Springer Proceedings in Materials

G. Kumaresan
N. Siva Shanmugam
V. Dhinakaran *Editors*

Advances in Materials Research

Select Proceedings of ICAMR 2019

Springer

Springer Proceedings in Materials

Volume 5

Springer Proceedings in Materials publishes the latest research in Materials Science and Engineering presented at high standard academic conferences and scientific meetings. It provides a platform for researchers, professionals and students to present their scientific findings and stay up-to-date with the development in Materials Science and Engineering. The scope is multidisciplinary and ranges from fundamental to applied research, including, but not limited to:

- Structural Materials
- Metallic Materials
- Magnetic, Optical and Electronic Materials
- Ceramics, Glass, Composites, Natural Materials
- Biomaterials
- Nanotechnology
- Characterization and Evaluation of Materials
- Energy Materials
- Materials Processing

To submit a proposal or request further information, please contact one of our Springer Publishing Editors according to your affiliation:

European countries: **Mayra Castro** (mayra.castro@springer.com)
India, South Asia and Middle East: **Priya Vyas** (priya.vyas@springer.com)
South Korea: **Smith Chae** (smith.chae@springer.com)
Southeast Asia, Australia and New Zealand: **Ramesh Nath Premnat** (ramesh.premnath@springernature.com)
The Americas: **Michael Luby** (michael.luby@springer.com)
China and all the other countries or regions: **Mengchu Huang** (mengchu.huang@springer.com)

More information about this series at http://www.springer.com/series/16157

G. Kumaresan · N. Siva Shanmugam ·
V. Dhinakaran
Editors

Advances in Materials Research

Select Proceedings of ICAMR 2019

Springer

Editors
G. Kumaresan
Bannari Amman Institute of Technology
Erode, Tamil Nadu, India

V. Dhinakaran
Centre for Applied Research
Chennai Institute of Technology
Chennai, Tamil Nadu, India

N. Siva Shanmugam
Department of Mechanical Engineering
National Institute of Technology
Tiruchirappalli
Tiruchirappalli, Tamil Nadu, India

ISSN 2662-3161 ISSN 2662-317X (electronic)
Springer Proceedings in Materials
ISBN 978-981-15-8318-6 ISBN 978-981-15-8319-3 (eBook)
https://doi.org/10.1007/978-981-15-8319-3

This Springer imprint is published by the registered company Springer Nature Singapore Pte Ltd.
The registered company address is: 152 Beach Road, #21-01/04 Gateway East, Singapore 189721, Singapore

Preface

International Conference on Advances in Materials Research (ICAMR 2019) is organized by Bannari Amman Institute of Technology in association with Indian Society of Technical Education (ISTE). The advances in materials research report the latest researches performed in basic materials and their science in the fields of composites, metals and alloys, fracture of materials, biomaterials, energy materials, polymers, etc. The researches in material science relate the desired properties and their performance enhancement/deterioration with respect to the atomic structure of the materials. The atomic interactions resulting from the density change, and covalent and polar bonds are characterized using latest characterization technologies. The original research includes both experimental and theoretical analyses, and peer-reviewed papers are systematically reported in this proceedings.

ICAMR is one of the interdisciplinary forums for researchers working in the areas of basic and applied materials research. The main objective of ICAMR 2019 is to encourage the wide range of applications towards the development of human society with the invention of new materials in the trusted area like development of lightweight composite materials in energy applications, construction, instrumentation, environment, communications, safety and ecology and thus contribute to societal well-being and prosperity. It will create a competent prospect for discussion of major issues related to advanced research in materials for their economic exploitation, long-term conservation, new development and imaginative uses. It also envisages global networking to inspire innovative research to provide solutions and drive systemic change. Further, eminent scientists across the globe will share their research and future scope for betterment of mankind.

ICAMR 2019 brings leading researches from academia, R&D organization and industries from various regions of the world under one roof. This also helps to identify the current demand and emerging area of the basic and applied materials research. This two-day conference is organized in association with Indian Society of Technical Education (ISTE) which includes the peer-reviewed articles and invited talks of expert from India, South Korea and Malaysia.

The articles published in the proceedings are reviewed by the experts from prestigious Indian institutions like IIT, NIT, Anna University, VIT, etc. The plagiarism of all submitted articles is verified using "Turnitin" software, and a double-blind review system is followed before to the submission of chief editorial board.

Erode, India — Dr. G. Kumaresan
Tiruchirappalli, India — Dr. N. Siva Shanmugam
Chennai, India — Dr. V. Dhinakaran

Contents

Effect of Ultraviolet (UV) Radiation on Mechanical Behavior of Bi-directional Carbon Fabric Reinforced Epoxy Composites Impregnated with Fly Ash Cenosphere Particles 1
S. M. Vinu Kumar, K. L. Senthil kumar, and B. Suresha

Performance Analysis of CO_2 Heat Pump for Milk Pasteurization Application 11
C. Subramaniyan, M. Jegadeeshwari, A. M. Sridhar, and S. Suresh

Applications of Additive Manufacturing—A Review 21
S. Madheswaran, Karuppan Sivakumar, E. Prakash, S. Kalaivanan, N. Someswaran, and J. Vishnudeepan

Review on Recent Additive Manufacturing Technologies 29
E. Prakash, M. Subramaniyan, Anandha Moorthy Appusamy, P. Mathan Kumar, M. Dinesh, M. Naveen, and C. Santhosh

Studies on Electric Discharge Machining of AA6063 Alloy Using Taguchi Approach 35
C. Boopathi, C. Veera Ajay, S. Manoj Vignesh, and S. M. Saravanakumar

Design and Analysis of 2D Steady Flow Over an Underwater Vehicle with Different Cavitators 47
D. Rohini, S. Vignesh, D. Nivitha, P. Preetha, and K. P. Arulshri

Investigation of Drying Rate in Moringa Leaves Under Periodic and Continuous Airflow in Vacuum Condition 61
M. Ashok Kumar, G. Kumaresan, and S. Rajakarunakaran

Patient Medicine Reminder System 73
M. Neela Harish

Audio Signal Processing for Cochlear Implants 81
K. T. Maheswari, R. Baranikumar, D. Lavanya, A. Nandhakumar, and M. Srinivasan

Investigation of Hybrid Concrete Using Steel and Polypropylene Fibres 89
M. Ranjitham, S. K. Deepika Sree, and M. B. Danyaa

Experimental Investigation on Geopolymer Bricks 97
M. Ranjitham, K. Vishvapriya, and L. U. Vishnu Pavya

Optimization of Mechanical Behaviors of Boiled Egg shell Particulate-banana fiber Reinforced Polyester Composites 107
K. Nijandhan, M. Raghunath, B. Monish Kanna, P. Nithish, G. Vishnu Prakash, and E. Logesh

Particle Swarm Optimization Tuned Fuzzy Controller for Vibration Control of Active Suspension System 115
K. R. Bharath Kumar, P. Senthil Kumar, K. S. Dharaneeshwarakumar, and B. Deepak

Additive Manufacturing Parameter Optimization with Automated Post-printing Flaw Detection Using Convolutional Neural Networks 127
E. Prakash, M. Subramaniyan, Anna Kalyani Naveen Sankar, and Kumaraguru Chandra Kumar

Design and Fabrication of 3D-Printed Acrylonitrile Butadiene Styrene (ABS) Dam Automation Structure with Integrated Flood Monitoring System Using Data Analysis and Computation Techniques 137
R. Sivabalakrishnan, M. Dineshkumar, B. P. Sharon, P. Naveenkumar, and S. Vignesh

Influence of Human Hair Fibre, Geogrid and PVC Grid on the Performance of CBR of Clayey Soil 147
V. Jayanthi, B. Soundara, S. Priyadharshini, J. Adhithya, M. Sharmaa Devi, and S. Amritha Shankar

Optimizing Performance Characteristics of Blower for Combustion Process Using Taguchi Based Grey Relational Analysis 155
K. B. Prakash, A. Amarkarthik, M. Ravikumar, P. Manoj Kumar, and S. Jegadheeswaran

Optimization of Process Parameters in Disc Plate Using Thermo-structural Analysis 165
N. Nandakumar, T. Allwin Raja, and P. Arunkumar

Implementing Biomimicric Owl Wing Pattern for Noise Reduction in Turbine Blade 175
B. Premkumar and N. Nandakumar

Modal Analysis of Profile Deck Sheets in Composite Structural System 183
V. Preetha, V. Senthilkumar, S. Govindhan, D. Vishnu, and K. RanjithSelvan

Experimental Investigation of Exhaust Emission Reduction in a CI Engine by Using Titanium Dioxide Nanoparticle-Blended Methyl-Esterified Neem Oil Biodiesel 193
G. Shaik Usmansha, K. Senthil Kumar, Praveen Maruthur, R. Rejumon, and S. Dhanesh

RFID-Based Real-Time Monitoring System for Drill Bit Manufacturing Process 201
N. Ikram, M. Pravin Savaridass, S. Amuthabharathi, and R. Karthickkumar

Efficient Data-Secured Cryptography Using FRQI Algorithm 209
A. Shyamalaprasanna, B. Ragavi, S. Saranya, L. Pavithra, and P. Santhya

Studies on Influence of Reinforcement Characteristics on Mechanical Properties of Banana Fiber Nonwoven Composite Structures 219
T. Murugan and B. Senthil Kumar

Effect of Lateral Load on Response of Pile Foundation 233
M. Mahalakshmi and M. Arulsurya

Investigation of Some Mechanical Properties of Cast Iron Coated with Chromium and Zirconia for Sliding Application 241
S. Pranesh, T. Nithish Raj, S. Sudhakar, D. Deepan Kumar, and K. Suwinraj

Performance Study of Low-Pressure Vertical Feedwater Heater with SS304 as the Tube Material 247
S. Jeeva, A. Abubakkar, S. Dinesh Kumar, and M. R. Ahamed Buhari

Behaviour of Concrete Structure Subjected to Open Fire—State of Art 255
C. Aravindhan and S. Nayannathara

Risk Assessment of Machining and Assembly Line in Automotive Industry 263
T. Rajpradeesh, M. Saravanamani, R. Manikandan, and P. Venkumar

Machining of Metal Matrix Composite Using Abrasive Water Jet Machine 277
E. Soundrapandian, A. Tajdeen, K. Kamal Basha, and P. Vivekkumar

Design and Automation of Shell Facing Machine 291
A. Tajdeen, E. Soundrapandian, E. Sakthivelmurugan, S. Nachimuthu, P. Dinesh, and S. Praveenkumar

Experimental Study of Electrochemical Micromachining on Titanium (Ti–6Al–4V) Alloy 301
P. Vivekkumar, E. Soundrapandian, A. Tajdeen, and T. Prashanth

Simulation and Analysis with Material Optimization of Automobile Suspension Using Multi-body Dynamic 309
S. Deepankumar, B. Saravanan, D. Yuvaraj, T. Ramesh Kumar, M. Sureshkumar, and K. Vinoth Simmon

Mathematical Analysis of Rectangular Reinforced Concrete Beam Externally Laminated with GFRP Sheet 321
N. V. Manjunath, M. Ranjitham, V. Manickavasakam, and Sujith Selvaraj

Effects of Drilling Process Parameters Using ANOVA and Graphical Methods 331
S. P. Sundar Singh Sivam, Ganesh Babu Loganathan, K. Saravanan, S. Dinesh Guhan, and Aishik Banerjee

A Low-Cost Fabrication Approach of UV, VIS and NIR Dielectric Reflectors 355
Venkatesh Yepuri, R. S. Dubey, and Brijesh Kumar

Job Safety Analysis for Various Operations in Cement Industry Using Risk Assessment Matrix 363
R. Manikandan, G. Rampranav, T. Rajpradesh, and S. Rajesh

To Reduce the Setting Piece Rejection Rate in Gear Hobbing Process by Advanced Product Quality Planning 375
R. Sivakumar, A. Boobal, M. Gowtham, and P. Senevasa Perumal

Development of Linear Automation in Butt Joint Fixture to Enhance Welding Characteristics 385
R. Sivakumar, S. Bhoopathi, R. Muralirajan, and E. Chinnayan

Corrosion Behavior of Brass in Methanol-Gasoline Fuel Blends 393
H. N. Meenakshi and Shraddha Dilip More

Quantitative Risk Analysis Using HIRA in an Automotive Manufacturing Sector 403
RajPradeesh Thangaraj, A. Rama Pandian, Venkumar Ponnusamy, and Manikandan Rajenderan

Thermal Analysis and Characterization of Catalytically Cracked Jatropha Bio-Oil 417
L. S. Gokul, S. Jegadheeswaran, and C. Sasikumar

Dynamic Risk Assessment of an Ammonia Storage Tank Based on Bow-Tie and Bayesian Approaches 427
T. Jishin Jayan, K. Muthukumar, and R. Rajiev

Risk Assessment Using Bow-Tie Tool in Cement Industry 437
R. Manikandan, P. Pradeep Kannan, T. Rajpradeesh, and S. Rajesh

A Novel Technique and Analysis for Efficient Opportunistic Routing in Mobile Ad Hoc Networks 447
K. P. Sampoornam, S. Hemavikasini, V. Vakula, and S. Vidhya

Harvesting of Electricity from Handloom Weaving Machine Coupled with Dynamo 459
N. Bhuvanesh, G. Kumaresan, C. Subramaniyan, C. Sasikumar, and R. Mukeshu

Removal of Rain Particles from the Single Captured Image 467
K. P. Sampoornam, S. Saranya, S. Vigneshwaran, J. Roshini Roy, and P. Santhya

Effects of Chemical Curing on the Mechanical Properties of Mineral Admixtures Blended Concrete 477
V. Kannan and N. Karthiga Shenbagam

Emulator for Efficiency Enhancement of Heave Type Wave Energy Converter 485
Nagulan Santhosh, M. Srinivasan, Ragupathy Karu, and Eswaramoorthy Santhosh Kumar

Characterization and Fabrication of ABS and PLA-Based Polymer Matrix Composites Using 3D Printing 499
Anandha Moorthy Appusamy, E. Prakash, S. Madheswaran, Arunkumar Rajamanickam, Vinoth Kumar Selvakumar, and P. Chandrasekar

An Investigation on Wear Process Parameter of Metal Matrix Composite Using Optimization Technique 511
S. Vignesh Kumar and N. V. Dhandapani

Experimental Investigation on Tribological Behaviour of Alumina Nano Particles Reinforced with Aluminium Alloy Composite Material 521
K. Ramachandra Raju, G. Senthilkumar, Y. Arivu, D. Sathya, A. Sathya, and S. Sandeep

Comprehensive Study of Hydrogenated Diamond-Like Carbon Coated AISI 5140 Alloy Steel 531
R. Sivakumar, P. Senthilkumar, M. Sreenivasan, and Ram Krishna

Review on Thermal Energy Storage with Phase Change Materials and Its Applications 543
Athimoolam Sundaramahalingam, S. Jegadheeswaran, Muthusamy Ponmurugan, and C. Sasikumar

A Review on Passive Cooling Methods for Green Energy Buildings 555
Muthusamy Ponmurugan, M. Ravikumar, and Athimoolam Sundaramahalingam

Enhancement of Soil Using Pyrolyzed *Cocus nucifera* Midrib Carbon 565
M. Angelina Thanga Ajisha, Jaslin J. Christopher, A. S. Jebamalar, and I. Regina Mary

Experimental Studies on Milling Parameters for Al6061 Hybrid Metal Matrix Composite 575
K. Ramachandra Raju, G. Senthilkumar, Y. Arivu, M. Vignesh, D. Thangeswaran, and G. Vivek

Experimental Studies on Mechanical Behaviour of Polylactide (PLA) Matrix—Aluminium Oxide (Al_2O_3) Particles Reinforced Composites 589
R. Girimurugan, M. Vairavel, A. Anandha Moorthy, E. Prakash, and S. Madheswaran

The Effect of Mg and Mn Addition on Hardness, Tensile and Wear Properties of LM6 Aluminum Alloy 599
S. Manojkumar, M. Kumar, M. Ananth, G. Mageshwaran, and P. Hariprakash

Investigation of Geopolymer Concrete with Ceramic Waste as a Partial Replacement of Coarse Aggregate 607
V. Vignesh Prabu, S. Velmurugan, and O. P. Deepak

Numerical Investigation on Cold-Formed Steel Web Stiffened Lipped Channel Columns Subjected to Local-Distortional Interaction Mode Buckling 615
O. P. Deepak and P. Aravinth

Experimental Investigations on Mechanical Properties and Morphological Analysis of Carbon Steel Grade III Leaf Spring Steel 629
A. Anandha Moorthy, E. Prakash, S. Madheswaran, C. Sasikumar, M. Vairavel, and R. Girimurugan

Degassing of Aluminum Metals and Its Alloys in Non-ferrous Foundry 637
Bhaskar M. Reddy and Tamilselvam Nallusamy

Design and Fabrication of Hybrid Mobility Scooter 645
N. Ramachandran, R. Sivasubramanian, R. Palanivel, P. Nishanth Kalathil, and B. Nirmal

Optimization of Process Parameters to Reduce the Green Sand Casting Defects 655
M. Nandagopal, K. Sivakumar, M. Sengottuvelan, and S. Velmurugan

Optimization of Welding Parameters in CMT Welding of Al 5083 . . . 663
S. Suryaprakash, S. Vishal, M. Sethu Raman, S. Rajendra Kumar, M. Umar, and T. Deepan Bharathi Kannan

Effect of Cyclic Annealing on the Grain Size of Low-Carbon Steel: An Image-Processing Approach 673
K. Gajalakshmi and S. Saravanan

Assessment of Start-Up Agility Using Multi-grade Fuzzy and Importance Performance Analysis 685
Edrion Chacko and M. Suresh

Design and Analysis of Pre-engineered Buildings Using Staad Pro . . . 695
C. Kavitha, S. Suryaprakash, N. Lavanya, and S. Durgadevi

Effect of Compression Ratio on the Performance, Emission, and Combustion Characteristics of C.I. Engine Using Waste Cooking Oil and Its Emulsion as Fuel 701
Selvakumar Raja, Jaikumar Mayakrishnan, Sasikumar Nandagopal, and Sangeethkumar Elumalai

Agile Practices in Human Resource Management 713
R. Kavitha and M. Suresh

Assessment of Organizational Agility Using Multi-grade Fuzzy: A Case of Adhesives Manufacturing Organization 723
Aravind Hariharan and M. Suresh

Advertising Media Selection Framework Using Fuzzy VIKOR Approach: A Case of New Insurance Product 733
M. Suresh and Deepak Joshy

Modelling the Factors of Store Environment on Impulse Buying Behavior Using TISM 741
M. Suresh and R. Dev Abhishek

Modelling the Factors of Environmental Sustainability in Healthcare Dispensaries 753
M. Suresh and S. V. Krishnan

Manufacturing Flexibility Assessment Using Multi-Grade Fuzzy: A Case of Garment Industry 763
R. Sowmiyaa Sri and M. Suresh

Leanness Assessment Using Multi-grade Fuzzy: A Case of Textile Manufacturing Company 773
S. Sreedharshini and M. Suresh

Pairwise Nonparametric Model Analyzed Advanced ICT Skills and Adaption of E-Health Solution in India 783
K. Ravichandran

Modelling of Surface Roughness in Wire-EDM Using Response Surface Methodology Technique 791
P. Mathan Kumar, D. Dinesh, G. Sundarraju, S. Madheswaran, and K. Perumal

Experimental Investigation on Mechanical Properties of TIG Welded Dissimilar AISI 304L and AISI 316L Stainless Steel 801
A. Ramakrishnan, T. Ramesh Kumar, G. Rajamurugan, V. D. Tamilarasan, and M. Vijayakumar

Modelling of Factors Influencing Saving Behaviour of Women in India: An Interpretive Structural Modelling 809
M. Suresh, D. Sangeetha, and Sumathi Kumaraswamy

Modelling the Factors of Job Stress in Audit Firms: A TISM Approach 819
M. Suresh, R. Srividya, and Sumathi Kumaraswamy

Performance Analysis of Flat-Plate Solar Collector Using Tungsten Trioxide Nanofluid 831
J. Vinoth Kumar, A. Amarkarthik, R. Harish, S. Mugundan, and R. R. Suriyaa

Investigation on Characteristics of Stir-Casted Aluminum Matrix Composites—A Review 841
P. Raghuvaran, M. Suresh, J. Baskaran, S. Arun Prasadh, M. K. Charan, and T. Dhananjayan

Mechanical Behavior Investigation of Copper-Added A356 Alloy 853
J. Baskaran, M. Suresh, P. Raghuvaran, V. K. Dharsan, A. Afesul Gayoom, and S. Dharaneetharan

Review on Manufacturing and Development of Ni-Ti Shape Memory Alloys 859
M. Sureshkumar and S. Madan Mohan

Kinematic and Dynamic Modelling and PID Control of Three Degree-of-Freedom Robotic Arm 867
K. Renuka, N. Bhuvanesh, and J. Reena Catherine

Investigation on Normal Hard Turning of AISI 4340 Steel 883
N. Jayakumar, G. Senthilkumar, M. Vignesh, and V. Gokul

Estimation of Thermo Oxidation on Chromel–Alumel Thermocouple 897
P. Narendra Ilaya Pallavan, S. Srinivasan, and V. Arumugam

Experimental Investigation of Solar-Based Air Heater Rectangular Duct Having Uniform Spaced Dimple Shaped as Roughness Element on the Absorber Plate 903
P. Rajesh Kanna, M. Chandrasekaran, and M. Ravikumar

Investigation and Experimental Study on Microstructure and Characterization of Silicon Carbide Synthesized by High Energy Ball Milling 913
M. Kalil Rahiman, S. Santhoshkumar, and P. Mathan Kumar

Advanced Bidirectional Switches-Based Three-Phase to N-Phase High-Power Impedance Source Matrix Converter 923
S. Manivannan, N. Shankar, A. Santhoshkumar, P. Selvabharathi, and N. Saravanakumar

Design Implementation and Evaluation of Password Protected Circuit Breaker for Reliable Power System Protection and Maintenance 933
S. Manivannan, S. Sudhahar, G. M. Oorappan, K. Rajalashmi, and N. Saravanakumar

Surface Texturing in Piston Ring Cylinder Liner Pair for Friction Reduction: A Review 943
S. Prakash, C. Sasikumar, S. Aravind, V. Mohan Prasath, and C. Udhayakumar

Mitigation of Frequency Variation Through Voltage Control in Islanded Microgrid 953
C. Kokila Vani, E. Sarangapani, and R. Kumaresan

Analyzing the Performance of CO_2 Heat Pump for Mushroom Drying Application 963
C. Subramaniyan, R. Naveen Kumar, S. Siva Ranjith, and S. Thiyagu

System Identification Using Adaptive Algorithms 971
J. Reena Catherine, N. Bhuvanesh, M. Prasanna, and S. Manojj

Design of Compact Paper Counting Machine 987
C. Sathishkumar, J. Selvakumar, S. R. Venkatesh, and M. Thoufeekahamed

Sports Prediction Based on Random Forest Algorithm 993
G. Shobana and M. Suguna

Experimental Study on Machinability of Metal Matrix Composite by Abrasive Water Jets 1001
B. Siddharthan and A. Kumaravel

Study on Effect of Deposition Thickness on Temperature Distribution of Various Shaped 3D Printed Components 1015
Arundeep Murugan, Mulatu Mengistayehu, N. Ummal Salmaan, and C. Sasikumar

Computer-Aided Thermal Control System of 3L-ANPCI Using LabVIEW 1025
E. Sarangapani, N. Narmadhai, and C. Kokila Vani

Experimental Investigation and Optimization of Machining Parameters of Aluminum Composite Material 1035
K. Ramachandra Raju, G. Senthilkumar, D. Deepakraja, M. Vignesh, S. K. Surya, and G. Vivek

FEM and Execution Analysis of Hardfaced Aluminium Alloy Impeller 1047
C. Ramesh, P. Prakash, P. Sankar, and R. Prakash

Sensor-Based Gamified Rehabilitation Therapy to Enhance and Manage Human Physical Kinematics 1059
S. J. Syed Ali Fathima, S. Amritha Shankar, and A. Ahamed Thajudeen

A Review on Analysis of Performance Parameters in Low Voltage Current Mirror Circuits 1069
S. Saranya, R. Saravana Kumar, S. Praveen Kumar, S. Dharani, and P. M. Rubesh Anand

Experimental Investigation on Mechanical Properties of Banana Fiber Reinforced Vinyl Ester Resin Composites 1079
J. Harish Kumar, S. Prabhakaran, K. Alagar Pandi, and K. N. Karthick

Wear Characterization of AlTiCrN and TiCN Coatings on SG Cast Iron 1095
P. Sivasankar, S. K. Rajesh Kanna, N. Lingaraj, and P. Chandrasekar

Optimization of Process Parameters on the Electrical Discharge Machining of Al6061-SiC MMC Through Evolutionary Approach 1103
S. K. Rajesh Kanna, N. Lingaraj, P. Sivasankar, and P. Chandrasekar

Numerical Investigation on Aluminum Alloys Under Medium Velocity Impact of Projectiles 1113
N. Nandhini, M. Vijayan, and M. A. Rajesh Kumar

Priority-Based Task Allocation and Scheduling in WSN Using DMPS 1123
M. Suguna, D. Prakash, G. Shobana, and J. Cynthia

Characterization of Conformal Antenna for 5G-Enabled Industrial Robots 1133
P. Hamsagayathri, P. Ramya, T. Perarasi, and R.Gayathri

Performance Analysis of Booth Multiplier-Based FIR in DWT Image Processing Applications 1143
S. Tamilselvan, R. Ramesh, K. Hema Priya, and B. Nithya

Structural and Optical Studies on Radio Frequency (Rf) Magnetron Sputter Deposited Nickel Oxide Thin Films 1151
K. S. Usha, R. Sivakumar, and C. Sanjeeviraja

Classification and Detection Techniques of Fault in Solar PV System: A Review 1155
V. Mohanapriya, B. Sharmila, and V. Manimegalai

Power Generation Enhancement Using Hybrid Thermoelectric Generator with Synthetic Oil-Based Nanofluids 1165
V. George Samuel Raj, Godson Asirvatham Lazarus, Elangovan Daniel, Anitha Angeline Appadurai, and Stephen Manova

Performance Analysis of Automobile Radiator Using Tungsten Trioxide Nano-Fluid 1175
J. Vinoth Kumar, A. Amarkarthik, T. Santhosh, R. Solomon Allenjudah, and U. Sundreswaran

Experimental Investigation on Corrosion Behaviour of Aluminium Alloy Nanoparticles Composite Material 1183
K. Ramachandra Raju, G. Senthilkumar, Y. Arivu, T. Santhosh, T. Prasanth, and R. Pradeep

Applications of Fuzzy Logic Approach for Assessment 1191
V. Vaishnavi and M. Suresh

Study and Testing of Pneumatic Control of Ball Valve Using Actuator 1199
G. Dinesh Kumar, K. S. Karthikeyan, and C. Sathishkumar

Analysis of Six Sigma—Implementation of DIMAC Methodology in Foundry Industry 1213
P. Nethaji, P. Kaliyappan, R. Sathya, S. R. Hariprakash, and K. Prakash

Novel Metal-Organic Polymer [Ruthenium Bis(II) (2,2′–Bipyridyl 4,4′–Dicarboxylic Acid) (N-Methyl morpholine)]$_n$ (BF_4)$_{2n}$ for Dye-Sensitized Solar Cell Application 1223
Sathishkumar Chinnasamy, Mohanraj Shanmugam, and Sivasubramanian Ramanathan

Effect of Different SiCp Particle Sizes on the Behavior of AA 7075 Hot Deformation Composites Using Processing Maps 1233
M. Rajamuthamilselvan, S. Rajakumar, and S. Kavitha

Experimental Analysis of Forced Turbulent Convective Heat Transfer in a Circular Cross-Sectional Tube With Al_2O_3-Water Nanofluid 1245
V. D. Tamilarasan, T. Rameshkumar, S. Saravanan, and A. Ramakrishnan

Modelling the Factors of Buying Behaviour of Paint Products 1259
M. Suresh and S. Bala Yogesh

About the Editors

Dr. G. Kumaresan is presently an Associate Professor in the Department of Mechanical Engineering, Bannari Amman Institute of Technology, Tamil Nadu, India. He received his Doctoral degree in 2015 from National Institute of Technology, Tiruchirappalli. He has published 22 original research articles in highly reputed national and international peer-reviewed journals and also filed two patents. He completed his Master's Degree from Government College of Technology, Coimbatore, and Bachelor's Degree from Anna University, Chennai. He is an active review member of more than 12 international journals and served as a guest editor of Elsevier – Materials Today Proceedings. He has delivered several invited talks at various engineering institutions and industries. He is handling two research projects funded by TEQIP and DST. His research interests include phase change heat transfer, heat pipes nanofluids and computational fluid dynamics.

Dr. N. Siva Shanmugam is an Associate Professor in the Department of Mechanical Engineering, National Institute of Technology, Tiruchirappalli, India. He received his Doctoral degree in 2012 from National Institute of Technology, Tiruchirappalli. He has published numerous papers in reputed national and international peer-reviewed journals. He is actively associated with different national and international societies and academies. He has delivered several invited talks at various engineering institutions and industries situated in different parts of India such as Tamil Nadu, Kerala and Andhra Pradesh. He has completed several research & consultancy projects, further, he is handling multiple consultancy and sponsored projects for Bharat Heavy Electrical Limited (BHEL) and ISRO, Government of India. His research targets FE simulation of welding processes, ergonomics study, and biomechanics.

Dr. V. Dhinakaran is an Associate Professor at Chennai Institute of Technology, Chennai, India. He received his B.E in Mechanical Engineering from Arulmigu Kalasalingam College of Engineering in 2002; M.E from the Department of Aeronautical Engineering, Sathyabama University in 2012; and Doctoral degree in 2017 from National Institute of Technology, Tiruchirappalli. He is heading the

Centre for Applied Research in Chennai Institute of Technology. He is an active participant in academic and industrial research. He has published 17 articles in reputed national and international peer-reviewed journals. He is a life member of Indian Society for Technical Education (ISTE), Indian Cryogenic Council (ICC) and the International Association of Engineers (IAENG). His areas of research include welding, additive manufacturing, finite element method and computational fluid dynamics.

Effect of Ultraviolet (UV) Radiation on Mechanical Behavior of Bi-directional Carbon Fabric Reinforced Epoxy Composites Impregnated with Fly Ash Cenosphere Particles

S. M. Vinu Kumar, K. L. Senthil kumar, and B. Suresha

Abstract The present paper discusses about the effect of ultraviolet (UV) radiation on the mechanical properties of unfilled and fly ash cenosphere (CSP) filled carbon-epoxy (C-E) composites. The laminates of composites were fabricated using hand layup process and followed by autoclave curing technique. Fabricated composites were exposed UV radiation (320 nm of wave length) for 336 hours under the constant temperature of 50 degree celcius. Results showed that as weight gain (%) for the flexural sample decreases as the period of UV exposurer increases. However, impact samples showed synergetic behavior in weight gain (%). Flexural strength and flexural modulus were found to be high for UV exposed sample compared to unexposed one. In overall, unconditioned sample exhibited higher impact strength compared to UV exposed samples.

Keywords Carbon-epoxy composites · UV radiation · CSP filler · Flexural strength

1 Introduction

In today's era of material science, composites are highly preferred over the conventional metals/alloys due to their exceptional properties like high strength to weight ratio, corrosion resistance, and superior fatigue performance which can be tailored based on the requirements, and thus, it has become ideal choice in many of the applications. Amongst the composites materials, polymer-based (reinforced) are used in diverse and reaching all the industrial sectors covering the range from commercial aircrafts to bathtub because of non-difficulties in processing and cost of production

S. M. Vinu Kumar (✉) · K. L. Senthil kumar
Department of Mechanical Engineering, Bannari Amman Institute of Technology, Sathyamangalam, Erode 638401, Tamil Nadu, India
e-mail: vinukmr1988@gmail.com

B. Suresha
Department of Mechanical Engineering, The National Institute of Engineering, Mysore, Karnataka 570008, India

G. Kumaresan et al. (eds.), *Advances in Materials Research*, Springer Proceedings in Materials 5, https://doi.org/10.1007/978-981-15-8319-3_1

is quite low. Aerospace and marine parts made from the carbon reinforced epoxy composites are often exposed to extreme natural atmosphere (weathering) like heat, rain, sunshine, humidity, and also sometimes it will be prone to atmosphere pollutants like sand dust, hydrocarbons, all of these weathering factors tends to cause severe damages to the Parts (made of polymer composites).

Polymer reinforced composites once they exposed to UV radiation, then it absorbs UV rays which in turn initiate photo oxidation reaction, which include oxidation, chain scission, and cross linking subsequently weight loss result of which reduces the viability of material usage in structural application. Prolonged exposure during the service to UV rays would adversely affect the viscoelastic properties in the form of raising temperature, lowering the storage modulus, and glass transition temperature. Also, Aerospace and marine partspolymer composite becomes susceptible to impact damages due to relative brittleness [1–3]. Only few studies have reported the environmental effect on mechancial properties of polymer reinforced composites.

Kumar et al. [1] studied the degradation effect on carbon-epoxy composites by subjecting them to ultraviolet radiations and condensation. They reported that there were no appreciable changes in longitudinal elastic modulus and longitudinal tensile strength in any of the exposure condition due to fiber dominated properties. Also, they indicated that there was 4.2 and 2.8% decreases in transverse modulus which are resulted from exposure to only UV and only condensation at 500 h, respectively. Further result showed that there was 9 and 20% decreases in tensile strength which are resulted from exposure to only UV and only condensation at 500 h, respectively. But at sequential exposure to UV and condensation at 1000 h, tensile strength was found to be decreased by 21% compared to unconditioned samples. Tcherbi-Nartech et al. [2] reported on synergetic effect of UV radiation and condensation on mechanical and thermal properties of carbon-epoxy composites impregnated with nanoclay. They reported that modulus of all samples increases while strength decreases when compared to unconditioned samples at room temperature; they also concluded that as exposure time increases compression strength decreases for neat system. But compression strength increases for 1 and 2 wt% (MMT) samples after 10 days of conditioning. The addition of nanoclay enhanced the glass transition temperature of the unconditioned samples at room temperature; however, glass transition temperature decreases after conditioning. According to Zainuddin et al. [3], nanoclay addition improved the strength and modulus of the composites by 19 and 13%, respectively, at room temperature. Further, when the samples exposed to synergetic condition, again nanoclay reinforced composites showed improvement in mechanical properties over neat samples.

From the literature survey, it is understood that, less attention has been given to study about the effect of weathering condition on the mechanical performance of polymer reinforced composites. Therefore, present work pertains to study the influence of cenosphere particle on mechanical properties of composites when they are exposed to UV radiation.

Table 1 Composition of unfilled and CSP filled C-E composites

Sl. No.	Composite designation	Quantity of constituents (wt%)		
		Bi-directional carbon fabric	Epoxy matrix	Cenosphere particle
1	C-E	60	40	–
2	4 CSP	60	36	4
3	6 CSP	60	34	6

2 Materials and Methods

2.1 Fabrication

In the present investigation bi-directional carbon fabric, aerial density of 206 g/m^2 used as main reinforcement system. Epoxy resin LY-556 and its hardener araldite HY-95 have been selected as polymer matrix material. Cenosphere microparticles in the range of 20–22 microns are used as filler materials. The complete fabrication of the composites slab has been explained in our previous study [4]. The composition and quantity of resin and reinforcement in weight fraction are detailed in Table 1.

2.2 Weathering Test: UV Radiation Exposure Studies

In order to study the degradation effect of UV radiation, the fabricated samples were kept in the environmental chamber according to ASTM-G 53-96. The samples were continuously exposed to UV radiation for a period of 336 h at 320 nm wave length under maintained temperature of 50 °C. The samples were taken out periodically and weighed immediately using high precision weighing digital balance of 0.1 mg accuracy to find out any changes in the weight of samples. The percentage in weight loss or gain was calculated by Eq. (1)

$$\text{Weight loss/gain}(\%) = \frac{W_x - W_i}{W_x} \times 100 \tag{1}$$

where W_x is the final weight of the sample measured at every 24 h. W_i is the initial weight of the sample.

2.3 Flexural Behavior

Bending tests were performed on the composite samples at room temperature to evaluate its flexural strength. Three point bending test was conducted as per ASTM-D790 using universal testing machine. Comparison of specimen before and after flexural test for various compositions of C-E composites is shown in Fig. 1.

2.4 Impact Strength

Izod test was performed according to ASTM G256—7J to study the toughness of the composites, and it is determined using a CEAST pendulum testing machine. Impact energy used for fracturing the specimen is 7 J with impact speed of 3.7 m/s at hammer angle 149.75°. Impact test specimen before and after test is shown in Fig. 2.

Fig. 1 Shows comparison of flexural test specimen before and after test

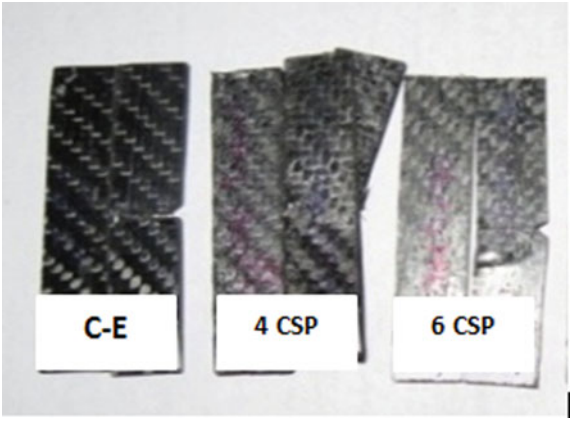

Fig. 2 Shows comparison of impact test specimen before and after test

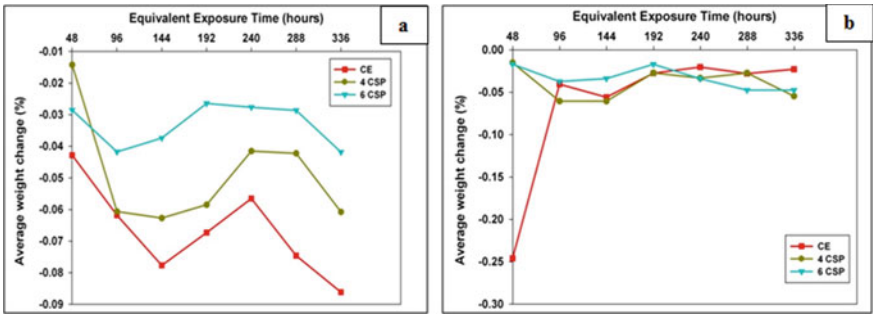

Fig. 3 Shows change in specimen weight of unfilled and CSP filled C-E composite test specimens as a function of time for exposure to only UV radiation for 336 h. **a** Flexural test specimen, **b** impact test specimen

3 Result and Discussion

3.1 UV Radiation Absorption

Figure 3 illustrates the weight changes (in percentage) as a function of UV radiation absorption in flexural and impact specimens. It is clear that higher filler loading showed minimum changes in weight gain compared to unfilled C-E. Further, it is evident that, bending test and impact test specimen of unfilled C-E exhibited maximum decrease in weight loss at 336 hour and 48 hours respectively, as shown in Fig. 3. The cause for the weight decrease in the specimen is due to the process of chain scission when polymer exposed to UV radiation [5]. Also, polymer chain tends to produce molecules, and these molecules vulnerable for atmospheric air which tries to migrate out of specimen. Moreover, epoxy resin itself less resistance to UV radiation [6]. Thus, diffused oxygen inside the polymer may cause its degradation.

3.2 Density

A test result of the various composites for different weathering condition is shown in Tables 2 and 3. Density of the composites is an essential part of the characterization. From Fig. 4, it is observed that as the addition of fly ash cenosphere increases, density decreases. Lowest density is found for 6 CSP filled C-E composites. Density decreases due to the filler property since filler is low dense and hollow sphere [4]. Therefore, CSP filler can be recommended for fabricating lightweight composites.

Table 2 Physico-mechanical properties of unexposed composites

Sample codes	Density (g/cc)	Flexural strength (MPa)	Flexural modulus (GPa)	Impact strength (J/m)	Barcol hardness
C-E	1.41	751	39.59	1076.67	72.4
4 CSP	1.12	654	32.64	1126.12	73
6 CSP	1.03	683	48.90	1842.7	73.5

Table 3 Physico-mechanical properties of UV exposed composites

Sample codes	Flexural strength (MPa)	Flexural modulus (GPa)	Impact strength (J/m)
C-E	822.18	46.11	843
4 CSP	899.25	63.34	820
6 CSP	900.85	74.03	965

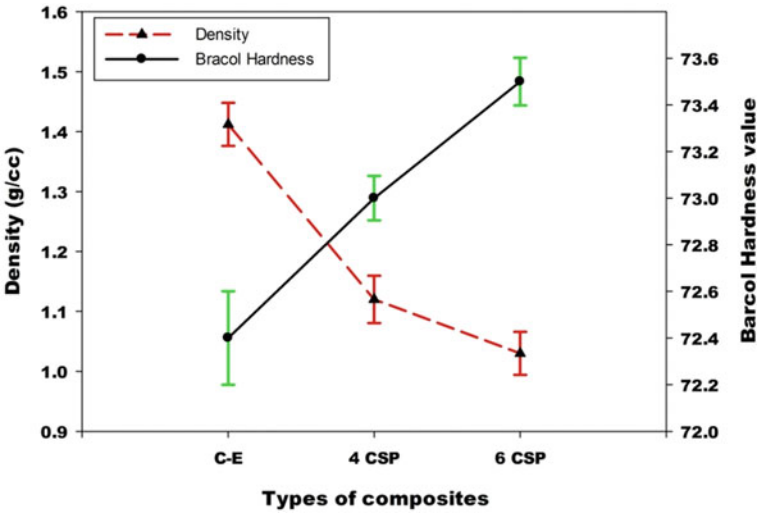

Fig. 4 Density and barcol hardness number of fabricated composites

3.3 Hardness

The improvement in the hardness of the composites has been observed when the CSP filler is added to neat C-E composites. Figure 4 clearly tells that hardness is increased may be due to composition of the filler. SiC content in the CSP filler induces hardness on the hybrid composites [4]. Also, it can be said that, as the addition of filler increases, distance between particles is reduced which in turn increases the hardness of the composites.

3.4 Flexural Behavior

The flexural strength and modulus of unfilled and CSP filled C-E composite during unexposed and UV exposed condition are shown in Fig. 5. It can be seen that flexural strength and modulus increases with the addition of cenosphere particles. This trend is observed in both the testing conditions. From the plot, it is noted that, UV exposed composites showed improvement in flexural strength compared to unexposed samples. Unfilled composites showed 9.4% improvement in bending strength, whereas 4 CSP and 6CSP filled C-E composites showed 37.46 and 31.7% increases in flexural strength, respectively. This may be due to the consequences of UV radiation. During absorption of UV radiation, chain scission and chain linking are competing each other on polymer chains. Chain scissions lower the weight of composites, and chain cross link increases strength [1, 7].

Flexural modulus behavior with respect to UV exposure for different weight percentage of C-E composites is shown in Fig. 6, and it can be seen that flexural modulus increases with increase in the CSP filler content. In case of unexposed condition, amongst the filled composites, 6 CSP filled C-E showed 23.39% increase in flexural modulus compared to neat carbon-epoxy composites. After subjecting the samples for 336 hrs continuously for UV exposure, the UV exposed specimen showed increase in flexural modulus compared to unexposed. However, 2 CSP filled C-E composites showed unchanged in flexural modulus.

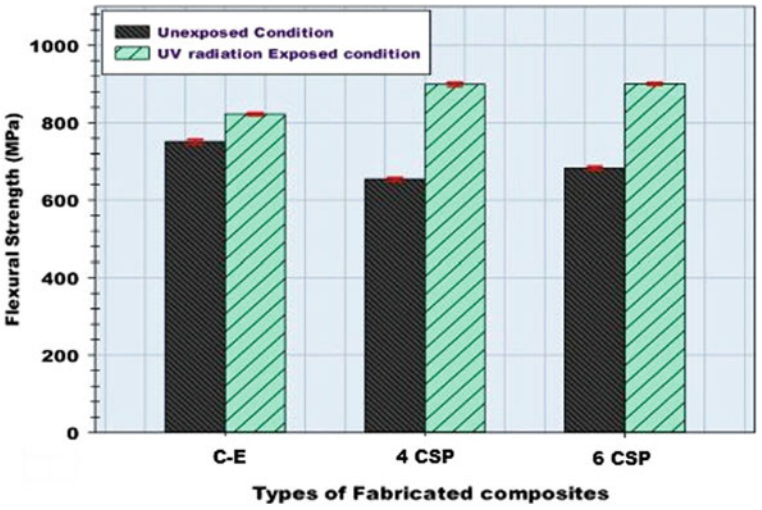

Fig. 5 Flexural strength of the unfilled and CSP filled C-E composites at unexposed and UV exposed condition

Fig. 6 Flexural modulus of the unfilled and CSP filled C-E composites at unexposed and UV exposed condition

3.5 Impact Strength

Figure 7 shows the trend in the impact strength of C-E composites with and without CSP fillers at different weathering conditions. It can be seen from the plot that degradation of the epoxy matrix leads to significant deterioration of the impact strength of

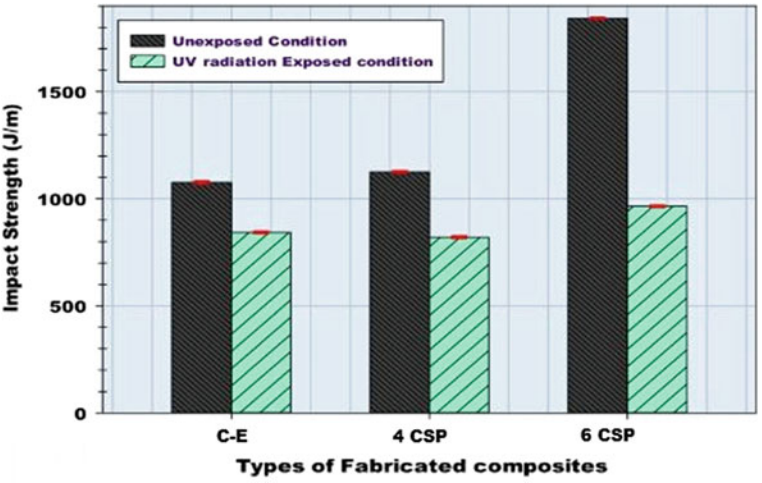

Fig. 7 Impact strength of the unfilled and CSP filled C-E composites at unexposed and UV exposed condition

the composites. Further, composites which are exposed 336 h continuously for UV radiation exhibited lower strength compared to unexposed one. Amongst the fabricated laminates, 6 CSP filled C-E composites showed remarkable changes in strength when exposed to UV weathering condition, i.e., 47% decreases in impact toughness, and this may be attributed to chain scission of polymer chain which reduces the overall property of the composites [1, 7].

4 Conclusions

In this paper, effect of UV radiation on fabricated C-E hybrid composites has been experimentally studied. From this study, the following inferences are drawn:

- Density and hardness of the C-E hybrid composites decrease and increase, respectively, as the cenosphere particles loading increases.
- During the UV exposure for 360 h, flexural sample reduced their weight compared to unexposed sample. But impact test samples showed synergetic behavior under the same weathering condition.
- UV exposed 4 CSP composites showed 37.1% improvement in the flexural strength when compared with unexposed composites. However, impact property has been found to be superior for unconditioned samples.

References

1. Kumar BG, Singh RP, Nakamura T (2002) Degradation of carbon fiber-reinforced epoxy composites by ultraviolet radiation and condensation. J Compos Mater 36(24):2713–2733
2. A. Tcherbi-Narteh, M. Hosur, S. Jeelani (2011) Mechanical and thermal properties of carbon/epoxy nanoclay composites exposed to synergistic effect of UV radiation and condensation. In: Proceedings of the 18th international conference on composite materials
3. Zainuddina S, Hosura M, Ashok Kumar JS (2010) Durability studies of nanophased FRP composites under synergistic exposure conditions. Mater Sci Eng A 527:3091
4. Kumar SMV, Suresha B, Rajamurugan G, Megalingam A (2018) Mechanical and abrasive wear behavior of cenosphere filled carbon reinforced epoxy composites using Taguchi-Grey relational analysis. Mater Res Exp 6(1):015307
5. Zainuddin S, Hosur M, Barua R, Kumar A, Jeelani S (2011) Effects of ultraviolet radiation and condensation on static and dynamic compression behavior of neat and nanoclay infused epoxy/glass composites. J Compos Mater 45(18):1901–1918
6. Liau W, Tseng F (1998) The effect of long-term ultraviolet light irradiation on polymer matrix composites. Polym Compos 19(4):440–445
7. Woo RS, Chen Y, Zhu H, Li J, Kim J-K, Leung CK (2007) Environmental degradation of epoxy–organoclay nanocomposites due to UV exposure. Part I: Photo-Degradation. Compos Sci Technol 67(15–16):3448–3456

Performance Analysis of CO_2 Heat Pump for Milk Pasteurization Application

C. Subramaniyan, M. Jegadeeshwari, A. M. Sridhar, and S. Suresh

Abstract This paper presents performance studies on the transcritical CO_2 heat pumps for heating of milk in pasteurization process. As CFCs and HCFCs were deemed unfit as working fluids in refrigeration, air conditioning, and heat pump applications, there has been an increase in research on carbon dioxide technology. Heat pump is one such application where theoretical and experimental investigations are performed by varying input parameters. Milk is treated in milk processing industry for purification and sterilization so as to increase its shelf life. Pasteurization (heat treatment) is the process done in milk by which the microbial activity is completely eradicated. In the heat treatment process, milk is subjected to high temperature for a period of time to sterilize it and increase the quality of milk. Heat treatment is done in vapour compression heat pump system. The refrigeration fluid used is CO_2 instead of other chemical refrigerants. The efficiency of pasteurization process is analyzed by the performance of heat pump. By varying the mass flow rates of milk in the condenser, the COP of the system and final temperature of milk are investigated. The study shows that both the milk mass flow rate and inlet temperature have a significant effect on system performances.

Keywords Energy · Heat pump · CO_2 refrigerant · HTST pasteurization

1 Introduction

Due to increase in global warming and environmental pollution, it is necessary to use natural and non-polluting substances in industrial sectors. Regarding this, CFC and HFC used as refrigerant are banned in many sectors due to its harmful effects on environment. Further, new innovative technologies and less polluting refrigerants are discovered by scientists. One such refrigerant is CO_2 which can be used in vapour compression systems for refrigeration, heating, and other applications. When heating

C. Subramaniyan (✉) · M. Jegadeeshwari · A. M. Sridhar · S. Suresh
Department of Mechanical Engineering, Bannari Amman Institute of Technology, Sathyamangalam 638401, India
e-mail: subra.csm@gmail.com

G. Kumaresan et al. (eds.), *Advances in Materials Research*, Springer Proceedings in Materials 5, https://doi.org/10.1007/978-981-15-8319-3_2

is considered, milk pasteurization is one of the major applications, which needs a non-polluting, non-toxic cooling fluid, where CO_2 is a perfectly suitable refrigerant. CO_2 is more efficient in cooling when compared with other refrigerants. It gives high-temperature change in condenser which is useful to transfer heat to other applications. CO_2 has low critical temperature of 31.1 °C which is a distinct remarkable property required for a refrigerant. Vapour compression systems with CO_2 as working fluid at normal refrigeration, heat pump and air-conditioning temperatures will work near or above the critical pressure of 7.38 MPa. Heat rejection will also take place at supercritical pressure, which leads to high-pressure level in the system, and the cycle is in 'transcritical' stage. Transcritical stage means the process with subcritical low-side pressure and supercritical high-side pressure (for a single-stage cycle). Hence to obtain optimum efficiency, the high-side pressure has to be controlled. The efficiency of a heat pump is defined as the ratio of the energy output (enthalpy difference at heat rejection) to the power input to the compressor (enthalpy difference during compression).

Maximum efficiency is obtained with low power consumption with high heat rejection [1]. In order to reduce the losses in expansion process with high-temperature change, the temperature of refrigerant at the exit of compressor can be reduced by multistage compression with intercooling [2]. To improve the working of vapour compression system, the thermodynamic cycle of refrigerant must be similar to Carnot ideal i.e., a rectangle on the T-S diagram. The irreversibility in the system with CO_2 as refrigerant is its high temperature of heat rejection and the losses in the expansion process. In order to reduce the loss, the refrigerant can be cooled [3]. Hall and Trogt mentioned that pasteurization is a time temperature-dependent process. The microbial reduction is achieved when milk is heat-treated at 72 °C for 15 s or 127 °C for 4 s [4]. The COP and heat transfer increases with increase in water mass flow rate. LMTD decreases with increase in mass flow rate and pressure decreases [5].

A theoretical study on CO_2 heat pumps for hydronic heating application are studied in which the desired temperature of water is obtained by reducing the mass flow rate of water and resulted in increase in efficiency without loss [6]. Fouling in heat exchanger is a major disadvantage in pasteurization process over a period of time because of high surface temperature. Merlin and Rosenthal concluded that batch heating in microwave will be more efficient in pasteurization when compared to conventional heating systems. A design of heat pump system based on liquid to liquid principle is made to undergo pasteurization process at 69 °C and then cool to temperature of 32 °C [7].The mixing of CO_2 in milk at 6.9 MPa, 45 °C for 60 min shows a low microbial activity. The activities of micro-organisms are totally inactivated by CO_2 treatment at 10 MPa and 36 °C [8].In a simulation model for CO_2 heat pump, it is declared that pressure and isentropic efficiency of compressor depends on swept volume and heat transfer rate of gas cooler depends on refrigerant flow rate [9]. The proposed transcritical CO_2 Heat pump shows that the highest primary energy-saving rate of 51.5% in dairy industries [10].

The functional designs of heat exchangers, expansion devices, and compressors have been playing a pivotal role in performance of CO_2 HP by using different CO_2 HP

cycles coupled with auxiliary components, hybrid systems, and refrigerant mixtures [11]. A suitable transcritical CO_2 refrigeration system for continuous pasteurization and milk chilling process in a dairy plant has been obtained and analyzed [12]. To reduce the power consumption, a heat pump is used for both cold and heat generations. The evaporating, compensating temperatures, engine rotation are the factor influences heat-pump performance [13]. The CO_2 heat pumps provide slightly lower COP (5–25%) related to other conventional refrigerants in industrial heat pumps, they offer significantly higher volumetric capacity and lower pressure ratios of (3–4 times) [14]. The general performance and study for installation of heat pump that generated 184 °C using district heating as a heat source has been investigated [15].

2 Methodology

2.1 Pasteurization

Pasteurization is the process of eliminating micro-organisms in packed foods to increase the shelf life of industrial products. Milk is suitable for microbial growth. To achieve food preservation and safety, pasteurization is to be done before it is packed in the factory. Milk is heat-treated to prevent diseases like tuberculosis, diphtheria, scarlet fever and Q-fever. It kills harmful bacteria like Staphylococcus aureus, Salmonella, Yersinia, Campylobacter and Escherichia coli. High-temperature short-time (HTST) pasteurization means the treatment of milk to a high temperature of 71 °C for a time period of 15 s to kill the pathogens in milk and ensure the safety. It can provide a shelf life of about 15 days. Alkaline phosphatase present in milk is sterilized by pasteurization process which practically kills the bacteria in milk.

2.2 Vapour Compression System

Heat engine working in reverse process, i.e., Reverse Carnot cycle is the fundamental principle of vapour compression system. Here, heat is transferred from cold body to hot body. Work has to be done to transfer heat. It is a compression process in which the refrigerant pressure is increased by the compressor and flows through condenser to transfer heat and then flows to evaporator with initial low pressure through expansion valve. The compressor used in the cycle can be screw, centrifugal or reciprocating types. The refrigerant (CO_2) enters the compressor at low pressure and low temperature in gaseous state and leaves at high temperature and high pressure. In this process, electric motor is used to produce work. The condenser is a heat exchanger. Here, heat is transferred from refrigerant to the fluid to which the heat is to be transferred. Phase change occurs in refrigerant and the refrigerant is in liquid state when leaving the condenser.

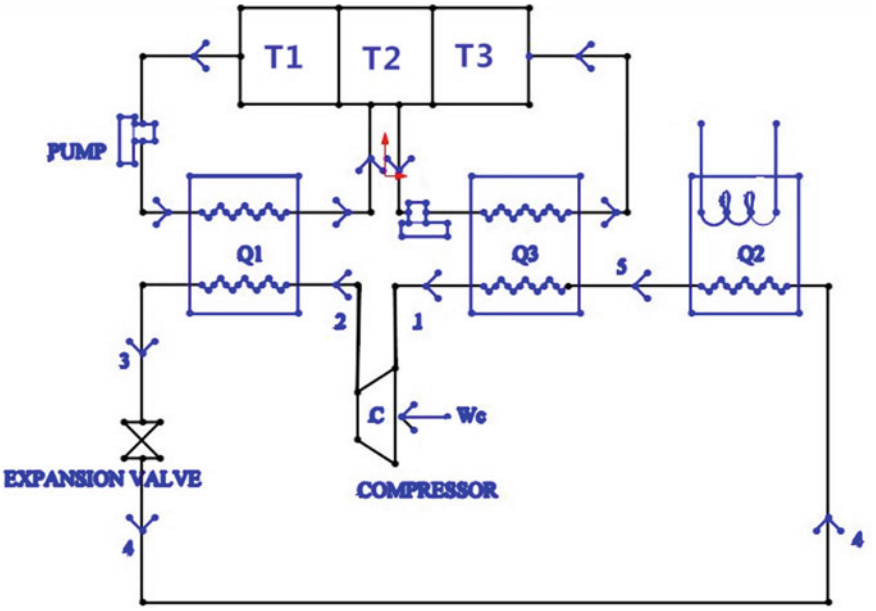

Fig. 1 Proposed layout of experimental setup

For safety reasons, there are pressure control devices to control and monitor the equipment. It reduces the pressure of refrigerant and consequently, reduces the temperature. As these changes occur, the refrigerant will be in liquid vapour mixture stage at the exit with 75% and 25% respectively. The refrigerant enters at low temperature and absorbs latent heat of vapourization. Heat is extracted from the surrounding, phase change occurs and the refrigerant will be in vapour state at the exit of evaporator.

Milk is heat-treated to prevent diseases like tuberculosis, diphtheria, scarlet fever and Q-fever. It kills harmful bacteria like Staphylococcus aureus, Salmonella, Yersinia, Campylobacter and Eschericha coli. High-temperature short-time (HTST) pasteurization means the treatment of milk to a high temperature of 71 °C for a time period of 15 s to kill the pathogens in milk and ensure the safety. It can provide a shelf life of about 15 days. Alkaline phosphatase present in milk is sterilized by pasteurization process which practically kills the bacteria in milk (Fig. 1).

3 Mathematical Modelling of Equation

Heat transferred from the heat exchanger to tank is denoted by Q_1 and the heat transfer is given by the the following equation (Eq. 1)

$$Q_1 = \dot{m} C_P (T_2 - T_1) \tag{1}$$

Heat transferred from tank 2 to tank 3 is denoted by Q_3 and it is given by following equation (Eq. 2)

$$Q_3 = \dot{m} C_P (T_2 - T_3) \tag{2}$$

From the following equation (Eq. 3), the enthalpy h_3 value can be determined, where h_2 is taken from CO_2 refrigerant chart (R744)

$$Q_1 = h_2 - h_3 \tag{3}$$

At initial temperature of 25 °C, the enthalpy h_1 is taken as constant, $h_1 = 400$ kJ/kg, Work output W_C from the compressor is given by the following equation (Eq. 4)

$$W_C = h_2 - h_1 \tag{4}$$

The enthalpy h_5 can be calculated from the following equation (Eq. 5)

$$h_5 = h_1 + Q_3 \tag{5}$$

The heat given to the heat exchanger is denoted by Q_2 and the heat transfer is given by the following equation (Eq. 6)

$$Q_2 = h_5 + h_3 \tag{6}$$

The coefficient of performance COP can be determined by the following equation (Eq. 7)

$$\text{COP} = \frac{(Q_1 + Q_3)}{W_C} \tag{7}$$

4 Analysis

In heat pump system, the inlet temperature of refrigerant is assumed to be at 25 °C i.e., at atmospheric temperature Milk must be heated to 70 °C in the first stage. The refrigerant could be set to a temperature of 80 °C. But in order to avoid subcooled conditions of refrigerant, the outlet temperature of refrigerant from compressor is assumed from 100 °C so that after expansion, the refrigerant will not fall in subcooled temperature as it is not suited for real-time application. The outlet temperature of the refrigerant from compressor is varied from 100 to 140 °C to find the maximum efficiency of the system at various working conditions (Table 1).

Table 1 Experimental result for the working temperature of refrigerant after compression (120 °C)

S. No.	P	h_2	h_3	W_C	h_5	Q_2	COP
	Bar	kJ/kg	kJ/kg	kJ/s	kJ/kg	kJ/s	–
1	90	540	280	140	576.85	296.85	3.120
2	100	530	270	130	576.85	306.85	3.360
3	110	520	260	120	576.85	316.85	3.640
4	120	515	255	115	576.85	321.85	3.798
5	130	510	250	110	576.85	326.85	3.971

5 Result and Discussion

COP of the system increases with increase in pressure. When temperature is increased, the COP of system decreases. For 100 °C, the COP of system ranges between 4 and 8. For 140 °C, the COP of system is decreased. Hence, the refrigerant must be compressed to give an optimum temperature of 100 °C to get maximum COP. Increased work of compressor to achieve 140 °C leads to inefficient system (Figs. 2, 3, 4 and 5).

The work of compressor decreases with increase in pressure. The work input of compressor for 100 °C is much lower when compared with that of 140 °C. In order to achieve a higher COP the work input of compressor must be minimum. Enthalpy of refrigerant at various stages of system is compared. Here, the enthalpy is maximum

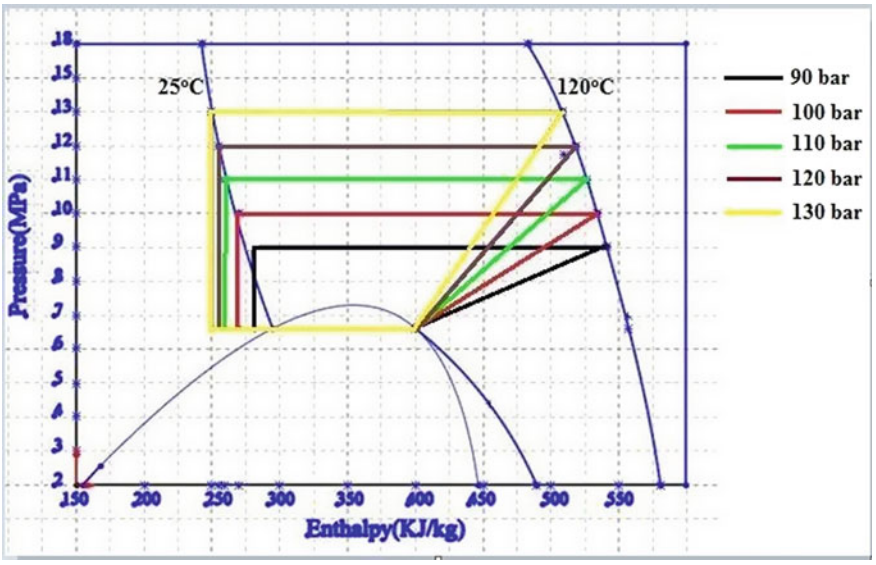

Fig. 2 Pressure-enthalpy diagram

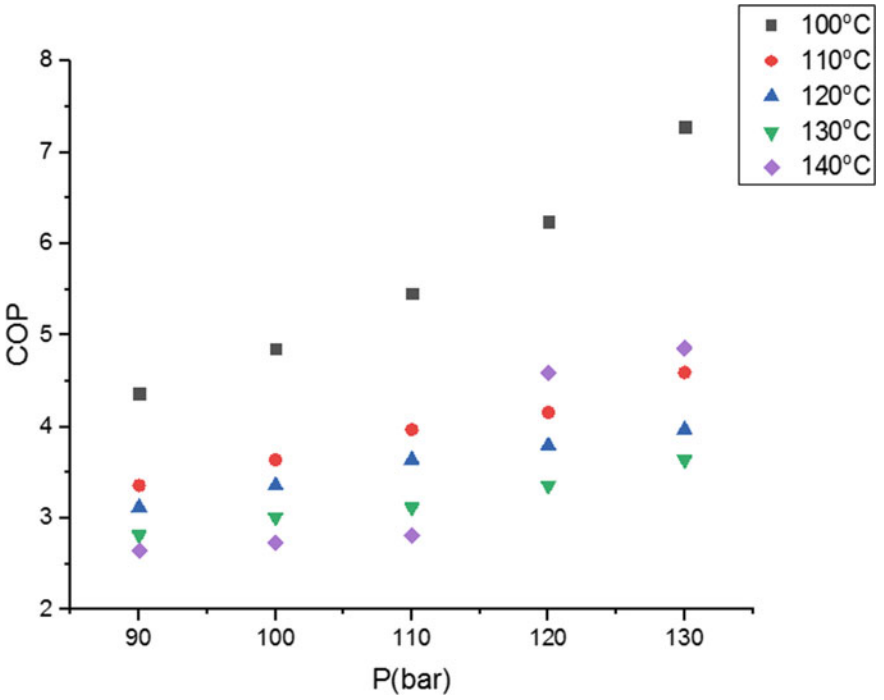

Fig. 3 Coefficient of performance for different pressure

after the supply of heat from heat source (h_5) and minimum after heat supplied at stage 1 (h_3).

6 Conclusion

Heat pump system is used in many applications in day-to-day life. In industries, to expand the production and increase the efficiency of working systems, research and development is done in every unit. The idea of using CO_2 as refrigerant is an advanced system in heat pump industries. Conducting experiments by varying input parameters and achieving optimum results than earlier methods is done to increase the efficiency of production unit. Study of theoretical concepts and analysis of calculated readings and interpretation of results is done for heat pump system to be used in milk pasteurization unit.

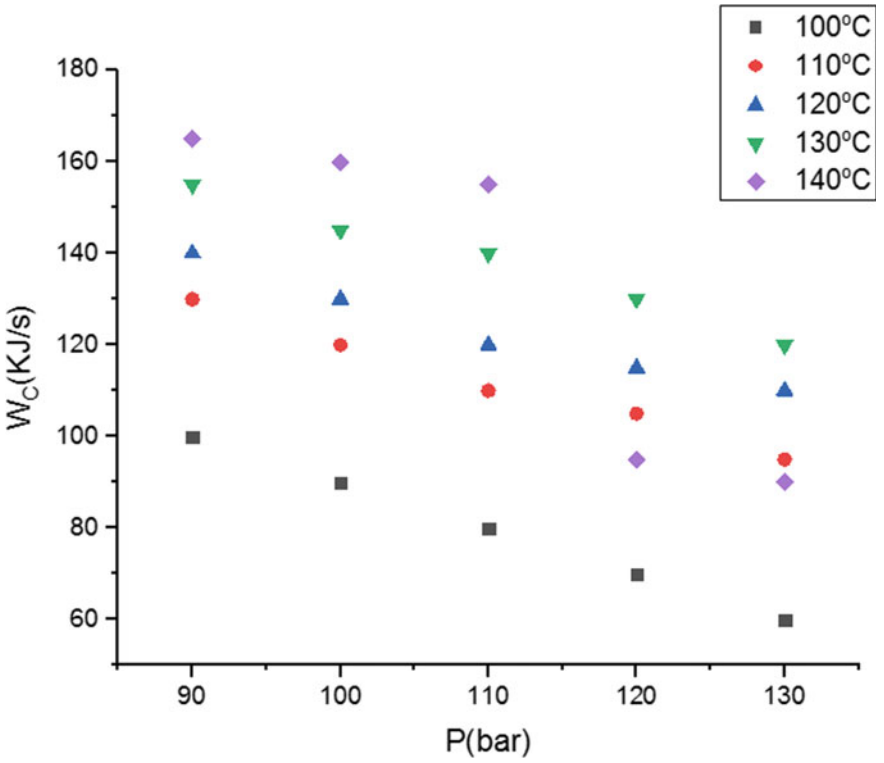

Fig. 4 Work input for compressor with respect to different pressure

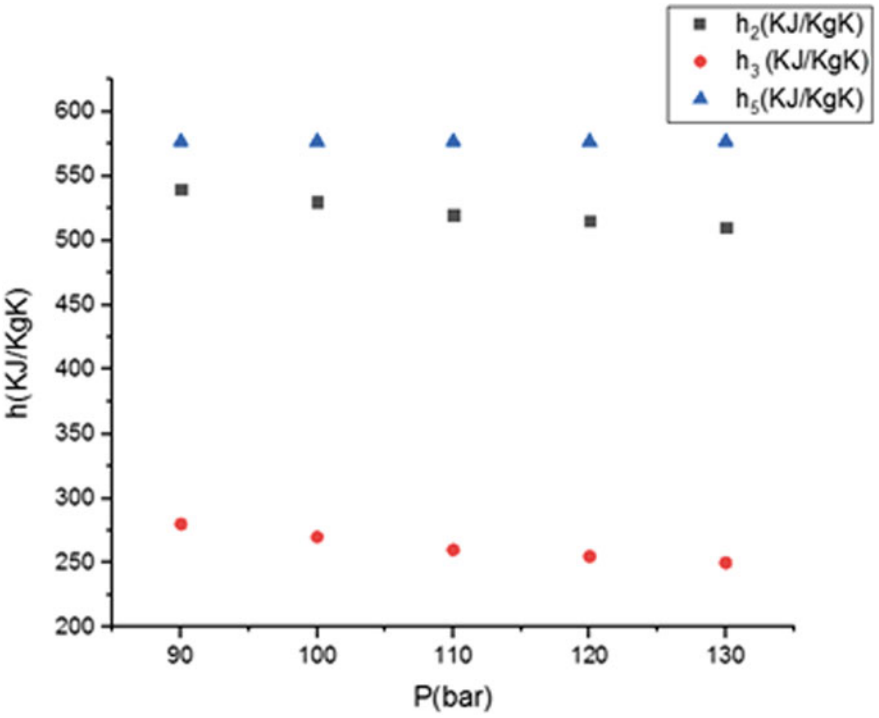

Fig. 5 Enthalpy of refrigerant for different pressure

References

1. Cavallini A, Zilio C (2007) Carbon dioxide as a natural refrigerant. Int. J. Low-Carbon Technol. 2(3):225–249
2. Bullard C (2004) Transcritical CO_2 systems—recent progress and new challenges. Review article. Bull IIR
3. Försterling S, Tegethoff W, Köhler J (2002) Theoretical and experimental investigations on carbon dioxide compressors for mobile air conditioning systems and transport refrigeration
4. Van Kudra T, de Voort FR, Raghavan GSV, Ramaswamy HS (1991) Heating characteristics of milk constituents in a microwave pasteurization system. J Food Sci **56**(4):931–934
5. Nekså P (2004) CO_2 as refrigerant for systems in transcritical operation. Principl Technol Status EcoLibrium 3(9):26–31
6. Neksa P, Aarlien R (1998) Current status on heat pumps with carbon dioxide as working fluid
7. Çomakli Ö, Yüksel B, Kara YA, Çağlar A, Tülek Y (1994) Heat pump utilization in milk pasteurization. Energy Convers Manage 35(2):91–96
8. Yamaguchi S, Kato D, Saito K, Kawai S (2011) Development and validation of static simulation model for CO_2 heat pump. Int J Heat Mass Transf 54(9–10):1896–1906
9. Smitt SM (2017) Integrated Energy concepts for high performance hotel buildings. Master's thesis, NTNU
10. Liu Y, Groll EA, Kurtulus O, Yazawa K (2014) Study on energy-saving performance of a novel CO_2 heat pump with applications in dairy processes
11. Rony RU, Yang H, Krishnan S, Song J (2019) Recent advances in transcritical CO_2 (R744) heat pump system: a review. Energies 12(3):457

12. Ahammed ME, Bhattacharyya S, Ramgopal M (2018) Analysis of CO_2 based refrigeration systems with and without ejector for simultaneous pasteurization and chilling of milk. Int J Refrig 95:61–72
13. Jordan RA, Cortez LA, Barbin DF, Lucas Junior JD (2016) Heat pump for thermal power production in dairy farm. Engenharia Agrícola 36(5):779–791
14. Sarkar J, Bhattacharyya S, Gopal MR (2004) Transcritical carbon dioxide based heat pumps: process heat applications
15. Tveit TM (2017) Application of an industrial heat pump for steam generation using district heating as a heat source. In: 12th IEA heat pump conference 2017. HPC 2017, Rotterdam, May 2017

Applications of Additive Manufacturing—A Review

S. Madheswaran, Karuppan Sivakumar, E. Prakash, S. Kalaivanan, N. Someswaran, and J. Vishnudeepan

Abstract 3D printing produces components with complicated geometries without complexity. Printed part's strength depends on the material property. Optimizing the printing parameters provides improved mechanical properties of the printed parts. Even though it is not improved as expected, another method is to introduce the composite material. Polymer composites have increased mechanical properties, and so they are used in producing high-quality objects. 3D printing is helpful in various composites fabrication having high good-quality, high accuracy and custom designed model. Here, we present detailed theoretical study on various 3D printing technologies that use polymer composite as raw material. Due to various advantages in 3D printing technologies, they play an important role in biomedical, aerospace, automobile and electrical engineering. Common 3D printing technologies are selective laser sintering, stereolithography, fused deposition modeling which are studied. Further, we studied about acrylonitrile butadiene styrene (ABS) and injection molding process. In this work, we study on particles, fiber and nonmaterial composite.

Keywords Fusion deposition modeling (FDM) · 3D printing · Selective laser sintering (SLS) · Nonmaterial polymer composite

1 Introduction

3D printing, also known as additive manufacturing (AM), rapid prototyping (RP) is a addition process that was defined by Charles Hull in 1986 [1, 2]. Since objects are created in addition manner, waste gets reduced and accuracy gets improved [3]. The mesh information is cut by a construct document of two-dimensional parts and dispatched to the 3D print machines. Thermoplastic polymer substances inclusive of acrylonitrile butadiene styrene (ABS) [4] got lots of properties that include

S. Madheswaran (✉) · K. Sivakumar · E. Prakash · S. Kalaivanan · N. Someswaran · J. Vishnudeepan
Department of Mechanical Engineering, Bannari Amman Institute of Technology, Sathyamangalam, Erode 638401, Tamil Nadu, India
e-mail: madhesbannariamman@gmail.com

G. Kumaresan et al. (eds.), *Advances in Materials Research*, Springer Proceedings in Materials 5, https://doi.org/10.1007/978-981-15-8319-3_3

lightweight, abrasion resistance, etc. This is useful for industrial application. Polylactic acid (PLA) [4–6], polyamide (PA) and polycarbonate (PC) [7] as well as thermosetting polymer substances like epoxy resins will be processed by means of 3D printing. Therefore, epoxy resins are suitable for UV or warmth-assisted printing process. Due to numerous alternatives of substances, 3D printing of polymers has been used in areas such as aerospace industries for growing complicated lightweight systems, architectural companies for structure models, art fields for replication or change and clinic field for print the tissue and organ [8]. But most of the 3D print polymers produced are now used for in preference to useful additives, considering the fact that non-polymer composite materials made by means of 3D printings loss of power as full practical elements. Those problems give restrict to huge commercial utility of 3D print polymers. 3D printing solves the material variety and power loss problems together by processing of different materials using single universal machines which replaces many conventional machines.

2 3D Printing Technologies

3D printing is a method that build 3D model by primarily by CAD models [9]. Many printing methods are used to produce polymers which include fused deposition modeling etc. Other 3D printing technique is under development process. Each 3D technique has its personal advantages and limitations in generating composite products. The choice of fabrication method depends on the starting materials, necessities of processing velocity and resolution, expenses and performance necessities of final products.

2.1 Fused Deposition Modeling (FDM)

Fused deposition modeling (FDM) is also known as fused filament fabrication (FFF) which is a 3D printing process that uses thermoplastic filament which has a raw material, and the thermoplastic materials such as PC, ABS and PLA are used since they have low melting temperature. We study that in FDM the filament is continuously fed through the heated extrusion nozzle where the filament gets melted and it forms layer by layer on the platform which is shown in Fig. 1. The excellent of published components are controlled by means of altering various printing parameters. Outcomes of process are mentioned by Sood et al. [10].

In this paper, we made a study that filament-shaped composite material can only be printed by FDM process. Homogeneous disperse reinforcements are difficult to produce in FDM process. Also, whole elimination of support material is used throughout printings that is difficult. Many printers has advantages such as large height-shaped objects which can produce high-dimensional accuracy and simplicity.

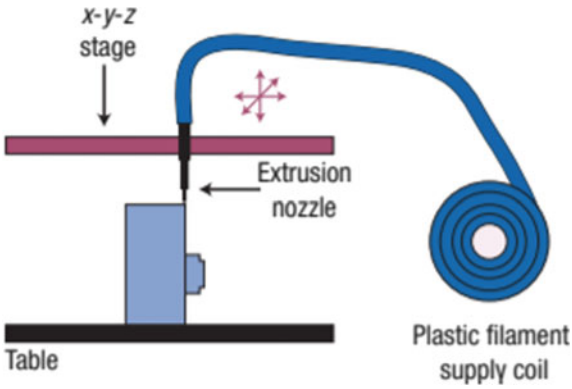

Fig. 1 Layer-by-layer object build up in FDM process using filament as raw material [11]

2.2 Stereo Lithography (SLA)

Stereo lithography is a process which uses liquid photo polymeric resin in the state of monomer as a raw material and works based on photo polymerization principle. Upon exposure to concentrated UV rays, the monomer turns to a polymer. This process repeated in 2D layer by layer pattern is repeated untill the component completely fabricated. Typical polymer substances utilized in SLA are acrylic and epoxy resins.

Understanding the curing reactions happening for the duration of polymerization is vital to govern the excellent of final printed elements. Intensity of laser strength, scan pace and duration of publicity has an effect on the curing time and printing decision. Photoinitiators and UV absorbers may be introduced to the resin to control the depth of polymerization. The primary gain of SLA printing generation is the capability to print components with excessive decision. Since SLA does not uses nozzle feeding which avoids material clogging issues. Even though it has many merits, the parts produced tends to shrink and become brittle since it is exposed to UV rays present in the atmosphere.

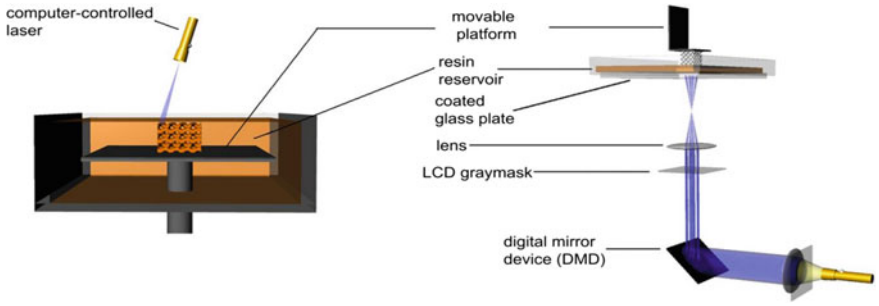

Fig. 2 Object is build in the platform layer by layer, on concentration of UV laser over resin reservoir [12]

2.3 Selective Laser Sintering (SLS)

Selective laser sintering technique is much like other 3DP method, and they uses powder as a raw material. liquid binder is not used in SLS; in SLS, laser beam gets scanned on the powder; due to high intensity of laser over the powder, the powder gets fused with neighbor powder through molecular diffusion and the object is build layer by layer over the platform, and unused powder is used for further process, and they are used mainly for aerospace applications [13]. The feature resolution is determined with the aid of length, light energy and test pace. Also theoretically any geometry can be produced using SLS approach, sintering cures and creates a voidless dense components [14]. To date, polycaprolactone (PCL) and polyamide (PA) are broadly used laser sintering substances.

3 3D Printing of Polymer Matrix Composites

Polymer substances are widely used in 3D printings technology. They have properties such as low-melting point and process flexibilities. 3D printed polymers must have geometric functionality, and loss of mechanical power is a large task for extensive application. In current year, improvement of composites material leads to development in complex shapes. Particles strengthen the printed composite substance.

3.1 Particle-Reinforced Polymer Composite

We studied that particle-reinforced materials are used in many field because of the low cost, and this is to improve the residence of polymer matrix composites. SLS and SLA use the powder form materials. And also the FDM process uses the same materials. Glass beds [15], tensile and garage modulus are the most of the problems in the 3D printing technology. SLA technique was developed by Kalsoom et al. [16] for production of warmth sink composite structure. And the addition of diamond debris results in warmness.

3.2 Fiber-Reinforced Polymer Composites

The properties of polymer matrix substance are increased due to the fiber reinforcement. FDM and direct method techniques are the most same 3D printing methods to build fibers, and also, it is widely used in many applications. Composite filament used in FDM process are fabricated by extrusion method with uniform blend of polymer

and fibers in required proportion using double extrusion process. And in the direct writing method, fibers and Polymer are blended and extruded out, and creation of pure form of powder fiber mixture is very difficult to produce in any other 3D printing technologies [17].

3.3 Nanocomposites

The additions of nonmaterials with the polymers always results in good performance of composite materials. That is why the nonmaterials together with carbon, graphite and steel nano-particles have good mechanical, electrical and thermal properties in a good manner.

Nano materials are often used as an additive with composites to improve mechanical properties. The addition of some of the composites results in good polymer parts compared to other polymers. And also, all composite parts are used to to reduce the length. Lin et al. [18] proved that photopolymer composite truss by the SLA method shown in Fig. 3. Carbon nanofiber, carbon black ok and carbon nanotube are some of the stronger electric property nanomaterials.

4 Biomedical Application

Development of additively manufactured composite materials find a significant applications in medical industries [20]. By use of the derived photo-informations, patient rare tissues and organs with different difficult 3D micro-architecture are build by the 3D printings technologies. Polymer materials now widely use for printing the sides.

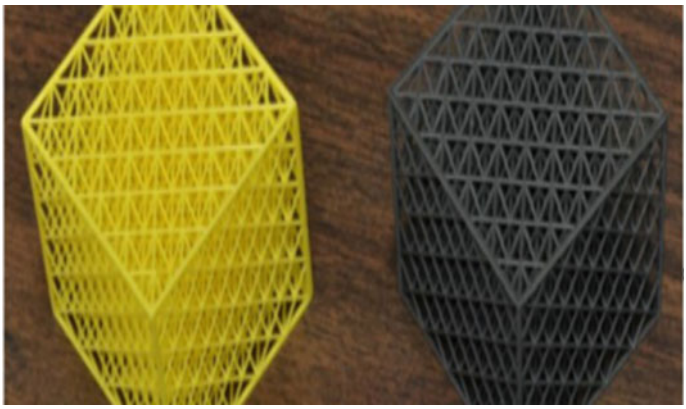

Fig. 3 Shows the polymer truss with GOs reinforced that have good ductility [19]

The common developments of printable things for biomedical bags are printability, biocompatibility and perfect mechanical properties. It is important for good feature to ensure that produced 3D part has an amazing work with all tissue [19].

4.1 Electronics

In this work, we studied that 3D printing can be used in various digital prototypes with less time development [21]. 3D printed composites are combined with electrical conduit materials which are used as digital device. FDM prints the pizeo-resistive and capacitive sensors. 3D printing applications are done by those two sensors very effectively and successfully, and finished part is done by PLA usage. Evaporation of solvents occurred, and continually 3D microstructure is formed. Simon et al. fabricated electronic sensor that ranges from piezo-resistive sensor to capacitive sensor [11]. The piezo-resistive sensors sense mechanical flexing which is embedded into clever vessels to locate the presence and shortage of water.

4.2 Aerospace Applications

Time-consuming and high production cost is the only defect in aerospace industries. So, this method is well suited for improvement of components. Now, turbine blades are made of metal materials [22, 23], because metals have good strength and flammable than polymer.

5 Results and Conclusion

3D printing offers accurate-shaped objects that are eco-friendly one, and it also reduces time- and cost-efficient method. Thermoplastic materials such as ABS, PLA are used for various 3D printing processes. As per our study on these ABS composite materials, this is widely used for a aerospace applications and biomedical field. Using 3D printing technologies produced, composites have fatigue strength and corrosion resistance. In this study, we knew that there is no material wasted. In this work, we theoretically studied about various processes of 3D printing and polymer composite for 3D printing process briefly.

References

1. Standard A (2012) F2792, standard terminology for additive manufacturing technologies. ASTM International, West Conshohocken
2. Hull CW (1986) Apparatus for production of three-dimensional objects bystereolithography. Google Patents
3. Levy GN, Schindel R, Kruth JP (2003) Rapid manufacturing and rapid tooling with layer manufacturing (LM) technologies, state of the art and future perspectives. CIRP Ann Manuf Technol 52(2):589e609
4. Tymrak B, Kreiger M, Pearce J (2014) Mechanical properties of components fabricated with open-source 3-D printers under realistic environmental conditions. Mater Des 58:242e6
5. Tran P, Ngo TD, Ghazlan A, Hui D (2017) Biomaterial 3D printing and numerical analysis of bio-inspired composite structures under in-plane and transverse loadings. Compos Part B Eng 108:210e23
6. Melnikova R, Ehrmann A, Finsterbusch K (2014) 3D printing of textile-based structures by Fused Deposition Modeling (FDM) with different polymer materials. In: IOP conference series: materials science and engineering. IOP Publishing
7. Garcia CR, Correa J, Espalin D, Barton JH, Rumpf RC, Wicker R, Gonzalez V (2012) 3D printing of anisotropic materials. Prog Electromagn Res Lett 34:75e82
8. Murphy SV, Atala A (2014) 3D bio printing of tissues and organs. Nat Biotechnol 32(8):773e85
9. Rengier F, Mehndiratta A, von Tengg-Kobligk H, Zechmann CM, Unterhinninghofen R, Kauczor H-U, Giesel FL (2010) 3D printing based on imaging data: review of medical applications. Int J Comput Assisted Radiol Surg 5(4):335e41
10. Sood AK, Ohdar R, Mahapatra S. Parametric appraisal of mechanical property of fused deposition modeling processed parts. Mater Des 2010;31(1):287e95.
11. Leigh SJ, Bradley RJ, Purssell CP, Billson DR, Hutchins DA (2012) A simple, low-cost conductive composite material for 3D printing of electronic sensors. PloS one 7(11):e49365
12. Melchels FP, Feijen J, Grijpma DW (2010) A review on stereo lithography and its applications in biomedical engineering. Biomaterials 31(24):6121e30
13. Gu D, Meiners W, Wissenbach K, Poprawe R (2012) Laser additive manufacturing of metallic components: materials, processes and mechanisms. Int Mater Rev 57(3):133e64
14. Goodridge R, Shofner M, Hague R, McClelland M, Schlea M, Johnson R, Tuck C (2011) Processing of a Polyamide-12/carbon nanofibre composite by laser sintering. Polymer Test 30(1):94e100
15. Chung H, Das S (2006) Processing and properties of glass bead particulate-filled functionally graded Nylon-11 composites produced by selective laser sintering. Mater Sci Eng A 437(2):226e34
16. Kalsoom U, Peristyy A, Nesterenko P, Paull B. A 3D printable diamond dipolymer composite: a novel material for fabrication of low cost thermally conducting devices. RSC Adv 6(44):38140e7
17. Guo N, Leu MC (2006) Additive manufacturing: technology, applications and research needs. Front Mech Eng 8(3):215e43. Rapid Prototype J 12(5):292e303
18. Lin D, Jin S, Zhang F, Wang C, Wang Y, Zhou C, Cheng GJ (2015) 3D stereolithography printing of grapheme oxide reinforced complex architectures. Nanotechnology 26(43):434003
19. Hollister SJ. Porous scaffold design for tissue engineering. Nat Mater2005;4(7):518e24.
20. Meaney J, Goyen M (2007) Recent advances in contrast-enhanced magnetic resonance angiography. Eur Radiol 17:B2e6
21. MacDonald E, Salas R, Espalin D, Perez M, Aguilera E, Muse D, Wicker RB. 3D printing for the rapid prototyping of structural electronics. Access, IEEE 2:234e42
22. Watkins T, Bilheux H, An K, Payzant A, Dehoff R, Duty C, Peter W, Blue C, Brice CA (2013) Neutron characterization for additive manufacturing. Adv Mater Process 171(3):23e7
23. Malhotra SK, Goda K, Sreekala MS (2012) Part one introduction to polymer composites. In: Polymer composites, 1st edn. Wiley, New York

Review on Recent Additive Manufacturing Technologies

E. Prakash, M. Subramaniyan, Anandha Moorthy Appusamy, P. Mathan Kumar, M. Dinesh, M. Naveen, and C. Santhosh

Abstract Additive manufacturing (AM) is the best technology in manufacturing the components without complexity. This technology is classified as seven categories by ASTM standards. Based on types of materials, it is classified into two. Materials and types of technology define the property of fabricated parts. Single material printed parts give less material property, to improve this property industries fetching towards making composite material to improve the mechanical strength and making functional parts. Ceramic matrix composites are substances which can be applied for excessive heat considered for different areas consisting of a glass, aerospace and so on. It may be hard to manufacture CMC using conventional mould techniques because of hardness and brittle. Additive manufacturing technology is virtual production technology that provides a couple of merits over traditional manufacturing process, together with producing complex elements, matrix-unfastened production, quick improvement process and so on. AM era has the same fashioning abilities in forming ceramics components, but the lack of bonding creates a lack of toughness, these properties are created prone to ceramic components fabrication failure.

Keywords Ceramic matrix · Fibres · Selective laser sintering

1 Introduction

Ceramic matrix composites are materials consisting of a ceramic matrix companied with a ceramic (oxides and carbides) dispersed phase. Ceramics that have crystal structures consist of positive ions. The traditional ceramics are based mainly on pure raw material of clay and silicates, polymers. CMCs are reinforcement by either continues fibres or discontinuous fibres. Such fabrication routes are successfully employed for preparing composite reinforced with a discontinuous phase.

E. Prakash (✉) · M. Subramaniyan · A. M. Appusamy · P. Mathan Kumar · M. Dinesh · M. Naveen · C. Santhosh
Department of Mechanical Engineering, Bannari Amman Institute of Technology, Sathyamangalam, Erode, Tamil Nadu 638401, India
e-mail: prakashe@bitsathy.ac.in

G. Kumaresan et al. (eds.), *Advances in Materials Research*, Springer Proceedings in Materials 5, https://doi.org/10.1007/978-981-15-8319-3_4

Which decreases the efficiency and yield charge? A difference of AM technology had been applied to produce CMC elements along with direct ink writing (DIW), three-dimensional printing (3DP), selective laser sintering (SLS), laminated object modelling (LOM), and stereolithography (SL). Many polymer composite materials are heat resistant and non conductive compare to steel [1, 2]. The fibre weaving approach has been extensively taken, wherein fibre reinforcement efficient and excessive mechanical homes of the composites display exquisite improvements evaluating with gel-casting.

2 Ceramic Matrix Composites for Additive Manufacturing

These sequences in CMC element manufacturing process performed on this method are regular to the conventional CMC components producing procedure. In recent, these components production totally on robocasting, 3D printing and different technology belong to production era. Ceramics, glass and carbon fibres among the most advanced rapid growth due to investments in CMCs and hybrid parts become increasingly important. And this type of SLS era is referred to as direct selective laser sintering (DSLS) that much like precept of direct metal laser melting (DMLM) for metal substances.

2.1 Robocasting

In the production manner, ceramic composite components are less frequent as direct write assembly or micro-robotizes deposition of AM technology based on direct extrusion of slurry-based inks. The ceramic element is finished with some other ceramic techniques. The transformed and concentrated equipment is the key part of utilizing direct ink writing ([2, 3, 4, 5, 6]). An ink with appropriate rheological properties for robocasting must be able to own through the nozzles which are the important thing aspect for combining the printing system and the homes of the composite material properties. These houses of the ink and the microstructure houses of broadcast materials are mentioned.

2.1.1 Rheological Properties

Ceramic particle reinforced steel composites are widely used in electronics, aerospace and other industries. The investigation of rheological behaviour of semi-solid alloys imposed with other particles. Direct ink writing era has necessities the rheological residences of combined ink. The ink desires certain behaviour [2, 7, 8] which allows the combined ink to be without difficulty exposed via the micro-head

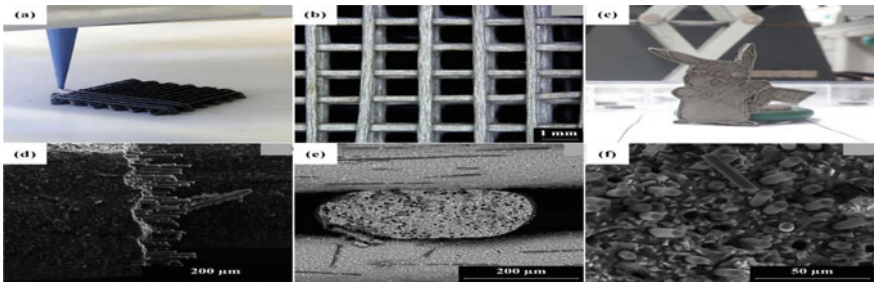

Fig. 1 Mechanical properties and microstructure correlation

to pass much sufficient yield strength to regain shape. A vital density for combined ink needs to keep the head from closing that easily retrieved by section parts.

2.1.2 Mechanical Properties and Microstructure

The hard ceramic particulate fibre improved the mechanical properties especially hardness and microstructure refinement while mixing it with the appropriate resin. The microstructure as well as certain properties of the manufacturing composite is analysed as shown in Fig. 1. The orientated fibre proves the electricity in neighbourhood location of the broadcast part, which gives fashionable to education for change in direction along with object for ceramic matrix composite.

Recently, the contribution of fibres has presented an practical investigations, but most lectures of applications and derivations were suggested [9]. The inks had been fantastically wide variety of fibres, SiC powder and methyl silsesquioxane.

2.2 3D Printing

Three-dimensional printing also called [10, 11]. 3D printing is a powdered bed typed on totally printing technology. In this manner of producing, those components are totally powder that is flippantly blended. In these types of processes, the excessive material wastes have been avoided. In this material production, the support material is used to withstand the finished product.

2.3 Selective Laser Sintering (SLS)

The working volume of SLS is maintained with appropriate temperature so that laser supplies the energy required to cross the threshold sintering temperature. An inert

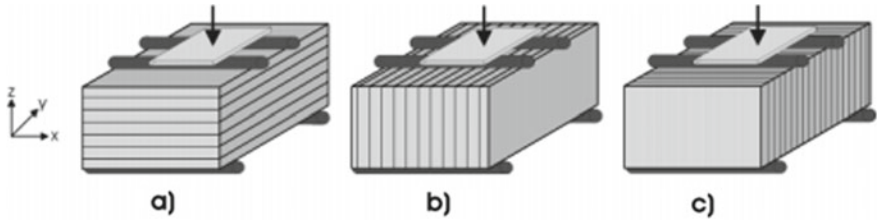

Fig. 2 Layer orientations and loading directions

environment is created using continuous supply of gas such as nitrogen/argon [5, 12, 13]. This is to minimize fire hazards as the fine particles have high activation.

Laser beam is positioned using a pretty mirror capable of deflecting in two directions. Therefore, this has very low inertia and hence high speed and accuracy; in spite of low production rate, the 3D printing components need more than one precipitation cycle.

2.4 Laminated Object Manufacturing (LOM)

It has to produce ceramic where a product is developed by good surfacing layers of required material bending the temperature and pressure. This is used to produce the laminated objects [8]. They can be easily renewable. The most common materials used in LOM are thermoplastics such as PVC. Figure 2 shows layer orientations and loading directions of laminated object manufacturing.

It is the major difference in AM technique compared with CNC, various reinforce substances occur as a debris in LOM. It can be contouring and applying of sheet material. The materials can be used as foil like paper, metals, plastics, fibre glass and composite [14].

2.5 Stereolithography (SLA)

Stereolithography is a technique which is used to produce projected model. UV laser is used as the light energy source. When it is scanned on the seceded region over a layer of liquid polymer, that region becomes solid. In this way, required layer can be realized over a liquid surface [15]. Figure 3 shows that the SLA technology is ideal for producing particle of reinforced ceramics.

The stress concentration of laser beam is positioned using a small mirror capable of deflecting in two directions. Therefore, this has very low inertia and hence high speed and accuracy. The power of the laser decides the layer thickness [1, 16, 17]. SLS and Quick cast are used for fabricating direct metal parts and tools like KeITool used

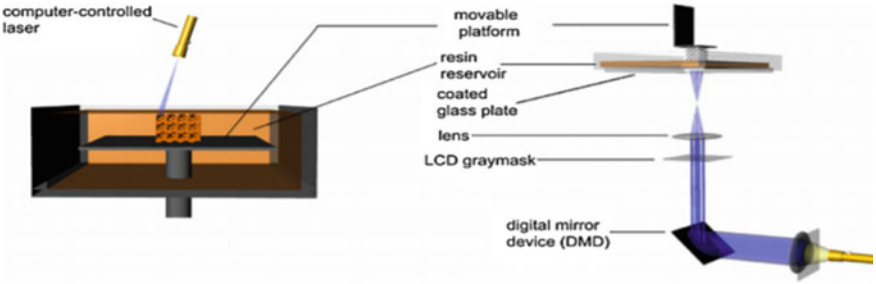

Fig. 3 SLA 3D printing stereolithography

for indirect tooling [8]. So a complete solution for physically prototyping is available from one source. Quick cast is suitable for producing castings of any metals with the fine surface finish which are ideal for photo-elasticity.

3 Results and Conclusion

The ceramics developed by the 3D printing technologies were initially found to have some favourable properties which promote intensive work for their use in industries and in heat conversion devices. 3D printed ceramics matrix composites toughness increases due to reinforcement, and there is no sudden failure occurs in ceramics. In this study, we know that ceramics have high strength to weigh ratio, wear and corrosion resistance and lower cost compared to other composites. Thus, the ceramics are used in aerospace applications and in various fields, etc. Improvement in the toughness of these ceramics is possible by making composites with ceramics using 3D printing technologies.

References

1. Frketic J, Dickens T, Ramakrishnan S (2017) Automated manufacturing and processing of fiber-reinforced polymer (FRP) composites: an additive review of contemporary and modern techniques for advanced materials manufacturing. Additive Manuf 14:6986. https://doi.org/10.1016/j.addma.2017.01.003
2. Kumar S, Kruth JP (2010) Composites by rapid prototyping technology. Mater Des 31(2):850–856. https://doi.org/10.1016/j.matdes.2009.07.045
3. Beaman JJ, Deckard CR (1990) Selective laser sintering with assisted powder handling. Google Patents
4. Misra AK, Joseph EG, Carter R (2015) Additive manufacturing of aerospace propulsion components. In: Additive manufacturing conference
5. Lewicki JP, Rodriguez JN, Zhu C, Worsley MA, Wu AS, Kanarska Y, Horn JD et al (2017) 3D-printing of meso-structurally ordered carbon fiber/polymer composites with unprecedented orthotropic physical properties. Sci Rep 7:43401. https://doi.org/10.1038/srep43401

6. Peng J, Lin TL, Calvert P (1999) Orientation effects in freeformed short-fiber composites. Compos A Appl Sci Manuf 30(2):133–138
7. Meteyer S, Xin Xu, Perry N, Zhao YF (2014) Energy and material flow analysis of binder-jetting additive manufacturing processes. Procedia CIRP 15:19–25. https://doi.org/10.1016/j.procir.2014.06.030
8. Sachs EM, Haggerty JS, Cima MJ, Williams PA (1995) Three-dimensional printing techniques
9. Franchin G, Wahl L, Colombo P (2017) Direct ink writing of ceramic matrix composite structures. J Am Ceram Soc 100(10):4397–4401. https://doi.org/10.1111/jace.15045
10. Conner BP, Manogharan GP, Martof AN, Rodomsky LM, Rodomsky CM, Jordan DC, Limperos JW (2014) Making sense of 3-D printing: creating a map of additive manufacturing products and services. Additive Manuf 1–4:64–76. https://doi.org/10.1016/j.addma.2014.08.005
11. Gaytan SM, Cadena MA, Karim H, Delfin D, Lin Y, Espalin D, MacDonald E, Wicker RB (2015) Fabrication of barium titanate by binder jetting additive manufacturing technology. Ceram Int 41(5, Part A):6610–6619. https://doi.org/10.1016/j.ceramint.2015.01.108
12. Liu R-Z, Chen P, Jia-Min Wu, Chen S, Chen A-N, Chen J-Y, Liu S-S, Shi Y-S, Li C-H (2018) Effects of B4C addition on the microstructure and properties of porous alumina ceramics fabricated by direct selective laser sintering. Ceram Int 44(16):19678–19685. https://doi.org/10.1016/j.ceramint.2018.07.220
13. Calvert P, Lin TL, Martin H (1997) Extrusion freeform fabrication of chopped-fibre reinforced composites. High Perform Polym 9(4):449–456
14. Windsheimer H, Travitzky N, Hofenauer A, Greil P (2007) Laminated object manufacturing of preceramic-paper-Derived Si–SiC Composites. Adv Mater 19(24):4515–4519. https://doi.org/10.1002/adma.200700789
15. Bae C-J, Halloran JW (2011) Influence of residual monomer on cracking in ceramics fabricated by stereolithography. Int J Appl Ceram Technol 8(6):1289–1295. https://doi.org/10.1111/j.1744-7402.2010.02578.x
16. Vaidyanathan R, Green C, Phillips T, Cipriani R, Yarlagadda S, Gillespie WJ, Effinger M, Cooper KC (2002) Rapid prototyping of continuous fiber reinforced ceramic matrix composites. Program of Annual Meeting of Ksiam
17. Lukaszewicz DHJA, Ward C, Potter KD (2012) The engineering aspects of automated prepreg layup: history, present and future. Compos B Eng 43(3):997–1009. https://doi.org/10.1016/j.compositesb.2011.12.003

Studies on Electric Discharge Machining of AA6063 Alloy Using Taguchi Approach

C. Boopathi, C. Veera Ajay, S. Manoj Vignesh, and S. M. Saravanakumar

Abstract Electric discharge machining is a non-traditional electrothermal machining process, in which electrical energy is used to generate electrical spark and material removal occurs due to thermal energy produced by the spark. Electric discharge machining can be used to machine irregular geometries in small batches or even on job-shop basis. In this research work, the impact of EDM input parameter such as peak current (I), voltage (V), pulse-on time (T_{ON}), and flushing pressure (P_f) on material removal rate (MRR), electrode wear rate (EWR), and surface roughness (SR) in aluminum alloy AA6063 was studied and discussed the same in detail. Taguchi approach (L_9 orthogonal array) was used to design the experimental layout.

Keywords Electrical discharge machining · Electrode · Current · Pulse-on time · Taguchi approach

1 Introduction

Electrical discharge machining (EDM) is an electrothermal machining process used to machine high strength temperature-resistant alloy and materials difficult-to-machine. The process is most commonly used in tool and die, aerospace, automobile, chemical, and biomedical industries. EDM process has been used to machine complex geometrics with high accuracy. Chandramouli and Eswaraiah [1] studied the effect of input process parameters such as T_{ON}, T_{OFF}, tool lift time, and I on output response such as SR and MRR in stainless steel (SS) workpiece machined with electrode made of copper tungsten. L_{27} Orthogonal array (OA) was used to frame the experimental design layout. ANOVA method was carried out to analysis

C. Boopathi (✉) · S. Manoj Vignesh · S. M. Saravanakumar
Department of Mechanical Engineering, Bannari Amman Institute of Technology, Sathyamangalam 638506, Tamil Nadu, India
e-mail: boopathichinnakannan@gmail.com

C. Veera Ajay
Department of Mechanical Engineering, National Engineering College, Kovilpatti 628503, Tamil Nadu, India

G. Kumaresan et al. (eds.), *Advances in Materials Research*, Springer Proceedings in Materials 5, https://doi.org/10.1007/978-981-15-8319-3_5

the influencing process parameter over response parameters. The authors optimized the input parameter by considering the response parameters which having minimum surface roughness (SR) and maximum MRR. Rajmohan et al. [2] studied the impact of selected input process parameters over response parameter such as MRR while machining 304 SS workpiece. L_9 OA was used to frame the experimental design layout. The authors concluded that pulse-OFF time and selected current are the most influencing process parameters. Das et al. [3], the authors concluded that response surface methodology (RSM) and Jaya algorithm (JA) are found to be effective tool for modeling and optimizing the EDM process. Selvarajan et al. [4] studied the influences of input parameters such as dielectric flushing pressure, T_{ON}, T_{OFF}, and I on output response parameters such as TWR, MRR, perpendicularity (PER), cylindricity (CYL), and circularity (CIR) in ceramic composite (Si_3N_4–TiN) workpiece machined with copper-based electrode. The authors determined the optimal machining parameter using the gray relational grade (GRG). Bhaskar et al. [5] proposed the multi-response optimization method for EDM of aluminum alloy. The result indicated that pulse-on time and peak current increase with increases in TWR, MRR, overcut, and surface roughness. Krishnaraj [6] used the EDM for machining titanium alloy. Hole taper, TWR, and MRR were selected as response parameter. Multiple regression analysis was used to extend the mathematical models. The author concluded that Ton and I_p are the most influencing parameter in the EDM process. Dewan et al. [7] used the electrical discharge machining for machining Nimonic 90 work material.

The optimal process parametric combination was obtained using gray relational analysis. The result shows that as T_{ON} increases there will be increases in surface roughness because discharging duration available is more. Assarzadeh et al. [8] optimized the input parameters in EDM process based on statistical technique. The significant factor affecting TWR is T_{ON}, I and duty cycle. The surface roughness is mostly influenced by I, duty cycle and T_{ON}. Daneshmand et al. [9] studied the effects of EDM parameter on NiTiSMA workpiece machined using copper electrode. The authors concluded that TWR and MRR increase with an increase in T_{ON} and I. TWR is minimum while using de-ionized water as flushing medium rather than kerosene. Pradhan and Biswas [10] machined the AISI D2 tool steel workpiece using copper electrode in EDM machine. RSM approach was implemented for the experimentation. It can be observed from this research work that SR has a direct association with the I and T_{on}.

2 Materials and Method

The experiments were performed on RELIABLE-make EDM machine shown in Fig. 1. The workpiece material chosen for the experiment is aluminum alloy AA 6063 having dimension of 10 mm × 10 mm × 4.1 mm. Electrodes made of brass with 2 mm diameter were used as tool, and commercial EDM oil was used as dielectric fluid. The investigational samples are shown in Fig. 2 (Table 1).

Fig. 1 RELIABLE-make EDM machine

3 Results and Discussions

3.1 Material Removal Rate

The regression equation for MRR is shown in Eq. 1.

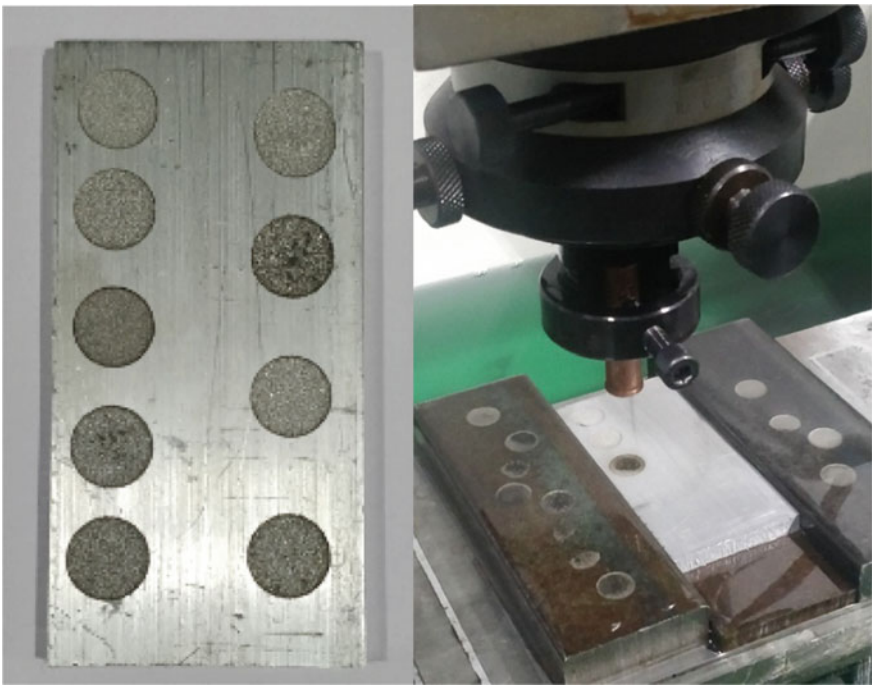

Fig. 2 Experimental samples

Table 1 Experimental design layout

S. No	I (A)	V (V)	T_{ON} (μs)	P_F (Mpa)	MRR (g/min)	TWR (g/min)	SR (μm)
1	5	20	150	0.25	0.0377	0.0027	5.78
2	5	40	300	0.5	0.0320	0.0036	6.06
3	5	60	450	0.75	0.0210	0.0048	6.88
4	10	20	300	0.75	0.1187	0.0066	6.91
5	10	40	450	0.25	0.0908	0.0075	7.70
6	10	60	150	0.5	0.0520	0.0042	6.19
7	15	20	450	0.5	0.1825	0.0059	7.60
8	15	40	150	0.75	0.1297	0.0038	6.82
9	15	60	300	0.25	0.1015	0.0082	8.02

$$\text{MRR} = -0.00583 + 0.010765I - 0.001370V + 0.000083T_{\text{ON}} + 0.02633T_{\text{f}} \quad (1)$$

The R^2 value is 0.9961 for MRR which states that the model is 99.61% accomplished to predict the response value. The R^2 value is in better accord with the adjusted R^2 (0.9921). The ANOVA value obtained in minitab for MRR is shown in Table 2.

From Figs. 3 and 4, it is observed that increasing the current (I_p) from 5 to 15 A

Table 2 ANOVA for MRR

Source	DF	Adj-SS	Adj-MS	*F*-Value	*P*-Value
Regression	4	0.023083	0.005771	253.39	0.000
I	1	0.017384	0.017384	763.31	0.000
V	1	0.004506	0.004506	197.84	0.000
T_{on}	1	0.000934	0.000934	41.00	0.003
T_f	1	0.000260	0.000260	11.42	0.028
Error	4	0.000091	0.000023		
Total	8	0.023174			

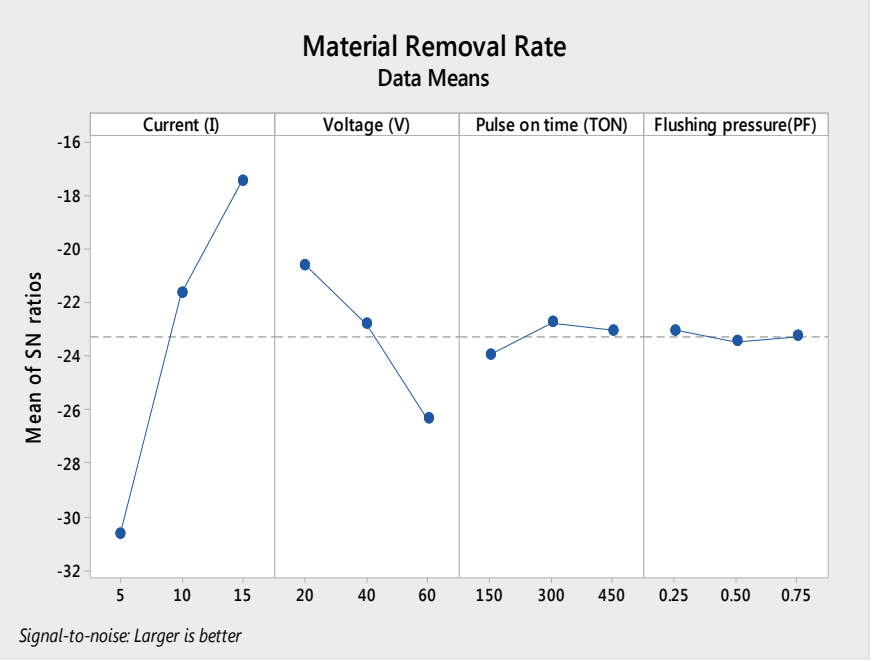

Fig. 3 Mean of SN ratio plot for MRR

result in increased MRR. The increase in I_p produces larger spark which creates a higher temperature in the workpiece, which causes large amount of material removal from the workpiece. MRR increases slightly and then decreases with rise in T_{ON}. Rise in T_{ON}, increases the supply of spark energy to the metal which result in increased MRR. The MRR increases with decreases in voltage.

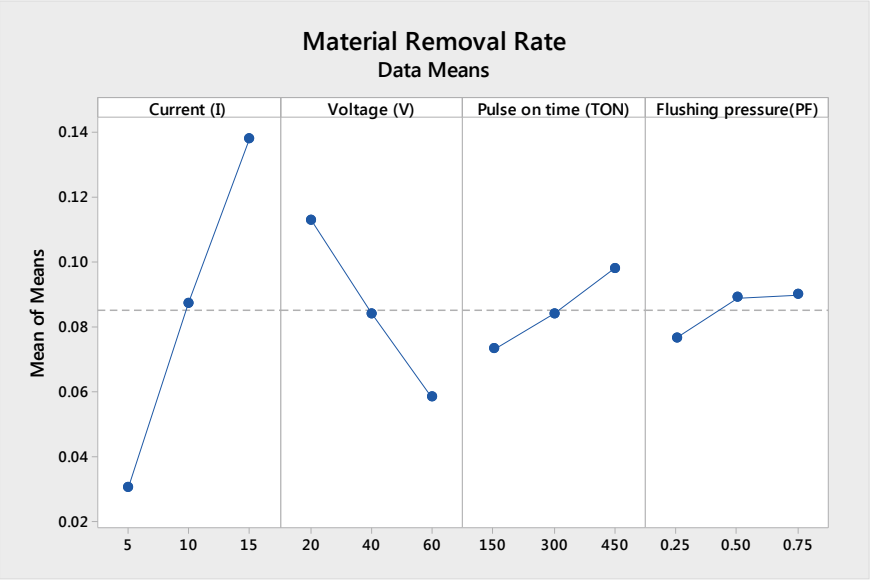

Fig. 4 Mean of means plot for MRR

3.2 Tool Wear Rate

The regression equation for TWR is shown in Eq. 2.

$$\text{TWR} = 0.00089 + 0.000227I + 0.000017V + 0.000008T_{\text{ON}} - 0.00213T_{\text{f}} \quad (2)$$

The R^2 value is 0.6792 for MRR which states that the model is 67.92% accomplished to predict the response value. The R^2 value is in better accord with the adjusted R^2 (0.3585). The ANOVA value obtained in minitab for TWR is shown in Table 3.

From Figs. 5 and 6, it is observed that increasing the current (I_{p}) from 5 to 15 A result in increased TWR. The increase in I_{p} produces larger spark which creates a

Table 3 ANOVA for TWR

Source	DF	Adj-SS	Adj-MS	*F*-value	*P*-value
Regression	4	0.000019	0.000005	2.12	0.243
I	1	0.000008	0.000008	3.36	0.141
V	1	0.000001	0.000001	0.29	0.619
T_{on}	1	0.000009	0.000009	4.08	0.113
T_{f}	1	0.000002	0.000002	0.74	0.437
Error	4	0.000009	0.000002		
Total	8	0.000029			

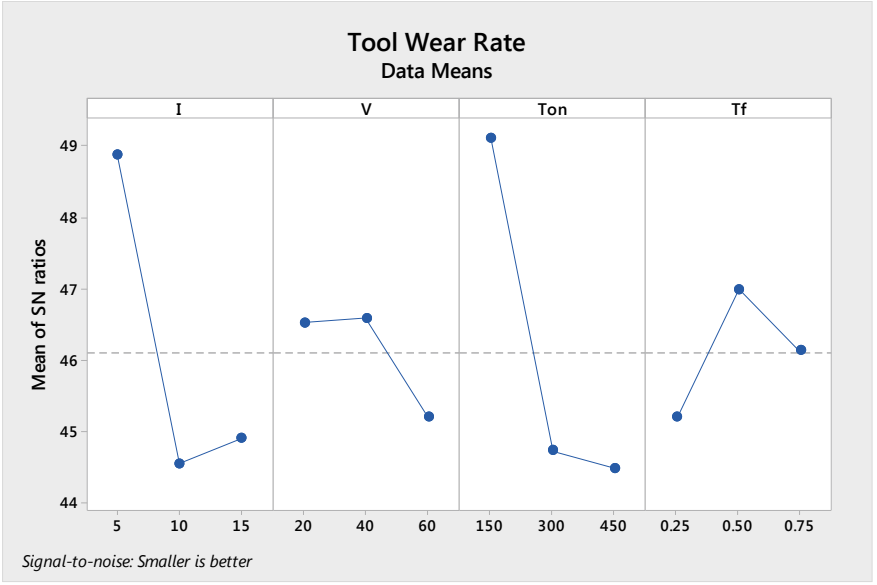

Fig. 5 Mean of SN ratio plot for TWR

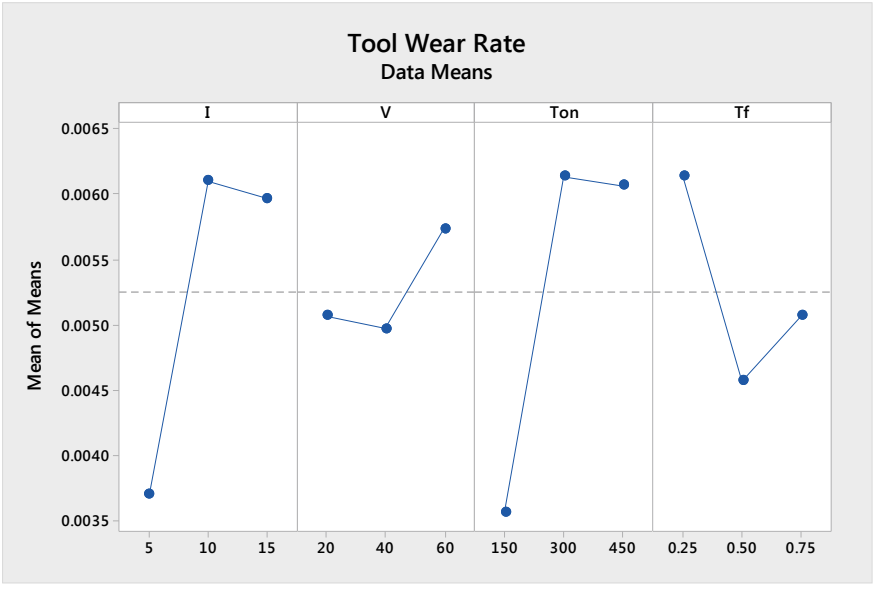

Fig. 6 Mean of means plot for TWR

Table 4 ANOVA for SR

Source	DF	Adj-SS	Adj-MS	*F*-value	*P*-value
Regression	4	4.4604	1.11511	11.36	0.019
I	1	2.3064	2.30640	23.49	0.008
V	1	0.1067	0.10667	1.09	0.356
T_{on}	1	1.9153	1.91535	19.51	0.012
T_f	1	0.1320	0.13202	1.34	0.311
Error	4	0.3928	0.09820		
Total	8	4.8532			

higher temperature in the tool, which causes large amount of material removal from the tool. TWR increases highly and then decreases with rise in T_{ON}. Rise in T_{ON}, increases the supply of spark energy to the metal which result in increased TWR. The TWR increases with increase in voltage.

3.3 Surface Roughness

The regression equation for SR is shown in Eq. 3.

$$SR = 4.544 + 0.1240I + 0.00667V + 0.003767T_{ON} - 0.593T_f \quad (3)$$

The R^2 value is 0.9191 for MRR which states that the model is 91.91% accomplished to predict the response value. The R^2 value is in better accord with the adjusted R^2 (0.8381). The ANOVA value obtained in minitab for SR is shown in Table 4.

From Figs. 7 and 8, it is observed that increasing the current (I_p) from 5 to 15 A and T_{ON} from 150 to 450 µs result in decreased SR. Increased T_{ON} generates more amount of discharge energy that creates the larger crater on the work surface result in poor surface finish. The SR increases with decreases in voltage.

3.4 Optimization

The optimized machining condition predicted for the minimum SR, minimum TWR, and maximum MRR is 6.14 µm, 0.0033 g/min, and 0.1159 g/min for a peak current (I) of 10 A, voltage (V) of 20 V, pulse-on time (T_{on}) of 150 µs, and flushing pressure (T_f) of 0.750 MPa (Fig. 9).

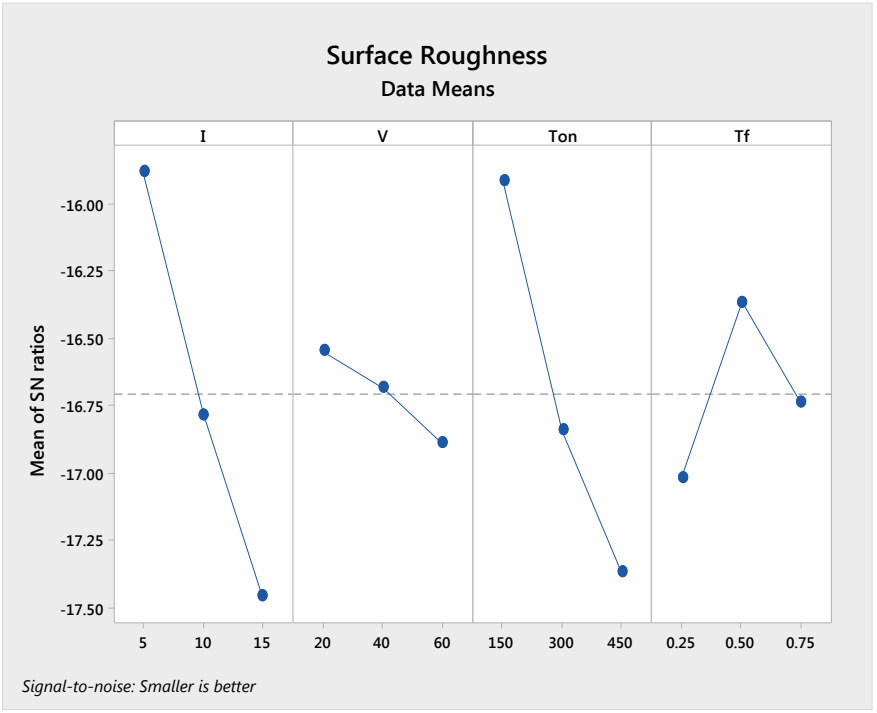

Fig. 7 Mean of SN ratio plot for SR

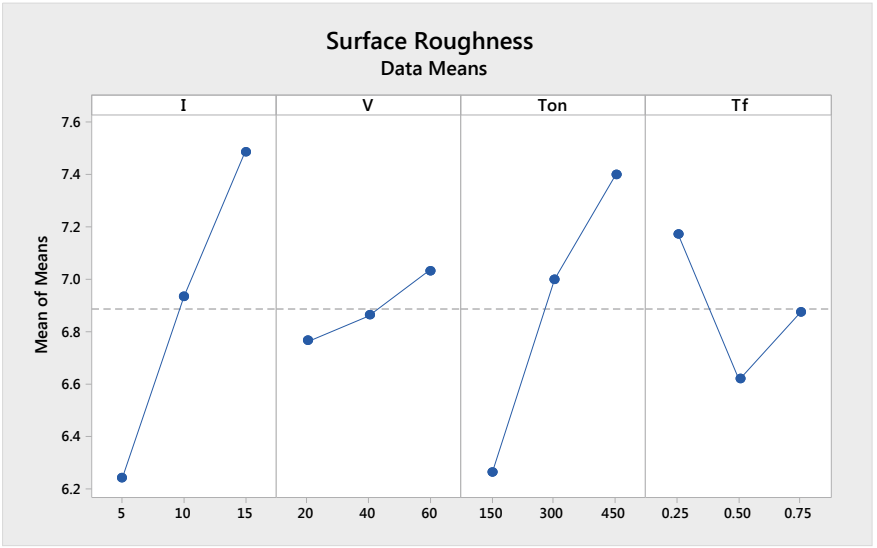

Fig. 8 Mean of means plot for SR

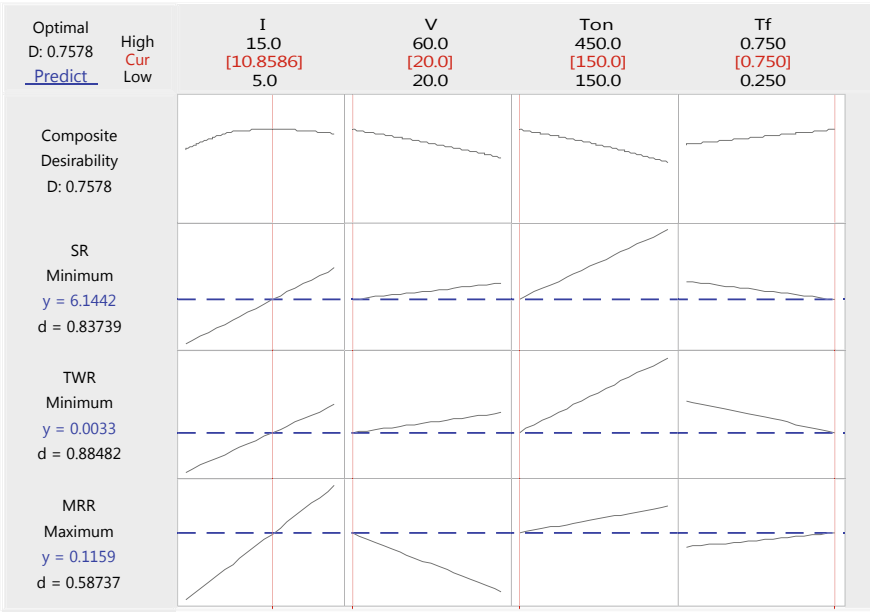

Fig. 9 Optimization plot

3.5 Optical Microscope

The optical microscope was used to carry out the microscopic analysis to observer the surface morphology of the machined surface. The microscopic images (about 50 μm) of the machined surface were shown in Fig. 10. The three image shows the presence of deposited distributed particles on the machined surface in different machined surfaces. Due to subsequent sparking, craters are formed on the deposited layer surface. This results in poor surface finish of the machined surface. The workpiece machined with less T_{on} produces a thin deposition with less roughness, but workpiece machined with high current and T_{on} results in deeper craters on surface. Hence, it can be accomplished that increase in peak current and T_{on} would deposit thicker layer with deeper craters.

4 Conclusion

In this work, the influence of EDM parameters of AA 6063 alloy on various output response variables such as surface roughness, material removal rate, and tool wear rate were found out. Electrodes made of brass with 2 mm diameter were used as tool and commercial EDM oil was selected as dielectric fluid.

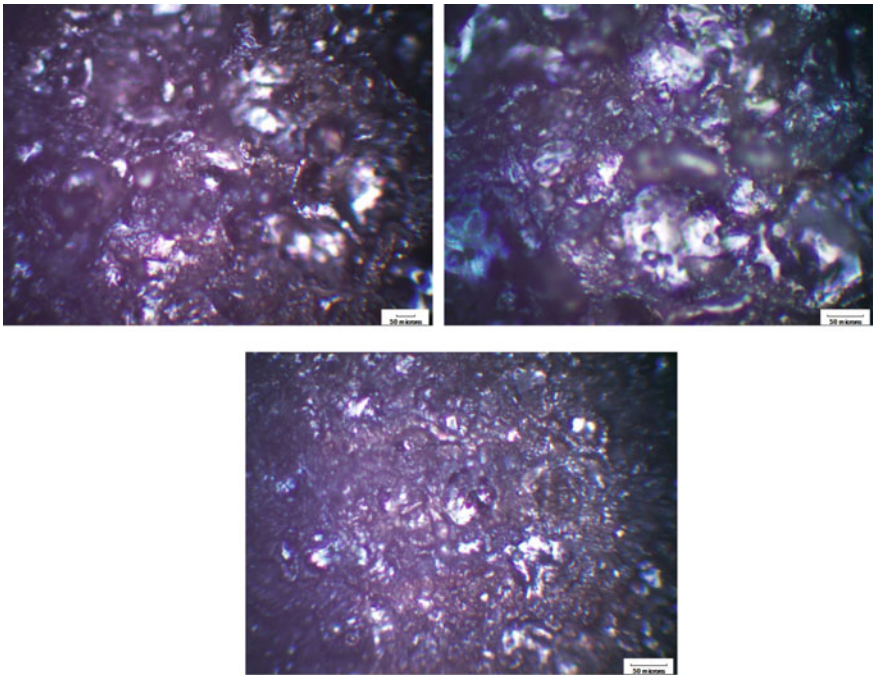

Fig. 10 Microscopic images of the machined surface (about 50 μm)

1. Increasing the current (I_p) result in increased MRR, TWR. The increase in I_p produces larger spark which creates a higher temperature in the workpiece, which causes large amount of material removal from the workpiece. MRR, TWR increases and then decreases with rise in T_{ON}.
2. Increasing the current (I_p) from 5 to 15 A and T_{ON} from 150 to 450 μs results in decreased SR. Increased T_{ON} generates more amount of discharge energy that creates the larger crater on the work surface result in poor surface finish. The SR increases with decreases in voltage.
3. The optimized machining condition predicted for the minimum SR, minimum TWR, and maximum MRR is 6.14 μm, 0.0033 g/min, and 0.1159 g/min for a peak current (I) of 10 A, voltage (V) of 20 V, pulse-on time (T_{on}) of 150 μs, and flushing pressure (T_f) of 0.750 MPa.

References

1. Chandramouli S, Eswaraiah K (2017) Optimization of EDM process parameters in machining of 17–4 PH steel using Taguchi method. Mat Today Proc 4:2040–2047

2. Rajmohan T, Prabhu R, Subba Rao G, Palanikumar K (2012) Optimization of machining parameters in electrical discharge machining (EDM) of 304 stainless steel. Procedia Eng 38:1030–1036
3. Das M, Rudrapati R, Ghosh N, Rathod L (2016) Input parameters optimization in EDM process using RSM and JAYA algorithm. Int J Curr Eng Technol 6:109–112
4. Selvarajan L, Sathiya Narayanan C, JeyaPaul R (2015) Optimization of EDM parameters on machining Si_3N_4-TiN composite for improving circularity, cylindricity and perpendicularity. Mat Manuf Proces 31(4):405–412
5. Kandpal BC, Kumar J, Singh H (2017) Optimization and characterization of EDM of AA 6061/10%Al_2O_3 AMMC using Taguchi's approach and utility concept. Prod Manuf Res 5(1):351–370
6. Krishnaraj V (2016) Optimization of process parameters in micro-EDM of Ti-6Al-4V alloy. J Manuf Sci Prod 16(1):1–9
7. Dewan PR, Lepcha LP, Khaling AN, Prasad N, Rai S (2018) Experimental analysis and optimization of EDM process parameters. IOP Conf Ser Mat Sci Eng 377(1):012220
8. Assarzadeh S, Ghoreishi M (2013) Statistical modeling and parametric optimization of process parameters in electro-discharge machining of cobalt-bonded tungsten carbide composite WC/6%Co. Elsevier Procedia CIRP 6:463–468
9. Daneshmand S, Kahrizi EF, Neyestanak AA, Ghahi MM (2013) Experimental investigation into EDM of NiTi SMA using rotational tool. Int J Electrochem Sci 8:7484–7497
10. Pradhan MK, Biswas CK (2009) Modeling and analysis of process parameters on surface roughness in EDM of AISI D2 tool steel by RSM approach. Int J Eng Appl Sci 5(5):346–351

Design and Analysis of 2D Steady Flow Over an Underwater Vehicle with Different Cavitators

D. Rohini, S. Vignesh, D. Nivitha, P. Preetha, and K. P. Arulshri

Abstract The concept of super-cavitation in the incompressible liquid flow has been analyzed and simulated using ANSYS Fluent. The work has been carried out by considering the high-speed flow of water over two-dimensional flows with different cavitators. The flow is said to be analyzed at three different angles, such as 6°, 12°, and 15°, and two different velocities, such as 55 and 60 m/s. The results obtained through the research work have been compared in order to ensure effective drag reduction. The drag force tends to originate in different forms through various sources. The hydrodyne drag is mainly caused by the viscosity of the medium as the molecules tend to move along the surface of the body. The most dominant drags, such as pressure and viscous, are said to be available in the body moving in water. In order to function effectively, the model should be designed for overcoming the drag. Thus, it becomes a stimulating task to design the competent models for vehicles, boat hulls, and underwater missiles. The influences of cavitator effect and speed of flow on the super-cavitation bubble have been investigated. The obtained results clearly depict that the drag tends to reduce at different velocities and angles.

Keywords Super-cavitation · Hydrodyne drag · Cavitator · ANSYS fluent · Underwater missile

D. Rohini (✉) · D. Nivitha · P. Preetha
Department of Aeronautical Engineering, Bannari Amman Institute of Technology, Sathyamangalam, Erode, Tamil Nadu 638401, India
e-mail: rohinidharmaraj90@gmail.com

S. Vignesh
Department of Mectronics Engineering, Bannari Amman Institute of Technology, Sathyamangalam, Erode, Tamil Nadu 638401, India

K. P. Arulshri
Department of Mechanical Engineering, Nehru Institute of Technology, Coimbatore, Tamil Nadu 641105, India

G. Kumaresan et al. (eds.), *Advances in Materials Research*, Springer Proceedings in Materials 5, https://doi.org/10.1007/978-981-15-8319-3_6

1 Introduction

Few decades back, the design of cavitator using super-cavitation phenomenon has been carried out by the computational fluid dynamic approach. The process mainly focuses on numerical analyses of supercavitation effect subjected to cross sections. This will show us the distribution of drag at which the flow passes over the cross section under different working conditions. The underwater missile has been designed using ANSYS Fluent. The process of meshing and analysis has been accomplished simultaneously. The vapor cavities will be generated if the pressure reduction appears in the fluid flow. This is a notable phenomenon found in many of the compressible flow of liquids [1]. Water is the fluid which has a special thermodynamic property where the phase changes would be observed in many experimental conditions. The damages caused due to the effect of water cavitation are said to be an undesirable condition. Also, the effect of cavitation effect plays a significant role in the field of engineering and industrial application to reduce the skin friction drag on the moving underwater body. When the sharp-edged solid body travels in water with maximum high speed, there envelopes cavitation vapor pockets with the overall body which causes a significant reduction in the skin friction drag [2]. In order to reduce the drag in a more effective manner, the variances in liquid and vapor viscosities are to be considered. Thus, it is clear that the stable super-cavitation can be attained through the velocity possessing maximum or minimum difference in pressure. The minimum difference in pressure can be acquired through the process of maximizing cavitation pressure [3].

2 Literature Review

Underwater vehicles like submarines and torpedoes are limited to high speed because of significant amount of drag produced on the hull skin due to friction. The concept of super-cavitation is a gaseous formation which envelops the whole body, as the atmospheric pressure falls lesser than the saturated vapor pressure. Skin drag is mostly neglected because the moving body throughout the length does not have any form of connection with the phases of liquid [4]. Supercavitation depends on the cavitation number and decreases the viscous drag on underwater bodies tremendously, especially at speeds above 50 m/s [5]. The two-stage Riemann solver (one-liquid strategy) is utilized for displaying the cavitation procedure with constant temperature and reliable condition of stage with the physical contact of the water. Hargrove [3] investigated the impact of the cavitator head and stream speed on the super-cavitation bubble. A rapid super-cavitating stream around a two-dimensional symmetric wedge-shaped cavitator was considered. The computational technique was utilized to check the stream over a hemispherical head was mimicked and approved against existing exploratory information [6].

The super-cavitating body is designed in such a way that it produces a cavitation bubble at the front part which prolong till the end of the body significantly reducing frictional drag on the skin [7]. An attribute of the super-cavitating object consists of a specially designed nose, normally flat shaped with a sharp edge streamlined body. Super-cavitating bodies can be achieved at very high speeds underwater because of reduced drag. The cavitation bubble is generated at the nose with proper design, and the friction on the skin is substantially reduced as the viscosity and density of the gas are remarkably lower than the seawater. If the body is designed suitably, the presence of pressure drag can be maintained at least level and the overall drag of the body tends to reduce. Super-cavitation usually occurs when the cavitation number tends to be less than 0.1. In general, the entire pressure field cannot be determined. Hence, the probability of the flow to cavitate can be determined [5]. Super-cavitation has been widely used in military purposes and high-performance racing boats. For instance, let us imagine a boat which moves through the water [8]. This uses super-cavitation principle where the formation of gaseous bubble layer around the hull reduces friction underwater. This will attain maximum speed at relatively low fuel cost.

3 Methodology

The ANSYS Fluent has been used to design the projectile with cone and disk cavitator. The domain is created, and the fine mesh is obtained through Gambit. The boundary conditions are fixed for the projectile which tends to carry out the steady flow analysis. The contour has been predicted, and the optimization of the cavitator has been carried out. The detailed steps are provided in Fig. 1.

4 Results and Discussion

4.1 Modeling

The model which has been taken into consideration in the present research is Varunastra Torpedo. The scaled model of the torpedo has been taken, in which, the disk diameter of nose of the section has been considered to be 1 mm, 2 mm with respect to the consideration of different cone angles. Torpedo's design is an emerging one in the research field due to its various advancement in the field of submarines. It is the most preferable torpedo due to their effectiveness when compared with others. The cone cavitator with a nose angle of 6° along with the projectile is shown in Fig. 2. The torpedo nose cone angle of 6° with the diameters 1 and 2 mm is shown in Figs. 3 and 4, respectively. Likewise, the design geometry has been created for torpedo nose cone angle 12° and 15° with the diameters 1 and 2 mm, respectively. In

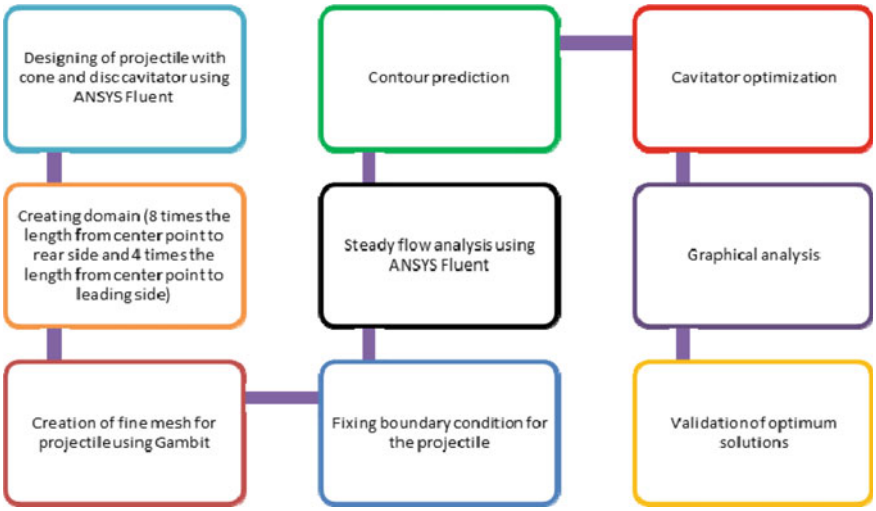

Fig. 1 Steps involved in the process of computational analysis of 2D flow over an underwater vehicle with different cavitators

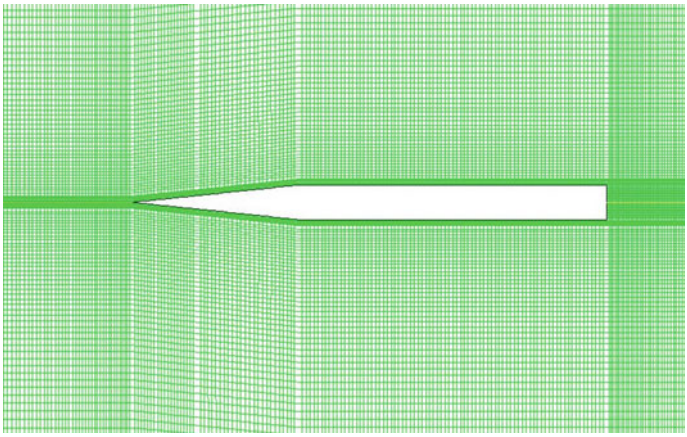

Fig. 2 Cone cavitator with projectile (Nose angle: 6°)

Figs. 2, 3, and 4, the scaled model of the varunastra torpedo is shown and the length of the macroscopic image is 63 mm.

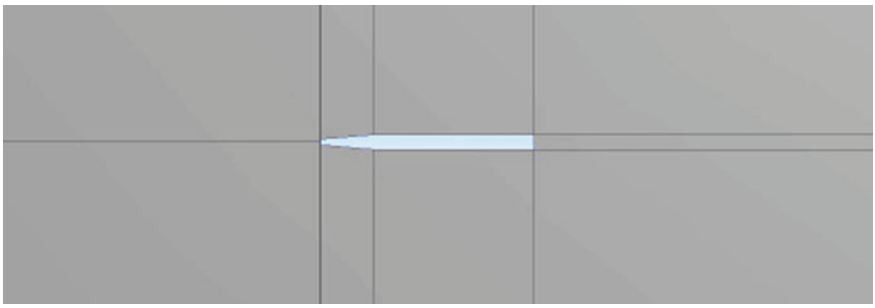

Fig. 3 Disk cavitator with projectile (Nose angle: 6°, disk diameter: 1 mm)

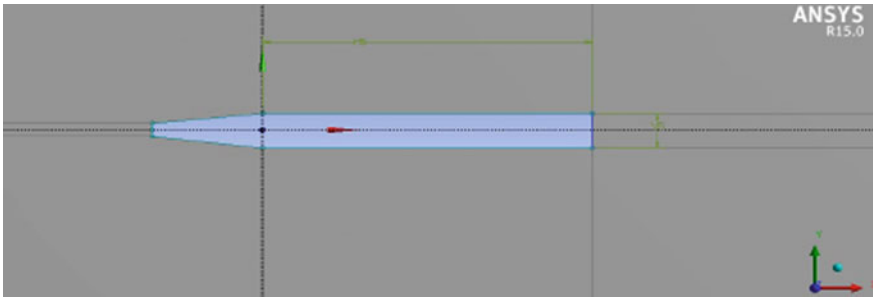

Fig. 4 Disk cavitator with projectile (Nose angle: 6°, disk diameter: 2 mm)

4.2 Meshing

An inflated boundary of the elements was utilized near cone surface in order to improve the spatial resolution and to gain better understanding of the boundary layer phenomenon. An unstructured mesh with quadrilateral elements was used for volume meshing. The simulations were carried out with cavitator model which has been coupled with a blend factor. The computational mesh was constructed automatically using quadrilateral cells, surrounded at the solid boundaries. The quadrilateral cells tend to fill space in a more efficient manner than other elements. The quadrilateral cell count is said to be 25,400. The mesh node is shown in Fig. 5. The flow parameters considered for the investigation are variation of drag force along the model, variation of pressure, velocity vectors, and variation of density. In Fig. 5, scaled model of varunastra is meshed and shown in (a) and the zoomed view of meshed model is shown in (b).

The boundary conditions such as inlet velocity and flow condition are fed in an appropriate manner. The flow conditions are assigned as 55 and 60 m/s. The pressure outlet condition is provided to the outlet and in the case of projectile (bullet), no-slip condition is raised. In the case of wall (upper and lower boundary condition), shear condition is raised. The solutions were obtained using the concept of PISO approach

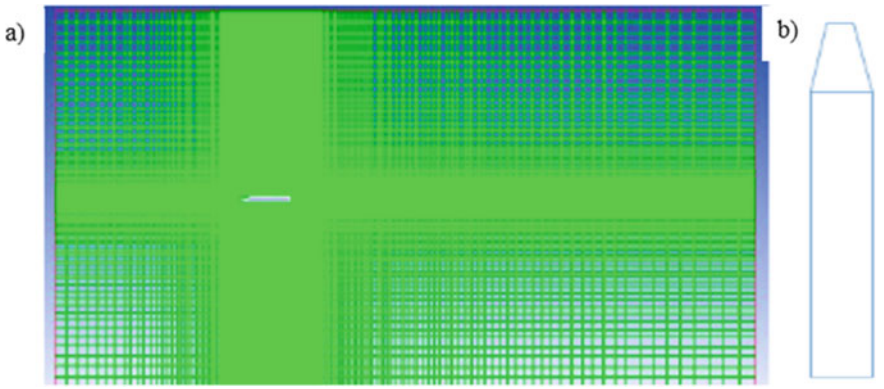

Fig. 5 **a** View of mesh visible around the object, **b** zoomed view of meshed model

as it is highly recommended for all the transient flow calculations. Basically, the K-epsilon specific feature model is based on the pressure analysis. The two phases such as 'water liquid' and 'water vapor' have been considered in the present analysis. However, the model undergoes the change from one phase to another (i.e., liquid to vapor). The changes in density from 'water' to 'water vapor' are limited within the range 1000–0.5542 kg/m^3.

4.3 Analysis of Projectile (Cone and Disk Cavitators)

The projectile is analyzed for the cone and disk cavitators, and the super cavity formation for the two cavitators with different nose angles and flow velocities are provided in Table 1. From Figs. 6, 7, 8, 9, 10, 11, 12, 13, 14, 15, 16, 17, 18, 19, 20 and 21, the variation of density in cavitator at different cone angle and at different velocity is shown. However, the variation of density contour plot is minimum only a small difference in the figure is visualized.

The plots for pressure and viscous drag between coefficient of drag and diameter of the cavitator have been shown in Figs. 22 and 23, respectively. It is evident that the total drag tends to decrease at the flow velocity of 55 m/s in cavitator disk of 1 mm at the nose angle of 6°.

5 Conclusion

In the present research, the drag force and variation of density along the surface of the model were analyzed clearly with various velocities such as 55 and 60 m/s along with various nose angles 6°, 12°, and 15°. There are about four parameters

Table 1 Details of the contour density analysis

Sl. No.	Contour	Type of cavitators	Nose angle (in degrees)	Flow velocity (in m/s)	Plot
1	Density	Cone	6	55	Figure 6
2		Cone	6	60	Figure 7
3		Disk (1 mm)	6	55	Figure 8
4		Disk (1 mm)	6	60	Figure 9
5		Disk (2 mm)	6	55	Figure 10
6		Disk (2 mm)	6	60	Figure 11
7		Cone	12	55	Figure 12
8		Cone	12	60	Figure 13
9		Disk (1 mm)	12	55	Figure 14
10		Disk (1 mm)	12	60	Figure 15
11		Disk (2 mm)	12	55	Figure 16
12		Disk (2 mm)	12	60	Figure 17
13		Cone	15	55	Figure 18
14		Cone	15	60	Figure 19
15		Disk (1 mm)	15	55	Figure 20
16		Disk (1 mm)	15	60	Figure 21
17		Disk (2 mm)	15	55	Figure 22
18		Disk (2 mm)	15	60	Figure 23

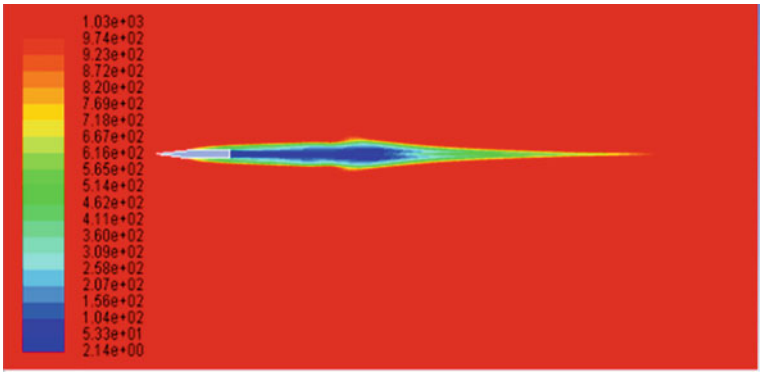

Fig. 6 Density contour for 6° cone cavitator at 55 m/s velocity

considered in the present investigation for designing the cone and disk cavitators. The computational processing has been carried out. The meshed geometry has been analyzed using the prescribed boundary conditions specified for ANSYS Fluent. The results obtained were found to be efficacious. The graph has been plotted showing the variation of flow parameters involved in the research. The analysis clearly indicates

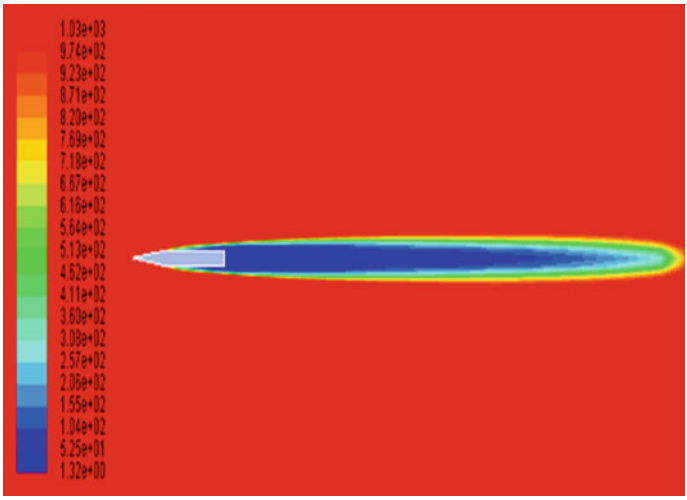

Fig. 7 Density contour for 6° cone cavitator at 60 m/s velocity

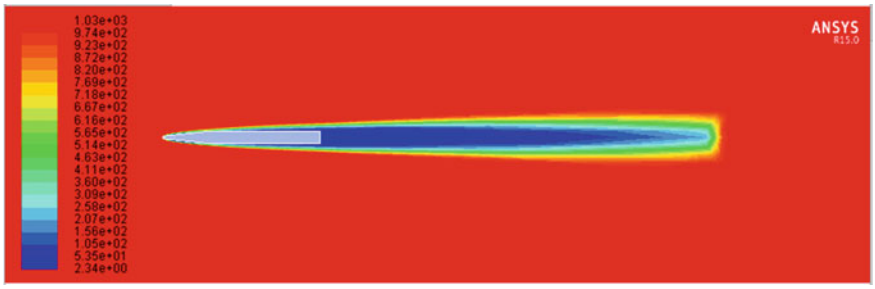

Fig. 8 Density contour for 6° with 1 mm cavitator disk 55 m/s velocity

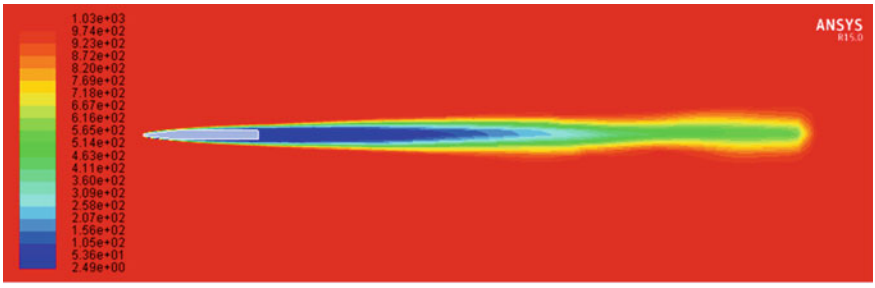

Fig. 9 Density contour for 6° with 1 mm cavitator disk 60 m/s velocity

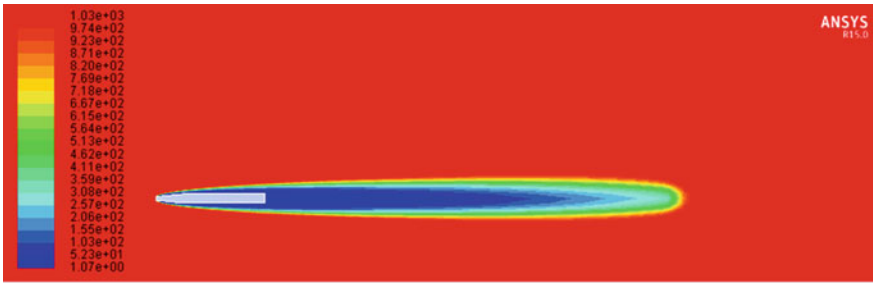

Fig. 10 Density contour for 6° with 2 mm cavitator disk 55 m/s velocity

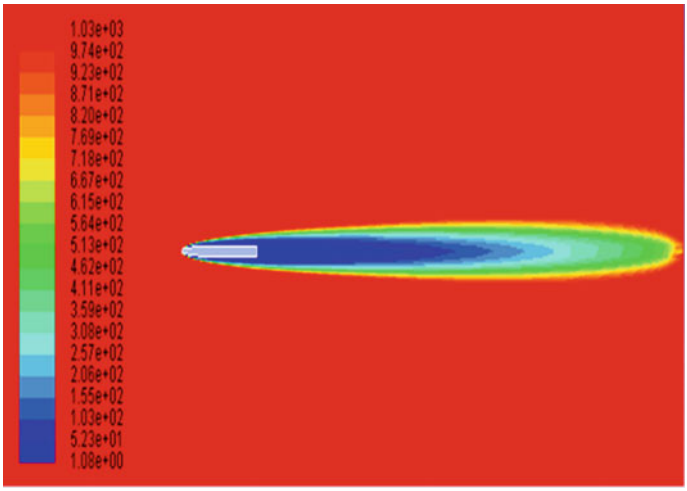

Fig. 11 Density contour for 6° with 2 mm cavitator disk 60 m/s velocity

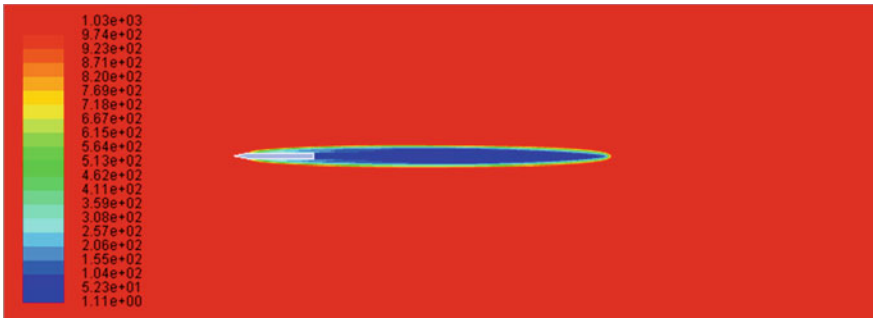

Fig. 12 Density contour for 12° cone cavitator at 55 m/s velocity

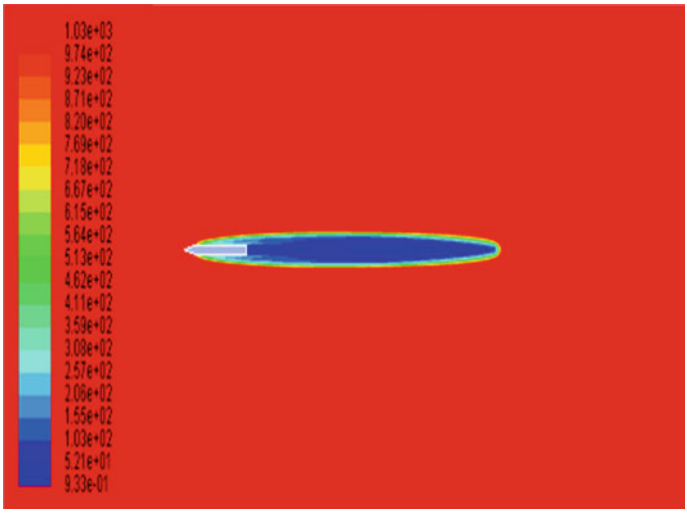

Fig. 13 Density contour for 12° cone cavitator 60 m/s velocity

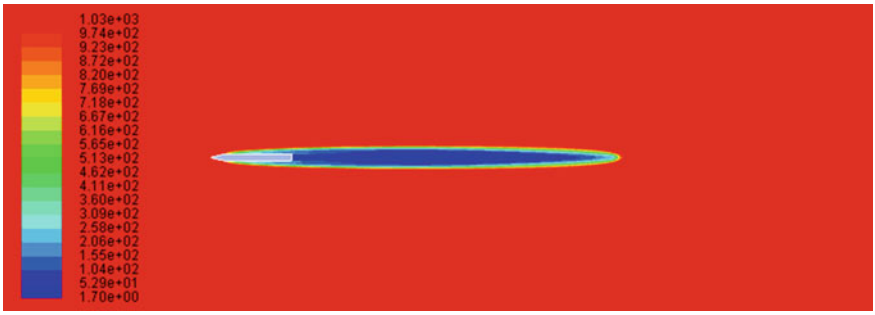

Fig. 14 Density contour for 12° with 1 mm cavitator disk 55 m/s velocity

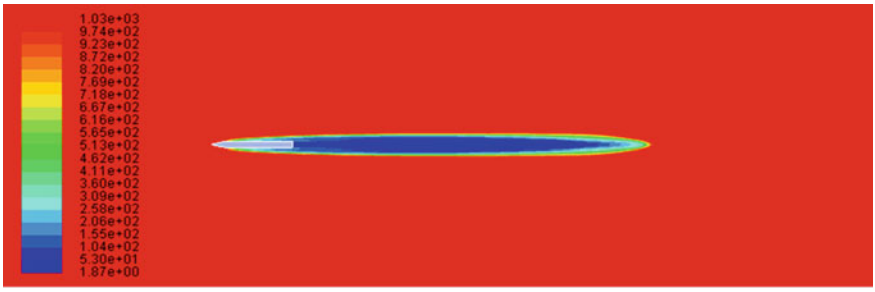

Fig. 15 Density contour for 12° with 1 mm cavitator disk 60 m/s velocity

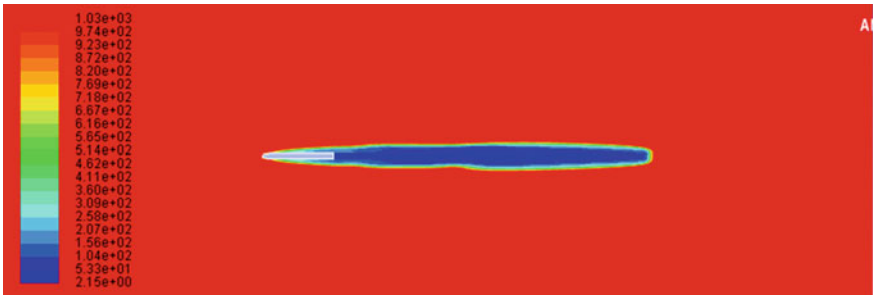

Fig. 16 Density contour for 12° with 2 mm cavitator disk at 55 m/s velocity

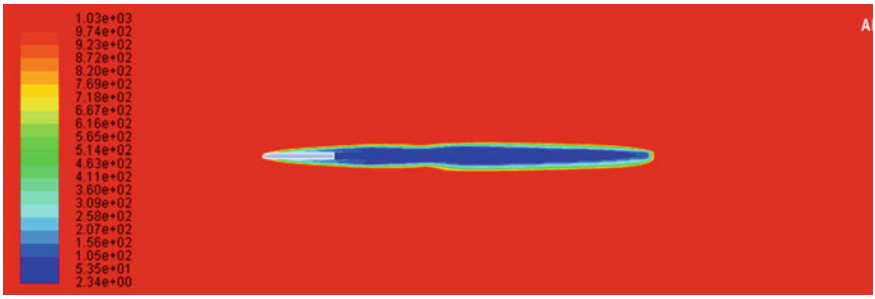

Fig. 17 Density contour for 12° with 2 mm cavitator disk 60 m/s velocity

Fig. 18 Density contour for 15° cone cavitator at 55 m/s velocity

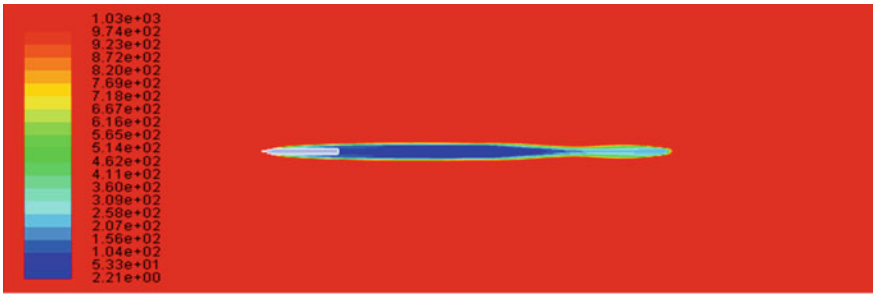

Fig. 19 Density contour for 15° cone cavitator at 60 m/s velocity

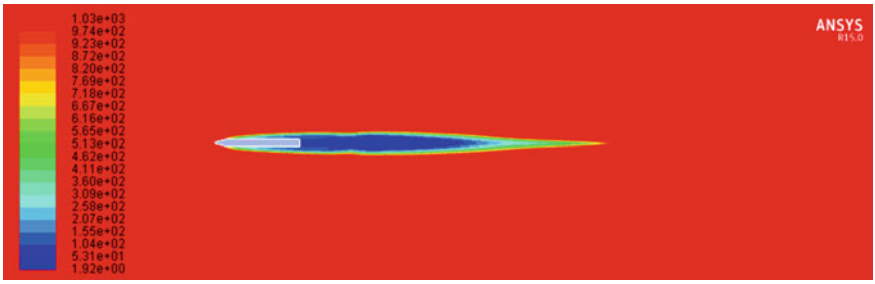

Fig. 20 Density contour for 15° with 1 mm cavitator disk at 55 m/s velocity

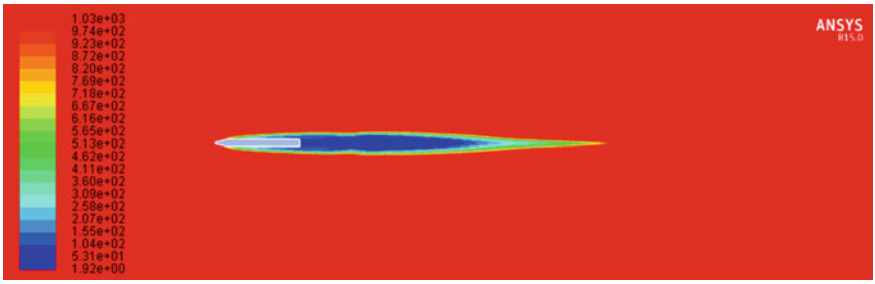

Fig. 21 Density contour for 15° with 1 mm cavitator disk at 55 m/s velocity

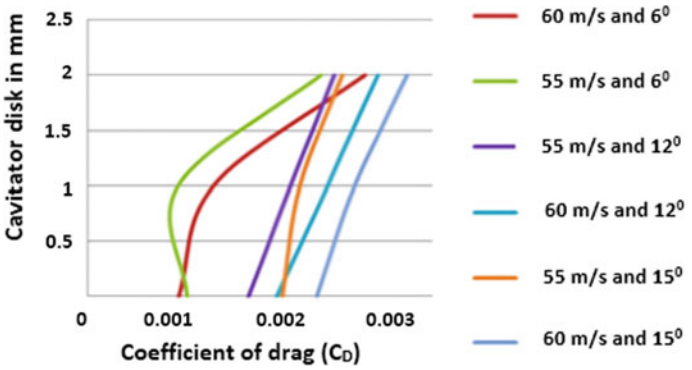

Fig. 22 Pressure drag for the model with different cavitators at various angles and velocities

that the diameter of cavitator tends to increase as the envelope gets enlarged. The aspect ratio of the model increases as the velocity tends to decrease in a gradual manner. Thus, the method would be capable of generating efficient model working for underwater missiles.

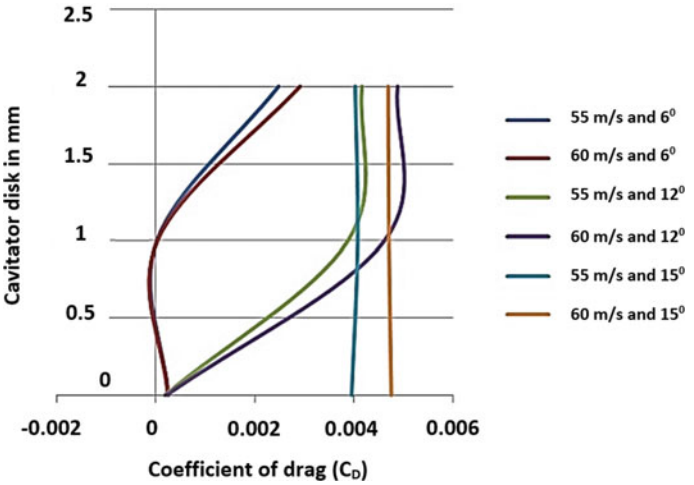

Fig. 23 Viscous drag for the model with different cavitators at various angles and velocities

References

1. Kwack YK, Ko SH (2013) Numerical analysis for supercavitating flows around axisymmetric cavitators. Int J Naval Archit Ocean Eng 5(3): 325–332
2. Choi JH, Penmetsa RC, Grandhi RV (2005) Shape optimization of the cavitator for a supercavitating torpedo. Struct Multidiscip Optim 29(2):159–167
3. Hargrove J (2004) Supercavitation and aerospace technology in the development of high-speed underwater vehicles. In: 42nd AIAA Aerospace Sciences Meeting and Exhibit 5–8 Jan 2004, Reno, Nevada AIAA 2004-130
4. Yang D, Xiong YL, Guo XF (2017) Drag reduction of a rapid vehicle in supercavitating flow. Int J Naval Archit. Ocean Eng **9**(1):35–44
5. Jafarian A, Pishevar A (2016) Numerical simulation of steady supercavitating flows. J Appl Fluid Mech 9(6):2981–2992. ISSN 1735-3572. EISSN 1735-3645
6. Cheng MA, Jia D, Qian Z, Feng D (2006) Study on cavitation flows of underwater vehicle. J Hydrodyn 18(supplement 1):365–369
7. Parka S, Rheeb SH (2012) Computational analysis of turbulent super-cavitating flow around a two-dimensional wedge-shaped cavitator geometry. Comput Fluids 70:73–85
8. Jiang J, Liu Z, Liu W, Zhou W (2009) Shape optimization of the cavitator for a supercavitating vehicle based on genetic algorithm. Published in 2009 International Conference of Information Engineering and Computer Science, print ISSN-2156-7379, electronic ISSN-2156-7387

Investigation of Drying Rate in Moringa Leaves Under Periodic and Continuous Airflow in Vacuum Condition

M. Ashok Kumar, G. Kumaresan, and S. Rajakarunakaran

Abstract In herbal powder manufacturing industries, drying herbal with less colour and nutrient loss is a challenging problem. Commercially, there are many methods that is being used for drying the leaves. Still, there are many problems encountered such as nutrient degradation, colour loss and power consumption. Drying leaves by dehumidified air is one of the promising methods to overcome the above issue. The dehumidified air passes to the drying chamber through two modes one by periodic and other by continuous. In this study, the adiabatic dehumidification system with the periodic flow and the heat pump dryer with the continuous flow is designed and developed to compare the performance of both modes of flow. The experimental study was carried out in Moringa leaves to compare the drying rate. The experiments were conducted in a vacuum drying chamber which is maintained at 0.9 and 0.8 bar in periodic flow and with the same pressure in closed-loop heat pump dryer with the continuous flow at the velocity of 1.1 m/s for the same capacity dehumidification system. At various periods, the drying rate is compared and the experiment result shows that under continuous mode with low pressure has a significantly higher drying rate than periodic mode with the same vacuum conditions.

Keywords Heat pump drying · Vacuum drying · Dehumidification drying · Leaf drying

1 Introduction

India is a country well rich in herbals and origin of Ayurveda, Siddha. Most of the Ayurvedic industries across India are facing problems in drying herbal leaves to

M. Ashok Kumar (✉) · S. Rajakarunakaran
Department of Mechanical Engineering, Ramco Institute of Technology, Rajapalayam, 626117 Tamil Nadu, India
e-mail: ashokkumar@ritrjpm.ac.in

G. Kumaresan
Department of Mechanical Engineering, Bannari Amman Institute of Technology, Sathyamangalam, Erode 638401, Tamil Nadu, India

G. Kumaresan et al. (eds.), *Advances in Materials Research*, Springer Proceedings in Materials 5, https://doi.org/10.1007/978-981-15-8319-3_7

extract powder to produce medicines. The high-temperature drying process degrades the quality of the products. High power consumption of the drying process leads to the high cost of drying and consequently increases the price of the product. Nutrients degradation, colour loses and high power consumption are major problems which are encountered by most of the herbal industries. Evolution of science and technology has identified some techniques such as sun drying, freeze-drying, microwave drying, infrared drying, lyophilization to dry the leaves quickly by using thermal energy in different forms. But the use of thermal energy drastically deteriorates the herbal quality of leaves.

In the progressive drying process like forced convection drying, drying by chemical, microwave drying with vacuum condition, batch fixed bed drying, continuous fluidized bed drying and heat pump drying, the better drying rate is achieved without conceding the quality such as nutrient content and colour of the herbal leaves [1]. Drying the clothes by heat pump dryer with relative humidity (RH) of 10% of dehumidified air significantly reduced the thermoelectric power consumption and the drying period [2]. The mathematical model for a heat pump dryer was developed for drying aromatic plant and the simulated result agreed well with the experimental results. The results indicate that at an average drying temperature of 36.84 °C with a relative humidity of 20% conditioned dehumidified air takes 89 h to reduce the moisture content of valerian roots from 89 to 9% [3]. Drying characteristic of nettle and mint was investigated experimentally in heat pump drier at 35 °C with RH 40%, increasing flow velocity from 0.2 to 0.6 m/s is reducing the drying period by 6.9%. The drying time reduced by 41.6% for nettle leaves and 37.5% for mint leaves at the average drying temperature of 35 °C with velocity 0.2 m/s, reducing the RH from 70 to 40% [4]. The influence of air velocity and air temperature in drying process was investigated; increasing the air temperature and air velocity leads to high evaporation rate; and in this study, it is observed that the effect of temperature is less significant at high temperature, and also, the evaporation rate gets reduced over the period because of the moisture content present in the leaves is low [5]. The performance of a vacuum heat pump dryer with different temperature and pressure conditions is investigated, and the results show that the drying rate is significantly increased with increasing the drying temperature and by reducing the pressure. However, the drying pressure is not influenced more as strong as the drying temperature [6]. The leaves are rich in macronutrients, and micronutrients Moringa oleifera hold its nutrient quality in the drying process while the drying temperature does not exceed 50 °C [7]. The drying kinetics and colour of Moringa leaves at three different temperature 40, 50, and 60 °C were examined, and the result insisted that the drying temperature decreases drying time and 50 °C is an optimum operating temperature at which the degradation of moisture ratio has been better in quality in terms of nutrient content present in the leaves and colour [8].

The drying rate of the eggplant is increasing with the increase in moisture content present in plant, and at vacuum drying condition, the moisture removal rate (MRR) increases linearly with increasing the operating temperature. The effect of moisture diffusivity of the eggplant samples within a moisture ratio range from 1 to 0.35 varied from 1.653×10^{-9} to 3.417×10^{-9} m^2/s according to the drying condition [9].

The heat and mass coupling transfer model was developed and concluded that the moisture content in the wood, and drying rate is decreased with increasing the drying time at a vacuum condition and also the total coefficient of diffusivity decreases with increases of drying time [10]. The mathematical model was developed for combined far-infrared and vacuum drying for the banana slice and the developed model predict adequately in changes of the moisture content [11]. The aim of this study is observing and comparing the effect of the drying rate of Moringa leaves under vacuum conditions in the periodic and continuous flow of dehumidified air.

2 Materials and Methods

2.1 Materials

Moringa leaves were taken as herbal leaves for this experimental study. The leaves were purchased from the local market where the farmers directly sell their products to the consumers. The leaves were selected for this experiment based on size and colour.

2.2 Sample Preparation

The stem-free Moringa leaves without any foreign particles like mud and sand were prepared by cleaning with pure water, and it is covered by moisture absorption paper for 3 min two times to remove water content present in the leaves during cleaning. The 500 g of the sample was prepared whenever it is required to avoid the natural drying.

2.3 Design and Development of Experimental Device

2.3.1 Design

Two experimental set-ups were designed and developed.

1. Adiabatic dehumidification system for conducting the experiment in periodic mode—The schematic diagram is shown in Figs. 1 and 2. Closed-loop heat pump dryer for conducting the experiment in continuous mode—The schematic diagram is shown in Fig. 2.

A 20-L per 24 h capacity dehumidifier was used in both the adiabatic dehumidification system and in heat pump dryer. The working fluid in both systems was R134a. The vacuum is generated in both a system by vacuum pump with a capacity of 2

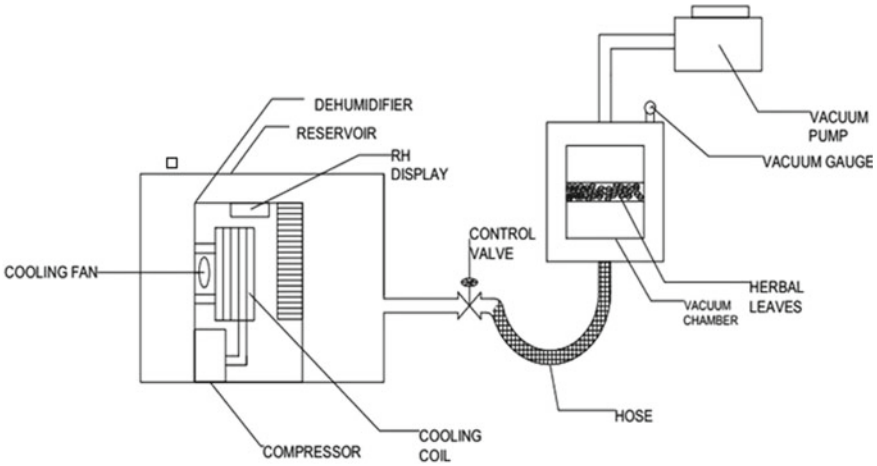

Fig. 1 Adiabatic dehumidification system (periodic flow)

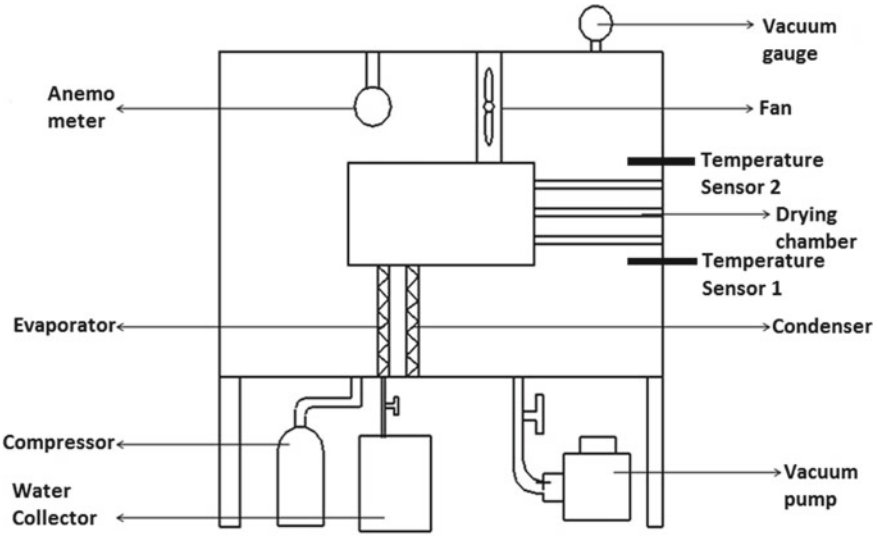

Fig. 2 Heat pump dryer (continuous mode)

CFM (cubic feet per minute). A model heat pump dryer was designed and built with dimensions 0.9 m × 0.6 m × 0.34 m with a drying chamber volume of 0.023m^3 and a fan with a capacity of 163 m^3/h is installed.

Both experimental setups were completely fabricated with a 5-mm-thick steel sheet. Specifications of measuring instruments used in both experimental set-ups are given below:

Thermocouple: K-type thermocouple.

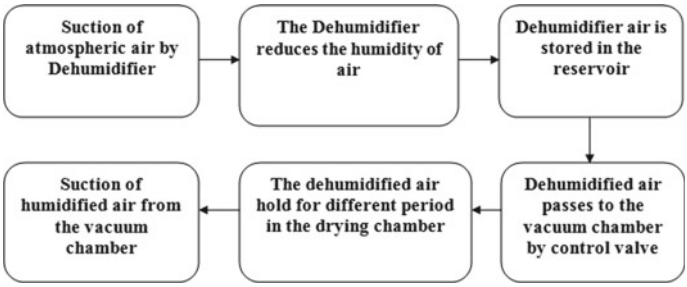

Fig. 3 Process flow diagram—periodic flow

Anemometer: 0.1–5 m/s.
Vacuum gauge: 0–760 mm of Mercury.

2.3.2 Operation

Adiabatic Dehumidification System-Periodic Flow

The adiabatic dehumidification system has been involved in two drying techniques such as vacuum drying and dehumidified air drying. Under vacuum pressure, the corresponding saturation temperature of the moisture decreases so evaporation can take place at atmospheric temperature itself. In this condition, moisture content present in the leaves pull out from the leaves and it came to the surface of the leaves. During vacuum drying, boiling of water occurs in the pores of leaves even at low temperatures and the drying rate decreases compared to the open sun drying method. The leaves to be dried are placed in the tray which has been placed in the vacuum chamber where the pressure (0.9 and 0.8 bar) is maintained by 2 CFM vacuum pump. The dehumidified air that is derived from the dehumidification chamber is sent to the drying chamber where the low relative humidity air at vacuum pressure starts to absorb the moisture and drying in happening. The process flow diagram is given in Fig. 3.

Heat Pump Dryer—Continuous Flow

This device has been involved in two drying techniques like in the adiabatic dehumidification system. To circulate the air at 1.1 m/s, the fan is mounted in the dryer. During the continuous circulation of air, the cooling and dehumidification process has occurred in the evaporator. The air comes out from the evaporator which is at 100% RH. The relative humidity air is then reduced by the heat released from the condenser during continuous circulation. The air temperature higher than 50 °C in the drying chamber leads to phytochemical and colour lose, and it can be avoided

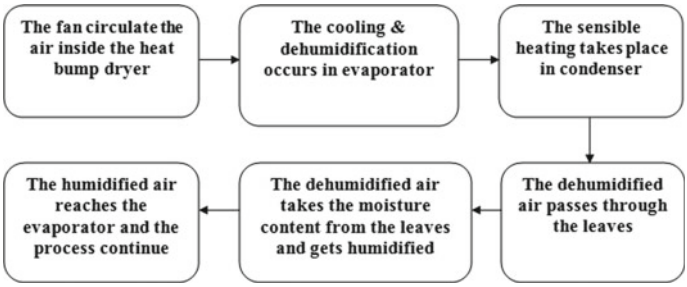

Fig. 4 Process flow diagram—continous flow

by increasing the velocity of air by which the temperature can maintain at required level. The process flow diagram is given in Fig. 4.

2.4 Methods

Unfavourable losses in nutrient in the object may lead to a decrease in quality. The predominant parameter causes for a loss in phytochemical and nutrients of leaves is the drying temperature. The optimal drying temperature for Moringa leaves is 50 °C [12]. At the pressure, lower than atmosphere the corresponding saturation temperature of the moisture gets reduced. So the rate of evaporation increased significantly at vacuum conditions [13]. To improve evaporation rate, the vacuum was introduced in both drying process and the temperature which is controlled by controlling the velocity of air. Thus, the experiment was conducted in both experimental setup with the pressures of 0.8 and 0.9 bar. For each drying 500 g of Moringa leaves were tested in the period of 30 min. The temperature readings before and after the drying chamber were taken for every minute, and the mass of dried leaves was measured every five minutes. The operational flowchart for heat pump drying-continuous is shown in Fig. 5.

2.4.1 Evaporation Rate

The initial moisture content of Moring leaves is 81% as per the Association of Official Analytical Chemists (AOAC). The leaves' weight was measured as quickly as possible to avoid further mass transfer between leaves and atmospheric air (less than 30 s). The evaporation rate is calculated by the following equation [14].

$$\dot{m}_{\mathrm{ev}} = \frac{m_{\mathrm{t}} - m_{\mathrm{f}}}{t} \tag{1}$$

where

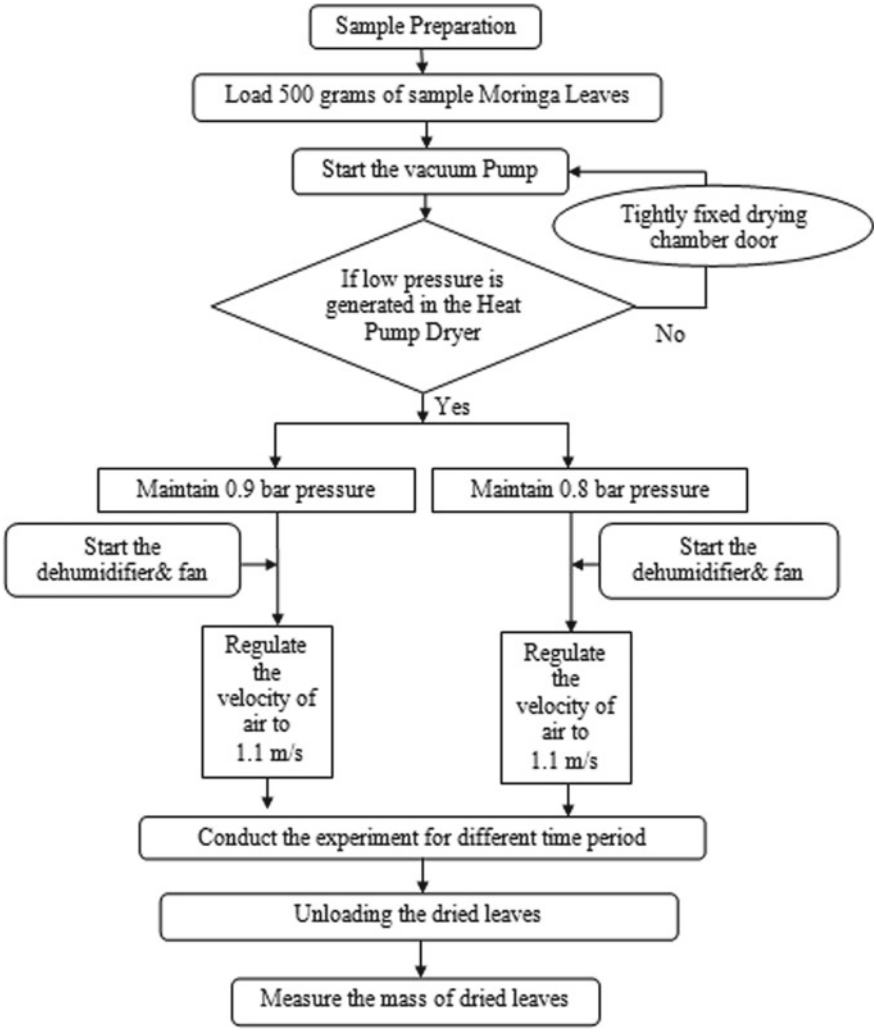

Fig. 5 Operational flowchart for continuous flow

m_t is the mass of leaves before drying process in grams.
m_f is the mass of leaves after drying process in grams.
t is the drying time in seconds.

2.4.2 Moisture Ratio

During drying, the moisture content of the leaves at any time can be calculated with moisture ratio. Moisture ratio relates the initial moisture content, equilibrium

moisture content, and the moisture content to be achieved after a certain period of drying. Moisture ratio (MR) expressed as [12].

$$\mathrm{MR} = \frac{M - M_\mathrm{e}}{M_\mathrm{i} - M_\mathrm{e}} \tag{2}$$

where M is the moisture content of the product at any time.

t in kg water/kg dry solid, M_e is the equilibrium moisture content of the product in kg water/kg dry solid and M_i is its initial moisture content.

Equilibrium moisture content can be calculated with the aid of Hailwood–Horrobin equation [15].

$$M_\mathrm{e} = \frac{1800}{w}\left[\frac{kh}{1-kh} + \frac{k_1 kh + 2k_1 k_2 k^2 h^2}{1 + k_1 kh + k_1 k_2 k^2 h^2}\right] \tag{3}$$

where w, k, k_1, k_2 are constant, and h is relative humidity (RH) of air. The constants can be calculated by using the following expressions:

$$w = 330 + 0.452T + 0.00415T^2 \tag{4}$$

$$k = 0.791 + 4.63 \times 10^{-4}T - 8.44 \times 10^{-7}T^2 \tag{5}$$

$$k_1 = 6.34 + 7.75 \times 10^{-4}T - 9.35 \times 10^{-5}T^2 \tag{6}$$

$$k_2 = 1.09 + 2.84 \times 10^{-2}T - 8.44 \times 10^{-7}T^2 \tag{7}$$

where T is the temperature of the air in °C.

3 Result and Discussion

3.1 Effect of Temperature at 0.9 and 0.8 bar

The experiment was conducted for various periods from 5 to 30 min in both periodic flow and continuous flow. The variance in temperature at 0.9 bar and 0.8 bar is shown in Fig. 6. The temperature of the air during the drying process in periodic flow is decreased from 48 to 32.7 °C at 0.9 bar starting pressure, and the temperature of the air decreases from 48 to 31.2 °C for the starting pressure of 0.8 bar. However, in continuous mode, the temperature is increased continuously from 34.1 to 46.9 °C at 0.9 bar and from 32.3 to 43.3 °C at 0.9 bar.

Temperature is a predominant parameter that influenced more in the moisture removal rate (MRR). A higher in temperature leads to an increase in MRR and

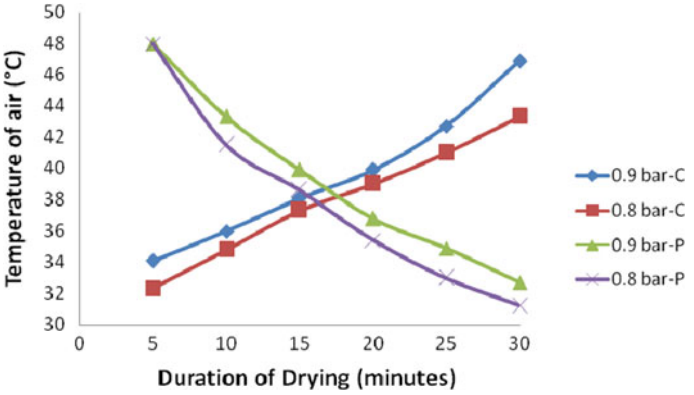

Fig. 6 Change in temperature with respect to time

reducing the drying time. At the starting time of drying, the moisture present in the leaves will be higher and the moisture present in the dehumidified air will be lower. So the density difference is higher at the initial period, it leads to a higher drying rate.

In the case of periodic flow, the temperature is decreasing for time and also the density difference of moisture between leaves and air is reduced. So it is concluded from the graph and discussion, both the temperature and density differences which are directly proportional to the moisture removal rate are decreased. Meanwhile, in continuous flow (heat pump dryer), the temperature of the air is increasing with respect to time and also the density difference of moisture between leaves and dehumidified air is reduced but a decrease in density difference is lower compare to periodic flow. So it is concluded that from the graph and discussion the temperature is increased and the density difference is decreased lower than periodic flow in closed-loop continuous flow heat pump dryer.

3.2 Effect of Periodic Flow and Continuous Flow in Evaporation Rate

The evaporation rate with respect to time in periodic flow and in continuous flow is given in Fig. 7.

It is clear from the graph that the evaporation rate is decreased exponentially in the case of periodic flow and increasing continuously in the case of continuous flow. The average evaporation rate in periodic flow at 0.9 bar is 75.67 g/h and at 0.8 bar is 81.5 g/h. From this value, it can be concluded that the vacuum plays a vital role in the evaporation rate. The average evaporation rate is increased by 5.83 g/h by decreasing the operating pressure by 0.1 bar. At the same time, the average evaporation rate in continuous flow at 0.9 bar is 88.28 g/h and at 0.8 bar is 108.5 g/h. The evaporation

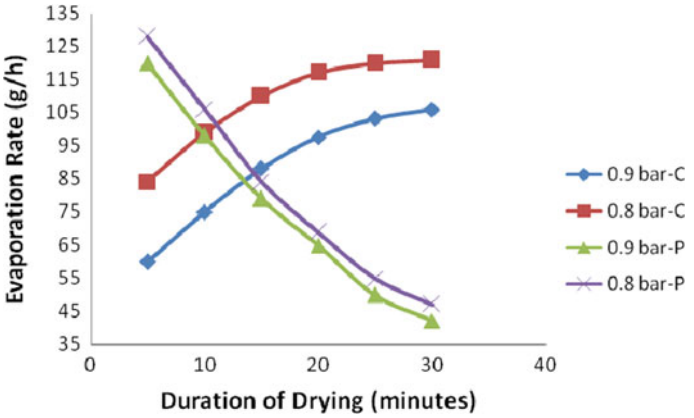

Fig. 7 Change in evaporation rate with respect to time

rate is increased by 20.22 g/h by decreasing the pressure by 0.1 bar. It is proved that in continuous flow, the role of pressure is higher than the periodic flow.

4 Conclusion

An adiabatic dehumidification system and a heat pump dryer working on vacuum pressure have been developed to dry the Moringa leaves. The influence of periodic and continuous flow with a vacuum drying chamber was examined. The experimental result shows that the drying rate was significantly increased by introducing a vacuum in periodic and continuous flow. The evaporation rate is increased by 7.15% by changing the flow from periodic to continuous at 0.9 bar pressure and 18.63% by flow changing at 0.8 bar. Totally, the evaporation rate has increased by 30.25% by introducing continuous flow at low pressure in the dehumidification drying process. The investigation of this study is also concluding that the drying rate is increased with an increase in temperature of approximately linear. The dehumidification process under vacuum condition along with the continuous flow is a promising technique to increase the drying rate and reducing the drying time significantly.

Acknowledgements The authors sincerely thank the Department of Science and Technology (DST), Government of India, for providing a financial grant (F.No. DST/SSTP/2018/161(C)) for this work under the scheme of State Science and Technology Programme (SSTP).

References

1. Babu AK, Kumaresan G, Antony Aroul Raj V, Velraj R (2018) Review of leaf drying: Mechanism and influencing parameters, drying methods, nutrient preservation, and mathematical models. Renew Sustain Energy Rev 90:536–556
2. Patel VK, Kyle R, Gluesenkamp DG, Gehl A (2018) Experimental evaluation and thermodynamic system modeling of thermoelectric heat pump clothes dryer. Appl Energy 217:221–232
3. Hossain MA, Gottschalk K, Hassan MS (2013) Mathematical model for a heat pump dryer for aromatic plant. In: Procedia engineering, 5th BSME international conference on thermal engineering, vol 56, pp 510–520
4. Kaya A, Aydin O (2009) An experimental study on drying kinetics of some herbal leaves. Energy Conserv Manag 50:118–124
5. Putra RN, Ajiwiguna TA (2017) Influence of air temperature and velocity for drying process. In: Engineering physics international conference, EPIC, pp 516–519
6. Artnaseaw A, Theerakulpisut S, Benjapiyaporn C (2010) Drying characteristics of Shiitake mushroom and Jinda chili during vacuum heat pump drying. Food Bioprod Process 88:105–114
7. Alakali JS, Kucha CT, Rabiu IA (2015a) Effect of drying temperature on the nutritional quallity of Moringa oleifera leaves. African J Food Sci 9(7):395–399
8. Ali MA, Yusof YA, Chin NL, Ibrahim MN, Basra SMA (2014) Drying kinetics and colour analysis of *Moringa oleifera* leaves. In: Agriculture and agricultural science Procedia, 2nd international conference on agricultural and food engineering, vol 2, pp 394–400
9. Long Wu, Orikasa T, Ogawa Y, Tagawa A (2007) Vacumm drying characteristics of eggplants. J Food Eng 83:422–429
10. He Z, Qian J, Lijie Qu, Wang Z, Yi S (2019) Simulation of moisture transfer during wood vacuum drying. Results Phys 12:1299–1303
11. Swasdisevi T, Devahastin S, Sa-Adchom P, Soponronnarit S (2009) Mathematical modeling of combined far-infrared and vacuum drying banana slice. J Food Eng 92:100–106
12. Alakali JS, Kucha CT, Rabiu IA (2015b) Effect of drying temperature on the nutritional quallity of *Moringa oleifera* leaves. Afr J Food Sci 9(7):395–399
13. Thirunanasambandham K, Sivakumar V (2016) Enhancement of shelf life of *Coriandrum sativam* leaves using vacuum drying process: modeling and optimization. J Saudi Soc Agricult Sci 15:195–201
14. Putra RN, Ajiwiguna TA (2017) Influence of air temperature and velocity for drying process. In: Engineering physics international conference EPIC, pp 516–519
15. Kukule A, Rocens K, Lukasenoks A, Frolovs G (2017) Change of moisture distribution in ribbed plate with different opposite surface temperatures. Modern Build Mater Stuct Tech Procedia Eng 172:612–619

Patient Medicine Reminder System

M. Neela Harish

Abstract Automatic reminder for medicine is useful to all patients. Nowadays, specialist care of subjects is very judgmental. Regular checkup by the medical practitioner suggests correct dose at regular time intervals. At several circumstances, patient's antibiotics were not taken at regular and correct dosages. In this paper, a patient medicine reminder system is introduced. This system can be customized through keyboard input depending upon the dosage, name of medicine and intervals. In the LCD, display of the uploaded prescription of patients is as per timing, and dosage of each tablet can be viewed. Thus, the heath of patients is controlled regularly by doctors. This is implemented using Unified Technology Learning Platform.

Keywords UTLP kit · OMAP 3530 processor · ULK · Eclipse · Character LCD · Graphics LCD · Keyboard · Touch panel

1 Introduction

Health care and pharmaceutical play a vital role in emergency situations or centers such as the Intensive Care Unit (ICU) and Surgical Intensive Care Unit (SICU). The main aim is to keep track over the heath of the patient throughout the day without making them staying in hospital. Modern solutions are employed as solutions to the abovementioned proposals. But the main challenges in this are staff of centers and their record maintenance to enhance the patient's drug delivery system. It may be helpful for research institutions, health software managements and NGOs for medical administration. This system has been implemented at various rural and urban hospital centers and to improve reminder-based medication for each patient [1].

Abbey et al. [2] described the importance of medication adherence with instruments of purpose of alerting on a timely basis the dosage intake and medical records. The software uses a medication box which is processed as a web-based module

M. N. Harish (✉)
Department of Biomedical Engineering, Rajalakshmi Engineering College, Thandalam, Tamil Nadu 602105, India
e-mail: neelamadhu_psbb@yahoo.co.in

G. Kumaresan et al. (eds.), *Advances in Materials Research*, Springer Proceedings in Materials 5, https://doi.org/10.1007/978-981-15-8319-3_8

through mobile customized for each patient needs. IT provides continuous data about the patient as per the executed code. The GUI interface with each doctor and patient link established displays the daily dosage, pills and their corresponding timings.

Dalgaard et al. [3] described a Med iFrame: a android-based application to alert, recall and maintain elderly patient's health condition. As elderly people are left alone at home, they face difficulties to inform hospitals in case of any emergency situations arise when their health deteriorates suddenly. Med iFrame is a private pill reminder application to aid elderly people at non-clinical environment.

DeMeo et al. [4] described the pill-taking process using a smart system. Physician can abidance by a not wired and power-efficient drug delivery model. By this model, a solution to a never-ending problem to patient monitoring has been initiated. It demonstrates a real-world solution using a bottle with advanced pill detection and wireless connectivity to a cloud infrastructure. The infrastructure aggregates the information and reminds patients to take their medication at appropriate times.

Finite element (FE) analysis [5] has been made at four different locations to study the temperature distribution and determine the microstructure of the metal plate. Also sudden cooling done to the electron beam allows the development of dendrites, which makes the structure visible. The multi-parameter model is designed at different stages of manufacturing with goals such as to reduce the cost. Give prior to worst probabilities and achieve highest customer needs. Three stages of production are developed using a two-stage stochastic prototype [6]. The dynamometer is fixed with stress gauge and cylindrical bar [7] to achieve higher sensitivity and decrease cross-interference. AISI 4140 metal is used as the base material to measure the circumferential strain using a Wheatstone bridge. It describes that brain and mind are not dependent on each other [8], which is termed as dualism, and also the treatment way to mental disorder changes from each aspect. AS for instance the person's fear can be asked as interrogative by brain and emotional quotient as from the mind aspect. The main goals of this system were workers cost-effectiveness [9], not available due to changing climatic conditions which makes always open during emergency. A robotic arm has been set up at a distance to fuel tank, and once the car enters the station and sips the amount or payment, the equivalent fuel is filled with the mechatronics design. Parameter-based data collection process has been done [10] for a specific foundry idea. ANOVA test for tensile and bonding strength is validated and increased by communication using carbon fiber [11]. The aspect ratio of nanoparticles is increased stability by continuous loading of Buparvaquone [12] by intravenous method. Renal failure can be reduced using nanoparticles made of gold, which was tested using three sections of rates with various dosages [1].

2 Materials and Methods

2.1 Experimentation

Mohammed et al. [13] described that reminder to the patients to intake their drug dosage at regular intervals. But it was not a successful system as if patient fails to have medicine, it can lead to emergency situation or also fatal death. To avoid all such worst-case condition, a home system for elderly and nurses at home for effective healthcare management has been designed. This prototype was programmed and executed successfully for a list of patients. Now, more importantly, it is given to decrease the cost and size to make it affordable and comfortable for all range of patient monitoring purposes. Ventricular drug is infusion [14] to the epicardium of the rat heart and tested with high and low dosage to observe the hemodynamic.

Silva et al. [15] present a SapoMed, a graphic user interface in mobiles for healthcare administration. It has various forms of inputs such as sound, images and tactile sensations to remind their dosage at regular intervals. Additionally, the barcode of pharmaceutical is recorded through camera service, and useful information can be obtained using advanced mobile technology. Zao et al. [16] mentioned that the most likely error detection area was recording of the daily patient's medicine, dosage and treatment. It presents a smartphone application that helps patients to avoid most medication administration errors. For enzyme replacement therapy [17], hydrogels are given at a faster rate to paralyzed patients to increase stability, no overdosage and four-time slower rate to diffuse correctly. Terconazole ocular drug infusion [18] is done interfusion without any side effects. It also maintains the deocyalte levels to safeguard against immune infection. Carboxymethyl cellulose (CMC) [19] which is employed is the process of wound treatment based on polymers-based and maintains release rate, varying rate of infusion and test of wound recovery depending upon the patient condition.

2.2 Description

The block diagram of patient medication reminder system is shown in Fig. 1. The program is coded using C language and complied using eclipse software. After compilation, the UTLP kit is linked with Unified Learning Kit (ULK). Then the system code is loaded to execute the program. The execution is done with the aid of two devices—Texas OMAP 3530 processor and Xilinx spartan6 FPGA. The exhibited displays using seven segments and LCD are corresponding to the patient data customized.

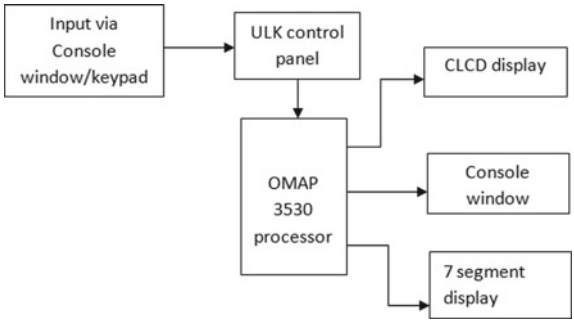

Fig. 1 Block diagram of patient medicine reminder system

2.3 Eclipse

Integrated development environment (IDE) discovered a Java-based operating software to work on different languages designed a plug-in system known as eclipse an. Various plans and plug-in systems for other languages including Ada, C++, COBOL, FORTRAN are employed. In UTLP, C-based proposals using IDE tool have been developed.

2.4 Unified Learning Kit-Control Panel

Ubuntu Corporation recommended a programming-based ULK kit. Ubuntu host personal computer and the Unified Technology Learning Platform (UTLP Kit) are connected using this software. At different modes of operation, UTLP can be operated at the purpose of running and booting-up process. Figure 2 demonstrates the interfacing of the server computer and end user.

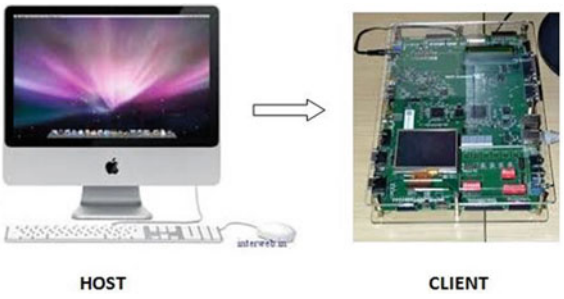

Fig. 2 Interfacing host computer and client

2.5 Texas Omap3530 Processor

The ULK is application-based Spartan-6 FPGA by Texas instrument. To help in performance-oriented and multi-thread applications, Texas Instruments OMAP 3530 is used. Various built-in functions such as Bluetooth, camera connector, touch screen LCD and NAND Flash are supported by OMA architecture. Also interfaces such as Ethernet, USB two SD cards, I/O expansion connector, I2C header for GPS and LCD connector are supported by this processor.

2.6 Interfaces in UTLP

UTLP has an additional feature of interfacing devices which has the capability to perform in both normal and lab modes. The list of devices such as different forms of display—seven segments, graphics, character, LCD, touch panel, etc.—can be programmed and executed in the normal mode.

API—Libraries provide the processes and built-in functions. By using the functions or processes from the library, the programs for an interfacing can be performed. At the linking time, the API library binaries conversion of the binary program to code file is executed during the connection between the host and client. There are many interface libraries available for different devices with different functionalities in normal mode of UTLP.

2.7 Liquid Crystal Display Based on Character

The display panel has two rows of lines, and each line can contain 16 characters as shown in Fig. 3. The size of the panel is 16 × 2, and dimensions of each matrix in display are 5 × 7 pixel which is linked through interface I2C. Character LCD has a controller built in them called HD44780. There are several registers for the initial storage and manipulation functions in this controller.

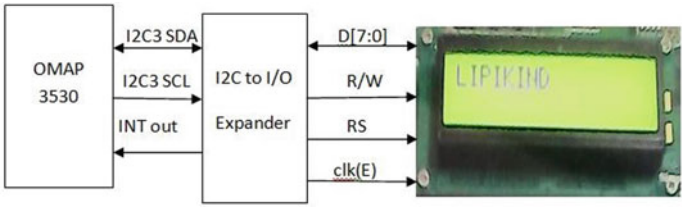

Fig. 3 Character LCD

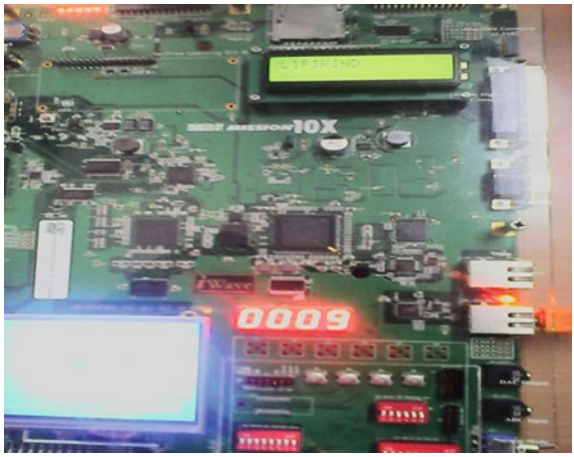

Fig. 4 Character LCD and seven-segment display output

2.8 Implementation and Methodologies

The enhanced version is checked with higher efficiency in power and over performance of cortex-A8 prototype by ARM. The momentum of cortex-A8 ranges from 600Mhz to 1Ghz because of its system architecture. Power efficiency has been improved to a great extent in this version such that mobile devices can be operated at power level of 300mW. The representation of the executed program in UTLP kit is through the seven segments and CLCD. Application programming interface is the main software processed in the flow of displaying.

3 Results and Discussions

Thus, the program was written and executed in embedded C using the Eclipse software. ULK kit is linked with UTLP, once the program has been executed without any failure. The above connection is represented in Fig. 4. The different modes of display options are the segment display, character LCD and touch panel. In [20] such devices would be helpful in assisiting the elderly or bed ridden patients for their daily needs without any other assistance.

4 Conclusions

This paper helps the patients for the intake of medicines at the right time. In recent days, people get affected by many diseases, even at early ages so that they need to take medicines every day to maintain their health condition. Because of their busy

schedule, they forget to take their prescribed medicines. This makes them to be failed in maintaining their health conditions. This project was implemented to remain the list of medicines, and timing for the intake of medicines will be helpful for the patients. Thus, this system helps them to avoid the difficulties which are faced by the patients failed to keep track of regular time intervals of fetching their pharmaceutical.

References

1. Alomari G, Al-Trad B, Hamdan S et al (2020) Gold nanoparticles attenuate albuminuria by inhibiting podocyte injury in a rat model of diabetic nephropathy. Drug Deliv Transl Res 10:216–226. https://doi.org/10.1007/s13346-019-00675-6
2. Abbey B, Alipour A, Gilmour L, Camp C, Hofer C, Lederer R et al (2012) A remotely programmable smart pillbox for enhancing medication adherence. In: Computer-based medical systems (CBMS), 2012 25th international symposium, pp 1, 4, 20–22
3. Dalgaard LGG, Gronvall E, Verdezoto N (2013) Med iframe: a tablet application to plan, inform, remind and sustain older adults. In: Medication intake, healthcare informatics (ICHI), IEEE international conference, pp 36, 45, 9–11 Sept 2013
4. DeMeo D, Morena M (2014) Medication adherence using a smart pill bottle. Emerging technologies for a smarter world (CEWIT), 11th international conference & expo, 29–30 Oct 2014
5. Das D, Pratihar DK, Roy GG (2016) Electron beam melting of steel plates: temperature measurement using thermocouples and prediction through finite element analysis. Robot Factor Fut Lect Notes Mech Eng. https://doi.org/10.1007/978-81-322-2740-3_57,SpringerIndia
6. Felfel H, Ayadi O, Masmoudi F (2015) A multi-objective multi-site supply chain planning problem under risk and uncertainty. design and modeling of mechanical systems—II. Lecture notes in mechanical engineering. Springer International Publishing, Switzerland. https://doi.org/10.1007/978-3-319-17527-0_1
7. Jain R, Rathore JK, Gorana VK (2016) Design, development and testing of a three component lathe tool dynamometer using resistance strain gauges. In: CAD/CAM, robotics and factories of the future. Lecture notes in mechanical engineering. Springer India. https://doi.org/10.1007/978-81-322-2740-3_2
8. Matthews E (2019) Mind-brain dualism and its place in mental health care. Handbook of the philosophy of medicine. https://doi.org/10.1007/978-94-017-8706-2_15-1#SpringerScience+BusinessMediaDordrecht
9. Sheth S, Patel KH, Patel H (2016) Design of automatic fuel filling system using a mechatronics approach. In: CAD/CAM, robotics and factories of the future. Lecture notes in mechanical engineering. Springer, India. https://doi.org/10.1007/978-81-322-2740-3_76
10. Sika R, Ignaszak Z (2020) Data acquisition procedures for A&DM systems dedicated for the foundry industry. In: Ivanov V et al (eds) Advances in design, simulation and manufacturing II. DSMIE 2019. Lecture notes in mechanical engineering. Springer, Cham
11. Ramadhoni BF, Rizkyta AG, Bintoro A, Nugroho A (2020) Effect of glass fibers and aramid fiber on mechanical properties of composite based unmanned aerial vehicle (UAV) skin. In: Osman Zahid M, Abd. Aziz R, Yusoff A, Mat Yahya N, Abdul Aziz F, Yazid Abu M (eds) iMEC-APCOMS 2019. Lecture notes in mechanical engineering. Springer, Singapore
12. Maithania HV, Mohanty BS, Chaudhari PR et al (2020) Shape mediated splenotropic delivery of buparvaquone loaded solid lipid nanoparticles. Drug Deliv Transl Res Res 10:159–167. https://doi.org/10.1007/s13346-019-00670-x
13. Mohammed MNA, Ahmed AHM, Salih TS (2013) Designing low cost digital dose reminder system. In: Computing, electrical and electronics engineering (ICCEEE), 2013 international conference, pp 357, 362, 26–28 Aug 2013

14. Li XM, Li R et al (2020) An epicardial delivery of nitroglycerine by active hydraulic ventricular support drug delivery system improves cardiac function in a rat model. Drug Deliv Transl Res 23–33. https://doi.org/10.1007/s13346-019-00656-9
15. Silva BM Lopes IM Marques MB, Rodrigues PML (2013) A mobile health application for outpatient's medication management. In: Communications (ICC), 2013 IEEE international conference, pp 4389, 4393, 9–13 June 2013
16. Zao JK, Wang M-Y, Tsai P, Liu JWS (2010) Smart phone based medicine in-take scheduler, reminder and monitor. In: e-health networking applications and services (Healthcom), 2010 12th IEEE international conference, pp 162, 168, 1–3 July 2010
17. Jain E, Flanagan M, Sheth S et al (2020) Biodegradable polyethylene glycol hydrogels for sustained release and enhanced stability of rhGALNS enzyme. Drug Deliv Transl Res. https://doi.org/10.1007/s13346-020-00714-7
18. Yousry C, Zikry PM, Salem HM et al (2020) Integrated nanovesicular/self-nanoemulsifying system (INV/SNES) for enhanced dual ocular drug delivery: statistical optimization, in vitro and in vivo evaluation. Drug Deliv Transl Res. https://doi.org/10.1007/s13346-020-00716-5
19. Amanat S, Taymouri S, Varshosaz J et al (2020) Carboxymethyl cellulose-based wafer enriched with resveratrol-loaded nanoparticles for enhanced wound healing. Drug Deliv Transl Res. https://doi.org/10.1007/s13346-020-00711-w
20. Suzuki T, Jose Y, Nakauchi Y (2011) A touchscreen-equipped medicine case as a medical interface for assisting an elderly person in medication management. In: Engineering in Medicine and Biology Society, EMBC, 2011 Annual international conference of the IEEE, pp 5335, 5338, Sept 2011

Audio Signal Processing for Cochlear Implants

K. T. Maheswari, R. Baranikumar, D. Lavanya, A. Nandhakumar, and M. Srinivasan

Abstract Cochlear implants are a minor, complicated electronic gadget that may offer assistance to afford a feel of sound to an individual who is significantly hard of hearing or essentially tough-of-hearing. Unlike, cochlear implant does not simply make bigger sound. They imitate herbal listening for the purpose of the internal ear thru electronic simulation. The implant consists of an outside element that is in the backside ear and second part which is surgically located underneath the skin. Both these gears are coupled with the usage of an effective magnet. The outside setup of a cochlear implant is made up of three parts such as microphone, speech processor and transmitter. The microphone and speech processor are bounded collectively in a small unit that appears to be at the back-of-the-ear hearing useful resource. A small wire connects them and the transmitter. The transmitter is placed over an internal part of the tool. The inner part of implant accommodates a receiver (which is located below skin at temporal bone) and one or greater electrode arrays. In this paper, the proposed system has been simulated in MATLAB/Simulink, and the experimental setup has been implemented to verify the results.

Keyword Cochlear implant · Electrode array · Microphone · Receiver speech processing transmitter

1 Introduction

The ear is made from three segments specifically outer, middle and inner. The outer ear comprises of pinna and ear canal. Pinna in the outer ear, captures the sound waves and funneling them into the ear canal. The center ear contains the eardrum and an air-stuffed cavity encompassing small bones denoted as ossicles [1]. Discrete parts are hammer (malleus), anvil (incus) and stirrup (stapes)—and they vibrate together while eardrum moves. The inner ear consists of complex collection of channels and

K. T. Maheswari (✉) · R. Baranikumar · D. Lavanya · A. Nandhakumar · M. Srinivasan
Department of Electrical and Electronics Engineering, Bannari Amman Institute of Technology, Sathyamangalam, Erode, Tamil Nadu 638401, India
e-mail: maheswarikt@bitsathy.ac.in

G. Kumaresan et al. (eds.), *Advances in Materials Research*, Springer Proceedings in Materials 5, https://doi.org/10.1007/978-981-15-8319-3_9

chambers. For listening to, the precarious organ is the spiral-shaped cochlea. Roughly the scale of a pea, the cochlea encloses fluid and about 15,000 tiny hair cells [2]. Each and every hair cell is attached to the auditory nerve. The sound waves hit eardrum, and immediately, it vibrates.

Tiny ossicles vibrate with the eardrum and transfer the sound to the cochlear through the middle ear [3]. These hair cells trade the motion into electric powered impulses which might be dispatched alongside the auditory nerve to the brain. The listening to center of the mind interprets the impulses as sound. The ear is an amazingly complicated but efficient listening to machine, and the whole method best takes fraction of a 2d. Hearing aids help numerous human beings who lost listening. However, it cannot assist each. When human beings with intense to profound listening to loss do not benefit from listening to aids, health workers bear in mind a cochlear implant to be a more effective long-time period answer [4, 5]. Unlike hearing aid, cochlear implants do not simply expand sounds. They mimic herbal listening to function of inner ear thru digital stimulation. Incoming sounds are processed into electric signal after which transmitted to hearing nerve, bypassing the broken components of inner ear.

2 Cochlear Implants (CIs)

CIs comprise of electrodes which are found inside cochlea to stimulate 8th nerve (nVIII). Such electrode therefore generates electric currents which cause compound motion potentials in fibers that could be transmitted to the cerebrum for elucidation. CIs sidestep broken or missing external hair cells inside the cochlea that would commonly happen as code sound. All CIs have typical segments, and on the other hand, there are varieties in procedures which are used to process sounds, transmit insights to inward embed and invigorate anodes. There are various anodes to be had from every maker, including a diminished cluster utilized with half and half CIs [6].

2.1 Internal Components

Implanted components in CIs must be bio-compatible and not lead to long-term damage to adverse tissue as shown in Fig. 1.

Stimulator
Stimulator is one of the inner components which are sometimes called as the internal coil, that is, embedded in a smoothed or recessed piece of the skull back to and scarcely over the pinna, since it gets vitality and disentangles directions from the discourse processor. Stimulator converts electrical sign into digital code and again to electric sign, which are added to the cathodes in cochlea [7]. It receives stimulus

Fig. 1 Internal component of cochlear implants

records via radio frequency (RF) transmission from the outside coil housed within the headpiece. Thus, approach of coupling is referred to as transcutaneous link.

Electrode Arrays
Multi-channel gadgets have an as great deal as 22 lively electrodes. Researches were indicated that greater electrodes commonly bring about higher speech perception. Nevertheless, this is not always a one-to-one relationship, as many people gain very good speech belief without the usage of all the electrodes of their array. The residual auditory nerve fibers are stimulated by an electrode array along modiolus. CI electrodes designed for replacement in scala of cochlea. Keeping the cathodes especially close to the winding ganglion cells is useful for the sound-related nerve's kept incitement. Various cathodes ideally invigorate unprecedented sub-populaces of cochlear neurons. Neurons close to the base of the cochlea (first turn) answer to high-repeat sounds, and neurons in pinnacle of cochlea reply to low-frequency sounds [8].

2.2 External Components

The external setup of a cochlear implant involves a microphone, a speech processor and a transmitter for the process as shown in Fig. 2

Microphone
The microphone, which is normally located on the speech processor, is a device used to collect and process incoming audio signal. It senses valid stress signals and transforms into electrical signals. Generally, electrical signals are transmitted to a pre-amplifier to improve noise ratio, providing at higher frequencies. The microphone has a broad frequency reaction, but reduces responses to lower-frequency vibrations, which includes those produced by head and frame actions. Producers offer a couple of microphones, increasing the selectivity of the directional sample to useful resource speech expertise discourse in boisterous circumstances [9]. Directional receivers underscore sounds before the amplifier and smother sounds exuding from various guidelines. All three producers have multiple microphone options to be had to lower wind noise and to assist with speech know-how in historical past noise. All manufacturers have applications/functions to permit the microphones to be

Fig. 2 External component in cochlear implant

self-adjusting by listener's surroundings. The microphone sends this rectified signal to external speech processor.

Speech Processor

The speech processor of a CI utilizes sound from the receiver to make a great deal of electrical upgrades for electrode terminals. The obtained signal is broke down by an advanced digital signal processor (DSP) to segregate the input in line with intensity, frequency and time domain names, to be able to be represented on the nVIII. Producers dedicate a splendid arrangement important to growing new and propelled preparing plans.

Regularly the new plans can be fused into existing processors through a product program update. Substitution of the inner parts is once in a while, if at any time, essential to utilize new discourse preparing plans. The discourse processor takes the handled electric sign and transmits it through a string to the headpiece. The discourse processor is fueled through batteries—both liked and battery-powered. Run of the battery presence is over 12 h for a body-worn processor and typically really much less for a back-of-the-ear processor.

Headpiece

The headpiece situates at the outside loop of the CIs and situates in region over the inside trigger (inward curl) with magnets. The headpiece transmits electrical sign, subsequent to transforming it to an electromagnetic sign, to the inward trigger through radio recurrence (RF). The RF curl sign also fills in as power supply for internal trigger. The RF coil sign additionally serves as electricity supply for inner stimulator.

3 Experiment and Results

This experiment has been composed of three processes. First, the audio signal has to be obtained and split into different frequency bands; second, electrical pulse generation for each frequency band; and third, the reconstruction of the original signal. In an actual cochlear implant, there is a transistor and receiver integrated into this system to transmit the electric signals and receive them inside the ear, which is not done due to practical unfeasibility [10].

The original MATLAB Simulink model for a cochlear implant is available in MATLAB library. The model is used by replacing the embedded inputs by external inputs at runtime and by also changing implemented filter parameters, using different rate transition and different sampling rate. With few listed changes, the model is working fine for prerecorded inputs. But, when tried implement on FRDM-K64F board, we encounter many errors since the Simulink model from the library was not compatible with the CMIS RTX delay rates [11]. Hence, a new Simulink model was made keeping the idea the same. This newly implemented model runs successfully.

Block Diagram

Figure 3 shows the Block diagram for simulation of audio signal processing.

Splitting of signal

To show the working of the model, an audio flag is recorded in mp3 format and gated it as the input to a bank of 8 (as per investigation, eight channels are best for great sound-related hearing for an individual with a cochlear implant) band-pass FIR channels. The stop-band and passband frequencies of each filter were calculated by utilizing center frequency of the recorded wave and utilizing sampling frequency as 2.25 times the center frequency. The band-pass filters divide the input signal into different frequency by the given passband and stop-band frequencies.

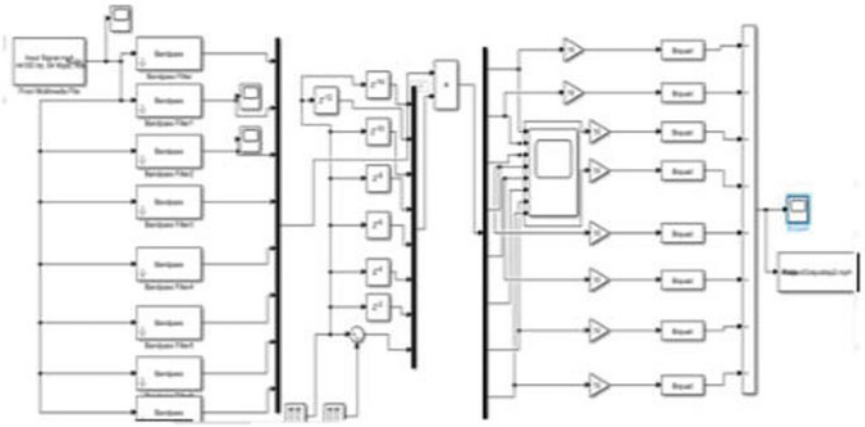

Fig. 3 Block diagram for simulation of audio signal processing

Pulse Generation

Every eight signals of different frequencies are encoded with an electrical pulse to transmit it to the internal part of the cochlear implant. For implementing this feature, we used a pulse generator to provide a pulse to different channels with different delays (interleaved manner for better results). The corresponding input pulses modulated the electrical pulses in each channel by use of a multiplier. Now, these signals are ready to be transmitted to the internal part of the implant [12]. Figure 4 shows the input signal for cochlear and the waveforms of input and eight-channel split output (after superimposing with electrical beats) are appeared underneath in Fig. 5.

Reconstruction

This part is used to check whether the split signal is correct, and do they properly recombine to form the original signal? For this process, we add "gain" (for compensating random noise and filter losses) to each signal and feed them to a "Biquad" blocks [13]. The summation of outputs from these eight Biquads reconstructed the signal. The output waveform of the reconstructed signal is shown in Fig. 6.

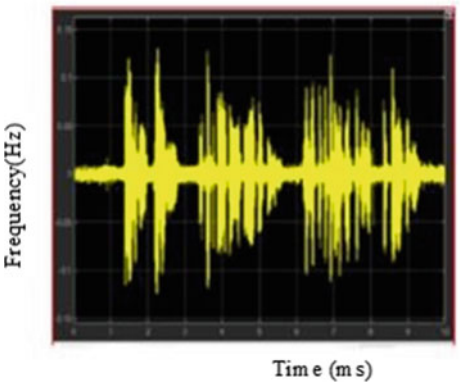

Fig. 4 Input signal for cochlear

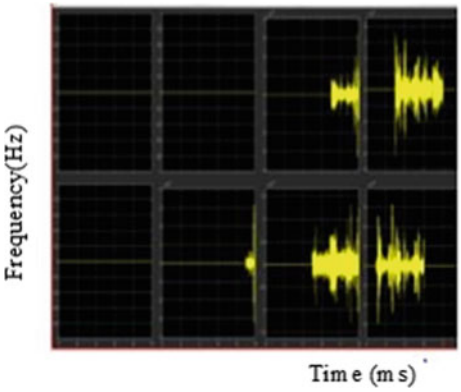

Fig. 5 Simulation during split signal

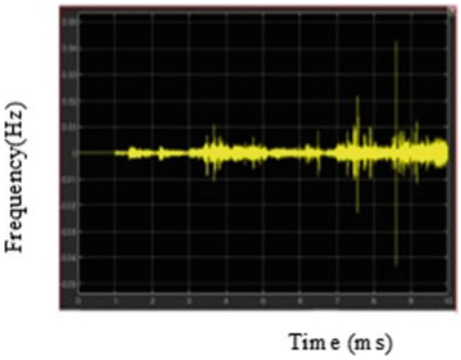

Fig. 6 Simulation of audio signal during reconstruction

4 Conclusion

In common, the enhancement in auditory perception following cochlear implantation varies broadly from user to user and can range from speech perception to music enjoyment. By compensating for the loss of hair cells in the ear and stimulating the neurons in the brain, the cochlear implants restore some hearing [14]. Benefits of cochlear implants include hearing conversation and environmental sounds at discussion and natural sounds at open to listen, distinguish and recognize sounds in the earth, for example, doorbell, vehicle horns, keep their vocal din at a fitting level, comprehend others all the more precisely and with less exertion, comprehend discourse by listening alone (without lipreading). Whole implementation requires a bank of filters and modulation technique to first separate the acoustic signal into different frequencies waveform and then reconstructing [15]. Thus, the proposed in this paper is successfully imitating the concept by designing our filter banks, multiplexers, demultiplexers and modulators in MATLAB.

References

1. Implants: Who, How And Why?—Healthy Hearing. https://www.healthyhearing.com/help/hearing-aids/cochlearimplants (Cochlear accessed December 02, 2018)
2. AdvancedBionics, LLC. (2012) Retrieved Oct 2012 from https://www.advancedbionics.com/us/en/home.html
3. Audioscan (2006) Verifit test drive. Retrieved November 2009 from https://www.audioscan.com/webpages/verifit/vf1testdrive/recdtest.htm
4. Beauchaine K, Stelmachowicz P (2002) Amplification for infants. ASHA Leader, 7, 67. Centers for Disease Control and Prevention
5. Cochlear Americas Corporation (2012) Retrieved October 2012 from https://www.cochlearamericas.com/?ctcampaign=1312&ctkwd=cochlear%20
6. Cooper HW, Craddock LC (eds) (2006) Cochlear implants: a practical guide. Whurr Publishers, London
7. Desired Sensation Level Method (2005) Hearing aid selection. Retrieved 20 Jan 2007, from https://www.dslio.com

8. Dillon H (2006) What's new from NAL in hearing aid prescriptions? Hearing J 59(10):10–16
9. Dunn C et al (2008) Comparison of speech recognition and localization performance in bilateral and unilateral cochlear implant users matched on duration of deafness at age of implantation. Ear Hear 29(3):352–359
10. Ramsden R, Greenham P, O'Driscoll M et al Evaluation of bilaterally implanted adult subjects with nucleus 24 cochlear implant system. Otol Neurotol 26:988–998
11. Rubinstein JT, Parkinson WS, Tyler RS et al (1999) Residual speech recognition and cochlear implant performance: effects of implantation criteria. Am J Otol 20:445–452
12. Schleich P, Nopp P, D' Haese P (2004) Head shadow, squelch, and summation effects in bilateral users of the med-el combi 40/40+ cochlear implant. Ear Hear 25:197–204
13. Seeber B, Baumann U, Fastl H (2004) Localization ability with bimodal hearing aids and bilateral cochlear implants. J Acoust Soc Am 116:1698–1709
14. Seen P, Martin K, Vischer M et al (2005) Minimum audible angle, just noticeable interaural differences and speech intelligibility with bilateral cochlear implants using clinical speech processors. Audiol Neurootol 20:342–352
15. Shannon RV, Fu Q, Galvin J et al (2004) Speech perception with cochlear implants. In: Zeng G, Popper AN, Fay RR (eds) Cochlear implants: auditory prostheses and electric hearing (Chap. 8). Springer, New York, pp 334–376

Investigation of Hybrid Concrete Using Steel and Polypropylene Fibres

M. Ranjitham, S. K. Deepika Sree, and M. B. Danyaa

Abstract The addition of the hybrid fibres which greatly influences the mechanical properties such as compressive strength, split tensile strength and the flexural strength of the concrete is discussed in this paper. These fibres are widely used in many pavements such as rigid pavements, flexible pavements and many structures such as bridge, and also in many hydraulic structures. The word hybridization is the integration of many types of fibres. One of the main purpose of the combination of many types of fibres is that it increases the characteristics of concrete. Concrete is made by the addition of 1% of the steel fibres and 0.035% of polypropylene fibres and mixing them together. The efficiency of the mechanical properties of this compound is far more greater than the conventional reinforced concrete. The fracture characteristics of concrete are increased by adding polypropylene fibre.

Keywords Steel fibres · Polypropylene fibres

1 Introduction

Most popular material in the field of construction purpose is concrete. Concrete is strong in compression but weak in tension as well as in flexural strength also. The introduction of high strength concrete into the construction field has many advantages. The fibre reinforced concrete (FRC) is the addition of short discrete fibres like steel fibres, glass fibres, synthetic fibres or natural fibres which are distributed

M. Ranjitham (✉) · S. K. Deepika Sree · M. B. Danyaa
Department of Civil Engineering, Bannari Amman Institute of Technology, Sathyamangalam, Erode, Tamil Nadu 638401, India
e-mail: Ranjitham3391@gmail.com

S. K. Deepika Sree
e-mail: deepikasree.ce17@bitsathy.ac.in

M. B. Danyaa
e-mail: danyaa.ce17@bitsathy.ac.in

G. Kumaresan et al. (eds.), *Advances in Materials Research*, Springer Proceedings in Materials 5, https://doi.org/10.1007/978-981-15-8319-3_10

uniformly in the concrete. These fibres when added to the concrete greatly influence the mechanical properties of the concrete. These fibres alter the fibre matrix compound once it gets cracked, and thereby, it increases the toughness. Mixing fibres to the concrete thereby makes it as a composite structure and gives it more strength to the concrete mixture. Hence, this type of concrete mixture is known as the hybrid fibre reinforced concrete (HFRC).

Waste plastic fibre is more productive in managing the cracks [1] and the effects of strength and workability in concrete. For increasing the fracture characteristics of concrete [2], the addition of fibres is very helpful in improving the impermeability, resistance to frost and also mechanical properties of fibre reinforced concrete when compared with conventional concrete [3]. The study on the hybridization of steel fibres and polypropylene indicate that the use of hybrid fibres in specimen increases the flexural toughness, rigidity and the overall performance. The resistance to elevated temperature of HF self-compacting concrete is better than single fibre reinforced self-compacting concrete. Using polypropylene resists the initial crack and shrinkage. To increase the strength parameters, the steel fibres are used [4–6].

2 Objective

The main objective is to increase the strengths of various joints in many precast structures and also to increase the ductile connection for the precast concrete member in an earthquake zone. Another main objective is to study in depth about the properties and effects of hybrid fibre concrete.

3 Test Specimens

3.1 Cube Specimen

Cubes of nominal size 150 × 150 × 150 mm were used to test the compressive strength of conventional concrete and HFRC concrete cubes.

3.2 Cylinder Specimen

The cylinders having diameter 150 mm and height 300 mm were tested for split tensile strength.

Table 1 Concrete mix proportion design is given in

Type of concrete	Cement in kg/m^3	Fine aggregate in kg/m^3	Coarse aggregate in kg/m^3	Water (l)	Steel fibres	PP fibres
Conventional concrete	375.5	590.6	1177	188	0	0
HFRC	375.5	590.6	1177	188	1	0.035

3.3 Beam Specimen

Beams of size 1500 × 150 × 100 mm with main reinforcement of 10 mm and distribution reinforcement of 8 mm which are of 4 numbers were spaced at 90 mm were tested for the flexural strength.

3.4 Mix Proportion

See Table 1.

4 Concrete Ingredients

4.1 Cement

Binding agent used here is cement. It adheres to the materials and binds all of them together. The specific gravity of cement is 3.14 and has a normal consistency of 32%. Ordinary Portland cement of grade 53 is used here.

4.2 Fine Aggregate

Aggregates which pass through IS sieve 4.75 are known as coarse aggregate. Here, M sand is used as fine aggregate. M sand has the water absorption capacity of 1.93%.

4.3 Coarse Aggregate

Aggregates which are retained on IS sieve 4.75 are known as coarse aggregate. Here, coarse aggregate of size 20 mm was used. Many tests were performed on these aggregates.

4.4 Water

Potable water is used here. The water used should be fresh and should lack hazardous impurities like acids, alkalis, etc.

4.5 Steel Fibre

Steel fibres have excellent mechanical properties which also include high tensile strength. Adding steel fibres to the concrete greatly improves the resistance to cracks. Steel bars are placed to increase the tensile strength of concrete in any one direction, but the steel fibres are used for reinforcement in many directions. The steel fibres used here are of hooked ends.

4.6 Polypropylene Fibre

The polypropylene fibre is very light in nature and is very light in nature. The polypropylene has a melting point of 170. It has a water absorption capacity of 0.3%.

5 Tests Performed

5.1 Compression Test

The cube's compressive strength was determined at the end of 28 days.

Compressive strength of the cube can be found by

$$f = P/A \text{ N mm}^2$$

5.2 Split Tensile Test

The cylinder's split tensile strength was determined after 28 days.

The formula used for finding out the tensile strength is

$$\text{Split Tensile strength} = 2P/3.14LD$$

5.3 Flexural Strength

The beam's flexural strength was determined at the end of 28 days. The formula used for finding out the flexural strength is

$$\text{Flexural strength} = \text{PL/bd}^2\text{(or)3Pa/bd}^2$$

6 Test Results

6.1 Compressive Strength

See Chart 1 and Table 2.

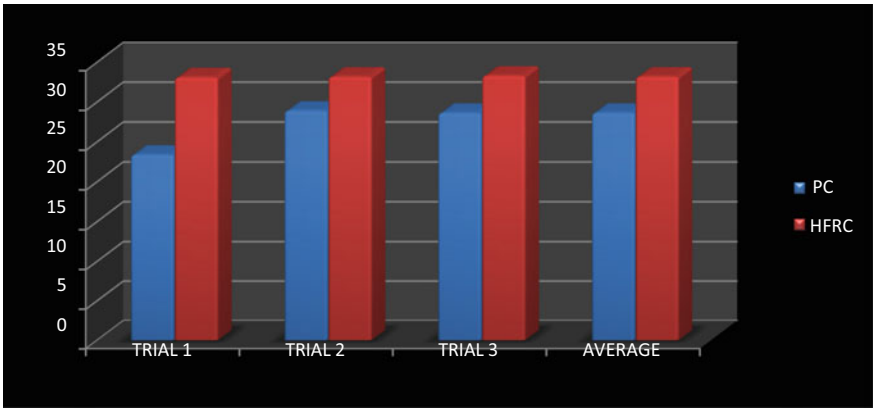

Chart 1 Compressive strength test

Table 2 Compressive strength at 28 days

Index	Compressive strength, Mpa			Average stress, N/mm^2
	Trial 1	Trial 2	Trial 3	
Conventional concrete	28.38	28.90	28.0.62	28.63
Hybrid fibre reinforced concrete	33.09	33.17	33.29	33.18
Net % increase				13%

6.2 Split Tensile Test

See Chart. 2 and Table 3

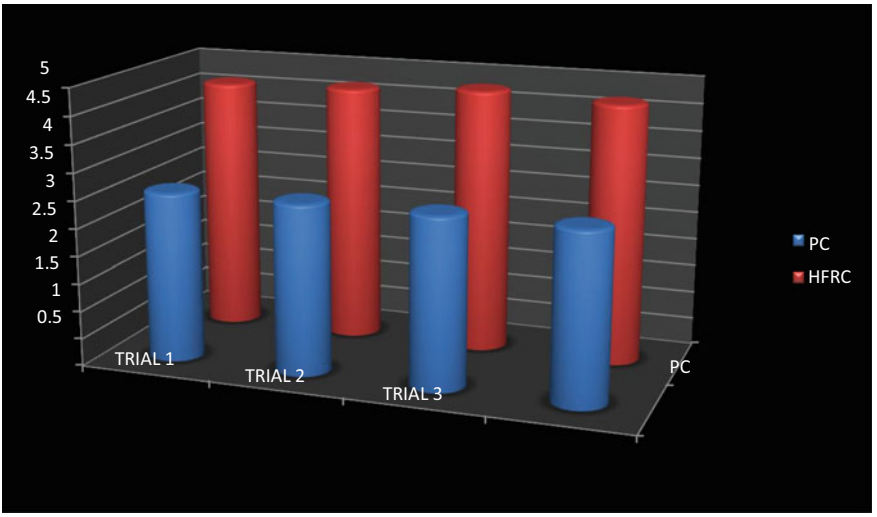

Chart 2 Split tensile strength

Table 3 Split tensile strength at 28 days

INDEX	Split tensile strength, N/mm^2			Average stress, N/mm^2
	Trail 1	Trail 2	Trail 3	
Conventional concrete	3.08	3.09	3.10	3.09
Hybrid fibre reinforced concrete	4.62	4.67	4.78	4.69
Net % increase				48%

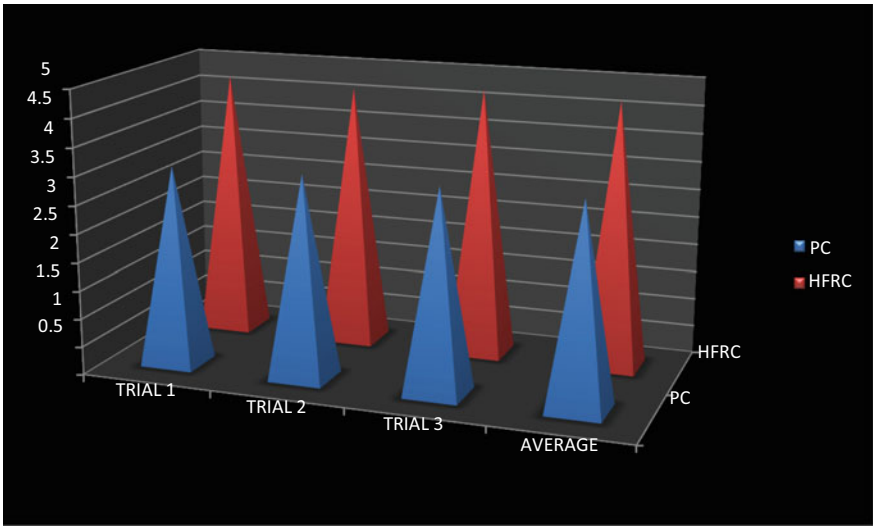

Chart 3 Flexural strength

Table 4 Flexural strength at 28 days

Index	Flexural strength, N/mm^2			Average stress, N/mm^2
	Trail 1	Trail 2	Trail 3	
Conventional concrete	3.54	3.58	3.57	3.56
Hybrid fibre reinforced concrete	4.74	4.65	4.77	4.72
Net % increase				31%

6.3 Flexural Strength

See Chart 3 and Table 4

7 Conclusion

The experimental investigations are conducted on the cube, cylinder, and beam. The compressive strength, split tensile strength, the flexural strength of the elements are compared with the hybrid fibre reinforced concrete. The following conclusions were arived.

1. The Strength of the hybrid fibre reinforced concrete is increased gradually without any addition of admixtures.

2. The compressive strength of HFRC at the end of 28 days is 33.18 N/mm^2 which is more than that of conventional concrete. Thus, 13% is the average increase of compressive strength.
3. The split tensile strength of HFRC at the end of 28 days is 4.69 N/mm^2 which is more than that of conventional concrete. Thus, 48% is the average increase of split tensile strength.
4. The flexural strength of HFRC at the end of 28 days is 4.72 N/mm^2 which is more than that of conventional concrete. Thus, 31% is the average increase of flexural strength.

References

1. Prahallada MC, Prakash KB (2011) Strength and workability characteristics of waste plastic fiber reinforced concrete produced from recycled aggregates. Int J Eng Research Appl 1(4):1791–1802. ISSN 2248-9622
2. Shao YD, Wang WF (2012) Experimental study on fracture properties of hybrid fiber reinforced concrete. Adv Mater Res 450–451:518–522
3. Gao S, Tian W, Wang L, Chen P (2012) Comparison of the mechanics and durability of hybrid fiber reinforced concrete and frost resistant concrete in bridge deck pavement. Transp Infrastruct Construct Emerg Technol 2927–2935
4. Dawood ET, Ramli M (2011) Contribution of hybrid fibers on the hybrid fibers on the properties of high strength concrete having high workability. In: Proceedings of Twelfth East Asia—Pacific conference on structural engineering and construction. Procedia Eng 14:814–820
5. Ravi K, Prakash KB (2008) Strength characteristics of hybrid fiber reinforced self compacting concrete subjected to sustained elevated temperature. In: Proceedings of 33rd conference on our world in concrete and structures, Singapore, Aug 2008, pp 25–27
6. Jirobe S, Brijbhushan S, Maneeth PD (2015) Experimental investigation on strength and durability properties of hybrid fiber reinforced concrete. Int Res J Eng Technol (IRJET) 02(05)

Experimental Investigation on Geopolymer Bricks

M. Ranjitham, K. Vishvapriya, and L. U. Vishnu Pavya

Abstract The product material of combustion of coal is known as fly ash. It contains fine particles and fuel gases emitted from boilers. During combustion, mineral impurities in the coal (clay, feldspar, quartz and shale) fuse in suspension and float out of the combustion chamber with the exhaust gases. As the fused material rises, it cools and solidifies into spherical glassy particles called fly ash. Class F fly ash (contains less than 20% lime) is collected. Due to the puzzolanic nature of the fly ash, it is used in the manufacture of hydraulic cement and also in the partial or complete replacement of PC in the manufacture of concrete. Fly ash can not only be used in the cement industries but can also be used in the manufacture of brick. This is more eco friendly. The main objective of this paper is to examine and monitor the purpose of geopolymer brick which contains fly ash as the chief constituent. The geopolymer bricks were prepared and casted with clayey soil and fly ash in various proportions such as 100:0, 80:20, 70:30, 60:40 and 50:50. The sodium fume solution was added in the ratio of 1:2 ratio of water. The sodium fume solution acts as an alkaline activator. This is now added to NaOH solution which acts as a binder. The w/b ratio was taken as 0.416 for dimension of 200 × 100 × 100. The obtained results were compared with that of conventional bricks and studied.

1 Introduction

The production of conventional bricks in the industries uses 2200 m^3 per billion bricks per annum of soil. The thermal power plants produce nearly 110 million of

M. Ranjitham (✉) · K. Vishvapriya · L. U. Vishnu Pavya
Department of Civil Engineering, Bannari Amman Institute of Technology, Sathyamangalam, Erode, Tamilnadu 638401, India
e-mail: ranjitham3391@gmail.com

K. Vishvapriya
e-mail: vishvapriya.ce17@bitsathy.ac.in

L. U. Vishnu Pavya
e-mail: vishnupavya.ce@bitsathy.ac.in

G. Kumaresan et al. (eds.), *Advances in Materials Research*, Springer Proceedings in Materials 5, https://doi.org/10.1007/978-981-15-8319-3_11

fly ash annually and nearly 250 tonnes of coal. The complication in the manufacture of bricks, production of fly ash and urbanization is increasing rapidly.

Concrete is one of the major components for the construction of bricks. The industries manufacturing cement use fly ash as a complete replacement or partial replacement to Portland cement. The ordinary Portland cement usually generates large amount of CO_2 into the atmosphere. This ultimately leads to greenhouse gas emissions. It is high time to find an alternative material for the manufacture of bricks. The geopoymer bricks are an innovative building material which depletes the greenhouse gas emission to nearly 80%. In this paper, the production of geolpolymer solid brick using class F fly ash as the chief ingredient and its physical properties has been studied.

1.1 Geopolymer

Geopolymer concrete is manufactured by utilizing the waste materials like fly ash and ground granulated blast furnace slag also known as GGBS. Fly ash is obtained from the byproduct obtained from thermal power plants, whereas ground granulated blast furnace slag is obtained from the byproduct obtained in steel plants. Both fly ash and GGBS are processed by technology which is used in the form of geopolymer concrete. The use of geopolymer concrete helps in decreasing the wastes and reducing carbon emission by decreasing the demand of Portland cement. Silicon and aluminium are the main constituents which are provided by thermally activated natural materials (e.g. kaolinite) or industrial byproducts (e.g. fly ash or slab) and an alkaline activating solution [1]. They polymerize these materials into molecular chains to create binder. The applications of polymer-based binder material can be highly used in the civil engineering field since conventional cement production is energy intensive. Moreover, it also consumes a certain amount of natural resources for large-scale productions to meet the demand [2]. On the other hand, the usage of cement concrete is on the increase and necessitates looking for an alternative binder to make concrete. The origin of geopolymer is derived from the rock-forming raw materials. In the synthesis process of silicon-based polymers, geopolymers are used [3].

1.2 Development of Geopolymer Bricks

Generally, fly ash reacted to form gel formation is known as the binder in brick production. The binder replaces the requirement of cement. Fly ash of class F is rich in silica and alumina. The reaction of alkali-activated pre-mixed sodium hydroxide and sodium silicate with the higher amount of silica and alumina results in the gel formation [4].

2 Objectives

The main objective is

I. To implement and investigate casting and curing process.
II. Developmental study of salient properties of geopolymer bricks.
III. To produce substantial light-weighted bricks for field construction.

3 Materials Required

3.1 Clay Soil

Sediments deposited by rivers are known as alluvial soil. Alluvial soil contains sand, silt and clay. Clay soil is rich in northern plains, deltas of different rivers such as Godavari, Kaveri, Krishna and Mahanadi in Peninsular India.

3.2 Fly Ash

Fly ash is a byproduct from burning pulverized coal in electric power generating plants. During combustion, mineral impurities in the coal (clay, feldspar, quartz, and shale) fuse in suspension and float out of the combustion chamber with the exhaust gases. As the fused material rises, it cools and solidifies into spherical glassy particles called fly ash. Class F fly ash (contains less than 20% lime) is collected. Specific gravity of fly ash is 2.30 and fineness modulus is 7.86 (Table 1).

Table 1 Fly ash

Constituents	Percentage of content %
SiO_2	46.2
Al_2O_3	26.4
$Fe2O_3$	10.7
CaO	7.60
SO_2	1.80
Loss on ignition	0.20

3.3 Water

In this project, casting and curing of specimen were done using potable water which is free from all harmful materials. The role of water is to impart workability to the mix.

3.4 Sodium Hydroxide

Sodium hydroxides are available in form of pellets and flakes. These are colourless. Chemical composition of sodium hydroxide is assay, carbonate, chloride, sulphate, lead, iron and zinc.

3.5 Sodium Silicate

Sodium silicate is also known as water glass or liquid glass, is available in liquid (gel) form. As per the manufacturer, silicates are supplied to the detergent company and textile industry as bonding agents.

4 Mix Design and Proportioning

4.1 Preparation of Alkaline Solution

1. **Sodium silicate (Na_2SiO_3) solution**
   Sodium silicate (Na_2SiO_3) solution As we are aware, the molecular weight of Na_2SiO_3 powder is 212.14 g. For a 1 M solution, 212.14 g of Na_2SiO_3 needs to be dissolved into 1000 ml of refined water. So for a 1 M solution, we utilize a little amount of water (e.g. 100 ml of water); the necessary measure of Na_2SiO_3 powder will be 2.12 g.
2. **Sodium hydroxide solution**
   Essentially, the molecular weight of NaOH pellets is 40 g. For 1 M arrangement, 40 g of NaOH should break up into 1000 ml of refined water. So for the arrangement of 10 M solution, 40 g of NaOH disintegrated in 100 ml of refined water.

4.2 Mix Proportioning and Material Quantity

Different proportions of materials were used for making geopolymer bricks.

1. 100% soil + water
2. 50% soil + 50% fly ash + alkaline solution ($NaOH + Na_2SiO_3$) + water
3. 60% soil + 40% fly ash + alkaline solution ($NaOH + Na_2SiO_3$) + water
4. 70% soil + 30% fly ash + alkaline solution ($NaOH + Na_2SiO_3$) + water.
5. 80% soil + 20% fly ash + alkaline solution ($NaOH + Na_2SiO_3$) + water.

With some amount of water, sodium hydroxide and sodium silicate are being mixed. The solution was prepared just before adding it to the dry mix. During the former stages for all the materials portions, the molar ratio of the alkaline solution used was in the ratio 1:10. Then, in the latter stages, the soil to fly ash ratio was kept as 70:30. Keeping the soil to fly ash ratio as constant, the molar ratio of the alkaline solution was 1:8, 1:12, 1:14 (Tables 2 and 3).

5 Mixing, Casting and Curing

The moulds in rectangular shape having a cross section of 20 cm × 10 cm × 10 cm were prepared. The basic components like clay soil and fly ash were taken, and they are weighed in a proper ratio. Mixing takes place with dry hands until it reaches a proper uniform colour. This occurs after a time interval of 3 min approximately. By using sodium silicates and sodium hydroxides, the alkaline solutions are prepared.

Table 2 Quantity of the material having constant alkaline ratio of 1:10

Proportion	Soil (kg)	Fly ash (kg)	Molar ratio	Na_2SiO_3	NaOH (ml)
100:0	3.5	0	1:10	10	40
50:50	1.62	1.62	1:10	10	40
60:40	1.95	1.29	1:10	10	40
70:30	1.97	0.87	1:10	10	40
80:20	2.4	0.3	1:10	10	40

Table 3 Quantity of the material having constant soil to fly ash ratio

Proportion	Soil (kg)	Fly ash (kg)	Molar ratio	Na_2SiO_3	NaOH (ml)
70:30	1.97	0.87	1:10	10	40
70:30	1.97	0.87	1:8	20	60
70:30	1.97	0.87	1:14	30	70
70:30	1.97	0.87	1:12	20	80
70:30	1.97	0.87	1:10	10	50

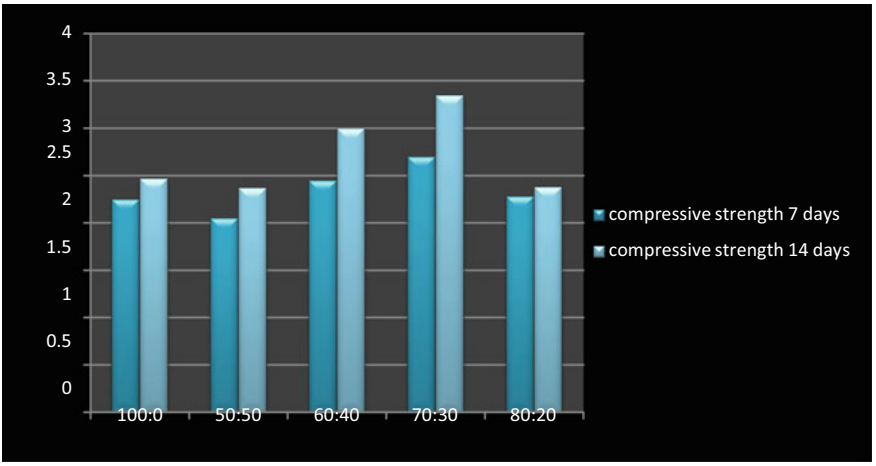

Chart 1 Compressive strength of Geopolymer brick taken after 7 days and 14 days

The dry mixes together with alkaline solutions are mixed until a uniform mix is formed. This is considered to be the final mix (approximately 3–4 min). During the casting process, limited amount of water is added. This is then directly transferred to the moulds by performing required compactions. Surface finishing was done to each mould. The specimen is then made to dry cure at an average temperature of 60 °C inside the oven. Even after curing, the specimen is left inside the mould for at least 6 h. The specimen is demoulded after 6 h and left to air dry until the day of test in the laboratory.

6 Tests and Results

6.1 Compressive Strength Test

Compressive testing machine is used to test the compressive strength of the brick. The capacity of CTM is 2000 KN. It is loaded at a rate of 200 kg/cm^2/min. The seventh and fourteenth day compressive strength is tested. The results are as follows (Charts 1 and 2; Tables 4 and 5):

6.2 Water Absorption Test

This is to check the durability property which includes behaviour under weather action. The dry specimen of brick is kept inside the oven till it reaches its constant

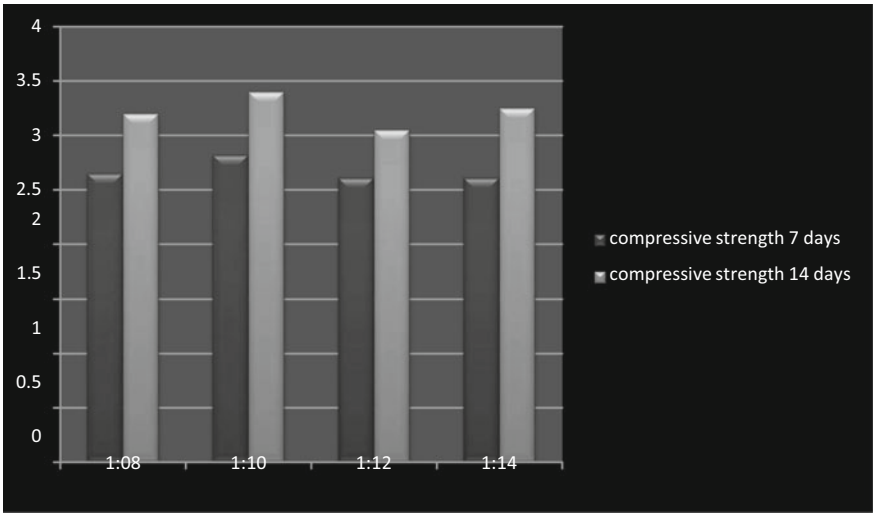

Chart 2 Compressive strength of geopolymer brick

Table 4 Compressive strength of Geopolymer brick at various concentrations

Molar ratio of alkaline solution (1:10)				
Material ratio (soil:fly ash)	Results for 7-day specimen		Results for 14-day specimen	
	Weight of bricks (kg)	Compressive strength (N/mm^2)	Weight of bricks (kg)	Compressive strength ($N/mm^{2)}$
100:0	3.18	2.25	3.10	2.47
50:50	2.68	2.05	2.62	2.37
60:40	2.74	2.45	2.75	3.00
70:30	2.78	2.70	2.67	3.35
80:20	2.92	2.28	2.86	2.38

Table 5 Water absorption of geopolymer brick (70:30)

Molar ratio (clay soil:fly ash = 70:30)				
Material ratio (soil:fly ash)	Results for 7-day specimen		Results for 14-day specimen	
	Weight of bricks (kg)	Compressive strength (N/mm^2)	Weight of bricks (kg)	Compressive strength (N/mm^2)
1:8	2.80	2.65	2.72	3.20
1:10	2.80	2.82	2.65	3.40
1:12	2.78	2.61	2.75	3.05
1:14	2.78	2.61	2.78	3.25

mass at 105–115 °C. Then, it is allowed to cool at room temperature. The weight is now noted as (W1). The dry specimen is then immersed in clean water for 24 h. Finally, the specimen is removed, cleaned and weighed and noted as (W2) (Charts 3 and 4; Tables 6 and 7).

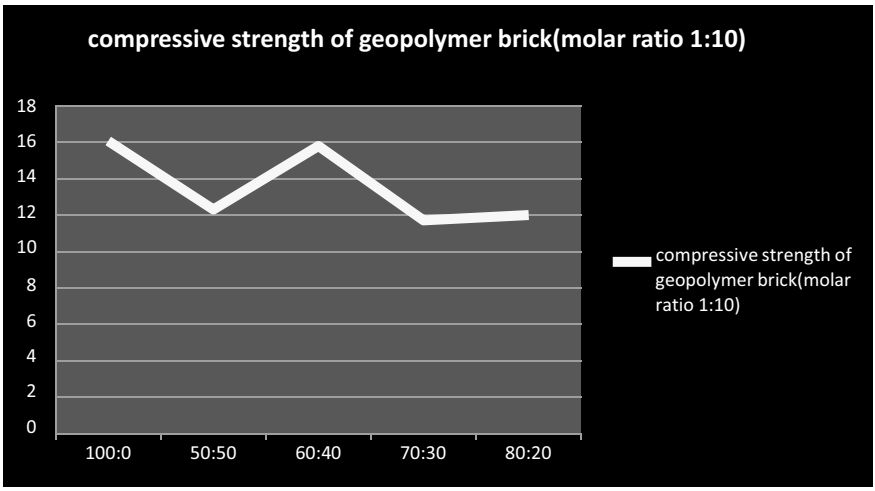

Chart 3 Graphical representation of water absorption of geopolymer brick (1:10)

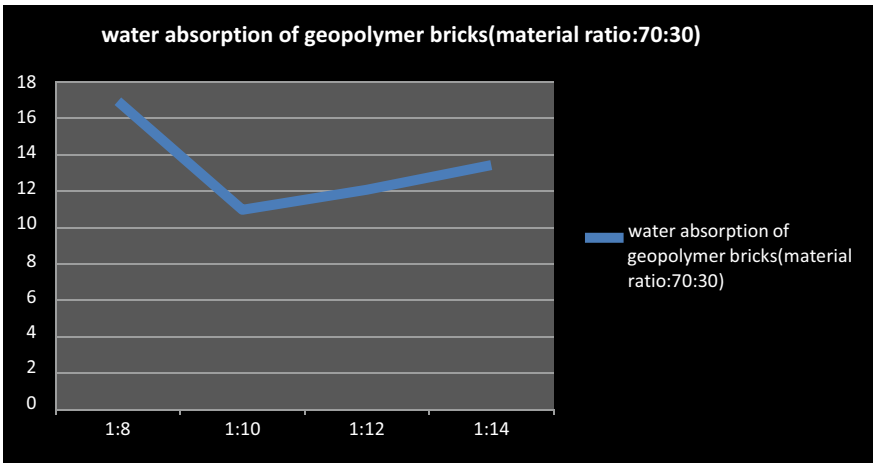

Chart 4 Graphical representation of water absorption of geopolymer brick (70:30)

Table 6 Water absorption of geopolymer brick (1:10)

Molar ratio of alkaline solution (1:10)			
Material ratio (soil:fly ash)	Initial dry weight ($W1$) in kg	Final weight after water absorption ($W2$) in kg	% of water absorption
100:0	3.10	3.62	16.20
50:50	2.63	2.95	12.43
60:40	2.75	3.18	15.93
70:30	2.68	3.00	11.84
80:20	2.86	3.20	12.13

Table 7 Water absorption of geopolymer brick (70:30)

Molar ratio (soil: fly ash = 70:30)			
Material ratio (soil:fly ash)	Initial dry weight ($W1$)in kg	Final weight after water absorption ($W2$) in kg	% of water absorption
1:8	2.73	3.20	17.06
1:10	2.68	2.97	11.10
1:12	2.76	3.10	12.20
1:14	2.78	3.15	13.55

6.3 Efflorescence Test

It is a whitish crystalline salt compound. It consists of magnesium sulphate, calcium sulphate and carbonates of sodium and potassium. Efflorescence deposits on the surface of the brick are mainly due to moist conditions and low temperature. The presence is mentioned as nil, slight and moderate.

6.4 Dimension Test

Few sample bricks are selected for dimension test. The length, width and height are noted. The variations in dimensions are limited within 3% for class 1 and 8% for the other remaining classes.

7 Conclusion

From the geopolymer bricks obtained by different material ratios and ratios of alkaline solutions, it is concluded that

i. Geopolymer bricks have low weight compared to normal bricks.

ii. Considering the 7-day and 14-day strength, the maximum compressive strength was obtained by the brick with the material ratio 70:30.
iii. The maximum compressive strength obtained with different percentages of alkaline solutions of geopolymer bricks of 1:10 ratio remains the same after 7 days and 14 days.
iv. The water absorption and the penetration obtained from the test are comparatively less for geopolymer bricks than the normal bricks.
v. Due to the oven curing method and geopolymerization, small amount of was restrained in the production of geopolymer bricks.
vi Therefore, we come to a conclusion that the geopolymer bricks are light in weight and environmental friendly. Approximately, they have the nearest compressive strength and decreased factor of water absorption than the normal bricks.

References

1. Khater HM, Ezzat M, El Nagar AM (2016) Engineering of low cost geopolymer building bricks applied for various construction purposes. Int. J. Civil Eng. Technol. **7**(4), 81–99 (2016)
2. Banupriya C, John S, Suresh R, Divya E, Vinitha D (2016) Experimental investigations on geopolymer bricks/paver blocks. Indian J. Sci. Technol. **9**(16) (2016)
3. Zivica V, Palou MT, Krizma M (2014) Geopolymer cements and their properties: a review. Build. Res. J. **61**(2), 85–100 (2014)
4. Saravanan G, Jeyasehar CA, Kandasamy S (2013) Flyash based geopolymer concrete–a state of the art review. J. Eng. Sci. Technol. (Review article), Review **6**(1), 25–32 (2013)

Optimization of Mechanical Behaviors of Boiled Egg shell Particulate-banana fiber Reinforced Polyester Composites

K. Nijandhan, M. Raghunath, B. Monish Kanna, P. Nithish, G. Vishnu Prakash, and E. Logesh

Abstract The natural fiber-reinforced polymer composites are recognized as an alternative to wood and plastics in recent years. The natural plant fibers are extracted from various parts of the tree and are used in polymer composites. Natural fibers have gained popularity over synthetic fibers because of their low cost, lightweight, abundance as natural and renewable resources, and versatile mechanical properties, among others. Natural fibers in numerous applications in many fields such as automotive, textile, fiberboard, cushion, paper, mattress, door, wall panel, air cleaner, dashboard and insulation mat manufacturing, as well as in the construction and transportation industries. This present investigation focuses on boiled eggshell particulated banana fiber-polyester composites. The resin content of 60% is maintained constantly, and reinforcement is maintained as fiber content of 40-x%, where x is the particulate content in weight % was maintained for the different combination of fabrication parameters. The tensile strength of fabricated composites has been evaluated as per ASTM standards. The effect of fiber length and filler content on the mechanical behaviors of banana fiber-polyester composites was studied using ANOVA and surface plots. The nonlinear regression models have developed for the prediction of mechanical behaviors over the specified range of conditions and optimized the better values of parameter.

Keywords Banana fiber · Boiled shell · Polyester resin · Tensile strength · Response surface methodology

1 Introduction

Natural fibers are potential alternatives to artificial fibers such as glass, aramid and carbon fibers. The natural fibers have abundant, environment-friendly, low cost, no hazard during handling, etc. There is a growing interest in development of new

K. Nijandhan (✉) · M. Raghunath · B. M. Kanna · P. Nithish · G. Vishnu Prakash · E. Logesh
Department of Mechatronics Engineering, Bannari Amman Institute of Technology, Sathyamangalam 638402, Tamil Nadu, India
e-mail: nijandhan@bitsathy.ac.in

G. Kumaresan et al. (eds.), *Advances in Materials Research*, Springer Proceedings in Materials 5, https://doi.org/10.1007/978-981-15-8319-3_12

materials which enhance optimal utilization of natural resources and, particularly, of renewable resources. Natural fibers such as jute, coir and sisal belong to this category. The usage of natural fibers as reinforcement in engineering field is increasing in trend. Many composites exhibit great weight to strength ratio, corrosion, oxidation, wear, etc. This natural composite has unique characteristics which provide engineer with design opportunities [1]. Many manufacturing processes for composites are well adapted to the fabrication of large, complex structures, which allows consolidation of parts, reduction of manufacturing costs [2]. The composite strength depends on the verity of reinforcement, fiber content, fiber length, process temperature, operating pressure, manufacturing method, etc. Owolabi et al. [3] fabricated the coir fiber with phenol–formaldehyde resins composites. The mechanical properties were studied and concluded that coconut fiber has potential for reinforcement [4]. The other fibers such as sisal-polymer composites were successfully proved in composite applications. Most of the research was carried out on sisal-polymer composites in the mid-1990s. On the other hand, the people incorporated the particles as reinforcement for its increasing nature of mechanical properties of composites. The particles have two different types, one is organic and another one is inorganic particles. Chi-Ming et al. [5] developed the polypropylene (PP) and calcium carbonate-based composites and reported that the particulates were improved the mechanical properties of the composites [6]. Leong et al. [7] studied the polypropylene-based hybrid composites. The mechanical and thermal properties of hybrid (PP) composites made from calcium carbonate ($CaCO_3$) and talc—PP composites of different filler weight ratios (talc/$CaCO_3$) were evaluated and found that particulates were improved the composite properties [8]. Mohanty et al. studied the influence of different surface modifications and fiber content on the performance of the biocomposites [9]. Increasing the fiber content will lead to improvement of composite strength at a certain level; thereafter, it will reduce the strength of composites. Jute fiber content also affected the biocomposite performance and about 30% by weight of jute showed optimum properties of the biocomposites [10–15].

Moreover, a large number of researchers incorporated new organic filler into composites for the further improvement of composites. Further, they found the optimum parameters for better mechanical properties using the techniques such as heuristic and non-heuristic optimization techniques. Kailainathan et al. [16]) investigate the effect of process temperature and particulate content on sisal fiber-reinforced composite. The impact behavior of fabricated composite specimens were optimized using pattern search optimization and validate the results, which shows there is small value of error in between in experimental and optimized values [17–19]. In the present investigation, the composites were fabricated using natural fiber and boiled eggshell particles and evaluate their mechanical properties in terms of changing the fiber length and filler weight content (%). To develop the regression equation for the mechanical behaviors of banana fiber, boiled eggshell polyester composites found the better parameters for better mechanical properties using genetic algorithm.

Table 1 Parameters and levels

SI. No.	Parameters	Level 1	Level 2	Level 3	Level 4	Level 5
01	Fiber length (mm)	10	20	30	40	50
02	Particulate wt content (%)	5	10	15	20	25

2 Experimental Procedure

2.1 Materials and Methods

The banana fiber (diameter 0.8–1.2 mm) and boiled shells (size 40 μm) are collected from local areas of erode. The experiments were conducted as per the full factorial design. Table 1 shows the parameters and levels used in this experiment. The unsaturated polyester is used as a matrix material. The matrix system consists of unsaturated polyester resin, cobalt actuate accelerator and MEKP catalyst in the ratio of 1:0·015:0·015. The composites were fabricated in the mold size of 300 × 300 × 3 mm^3 using compression molding process in the operating pressure of 2.3 MPa and curing temperature of 60 °C in 45 min. The composite sheets allowed for curing 24 h in room temperature. After curing, the tensile specimens were cut as per the ASTM standards.

2.2 Mechanical Testing

The tensile behavior of egg cell particulate incorporated banana fiber-polyester composites was measured using the Universal Testing Machine (Make: Shimadzu & Model: AG-IS) at a cross-head speed of 5 mm/min (Fig. 2) as per the ASTM D638-08 standard. The specimens (Fig. 1) were cut from the fabricated composite in the approximate length, width and thickness of 165 mm, 25 mm and 3 mm, respectively. Five identical specimens were tested to obtain the average tensile strength value. Table 2 shows the tensile properties of banana-boiled eggshell particulate.

2.3 Regression Modeling and Optimization

The statistical tool regression analysis helps to estimate the value of one variable from the given value of another. The nonlinear regression equations were developed for determining the tensile properties within the lower and upper limits of the fiber parameters. The quadratic model was selected, based on the fit summary and R^2 value. The coefficient of determination, R^2, is used in the context of the statistical models whose main purpose is the prediction of future outcomes, on the basis of other

Fig. 1 Tensile properties of banana-boiled shell particulate

Fig. 2 Photographic image of tensile testing machine

related information. Table 3 shows the regression equation of tensile strength models of banana fiber-boiled eggshell polyester composites. Genetic algorithm is a method to solve the constrained and unconstrained optimization problems which is based on natural selection, the process that drives biological evolution. The parameters of genetic algorithms are shown in Table 2 response surface and contour plots for the tensile strength.

3 Result and Discussion

The effect of tensile strength on fiber length and particulate content of banana-boiled eggshell particulate incorporated composites were shown in Fig. 3. The strength of composites increased up to 30 mm thereafter it reduced, this is due to the more length of fibers gets more fiber-fiber contact which may reduce strength of composites. On the other hand, the small length of fiber tends to less strength transfer of fiber, this is due to the fiber gets more stress concentration leads to quick failure. In the case of particulate content, the high strength obtained at 15% weight content. The high

Table 2 Tensile properties of fabricated composites

Run	Fiber length(mm)	Particulate wt content (%)	Tensile strength (Mpa)
S1	10	5	11.7
S2	10	10	12.7
S3	10	15	15
S4	10	20	13.1
S5	10	25	12.1
S6	20	5	14.8
S7	20	10	17.4
S8	20	15	20
S9	20	20	18.1
S10	20	25	15.7
S11	30	5	17.7
S12	30	10	21.2
S13	30	15	25
S14	30	20	22.1
S15	30	25	18.5
S16	40	5	15.3
S17	40	10	17
S18	40	15	19
S19	40	20	17.6
S20	40	25	15
S21	50	5	12.3
S22	50	10	14.1
S23	50	15	15.8
S24	50	20	14.6
S25	50	25	13.4

Table 3 Regression equation of tensile tested specimens

Parameters	Equation	R^2
t_s	$6.74 + 0.937*\text{fl} + 1.357*\text{ fc} + 0.0004*\text{ fl} * \text{fc} - 0.015*\text{fl}^2 - 0.004*\text{ fc}^2$	0.9

content of boiled egg shell particulate leads to insufficient resin to wet the fibers and particulate and low fiber content tends to small amount fiber and particulate carry the load. The regression equation of mechanical properties was formulated (Fig. 4).

The regression equation has R^2 value of 0.9 which shows the predicted models were well fit into the experimental values.

The surface response plot and contour plots were shown in Fig. 5. The genetic algorithm is used to optimize the mechanical properties of composites. The maximum

Fig. 3 Photographic image of tensile test specimen after fracture

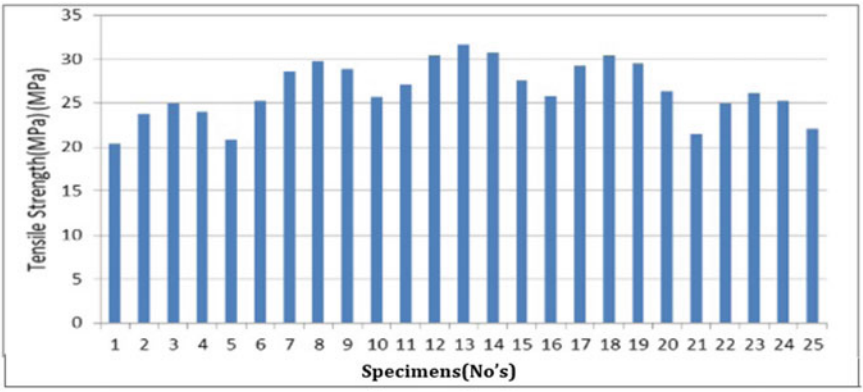

Fig. 4 Validation of particulated polyester composites

values of tensile strength are 26.2 MPa in the fiber length of 35.5 mm and particulate content of 17.49 wt.% was the optimized values of banana fiber-boiled eggshell particulate composites. The optimized values were validated through *V* experimentation and found the minimum value of error.

3.1 Genetic Algorithm

Genetic algorithm is a heuristic optimization technique. The genetic algorithm is used to solve both constrained and unconstrained optimization problems that is based on

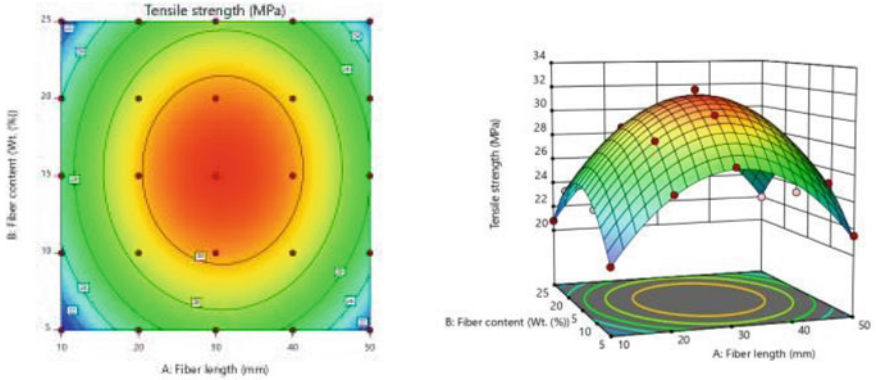

Fig. 5 3D contour plot

natural selection, the process that drives biological evolution. The genetic algorithm repeatedly modifies a population of individual solutions. The optimal parameters of composites were found genetic algorithm. The maximum value of 25 MPa as a optimized value, in the fiber length of 30 mm and particulate content of 15% wt.

4 Conclusion

The tensile properties if banana fiber-reinforced boiled eggshell particulates were evaluated. The experimental results show the fiber length of 30 mm and particulate content of 15% wt. gives the tensile strength of 25 MPa, respectively. The regression equation is used to predict the mechanical properties, and its significance is verified by 3D response surface and contour plots. Using genetic algorithm, the optimal parameters were found and it is verified by validation tests. The results were shows that banana fiber-boiled eggshell particulate improve the strength of the composite and it can be potential reinforcement of lightweight components in the field of automotive, construction, aero applications.

References

1. Felix Prasad C, Jayabal S, Natarajan U (2007) Optimization of tool wear in turning using genetic algorithm. Indian J Eng Mater Sci 14:403– 407
2. Cus F, Balic J (2003) Optimization of cutting process by GA approach. Robot CIM-Int Manuf 19:113–121 (for solving constrained and unconstrained optimization problem)
3. Owolabi O, Czvikovszky T, Kovács I Coconut-fiber-reinforced thermosetting plastics. J Appl Polym Sci 30(5):1827–1836
4. Onwubolu GC, Kumalo T (2001) Optimization of multipass turning operations with genetic algorithms. Int J Prod Res 39:3727–3745

5. Lo C-M, Ngan H, Tso W-K, Liu C-L, Lam C-M, Poon RT-P, Fan S-T, Wong J (2002) Randomized controlled trial of transarterial lipiodol chemoembolization for unresectable hepatocellular carcinoma. Hepatology 35(5):1164–1171
6. Deb K, Goyal M (1997) Optimization for engineering designs using a combined genetic search. In: Proceedings of the seventh international conference on genetic algorithms, pp 521–528
7. Dang W, Kadiyala I, Zhao Z, English JP, Mao H-Q, Leong KW (2004) Biodegradable compositions comprising poly (cycloaliphatic phosphoester) compounds, articles, and methods for using the same. U.S. Patent 6,800,672, issued October 5, 2004
8. Gupta R, Batra JL, Lal GK (1995) Determination of optimal sub division of depth of cut in multi pass turning with constraints. Int J Prod Res 33:2555–2565
9. Caprino G, Diterlizzi A, Tagliaferri V (1990) Damage in drilling glass fiber reinforced plastics. Int J Mach Tools Manufact 301:77–84
10. Deb K (2004) Optimization for engineering design: algorithms and example. Prentice-Hall of India, New Delhi
11. Das G, Biswas S (2016) Physical, mechanical and water absorption behaviour of coir fiber reinforced epoxy composites filled with Al_2O_3 particulates. In: IOP conference series: materials science and engineering, vol 115, No. 1, p 012012. IOP Publishing
12. Biswas S, Debnath K, Patnaik A (2012) Mechanical behaviour of short bamboo fiber reinforced epoxy composites filled with alumina particulate
13. Navaneethakrishnan S, Athijayamani A (2015) Taguchi method for optimization of fabrication parameters with mechanical properties in fiber and particulate reinforced composites. Int J Plast Technol 19(2):227–240
14. Durowaye SI, Lawal GI, Akande MA, Durowaye VO (2014) Mechanical properties of particulate coconut shell and palm fruit polyester composites. Int J Mater Eng 4(4):141–147
15. Mishra V, Srivastava A (2014) Epoxy/wood apple shell particulate composite with improved mechanical properties. Int J Eng Res Appl 4(8):142–145
16. Kailainathan S, Muralikannan R, Kalyana Sundaram S, Nijandhan K (2015) Statistical analysis and pattern search optimization on the impact properties of talk particulates impregnated sisal fiber reinforced polyester composites. Trans Indian Inst Met 68(5):859–865
17. Rao SS (1996) Engineering optimization: theory and practice. New Age, New Delhi
18. Latif A, Abrar M, Manaf A, Edeerozey M, Firdaus MIS, Maslamany L, Munawar RF (2016) Effects of particulate types on biomass particulate filled kenaf/polypropylene composite. In: Key engineering materials, vol 694, pp 23–28. Trans Tech Publications Ltd.
19. Chang WP, Kim KJ, Gupta RK (2009) Moisture absorption behavior of wood/plastic composites made with ultrasound-assisted alkali-treated wood particulates. Compos Interfaces 16(7–9):937–951

Particle Swarm Optimization Tuned Fuzzy Controller for Vibration Control of Active Suspension System

K. R. Bharath Kumar, P. Senthil Kumar, K. S. Dharaneeshwarakumar, and B. Deepak

Abstract This paper focus on the development of Particle Swarm Optimization (PSO) tuned fuzzy logic controller for vibration control of hydraulic actuated active suspension. A 2 Degrees of Freedom (DoF) of quarter car model with hydraulic actuator dynamics has been developed to measure performance of active suspension for various road conditions. A fuzzy controller was proposed for active suspension in order to handle the complexity of active suspension and nonlinearity in actuator dynamics. The effective control of fuzzy logic largely depends on optimum value of membership function which has been tuned by knowledge of user. A novel PSO algorithm is proposed to overcome the limitation of manual tuning in fuzzy controller. The optimum tunable parameters for membership function are obtained based on fitness function of PSO algorithm. The simulation of quarter car model based nonlinear active suspension is carried out for bump and random profile. The results from experiment confirm the feasibility of proposed PSO tuned fuzzy controller for hydraulic actuated nonlinear active suspension in terms of body displacement, acceleration, and suspension travel.

Keywords Active vibration control · Quarter car model · Particle swarm optimization · Fuzzy logic · Actuator dynamics

K. R. Bharath Kumar (✉) · P. Senthil Kumar · K. S. Dharaneeshwarakumar · B. Deepak
Department of Mechanical Engineering, Bannari Amman Institute of Technology, Sathyamangalam, Tamil Nadu 638402, India
e-mail: bharathkumar14899@gmail.com

P. Senthil Kumar
e-mail: senthilkumarp@bitsathy.ac.in

K. S. Dharaneeshwarakumar
e-mail: dharaneeshwarakumar.me17@bitsathy.ac.in

B. Deepak
e-mail: deepak.me17@bitsathy.ac.in

G. Kumaresan et al. (eds.), *Advances in Materials Research*, Springer Proceedings in Materials 5, https://doi.org/10.1007/978-981-15-8319-3_13

Nomenclature

m_w	Wheel mass
m_b	Body mass
K_s	Suspension stiffness coefficient
k_t	Tire stiffness coefficient
x_w	Wheel displacement
v_t	Total volume of actuator
C_{tp}	Total leakage coefficient
C_d	Discharge coefficient
W	Slope of spool valve area
U	Servo voltage
Q	Fluid flow rate
$r(t)$	Reference signal
$y(t)$	Suspension travel
b_s	Suspension damping coefficient
x_p	Particle best of particles
x_g	Global best of particles
P_l	Pressure drop
A_a	Actuator ram area
r	Road profile
b_s	Damping force
f_s	Actuator force
x_b	Body displacement
x_v	Wheel displacement
r	Road profile
X	Position of particles
V	Velocity of particles
$i, i+1$	Current and next iteration position
Ω	Momentum factors
r_1, r_2	Random numbers
$C_{1,}C_2$	Cognitive acceleration factor
h_1, h_2	Road height
A, B, C	Scaling factors
P_s	Pressure of hydraulic actuator

1 Introduction

The purpose of suspension system is to reduce the road disturbance by minimizing displacement and acceleration of vehicle body. Design of suspension involves an optimization process where the design elements are selected by compromising on soft and hard suspension. Nowadays, many researcher focusing their research on active

suspension systems due to its ability to operate on wide range of frequency [1–6]. The development of computer and micro-processor improved practical implementation of active suspension in automotive industries [7, 8].

Alleyne and Liu proposed a nonlinear control technique for hydraulic operated quarter car model based active suspension [9]. A nonlinear control law formulated to control dynamic nature of hydraulic actuator. The quarter car model is a simplified model of car with 2 DoF by using that the vertical motion of car body and wheel has been measured for active suspension [10]. Rajendran first introduced fuzzy logic to practical application for quarter car model [11]. Fuzzy logic has an ability to control a system without any mathematical model. Further, fuzzy controller is simple and handle parameter uncertainty and nonlinearity in system very well compare to model based control. Palanisamy et al. formulated fuzzy control algorithm by considering states of sprung mass velocity and acceleration for quarter-car model [12]. Cherry and Jones investigated the application of fuzzy control to continuously variable damping automotive suspension using full car model [13]. Huang and Chao employed grey predictor with fuzzy controller to remove the tire deformation from feedback signal of active suspension [14]. D'Amato and Viassolo proposed double loop fuzzy control to avoid rate space issue in active suspensions [15].

However, the optimum performance of traditional controller depends on appropriate fuzzy rules and membership functions. There are no proper guidelines to tune fuzzy parameters and this time-consuming tuning process is often carried out by knowledge of expert [16]. Hence, intelligent optimization algorithms were introduced into fuzzy controller to tune fuzzy parameters-based performance index in order to reduce the time consumption of tuning process. Rao and Prahlad developed tunable fuzzy logic controller in which input membership functions are fine-tuned by trial and error methods using look-up table [17]. Shao proposed a self-organizing fuzzy controller (SOFC) to establish membership function without the intervention of human expert [18]. However, they need a complicated learning mechanism and its rules increase exponentially in terms of number of dimension make it difficult for real-time implementation. Hence, in this paper PSO algorithm is introduced to fuzzy logic controller to tune the membership function.

2 System Modeling

The 2 DoF of quarter car model is represented in Fig. 1. The sprung and unsprung mass are coupled together by the spring, damper, and hydraulic actuator to generate active force. The equation of motion for the 2 DoF of quarter car model is derived from Newton's second law of motion as described in Eq. (1)–(3).

$$m_b\ddot{x}_b + b_s(\ddot{x}_b - \dot{x}_w) + k_s(x_b - x_w) = f_s \tag{1}$$

$$m_w\ddot{x}_w + b_s(\dot{x}_w - \dot{x}_b) + k_s(x_w - x_b) + k_t(x_w - r) = -f_s \tag{2}$$

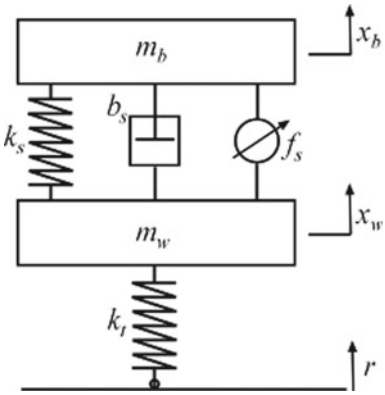

Fig. 1 Quarter car model of active suspension

$$\dot{f_s} = -\beta f_s - \alpha A_a^2(\dot{x}_b - \dot{x}_w) + \tau A_a x_v \sqrt{P_s - \frac{\text{sgn}(x_v) f_s}{A_a}} \tag{3}$$

The hydraulic actuator is modeled with four-way piston–valve arrangement. The force exerted by actuator is $f_a = A_a P_L$ where A_a and P_L represent area of piston and pressure drop inside cylinder respectively. The rate of change of pressure drop expressed as in Eq. (4).

$$\frac{V_t}{4\beta_e} \cdot P_L = C_{tp} P_L - A_a(\dot{x}_{as} - \dot{x}_{au}) + Q \tag{4}$$

Hydraulic flow in cylinder is derived from Eq. (5)

$$Q = C_d w x_v \sqrt{\frac{1}{\rho}\left[P_s - \text{sgn}(x_v) P_L\right]} \tag{5}$$

Hence, the actuator force developed by hydraulic actuator is described by the nonlinear Eq. (6).

$$u_a = -\beta f_s - \alpha A_a^2(\dot{x}_{as} - \dot{x}_{au}) + \tau A_a x_v \sqrt{P_s - \frac{\text{sgn}(x_v) u_a}{A_a}} \tag{6}$$

where $\alpha = 4\beta e/Vt$, $\beta = \alpha Ctp$, $\Gamma = \alpha\ cd\ w\ \sqrt{1/\rho}$ and $x_v = k_c U$. The parameters and values assigned for the quarter car active suspension system with hydraulic actuator represented in Table 1.

The equation of motion for quarter car model with hydraulic actuator dynamics is described below.

$$\dot{x_1} = x_2 \tag{7}$$

Table 1 Parameters for active suspension

Symbol	Value	Unit
m_w	60	kg
m_b	300	kg
k_s	16,000	N/m
k_t	19,000	N/m
b_s	1000	Ns/m
P_s	10,342,500	Pa
A_a	$3.35 * 10^{-4}$	m^2
k_c	0.001	m/V
α	4.515×10^{13}	N/m^5
B	1	s^{-1}
Γ	1.545×10^9	$N/m^{5/2}\ kg^{1/2}$

$$\dot{x_2} = \frac{1}{m_s}[k_s(x_3 - x_1) + c_s(x_4 - x_2) + x_5] \tag{8}$$

$$\dot{x_3} = x_4 \tag{9}$$

$$\dot{x_4} = \frac{1}{m_{us}}[k_s(x_1 - x_3) + c_s(x_2 - x_4) + k_t(z_r - x_3) - x_5] \tag{10}$$

$$\dot{x_5} = -\beta x_5 - \alpha A_a^2(x_2 - x_4) + \Gamma A_a x_v \sqrt{P_s - \frac{\text{sgn}(x_v)x_5}{A_a}} \tag{11}$$

3 Controller Design

3.1 Fuzzy Logic Controller

The plant that is difficult to obtain mathematical models can be easily controlled by fuzzy logic. The estimation of road surface deviation and tire deformation is difficult in active suspension. Hence, the model-free fuzzy logic controller is proposed to control the active suspension without the need for mathematical model. The error (e) and error rate (Δe) of suspension travel is obtained from Eqs. (12 and 13).

$$e(t) = r(t) - y(t) \tag{12}$$

$$\Delta e(t) = \frac{e(t) - e(t-1)}{T} \tag{13}$$

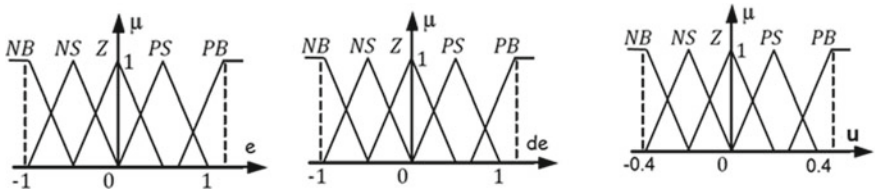

Fig. 2 Membership function for fuzzy logic

Table 2 Fuzzy rules table

	ΔE				
E	NEB	NES	ZER	PES	PEB
NEB	NEB	NEB	NES	NES	ZER
NES	NEB	NES	NES	ZER	PES
ZER	NES	NES	ZER	PES	PES
PES	NEM	ZER	PES	PES	PEB
PEB	ZER	PES	PES	PEB	PEB

The degree of membership function is represented in Fig. 2 with linguistic variables. The input and output membership functions are normalized between −1 and 1. The error in suspension travel is relatively large, so each membership function are expressed by a triangular function.

The total number of possible fuzzy rules are $5 \times 5 = 25$. The empirical fuzzy rule base for active suspension is summarized in Table 2. The rule base for the fuzzy controller has rule of the form as below: R_n: If e is NEB and Δe is NEB then u is NEB. Where R_n is the nth rule. e and Δe are fuzzy input variables. u is control output of fuzzy system. NEB is linguistic terms used in fuzzy system.

3.2 PSO Tuned Fuzzy Logic Controller

The major drawbacks of designing the fuzzy controller are that it requires the experience of human experts to tune the scaling factor of membership function. The time-consuming manual tuning process can be eliminated by fuzzy learning system. Hence, a novel PSO tuning algorithm is proposed as shown in Fig. 3 for fuzzy learning system to adjust the scaling factor of fuzzy logic.

PSO is population-based heuristic search algorithm inspired by swarm methodology for optimization of continuous function [19–22]. The algorithm starts with random population and search for optimum solution by updating population similar to genetic algorithm [23]. Each element in the population is called as particle in PSO. Each particle moves with certain velocity in the search space. The magnitude of velocity decides the movement of particle in the search space. The particle velocity

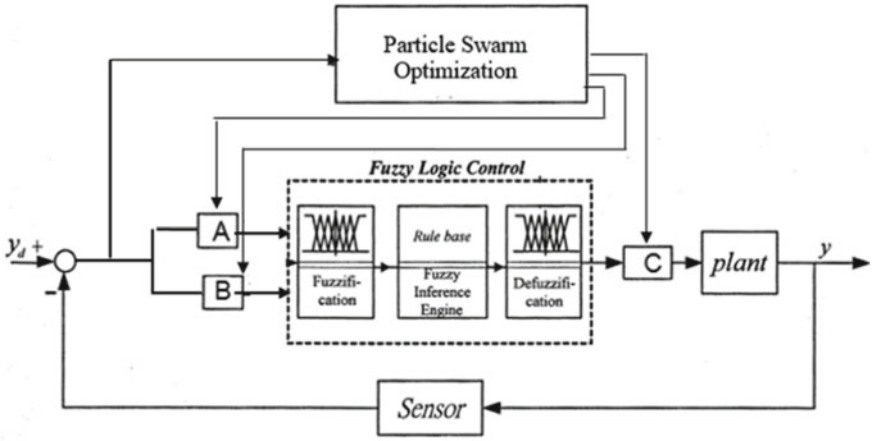

Fig. 3 PSO-tuned fuzzy controller for active suspension

and position are updated based on global best and particle best values as follow;

$$v(i+1) = w \times v(i) + c_1 \times r_1 \times (x_p - x(i)) + c_2 \times r_2 \times (x_g - x(i)) \quad (14)$$

$$x(i+1) = x(i) + v(i+1) \quad (15)$$

The searching algorithm of PSO is described as follows:

Step 1: Select population size and maximum iteration number.

Step 2: Initialize swarm velocity and position randomly for PSO.

Step 3: Select range of scale factors for membership function. The particle positions are defined as scaling factor A, B and C.

Step 4: The fitness function is used for measuring performance index.

Step 5: Calculate the value of the fitness function for each particle using SIMULINK model.

Step 6: Update the x_{p}, x_{g} value by classifying fitness values. If the x_{p} of all current particle is better than x_{g}, then update the value of the global best solution.

Step 7: Modify swarm velocity and position for updated x_p and x_g.

Step 8: Repeat Steps 5 to 8 until the iterations reach its maximum limit to determine the corresponding optimal solution.

4 Simulation

This section presents simulation of hydraulic actuated full car model based active suspension for control algorithm developed in previous section. For comparison, the

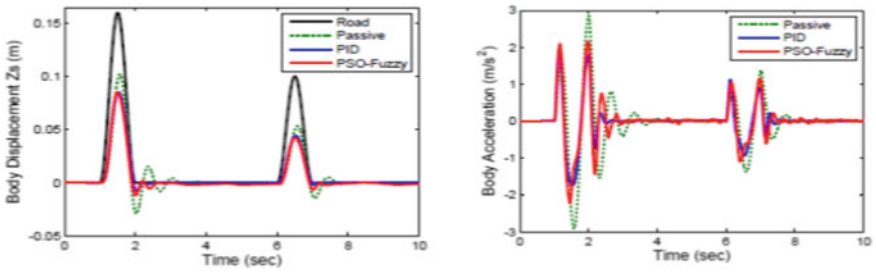

Fig. 4 Response of active suspension for bump road

PID controller introduced for active suspension to demonstrate the effectiveness of proposed controller.

Bump road is always assumed as sinusoidal waveform and the ground disturbances as depicted in Eq. (16) is used for simulation.

$$r(t) = \begin{cases} h_1(1 - \cos(8\pi t)/2) & \text{if } 1 \le t \le 2 \\ h_2(1 - \cos(8\pi t)/2) & \text{if } 6 \le t \le 7 \\ 0 & \text{otherwise} \end{cases} \tag{16}$$

$h_1 = 15$ cm, $h_2 = 10$ cm. The response of passive, PID, and PSO tuned fuzzy controller for body displacement, acceleration is illustrated in Fig. 4. It is clear from the figure that body displacement and acceleration of active suspension is significantly reduced in PSO tuned fuzzy controller.

Table 3 gives the Root-Mean Square (RMS) values for bump road. The performance of suspension parameters are effectively measured using RMS values. The RMS value of the body displacement and acceleration indicates ride quality of the passengers and the amount of vibration reduced by suspension system.

The RMS value of body acceleration is reduced from 0.61 to 0.31 m/s^2 which means 49% of reduction in acceleration is achieved by PSO tuned fuzzy controlled active suspension. Similarly, the percentage of reduction in body displacement, pitch angle and roll angle are 33%, 70% and 31% respectively. It is clear from the table that displacement and acceleration of vehicle are considerably reduced by PSO fitness function which further improves ride comfort and stability of vehicle.

In real time, road disturbance is specified as random process with sequence of $N(0, 2\pi n0\sqrt{G0V})$ random variables, where $G0$ is road roughness coefficient and $n0 = 0.1$ is spatial frequency. The road roughness of D with ISO2631 standards road is selected to generate the random road profile. The response of suspension parameter

Table 3 RMS value for bump road

Parameter	Passive	Active PID	PSO Fuzzy
Displacement (cm)	1.83	1.58	1.22 (↓33%)
Acceleration (m/s^2)	0.61	0.41	0.31 (↓49%)

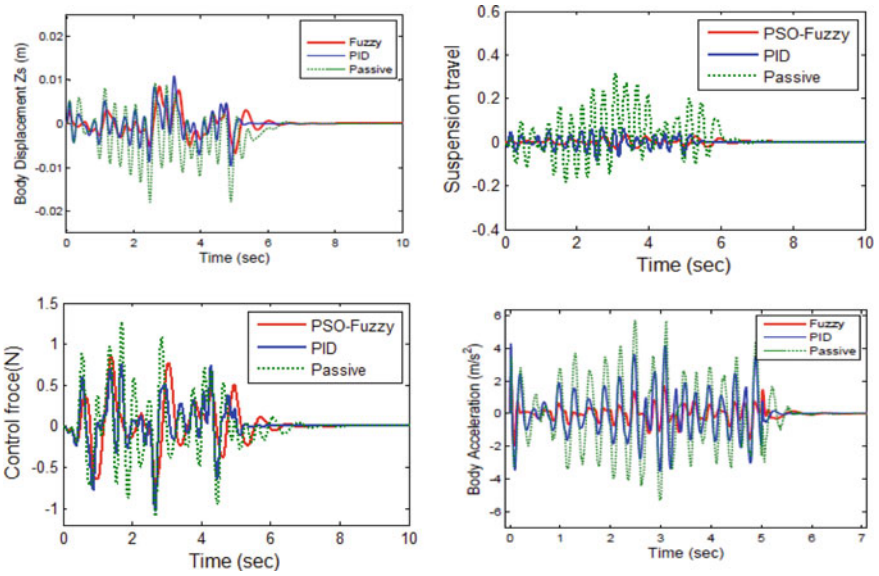

Fig. 5 Response of active suspension for random road

Table 4 RMS value for bump road

Parameter	Passive	Active PID	PSO fuzzy
Displacement (cm)	3.83	2.09	1.81 (↓52%)
Acceleration (m/s^2)	1.34	0.86	0.31 (↓76%)

for random road is compared with passive and PID-controlled suspension system as illustrated in Fig. 5. It is seen from the figure that fuzzy controller auto tuned by PSO algorithm impressively reduce body displacement and acceleration of suspension system.

Table 4 gives the RMS values of the body displacement, body acceleration, pitch angle, and roll angle for random road. The PSO-tuned fuzzy active suspension reduces body acceleration from 1.34 to 0.31 m/s^2 and body displacement from 3.83 to 1.81 cm. From this table, it is clear that greater degree of reduction in suspension parameters can be achieved from PSO tuned fuzzy controller for the random road inputs, which further confirms the possibility of the proposed PSO tuned fuzzy controller for nonlinear active suspension.

5 Conclusions

A 2 DoF of quarter car model was developed for nonlinear hydraulic actuated active suspension system to measure heave motion of vehicle. PSO algorithm was proposed

for fuzzy controller to overcome the limitation in manual tuning of membership function. The scaling factor of membership function was tuned by PSO based on the fitness function of active suspension. The fitness function was defined in such a way that will minimize the sprung mass acceleration and suspension travel of vehicle. The simulation of quarter car model-based nonlinear active suspension was carried out for bump and random profile. The results of experimentation confirm that the proposed PSO tuned fuzzy controller significantly reduces body displacement, acceleration of active suspension to improve the ride comfort of vehicle.

References

1. Cao. J, Liu. H, Li P, Brown DJ (2008) State of the art in vehicle active suspension adaptive control systems based on intelligent methodologies. IEEE Trans Intell Transp Syst 9(3):392–405
2. Yazici H, Sever M (2017) Output derivative feedback vibration control of an integrated vehicle suspension system. Proc Inst Mech Eng Part I J Syst Control Eng (2017)
3. Li H, Gao H, Liu H, Liu M (2012) Fault-tolerant H∞ control for active suspension vehicle systems with actuator faults. Proc Inst Mech Eng Part I J Syst Control Eng 226(3):348–363
4. Wilson DA, Sharp RS, Hassan SA (1986) The application of linear optimal control theory to the design of active automotive suspensions. Veh Syst Dyn 15(2):105–118
5. Kamalakkannan K, Elayaperumal A, Managlaramam S (2013) Input advanced control of semi active half car heave model. J Mech Sci Technol 27(5):1225–1231
6. Rajamani R, Hedrick JK (1995) Adaptive observers for active automotive suspensions: theory and experiment. IEEE Trans Control Syst Technol 3(1):86–93
7. Sun W, Pan H, Gao H (2016) Filter-based adaptive vibration control for active vehicle suspensions with electrohydraulic actuators. IEEE Trans Veh Technol 65(6):4619–4626
8. Yagiz N, Hacioglu Y (2008) Backstepping control of a vehicle with active suspensions. Control Eng Pract 16(12):1457–1467
9. Alleyne AG, Liu R (2000) Systematic control of a class of nonlinear systems with application to electrohydraulic cylinder pressure control. IEEE Trans Control Syst Technol 8(4):623–634
10. Sathishkumar P, Jancirani J, John D (2014) Reducing the seat vibration of vehicle by semi active force control technique. J Mech Sci Technol 28(2):473
11. Rajendiran S, Lakshmi P (2016) Simulation of PID and fuzzy logic controller for integrated seat suspension of a quarter car with driver model for different road profiles. J Mech Sci Technol 30(10):4565–4570
12. Palanisamy S, Karuppan S (2016) Fuzzy control of active suspension system. J Vibroeng 18(5)
13. Cherry AS, Jones RP (1995) Fuzzy logic control of an automotive suspension system. In: IEEE Proc Control Theory Appl 142(2):149–160
14. Huang SJ, Chao HC (200) Fuzzy logic controller for a vehicle active suspension system. Proc Inst Mech Eng Part D J Automob Eng 214(1):1–12
15. D'Amato FJ, Viassolo DE (2000) Fuzzy control for active suspensions. Mechatronics 10(8):897–920
16. Zareh SH, Sarrafan A, Khayyat A, Zabihollah A (2012) Intelligent semi-active vibration control of eleven degrees of freedom suspension system using magnetorheological dampers. J Mech Sci Technol 26(2):323–334
17. Rao MVC, Prahlad VA tunable fuzzy logic controller for vehicle-active suspension systems. Fuzzy Sets Syst 85(1):11–21
18. Shao S (1988) Fuzzy self-organizing controller and its application for dynamic processes. Fuzzy Sets Syst 26(2):151–164

19. Nikranajbar A, Ebrahimi MK, Wood AS (2010) Parameter identification of a cage induction motor using particle swarm optimization. Proc Inst Mech Eng Part I J Syst Control Eng 224(5):479–91
20. Moghaddam JJ, Bagheri A (2015) A novel stable deviation quantum-behaved particle swarm optimization to optimal piezoelectric actuator and sensor location for active vibration control. Proc Inst Mech Eng Part I J Syst Control Eng 229(6):485–94
21. Sedraoui M, Boudjehem D (2012) Robust fractional order controller based on improved particle swarm optimization algorithm for the wind turbine equipped with a doubly fed asynchronous machine. Proc Inst Mech Eng Part I J Syst Control Eng 226:1274–86
22. Ab Talib MH, Mat Darus IZ (2017) Intelligent fuzzy logic with firefly algorithm and particle swarm optimization for semi-active suspension system using magneto-rheological damper. J Vibration Control 23:501–14
23. Sarathambekai S, Umamaheswari K (2017) Intelligent discrete particle swarm optimization for multiprocessor task scheduling problem. J Algorithms Comput Technol 11:58–67

Additive Manufacturing Parameter Optimization with Automated Post-printing Flaw Detection Using Convolutional Neural Networks

E. Prakash, M. Subramaniyan, Anna Kalyani Naveen Sankar, and Kumaraguru Chandra Kumar

Abstract In additive manufacturing, the printing quality and errors are inevitable nowadays. The quality errors such as not extruding at start of the print, not sticking to the bed, stringing or oozing, layer shifting, layer separation and stops extruding mid print can lead to complete wastage of material and time. Detecting such defects while printing the piece will help eradicating the wastage of material and saves lots of valuable time. Providing a proper checkpoints and critical design identification where the defects are highly vulnerable can help us perform corrective measures in the early stages of printing. Here we present our findings on a novel approach based on visual pattern mining using volumetric elemental pixels popularly known as Voxels. The proposed finding provides an accelerated process monitoring and detection of printing failure conditions—by the method of classifying every layer of the printing 3D model into critical and normal layers using advanced deep learning pattern mining approach with convolutional neural networks and automatic choice of critical checkpoints from the classification, to calculate error deviation between the Voxel image of critical 3D printed layer with actual image of same layer from the semi-finished part. Integration of a camera in 3D printer, Voxel separation and processing, pattern mining, and deep machine learning provides the above-proposed system which results in high test accuracy >93% on unknown raw models. Images of parts are taken at various stages of the printing process according to the part geometry, and Voxel images are extracted from >20k 3D models. A deep learning method, convolutional neural networks (CNN), is proposed to classify the parts into either 'normal' or 'critical' category. Parts using PLA and FDM materials were printed to demonstrate the proposed framework. We demonstrate that this methodology precisely and unambiguously detects the print failure in most cases and stops the print for manual corrective measure.

Keyword Voxels · Pattern mining · Convolutional neural network · 3D printing · Critical point

E. Prakash (✉) · M. Subramaniyan · A. K. Naveen Sankar · K. Chandra Kumar
Department of Mechanical Engineering, Bannari Amman Institute of Technology, Sathyamangalam, Erode, Tamil Nadu 638401, India
e-mail: prakashe@bitsathy.ac.in

G. Kumaresan et al. (eds.), *Advances in Materials Research*, Springer Proceedings in Materials 5, https://doi.org/10.1007/978-981-15-8319-3_14

1 Introduction

The new ability of creating complex geometrical shape with more manufacturing options using the design software, termed 3D printing, has become a viable option for production.

Various applications have been arised over these technologies significantly in several fields, but they do not have any designated system to track and monitor the printing progress. This causes the 3D printers to print the part even though filament ran out or any other potential defects occur in the filament extruding process causing the wastages and unease of printed components. Hence, a system is required to detect the defect which occurs during printing stages and not only defect and also to ensure the perfectness in printed components. Continuous detection may also not end up productive; hence, effective monitoring of critical stages will be effective [1]. Automated monitoring system is mostly viable for production-scale 3D printing farm where multiple printers are being functioned at same time.

New method has been proposed to for error solving by monitoring the 3D printer's printing functionalities [8] at various checkpoints by pausing and comparing with the Voxel-layer image (Fig. 1) to resolve the defect identification and to decide whether to continue or hold the printing process.

The critical checkpoints defined used the new area of machine learning coined 'Deep Learning' which provides the solution for figuring out the critical points. More than 10,000+ Cad model files have been learned by the proposed method with annotated critical point, thereby getting the capabilities of finding the critical points.

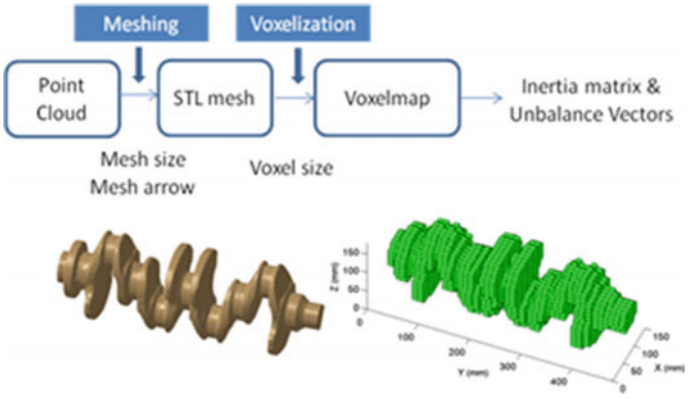

Fig. 1 3D model to Voxel conversion

2 Methodology

The process begins with the algorithm of segregating the images to figure out the critical points in the components. Initially, the 3D component is sliced into layers based on layer thickness and each consecutive layer is summed up to figure up with consolidated layer. Figure 2 indicates the separated layers, Fig. 2b indicate the consolidated layers. Once the image splits into layers it undergoes the below methodology to figure out the critical points.

2.1 Local Receptive Fields

Each neuron in the first hidden layer will be connected to a small region of the input neurons. This region in the input image is called the local receptive field for the next hidden neuron (Fig. 3). Then, we slide the local receptive field across entire input image pixels [2]. For each field, there will be different hidden neuron in the first hidden layer.

2.2 Shared Weights and Biases

Each hidden neuron has a bias and 3×3 weights connected to its receptive fields [3]. We are going to use the same weights and biases for 148×148 neurons.

$$\sigma\left(b + \sum_{l=0}^{4}\sum_{m=0}^{4} \omega_{l,m} a_{j+l,k+m}\right)$$

This means that all the neurons in the first hidden layer detect exactly the same feature at different locations in the input image. These shared weights and biases are used to define a kernel/filter/feature map. For critical point identification, we use

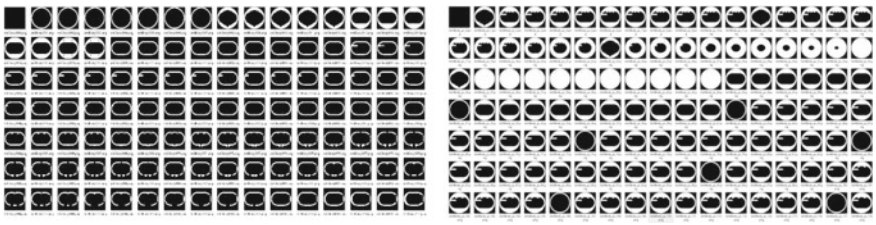

(a) Separated Layers (b) Consolidated Layers

Fig. 2 **a** Separated layers, **b** consolidated layers

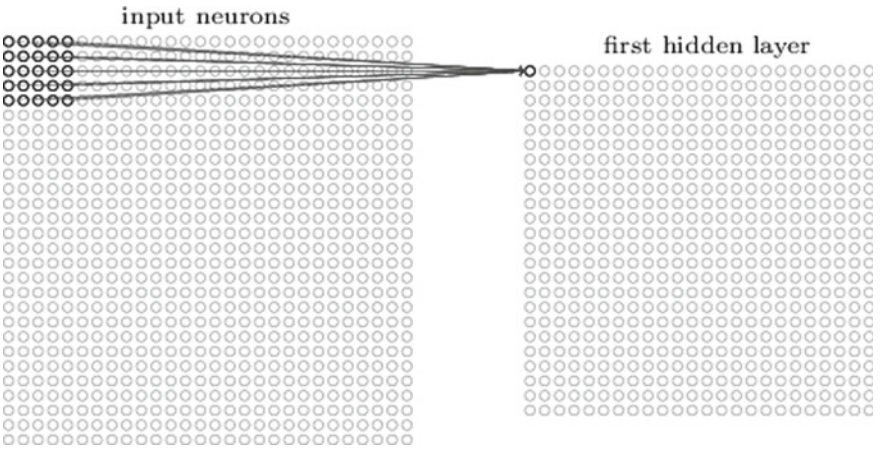

Fig. 3 Hidden layer of input neurons

multiple three-dimensional feature maps in different convolutional layer which can detect all localized features (Fig. 4).

$$a^1 = \sigma(b + w * a^0)$$

where
a^1—denotes the set of output activations from one feature map,
a^0—is the set of input activations,
$*$ —is called a convolution operation,
b—is biases
w—is weights

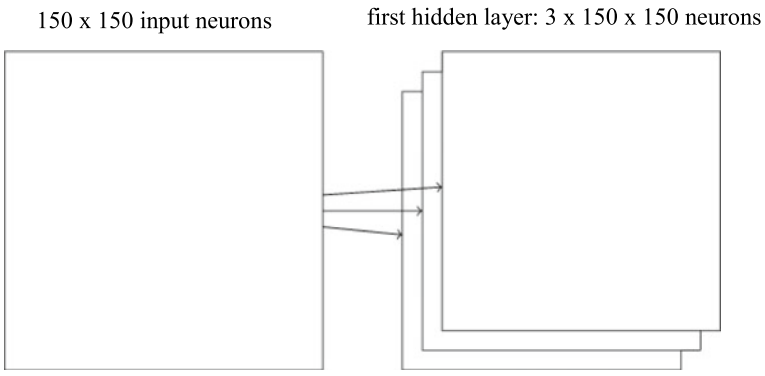

Fig. 4 Featuring of taken image to 150 × 150 pixels

2.3 Pooling Layers

To simplify the information in the output from the convolutional layer, we are using a max pooling layer. This layer takes each feature map output from the convolutional layer and forms a condensed feature map. In max pooling, a pooling unit simply outputs the maximum activation in the 2 × 2 input region [4] (Fig. 5).

Since we have 148 × 148 neurons output from the convolutional layer, after pooling we have 74 × 74 neurons (Fig. 6).

In addition to these, we add three more convolutional and max pooling layers with 64, 128, 128 filters and ReLU activation function, respectively [5]. Before connecting the output of these partial layers to a fully connected layer, we used a dropout layer with the rate of 0.5 (50% random neurons to drop in each epoch) to prevent overfitting [6].

This is followed by a flatten layer to flatten the output neurons to 1D layer with (6272 neurons) to feed it to the fully connected layer. After flatten layer, a dense

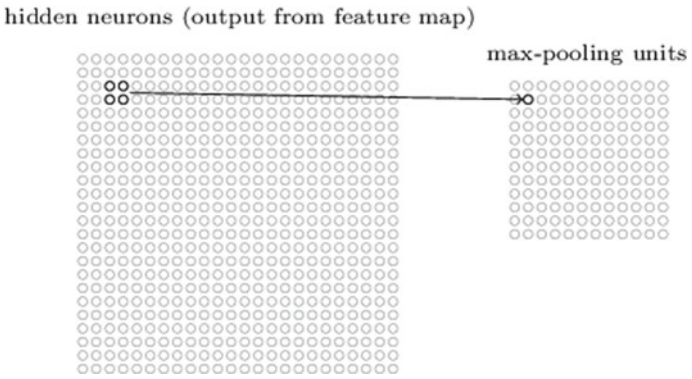

Fig. 5 Pooling unit conversion

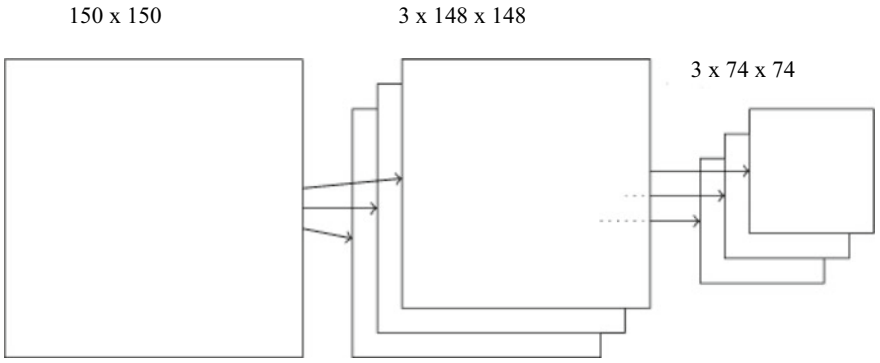

Fig. 6 Output from convolutional layer

Layer (type)	Output Shape	Param #
conv2d_1 (Conv2D)	(None, 148, 148, 32)	896
max_pooling2d_1 (MaxPooling2	(None, 74, 74, 32)	0
conv2d_2 (Conv2D)	(None, 72, 72, 64)	18496
max_pooling2d_2 (MaxPooling2	(None, 36, 36, 64)	0
conv2d_3 (Conv2D)	(None, 34, 34, 128)	73856
max_pooling2d_3 (MaxPooling2	(None, 17, 17, 128)	0
conv2d_4 (Conv2D)	(None, 15, 15, 128)	147584
max_pooling2d_4 (MaxPooling2	(None, 7, 7, 128)	0
dropout_1 (Dropout)	(None, 7, 7, 128)	0
flatten_1 (Flatten)	(None, 6272)	0
dense_1 (Dense)	(None, 512)	3211776
dense_2 (Dense)	(None, 2)	1026

Total params: 3,453,634
Trainable params: 3,453,634
Non-trainable params: 0

Fig. 7 Trainable parameters

fully connected layer with 512 neurons [7] is used and followed by a softmax layer with 2 neurons to classify critical and normal points in each binary image. This in turn creates total trainable parameters of 3,453,634 (Fig. 7).

2.4 CNN Architecture of the model

See Fig. 8.

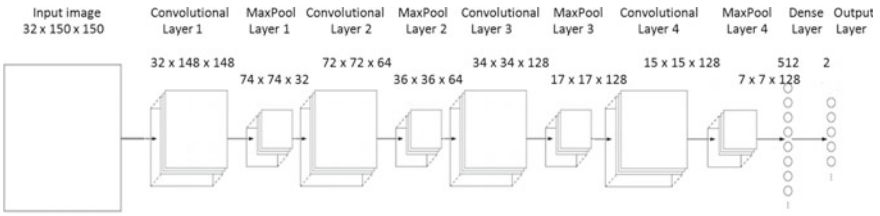

Fig. 8 CNN architecture

3 Result and Discussion

The critical point classified by the DCNN model is used as a checkpoint to pause the printing process, and a snap of that printed piece is taken with an e-CAM131_CUMI1335_MOD camera and cost function will be calculated with the printed image with original image sliced from the stl file using the below formula

$$J(\theta) = \frac{1}{2}\sum_{i=1}^{n}\left(h_\theta\left(x^{(i)}\right) - y^{(i)}\right)^2$$

The threshold value of 8% is set as the decision boundary. If the cost function is above this level, printing process will be stopped for manual correction or supervision, else printing will be resumed to complete all critical checkpoints in the same methodology (Figs. 9 and 10).

Fig. 9 Model graph

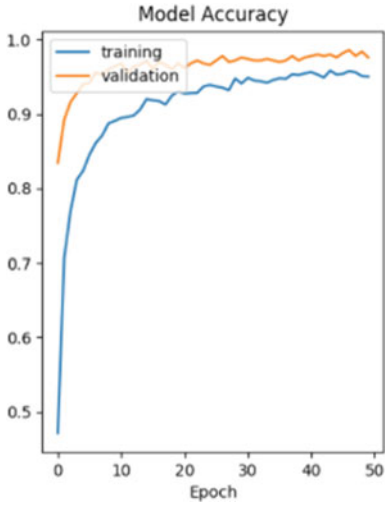

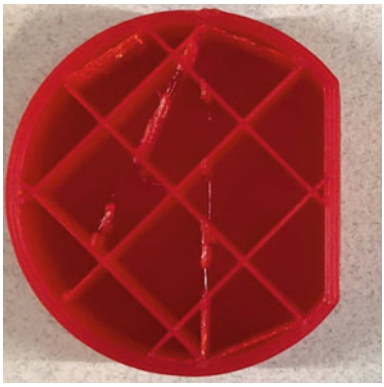

Fig. 10 Printed component

4 Conclusion

This paper proposes a cost-effective additive manufacturing flaw detection system for the time and material cautious using deep convolutional neural networks based on Voxel modeling. By slicing design (stl mesh) files into individual layers and feeding layer images to the pre-trained DCNN model, to classify different layers into normal and critical points. The latter is used as a checkpoint to pause the printing process, and a snap of that printed piece is taken, and error will be calculated with the printed image with original image. Based on the threshold value, the printing process will be stopped for manual correction which can overcome several material wastage, and time can be saved, and human supervision is avoided. Experimental results manifests that the proposed additive manufacturing flaw detection system with 93.4% accuracy will be fascinating and attractive to every 3D printing engineers and the additive manufacturing industry.

References

1. White G (2015) Industry analysis: the pros and cons of 3D printing. Retrieved from https://www.manufacturingglobal.com/
2. Straub J (2015) Initial work on the characterization of additive manufacturing (3D printing) using software image analysis. J Mach 3:55–71
3. Wuest T, Irgens C, Thoben KD (2014) An approach to monitoring quality in manufacturing using supervised machine learning on product state data. J Intell Manuf 25:1167–1180
4. Fastowicz J, Okarma K (2016) Texture based quality assessment of 3D prints for different lighting conditions. In: Proceedings of the international conference on computer vision and graphics, ICCVG, pp 17–28.
5. Vaezi M, Chua CK (2011) Effects of layer thickness and binder saturation level parameters on 3D printing process. Int J Adv Manuf Technol 53:275–284
6. Taylor JS, Cristianni N (2004) Kernel methods for pattern analysis. Cambridge University Press

7. Roberson DA, Espalin D, Wicker RB (2015) 3D printer selection: a decision-making evaluation and ranking model. Virtual Phys Prototyp 8(3):201–212
8. Wang WM, Zanni C, Kobbelt (2016) Improved surface quality in 3D printing by optimizing the printing direction. Eurographics

Design and Fabrication of 3D-Printed Acrylonitrile Butadiene Styrene (ABS) Dam Automation Structure with Integrated Flood Monitoring System Using Data Analysis and Computation Techniques

R. Sivabalakrishnan, M. Dineshkumar, B. P. Sharon, P. Naveenkumar, and S. Vignesh

Abstract In general, the natural catastrophic event causes damage to the life and economy. The proposed work focuses on forecasting of flood using Internet of things (IoT). The correlation techniques for multivariate datasets acquired from sensors have been used for better flood forecasting scheme. The flood forecasting system incorporates monitoring features, such as water level of dam, humidity, water flow and rate of rainfall. These parameters are to be analyzed to monitor and control the release of water from the dam at moderate rate in advance to avoid any losses on downstream due to the flood. The datasets are collected by the wireless sensor network (WSN) via PLC. The sensor information can be analyzed using correlation techniques and system creates an alert to the people community, dam authorized person through siren, alert message using a smart communication device and IoT dashboard. The analyzed result can be appended to show a considerable development over the current existing methods. The manual gate control mechanism results in the insufficient supply of water due to the flow of excess water and human errors which leads to failure in monitoring and controlling the opening and closing of shutter. The water leakage in dam is due to poorly sealed pipes or the improper concrete structure. The designed flood control system was intended to acquire the real-time data for flood prediction by correlation techniques for integrated PLC and servo-based control of dam and canal shutter instantaneously without any time lag. Further, the webpage and mobile application can be created in which the data could be monitored frequently by the officials and the people who live in that locality thereby creating an alert.

Keywords Wireless sensor networks · Correlation method · Data analysis · Automation and PLC-based servo control · Internet of things (IoT)

R. Sivabalakrishnan (✉) · M. Dineshkumar · B. P. Sharon · P. Naveenkumar · S. Vignesh
Department of Mechatronics, Bannari Amman Institute of Technology, Sathyamangalam, Erode 638401, Tamil Nadu, India
e-mail: sivaeinfo@gmail.com

G. Kumaresan et al. (eds.), *Advances in Materials Research*, Springer Proceedings in Materials 5, https://doi.org/10.1007/978-981-15-8319-3_15

1 Introduction

A dam is constructed mainly for irrigation, flood prevention and power generation. More than 2.3 billion people were facing severe crisis due to flood in the last 20 years. On the other hand, due to unplanned opening of dam's water, scarcity goes on increasing. Comparatively, there are numerous reports showing the rapidity of increase in domestic and industrial demand for water, apart from agriculture. The rapid growth in demand for water will occur in the countries with developing or emerging economies [1]. The energy production through hydropower plants is one of the best renewable green energy sources. Globally, the hydroelectric power plants have a combined capacity of 675,000 MW that generates over 2.3 trillion kW-h of electrical power every year, supplying 24% of the world's electricity. It is essential to uphold the speed of the turbine for achieving a good efficient model [2]. In order to prevent flooding, the shutter level should be maintained based on the prior prediction of flood from several scenarios, such as rainfall in water catchment areas, water level in dams and allowing calculated amount of water through canal branches. The study proposed to forecast the river flow using ANN model and validated the accuracy on upstream locations. These approaches have been evaluated to predict the flood at Dongola station [3]. The repetitive flood damage is to be protected by nomograph-based flood forecasting method for saving human lives from real-time rainfall analysis [4]. The research proposed IoT-based smart flood monitoring and forecasting architecture by combining big data and HPC.

2 Literature Survey

The *K*-mean clustering algorithm tends to predict the status of flood, and the forecasting has been carried out using Holt-Winter's method [5]. Sun et al. [6] discussed the real-time monitoring of the inundated line, confiscated water level and deformation of dam. IoT-based monitoring of dam safety to provide safety alert information during critical weather condition was discussed. The manual system is lagging in terms of speed of the process. In order to open or close the shutter, the traditional methodology involves getting access from ministry, communication between ministry and control room, manual calculation of water quantity allowed in each canal and so on. For eliminating the above-mentioned problems, an automated system would be the ultimate solution [7]. The issues in the current system tell that the advanced development of automated unit would provide regular control over every process in a dam [8]. The most critical challenge in automation system is gathering the information about the individual process in each section of the dam setup. The increase in water level and inrush flow of water in the dam due to rainfall will damage the routine life of the habitants [9]. In order to avoid the damage, IoT dashboard creates an alert to the surrounding people through short message service (SMS) which can help people to evacuate from the place, thereby preventing the loss of life

[10] and [11]. The developed application can be useful to assist the people to check the water level, rainfall and flow rate in the dam. The data science management can predict the flood using appropriate data in the cloud computing. The officials can see the level of water and can schedule the opening of shutter accordingly [12] and [13].

The proposed system is to design an intelligent control system for automation of dam and shutter gate integrated with flood monitoring system for preventing the in-rush flow of water during flood by analyzing the sensor data using correlation method. The system uses an IoT technology to incorporate the details regarding dam, canal and flood monitoring areas with visualization of sensor data and timely prediction of flood by analyzing the parameters, such as level, water discharge (inside and outside dam areas) and rainfall.

3 Methodology

The digitization of automation process is to be effectively included in the dam automation with integrated flood forecasting system that infers the real-time data from which the statistics can be analyzed by correlation method based on the information stored using cloud computing. The IoT device communicates with all other devices to exchange the information remotely thereby monitoring and controlling the process. The cloud computing technology provides a platform to access the stored information about the products for monitoring and analyzing. It gives feedback to the dam automation system through API. The flood forecasting system involved in our prototype offers frequent monitoring of dam water level, outflow of water, temperature and humidity with the help of ultrasonic, humidity, rainfall and flow sensor. The data from all the sensors will be investigated and appropriate relationship will be established using data analysis method. The flood prediction system will determine the occurrence of flood for controlling dam shutter in an automated manner. The habitants near the dam are alerted by sending updates in the case of high out flow of water from dam. This process ensures the prevention of life due to natural disasters. The flood can be predicted by the data retrieved from the sensors. This can be used by data science management structure as shown in Fig. 1.

In the case of real-time implementation of the process, the use of LIDAR sensor is exercised for monitoring the water level. The LIDAR sensor is used for surveying method which calculates distance by transmitting laser light and measuring reflected light with sensor. The surface temperature is to be measured with the help of STS-51 (Thermistor). The temperature and humidity can be measured in a real-time manner using thermo-hygrometer.

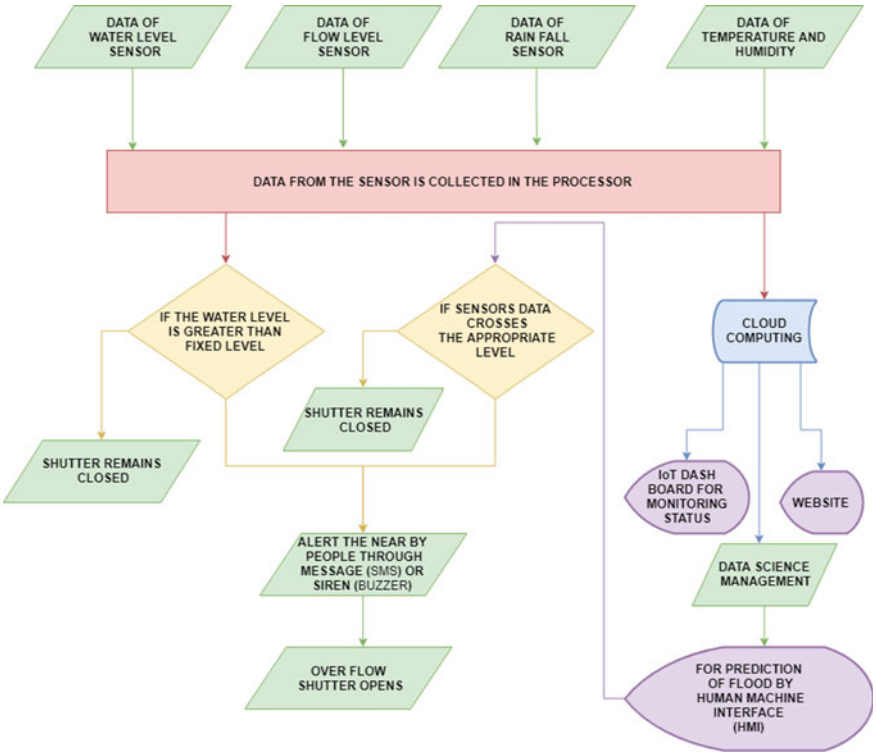

Fig. 1 Data science management structure

3.1 Conceptual Design

The retrofit sensors are provided to the system in an appropriate manner. The data from the respective sensor is collected by the PLC and then pushed into the cloud using MODBUS communication. Using big data analysis, the correlation method is executed for processing the collective datasets from variant sensors for prediction of flood. The data related to flood prediction is to be read by the PLC using RTU protocol which gives input the servo drive to control the position for stabilizing the outflow of water from dam and canal within the appropriate response time.

The system has to send an alert through GSM module. The data retrieved from the cloud is used for predicting flood, creating alert and controlling dam shutter.

The entire process is to be monitored by web dashboard and mobile application. Figure 2 shows the conceptual design of the proposed system.

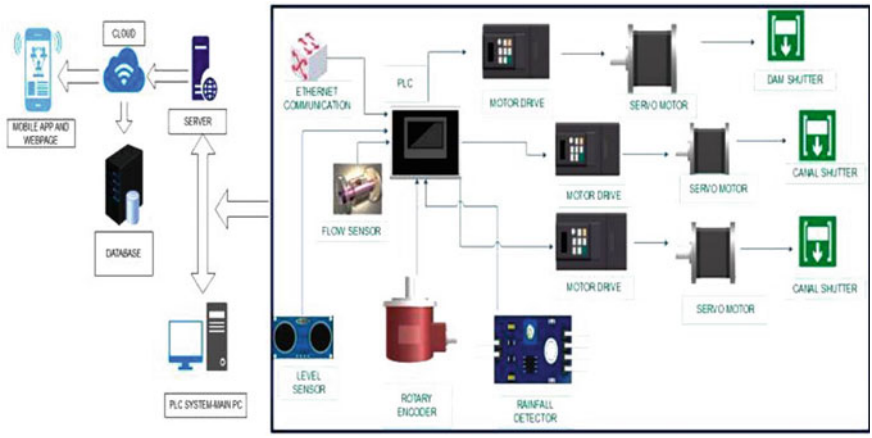

Fig. 2 Conceptual design of DAM automation and flood monitoring system

4 Experimental Setup

The IoT-based dam automation and flood monitoring system is incorporated with the features, such as self-monitoring and intelligent alerting. The sensors used in the prototype are ultrasonic sensor for water level measurement, raindrop sensor for measuring the rainfall, and temperature and humidity sensor for forecasting the weather, and flow sensor to calculate the outflow of water from the dam. The data from various sensors is to be analyzed using correlation method for predicting the occurrence of flood. The proposed structure shown in Fig. 3a was designed with requirement parameter and dimensions in solidworks. The structure shown in Fig. 3b is made of acrylonitrile butadiene styrene (ABS) using rapid prototyping. ABS is amorphous and therefore has no true melting point; it is insoluble in water. The ABS material is recyclable and eco-friendly. It holds pressure up to 450 psi. The

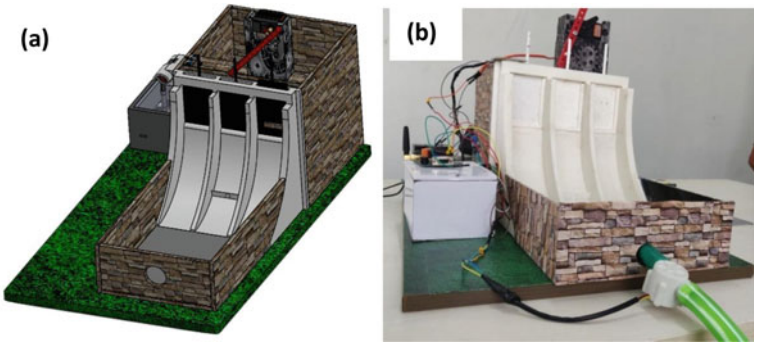

Fig. 3 **a** CAD design, **b** system structure with retrofit sensors and control system

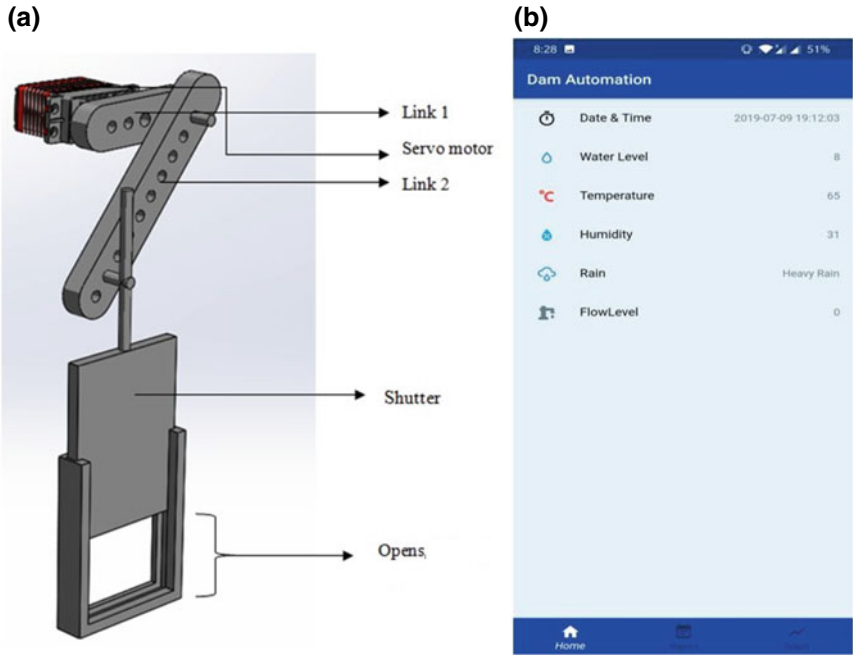

Fig. 4 **a** Shutter control mechanism, **b** graph visualization in mobile applications

conceptual design was made using SolidWorks, and the model is made using rapid prototyping in the form of injection modeling technique.

4.1 Mechanism for Shutter Control

The link 1 rotates in circular path in which link 2 is connected. When servo motor is actuated to rotate link 1, it makes the link 2 to move in translated path. The dam shutter is fixed to link 2 in an inclined manner. When link 2 translates, it makes the shutter to open. It receives feedback from data analysis system based on flood prediction method. When the desired distance is achieved, the motor actuates and opens the shutter in Fig. 4a.

4.2 Implementation of IoT and Data Analysis

The mobile application is developed for android users made from an algorithm for viewing the real-time update of the retrieved data. Google firebase cloud system can be used for data retrieval and authentication. The data acquired is stored in our firm's

server and they are uploaded to mobile application which is used for monitoring. The mobile application consists of a login page incorporated with an introduction panel for real-time data visualization which is updated for every 7 s from PLC as shown in Fig. 4b.

It tends to provide a graphical representation of the stored data in the form of analytical data. The webpage holds the data, such as date, time, water level, temperature, humidity and rainfall. It was developed using HTML program for scaling the background of the work.

The IoT dashboard has created for importing the report of data collected from dam with its appropriate details for the particular period. The correlation method of data analysis is a statistical technique for making relationship among the time-related multivariable data sets captured from various sensors. The multivariate data sets provide appropriate information for predicting the occurrence of flood. In this method, the temperature is independently varying with humidity; water level is dependently varying with inlet flow to the dam. Rainfall is also dependent with respect to temperature and humidity. The correlation infers the variation in one parameter related to the other. The variation tells the forecasting of flood based on collective data sets from different sensors.

This method is used to quantify the association between two continuous variables between three dependents, such as rainfall, water level, water flow, and independent variables such as temperature and humidity. The correlation of parameters from the sensors are marked with different color indications by mentioning proper weightage as shown in Figs. 5 and 6. The correlation points are strongly associated in the range 0.5–6% and 21–22% of water level with 0 to 10% of water flow which was shown in x and y axis functions for the prediction of flood. Figure 6 shows the percentage of variation of flood during various seasons in every year.

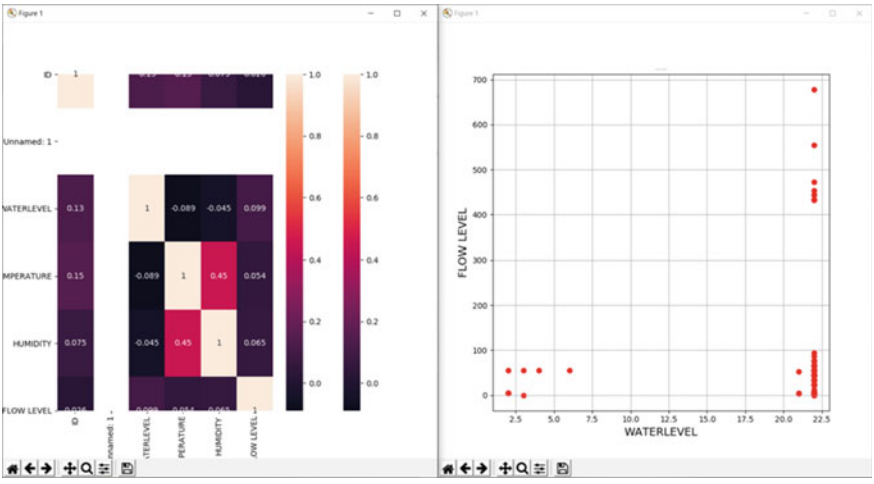

Fig. 5 Graph visualization in IoT dashboard

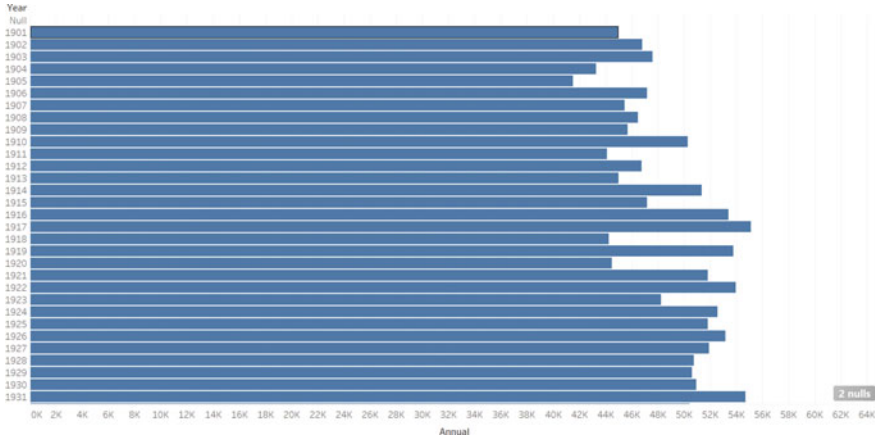

Fig. 6 Analysis of data in Tableau

5 Conclusions

The data is made available on the webpage after retrieving it from the cloud storage. It helps in executing the analysis and prediction of flood based on correlation method of multivariate datasets. After utilizing the proposed system, it is having the facility to control or monitor the dam's shutter prior to the occurrence of flood based on forecasting. The IoT technology is implemented to visualize the dynamic changes in data sets. It creates an alert and provides possible control over the flow of water to prevent flood. Furthermore, this system can run without any human intervention, and an alert system is incorporated which will be helpful in the case of emergency situation. Based on the implementation of the data analysis approach, the system is able to predict the occurrence of flood through information acquired from the database about the environment for a period of five years.

References

1. Mishra V, Shah H (2018) Hydro climatological perspective of the Kerala flood of 2018. J Geol Soc India 92(5):645–650
2. Chang HLH, Kim E, Jeon G, Azam M (2015) The change of flood according to dividing sub-basin at Mu-sim river. J Inst Constr Technol 34:99–104
3. Elsafi SH (2014) Artificial neural networks (ANNs) for flood forecasting at Dongola Station in the River Nile, Sudan. Alexandria Eng J 53(3):655–662
4. Lee E, Kim J, Choo Y, Jo D (2018) Application of flood nomograph for flood forecasting in urban areas. Water 10(1):53
5. Sood SK, Sandhu R, Singla K, Chang V (2018) IoT, big data and HPC based smart flood management framework. Sustai Comput Inf Syst 20:102–117
6. Sun E, Zhang X, Li Z (2012) The internet of things (IOT) and cloud computing (CC) based tailings dam monitoring and pre-alarm system in mines. Saf Sci 50(4):811–815

7. Nof SY (2009) Automation: what it means to us around the world. In: Handbook of automation. Springer, Berlin, pp 13–52
8. Nico G, Di Pasquale A, Corsetti M, Di Nunzio G, Pitullo A, Lollino P (2015) Use of an advanced SAR monitoring technique to monitor old embankment dams. In: Engineering Geology for Society and Territory, vol 6, pp 731–737. Springer, Cham
9. Azam M, San Kim H, Maeng SJ (2017) Development of flood alert application in Mushim stream watershed Korea. Int J Disaster Risk Reduct 21:11–26
10. Joo J, Kjeldsen T, Kim HJ, Lee H (2014) A comparison of two event-based flood models (ReFH-rainfall runoff model and HEC-HMS) at two Korean catchments, Bukil and Jeungpyeong. KSCE J Civil Eng 18(1):330–343
11. Ratnam KN, Srivastava YK, Venkateswara Rao V, Amminedu E, Murthy KSR (2005) Check dam positioning by prioritization of micro-watersheds using SYI model and morphometric analysis—remote sensing and GIS perspective. J Indian Soc Remote Sen 33(1):25
12. Hong Y, Adler RF, Negri A, Huffman GJ (2007) Flood and landslide applications of near real-time satellite rainfall products. Nat Hazards 43(2):285–294
13. Tang E, Chen F, Zhu Q (2013) Environment monitoring system based on internet of things. In: Emerging technologies for information systems, computing, and management. Springer, New York, pp 125–132

Influence of Human Hair Fibre, Geogrid and PVC Grid on the Performance of CBR of Clayey Soil

V. Jayanthi, B. Soundara, S. Priyadharshini, J. Adhithya, M. Sharmaa Devi, and S. Amritha Shankar

Abstract Thickness of pavement layers over the subgrade decides the strength of pavement. Stronger subgrade reduces the thickness of pavement layers, whereas the weaker subgrade needs improvement in deciding the strength of pavement. This paper addresses the effectiveness of the inclusion of natural and synthetic reinforcement material on clayey soil. The California Bearing Ratio of the subgrade is considered to assess the thickness of the pavement. The effect of natural and synthetic material on overall performance of the system in terms of bearing ratio has been systematically studied through a series of tests. The natural reinforcement material such as human hair was mixed uniformly with the soil, and geosynthetic reinforcement materials, namely geogrid and PVC grid, were introduced as mats in single and two layers within the thickness of clayey soil at equal interval. The specimen for the unsoaked CBR test was prepared at optimum moisture content and dry density obtained from standard proctor compaction test. From the test results, it is observed that the unsoaked CBR of reinforced clay is greater than the unreinforced clay irrespective of the inclusion material. Also it is observed that the value of CBR is increased with increase in the number of inclusion of reinforcing material. The results from the serial of trial section the double layer geogrid gives the better result compared to others. Even though the human hair fibre also suggested for small works, it is having some bearing strength.

Keywords Clay · Reinforcement · CBR · Human hair · Geogrid · PVC grid

V. Jayanthi (✉)
Assistant Professor, Bannari Amman Institute of Technology, Sathyamangalam, India
e-mail: jayanthiv@bitsathy.ac.in

B. Soundara
Professor & Head, Bannari Amman Institute of Technology, Sathyamangalam, India

S. Priyadharshini · J. Adhithya · M. S. Devi · S. A. Shankar
Graduate Student, Bannari Amman Institute of Technology, Sathyamangalam, India

G. Kumaresan et al. (eds.), *Advances in Materials Research*, Springer Proceedings in Materials 5, https://doi.org/10.1007/978-981-15-8319-3_16

1 Introduction

Since the introduction of ground improvement techniques, improving the strength behaviour of weak soil is a major concern for engineers. In order to improve the engineering properties of weak soil, many methods were introduced by the engineers such as inclusion of reinforcement into the soil, replacement of weak soil by strong soil to a particular depth and improvement of relative density of soil [1]. The strength of road pavements depends on the subgrade, subbase and subbase materials. The subgrade soil should have the capacity to transfer the load from the pavement to the layer beneath. The desirable properties of subgrade soil are influenced by stability, incompressibility, volume changes, good drainage and ease of compaction.

The construction of concrete or asphalt pavements on weak soil is quite difficult. Because in this case, due to an environmental concern, the pavement will get cracks easily on its surface so that the road becomes worthless. Soil has the capability to carry compressive and shear forces. In order to carry the tensile forces, many natural and synthetic materials are used to increase the strength of subgrade. The thickness and bearing capacity of the subgrade are determined by the penetration test commonly known as California Bearing Ratio (CBR) test. CBR value of soil depends on many factors like index properties, type of soil, permeability of soil, optimum moisture content (OMC) and on soaked and unsoaked conditions of soil.

From the past few decades, planar structure has been used for various purposes like pavements, foundations and walls. Afterwards, geocell was first initiated by US Army Corps of Engineers for stabilization of sand beach [2]. Muthulakshmi et al. have done the research on soaked and unsoaked CBR values and concluded that soaked and unsoaked CBR values have been increased with the increment of OMC [3]. Aboshio analysed and concluded that a strong relationship exists between undrained triaxial compressive strength (UTCS) and CBR [4]. Based on this research, it was suggested that UTCS results can possibly replace the CBR test results in the characterization of lateritic soils for pavement design and construction.

Hegde and Sitharam [5] conducted an experimental study to improve the bearing capacity of soft ground. Vaitkus and Laurinavicius [6] discussed the strengthening of existing road pavements using geocells in Lithuania adopted by Lithuanian road administration in 1998. Humayoon et al. [7] used plastic mat as geocell to calculate the CBR value of soil. In this experiment, various thicknesses of plastic mats such as 1, 2, 3, 4 and 5 cm were placed at depths about 2, 4, 6 and 8 cm from the top of CBR mould. They concluded that the optimum value of plastic mat is 3 cm thickness at 4 cm depth. The geocell application was successfully implemented in Latin America by Lavoie and Botelho [8]. Leschinsky and Ling [9] concluded the geocell reinforced embankment minimized the vertical settlement under monotonic and cyclic loading conditions.

Many researchers have attempted to use different materials for strengthening subgrade. Kuity and Roy [10], Singh and Gill [11] and Chauhan and Sharma [12] suggested that geogrid layered inclusions provided the better result compared to natural material inclusions like plastic waste, fly ash, etc. Ramakrishna and Naga

Malleswara Rao [13] conducted an experiment on CBR using geosynthetics. From this, he has suggested that geogrid gives more value in sandy soils. Robert Koerner [14] discussed the stabilization of soil slopes using geosynthetics in the field. The tensile reinforcement was provided to the soil provided by tensioned soil anchors connected with the geosynthetic surface. The selected ground surface was covered using geotextile from the top of slope. To enhance the bearing capacity as well as the shearing of a clayey soil, the natural fibre human hair is distributed in clayey soil samples [15]. This improves the strength significantly and also prevents the sample from cracking.

Geosynthetics are the synthetic products generally known as polymeric products used for many purposes in civil engineering. Geosynthetics may be in the form of geomembrane, geocell, geogrid, geotextile, etc., and the functions of these geosynthetics mainly depend on the purpose of filtration, separation, reinforcement, etc.

Form the past studies, the soil properties have been improved by the introduction of reinforcement materials. Out of the reinforcement elements, randomly distributed elements have been the main attraction of many engineers in the past few years. Based on these conclusions, the present study has been taken up for the introduction of the waste material as an alternate for geosynthetic products in ground improvement. Using this reinforcement, the bearing capacity of pavement with the waste materials such as human hair and PVC grid is to be increased, and finally, it is compared with the geogrid reinforcement.

2 Material Tests

2.1 Soil

Soil used in this test was collected from Sathyamangalam, Erode District. To perform the CBR test, the basic tests were performed on the collected clay. For that, the collected soil was dried for 24 h, and the basic tests were conducted and the results were compared with the corresponding IS codes. The basic tests like particle size distribution using sieve analysis (IS 460-1962), specific gravity (IS 2720-1980—Part 3), Atterberg limit (IS 2720-1985—Part 5) and modified proctor compaction test (IS 2720) results were tabulated in Table 1. According to Unified Soil Classification System, the soil was designated as CL (clay of low compressibility).

2.2 Natural and Synthetic Fibre

When the fibre introduced into the subsoil and base course, the fine-grained soil interlocks with the synthetic products. Thus, the required bearing capacity can be

Table 1 Material properties

S. No.	Tests performed	Results obtained
1	Particle size distribution	Sand—2.61% Silt—78.92% Clay—18.47%
2	Specific gravity	2.69
3	Atterberg limit	Liquid limit—27% Plastic limit—18% Plasticity index—9%
4	Modified proctor compaction test	OMC—11.48% MDD—1.4173 g/cc

Table 2 Fibre properties

S. No.	Material	Properties
1	Human hair	Length—25 mm Diameter—50 μm Flexural strength—25–30 MPa
2	PVC grid	Aperture size—40 mm × 40 mm
3	Geogrid	Aperture size—40 mm × 40 mm

achieved without additional expensive soil exchange, and also sometimes, the base course thickness can be reduced. The fibres used in this research were human hair, PVC grid and geogrid, and the dimensions are tabulated in Table 2.

3 Experimental Setup

The soil sample was prepared with OMC for CBR test. Unsoaked CBR tests were conducted for both reinforced and unreinforced soil samples. The prepared samples were placed in the CBR testing apparatus, and the strain rate of 1.25 mm per minute was applied during the CBR test.

3.1 Strengthening by Human Hair

The inclusion of human hair fibre into the soil for the improvement of shear strength, as well as bearing capacity was successfully studied by Butt et al. [15]. In this research to evaluate the bearing capacity of weak soil, the human hair was used as an additive to the soil by weight (0.25, 0.5, 0.75 and 1%) of soil. With increase in fibre content, the fibre may not be perfectly blended with the soil matrix. But at the optimum content, the fibre produces good bearing capacity properties. The

Fig. 1 CBR with geogrid and PVC grid

experimental study concluded that the addition of human hair fibre enhances the bearing capacity of clayey soil.

3.2 Strengthening by Geogrid and PVC grid

To prepare a reinforcement sample, two geogrids and PVC grids are provided separately in the cylindrical mould at heights of 60 and 120 mm. The first layer was placed after compacting the clay to the maximum dry density by giving 56 blows using the hammer. Further, clay was poured over the first layer of geogrid, PVC grid and then the clay layer was compacted. Over that the second layer, the next layer of clay was compacted. The provision of geogrid and the results were shown in Fig. 1.

4 Results and Discussion

The type of reinforcement and their corresponding 2.5 and 5 mm penetration was tabulated in Table 3, and it is shown in Fig. 2.

The major conclusion from this study is summarized as follows:

- The inclusion of reinforcing materials in soils improves the CBR and decreases the surface penetration and deformation.
- The CBR value of double layer of geogrid in 5 mm penetration is increased about 60.64% than the unreinforced section.
- The CBR value of dispersion of human hair is increased in 5 mm penetration about 12.8% than the unreinforced sample.
- The CBR value of double-layer PVC grid in 5 mm penetration is reduced to 3.1% when compared to the dispersion of human hair.

Table 3 CBR test results

S. No.	Reinforcement details	CBR value	
		2.5 mm penetration	5 mm penetration
1	Without reinforcement	1.18	1.09
2	Human hair	1.23	1.25
3	Single layer of PVC grid	1.28	1.23
4	Double layer of PVC grid	1.29	1.29
5	Single layer of geogrid	1.97	1.85
6	Double layer of geogrid	2.90	2.77

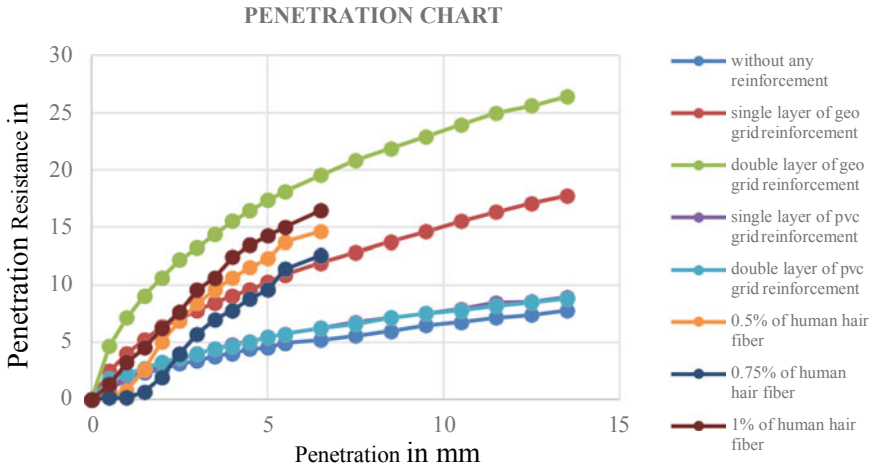

Fig. 2 CBR test results

5 Conclusion

In the past few decades, geosynthetics predominantly occupy a major role in ground improvement techniques. The application of geocell in various building (infrastructure) projects such as pavements and embankments has been popularized nowadays due to its various benefits. This paper recognized the application of natural and synthetic fibre reinforcement in various research activities. From the series of test results, the addition of natural and synthetic fibre into the soil enhances the bearing ratio of weak soil. Compared to geogrid, human hair and PVC are available in abundance at a very low cost. This recycled method reduces the negative impact to the

environment and also helps in sustainable development of various infrastructures by utilizing these wastes effectively.

References

1. Sharma V, Kumar A (2017) Influence of relative density of soil on performance of fibre reinforced soil foundations. Geotext Geomembr 499–507
2. Webster SL (1979) Investigation of beach sand traffic ability enhancement using sand-grid confinement and membrane reinforcement concepts, Rep. GL-79–20(1). U.S. Army Engineer Waterways Experiment Station, Vicksburg, MS
3. Muthu Lakshmi S, Subramanian S, Lalithambikhai MP, Mithra Vela A, Ashni M (2016) Evaluation of soaked and unsoaked CBR values of soil based on the compaction characteristics. Malaysian J Civil Eng 172–182
4. Aboshio A (2010) Comparative study of the California bearing ratio test and undrained triaxial compressive strength test for lateritic soils. J Engi Technol 1–4
5. Hegde A, Sitharam GT: 3-Dimensional numerical analysis of geocell reinforced soft clay beds by considering the actual geometry of geocell pockets. Can Geotech J 52:1–12 (2015)
6. Vaitkus A, Laurinavicius A (2010) Use of geosynthetics for the strengthening of road pavement structure in Lithuania. In: 9th international conference on geosynthetics, Brazil
7. Humayoon H, Gopinath B (2016) A study on the improvement of CBR using waste plastic mat as Geocell. Int J Eng Res Technol 5:9. Int J Res Eng Technol 423–427 (2005)
8. Lavoie FL, Botelho C (2016) The application of geocells in Latin America. In: 3rd Pan American conference on geosynthetics
9. Leshchinsky B, Ling H (2013) Effects of geocell confinement on strength and deformation behavior of gravel. J Geotech Geoenviron Eng 340–352
10. Kuity A, Roy TK (2013) Utilization of geo grid mesh for improving the soft subgrade layer with waste material mix compositions. Procedia Soc Behav Sci 255–263
11. Singh P, Gill KS (2015) CBR improvement of clayey soil with geo-grid reinforcement. Int J Emerg Technol Adv Eng 315–318
12. Chauhan R, Sharma R (2014) An experimental investigation on CBR improvement of sand—fly ash mix using geo-grid layers. J Civil Eng 10–14
13. Rama Krishna M, Naga Malleswara Rao B (2015) Evaluation of CBR using geo-synthetics in soil layers. Int J Res Eng Technol 04(05)
14. Koerner RM (2015) Koerner: in-situ stabilization of soil slopes using nailed or anchored geosynthetics. Int J Geosynth Ground Eng 1:2
15. Butt WA, Mir BA, Jha JN (2016) Strength behavior of clayey soil reinforced with human hair as a natural fibre. Geotech Geol Eng 34:411–417

Optimizing Performance Characteristics of Blower for Combustion Process Using Taguchi Based Grey Relational Analysis

K. B. Prakash, A. Amarkarthik, M. Ravikumar, P. Manoj Kumar, and S. Jegadheeswaran

Abstract Complete combustion in a furnace must be achieved to reduce the emissions. In order to achieve the same, this work focuses on the optimization of performance parameters of centrifugal blower for complete combustion in the furnace with the aid of one the optimization techniques, i.e., Taguchi-based grey relational analysis. The type of blade and percentage of the opening of the blower duct is selected as input parametric characteristics. For experimental design, tests are planned based on Taguchi's L12 orthogonal array and by conducting experiments as design, the output process parameters i.e. velocity, discharge, input power, output power, and mechanical efficiency are calculated and found the operating settings of the blower by manipulating grey relational grade with Taguchi optimization technique. The test results propose that the type of blade has the most noteworthy impact on the multiple performance qualities rather than the percentage of the opening of duct and blower with a backward blade and 50% opening of duct shows the best-operating conditions.

Keywords Optimization · Taguchi-based grey relational analysis · Blower performance · Velocity · Combustion process

1 Introduction

There are several factors that affect the combustion process, i.e., oxygen required and velocity of air from blower, lack of that parameter leads incomplete combustion in the boiler furnace. Due to the same, emissions expelled are more and which leads to greenhouse effects and ozone layer depiction. To account for the same, incomplete combustions should be avoided to decrease the emissions from the furnace [1]. One

K. B. Prakash (✉) · A. Amarkarthik · M. Ravikumar · S. Jegadheeswaran
Department of Mechanical Engineering, Bannari Amman Institute of Technology, Sathyamangalam, Erode 638401, Tamil Nadu, India
e-mail: kbprakash404@gmail.com

P. Manoj Kumar
Department of Mechanical Engineering, KPR Institute of Engineering and Technology, Arasur, Coimbatore 641407, Tamil Nadu, India

G. Kumaresan et al. (eds.), *Advances in Materials Research*, Springer Proceedings in Materials 5, https://doi.org/10.1007/978-981-15-8319-3_17

of the main reasons for the incomplete combustion is blower operating settings. By setting or operating the blower at optimum conditions, the above-said problems can be eliminated. So the attempt has been done to operate the blower at optimum conditions and setting the parameters at optimum level using Taguchi-based Grey Relational Analysis.

Combustion process in furnace depends upon the oxygen supplied to it. The volume flow rate of air and velocity of should be 0.2–0.3 m^3/s and 16–20 m/s [2]. In the performance vice, mechanical efficiency should be high and input power to the blower should be less for the given output. To satisfy the above condition, power required is being high. So these problems can be eliminated by setting the best operating condition of the centrifugal blower.

This work concentrates on finding the optimal operating setting of centrifugal blower using the optimization techniques of Taguchi based grey relational analysis and different type of blade and percentage of opening of blower duct are streamlined to achieve the best performance characteristics of blower for combustion process. Taguchi configuration approach is utilized for test arranging during testing with blower. The results are analyzed to achieve optimal performance parameters i.e. velocity, input and output power and efficiency of blower. GRA examination was performed to join the various responses into single numerical value, rank this value, and choose the ideal blower working parameter settings. ANOVA is executed to explore all the impacting parameters on the different exhibition attributes [3–5].

2 Experimental Methods

Experiments are conducted in centrifugal blower test rig with different blade and setting conditions after finalizing design of experiments. They are explained in the following section in detail.

2.1 Experimentation

The test unit, which is appeared in Fig. 1, comprises a centrifugal blower driven by an AC motor through a stage pulley course of action to acquire three distinctive test speeds. The motor is mounted on an adjustable bed and can be moved in and out, to position the fan belt at the required pulley. At the blower outlet, a sluice valve is used to control the discharge. An orifice device is fitted at outlet of the pipeline to quantify the actual volume flow rate.

A lot of pitot tube and thermometer is given at the outlet to quantify the velocity of air and temperature of air. U-tube manometers are given to gauge the pressure difference over the opening in the pitot tube and exit pressure. Three kinds of compatible impellers-with outspread (Radial) vanes, in reverse bended vanes and forward bended vanes are given the test apparatus to think about the impacts of various vane types.

Fig. 1 Blower experimental setup

Table 1 Input parameters and their levels

Sl. No	Run No.	Type of blade	% of Fresh air opening
1	1	F	25
2	2	F	50
3	3	F	75
4	4	F	100
5	5	B	25
6	6	B	50
7	7	B	75
8	8	B	100
9	9	R	25
10	10	R	50
11	11	R	75
12	12	R	100

Table 2 Experimental design ($L12$)

Factors	Level 1	Level 2	Level 3	Level 4
Type of blade (B)	F	B	R	–
% of opening duct (O)	25	50	75	100

Taguchi's trial configuration was utilized to and examines the impact of controllable factors on responses. The input controllable components which are measured in this examination are a sort of blade, i.e., forward blade, backward blade, and radial blade and level of the opening of the conduit. The various levels of these variables are shown in Table 1. The full factorial clusters were chosen and appeared in Table

Table 3 Experimental result (samples)

Type of blade	Delivery valve position open %	Orifice manometer reading (cm)		Delivery pressure manometer reading		Energy consumption t (s)
		H_3	H_4	H_1	H_2	
F	25	57.6	19.5	38.2	37.4	12
F	50	57.9	19.4	44	31.4	8.5
F	75	56.2	21.1	60	14.6	5.8
F	100	54.2	23.1	69	6	4.8

Table 4 Output parameters (samples)

Sl. No.	Discharge (m^3/s)	Velocity (m/s)	Input power (kW)	Output power (kW)	Blower efficiency (%)
1	0.006	0.4	1.6	0.3	16
2	0.264	19.6	2.1	1	46.9
3	0.501	37.2	3.1	1.7	55.5
4	0.59	43.8	3.8	1.8	48
5	0.066	4.9	1.3	0.2	17.1
6	0.233	17.3	1.7	0.8	46.6

2. It was utilized on the grounds that it requires just twelve keeps running for blends of two controllable components shifted at three levels and four levels individually.

The experiments were conducted in the centrifugal blower for the twelve runs as per the procedure which is shown in Table 3. The experiments were conducted by the following procedures. Close the delivery valve completely. Start the motor. Open the valve slowly and for various stages of opening with Forward blade and readings were noted. Next radial blade and backward blades were fitted and same procedures were adopted to note remaining readings. From the experimentations output parameters i.e. velocity of air, discharge, input and output power of the blower and finally blower efficiency were calculated and tabulated in Table 4.

2.2 Optimization Method—Taguchi-Based Grey Relational Analysis

In the point of acquiring output responses from the run, that is utilized to change over a multi-objective problem into a single objective problem by Taguchi based GRA. The accompanying advances are done to get the GRG. They are,

2.2.1 Data Preprocessing

The primary step is to grouping and separating the responses based responses values to be like nominal the better, smaller the better and larger the better. On the off chance that the objective estimation of unique grouping is limitless, at that point it has a normal for "the-bigger the-better" [6, 7]. Here the yield parameters i.e. blower efficiency and output power ought to be bigger the better and the first succession can be standardized as Eq. (1).

$$x_i^*(k) = \frac{x_i^{(o)}(k) - \min x_i^{(o)}(k)}{\max x_i^{(o)}(k) - \min x_i^{(o)}(k)} \tag{1}$$

At the point when the smaller, the better is normal for the first grouping then the first arrangement ought to be standardized as conditions (2) and input power to the blower should be smaller [7].

$$x_i^*(k) = \frac{\max x_i^{(o)}(k) - x_i^{(o)}(k)}{\max x_i^{(o)}(k) - \min x_i^{(o)}(k)} \tag{2}$$

In any case, for the velocity of air and volume flow rate of air from the blower is to be clear target an incentive to be accomplished; at that point, the first succession will be standardized as Eq. (3).

$$x_i^*(k) = 1 - \frac{\left| x_i^{(o)}(k) - OB \right|}{\max\{\max x_i^{(o)}(k) - OB,\ OB - \min x_i^{(o)}(k)\}} \tag{3}$$

Or then again, the first succession can be basically standardized by the most fundamental procedure, i.e., the values are estimated by dividing original sequence with first value of the sequence.

$$x_i * (k) = \frac{x_i^{(o)}(k)}{x_i^{(o)}(1)} \tag{4}$$

where $x_i^{(o)}(k)$ is the original sequence, $x_i * (k)$ the sequence after the data processing maximum $x_i^{(o)}(k)$ the largest value of $x_o^{(o)}(k)$ and minimum $x_i^{(o)}(k)$ the smallest value of $x_o^{(o)}(k)$. The normalization matrix has been found using the above relations and that is Table 5.

2.2.2 Grey Relational Grade (GRG)

After information preprocessing is completed, a grey relational coefficient (GRC) can be determined with the preprocessed successions. The GRC is characterized

Table 5 Normalized matrix (samples)

Responses to be nominal		Responses to be smaller	Responses to be larger	
Discharge	Velocity	Input power	Output power	Blower efficiency
1.000	0.822	0.898	0.031	0.000
0.122	0.017	0.661	0.500	0.739
0.684	0.721	0.265	0.950	0.945
0.986	0.999	0.000	1.000	0.766

as pursues and which has been shown in Table 6. Where $\Delta_{oi}(k)$ is the deviation sequence of the reference sequence $x_o*(k)$ and the comparability sequence is derived from Eqs. 5, 6 and 7 [8]. They are

$$\Delta_{oi}(k) = |(x_o*(k) - x_i^*(k))|, \tag{5}$$

$$\Delta_{\max} = \underset{\forall j \varepsilon i}{\max}\ \underset{\forall k}{\max} \left|(x_o*(k) - x_j^*(k))\right| \tag{6}$$

$$\Delta_{\min} = \underset{\forall j \varepsilon i}{\min}\ \underset{\forall k}{\min} \left|(x_o*(k) - x_j*(k))\right| \tag{7}$$

where, £ = distinguish co-efficient £, € (0, 1) and grey relational grade shown in Table 6 is a weighting-sum of the grey relational coefficient. It is gotten from conditions 8 and 9. They are,

$$\gamma(x_o*, x_i*) = \sum_{k=1}^{n} \beta_k \gamma(x_o*(k), x_i*(k)), \sum_{k=1}^{n} \beta_k = 1 \tag{8}$$

$$\gamma(x_o*(k), x_i*(k) = \frac{\Delta_{\min} + \zeta \Delta_{\max}}{\Delta_{oi}(k) + \zeta \Delta_{\max}}, \quad 0 \le \gamma(x_o*(k), x_i*(k) \le 1 \tag{9}$$

Here, GRG speaks to the degree of connection between the reference sequence and the comparability sequence.

Table 6 Grey relational co-efficient (samples)

Discharge	Velocity	Input power	Output power	Blower efficiency
1.00	0.73	0.83	0.34	0.33
0.33	0.33	0.60	0.50	0.66
0.58	0.64	0.40	0.91	0.90
0.97	1.00	0.33	1.00	0.68

Table 7 Grey relational grade and S/N ratio

Factors	Level 1	Level 2	Level 3	Level 4
Type of blade	−5.6989	−5.79058	−5.5587	–
% of opening of duct	−6.65492	−7.04238	−4.4860	−4.54763

3 Results and Discussions

3.1 S/N Ratio

Noise level loss function is communicated in condition 10. It is,

$$L_{ij} = (1/N) \sum_{k=1}^{n} (Y_{ij}k)^2 \tag{10}$$

Loss function is moreover changed into S/N proportion to choose the deviation of performance characteristics (PC) from the desired value [8–11]. The same is communicated in condition 10. It is,

$$\beta_{ij} = -10 \log(L_{ij}) \tag{11}$$

Utilizing the above relations, *S/N* proportion-based grey relational grade was discovered utilizing the above relations and optimum conditions were resolved and which is appeared in Table 6.

Table 7 clarifies that second level of blade and second level of opening gives the optimum performance of the centrifugal blower for the combustion process. It means that operating a blower at backward blade with 50% opening of duct gives the optimum level values i.e. velocity, discharge of air to the combustion process and higher output for lower input power. So it leads to operate a blower in the maximum efficiency.

3.2 Analysis of Variance (ANOVA)

The reason for doing ANOVA is, to analyze the parameters, which essentially influence the PC [12–15]. Hence, Values of ANOVA demonstrates that kind of type of blade plays the most critical parameter for execution of required output from the blower when it is utilized to improve the blower execution qualities for the combustion process.

3.3 GRG Validation

After finding the optimal level from the various variables, the last advance is to foresee the PC with optimal setting factors [16–18].

$$\gamma = \lambda m + \sum_{i=1}^{y} (\gamma_i - \gamma_m) \tag{12}$$

In light of the above condition [19, 20] the GRG utilizing the optimal setting parameters would then be able to be acquired. At starting conditions the GRG was 0.484 for B1O2 and after the enhancement anticipated condition is B_2O_2 (Backward blade and half opening of the conduit) and GRG for the equivalent is 0.586. Thus improved GRG value is 0.12.

4 Conclusions

S/N proportion-based GRG got from the GRA is utilized to enhance the performance of centrifugal blower for the complete combustion process. The experimental trial demonstrates that the type of blade has the most noteworthy impact on the performance of the blower. The aftereffect of the affirmation test result yielded an enhancement of 0.12 in GRG after validation. Thus, the combination of GRA and Taguchi Method can be used to streamline the process parameters and it assists to improve the effective burning.

References

1. Borman GL, Ragland KW (1998) Combustion engineering. McGraw-Hill, Inc., pp 155–162
2. Baukal CE (2013) Oxygen-enhanced combustion, 2nd edn. CRC press
3. Lin CL (2004) Use of the Taguchi method and grey relational analysis to optimize turning operations with multiple performance characteristics. Mater Manuf Processes 19(2):209–220
4. Pan LK, Wang CC, Wei SL, Sher HF (2007) Optimizing multiple quality characteristics via Taguchi method based Grey analysis. J Mater Process Technol
5. Balasubramanian S, Ganapathy S (2011) Grey relational analysis to determine optimum process parameters for wire electro discharge machining (WEDM). Int J Eng Sci Technol 3(1):95–101
6. Fung C-P (2003) Manufacturing process optimization for wear property of fiber reinforced polybutylene terephthalate composites with grey relational analysis. Int J Prod Res **41**(8)
7. Huang JT et al (2003) Optimization of machining parameters of Wire-EDM based on Grey relational and statistical analyses. Int J Prod Res 41(8):1707–1720
8. Jayabal S et al (2019) Modeling and optimization of thrust force, torque and tool wear in drilling of coir fibre reinforced composites using response surface method. Int J Mach Machinabil Mater 9(1/2):149
9. Saha A, Mondal SC 2016) Multi objective optimization of welding parameters in MMAW for nano-structured hard facing material using GRA coupled with PCA. Trans Indian Instit Metals

10. Agrawal DP, Gurav KV, Kamble DN (2014) Multi-objective optimization of photochemical machining process based on grey relational analysis method for spray etching. Appl Mech Mater
11. Kanigalpula PKC, Pratihar DK, Jha MN, Derose J, Bapat AV, Pal AR (2016) Experimental investigations, input-output modeling and optimization for electron beam welding of Cu-Cr-Zr alloy plates. Int J Adv Manuf Technol 85(1–4):711–726
12. Dhinakaran V, Shanmugam NS, Sankaranarayanasamy K (2017a) Experimental investigation and numerical simulation of weld bead geometry and temperature distribution during plasma arc welding of thin Ti-6Al-4V sheets. J Strain Anal Eng Des 52(1):30–44
13. Dhinakaran V, Shanmugam NS, Sankaranarayanasamy K (2017b) Some studies on temperature field during plasma arc welding of thin titanium alloy sheets using parabolic Gaussian heat source model. Proc Inst Mech Eng Part C J Mech Eng Sci 231(4):695–711
14. Kao PS, Hocheng H (2003) Optimization of electrochemical polishing of stainless steel by grey relational analysis. J Mater Process Technol 140(1–3), 22 Sept 2003:255–259
15. Mao S et al (2016) A novel fractional grey system model and its application. Appl Math Model 40(7–8):5063–5076
16. Wu L et al (2018) Using a novel multi-variable grey model to forecast the electricity consumption of Shandong Province in China. Energy 157(15):327–335
17. Zeng B (2018) Improved multi-variable grey forecasting model with a dynamic background-value coefficient and its application. Comput Industr Eng 118:278–290
18. Kothari CR (2004) Research methodology: methods and technique, new age international. (P) Limited, New Delhi
19. Pathak A et al (2018) Taguchi-grey relational based multi-objective optimization of process parameters on the emission and fuel consumption characteristics of A VCR petrol engine. Mater Proc Today 5(2), Part 1, 4702–4710
20. Fraley S, Oom M, Terrien B, Date JZ (2006) Design of experiments via taguchi methods: orthogonal arrays. The Michigan Chemical process dynamic and controls open text book, USA

Optimization of Process Parameters in Disc Plate Using Thermo-structural Analysis

N. Nandakumar, T. Allwin Raja, and P. Arunkumar

Abstract The objectives of the present paper are to perform coupled field steady-state thermal analysis and static structural analysis by using ANSYS Workbench to evaluate the temperature distribution, total deformation and von Mises stress in the disc plate. Thickness of disc plate, diameter of hole and selection of material are selected as process parameters which affect the thermal and structural behaviour of disc plate. The fuzzy logic modelling is developed to model the output parameters such as temperature distribution, total deformation and von Mises stress in the disc plate. The rule-based fuzzy logic modelling is used in the present investigation. It is resulted that there is an error percentage of 0.2, 0.51 and 0.15 between fuzzy and FEA results such as temperature, total deformation and von Mises stress, respectively. It is ensured that the fuzzy logic modelling can be used for output responses in designing disc plate due to lesser error percentage. The optimization of process parameters such as thickness of disc plate, diameter of hole and selection of material is carried out using Taguchi analysis. It is obtained from the optimization results that thickness of disc plate (3 mm), diameter of hole (5 mm) and selection of material (grey cast iron) are the optimized process parameters which provide the minimum value of output responses such as temperature, total deformation and von Mises stress.

Keywords Disc plate · Thermal analysis · Structural analysis · Fuzzy logic modelling · Taguchi method

1 Introduction

A disc brake is a device, used to retard the motion or stop the automobile by using artificial frictional resistance, and it is widely used in light motor vehicles. The optimization of influencing process parameters in disc brake is vital in the field of automobile, to improve the structural and thermal performance of the disc brake.

N. Nandakumar (✉) · T. Allwin Raja · P. Arunkumar
Department of Mechanical Engineering, Government College of Technology, Tamil Nadu, Coimbatore 641013, India
e-mail: nannthu@yahoo.com

G. Kumaresan et al. (eds.), *Advances in Materials Research*, Springer Proceedings in Materials 5, https://doi.org/10.1007/978-981-15-8319-3_18

There has been a great deal of research on analysis of disc plate, and a large body of the literature on brake disc plate modelling has been published. Lakshmi et al. [1] deal with the analysis of disc rotor of a Bajaj Pulsar 150 DTSi bike.

The results such as von mises stress, elastic strain, total deformation obtained from the static structural analysis of disc plate shows that grey cast iron gives better results when compared to aluminium alloy. The thermal analysis is also carried out in the disc plate to validate the appropriate material [2–9]. Khalanisohil et al. [10] modelled the brake with aluminium and grey iron materials and analysis for normal force, shear force and piston force. Vishal et al. [11] investigated on the single plate clutch to evaluate the stresses and forces using computer modelling and numerical method. Nishant et al. [12] have studied frictional plate of multi-plate clutch for cork and kevlar materials as friction lining and compared the von Mises stress. In recent times, fuzzy logic technique is one of the emerging technologies in artificial intelligence. Rajamani et al. [13] predicted the dimensional accuracy of polymer parts fabricated by selective inhibition sintering (SIS) process, using fuzzy logic technique. Latha and Senthilkumar [14] have done fuzzy rule-based modelling to predict the surface roughness in drilling process of fibre-reinforced composite materials. Peng et al. [15] have developed fuzzy inference system to model the dimensional error, warp deformation and built time in fused deposition modelling process. Taguchi's optimization technique is a distinctive and powerful optimization discipline that permits optimization with minimum variety of experiments. Athreya and Venkatesh [16] illustrate the procedure adopted in using Taguchi method to a lathe-facing operation. Liang et al. [17] performed optimization of process parameters to maximize the swimming speed of robotic fish using Taguchi method. Pundir et al. [18] utilized Taguchi method to optimize the process parameters for the maximization of copper and nickel removal in batch reactor. Arunkumar and Balasubramanian [19] developed theoretical model from thermo-structural analysis and performed Taguchi method for minimizing structural and thermal damage in polymer part during selective inhibition sintering process. Further, analysis of variance (ANOVA) is also performed to identify the influence of each parameter affecting biosorption.

In this present investigation, the coupled field steady-state thermal analysis and static structural analysis are performed by using ANSYS Workbench to evaluate the temperature distribution, total deformation and von Mises stress in the disc plate. The fuzzy logic modelling is developed to model the output parameters such as temperature distribution, total deformation and von Mises stress in the disc plate. Further, the optimization of process parameters such as thickness of disc plate, diameter of hole and selection of material is carried out using Taguchi analysis.

2 Thermo-structural Analysis

The steady-state thermal analysis and static structural analysis are coupled by using ANSYS Workbench to evaluate the temperature distribution, total deformation and von Mises stress in the disc rotor of a Bajaj Pulsar 150 DTSi bike. The process

Table 1 Process parameters and its levels

Process parameters	Level 1	Level 2	Level 3
Thickness (mm)	2	3	4
Diameter of hole (mm)	5	10	15
Selection of material	Al alloy (1)	Grey cast iron (2)	Structural steel (3)

Table 2 Experimental design

S. No.	Thickness (mm)	Diameter of hole (mm)	Selection of material
1	2	5	1
2	2	10	2
3	2	15	3
4	3	5	2
5	3	10	3
6	3	15	1
7	4	5	3
8	4	10	1
9	4	15	2

parameters such as thickness of disc plate, diameter of hole and selection of material are considered in the present investigation which is mentioned in Table 1.

Three process parameters and three levels are taken in the present study. L_9 and L_{27} orthogonal arrays are recommended for this condition. To minimize the experimental cost, L_9 orthogonal array is developed using design of experiments as shown in Table 2.

The steady-state thermal analysis is performed to evaluate the temperature distribution of disc plate. Thermal boundary condition such as heat flux of 38,000 W/m^2 and convection coefficient of 230 W/m^2°C are applied which is shown in Fig. 1a. The steady-state thermal analysis is coupled with static structural analysis to evaluate the total deformation and von Mises stress of disc plate. The inner wall of disc plate is fixed, and the results of thermal analysis are imported into structural analysis which is shown in Fig. 1b.

3 Fuzzy Logic Modelling

Fuzzy logic modelling technique is one of the artificial intelligences developed by Zadeh. It works under IF-THEN rules using Mamdani-based technique. It comprises

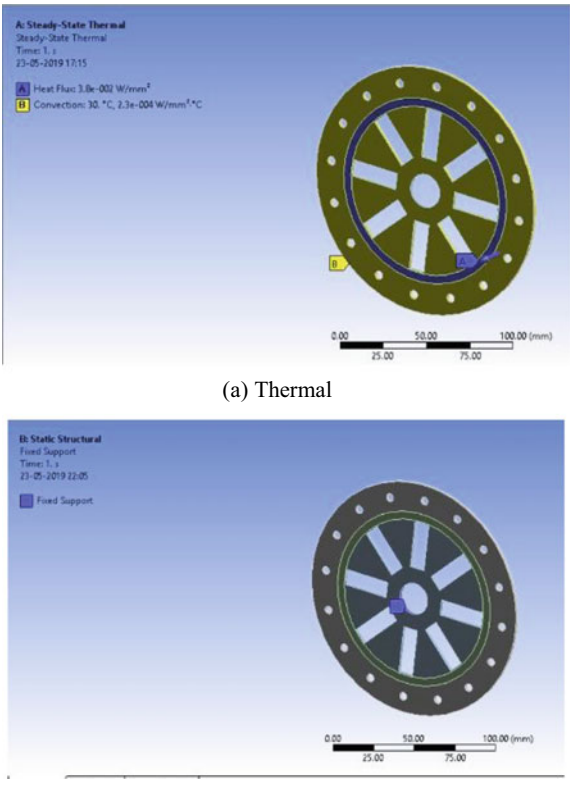

(a) Thermal

(b) Structural

Fig. 1 Thermal and structural boundary conditions at disc plate

three modules such as fuzzification module, inference module and defuzzification module which can be seen in Fig. 2.

In this present study, layer thickness of disc plate, diameter of hole and selection of material are input process parameters. Thermal and structural characteristics such as temperature distribution, total deformation and von Mises stress are output responses.

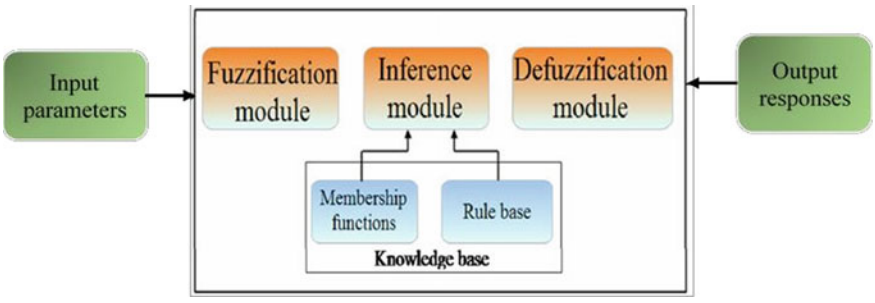

Fig. 2 Rule-based fuzzy logic modelling

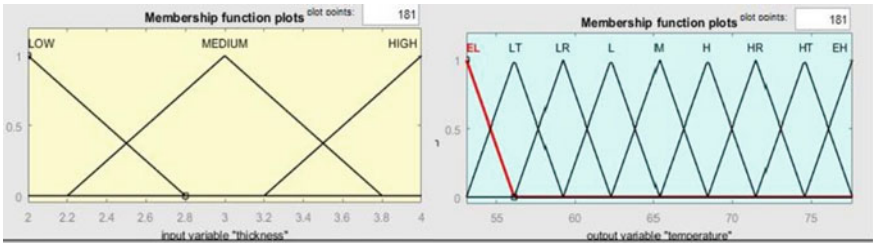

(a) Thickness of disc (b) Temperature

Fig. 3 Membership function for thickness of disc and temperature

Triangular-based membership function is adopted for both input and output variables to achieve the accurate results. Three and nine fuzzy sets are assigned for input and output variables, respectively, which can be seen in Fig. 3a, b.

4 Optimization Using Taguchi Method

The Taguchi method is a useful and powerful tool to optimize through statistical relationship between input process parameters and output responses. In this study, signal-to-noise ratio is performed in the optimization process to achieve the following condition: to minimize the temperature distribution, to minimize the von Mises stress and to minimize the total deformation. Further, main effect plot of SN ratio is used to provide the significance of each parameter on the thermal and structural characteristics of the brake disc plate.

5 Results and Discussion

5.1 Coupled Field Thermal and Structural Analysis

The coupled field thermal and structural analysis is performed and evaluated temperature distribution, total deformation and von Mises stress at various parameter conditions which is mentioned in Table 3.

5.2 Fuzzy Logic Modelling

Figure 4 depicts the fuzzy rule viewer of temperature distribution, total deformation and von Mises stress for L_9 experiments corresponding to input process parameters.

Table 3 Thermal and structural results

S. no.	Thickness (mm)	Diameter of hole (mm)	Selection of material	Temperature (°C)	Total deformation (mm)	von Mises stress (MPa)
1	2	5	1	57.660	0.0468	59.199
2	2	10	2	73.870	0.0234	48.476
3	2	15	3	77.650	0.0280	101.300
4	3	5	2	63.810	0.0220	36.214
5	3	10	3	63.670	0.0247	77.461
6	3	15	1	58.732	0.0489	70.639
7	4	5	3	58.010	0.0232	83.760
8	4	10	1	53.075	0.0442	72.138
9	4	15	2	65.368	0.0232	47.852

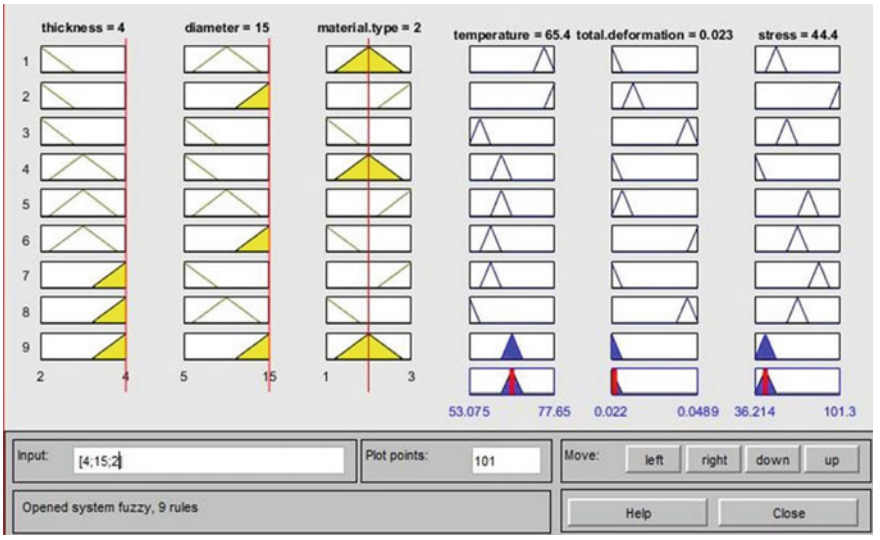

Fig. 4 Fuzzy logic performance of nine experiments

The experimental results are compared with the results obtained from fuzzy logic technique. It is identified that average error between experiment and fuzzy results is as follows: 0.31% for temperature, −0.51% for total deformation and −0.15% for von Mises stress which can be observed from Fig. 5a–c.

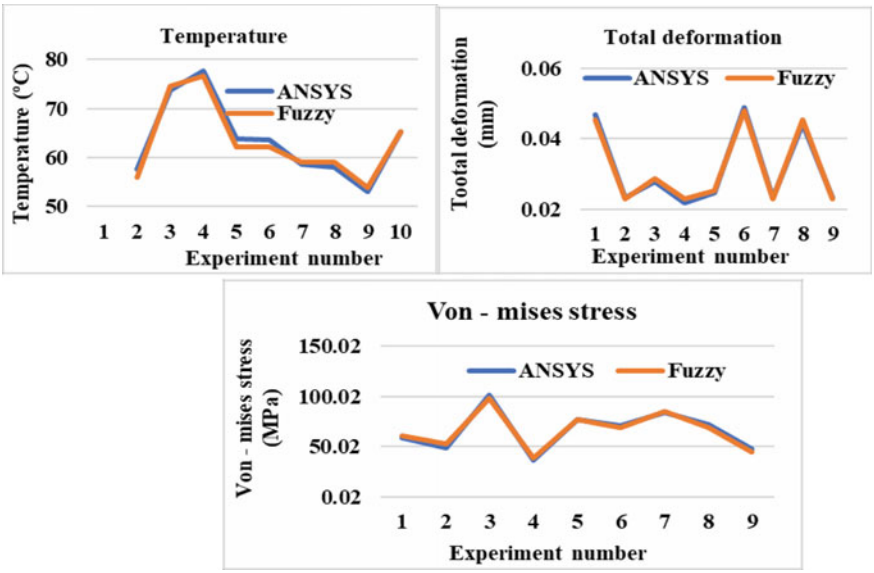

Fig. 5 Comparison of temperature, total deformation and von Mises stress between fuzzy and ANSYS results

5.3 Taguchi's Optimization Method

The optimization is carried out using Taguchi method to minimize the temperature distribution, total deformation and von Mises stress. Figure 6 shows response table for signal-to-noise ratio. It is evident that selection of material is most significant factor in the disc plate. Figure 7 shows the main effect plot for signal-to-noise ratio. The optimized process parameters such as thickness of disc plate (3 mm), diameter of hole (5 mm) and selection of material (grey cast iron) are shown in Table 4.

Fig. 6 Response table for signal-to-noise ratio

Response Table for Signal to Noise Ratios

Smaller is better

Level	A	B	C
1	-35.02	-33.83	-34.11
2	-34.09	-34.56	-33.36
3	-34.35	-35.08	-36.00
Delta	0.93	1.25	2.63
Rank	3	2	1

Fig. 7 Main effect plot for signal-to-noise ratio

Table 4 Optimized process parameters

Process parameters	Level
Thickness (mm)	3
Diameter of hole (mm)	5
Material type	Grey cast iron

6 Conclusions

The present paper deals with the analysis of disc rotor of a Bajaj Pulsar 150 DTSi bike. The steady-state thermal analysis and static structural analysis are coupled by using ANSYS Workbench to evaluate the temperature distribution, total deformation and von Mises stress. Three process parameters and three levels are taken, and hence, L_9 orthogonal array is developed using design of experiments. Further, fuzzy logic modelling is developed to model the output parameters. It is resulted that there is an error percentage of 0.2, 0.51 and 0.15 between fuzzy and FEA results such as temperature, total deformation and von Mises stress, respectively. It is ensured that the fuzzy logic modelling can be used for output responses in designing disc plate due to lesser error percentage. The optimization of process parameters such as thickness of disc plate, diameter of hole and selection of material is carried out using Taguchi method. Lower the better SN ratio is opted to minimize the output responses such as temperature, total deformation and von Mises stress. It is obtained from the optimization results that thickness of disc plate (3 mm), diameter of hole (5 mm) and selection of material (grey cast iron) are the optimized process parameters which provide the minimum value of output responses such as temperature, total deformation and von Mises stress.

References

1. Lakshmi Kala K, Hari Prasad T (2016) Modelling and structural analysis of disc plate with different materials by using ANSYS software. Int J Innov Res Sci Eng Tech 5(8)
2. Avinash ST, Dhakad (2018) Thermal analysis of disc brake using ANSYS. Int J Tech Innov Mod Eng Sci 4(6)
3. Maher B, Tarek L, Mohamed S (2013) FEA of in-plane shear stresses of preloaded sandwich plate with a viscoelastic core: application to the disk brake system. Des Model Mech Syst 289–296
4. Ayush G, Upadhyay M, Tapnokumarhotta (2017) Design and thermal analysis of a two-wheeler disc plate at different speeds using ANSYS software. Int J Adv Eng Res Dev 4(11)
5. Rakesh J, Anupam RJ, Anush K, Debayan D, Pawan J, Saurav R, Ankit B (2016) Structural and thermal analysis of disc brake using solid works and ANSYS. Int J Mech Eng and Tech 7(1):67–77
6. Viraj P, Kunal N, Dhale AD (2014) Structural and thermal analysis of brake disc. Int J Eng Dev Res 2(2)
7. Ishwar G, Gaurav S, Vikas M (2014) Thermal analysis of rotor disc of disc brake of Baja Sae 2013 car through finite element analysis. Int J Eng Res Appl. ISSN: 2248-9622
8. Babukanth G, Vimal TM (2012) Transient analysis of disk brake by using ANSYS software. Int J Mech Ind Eng 2(1). ISSN No. 2231–6477
9. Thilak VMM, Krishnaraj R, Sakthivel M, Kanthavel K, Deepan MMG, Palani R (2011) Transient thermal and structural analysis of the rotor disc of disc brake. Int J Sci Eng Res 2(8)
10. Khalanisohil, Seshagiri GVR, Anandkumar P (2016) Design and thermal analysis of disc brake using ANSYS. Int J Eng Educ Tech 4(4)
11. Vishal, Deshbhratar J, Nagnath U, Kakde (2013) Design and structural analysis of single plate friction clutch. Int J Eng Res Tech 2(10)
12. Nishant D, Ashish M, Ankit G (2018) Investigating behavior of multi-clutch plate frictional materials using ANSYS. Int J Appl Eng Res 13(16):12657–12662
13. Rajamani D, Balasubramanian E, Arunkumar P (2018) Study on dimensional accuracy of selective inhibition sintered HDPE parts using fuzzy logic. Mat Today Proceed 5(2):3817–3824
14. Latha B, Senthilkumar VS (2010) Modeling and analysis of surface roughness parameters in drilling GFRP composites using fuzzy logic. Mat Manu Proc 25(8):817–827
15. Peng A, Xingming X, Rui Y (2014) Process parameter optimization for fused deposition modeling using response surface methodology combined with fuzzy inference system. Int J Adv Manu Tech 73(1–4):87–100
16. Athreya S, Venkatesh YD (2012) Application of Taguchi method for optimization of process parameters in improving the surface roughness of lathe facing operation. Int Ref J Eng Sci 1(3):13–19
17. Liang L, Jiang LV, Wang C, Wei W, Xing Z, Guangming X (2016) Application of Taguchi method in the optimization of swimming capability for robotic fish. Int J Adv Rob Sys 13(3):102
18. Pundir R, Chary GHVC, Dastidar MG (2018) Application of Taguchi method for optimizing the process parameters for the removal of copper and nickel by growing *Aspergillus* sp. Wat Res Ind 20:83–92
19. Arunkumar P, Balasubramanian E (2017) Taguchi's parametric approach in optimizing selective inhibition sintering process variables. Innov Des Dev Pract Aero Auto Eng 263–269

Implementing Biomimicric Owl Wing Pattern for Noise Reduction in Turbine Blade

B. Premkumar and N. Nandakumar

Abstract The objective of this project is to reduce the noise level which is coming out from the turbine blade in jet engine by implementing owl wing pattern. During the take-off and landing, the noises coming out from the jet engines cause noise pollution. It also provides the irritating to nearby houses, colleges, and schools. During testing of jet engines, the noises from the jet engines cause irritation to technical staff, workers, and it may cause damages to their ears. Model the turbine blade by implementing the owl wing pattern and testing the noise level by modal, harmonic response, and harmonic acoustics analysis. This analysis gives the results in the form of sound pressure level (SPL) in dB. This experiment is modelled by the Catia V5R17. This analysis is done by Ansys 18.2. The comparison was made between the normal turbine blade and owl wing pattern turbine blade and the results are obtained from harmonic acoustics analysis. The SPL values are obtained from the normal turbine blade 143 dB which is greater than the owl wing pattern turbine blade 138 dB. Based on the SPL analysis, the serrated owl wing turbine blade is the best suitable design to reduce the noise which is coming out from the turbine blade.

Keywords Biomimicry · Owl wing pattern · Noise reduction · Turbine blade · Sound pressure level

1 Introduction

A turbine blade is the individual component which is used in turbine section of a gas turbine and aircraft engine. The blades are used for getting energy from the high temperature, high pressure gas produced by the combusto [1]. Aircraft turbines emit noise. The noise is generated by the movement of the blades through the air. This produces a swishing sound in rate with the rotation of the blades, as well as noise from the turbine machinery. Machine noise can have a tonal character which

B. Premkumar (✉) · N. Nandakumar
Department of Mechanical Engineering, Government College of Technology, Coimbatore, Tamil Nadu 641013, India
e-mail: premkumarsearch@gmail.com

G. Kumaresan et al. (eds.), *Advances in Materials Research*, Springer Proceedings in Materials 5, https://doi.org/10.1007/978-981-15-8319-3_19

is particularly annoying. Some of the ways to reduce the noise are changing the materials like acoustic absorbing material, designing blades using aerofoil shape like NACA 64-418 aerofoil. It reduces the noise range up to 115 dB. Introducing the porous surface at the trailing edges.

It reduces the noise range up to 112 dB. Finally, implementing the biomimicry pattern to the turbine blades is discussed in this paper. Objective of this project is to reduce the noise which is coming out from the turbine blade during the dynamic motion of the turbine by implementing the owl wing pattern at the edge of the turbine blade and reduce the material usage for manufacturing the turbine blade.

This present work consists of following methodology which starts from selection of materials, modelling dimensions and modelling of normal turbine blade to the modal, harmonic response and harmonic acoustics of the owl wing pattern turbine blade and compare the results of both analyses. Some of the information which was studied from related papers is Nedunchezian et al. [2] stated that the interplay between the wing motion, resulting unsteady aerodynamics, and aeroacoustics of a flapping wing flyer is investigated. The wing motion is varied in terms of the flapping amplitude, pitching amplitude, and the phase difference between flap and pitch. Two main sound generation mechanisms are found. The flapping motion induces the highest sound pressure level (SPL) in the stroke plane. Barone [3] Aerodynamic noise from wind turbine rotors leads to constraints in both rotor design and turbine siting. The primary source of aerodynamic noise on wind turbine rotors is the interaction of turbulent boundary layers on the blades with the blade trailing edges. Jianu et al. [4] studied that the global push toward sustainability has led to increased interest in alternative power sources other than coal and fossil fuels. One of these sustainable sources is to harness energy from the wind through wind turbines. Radun et al. [5] studied that wind turbine noise (WTN) increases the risk of WTN annoyance and self-reported sleep disturbance, which in turn can influence people's well-being.

2 Materials and Methods

2.1 Design Modification of Turbine Blade

In this section, the modelling of the normal aircraft jet engine turbine blade is modelled by using CATIA V5R17. It can be designed by using part design and wire frame design in Catia. Draw external profile in part design and revolve it. Draw the required profile on surface on the plane. Select any perpendicular plane and draw external profile of blade. Now, enter in wireframe. Use sweep command to extrude sweep-along pulling direction. Select law select linear and give required angle and surface design. Use extrude in given direction. Finally, the required 3D jet engine turbine blade models were obtained. In this analysis, three stage turbine was modelled. The normal turbine blade has not serrated edges at the end of blade; in case of modified turbine, blade contains serrated edges at the end of blade [6–10].

2.1.1 Turbine Blade Model

The model of normal turbine blade is shown in Fig. 1 and the model of owl wing pattern turbine blade which contains serrated edges at the end is shown in Fig. 2. Both models were designed by using the Catia V5R17.

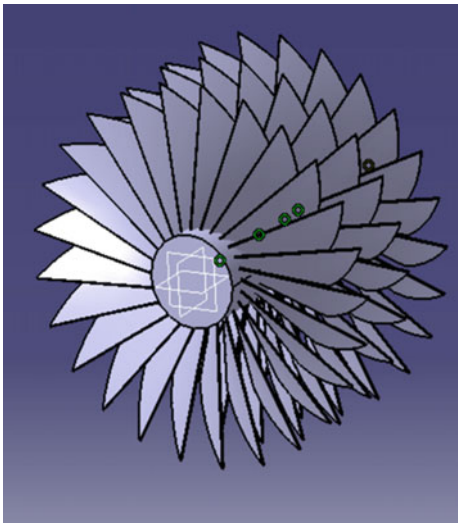

Fig. 1 Model of normal turbine blade

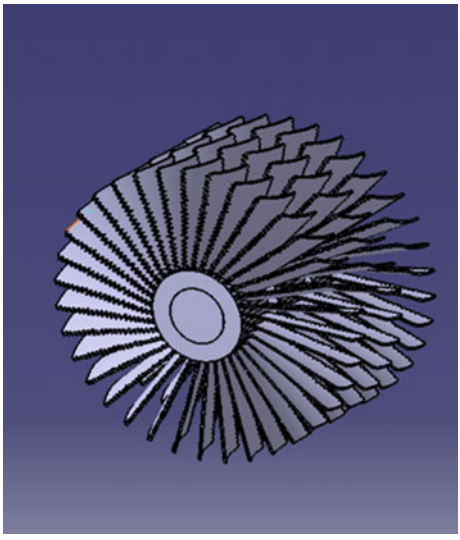

Fig. 2 Model of owl wing pattern turbine blade

2.1.2 Sound Pressure Level Analysis

The CATIA V5R17 modelled turbine blades were analyzed by using modal, harmonic response, harmonic acoustic analysis in ANSYS 18.2. The sound pressure analysis (SPL) is used to find the noise level which is coming out from the turbine blade. This analysis is carried out by finding the natural frequency of the turbine blade in the modal analysis. The solution from the modal analysis is connected to the setup file of the harmonic response of the ANSYS 18.2. The harmonic response of the turbine blade is performed by applying the input rotating force to the turbine blade. It gives the frequency versus amplitude with phase angle graph. Finally, this solution is connected to the harmonic acoustic analysis to find the SPL IN decibel by applying input load to the turbine by converting the harmonic frequency to the imported velocity to the turbine blade. To solve the harmonic acoustic solution to find the SPL of the corresponding turbine.

2.2 Statement of the Problem

- During the take-off and landing, the noises coming out from the jet engines causes noise pollution. It also provides irritating to nearby houses, offices, colleges, schools, etc.
- During testing of jet engine, the noise from the jet engines causes irritation to workers and it may cause damages to their ears.

3 Results and Discussions

3.1 Modal Analysis

In this model analysis, the natural frequency of different types of the turbine blades is shown. The natural frequency obtained from the turbine models was used in the harmonic analysis (Figs. 3 and 4).

3.2 Harmonic Response Analysis

In this harmonic analysis, the actual frequency and normalized frequency at different phase angle of the different types of the turbine blades are shown (Figs. 5 and 6).

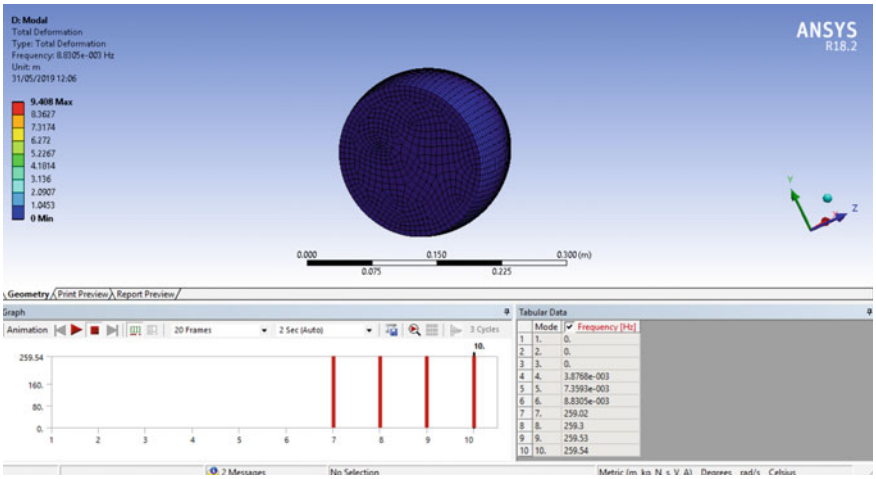

Fig. 3 Modal analysis of the normal turbine blade

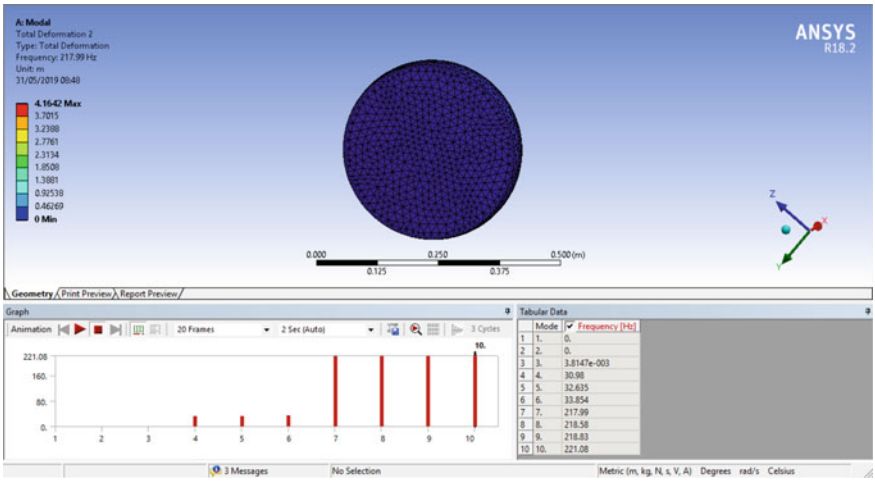

Fig. 4 Modal analysis of the owl wing pattern turbine blade

3.3 Harmonic Acoustic Analysis

In this harmonic acoustic analysis, the sound pressure level (dB) at different phase angle of the different types of the turbine blades is shown (Figs. 7 and 8).

Table 1 shows the harmonic and sound pressure level analysis of the both the models. The highest amplitude for the corresponding frequency of normal turbine blade at 250 Hz is 2.052e−16. Similarly, the highest amplitude for the corresponding frequency of owl wing pattern turbine blade at 250 Hz is 2.0e−19. The sound pressure

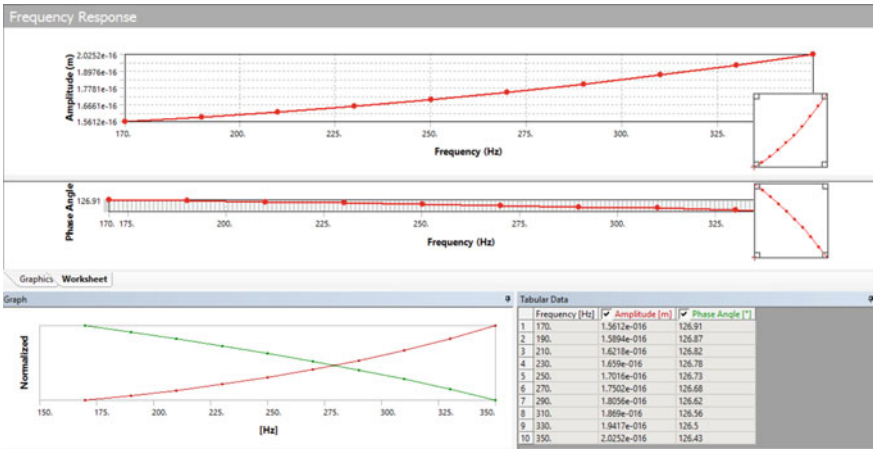

Fig. 5 Harmonic response analysis of the normal turbine blade

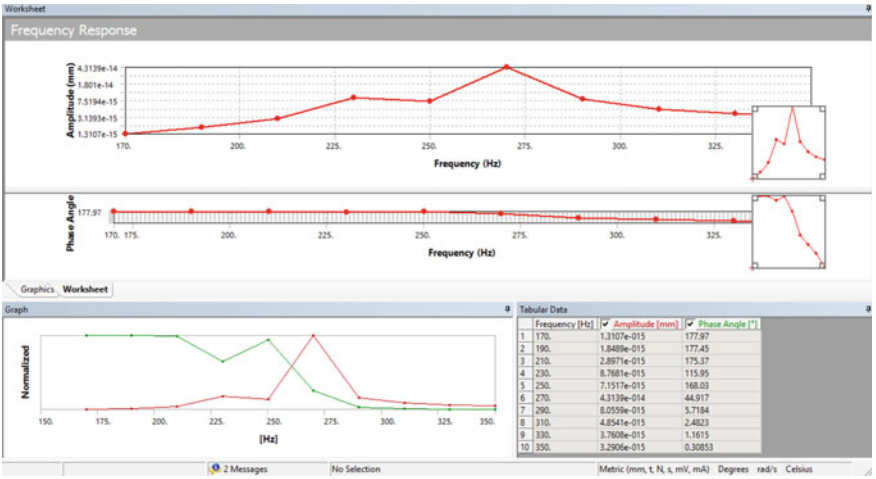

Fig. 6 Harmonic response analysis of the owl wing pattern turbine blade

level of the normal turbine blade is 143 dB. The sound pressure level of the owl wing pattern turbine blade is 138 dB. From this result, it should be absorbed that the noise level is reduced when implementing the owl wing pattern at the edge of the turbine blade.

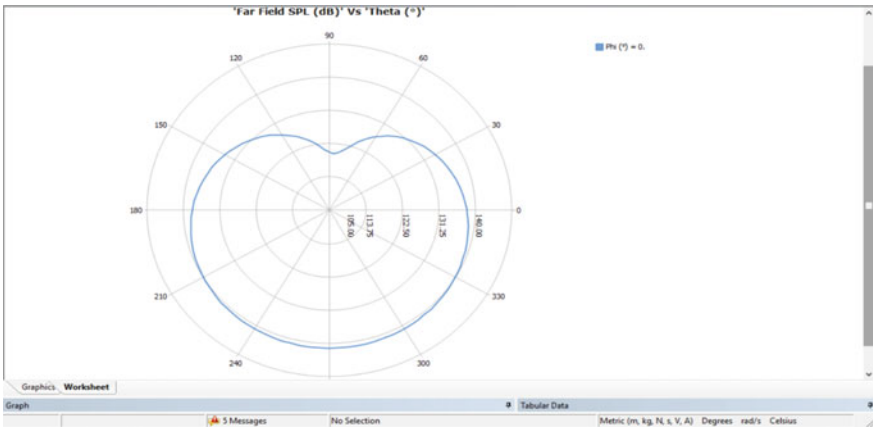

Fig. 7 Harmonic response analysis of the normal turbine blade

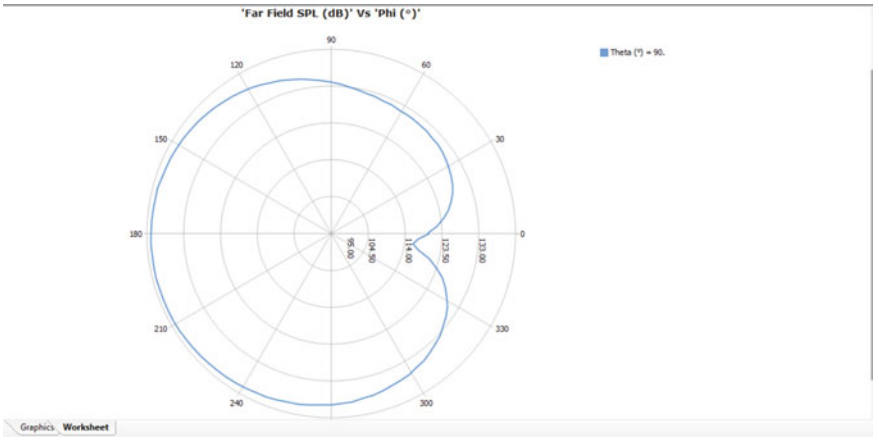

Fig. 8 Harmonic acoustic analysis of the owl wing pattern turbine blade

Table 1 Harmonic and sound pressure level analysis of both the turbine blade models

Parameters	Values
Harmonic frequency of models	For normal blade, $A = 2.052e{-}16$ For owl pattern blade, $A = 2.0e{-}19$
Sound pressure level of models	For normal blade, SPL = 143 dB For owl pattern blade, SPL = 138 dB

4 Conclusions

The present work of investigating the noise reduction of the turbine blade for the commercial aircraft by implementing the owl wing serrated pattern at the edge of the turbine blade has been successfully reduce the noise level up to 5–7 dB of the turbine during the rotation. So this analysis concluded that, by implementing the owl wing pattern at the edge of the turbine blade reduces the noise pollution. During the take-off, landing, and testing of aircraft engine, the noise coming out from the turbine should be reduced to certain level and gives comfort level for the engineering in testing of aircraft engine. In the future work, the noise reduction of the turbine blade can be analyzed by changing the shape of the serrated edges at the end.

References

1. Klän S, Burgmann S, Bachmann T, Klaas M, Wagner H, Schröder W (2012) Surface structure and dimensional effects on the aerodynamics of an owl-based wing model. Eur J Mech B/Fluids 33:58–73
2. Nedunchezian K, Kang CK, Aono H (2019) Effects of flapping wing kinematics on the aeroacoustics of hovering flight. J Sound Vib 442:366–383
3. Barone M (2011) Survey of techniques for reduction of wind turbine blade trailing edge noise. Prepared for Sandia National Laboratory
4. Jianu O, Rosen MA, Naterer G (2012) Noise pollution prevention in wind turbines: status and recent advances. Sustainability 4(6):1104–1117
5. Radun J, Hongisto V, Suokas M (2019) Variables associated with wind turbine noise annoyance and sleep disturbance. Build Environ 150:339–348
6. Laroulandie V (2016) Hunting fast-moving, low-turnover small game: the status of the snowy owl (*Bubo scandiacus*) in the Magdalenian. Quatern Int 414:174–197
7. Boonman A, Zadicario P, Mazon Y, Rabi C, Eilam D (2018) The sounds of silence: barn owl noise in landing and taking off. Behav Proc 157:484–488
8. Neise W, Enghardt L (2003) Technology approach to aero engine noise reduction. Aerosp Sci Technol 7(5):352–363
9. Liu WY (2017) A review on wind turbine noise mechanism and de-noising techniques. Renew Energy 108:311–320
10. Filippone A, Zhang M, Bojdo N (2019) Validation of an integrated simulation model for aircraft noise and engine emissions. Aerosp Sci Technol 89:370–381

Modal Analysis of Profile Deck Sheets in Composite Structural System

V. Preetha, V. Senthilkumar, S. Govindhan, D. Vishnu, and K. RanjithSelvan

Abstract Composite construction occupies a vital part in construction industry due to rapid completion of the projects. In composite systems, floor decking sheets involve a drastic study for effective replacement of conventional slab system. The composite floor deck system consists of profile deck sheet at the bottom above which minimum reinforcement is provided to take care of shrinkage stresses. The deck sheet acts as a temporary shuttering during concreting. The present work aims to investigate the vibration characteristics of profile deck sheet under various profile shapes employed for composite slab system. Modal analysis is a one of the technique adopted in which vibration studies can be determined for various profile shapes by involving parameters such as mode shape, natural frequency, plate stresses, and deformation by using finite element analysis. Based on the profile shapes the stiffness of the sheet varies with frequency.

Keywords Profile deck sheet · Modal analysis · Vibration studies · Natural frequency · Mode shape

1 Introduction

The enriched intention today imposed on building construction is efficient utilization of time and structural competency of structures. Steel–concrete composite elements are one such to satisfy these demands by integrating several developments of research in the field of composite construction. A composite slab, in which concrete is casted on top of the profiled deck sheets with the stud connection, functioning to tie the slab and beam together as a unit. The composite interaction of concrete with steel deck sheets having embossments in deck sheet to improve their shear bond characteristics. Provisions of deck sheets play a major role in composite construction. The investigation on elementary behavior of vibration characteristics on profile steel deck sheets

V. Preetha (✉) · V. Senthilkumar · S. Govindhan · D. Vishnu · K. RanjithSelvan
Department of Civil Engineering, Bannari Amman Institute of Technology, Sathyamangalam, Erode, Tamil Nadu, India
e-mail: preethav@bitsathy.ac.in

G. Kumaresan et al. (eds.), *Advances in Materials Research*, Springer Proceedings in Materials 5, https://doi.org/10.1007/978-981-15-8319-3_20

was determined by modal analysis method. The provision of profiled steel sheeting speeds up construction methodology. It is also often used with lightweight concrete to reduce the dead load due to floor construction. The profile deck sheet varies in shapes so that it imbibes more resistance. In this paper, the research is mainly focused on modal analysis on different profile deck sheets to analyze the frequency and the modal behavior under stipulated loading conditions. The shape involves flat plate as deck sheet, trapezoidal profile, and rectangular profile with variation in height of the profile. Besides the well-known analytical method, such as Fourier spectral element method, is preferred for the dynamic analysis of plate structures [1]. Many researchers have studied the modal analysis in different perspective of plates are summarized here. The plates with cracks are also been studied to determine the natural frequency and mode shape. Based on the presence of cracks in plates, the natural frequency will decrease with increase in peak amplitude [2]. The plates with stiffeners are also been analyzed under dynamic nature, wherein the strength and stiffness of the plate is increased by adding stiffeners. The addition of stiffeners prevents buckling of plate structures, thereby increasing the frequency [3, 4].

2 Literature Review

Li et al. [1] proposed the modal analysis with rectangular plates using the Fourier spectral element method. The compatibility conditions for the plates are assessed for two adjacent plates by 3D elastic couplers under translational and rotational stiffness. They involved the plates restrained along all the edges as simply supported condition. The accelerated Fourier series expansion formulations are performed to determine the flexural displacement fields on each plate. The expansion coefficients are assessed using various techniques. The results of finite element analysis were validated along with experimental data for box structures for different boundary conditions.

Al-Maliky [2] proposed the modal analysis to detect the cracks in stainless steel plates. By using ANSYS 18.2 program workbench, the free vibration studies on modal analysis on plate with central crack were done using finite element analysis. The square plates were meshed to form elements and nodes. The cracked percentage of length along with the square plates is from 10 to 40%. All the four cases of cracked plates were analyzed by using different boundary conditions. Based on crack length along with the modes, natural frequency, and plates. The parameters involving natural frequency as a function of crack's length were estimated for three modes. Finally, by their study of different techniques in the dynamic response of structures which provides a appropriate method to investigate the plates and also helps to predict the cracks of stainless steel plates.

Kumar and Arakerimath [3] studied about the dynamic nature of plates and predicted the various modes of vibrations. The plates with high strength-to-weight ratio used in structural applications are subjected to dynamic load often over its life span. The strength of the plate structures is increased usually by providing stiffeners in suitable position of plates. The bases of structures are formed by the analysis

of rectangular stiffened plates. Nastran and Hyper mesh is used to perform finite element analysis. Here, the modal analysis of a rectangular stiffened plate is done with the aspect ratio of 2.

Sonawane et al. [5] proposed the study on modal analysis for to evaluate the characteristics of vibration of structures with its components using major techniques. The parameters taken for the study include mode shapes, damping factor, and natural frequencies of structure. Comparison of the natural frequency mathematically, FEA, and experimentally was done. In this study, single rectangular cantilever beam was analyzed for modal analysis and compared the results by finite element analysis with experimental results. The rectangular cantilever plate of aluminum as material property proposed for the investigation was designed and analyzed by using ANSYS Workbench. A correlation study between the FEA, mathematical (Euler's Bernoulli's beam theory) and experimental data were observed. The results help in predicting the failure loads for different end conditions.

Ikechukwu et al. [4] proposed the modal analysis for the components under vibration excitation to evaluate the mode shapes. The results generated were compared with a number of resonances where the damping effect and frequency were predicted. The study on flat plate mounted with electromagnetic shaker enables the vibration studies on the plate, and the results of the responses were measured by using a transducer. By using CATIA software, the plate was modelled and analyzed using various FEA solvers, particularly the optimized results obtained by ANSYS 5 degree of freedom.

Zhong et al. [6] proposed the analysis for vibration of foundation plate with four discontinuous edges using finite cosine integral transform method. The Kirchhoff classical theory is used for rectangular plate. The foundation is modelled using Winkler elastic foundation. The frequencies and the modes of vibration were calculated by the integral transform method.

Subba Rao et al. [7] proposed the study on modal analysis of plates with cut outs. The investigation is to predict the natural frequency for the rectangular plate with different aspect ratios. The analysis involves rectangular plates with circular- and rectangular-type cutouts with simply supported end conditions. The changes in location of cut outs on the plates along its major axis line are varied.

Ramu and Mohanty [8] studied the analysis for functionally graded plates using finite element method. The modal analysis is to determine the parameters such as frequency and mode shapes. Based on the structure and composition of the material over its volume, corresponding changes are differentiated in the material constituents. The material composition is assumed to vary accordingly throughout its thickness.

Bhusnar and Sarawade [9] studied the behavior of rectangular plate with lap joints. The study is to analyze the dynamic behavior of elementary connections with rectangular plate involving bolted lap joint, welded lap joint, and single lap epoxy adhesive joint subjected to impact or shock loads. The factors that affect the response of joints were studied that include natural frequencies, mode shapes, and damping ratio. From this work, the effective bonding of joints was identified.

Khan and Awari [10] proposed the analysis for fixed plate condition. The analytical solutions are predicted in terms of mass and stiffness modifications for each plate.

The concept of uncertainty in plate structures is well addressed in this research study. By adding the uncertain mass, different dynamic characteristics of plate with same boundary conditions are used. Irregularity in mass to the bare plate not only shift its frequencies but it also affects the mode shapes of plate. Addition of the uncertain stiffness changes the dynamic characteristic of plate with the same boundary condition.

Kumar et al. [11] proposed the vibration analysis on cantilever plate using finite element analysis. The optimization functions are proposed to determine vibrations induced in beams and plates to get optimize results under transient response of dynamic characteristics. A cantilever flat plate has modeled to analyze for natural frequencies and mode shapes. It has found that it depends on the mode number the distribution of modal strain energy intensity varies.

Avitabile [12] proposed the experimental modal analysis of structures with various concepts of vibration and the tools to solve structural dynamic problems. The study involves identification of structures under vibration in a non-mathematical perspective. The simple explanations were described for structural vibration and the tools for the solution of structural dynamic problems. This was all achieved by detailed mathematical relationships.

Klimenda and Soukup [13] proposed the modal analysis of thin aluminum plate to evaluate the natural frequencies and mode shapes of thin plate. The modal analyses of thin aluminum (Al 99.9) isotropic plate with dimensions $0.10 \times 0.10 \times 0.002$ m were adopted for the study. The modal analysis was performed to predict the eigenvalues and the numerical solution of a thin isotropic plate was obtained. The solution was performed in the ANSYS program.

3 Materials and Methods

3.1 Profile Deck Sheet

The profile deck sheet is generally having the profile thickness which varies with 0.8–1.5 mm with galvanized coating. The profile heights are usually ranges from 38 to 75 mm with the corrugations in between the profile with pitch of 150 mm and 350 mm, respectively. The standard profile shapes available in the market include dovetail and trapezoidal profile with Web indentations. The common profile shapes as shown in figure: case II and case III compromise to enhance the bond between the interface by providing stability during concreting and other construction loads. Embossments on the rib of the deck sheet mobilize the bearing resistance with adhesion property to provide the shear transfer in composite slabs.

3.2 Finite Element Analysis

The finite element method is proposed to obtain solutions of boundary value problem. The boundary value problem is proposed with dependent variables to satisfy a differential equation within a domain of independent variables and to satisfy boundary conditions in that domain. The modal analysis of rectangular plate with different profile geometry is modeled using finite element method in ANSYS 19.2 software. The finite element formulations are arrived to determine the equation of motion by Hamilton's principle [8]. The equations for bending stiffness of plate in rectangular Cartesian coordinates are shown.

$$D\left(\frac{\partial^4 w}{\partial x^4} + 2\frac{\partial^4 w}{\partial x^2 \partial y^2} + \frac{\partial^4 w}{\partial y^4}\right) = -q(x, y, t) - 2\rho h \frac{\partial^2 w}{\partial t^2}.$$

For a uniform plate of thickness,

$$D := \frac{2h^3 E}{3(1 - \nu^2)}.$$

where D—Flexural rigidity

w—Plate deflection.

The plan dimension of the profile deck is 1.0 m × 0.9 m with plate thickness of 1 mm, respectively. The present study involves following material idealization of steel plate with profiles of variable height. The element chosen to study is SOLID185 for 3D modeling of solid plate structures. The assignment includes eight-noded element having three degrees of freedom at each node. It also has mixed formulation capability for simulating deformations of nearly incompressible elastoplastic materials, and fully incompressible hyper elastic materials. The forms of profile deck sheet considered for the modal analysis involve

Case I: Flat plate of 1 mm thickness

Case II: Trapezoidal deck sheet

Case III: Rectangular deck sheet.

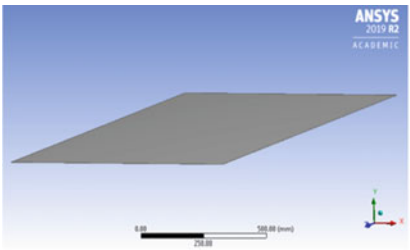

Case I: Flat plate of 1mm thickness

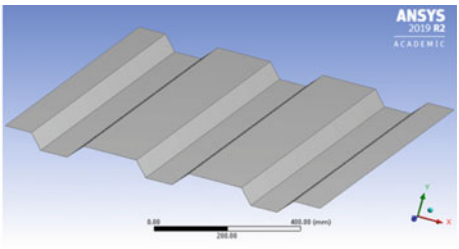

Case II: Trapezoidal deck sheet

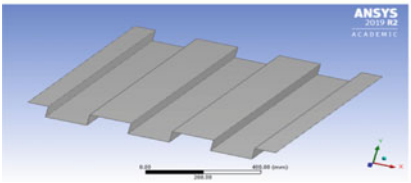

Case III: Rectangular deck sheet

3.3 Modal Analysis

The dynamic response of composite deck slab system through modal analysis is to determine the frequency and vibration modes for three different models. The finite element results obtained through an extensive parametric study were analyzed based on its sheet profile. The results obtained for each model is as shown in Figs. 1, 2 and 3 to identify the most suitable deck sheet. The natural frequency variations for various profile shapes with mode numbers are tabulated as in Table 1.

4 Results and Discussion

The modal analysis is performed for three different cases for profile deck sheet in composite slab system to determine the frequency and mode shape for different profile plate system for ten modes. The shapes of the modes are depicted in Figs. 1, 2 and 3 with different simulation profiles. The frequency variation slightly varies for flat plates. The frequency is high for trapezoidal plates (case II) when compared to other profile shapes. The frequency gradually increases with increase in stiffness of the plate based on its profile dimension. Figure 4 shows the variation of frequency for all cases with mode numbers.

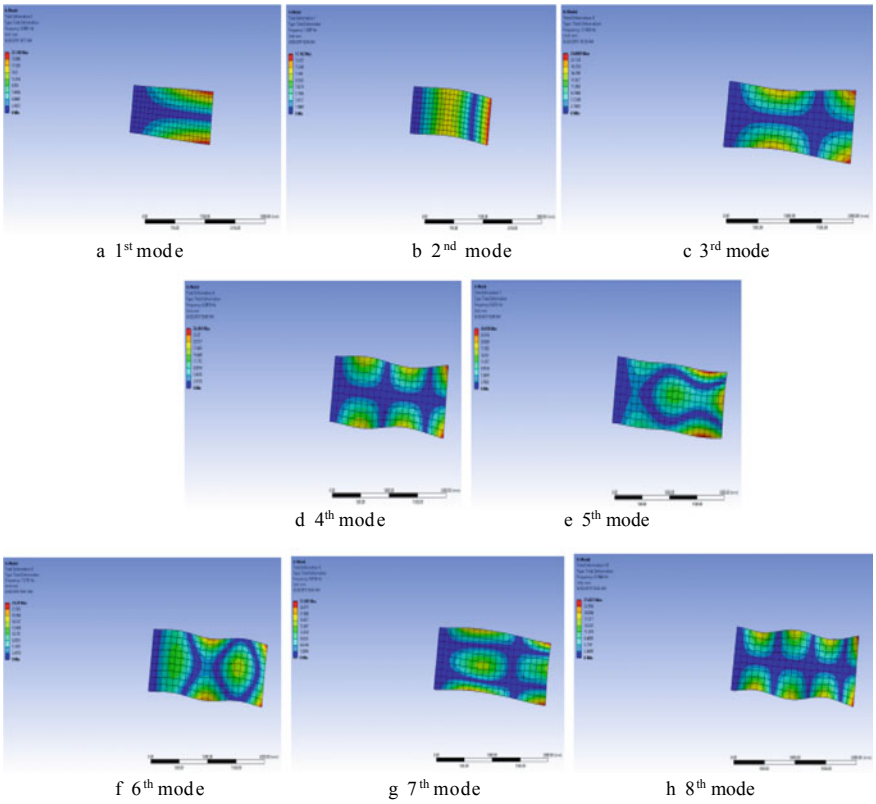

Fig. 1 Mode shape of flat plate deck sheet

5 Conclusion

In this work, the dynamic characteristics of fixed supported deck sheets are been analyzed by ANSYS 19.2. To judge the reliability of profile deck sheets in composite slabs, a comparison between various shapes has been made based on natural frequencies and mode shape. The variations of frequency are relatively small for rectangular and trapezoidal profile whereas the flat plate stiffness is low when compared to other cases. The variation of ten mode shapes with its frequency values varied a lot for flat plate and other profile plates due to increase in stiffness of plate. The deformed shape of various profile deck at specific frequency shows the mode of vibration characteristic of deck sheet. The main influence of deck sheet is characterized by vibration mode shape. The vibration mode shape reflects the failure pattern and delamination behavior of deck sheet with composite slab arrangement.

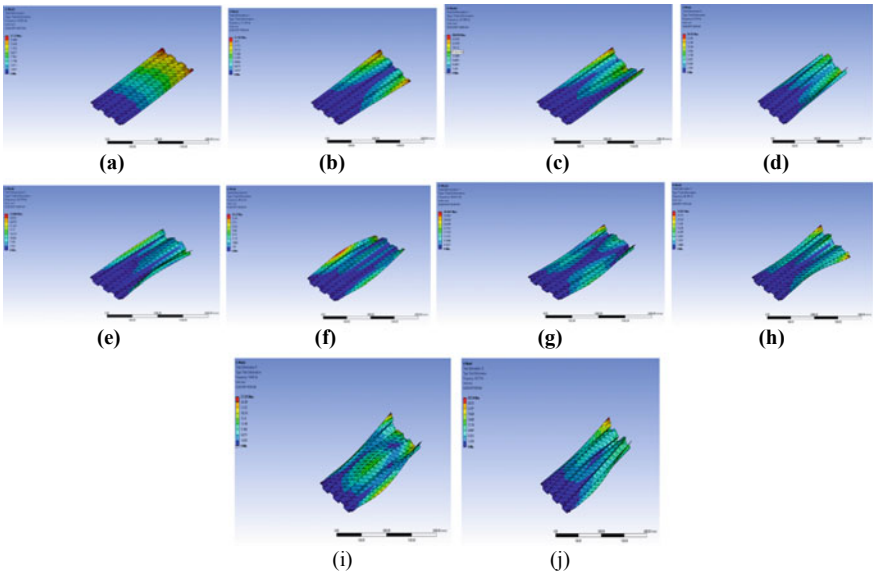

Fig. 2 **a–j** Mode shape of rectangular deck sheet

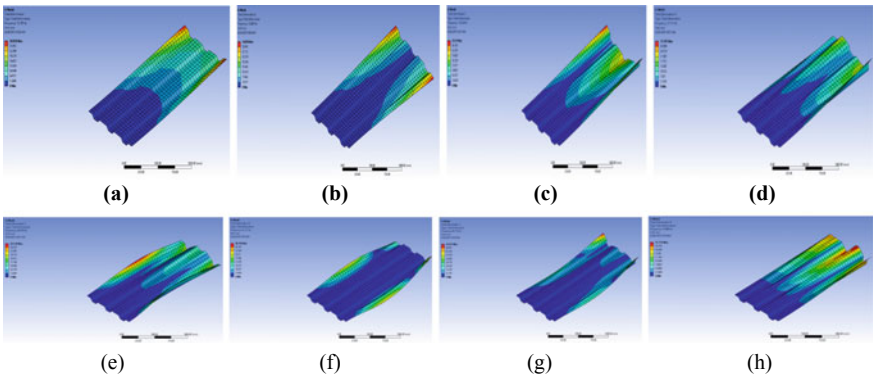

Fig. 3 **a–h** Mode shape of trapezoidal deck sheet

Table 1 Frequency variation based on deck sheet profile

Mode numbers	Frequency in Hz		
	Case I	Case II	Case III
1	0.209	15.655	12.195
2	0.988	17.124	12.630
3	1.309	25.799	17.414
4	3.183	47.390	27.111
5	3.679	76.779	40.759
6	6.007	85.220	41.117
7	6.825	89.672	41.172
8	7.379	95.791	57.899
9	9.019	116.92	86.757
10	9.766	132.77	87.133

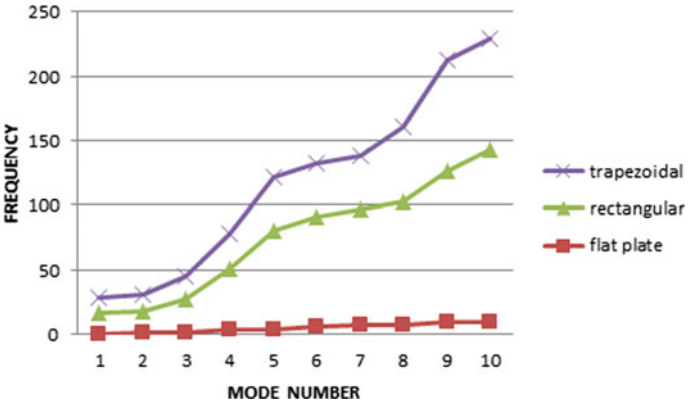

Fig. 4 Variation of frequency with mode numbers

References

1. Li W, Xu H, Du J (2015) Modal analysis of general plate structures. J Vib Acoust 136
2. Al-Maliky FT (2018) Modal analysis of central crack stainless steel plate using ANSYS program. Int J Mech Eng Technol 9(9):460–466
3. Kumar A, Arakerimath RR (2015) A review and modal analysis of stiffened plate. Int Res J Eng Technol 2(8):581–588
4. Ikechukwu O, Aniekan I, Pau S, Ikpe E (2016) Experimental modal analysis of a flat plate subjected to vibration. Am J Eng Res (AJER) 6:30–37
5. Sonawane AR, Talmale PS, Sapkal LGN (2017) Modal analysis of single rectangular cantilever plate by mathematically, FEA and experimental, pp 264–269
6. Zhong Y et al (1993) Vibration of plate on foundation with four edges free by finite cosine integral transform method. Lat Am J Solids Struct 1954:854–863
7. Merneedi A, Raonalluri M, Rao VVS (2017) Free vibration analysis of a thin rectangular plate with multiple circular and rectangular cut-outs. J Mech Sci Technol 31(11):5185–5186
8. Ramu I, Mohanty SC (2014) Method. MSPRO 6(Icmpc):460–467

9. Bhusnar M, Sarawade SS (2016) Modal analysis of rectangular plate with lap joints to find natural frequencies and mode shapes, pp 6–14
10. Khan IA, Awari GK (2014) Analysis of natural frequency and mode shape of all edge fixed condition plate with uncertain parameters. Int J Innov Res Sci Eng Technol 3(2):9277–9284
11. Waghulde KB, Kumar B, Garse TD, Patil MM (2011) Vibration analysis and control of cantilever plate by using finite element analysis. J Eng Res Stud Iii
12. Avitabile P. Experimental modal analysis. In: Modal analysis and control laboratory, pp 1–15
13. Klimenda F, Soukup J (2017) Modal analysis of thin aluminum plate. Procedia Eng 177:11–16

Experimental Investigation of Exhaust Emission Reduction in a CI Engine by Using Titanium Dioxide Nanoparticle-Blended Methyl-Esterified Neem Oil Biodiesel

G. Shaik Usmansha, K. Senthil Kumar, Praveen Maruthur, R. Rejumon, and S. Dhanesh

Abstract This experimental work is attempted to analyze the effect of titanium dioxide (TiO_2) blended into neem oil-based biodiesel mixture, and tested in CI engine. The experiment focuses on emission reduction along with performance enhancement of CI engine when powered with a bio fuel mixture into which a nanoparticle is blended in. Nanparticle TiO_2, is mixed into the neem oil biodiesel (B20) in two quantities: one is 200 ppm and other is 400 ppm. The test fuels used are neat diesel, B20, B20 + 200 ppm TiO_2, B20 + 400 ppm TiO_2. The test fuel has gone through high speed blending and stabilized using ultrasonic bath stabilization. The major result expected from this experimental study was emission reduction particularly of CO, HC and it is found to be less. Obviously, due to use of biodiesel, the NO_x emission is on the higher side compared to neat diesel fuel and addition of TiO_2 has reduced NO_x emission.

Keywords Diesel engine · Neem biodiesel · Brake thermal efficiency · Titanium dioxide

1 Introduction

As seen everywhere, major application of compression ignition engine is in heavy vehicles used for transportation. The reason for this is that diesel has greater calorific value; hence, it gives increased performance when compared to spark ignition engine. Nowadays, fossil fuel depletion news is very common and in and around for few years, so the search for alternate fuels are inevitable and happening briskly. Though

G. S. Usmansha (✉) · K. S. Kumar · S. Dhanesh
Department of Mechanical Engineering, SNS College of Engineering, Coimbatore, India
e-mail: shaikusmansha@gmail.com

P. Maruthur
Acharya Analytics, Palakkad, India

R. Rejumon
Department of Automobile Engineering, Nehru College of Engineering, Thrissur, India

G. Kumaresan et al. (eds.), *Advances in Materials Research*, Springer Proceedings in Materials 5, https://doi.org/10.1007/978-981-15-8319-3_21

electric vehicles are considered as the major alternative for IC engine, studies and experiments are happening in the area of biodiesel too. The reason for experimenting with biodiesel is that we do not have to change the IC engine working technology that much and recently most common experimenting technique followed is blending diesel and vegetable derived bio oils, they together forms a biodiesel. By doing so, many experiments have shoed up with many results majorly all demanding performance enhancement, but interestingly very few suggested emission reduction from these engines as it was commonly seen in all vegetable oil mixed biodiesel blends increase in NO_x emission. This experimentation is trying to prove along with NO_x and other emission values can be brought down drastically. Dorado et al. [1] reduced CO and NO_x values significantly by directly injection olive oil biodiesel when compared to neat diesel fuel. Narayanareddy and Ramesh [2] used jatropha fuel and by varying injection pressure and various other parameters achieved good performance results. Lakshminarayana Rao et al. [3] got emission reduction in CO, HC and a slight increase in NO_x emission while they were experimenting with rice bran oil-blended biodiesel test fuel and their test too suggested good performance improvement of IC engine. Banapurmath and Tewari [4] created a test engine rig where piston wall was coated with thermal barrier and they used honge oil along with its methyl-esterified version; interestingly, they put forward that methyl esterified honge oil fuel gave out less emissions when compared to honge oil blended biodiesel fuel. Hazer [5] studied performance and emission characteristics of a diesel engine coated with ceramic and used canola methyl-esterified blends as fuel. They came up with the result of about 8% reduction in specific fuel consumption along with power output increase, looking at emission side, the CO and smoke emission values were low but NO_x values were high which was common for vegetable derived oil-blended biodiesel. Prabakar and Rajan [6] did their experimentation using methyl-esterified pongmia fuel in titanium dioxide-coated piston cylinder IC engine arrangement and their result was decreased values for CO, CO_2 and HC, but increase in NO_x emissions. Arulmozhiselvan et al. [7] added cerium oxide nanoparticle into biodiesel–ethanol blend and compared the performance with neat diesel. They showed with result that the ignition delay can be overcome by addition of cerium oxide Nano particle and high ignition pressure was achieved by addition of ethanol along with few emission reduction values. The motto of this experiment is emission reduction by using titanium dioxide nanoparticle in CI engine.

2 Materials and Methods

2.1 Preparation of Biodiesel (Neem Oil Methyl Ester: NOME)

Methyl esterified neem oil is produced through trans-esterification process where the neem oil is made to react with methyl alcohol in the presence of catalyst NaOH. The

Table 1 Property comparison of various oils

Properties	Diesel	Neem oil	Neem oil methyl ester
Specific gravity	0.830	0.960	0.870
Kinematic viscosity (cSt)	3.8	34	4.1
Flash point (°C)	61	158	98
Fire point (°C)	65	167	106
Calorific value (MJ/Kg)	42,500	40,500	390,000
Cetane number	48	36	53

process gives glycerol and fatty acid as output. The quantity of methyl alcohol taken is 20 ml and 8 mg of sodium hydroxide and they react to form sodium methoxide. This sodium methoxide reacts with neem oil (1000 ml) which is heated to 65 °C and held at that temperature continuously for 2 h. Then the mixture is cooled down in a separating flask for 12 h. At the end of cooling, two layers will be formed: bottom layer will be heavier glycerol and upper layer was methyl ester. The fuel properties after trans-esterification is tabulated as Table 1. Experimentation is carried out with neat fuel, biofuel-diesel blend (B20) at 20–80 proportion, B20 with 200 ppm TiO_2, B20 with 400 ppm TiO_2.

2.2 Experimental Setup

Experiments were conducted on a 4-stroke DI single cylinder water-cooled diesel engine, specifications of which are given in Table 2. The engine was running at constant speed of 1500 rev/min and the tests were conducted on diesel engine using pure diesel, neem oil methyl ester with and without nanoparticle addition from no load to maximum load. The volumetric fuel flow rate was measured and kept as 50 cm^3. The emissions like CO, HC, and NO_x were measured by using AVL five gas analyzer.

Table 2 Diesel engine specifications

Engine	Kirloskor
Power	4.4 KW
Bore (mm)	87.5
Stroke (mm)	110
Compression ratio	17.5:1
Speed (rpm)	1500
Injection pressure (bar)	200
Injection timing	23° bTDC

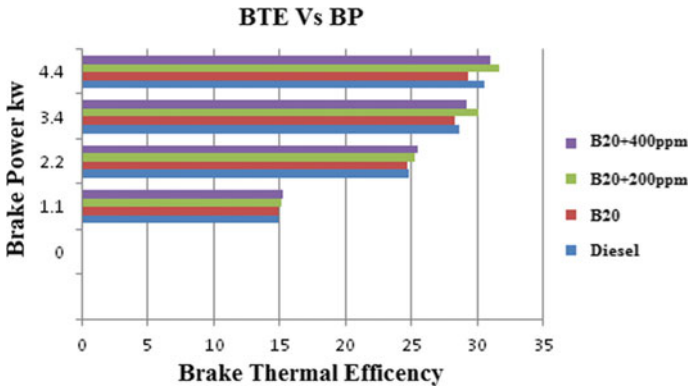

Fig. 1 Brake thermal efficiency versus brake power

3 Results and Discussions

3.1 Brake Thermal Efficiency

Figure 1 shows the variations of brake thermal efficiency with load for diesel and biodiesel (B20) and with nanoparticle is. It was observed that there is an increase in BTE while using B20 + 200 ppm TiO2 fuel when compared to other fuel samples. The maximum brake thermal efficiency obtained for B20 biodiesel blend with 200 and 400 ppm nanoparticle is 31.64 and 30.92% and for diesel, it is 30.48% at full load.

3.2 Brake Specific Fuel Consumption

Figure 2 shows the variation of brake specific fuel consumptions (BSFC) with load for diesel and biodiesel (B20) and with nanoparticle. BSFC of B20 biodiesel is higher when compared to all other test fuel sample which may due to lower calorific value of biodiesel blend. The lowest BSFC is obtained as 0.226 kg/kWh and 0.30 kg/kWh for 200 ppm and 400 ppm nanoparticle added with B20, respectively, whereas it is 0.32 kg/kWh for B20 at maximum load.

3.3 Carbon Monoxide Emission (CO)

The graph (Fig. 3) itself shows that the CO emission values grow very slowly upto ¾ of the full load and there is a sudden jump in the emission value when the test rig

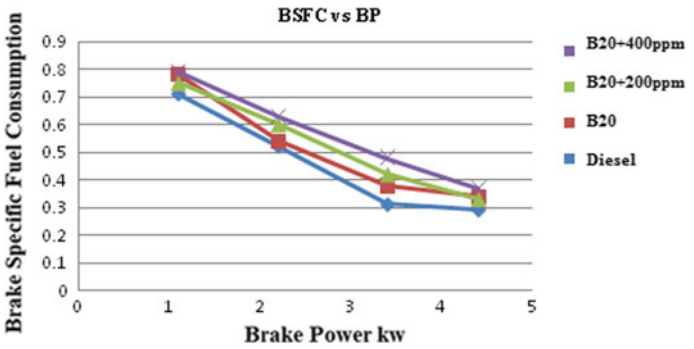

Fig. 2 BSFC versus BP

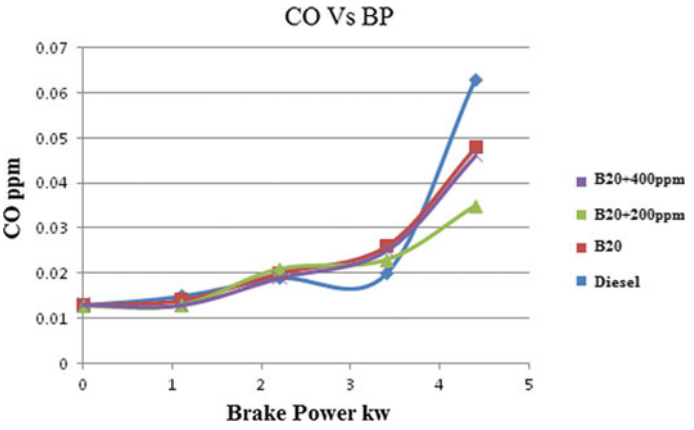

Fig. 3 CO versus BP

is at its full load for all the test fuels and evidently, there is CO emission reduction when titanium dioxide is added.

3.4 Hydrocarbon Emission (HC)

Figure 4 shows the variation of hydrocarbon emission with load. Adding of titanium oxide decreases the hydrocarbon emission when comparing with pure diesel and biodiesel blend. The least HC emission is obtained for 200 ppm and 400 ppm nanoparticle with B20 are 22 ppm and 21 ppm, respectively, whereas B20 is 24 ppm at maximum load.

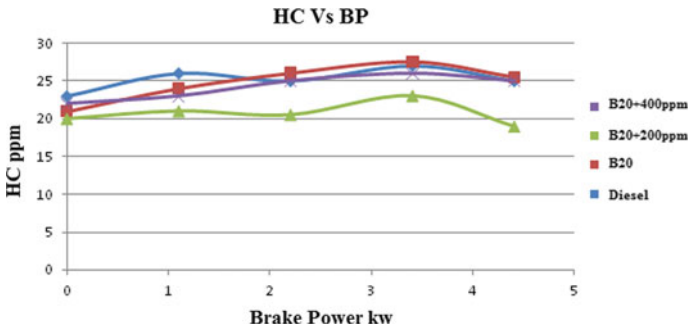

Fig. 4 HC versus BP

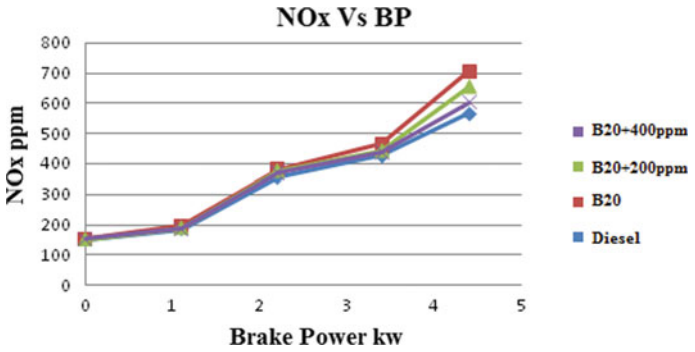

Fig. 5 NO_x versus BP

3.5 Nitrogen Oxide Emission (NO)

The effect of nanoparticle additives (Fig. 5) improves the combustion and the longer ignition delay result in faster premixed combustion is the cause for higher combustion temperature and the subsequent higher NO_x emission. The lowest NO_x emission obtained for 200 ppm and 400 ppm nanoparticle with B20 are 654 ppm and 641 ppm, respectively, whereas for diesel and B20 are 605 ppm and 676 ppm, respectively, at maximum load.

4 Conclusions

The engine performance and exhaust emission characteristics of a diesel engine with diesel–neem biodiesel blends with the influence of titanium oxide nanoparticles were investigated and the derived conclusions are given. The brake thermal efficiency was increased by 1.32% for B20 with 200 ppm of TiO_2. The CO and HC emissions

were decreased by 23% and 16.5%, respectively, for 200 ppm TiO_2 added with B20 as additives at full load. The NO_x emissions increased about 5% for 200 ppm TiO_2 added with B20 diesel–biodiesel blends compared to 400 ppm TiO_2 with B20 diesel–biodiesel blends and without nanoparticle addition with B20 blend at full load. So it can be concluded that the addition of 200 ppm titanium oxide nanoparticle as additive with biodiesel blends will reduce emission even though there is marginal increase in NO_x emission.

References

1. Dorado MP, Ballesteros E, Arnal E, Gomez J, Lopez FJ (2003) Exhaust emissions from a diesel engine fuelled with transesterified waste olive oil. Fuel 82(11):1311–1315
2. Narayanareddy J, Ramesh A (2006) Parametric studies for improving the performance of a Jatropha oil-fuelled compression ignition engine. Renew Energy 31:1994–2016
3. Lakshminarayana Rao G, Saravanan S, Sampath S, Rajagopal K (2008) Combustion and emission characteristics of diesel engines fueled with rice bran oil methyl ester and its diesel blends. Therm Sci 12:139–150
4. Banapurmath NR, Tewari PG (2008) Performance of a low heat rejection engine fuelled with low volatile honge oil and its methyl ester. Proc IMechE Part A J Power Energy 222:323–330
5. Hazer H (2009) Effects of biodiesel on a low heat loss diesel engine. Int J Renew Energy 34:1533–1537
6. Arulmozhiselvan V, Anand RB, Udayakumar M (2009) Effects of cerium oxide nanoparticle addition in diesel and diesel-biodiesel-ethanol blends on the performance and emission characteristics of a CI engine. ARPN J Eng Appl Sci 4(7):01–06
7. Karhikeyan R, Mahalakshmi NV (2005) Performance and emission characteristics of a turpentine diesel dual fuel engine. Energy 32:1202–1209
8. Panwar NL, Shrirame Hemant Y, Rathore NS, Sudhakar J, Kurchania AK (2010) Performance evaluation of a diesel engine fuelled with methyl ester of castor seed oil. Appl Therm Eng 30:245–249
9. Kumar AA (2007) Biofuels (alcohols and biodiesel) applications as fuels international combustion engines. J Energy Combust Sci 33:233–271
10. Ramanik PK (2003) Properties and use of jatropha curcas oil and diesel fuels blends in compression ignition engine. Int J Renew Energy 28:239–248
11. Agarwal D, Agarwal AK (2007) Performance and emission characteristics of jatropha oil preheated and blend in a direct injection compression ignition engine. Appl Therm Eng 27:2314–2323
12. Sahoo PK, Das LM (2009) Process optimization for biodiesel production from jatropha, karanja and polanga oils. Fuel 88:1588–1594
13. Kalam MA, Husunawan M, Masjuki H (2003) Exhaust emission and combustion evaluation of coconut oil-powered indirect injection diesel engine. Renew Energy 3:2405–2415
14. Jindhal S, Nandwana BP, Rathore NS, Manistha V (2009) Experimental investigation of the effect of compression ratio and injection pressure in a direct injection diesel engine running on jatropha methyl ester. Appl Therm Eng
15. Muralidhram K, Vasudevan D (2011) Performance emission and combustion characteristics of a variable compression ratio engine using ester of waste cooking oil and diesel blends. Appl Energy 88:3959–3968

RFID-Based Real-Time Monitoring System for Drill Bit Manufacturing Process

N. Ikram, M. Pravin Savaridass, S. Amuthabharathi, and R. Karthickkumar

Abstract Manufacturing industries undergo several process and techniques for making an end product. Each process is monitored and controlled by localized superior in that particular process. The communication between the processes is done manually; it leads to a lag of connectivity in data sharing between each process. This may cause human error and it incorporates to the lag of efficiency in manufacturing process. Manual tracking of each and every component in manufacturing industries is difficult and also highly unreliable. This paper introduces real-time RFID technology for tracking and monitoring each and every steps of process to improve the efficiency of the production throughout the process. This technology also simplifies the problem of tracking the component in every process. This RFID implementation makes the connection between the several processes in an industry to develop a finalized product. Further, this paper proposes an automated technology for indicating the defect in the product in every stage of the process. This RFID technology implements specifically for identifying the defects and efficiency lag in the drill bit manufacturing process. RFID technology plays a vital role in improving the process in logistics and manufacturing. The exact position and defects are supervised and located throughout its flow in the whole production process of an industry. RFID enables better monitoring of production processes with appropriate material flow.

Keyword RFID drill bit tracking process automation

N. Ikram (✉) · M. P. Savaridass · S. Amuthabharathi · R. Karthickkumar
Department of Electronics and Instrumentation Engineering, Bannari Amman Institute of Technology, Sathyamangalam, Tamil Nadu 638401, India
e-mail: ikram@bitsathy.ac.in

G. Kumaresan et al. (eds.), *Advances in Materials Research*, Springer Proceedings in Materials 5, https://doi.org/10.1007/978-981-15-8319-3_22

1 Introduction

1.1 RFID Observance System

RFID technology has strong identification and tracking facilities, so it is implemented in various applications. In every places, wherever there are different things accessed by several users, the tendency of losing the tracking information about the product is quite high, because of weakness in material observance. The aim of the analysis is to figure out a generic approach in tracking of product in manufacturing process. Typical approach of checking materials for each product is tough for manual tracking system. These ends up in a challenge for administrator to monitor the flow and process of the materials continually. To automate these method, Radio Frequency Identification (RFID) is a well known in concert of the foremost sensible and implementable in real-time in-line with process. In this paper, solution has been provided for the continuous monitoring encountered within the manufacturing process. So RFID-based observance system has been designed and developed to explore the material handling system of industrial product.

1.2 RFID Technique and RFID Tag

RFID known as Radio Frequency Identification is a technology where the data encoded in the RFID smart card are decoded by the RFID reader module to retrieve the data. RFID structures consist of three components: an RFID tag or smart label, an RFID reader, and an antenna. RFID tags incorporate an integrated circuit and an antenna, which are used to transmit information to the RFID reader. RFID tag will store the data and it can be scanned and read through RF reader module and it has a huge storage capability than the bar code technique. Two major components of RFID system are transponder and RFID reader. The product which is to be scanned have a transponder or RFID tag and the reader can be either just a read or a write device, depending upon the system design and the requirement. RFID reader contains a radio frequency module, configurable control unit, a display device, and an antenna. In added to that, a number of RFID readers are integrated with an extra interface allowing them to forward the data received to another system. Radio waves are converted to an accessible data by the reader. Information generated by the label is transmitted through the communication interface to the host computer system where data can be stored and analyzed in a database. RFID utilizes electromagnetic fields to naturally recognize and track labels appended to objects. The tags contain electronically stored information. Passive tags collect energy from a nearby RFID reader's interrogating radio waves. Active tags have a local power source (such as a battery) and may operate hundreds of meters from the RFID reader. Unlike a barcode, the tag need not be within the line of sight of the reader, so it may be embedded in the tracked object.

Table 1 Specification of RFID's

Frequency	Range	Different modules	Applications
125–150 kHz	5–20 cm	EM-18 and ILA-12	Factory data collections
13.56 MHz	10 cm–1 m	MFRC522 and SM 130	Smart cards

2 Materials and Methods

2.1 EM-18 RFID Card Reader Module

EM18 RFID is used for industrial applications with different range and frequencies. EM18 RFID reader which is used to read RFID tags of frequency in the range of 125 kHz. After reading tags, it transmits unique ID serially to the PC or microcontroller using UART communication or Wiegand format on respective pins.

EM18 RFID reader reads the data from RFID tags which contains 12 bytes stored ID. This reader does not require line-of-sight, also it has short identification range of few centimeters (Table 1).

2.2 Literature Survey

McFarlane and Sheffi [1] propose supply chain operation involved with automatic identification smart cards (RFID) and also show the challenges occurred in supply chain operations. Lu and Cheng [2] reviewed the fundamental issues, methodologies, applications, and potential of RFID-enabled manufacturing and a simulated RFID machining process and finally proposed a methodology, framework, and five-step deployment process aimed at developing a holistic approach to implement RFID-enabled manufacturing. Sarac et al. [3] surveyed the state-of the-art on RFID technology deployments in supply chains and analyzed the impact on the supply chain performance. da Costa and de Oliveira [4] show the study of Radio Frequency Identification (RFID) technology contribution to the optimization of production process. Wang et al. [5] proposed a RFID-based manufacturing process and a framework manufacturing process for a cloud MES system centered on machine tools constructed. In this, RFID configuration and cloud processing are analyzed.

2.3 Implementation of RFID System

Tracking of RFID attached to the raw material and components is done automatically and this RFID collects the material flow data from each process and updates it to the

superior controlling system periodically. These data are been stored for statistical analysis and future reference. The implementation of RFID in process station brings continuity and connection between each stage of the process in manufacturing [6]. The accurate and precised data are derived and rectified by implementing this RFID and the progress flow will be obtained during the manufacturing process itself. RFID makes the individual process to a combined process by establishing the connectivity with each process. Implementing RFID system requires EM18 RFID module which has an inbuilt integrated chip for process and an antenna for signal receiving and these are the RFID readers consist of hardware part which directly interact with RFID tags, RFID tags where the data are processed, stored and data are transmitted to the module by scanning the tags. Implementing of RFID technology in individual stage of manufacturing process involves analysis of raw material for particular process, tagging of raw materials, tracking the process materials, and reading of data in RFID tags. Some of the factors which will affect the RFID property like temperature, distance factor, etc., will be considered and take actions to overcome this problems before implementing the RFID tags with process materials [7]. The proper RFID tags will be chosen for process by considering the property of RFID and also the working or process environment. The first stage of implementing is the analysis of raw material; in this stage, the raw material used for the particular process is analyzed. The second stage is the tagging of RFID to the raw materials; here, the raw materials are undertaken to attach the RFID tags to it. While attaching the RFID tags, the data of each and every raw materials are noted and these data are stored electronically in the RFID tags. Tagging is done to each raw material individually. The data stored in the RFID are transmitted to the system before move on to the process. The next stage is tracking of process materials; in this stage, the tagged processing materials are tracked for the material status. The final stage of implementation of RFID is scanning; in this stage, the end materials from each process are scanned by using RFID module. While scanning, the material data are transmitted from RFID tag to the module and these data in module are transmitted to the superior system, and the status of the process is done and verified. 3.1 Work flow of RFID system (Fig. 1) [8].

When drill bit reaches the starting position of the process, it gets scanned and updated to the system. If drill bit not completing any stage of the process or else damaged, it is marked in the system which get updated to the central system. So that it could not reach further process of manufacturing. Skipping of the process is also identified by this RFID technique. Drill bit could not enter any further steps without completing the previous process. The status of each product can be monitored continuously anytime by the quality team. The loss of material can be easily identified by the team members of quality through this technology. If any of the stage is skipped during the process of manufacturing, it can be easily identified and also any of the product gets rejected or damaged in the manufacturing process, it can be tracked and undergoes corresponding remedial actions. When all the process is completed, the overall efficiency of manufacturing can be easily identified by the stored data which can be easily accessed through the system [9].

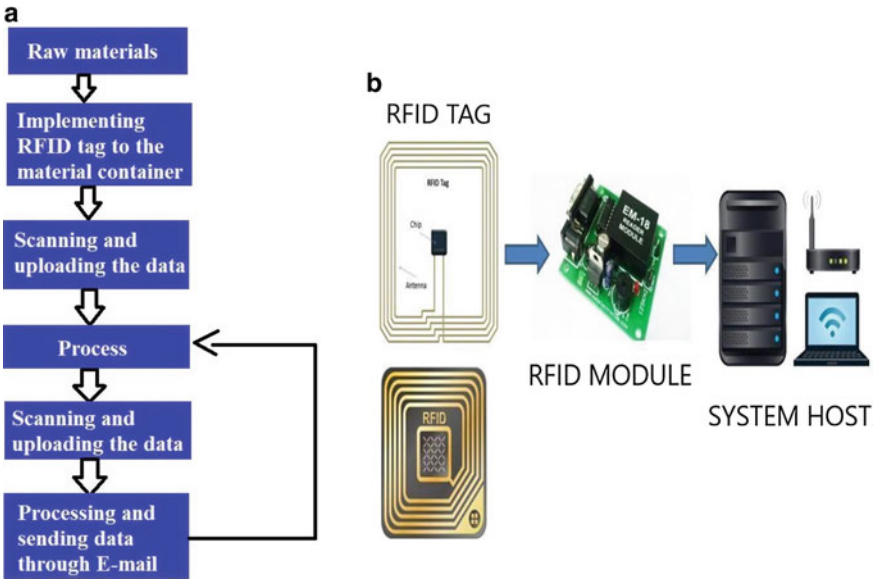

Fig. 1 **a** RFID system work flow. **b** Implementation of RFID system

3 Results and Discussions

In this paper, Arduino software and Python programming are implemented for the proposed technique. By using the RFID reader module, data are updated to the server. The data are continuously transferred to the authorized persons through e-mail. The defective products can be easily updated to the system through authorized persons [10]. The status of the products can be easily verified through system. This technique will improve the efficiency of the manufacturing process. The output of the process will be displayed in the monitor. The comparison analysis of drill bit manufacturing process by manual system and RFID implemented automated system is showed in Tables 2 and 3. The overall analysis shows the RFID implemented system causes

Table 2 Analysis of batch process for drill bit manufacturing for a day by manual process

Shift batch	Number of product of scanned	Number of products undergoes all process	Number of products missing the process	Number of defected products	Number of products undergoes remedial action
Shift 1	100	93	4	3	2
Shift 2	100	91	5	4	4
Shift 3	100	93	3	4	3

Table 3 Analysis of batch process for drill bit manufacturing for a day using RFID

Shift batch	Number of product scanned	Number of products undergoes all process	N missing the process	Defected products	Number of products undergoes remedial action
Shift 1	100	92	6	2	8
Shift 2	100	91	4	5	9
Shift 3	100	93	3	4	7

more efficiency in the manufacturing process by identifying all the missed-out and defected products and finally undergoes the remedial actions [11].

4 Conclusions

A real-time observance system for an industry has been successfully developed using RFID system. The RFID technique provides more advantages over standard method of observance. The proposed method provides several advantages over conventional method of monitoring the process in an industry. The proposed system is portable and compact. The result can be viewed through the e-mail to the particular authorities from the system automatically. The finalized results are displayed in the screen. The future scope of this process is to fetch the scanned data of the objects in industrial process and transmitted to the cloud storage management. This cloud storage management simplifies the whole process storage. The real-time monitor will be updated by developing a backend database. Another main challenge in this RFID monitoring system is that it cannot withstand in all the industrial environment. The future work will be that this problem will be rectified with an optimal solution [12]. Furthermore, the sensors implementation and automate the device in order to develop a smart manufacturing unit.

References

1. McFarlane D, Sheffi Y (2003) The impact of automatic identification on supply chain operations. MCB UP Ltd 14(1):1–17
2. Lu B, Cheng K (2005) A framework for RFID based manufacturing system. In: ICAM international conference on agility (1), pp 73–92
3. Sarac A, Absi N, Dauzere-Peres S (2010) A literature review on the impact of RFID technologies on supply chain management. Int J Prod Econ 1:77–95
4. da Costa C, de Oliveira LR (2015) RFID applications to the optimization of discrete manufacturing process. Res Gate Publ 5:8–12
5. Wang C, Chen X, Soliman A-HA, Zhu Z (2018) RFID based manufacturing process of cloud MES. Future Internet Publ 104(2):6–11

6. Kwon K-B, Song C-H, Park J-Y, Oh J-Y, Lee J-W, Jung WC (2014) Evaluation of drilling efficiency by percussion testing of a drill bit with new button arrangement. Int J Publ 1:1–3
7. Lee WB, Cheung BCF, Kwok SK (2009) Springer hand book of automation, vol 49(1), pp 867–877. Verlag, Berlin Heidelberg
8. Brewer A, Sloan N, Landers T (1999) Intelligent tracking in manufacturing. J Intell Manuf 10(3–4):245–255
9. Huang GQ, Zhang YF, Jiang PY (2008) RFID-based wireless manufacturing for real-time management of job shop WIP inventories. Int J Adv Manuf Technol 36:752–764
10. Curtin J, Kauffman RJ, Riggins FJ (2007) Making the most out of RFID technology: a research agenda for the study of the adoption, usage, and impact of RFID. Inf Technol Manag 8(2):87–110
11. Saksala (2011) Numerical modelling of bit-rock fracture mechanisms in percussive drilling with a continuum approach. Int J Numer Anal Methods Geomech 35:1483–1505
12. Zhang D, Huang H, Jo M (2005) Future RFID technology and applications: visions and challenge. Telecommun Syst 58(3):193–194

Efficient Data-Secured Cryptography Using FRQI Algorithm

A. Shyamalaprasanna, B. Ragavi, S. Saranya, L. Pavithra, and P. Santhya

Abstract The Web clients are consistently expanding step by step. After the starting of the 4G or IMT—Advanced administrations, correspondence over Web expanded definitely. Individuals over every one of the networks like social, monetary, business, money related, and so forth are doing correspondence or trading their esteemed reports over Web. The interest for verifying the information in productive manner has been expanded. As cryptography is the most ideal approach to verify the correspondence. In FRQI, the compression ratio of quantum images is more efficient and achieves quadratic speed in quantum images. Here, BB84 protocol convention is used to execute QKD. It manages the harmonization states that want to transmit the media transmission information with elevated level of security utilizing a glass or optical fiber.

Keywords Quantum cryptography · Qubits · Image compression · FRQI · QKD protocol

1 Introduction

Securing the data content in advanced image basic today for differing purposes, from military to medicinal services frameworks. Propelled encryption procedures such as protected transmission, recovered quantum pictures are progressively required for an assortment of picture preparing applications, particularly for restorative pictures. The encrypt of sender or client data before its transference over a correspondence channel or Internet of thing system is significant tolerant classification.

A. Shyamalaprasanna (✉)
Department of Electronics and Communication Engineering, Faculty of ECE, Bannari Amman Institute of Technology, Sathyamangalam, Erode, India
e-mail: shyamalaprasanna@bitsathy.ac.in

B. Ragavi · S. Saranya · L. Pavithra · P. Santhya
Department of Electronics and Communication Engineering, Bannari Amman Institute of Technology, Sathyamangalam, Erode, India
e-mail: ragavi.co19@bitsathy.ac.in

G. Kumaresan et al. (eds.), *Advances in Materials Research*, Springer Proceedings in Materials 5, https://doi.org/10.1007/978-981-15-8319-3_23

Quantum mechanics lead to the formation of qubit information, calculation, and later quantum PCs take care of issue that cannot be proficiently understood in customary computers. Various quantum picture portrayal models have been proposed to use quantum mechanics to heap and proceeding picture data. For example, Qubit, Entangled Image, Real Ket, and adaptable portrayal of quantum pictures (FRQI) Some straightforward picture handling calculations have been created [1]. FRQI is the most recent portrayal among the current trends. FRQI utilize standardized emplacement to reserve every one of the pixels in a picture, the equivalent activities execute the same time on all pixels, and hence FRQI can clarify the ongoing calculation issue of picture handling applications. Nonetheless, since FRQI utilizes just a solitary quantum bit to store dim scale data to every pixel in a picture, some computerized picture preparing tasks, for instance certain complex shading activities, is impossible based on FRQI. In this proposed model, FRQI can improve an quantum port for advanced pictures. The modernized utilized the premise condition of a quantum bit succession to reserve the dark scale estimation of each picture element.

Along these lines, to store the computerized picture utilizing quantum mechanics, two snared quantum bit successions are utilized in NEQR to reserve the entire picture, which speak to the dark scale and locational data of the considerable number of picture element [2]. Specialists have built up a great deal of cryptographic calculations; however, most calculations are proposed to scramble messages in content structure.

Propelled calculation for cryptography which is absolutely reliant on hashing capacity method to produce a mystery key which is additionally used to encode and unscramble the significant data. QKD gives a special method for sharing irregular arrangement of bits between clients with a degree of security not achievable with any other old style cryptographic strategies [3].

In this paper, a protocol called BB84 is utilized to execute. QKD that manages the photon polarization states is used to transmit the media transmission data with elevated level of security utilizing optical fiber. QKD gives a special method for sharing irregular arrangement of bits between clients a degree of security not achievable in old style cryptanalysis [4]. In the reserved computerized picture utilizing quantum mechanics, two caught quantum bit groupings are utilized in FEQR to store the entire picture, which speak to the dark scale and positional data of the considerable number of pixels.

2 Illustration of FRQI

Through investigations and correlations with FRQI, the accompanying focal points of FRQI have been illustrated:

The time complexity of setting up the NEQR quantum picture shows a roughly quadratic diminishing contrasted with FRQI.

For picture pressure dependent on minimization of Boolean articulations, the pressure proportion of NEQR can be expanded to 1.5X that of FRQI.

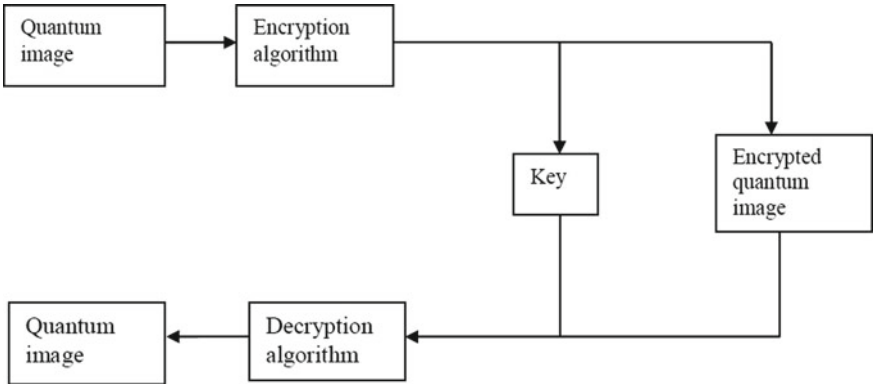

Fig. 1 Basic encryption and decryption

Through quantum estimations, the first old style picture can be recovered precisely from the NEQR quantum picture, not feasibility as with FRQI.

More picture activities can be accomplished helpfully dependent on NEQR than FRQI. For example, incomplete shading activities what is more, factual shading activities which are depicted (Fig. 1).

In light of these points of interest, the recently proposed model for quantum picture handling is progressively adaptable and more qualified crucial model than all other existing quantum picture portrayals.

2.1 Approach of QKD

Quantum mechanical impacts can be utilized to move data from sender to receiver and any endeavored by hacker will consistently be perceptible.

Related Work

This quantum picture portrayal model can be communicated for a $2n \times 2n$ picture [5]. In FRQI, the position data of each pixel is put away in a premise condition of a two-dimensional quantum bit arrangement, and the dark scale information reserved as the likelihood adequacy of a solitary qubit which is caught with the quantum bit arrangement.

Numerous examinations on quantum picture handling have been done dependent on FRQI examined basic geometric and shading activities dependent on FRQI and demonstrated the extraordinary execution development of these quantum tasks contrasted and traditional picture tasks extended FRQI utilizing three shading qubits to reserve the full-shading data of a RGBα picture structured quantum watermarking calculations in view of FRQI [6], acquiring great execution.

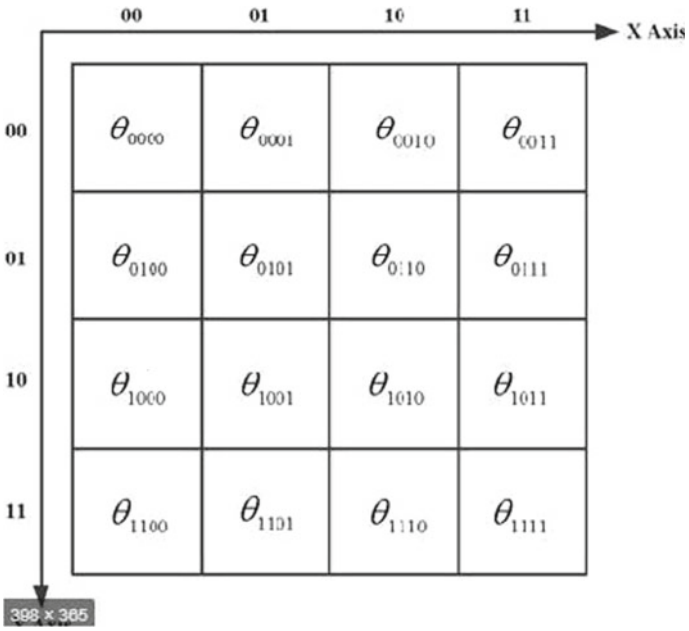

Fig. 2 FRQI qubit image

All in all, all past examinations based on FRQI have concentrated on certain basic activities and calculations in advanced picture preparing. The primary explanation behind this is the FRQI model has a few downsides (Fig. 2).

The time multifaceted nature of quantum picture arrangement for FRQI is excessively high. To disentangle planning of a FRQI quantum picture, the Boolean articulation reduction strategy is utilized to execute picture pressure [7]. In any case, it has been discovered that the FRQI pressure proportion relies upon the dim scale distribution of the computerized picture; particularly, when the picture is exceptionally scattered, the FRQI pressure proportion is low, in any event, moving toward zero. Since FRQI reserves the dark scale data of the picture element as the likelihood Plentifulness of a solitary quantum bit, it is difficult to get precise likelihood plentifulness for this qubit through limited quantum estimations [8]. At the end of the day, exact picture recovery is a unimaginable assignment for the Flexible Representation Of Quantum Image model. FRQI reserve the computerized picture into the protector of a qubit arrangement concurring to the position data of various pixels [9]. Subsequently, all activities which are appropriate for FRQI ought to play out similar tasks for pixels at various positions. Different tasks cannot be obliged. These drawbacks of FRQI have moved toward becoming restrictions on the investigation of complex quantum picture preparing calculations.

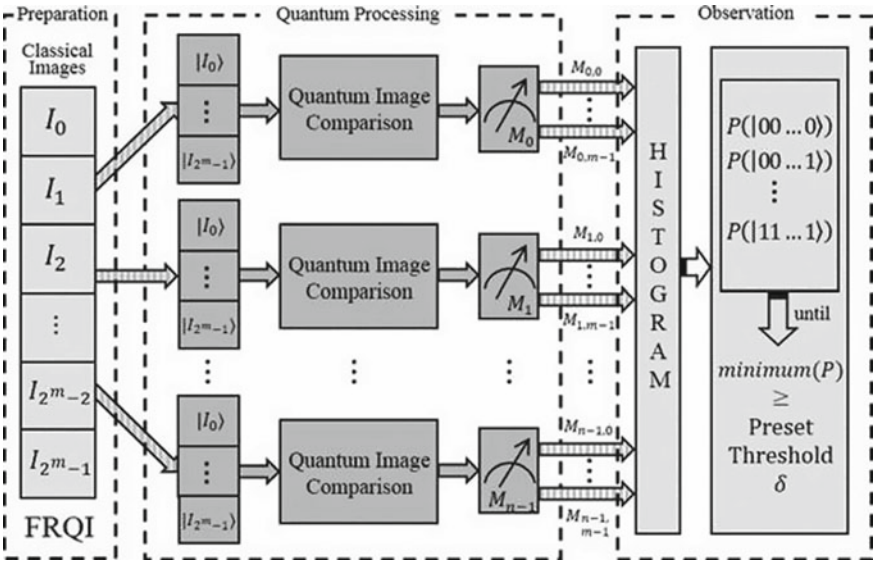

Fig. 3 Representative expression of FRQI

3 Representation, Compression, and Preparation of Quantum Images

3.1 FRQI

Through investigation of the FRQI quantum picture model, it is realized that the upsides of FRQI come about because of utilizing the protector of a quantum bit succession to reserve the locational data of the considerable number of picture elements, so all can be worked on all the while. In any case, the primary explanation behind the disadvantages of this model is that FRQI utilizes just a solitary qubit to store the dark scale data for every pixel [10]. To improve Flexible Representation of Quantum Image, uses two snared quantum bit arrangements to store the dim scale and position data, and stores the entire picture in the protector of the two qubit arrangements (Fig. 3).

3.2 Quantum Picture Planning

To take advantages of quantum mechanics to process a picture, the picture data should initially be put away in a quantum state [11]. The arrangement method for FRQI will currently be depicted. From the portrayal of FRQI, $q + 2n$ qubits are expected to develop the quantum picture for a $2n \times 2n$ picture with dark range $2q$ (Fig. 4).

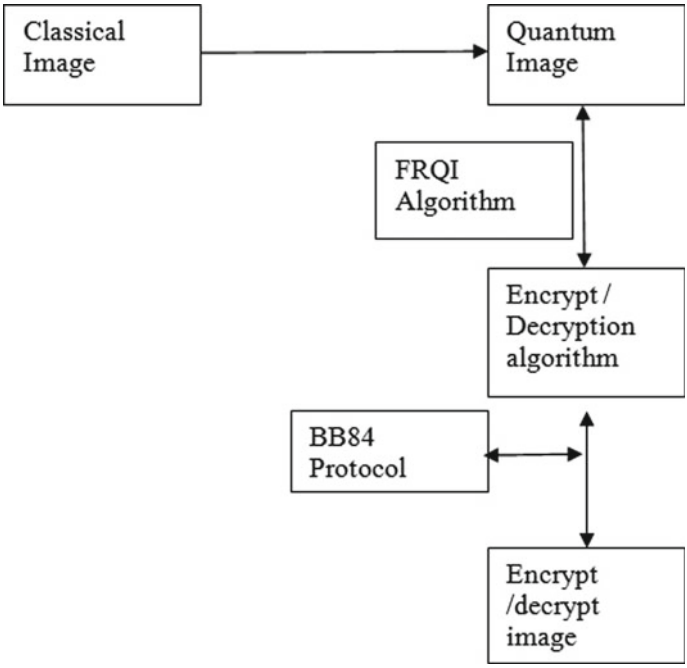

Fig. 4 Block diagram of encryption and decryption of FRQI

The classical images are first converted into quantum images, and by using an FRQI algorithm, we encrypt the data by transmitting form sender to receiver. The image can be encrypted by high secured-level decrypting method; the BB84 protocol can be decrypted by getting a original image [12].

4 Compression Ratio

$$\text{Compression Ratio} = \frac{1}{\text{Compression/Before Compression}} * 100$$

4.1 Framework Implementation

The secured image can be converted into a quantum image by implementing a algorithm called FRQI algorithm [13]. Figure 5 shows the quantum image can be encrypted by using a same algorithm with the implementation of BB84 protocol to transfer an efficient secured data.

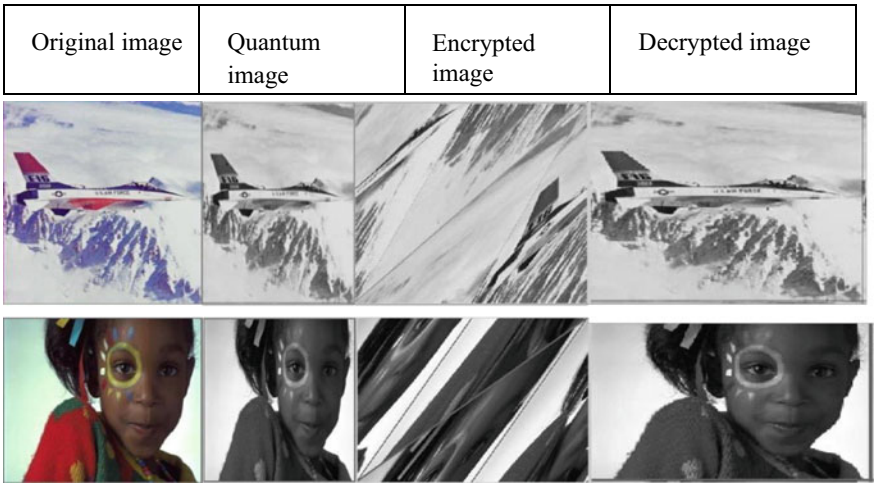

Fig. 5 Experimental result

Read the image file.
Convert the image into gray scale image.
Identify each pixels and position of the image.
Convert it into quantum image using FEQR algorithm.
Read the color pixel RGB.
The encrypted imaged position is to be calculated by position of X, Y.
RGB pixels to the image to be random and cannot be recognized.

The distinction between the first picture and the encoded picture is contrasted and found with be of in significant distinction with no picture data. The entropy of the quantum and unique picture is contrasted and found with be equivalent [14]. Entropy of a picture is the proportion of picture data content, which is deciphered as the normal vulnerability of data source.

5 Simulation Result

In image, entropy is defined as corresponding states of intensity level which individual pixels can adapt. Table 1 represents the entropy comparison of the original image and quantum image. These values are compared to be more or less equal.

Table 1 Entrophy comparison of original and quantum image

Original image	Quantum image
7.770	7.675
7.883	7.762

To break down the existing methodologies, a PC with 6 GB RAM and Intel center CPU furnished with MATLAB R2014a is used to perform quantum activities on quantum pictures [15]. Demonstrates the reenactment after effect of the picture changed over into quantum picture and the encoded picture utilizing FRQI calculation too the picture is unscrambled by utilizing a BB84 convention to get the first picture to transfer an information with unqualified security. Picture of various size is taken as the info picture and the accompanying reenactment results are examined as beneath.

6 Conclusion

A highly secure quantum image cryptography approach is shown in this work. FRQI algorithm is good enough to secure a digital image, especially in the security pixel mostly algorithm cryptography secures files or specific to text, with other algorithms, FRQI map could safeguard the image of a well without reducing the value or information of a digital image and by decrypting a data with highly secured BB84 protocol to transfer a data with unconditional security.

References

1. Shankar K, Eswaran P (2016) A new k out of n secret image sharing scheme in visual cryptography. In: 2016 10th international conference on intelligent systems and control (ISCO). IEEE
2. Sklavos N, Zhang X (2007) Wireless security and cryptography: specifications and implementations
3. Martinez-Mateo J, Ciurana A, Martin V (2014) Quantum key distribution based on selective post-processing in passive optical networks. IEEE Photonics Technol Lett 26(9)
4. Le PQ, Iliyasu AM, Dong F, Hirota K (2011) Strategies for designing geometric transformations on quantum images. Theor Comput Sci 412:1406–1418
5. Comandar LC, Lucamarini M, Fröhlich B, Dynes JF, Sharpe AW, Tam SW-B, Yuan ZL, Penty RV, Shields AJ (2016) Quantum key distribution without detector vulnerabilities using optically seeded lasers. Nat Photonics 10:312
6. Coles PJ, Metodiev EM, Lütkenhaus N (2016) Numerical approach for unstructured quantum key distribution. Nat Commun 7:11712
7. Lydersen L, Makarov V, Sokar J (2011) Secure gated detection scheme for quantum cryptography. Phys Rev A 83:032306
8. Mitanni M, Curty CCW, Lim NI, Tamaki K (2015) Finite-key security analysis of quantum key distribution with imperfect light sources. New J Phys 17:093011
9. Scarani V, Acín A, Ribordy G, Gisin N (2004) Quantum cryptography protocols robust against photon number splitting attacks for weak laser pulse implementations. Phys Rev Lett 92:057901
10. Kurochkin VL, Neizvestny IG (2009) Quantum cryptography. In: 10th international conference and seminar EDM'2009, Section III, 1–6 July, Erlagol
11. Gonzalez RC, Woods RE, Eddins SL (2002) Digital image processing. Publishing House of Electronics Industry, Beijing
12. Venegas-Andraca SE, Bose S (2003) Storing, processing and retrieving an image using quantum mechanics. In: Proceeding of the SPIE conference quantum information and computation, pp 137–147

13. Fu X, Ding M (2009) A new quantum edge detection algorithm for medical images. In: Proceeding of medical imaging, parallel processing of images and optimization techniques. SPIE, vol 7497
14. Iliyasu AM, Le PQ, Dong F, Hirota K (2012) Watermarking and authentication of quantum images based on restricted geometric transformations. Inform Sci 186:126–149
15. Durr C, Hoyer P (1996) A quantum algorithm for finding the minimum. arXiv:quant-ph/9607014

Studies on Influence of Reinforcement Characteristics on Mechanical Properties of Banana Fiber Nonwoven Composite Structures

T. Murugan and B. Senthil Kumar

Abstract The influence of banana fiber length, fiber volume fraction, alkali concentration during surface treatment on mechanical properties such as tensile strength and flexural strength of the composite materials. Eighteen different composite samples were produced by changing the fiber length (such as 4, 6, and 8 cm), fiber volume fraction (30%, 40%, and 50%), contraction of alkali while giving surface treatment on the fiber (such as 3%, 5%, and 7%), and fiber alignment (such as machine direction and cross direction) through needle punched nonwoven batt. As per the ASTM standard, tensile and flexural studies were carried out for all the samples using Instron tester. The following results were found such as the composite made up of 50% fiber volume fraction and 5% alkali treatment shown highest tensile and flexural strengths. In the case of fiber length is concerned, 6 cm length-based nonwoven reinforcement yields highest mechanical properties and cross direction reinforcement is shown higher mechanical strength than machine direction reinforcement laying.

Keywords Banana fiber · Composites · Hand lay-up · Epoxy · Mechanical property

1 Introduction

Recent days, the use of natural fiber-reinforced polymer composites was getting higher attention due to ecological aspects [1]. The natural fibers are low density, good thermal and acoustic properties, low cost and environmentally friendly production and disposal system are the attractive features of natural fiber reinforcement [2].

T. Murugan (✉)
Department of Fashion Technology, National Institute of Fashion Technology (NIFT), Chennai, India
e-mail: murugan.thangaraj@nift.ac.in

B. S. Kumar
Department of Rural Industries and Management, Gandhigram Rural Institute–Deemed University, Gandhigram, Dindigul, India
e-mail: Senthil.b1980@gmail.com

G. Kumaresan et al. (eds.), *Advances in Materials Research*, Springer Proceedings in Materials 5, https://doi.org/10.1007/978-981-15-8319-3_24

Presently, most of the green fibers such as jute, flax, kenaf, and coconut fibers have been considered as reinforcement along with thermoplastic and thermoset matrices due to abundant availability [3]. The mechanical properties of any polymer composites have been depending upon various matrix parameters as well as reinforcement parameters and fiber matrix interaction and hybridization is one such important properties. Many research works have been undertaken to investigate the effect of surface treatment of banana fiber on reinforced with thermoplastic and thermosetting polymer [4, 5]. According to Merlini et al., the surface treatment improved the fiber matrix interfacial shear stress and overall mechanical strength of the composites [6]. Prasanna and Subbaiah fabricated surface-modified banana fiber reinforced with polyurethane matrix and found that 20% surface-treated fiber holds higher tensile strength than 10% surface treatment reinforcement [7]. Shankar et al. reported that fiber volume fraction has significantly affected the mechanical properties of the composite. There is a 5% increase from the optimum level of jute fiber-reinforced composite, the overall decrease in tensile strength was 15–20%, and reduction in flexural strength was 5–10% [8]. Sumaila et al. have developed the random fiber composite using banana chopped fibers with different fiber lengths with epoxy resin and found that the composites having 15 cm length have shown highest tensile strength among the other ranges but the flexural strength of the composite was shown increasing mode up to 25 mm fiber lengths [9]. Laban et al. have studied the influence of fiber length on mechanical properties of the composite materials and found that the tensile strength was highest with 30 mm fiber length reinforcement composites whereas the impact strength was highest with 40 mm length reinforcement composites [10]. To study aim to analyze the effect of fiber length, fiber volume fraction, alkali treatment, and fiber alignment on mechanical properties such as tensile and flexural strength of the composite materials.

Recent days, natural fibers are considered as important reinforcement for composite making due to the environmental concern as a replacement for synthetic fibers [11]. The fibers such as jute, flax, banana fiber, kenaf, ramie, and bagasse are popularly used for natural fiber-reinforced composite production due to its low density, good in mechanical properties, recyclable, and higher length-to-strength ratio [12, 13]. Further to this, the natural fibers are sustainable, renewable, and eco friendly in nature. These types of green composites were largely used in automobile and construction industries [14]. Some of the natural fibers are formed as agriculture wastages and creates environmental pollution, if it is not reused. One such waste fibrous material is known as banana fiber [14]. Banana fiber has hard fibrous part called rind and soft non-fibrous part called pith and consists of 45–55% of cellulosic material, 20–25% hemicelluloses, and 18–24% lignin [15].

Table 1 Physical properties of banana/palm fiber

Types of fiber	Avg. linear density (g/cc)	Avg. tensile strength (MPa)	Avg. modulus (GPa)	Avg. breaking extension (%)
Banana fiber	1.3	310	42	1.20
Palm fiber	0.7–1.55	400–500	47	4

2 Experimental Details

2.1 Materials

Banana fiber has been extracted from dried stem of the banana tree. The extraction process was done at the Laboratory of Department of Rural Industries and Management, The Gandhigram DU. Then, the fibers were dried in the room temperature for about 30 h. The fibers were cut into 4, 6, and 8 cm lengths, washed with distilled water and oven-dried for obtaining a constant weight. The physical properties of the extracted fibers were measured and shown as in Table 1.

2.2 Experimental Design

This study was conducted in two different phase.

Phase-1: During the first phase of analysis, six composite samples were produced using banana fibers by changing the fiber volume fraction (three levels such as 30%, 40%, and 50%) and alkali concentration to improve the surface roughness of the reinforcement (three levels such as 3%, 5%, and 7%). Then, the tensile and flexural studies were undertaken to measure the influence of alkali concentration and fiber volume fraction on banana fiber-reinforced composite.

Phase-II: During the second phase of analysis, six composite samples were produced using banana fibers by changing the fiber volume fraction (three levels such as 35%, 40%, and 45%) and fiber length concentration to improve the strain propagation of the composite (three levels such as 4 cm, 6 cm, and 8 cm). Then, the tensile and flexural studies were undertaken to measure the influence of fiber length and fiber volume fraction on banana fiber-reinforced composite.

2.3 Alkali Treatment for Surface Modification

A portion of cut banana fibers was then treated with NaOH in three different such as 3%, 5%, and 7% W/W of solution at ambient temperature (30 ± 2 °C) for 30 min duration and the material liquor ratio was 1:50 (w/v). Subsequently, treated fibers

Table 2 Physical properties of alkali-treated banana fiber

Types of fiber	Avg. linear density (tex)	Avg. tensile strength (MPa)	Avg. modulus (GPa)	Avg. breaking extension (%)
Untreated	2.74	310	42	1.20
3% alkali treated	2.68	350	44	1.34
5% alkali treated	2.61	420	48	1.42
7% alkali treated	2.34	380	36	1.36

were then neutralized with 5 wt.% acetic acid solution and subsequently, washed with distilled then the fibers were air-dried at room temperature for 24 h and then oven-dried to obtain a constant weight. The fiber properties of the alkali treated and untreated banana fiber are tabulated as in Table 2.

2.4 Needle Punching Process

All the reinforcement samples with different combination as per the phase-1 and phase-II study were presented in to the mouding section in the form of needle punched non-woven batt. This needle punched samples were executed through technical textile laboratory at Avinashilingam Deemed University.

In phase-I study, Nine different types of needle punched nonwoven batt were prepared by changing the fiber volume fraction such as 30%, 40%, and 50% and alkali concentration such as 3%, 5%, and 7% alkali concentration. These fibers were opened and carded and subsequently, passed through a cross-lapper to form cross-laid webs and parallel–lapper for parallel laid batt. Both the type of batts were then made to pass through the needle punching process to prepare the nonwovens of nominal mass per unit area of 400 g/m^2. The process parameters (punch density of 150 cm^{-2}, depth of needle penetration of 12 mm) were kept constant during the fabrication of nonwoven samples.

In phase-I study, nine different types of needle punched nonwoven batt were prepared by changing the fiber volume fraction such as 35%, 40%, and 45% and fiber length such as 4 cm, 6 cm, and 8 cm. These fibers were opened and carded and subsequently passed through a cross-lapper to form cross-laid webs then taken for needle punching machine to produce the nonwoven batt.

2.5 Mold Size

A wooden mold was fabricated with the dimension of 15 cm × 15 cm × 2 cm and it is utilized for composite preparation. During the composite preparation, aluminum

foil was also used as a base material to protect the resin leakages during molding process.

2.6 Composite Fabrication

As per the sample plan in phase-I and phase-II, the molding process was executed separately. The composite prepared from the banana fiber nonwoven structure is as follows. The mold of 200 mm × 200 mm × 10 mm. It was interlined with aluminum foil to avoid the resin leakages. Then, the epoxy resin was poured stage by stage into the mold. The nonwoven batt was laid into the mold in alternative layers with resin. Once the process is completed, then, the mold unit is transferred to the compression molding machine. There are about 30 bar pressure was given to the mold by the machine. After that, composite samples were removed and the specimens were cut for various mechanical tests.

3 Characterization

3.1 Mechanical Testing

The tensile and flexural strength of the composite samples were carried out using Instron Universal testing machine (Zwick Roell-Z010 Universal Testing machine) based on ASTM D3039M and ASTM D790, respectively. Specimen dimensions used for the tensile and three-point bending tests were 150 × 25 × 10 mm and 75 × 15 × 10 mm, respectively. A cross-head speed of 2 mm/min was used in the tensile tests whereas the bending tests were performed at a speed of 2.8 mm/min. It should be noted that the edges of composite samples were smoothened by sandpaper in order to avoid stress concentration during the tensile and bending tests.

4 Results and Discussions

4.1 Analysis of Alkali Concentration on Composite Properties

4.1.1 Mechanical Properties of Banana Fiber Composite with MM Fiber Alignment

The composites were prepared with aligning the needle punched nonwoven in the machine direction (MM) with changes in fiber volume fraction and surface treatment concentration with alkali. The mechanical properties of those composites were reported as Table 3.

In the case of MM-aligned banana fiber composite with different alkali concentration, the alkali pretreatment has influenced the tensile strength and flexural strength of the composite. The composite made up of 50% fiber volume fraction and 5% alkali treatment shown highest tensile and flexural strengths. This is due to optimum fiber content has increased the tensile strength of the composite and the pretreatment with alkali has increased the bond strength of resin–matrix interface (Fig. 1).

4.1.2 Mechanical Properties of Banana Fiber Composite with MX Fiber Alignment

The composites were prepared with laying reinforcement in both machine and cross direction alternatively, which is technically called as anisotropic composite structure and its tensile strength and flexural properties were studied and it is tabulated as in Table 4.

In the case of MX-aligned composite, the alkali pretreatment has also influenced the tensile strength and flexural strength of the composite. The composite sample produced with 5% alkali concentration and 50% fiber volume fraction showed maximum tensile strength and flexural strengths.

4.2 Analysis of Fiber Length on Composite Properties

In the phase-II study, the fiber length of the banana fiber has been changed while fabrication the composite materials and analyzed its influence on mechanical properties of the composite. The nonwoven batt was prepared using 4 cm, 6 cm, and 8 cm lengths fibers separately with three different fiber volume ratio such as 35%, 40%, and 45% and its tensile strength and flexural strength were measured and it is tabulated as in Table 5.

In this case of fiber length, fiber volume fraction and blend proportion of banana and palm have influenced the tensile strength of the composite. In the case of 40% fiber volume fraction and 6 cm fiber length yield higher tensile strength of 42 MPa

Table 3 Mechanical properties of banana fiber composite with MM fiber alignment

Fiber volume fraction (%)	Alkali concentration					
	Tensile strength (3% alkali concentration) (MPa)	Flexural strength (3% alkali concentration) (MPa)	Tensile strength (5% alkali concentration) (MPa)	Flexural strength (5% alkali concentration) (MPa)	Tensile strength (7% alkali concentration) (MPa)	Flexural strength (7% alkali concentration) (MPa)
30	18	22.8	19.5	24.5	21	26
40	20.2	26.3	25.5	29.3	22.4	27.6
50	23.5	27.6	32.4	37.4	31.2	31.2

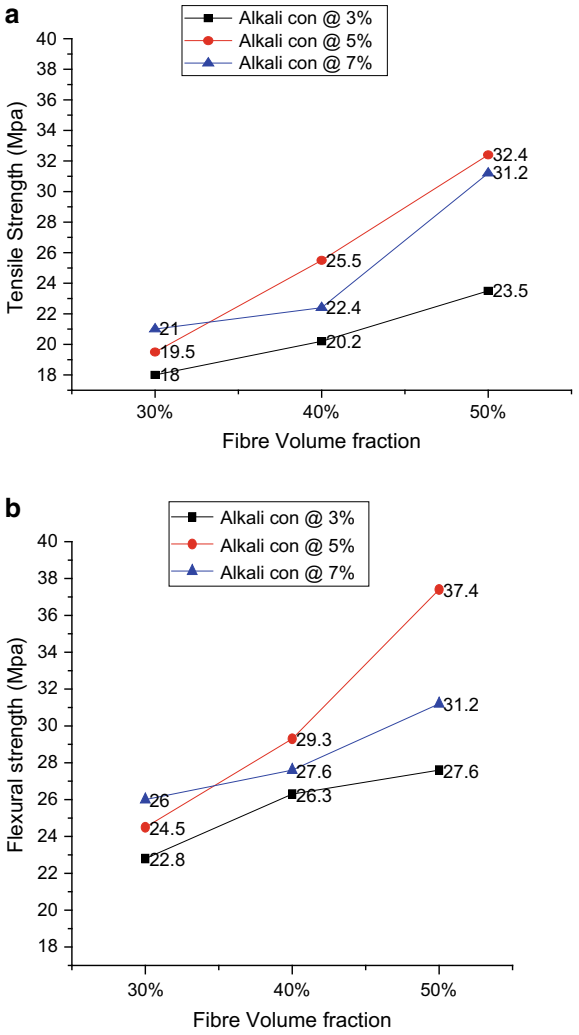

Fig. 1 **a** Tensile strength of banana fiber composite with MM fiber alignment. **b** Flexural strength of banana fiber composite with MM fiber alignment

and flexural strength of 44.7 MPa. When the fiber volume fraction increases, the tensile strength of the composite was also increased up to certain level more than 40% the fiber matrix wetting property was affected, which leads to reduction in tensile strength. Similarly when the fiber length of the reinforcement increases, which increases the tensile strength of the composite but more than 6 cm, the fiber extend was getting minimized due to curly nature of textile fiber, which leads to strength reduction (Figs. 2 and 3).

Table 4 Mechanical properties of banana fiber composite with MX fiber alignment

Fiber volume fraction (%)	Alkali concentration for surface treatment					
	Tensile strength (3% alkali concentration) (MPa)	Flexural strength (3% alkali concentration) (MPa)	Tensile strength (5% alkali concentration) (MPa)	Flexural strength (5% alkali concentration) (MPa)	Tensile strength (7% alkali concentration) (MPa)	Flexural strength (7% alkali concentration) (MPa)
30	20	26	23	29.4	21	26
40	22	28.2	27	33.4	24	30.3
50	28	36.3	35	41.3	32	39.2

Table 5 Mechanical properties of banana fiber composite with different fiber length

Fiber volume fraction (%)	Fiber length variation					
	Tensile strength (4 cm fiber length) (MPa)	Flexural strength (4 cm fiber length) (MPa)	Tensile strength (6 cm fiber length) (MPa)	Flexural strength (6 cm fiber length) (MPa)	Tensile strength (8 cm fiber length) (MPa)	Flexural strength (8 cm fiber length) (MPa)
35	34	35.4	36	38.4	34	36.2
40	36	38.4	42	44.7	38	40.3
45	34	36.4	39	40.9	35	38.8

5 Conclusion

Banana fiber-reinforced polymer composites were produced in two-phase of research work. In phase-I, samples were produced with changes in fiber volume fraction, fiber alignments such as machine direction and cross direction and alkali concentration. It is found that the samples produced through cross direction have shown higher performance than machine direction alignment specimen. It specifically found that around 7–10% of improvement was found between the cross-direction fiber alignment samples to machine directional fiber alignment. Fiber volume fraction has direct effect on mechanical properties of the composite. In all the cases, around 50–55% improvement was found from 30% fiber volume fraction to 50% fiber volume fraction. In the same line, alkali concentration also significantly influenced the mechanical properties of the composite. In this research, it is found that 5% alkali concentration yield higher performance than 3% alkali concentration and 7% alkali concentration. It is found that in all the samples, around 40–45% improvement was identified from 3% alkali concentration. In phase-II, research work, composite samples were produced with changes in banana fiber length. It is found that 6 cm length of fiber shown highest performance than 4 cm fiber and 8 cm fibers. The variations were found around 2–5%.

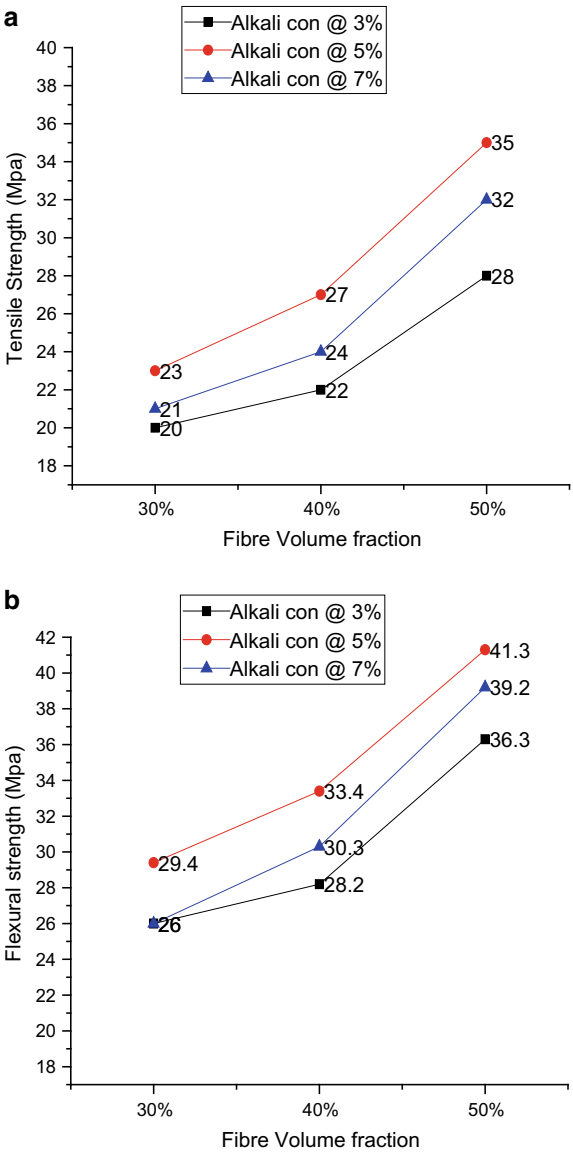

Fig. 2 **a** Tensile strength of banana fiber composite with MX fiber alignment. **b** Flexural strength of banana fiber composite with MX fiber alignment

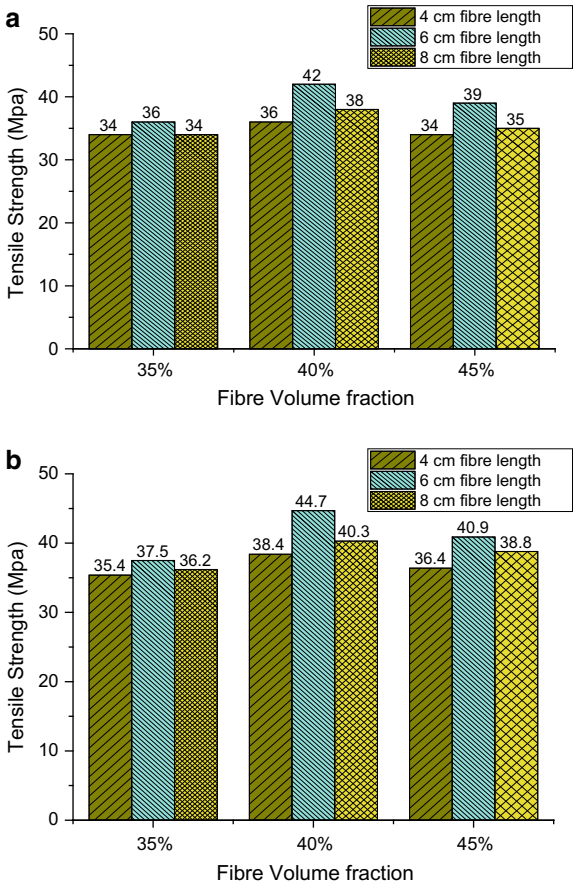

Fig. 3 **a** Tensile strength of banana fiber composite with the change in fiber length. **b** Flexural strength of banana fiber composite with the change in fiber length

References

1. Bos HL, Molenveld K, Teunissen W, Van Wingerde AM, Van Delft DRV (2004) Compressive behaviour of unidirectional flax fiber reinforced composites. J Mater Sci
2. Placet V (2009) Characterization of the thermo-mechanical behaviour of hemp fibers intended for the manufacturing of high performance composites. Compos Part A Appl Sci Manuf
3. Munikenche Gowda T, Naidu ACB, Chhaya R (1999) Some mechanical properties of untreated jute fabric-reinforced polyester composites. Compos Part A Appl Sci Manuf 30(3):277–284
4. Venkateshwaran N, Elaya Perumal A, Alavudeen A, Thiruchitrambalam M (2011) Mechanical and water absorption behaviour of banana/sisal reinforced hybrid composites. Mater Des
5. Udaya Kiran C, Ramachandra Reddy G, Dabade BM, Rajesham S (2007) Tensile properties of sun hemp, banana and sisal fiber reinforced polyester composites. J Reinf Plast Compos
6. Merlini C, Soldi V, Barra GMO (2011) Influence of fiber surface treatment and length on physico-chemical properties of short random banana fiber-reinforced castor oil polyurethane composites. Polym Test 30:833–840
7. Prasanna GV, Subbaiah K (2013) Modification, flexural, impact, compressive properties & chemical resistance of natural fibers reinforced blend composites. Malays Polym J 8:38–44

8. Shankar P, Reddy D, Sekhar V, Sekhar V (2013) Mechanical performance and analysis of banana fiber reinforced epoxy composites. Int J Recent Trends Mech Eng
9. Sumaila M, Amber I, Bawa M (2013) Effect of fiber length on the physical and mechanical properties of random oriented, nonwoven short banana (*Musa balbisiana*) fiber/epoxy composite. Asian J Nat Appl Sci 2:39–49
10. Laban BG, Corbiere-Nicollier T, Leterrier Y, Lundquist L, Manson J-AE (2001) Life cycle assessment of biofibers replacing glass fibers as reinforcement in plastics. Resour Conserv Recycl 33:267–287
11. Salleh EM, Razali NAM, Ya'Acob WMHW, Aziz FA (2019) Dynamic mechanical analysis of epoxy reinforced by nanocellulose rice straw composite. AIP Conf Proc
12. Haque MM, Hasan M, Islam MS, Ali ME (2009) Physico-mechanical properties of chemically treated palm and coir fiber reinforced polypropylene composites. Bioresour Technol
13. Ashori A (2008) Wood-plastic composites as promising green-composites for automotive industries! Bioresour Technol
14. Nechita P, Ionescu ŞM (2018) Investigation on the thermal insulation properties of lightweight biocomposites based on lignocellulosic residues and natural polymers. J Thermoplast Compos Mater
15. Lee SC, Mariatti M (2008) The effect of bagasse fibers obtained (from rind and pith component) on the properties of unsaturated polyester composites. Mater Lett

Effect of Lateral Load on Response of Pile Foundation

M. Mahalakshmi and M. Arulsurya

Abstract The seismic soil-structure interaction involves the investigation of the collective response of the structure, the foundation and its surroundings, to a predetermined free-field ground motion. In this investigation, the pile foundation is analyzed for earthquake loads. The piles are modeled in SolidWorks software and analyzed in ANSYS workbench. The vertical and lateral load is applied on long and short pile. Due to impact of lateral force, huge overturning and displacement occurred in long pile, combined with small ground displacements. In short pile, settlement of pile was observed along with large ground displacement.

Keywords SSI · Piles · Earthquake analysis · Deformation · ANSYS

1 Introduction

Pile foundations are exploited to distribute the load from elevations, through mid-layer which can be water, or rigid soil. They are eventually for tall buildings, skyscrapers and mainly accomplished where top settlement is averted. Pile is also called as concrete columns which are constructed in subsoil strata. In small buildings, they are generally adopted up to 2–4 m depth, and diameter ranges from 250 to 350 mm. The long slender column used for piles is generally made up of steel, timber and reinforced concrete in order to carry the vertical load and seismic loads. The laterally loaded piles embedded in sand were analyzed using Plaxis by Elhakim et al. [1]; it was found that the pile response depended upon pile spacing and relative density of sand. Also, the fixity of pile head effects was examined under lateral loading. Nonlinear analysis was used to analyze the load carrying capacity and load deformation behavior of single pile by Ahmed et al. [2, 3]; one of the main difficulties in design was to predict the maximum deflection of the pile. Therefore, the 2D models were created to study the lateral behavior of piles in horizontal plane.

M. Mahalakshmi (✉) · M. Arulsurya
Department of Civil Engineering, Bannari Amman Institute of Technology, Sathyamangalam, Erode, Tamil Nadu, India
e-mail: mahalakshmice@gmail.com

G. Kumaresan et al. (eds.), *Advances in Materials Research*, Springer Proceedings in Materials 5, https://doi.org/10.1007/978-981-15-8319-3_25

Design of foundation for seismic loading is described briefly in this paper. SAP 2000 finite element software was used to analyze the variation of supports in structure and bearing forces. Deflection, moment and reaction of a column are briefly discussed by Abbas et al. [4]; reinforced concrete (RC) micro-piles and reactive powder concrete (RPC) were invented and designed by Cheng et al. [5] to examine the dynamic response parameters such as strain, bending moment, pile soil system and their time history. The pile deformation on dynamic response of micro-pile soil interaction is performed by shaking table test. The result indicated that the strain response of piles is buried about a depth of 4.2D. The 1D model is derived from the 2D model to imitate the nature of actions on piles by Sugimura et al. [6]. In general it is not possible to design, but here, an attempt was made to investigate the displacement response of ground. The experimental study of pile was carried out by Bisaws et al. [7] based on the numerical study and also to calculate the coefficient of lateral modulus of subsoil forces. Three dimensional finite difference analysis was carried out by Chourasia et al. [8] to compute The long free headed and short free headed piles of similar or layered soil media are tested. The parameters such as slenderness ratio, relative density of sand and embedment ratio of pile were tested by varying their data with the help of model pile test. The numerical study was undergone by Plaxis 3D foundation software. The lateral load–displacement curve, pile deflection and bending moment distribution were obtained from the pile foundation. The depth for bed rock is established between 3 and 20 m. The effect of the bedrock on the curves was evaluated from *p*–*y* curves which were collected at depths of 2.0–4.5 m.

It was observed that the p-y curves were significantly affected by the material properties of the bedrock if the rock is located in close proximity (within 3D). Analysis of laterally loaded piles in 18 node triangular prism elements was done using detailed three-dimensional finite element formulation. Numerical formulation has been illustrated to develop in the pile which is located at the crest of the slope and at some edge distance from the crest. The displacement and bending moment increase with an increase in slope of the ground, whereas they decrease with increasing edge distance which is also industrialized by numerical study carried out by Vishwas et al. [9]. Ayothiraman et al. [10] conducted shake table test on model to study the adaptability of foundation. In this paper, the effect of flexibility of foundation which is subjected to lateral earthquake loads has been studied, and also, the effect of lateral load on long and short pile foundation is also analyzed using Ansys workbench software.

2 Model Using Solid Work

The pile foundation system is modeled using the software package SolidWorks. The major feature of this package is simplified part creation and assembled (Figs. 1, 2 and 3).

Fig. 1 Part – pile with cap

Fig. 2 Part – soil continuum

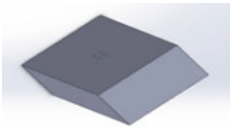

Fig. 3 Assembled system

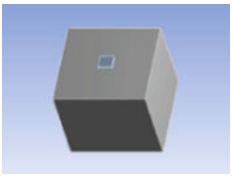

3 Analysis Using Ansys

The 2 × 2 pile foundation embedded in sandy soil with both short and long piles is studied by applying dynamic loading to the system. The model combined both pile with cap and soil continuum as assembled system has the interactions and loadings. The raft thickness remained the same for both short and long piles. *L*/*d* ratio greater than 15 was adopted to study the behavior of long piles, and *L*/*d* ratio lesser than 15 was adopted to study the behavior of short piles. As vertical and lateral load is applied, an enormous eccentricity develops. Tables 1 and 2 define the parameters of pile, and the parameters of soil and model specifications are defined in Table 3.

Table 1 Parameters of pile

Density	2300 kgm^3
Young's modulus	3E + 10 pa
Poisson's ratio	0.18
Bulk modulus	1.56525E + 10 pa
Compressive strength of concrete in the pile	M40

Table 2 Parameters of soil

Density	1700 kgm^3
Young's modulus	5.014E + 10 pa
Poisson's ratio	0.3
Bulk modulus	4.36E + 10 pa
Mohr's coulomb parameters	
Initial inter-friction angle	25°
Initial cohesion	5000 pa

Table 3 Specification of models

Description	Condition	Model
Long pile	$L/d > 15$	Pile length = 7.5 m Pile dia = 500 m Pile cap size = 3 m × 3 m Soil continuum = 20 m × 20 m 18.5 m
		Pile diameter = 500 mm Pile dia = 500 m Pile cap size = 3mx3m Soil continuum = 20 m × 20 m × 18.5 m
		Pile cap size = 3 m × 3 m
		Soil continuum = 20 m × 20 m × 18.5 m
Short pile	$L/d < 15$	Pile length = 3 m Pile dia = 200 mm Pile cap size = 2 m × 2 m Soil continuum = 10 m × 10 m × 7.5 m
		Pile diameter = 200 mm
		Pile cap size = 2 m × 2 m
		Soil continuum = 10 m × 10 m × 7.5 m

3.1 Boundary Condition

The boundary condition was allowed to be simulated in the initial step itself. The bottom boundary must be arrested against vertical translation while the vertical boundary must be arrested against lateral translation. All surfaces of soil continuum except the top and left side surface were restrained mechanically by providing fixed supports in order to eliminate the effect of boundary conditions, a large soil continuum was necessary.

The dynamic analysis of laterally loaded long and short piles installed in sandy soils was evaluated by applying horizontal velocities at the soil continuum, and the

pile load variation settlement in soil was monitored. A lateral load of 7 Richter scale was applied. A vertical load of 16,802 KN was applied to the foundation as loading from the superstructure based on Kanaujia et.al. [10].

4 Validation of Model

The present model is based on 3D modeling of seismic load on pile groups resting in sand by Elhakim et al. [1]. In this investigation, three-dimensional model is analyzed by ANSYS workbench, and moreover, the loading parameter adopted is in accordance with Kanaujia et.al. [10].

5 Result and Discussion

5.1 Behavior of Long Piles Under Lateral Force

The dynamic lateral load of 7 Richter scale was applied on the model having greater L/d ratio to study the behavior of displacement, settlement, pile head displacement and ground displacement after the application of vertical load.

From this analysis, as an impact of lateral force overturning of pile is observed which is in accordance with [1] and small ground displacement is occurring, then the pile is largely displaced as shown in Figs. 4 and 5. Load versus displacement curve for long pile is shown in Fig. 6. It indicates that as the load increases in the presence of lateral load, the pile displacement is also reportedly high.

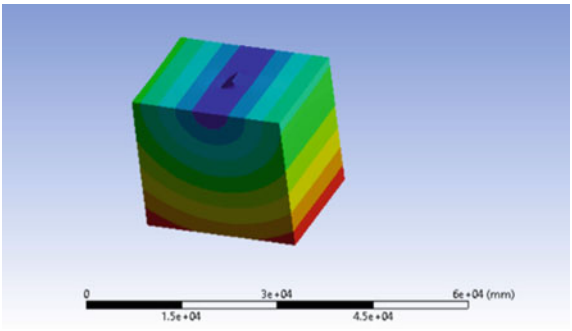

Fig. 4 Total deformation of long pile setup

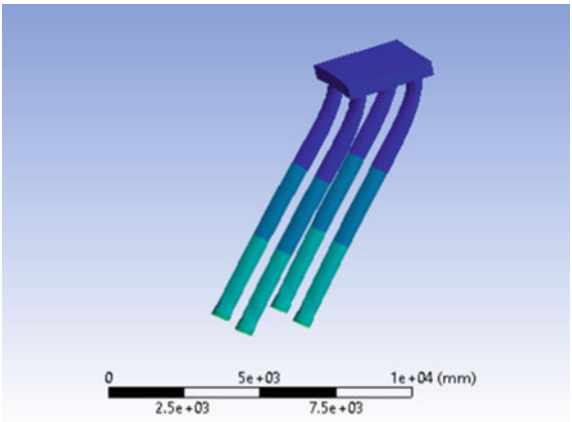

Fig. 5 Total deformation of long pile

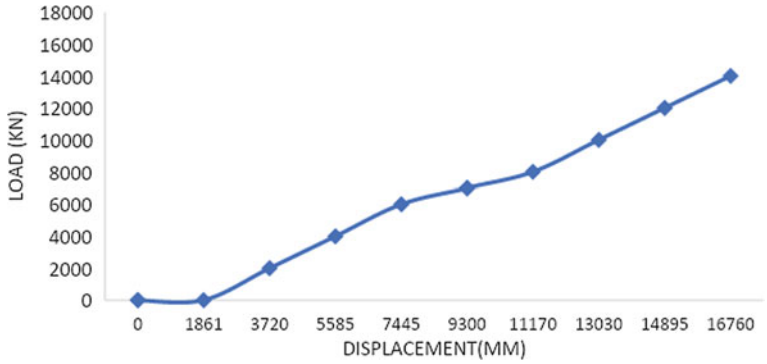

Fig. 6 Load versus displacement graph for long pile

5.2 Behavior of Short Piles Under Lateral Force

The analysis of short piles having lesser *L*/*d* ratio is done using the same dynamic lateral load in the presence of vertical load.

It was found that due to the impact of lateral force, large ground displacement was observed as shown in Fig. 7. The load vs displacement curve for the short piles shown in Fig. 8 represents less displacement compared to the long piles. Since short piles behave partially plastic and partially elastic, long piles completely behave as plastic.

6 Conclusion

From the study, it was concluded that

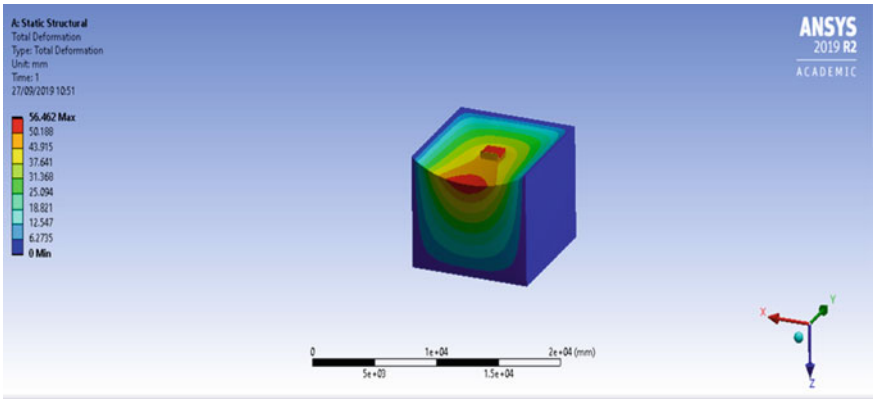

Fig. 7 Total deformation of short pile

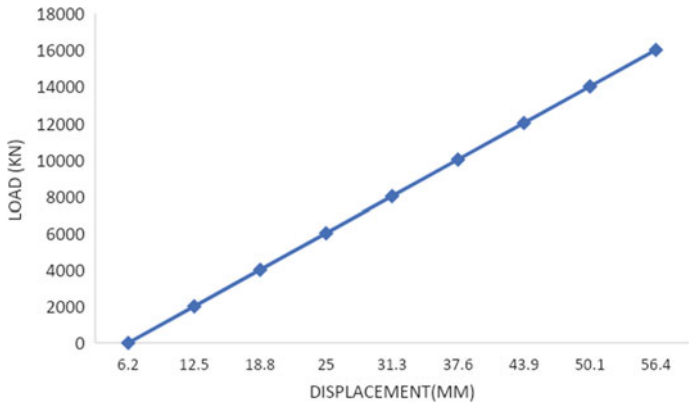

Fig. 8 Load versus displacement graph for short pile

- During the impact of lateral force, the pile is largely displaced, and then, it leads to overturning.
- When the *L*/*d* ratio increases, the settlement decreases for short pile compared to long pile where the settlement increases when the pile length increases.
- The pile cap is dislocated, and small ground displacement occurs due to lateral force in long pile, whereas large ground displacement occurs in short pile.

References

1. Elhakim AM, El Khouly MAA, Awad R (2014) Three-dimensional modeling of laterally loaded pile groups resting in sand. HBRC J 1687–4048

2. Ahmed MY, Neelima SD (2009) Numerical analysis of a pile subjected to lateral loads. IGC 2009, Guntur, India
3. Abbas JM, Chik Z, Taha MR (2018) Modelling and assessment of a single pile subjected to lateral load. Studia Geotechnica et Mechanica 40(1):65–78
4. Ray RP, Wolf Á (2013) Analysis and design of piles for dynamic loading. In: 18th international conference on soil mechanics and geotechnical engineering, Paris
5. Cheng J, Luo X, Zhuang Y, Xu L, Luo X (2019) Experimental study on dynamic response characteristics of RPC and RC micro piles in SAJB. Appl Sci 9:2644. www.mdpi.com/journal/applsci
6. Sugimura Y, Karkee MB (2001) Nature of damage to pile foundation of buildings in recent earthquakes and some proposals for seismic design. Sugimura & Karkee/01
7. Bisaws SK, Mukherjee S, Chakrabarti S, De M (2015) Experimental investigation of free head model piles under lateral load in homogenous and layered sand. Int J Geotech Eng. ISSN: 1938-6362 (Print) 1939-7879 (Online) Journal homepage: https://www.tandfonline.com/loi/yjge20
8. Chourasia J, Pendharkar U, Singh R (2018) Numerical analysis of laterally loaded piles affected by bedrock depth. Hindawi Adv Civ Eng 2018(Article ID 5493579):9
9. Sawant VA, Shukla SK (2012) Finite element analysis for laterally loaded piles in sloping ground. Coupled Syst Mech 1(1):59–78
10. Kanaujia VK, Ayothiraman R, Matsagar VA (2012) Influence of superstructure flexibility on seismic response pile foundation in sand. 15 Wccee Lisboa

Investigation of Some Mechanical Properties of Cast Iron Coated with Chromium and Zirconia for Sliding Application

S. Pranesh, T. Nithish Raj, S. Sudhakar, D. Deepan Kumar, and K. Suwinraj

Abstract In this project work, aluminium oxide/zirconia (30% Al_2O_3 + 70% ZrO_2) and aluminium oxide/chromium (30% Al_2O_3 + 70%Cr) were coated through atmospheric plasma spray technique (APS) over cast iron as a base material, and some of its mechanical properties were studied experimentally. The hardness, wear and SEM and EDX of Al_2O_3/ZrO_2, Al_2O_3/Cr coated and non-coated cast iron were taken, and the results were compared. Hardness, SEM and EDX results show that the chromium is better fused with cast iron than zirconium.

Keywords Atmospheric plasma spray · Hardness · SEM and EDX

1 Introduction

Nowadays, there is an increasing demand for engineering components to work in severe working environments [1]. Due to its high-temperature application, there is a need for some special types of coating in the surface of the components. Alumina oxide coatings are excellent medium for providing a better protection against wear and also resistant to high-temperature wear [2]. These coatings are used in hot temperature applications such as turbine blades, internal combustion engine pistons, petrochemical pipelines, hydraulic pumps and shafts. [3, 4]. Plasma spraying is one of the best techniques to coat various materials on a variety of metal substrates [5, 6]. Coatings which are done with plasma spraying will exhibit a better bonding with the metal substrate, wear resistance, excellent corrosion resistance and also high thermal resistance.

S. Pranesh (✉) · T. N. Raj · S. Sudhakar · D. D. Kumar · K. Suwinraj
Sri Krishna College of Engineering and Technology, Coimbatore, India
e-mail: praneshs@skcet.ac.in

G. Kumaresan et al. (eds.), *Advances in Materials Research*, Springer Proceedings in Materials 5, https://doi.org/10.1007/978-981-15-8319-3_26

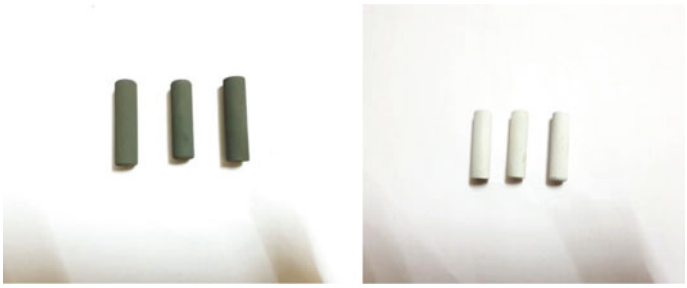

Fig. 1 **a** Chromium-coated material; **b** zirconia-coated material

2 Materials and Methods

Plasma spray coating is been done on base material cast iron (GC-211) which is specially used for variety of piston rings in reciprocating or in rotatory applications. Thick coatings (450–500 μm) were deposited on the base material by using plasma spraying gun with 7 mm internal diameter nozzle. Cast iron (GC-211) was sand blasted by using alumina particles in order to improve the surface roughness value and also the bonding between the coating and the metal surface [7]. Finally, the samples are mounted on the specimen catcher, and it is been coated [8]. Three variety coating materials, namely aluminium oxide, zirconia and chromium, were used. The coating was done with different chemical compositions. Figure 1a shows the cast iron coated with 30% aluminium oxide and 70% chromium (wt.%).Fig. 1b shows the cast iron coated with 30% aluminium oxide and 70% zirconia.

3 Results and Discussion

3.1 Hardness

In the present study, aluminium oxide, zirconia and chromium coatings were done on the cast iron by plasma spray technique, and their mechanical properties were characterized [9, 10]. \query{Please check the edits made in the sentence 'The hardness of pure aluminium oxide coatings was about 81 HRC...'.}The hardness of pure aluminium oxide coatings was about 81 HRC, the hardness of Al_2O_3 + Zirconia coatings was about 85.7 HRC, and the hardness of Al_2O_3 + Chromium was about 88 HRC. Figure 2 explains the bar chart displaying the variation in Rockwell hardness with a variety of coating materials. \query{Please check the clarity of the sentences 'Cast iron 211 has an 84.2 HRC when...', 'And also, when compared with Al2O3 + chromium is 3.8 HRC is comparability low', and 'When comparing the two coated materials Al2O3 + Zirconia and Al2O3 + chromium has 2.3 HRC...'.}Cast iron

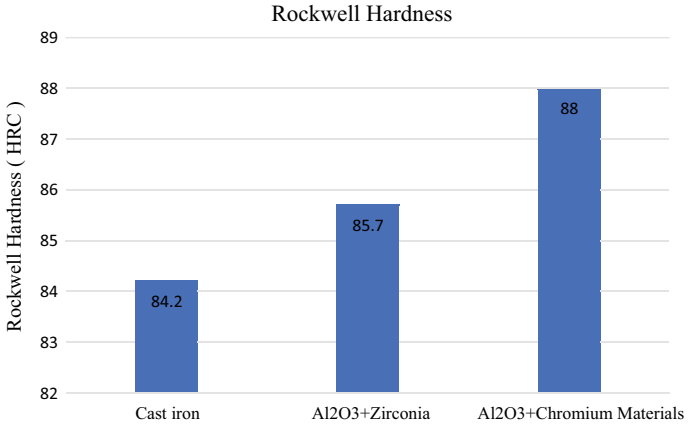

Fig. 2 Bar chart displays the variation in Rockwell hardness

211 has an 84.2 HRC when compared with the coated materials Al2O3 + Zirconia is 1.5 HRC is low. And also, when compared with Al2O3 + chromium is 3.8 HRC is comparability low. When comparing the two coated materials Al2O3 + Zirconia and Al2O3 + chromium has 2.3 HRC is the difference. The above graph shows that Al2O3 + chromium-coated sample has high hardness value when compared to the other two materials because the chromium generally has high hardness property [11, 12].

3.2 SEM Analysis

Ceramic-coated samples were been cut by medium-speed diamond saw cutter and polished upto 0.26 μm. Then, the polished specimen cross sections were then analysed using scanning electron microscopy. For each sample, various micrographs at different magnification ranges, i.e., 100X–2000X, were been processed and analysed. From Fig. 3, it is clear that both the coatings exhibit a porosity and microholes [13, 14]. The presence of fine pores and also the presence of microcracks are also homogeneously distributed [15]. Figure 4 shows some patches and interlamellar microcracks (denoted by yellow arrows). Partially melted particles were also observed in some areas.

4 Conclusion

In the present work, some mechanical properties of cast iron coated with chromium and zirconia for sliding application have been investigated. The result obtained from

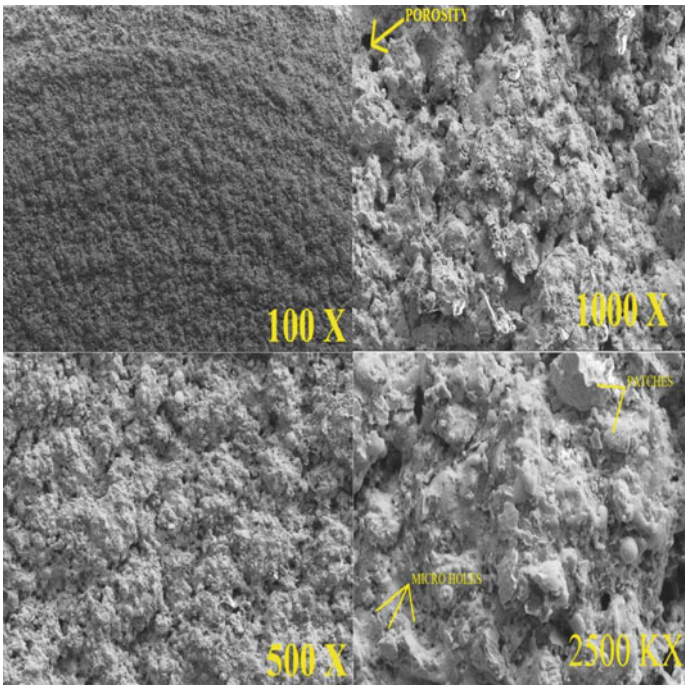

Fig. 3 Al2O3/Cr-coated cast iron

the Rockwell hardness tester shows that hardness is higher for Al2O3 + Chromium when compared with Al2O3 + Zr and non-coated cast iron. The result obtained from SEM and EDX shows that the chromium is better fused with cast iron than zirconia and also does not have much porosity and cracks when compared with other material.

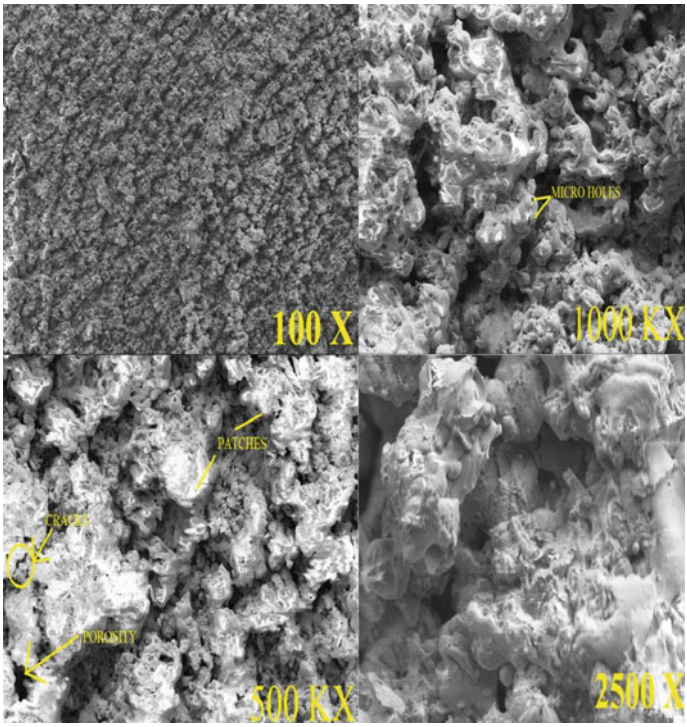

Fig. 4 Al2O3/Zr-coated cast iron

References

1. Davis JV (2005) Handbook of the thermal spray technique. ASTM International, Material Parks, OH
2. Pantels DS, Psylaki R, Alexopolos N (2001) Tribologicall behaviours of plasma arc sprayed aluminium oxide coatings under the severe wearing conditions. Wear 237:198–205
3. Bandyoopadhay PR, Cicot D, Venkateswarlu B, Racerla V, Decopman X, Lesagse J (2013) Mechanical properties of the conventional and also nanostructured plasma arc sprayed alumina coating. Mech Mater 54:61–71
4. DeMasi-Marcin JT, Gupta Pratt DK (1994) Protective coatings in the gas turbine engine, 400 Main Street, East Hartford, CT06108, USA
5. Knotek K (2002) Thermal arc spraying technique and detonation gun method. In: Bunsha RK (ed) Handbook of the hard coating technique. Noyes Publications, New Yersy, pp 79–108
6. Heimann RB (1996) Applications of plasma-sprayed ceramic coatings. Key Eng Mater 122–124:399–442
7. Zhu D, Miller RA (2004) Development of advanced low conductivity thermal barrier coatings. NASA John H. Glenn Research Center at Lewis Field, 21000 Brookpark Road, Cleveland, OH 44135
8. Lima RS (2007) Thermal spray coatings engineered from nanostructured ceramic agglomerated powders for structural, thermal barrier and biomedical applications: a review 191:389–397

9. Suresh Babu P, Rao DS, Rama Krishna L, Sundararajan G (2017) Weibull analysis of hardness distribution in detonation sprayed nano-strucutred WC-12Co coatings. Surf Coat Technol 319–394–402
10. Vargas Garcia JR, Goto T (2003) Thermal barrier coatings produced by chemical vapor deposition. Institute for Materials Research, Tohoku University, Sebdau 980-8577, Japan. Received 14
11. Matikainen V, Niemi K, Koivuluoto H, Vuoristo P (2014) Abrasion, erosion and cavitation erosion wear properties of thermally sprayed alumina based coatings. Coatings 4:18–36
12. Khor KA, Dong ZL, Gu YW (1998) Plasma sprayed functionally graded thermal barrier coatings. School of Mechanical and Production Engineering, Nanyang Technological University, Singapore. Received 7
13. Sarekaaya P (2006) Effects of the some parameters on the microstructure and hardness of an alumina coatings done by the air plasma arc spraying technique. Surf Coat Techn 191:389–394
14. Beardsley MB, Fairbanks J (eds) (1990) Proceedings of the 1990 coatings for advanced heat engines workshop. Department of Energy, Washington DC, USA, p 1153
15. Rana H (2006) A review paper on thermal barrier coatings (TBC) to improve the efficiency of gas turbine 237:198–210

Performance Study of Low-Pressure Vertical Feedwater Heater with SS304 as the Tube Material

S. Jeeva, A. Abubakkar, S. Dinesh Kumar, and M. R. Ahamed Buhari

Abstract Most of the power generated comes from the steam power plant based on modified Rankine cycle. Researchers always attempt to increase the thermal efficiency of the steam power cycle. Due to increasing competition, it has become necessary for electric utilities to operate their facilities in the most cost-effective way possible. Even a slight increase in thermal efficiency reduces fuel consumption, and subsequently, the fuel cost is also saved. Feedwater heater is one of the components that increase the cycle efficiency. Low-pressure feedwater heater is used in a steam power plant to preheat the feedwater. But the tubes of the heater are subjected to frequent failures. So it becomes necessary to study the performance of the heater to check for its degradation. Effective monitorization of the process can be a very useful tool for diagnostic purposes. The performance of feedwater heaters can be studied by measuring a few thermodynamic properties. Terminal temperature difference (TTD), drain cooler approach (DCA), pressure drop and temperature rise are the four main parameters used in the analysis of feed water heaters. A simplified routine performance test on feedwater heater at a frequency of five minutes is conducted for a period of two hours. Using this test, the actual performance parameters are calculated. These results are compared with the computed values. This will help in identifying the deviations of the performance parameters under normal conditions. Based on the comparison, suitable decision can be made of whether to operate the heater or to replace it.

Keywords Terminal temperature difference · Drain cooler approach · Feedwater · etc.

S. Jeeva (✉) · A. Abubakkar · S. Dinesh Kumar · M. R. Ahamed Buhari
Department of Mechanical Engineering, Kongu Engineering College, Tamil Nadu, Erode 638060, India
e-mail: jeeva.mech@kongu.edu

G. Kumaresan et al. (eds.), *Advances in Materials Research*, Springer Proceedings in Materials 5, https://doi.org/10.1007/978-981-15-8319-3_27

1 Introduction

A feedback heater is a heat exchanging device in which by mixing the two streams or without mixing the steams, the heat is transferred from steam to the boiler feedwater [1]. In feedback heater, the Rankine cycle efficiency can be increased by raising the feedwater temperature that is supplied to the steam generator. More power will be wasted if the exiting water from the heater does not have specific temperature or if the mass flow or the specific enthalpy going to the heater from the extraction point is higher than the specific level. Effective monitorization of the process parameters can provide meaningful results for diagnostic purposes. As compared to the open heater, the closed heater does not attain a high feedwater temperature. The closed feedwater heaters are of shell and tube heat exchangers type. The degradation mechanisms of heat exchangers can be studied by measuring the temperature and pressure [2]. The LP heaters are usually located between the condensate extraction pump and the deaerator, which is followed by the boiler feed pump. LP heaters are employed to increase the overall efficiency of the regenerative cycle by heating the feedwater, coming from the condensate extraction pump. In boiler–turbine systems, the economy of the system causes too much problems. The load tracking system used in the past cannot measure the economy of the boiler–turbine systems effectively [3]. If malfunction of feedwater heater occurs, it affects the power plant efficiency by increasing the heat rate and/or decreasing generation capacity. Severe malfunction leads to complete shutdown of power plant unit. Heat exchanger tubes are the vulnerable part in the heat exchanger. Analysis showed that failure was due to the flushing operation with the initial water pressure of 2300 kgf/cm^2 [4]. Flow-accelerated corrosion causes in thinning of the deaerator walls and in some places results a leaky hole. Microstructure observation revealed that leaky hole was formed at places where the microstructure underwent recrystallization during the initial manufacturing process. The x-ray diffraction, scanning electron microscopy and optical microscopy techniques were used in the past for the microstructure analysis of deaerating feedwater heater. The results showed that the flow-accelerated corrosion (FAC) at the bottom of the deaerator can lead to the failure of feedwater heater [5]. A basic understanding of the operation of feedwater heater is necessary in realizing the impact of this system and subsequent control on plant efficiency. The thermal efficiency and cost of the shell and tube heat exchangers are two parameters which are difficult to optimize [6]. Feedwater heaters take advantage of the heat of condensation to preheat water supplied to the boiler. This reduces the amount of fuel required to bring the water up to required temperature. Model codes have been developed to solve the governing equations encountered in heat transfer problems. For the analysis of shell and tube heat exchanger, computer program can be incorporated for variety of heat exchanger configurations [7].

Barszcz and Czop [8] proposed a model of the feedwater and a method for it. They studied the parameters affecting the performance of the feedwater. The variations can be easily tracked by the PC workstations. The model was implemented in a 225 MW coal-fired plant and the operational data were tracked successfully.

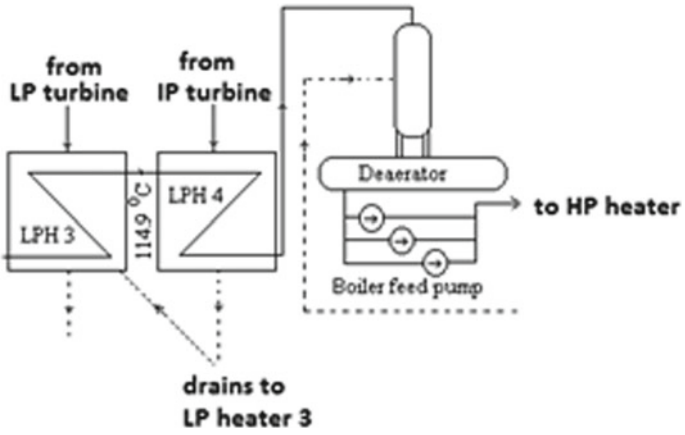

Fig. 1 Schematic diagram of the low-pressure heater

2 Zones in Feedwater Heater

As shown in Fig. 1, the LP heater 4 is located between the LP heater 3 and the deaerator. The feedwater enters the LP heater 4 from LP heater 3 and then leaves to deaerator.

The steam is extracted from intermediate pressure turbine, and the drains from HP heater 6 are fed to LP heater 4 for heating of feedwater. The drain outlet is sent to LP heater 3. Each feedwater heater contains one to three separate heat transfer area or zone. The Design parameters of the feedwater heater are determined by plant requirement and economics of design. The feedwater heater in this experimental study consists of two zones—condensing zone and sub-cooling or drain cooling zone. Low-pressure feedwater heater (LPH-4) is two-zone, vertical, channel down, U-tube type shell and tube heat exchanger with a removable shell. Condensate passing on the tube side with two passes is heated by the extraction steam from turbine exit on the shell side. The tube bundle of heater is divided into two distinct zones on the shell side: condensing zone and drain cooling zone. Steam enters the condensing zone where it is fully condensed. The drain is sub-cooled in the integral drain cooling zone.

3 Case History of the Previous Failures

The tubes of the previous low-pressure heater were made of ASTM B 395 Alloy C. Due to the frequent failures in the tube, the tube was plugged to avoid further performance deterioration. But there is a limit to the number of tubes that can be plugged, which is approximately 10% of the total number of the tubes.

The total number of tubes in the heater was 659. More than 10% of the tubes were plugged. Therefore, the tube material was changed to SA 688 TP 304, and the performance study of the low pressure with stainless steel 304 is made. The SS 304 shows greater resistance to erosion and corrosion and is immune to ammonia attack and to ammonia-induced stress corrosion cracking.

3.1 Causes of Tube Failure

The presence of $CaSiO_2$ and Na_2FeO_2 causes caustic corrosion. Also, due to the overheating of tube and its rupture, the NaOH in the water causes caustic corrosion [9]. Tensile test and micro-hardness tests carried out on ASTM SA 210C tubes showed that ductile mode failure caused the tubes to fail [10]. Farrahi et.al. [11] investigated the failure of shell and tube heat exchanger due to the plugging of tubes. To study this, the tubes were inserted with a series of rods and the tube-sheet failure because the effect of plugging of tubes was investigated by CFD analysis. The pressure, temperature, stresses and deformations of these tubes were examined. The stress corrosion cracking is a concern for high-pressure water heater tubes. When these tubes were exposed to certain environments, they tend to fail. Rao et al. [12] investigated the high-pressure heater tube made of stainless steel 316L. Also, different materials with different environmental combinations were used to find the reason for stress corrosion cracking. The failure of a boiler tube in a petrochemical plant was studied by Hosseini and Yareiee [13]. The microstructure analysis was done by optical microscopy, scanning electron microscopy and x-ray diffraction. The hardness measurements were also done. The results showed that the short-term overheating has caused the boiler tube to fail. Copper tube failure is due to the interaction of both the ant net and stress corrosions [14].

3.2 Effects of Tube Failure in the Heater

Normally, the heaters are designed with 10% of excess tubes to take care of tube failures during life time. If 10% of tube fails, then the velocity will increase due to throttling at the entry of the tube. This may lead to erosion. Next, the heater outlet temperature will fail, and the steam requirement for deaeration will increase.

4 Performance Analysis of the Feedwater Heater

The performance of the feedwater can be analysed by comparing the actual performance parameters with the computed ones. Power generation systems consisting

of feedwaters have high complaints on the performance degradation due to the uncertainties involved in the feedwater systems [15].

4.1 Calculation of Actual Performance Parameters

The parameters for feedwater analysis are terminal temperature difference, drain cooler approach, temperature rise and pressure rise. The performance of the heater is said to be deteriorating if the actual values of TTD, DCA and pressure rise are greater than the computed values. Similarly, the actual temperature rise should be greater than the computed values for its better working.

The numerical values of the actual performance parameters can be found out by measuring the pressure and temperature of the feedwater and the steam at inlet and outlet. The observations were made for a period of 2 h. The minimum and maximum values of each of the measured parameter are indicated in Table 1.

The actual performance parameters [16] are found using the formula given below.

4.1.1 Terminal Temperature Difference (TTD)

The terminal temperature difference is the difference between the saturation temperature corresponding to the inlet extraction steam pressure to the heater and the outlet feedwater temperature. It is the major factor affecting the heat exchanger performance [6].

$$\text{TTD} = t_{\text{sat}} - T_2 \tag{1}$$

4.1.2 Drain Cooler Approach (DCA)

The drain cooler approach is temperature difference between the drain leaving the shell side of the heater and the entering feedwater on the tube side.

$$\text{DCA} = t_{od} - T_1 \tag{2}$$

Table 1 Observed properties of feedwater and steam at inlet and outlet

Range	Feedwater temperature in °C		Feedwater pressure in kg/cm^2		Steam temperature in °C		Steam pressure kg/cm^2	
	Inlet	Outlet	Inlet	Outlet	Inlet	Outlet	Inlet	Outlet
Minimum	113.9	147.2	15.47	15.17	279.1	118.6	4.67	4.64
Maximum	114.6	147.9	16.4	15.7	281.2	119.2	4.77	4.74

4.1.3 Temperature Rise (TR)

The temperature rise is temperature difference between the feedwater outlet temperature to the feedwater inlet temperature.

$$\Delta T = T_2 - T_1 \tag{3}$$

4.1.4 Tube Side Pressure Drop

The tube side pressure drop consists of the frictional losses in the tubes, including inlet and outlet channel losses. It is difference between the feedwater inlet pressure to the feedwater outlet pressure.

$$\Delta P_{1-2} = P_1 - P_2 \tag{4}$$

4.2 Calculation of Design Values of Performance Parameters

The design calculations are based on ASME PTC 12.1 [17]. It is mostly widely accepted for calculating the performance of closed feedwater heater. Based on the calculations, design values are obtained. Figure 2 shows the comparison of actual and design values of the four performance parameters.

5 Consequences and Discussion

The main objective of the paper is to highlight the method used to analyse the performance of closed feedwater heater. Not much studies are found which compares the actual and design parameters with codes. Here, an attempt is made to find out whether the feedwater heater is working satisfactorily or not based on the ASME test codes. The actual performance parameters based on operating variables and design parameters based on design variables are calculated and compared. It can be inferred that the performance parameters (TTD, DCA and ΔP) calculated from the observation readings are lower than their corresponding performance parameters based on the design values (TTD^*, DCA^*, ΔP^*). The calculated temperature rise is larger than design temperature rise. For a normal closed feedwater heater, the actual temperature rise should be greater than the temperature rise based on design values. The other parameters should be lower than the design values. The above trend is seen in the feedwater heater under investigation. So it can be concluded that the low-pressure heater is working under satisfactory condition.

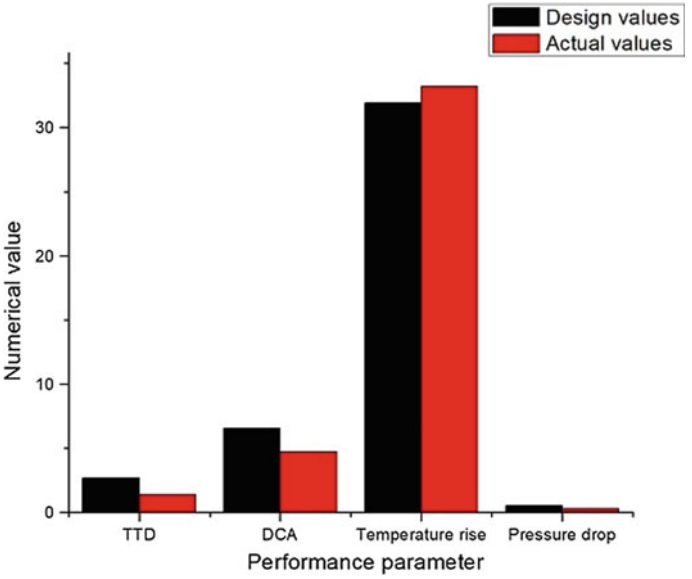

Fig. 2 Comparison of actual and design values

Nomenclature

T_1	Feedwater inlet temperature, °C
T_2	Feedwater outlet temperature in °C
P_1	Feedwater inlet pressure in kg/cm^2
P_2	Feedwater outlet pressure in kg/cm^2
t_1	Steam inlet temperature in °C
t_2	Steam outlet temperature in °C
P_{s1}	Steam inlet pressure in kg/cm^2
P_{s2}	Steam outlet pressure in kg/cm^2
t_{sat}	Saturation temperature corresponding to the inlet extraction steam pressure to the heater in °C
t_{od}	Temperature of the drain leaving the shell of the heater in °C
TTD	Terminal temperature difference in °C
DCA	Drain cooler approach in °C
R	Temperature rise in °C
ΔP	Pressure drop in N/m^2

Exponents

*	Computed parameters from design values

References

1. Kakac S, Liu H, Pramuanjaroenkij A (2002) Heat exchangers: selection, rating, and thermal design. CRC press
2. Addepalli S, Eiroa D, Lieotrakool S, François AL, Guisset J, Sanjaime D, Kazarian M, Duda J, Roy R, Phillips P (2015) Degradation study of heat exchangers. Procedia Cirp 38:137–142
3. Liu X, Cui J (2018) Economic model predictive control of boiler-turbine system. J Process Control 66:59–67
4. Ni TW, Fei JL, Wang SH, Gong Y, Yang ZG (2020) Failure analysis on unexpected perforation of heat exchanger tube in methacrylic acid reboiler of specialty chemical plant. Eng Fail Anal 108:104267
5. Zangeneh S, Bakhtiari R (2019) Failure investigation of a deaerating feed-water heater in a power plant. Eng Fail Anal 101:145–156
6. Mirzaei M, Hajabdollahi H, Fadakar H (2017) Multi-objective optimization of shell-and-tube heat exchanger by constructal theory. Appl Therm Eng 125:9–19
7. Kara YA, Güraras Ö (2004) A computer program for designing of shell-and-tube heat exchangers. Appl Therm Eng 24(13):1797–1805
8. Barszcz T, Czop P (2011) A feedwater heater model intended for model-based diagnostics of power plant installations. Appl Therm Eng 31(8–9):1357–1367
9. Kim YS, Kim WC, Kim JG (2019) Bulging rupture and caustic corrosion of a boiler tube in a thermal power plant. Eng Fail Anal 104:560–567
10. Prabu SS, Choudhary A, Mittal N, Gupta S, Ramkumar D, Natarajan A (2019) Failure evaluation of SA 210C riffle water wall tubes in 70 MW CFBC boiler. Eng Fail Anal
11. Farrahi GH, Chamani M, Kiyoumarsioskouei A, Mahmoudi AH (2019) The effect of plugging of tubes on failure of shell and tube heat exchanger. Eng Fail Anal 104:545–559
12. Rao MA, Babu RS, Kumar MP (2018) Stress corrosion cracking failure of a SS 316L high pressure heater tube. Eng Fail Anal 90:14–22
13. Hosseini RK, Yareiee S (2019) Failure analysis of boiler tube at a petrochemical plant. Eng Fail Anal 106:104146
14. Zhou J, Yan L, Tang J, Sun Z, Ma L (2018) Interactive effect of ant nest corrosion and stress corrosion on the failure of copper tubes. Eng Fail Anal 83:9–16
15. Kang YK, Kim H, Heo G, Song SY (2017) Diagnosis of feedwater heater performance degradation using fuzzy inference system. Expert Syst Appl 69:239–246
16. Hansen E, Godwin R, Wood D, Turner L (1996) Early detection of feedwater-heater leaks
17. ASME (2000) Closed feedwater heaters: performance test codes. ASME PTC-12.1-2000

Behaviour of Concrete Structure Subjected to Open Fire—State of Art

C. Aravindhan and S. Nayannathara

Abstract When the structure is subjected to fire, they undergo deformation and result in spalling and cracking and final lead to the distortion of the structures. The study intensifies to improve the prolong time failure of the structure which are subjected to fire outrage and applies the rehabilitation techniques to improve the life span of the damaged structure for prolonged time. The retrofitting is applied in order to improve the brittle failure. In this project, the beam is considered for investigating purpose and used to examine the beam behaviour before and after exposing to the fire. The retrofitting techniques are applied over the beam, and their compressive strength is computed.

Keywords Reinforced concrete structures · Retrofitting techniques · CFRP · Fibre-reinforced polymer (FRP) · Rubberized coir fibre sheets (RCFS)

1 Introduction

In the modern world, they are upgrading different technologies. The present trending and remarkable development in technologies may also lead to different challenges in the construction field. In this modern world, the fire disasters are arriving as a threat to structural buildings. The major constituents for fire are fuel, oxygen and heat. The fire calamities occurring in the building cause damage to the structural elements. The major reasons for these hazards are volatile materials, electrical equipments, household appliances and human transgressions. These rationales direct them to destruction of the structural building. This may also affect the lifelines of living creatures and wealth losses.

C. Aravindhan (✉)
Department of Civil Engineering, Bannari Amman Institute of Technology, Sathyamangalam 638401, Tamil Nadu, India
e-mail: aravindhanc@bitsathy.ac.in

S. Nayannathara
Bannari Amman Institute of Technology, Sathyamangalam 638401, Tamil Nadu, India

G. Kumaresan et al. (eds.), *Advances in Materials Research*, Springer Proceedings in Materials 5, https://doi.org/10.1007/978-981-15-8319-3_28

2 Literature Review

2.1 Lilly Grace Murali et al. (2014)

It represents the case studies of four fire accidents happened in four different places. The huge fire disasters occurred in case study, and they have discussed about the planning of the building and represented the reason for the occurrence of the fire, materials that feed the fire to the next stages, failure of the structure, reasons behind the life losses and wealth losses and remedial measure for each building which are also enumerated in the case study. The major aspect behind the failure of the structure is improper design of the buildings; the passive and active measurements are recommended to avoid the failure of the structure.

2.2 J. Gopi Krishnan et al.

The existing reinforced concrete structures need repair works, rehabilitation, because of deterioration due to various factors like corrosion, lack of detailing, failure of bonding between beam-column joints, increase in service loads, improper design and unexpected external lateral loads such as wind or seismic forces acting on a structure, environment and accident events, etc., leading to cracking, spalling, loss of strength, deflection, etc. Strengthening of the existing reinforced concrete structures is necessary to obtain an expected life span and achieve specific requirements. The need for efficient rehabilitation and strengthening techniques of the existing concrete structures has resulted in research and development of composite strengthening systems. Recent experimental and analytical research has demonstrated that the use of composite materials for retrofitting the existing structural components is more cost-effective and requires less effort and time than the traditional means. Fibre-reinforced polymer (FRP) composite has been accepted in the construction industry as a capable substitute for repairing and strengthening of RCC structures. Static load responses of all the beams under two-point load method have been evaluated in terms of flexural strength, crack observation, compositeness between CFRP fabric and concrete, and the associated failure modes. The deflections of the beams are decreased due to full wrapping technique around all the four facets of the beam. The flexural strength and ultimate load capacity of the beams enhanced due to external strengthening of beams.

2.3 Poorna Prasad Rao O. L. et al.

This paper offers retrofitting of strengthened concrete beams using rubberized coir fibre, a herbal laminate, in both flexure and shear that is subjected beneath two-point

loading. The essential aim of this look is to rehabilitate the structurally deficient beam and to make it serviceable in each flexure and shear. The beams retrofitted with rubberized coir fibre sheets (RCFS) are used to make structure green and to repair stiffness and strength values greater than those of manage beams. Understanding the reaction of these components all through loading is important to the improvement of an overall efficient and safe shape. Formation of first cracks, RCFS debonding and onset of concrete crushing are compared and discussed. Load–deflection conduct, failure modes and crack propagation patterns are studied notably. The presence of shear straps to enhance shear electricity has the twin gain of delaying debonding of RCFS sheets used for flexural strengthening. The check results confirmed that the stiffness of the RCFS retrofitted beams is significantly increased compared to the manage beams, and additionally, the deflection of retrofitted beams was decreased predominantly on the early levels of loading. The closing loads at failure of the specimen were extended. Instead of replacing the entire structure, it might be better to go for retrofitting (Figs. 1 and 2).

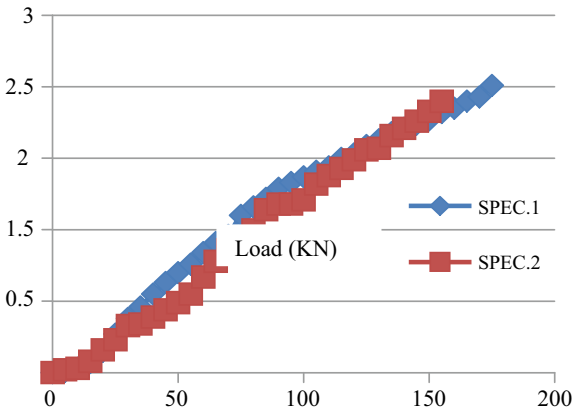

Fig. 1 Load versus deflection curve comparison of RS1 and RS2 with retrofitted beam

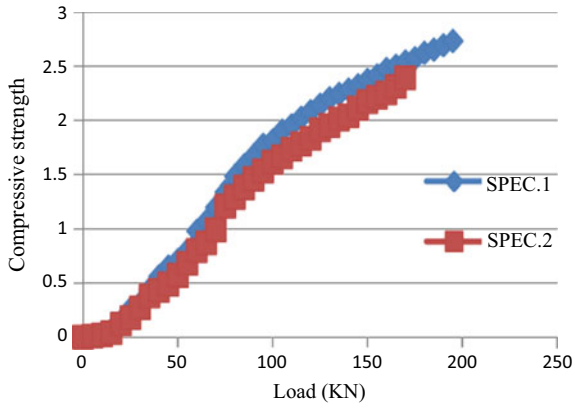

Fig. 2 Load versus deflection curve comparison of RS1 and RS2 with retrofitted beam

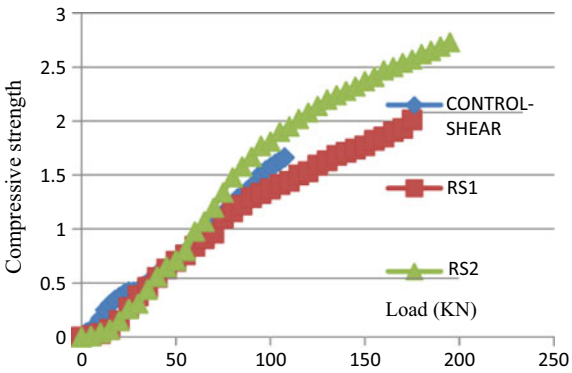

Fig. 3 Load versus deflection curve comparison of RS1 and RS2 with control beam

2.4 Liu Ming et al. (2013)

This paper undergoes a study about three-storey industrial building occurred in January 2010. Reinforcement enlarging section method is enhanced to rectify the damage caused during fire causalities. Polymer mortar and gules CFRP are also adopted for strengthening the damaged structural elements. CFRP reinforcement is provided on each side of the column. Dealing with the ventures building harmed by fire can give us a decent reference of fixing the comparative enterprises building. The distinctive harmed individuals were reinforced with various support strategies, for model shot solid support strategy, utilizing CFRP sheets fortification method, embedded steel bars with enlarger segment supportive technique and so forth. The use of an assortment of support strategies arrives at load-conveying limit prerequisite and expands less asserts (Figs. 3, 4, 5, 6 and Table 1).

3 Conclusions

In the present work, an attempt has been made to optimize the bead profile of the plasma arc welded BoP weld geometry of Inconel 617 plates using two non-traditional optimization techniques, namely GA and IWO. The regression equations obtained with the help of the response surface methodology are used to establish the objective functions for the study. It is observed that both the optimization methods are seen to perform with reasonably good accuracy. But the convergence rate of IWO is faster when compared with GA. The results of optimization also show that IWO algorithm is found to perform better than GA in terms of both the bead width and bead height of the BoP weld.

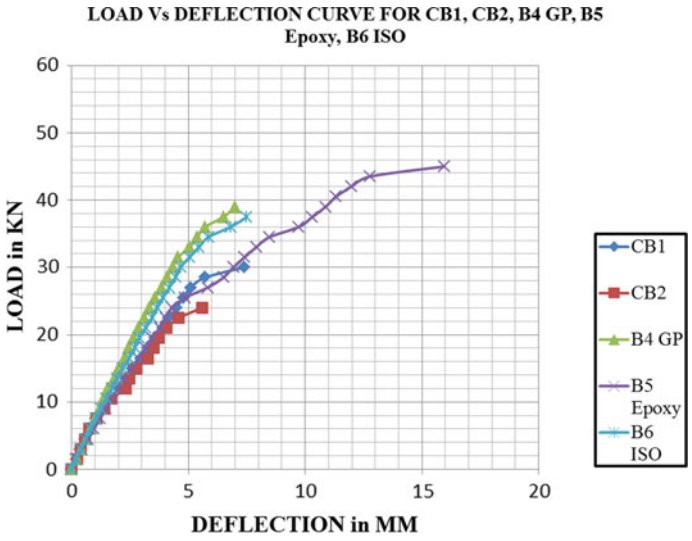

Fig. 4 Load versus deflection curve comparison of CB cube; orthophthalic resin (GP), epoxy resin and ISO resin

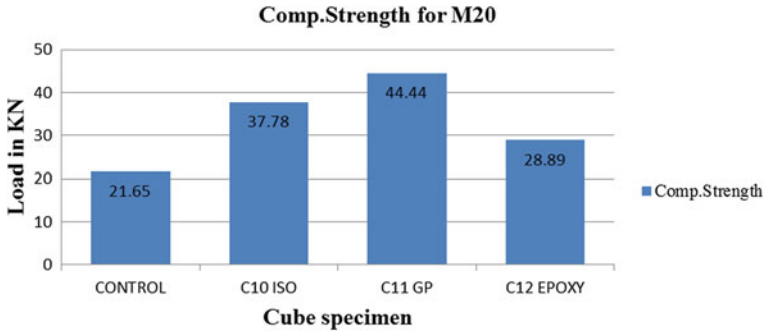

Fig. 5 Compression strength for M20 in CB cube; orthophthalic resin (GP), epoxy resin and ISO resin

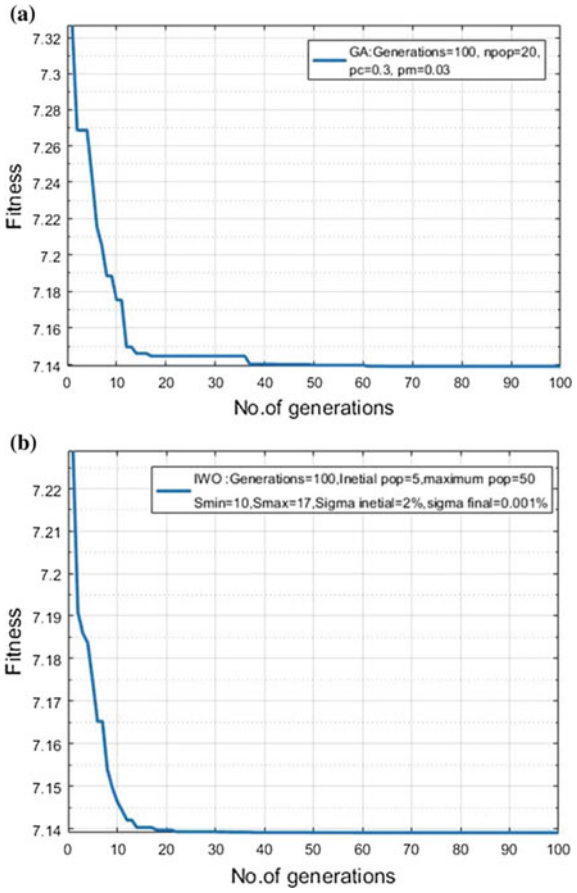

Fig. 6 Convergence graphs for **a** GA and **b** IWO algorithms

Table 1 Optimal values of the process parameters and their responses

Optimization method	Welding current (I)	Welding speed (N)	Plasma gas flow rate (G)	Bead width (BW) in mm	Bead height (BH) in mm
GA	86.001	300.00	2.296	5.600	1.656
IWO	86.049	300.00	2.298	5.666	1.620

References

1. Murali LG, Murali PLG, Vijayalakshmi M (2014) Fire accidents in buildings–case studies. Int J Eng Trends and Technol (IJETT) 11(4)
2. Krishnan JG, Reddemma S, Murthy NPN (2015) Retrofitting of reinforced concrete beam with externally bonded CFRP. Int J Innovative Res Sci Technol 2(7)

3. Poorna Prasad Rao OL, Rama Mohan Rao P (2016) Retrofitting of reinforced concrete beam using rubberized coir fiber sheets SSRG. Int J Civ Eng 3(3)
4. Liu M, Fan X-H, Zuo YZ, Song BF (2013) Strengthening and retrofitting of the industries building after fires. Adv Mater Res 671–674, pp 778–781

Risk Assessment of Machining and Assembly Line in Automotive Industry

T. Rajpradeesh, M. Saravanamani, R. Manikandan, and P. Venkumar

Abstract In this present digital world, the automotive industries have started adopting the applications of Industry 4.0. It is an essential backbone of India as well as most developing countries. The corresponding work processes are involved in the automotive industry (machining and assembly section) like grinding, milling, welding, etc. Most of the safety systems are followed in the workshop floor. However, some minor or major accidents have happened apart from the safety protection system due to poor maintenance of machining, lack of knowledge, worker awareness, and unsafe act/conditions. Initially, necessary safety precautions take place to prevent the injuries and improve the safety culture. The present study analyzes the risks of industries using the corresponding checklist to identify the hazards. The study has assessed the risk using risk assessment tool in machining and assembly area. Further, the results of the study recommend flexible implementation of safety measures with the existing system.

Keywords Hazard · Risk assessment · Machining area · Hazard identification and risk assessment (HIRA)

1 Introduction

In the recent industries' emerging scenario, though most of the automotive industries use the process of industry 3.0, some of the companies move to advanced level with industry 4.0 process. On the one hand, the technology development focuses on customer satisfaction, requirements and product demand, and on the another hand, there is a need to protect the employees in the working area. All kind of techniques aims to protect the workers with many safety measures.

In general, the automotive industry is a huge organization to participate in various department activities like design, development, manufacturing, marketing

T. Rajpradeesh (✉) · M. Saravanamani · R. Manikandan · P. Venkumar
Department of Mechanical Engineering, Kalasalingam Academy of Research and Education, Krishnankoil, Tamil Nadu 626126, India
e-mail: rajpradeesh29@gmail.com

G. Kumaresan et al. (eds.), *Advances in Materials Research*, Springer Proceedings in Materials 5, https://doi.org/10.1007/978-981-15-8319-3_29

(distributing) and finally, services. All the above functions are dealt with a different prominent role. However, in the manufacturing department, the employees face the safety problem associated with machining and assembly lines. There are a few studies that consider and eliminate the problem with respective path and solve the problem from various methods. The study conducted by R. Ramesh et al. reported that assessment tool establishes possible category of hazards in each department. Their proposed category risks are split up with high and low risks and also recommend possible control measures [1]. The study of Bambang Suhardi et al. has reported the potential hazards that occur at the printing industry. Their study recommends the practical solution to health and safety at the workplace to conduct risk assessment performance by using HIRA and HAZOP. The study has categorized with five different points of view like work attitude, work posture, work procedure, work station and physical environment. The safety assessment activities have obtained the value from higher to lower risk category and finally propose a practical solution for the hazards [2]. Khairul Akmal Shamsuddin et al. have reported HIRA to the determination of the necessity of control for an operational process at the solar company. The goal of the study is to achieve "zero accident" with a safe work system recommended by hierarchy control measures, before that their study evaluates and reviews the risks. Their findings record the harmful factors of the working environment [3]. John R. Etherton has investigated the work-related death and safety challenges of employees who work with machinery. This study has also used a guide to determinate, evaluate, and reduce risk relevant to machine tool created by international safety standards ISO14121 followed in the US guidelines associated with identified hazards and risk assess [4].

Magdalena Mazur has reported the analysis of risks in the marking process of industries and uses FMEA techniques to calculate RPN number, which is used to split up the category from higher to lower risks. It also compares the existing processing system control of the workplace by using the guidelines of the standard operating procedure that is generated by FMEA techniques [5]. The study of Rajpradeesh T. et al. has investigated and reduced hazards in the workplace. It is related to workers operation by using HIRA and FMEA and has three main stages of analysis of the potential hazards. After assessing the risk, their study finally reduces the risk by using the worksheet data [6]. Faisal, I et al. reported the use of HIRA and conducted the HAZOP tool using computer. The results obtained by fuzzy computation probability and likelihood impacts of effective and risk assessment exercise provide the safety [7]. Paithankar et al. analyze the hazards and address the hazards from the sources using HIRA techniques. Their study establishes the level of risk and categorizes the risks like low, medium and high. It proposes the method to reduce risks and develops the modified work station with safety [8].

2 Process

The corresponding workflow processes involve in the automotive industry, and each department is having a significant role in the outcome of the product (Mention Fig. 1).

2.1 Tool Description

i. **HIRA**

The Control Measures are taken using the HIRA Tool and Identify the Hazards and Risks in the workplace after that it can be reduced to the Low risk. For that purpose, HIRA method is used as a step-by-step operation.

HIRA tool reviews may be performed at any process or any operations in the working area like machining, construction, ongoing operation, installation work, commissioning or decommissioning and demolition.

A group of field experts typically performs a HIRA study with the qualified staff on the process, the work activities and the materials. The personnel have the training on risk assessment methods after applying the control measures (if necessary) with a possible solutions like elimination, substitution, isolation, administrative control, engineering control and personal protective equipment. When the study is completed, it decides to control the measures to implement the corrective action taken from high-level risks to low-level risks.

A study is suitable for a simple process by single experts—complex process risks by the multidiscipline team to conduct the risk analysis [9]. Papazoglou et al. have reported the integrated technical method, which is used to analyze risk management, and their study has been conducted in chemical installation unit [10].

ii. **HIRA Process**

The purpose of this work is to identify the hazards and analyze the risks of every process involved in various activities in the machining line and assembly line and gives recommendations to reduce or eliminate the risk assessment.

The success of the industry does not only depend on the production but also deal with the safety of the employees in the working area. While using HIRA action, it reduces the risks to considerable level.

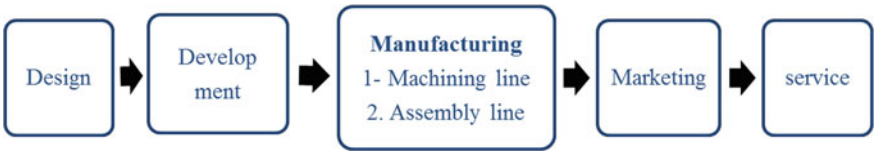

Fig. 1 Process in the automotive industry

The step-by-step process of HIRA is explained as follows. It starts from analyzing various activities, such as field survey, identifying the hazards, analyzing the level of risk category and controlling the risks. Suhardi et al. have reported an analysis of the hazards, and their study uses HIRA and HAZOP methods [11].

3 Methodology

3.1 Hazard Identification

Hazard
The main purpose of hazard identification is to mention the harmful operation or critical process of tasks. Working area hazards can be identified in several ways. Hazard identification is a major role and the first step in the HIRA process. The identification process is useful for workers to work in a safe zone. The hazard identification process is conducted to identify all hazards in the working environment. Chinnah et al. have reported risk conditions that can be reduced using this tool [12]. Erbay et al. reveal fuzzy and FMEA tools that can be used for risk assessment in Software Project Applications [13].

Hazards Factors
Generally, hazards can be classified into various types in the workplace;

- Physical hazards (slippery floor, poor lighting, excessive noise, etc.);
- Chemical hazards (chemical solvents, gases, liquids, etc.);
- Electrical hazards (electric shocks, damage switchboard, poor wire connection, etc.);
- Mechanical hazards (running machinery, rotatory parts, etc.);
- Ergonomics hazards (manual handling, poor design of a workstation, types of equipment, etc.);
- Height work (ladder, plant top, roof, wall, etc.);
- New workers and visitors.

Hazard Identification Techniques
HIRA methodology considers the following factors/information that will help to identify the hazards in the worksite/jobs.

- Inspect regularly by walking around the workplace
- Suggestions from employees who have noticed any critical thinks
- Review the previous accident/incident investigation reports.
- Any results of workplace inspections.

Fig. 2 Information sources

Hazard Identification Sources
Step 1: Classify the work activities

Describe the separate activities in the work station with various roof case and different operations.

Step 2: Information sources (Fig. 2)

Step 3: Checklist preparation

Ensuring of our job has to be done on time with an organization by the checklists, apart from information sources and techniques to fulfill the HAZID process by the checklist preparation. The hazards can be identified and assessed from the checklist by risk methods with respective hazards.

Kiurski et al. have reported that the hazards are registered, and sustainable development is done by safety tool in printing industry [14].

During the preparation of the checklist, it considers observation of the workplace environment, observation of work in progress, work in patterns, physical and social factors, maintaining conditions and basic parameters like date, machine line, operation number, location, assessed by, checked by, valid by, task/premises, activities, hazard with Yes or No option, etc.

3.2 Risk Assessment

Risk
Risk is the uncontrolled loss; it leads to potential incidents and causes injury. Jacxsens et al. have reported risk assessment done by quantitative-based challenge [15]. The

Authors that they are Reviewed the Land-Use Palnning Risk assesment in Four ways they are follow as Before the work carried out, After the work carried out and Upcoming the Future Conditions [16].

Risk Assessment

- Analyze and evaluate the risk assessment with hazards after identifying the hazards and risk factors (potential to cause harm);
- The risk assessment can help to assess the risk levels like high, medium and low from identifying the problems in the operations.
- Risk assessment helps to provide information on the consequence and likelihood of harm by the hazards.
- A combination of consequence and likelihood rate can be decided on risk assessment.

Risks Rating

- One of the easy ways to assess the risk by risk rating method is to rate the assessment of risk as high, medium or low—based on how likely causes harm and how serious harm it is. It is called risk rating.
- This method is used to evaluate the risk level by Risk Priority Number (RPN) for each hazard.

$$\textbf{Risk Rating}(\textbf{Risk score}) = \textbf{Severity rate} \times \textbf{Probability rate}$$

A. **Severity Rate**

- Severity means "HOW SERIOUS" hazardous to peoples.
- How serious harm from hazard was realized in severity.
- Severity is based on the increasing level of consequence to an individual safe, health and environmental or property.
- Severity defines as the effect on the person either injury or ill health.
- Severity rating from a minor loss to death is divided into five different categories.
- The severity rating is mentioned in the following Table 1.

B. **Probability Rate**

- Probability means "HOW LIKELY" the event occurs.
- Likelihood deciding how likely harm occurs from a hazard.
- Factors considering in likelihood include the number of times the situation occurs, duration of exposure and frequency.
- Likelihood can divide into five categories from rare cases to most likely.
- Probability of rate is mentioned in the following Table 2.

Table 1 Severity rating

Severity	Meaning	Rating
Extreme	Multiple death Destroyed property damaged	5
Major	Major property damage Fatal Burn injury	4
Moderate	Fracture Serious injury Permanent disability (Non-fatal)	3
Minor	Minor incident Not permanent injury	2
Negligible	Little consequence First aid injury	1

Table 2 Probability rating

Probability	Meaning	Rating
Most likely	Very high probability of damage (constant exposure) event is realized.	5
Likely	High probability of damage(frequent exposure) not unusual	4
Possible	Moderate probability of damage (occasional exposure) occurs sometimes in the future.	3
Unlikely	Low probability of damage(exposure) occurs after many years	2
Rare	Very low probability of damage (no reported) is never occurred	1

C. **Risk Matrix**

Corresponding severity and probability rating multiplication of value need to be considered as final risk assess value, and it is also categorized as four classes, such as low, medium, high and very high. Based on the hazards and risk present, the workplace will be analyzed and evaluated by risk matrix. Risk matrix level is given in Tables 3, 4 and 5.

3.2.1 Risk Analysis

- Table 6 shows the categories of risk level based on the risk assessment worksheet
- Table 7 mentions the corrective action plan of the workplace based on the risk score from the worksheet.

Table 3 Risk matrix

PROBABILITY RATE	SEVERITY RATE				
	Negligible 1	**Minor 2**	**Possible 3**	**Major 4**	**Extreme 5**
Most likely 5	Medium 5	High 10	High 15	Very high 20	Very high 25
Likely 4	Medium 4	Medium 8	High 12	High 16	Very high 20
Possible 3	Low 3	Medium 6	Medium 9	High 12	High 15
Unlikely 2	Low 2	Medium 4	Medium 6	Medium 8	High 10
Rare 1	Low 1	Low 2	Low 3	Medium 4	Medium 5

4 Control Measures

It is a process of elimination or reduction of hazards due to risks in the workplace or equipment. Hazards should be controlled by a hierarchy of control techniques to the risks.

The control measures **is the** final step in HIRA that deals with determining and implementing appropriate measures to control risk [9] (Fig. 3).

Evaluation: Hierarchy of control step is used for checking after the introduction of changes related to hazards and risk factors from the previous one.

Implementation: As discussed as in risk matrix chapter, (Table 5.1) very high risk action takes in urgent based on that very high risk is controlled at first (Table 8).

5 Result and Discussion

A. **Risk Level**
B. **Implementation**

From Fig. 4, the HIRA tool risk score displays low, medium, high and very high risks based on the risk matrix table corresponding to severity and probability. The low risk represents the workplace as it is a safe category, whereas the medium risk causes small and minor injury of workplace. However, the high risk causes a major injury to the workers in all of the above workplace taken into assessments. Very high risk causes the major probability of accidents in the workplace. In these HIRA Tool, it can inferenced the Grooving Operations Represents Medium amount of Risk can be Present in the workplace during before the Changes can be Implemented in that workplace. The three processes of workplaces are at a very safe level—brake chamber, valve and crank chamber.

From Fig. 5, it represents initial score and actual score during HIRA on machine

Table 4 Machining line worksheet (risk assessment worksheet)

HIRA - WORK SHEET

NAME OF THE COMPANY :AUTOMOTIVE INDUSTRY

PLANT : VALUE STREAM 1 LNE: MACHIING LINE

S. NO	LOCATION	OP. NO	OPERATION NAME	HAZARD FINDINGS	HAZARD DESCRIPTION	RISKS	RISK RATING		RISK SCORE	LEVEL OF RISKS
							S	P	M	
1	Crank Case	80	Leak Test	Absence of cylinder gap while return movement	Piston and cyclinder movement in pnematic system ,up and down operational process ,during the return state no gap may be workers finger to be damage.	Demage to human finger	3	3	9	Medium
2	Crank Case	50	VMC - drilling &Tapping	Wires are not properly routed	CNC machine number of wires are open in working space in the machine	Electric Shock	4	3	12	High
3	Crank Case	100	Washing	Actuating piston and cylinder movement in side not covered	Piston movement in cylinder towards machine,the movement excess to the machine area, so it may demage to workers in machining time.	Damage to human body	3	2	6	Medium
4	Crank Case	80	Leak Test	Presence of mannual mode operation	During Manual mode safety sensor are not in working and manual opetion only for maintenance purpose control with lock and key type, but work with manual operation is high risk.	serious injury to worker	4	5	20	Very High
5	DDSBA Flange	30	Washing and drying	Photo sensor minimum clearing distance is less than 250mm (Type 2 sensor)	To protect human hands from machine using photo guard sensor , but in the sensor clearing distance should be maintanance minimum 250mm , less then this distance may be damage the human hand.	Injury to human	4	4	16	High
6	DDSBA Flange	40	Leak Test	Absence of bottom coverage	In Leak test movements of cylinders at bottom,its not covered	Injury to human legs	2	4	8	Medium
7	DDSBA Flange	20	Marking	Absence of checking tool	Every shift starting time check the photo guard sensor to working or not by checking tool ,it absent in the place	Occur Minor accident	1	2	2	Low
8	TriStop Flange	20	Marking	Declaming Sensor not in working	Claiming and declaming process by automatically , here error on declaming	Occur major accident	4	5	20	Very High
9	E6 valve	50	Leak test	Emergency button broken	In case of any mistake , emergency button only stop the process ,now its not working	serious injury to worker	5	5	25	Very High
10	Trailer ABS Housing	80	Rotary type washing	Photo sensor minimum clearing distance is less than 200mm (Type 4)	To protect human hands from machine using photo guard sensor , but in the sensor clearing distance should be maintanance minimum 200mm , less then this distance may be damage the human hand.	Injury to human	4	4	16	High
11	Crank shaft	100	Journal Grinding	Coolant oil leaking from door while operation	Oil leaking from the machine by over flow andinsuffient to store the oil in the storage tank .	Slip to floor	3	5	15	High
12	Crank shaft	140	High pressure washing	Back side Guarding Absence	Washing sticks move with excess in back side and its not covered	Injury to human	2	2	4	Medium
13	E6 valve	50	Leak test	Absence of double hand push button	To aviod accident worker machine start by double hand push button , here its absend	Injury to human	1	1	1	Low
14	Crank shaft	140	High pressure washing	Presence of mannual mode operation key push button	During Manual mode safety sensor are not in working and manual opetion only for maintenance purpose control with lock and key type, but work with manual operation is high risk.	serious injury to worker	4	5	20	Very High
15	Crank shaft	15	Name plate marking	switchs not in specified colour	Operation switches having sperate colour for aviod confusion , but here not in specfic colour	Injury to human	1	3	3	Low
16	CYLINDER HEAD		PDI - air gun	Air leakage in housing	Excess of air may harm to workers	Minor injury	2	4	8	Medium
17	DDSBA 1	40	Ring Hose assembly	Photo guard sensor not in correct poisition	Top and bottom side photo guard sensor having some space its danger to workers	Injury to human	3	4	12	High
18	DDSBA Hub	20	Grooving	Absence of CLIA check sheet past 2 days	Check sheet followed by daily , if not proper follow the check sheet accident will happen.	property damage	5	4	20	Very High

safety. The initial score is taken before control measures, and the actual score is taken after completion of HIRA study. While comparing both, the actual score is less than the initial score. From the results, it is observed that after HIRA study, the hazards will be minimized.

Table 5 Assembly line worksheet

HIRA - WORK SHEET

NAME OF THE COMPANY :AUTOMOTIVE INDUSTRY

PLANT : VALUE STREAM 1 LINE: ASSEMBLY LINE

S. NO	LOCATION	OP. NO	OPERATION NAME	HAZARD FINDINGS	HAZARD DESCRIPTION	RISKS	RISK RATING		RISK SCORE	LEVEL OF RISKS
							S	P	M	
1	VS 1 - Assembly	-	General	Fire extinguishers placed at unmarked and improper position	fire extinguishers are placed no visible place with specific marking , in case of emergency difficult to manage	Property damage	5	3	15	High
2	VS 1 - Assembly	-	General	No emergency EXIT marking for Exit path	No exit marking in Assembly. A room with air conditioning and closed room, if any emergency exit it do be difficult	fall down	2	3	6	Medium
3	MTS 2	50 B	Performance test	Electrical panal are not closed	Many more wires are in Electrical panel , it is open condition	short circuit	4	4	16	High
4	Door cylinder	70	Lip seal assembly	Cycle start button not in green colour	Operation switches having sperate colour for aviod confusion , but here not in specfic colour	Injury to human	1	3	3	Low
5	Emergency cock 2/2	30	Valve ,Bracket assembly	Photo sensor minimum clearing distance is less than 250mm (Type 2 sensor)	To protect human hands from machine using photo guard sensor , but in the sensor clearing distance should be maintanance minimum 250mm , less then this distance may be damage the human hand.	Injury to human	4	4	16	High
6	E6 SS (Stroke sensor)	20	Upper body asembly	Photo sensor checking tool is not available	Every shift starting time check the photo guard sensor to working or not by checking tool ,it absent in the place	Occur Minor accident	1	2	2	Low
7	DDSBA 1	120	Painting	Absence of extinguisher tank.	Incase of fire to control by extinguisher , but No extinguisher tank in Painting booth.	Property damage	4	3	12	High
8	DDSBA 1	130	End piece pressing	Absence of Restart botton	If any mistake or error in operation to press thr reset button to function from starting,but no reset button in machine.	Injury to human	1	1	1	Low
9	DDSBA 1	150	Leak Test 1	Bottom Guarding is not fastened	bottom door is available ,but its not fastened. Danger to workers , because of movements in bottom of machine.	Injury to human	2	2	4	Medium
10	Breake Chamber	40	End piece pressing	Photo sensor minimum clearing distance is less than 200mm (Type 4 sensor)	To protect human hands from machine using photo guard sensor , but in the sensor clearing distance should be maintanance minimum 200mm , less then this distance may be damage the human hand.	Injury to human	4	4	16	High
11	Breake Chamber	20	NPC Sub assembly	Absence of safity guard	Permanent safety guard is needed for this operation . But safety guard is absend.	Injury to human	4	3	12	High
12	Breake Chamber	30	Clamp ring assembly	Absence of front movement guarding	Assembly the ring sometimes due to over pressure the child parts fly over .here front movement guard is absend	serious injury	5	4	20	Very high
13	Breake Chamber		End piece pressing	Absence of zebra marking at rotating parts	Rotating parts not covered by zebra label	minor injury	2	2	4	Medium
14	DDSBA 1	110	Functional leak test	In bottom rail is in unsafe condition	Movement of gauge by rail , the rail path loose connection	minor injury	2	3	6	Medium
15	DDSBA 1	180	Fork assembly	sharp edges on machines	End piece pressing by hub is sharp edged.	serious injury	4	4	16	High

Table 6 Category of risks level

Value Stream Plant 1	Low Risks	Medium Risks	High Risks	Very high Risks	No.of Risk Assessed
Machining line	3	5	5	**5**	18
Assembly line	3	4	6	**2**	15
TOTAL	6	9	11	**7**	33

Table 7 Corrective action plan

RISK	DESCRIPTION	ACTION
20-25	Critical	• A risk identifies as Very high, urgent action to control the hazards • Action taken must be recorded. • Should be monitor daily. • Notification to senior executives includes plant heads.
10-16	Serious	• A risk identifies as high, immediate action to control the hazards • Action taken must be recorded. • Should be monitor weekly. • Notification to senior manager
4-9	Moderate	• A risk identifies as a medium, controls the hazard and applies temporary measures. • Action taken must be recorded. • Must be monitor and review monthly.
1-3	Minimal	• A risk identifies as low risk and considers as an acceptable level • Little or no impact • Should be monitor on quarterly • No explicit action is required.

Fig. 3 Hierarchy controls

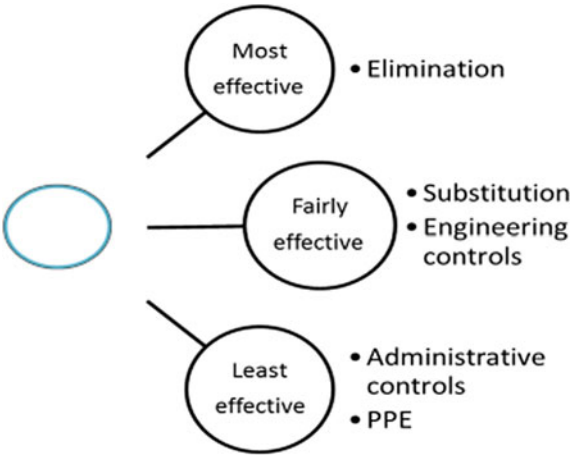

6 Conclusion

The consolidated risk score of each activity can be minimized using the HIRA tool in the automotive industry manufacturing process. All the workplaces are monitored intensely and assessed the risk before implementation and after implementation. From that HIRA tool, it identifies serious potential hazard that causes severe injury in all the process. The work checklist has been prepared based on machining line and operating line. Those checklists have been used for the HIRA tool. It is done based on the risk assessment comparison like before and after the implementation of the tool. The HIRA tool is found to minimize the hazards through the implementation of control measures provided by the tool.

Table 8 Implementation of HIRA

LINE	Location	Operation Name	Op. no	Hazard findings	Initial score			Level of risks	Control measures	Actual score.			Level of risks
					S	P	M			S	P	M	
ML	Crankcase	Leak test	80	Presence of manual mode operation	4	5	20	Very high	The maintenance team has to act and cut of the manual mode in the control panel (by elimination).	1	2	2	Low
ML	Tri stop flange	Marking	20	Declaiming Sensor not in working	4	5	20	Very high	To stop the work and put the tag system and service the sensor problem by engineering control	1	1	1	Low
ML	E6 valve	Leak test	50	Emergency button broken	5	5	25	Very high	Stop the machine and service by the maintenance department to change the new button.	1	2	2	Low
ML	Crankshaft	High pressure Washing	140	Presence of manual mode operation	4	5	20	Very high	The maintenance team has to act and cut of the manual mode in the control panel by elimination	1	2	2	Low
ML	DDSBA Hub	Grooving	20	Absence of CLIA check sheet past 2 days	5	4	20	Very high	Prepare Check sheet includes all safety point of view inspection and implemented by line in charge	2	2	4	Medium
AL	Brake Chamber	Clamp ring assembly	30	Absence of front movement guarding	5	4	20	Very high	Provide the safety guard on the front of the machine by engineering control	1	2	2	Low
AL	DDSBA 1	Fork assembly	180	sharp edges on machines	5	4	20	Very high	To remove the parts or replace them with a normal corner surface to that place.	1	1	1	Low.

ML-Machining line 1 AL-Assembly line 1 S-Severity l P-Probability l M –Risk matrix Score.

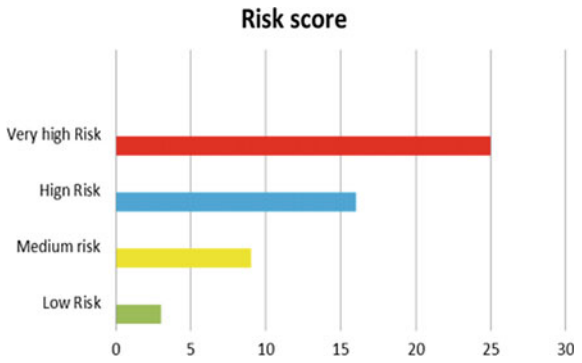

Fig. 4 Risk level

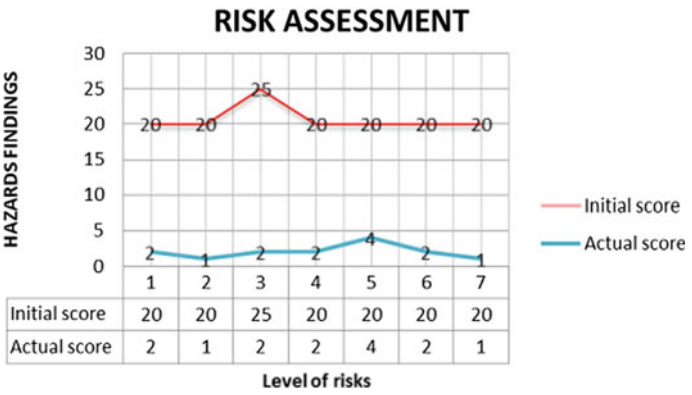

	1	2	3	4	5	6	7
Initial score	20	20	25	20	20	20	20
Actual score	2	1	2	2	4	2	1

Fig. 5 Risk assessment

References

1. Ramesh R et al (2017) Hazard identification and risk assessment in automotive industry. Int J ChemTech Res 10(4):352–358
2. Bambang S, et al (2018) Analysis of the potential hazard identification and risk assessment (HIRA) and hazard operability study (HAZOP): case study. Int J Eng Technol 7(3, 24):1–7
3. Khairul Akmal S, Che Ani MN, Ismail AK (2015) Investigation the effective of the hazard identification, risk assessment and determining control (HIRADC) in manufacturing process. Int J Innov Res Adv Eng 2(8):80–84
4. Etherton JR (2007) Industrial machine systems risk assessment: a critical review of concepts and methods. Risk Anal Int J 27(1):71–82
5. Magdalena M (2018) Analysis of production incompatibilities and risk level in series production of assembly elements for the automotive industry. In: MATEC web of conferences, vol 183. EDP Sciences
6. Rajpradeesh T, et al (2019) Hazard identification on cabtrim in manufacturing industry. In: AIP conference proceedings, vol 2128, no 1. AIP Publishing
7. Khan FI, Abbasi SA (1998) Techniques and methodologies for risk analysis in chemical process industries. J Loss Prev Process Ind 11(4):261–277
8. Paithankar A (2011) Hazard identification and risk analysis in mining industry. Dissertation
9. Purohit DP, et al (2018) Hazard identification and risk assessment in construction industry. Int J Appl Eng Res 13(10):7639–7667
10. Papazoglou IA et al (2003) I-risk: development of an integrated technical and management risk methodology for chemical installations. J Loss Prev Process Ind 16(6):575–591
11. Suhardi B, et al (2018) Analysis of the potential hazard identification and risk assessment (HIRA) and hazard operability study (HAZOP): case study. Int J Eng Technol 7(3, 24):1–7
12. Chinniah Y, Aucourt B, Bourbonnière R (2017) Safety of industrial machinery in reduced risk conditions. Saf Sci 93:152–161
13. Erbay Barbaros, Özkan Coşkun (2018) Fuzzy FMEA application combined with fuzzy cognitive maps to manage the risks of a software project. Eur J Eng Formal Sci 2(2):6–21
14. Kiurski J, et al (2012) Register of hazardous materials in printing industry as a tool for sustainable development management. Renew Sustain Energy Rev 16(1):660–667
15. Jacxsens L, Uyttendaele M, De Meulenaer B (2016) Challenges in risk assessment: quantitative risk assessment. Procedia Food Sci 6:23–30
16. Pasman H, Reniers G (2014) Past, present and future of quantitative risk assessment (QRA) and the incentive it obtained from land-use planning (LUP). J Loss Prev Process Ind 28:2–9

Machining of Metal Matrix Composite Using Abrasive Water Jet Machine

E. Soundrapandian, A. Tajdeen, K. Kamal Basha, and P. Vivekkumar

Abstract Abrasive water jet machining (AWJM) is one of the unconventional machining processes, in which the material is removed by the impact of high-pressure water, along with entrained abrasives. The input parameters involved in the AWJM system are water jet pressure, abrasive flow rate, orifice diameter, nozzle diameter, particle size of the abrasive, abrasive type, etc. Metal matrix composites (MMC) are widely used in the industries such as automobile, defense and aerospace. This work is an attempt to study on machinability of aluminum alloy 7074 (Al 7074) reinforcement with 10% silicon carbide (SiC) particulate. AWJM experiments were conducted on trapezoidal-shaped metal matrix composite by varying abrasive mesh size, abrasive flow rate, water jet pressure and traverse rate to obtain higher material removal rate, depth of cut and better surface finish. The experiments are carried out based on response surface methodology (RSM) designed using Box–Behnken method for four parameters into three levels. Using response surface graph, the significant AWJM machining parameters and their levels are identified to achieve higher material removal rate, depth of cut and better surface finish.

Keywords Abrasive water jet machining · Metal matrix composite · Machinability · Response surface methodology

1 Introduction

In abrasive water jet machining, kerf top width and taper angle were influenced by the parameters such as transverse speed, standoff distance and mass flow rate [1]. The standoff distance has a predominant influence on the workpiece quality, and also the RMS and ACS values are lower when machining lower thickness workpiece [2]. In order to evaluate the Ra on the machined surface of MMC, increased in Ra value was observed due to increase in water jet pressure [3]. In the cases

E. Soundrapandian (✉) · A. Tajdeen · K. K. Basha · P. Vivekkumar
Department of Mechanical Engineering, Bannari Amman Institute of Technology, Sathyamangalam, Erode 638401, Tamil Nadu, India
e-mail: soundrapandian@bitsathy.ac.in

G. Kumaresan et al. (eds.), *Advances in Materials Research*, Springer Proceedings in Materials 5, https://doi.org/10.1007/978-981-15-8319-3_30

of slot cutting and piercing in MMC, the kerf taper will increase with increase in transfer rate and particle size but in the case of piercing kerf taper increases with increase in standoff distance [4]. On varying the abrasive mass flow rate, abrasive mesh size and jet impact angles on MMC found that erosion rate increases with increase in jet impact angles [5]. In machining of MMC, the depth of cut is higher when the mesh size is lesser due to lesser kinetic energy of the smaller size aggregate [6]. The machining aspects of MMCs were carried out in various non-conventional machining processes such as EDM, laser cutting and AWJM; in AWJM the mechanism of material removal was observed as ductile shearing and also there were no thermal damage and burr formation in the AWJM [7]. The process parameters of AWJM greatly influence its machining performance. It is widely classified into four types, namely [8] abrasive parameters: abrasive mass flow rate, abrasive size distribution, abrasive particle shape, diameter and hardness, etc.; [9] cutting parameters: standoff distance, impact angle, number of passes, traverse rate, etc.; mixing chamber and acceleration parameters: focusing nozzle length, focusing nozzle inside diameter, etc., and [10–12] hydraulic parameters: water flow rate, pump pressure, orifice diameter, etc. Each of these parameters has been investigated by several researchers using experimental trials and their optimum values have been found. These values become indispensable when one advances toward condition monitoring [13]. For any process to be completely automated and monitored, an in-depth understanding of the interaction between the machine, workpiece and tool is required. Hence, condition monitoring of AWJM is of primary importance for full automation. Condition monitoring is the continuous/periodic verification of few or all parameters of the system. It is usual to make sure that all system components are performing in close agreement to the optimum level or as a fault detection system [14, 15]. A comprehensive review on major research activity carried out so far by several researchers on condition monitoring of AWJM is also discussed here.

2 Experiment Details

2.1 MMC Casting Procedures

An electric furnace is used for preheating the reinforcements, and electric resistance furnace is used for melting the matrix material. MMCs are made by liquid-state stir casing process. The stir casting furnace is used for preheating the reinforcement of Si at the temperature of 700 °C. The trapezoid-shaped die is used for preparing the workpieces. The size of the workpieces is 10 mm diameter rods. Casted component (Al7074 alloy with 10% of SiC) is a poured in trapezoid-shaped die.

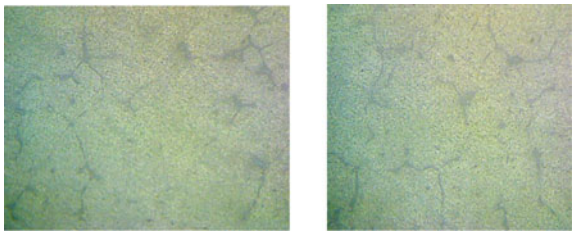

Fig. 1 Optical micrographs of MMCS

a)Al 7074 + 10% SiC **b)Al 7074 + 10% SiC**

2.2 Microstructure

To study the microstructure of the specimens, they were cut and prepared as per the standard metallographic procedure. The specimen plates were prepared by grinding through 600 mesh size grit abrasives. Velvet cloth was polished by using 240, 400, 600 and 1000 mesh size to get the fine surface finish. After that specimens were further polished by using Nital reagent (etched). All these specimens were kept in dry air. The microstructure etched specimens were observed using optical microscope. The presence of SiC in the composites materials has been identified using microscope images captured with (Dewinter Metallurgical Microscope). It is observed from Fig. 1 the uniform distribution of SiC particles. This can be attributed to the effective stirring action and the use of appropriate process parameter.

2.3 Response Surface Methodology (RSM)

In this technique, the main objective is to optimize the response surface that is influenced by various process parameters. RSM also quantifies the relationship between the controllable input parameters and the obtained response surfaces.

If all variables are assumed to be measurable, the response surface can be expressed as follows:

$$Y = f(X_1, X_2, \ldots, X_n)$$

where

Y is the answer of the system and is the variable of action called factors.

The goal is to optimize the response variable y. In this work, the response y is MRR and Ra.

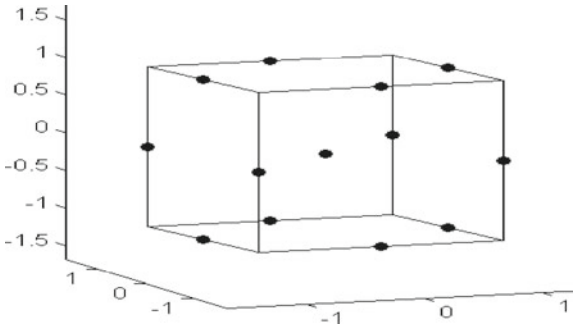

Fig. 2 Box–Behnken design

2.4 Box–Behnken Design

In this study, the Box–Behnken experimental design was chosen for finding out optimized WEDT parameters and regression equations which gives the relationship between the response functions (MRR and Ra) and variables pulse on time, voltage, spindle speed and pulse off time. Box–Behnken design is rotatable second-order designs based on three-level fractional factorial designs. The geometry of a Box–Behnken design is shown in Fig. 2.

Reason for the selection of Box–Behnken design over central composite design is for fewer no. of input factors (here four) and lesser no. of experiments are required than central composite design.

2.5 Level Input Parameter Using RSM

See Tables 1 and 2.

3 Result and Discussion

See Table 3.

Table 1 AWJM input parameters

S. No.	Description	Low	Medium	High
1	Water jet pressure (MPa)	124	200	274
2	Abrasive flow rate (g/min)	240	340	440
3	Abrasive mesh size (#)	80	100	120
4	Traverse speed (mm/min)	60	90	120

Table 2 Observation results

S. No.	Abrasive mesh size (#)	Abrasive flow rate (g/min)	Water jet pressure (Mpa)	Traverse rate (mm/min)	Metal removal rate (mm^3/min)	Depth of cut (mm)	Kerf tapper angle (°)	Surface roughness (μm)
1	80	240	200	90	677	20.04	0.1	4.067
2	120	240	200	90	491	14.44	0.2	3.047
3	80	440	200	90	844	24.03	0.0	3.647
4	120	440	200	90	423	14.4	0.1	2.32
4	100	340	124	60	410	18.24	0.1	2.708
6	100	340	274	60	422	23.18	0.1	3.294
7	100	340	124	120	402	11.14	0.2	3.479
8	100	340	274	120	409	11.3	0.3	3.377
9	80	340	200	60	424	23.27	0.2	3.383
10	120	340	200	60	230	10.2	0.2	3.032
11	80	340	200	120	423	9.4	0.4	2.367
12	120	340	200	120	414	9.21	0.4	2.44
13	100	240	124	90	440	13.33	0.2	3.969
14	100	440	124	90	442	13.39	0.1	2.397
14	100	240	274	90	444	13.14	0.2	3.439
16	100	440	274	90	443	16.1	0.2	3.012
17	80	340	124	90	400	14.82	0.2	3.424
18	120	340	124	90	374	11.1	0.2	3.27
19	80	340	274	90	447	16.2	0.1	3.449
20	120	340	274	90	343	10.14	0.2	2.647
21	100	240	200	60	333	14.8	0.1	3.114
22	100	440	200	60	340	14.1	0.2	3.197
23	100	240	200	120	371	8.24	0.4	2.716
24	100	440	200	120	619	13.76	0.4	3.447
24	100	340	200	90	474	14.06	0.3	4.727
26	100	340	200	90	491	14.44	0.3	2.342
27	100	340	200	90	491	14.44	0.2	2.444
28	100	340	200	90	407	14.03	0.2	3.146
29	100	340	200	90	491	14.44	0.3	3.889

3.1 Response Surface Methodology

See Fig. 3.

Table 3 Box–Benkhen L29 I/O parameter

S. No.	Abrasive mesh size (#)	Abrasive flow rate (g/min)	Water jet pressure (MPa)	Traverse rate (mm/min)	Metal removal rate (mm^3/min) Al + 10% SiC	DoC (mm)	Surface roughness (μm)
1	80–120	240–440	125	60	647.448	22.354	2.21
2	80–120	240–440	200	60	630.845	25.919	2.21
3	80–120	240–440	275	60	615.327	28.701	2.42
4	80–120	240–440	125	90	457.579	19.080	2.51
5	80–120	240–440	200	90	591.829	21.447	2.59
6	80–120	240–440	275	90	626.155	23.032	2.72
7	80–120	240–440	125	120	381.547	13.961	2.68
8	80–120	240–440	200	120	527.505	15.131	2.58
9	80–120	240–440	275	120	590.015	15.518	2.29
10	80–120	240	125–275	60	631.011	25.391	2.84
11	80–120	340	125–275	60	612.223	26.076	2.59
12	80–120	440	125–275	60	624.928	28.701	2.21
13	80–120	240	125–275	90	521.571	17.157	2.75
14	80–120	340	125–275	90	558.8	19.105	2.73
15	80–120	440	125–275	90	627.376	23.032	2.51
16	80–120	240	125–275	120	373.165	11.601	2.21
17	80–120	340	125–275	120	466.296	11.436	2.36
18	80–120	440	125–275	120	590.015	15.518	2.54
19	80–120	240	125	60–120	586.69	21.934	3.30
20	80–120	240	200	60–120	630.845	24.054	2.75
21	80–120	240	275	60–120	534.283	25.391	2.21
22	80–120	340	125	60–120	534.023	21.174	2.59
23	80–120	340	200	60–120	609.134	24.017	2.58
24	80–120	340	275	60–120	584.321	26.076	2.36
25	80–120	440	125	60–120	503.117	22.354	2.21
26	80–120	440	200	60–120	609.575	25.919	2.23
27	80–120	440	275	60–120	627.851	28.701	2.42
28	80	240–440	125–275	60	631.011	28.701	2.55
29	100	240–440	125–275	60	393.444	20.192	2.37
30	120	240–440	125–275	60	192.263	13.482	2.21
31	80	240–440	125–275	90	627.376	22.853	2.98
32	100	240–440	125–275	90	467.009	17.651	2.97
33	120	240–440	125–275	90	343.035	13.507	2.53

(continued)

Table 3 (continued)

S. No.	Abrasive mesh size (#)	Abrasive flow rate (g/min)	Water jet pressure (MPa)	Traverse rate (mm/min)	Metal removal rate (mm^3/min) Al + 10% SiC	DoC (mm)	Surface roughness (μm)
34	80	240–440	125–275	120	590.015	15.518	2.77
35	100	240–440	125–275	120	537.946	13.669	2.67
36	120	240–440	125–275	120	521.431	13.311	3.37
37	80	240–440	125	60–120	586.69	22.354	2.56
38	100	240–440	125	60–120	367.856	16.601	2.41
39	120	240–440	125	60–120	381.547	13.211	2.12
40	80	240–440	200	60–120	630.845	25.919	3.24
41	100	240–440	200	60–120	497.521	18.138	2.81
42	120	240–440	200	60–120	498.8	13.389	2.22
43	80	240–440	275	60–120	627.851	28.701	2.87
44	100	240–440	275	60–120	537.441	20.192	2.67
45	120	240–440	275	60–120	516.13	13.518	2.31
46	80	240	125–275	60–120	631.011	25.391	2.78
47	100	240	125–275	60–120	397.42	18.892	2.71
48	120	240	125–275	60–120	364.411	13.482	2.23
49	80	340	125–275	60–120	612.298	26.076	3.43
50	100	340	125–275	60–120	428.849	18.572	2.92

3.2 Analysis of MRR for Al 7075 + 10% SiC

Table 3 (S. No. 1–9) indicates that MRR values are achieved by varying abrasive mesh size (#80–#120) and abrasive flow rate (240–440 g/min), while water jet pressure and traverse rate are varied at different levels of combinations. Among the combinations, it is observed that high water jet pressure and low traverse rate result in high MRR of 647 mm^3/min. From the analysis (Table 3, S. No. 1–54 and Fig. 4), it is observed that the combinations of input process parameter and their levels such as low abrasive mesh size, high abrasive flow rate, high water jet pressure and low traverse rate result in high MRR(648 mm^3/min) for Al 7075 + 10% SiC. It is observed that higher MRR is achieved with size (#80) and lower MRR is achieved with size (#120). Due to the fact that smaller size of abrasive is likely to possess lesser kinetic energy than resulting in lower MRR, higher size of abrasive is likely to possess higher kinetic energy than resulting in higher MRR.

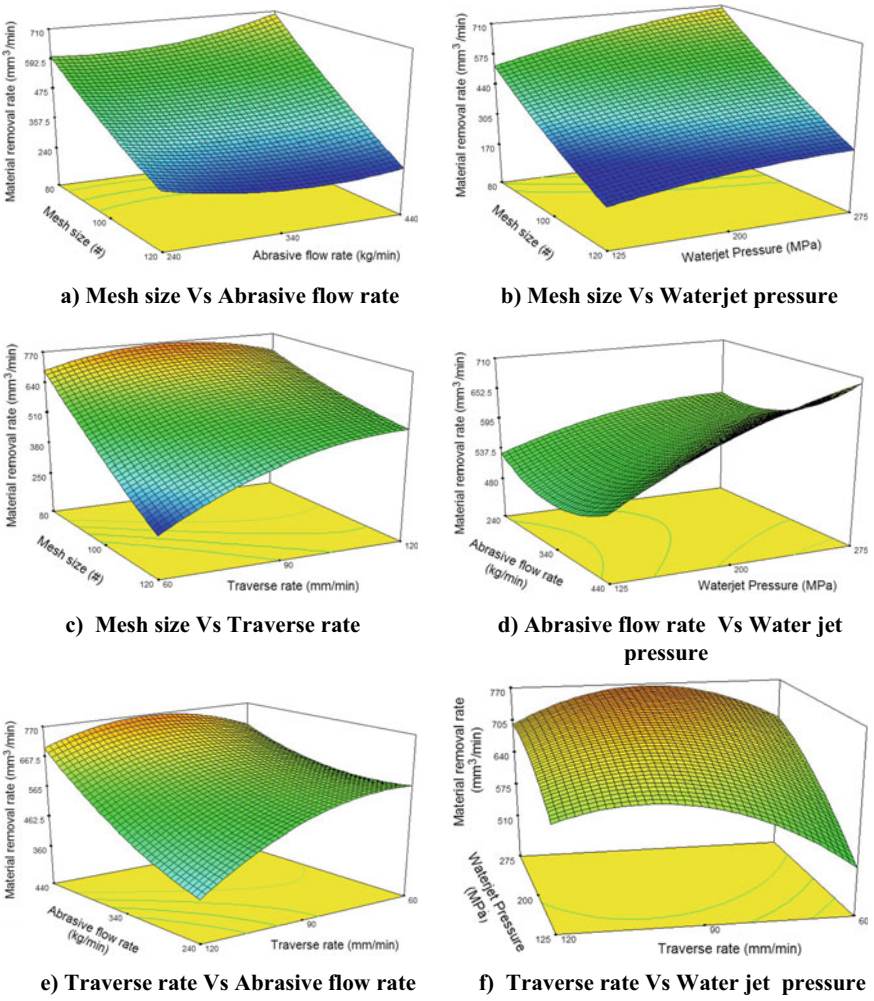

a) Mesh size Vs Abrasive flow rate

b) Mesh size Vs Waterjet pressure

c) Mesh size Vs Traverse rate

d) Abrasive flow rate Vs Water jet pressure

e) Traverse rate Vs Abrasive flow rate

f) Traverse rate Vs Water jet pressure

Fig. 3 Response surface of MRR (Al 7075 + 10% SiC) for various combinations

The relationship between the input process parameter and the response (MRR) for MMC is expressed in the form of regression equation, and it is given below.

$$\begin{aligned}\text{MRR Al 7075} + 10\%\ \text{SiC} = {} & +3977.58 - (28.00 * \text{MS}) - (5.43 * \text{AFR}) \\ & + (4.98 * \text{WP}) - (24.21 * \text{TR}) - (8.14\text{E} - 003 * \text{MS} * \text{AFR}) \\ & - (0.030 * \text{MS} * \text{WP}) + (0.25 * \text{MS} * \text{TR}) + (8.25\text{E} - 004 * \text{AFR} * \text{WP}) \\ & + (0.031 * \text{AFR} * \text{TR}) + (0.025 * \text{WP} * \text{TR}) - (0.015 * \text{MS2}) \\ & + (3.42\text{E} - 003 * \text{AFR2}) - (0.015 * \text{WP2}) - (0.079 * \text{TR2})\end{aligned}$$

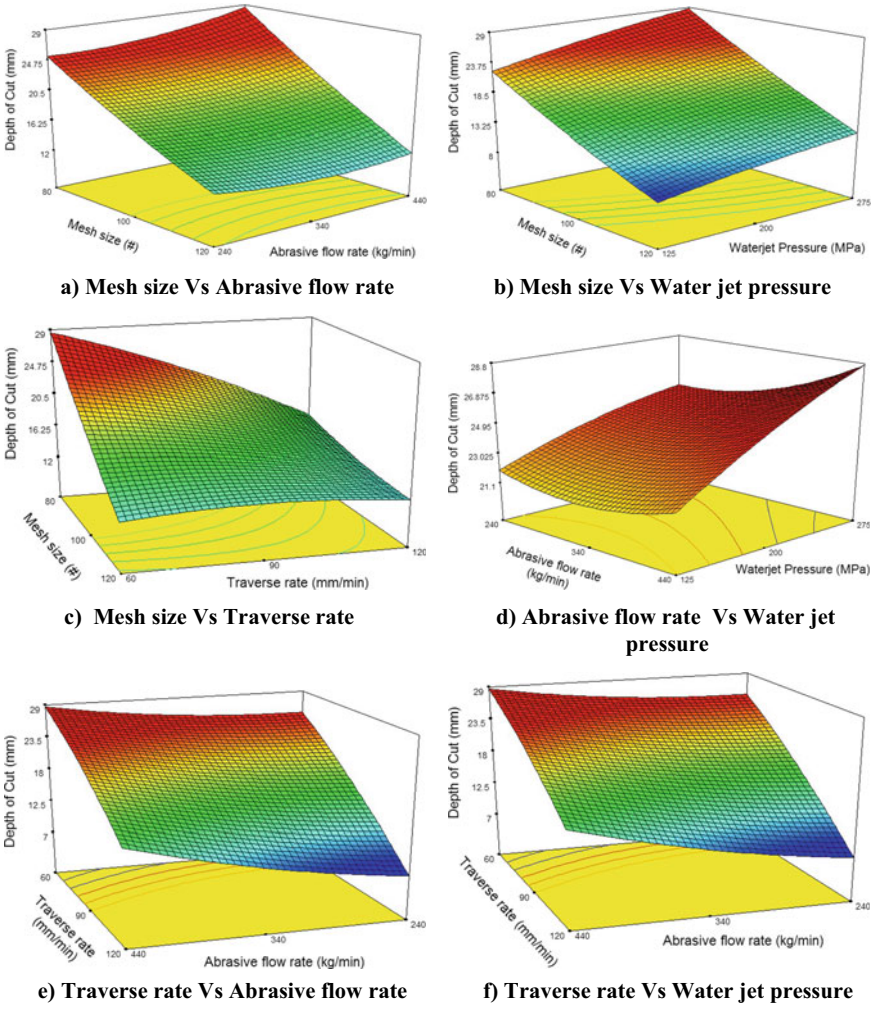

a) Mesh size Vs Abrasive flow rate

b) Mesh size Vs Water jet pressure

c) Mesh size Vs Traverse rate

d) Abrasive flow rate Vs Water jet pressure

e) Traverse rate Vs Abrasive flow rate

f) Traverse rate Vs Water jet pressure

Fig. 4 Response surface of DoC (Al 7075 + 10% SiC) for various combinations

3.3 Analysis of DoC for Al 7075 + 10%SiC

Table 5 (S. No. 1–9) indicates that DOC values are achieved by varying abrasive mesh size (#80–#120) and abrasive flow rate (240–440 g/min), while water jet pressure and traverse rate are varied at different levels of combinations. Among the combinations, it is observed that high water jet pressure and low traverse rate result in high DOC of 29 mm (Table 3 S. No. 3). Due to the fact that smaller size of abrasive is likely to possess lesser kinetic energy than resulting in lower DOC, higher size of abrasive is likely to possess higher kinetic energy than resulting in higher DOC. Similarly,

Table 4 Analysis of variance table for MRR (Al 7075 + SiC 10%)

Source	Sum of squares	d*f*	Mean square	*F* value	*p*-value prob > *F*	
Model	368.628	14	26.3302	3.209775	0.0184	Significant
A-abrasive-e mesh	120.7771	1	120.7771	14.72329	0.0018	
B-AFR	18.1548	1	18.1548	2.213155	0.1590	
C-water pressure	5.400208	1	5.400208	0.658311	0.4307	
D-reverse rate	145.0465	1	145.0465	17.68185	0.0009	
AB	4.0401	1	4.0401	0.492507	0.4943	
AC	1.357225	1	1.357225	0.165452	0.6903	
AD	41.4736	1	41.4736	5.055826	0.0412	
BC	2.088025	1	2.088025	0.25454	0.6217	
BD	6.786025	1	6.786025	0.827248	0.3785	
CD	5.736025	1	5.736025	0.699248	0.4171	
A^2	1.812327	1	1.812327	0.220931	0.6456	
B^2	6.101038	1	6.101038	0.743745	0.4030	
C^2	0.993775	1	0.993775	0.121146	0.7330	
D^2	5.522035	1	5.522035	0.673162	0.4257	
Residual	114.8438	14	8.20313			
Lack of Fit	114.3733	10	11.43733	97.23971	0.0002	Significant
Pure Error	0.47048	4	0.11762			
Cor Total	483.4666	28				

it is observed that increased water jet pressure and decreased traverse rate lead to increased DOC and further observed that increases in abrasive flow rate and abrasive particle size result in higher DOC.

3.4 Analysis of Surface Roughness for Al 7075 + 10% SiC

Table 6 (S. No. 1–9) indicates that fine surface finish values are achieved by varying abrasive mesh size (#80 – #120) and abrasive flow rate (240–440 g/min. From the analysis (Table6, S. No. 1–54 and Fig. 5), it is observed that the combinations of input process parameter and their levels such as low abrasive mesh size, high abrasive flow rate, high water jet pressure and low traverse rate result in better surface finish (2.1 μm) for Al 7075 + 10% SiC. Due to the fact that smaller size of abrasive is likely to possess lesser kinetic energy than resulting in better Surface finish, higher size of abrasive is likely to possess higher kinetic energy than resulting in better surface

Table 5 Analysis of variance table for DoC (Al 7075 + SiC 10%)

Source	Sum of squares	d*f*	Mean square	*F* value	*p*-value Prob > *F*	
Model	368.6228	14	26.3302	3.209775	0.0184	Significant
A-abrasive mesh	120.7771	1	120.7771	14.72329	0.0018	
B-AFR	18.1548	1	18.1548	2.213155	0.1590	
C-water pressure	5.400208	1	5.400208	0.658311	0.4307	
D-reaverse rate	145.0465	1	145.0465	17.68185	0.0009	
AB	4.0401	1	4.0401	0.492507	0.4943	
AC	1.357225	1	1.357225	0.165452	0.6903	
AD	41.4736	1	41.4736	5.055826	0.0412	
BC	2.088025	1	2.088025	0.25454	0.6217	
BD	6.786025	1	6.786025	0.827248	0.3785	
CD	5.736025	1	5.736025	0.699248	0.4171	
A^2	1.812327	1	1.812327	0.220931	0.6456	
B^2	6.101038	1	6.101038	0.743745	0.4030	
C^2	0.993775	1	0.993775	0.121146	0.7330	
D^2	5.522035	1	5.522035	0.673162	0.4257	
Residual	114.8438	14	8.20313			
Lack of Fit	114.3733	10	11.43733	97.23971	0.0002	Significant
Pure Error	0.47048	4	0.11762			
Cor Total	483.4666	28				

finish. Similarly, it is observed that increased water jet pressure and decreased traverse rate lead to better surface finish, and further observed that increases in abrasive flow rate and abrasive particle size result in better Surface finish.

4 Conclusion

In this present work, an attempt is made to investigate the material removal rate, depth of cut and surface roughness of AWJM, for various input parameters. In this study, aluminum alloy (AL7075) is reinforced with 10% SiC by using stir casting process. The experiments are conducted using RSM with Box–Behnken design. The signification AWJM process parameters and their levels are identified for achieving

Table 6 Analysis of variance table for surface roughness

Source	Sum of squares	d*f*	Mean square	*F* value	*p*-value Prob > *F*	
Model	2.938214	14	0.209872	0.434522	0.9346	significant
A-abrasive mesh	1.198272	1	1.198272	2.480917	0.1376	
B-AFR	0.449694	1	0.449694	0.931052	0.3510	
C-water pressure	0.000533	1	0.000533	0.001104	0.9740	
D-reverse rate	0.052404	1	0.052404	0.108498	0.7467	
AB	0.026732	1	0.026732	0.055347	0.8174	
AC	0.107912	1	0.107912	0.223423	0.6437	
AD	0.044944	1	0.044944	0.093053	0.7648	
BC	0.273006	1	0.273006	0.565235	0.4646	
BD	0.14402	1	0.14402	0.298181	0.5936	
CD	0.118336	1	0.118336	0.245004	0.6283	
A^2	0.155436	1	0.155436	0.321816	0.5795	
B^2	0.000167	1	0.000167	0.000346	0.9854	
C^2	0.004624	1	0.004624	0.009574	0.9234	
D^2	0.364878	1	0.364878	0.755447	0.3994	
Residual	6.761939	14	0.482996			
Lack of Fit	2.893358	10	0.289336	0.299165	0.9446	Significant
Pure Error	3.868581	4	0.967145			
Cor Total	9.700153	28				

higher MRR, DoC and fine surface roughness. This investigation revealed the choice of #80 mesh size garnet for achieving the higher MRR of AWJM in Al7075 + SiC. MMCs can depend on the size of SiC particulate in MMCs. Hence, the combinations of input process parameter and their levels are recommended for higher MRR from the analysis of optimal value that are abrasive mesh size (#80), abrasive flow rate (440 g/min), water jet pressure (275 MPa) and traverse rate (60 mm/min), and the minimum MRR can be achieved by high abrasive mesh size (#120), abrasive flow rate (240 g/min), water jet pressure (125 MPa) and traverse rate (120 mm/min). Similarly, higher DoC is achieved with size (#80) and lower DoC is achieved with size (#120). Due to the fact that smaller size of abrasive is likely to possess lesser kinetic energy than resulting in lower DoC, higher size of abrasive is likely to possess higher kinetic energy than resulting in higher DoC. Similarly, it is observed that increased water jet pressure and decreased traverse rate lead to increase DoC, and further observed that increases in abrasive flow rate and abrasive particle size (μm) result in higher DoC. It is observed that better surface finish is achieved with size (#80), and rough surface finish is achieved with size (#120). Due to the fact that

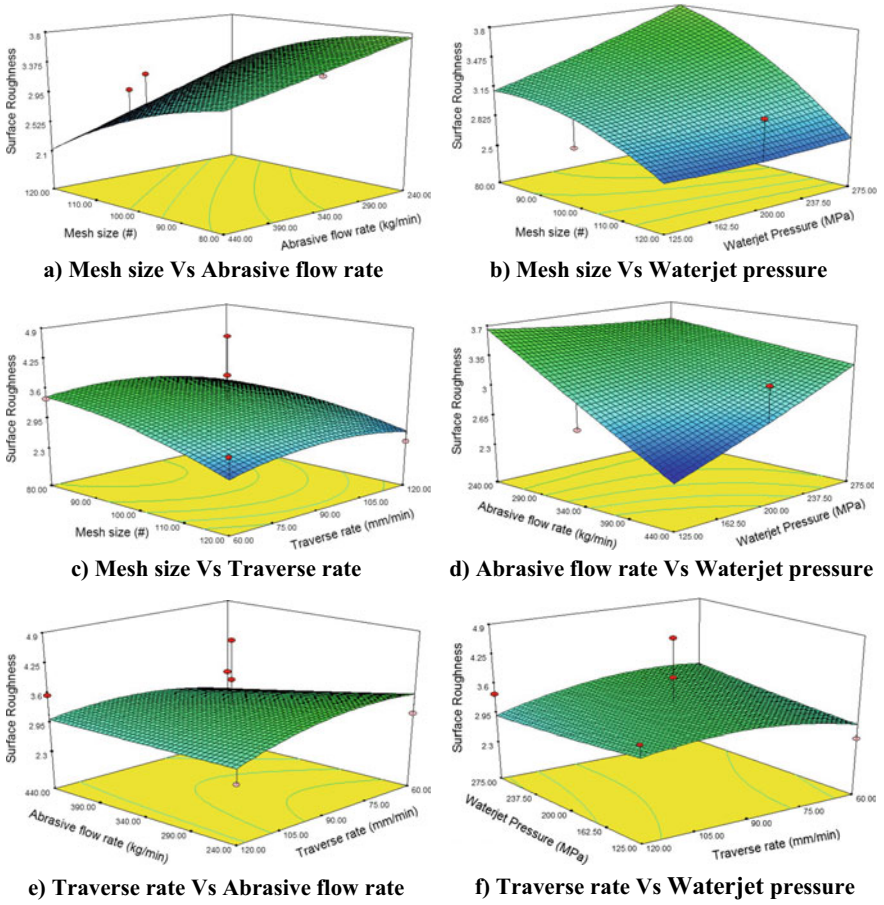

a) Mesh size Vs Abrasive flow rate

b) Mesh size Vs Waterjet pressure

c) Mesh size Vs Traverse rate

d) Abrasive flow rate Vs Waterjet pressure

e) Traverse rate Vs Abrasive flow rate

f) Traverse rate Vs Waterjet pressure

Fig. 5 Response surface of surface roughness (Al 7075 + 10% SiC) for various combinations

smaller size of abrasive is likely to possess lesser kinetic energy than resulting in better surface finish, higher size of abrasive is likely to possess higher kinetic energy than resulting in better surface finish. Similarly, it is observed that increased water jet pressure and decreased traverse rate lead to better surface finish, and further observed that increases in abrasive flow rate and abrasive particle size result in better surface finish.

References

1. Shukla R (2017) Experimentation investigation of abrasive water jet machining parameters using Taguchi and evolutionary optimization techniques. Swarm Evol Comput 32:167–183

2. Jurisevic B (2004) Monitoring of abrasive water jet (AWJ) cutting using sound detection. Int J Adv Manuf Technol 24:733–737
3. Savrun E (1988) Surface characterization of SiC whisker/2124 aluminum and Al_2O_3 composites machined by abrasive waterjet. J Mater Sci 23:1453–1458
4. Hamatani G (1990) Machinability of high temperature composites by abrasive waterjet. J Eng Mater Technol 318–386
5. Ramulu M, Raju SP (1993) Hydro-abrasive erosion characteristic of 30 vol%SiC/6061-T6 Al composite at shallow impact angles. Wear 166:55–63
6. Srinivas S, Rameshbabu N (2011) Role of garnet and silicon carbide in abrasive waterjet of aluminum-silicon carbide particulate metal matrix composites. Int J Appl Res Mech Eng 109–122
7. Muller F, Monaghan J (2000) Non-conventional machining of particle reinforced metal matrix composite. Int J Mach Tools Manuf 1351–1366
8. Momber AW, Kovacevic R (1998) Principle of abrasive waterjet machining. Springer, London
9. Kovacevic R, Hashish M, Mohan R, Ramulu M, Kim TJ, Geskin ES (1997) State of the art of research and development in abrasive waterjet machining . Trans ASME J Manuf Sci Eng 119:776–785
10. Hashish M (1989) A model for abrasive water jet (AWJ) machining. Trans ASME J Eng Mater Technol 3:154–162
11. Kovacevic R, Fang M (1994) Modeling of the influence of the abrasive waterjet cutting parameters on the depth of cut based on fuzzy rules. Int J Mach Tools Manuf 55–72
12. Fredin J, Jonsson A (2011) Experimentation on piercing with abrasive waterjet. World Acad Sci, Eng Technol 5:11–21
13. Brandt C, Louis H, Meier G, Tebbing G (1994) Abrasive suspension jets at working pressures up to 200MPs. Jet Cut Technol, Allen, pp 489–509
14. Kovacevic R (1991) A new sensing system to monitor Abrasive waterjet nozzle wear. J Mater Process Technol 28:117–125
15. Kovacevic R (1992) Monitoring the depth of the waterjet penetration. Int J Mach Tools Manuf 32:725–736

Design and Automation of Shell Facing Machine

A. Tajdeen, E. Soundrapandian, E. Sakthivelmurugan, S. Nachimuthu, P. Dinesh, and S. Praveenkumar

Abstract As production industries strive to remain competitive, they are also seeking to improve efficiency. Today's manufacturing environment has pushed companies into a constant search for improved production and better management. Each company needs a unique product flow. The flow depicts each step a product goes through from start to finish. Every conservation is one of the most important factor considerations of each and every production industries. In the production industries, the operations are carried out by different methods. It is used for the purpose of increased productivity, improved the working more safety to operators reduction in power consumption. In valve stem seals production industries, after pressing, lathe is used for shell facing operation. The objective is to reduce the time consumption, fatigue of laboratory our and manual work. In the existing process of companies, the shell is loading, unloading, and facing manually in lathe. By the design of the new machine, the productivity could be improved and so the production target could be achieved easily. For that, we designed fully automated machine for shell facing process. Production is increased and man power is reduced; those man powers are effectively used for other process.

Keywords Shell facing · Automation · Sheet metal pressing · Fatigue · Manual work

1 Introduction

In the assembly, components such as punches and dies, automotive components, precision tools, valve body, etc., require high accuracy and precision. So, to meet these requirements, lead to introduction of semi-automatic and automatic machines. In conventional CNC lathe, the piezoelectric-based fast tool servo was mounted in

A. Tajdeen (✉) · E. Soundrapandian · E. Sakthivelmurugan · S. Nachimuthu · P. Dinesh · S. Praveenkumar
Department of Mechanical Engineering, Bannari Amman Institute of Technology, Sathyamangalam, Erode, Tamil Nadu 638401, India
e-mail: tajdeena@bitsathy.ac.in

G. Kumaresan et al. (eds.), *Advances in Materials Research*, Springer Proceedings in Materials 5, https://doi.org/10.1007/978-981-15-8319-3_31

same CNC lathes turrets for precision turning operation. The conventional CNC lathe is used to semi-turning on a shaft and piezoelectric-based fast tool servo is used to finish turning which is mounted on the same CNC lathe's turret. During cutting, cutting force disturbances were compensated by sliding mode controller [1]. The simple and compact design features are used for solid flexures to transmit motion from a high voltage piezo-stack actuator to single-axis piezo-based fast tool servo turning tool assembly. Finite element analysis models and analytical of the flexures were designed with actuator that has a 38 μm stroke, 370 N/μm stiffness, and 3200 Hz natural frequency. Cutting force disturbances and piezo-ceramic nonlinearity during step turning, taper turning, and profile turning are machined to verify the control commend [2].

Nowadays, complex shape products required high precision and accuracy. So products can be produced by latest technology machines. In our country, there are many conventional lathe machines in idle condition. By retrofitting methodology, these conventional lathe machines were converting into semi-automatic control lathe machine or automatic control lathe machine. In conversion and changing stages are required three portions, such as mechanical, electronics, and hydraulic. In initial stage of retrofitting ball screw in place of lead screw for better accuracy and remove some unnecessary component like gears for providing space for motors. Hydraulic circuits installed for cooling purpose and stepper/servo motor for Z and X axis for efficient operation [3]. All kinds of vehicles are using brake components, for making brake components required CNC machines but which is very costly compared to a conventional lathe. Implementing the automation and control in conventional lathe, we achieve Just in Time (JIT) concept and also increase the productivity. Pneumatic actuators were used to automate the conventional lathe in very economical manner [4]. Retrofitting is anticipated benefits include a lower cost investment compared to purchasing a new machine. In retrofitting, typically includes the repair or replacement of some worn mechanical components such as ball screws, lubrication pumps, safety interlocks, guards, hoses, belts, and electrical wiring [5]. Lathe machine is the oldest machine as compare to the all other conventional machines. The drilling operation can be done using tailstock mechanism of conventional lathe machine [6]. In leveling machine, the exiting laser-based-controlled machine redesigned through a mechanical design was adapted for automation. Mechanization and automation works are carried out to improve the operational efficiency of the laser-controlled land leveling machines and to design a more precise, ergonomic, economical, and reliable system [7].

The batch production in small- and medium-scale industries, tool, and mold making was required computer-based shop floor control. To achieve more production with high quality, it is necessary to empower the human skills with latest technology and automation to create synergetic effects [8]. In my work, the shell facing machine was designed and automated for small size of shells. The detailed process was explained in this paper.

Fig. 1 Shell

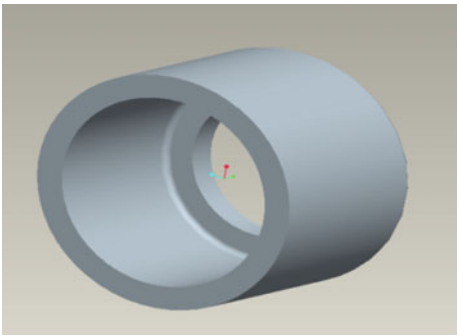

Table 1 Specification of shell

S. No.	Description	Size in mm
1	Outer diameter (OD)	10.2
2	Inner diameter (ID)	6
3	Thickness (t)	2
4	Height (H)	6.6

2 Problem Identification

2.1 Product Description

Many industries manufacture the valve stem seals; it consists of three major components, and they are shell, rubber, and springs. To manufacture shell components, the received raw material sheets are pressed to form the shell component. Variations in the shell height are corrected by turning in the lathe. However, for smaller shell components are very tedious and it is difficult to load and unload the shell and perform manual turning for height correction. To overcome this problem, we have taken care for ease of manufacturing the component. Figure 1 shows 3D view of the shell and Table 1 gives the specification of the shell.

2.2 Shell Facing Preparation

Figure 2 shows the various steps involved in the valve stem seals manufacturing. The pressing operation is the stage 1 process followed by shell facing operation stage 2 which is indicated with red color; this shell facing operation involves loading, fixing, facing, and unloading. These processes consumes more time because it is a very small component, so loading and unloading are difficult one. Our objective is to automate the machine for the shell so that turning process of shells can be done in a single machine irrespective of the size and it will be a cost effective one.

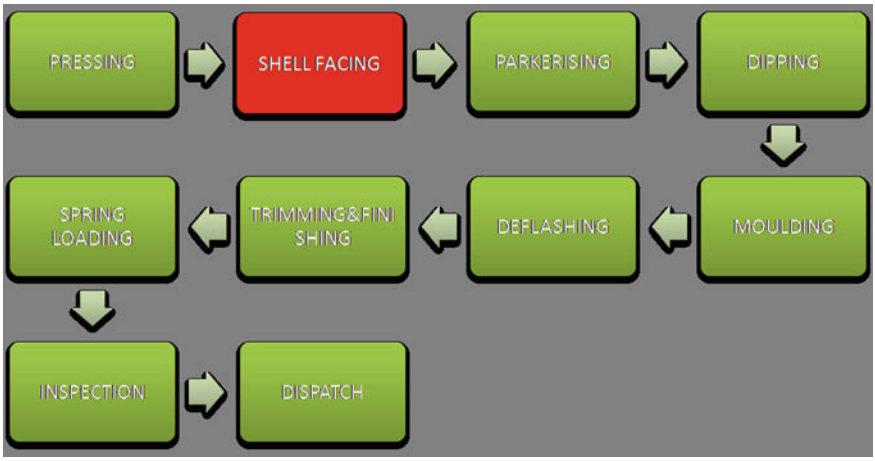

Fig. 2 Shell facing operation

3 Existing Methodology

3.1 Conventional Lathe for Shell Facing Operation

In conventional lathe, the pressed shell component was loaded on the lathe by a manual spring mechanism. Then, the tool is engaged using a lever mechanism and brought closer to the shell. After turning is over, the lever is disengaged and the tool is retracted, to unload the shell component. This process steps were repeated. Figure 3 shows the exiting conventional lathe used for shell facing.

Fig. 3 Shell facing lathe

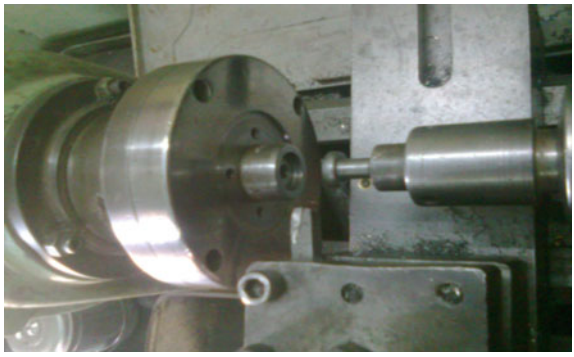

3.2 Analyzing the Problems in Conventional Lathe

In existing, conventional lathe is modified with manual spring back mechanism instead of tail stock and lever mechanism added in tool post carriage. So, production rate is low because it required skilled persons to operate that lathe. The targets are not achieved because more time consumption and continuous work energy is needed for operating this lathe.

4 Operational Analysis and Automation

4.1 Automation in Conventional Lathe (Design Trial-1)

Small automation is carried out in lathe tail stock and cross slide by using pneumatic cylinders. While testing this design, we experienced difficulties in loading as the shell has to be positioned axially. So we are looking for an alternate design which could eliminate this loading problem. Figure 4 shows the modified conventional lathe.

Disadvantages

- Skilled operator is needed
- Continuous work energy is needed
- Difficult to the load shell in axially
- Difficult to automate the tail stock
- Impossible to be fully automated.

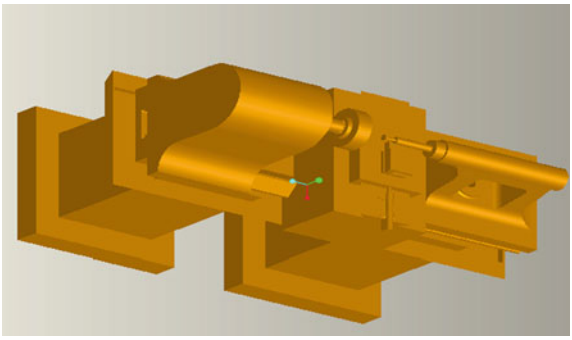

Fig. 4 Conventional lathe after retrofitting

4.2 Shell Facing Machine—New Design for Automation (Design Trial 2)

After pressing, the shells are put in the vibrator. The function of vibrator is to carry the work pieces to the shell facing machine. The shell facing machine is controlled by Programmable Logic Controller (PLC) and it works by receiving the signal from sensors. The work pieces in the vibrator are brought near the loading gripper one by one. These jobs are aligned in a row by using the vibration which helps the gripper to load the work piece easily.

Now, the loading gripper picks the job at the tip of the vibrator then the loading pillar is raised by the PLC signal. The loading cylinder moves the piston toward the spindle mounting and it places the job. Then the gripper retracts by the cylinder to its original position. When the job is loaded in the mounting, the vertical loader senses the signal and it starts moving down to clamp the job. At this moment, the facing tool is in forward position and the chamfering tool is in inward position. Now, the vertical loader holds the job and the facing of the job is done in the retract motion of the facing tool cylinder. When the facing is done simultaneously, the chamfering tool chamfers the shell in its forward motion. Now both the operation is finished and the vertical loader moves upward. As in the initial stage, the facing tool is forwarded and chamfering tool is retracted. At the same time, the unloading cylinder picks the shell from the spindle mounting and drops it in the slope which leads to the collecting tray. Figure 5 shows the automated shell facing machine and Fig. 6 shows detailed views of automated shell facing machine.

5 Design Specification

5.1 Design Specifications of Automated Machine

The following are the design specifications for the automated machine

- Stroke length for loading cylinder = up to 150 mm
- Stroke length for unloading cylinder = up to 150 mm
- Stroke length for vertical loading cylinder = up to 50 mm
- Stroke length for facing tool cylinder = up to 10 mm
- Stroke length for chamfering tool cylinder = up to 10 mm
- Stroke length for gripper = up to 10 mm.

6 Results and Discussions

While comparing the proposed design to existing methodology, the manpower is reduced and this leads to increase the production. The comparison is shown as below

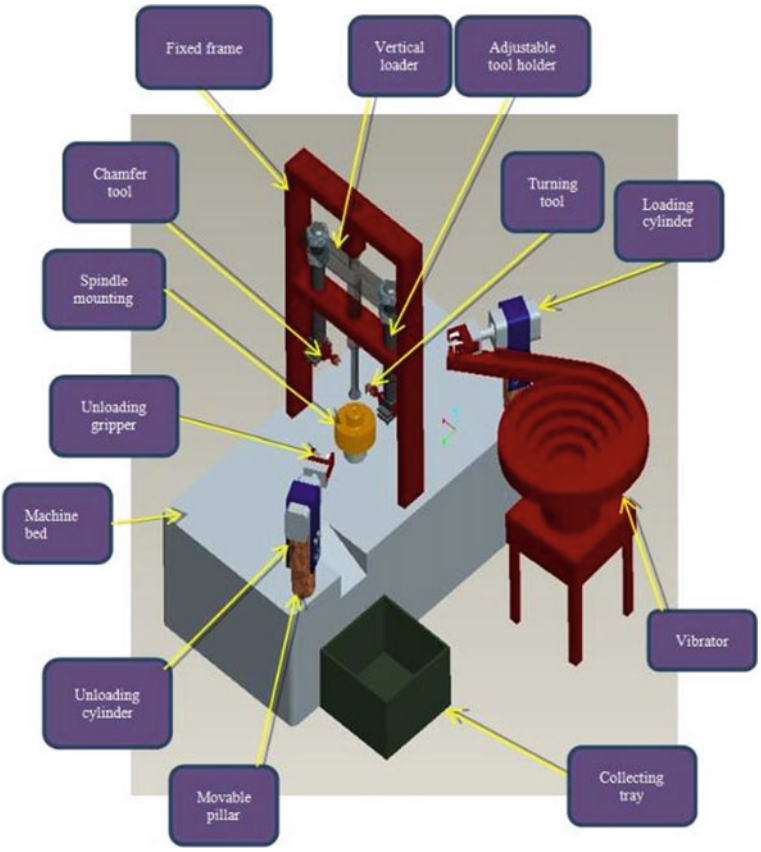

Fig. 5 Automated shell facing machine

6.1 Production Improvements

In the conventional machine, 4000 shell components are produced per shift. But, in the proposed design more than 6000 components are produced per shift with lesser manpower. The output of the existing and proposed design is depicted in Fig. 7.

In proposed new design will produce 6000 and more components per shift with very minimum man power.

6.2 Manpower Reduction

The conventional machine requires continuous manpower to operate the machine. But, in the proposed design continuous manpower is not required to operate the

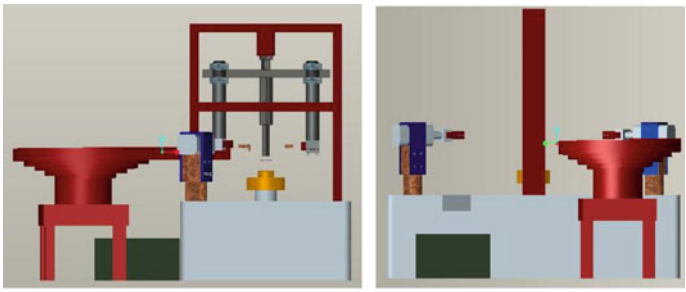

Front View Side View

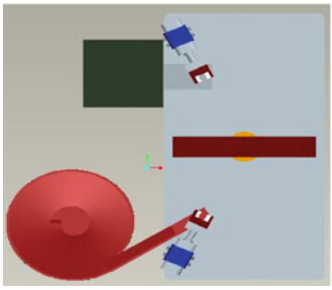

Top view

Fig. 6 Detailed view of automated shell facing machine

Fig. 7 Output chart

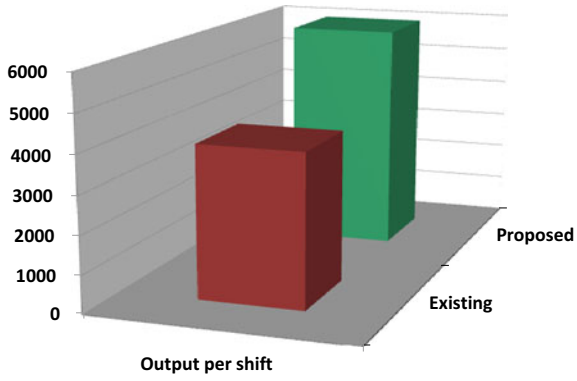

machine. The manpower requirement is only for monitoring and troubleshooting purposes in the proposed design. The manpower requirement for existing and proposed design is depicted in Fig. 8.

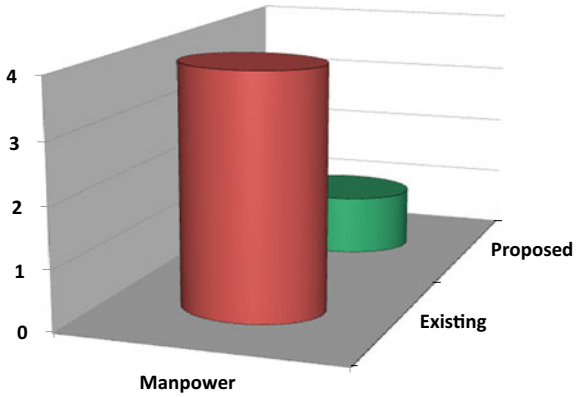

Fig. 8 Manpower chart

7 Conclusion

In conventional machines can be avoided for shell components because of less production due to time consumption, production target is difficult to achieve, difficult to reduce manpower, and difficulty in achieving the quality.

In this work, fully automated shell facing machine was designed to reduce the man power without affecting the productivity. By these automation,

- The cycle time is reduced
- Production rate is increased
- Man power is reduced
- Unskilled operator can work easily
- Easy to operate
- Occupies less space
- The machine was designed with lesser weight.

References

1. Zhu W-H, Jun MB, Altintas Y (2001) A fast tool servo design for precision turning of shafts on conventional CNC lathes. Int J Mach Tools Manuf 41:953–965
2. Woronko A, Huang J, Altintas Y (2003) Piezoelectric tool actuator for precision machining on conventional CNC turning centers. Int J Precis Eng 27:335–345
3. Parmar PN, Gondalia VR, Mehta NC (2014) Review on advance automation of conventional lathe machine. Int J Eng Dev Res 2:2452–2456
4. Abhishek, Kumar D, Karthik A, Ajay (2017) Automation of lathe using pneumatic actuators. Int J Mech Eng Technol 8:419–425
5. Pagar HA, Jadhav DC, Mandalik SM, Patil HS, Shinde KU (2016) Enhancement in conventional lathe machine. Int Res J Eng Technol 3:497–499
6. Rana CP, Gandhi HN, Patel SH, Soni SS (2017) Drilling by tailstock mechanism of conventional lathe machine—review. IJARII 3:119–127

7. Irsel G, Tahir Altinbalik M (2018) Adaptation of tilt adjustment and tracking force automation system on a laser-controlled land leveling machine. Int J Comput Electron Agric 150:374–386
8. Erbe H-H (2002) Low cost intelligent automation in manufacturing. In: 15th triennial world congress, Barcelona, pp 373–378

Experimental Study of Electrochemical Micromachining on Titanium (Ti–6Al–4V) Alloy

P. Vivekkumar, E. Soundrapandian, A. Tajdeen, and T. Prashanth

Abstract Electrochemical machining is an unconventional process where metal removal takes place due to the action of electrochemical process. ECM is used to process extremely hard material which is difficult to machine using conventional machining process. Titanium grade 5 has very good application in aerospace and medical industry. Performing micromachining operation on titanium is very difficult using conventional process. Therefore, electrochemical micromachining is done to perform machining operation with less external force, thus avoiding tool wear. An attempt has been made in this project to optimize the parameters like voltage, electrolyte concentration and frequency to achieve geometric accuracy and better surface finish (R_a). Machined material was scanned using microscopic system to measure conicity and overcut of the drilled hole, and profilometer was used to measure surface roughness of the machined surface to determine the optimum machining parameter. Taguchi Analysis of Variance was performed to determine each parameter influence over material removal rate, circularity and overcut of drilled hole. From the above experimental work, electrolyte concentration plays a vital role among the electrolyte concentration, voltage and frequency in material removal rate, as acidic nature of the electrolyte affects the machining/material removal rate. Voltage ranks first in affecting conicity of the drilled hole among the three input parameters. Optimum input parameters were determined by carrying out S/N ratio analysis with respect to MRR and conicity. A linear regression model was developed with respect to deviation occurrence with the mean, which is also simulated with programming tool to generalize the model development.

Keywords Electrochemical machining · Surface finish · Taguchi · Conicity

P. Vivekkumar (✉) · E. Soundrapandian · A. Tajdeen · T. Prashanth
Department of Mechanical Engineering, Bannari Amman Institute of Technology, Erode 638401, Tamil Nadu, India
e-mail: vivekkumar@bitsathy.ac.in

G. Kumaresan et al. (eds.), *Advances in Materials Research*, Springer Proceedings in Materials 5, https://doi.org/10.1007/978-981-15-8319-3_32

1 Introduction

Micromachining is the process of removing material in micron level of measurement in the form of chips or debris. The various techniques which are employed for the manufacturing of microproducts are microelectromechanical systems (MEMS). The manufacturing technique uses photolithography, plating, chemical etching, laser fabrication and LIGA [1], while non-MEMS-based manufacturing process often uses techniques such as laser drilling, electrical discharge machining (EDM), mechanical machining, laser cutting, electrochemical machining (ECM), laser patterning, embossing, injection molding, forging, extrusion and stamping [2]. Among the various capable techniques, electrochemical micromachining (EMM) is considered for its advantages such as high material removal rate (MRR), and small forces acting on the workpiece are required as well as low stresses and better accuracy [3, 4]. In electrochemical machining (ECM), metal removal takes place due to the action of electrochemical process. This kind of machining is preferred for machining hard materials which cannot be machined using conventional machining process [5]. The main barrier in implementing this kind of machining process is material which is electrically conductive and can alone be used [6]. ECM can be used to machine small, intricate contours or cavities in hard, exotic metals and odd-shaped angles such as titanium aluminides, cobalt Inconel, Waspaloy, rhenium alloys and high nickel [7].

ECM is capable of machining both external and internal geometry. ECM is characterized as reverse electroplating, i.e., it is a subtractive process [8]. Both the ECM and EDM are similar in their working principle where electric current is allowed to pass through between an electrode and the part to be machined, due to which electrolytic material removal process having a negatively charged electrode acts as a cathode, a dielectric fluid (electrolyte) and a conductive workpiece acts as a anode; however, in ECM there is no tool wear. MRR is main parameter to evaluate the efficiency of unconventional machining process [9, 10]. In ECM, the metal removal occurs due to the atomic dissolution of the workpiece material.

From Faraday's first law for electrochemical dissolution, the quantity of electrochemical dissolution used is directly proportional to the quantity of charge passed through the electrochemical cell [11]

$$m \propto Q, \tag{1}$$

where $m =$ mass of the material dissolved, and

$Q =$ amount of the charge passed through the electrochemical cell.

From the second law states, the amount of material dissolved further depends on the electrochemical equivalence (ECE) of the material

$$m \propto \text{ECE} \propto \frac{A}{v} \tag{2}$$

.

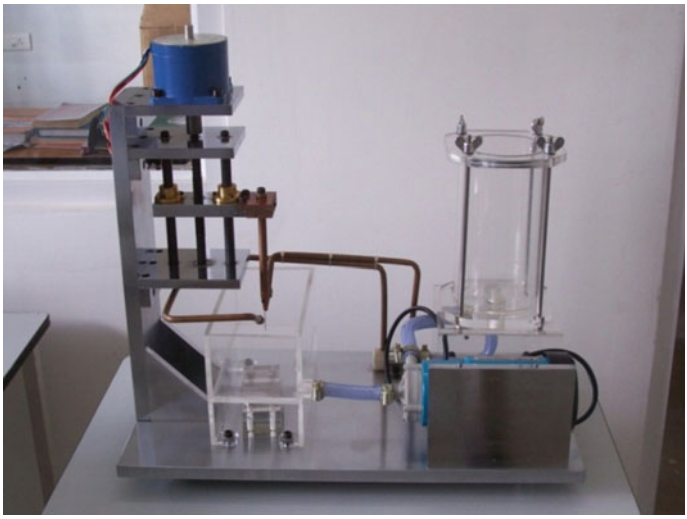

Fig. 1 Photographic view of the ECMM setup

2 Experimental Setup

Fig. 1 shows the experimental setup of the electrochemical machining. It has a five-phase step motor with an accuracy of 0.1 μm.

3 Design of Experiments

Taguchi's L9 orthogonal array was used to carry out in machining, which helps to determine the optimum and best responsive factor in less number of trials [12, 13].

3.1 Design of Experiment for Ecmm

Steps involved in defining the DOE of our experiments are as follows,

1. Choosing the independent variables,
2. Fixing of orthogonal array,
3. Allocating the independent variables,
4. Experimentation,
5. Analyze the data,
6. Inference.

Table 1 Process parameters and its level

Level	Process parameters		
	A (voltage)	B (concentration)	C (frequency)
1	18	0.05	40
2	19	0.075	60
3	20	0.1	80

3.2 Process Parameter and Its Level

Prior to selecting the orthogonal array, the number of experiments to be conducted will be defined based on the total number of degrees of freedom. It is found that the minimum number of experiments to assess the factors be more than the total DOF available. The number of degrees of freedom related to each factor study is less than the number of levels available for that factor [14].

Table 1 tabulates the three study parameters and its levels of experiments that are carried out in this project to determine the high response factor and also the optimum value.

3.3 Selection of An Orthogonal Array

Orthogonal array requires only a few number of experimental trails to find out the important factors which has an effect on system output. The minimum number of experiments to be conducted before selecting orthogonal array to be finalized based on Taguchi's Eq. (3)

$$N \text{ Taguchi} = 1 + \sum_{(i=1)}^{NV} (Li - 1) \tag{3}$$

N Taguchi = No. of experiments

NV = No. of testing parameters

L = No. of levels

For our work

We take $NV = 3$ and $L = 3$

$$\text{Then will be } N \text{ Taguchi} = 1 + 4(3 - 1) = 9 \tag{4}$$

From the above calculation, it is found that nine experiments to be conducted based on orthogonal array (OA) are to be selected which has at least nine rows.

Table 2 Input parameters for machining

Voltage	Concentration (Molar)	Frequency (Hz)	Duty cycle	Pulse		Current (A)
				ON	OFF	
18	0.05	40	50	12.5	12.5	4
19	0.05	60	60	10	6.67	4
20	0.05	80	70	8.75	3.75	4
18	0.1	60	70	11.66	4.99	4
19	0.1	80	50	6.25	6.25	4
20	0.1	40	60	15	10	4
18	0.075	80	60	7.5	5	4
19	0.075	40	70	17.5	7.5	4
20	0.075	60	50	8.33	8.33	4

The standard orthogonal arrays which are commonly used in the design of experiments are as follows:

1. 2-level arrays: L4, L8, L12, L16, L32,
2. 3-level arrays: L9, L18, L27,
3. 4-level arrays: L16, L32.

Input Parameter

Electrochemical micromachining was carried out, following L9 orthogonal array, by which nine experiments were carried as shown in Table 2.

Voltage and concentration ranges are varied based on the experiments that are studied over other materials. But, frequency (Hz), duty cycle and pulse on and off time are interrelated. Another major and influencing input parameter that is varied in this experiment was electrolyte concentration.

4 Results and Discussions

4.1 Inference from the Experiment

Electrochemical micromachining was performed, and base material was observed under microscope to measure diameter to determine the conicity and overcuts. Difference in weight of the base material was measured to calculate the MRR, and analysis was carried out using Taguchi to determine the influencing parameter [15].

Table 3 MRR calculation

Exp. No.	Time (s)	Initial weight	Final Weight	Initial wt − Final wt	MRR per s (g/s)
1	1224	3.7311	3.5942	0.137	0.000112
2	1083.6	3.4633	3.3108	0.153	0.000141
3	965.4	3.4867	3.4427	0.044	4.56E−05
4	241.2	3.5215	3.4783	0.043	0.000179
5	456.6	3.5789	3.5036	0.075	0.000165
6	223.2	3.5680	3.5300	0.038	0.00017
7	578.4	2.9341	2.9024	0.032	5.49E−05
8	514.8	3.2036	3.1758	0.028	5.41E−05
9	631.8	3.2907	3.2690	0.022	3.45E−05

4.2 Material Removal Rate

MRR is defined as the rate at which material is removed from the workpiece during machining.

Material removal rate is calculated based on Eq. 5

$$\text{MRR} = \frac{\text{Intialweight} - \text{finalweight}}{\text{time}} (\text{g/s}) \tag{5}$$

Equation (5) was substituted in the nine experiments to get material removal rate as shown in Table 3.

Time denotes the time taken to machine or drill single workpiece. From the overall observation of Table 3, it is clear that MRR moves in increasing trend when concentration is increased.

4.3 Conicity

Conicity is defined as the degree of straightness of the through hole that was machined. Conicity is preferred to be zero for effective and straight through hole. Conicity is explained as shown in Figs. 2, 3 and 4.

Base material was observed under microscope, to measure conicity. Below shown are the images of the material that was machined using ECMM.

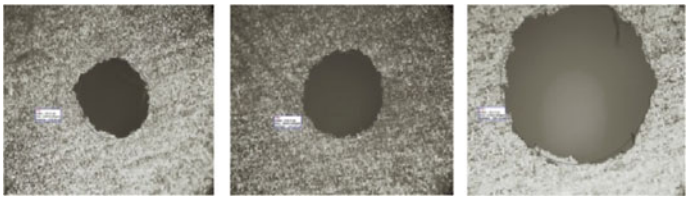

Fig. 2 Microscopic image (0.05 molar concentration)

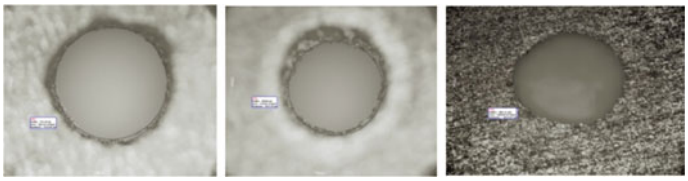

Fig. 3 Microscopic image (0.075 molar concentration)

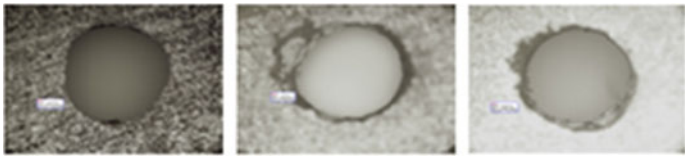

Fig. 4 Microscopic image (0.1 molar concentration)

5 Conclusion

- Base material purchased was tested for its chemical composition, and it is listed in Table 3. Machining was carried out by which micro-hole was machined.
- It is found that concentration influences the most for MRR, i.e., concentration influences about 87% and remaining 13% from voltage, frequency and current.
- Voltage and frequency influence the equal percentage in conicity, i.e., equal of about 40% each.
- Similarly, for overcut, concentration plays a major role, contributing about 78%, by which it is suggested that concentration selection is most important in electrochemical machining of titanium grade 5.
- In addition to the parameter influenced study, a generalized linear model was developed based on the response characteristics to the supplied input characteristic. This process of developing a model was simulated using a developer software tool for L9 orthogonal array with three-level inputs.

References

1. Bhattacharyya B, Malapati M, Munda J (2005) Experimental study on electrochemical micromachining. J Mat Proc Tech 169(3):485–492
2. Bahre D, Weber O, Rebschlager A (2013) Investigation on pulse electrochemical machining characteristics of lamellar cast iron using a response surface methodology-based approach. Procedia CIRP 6:362–367
3. Ghoshal B, Bhattacharyya B (2013) Influence of vibration on micro-tool fabrication by electrochemical machining. Int J Mach Tools Manuf 64:49–59
4. Kozak J, Rajurkar KP, Makkar Y (2004) Selected problems of micro-electrochemical machining. J Mater Process Technol 149(2004):426–431
5. Fang JC, Jin ZC, Xu WJ, Shi YY (2002) Magnetic electrochemical finishing machining. J Mater Process Technol 282–287
6. Koyano T, Kunieda M (2013) Ultra-short pulse ECM using electrostatic induction feeding method. Procedia CIRP 6:390–394
7. Holstein N, Krauss W, Konys J (2011) Development of novel tungsten processing technologies for electro-chemical machining (ECM) of plasma facing components. Fusion Eng Des 86(2011):1611–1615
8. Mi D, Natsu W (2015) Proposal of ECM method for holes with complex internal features bycontrolling conductive area ratio along tool electrode. Prec Eng 42(2015):179–186
9. Das MK, Kumar K, Barman TK (2014) Optimization of surface roughness and MRR in electrochemical machining of EN31 tool steel using Grey-Taguchi approach. Procedia Mater Sci 6:729–740
10. Bahre D, Weber O, Rebschlager A (2013) Investigation on pulse electrochemical machining characteristics of lamellar cast iron using a response surface methodology based approach. Procedia CIRP 6:363–368
11. Klocke F, Zeisa M, Harsta S, Klinka A, Veselovaca D, Baumgärtner M (2013) Modeling and simulation of the electrochemical machining (ECM) material removal process for the manufacture of aero engine components
12. Das MK, Kumar K, Barman TK, Sahoo P (2014) Optimization of surface roughness and MRR in electrochemical machining of EN31 tool steel using Grey-Taguchi approach 729–740
13. Nagaraju N, Venkatesu S, Ujwala NG (2018) Optimization of process parameters of EDM process using fuzzy logic and taguchi methods for improving material removal rate and surface finish 7420–7428
14. De Silva A, McGeough JA (1998) Process monitoring of electrochemical machining. J Mater Process Technol 76:165–169
15. Datta M (1998) Microfabrication by electrochemical metal removal. IBM J Res Dev 42(5):655–669

Simulation and Analysis with Material Optimization of Automobile Suspension Using Multi-body Dynamic

S. Deepankumar, B. Saravanan, D. Yuvaraj, T. Ramesh Kumar, M. Sureshkumar, and K. Vinoth Simmon

Abstract Suspension system is considered as one of the most critical systems in automobile vehicles. This project aims to calculate multi-axial forces acting on various linkages of McPherson suspension system. Multi-body dynamics concept is used for the calculation of multi-axial forces acting on suspension system. The obtained forces are verified by using analytical calculation for its accuracy. Since steering knuckle is a main automotive component that requires a lot of attention in taking care of it, the effect on forces acting on strut mount, lower ball joint, steering tie rod and wheel axis on the steering knuckle is analyzed. Structural analysis of the steering knuckle is performed to research and analyze the impact of the multi-axial forces acting on the steering knuckle. Further, it is subjected to impact and fatigue loads due to the uneven road surface. Hence, impact analysis is performed to support the design. Vibration is an important characteristics of automobile vehicle component. It should not be a resonance frequency. It greatly influences the component life and performance. So, it has to consider the vibration characteristics of component. Hence, modal analysis is performed to predict the behavior of steering knuckle under vibration. The results of the above analysis provide a foundation for optimization of suspension components.

Keywords Multi-body dynamics · Steering knuckle · Link forces · Modeling · Vibration

1 Introduction

In this time of constant advancement in assembling part, plan and weight streamlining is the prime goal. This goal is lead to the improvement of different metal

S. Deepankumar (✉) · B. Saravanan · D. Yuvaraj · T. Ramesh Kumar · M. Sureshkumar · K. V. Simmon
Department of Automobile Engineering, Bannari Amman Institute of Technology, Sathyamangalam, Erode, Tamil Nadu 638401, India
e-mail: deepanauto@gmail.com

G. Kumaresan et al. (eds.), *Advances in Materials Research*, Springer Proceedings in Materials 5, https://doi.org/10.1007/978-981-15-8319-3_33

amalgams and composite materials. As a material, mechanical properties and assembling parameters assume definitive jobs, and the shortcomings and qualities of each assembling procedure should be accessible to planners in these regards, to empower them to pick the ideal decision for the particular segment and application [1].

In car industry, the critical increment of the interest for lighter, more eco-friendly vehicles, diminished plan testing cycles and tasteful dependability level has advanced the selection of ideal materials and parts. The present pattern in the car business is to deliver safe yet lightweight vehicles [2]. To accomplish this objective with at least costly model testing, new structures must be researched logically as far as quality and weakness disappointment. In car, suspension and controlling framework is in charge of giving ride solace and soundness. The exhibition of both the frameworks relies upon the presentation of directing knuckle which consolidations both the frameworks [3].

Directing knuckle is one of the principal parts utilized in controlling frameworks of cars, and they are exposed to a huge number of fluctuating anxieties cycles prompting the exhaustion disappointment. Because of the basic usefulness of directing knuckle, its structure just as weight streamlining is required [4].

This need requests the exhaustive investigation and understanding the conduct of directing knuckle under static and weakness loads. In this way, the static and weakness examination of the controlling knuckle will fill in as the establishment for the utilization of elective materials, for example, aluminum amalgams and composite materials [5].

To accomplish the previously mentioned things, the current steering knuckle force count is significant one. The goal is that we ascertaining the multi-body dynamic simulation and analysis of automobile suspension system [6].

2 Selection of Suspension System

MacPherson suspension system is a most common suspension used in all commercial cars. Steering knuckle is a critical component in the suspension system, which is used to control the stability of the vehicle. Riding comfort and stability are the important factors for driving the vehicle, and these can be considerably achieved by optimizing the shape and size of the steering knuckle. Figure 1 shows MacPherson suspension system and its attachments [7].

3 Geometric Modeling of Compact Car Suspension System

Suspension system model is developed by using SolidWorks software, which is shown in Fig. 2.

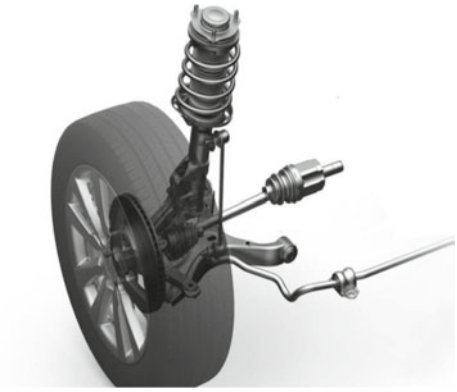

Fig. 1 MacPherson strut suspension

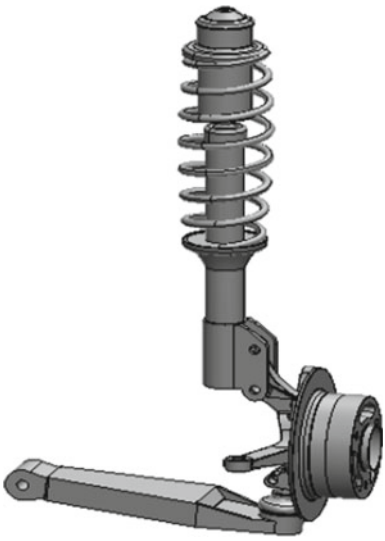

Fig. 2 Model of compact car suspension component

3.1 Lateral Load Transfer

While cornering, load transfer takes place from the inside pair of wheels to the outer wheels. This is termed as lateral load transfer. Thus, the outer tires are subjected to maximum lateral force [8], which is shown in Fig. 3.

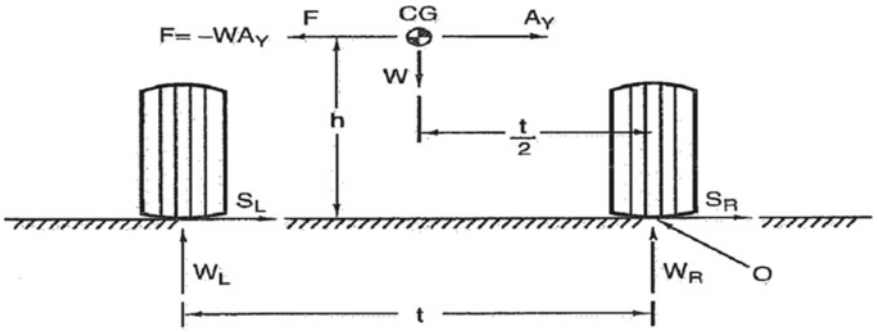

Fig. 3 Lateral load transfer

3.2 Longitudinal Load Transfer

As shown in Fig. 4 while braking or accelerating, load shifts from rear to front (braking) or vice versa (acceleration) due to inertia forces. This is termed as longitudinal load transfer. Thus, the front tires are experienced greater braking force while the rear tires are loaded under acceleration [9].

4 Resolving Loads on Strut Mount in *X*-, *Y*- and *Z*-Axis

To calculate the forces acting on the steering knuckle on the strut mounting point, the force transferred by the strut to the steering knuckle is resolved into three components along the three axes. The angles of inclination of the strut to the axes are used to

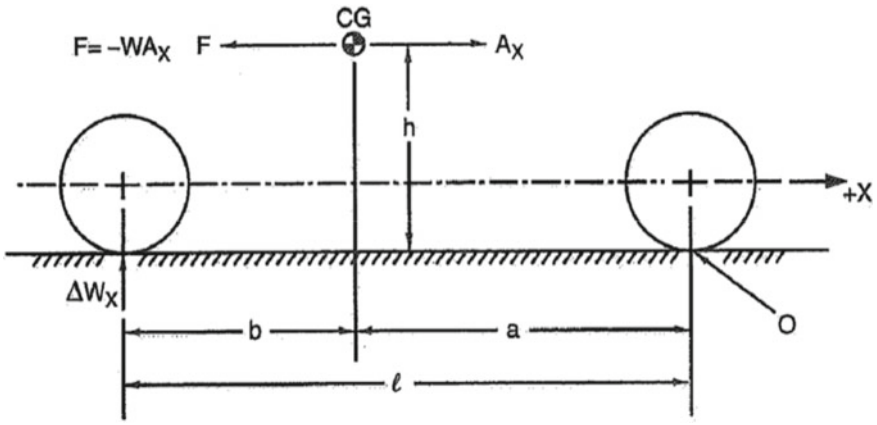

Fig. 4 Longitudinal load transfer

resolve the force in the three axes. First, in order to calculate the angles, the hard points of the suspension system are measured for the considered vehicle by initially setting the tire-road contacting point as origin. Then the distance of each point in all the axes is measured. The angle of inclination is calculated by plotting the hard points in CAD modeling in three-dimensional line sketch as free body diagram and is measured from the model [10].

$$F_x = F\cos(\theta_x)$$
$$F_y = F\cos(\theta_y)$$
$$F_z = F\cos(\theta_z)$$

4.1 Hard Points of Steering Knuckle

See Table 1 and Figs. 5 and 6.

5 Model Calculation

The resolved strut forces act on the steering knuckle along corresponding axes. In order to calculate the other forces at the other three points such as hub mounting point, tie rod mounting point and lower ball joint, the steering knuckle is assumed to be in equilibrium condition [11–14].

For equilibrium,

$$\sum F = 0; \sum M = 0.$$

In case of three-dimensional non-coplanar forces,

$$\sum F_x = 0; \sum F_y = 0; \sum F_z = 0;$$
$$\sum M_x = 0; \sum M_y = 0; \sum M_z = 0;$$

Table 1 Hard points of steering knuckle

S. No.	Position	*X*-axis	*Y*-axis	*Z*-axis
1	Strut mount	$X1 = 647.7996$	$Y1 = 431.1444$	$Z1 = 1726.6613$
2	Tie rod end	$X2 = 696.1035$	$Y2 = 292.8793$	$Z2 = 1919.9281$
3	Hub center point	$X3 = 759.4955$	$Y3 = 305$	$Z3 = 1737$
4	Lower ball joint	$X4 = 689.3451$	$Y4 = 167.1837$	$Z4 = 1758.1414$

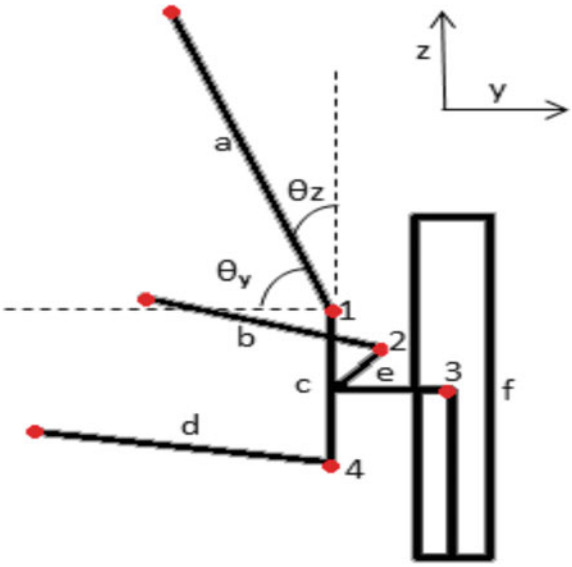

Fig. 5 Diagram of steering knuckle in *YZ*-plane. a = strut, b = tie rod, c = knuckle, d = lower control arm, e = hub, f = wheel; 1 = strut mounting point, 2-tie rod mounting point, 3 = hub mounting point, 4 = lower ball joint; θ_x = angle of inclination of strut to the *X*-axis; θ_y = angle of inclination of strut to the *Y*-axis; θ_z = angle of inclination of strut to the Z-axis

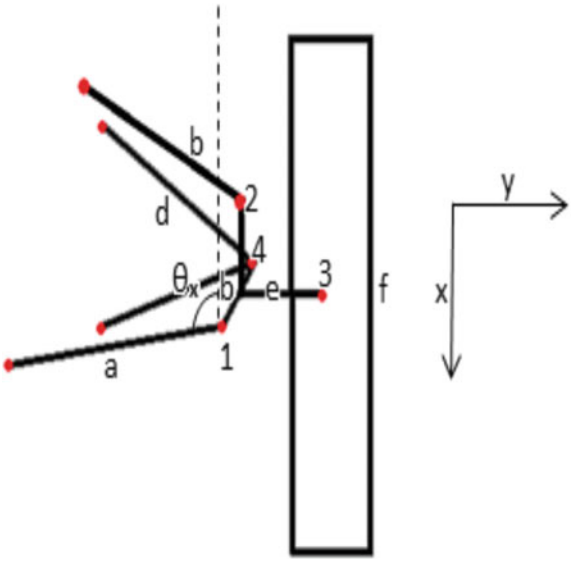

Fig. 6 Diagram of steering knuckle in*XY*-plane. a = strut, b = tie rod, c = knuckle, d = lower control arm, e = hub, f = wheel; 1 = strut mounting point, 2-tie rod mounting point, 3 = hub mounting point, 4 = lower ball joint; θ_x = angle of inclination of strut to the *X*-axis; θ_y = angle of inclination of strut to the *Y*-axis; θ_z = angle of inclination of strut to the Z-axis

Say three forces per joint, and totally nine forces are to be calculated. Thus, nine unknown reaction forces are acting on the steering knuckle. For calculating these nine forces, nine equations with nine unknowns have to be formed. Hence, considering the steering knuckle in equilibrium condition, the equations are formed equating the forces along a direction to zero and equating the moments about point in a plane to zero [15].

So, the forces along *X*-direction

$$\sum F_x = 0$$
$$R_{\text{hubx}} + R_{\text{strx}} + R_{\text{lbjx}} = F_x$$

The forces along *Y*-direction

$$\sum F_y = 0$$
$$R_{\text{huby}} + R_{\text{stry}} + R_{\text{lbjy}} = F_y$$

The forces along *Z*-direction

$$\sum F_z = 0$$
$$R_{\text{hubz}} + R_{\text{strz}} + R_{\text{lbjz}} = F_z$$

Taking moment about LBJ:
In *yz*-plane:

$$R_{\text{huby}} \times z_{34} - R_{\text{hubz}} \times y_{34} + R_{\text{stry}} \times z_{24} - R_{\text{strzy}} \times y_{24} = -F_z \times y_{14} - F_y \times z_{14}$$

In *xz*-plane:

$$R_{\text{hubr}} \times z_{34} - R_{\text{hubz}} \times x_{34} - R_{\text{strx}} \times z_{24} + R_{\text{strz}} \times r_{24} = F_x \times z_{14} + F_z \times x_{14}$$

In *xy*-plane:

$$R_{\text{hubx}} \times y_{34} + R_{\text{huby}} \times x_{34} + R_{\text{strx}} \times y_{24} - R_{\text{stry}} \times x_{24} = -F_y \times x_{14} - F_x \times y_{14}$$

Taking moment about HUB:
In *yz*-plane:

$$-R_{\text{stry}} \times z_{23} + R_{\text{strz}} \times y_{23} - R_{\text{ibj}} \times z_{43} + R_{\text{lbj}} \times \text{distance} = -F_z \times y_{13} - F_y \times z_{13}$$

In *xz*-plane:

$$R_{\text{strx}} \times z_{23} + R_{\text{strz}} \times x_{23} + R_{\text{ibjx}} \times z_{43} + R_{\text{ibjz}} \times x_{43} = +F_x \times z_{13} + F_z \times x_{13}$$

In *xy*-plane (Fig. 7):

$$-R_{\text{strx}} \times y_{23} - R_{\text{stry}} \times x_{23} - R_{\text{lbjx}} \times y_{43} - R_{\text{ibjy}} \times x_{43} = +F_x \times x_{13} - F_y \times x_{13}$$

$$R_{\text{hubx}} + R_{\text{strx}} + R_{\text{lbjx}} = -3370.87$$

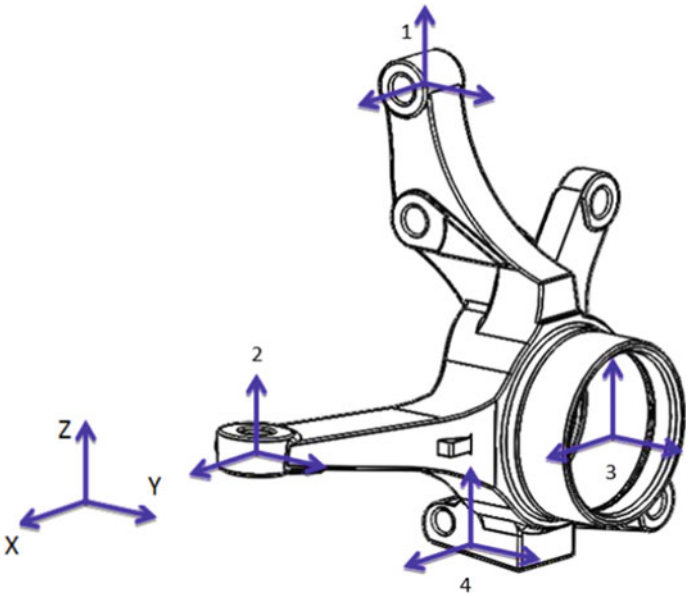

Fig. 7 Reaction forces on knuckle linkages

$$R_{huby} + R_{stry} + R_{\text{ibjy}} = 4026.92$$
$$R_{\text{hubz}} + R_{\text{strz}} + R_{\text{lbjz}} = -9545.15$$

$$R_{\text{huby}} \times 21.141 - R_{\text{hubz}} \times 137.82 + R_{\text{stry}} \times 161.79 - R_{\text{strzy}} \times 125.695 = -F_z \times 263.96 - F_y \times 31.48$$

$$-R_{\text{hubx}} \times 21.141 - R_{\text{hubz}} \times 70.15 - R_{\text{strx}} \times 161.7867 + R_{\text{strz}} \times 6.758 = F_x \times 31.48 + F_z \times 41.55$$

$$R_{\text{hubx}} \times 137.816 + R_{\text{huby}} \times 70.15 + R_{\text{strx}} \times 125.695 - R_{\text{stry}} \times 6.758 = -F_y \times 41.55 - F_x \times 263.96$$

$$-R_{\text{stry}} \times 182.93 + R_{\text{strz}} \times 12.12 - R_{\text{lbjy}} \times 21.14 + R_{\text{lbjz}} \times 173.82 = -F_z \times 126.14 - F_y \times 10.34$$

$$R_{\text{strx}} \times 182.93 + R_{\text{strz}} \times 63.392 + R_{\text{lbjx}} \times 21.14 + R_{\text{lbjz}} \times 70.15 = +F_x \times 10.34 + F_z \times 111.69$$

Table 2 MATLAB readings

Conditions	Axis	Strut. mount	Tie rod	Lower ball joint	Wheel hub
Cornering	*X*	−3361 N	−1817 N	−841 N	−507.3 N
	Y	4015 N	6850 N	−4571 N	−5356 N
	Z	−9515 N	24,109 N	−2137 N	2539 N
Acceleration	*X*	2300 N	2420 N	−652 N	−239 N
	Y	−1970 N	−5475 N	−1474 N	5433 N
	Z	−2440 N	−5577 N	−4621 N	−5633 N
Braking	*X*	4278 N	4502 N	−1213 N	−446 N
	Y	−3680 N	−10,186 N	−2742 N	10,107 N
	Z	−4539 N	−10,374 N	−8597 N	−10,480 N

$$-R_{\text{strx}} \times 12.12 - \text{R}_{\text{stry}} \times 63.39 - R_{\text{lbjx}} \times 137.82 - R_{\text{lbjy}} \times 70.15 = +F_x \times 111.69 - F_y \times 126.144$$

On solving these nine equations for nine unknowns, we get R_{hubx}, R_{huby}, R_{hubz}, R_{strx}, R_{stry}, R_{strz}, R_{lbjx}, R_{lbjy} and R_{lbjz}. But solving nine equations with nine unknowns is a tedious process, so we go for MATLAB (Table 2).

6 Experimental Results

6.1 Camper Versus Time

The camber versus time characteristics varies in a sinusoidal way in reaction to the sinusoidal input at the wheel over the hydraulic lift. As the difference of camber angle is less for the proposed system, it ensures better handling and maneuverability of the vehicle. This provides better dynamic characteristics of the vehicle during real-time operations (Fig. 8).

6.2 Toe Versus Time

Similar to the camber analysis, both the systems were subjected to undergo wheel travel, and the corresponding changes in toe characteristics are presented in the following section.

The toe angle response of the suspension systems during simulation process is shown in Fig. 9. The maximum toe angle obtained from the suspension system is −

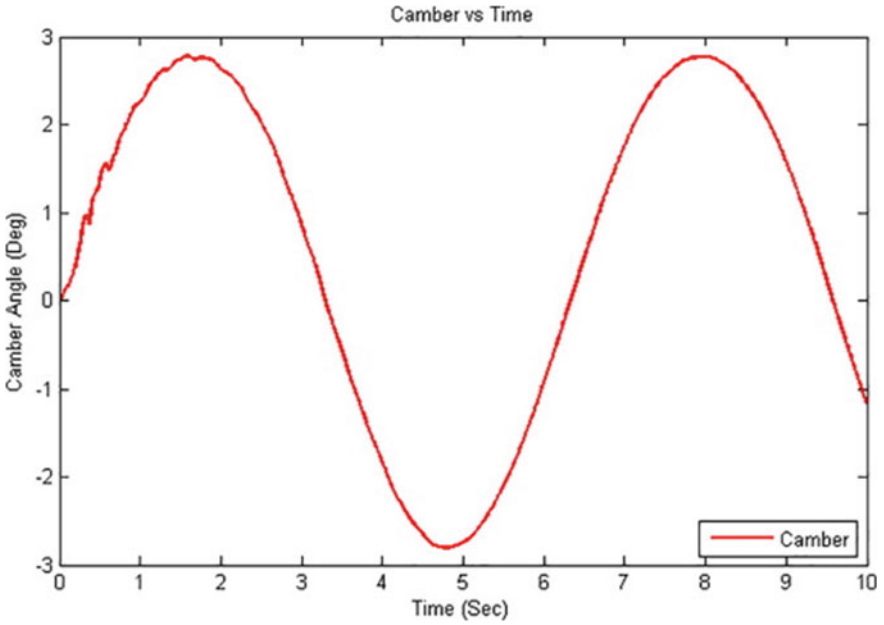

Fig. 8 Camber versus time

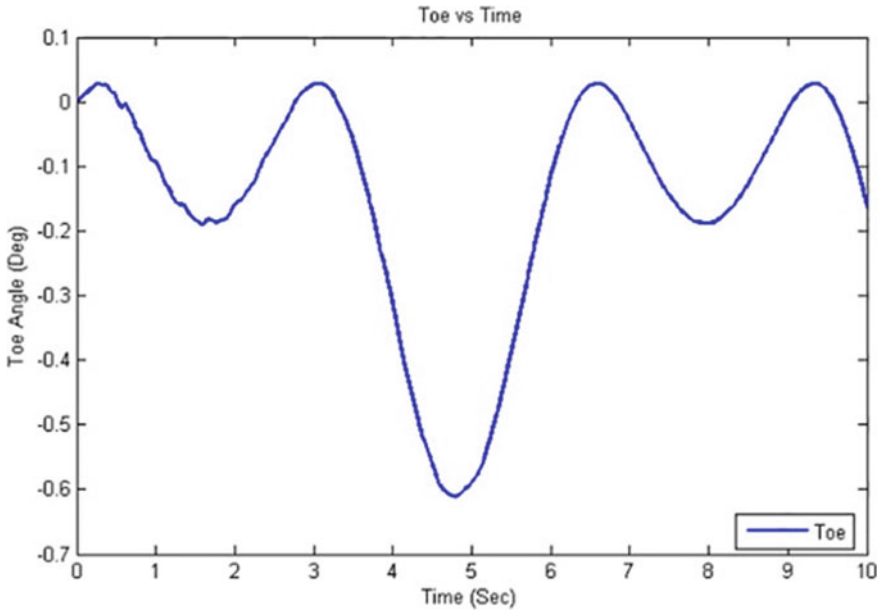

Fig. 9 Toe versus time

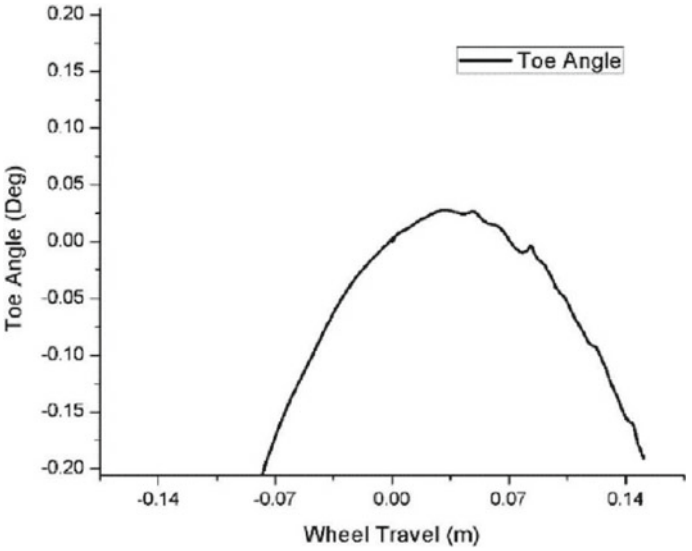

Fig. 10 Toe response with wheel travel

0.6°. This ensures a larger area of wheel contact patch, which results in better wheel traction.

6.3 Toe Response of Suspension System

Toe characteristics of suspension system with respect to the wheel travel are shown in Fig. 10. The plots show a significant reduction in the toe angle variation of the active suspension system due to active control of the tie rod by the servo actuator. The maximum toe angle obtained from suspension system is about 0.6 degrees. Also, the confounding variations in the toe angle as seen in Fig. 10 are due to the same inertial effects and imbalance which affected the camber characteristics.

7 Conclusion

Methodology of multi-axial force acting on steering knuckle during acceleration, braking and cornering is studied, and the forces acting on the steering knuckle of a commercial hatchback car are developed using MATLAB. The multi-axial forces acting on the steering knuckle for the three conditions are computed. Thus, a MATLAB program is developed to obtain the forces on steering knuckle for various riding conditions for the given input of vehicle specification by using this procedure,

and by only varying the input data of any hatchback model car with MacPherson strut suspension system, we can find the forces acting on the steering knuckle. Thus, it will be helpful and can be used as a template for modifying the design of steering knuckle and to analyze using the obtained load. It can be used for FEA analysis of steering knuckle and optimization of the same.

References

1. Mukras S, Mauntler NA, Kim NH, Schmitz TL, Gregory W (2009) Modelling a slider—crank mechanism with joint wear. Sawyer University of Florida
2. Jadav CS, Gautam JR (2014) Multi-body dynamics analysis of the suspension using adams. IJSRD Int J Sci Res Dev, 2(03). ISSN: 2321-0613
3. Kocer F, Sundaresh K, Ravikoti S, Cardoso V (2012) Random response and fatigue optimization in the frequency domain. Altair Engineering Inc.
4. Bumham P, Mclaren (2010) Simulating the suspension response of a high performance sports car. Automotive McLaren Technology Centre, Chertsey Road, Woking, Surrey, GU21 4YH
5. Vadhe R, Dave V (2008) Multi-body simulation of earthmoving equipment using motion view/motionsolve, HTC
6. Kruger WR (2011) Multibody analysis of whirl flutter stability on a tiltotor wind tunnel mode. Institution Mechanical Engineer
7. Gonzalez F, Masarati P, Cuadrado J, Naya MA (2017) Assessment of linearization approaches for multibody dynamics formulations. J Comput Nonlinear Dyn 12(4), paper 041009
8. González F, Naya MA, Luaces A, González M (2011) On the effect of multi-rate co-simulation techniques in the efficiency and accuracy of multibody system dynamics. Multibody Syst Dyn 25(4):461–483
9. Cao D, Song X, Ahmadian M (eds) (2010) Perspectives: road vehicle suspension design, dynamics, and control. University of waterloo, Canada, Taylor and Francis
10. Fallah MS, Mahzoon M, Eghtesad M (2008) Department of mechanical engineering, Shiraz University, Iran. Iran J Sci Technol
11. Attia HA (2001) Dynamic modeling of the double wishbone motor vehicle suspension system. Department of Mathematics, College of Science, King Saud University, Elsevier
12. Deepan Kumar S (2019) Experimental analysis of performance and emission characteristics of single cylinder direct injection diesel engine using algae as a biodiesel and barium oxide as a nano-fuel additive. Int J Mech Prod Eng Res Dev (IJMPERD) 9(1):35–42
13. Deepankumar S (2019) Experimental investigation of mechanical and corrosion characteristics of friction stir welded aluminum alloy 7075-T6 2019-28-0175. SAE Technical Paper, vol 2019, no 28
14. Deepankumar S (2019) Experimental analysis of performance and emission characteristics of diesel-electronic waste plastics pyrolyis oil (Ewppo) blends in diesel engine. Int J Mech Prod Eng Res Dev (IJMPERD) 9(1):148–155
15. Rajamurugan G, Deepankumar S, Ramakrishnan A, Krishnasamy P, Dhanabalan D (2019) Corrosion characteristics on friction stir welding of dissimilar AA2014/AA6061 alloy for automobile application. SAE Technical Paper, vol 2019, no 28

Mathematical Analysis of Rectangular Reinforced Concrete Beam Externally Laminated with GFRP Sheet

N. V. Manjunath, M. Ranjitham, V. Manickavasakam, and Sujith Selvaraj

Abstract Reinforced construction structures are constructed manually to the reinforced concrete structure, and the rehabilitation progression was held to avoid the damaged structures due to static loads. In the thesis related, the finite element model is to stimulate the beam to analyze with the design criteria to externally wrapped RCC beam. This process is one of the achievements in the modern civil engineering field. The thesis presents the retrofitting method to improve their force and rigidity by the cover of the GFRP sheet on externally reinforced material. An analytical representation is proposed to predict the shear capacity strengthened through the glass fiber reinforced polymer sheet (GFRP). The two-point load was applied at the beam bottom surface at a specific distance and held constant during the test. The beam setup should be simply supported under the two hinged support, and the edges are free in condition and externally strengthened by the GFRP sheet. The GFRP sheets enhancing the ductility and to transmit the collapse method to hold up the shear collapse manner of load augmentation. The force and deflection result is evaluated to define by a strengthen beam and unstrengthen beam. This numerical analysis method shows that the RCC arrangement strengthened among the GFRP sheet can increase their force, rigidity and energy dissipation capacity.

Keywords Retrofitting · GFRP sheet · Two-point loading

1 Introduction

FRP is solid only in the ways of strands. The fiber headings in FRP composites might be unidirectional, bi-directional or multi-directional as appeared in below figure. The utilization of strands in two ways can be valuable as for shear opposition regardless of whether reinforcing for turned around stacking is not required, aside from an impossible case in which one of the fiber headings is parallel to the shear breaks.

N. V. Manjunath (✉) · M. Ranjitham · V. Manickavasakam · S. Selvaraj
Department of Civil Engineering, Bannari Amman Institute of Technology, Sathyamangalam 638401, India
e-mail: manjunathnv@bitsathy.ac.in

G. Kumaresan et al. (eds.), *Advances in Materials Research*, Springer Proceedings in Materials 5, https://doi.org/10.1007/978-981-15-8319-3_34

With the increment in research and presentation of new materials and innovation, there are better approaches for retrofitting the structure with many included points of interest.

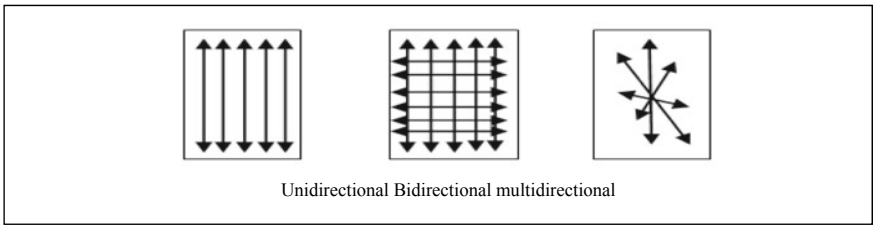

2 Glass Fiber Reinforced Polymer (GFRP)

Glass fiber reinforced polymer (GFRP) is distinct from the complex material. GFRP is accessible in numerous structures and is utilized as basic support for the solid structures. Some of these structures are bars, plates and sheets. The FRP sheets are all the more generally used to fortify the current structures within the beam of more noteworthy adaptability contrasted by different structures. FRP fix is a basic method to increment both the quality and plan life of a structure.

2.1 Fiber Disappointment

It happens when the pliable worry in the filaments surpasses the rigidity. It is portrayed by a quick dynamic fiber disappointment in the composite, especially for sheets, yet the disappointment is fragile in the majority of the cases. The direction of the strands as for the chief strain in solid influences the flexibility of the composite.

2.2 Bond Disappointment

Bond disappointment is administered by the property of the flimsier materials within contact, for example, solid concrete and glue. At the point when the sheer quality of one of these surpasses the power, at that point move cannot be guaranteed any longer and a “slip” is created. The debonding can happen in the solid, between the solid and the cement, and in the glue, between the glue and the filaments. The most widely recognized debonding disappointment watched is at the outside of the solid, which is a reasonable wonder since the solid is the weakest component in this “communication chain”. The bond disappointment is considered riskier failure mode

Table 1 GFRP material property

FRP composite	Elastic modulus (Mpa)		Tensile strength (Mpa)	Shear modulus	Thickness of laminate
GFRP	$\varepsilon_x = 2.5e^5$	$\upsilon_{xy} = 0.22$	$3.5e^3$	$G_{xy} = 1.18e^4$	1
	$\varepsilon_y = 1.8e^5$	$\upsilon_{xz} = 0.22$		$G_{xz} = 1.18e^4$	
	$\varepsilon_z = 1.79e^4$	$\upsilon_{yz} = 0.33$		$G_{yz} = 6.8e^4$	

than ductile disappointment since it can neither be predicted nor be prohibited (Table 1).

3 Cementitious Matrix

Apply of the cementitious matrix be in practice for transfer of stresses more efficient through the application epoxy resin strengthening adhesive after cement matrix. It has a high resistance to fatigue. It has high resistance to freeze-thaw and delayed contraction and cracking. GFRP improves the compressive force and improves the fracture propagation.

4 Shear Failure of Externally Bonded GFRP Wrapped

A typical detail of externally bonded GFRP on beam. Since the load acting is better, the compressive force changes the beam to bend up the bars inside with the deterioration of the bond performance of the standard position. It was generating the tensile strength to oblique the bent-up bars which structure the crack propagation. Architectural Institute of Japan (AIJ) design guideline (AIJ 1999) defines the equation for link force. The state of the minimum joint as volume as 0.3% between the beam and GFRP. This design equation gives an enhanced strength on the dislocation of beam elastic, and it becomes safe guideline.

5 Specimen Measurement

The span of the beam = 1700 mm, the width of the beam = 500 mm, and the depth of the beam = 750 mm.

6 Reinforcement Details

5 numbers of 12 mm diameter bars and the 8 mm diameter stirrups @ 150 mm C/C distance.

7 Finite Element Modeling

7.1 Introduction

The limited component strategy is anything but difficult to dissect the structure in a numerical investigation of the method. ANSYS is universally useful inside the bar to the thorough investigation of holding among the strengthening and steel.

7.2 Concrete Demonstrating

Basically, the solid gets a breakdown among the hold of total and mortar because of effect stacking, and it shows a bigger number of miniaturized scale splits. The mechanical conduct of cement, since their engendering level of breaks, adds to non-direct low pressure and causes volume broad, isolation, shrinkage and warm far-reaching of the mortar. It might create distinction in solidness between their total and mortar. Its interface has a fundamentally lower elasticity than mortar and establishes weakest in the composite framework. Since the solid is for the most part in force, the stress–strain link is essentially intriguing. Part properties unyielding are utilized for 3D display of solids with or without fortifying bars (rebar). The strong is equipped for breaking in strain and pulverizing in pressure. For which the component is likewise pertinent would be fortified composites (e.g., fiberglass) and topographical material, for example, shake. The component is characterized by eight hubs having three levels of opportunity at every hub interpretation in the nodal arrange x, y, z headings. Steel support to show solid fortification discrete into limited component demonstrating is accepting that bond among steel and cement is 100%. Shaft segment has six levels of opportunity at every hub. These incorporate interpretations in the x, y, z bearings and pivots. This component is appropriate for direct, huge turn and strain nonlinear applications.

7.2.1 Overlays

To show overlaid composites, SHELL 91 is utilized for layered uses of an auxiliary shell model or for displaying thick elective structures. Up to 100 unique layers are allowed for applications with the sandwich alternative turned out. When building a

Table 2 Different material property

Material	Density (Kg/m^3)	Elastic modulus (Mpa)	Poisson ratio	Fck (Mpa)	Fy (Mpa)	Elements used
Concrete	2200	22,360	0.2	20	–	Solid 65
Steel reinforcement	7850	$2e^5$	0.3	–	415	Beam 88

model SHELL 91 is more capable than SHELL 99. The direct investigation considered for displaying the RC bar depicts the material property and mechanism utilized (Table 2).

8 Externally Wrapping RC Beam with no GFRP

The structural geometry of the exterior beam has been modeled for the mentioned dimension and analyzed using ANSYS. It has been analyzed without GFRP wrapping under the bottom of the beam is constrained in all degrees of freedom. The two-point load up to 25 KN is applied on the beam (Fig. 1).

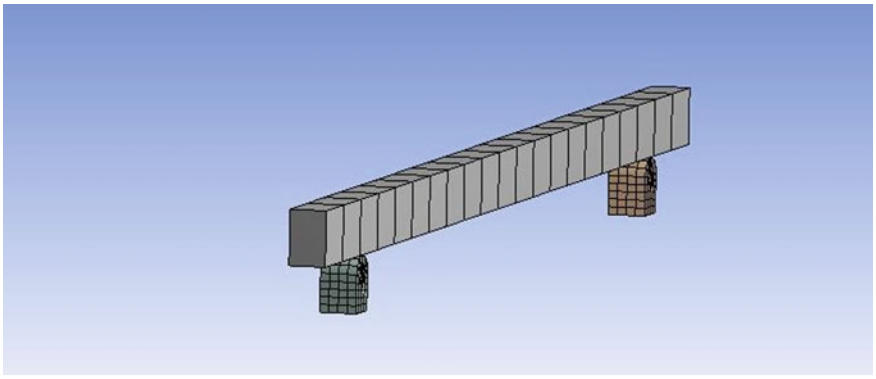

Fig. 1 Exterior RCC beam model without GFRP

9 Exterior RC Beam with and with no GFRP Wrapping

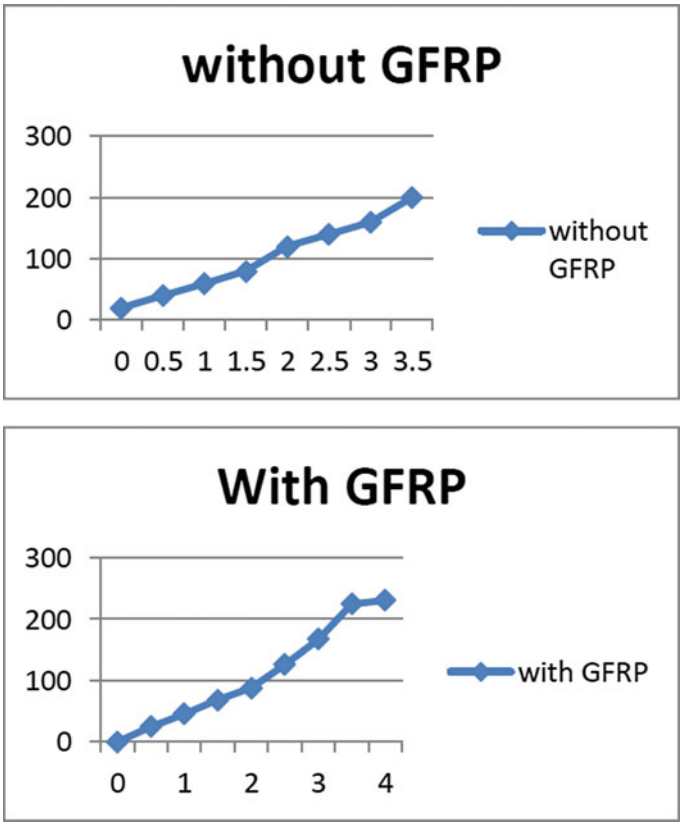

The structural geometry of the exterior beam has been modeled for the mentioned dimension and analyzed using ANSYS. It has been analyzed with no GFRP wrapping under the bottom of the beam is constrained in all degrees of freedom. The two-point load up to 55 KN is applied on the beam (Figs. 2, 3, 4, 5, 6 and 7).

In the postulation, the numerical aftereffects of together with GFRP wrapping and without CFRP wrap are translated. Their conduct all through the examination is contemplated from the recorded information acquired from the diversion conduct and burden conveying limit utilizing ANSYS. The reinforced and strengthened bars are tried for their definitive quality.

1. The heap conveying limit of the retrofitted example is 30% more than the strengthened example.
2. The heap distortion conduct likewise improves to the huge degree if there should arise an occurrence of retrofitted example over unstrengthen example.

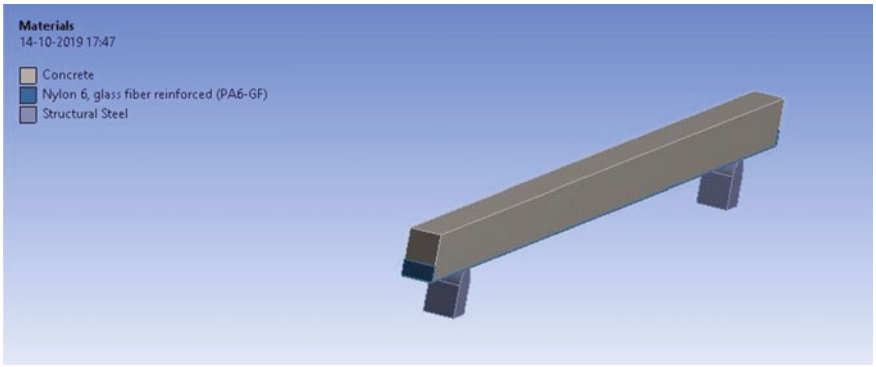

Fig. 2 Exterior RCC beam model

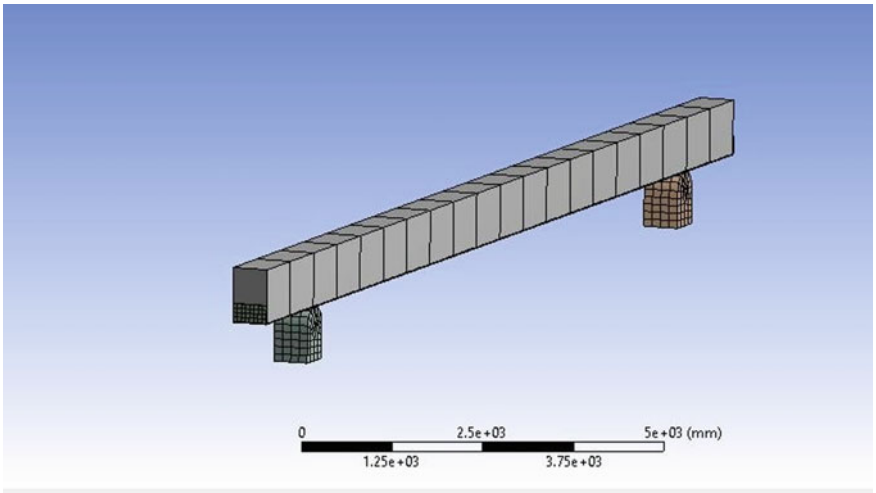

Fig. 3 Exterior RC beam model with GFRP

3. The malleability of the retrofitted example will be more noteworthy when contrasted and the typical example.
4. GFRP retrofitting example of the shaft segment joint moved the disappointment of the joint from section bit to the bar segment of the joint which will anticipate dynamic breakdown.

10 Conclusion

The accompanying perceptions and ends can be attracted by the explanatory aftereffects of the examination.

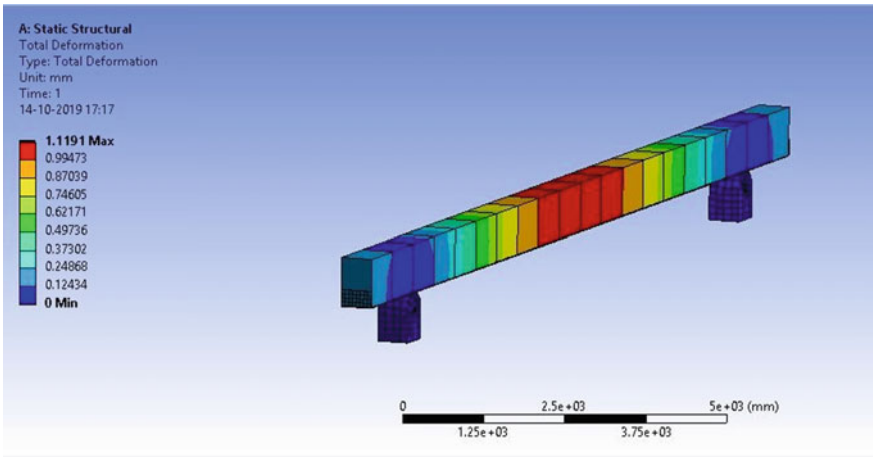

Fig. 4 Total deformation of exterior RCC beam model with GFRP

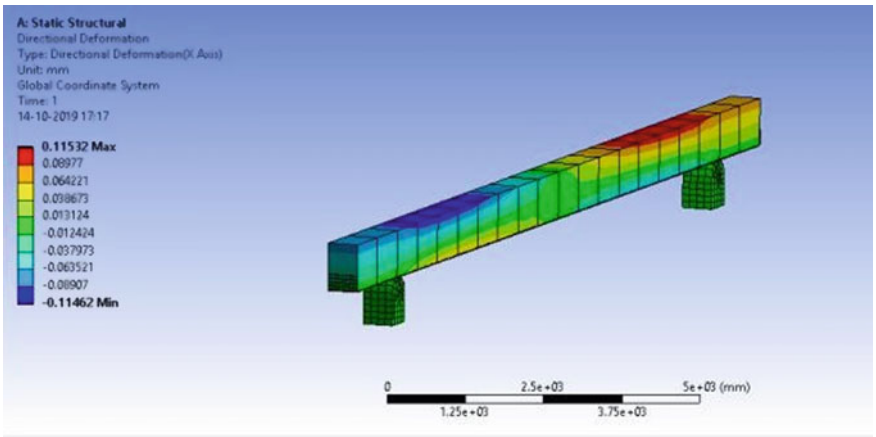

Fig. 5 Directional deformation of exterior RCC beam model with GFRP

1. Looking at the numerical examination we ought to assert with the purpose of the avoidance within the reinforced example is lesser than to facilitate of the strengthened example.
2. It is seen that the worry in the example is better in the retrofitted with GFRP example when contrasted and the ordinary example without GFRP wrapping.
3. From the theory, it very well may be presumed that the fortifying with the GFRP structure will expand the workableness of the structure.

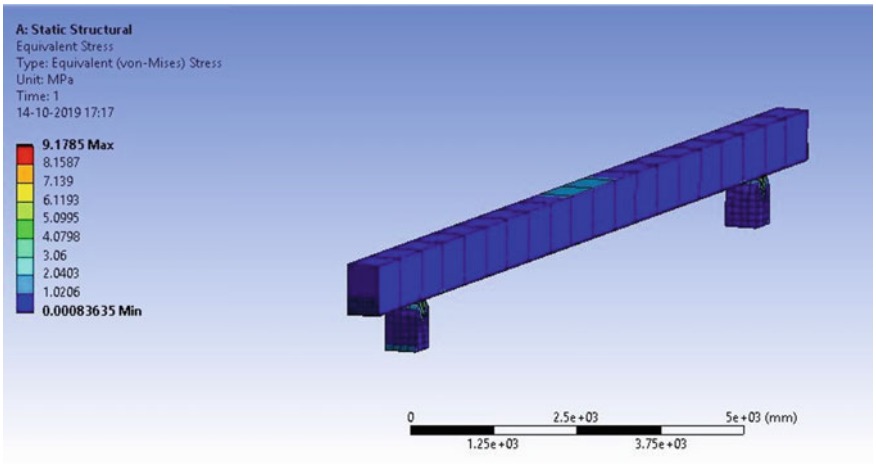

Fig. 6 Equivalent stress of exterior RCC beam model with GFRP

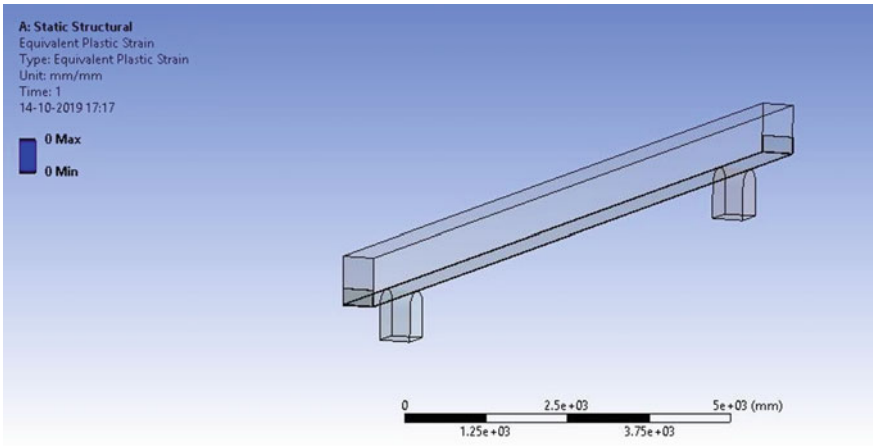

Fig. 7 Equivalent elastic strain of exterior RCC beam model with GFRP

References

1. Naveenai N, Ranjitham M (2016) Numerical study on retrofitting of pillar segment joint fortified with CFRP
2. Wang G-L, Dai J-G, Teng JG (2010) Shear quality model for RC shaft section joints under seismic loading 48–60
3. Kwon H, Cho S, Kawasaki A, Leparoux (2012) Dual-nanoparticulate-reinforced aluminum matrix composite materials published on International Nuclear Information System (INIS) March 2012-01-01
4. Kadhim (2012) Impact of CFRP sheet length on the conduct of HSC persistent beam 00

5. Fbi notice 14, Design and use of remotely fortified fiber strengthened polymer support (FRP EBR) for fortified cement structure, July 2001
6. Sobuzl HR, Ahmed E, Sadiq Hasan NM, Habibur Uddin MA (2011) Intercontinental paper of common and structural engineering
7. Department of Indian Standard. IS 456:2000 Simple and reinforced concrete-code of practice
8. Meikandaan TP, Ramachandramoorthy A (2017) International paper of civil engineering and technology (IJCIET) 8(2)
9. Raju A et al (2013) Retrofitting of RC beams using FRP. Int J Eng Invest Technol (IJERT) 2(1). ISSN: 2278-0181
10. Alferjani MBS et al (2013) Exploit of carbon fiber reinforced polymer laminate for fortifying strengthened solid bar in shear. A review. Int Ref Pap Eng Sci (IRJES) 2
11. Vimala S, Shanna V (2017) Strongest persistent multicast routing convention for reliable transmission in both ad-hoc and mobile ad-hoc networks. Worldwide J Civ Eng Technol 8(1):976–986
12. Jisten B (2003) Strengthening solid bars for shear through CFRP sheet. Constr Struct Mater
13. Shang X-y, Yu J-T, Shy L, Dao Z (2019) Strengthening of RC structures by using engineered cementitious composites
14. Kumar AA, Sharma O, Banal S, Songhai (2018) Quality, and strength of superior designed cementitious composites
15. Gabo S, Wang Z, Wang W, Quid H (2018) Emit of shrinkage-lessening admixture and far-reaching operator lying on automatic properties and drying expansion of designed cementitious composites (ECC). Constr Manuf Mater 179:172–185
16. Jang SJ, Kim JH, Kim SW (2019) The expel of shrinkage-pay on the exhibition of strain-solidifying bond composite (SHCC). Maintainability 11:1453
17. Costa FBP, Richie DP (2019) Grave, experimental learning of some stability property of ECC with every creature the more earth practical rice husk debris and high steadiness polypropylene fibers. Constr Constr Mater 213:505–513
18. Deng MK, Yang S (2018) Cyclic testing of unreinforced stonework dividers retrofitted with designed cementitious composites. Constr Assemble Walk
19. AL-Gemeel AN, Huge Y An exploratory examination of material strengthened build cementitious composite (ECC) for square solid segment confinement

Effects of Drilling Process Parameters Using ANOVA and Graphical Methods

S. P. Sundar Singh Sivam, Ganesh Babu Loganathan, K. Saravanan, S. Dinesh Guhan, and Aishik Banerjee

Abstract Magnesium alloys are highly preferred for use in the automobile sector and aerospace industry because of their low density and superior strength. Due to the lightweight and high strength of magnesium alloys, they are continuously being used for engineering applications. The transport industry has benefitted a lot as weight reduction is of prime importance in terms of cost saving. AM60 magnesium alloy also has good resistance to corrosion especially when compared with the rusting of mild steel in the same atmosphere. The paper makes an attempt to determine the best machining conditions to manufacture magnesium goods, especially AM60 magnesium alloy. Drilling operation is carried out on AM60 magnesium alloy, and the results obtained are optimized using ANOVA technique. The output responses analysed are residual stress, thermal stress, surface roughness, maximum amplitude of vibration, deviation from concentricity, deviation from cylindricity, deviation from diameter and deviation from perpendicularity. These responses are analysed using ANOVA in order to check the productivity of drilling operation at controlled input parameters such as cutting speed, feed, time and drill bit treatment. Cryogenically

S. P. S. S. Sivam (✉) · S. Dinesh Guhan · A. Banerjee
Department of Mechanical Engineering, SRM Institute of Science and Technology, Kancheepuram, Kattankulathur, Tamil Nadu 603203, India
e-mail: legendsundar2k6@gmail.com

S. Dinesh Guhan
e-mail: dinesh6.ksguhan@gmail.com

A. Banerjee
e-mail: aishikbanerjee97@gmail.com

G. B. Loganathan
Department of Mechatronics Engineering, Tishk International University, Erbil, Kurdistan Region, Iraq
e-mail: ganesh.babu@ishik.edu.iq

K. Saravanan
Department of Mechatronics Engineering, SRM Institute of Science and Technology, Kancheepuram, Kattankulathur, Tamil Nadu 603203, India
e-mail: sarav3186@gmail.com

G. Kumaresan et al. (eds.), *Advances in Materials Research*, Springer Proceedings in Materials 5, https://doi.org/10.1007/978-981-15-8319-3_35

treated drill bits with different tempering cycles are used as one of the input parameters. The input parameters are pre-defined and then applied in the drilling operation, and the corresponding results obtained are analysed.

Keywords ANOVA · AM60 · Cryogenic treated drill tools · Hole quality

1 Introduction

Drilling is one of the most popular machining processes. It is widely used in automotive, aerospace, aircraft, dies and mould industry, home appliances, etc. Thus, cost-effectiveness is one of the most important criteria along with superior quality of products. In today's world, it has become very necessary to apply optimization techniques in machining processes so as to obtain the most efficient result in the shortest span of time possible. In this paper, ANOVA method determines the influence (percentage of contribution) of the input parameters on the output responses. AM60 magnesium alloy has been chosen to carry out the drilling operation. Magnesium alloy is one of the most popular lightweight materials. Magnesium alloy absorbs vibrations and has high strength density ratio. Magnesium alloy has varied applications. They are used in various fields like electronics, automobiles and aerospace due to its good strength to weight ratio and low density. Magnesium alloys are regarded as one of the lightest among the metallic materials as aluminium alloys are approximately 35% heavier than magnesium alloys [1]. Drilling is one of the most vital processes which have been investigated extensively by researchers. Chen et al. [2] incorporated the splitting parameters for the drilling process using a split point drill. An effort was made to minimize the thrust force and torque during drilling. Chen and Tsao [3] concluded that differently coated drills resulted in varied performance on the drill life and the quality of drilled hole. Optimization methods are of prime importance in metal cutting processes, which is also considered to be of great importance for continuous improvement in output quality [4]. Chavan and Guja [5] used Analysis of Variance, i.e. ANOVA, to determine the significant inputs affecting the surface roughness. He used different twist drills under dry cutting conditions on SG500/7 plate. Alagarsamy et al. [6] used the Taguchi method to investigate the effects of drilling parameters on aluminium alloy 7075 using HSS drill. Cutting speed, feed and depth of cut were used as the parameters. Vankanti and Ganta [7] optimized process parameters such as cutting speed, feed, point angle and chisel edge width in drilling of glass fibre-reinforced polymer (GFRP) composites. ANOVA was also done to determine the significance of each input in the drilling operation. Tripathi et al. [8] carried out experiments to find the optimal drilling parameters on aluminium 6061 so as to obtain the minimum value of torque and thrust. Grigoraş and Brabie [9] conducted ANOVA analysis for milling operation on AZ61A, a magnesium–aluminium alloy. The results revealed that only speed and feed have a considerable impact. Erkan et al. [10] performed the Taguchi method and GONNs to find out the machinability of milling composite materials. ANOVA analysis was conducted to

Table 1 Factors and levels

Constraints	Unit	Levels		
		1	2	3
Cutting speed (V)—IP1	Rpm	2000	2500	3000
Feed (F)—IP2	mm/rev	0.24	0.3	0.36
Machining time—IP3	s	60	120	180
Drill bit treatment—IP4	-	1	2	3

show that the cutting speed is the most significant factor affecting surface roughness. Despite the fact that Taguchi method could have been used, however, it would have been difficult to handle the multi-objective optimization problem. In order to better the multiple quality characteristics, Taguchi with grey relational analysis is regarded as an efficient optimization method in various machining processes [11–29].

2 Experimental and Measurement Process

In order to carry out the drilling operation on AM60 magnesium alloy, many experiments were performed with varied sets of input parameters. The AM60 magnesium alloy was used, and the drilling was done in VMC manufactured by Lakshmi Works Machine LV45. The measurement of the residual stresses—OP1—was obtained by combining experimental as well as analytical concepts. Initially, the chips obtained after machining were collected and observed under the XRD machine. Through this, we obtained the angle of diffraction, which was then used in the analytical equations to determine the overall residual stress used for calculating the residual stress. Talysurf instrument was used for measuring surface roughness—OP2. The values in the thermal stress equation and infrared thermometer were used for measuring the thermal stress—OP3. Kistler type 3-axis accelerometer and vibration sensors, and tri-axial accelerometer instrument was used for measuring the maximum amplitude of vibration (mm)—OP4. Deviation from perpendicularity (mm)—OP5—was measured by (coordinate measuring machine), deviation from concentricity (mm)—OP6—was measured by (coordinate measuring machine), deviation from diameter (mm)—OP7—was measured by (coordinate measuring machine), and deviation from cylindricity (mm)—OP8—was measured by (at least two circles over the hole) (Tables 1, 2 and 3).

3 Results and Discussion

Figure 1 tells us that as the cutting speed increases, the residual stress decreases initially, reaches a minimum value and then increases again. The curve is steepest

Table 2 Output parameters

Symbol	Criteria
OP1	Residual stress(KN/mm^2)
OP2	Surface roughness (mm)
OP3	Thermal stress (KN/mm^2)
OP4	Max amplitude of Vibration(mm)
OP5	Deviation from perpendicularity (mm)
OP6	Deviation from concentricity (μm)
OP7	Deviation from diameter (mm)
OP8	Deviation from cylindricity (μm)

Table 3 Outcomes

Trail No.	IP1	IP2	IP3	IP4	OP1	OP2	OP3	OP4	OP5	OP6	OP7	OP8
A1	2000	0.24	60	1	26.5	2.1794	7.9	0.051	1.71	116.63	1.71	116.63
A2	2000	0.3	120	2	48.1	2.1687	16.6	0.155	1.49	75.12	1.49	75.12
A3	2000	0.36	180	3	159.2	3.2348	265.5	0.258	2.68	208.87	2.68	208.87
A4	2500	0.24	60	1	28.4	2.4434	20.65	0.064	1.76	110.86	1.76	110.86
A5	2500	0.3	120	2	50.6	2.2298	30.65	0.368	1.18	67.20	1.18	67.20
A6	2500	0.36	180	3	81.4	3.1769	430.6	0.498	3.04	138.50	3.04	138.50
A7	3000	0.24	60	1	95.4	1.6616	29.95	0.087	1.64	79.69	1.64	79.69
A8	3000	0.3	120	2	185.3	1.3761	40.64	0.487	0.34	76.83	0.34	76.83
A9	3000	0.36	180	3	431.9	4.1131	479.79	0.798	2.50	62.98	1.50	82.98

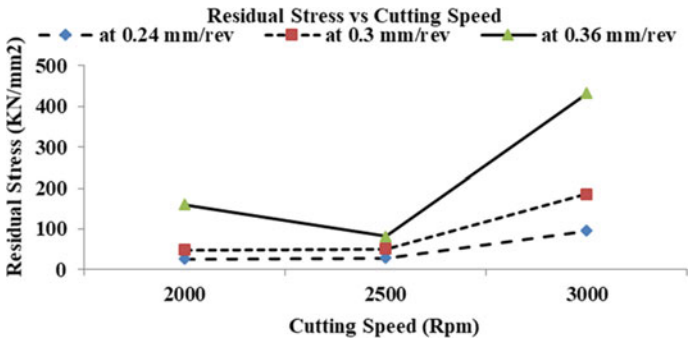

Fig. 1 Graph between residual stress and cutting speed

at a feed rate of 0.36 mm/rev. As the feed rate decreases, the steepness of the curve also lowers. In Fig. 2, we note that the residual stress increases with an increase in the feed. The difference in the residual stress values between cutting speeds of 3000 and 2500 rpm is also significant. The curve in Figs. 3 and 4 also follows a

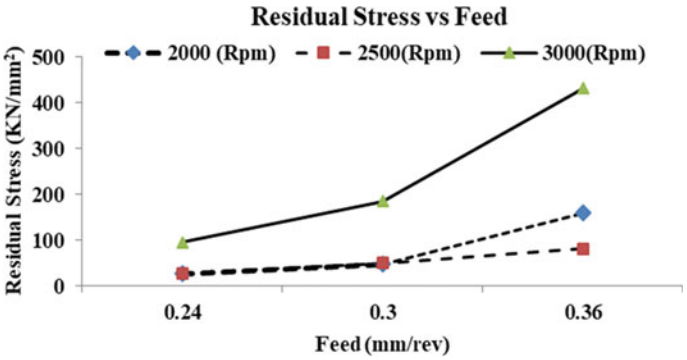

Fig. 2 Graph between residual stress and feed

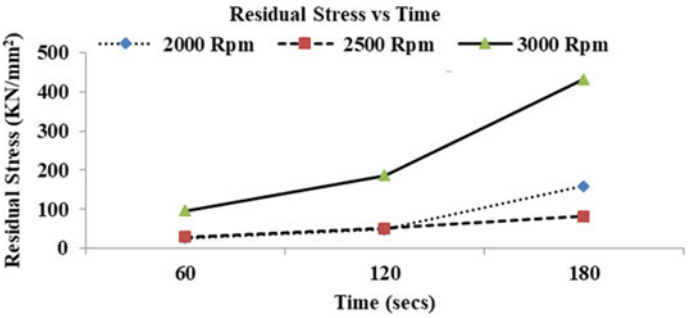

Fig. 3 Graph between residual stress and time

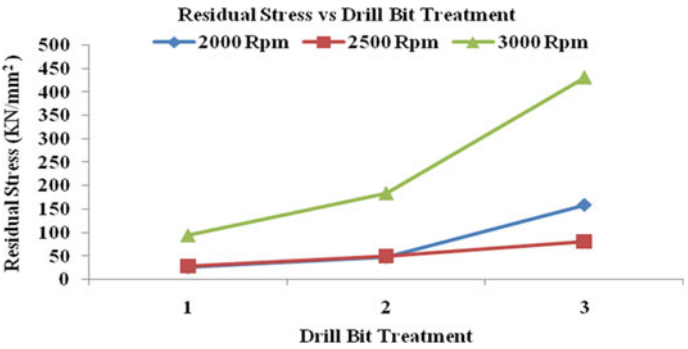

Fig. 4 Graph between residual stress and drill bit treatment

similar trend. The residual stress, as expected, increases with an increase in time and with a change in drill bit treatment. The ANOVA table on residual stress also shows that the residual stress is affected by cutting speed (7.03%), feed (34.23%),

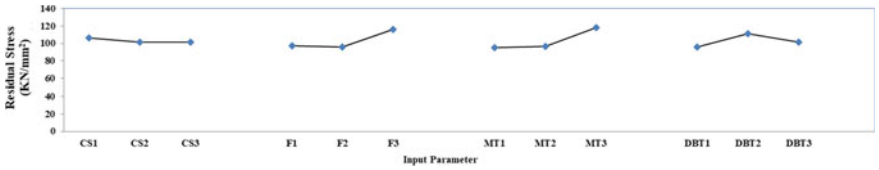

Fig. 5 Effects on residual stress (KN/mm^2)

machining time (45.53%) and drill bit treatment (13.21%). The highest influence is from machining time. Figure 5 indicates that a cutting speed of 2000 rpm, feed of 0.36 mm/rev, machining time of 180 s and drill bit treatment of 2 are the optimum conditions required to obtain residual stress (Table 4).

In Fig. 6, it is observed that with increase in the cutting speed, the thermal stress also increases. It can be seen that there is considerable difference between the thermal stress values between feed rates of 0.24 mm/rev and 0.36 mm/rev, while the values at feed rate of 0.3 mm/rev is rising with very little fluctuation. We can therefore infer

Table 4 ANOVA on residual stress (KN/mm^2)

Source of variation	Sum of squares	DOF	Mean Square	*F*	*F* table	Contribution %
Cutting speed (V)—IP1	1061.1289	2	530.5644	2,652,822.22	4.2	7.03
Feed (F)—IP2	5168.5356	2	2584.2678	12,921,338.89	4.2	34.23
Machining time—IP3	6876.1156	2	3438.0578	17,190,288.89	4.2	45.53
Drill bit treatment—IP4	1995.5489	2	997.7744	4,988,872.22	4.2	13.21
Error	0.002	9	0.000200	–		
SST	15,101.3289	17				

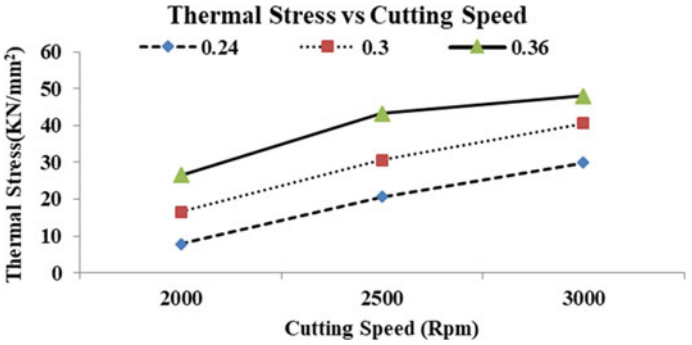

Fig. 6 Graph between thermal stress and cutting speed

that by increasing the feed rate, the thermal stress also increases. The above point is further proved in Fig. 7 where we can see that by increasing the feed rate, the thermal stress increases. There is a significant difference between the thermal stresses at 2000 and 3000 rpm. Hence, by increasing the cutting speed also, the thermal stress will increase. In Fig. 8, a similar nature of the curve follows where the thermal stress is seen increasing with increase in time. In Fig. 9, the thermal stress remains almost constant up to drill bit treatment number 2, followed by a sharp increase in its value. The ANOVA table on thermal stress also shows that the thermal stress is affected by cutting speed (21.83%), feed (34.70%), machining time (21.75%) and drill bit treatment (21.72%). The highest influence is from feed. Figure 10 indicates that a cutting speed of 2500 rpm, feed of 0.36 mm/rev, machining time of 60 s and drill bit

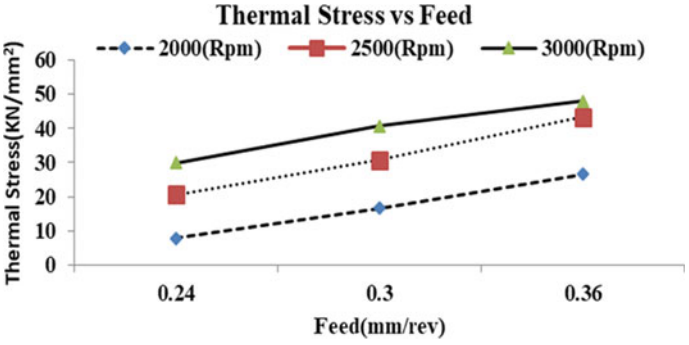

Fig. 7 Graph between thermal stress and feed

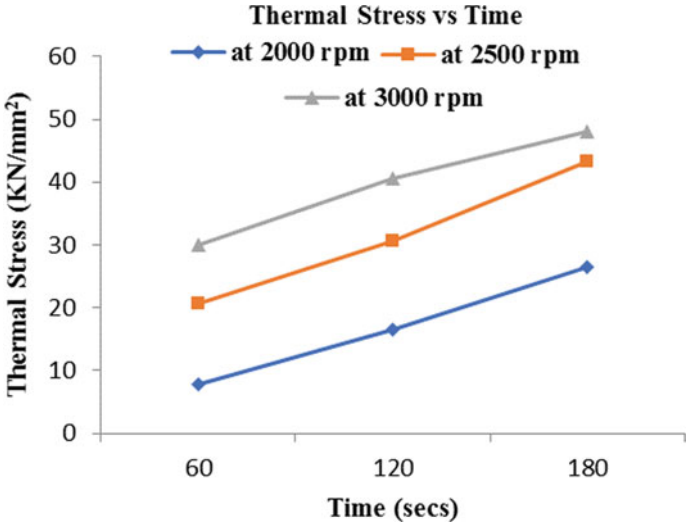

Fig. 8 Graph between thermal stress and time

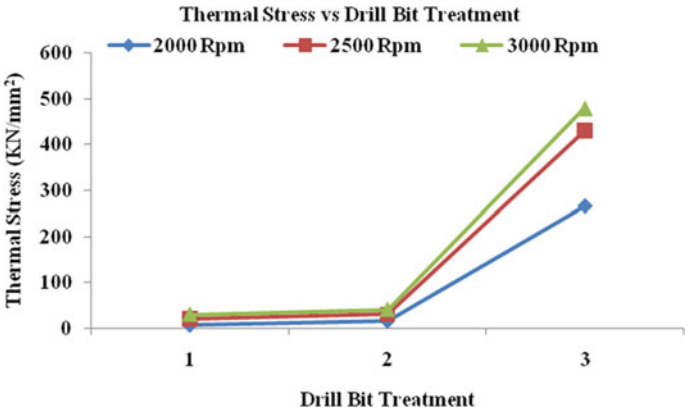

Fig. 9 Graph between thermal stress and drill bit treatment

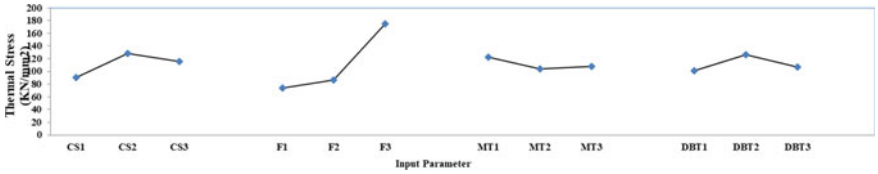

Fig. 10 Effects on thermal stress (KN/mm^2)

treatment of 2 are the optimum conditions required to obtain thermal stress (Table 5).

Figure 11 predicts that the surface roughness values do not undergo much change with increase in cutting speed. However, at higher cutting speeds, the surface roughness slightly increases for higher feed rates while it decreases for lower feed rates. From Fig. 12 also, we can infer that the surface roughness increases with an increase in feed rate, thus lowering the quality of surface finish of the alloy. As a result, separate surface finishing techniques like honing, grinding, etc. must be used to increase the smoothness. In Figs. 13 and 14 also, the curve follows the same nature. The ANOVA table on surface roughness also shows that the surface roughness is affected by cutting speed (1.42%), feed (77.45%), machining time (12.68%) and drill bit treatment (8.45%). The highest influence is from feed. Figure 15 indicates that a cutting speed of 2500 rpm, feed of 0.36 mm/rev, machining time of 120 s and drill bit treatment of 1 are the optimum conditions required to obtain deviation from surface roughness (Table 6).

Figure 16 shows that as the cutting speed is increased, the vibration amplitude also increases. The slope of the curve rises as the feed rate increases. At a feed rate of 0.24 mm/rev, there is hardly any fluctuation in the curve. However, as the feed rate increases, the slope gets steeper. Figures 17, 18 and 19 predict that the maximum amplitude of vibration increases with increase in the feed rate and time.

Table 5 ANOVA on thermal stress (KN/mm^2)

Source of variation	Sum of squares	DOF	Mean square	*F*	*F* table	Contribution %
Cutting speed (V)—IP1	3,499,109.8739	2	1,749,554.9369	8,747,774,684.67	4.2	21.83
Feed (F)—IP2	5,561,690.0205	2	2,780,845.0102	13,904,225,051.17	4.2	34.70
Machining time—IP3	3,486,600.8595	2	1,743,300.4297	8,716,502,148.67	4.2	21.75
Drill bit treatment—IP4	3,481,391.3498	2	1,740,695.6749	8,703,478,374.50	4.2	21.72
Error	0.002	9	0.000200	–		
SST	16,028,792.1036	17				

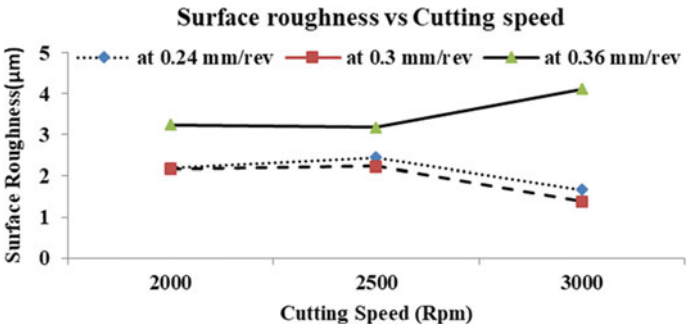

Figure 11 Graph between surface roughness and cutting speed

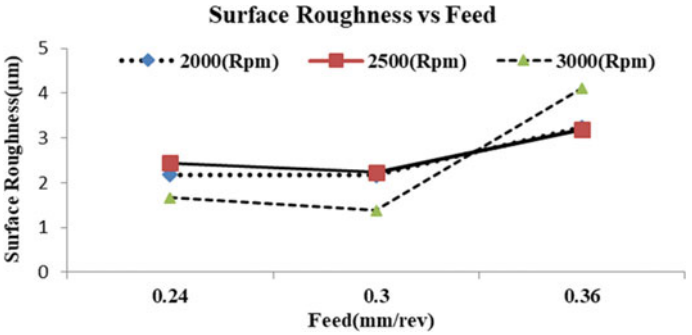

Fig. 12 Graph between surface roughness and feed

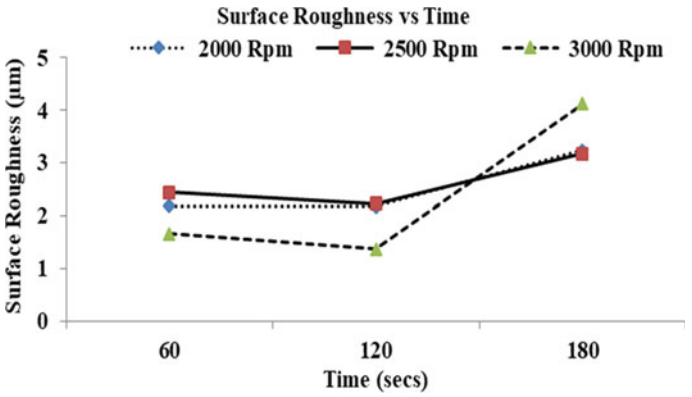

Fig. 13 Graph between surface roughness and time

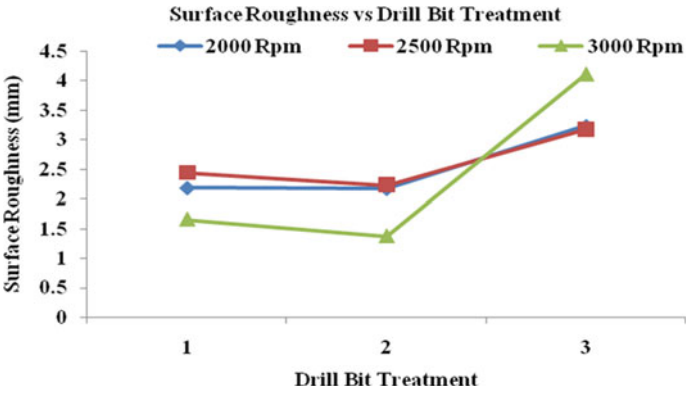

Fig. 14 Graph between surface roughness and drill bit treatment

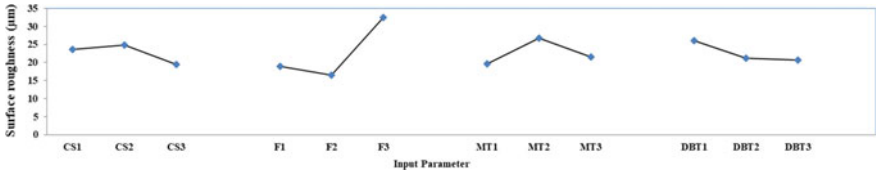

Fig. 15 Effects on surface roughness (μm)

Table 6 ANOVA on surface roughness (μm)

Source of variation	Sum of squares	DOF	Mean Square	*F*	*F* table	Contribution %
Cutting speed (V)—IP1	0.0830	2	0.0415	207.54	4.2	1.42
Feed (F)—IP2	4.5339	2	2.2670	11,334.80	4.2	77.45
Machining time—IP3	0.7426	2	0.3713	1856.43	4.2	12.68
Drill bit treatment—IP4	0.4948	2	0.2474	1236.88	4.2	8.45
Error	0.002	9	0.000200	–		
SST	5.8543	17				

At higher feed rate and at greater cutting speed, there is a huge difference between the vibration amplitudes. Figure 18 also tells us that as the time increases, the vibration amplitude difference for cutting speed of 2000 and 3000 rpm also increases significantly. The ANOVA table on maximum amplitude of vibration also shows that the maximum amplitude of vibration is affected by cutting speed (26.84%), feed (60.24%), machining time (4.28%) and drill bit treatment (8.65%). The highest influence is from feed. Figure 20 indicates that a cutting speed of 3000 rpm, feed of

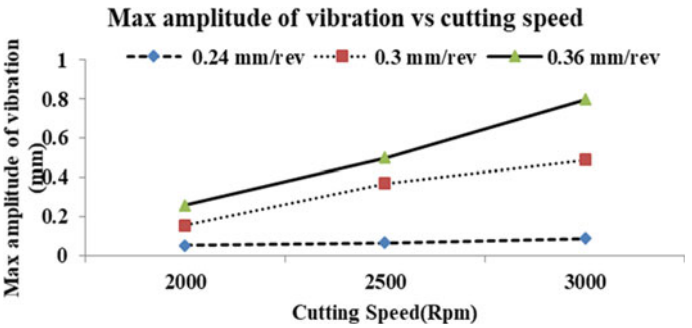

Fig. 16 Graph between max amplitude of vibration and cutting speed

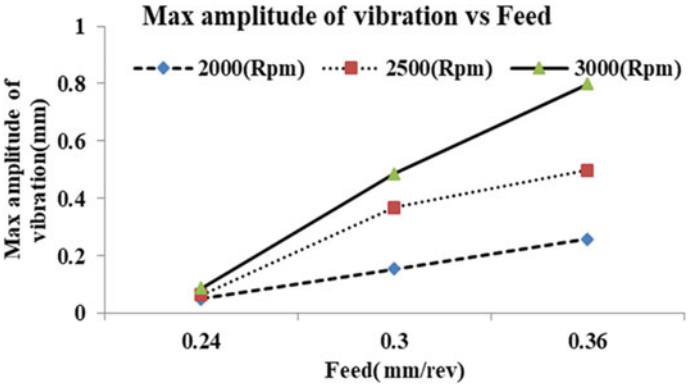

Fig. 17 Graph between max amplitude of vibration and feed

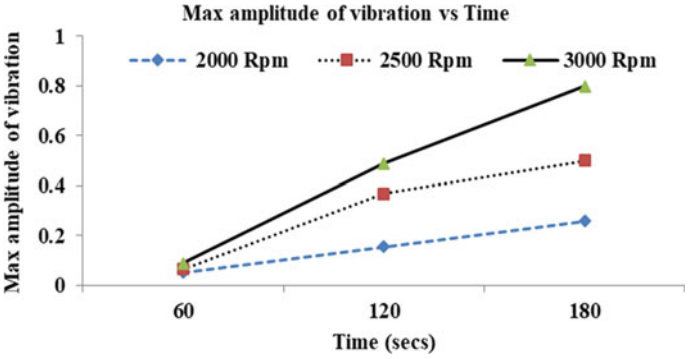

Fig. 18 Graph between max amplitude of vibration and time bit

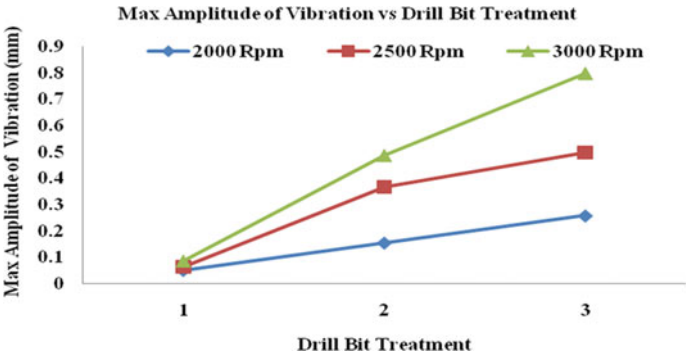

Fig. 19 Graph between max amplitude of vibration and drill treatment

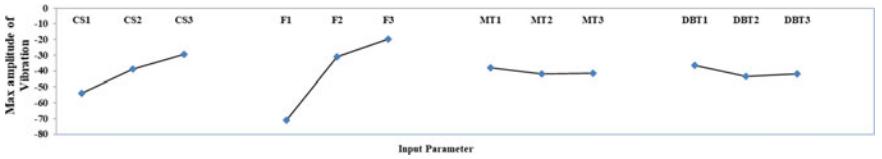

Fig. 20 Effects on max amplitude of vibration

0.36 mm/rev, machining time of 60 s and drill bit treatment of 1 are the optimum conditions required to obtain maximum amplitude of vibration (Table 7).

Figure 22 predicts that the concentricity decreases with an increase in the cutting speed. The slope of the curve is steepest for feed rate of 0.36 mm/rev and time of 180 s. In Fig. 21, however, the curve more or less does not fluctuate much for lower feed rates, i.e. at feed rates of 0.24 and 0.3 mm/rev. Figure 23 also follows a similar nature, where the time at 60 and 120 s does not fluctuate much with an increase in the cutting speed. In Fig. 24 also, the curve has a similar nature. The ANOVA table

Table 7 ANOVA on max amplitude of vibration

Source of variation	Sum of squares	DOF	Mean square	*F*	*F* table	Contribution %
Cutting speed (V)—IP1	0.1374	2	0.0687	343.61	4.2	26.84
Feed (F)—IP2	0.3085	2	0.1543	771.31	4.2	60.24
Machining time—IP3	0.0219	2	0.0110	54.75	4.2	4.28
Drill bit treatment—IP4	0.0443	2	0.0222	110.77	4.2	8.65
Error	0.002	9	0.000200	–		
SST	0.5122	17				

on deviation from concentricity also shows that the deviation from concentricity is affected by cutting speed (31.13%), feed (34.70%), machining time (11.91%) and drill bit treatment (22.26%). The highest influence is from feed. Figure 25 indicates that a cutting speed of 2000 rpm, feed of 0.36 mm/rev, machining time of 60 s and drill bit treatment of 3 are the optimum conditions required to obtain deviation from concentricity (Table 8).

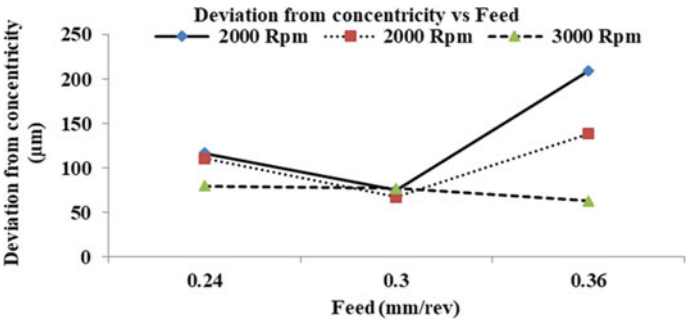

Fig. 21 Graph between deviation from concentricity and feed

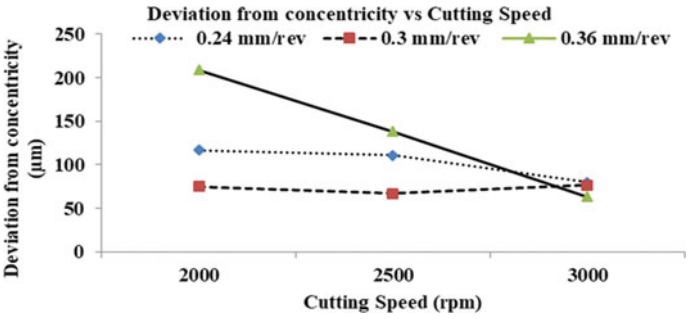

Fig. 22 Graph between deviation from concentricity and cutting speed

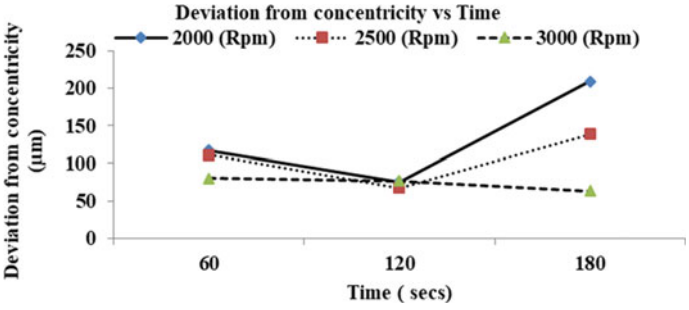

Fig. 23 Graph between deviation from concentricity and time

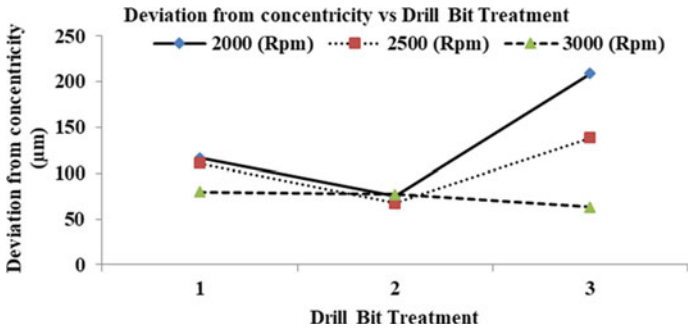

Fig. 24 Graph between deviation from concentricity and drill bit treatment

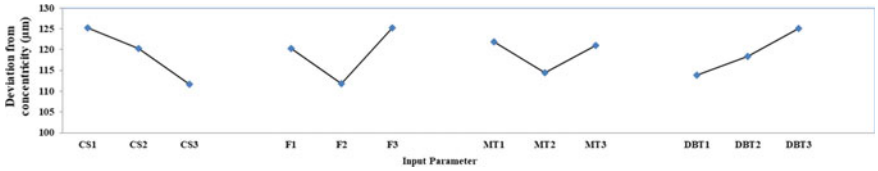

Fig. 25 Effects on deviation from concentricity (µm)

Table 8 ANOVA on deviation from concentricity (µm)

Source of variation	Sum of squares	DOF	Mean square	*F*	*F* table	Contribution %
Cutting speed (V)—IP1	5476.7980	2	2738.3990	13,691,994.89	4.2	31.13
Feed (F)—IP2	6105.6411	2	3052.8205	15,264,102.72	4.2	34.70
Machining time—IP3	2095.7422	2	1047.8711	5,239,355.56	4.2	11.91
Drill bit treatment—IP4	3916.4306	2	1958.2153	9,791,076.39	4.2	22.26
Error	0.002	9	0.000200	–		
SST	17,594.6118	17				

Figure 26 predicts that as the cutting speed increases, the deviation from cylindricity decreases. The slope of the curve is steepest for feed rate of 0.36 mm/rev and time 180 s, and we also note that there is considerable difference between the deviations from cylindricity values between feed rate of 0.36 and 0.3 mm/rev. The curve, however, does not fluctuate much for lower feed rate and time. The curves in Figs. 27, 28 and 29 follow a similar trend. The ANOVA table on deviation from cylindricity also shows that the deviation from cylindricity is affected by cutting speed (26.55%), feed (46.01%), machining time (8.22%) and drill bit treatment (19.21%). The highest influence is from feed. Figure 30 indicates that a cutting speed of 2000 rpm, feed of

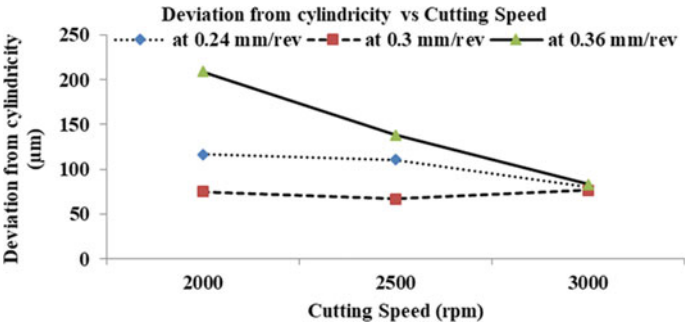

Fig. 26 Graph between deviation from cylindricity and cutting speed

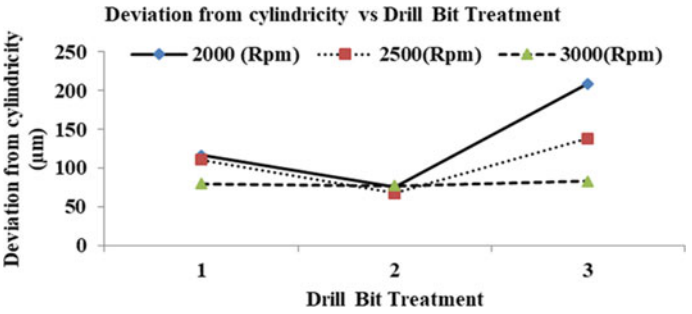

Fig. 27 Graph between deviation from cylindricity and drill bit treatment

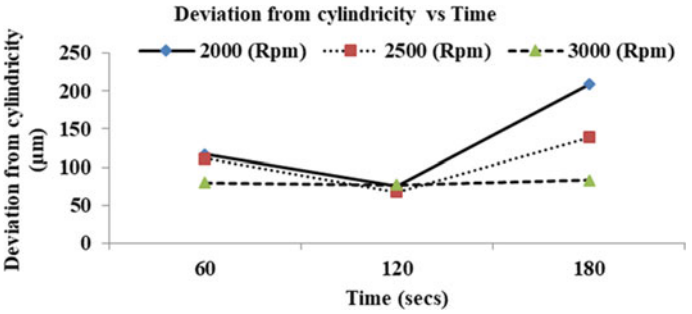

Fig. 28 Graph between deviation from cylindricity and time

0.36 mm/rev, machining time of 60 s and drill bit treatment of 3 are the optimum conditions required to obtain deviation from cylindricity (Table 9).

In Fig. 31, we see that the deviation from diameter is minimum for drill bit number 2 and that too for a cutting speed of 3000 rpm. The deviation from diameter is on the higher side for drill bit number 3. In Fig. 32, we see that as the cutting speed increases, the slope initially increases and then tilts downwards. Figures 33 and 34

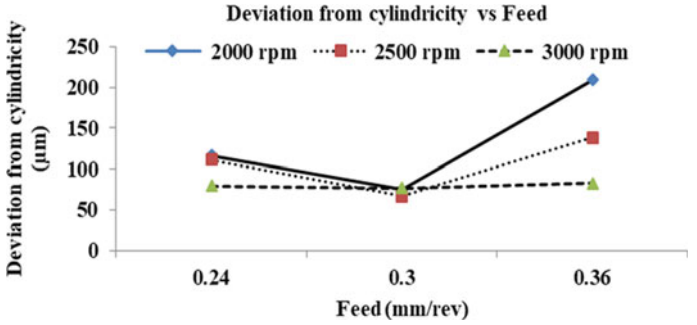

Fig. 29 Graph between deviation from cylindricity and feed

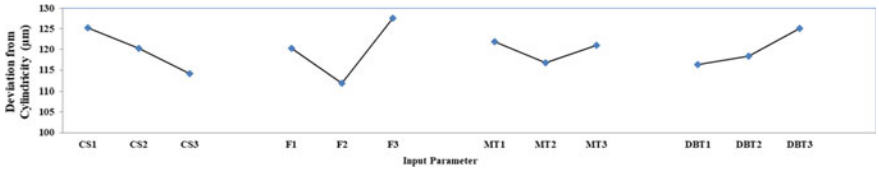

Fig. 30 Effects on deviation from cylindricity (µm)

Table 9 ANOVA on deviation from cylindricity (µm)

Source of variation	Sum of squares	DOF	Mean square	*F*	*F* table	Contribution %
Cutting speed (V)—IP1	4329.3313	2	2164.6656	10,823,328.22	4.2	26.55
Feed (F)—IP2	7502.8411	2	3751.4205	18,757,102.72	4.2	46.01
Machining time—IP3	1341.0756	2	670.5378	3,352,688.89	4.2	8.22
Drill bit treatment—IP4	3133.0972	2	1566.5486	7,832,743.06	4.2	19.21
Error	0.002	9	0.000200	–		
SST	16,306.3452	17				

follow a similar pattern. The ANOVA table on deviation from diameter also shows that the deviation from diameter is affected by cutting speed (26.89%), feed (59.47%), machining time (1.89%) and drill bit treatment (11.75%). The highest influence is from feed. Figure 35 indicates that a cutting speed of 2000 rpm, feed of 0.36 mm/rev, machining time of 180 s and drill bit treatment of 2 are the optimum conditions required to obtain deviation from diameter (Table 10).

Figure 36 tells that as the cutting speed increases, the deviation from perpendicularity remains more or less constant, but after 2500 rpm, the slope tilts downwards. In Fig. 37, the slope of the curve initially moves downwards, and after a feed of

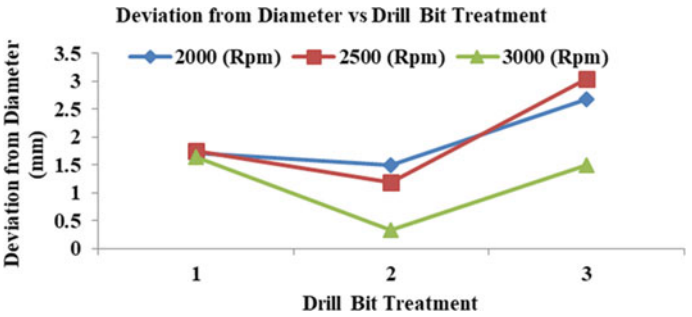

Fig. 31 Graph between deviation from diameter and drill bit treatment

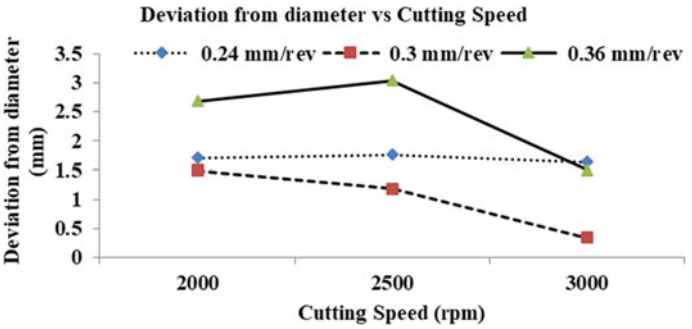

Fig. 32 Graph between deviation from diameter and cutting speed

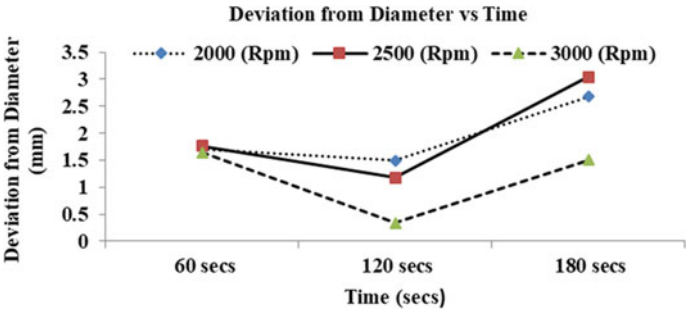

Fig. 33 Graph between deviation from diameter and time

0.3 mm/rev, the slope tilts upwards. The same nature of the curve is followed in Figs. 38 and 39 as well. The ANOVA table on deviation from perpendicularity also shows that the deviation from perpendicularity is affected by cutting speed (8.61%), feed (84.09%), machining time (1.36%) and drill bit treatment (5.94%). The highest influence is from feed. Figure 40 indicates that a cutting speed of 2000 rpm, feed of

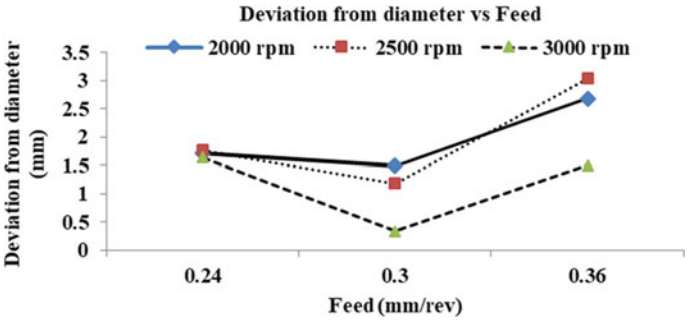

Fig. 34 Graph between deviation from diameter and feed

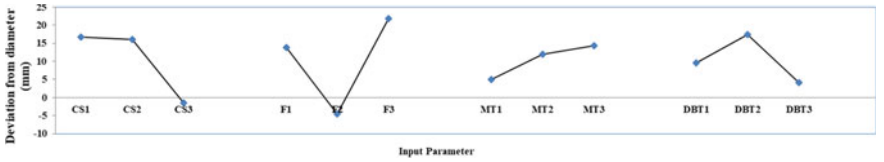

Fig. 35 Effects on deviation from diameter (mm)

Table 10 ANOVA on deviation from diameter (mm)

Source of variation	Sum of squares	DOF	Mean square	*F*	*F* table	Contribution %
Cutting speed (V)—IP1	1.3356	2	0.6678	3338.89	4.2	26.89
Feed (F)—IP2	2.9540	2	1.4770	7385.06	4.2	59.47
Machining time—IP3	0.0940	2	0.0470	235.06	4.2	1.89
Drill bit treatment—IP4	0.5836	2	0.2918	1459.06	4.2	11.75
Error	0.002	9	0.000200	–		
SST	4.9672	17				

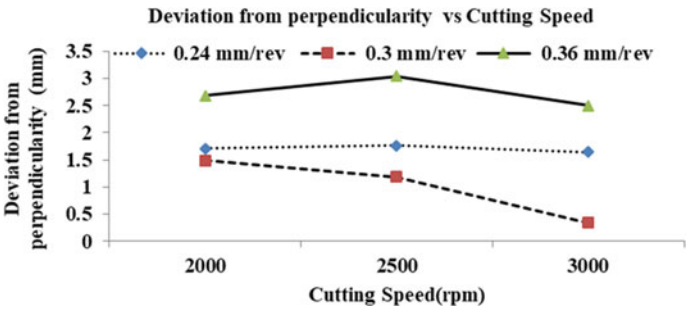

Fig. 36 Graph between deviation from perpendicularity and cutting speed

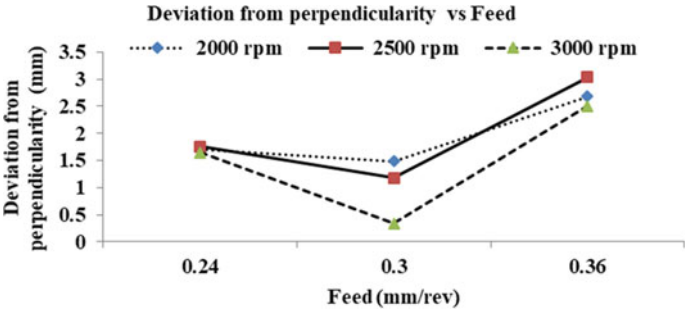

Fig. 37 Graph between deviation from perpendicularity and feed

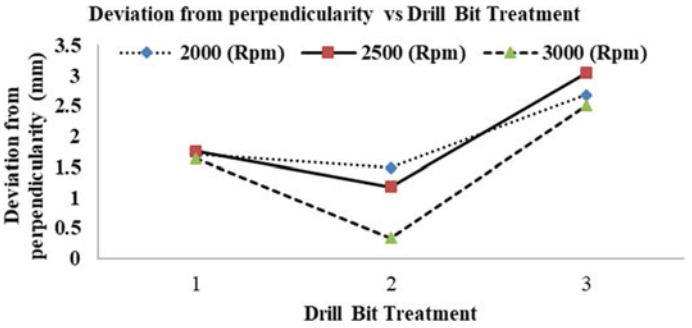

Fig. 38 Graph between deviation from perpendicularity and drill bit treatment

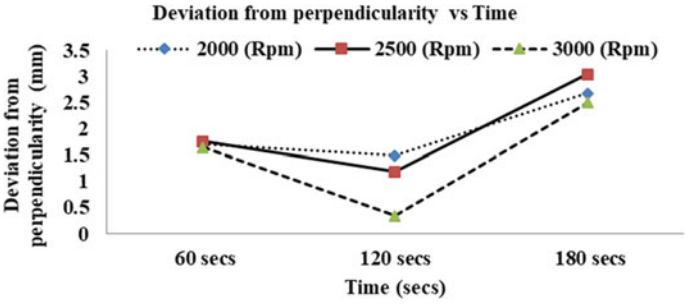

Fig. 39 Graph between deviation from perpendicularity and cutting speed

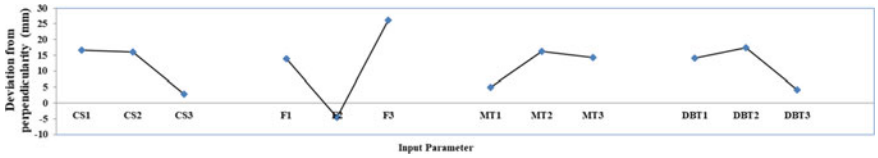

Fig. 40 Effects on deviation from perpendicularity (mm)

Table 11 ANOVA on deviation from perpendicularity (mm)

Source of variation	Sum of squares	DOF	Mean square	*F*	*F* table	Contribution %
Cutting speed (V)—IP1	0.4689	2	0.2344	1172.22	4.2	8.61
Feed (F)—IP2	4.5807	2	2.2903	11,451.72	4.2	84.09
Machining time—IP3	0.0740	2	0.0370	185.06	4.2	1.36
Drill bit treatment—IP4	0.3236	2	0.1618	809.06	4.2	5.94
Error	0.002	9	0.000200	–		
SST	5.4472	17				

0.36 mm/rev, machining time of 120 s and drill bit treatment of 2 are the optimum conditions required to obtain deviation from perpendicularity (Table 11).

4 Conclusions

The following are the output responses that were obtained and studied during the drilling operation of AM60 magnesium alloy. These output responses are very important during the machining of this alloy. It can be concluded that cutting speed, feed, machining time and drill bit treatment have high impact on the final outputs mentioned above. It is desired that we select the best combination of the input parameters so as to obtain the desired results. The ANOVA technique is used to obtain the results. The inputs have a unique effect on the output parameters. The highest impact of cutting speed is on deviation from concentricity and that of feed is on deviation from perpendicularity. The highest contribution of machining time is on residual stress and that of drill bit treatment is on thermal stress.

References

1. Xue-Nan GU et al (2014) Magnesium based degradable biomaterials. Front Mater Sci 8(3):200–218
2. Chen WC, Fuh KH, Wu CF, Chang BR (1996) Design optimization of a split-point drill by force analysis. J Mater Process Technol 58:314–322
3. Chen WC, Tsao CC (1999) Cutting performance of different coated twist drills. J Mater Process Technol 88:203–207
4. Mundheka AR, Jadhav SR (2015) Optimization of drilling process parameters: a review. Int J Res Appl Sci Eng Technol (IJRASET) 3(II). ISSN: 2321-9653
5. Chavan P, Gujar A (2017) Study the effect of machining parameter on surface roughness in drilling of SG 500/7 material. Int J Adv Eng Res Dev 3(7). e-ISSN (O): 2348-4470 p-ISSN (P): 2348-6406 at: https://www.researchgate.net/publication/309211582

6. Alagarsamy SV, Arockia S, Sagayaraj V, Raveendran P (2016) Optimization of drilling process parameters on surface roughness and material removal rate by using Taguchi Method. Int J Eng Res Gen Sci 4(2). ISSN 2091-2730. https://www.researchgate.net/publication/304894900
7. Vankanti VK, Ganta V (2013) Optimization of process parameters in drilling of GFRP composite using Taguchi method. Received 4 May 2013. Accepted 16 Oct 2013 Available online 21 Nov 2013 Elsevier. © 2013 Brazilian Metallurgical, Materials and Mining Association. Published by Elsevier
8. Tripathi A, Singari RM, Dahiya V (2016) Optimization of process parameters with effect of thrust and torque in drilling operation. IJAPIE 1(2):1–12. https://www.researchgate.net/publication/301298419
9. Grigoraş CC, Brabie G (2015) The influence of milling parameters on the surface roughness in the case of magnesium alloy AZ61A. Int J Mod Manuf Technol VI(2):57–61
10. Erkan Ö, Demetgül M, Işik B, Tansel İN (2014) Selection of optimal machining conditions for the composite materials by using Taguchi and GONNs. Measurement 48:306–313
11. Lin CL, Lin JL, Ko TC (2002) Optimisation of the EDM process based on the orthogonal array with fuzzy logic and grey relational analysis method. Int J Adv Manuf Technol 19:271–277
12. Tsao CC (2007) Grey-Taguchi method to optimize the milling parameters of aluminum alloy. Int J Adv Manuf Technol 40:41–48
13. Pawade RS, Joshi SS (2011) Multi-objective optimization of surface roughness and cutting forces in high-speed turning of Inconel 718 using Taguchi grey relational analysis (TGRA). Int J Adv Manuf Technol 56:47–62
14. Prasanna J, Karunamoorthy L, Raman MV, Prashanth S, Chordia DR (2014) Optimization of process parameters of small hole dry drilling in Ti–6Al–4V using Taguchi and grey relational analysis. Measurement 48:346–354
15. Mondal S, Paul CP, Kukreja LM, Bandyopadhyay A, Pal PK (2013) Application of Taguchi-based gray relational analysis for evaluating the optimal laser cladding parameters for AISI1040 steel plane surface. Int J Adv Manuf Technol 66:91–96
16. Sivam SP, Singh S et al (2017) Multi response optimization of setting input variables for getting better product quality in machining of magnesium AM60 by grey relation analysis and ANOVA. Periodica Polytech Mech Eng 62(2):118–125
17. Sivam SPSS, Gopal M, Venkatasamy S, Singh S (2015a) An experimental investigation and optimisation of ecological machining parameters on aluminium 6063 in its annealed and unannealed form. J Chem Pharm Sci 9:46–53
18. Sivam SPSS, Gopal M, Venkatasamy S, Singh S (2015b) Application of forming limit diagram and yield surface diagram to study anisotropic mechanical properties of annealed and unannealed SPRC 440E steels. J Chem Pharm Sci 9:15–22
19. Sivam SPSS, Abburi LK, Sathiya MK, Rajendra K (2016) Investigation exploration outcome of heat treatment on corrosion resistance of AA 5083 in marine application. Int J Chem Sci 14:453–460
20. Sivam SPSS, Sekar VGU, Mishra A, Mishra S, Mondal A (2016) Orbital cold forming technology—combining high quality forming with cost effectiveness—a review. Indian J Sci Technol 9(38):1–7
21. Sivam SPSS, Kumaran D, Natarajan H, Mishra A (2019) Numerical simulation of cold orbital forging process for gear manufacturing. Int J Mod Manuf Technol X(2):126–132. ISSN 2067-3604
22. Sivam SPSS, Saravanan K, Pradeep N, Moorthy K, Rajendrakumar S (2019) The grey relational analysis and anova to determine the optimum process parameters for friction stir welding of Ti and Mg Alloys. Periodica Polytech Mech Eng. https://doi.org/10.3311/PPme.12117
23. Sivam SPSS, Rajasekaran A, RajendraKumar S, SathiyaMoorthy K, Gopal M (2019) A study of cooling time, copper reduction and effects of alloying elements on the microstructure and mechanical properties of SG iron casting during machining. Aust J Mech Eng. https://doi.org/10.1080/14484846.2018.1560679
24. Sivam SPSS, Kumaran D, Saravanan K, Umasekar VG, Rajendrakumar S, Moorthy KS (2018) Thickness distribution and numerical modelling of conventional superplastic forming in AA2024 alloy. Int J Mod Manuf Technol X(2):76–85. ISSN 2067-3604

25. Sivam SPSS, Loganathan GB, Umasekar VG, Suresh Kumar PS, Raja S (2019) Study on micro structural characteristics and mechanical behaviour of AISI1050 steel under various heat treatments. Int J Veh Struct Syst 11(1):15–20. https://doi.org/10.4273/ijvss.11.1.04
26. Sivam SPSS, Loganathan GB, Saravanan K, Umasekar VG, Rameez TPM (2019) Optimization of passenger car door impact beam using quasi static CAE analysis. Int J Veh Struct Syst 11(1):21–26. https://doi.org/10.4273/ijvss.11.1.05
27. Sivam SPSS, Saravanan K, Loganathan GB, Kumaran D, Rajendrakumar S (2019) Root cause analysis for failure of door lock case assembly during caulking process. Int J Veh Struct Syst 11(1):11–14. https://doi.org/10.4273/ijvss.11.1.03
28. Sivam SPSS, Loganathan GB, Ganesh Babu L, Kumaran D (2019) Enhancing the mechanical properties and formability of cold rolled closed annealed sheet for automobile applications. Int J Veh Struct Syst 11(4):15–20. https://doi.org/10.4273/ijvss.11.4.17
29. Sivam SPSS, UmaSekar VG, Saravanan K, RajendraKumar S, Karthikeyan P, Sathiya Moorthy K (2016) Frequently used anisotropic yield criteria for sheet metal applications: a review. Indian J Sci Technol 9(47):1–6

A Low-Cost Fabrication Approach of UV, VIS and NIR Dielectric Reflectors

Venkatesh Yepuri, R. S. Dubey, and Brijesh Kumar

Abstract Reflectors are the primary need of several optical instruments that have been demanded their potential applications in solar cells, LEDs, lasers, and so forth. In this paper, we present the fabrication and characterization of ultraviolet (UV), visible (VIS), and infrared (NIR) dielectric reflectors composed of TiO_2 and SiO_2 films by varying the solution chemistry. Due to the tuning of solution chemistry, we could produce UV, VIS, and NIR reflectors having 100% reflectance within their respective spectrums. By UV–Vis spectroscopy investigation, the center wavelengths are found to be 380, 563, and 832 nm for the UV, VIS, and NIR reflectors, respectively. Scanning electron microscopy analysis showed the formation of the periodic structure of TiO_2 and SiO_2. Finally, our study demonstrates the easy and rapid fabrication of optical reflectors for the desired reflectance band.

Keywords Reflectors · Optical coating · Periodic layers · Reflectance · Dielectric films

1 Introduction

The sunlight which falls on earth consists of a massive spectrum of ultraviolet (UV), visible (VIS), and infrared (IR) light rays. Among these, ultraviolet and infrared light radiations are harmful to the human bodies if exposed for a long time, whereas visible light radiation is helpful for visualization of the objects. It means the molding of a particular band or multi-band solar spectrum is needed for their application, like UV/IR reflection/transmission. In this way, sunlight can be harvested to enhance the light absorption in thin-film solar cells or UV protection to overcome the problem of skin burn [1, 2].

V. Yepuri · R. S. Dubey (✉)
Advanced Research Laboratory for Nanomaterials & Devices, Department of Nanotechnology, Swarnandhra College of Engineering and Technology, Seetharampuram, Narsapur, A.P, India
e-mail: rag_pcw@yahoo.co.in

B. Kumar
Amity Institute of Nanotechnology, Amity University, Gurgaon, Haryana, India

G. Kumaresan et al. (eds.), *Advances in Materials Research*, Springer Proceedings in Materials 5, https://doi.org/10.1007/978-981-15-8319-3_36

Thus, light propagation can be manipulated by using optical coating by the mechanism of reflection/transmission/anti-reflection phenomena. The coating is nothing but the preparation of the thin film on the desired substrate to have either a reflection or antireflection property. The multilayer dielectric coatings have been demanded as the passive device in solar cells, light-emitting diodes, vertical-cavity surface-emitting diodes, waveguides, etc. [3–6]. The reflectors based on transparent coating of dielectric films have attracted the attention of scientists over the metallic reflectors owing to their high maintenance cost and less durability. In addition, dielectric optical coatings have the capability of self-cleaning due to their hydrophobic nature [7]. The propagation of light waves is strongly influenced by the refractive index and thickness of the films.

The most preferred dielectric materials used to fabricate reflectors are TiO_2, ZnO, Al_2O_3, ZrO2, and SiO_2. However, the combination of TiO_2/SiO_2 thin films has been reported as the better ones due to their large refractive index contrast [8]. There are various fabrication techniques available to prepare these reflectors, such as sputtering, e-beam evaporation, chemical vapor deposition, sol–gel spin coating etc, [9–11]. However, the fabrication cost is high with the standard fabrication methods except the sol–gel spin coating, which is the simplest and cost-effective ones [12]. Besides, no high vacuum is required to deposit these films, and hence, it reduces the fabrication time, particularly for the preparation of multilayer structures. The great advantage of the sol-gel spin coating technique is the easy tuning of process parameters [13, 14]. With these prospects, the sol–gel spin coating technique is the facile method to fabricate the dielectric reflectors having the reflection band of interest. Dubey et al. reported the fabrication of visible reflector based on multilayer films of TiO_2/SiO_2 and explored the optical reflectance. The fabricated reflector showed 100% reflectance in the visible spectrum with its center wavelength of 568 nm [15]. Nagayoshi et al. presented the fabrication of near-infrared reflectors based on TiO_2 film using nanoparticles and SiO_2 thin film using a solution. The fabricated reflector endorsed 90% reflectance in the near-infrared wavelength. They further suggested the application of the fabricated reflector as the backend reflector for the thin-film solar cells [16]. Deopura et al. prepared the omnidirectional visible reflector composed of 19 alternating layers of tin sulfide and silica by using the thermal evaporation technique. Though reflectivity was good, the high-fabrication cost and more processing time cannot be ignored [17]. Similarly, Isabella et al. fabricated a visible reflector composed of eight layers of hydrogenated amorphous silicon and silicon nitride films using RF plasma-enhanced chemical vapor deposition method [18]. The multilayer structure endorsed 100% reflectance in the visible region with its center wavelength 600 nm, and further, the investigation was explored for its solar cell application. Rabaste et al. studied the sol–gel process parameters of the dielectric TiO_2/SiO_2 reflectors [19]. They fabricated the fourteen layers of TiO_2/SiO_2 to achieve visible light reflection, and a maximum 100% reflectance was achieved with its center wavelength of 650 nm. The study was suggested the higher annealing temperature at 900 °C in order to remove the cracks from the films. Choi et al. developed a near-infrared reflector using $TiO_2/SiO_2/TiO_2$ structure by using a sol–gel spin coating technique [20]. The multilayer structure showed about 62% reflectance

in the near-infrared region with its center wavelength of 1000 nm. However, to achieve 100% reflectance in the desired wavelength region, it needs more number of layers. Wang et al. fabricated a multilayer structure using Al/MgF_2 by using e-beam evaporation technique [21]. The multilayer structure endorsed about 70% reflectance in the ultraviolet region with its center wavelength of 160 nm. In another study, Dubey et al. fabricated the multilayer structures of TiO_2/SiO_2 using sol–gel spin coating technique [22]. The reported multilayer structure could show 78% reflectance in the near-infrared region with its center wavelength of 829 nm.

In this paper, we present the fabrication of various dielectric reflectors based on TiO_2/SiO_2 films. This study explores the preparation of ultraviolet (UV), visible (VIS), and near-infrared (NIR) reflectors by varying the respective chemistry.

2 Materials and Methods

Titanium isopropoxide (TTIP) and tetraethyl orthosilicate (TEOS) purchased from Sigma-Aldrich were used as precursors for the preparation of TiO_2 and SiO_2 thin films, respectively. Acetic acid and hydrochloric acid were used as the chelating agents, while ethyl alcohol and de-ionized water were preferred as the solvents. For the fabrication of ultraviolet (UV), visible (VIS), and near-infrared (NIR) reflectors, we have prepared the different gels of TiO_2 and SiO_2 as described here. For the fabrication of UV, VIS, and NIR reflectors, the TiO_2 gels were prepared by using ethanol: DI water: TTIP: Hcl in the molar ratio 10:0.5:0.5:0.1 (Solution A1), ethanol: DI water: TTIP: Hcl, in the molar ratio 10:0.5: 0.75: 0.1 (Solution A2), and ethanol: Hcl: Acetic acid: TTIP in the molar ratio 10:0.2:2.4:2.4 (Solution A3), respectively. The solvent was mixed with the chelating agent under constant stirring for 15 min. Later, the precursor was added in the above-prepared solution under constant stirring and further stirred for 4 h and then kept for 24 h aging. Similarly, to fabricate the UV, VIS, and NIR reflectors, the SiO_2 gels were prepared by using ethanol: DI water: TEOS: Hcl in the molar ratio 10:4:0.5:0.1 (Solution B1), ethanol: DI water: TEOS: Hcl, in the molar ratio 10: 4: 0.75: 0.1 (Solution B2), and ethanol: Hcl: Acetic acid: TEOS in the molar ratio 10:0.2:2.4:2.4 (Solution B3), respectively. Initially, the solvent was mixed with chelating agents under 15 min stirring. Later, drop by drop TEOS was added to the resultant solutions. The prepared SiO_2 solutions of respective reflectors were kept for 48 h aging. After aging, both solutions of TiO_2 and SiO_2 were found as the transparent gels. The prepared TiO_2 and SiO_2 gels were spin-coated on cleaned glass substrates with the spin speed 3000 RPM for 30 s to fabricate the TiO_2 film (high-refractive-index layer) and SiO_2 film (low-refractive-index layer) film alternatively. Each spin-coated film was dried in hot air oven under 100 °C for 30 min and then sintered at 500 °C for a period of 1 h. The fabricated UV, VIS, and NIR reflectors were characterized to study the cross-section of multilayer structures using scanning electron microscopy (SEM, MIRA3 TESCAN) and reflectance by using UV–Vis spectrophotometer integrated with a specular reflectance attachment (UV1800 Shimadzu, Japan).

3 Results and Discussions

By varying the solution chemistry, we have prepared the UV, VIS, and NIR reflectors. For the preparation of UV reflector, the solutions A1 and B1 were used to prepare the TiO_2 and SiO_2 thin films, respectively. Figure 1a shows the reflectance of UV

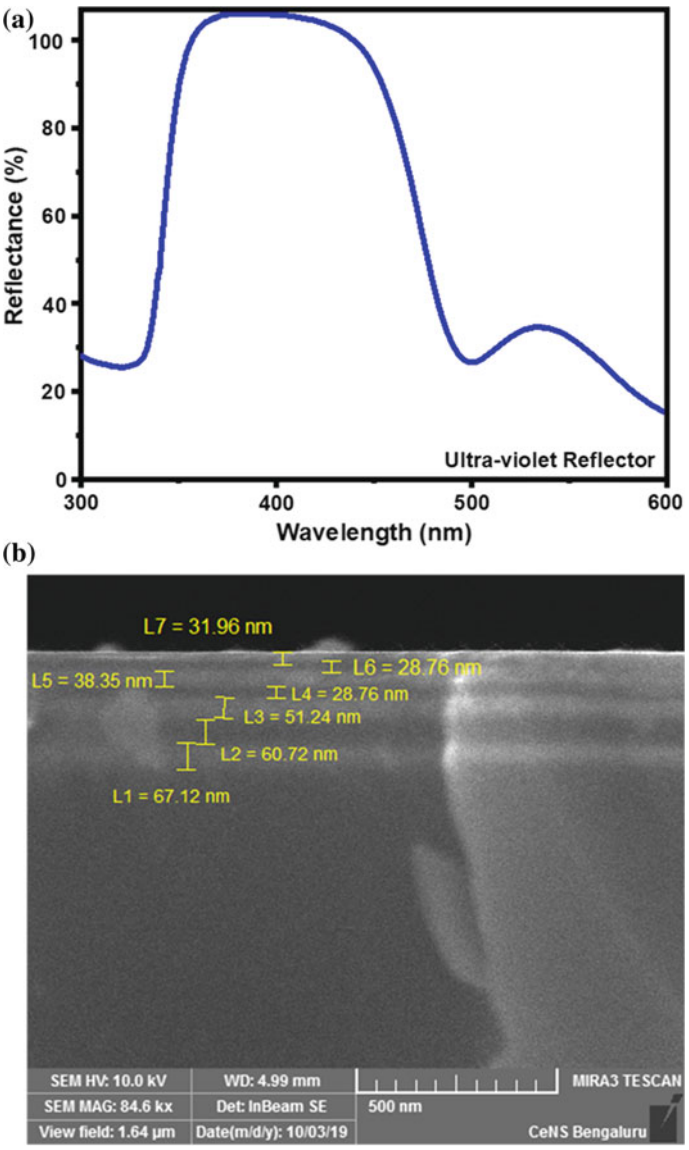

Fig. 1 Reflectance spectra (**a**) and cross-sectional image (**b**) of the ultra-violet reflector

reflector composed of 3.5 pairs of TiO_2/SiO_2 layers.

We can observe 100% reflectance with its center wavelength of 380 nm. The preparation of 3.5 pairs of TiO_2 and SiO_2 films was confirmed by the cross-sectional SEM measurement, as depicted in Fig. 1b. The brighter and darker layers represent spin-coated films of TiO_2 and SiO_2, respectively. The estimated thicknesses of individual layers TiO_2, SiO_2, TiO_2, SiO_2, TiO_2, SiO_2, and TiO_2 were 67.12 nm, 60.72 nm, 51.24 nm, 28.76 nm, 38.35 nm, 28.76 nm, and 31.96 nm, respectively.

Further, we have fabricated the visible reflector (using solutions A2 and B2) and found that the multilayer structure of 2.5 pairs of TiO_2/SiO_2 was sufficient to have 100% reflectance in the visible region with its center wavelength of 563 nm, as shown in Fig. 2a. The multilayer films of $TiO_2/SiO_2/TiO_2/SiO_2/TiO_2$ were examined by SEM cross-sectional study and depicted in Fig. 2b. The estimated thicknesses of the constituent films of TiO_2, SiO_2, TiO_2, SiO_2, and TiO_2 were 95.33 nm, 196.28 nm, 117.77 nm, 145.81 nm, and 67.29 nm, respectively.

Finally, near-infrared (NIR) reflector was fabricated using solutions A3 and B3. The examination of reflectance was performed by using a UV–Vis spectrometer as shown in Fig. 3a. One can clearly observe a broad peak centered at wavelength of 831 nm.

Preparation of 2.5 pairs of TiO_2/SiO_2 films was found enough to achieve a 100% reflectance. The confirmation of 2.5 pairs of TiO_2/SiO_2 was carried out by doing SEM cross-sectional analysis as shown in Fig. 3b. We can clearly observe the layered structure of TiO_2, SiO_2, TiO_2, SiO_2, and TiO_2 films with their thicknesses of 186.36 nm, 130.45 nm, 105.79 nm, 124.24, and 130.45 nm, respectively.

4 Conclusions

Using a simple and inexpensive method, UV, VIS, and NIR optical reflectors were fabricated and characterized for their optical and morphological properties. By tuning the solution chemistry, we could successfully prepare the optical reflectors of TiO_2/SiO_2 having their reflection windows in the wavelength range of UV, VIS, and NIR. The reflectance investigation evidenced the desired reflection band centered at wavelengths of 380, 563, and 832 nm corresponds to the UV, VIS, and NIR spectrums. To achieve 100% reflectance in the VIS and NIR regions, 2.5 pairs of TiO_2/SiO_2 films were found sufficient, whereas to attain UV reflectance it was of 3.5 pairs. The cross-sectional investigations of various reflectors demonstrated the fabrication of the periodic layer of TiO_2 and SiO_2. In summary, the solution preparation chemistry played a significant role in fabricating the UV, VIS, and NIR reflectors that, too, in a cost-effective and straightforward way.

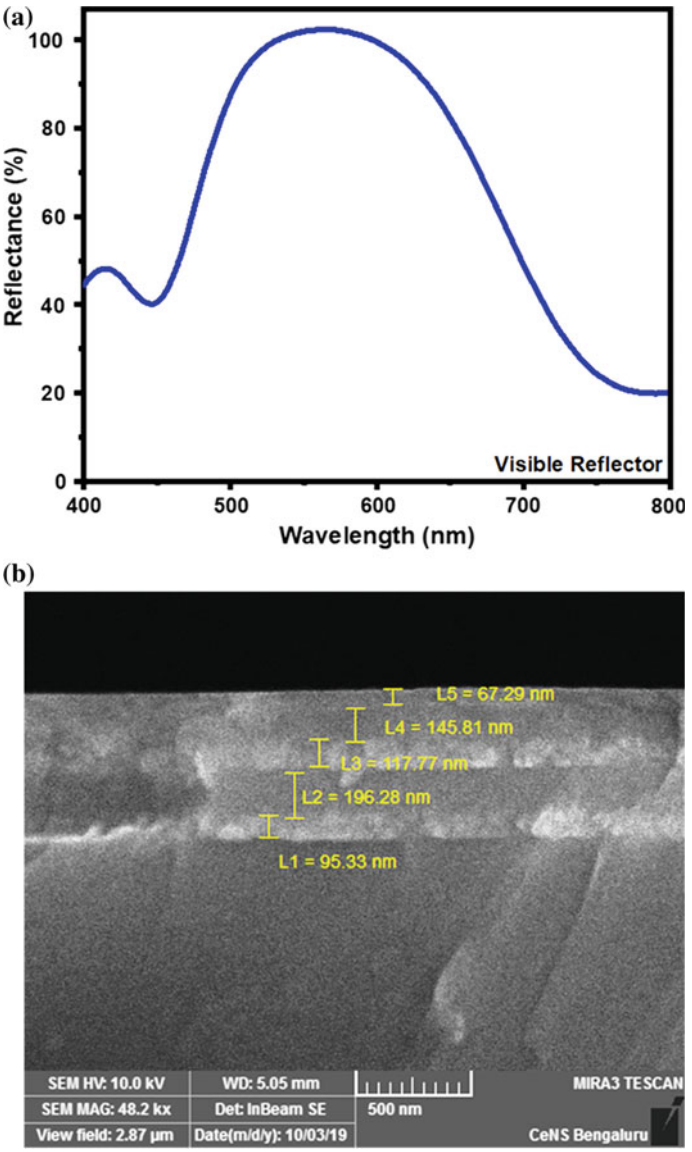

Fig. 2 Reflectance spectra (**a**) and cross-sectional image (**b**) of the visible reflector

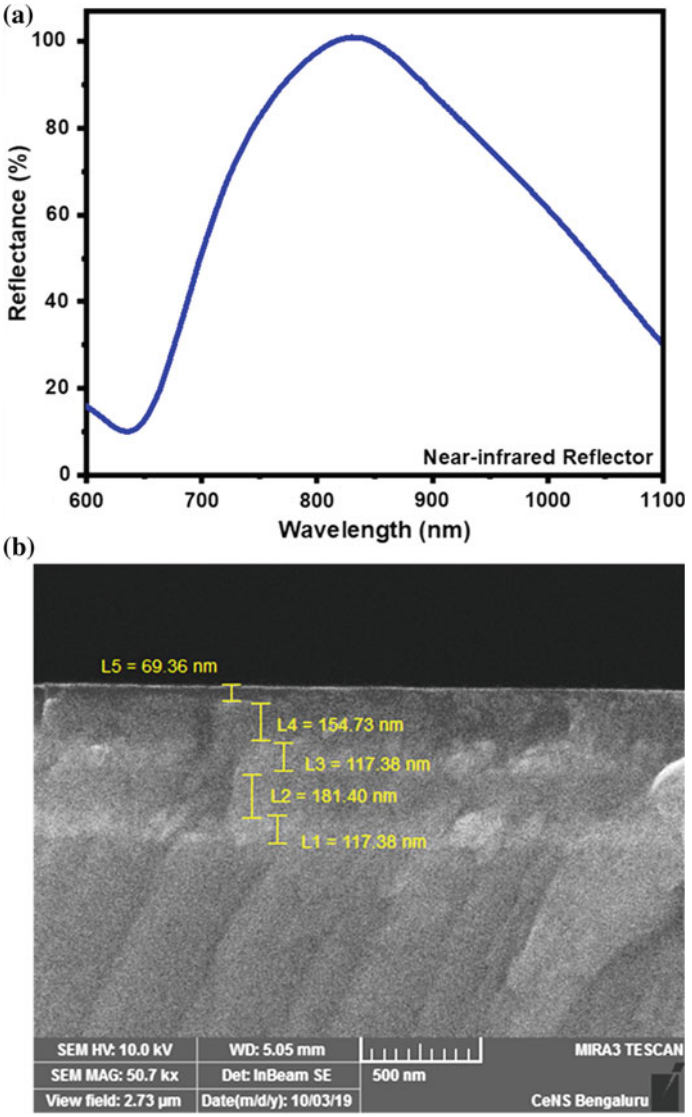

Fig. 3 Reflectance spectra (**a**) and cross-sectional image (**b**) of the near-infrared reflector

Acknowledgements This research grant was supported by the UGC-DAE Consortium for Scientific Research (Indore) under the collaborative research scheme.

References

1. Ren R (2018) Enhanced light absorption of silicon solar cells with dielectric nanostructured back reflector. Opt Commun 417:110–114
2. Castro Smirnov JR (2013) Selective UV reflecting mirrors based on nanoparticle multilayers. Adv Funct Mater 23(22):2805–2811
3. Mutitu JG (2010) Hybrid dielectric-metallic back reflector for amorphous silicon solar cells. Energies 3(12):1914–1933
4. Zhou S (2018) Effect of dielectric distributed bragg reflector on electrical and optical properties of GaN-based flip-chip light-emitting diodes. Micromachines 9(12):650
5. Hamaguchi T (2019) GaN-based vertical-cavity surface-emitting lasers incorporating dielectric distributed Bragg reflectors. Appl Sci 9(4):733
6. Ibanescu M (2000) An all-dielectric coaxial waveguide. Science 289(5478):415–419
7. Wu Z (2007) Structural color in porous, superhydrophilic, and self-cleaning SiO_2/TiO_2 Bragg stacks. Small 3(8):1445–1451
8. Macleod A (1999) The early days of optical coatings, J Opt A: Pure Appl Opt 1(S):779–783
9. Lissberger PH (1970) Optical applications of dielectric thin films. Rep Prog Phys 33(1):197–268
10. Anaya M, Rubino A, Calvo ME, Miguez H (2016) Solution processed high refractive index contrast distributed Bragg reflectors. J Mater Chem C 4(20):4532–4537
11. Chichibu SF (2006) Dielectric SiO_2/ZrO_2 distributed Bragg reflectors for ZnO micro cavities prepared by the reactive helicon-wave-excited-plasma sputtering method. Opt Exp 88(16):1619141–1619143
12. Chang T-H (2018) Investigation of TiO_2–$Al2O_3$ bi-layer films as Bragg reflector of blue light by using electron beam evaporation. Microsyst Technol 24(10):3941–3948
13. Lu TC (2002) InP/InGaAlAs distributed Bragg reflectors grown by low-pressure metal organic chemical vapor deposition. J Cryst Growth 250(4):305–312
14. Tyona MD (2013) A theoritical study on spin coating technique. Adv Mat Res 2(4):195–208
15. Dubey RS, Ganesan V (2017) Visible and near-infrared wavelength-selective dielectric reflectors for light management applications. Superlat Microst 111:1099–1103
16. Nagayoshi (2015) TiO_2 nanoparticle/SiO_2 composite back reflector for solar cells. Energy Procedia 77:242–247
17. Deopura M (2001) Dielectric omnidirectional visible reflector. Opt Lett 26(15):1197–1199
18. Isabella O (2012) Design and application of dielectric distributed Bragg back reflector in thin-film silicon solar cells. J Non-Cryst Solids 358(17):2295–2298
19. Rabaste S (2002) Sol–gel fabrication of thick multi layers applied to Bragg reflectors and micro cavities. Thin Solid Films 416(1–2):242–247
20. Choi J, Han K, Kim JH (2014) Enhanced near infrared reflectance of $TiO_2/SiO_2/TiO_2$ multilayer structure using a base-catalyzed SiO2 film. Thin Solid Films 569:100–103
21. Wang X-D (2015) Design and fabrication of far ultraviolet filters based on π-multilayer technology in high-k materials. Sci Rep 5(1):1–6
22. Dubey RS, Ganesan V (2017) Fabrication and characterization of TiO_2/SiO_2 based Bragg reflectors for light trapping applications. Results Phys 7:2271–2276

Job Safety Analysis for Various Operations in Cement Industry Using Risk Assessment Matrix

R. Manikandan, G. Rampranav, T. Rajpradesh, and S. Rajesh

Abstract Cement is a basic material which is used for buildings, and it is made up of various combinations of natural substances such as limestone, shells and chalk with clay, and silica sand. During working with cement manufacturing process, workers are exposed to various hazards in their working place. Not only the physical hazard but also the workers are affected mentally through noise, high temperature, and some kind of health risk. The workers should have safety awareness and knowledge to reduce the accidents. A job safety analysis (JSA) is a one of the safety tools and techniques to evaluate the potential hazards associated with each work and provide the proper control measures for the recognized hazards. In cement industry, the job is categorized into non-routine job, new job, and frequently occurring accident job, and this tool is applied. The outcome of this risk assessment methodology provides to control measures for the presence of health and safety hazards in the cement industry.

Keywords Job safety analysis · Risk assessment · Cement · Hazard · Accidents

1 Introduction

In our country, the cement sector is one of the most important branches in economic development. The labor power plays a major role in the supply and treatment of raw material. The cement plants exposed some risk to the workers like dust, noise, and vibration, and this kind of health risk must be protected. Ensuring safety and health for the employees who are working in the industry is more important. The accidents and health problems for the workers cannot be avoided, and also high temperature will affect the workers mentally. Basically, cement industry has more potential for hazard, because in the industry workers are exposed to cement dust, it affects human health [1]. The fundamental part of the industry is unsafe working environment and unsafe workplace due to the presence of hazard in their method [2]. The concept of job safety

R. Manikandan (✉) · G. Rampranav · T. Rajpradesh · S. Rajesh
Department of Mechanical Engineering, Kalasalingam University, Krishnankovil, Tamil Nadu, India
e-mail: rmanikandan198@gmail.com

G. Kumaresan et al. (eds.), *Advances in Materials Research*, Springer Proceedings in Materials 5, https://doi.org/10.1007/978-981-15-8319-3_37

analysis (JSA) and method of identifying the potential hazard from the workplace have been carried out from this paper. Engineering industry involves the production and manufacturing of large amount of products by handling hazardous equipment. The workers who engaged in material handling are met up with risk. It may lead to accidents, explosion, fire, and various hazards. Proper safety system is required for worker's safety life. Job safety analysis (JSA) is a technique which focuses on job task and identifies hazards before it occurs. It focuses on the relationship between the workers and their task. Selection of job is based on the accident frequency, severity, new job, and repetitive exposure [3]. This study was done at Chettinad Cement Corporations Ltd., Karur, and it aims at identifying the major hazards in the cement industry and provides guidelines to reduce the risk associated and to maintain the health of the employees. Not only the physical health issues but also the noise exposure issue and ergonomics of workers are studied. Though the company has ISO 14001/2004, certifications in the abovementioned suggestions will help the management to mitigate serious occupational health hazards and also reduce the compensation for workers through the occurrence of accidents or health hazards [4]. The purpose of the paper is to avoid accidents and health problems during the operation involved in the cement industry. The workers are exposed to dust, noise, and high-temperature effects which lead to many occupational hazards such as work injuries, allergic problems, and fatality. Safety risk scores to be identified for risk analysis. After determining the risks for the workers, the safety risk tables were prepared, and the possible risks were classified as high, moderate, and low-risk degrees concerning occupational and safety risk management system. It was found that the crusher, raw material and cement mills, and rotary kiln are the most dust, noise, and vibration producing units [5]. International Safety Standards state that the first step of risk assessment is to understand the situation and eliminates the hazard. Job safety analysis is the traditional method for risk assessment, where the operator can analyze the sequential tasks. This article possesses that equal emphasis should be given to the participants working in the workplace [6].

Because of certain accidents, JSA is compulsive to avoid such risk and to control the hazard in the workplace. Therefore, the cement industry should take corrective measurements, evaluation, and control of such risk. In industry, workers use chemicals and additives for the manufacturing process at a high temperature. If there any exploded happened, the environment and people will be effect. To forbid from any accidents or hazards happened, the safe procedure for the job should be improved. Every analyzing tool has its procedure to check for hazards and to give the control measure. The abnormal events and abnormal time sequence can be identified by using the graphical method. The risk assessment matrix method can address the amount of risk held during the operation [7].

2 Materials and Methods

In this paper, the risk analysis and assessment have been carried out in cement industry according to job safety analysis (JSA) tool. In this, the cement manufacturing process can be divided into five main sections which are as follows:

1. Raw grinding,
2. Storage and Transportation,
3. Raw milling,
4. Clinker,
5. Cement milling.

2.1 Summary of the Cement Plant

The first step in the cement production process is the raw materials that are used to manufacture cement (limestone and clay) which is blasted from the quarry. After crushing, the raw materials are transported to the plant by conveyor. Before homogenized, the plant stores the material. Too finely ground, the materials are transferred to the raw mill, to produce raw mix. The raw mix is preheated before it goes into the kiln, and by the flame, it can be heated to 2000 °c to produce clinker. When it leaves the kiln, the clinker is rapidly cooled with the atmosphere. This is the basic material to make cement. The gypsum and the secondary additives are added to the clinker, and it is transferred to the grinding for a very finely ground cement. That is transferred to silos to store the cement.

2.2 Methodology

A job safety analysis is a technique or a tool that focuses on a particular job to identify the potential hazard or risk before they occur. It helps to eliminate or reduce the hazard to an acceptable level. It is also called task-oriented risk assessment task which is used to review the hazard and errors in a particular work task and to ensure that suitable safeguards are in place to control those hazards and errors. To prevent harm to the individual(s), carrying out the task is the main goal of the analysis [8]. The JSA divides the job into steps which are based on the frequently occurring accident job, high severity job, non-routine job, and new job. By dividing the critical job into several steps, the potential hazard can be eliminated. Eliminating the hazard is more important than reducing the hazard. The JSA process covers Four major steps: They are identifying hazard, access the probability, and access the consequences [9]. The safe work procedure and practices have been identified by conducting effective Job Safety Analysis technique [10]. The final JSA result brings for the decision on whether the job which is carrying out is acceptable to proceed [11].

The basic steps of conducting the JSA are as follows:

1. Select the job to be analyzed.
2. Separate the job into a sequence of steps.
3. Identify the hazard in each step.
4. Provide preventive measures to overcome the hazard (Fig. 1).

To describe the potential risk as quantitatively or for comparing purpose, the risk assessment matrix table is used. In that table, the probability of risk can be divided into four types. They are very likely, probable, possible, and unlikely. And the severity can also be divided into four types. They are minor, marginal, critical, and fatality. Risk assessment technique consist of four different processes: identifying, analyzing, evaluating, and risk management [12]. It is inadequate to explain the illness at work and injuries occurred by hazard and stresses alone [13]. Numeric risk assessment matrix table is designed to describe the risks quantitatively and for comparison purpose [14]. It is presented to examine the conditions that leads to accident event and therefore to prevent the accident rate in the industry [15]. The risk assessment matrix is shown in Table 1.

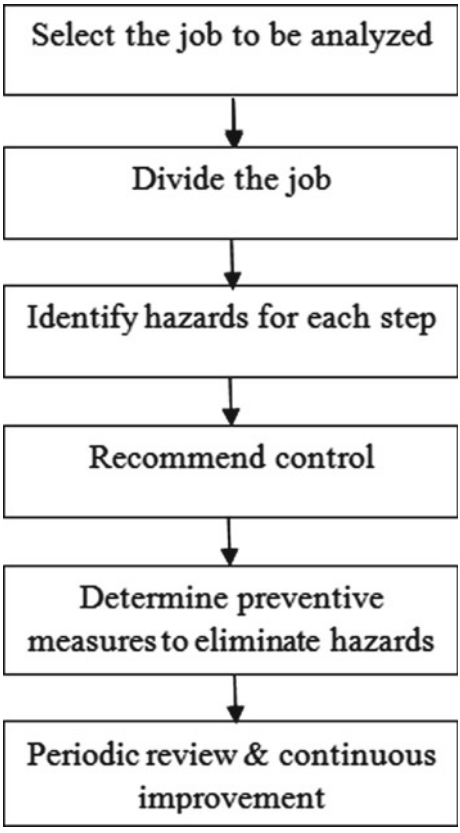

Fig. 1 Basic steps of JSA

Table 1 Risk assessment matrix [14]

Risk (R)		Consequence (C)			
		Minor	Marginal	Critical	Fatality
Probability (P)	Very likely	4	8	12	16
	Probable	3	6	9	12
	Possible	2	4	6	8
	Unlikely	1	2	3	4

Probability (P):
Very likely Events occur more than 5 times. The credit rating is 4.
Probable Events occur 3 to 4 times. The credit rating is 3.
Possible Events occur 1 or 2 times. The credit rating is 2.
Unlikely Events never occurred but should be noticed. The credit rating is 1.
Consequence (C):
Fatality: More than 1 person dies. The credit rating is 4.
Critical: 1 person die or more than 5 people get injured. The credit rating is 3.
Marginal: No death but 3 to 4 persons get injured. The credit rating is 2.
Minor: 1 or 2 persons get injured slightly. The credit rating is 1.

$$\text{Risk(R)} = \text{Consequence(C)} * \text{Probability(P)}$$

2.2.1 Problem Identification and Solution

This research focuses only on crushing operation, milling operation, silo cleaning operation, clinker operation, and filtering operation in cement industry. During these various types of operations, the number of hazards takes place.

Hazards in crushing operation are as follows:

1. Rotational movement of the parts of the crusher.
2. Exposure to noise and dust of the crusher.
3. Transportation of raw materials.
4. Maintenance activities inside the crusher.
5. Electrical problems (Table 2).

Hazards in milling operation are as follows:

1. Movement of the parts of the machinery.
2. Falling of material from the height in case of protection ducting is blocked.
3. Exposure of dust and noise.
4. Hurling of mill parts.
5. Airborne dust (Table 3).

Hazards in silo cleaning operation are as follows:

Table 2 Risk score in crushing operation

Step No	Potential hazards	Recommended action	Risk score		
			C	P	R
1	The moving part of the crusher comes in contact with the workers	• The machinery should be guarded • The safety line should be marked in moving machinery	2	3	6
2	During the maintenance of electrical parts and electric cables	• Authorized personnel must be involved • Electric cables should be coated with electrical tape	1	3	3
3	Exposure to noise and dust	• PPE like earplugs must be used • PPE like air respirators or masks can be used	2	4	8
4	During traveling of raw materials slip, trip or fall may occur	• The vehicle is positioned at load and discharge point at safe distance • Only qualified and authorized personnel are permitted for transporting	2	2	4

Table 3 Risk score in milling operation

Step No	Potential hazards	Recommended action	Risk score		
			C	P	R
1	Airborne dust in the milling area might harm	• Duct suction system can be used • PPE like respirators can be used to avoid inhalation	3	4	12
2	Excessive noise levels	• Try to minimize the noise at the source • Use proper PPEs like earplug and earmuff	2	4	8
3	Moving parts of the milling machine	• It should be properly guarded • The safety line should be marked near the moving part of the milling machine	2	2	4
4	Falling of material from height	• Use only licensed personnel who are appropriately trained • Experienced height workers	2	2	4

1. Internal cleaning of silos is high risk and frequent operation.
2. Confined space work.
3. Falling of material.
4. Falling of personnel from the working platform.
5. Exposure of dust.
6. Insufficient ventilation (Table 4).

Table 4 Risk score in silo cleaning operation

Step no	Potential hazards	Recommended action	Risk score		
			C	P	R
1	Working in a confined space inside the silo might cause harm	• PPE must be used • The work should be supervised • Make sure the oxygen level inside the confined space	4	4	16
2	Falling of personnel during accessing the work areas	• Approved and tested lifting device • Use only licensed personnel to do the work in height and make sure the personnel have all the insurance and certificate	3	3	9
3	Insufficient ventilation during cleaning the silos from the storage area	• Use an exhaust fan in the storage area • Use ridge vent or gable vent in the storage area	4	4	16
4	Exposure of dust inside the silo, might cause harm	• Use PPE like respirators and mask for covering the nose • Use duct suction system in the storage area	3	3	9

Hazards in clinker operation are as follows:

1. Contact with superheated materials.
2. Exposure to heat and noise.
3. Fall from height.
4. Confined space work.
5. Use of high-pressure pump (Table 5).

Hazards in filtering operation are as follows:

1. Electrical hazards (for electrostatic filters).
2. Exposure of dust.
3. Explosion due to the existence of increased concentration of CO in coal dust.
4. Operatives falling from height.
5. High temperature (Tables 6 and 7).

3 Result and Discussion

The potential hazards in the crushing, milling, silos-cleaning, clinkering, and filtering operating processes can be converted into a safe and excellent benefit method. Table 8 represents the risk ranking level during the various operations were carried out. The presence of risk level is reduced after implementing the JSA technique for all the oerations. It is higher before implementing the JSA technique.

Table 5 Risk score in clinkering operation

Step no	Potential hazards	Recommended action	Risk score		
			C	P	R
1	The personnel may contact with superheated material while working in hot work process	• Proper isolation of system • Proper PPE • Hoses in good condition • Proper fire extinguisher set up • Development of experienced personnel	3	4	12
2	Exposure of heat and noise	• Use proper PPE and fire suppression system • Use PPE like earplug and earmuff used to protect from the noise	2	3	6
3	During the pressure pump handling, some hazards may occur	• Never increase the test pressure more than maximum allowance pressure • Ensure that the personnel wearing the proper PPE • Isolate the equipment from all the sources of energy when not in use • Monitor the pressure gauge from a safe distance away from the potential source • Maintenance and check of high-pressure line	2	3	6

4 Conclusion

In cement industry, during manufacturing of cement, the various hazards are identified in crushing, milling, silo cleaning, clinkering, and filtering operation using JSA technique. The risk level is noted from the recognized hazards. The recognized hazards are eliminated, and recommended actions are also given using JSA technique. The recommended actions are implemented in their working place. In addition to safety tools, other methods like PPE, administrative, and engineering control are also playing main roles to control the hazards in hazardous working environment. This paper can support productive direction for the workers and supervisors who face the risk while doing the operation.

Table 6 Risk score of filtering operation

Step no	Potential hazards	Recommended action	Risk score		
			C	P	R
1	Short circuit can be created, if the filter is not earthed properly	• Adequate securing of the filter • Unplug electrical cord and retain control of plug during repair	3	2	6
2	Exposure of dust and high temperature	• Use PPE like respirators and dust masks • Thermal insulation of equipment • Use proper PPE for protecting us from the hot work	2	3	6
3	Explosion due to high concentration of CO in coal dust	• Immediate removal of CO source • Inform to the folks before start working under CO • Use proper PPE like respirator and mask • Immediate oxygen should be provided for the personnel who suffers by CO	2	2	4

Table 7 Risk score of after implementing JSA in all process

S. No.	Operation	Risk score		
		C	P	R
1	Crushing			
	The moving part of the crusher comes in contact with the workers	2	2	4
	During the maintenance of electrical parts and electric cables	2	1	2
	Exposure to noise and Dust	4	1	4
	During traveling of raw materials slip, trip or fall may occur	1	1	1
2	Milling			
	Airborne dust in the milling area might harm	4	2	8
	Excessive noise levels	4	1	4
	Moving parts of the milling machine	2	1	2
	Falling of material from height	1	1	1
3	Silo cleaning			
	Working in a confined space inside the silo might cause harm	2	3	6
	Falling of personnel during accessing the work areas	1	3	3
	Insufficient ventilation during cleaning the silos from the storage area	4	3	12
	Exposure of dust inside the silo might cause harm	2	2	4
4	Clinkering			
	The personnel may contact with superheated material while working in hot work process	2	2	4
	Exposure of heat and noise	2	2	4
	During the pressure pump handling, some hazards may occur	2	1	2
5	Filtering			
	Electricity can be created, if the filter is not earthed properly	2	1	2
	Exposure of dust and high temperature	2	2	4
	Explosion due to high concentration of CO in coal dust	2	2	4

Table 8 Risk rank for before and after implementation of JSA

S. No.	Operation	Risk rank	
		Before	After
1	Crushing	21	11
2	Milling	28	15
3	Silo cleaning	50	25
4	Clinker	32	10
5	Filtering	16	10

Fig. 2 Graphical presentation of before and after implementation of JSA

Acknowledgements The appropriate permission is received from the management persons to conduct the research activities.

References

1. Khahro SH, Ali TH, Memon NA, Memon ZA (2020) Occupational accidents: a comparative study of construction and manufacturing industries. Curr Sci 118(2):243
2. Sah DP, Chaudhary S, Shakya R, Mishra AK (2019) Occupational accidents in cement industries of Nepal. J Adv Res Alternat Energy Environ Ecol 6(3&4):22–28
3. Nandhakumar SMS, Gnanasekaran M (2014) Job safety analysis in material handling. Int J Sci Eng Technol Res 3(8):1408
4. Khaviya S, Kavitha S, Manoj S (2017) A risk assessment study on occupational hazards in cement industry. Int Res J Eng Technol 4(12)
5. Karahan V, Akosman C (2018) Occupational health risk analysis and assessment in cement production processes. Fırat Univ Turk J Sci Technol 13(2):29–37
6. Gopinath V, Johansen K (2016) Risk assessment process for collaborative assembly–a job safety analysis approach. Procedia CIRP 44:199–203
7. Li W, Cao Q, He M, Sun Y (2018) Industrial non-routine operation process risk assessment using job safety analysis (JSA) and a revised Petri net. Process Saf Environ Prot 117:533–538
8. Asl MM (2017) Job safety analysis (Human & equipment). Univ J Manag 5(7):355–363
9. Rozenfeld O, Sacks R, Rosenfeld Y, Baum H (2010) Construction job safety analysis. Saf Sci 48(4):491–498
10. Occupational Safety and Health Agency (OSHA) Publication #3071, Job Hazard Analysis
11. Albrechtsen E, Solberg I, Svensli E (2019) The application and benefits of job safety analysis. Saf Sci 113:425–437
12. Choi H-H, Cho H-N, Seo J-W (2004) Risk assessment methodology for underground construction projects. J Construct Eng Manag 130(2):258–272
13. Mattila MK (1985) Job load and hazard analysis: a method for the analysis of workplace conditions for occupational health care. Occup Environ Med 42(10):656–666
14. Li W, Zhang L, Liang W (2016) Job hazard dynamic assessment for non-routine tasks in gas transmission station. J Loss Prev Process Ind 44:459–464

15. Nezamodini Z, Ahmadabadi S, Mosavianasl Z (2019) Application of job safety analysis and inspecting the changes in identification of hazards in a cement industry in Fars province in 2017. Int J Biomed Public Health 2(1):26–30

To Reduce the Setting Piece Rejection Rate in Gear Hobbing Process by Advanced Product Quality Planning

R. Sivakumar, A. Boobal, M. Gowtham, and P. Senevasa Perumal

Abstract "Right the First Time" principle is to reduce the number of gear hobbing process rejection rate, reason of rework, scrap and change orders so customers are dissatisfied. The main objective of this project is to produce the first time right robust product, without setting piece rejection, also increasing the consistent product quality and productivity. While the machine setting changes, the first piece gets scrap due to improper tool selection and improper process parameters in Pfauter PE1000 machine for hobbing and skiving operation. In every setting change in Pfauter PE1000 machine for part number of 1000904, the first piece gets scrapped. To reduce the setting piece rejection rate, we found a proper root causes that are (1) part nominal height, (2) fixture locating height and (3) hob diameter. The permanent corrective action to prevent that setting rejection in Pfauter for part number of 1000904 is to measure the part with TRIMOS, dial gauge, coordinate measuring machine and micrometer that reduces the rejection rate from 14 to 1. Initial inspection, hob diameter and hob nomenclature are also reassigned to prevent the setting piece rejection. By advanced product quality planning, the Six Sigma value is increased from 3.9 to 4.9 and the rejection rate is decreased from 7458 to 441 PPM.

Keywords Pfauter PE1000 machine · Part nominal height · Fixture locating height · Hob diameter

R. Sivakumar (✉) · A. Boobal · M. Gowtham · P. Senevasa Perumal
Department of Mechanical Engineering, M. Kumarasamy College of Engineering, Karur, Tamil Nadu 639113, India
e-mail: sivamech637@gmail.com

A. Boobal
e-mail: boobalalagesan@gmail.com

M. Gowtham
e-mail: gowthammahendran99@gmail.com

G. Kumaresan et al. (eds.), *Advances in Materials Research*, Springer Proceedings in Materials 5, https://doi.org/10.1007/978-981-15-8319-3_38

1 Introduction

Defining the "Right the First Time" principle, the goal is to minimize the number of product issues that get past design release and cause rework, scrap and change orders, leading to displeased customers. This project was carried out in Sri Murugan Gears, Hosur, to improve productivity. Improved high productivity, timely export performance combined with lower costs, materials, overtime, scrap and other costs. You have implemented standard quality processes and applications, such as enterprise resource planning and quality management systems. However, your first time right (FDR) metrics may be as good as yours. You need to "implement" quality and plan and manage it. What your organization needs is integrated, customizable MES that helps predict and prevent quality problems before they occur. Gleason-Pfauter PE 1000 Gear Profile Grinding Machine is made for external, internal spur grinding and helical gears on cylindrical workpieces, as well as any other profile or form which can be ground by the single indexing. The machine is designed for the use of dressable grinding wheels as well as non-dressable single-plated CBN wheels. Pfauter machine is a gear cutter machine, which can be used for the hobbing and skiving operation for all angles such as (0°–130°).

COPQ is a calibrate of the cost an organization faces due to the provision of substandard products and services. Three types are available:

- Prevention
- Evaluation
- Failure.

It is expressed in numerical form as a percentage of sales and can be mathematically calculated using the above three factors

$$\text{COPQ} = \text{Prevention} + \text{Evaluation} + \text{Failure}$$

Correct and preventive action (CAPA, also known as corrective action or simply corrective action) consists of improvements in the processes of a company that has been taken to eliminate the causes of non-compliance or other undesirable circumstances. This usually requires the correction and removal of continuous inactivity that a company must take in the production, documentation, practices or systems of operations, laws or regulations. Adjustment and preventive action is designed by a team that includes quality assurance personnel and personnel. It should be duly implemented and observed for its ability to repeat such incompatibility repeatedly. Six Sigma strategies seek to improve the output quality of a process by identifying the causes of defects and reducing variability in manufacturing and business processes. It uses a suite of quality management systems, mainly for building on the experience, statistical methods and specialized infrastructure of those in the organization who are experts in these methods. Each Six Sigma project within a company follows defined steps and has specific value goals, for example: reducing process cycle time,

reducing pollution, reducing costs, increasing customer satisfaction and increasing profits.

2 Objective

- To produce the first time robust product and without setting piece rejection in gear hobbing process.
- To increase the consistent product quality and productivity of Pfauter PE1000 machine.
- To reduce the part per million (PPM) and increase the sigma value for quality improvement.

3 Problem Identification

- It was observed from the production logbook of Pfauter PE1000 machine for past two months that in majority of the causes the first piece is getting rejected during setup change resulting in increased setup time and also less production.
- The first piece of hobbing operation is getting reworked that increased setup time and less output in Pfauter.
- In Machine Setting Approval Chart/Statistical Process Control [MSAC/SPC] data book, we found a greater number of setting piece rejections in gear hobbing process of the part number 1000904.
- The quality plan/control plan chart cannot be maintained properly; due to that, the changed value of the part dimensions is not updated in the chart which causes rejection of workpiece.
- Improper measurement of part height and fixture height for setting the workpiece in Pfauter machine.

4 Solution

(1) Part height: To measuring the part height by using the TRIMOS and check with the instruction sheet and update of the free list. (2) Fixture height: To measuring the fixture height with dial stand by proper dialing and tighten the fixture with updating of free list. Two important components that assist in building and testing products are fixtures and jigs. To reduce the rejection rate by proper fixing of fixture. Fixtures locate, hold or test a work in progress (WIP) part or assembly during a manufacturing operation, while jigs hold and guide cutting tools in drilling and boring operations.

5 Literature Review

This paper shows a Six Sigma initiative guided by a semiconductor system dedicated to combining circuit cartridges for inkjet printers. They are tried by electricity in the last stage of the process of evaluating electrical properties to recognize or reject them. Power outage represents 50% of all things. Along these lines, it is important to set policy issues, causes and functions to reduce the dimension of defects. Through the use of Six Sigma, determining key components, distinguishing the best dimensions or resilience and development openings is imaginative [1]. The main considerations that were found through a structure of analyses 3 components and 2 levels were: grating weight (90–95 psi), stature of the instrument (0.06–0.05) and process duration (7000–8000 ms.). The improvement was a decrease in the electrical disappointments of around 50% [2]. The outcomes demonstrated that with legitimate use of this system and backing for the group and staff of the association, a positive effect on the quality and different highlights basic to consumer loyalty can be accomplished [3]. The motivation behind this thesis is basically to censor the green lean system and restrict it. Look at the similarity of green, lean and Six Sigma ideas and Six Sigma and uniquely its critical thinking system DMAIC. Indeed, gains and efficiencies and late consumer loyalty, quality and responsive spaces were the overall excitement for associations [4]. The move toward greener activities and items has constrained organizations to look for choices to consolidate these with green destinations and activities. Green lean is the consequence of this blend. In this manner, the paper reasonably proposes Green Lean Six Sigma [5]. Tools and techniques about production are widely used to eliminate various types of waste and increase the profitability of the system by making the process more efficient. The slim ones make extra: less time, inventory, space, people and money [6]. The lean manufacturing approach is to convert a value-added operation into a value-added process. Lean manufacturing has its impact on employees and customers [7]. The ultimate goal is to create the right value for the customer through an effective value creation system with zero waste. This article presents a literature review on lean tools and practical technique for lean manufacturing [8].

6 Experimental Work

According to QMS, we found that some of the important parameters of gear hobbing process are

1. Setting part
2. Setting time
3. Operator
4. First piece status
5. Running piece status
6. WIP tracking sheet

7. Quality plan/control plan
8. Instrument availability
9. MSAC/SPC.

6.1 Hob Selection

Pfauter machine setting requirements are:

1. Number of teeth
2. Module
3. Axis angle
4. Cutting depth
5. Part maximum diameter
6. Part minimum diameter
7. Fixture height
8. Part height
9. Hob diameter
10. Hob lead angle.

6.2 Gear Specifications

No of teeth: 42.
Normal module: 1.75 mm.
Minimum pressure angle: 13.339°
Maximum pressure angle: 39.878°
Axis angle: 90°
Tooth height: 3.661 mm.

6.3 Rejection Rate

In manufacturing, the rejection rate is

$$\begin{aligned} \text{RR} &= (\text{Rejected quantity}/\text{Produced quantity}) * 100 \\ &= (14/1845) * 100 \\ &= (0.00758) * 100 \end{aligned}$$

6.4 DPPM Six Sigma

DPPM represents the number of defects per million in the Six Sigma metric change. DPPM conversion is commonly used in manufacturing. DPPM is often used when estimating the rate of defect in a continuous object. The following table summarizes the parts of a million defects that can be converted into short-term or long-term process sigma.

Now, we can calculate the defects parts per million

$$\begin{aligned}\text{DPPM} &= (\text{Rejected quantity}/\text{Produced quantity}) * 1{,}000{,}000\\ &= (14/1845) * 1{,}000{,}000\\ &= 7588\end{aligned}$$

When applying the **advanced product quality planning (APQP)** (corrective actions) in Pfauter machine, we reduced first piece rejection rate.

No. of defects found = 1.

No. of settings change = 42.

No. of sample produced = 2264

$$\begin{aligned}\text{Output} &= \text{No. of rejections}/\text{No. of Settings}\\ &= 1/42\\ &= 0.023\end{aligned}$$

Six Sigma evaluation after advanced product quality planning.

Now, we calculated the defects parts per million after implementation

$$\begin{aligned}&\text{PPM} = (\text{Rejected quantity}/\text{Produced quantity}) * 1{,}000{,}000\\ &\text{No. of defects found} = 1\\ &\text{No. of settings change} = 42\\ &\text{No.of sample produced} = 2264\\ &= (1/2264) * 1{,}000{,}000\\ &= \left(4.4169 \times 10^{-4}\right) * 1{,}000{,}000\\ &= 441\ \text{PPM}\end{aligned}$$

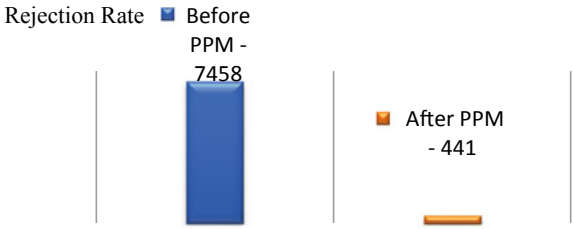

Fig. 1 Before and after implementation of advanced product quality planning (APQP)—rejection rate

7 Result and Discussion

7.1 Rejection Rate Comparison

Earlier PPM = 7458 (before APQP implementation).

Current PPM = 441 (after APQP implementation).

Figure 1 shows rejection rate comparison of the gear hobbing part 1000904, before implementation the PPM is 7458, and after implementation the PPM is reduced to 441. APQP helps to achieve low rejection rate in production industry.

7.2 Six Sigma Comparison

Before APQP implementation = 3.9–4.0

After APQP implementation = 4.8–4.9

Figure 2 shows comparison of Six Sigma value of the gear hobbing part 1000904, before implementation Six Sigma value is 3.9, after implementation Six Sigma value is increased to 4.9, and more Six Sigma value is indicated to more process capable and quality improvement.

Figure 3 shows overview of rejection rate, parts per million (ppm) and Six Sigma of the gear hobbing part 1000904. In that, rejection rate and PPM are reduced and then Six Sigma value is increased.

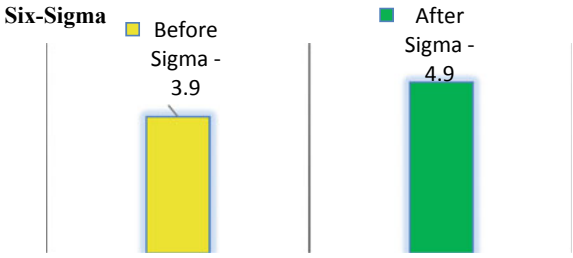

Fig. 2 Before and after implementation of advanced product quality planning (APQP)—Six Sigma value

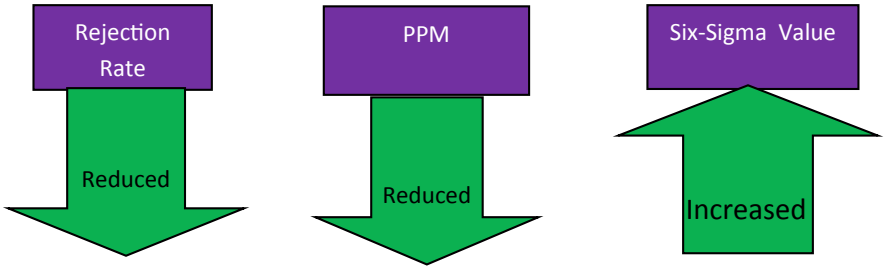

Fig. 3 Overview of rejection rate, parts per million (ppm) and Six Sigma

8 Conclusion

- This project works on to produce the first time right robust product, without getting setting piece rejection and also increasing the consistent product quality and productivity by advanced product quality planning (APQP) and Six Sigma center tools for reducing the cost of poor quality.
- In our project, we have taken the part 1000904, in that we found 14 rejections due to improper tool selection and improper process parameters so we took an action to reduce the rejection rate by the following root ways such as part height, fixture height and hob diameter.
- In this project, we reduced the rejection in Pfauter PE1000 machine with increasing the sigma and reducing the parts per million (PPM). This results in the Pfauter machine to perform the accurate hobbing and skiving with zero-piece rejection.

References

1. Valles A, Sanchez J, Noriega S, Nunez BG (2009) Implementation of six sigma in a manufacturing process. Int J Indust Eng 16(3):171–181
2. Enamul Kabir Md, Mahbubu IslamBoby SM, MostafaLutfi, (2013) Productivity improvement by using six sigma. Int J Eng Technol 3(12):1056–1084
3. Garza-Reye JA (2015) Green lean and the need for Six Sigma. Int J Lean Six Sigma 6(3):226–248
4. Salah S, Rahim A, Carretero JA (2009) Six sigma and total quality management (TQM): similarities, differences and relationship. Int J Six Sigma Competit Adv 5(3):237–250
5. Sivaraman B, Sivakumar R (2018) Optimization of grinding parameters in austenitic stainless steel AISI 317L using Taguchi method. Int J Mech Prod Eng Res Dev 8(2):1033–1038
6. Sivakumar R, Prasanna M, Pradeep K, Rajkumar VT, Raj Kumar S (2019) Wear characterization of ceramic tools (SiAlON and Al_2O_3+SiCWhisker) with dry and wet turning of Nimonic 75. In: AIP conference proceedings 2128:020022-1–020022-9

7. Balamurugan R, Zubar A (2019) An integrated approach to performance measurements, analysis, improvements and knowledge management in healthcare sector. Int J Knowl Manag Stud 10(1):84–99
8. Kamalakannan R, SudhakaraPandian R, Sivakumar P (2019) A simulated annealing for the cell formation problem with ratio level data. Int J Enterprise Netw Manag (IJENM) 10(1):78–90

Development of Linear Automation in Butt Joint Fixture to Enhance Welding Characteristics

R. Sivakumar, S. Bhoopathi, R. Muralirajan, and E. Chinnayan

Abstract In today's global economy, the survival of companies depends on their ability to innovate and improve quickly. Metal Inert Gas (MIG) welding can apply for many kinds of material such as mild steel, carbon steel, stainless steel, aluminum. This paper deals with the fabrication of MIG welding fixtures to clamp work piece and reduce the rejection ratio in production and reduce the welding distortion. The automation is used to welding the work piece for increasing the quality and production. Fixtures are essential components of the manufacturing process because they are required in most automated manufacturing, inspection, and assembly operations. The device is provided to support and control the work area with fixture providing a linear motion by the motor. Using fixing and automation welding often eliminates the need for verification, positioning, personal marking, and the same quality in the manufacturing process. These increase productivity and reduce operating time compared to manual welding. Automation welding process gives a best result compared to the manual welding. Some of the issues are occurred during manual welding (welding distortion, imperfect welding, less quality, and lower production rate). These problems can be solved by using automation welding process. In welding distortion, the automation rate of welding capacity increases 50% compared to manual welding rate. In imperfect welding joint, the fixture setup helps us to weld the work piece with 45% more efficiently.

Keywords Welding distortion · MIG welding fixture · Automation · Productivity rate

R. Sivakumar (✉) · S. Bhoopathi · R. Muralirajan · E. Chinnayan
Department of Mechanical Engineering, M. Kumarasamy College of Engineering, Karur, Tamil Nadu 639113, India
e-mail: sivamech637@gmail.com

S. Bhoopathi
e-mail: bhoopathisan@gmail.com

E. Chinnayan
e-mail: chinnayan90@gmail.com

G. Kumaresan et al. (eds.), *Advances in Materials Research*, Springer Proceedings in Materials 5, https://doi.org/10.1007/978-981-15-8319-3_39

1 Introduction

The project is carry out by the following company. In BULL, innovation is a way of life where quality is first priority. Bull, 54, of Ave. owned by the group; it has diversified companies employing more than 2000 people. Bull is the Indian leader in its class and division of loaders and backhoes. The company is ISO certified company 9001 and 2008. Fixture is required in various industries according to their use. The design of the new fixture has been replaced with the old one due to some flaws. Component positioning is done manually, so more rotation time is required to load and unload the component. Therefore, there is a need to create a system that helps reduce productivity, accuracy, and time. Over the past century, manufacturing has made significant strides. New machine tools, high-performance cutting tools, and modern manufacturing processes make today's businesses faster and better than ever before. The methods of holding the work have improved considerably, and the basic principles of tightening and finding are still intact. Mass production methods demand quick and easy positioning for precise operations. Fixtures are manufacturing tools used to precisely copy and transfer parts. The use of one component creates a very simple operation; otherwise, it takes a lot of skill and time. Fixtures position elements precisely to keep the components tight and prevent movement while working to provide greater productivity and part accuracy. Fixtures hold or capture a work area in a predetermined manner. Each component is designed to hold, support, and locate each component to ensure that it is drilled or machined within specified limits. The proper relationship and alignment between the weld holder and the work piece are maintained.

2 Objective

- To eliminate marking, punching, positioning, alignments while drilling and grinding the material, etc. Identify, support, and tighten the hollow, easy, fast, and stable position of the cutting tool in the welding process.
- Guidance for cutting tool like drill, reamer, etc.
- Increase productivity and maintain product quality after use of fixture assembly.
- To reduce the operator's labor and efficiency—the need for automation welding.
- Reduce its measurement cost.
- Improving the technical capability of linear butt joint welding machine tools.
- Reduce overall machining costs and increase transmission without affecting the company's revenue and source of income.

3 Problem Identification

- Weld distortion—while welding the component (arm). Distortion due to shrinkage due to large heat input during welding.
- Imperfect welding butt joint by manual welding. Overlaps may occur due to low currents, long arc length, and slow welding speed.
- Less quality in welding joints.
- Less production to achieve monthly target. Better welding productivity includes faster welding, more arc time, and less welding (less metal deposition).

4 Solution

- Fixtures are essential components of the manufacturing process, as they are required in most automated manufacturing, inspection, and assembly operations
- The device is provided to support and control the work area. Using fixing and automation welding often eliminates the need for verification, positioning, personal marking, and the same quality in the manufacturing process.
- These increase productivity and reduce operating time when compared to manual welding. The weld distortion can be avoided by using fixture. Perfect welding joint can be increased by automation welding.

5 Literature Review

Modular fixture are assembled by different quick acting universal elements designed and produced to meet the need for faster and economical way of fixturing [1]. There are all types and designs of welding positioners; some of which are fixed tables that are always vertical and are called headstock positioners. The type of tilt that is rotated and rotated in both directions which are often called welding positioners [2]. We have developed a clamping system and a tooling system for vertical grinding machine to measure Frictionless Welding (FSW) functions and process forces. A new type of adjustable fixture has been designed, with a view to creating space (i.e., lateral movement) and cross-movement of the workplace [3]. Welded using grade 317 steel fusion and resistance methods. This alloy oxyacetylene welding method is not preferred. You can use AWS E/ER317 or 317L filler metal for better results [4]. Trigger welding is the most straight forward application to a power inverter. Practical welders require power conditions of up to 1 MW simultaneously, while frequencies in the range of 200–500 kHz depend on pipe ignition [5]. Work analysis is a process used to understand what the important tasks of the job are, how they are perform, and what human attributes are important to carry them out successfully [6]. Annealing is the process work for controlled heating and cooling of a substance, the purpose of changing the microstructure to eliminate stress or to

change the properties of hardness, strength, or durability. There are frequent benefits of annealing in metals to eliminate stresses induced by cold work [7].

6 Experimental Work

Figure 1a Welding fixture without work piece is an initial setup which has holding arms for the work piece, then roller fitted to provide a linear motion for automation. Figure 1b Welding fixtures with work piece is an experimental setup for the linear automation butt joint welding. On the bottom, the bed is provided for carry the fixtures. Both side fixture is fixed to carry the work piece completely without any

Fig. 1 **a** Welding fixtures without work piece. **b** Welding fixtures with work piece

shaking, and at the top, the welding rod is fixed for linear welding work. Once work piece is fixed, we tight the fixture gets closure to the work piece. When switch on the machine, the welding process starts to happen in a linear motion produced by the motor, after complete one work piece. We release the arm and insert the another work piece. If the work piece is on different size, then the fixture will adjust according to the work piece sizes by manually. From this, we can easily weld the different size of work pieces with good quality manner.

7 Result and Discussion

Hold the gun at a 90° angle to the work piece, directing the filler material straight into the joint. By using the manual welding, the production rate is lower. The main reason is that the welder can't direct the gun at a 90° for a long period but in automation the gun can moved at 90° by using track (Table 1).

Figure 2 shows the comparison of manual welding and automation welding. From the first day of automation welding, the welded work piece material increases with less labor cost, problem rectifying factors like better finishing, improving the quality and quantity. As per results, we calculate the average for automation and manual welding to analyze overall advantages of the automation welding.

Ultrasonic test has carried out for manual and automatic welding parts to identify the defects of cracks, voids, pores, etc. In manual welding having higher defects rate when compared to the automatic welding, which is shown in Fig. 3.

7.1 Average for Number Pieces Welded by Automation Process

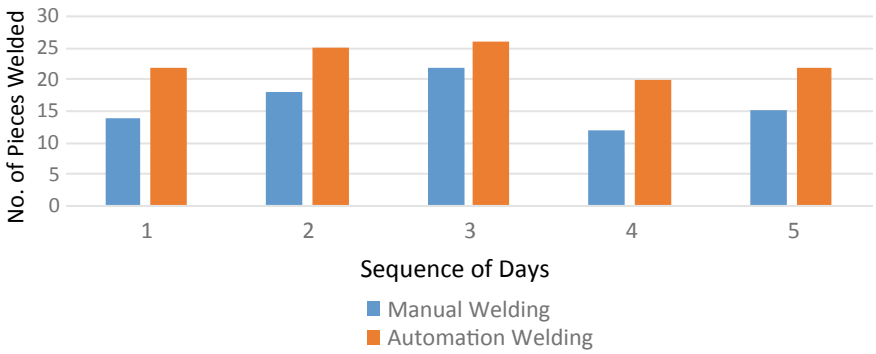

Fig. 2 Comparison of manual welding and automation welding

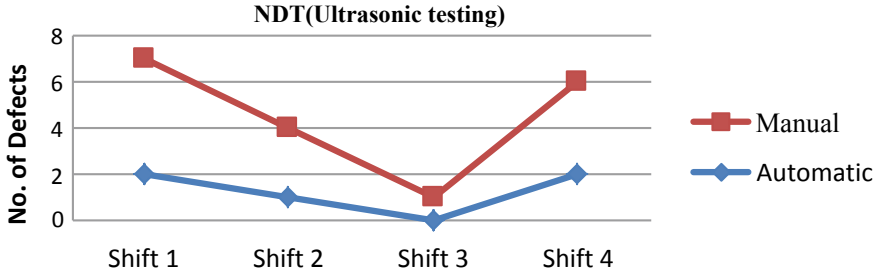

Fig. 3 Comparison of manual and automatic welding parts with ultrasonic test

$$= (22 + 25 + 26 + 20 + 22 + 20 + 24 + 23 + 21 + 28 + 19 + 28 + 22 + 21 + 24 + 26 + 27 + 22 + 24 + 20 + 24 + 29 + 27 + 24 + 22)/25$$
$$= 24 \text{ welded pieces per shift.}$$

7.2 *Average for Number of Pieces Welded by Manual Process*

$$= (22 + 25 + 26 + 20 + 22 + 20 + 24 + 23 + 21 + 28 + 19 + 28 + 22 + 21 + 24 + 26 + 27 + 22 + 24 + 20 + 24 + 29 + 27 + 24 + 22)/25$$
$$= 17 \text{ welded pieces per shift.}$$

- The difference between number of welded pieces for manual and automation 24–17 = **7 welded pieces per shift.**
- By using fixture automation, 7 welded pieces are increased per shift.
- Per day 14 welded pieces are increased in production rate.
- Approximately, per month (14 * 25) = **350 welded pieces.**
- Approximately, per year (350 * 12) = **4200 welded pieces** (Fig. 4)**.**

(a) Welding with distortion **(b)** Welding without distortion

Fig. 4. **a** Welding with distortion. **b** Welding without distortion

Table 1 Number of work piece welded by manual and automation MIG welding

Day	Manual welding (No. of pieces per shift)	Automation welding (No. of pieces per shift)
1	14	22
2	18	25
3	22	26
4	12	20
5	15	22

8 Conclusion

By manual welding process, the some of the issues are occurred (welding distortion, imperfect welding, less quality, and lower production rate). These problems can be solved by using automation welding process.

1. In welding distortion, the automation rate of welding capacity increases 50% compared to manual welding rate.
2. In imperfect welding joint, the fixture setup helps us to weld the work piece with 45% more efficiently.
3. In quality area, the compared result of automation welding to manual welding increases with the highest production rate of 40%.
4. Automatic welding process having lower defects compared to manual welding.

9 Future Scope

The future work of this project is that, to design and manufacture the all types of fixture in one fixture.

References

1. Shah P, Agrawal H, Joshi SP, Patel U (2011) Design and manufacturing of modular welding fixture national conference on recent trends in engineering & technology 21(17–25):415–427
2. Shinde SN, Kshirsagar S, Patil A, Parge T, Lomte R (2014) Design of welding fixtures and positioners. Int J Eng Res Gener Sci 2(5):2091–2730
3. Sivaraman B, Sivakumar R (2018) Optimization of grinding parameters in austenitic stainless steel AISI 317L using Taguchi method. Int J Mech Prod Eng Res Dev 8(2):1033–1038
4. Satpathy MP, Moharana BR, Dewangan S, Sahoo SK (2015) Modeling and optimization of ultrasonic metal welding on dissimilar sheets using fuzzy based genetic algorithm approach. Eng Sci Technol Int J 18(4):634–647
5. Sivakumar R, Prasanna M, Pradeep K, Rajkumar VT, Raj Kumar S (2019) Wear characterization of ceramic tools (SiAlON and Al_2O_3+SiCWhisker) with dry and wet turning of Nimonic 75. AIP Conf Proc 2128(1–9):020022–020022

6. Vasudevan M, Bhaduri AK, Raj B, Rao KP (2007) Genetic-algorithm-based computational models for optimizing the process parameters of A-TIG welding to achieve target bead geometry in type 304 L (N) and 316 L (N) stainless steels. Mater Manuf Processes 22(5):641–649
7. Dey V, Pratihar DK, Datta GL, Jha MN, Saha TK, Bapat AV (2009) Optimization of bead geometry in electron beam welding using a genetic algorithm. J Mater Process Technol 209(3):1151–1157

Corrosion Behavior of Brass in Methanol-Gasoline Fuel Blends

H. N. Meenakshi and Shraddha Dilip More

Abstract Alcohols have become attractive alternate to fossil fuels in the present oil crisis scenario because they can be obtained from varieties of natural and man-made sources and can reduce greenhouse gases from automobile emissions. Methanol production from biomass is one of the ways to convert waste into energy resources. Also methanol can be used directly in engines without changing the structure of the engines. Hence, methanol is the most attractive alcohol to be blended with fossil fuels. But methanol is hygroscopic in nature, and water content is always present in methanol-gasoline mixture because of strong affinity between the two substances which is a key factor for corrosion. Materials which are in contact with fuel in automobile applications can be grouped in three major categories: ferrous alloys, non-ferrous alloys, and elastomers. Metallic materials can undergo corrosion and wear when in contact with fuels. Corrosion occurred on metal surfaces in alcohol fuel blends are mainly due to alcoholate corrosion. Materials such as copper and its alloys (bronze and brass) can be oxidized on contact with automotive fuels and form sediments. Copper and its alloys present in some parts of engine fuel system such as fuel pump, bearing, and injectors are the mostly affected. Hence, the corrosion behavior of brass in methanol-gasoline blends was studied by mass loss method and potentiodynamic polarization method at room temperature and 40 °C with different time periods. Oxides and hydroxides of copper and zinc formed on the brass surface and corrosion products have been confirmed by X-ray diffraction (XRD).

Keywords Methanol · Gasoline · Brass · Corrosion

1 Introduction

Brass is one of the most common and worldwide used metal alloys in variety of industries for several reasons. The automotive industry is one of the top industries that use

H. N. Meenakshi (✉) · S. D. More
Centre for Incubation Innovation Research and Consultancy, Jyothy Institute of Technology, Tataguni, Off Kanakapura Road, Bengaluru, Karnataka 560082, India
e-mail: meenaparam75@gmail.com

G. Kumaresan et al. (eds.), *Advances in Materials Research*, Springer Proceedings in Materials 5, https://doi.org/10.1007/978-981-15-8319-3_40

these alloys in their manufacturing process. C-360, C26000, C26130 grades of brass are used in the manufacture of nozzles, bearings, and mechanical components used in automotive industry. These components when in contact with fuel cause significant damage to material as well as to the fuel. The existing literature highlighted that corrosivity of biodiesel, diesel, and their blends with different metals and metal alloys and results indicated that commercial diesel fuel was relatively lower in corrosive nature than biodiesel [1–3]. Due to the incompatibility of materials, low-percentage alternate fuel blends (diesel/gasoline) in volume are being used in engines at present.

Compared to diesel, these alternate fuels are more hygroscopic in nature and absorbed moisture and condensed water on the metal surface tend to create suitable condition for corrosion to occur. Corrosion of brass exposed to sunflower biodiesel blends becomes more severe than that of diesel fuel [4]. Also it was found that the highest corrosion rate of brass in petrol, followed by kerosene and least in diesel [5]. Aquino et al. highlighted that corrosion rates of copper and brass significantly decreases at higher temperature in the absence of oxygen but metallic ion accelerates the oxidation reaction [6]. The corrosivity of *Pongamia pinnata* biodiesel and its blends with commercial diesel on zinc and brass showed that zinc was highly corroded than brass [7]. Aluminum < mild steel < copper was the order of corrosion effect on the compatibility of metals with biodiesel-diesel-ethanol (BDE) fuel blends [8]. Fuel system materials and fuel degradation occurs in the presence of water, organic acids, aldehydes, peroxides, ketones, and esters in oxygenated fuel [9].

Being the most popular additives, alcohols have replaced all other additives as octane boosters in gasoline fuel. Alcohols can be promoted as alternative fuels in internal combustion engine since they do not contain sulfur or complex organic compounds [10]. The presence of alcohols in fuel causes corrosion to metallic fuel system components. Low blend rates could be used to diminish corrosion problems and make the best use of alcohols [11]. Recommended fuel blend in conventional vehicle engines is 10 vol % biofuels in gasoline. Previous studies have been investigated on the compatibility of aluminum, carbon steel, 304 stainless steel, and gray cast iron with ethanol-gasoline blends [12, 13]. There is a lack of research on compatibility of materials with methanol-gasoline fuel blends. Compatibility of fueling infrastructure materials with alternate fuels is necessary for confident usage of these fuels in high-level blends. Therefore, this paper is to investigate the corrosion behavior of brass in methanol-gasoline blends at various temperatures with different time periods.

2 Materials and Methods

Petrol used for this investigation was purchased from nearest Indian Oil petrol pump. Methanol anhydrous ($CH_3OH \geq 99\%$) used are analytical grade and provided by Bangalore scientific and industrial suppliers, Bengaluru. Commercially available brass was procured and having the elemental composition of 65% Cu, 34.95% Zn, 0.023% Sb, 0.006% Si, Sn and Pb, Ti, 0.005% Mn, 0.002% Ni, Al, Fe, and 0.001%

P was used for entire study. The test coupons were prepared as per ASTM standard G1-90 and weighed before and after immersion. Finally, immersed into the fuel blends M10 (10% methanol + 90% gasoline), M15 (15% methanol + 85% gasoline), M20 (20% methanol + 80% gasoline), M30 (30% methanol + 70% gasoline), and P100 (100% gasoline). Corrosion of brass in fuel blends were investigated at room temperature and 40 °C for various time periods (4 days, 10 days, and 30 days) under static and flow condition. At the end of the test, difference in mass was measured, and corrosion rate was calculated in miles per year as equation given in ASTM G1. The corrosion rates under flow condition were measured using rotating cage as per ASTM G184. The rotating cage description was detailed elsewhere [14]. Experimental procedure was given in previous publication [15].

Electrochemical analysis was carried out by using an electrochemical work station (CHI660E serial#:l1318 US model) with the conventional three electrode system of glass cell with platinum counter electrode and saturated calomel as a reference electrode. 1 cm^2 surface area was exposed to different blends (M10, M15, M20, and M30) at room temperature. The potentiodynamic polarization parameters such as corrosion current density (i_{corr}), corrosion potential (E_{corr}), anodic, and cathodic slopes (β_a and β_c) were obtained, and Eq. (1) is used to calculate polarization resistance (R_p) values.

$$R_p = \frac{\beta_a \beta_c}{2.3 \times i_{corr} \times (\beta_a + \beta_c)} \tag{1}$$

The fuel degradation, chemical structure, and functionalities for fuel blends were evaluated after the corrosion studies by Fourier transform infrared spectroscopy (FTIR) technique. The spectrum was recorded from the wave length from 4000 to 400 cm^{-1}, using Shimandzu ATR spectrophotometer used at 4 cm^{-1} resolution and total 64 scans. The surface morphology changes of brass in the various methanol-gasoline blends were characterized by scanning electron microscopy (SEM) using HITACHI, SU3500, and elemental analysis of the tested samples were investigated by energy dispersive spectroscopy (EDS). XRD investigations were conducted on BRUKER eco-D8 ADVANCE system working with Cu-Kα radiation (λ = 1.54 Å).

3 Results and Discussion

The corrosion rates of brass in methanol-gasoline fuel blends and in commercial petrol for various immersion period at different temperatures are depicted in Fig. 1. It is evident from the figure that M30 blend is more corrosive than other fuel blends. Also it proved the fact that when temperature increases corrosion rate increases. In all immersion periods and at different temperature, the corrosion rates of petrol were found to be lesser than methanol blended fuels. In general, the addition of methanol to petrol increases the corrosion rate. There was no significant change in the corrosion rates of brass on long-term exposure to studied fuel blends. The highest corrosion

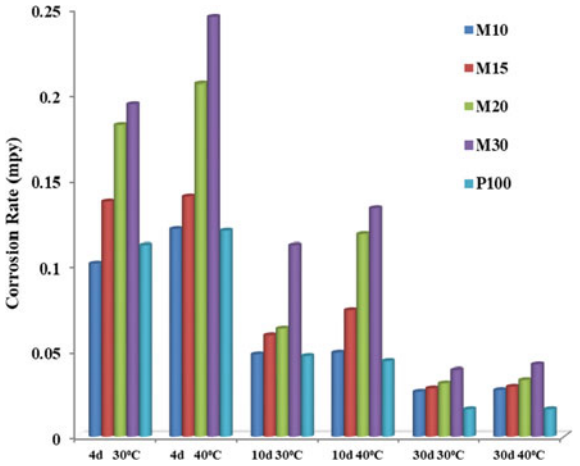

Fig. 1 Corrosion rates of brass in methanol-gasoline fuel blends

rate has been observed in M30 for 4 days (d) of immersion at 40 °C. The order of effect of time on the brass corrosion in methanol-gasoline blends was 4 days > 10 days > 30 days. Formation of film on the metal surface is protecting the brass surface and decreases the corrosion rate when extend the immersion time.

Table 1 shows the comparison of corrosion rates of brass in static and flow conditions after immersion of 4 days in M10, M15, M20, and M30 blends. As observed in static, corrosion rate increased when methanol percentage increases in the fuel blends under flow. The corrosion rates were more in flow condition than in static immersion test. Highest corrosion rate observed in M30 under flow condition was 0.314 mpy. Relative motion between metal and fuel is the major cause for higher corrosion rate under flow condition [16]. Flow leads to increase in wall shear stress thereby rupture the passive film formed on the metal surface, which causes the increase in corrosion rate. Oxygen concentration gradient increases with the increase in flow results in quick transfer of oxygen to the metal surface and caused the flow corrosion rate to increases in pipe flow system [17].

FT-IR spectra of gasoline and methanol-gasoline blends (P100, M30, M20, M15, and M10) before and after immersion of brass coupons have shown in Fig. 2. Methanol-gasoline fuel blends exhibit separate bands in the O–H stretching region between 3000 and 3600 cm^{-1}, and in the C-O stretching region from 1020 to

Table 1 Comparison of corrosion rates of brass at various conditions after immersion of 4 days in fuel blends

Medium	Corrosion rate (mpy)	
	Static	Flow
M10	0.101	0.124
M15	0.137	0.167
M20	0.182	0.225
M30	0.194	0.314

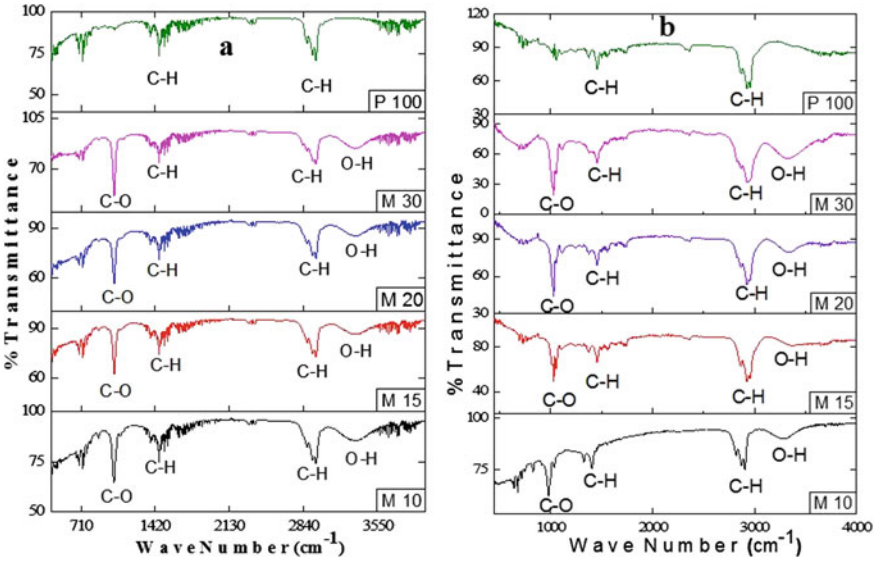

Fig. 2 FT-IR spectra of various fuel blends **a** before immersion **b** after 4 days of immersion of brass coupons

1120 cm^{-1} whereas absorption peaks in those regions are the absence in P100. O–H stretching band is observed at 3319 cm^{-1} for all fuel blends.

In addition to that methanol can be identified in the fingerprint region. The dominant peaks at 1046 and 1088 cm^{-1} can be assigned to the symmetric and asymmetric C–O stretches, respectively. In the C–H bending (1200–1600 cm^{-1}) and stretching (2800–3000 cm^{-1}) regions and overlapping vibrational bands of fuel blends and gasoline have been found. Figure 2 revealed the changes in the peaks intensities in the C–H bending and stretching regions, O–H stretching, and C–O stretching due to the degradation of fuel blends after immersion of brass coupons.

The obtained i_{corr}, E_{corr}, β_a, β_c, calculated R_p, and corrosion rate values of brass in various fuel blends from Tafel polarization method were given in Table 2, and corresponding plots are shown in Fig. 3. Increasing the methanol concentration increases the aggressiveness of the media. Values of E_{corr} and i_{corr} are increasing as

Table 2 Polarization parameters for the corrosion of brass in fuel blends

Medium	$i_{corr} \times 10^{-8}$(A)	E_{corr}(mV)	Tafel constant		$R_p \times 10^7 \Omega\ cm^2$	CR $\times 10^{-3}$(mpy)
			β_a(mV/dec)	β_c(mV/dec)		
M10	0.118	134	4.543	5.200	17.2	0.276
M15	0.140	114.9	5.23	5.039	15.8	0.327
M20	0.585	138.7	4.949	4.963	3.71	1.373
M30	2.78	141.8	4.959	4.886	0.788	2.931

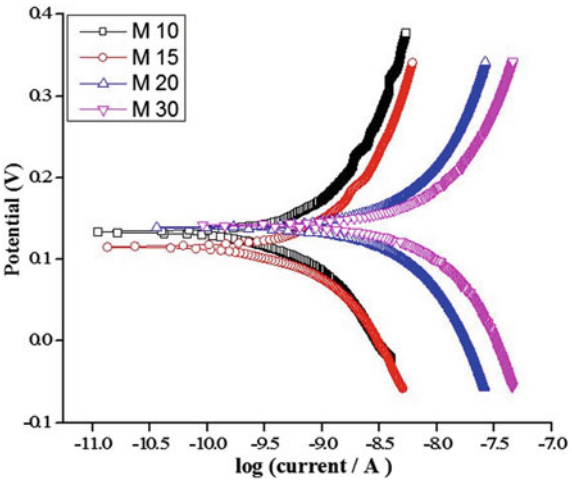

Fig. 3 Tafel plots of brass in M10, M15, M20, and M30

methanol concentration increases. R_p values for brass decreasing as the concentration of methanol is increasing.

The experimental results also proved that the corrosion rate of brass increases when alcohol concentration increases. This may be due the active behavior of brass in alcoholic environment. Not much changes in Tafel constants (β_a and β_c) for brass confirmed that there is no passive layer formation on the metal surface, and methanol concentration do not change the mechanism of the corrosion process. Therefore, corrosion rate increased progressively while increasing the methanol concentration in the fuel blends.

SEM images and elemental composition of polished brass and coupons immersed in M30 for 4 days under static and flow conditions are shown in Fig. 4a–c. Some scratches were observed on the surface of polished specimen under microscopic observation. The SEM images revealed that the surface damages occurred due to corrosion on the surface of metals exposed to blend when compared to the surface of polished coupon. Formations of occasional surface pits were observed on static immersion test coupon due to localized corrosion damage on the surface. Surface exposed to M30 under flow showed more number of pits and additional surface

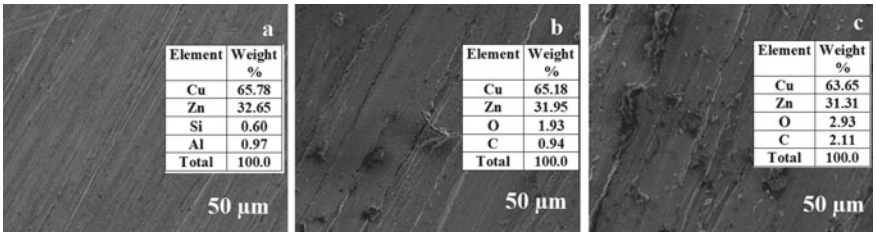

Fig. 4 SEM images of brass specimens **a** polished, **b** static immersion, **c** flow

roughness as compared to static confirmed the highest corrosion occurred on the brass surface. The presence of oxygen on the surface after immersion is due to the formation of corrosion products mainly oxides and hydroxides. The formation of oxides and hydroxides with their base metals increases with increased in corrosion process which has been proved by the higher oxygen % under flow condition than static immersion.

XRD pattern of brass coupon immersed in M30 for 4 days has shown in Fig. 5. Brass is an alloy of copper and zinc; hence, it has showed the high intense peaks of copper and zinc with $2\theta = 42, 49, 72, 88$ (PCPDF number-00-004-0836 and 00-004-0831). Mostly, copper and zinc will appear very closer because they have same energy level.

Oxides of base metals, namely cupric oxide (CuO) and zinc oxide (ZnO) are formed on the brass surface on immersion in M30 which has been proved by showing the CuO peaks with $2\theta = 32.49, 38.9, 79, 78, 80.18$ (PCPDF number-01-070-6831) and ZnO peaks at $2\theta = 56.55, 81.40$ (PCPDF number-00-005-0664). Also formation of cupric hydroxides [$Cu(OH)_2$] and zinc hydroxide [$Zn(OH)_2$] showed peaks at $2\theta = 33.79, 53.21, 63.39, 69.81$ (PCPDF number-00-013-0420) and at $2\theta = 37.0, 38.5, 46.99$ (PCPDF number-00-020-1435), respectively.

Products formed on brass surface in alcohol fuel blends are mainly due to alcoholate corrosion. Alcoholate corrosion is the type of localized corrosion that can occur on metal surface in methanol-gasoline blends in the presence of low water content. During corrosion reaction alcoholates, also called alkoxides or ethoxides are formed which cause pitting corrosion on the surface. These alcoholates decomposed to form oxides of base metals. Hydroxides of copper and zinc are formed when excess water is present in the fuel blends which have been confirmed by XRD analysis. Due to hygroscopic nature of methanol, gradual increase of water content in fuel blends is main cause for the formation of hydroxides as corrosion products on the brass surface immersed in methanol-gasoline blends.

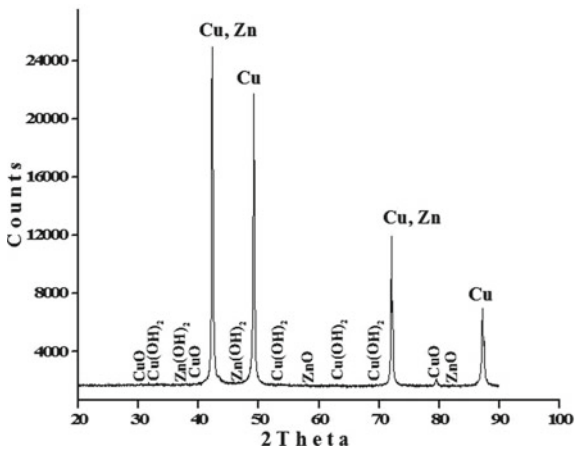

Fig. 5 XRD pattern of brass surface coupon immersed in M30 for 4 days

4 Conclusions

Corrosion rates of brass were evaluated in methanol-gasoline blends, and brass has undergone corrosion in tested fuel blends. The corrosion rates increase as the methanol percentage increases in the fuel blends; brass is subjected to higher corrosion attack in M30 fuel blend followed by M20, M15, and M10. The corrosion rates of brass are more in flow as compared to static immersion. Correlation between electrochemical corrosion rates and mass loss corrosion rates of brass in methanol-gasoline fuel blends were observed, and the polarization resistance of brass decreases with increasing the methanol amount. The corrosion products formed on the brass surfaces were mainly oxides and hydroxides of copper and zinc.

Acknowledgements The Authors would like to acknowledge the Department of Science and Technology (DST), Government of India for the financial support (TMD/CERI/MDME/2016/019), and the Center for Incubation Innovation Research and Consultancy (CIIRC), Jyothy institute of Technology, Bengaluru for providing necessary facilities to carry out this research.

References

1. Rocabruno-Valdes CI, Hernandez JA, Juantorena AU, Arenas EG, Lopez-Sesenes R, Salinas-Bravo VM, Gonzalez-Rodriguez JG (2018) An electrochemical study of the corrosion behaviour of metals in canola biodiesel. Corros Eng Technol 53:153–162
2. Ahmmad MS, Haji Hassan MB, Kalam MA (2018) Comparative corrosion characteristics of automotive materials in jatropha biodiesel. IJGE 15(6):393–399
3. Meenakshi HN, Anand A, Shyamala R, Saratha R (2017) Comparison on the corrosion rates of copper, zinc and brass in Pongamia and jatropha biodiesels. Indian J Chem Technol 24:417–423
4. Samuel OD, Gulum M (2018) Mechanical and corrosion properties of brass exposed to waste sunflower oil biodiesel-diesel fuel blends. Chem Eng Commun 206(5):682–694
5. Adetunji OR, Aiyedun PO, Kuye SI, Lateef DA (2014) Evaluation of the influence of fossil fuel on corrosion resistance of brass. J Miner Mater Character Eng 2(3):176–181
6. Aquino IP, Hernandez RPB, Chicoma DL, Pinto HPF, Aoki IV (2012) Influence of light, temperature and metallic ions on biodiesel degradation and corrosiveness to copper and brass. Fuel 102:795–807
7. Meenakshi HN, Lakshmi MPV, Anand A, Shyamala R, Saratha R (2016) Corrosivity of *Pongamia pinnata* biodiesel on zinc and its alloy—a comparison. Int J Environ Sustain Dev 15(3):264–271
8. Thangavelu SK, Ahmed AS, Ani FN (2016) Impact of metals on corrosive behavior of biodiesel–diesel–ethanol (BDE) alternative fuel. Renew Energy 94:1–9
9. Fazal MA, Haseeb ASMA, Masjuki HH (2014) A critical review on the tribological compatibility of automotive materials in palm biodiesel. Energy Convers Manage 79:180–186
10. Elfasakhany A (2015) Investigations on the effects of ethanol–methanol–gasoline blends in a spark-ignition engine: performance and emissions analysis. Eng Sci Technol Int J 18(4):713–719
11. Ozsezen AN, Canakci M (2011) Performance and combustion characteristics of alcohol–gasoline blends at wide-open throttle. Energy 36(5):2747–2752
12. Thomson JK, Pawel SJ, Wilson DF (2013) Susceptibility of aluminum alloys to corrosion in simulated fuel blends containing ethanol. Fuel 111:592–597

13. Lou X, Yang D, Singh PM (2009) Effect of ethanol chemistry on stress corrosion cracking of carbon steel in fuel-grade ethanol. Corrosion 65(12):785–797
14. Papavinasam S, Revie RW, Attard M, Demoz A, Michaelian K (2003) Comparison of laboratory methodologies to evaluate corrosion inhibitors for oil and gas pipelines. Corrosion 59(10):897–912
15. Meenakshi HN, Anisha A, Shyamala R (2013) A comparison of corrosion behavior of copper and its alloy in *Pongamia pinnata* oil at different conditions. J Energy Article ID 932976:4p
16. Meenakshi HN, Shyamala R (2015) Effect of flow and dissolved oxygen on the compatibility of *Pongamia pinnata* biodiesel with common construction materials used in storage and transportation. Int J Chem Eng, Article ID 463064, 9 p
17. Xingyue Y, Yaqin Z, Dongliang LI, Jing JI, Yixin QU, Jidong W (2011) Effect of near-wall hydrodynamic parameters on flow induced corrosion. Corr Sci Protect Technol 23(3):245–250

Quantitative Risk Analysis Using HIRA in an Automotive Manufacturing Sector

RajPradeesh Thangaraj, A. Rama Pandian, Venkumar Ponnusamy, and Manikandan Rajenderan

Abstract In industrial arena, all successful industry has to be safe, reliable and sustainable in its operations. The industry has to identify the hazards and assess the risks and to bring the risks to tolerable level. For this purpose, so many risk assessment tools are used by many industries. Like that, hazard identification and risk assessment is a basic safety tool, to be used for identifying hazards at workplace and assess risk level based on the severity and probability of that hazards. In this Paper, the Risk Assessment methodology was used to evaluate the potential risk encountered in that machinery and assembly sections in the automotive sectors. Most of the industrial accident acts due to machines to man. Arranging the machinery risk from higher to lower category based on their risk rating, possible control measures will be recommended.

Keywords Hazard · Risk machinery · Control · Hazard identification and risk assessment (HIRA)

1 Introduction

According to the department of labour, every year almost 6000 people are fatally injured at work. More than 4 four million more people suffer non-fatal injured. Injuries caused by machines are more severe and permanent. In moving machinery, danger can often be removed together by mechanical safeguards and better machine design or construction. In this Investigation Analysis, automotive industrial hazards were identified using the Checklist analysis in each machinery and assembly line operations. Before beginning the hazard identification and risk assessment, define my scope of this work, the aim of this work is implementing this procedure to all operating plants and project site of automobile industry. HIRA is a procedure to describe a hazard can be identified as an agent, condition or activity that has potential

R. Thangaraj (✉) · A. R. Pandian · V. Ponnusamy · M. Rajenderan
Department of Mechanical Engineering, Kalasalingam Academy of Research and Education, Krishnankoil, Tamil Nadu 626126, India
e-mail: rajpradeesh29@gmail.com

G. Kumaresan et al. (eds.), *Advances in Materials Research*, Springer Proceedings in Materials 5, https://doi.org/10.1007/978-981-15-8319-3_41

to cause illness, injury, loss of property or damage to environments. In this work, all hazards from the machinery and assembly sections in automobile industry are identified. Risk assessment is followed after finishing hazard identification.

Risk assessment is a systematic method of identifying and analysing the hazard associated with an activity and establishing a level of risk for each hazard [1], and for upcoming days, every industry followed risk assessment for all hazardous process, machinery operation and non-routine activities. Finally, control measures for all high hazardous process are noticed in this paper.

1.1 Machinery Safety

Where exposure to machinery hazards cannot be eliminated or substituted for machinery of improved design, risk assessment and risk control must be applied to the hazards to reduce the risk. Workplace health and safety laws require the highest order control be applied.

People must be provided with safe access and personal protective equipment [PPE] that is suitable for the work they perform in, on and around machinery. A work platform is suited to the nature of the work that allows for good posture relative to workers, sure footing, safe environment and fall prevention and PPE, which is a basic requirement [5]. Otherwise, the machines have some safety control devices for reducing the chance of hazard. Basically, some control devices are necessary for automotive industrial machines like photo guard sensor, double hand push button and limit switches. Photo guard sensor is one of the sensing devices which are placed both sides of dangerous area like cylindrical movement, it shut off the process, at that time it senses any movement nearby dangerous area, and in recent industries, type 2 and type 4 sensors are used. Double hand push button provides a highest level of safety by forcing the operator to keep the hands outside of the machine. And limit switch is an electromagnetic device which breaks the electrical connection when the bottom door will open.

2 Tool Description

In this paper, the HIRA tool has being applied, which can be performed in any industries like construction, mining, chemical, etc. It performs to identify hazard and to determine risk. Hazard Identification and Risk assessment to proactive rather than reactive methods for an automobile manufacturing sector to mitigate the potential hazards present in the Assembly and Machinery sections. [2]. Using this tool, we can analyse to control the potential and tolerable hazards.

A HIRA tool is performed by a team of qualified experts on the process, the machinery, hazards and work activities or a personal employee who have experienced on risk assessment methods usually lead these teams. Mostly, they are applying

the selected analysis technique with subject matter from engineering, operations, maintenance and discipline as needed [3]. The purpose of this tool is to identify hazards and risk in every activity and sequences and assess whether it is potential or tolerable and gives suggestion, in order to eliminate or substitute that hazards.

3 Methodology

In this Paper HIRA is a Processed Methodology Tool which is suitable to minimize the potential injuries and incidents encountered in automotive sector. It is also used to assessing the qualitative and Quantitative risk present in the workplace. In that process, hazards identification plays a vital role for analysing the hazards and risk in every machine by using a proper check sheet.

Hazard identification and risk assessment is a process of defining and describing hazard by characterising their severity and probability. Frequency and severity and evaluating adverse consequences, including potential loses and injuries [1]. In this work the author will chosen the five main sections and the working conditions also mentioned in that work, to assessing the risks in the workplace and it can be able applied in the five major units to identify the solution and implementation for the potential threats.

4 Hazard Identification

Hazard identification is the first step in this work. We have many sources to identify hazards inside automotive plant. Hazard identification sources are safety audit, workplace inspection, accident investigation, team consultant, incident illness report, health and environmental monitoring, employee complaints and observation [3].

In this Investigation Risk assessment, Workplace Inspection and observation is used a Hazard Identification Tool to identify the hazards. Using sample inspection prepares a proper checklist in Table 1 related to machinery hazard. In this checklist, all machinery hazard information are questioned including pneumatic and hydraulic system inside the machines. These are analysed in machinery and assembly section of plant 2 in automotive industry.

4.1 Hazard Findings

In this Investigation study applied the Hazard Identification Tool and the Checklist analysis method can be used to analysis major number of potential threats were identified in the Machining line sections as shown in Table 2 and assembly line as shown in Table 3 in plant 2. It is mostly based on safety control devices like photo

Table 1 Checklist for identify machinery hazard

S. No.	Checklist	Yes	No
1	Double hand push button working		
2	Double hand push button cannot be operated in single hand		
3	Check emergency button working		
4	Emergency button placed in easily accessible location		
5	Whether emergency button stops all hazardous process immediately		
6	Emergency button—red top with yellow bottom		
7	Check photo guard sensor working		
8	If type 2 sensor, minimum clearance distance is 250 mm		
9	If type 4 sensor, minimum clearance distance is 200 mm		
10	Photo guard sensor works for all sequences		
11	Photo sensor covers all hazardous movement		
12	Photo sensor checking tool available		
13	When interrupting photo sensor, cylinder should go to the home position. Check for all cylinders		
14	Safety guard available to avoid interruption from side and backside		
15	Safety guard available in bottom if required		
16	Bottom door has limit switch and is working		
17	If bottom door fastened, whether it can be removed by tool only		
18	Any sharp edges in machine		
19	Electrical panels are locked properly		
20	Wiring is properly routed		
21	Wire damage		
22	Any spillage of chemicals		
23	Check whether the chemicals are properly stored		
24	Check any manual mode operation		

guard sensor, double hand push button, cylinder gap, piston and cylinder movement. In hazard findings, the table includes cell number, operation number and operation name and abnormalities for both machining and assembly line. Finally, align all the abnormalities in both assembly and machining in the same table (Fig. 1). It is easy to see which hazard is higher level and which hazard is lower level (Fig. 2).

In assembly line, some other hazards are noticed and tabulated it. In assembly section, most of the machines work automated without manual power.

Table 2 Hazards in machining line

S. No.	Cell number	Operation number	Operation name	Abnormalities/hazards
1	1	PDI	Air gun	Air leakage in housing
	1	20	Dot marking	Double hand push button not working
3	1	75	Washing	Absence of back side coverage
4	1	80	High pressure washing	1. Cycle start damage 2. Photo sensor minimum clearing distance is less than 200 mm (type 4)
5	1	90 A	Dry leak test	Absence of double hand push button
6	1	90 B	Dry leak test LTM	1. Absence of side and back guarding 2. Wires are not properly routed and insulated 3. Photo sensor minimum clearing distance is less than 200 mm (type 4)
7	1	120	Bush pressing	Wires are not properly routed
8	1	140	Ultrasonic washing	Absence of side mesh (door operation)
9	1	60	Washing	Cycle start setup box not fastened
10	1	70	Leak test	Absence of cylinder gap while return movement
11	1	20	Marking	Absence of side and front coverage
12	1	180	Cap pressing	Absence of cylinder gap while return movement
13	1	190	Leak test	Control panel is not closed
14	1	20	Marking	Absence of one side guarding
15	1	70	High pressure washing	Absence of limit switches in bottom
16	1	80	Leak test	Absence of cylinder gap while return movement
18	1	20	Dot marking	Absence of one side guarding Photo sensor not in correct position

Table 3 Hazards in assembly section

S. No.	Cell number	Operation number	Operation name	Abnormalities/hazards
1	Assembly	20	Name plate marking	Absence of photo guard sensor
2	Assembly	60	Cylinder crimping	Absence of one side mesh
3	Assembly	30	Leak test	Absence of emergency button
4	Assembly	70A	Performance test	Absence of limit switches in bottom
5	Assembly	120	EOL test	Wires are not properly routed
6	Assembly	40	Air dryer assembly	Absence of double hand push button
7	Assembly	80	Welding station	Absence of front guarding
8	Assembly	160	Crane movement	Unsafe condition
9	Assembly	150	Cap pressing	Oil spillage
10	Assembly	40	Painting station	Absence of extinguisher tank in painting machine
11	Assembly	80	Subassembly cycle test	Absence of cylinder gap while return movement of cylinder
12	Assembly	60	Desiccant filling	Vacuum hose is in unsafe condition
13	Assembly	50	Riveting	Photo guard sensor not in proper position and not working sometimes
14	Assembly	80A	Support assembly	Sharp edges

5 Risk Assessment

Hazard is anything which is potential to cause harm, and risk is how high the chance that someone will be injured by that hazard. Risk assessment is the process used to determine whether the risk is potential or tolerable. For risk assessment, we have so many tools like HIRA, failure mode effect analysis [FMEA], etc. Most of the risk assessment is based on severity and probability. In this risk assessment, the risk rating and risk matrix are based on the severity and probability of collected abnormalities.

Fig. 1 HIRA process

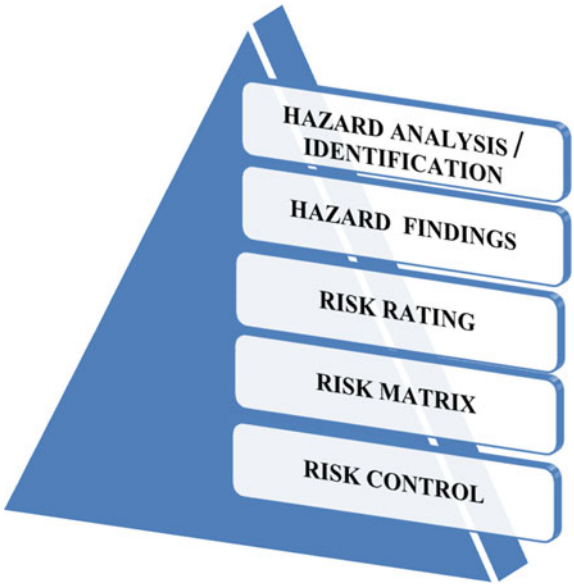

Fig. 2 Hazard identification sources

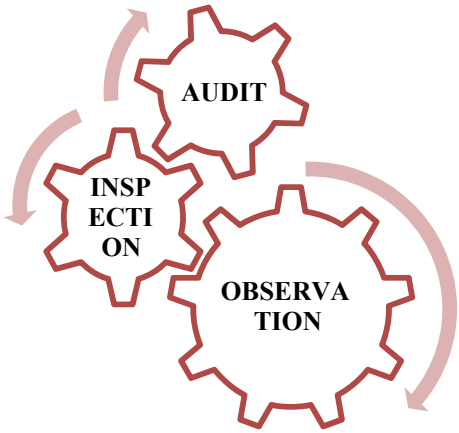

5.1 Risk Ratings

Risk rating is the process which separates the potential hazards and tolerable hazards using severity of probability score as shown in Tables 4 and 5. Uisng the Score Values

Table 4 Probability of occurrence

Rating	Description	Examples of description
5	Almost certain	Very high probability
4	Very likely	High probability
3	Likely	Moderate probability
2	Possible	Low probability
1	Unlikely	Very low probability

Table 5 Severity rating

Rating	Description	Examples of description
5	Severe	Fatality
4	Major	Injury or illness resulting in permanent impairment
3	Moderate	Injury or illness requiring hospital admissions
2	Minor	Injury or illness requiring medical treatment. Temporary impairment
1	Negligible	Minor injuries or discomfort. No medical treatment or measureable physical effect

represents the Risk and Hazards can be catergorized from major to minor range using the risk matrix table shown in Tables 4 and 5.

Probability of occurrence
Probability of occurrence is an estimate of that hazard or event occurs. It is defined mostly as total number of possibilities and detection of the problem observed in hazard identification [1].

Severity Rate
Severity is a state or condition of being severs. The severing rate describes the number of lost workdays of those workers. In some industry, the actual number of lost workdays times 200,000 (a standardised estimate of the hours worked by 100 employees) divided by the actual total number of hours worked by all the employees results in the severing rate. In this paper, the severity score is based on its impact, and it is described in Table 5.

Risk rating is a multiplication of severity and probability of the hazards. In these works, all machinery and assembly line hazards are separated based on their severity and probability (Tables 6, 7, 8 and 9).

$$\text{Risk Rating} = \text{Severity} * \text{Pr obability}$$

Table 6 Risk rating table

Hazard intimation letter	Hazard	Impact	Severity number	Probability number	Risk rating
A	Photo guard sensor less minimum clearance distance	Major hand injury	4	4	16
B	Wires are not properly routed and damage	fatality	5	5	25
C	Photo guard sensor not in proper position and not working sometimes	Major hand injury	4	2	8
D	Absence of bottom, front side guarding	Major injury	4	5	20
E	Emergency switch broken and not working sometimes	Machine damage, fatality	5	5	25
F	Air leak from air gun	Small injury	1	1	1
G	Electrical panel damaged	Fatality	5	4	20
H	Oil leakage	Minor injury or illness	2	3	6
I	Double hand push button not in working condition	Major injury	3	3	6
J	Absence of cylinder gap while return movement of cylinder	Major injury	3	5	15
K	Absence of limit switches in bottom door	Major injury	4	4	16
L	Fire extinguisher placed improper and unmarked position	Major injury	5	5	25
M	Electrical panel is in open condition	Fatality	5	1	5

(continued)

Table 6 (continued)

Hazard intimation letter	Hazard	Impact	Severity number	Probability number	Risk rating
N	Absence of extinguisher tank in painting machine	Fatality	5	4	20
O	Unrouted crane movement	Injury	4	2	8
P	Oil spillage at bottom of machine	Injury	2	3	6
Q	Vacuum hose is in unsafe condition	Machine damage	2	1	2
R	Sharp edges	Minor injury	2	2	4

Table 7 Risk matrix table

	NEGLIGIBLE [1]	MINOR [2]	MODERATE [3]	MAJOR [4]	SEVERE [5]
ALMOST CERTAIN [5]	M		J	N , K	B , L , E
VERY LIKELY [4]		O		A	G , D
LIKELY [3]		P , H ,I			
POSSIBLE [2]	Q	R		C	
UNLIKELY [1]	F				

Table 8 Colour intimation table

COLOUR INTIMATION	RISK LEVEL	SCORE
	HIGH RISK	20 – 25
	MEDIUM HIGH RISK	10 – 20
	MEDIUM RISK	6 – 10
	LOW MEDIUM RISK	4 – 6
	LOW RISK	1 – 4

5.2 Risk Matrix

A risk matrix is a graphical representation of the severity and probability scores of a risk. It is “5 × 5 matrix” because it contains five rows and five columns.

Table 9 Risk control chart

S.NO	HAZARD INTIMATE LETTER	HIGH AND MEDIUM HAZARD	CONTROL MEASURES	HIERARCHY CONTROL	S	P	RISK RATING
1	N	Absence of extinguisher tank in painting machine	Extinguisher tank is fixed in marked area	Engineering control	2	1	2
2	K	Absence of limit switches in bottom door	Fix any interlock device	Engineering control	2	2	4
3	B	Wires are not properly routed and damage	Proper maintenance [inspection]	Administrative Control	3	2	6
4	L	Fire extinguisher placed improper and unmarked position	Proper maintenance [inspection]	Administrative Control	2	2	4
5	E	Emergency switch broken and not working sometimes	Fix Machine fault intimate Alarm	Engineering control	1	1	1
6	G	Electrical panel damaged	Shock absorbance shoes, proper earthing	Engineering control , PPE	3	2	6
7	D	Absence of bottom, front side guarding	Fix auto adjustable Guarding	Engineering control	2	2	4

6 Risk Control

Controlling exposures to occupational hazards is the basic method of protecting workers. A hierarchy of controls has been used as a means of determining how to implement feasible and effective control solutions [6]. It defines.

1. ELIMINATE [eliminate the hazard by removing it]
2. SUBSTITUTE [substitute the hazard by replacing it]
3. ENGINEERING CONTROLS [application of interlocks, limit switches, installation of safety valve, alarm and detection System, etc.]
4. ADMINISTRATIVE CONTROLS [good housekeeping, safe systems at work, training, monitoring, procedures and laws, supervision, etc.]
5. PERSONAL PROTECTIVE EQUIPMENT [protect worker from hazards]

In this Investigation analysis, each potential hazard identified and it can be resolved using the Hierarchy control Methods to classify the High, Medium and Low risks matrix as shown in Table 7 because it is only a potential hazard to remove that as soon as possible. After implementing control measures, again calculate the risk rating score for that risks.

7 Result

From this Fig. 3, the risk ratings of high hazards are compared by using before HIRA and after HIRA. It represents risk ratings after HIRA is minimised a lot from risk

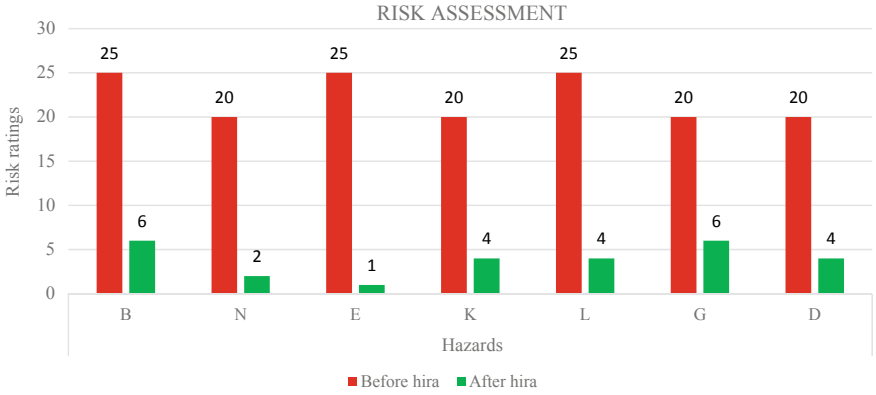

Fig. 3. Graphs for risk assessment before and after HIRA

ratings before HIRA. This statistics clearly describes that the high hazards will be minimised after HIRA process.

8 Conclusion and Discussion

This work explained about the HIRA methodological process through process analysing, checklist, hazard findings and risk assessment techniques. From that Risk assessment Investigation can be conducted in the above two sections (Machining and Assembly sections) were clearly. It is inference from the above investigation analysis more number of potential hazards are identified and their corresponding Control measures are recommended using the Hierarchy of controls methodology. We can use this HIRA process at any type of hazardous process in all types of industries. Using this process, we will reduce or eliminate that hazards which you found as high risk and medium-high risk.

References

1. Ramesh R et al (2017) Hazard identification and risk assessment in automotive industry. Int J ChemTech Res 10(4):352–358
2. Purohit DP et al (2018) Hazard identification and risk assessment in construction industry. Int J Appl Eng Res 13(10):7639–7667
3. Khan FI, Abbasi SA (1998) Techniques and methodologies for risk analysis in chemical process industries. J Loss Prev Process Indus 11(4):261–277
4. Shamsuddin KA, Mohd Norzaimi CA, Ismail AK (2015) Investigation the effective of the hazard identification, risk assessment and determining control (HIRADC) in manufacturing process. Int J Innov Res Adv Eng 2(8):80–84
5. Paithankar A (2011) Hazard identification and risk analysis in mining industry. PhD diss.

6. Khan FI, Abbasi SA (1998) Techniques and methodologies for risk analysis in chemical process industries. J Loss Prev Process Indust 11(4):261–277
7. Etherton JR (2007) Industrial machine systems risk assessment: a critical review of concepts and methods. Risk Anal Int J 27(1):71–82
8. Azadeh-Fard N et al (2015) Risk assessment of occupational injuries using accident severity grade. Saf Sci 76:160–167
9. Chinniah Y, Aucourt B, Bourbonnière R (2017) Safety of industrial machinery in reduced risk conditions. Saf Sci 93:152–161
10. Suhardi B et al (2018) Analysis of the potential hazard identification and risk assessment (HIRA) and hazard operability study (HAZOP): case study. Int J Eng Technol 7(3)24:1–7
11. Erbay B, Özkan C (2018) Fuzzy FMEA application combined with fuzzy cognitive maps to manage the risks of a software project. Eur J Eng Formal Sci 2(2):6–21
12. Kiurski J et al (2012) Register of hazardous materials in printing industry as a tool for sustainable development management. Renew Sustain Energy Rev 16(1):660–667
13. Jacxsens L, Mieke U, Bruno De M (2016) Challenges in risk assessment: quantitative risk assessment. Procedia Food Sci 6: 23–30
14. Pasman H, Reniers G (2014) Past, present and future of quantitative risk assessment (QRA) and the incentive it obtained from land-use planning (LUP). J Loss Prev Process Ind 28:2–9

Thermal Analysis and Characterization of Catalytically Cracked Jatropha Bio-Oil

L. S. Gokul, S. Jegadheeswaran, and C. Sasikumar

Abstract Global demand of fuel is to be increasing because of growth of population and industrialization that tends to development and research on alternative fuels. Alternative energy source has more advantages than diesel fuel. With a lot of research in over various alternative fuels, biodiesel is considered to be best due to its engine performance, cost and emission rates. After a brief study about it, non-edible vegetable oil (Jatropha) is selected. In this project, the catalytic reforming method is used for the biodiesel production, and cerium oxide (CeO2) is used as catalyst for the reforming. The catalyst is characterized using XRD and SEM. Then the fuel properties (flashpoint, density, viscosity, etc.) of the cracked biodiesel studied. Thermogravimetric analysis and gas chromatography/mass spectrometry analysis will be carried out. The results of these analyses show the characteristics of the bio-oil produced and that is compared with the commercial diesel.

Keywords Biodiesel · Thermal analysis · Catalyst · Fuel properties

1 Introduction

Nowadays, fossil fuels are not adequate to meet the world's demand due to vehicle population, and also the price of the fuel varies day by day due to national policies, needs and taxes. International Energy Agency (IEA) estimated the global energy demand in 2035 to be 18 billion tons for the current scenario of usage of oils. Fossil fuels present on our planet are limited. The increasing rate of fossil fuel consumption leads to greenhouse gas emissions [1].

It is a fuel other than petrol or diesel for powering motor vehicles. Some alternative fuels are biodiesel, bio-alcohol (methanol, ethanol), chemically stored electricity (batteries, fuel cells), hydrogen, propane, vegetable oil, biomass sources, etc. The main reason for using it in CI engine is that the consumption and demand of petroleum

L. S. Gokul (✉) · S. Jegadheeswaran · C. Sasikumar
Department of Mechanical Engineering, Bannari Amman Institute of Technology, Sathyamangalam, Erode, Tamil Nadu 638401, India
e-mail: gokulls@bitsathy.ac.in

G. Kumaresan et al. (eds.), *Advances in Materials Research*, Springer Proceedings in Materials 5, https://doi.org/10.1007/978-981-15-8319-3_42

by-products are increasing day by day due to urbanization and vehicle population. And also it reduces emissions produced by the engine. Vegetable oils are the main source of the production of biodiesel. The oils or fats filtered from their hydrocarbons and then combined with alcohol to produce biodiesel. The oil can either be mixed with diesel or used alone. It produces lesser air pollutants than diesel. The oils are renewable and low sulfur than the conventional fuels [4]. So, the resources like pongamia, jatropha curcas, cotton oil, mahua, calophyllum tobacco, etc. must be used instead of fossil fuels. Biodiesel production was found to be affordable and comparable to the existing diesel prices. Biodiesel is an eco-friendly and renewable fuel substitute for diesel [7]. Jatropha plant is developing well in poor soil. It is easy to initiate and grows very quickly, to producing seeds for 50 years. The jatropha oil can be used directly in an engine without any major medications required for a engine. While using jatropha oil, it is less pollutant as compared to the diesel fuel [8]. The plant has been shown in Fig. 1. It is one of the best non-edible oils which produce high yield compared to other oils. The average Jatropha seed is approximately 30–45 weight % oil. A low temperature should be maintained while producing the seed [10, 11]. This oil is considered for its cost as well as reduced emission. Environmental Protection Agency (EPA) has conducted a test, and the

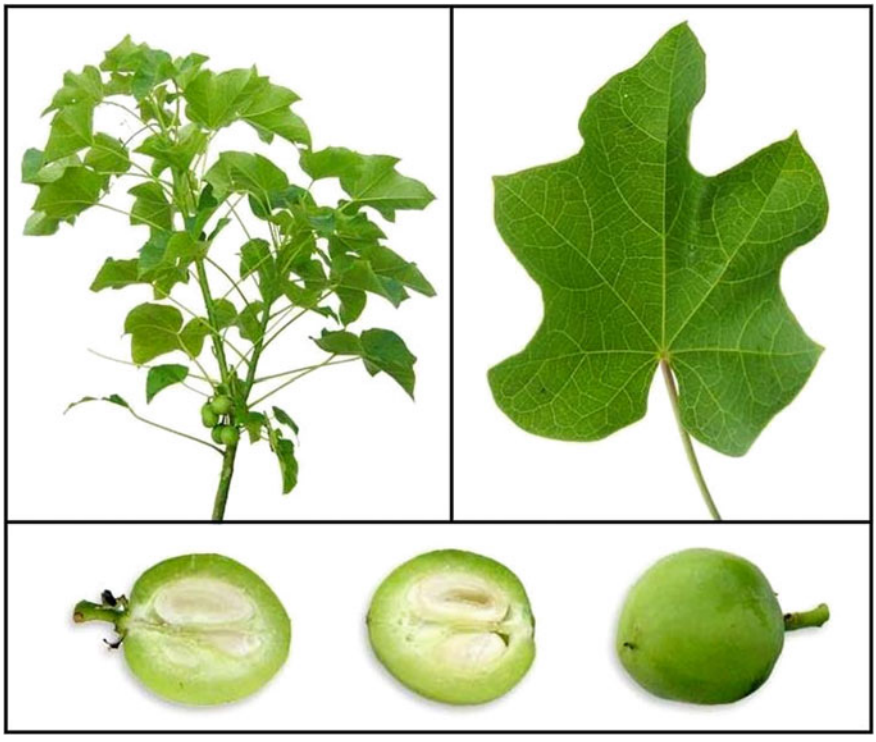

Fig. 1 Jatropha plant

Fig. 2 Jatropha oil

results of hydrocarbon emission of Jatropha oil are half that of fossil diesel [12]. It has higher cetane number compared to other oils. The extracted oil has been shown in Fig. 2

Biswas et al. [1] investigated the effect of different catalysts on the co-cracking of Jatropha oil. Co-processing of Jatropha oil and vacuum residue was investigated to determine behavior under atmospheric pressure and thermal heating conditions. The activity of various catalysts on co-cracking has been studied. CAT-R was the best catalyst used for the co-cracking, as it gives 45 and 49% gasoline and diesel hydrocarbons respectively in cracked liquid. In case of the co-cracking CAT-Z, it is about 37 and 35% for gasoline and diesel range hydrocarbons, respectively. Biswas and Sharma et al. [2] studied the effect of different catalysts on the cracking of Jatropha oil. They studied about catalytic cracking of Jatropha oil (JO) in a batch reactor, and they make experiments in nitrogen atmosphere and at temperature of 375°. They use catalysts like Zeolite Socony Mobil in the form of ZSM-5, ZSM-5 + SiAl (Silicon and aluminium) and NiMo/SiAl. In all that, Zeolite Socony Mobil–5+ Silica aluminium was the best for Jatropha Oil cracking which gives 36% gasoline and 58% diesel range hydrocarbons, respectively, and they also observed that the usage of catalyst has a positive effect on pH content.

Fan et al. [3] performed hydrocracking of Jatropha oil over nano-hydroxyapatite catalyst. The Ni-H3PW12O40 catalyst with H3PW12O40 was prepared through hydrocracking process, and they characterized the catalyst by using many methods which include powder X-ray diffraction and thermogravimetric analysis. The conversion of jatropha over various catalysts gives better liquid yield. The pour point of final product oil was 28 °C, and the catalyst was used without sulfurization.

Biswas et al. [5] studied on co-cracking of jatropha oil to obtain liquid, gaseous product and char. Co-cracking of jatropha oil was investigated on various heating rates from 5 to 35 K/min under nitrogen atmosphere. They employed various models for cracking process and observed with DTG curve and other curves. They made CG-MS and TGA tests and indicate presence of alkanes 47%, and various gaseous

products and char contained metal products are obtained from this co-cracking as a fuel source.

Laksmono et al. [6] performed the production of biodiesel from tar by using a method of biomass gasification. The cracking process has been done by using zeolite, magnesium oxide and aluminum oxide catalysts. Ong et al. [9] investigated the production of biofuel using catalytic cracking. There are several processes for biodiesel extraction but mostly by esterification or deoxygenate of triglycerides. By method of pyrolysis, bio-oil is produced. They completely discussed with the recent process, and the production of biodiesel by catalytic cracking method includes the important issues like reactor design and catalysts employed.

2 Objective and Methodology

To reduce the environmental pollution on earth caused by diesel engines for that to find an alternative fuel that has similar property of diesel can be used in the engine without any modification and to compare the characterization for the catalytically cracked oil to the commercial diesel. Methodology of jatropha oil production is shown below.

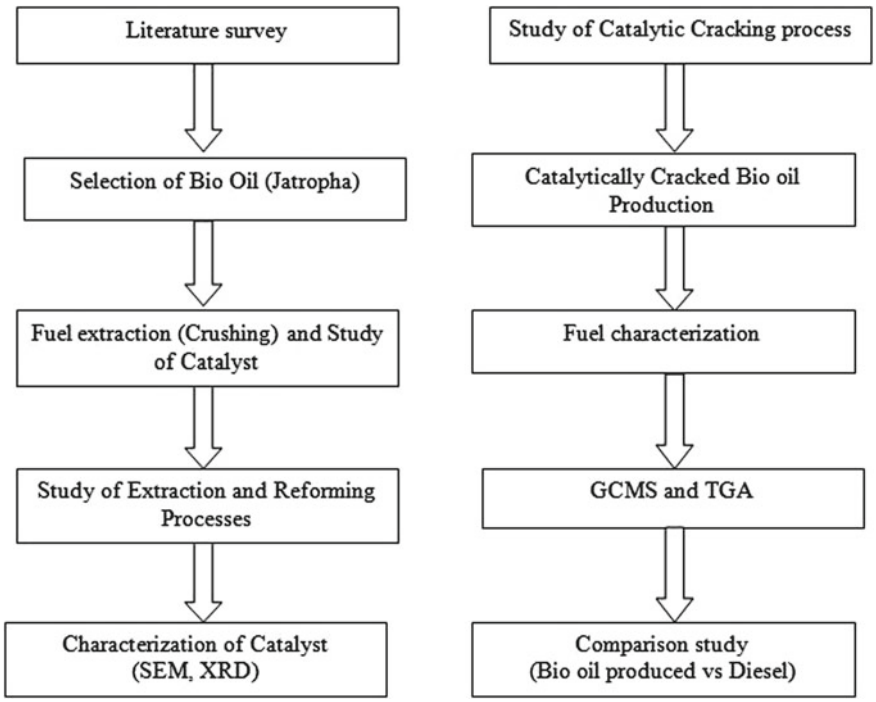

3 Production and Catalyst

3.1 Oil Extraction and Catalytic Reforming

The conversion of seed into oil is the oil extraction. Seed should be dried in the sun light for a duration of three week. Oil extraction can be made by enzymatically. The oil extracted by mechanical method of extraction (crushing) using Ram press. The cost of Jatropha oil was a Rs. 26/kg and that of seed cost was Rs. 6/kg in commercial market. Catalytic cracking is a process of chemical reactions that involves four chemical reactions that will be explained below.

3.2 Catalytic Reactions

Dehydrogenation: The process of conversion of methylcyclohexane to the new structure of toluene (Fig. 3).

Isomerization: The structure of the normal paraffins converted into the 2.5 Dimethylhexane (Fig. 4).

Aromatization: Normal heptane is to be converted into the toluene process (Fig. 5).

Hydrocracking: The given structure of the paraffins is converted into two or more number of smaller molecules by the process of cracking (Fig. 6).

Fig. 3 Dehydrogenation

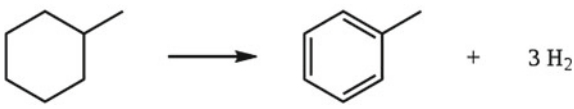

Fig. 4 Isomerization

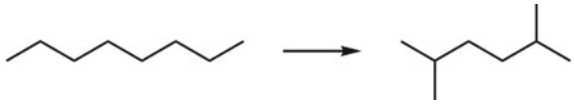

Fig. 5 Aromatization

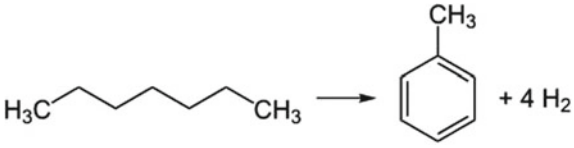

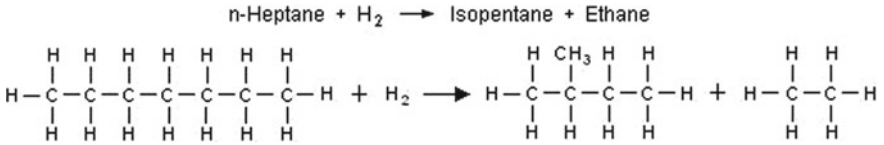

Fig. 6 Hydrocracking

3.3 Catalyst

Catalyst is used to enable faster chemical reaction under different conditions. It does not change the chemical reaction. Catalyst and its yield for the production of biodiesel using catalytic cracking are mentioned in Table 1

3.3.1 Cerium Oxide Catalyst

Cerium oxide used as a catalyst for this experiment. This catalyst is one of the best catalysts among other metal oxides, and it boosts the biodiesel yield. Cerium oxide is not used in any of the journals referred for jatropha for catalytic cracking. The CeO2 is mixed with NaOH to make pellets for the process. The catalyst has been shown in Fig. 7.

4 Characterization of Catalyst

A scanning electron microscope (SEM) was used to produce the accurate image of sample by scanning with a focused beam of electrons. SEM pictures of cerium oxide

Table 1 Yield % for various catalysts

Catalyst	Yield (%)
Zeolite	62–75
Magnesium oxide	55–66
Aluminum oxide	67–71
Ni–Al–MCM-41	57.9
V2O5	87.6
MoO3	55.1
ZSM-5	70
H2SO4	84.8
ZnO/KF	87
CO3O4	85.2
ZnCl2	77.6

Fig. 7 Cerium oxide

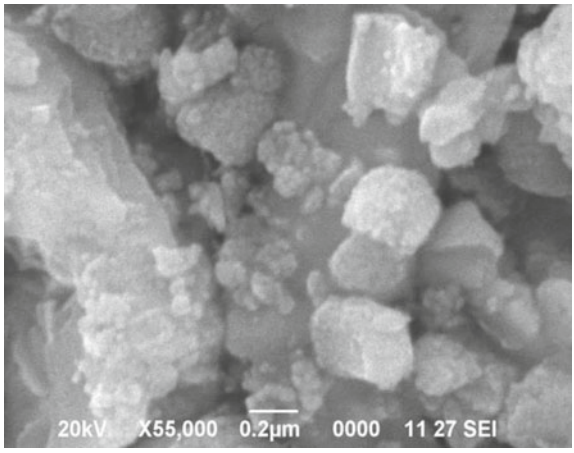

Fig. 8 SEM image of CeO_2 catalyst (55,000 x)

catalyst are shown in Figs. 8 and 9. All the particles are looks like a homogeneous in nature.

5 Characterization of Oil

After producing Jatropha oil, the fuel properties are measured. Then the properties of jatropha oil are compared with conventional fuel which is shown in Table 2.

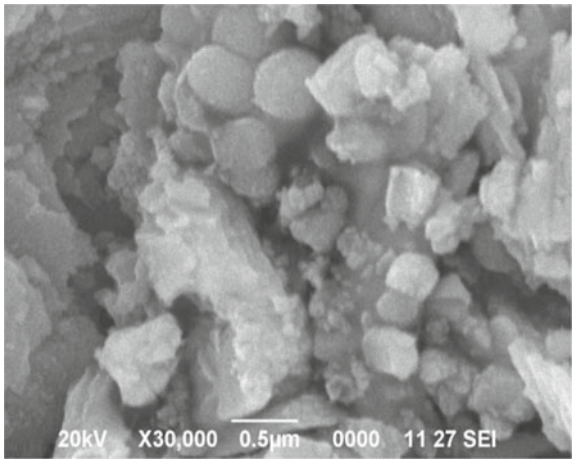

Fig. 9 SEM image of CeO_2 catalyst (30,000 x)

Table 2 Properties of diesel and Jatropha oil

Properties	Diesel	Jatropha oil
Calorific value (kJ/kg)	44,215	38,989
Mass density (kg/m^3)	0.852	0.926
Specific gravity	0.854	0.928
Kinematic viscosity (cSt)	3.91	47.3
Pour point in (°C)	−13	1
Flash point in (°C)	76	228
Fire point in (°C)	96	278
Cloud point in (°C)	−6	6

5.1 FTIR Testing

It is used to determine the rate of mixing of catalyst with oil with the help of infrared rays. It gives the intensity with the help of received and blocked wavelength of the passed infrared rays.

6 Conclusion

By the mechanical way of extraction, the oil is produced (crushing process). The extracted oil properties are almost matches with the diesel. So, the oil is selected for the cracking process to make it to equal. Discrete spherical and microlevel different particles are shown in the SEM image. From that, the formation of catalyst is homogeneous. These results show that cerium oxide catalyst can be used for the catalytic cracking.

The oil extracted from jatropha needs to be cracked using the characterized CeO2. Then the fuel properties of the cracked oil will be studied. Thermogravimetric analysis and gas chromatography/mass spectrometry analysis will be carried out for comparing with conventional fuel of diesel.

References

1. Biswas S, Majhi S, Mohanty P, Pant KK, Sharma DK (2014) Effect of different catalyst on the co-cracking of Jatropha oil, vacuum residue and high density polyethylene. Fuel 133:96–105
2. Biswas S, Sharmaa DK (2014) Effect of different catalysts on the cracking of Jatropha oil. J Anal Appl Pyrol 110:346–352
3. Fan K, Liu J, Yang X (2014) Hydrocracking of Jatropha oil over Ni- H3PW12O40/nano-hydroxyapatite catalyst. Int J Hydrogen Energy 39:3690–3697
4. Jain S, Sharma MP (2010) Prospects of biodiesel from Jatropha in India: a review. Renew Sustain Energy Rev 14:763–771
5. Biswas S, Mohanty P, Sharma DK (2013) Studies on co- cracking of jatropha oil with bagasse to obtain liquid, gaseous product and char. Renew Energy 63:308–316
6. Laksmono N, Paraschiv M, Loubar K, Tazerout M (2013) Biodiesel production from biomass gasification tar via therma l/catalytic cracking. Fuel Process Technol 106:776–783
7. Yigezu ZD, Muthukumar K (2014) Catalytic cracking of vegetable oil with metal oxides for biofuel production. Energy Convers Manage 84:326–333
8. Zhao X, Wei L, Julson J, Qiao Q, Dubey A, Anderson G (2015) Catalytic cracking of non-edible sunflower oil over ZSM-5 for hydrocarbon bio- jet fuel. New Biotechnol 32(2)
9. Ong YK, Bhatia S (2010) The current status and perspectives of biofuel production via catalytic cracking of edible and non-edible oils. Energy 35:111–119
10. Takase M, Zhao T, Zhang M, Chen Y, Liu H, Yang L, Wu X (2014) An expatriate review of neem, jatropha, rubber and Karanja as multipurpose non -edible biodiesel resources and comparison of their fuel, engine and emission properties. Renew Sustain Energy Rev 495–520
11. Yingying L, Houfang L, Wei J, Dongsheng L, Shijie L, Bin L (2011) Biodiesel production from crude Jatropha curcas L. oil with trace acid catalyst. Energy Resourc Environ Technol Chin J Chem Eng 20(4):740–746
12. Ramya G, Sudhakar R, Joice AI, Ramakrishnan R, Sivakumar T (2012) Liquid hydrocarbon fuels from Jatropha oil through catalytic cracking technology using AlMCM-41/ZSM-5 composite catalysts. Gener Appl Catal A 433–434

Dynamic Risk Assessment of an Ammonia Storage Tank Based on Bow-Tie and Bayesian Approaches

T. Jishin Jayan, K. Muthukumar, and R. Rajiev

Abstract The leakage of ammonia from the ammonia storage tank can cause harmful effects to human beings due to the toxic and flammable nature of the chemical. The ammonia leakage can result in the fire of various kinds such as flash fire, vapour cloud explosion, jet fire, and pool fire and causes harm to human health and environment due to toxic gas dispersion. An effective risk analysis is needed to prevent and mitigate such possible incidents. In this study, a bow-tie diagram is developed from the identified causes that can lead to leakage of the ammonia storage tank and its possible consequences. The prior failure probability data for all the basic events are identified, and updated failure frequency data are collected from the industry based on the practical component failure per year. The bow-tie model is further mapped to a Bayesian network for validating the results obtained from the bow-tie analysis using the forward prediction technique. The occurrence probability of the outcome (consequence) events obtained through the bow-tie analysis and the outcome event probability results from the Bayesian network (forward prediction technique) are similar, and hence, the results can be validated. The analysis is carried out on a 500 tonnes capacity ammonia storage unit of a fertilizer industry located in Kerala, India

Keywords Risk assessment · Bayesian network · Bow-tie analysis

1 Introduction

Ammonia is one of the important basic chemicals produced in the world and, as such, is produced in large quantities. The ammonia is the main chemical produced in every fertilizer industry for the production of nitrogen fertilizers, such as ammonium nitrate, urea, and ammonium sulphate. The liquid ammonia generally used to store in cylindrical flat bottom tanks of a single-walled or double-walled construction. The

T. Jishin Jayan (✉) · K. Muthukumar · R. Rajiev
Department of Mechanical Engineering, Bannari Amman Institute of Technology, Sathyamangalam, Erode, Tamil Nadu 638401, India
e-mail: jishin.jayan.jjt@gmail.com

G. Kumaresan et al. (eds.), *Advances in Materials Research*, Springer Proceedings in Materials 5, https://doi.org/10.1007/978-981-15-8319-3_43

ammonia leakage is highly dangerous due to the toxic and flammable nature of the chemical. The leakage can cause fires of various types, the fire of various kinds such as flash fire, vapour cloud explosion, jet fire, and pool fire, and it has the potential to affect human health and to cause damages to the environment. A risk analysis study of the ammonia storage tank is carried out to prevent such potential incidents.

The bow-tie analysis is very popular among the different techniques because it characterizes the accident scenario that completely includes the causes and consequences into a one single bow-tie model or diagram. One of the main disadvantages of the bow-tie model is that due to the static nature of its components, the bow-tie lacks dynamicity. It limits its application in real-time risk monitoring and in the updating of probabilities, which are the important features of dynamic risk analysis [1]. Abimbola et al. (2014) conducted a dynamic risk assessment study of the drilling operations where the real-time practical data, potential accident probabilities, and associated risks are updated and used for safety assessment. This method can be incorporated into a real-time risk monitoring device for field applications during drilling operations [2]. In every process plants, there is a strong demand for quantitative risk analysis. In dynamic risk analysis, the challenge is to define the process dynamic behaviour in case of system failures. The hazardous situations leading to major accidents are recognized, which allows the determination of consequences and quantification of severity [3].

A Bayesian network is an acyclic graph in which each link represents a conditional interdependence and each node corresponds to a single random event. The Bayesian network is a probabilistic method of inference, which can overcome the static limitation of the bow-tie method because of its probability updating mechanism; it can be used effectively to carry out forward prediction and backward diagnostic analysis. In this study, real-time data are obtained by monitoring and inspecting the system components based on their failure. These updated data from the industry are used as the initial inputs for the basic events of the bow-tie model developed, and the updated occurrence probability of the end-state consequences is estimated. The results obtained from the bow-tie analysis are compared with the Bayesian network developed, and the results can be validated. It is found that the bow-tie model is effective in estimating the updated occurrence probabilities of the outcome events when the real-time failure data are provided to the basic events. However, updating the bow-tie model with the updated failure probability data is time taking procedure that it needs to quantify both the fault tree and event tree whenever the failure frequency of the component subsystem changes. This lack of flexibility of the bow-tie model can be overcome by converting the static bow-tie model to a dynamic Bayesian network.

A Bayesian network is developed in a study, to model the maritime transport system, by taking into account its different representatives such as shipowner, shipyard, port, and their mutual influences. The Bayesian network is quantified by using conditional probability theories and by utilizing the experts' judgments finally; a sensitivity analysis has been carried out over the model to identify structure of the maritime transport system leading to a substantial reduction of accident probability during the operation [4].

A quantitative risk assessment is carried out focusing on evacuation from an offshore installation to improve the safety of the personnel working in the offshore installation. This work uses Bayesian concepts and binomial distribution to determine the impact of harsh environmental conditions to personnel performing escape and evacuation on offshore installations. The success probability of detecting the alarm by personnel depends upon the environmental conditions [5].

The Bayesian network-based modelling framework which can solve dynamic fault trees is developed in a study, where the complex behaviours and interactions are shown by dynamic system components, making combinative models unsuitable to resolve them. A novel reliability modelling and a framework based on Bayesian networks are proposed. The main concern in this paper is to define a Bayesian network-based modelling framework that can compute dynamic fault trees [6]. A new formalism is developed in a study, which helps to model dynamic system with regular and irregular changing variables. In this method, the time is assumed to be continuous to develop a continuous Bayesian network which provides sufficient flexibility to capture the dynamicity of real-world processes [7].

2 Risk Analysis of Ammonia Storage Tank Based on a Bow-Tie

Model and with Bayesian Approach—A Case Study

The study is carried out on an ammonia storage unit of a fertilizer industry with double-walled tank of 500 tonnes capacity. The current work is limited to single ammonia tank of capacity 500 tonnes and can be extended to the storage farm of the selected chemical industry.

2.1 Estimating the Failure Probabilities Using Bayesian Network

The Bayesian forward prediction technique is used to estimate failure probabilities of the outcome (consequence) events [8]. Consider the probability of the basic event E_{ii} be $PP\,(E_i)$, and the probability of the outcome event X is $PP\,(X)$ and then conditional probability of the outcome event X in the condition of the cause event E_{ii} be$PP\,(X|E_i)$, and then according to this forward prediction technique, PP (X) is given by,

$$P(X) = \sum_{i=1}^{n} P(E_i)(X|E_i) \tag{1}$$

2.2 Estimation of Prior Failure Probability Data

The generic (prior) failure probability values of the basic events are taken from the OREDA database. The prior failure frequency data of identified basic events and intermediate events are shown in Table 1. The updated failure frequencies of events based upon the real-time industrial data are also given in Table 1.

Table 1 Description of events in the fault tree with failure probability values

Events	Description with prior failure data	Updated failure data
Top event (TE)	Leakage of ammonia (2.5×10^{-5}/year)	1.428×10^{-4}/year
Intermediate event (IE)1	Tank over-pressurized (2.5×10^{-2})	1.428×10^{-1}
Intermediate event(IE) 2	Pressure relief system failure (1×10^{-4})	1×10^{-3}
Intermediate event (IE)3	Excess pressure in tank (8.76×10^{-9})	8.76×10^{-9}
Intermediate event(IE) 4	Failure of flare system (1×10^{-2})	9×10^{-2}
Intermediate event(IE) 5	Failure of refrigerating system (1×10^{-2})	1×10^{-4}
Intermediate event(IE) 6	HV 2703 fails closed (2.73×10^{-3})	2.73×10^{-3}
Intermediate event(IE) 7	Relief valve failure (2.74×10^{-3})	9.64×10^{-2}
Intermediate event(IE) 8	Isolation valves closed (0.01)	0.01
Intermediate event(IE) 9	Compressors fail to start (2.74×10^{-3})	2.74×10^{-3}
Intermediate event (IE)10	Pressurization of tank (1×10^{-4})	3.41×10^{-2}
Basic event (BE) 1	Failure of both SRVs (1.38×10^{-4})	1.38×10^{-4}
Basic event (BE) 2	Both isolation valves closed (1×10^{-4})	1×10^{-4}
Basic event (BE) 3	Isolation valves (V97-1,V97-2) closed (0.01)	0.01
Basic event (BE) 4	Pressure indicating failure/is closed(8.76×10^{-5})	8.76×10^{-5}
Basic event (BE) 5	External fire (5×10^{-3})	7.05×10^{-3}
Basic event (BE) 6	Warning system failure (5×10^{-3})	1×10^{-2}
Basic event (BE) 7	PS 2703 failure (9.64×10^{-4})	9.64×10^{-4}
Basic event (BE) 8	V 159 closed (0.01)	0.01
Basic event (BE) 9	V 438 closed (0.01)	0.01
Basic event (BE) 10	PS 2705 failure (9.64×10^{-4})	9.64×10^{-4}
Basic event (BE) 11	Power failure (2.74×10^{-3})	2.9×10^{-1}
Basic event (BE) 12	All compressors fail (1.98×10^{-5})	1.5×10^{-2}
Basic event (BE) 13	Control valve failure (2.74×10^{-3})	4.82×10^{-2}
Basic event (BE) 14	Air/power failure (2.74×10^{-3})	4×10^{-2}
Basic event (BE) 15	External factors (0.01)	0.1000002

2.3 Fault Tree Diagram

The fault tree diagram was first developed in 1961 at Bell laboratories to display the failure propagation of a system [9]. The fault tree analysis is a technique to explore the potential or actual causes of system or product failure. The fault tree analysis is a top–bottom analysis method where it starts with a cause until the consequence in a structured manner. It shows possible failure path that leads to the main critical event where all the events are connected through logic gates, which makes them easy to quantify. The fault tree diagram, with ammonia leakage as the top event, is drawn from the HAZOP study created from the available plant information, using SmartDraw (2018) software. The fault trees are usually positioned on the left side of the bow-tie diagram [10, 11]. The components and the subcomponents of the storage tank are identified, and failure causes as well as their failure frequency data are obtained from the plant. The identified basic events and the intermediate events with their description and failure frequencies are represented in Table 1.

2.4 Event Tree Diagram

An event tree is developed by taking continuous release of ammonia as the initiating event, and this initiating event with combination of several escalation factors may lead to several consequences such as vapour cloud explosion, pool jet fire, flash fire, and toxic gas dispersion. Event tree analysis is a forward logical modelling technique that explores responses through a single initiating event and lays a path for estimating the probabilities of outcome events. This technique is used to analyse the success and failure paths that the initiating events may lead to different consequences. This event tree analysis is generally carried out in a system during its early in the design stage to identify potential issues that may arise, rather than correcting the issues after they occur. The event tree diagram for the leakage of ammonia consisting of the safety barriers (escalation factors) with their occurrence probability values is shown in right side of the bow-tie diagram (Fig. 1).

2.5 Bow-Tie Diagram

The bow-tie model for the ammonia tank leakage is developed from fault tree and event tree diagrams, where the fault tree is placed over the left side of the bow-tie model and the event tree on the right side of the bow-tie model [12]. The resulting bow-tie diagram for the critical event of ammonia leakage which is obtained by combining their respective fault tree and event tree is shown in Fig. 1.

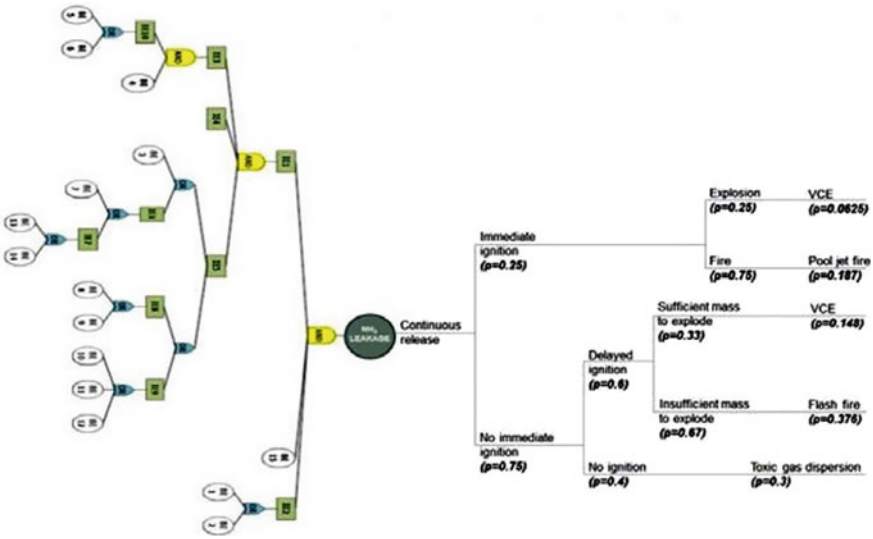

Fig. 1 Bow-tie model for ammonia storage tank leakage

2.6 Posterior (Updated) Failure Frequencies of Events

The posterior failure frequencies of the basic events are collected from practical data (incident reports) from the industry chosen. The new (updated) failure frequencies per year can be calculated by estimating storage tank components failure during the past entire working time of the ammonia storage tank. Since there were only some component failures, overtime the failure frequencies of some of the basic events are changed from the prior failure data. The fault tree and event tree are quantified again using the updated basic event failure probability in order to obtain the changed failure frequency of the critical event. The failure probability values of the critical event and the intermediate events based on the updated basic event failure probabilities are calculated, and updated values are shown in Table 1.

2.7 Bayesian Network for the Ammonia Storage Tank Failure

The Bayesian network is constructed by mapping the bow-tie model; the mapping procedure in Khakzad et al. [13] is adopted in this study. In the mapping algorithm, the basic events, intermediate events, and top event from the bow-tie model are taken as root nodes, intermediate nodes, and pivot nodes, respectively, within the Bayesian network.

The Bayesian network represents the connection between all the basic events (root nodes), the top event (pivot node), and the consequences through the arcs and

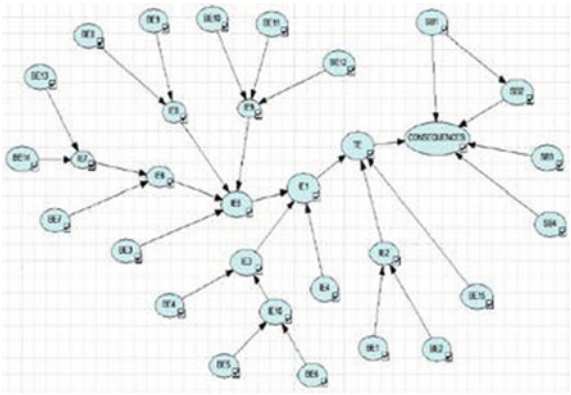

Fig. 2 Bayesian network

conditional probabilistic table [14]. The main advantage of using Bayesian network is its flexibility in updating the probability values of the variables. The prior probabilities of the variables are updated using Bayes' theorem to provide subsequent probabilities when new observations are made on the variables [15]. The Bayesian network of the ammonia tank leakage is developed using GeNIe software (version 2.3, Academic edition) and shown in Fig. 2. The Bayesian network is created from the bow-tie model, where all events from the bow-tie are converted into nodes and each node is linked logically through arcs. For each root node, the posterior failure probability values acquired from the practical data obtained from the industry are assigned, and for the other nodes, conditional probability tables are provided based on the logic gates(OR gate and AND gate).

The Bayesian network is shown in Fig. 2.

BE1–BE12 represents basic events from bow tie; IE1–IE10 represents intermediate events from bow tie; TE represents the top event (leakage of ammonia). SB1, SB2, SB3, SB4 represents barriers that could lead to different possible outcomes.

The Bayesian network can be studied through forward prediction and backward diagnosis analysis. The forward prediction technique in the Bayesian is used to estimate the occurrence probability of outcome events from the obtained probability values of the basic events and safety barriers. The estimation of the occurrence probability of outcome events can be performed easily by quantifying the bow-tie model. The occurrence frequency of end-state consequences obtained from the forward Bayesian technique and the bow-tie model is found to be similar.

3 Results and Discussions

The prior failure frequency of the ammonia leakage scenario is 2.5×10^{-5}/year. But when fault tree analysis was carried out using updated failure frequencies of

Table 2 Prior and the updated failure probability values of end-state consequences

Consequences	Prior failure frequency per year	Updated failure frequency per year
Toxic gas dispersion	2.25×10^{-7}	7.71×10^{-4}
Flash fire	3.83×10^{-7}	1.61×10^{-4}
Vapour cloud explosion	6.465×10^{-8}	3.67×10^{-5}
Pool/jet fire	8.76×10^{-8}	3.93×10^{-5}

components, the failure frequency of the top event became 1.428×10^{-4}, and therefore, there is a significant increase in the chance of top event occurrence compared to the initial probability. The event tree part of the bow-tie model is then quantified by taking the updated top event (initiating event) probability value to obtain the new failure frequencies of the end-state consequences, and the results from the prior failure data and the updated failure data of the end-state consequences are compared and tabulated in Table 2.

A Bayesian network is developed in which all the posterior failure frequencies of the basic events are assigned in the probability table of the root nodes. The Bayesian network is analysed through the forward prediction technique, and it was observed the occurrence frequency of end-state consequences obtained from the forward Bayesian technique (shown in Fig. 3) and the bow-tie model which are approximately the same.

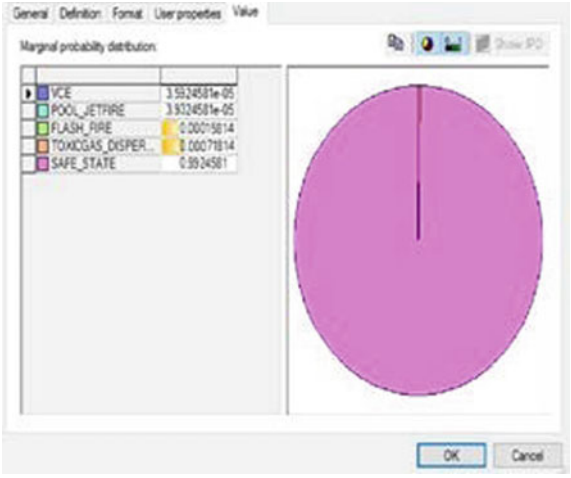

Fig. 3 Failure probability values of consequences

4 Conclusions

In this study, a quantitative risk analysis of an ammonia storage tank of a fertilizer industry located in Kerala is carried out using bow-tie model coupled with and Bayesian approaches. The following results are obtained from this study:

There is a significant chance of occurring the top event (leakage of ammonia) due to an increase in updated failure probabilities of the basic events when compared to prior failure probability data. Therefore, the top event probability should be reduced as low as reasonably practicable (ALARP).

The occurrence probability values of the end-state consequences obtained through quantifying the bow-tie model and the probability values obtained through the Bayesian network (forward prediction technique) are in conformity and can be used for validation purposes.

By analysing updated occurrence probability values of the end-state consequences, it is found that once the leakage of ammonia (TE) occurs, there is a greater chance of occurrence of flash fire and toxic gas dispersion. The study results can help experts to develop further measures to mitigate such potential accident scenarios and to decide where to take corrective measures to support in the risk managing process.

The current work is limited to a single ammonia tank of capacity of 500 tonnes and can be extended to the storage farm of the selected chemical industry.

References

1. Khakzad N, Khan F, Amyotte P (2011) Safety analysis in process facilities: comparison of fault tree and Bayesian network approaches. Reliab Eng Syst Saf 96(8):925–932
2. Abimbola M, Khan F, Khakzad N (2014) Dynamic safety risk analysis of offshore drilling . J Loss Prev Process Indust 30(1):74–85
3. Berdouzi F, Villemur C, Olivier-Maget N, Gabas N (2018) Dynamic simulation for risk analysis: application to an exothermic reaction. Process Saf Environ Prot 113:149–163
4. Trucco P, Cagno E, Ruggeri F, Grande O (2008) A Bayesian belief network modelling of organisational factors in risk analysis: a case study in maritime transportation. Reliab Eng Syst Saf 93(6):845–856
5. Norazahar N, Khan F, Veitch B, MacKinnon S (2018) Dynamic risk assessment of escape and evacuation on offshore installations in a harsh environment. Appl Ocean Res 79:1–6
6. Boudali H, Dugan JB (2005) A discrete-time Bayesian network reliability modeling and analysis framework. Reliab Eng Syst Saf 87(3):337–349
7. Liu M, Hommersom A, van der Heijden M, Lucas PJF (2017) Hybrid time Bayesian networks. Int J Approximate Reason 80:460–474
8. Shan X, Liu K, Sun PL (2017) Risk analysis on leakage failure of natural gas pipelines by fuzzy Bayesian network with a Bow-Tie Model. Sci. Program
9. Ericson C (1999) Fault tree analysis—a history Clifton A. Ericson II The Boeing Company; Seattle, Washington, pp 1–9
10. Markowski AS, Mannan MS, Bigoszewska A (2009) Fuzzy logic for process safety analysis. J. Loss Prev Process Ind 22:695–702
11. Jacinto C, Silva C (2010) A semi-quantitative assessment of occupational risks using bow-tie representation. Saf Sci 48(8):973–979

12. Shahriar A, Sadiq R, Tesfamariam S (2012) Risk analysis for oil & gas pipelines: a sustainability assessment approach using fuzzy based bow-tie analysis. J Loss Prev Process Ind 25(3):505–523
13. Khakzad N, Khan F, Amyotte P (2013) Dynamic safety analysis of process systems by mapping bow-tie into Bayesian network. Process Saf Environ Prot 91(1–2):46–53
14. Yuan Z, Khakzad N, Khan F, Amyotte P (2015) Risk analysis of dust explosion scenarios using bayesian networks. Risk Anal 35(2):278–291
15. Villa V, Paltrinieri N, Khan F, Cozzani V (2016) Towards dynamic risk analysis: a review of the risk assessment approach and its limitations in the chemical process industry. Safety Science

Risk Assessment Using Bow-Tie Tool in Cement Industry

R. Manikandan, P. Pradeep Kannan, T. Rajpradeesh, and S. Rajesh

Abstract In the cement industry, the employees are exposing by various health and safety issues during the manufacturing of cement products. The objective of this paper is to identify the existing hazards in workplace, and safety recommendations are given by using a bow-tie tool analysis. The bow-tie tool analysis is one of the safety tools, and it is used to provide the preventive measures for health and safety issues in the hazardous process of all industries. The cement has been made by using various processes like the selection of raw material, blending, pre-heater, kiln, and grinding, packing and shipping process. In the aforementioned processes, particularly during working with the kiln process, workers are exposed by different health hazards like dust, noise, vibration hazards, and it leads to many health problems like eye irritation, nose irritation, throat irritation, skin diseases, and upper respiratory problem. The silica exposure in the workplace leads to lung disorder and silicosis. So for the considerations of health and safety issues to employees, here the safety tool and technique is applied and the presence of hazards is reduced as expected level. This bow-tie safety tool is applicable to all the hazardous industries for assessing the risk level.

Keywords Hazard · Risk assessment · Ergonomics · Noise · Dust · Vibration

1 Introduction

Bow-tie tool analysis has become a public health priority in the industry [1]. The cement-producing process is one of these industries. Cement is mostly used to construct new or rebuilt the building. Because the cement is one of the strongest lifetimes for the buildings. Safety is important to the workers and environmental protection [2]. During the manufacturing process in the cement industry, various hazards have affected the workers especially dust particles, noise pollution, and

R. Manikandan (✉) · P. Pradeep Kannan · T. Rajpradeesh · S. Rajesh
Department of Mechanical Engineering, Kalasalingam Academy of Research and Education, Krishankoil, Tamil Nadu 626126, India
e-mail: r.manikandan@klu.ac.in; rmanikandan198@gmail.com

G. Kumaresan et al. (eds.), *Advances in Materials Research*, Springer Proceedings in Materials 5, https://doi.org/10.1007/978-981-15-8319-3_44

vibration are easily affected by the cement workers or people. It mainly affects the lung, stomach, etc., in the cement industry which is different types of products such as limestone, raw material, grinding, kiln, clinker packing [3].

In the cement industry process are commonly through the hazardous like dust particle, noise pollution, toxic gas, etc., They affected the workers' health, and they form some diseases in lungs, stomach, and cause eye irritation, etc. Cement industry is mainly hazardous because of confined space, falling or moving process, noise pollution, and vibration.

The objective of this work is to apply the bow-tie tool analysis to various manufacturing processes of cement, and the safety hazards are identified. And the recommended actions are given to avoid accidents.

2 Methodology

In the cement industry process are identified the various hazards and following through the recommendation due to the hazards (Fig. 1).

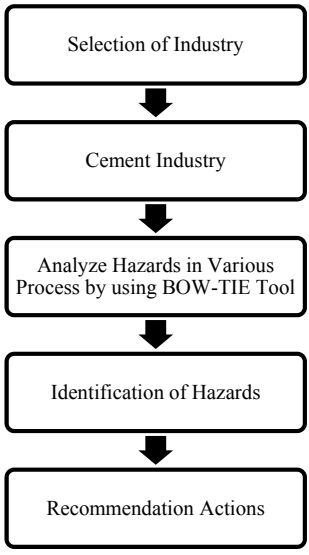

Fig. 1 Process involving in methodology

2.1 Process

This cement industry has various processes, involving the cement process, each and every process has the major or minor role of the cement industry, and the final result produces the cement (Fig. 2).

In the cement manufacturing process, the fine powder is added to the cement in the hydraulic compounds like silicate, aluminum, and alumina ferrites. Quite nasty raw materials of the area unit are divided into four basic classes: calcium, silicon, aluminum, and iron process. An area is the unit allowing the employed in the cement industry [4].

Cement industry produces the complicated method, starts with the crushing and raw material that like limestone rock and claimed clay, and to the fine powder also; it is like sand, crystalline mineral (quartz) or fine powder and fume known as raw material. These materials are heated with the high temperatures at 14,500–15,000 °C in cement microwave or micro-oven process [5]. During this one of the methods, the chemical bonds are the formation through the atom, ions, molecules, and ionic bonds are sharing through the electrons in covalent bonds of the raw material area unit [6]. They are decreased, and they have recombined the new method in the

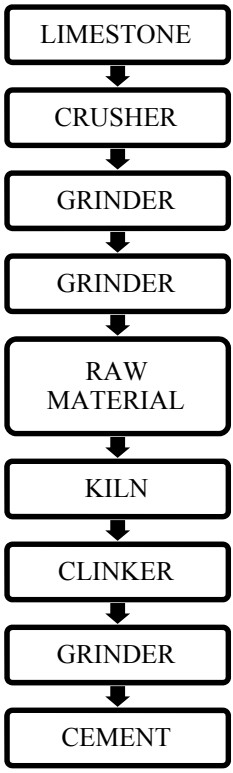

Fig. 2 Flowchart for the cement industry process

cement manufacturing process. This result is known as the clinker process that area unit rounded by the molecules between the 1000 and 2500 m across the area. The pulverized cement is mixed with the water, and the construction site is aggregated to create the best concrete that will employ [7].

2.2 Tool Description

Bow-Tie Tool
A bow-tie tool is a one of the safety tool, and diagram visualizes the risks in one step and easy to understand. The shape of a bow-tie tool analysis is creating clear difference between proactive (after the hazards are identified) and reactive (before hazards are identified) in risk management [8]. The power of the bow-tie tool analysis is an overview of hazard.

Bow-Tie Tool Process
The bow-tie tool is an analysis of the consequences of recovery barriers from the threat to the preventive barriers to hazard events.

Bow-tie tool analyzes the reviews of manufacturing the cement industry to the crusher, grinding, kiln process. In this process, maximum hazards have happened in the cement industry process.

Bow-tie tool analyses are to identify the hazards and risk management to the workers and preventive to the hazardous process. And it is used for the preventive of the hazard process through the workers during the working process.

Bow-tie tool analysis processes are shown in Fig. 3 and for preventive and proactive processes for hazard.

2.3 Hazard Identification

The main and major purposes of hazards are identified in the cement industry process. The hazard identification is the major step for one of the safety hazards, bow-tie tool analysis. The hazard identification process identifies all hazards in the cement industry process [9].

In the cement industry, hazards are classified into many types in the manufacturing process. They are,

Limestone quarrying process
Crushing plant process
Clinker process
Raw milling processes at the raw mill building
Filter process
Storage and transportation process

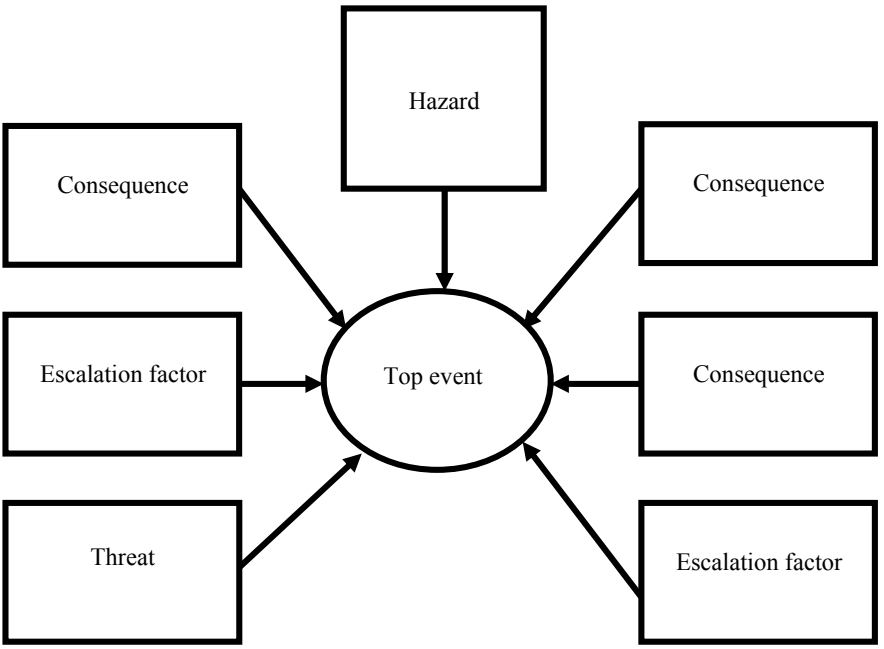

Fig. 3 Flowchart for bow-tie tool analysis process

Loading the vehicle
Fuel storage process for transport vehicle
Use of hazardous material process.

The cement manufacturing process identifies various hazards like dust particles, toxic gas, etc. [10]. From the cement industry, the main hazards identified from some cement manufacturing process [11] are shown in Table 1.

In the cement process, dust particles are filling the unit; it is one of the most effects of cement manufacture business all over the world and related to the handle and storage of raw material. The clinker process and material are introduced to the

Table 1 Hazards identification in the cement manufacturing process

Cement process	Hazard identifications
Limestone	A dust particle, vibration, and noise pollution
Raw material process	A dust particle, toxic gas like CO, CO_2, NO_X, SO_2, noise pollution, and heat pollution
Clinker burning process	A dust particle, toxic gas, high temperature, maximum workload for workers
Packing storage and delivery	A dust particle, overload vehicle, transfer the material

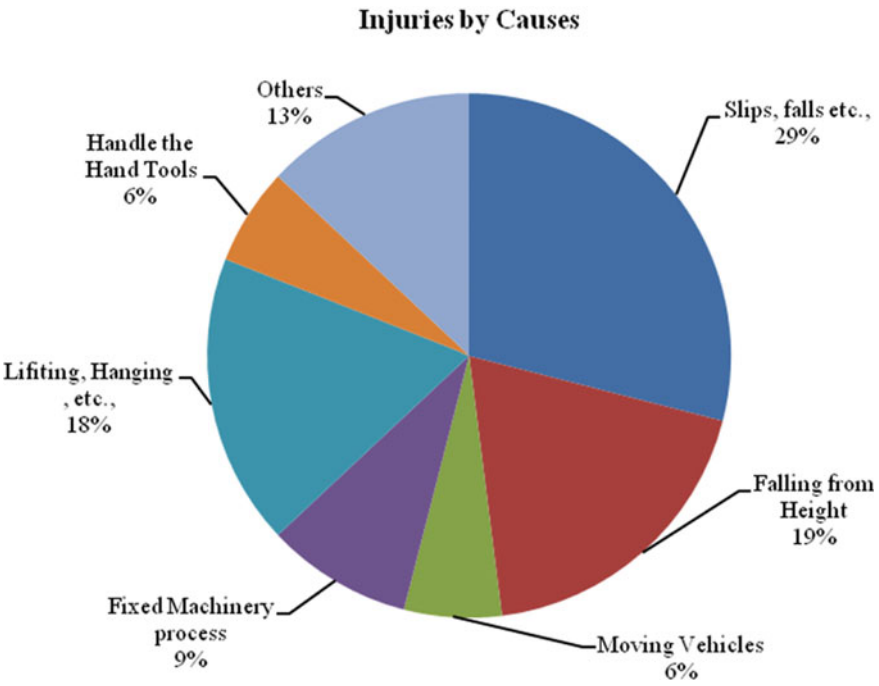

Fig. 4 Major injuries are affected in cement industry process

clinker process in limestone [12]. Packing within the most tried method for all cement industries [13] (Fig. 4).

3 Results and Discussions

3.1 Risk Score

Risk score and effects for the cement industry are shown in Table 2.

Table 2 Risk score for risk assessment in hazard's and effect's action

Risk score	Effect's
1–5	Low risk
6–10	Medium risk
11–15	High risk
16–20	Very high risk

3.2 Risk Assessment

In the cement manufacturing process, injuries and major risk assessment are identified, and recommended actions for hazards to preventive (before hazards) and reactive (after hazards) are shown in Table 3.

Table 3 Hazards for preventive action in the cement manufacturing plant

Hazards	Before	Preventive action	After
Slip, trips and falls	18	1. Tight workload 2. Fix the falling hazards 3. Use PPE (personal protective equipment)	3
Confined areas	17	1. Permission to work 2. Cleaning before the entry 3. Use the SCBA (self-containing breathing apparatus)	2
Electric process	16	1. Each panel must be labeled 2. Clean and neat 3. Use PPE for the working area	1
Falling/moving objects	18	1. Tight workload 2. Use PPE	2
Fire	17	1. Proper waste disposal 2. Use the heat detectors 3. Fire the extinguisher must be installed	2
Hot/cold surfaces	16	1. Usage PPE	2
Noise and vibration pollution	17	1. Technological of noise pollution 2. Wear ear protection 3. Use PPE	2
Vehicles	18	1. Must avoid overload 2. Must be back-up alarms for all vehicles in working conditions	2
Safeguards of machines	17	1. Use PPE 2. Maintain the conveyor belt	2
Manual handle process	18	1. Must be looked out the sharp edges, etc., 2. When lifting the overload objects, and then help the other workers 3. Use PPE	3
Dust	19	1. Usage of the automated package machines 2. Use the face mask 3. Use PPE	3
Cement dust	19	1. Usage of air, machine to avoid dust 2. Stay away from the automated packing machine 3. Use PPE	3

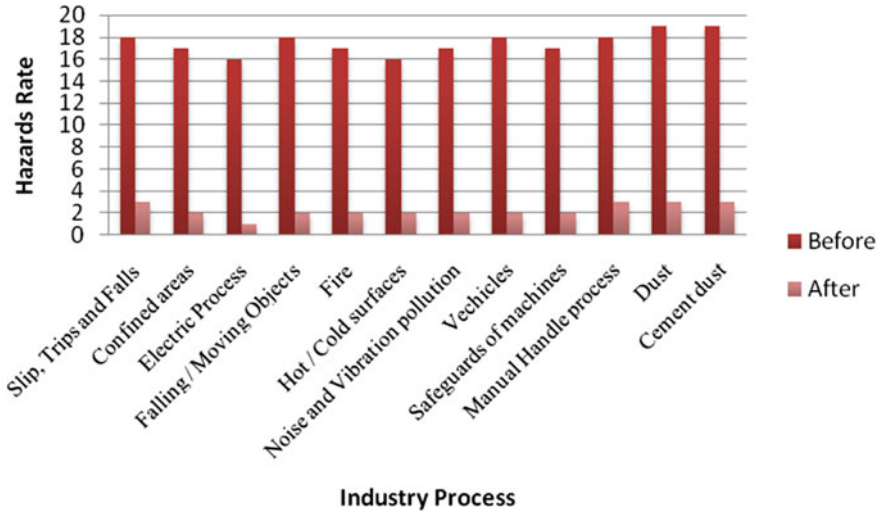

Fig. 5 Risk score for before and after hazards in cement industry

3.3 Graph

From this graph are identified the hazards in the cement industry process. And, the risk score for before and after the hazards is shown in Fig. 5.

4 Conclusions

The presence of hazards in the cement industry during the manufacturing of cement products is identified using the bow-tie tool analysis. The sources and effects of the existing hazards are recognized. The risk level is estimated using the nature of work, the probability of hazards and its effects. The risk level is categorized and as per the risk level, various safety recommendations are given to the working place inside the industry. This safety tool is suitable for any hazard-related process, and it is helpful to provide preventive measures for all the hazardous activity inside the working place.

References

1. Rachid C, Ion V, Irina C, Mohamed B (2015) Preserving and improving the safety and health at work: case of Hamma Bouziane cement plant (Algeria). Saf Sci 76:145–150
2. Zeb K, Ali Y, Khan MW (2019) Factors influencing environment and human health by cement industry: Pakistan a case in point. Manag Environ Qual Int J 30(4):751–767
3. Meo SA (2004) Health hazards of cement dust. Saudi Med J 25(9):1153–1159

4. Huntzinger DN, Eatmon TD (2009) A life-cycle assessment of Portland cement manufacturing: comparing the traditional process with alternative technologies. J Cleaner Prod 17(7):668–675
5. Zheng Y, Jensen AD, Windelin C, Jensen F (2012) Review of technologies for mercury removal from flue gas from cement production processes. Prog Energy Combust Sci 38(5):599–629
6. Worrell E, Price L, Martin N, Hendriks C, Meida LO (2001) Carbon dioxide emissions from the global cement industry. Ann Rev Energy Env 26(1):303–329
7. Karpiński B, Szkodo M (2015) Clay minerals–mineralogy and phenomenon of clay swelling in oil & gas industry. Adv Mater Sci 15(1):37–55
8. Mokhtari K, Ren J, Roberts C, Wang J (2011) Application of a generic bow-tie based risk analysis framework on risk management of sea ports and offshore terminals. J Hazard Mater 192(2):465–475
9. Kema Inc. (2005) Industrial case study: the cement industry. Report No. PGE0251.01
10. Bahino J, Yoboué V, Galy-Lacaux C, Adon M, Akpo A, Keita S, Gnamien S (2018) A pilot study of gaseous pollutants' measurement (NO_2, SO_2, NH_3, HNO_3 and O_3) in Abidjan, Côte d'Ivoire: contribution to an overview of gaseous pollution in African cities. Atmos Chem Phys 18(7):5173–5198
11. Marlowe I, Mansfield D (2004) 'Sub study 10: Environment. Health & Safety Performance Improvement', World Business Council for Sustainable Development
12. Tomar MK (2014) Study of occupational health, safety and environmental aspects in major cement manufacturing industry (Ultratech Cement Limited.). J Environ Earth Sci 4:117–120
13. WBCSD (World Business Council for Sustainable Development) (2004) Health and safety in the cement industry: examples of good practice. Cement Sustainability Initiative (CSI), Version 1.0.

A Novel Technique and Analysis for Efficient Opportunistic Routing in Mobile Ad Hoc Networks

K. P. Sampoornam, S. Hemavikasini, V. Vakula, and S. Vidhya

Abstract Wireless networks in terms of resources, forcefulness, and effectiveness are used for essential service applications. Many of the routing protocols of any cast pick complex and jammed midway nodes, resulting in frequent route failures and loss of packets. This paper is presented with a service-conscious routing scheme and mobility in wireless networks using three models: (1) stability in node movement, (2) channel blocking, and (3) route/link expiry time. Hence, to select the adjacent n-servers in route finding process, the above-mentioned three models are used. Based on low jamming, route/link expiry time, number of hops, and efficient constancy, a server is selected among n-servers. The results of the simulation show that proposed method demonstrates reduction in overhead control, route delay, and increased information delivery proportion compared to existing methods such as queue utilization, residual energy, and hub level.

Keywords Ad hoc · Routing · Round trip time · Energy consumption · QOS

1 Introduction

1.1 Wireless Networks

As the Wi-Fi network technology exploded, it has opened a brand-new view to users as it accelerated the data and application sharing with no trouble and unexpectedly [1]. Wireless networks use wireless generation without a pre-current infrastructure (get entry to points). As the name states, wireless networks consist of various mobile nodes, which can vary from notebooks, personal digital assistance (PDA) to any

K. P. Sampoornam (✉) · S. Hemavikasini · V. Vakula · S. Vidhya
Department of Electronics and Communication Engineering, Bannari Amman Institute of Technology, Sathyamangalam, Erode, Tamil Nadu 638401, India
e-mail: sampoornam@bitsathy.ac.in

G. Kumaresan et al. (eds.), *Advances in Materials Research*, Springer Proceedings in Materials 5, https://doi.org/10.1007/978-981-15-8319-3_45

electronic device that has the wireless RF transceiver and message managing functionality [2, 3]. Mobility and non-infrastructure form the idea of this community type

Mobility gives most freedom to customers, as they can be connected to the community, whether they are static or dynamic, until they are in the range of the community. Not like the constant networks or traditional wireless networks, wireless networks do not need any infrastructure to create and preserve communication among nodes. This belonging presents the capability to create a network unexpectedly and in pressing conditions right away, additionally without any greater cost [4, 5].

1.2 Structure of Ad hoc Networks

Any digital tool that has the Wi-Fi broadcast capability with right processing hardware can be part of a Wi-Fi networks. So, the nodes should have RF wireless transceivers as the community interface. However, for the reason that Wi-Fi transmission ranges according to broadcast sort of the antenna (omnidirectional, bidirectional), and the variations among transceivers at distinctive nodes affect the network shape of the wireless networks [6, 7].

At any given time, entities in the wireless networks are fixed without limitation, and they consist of portable hubs. Along these lines, their processing capacity is constrained. Likewise, control consumption of the versatile hubs is an unexpected factor on the architecture of the wireless networks [8, 9]. To make wireless networks pertinent and get greatest execution from them, consider these two aspects and structure any designs suitably. Remote networks are autonomous and decentralized systems. Through this way, the network can operate regardless of which nodes are connected or not connected with the system. Accessibility of centers just impacts the topology and coordinating of the framework, not the general tasks [10–12]. Since, wireless networks does not have any centralization; tasks are completed by circulation, so every center must have sufficient information about the framework and need to work independently [13, 14].

2 Research Methodology

2.1 Research Methodology

In previous work, the cross-layer and reliable opportunistic routing algorithm (CBRT) for MANETs is used. In CBRT, the contributions of the fuzzy logic system are the relative fluctuation (RF) measurements instead of the measurement values, which can diminish the quantity of fuzzy principles drastically. Besides, the quantity of fuzzy standards does not increment when the quantity of data sources increments. The hubs

are partitioned into various classes dependent on the quantities of hubs in their CRS. The hubs change their broadcast control dependent on respective classifications that they are associated with. The source hub decides the needs of the transfer hubs in CRS dependent on the services of these hubs. A hand-off hub which the utility is enormous has large handing-off need. In opportunistic routing, the large number of hubs in CRS, the large bundle conveyance proportion between the hub (sender) and the CRS is; the different way. Regardless, on account of the compactness of the center points in MANETs, the number of neighbors changes once in a while, so the bundle transport extent between the hub (sender) and the CRS changes as regularly as could be expected under the circumstances [1, 15, 16].

Drawbacks

- It experiences too many route breaks and route rediscovery methodology because of the event of communication hazy area.
- The additional calculation for connect security factor causes higher delay.
- The route recreation is decreased distinctly up to half (50%).
- Here, the information and encoding parcels has higher bundle overhead.
- Due to absence of connection limit assets, flows that could have been directed crosswise over adequately strong routes cannot be suited and are blocked.

2.2 Proposed System

The proposed work system uses Dynamic Source Routing (DSR) as essential path discovering convention alongside steadiness and QoS models. The commitments when contrasted with existing system are as per the following. (1) Manipulate a numerical model for choosing steady hubs (concerning position) in view of hub's own soundness, i.e., stability, and neighbor hubs security. (2) Manipulate a numerical method for choosing non blocked hubs dependent on channel burden and hub barrier occupancy. (3) Manipulate a numerical method for discovering join finishing time among pair of hubs. The effort made here proposes a directing convention that partitions the Spatial Wireless Ad Hoc systems (SWAH) into spine and non-spine systems to execute static routing and dynamic routing, separately. Creators demonstrate a security upgrade to DSR convention against wormhole assaults in ad hoc systems for multirate broadcasts which depend on count of round excursion time. It utilizes the handling as well as lining deferrals of taking an interest hub in the count of RTTs among neighbors. Along these lines it is needed to build up powerful and proficient development soundness and Quality of service-based conjunction conscious anycast directing plan in wireless networks. The three noteworthy structure models are proposed to deal with anycast routing disclosure issue. (1) Constancy model to distinguish steady hubs, (2) blockage system to consider over QoS by examining clog mindful constraints like channel burden, and buffer occupancy and (3) connect finishing period model to ensure the connection term will drop inside a satisfactory range. The architectural design of the proposed system is shown in Fig. 1.

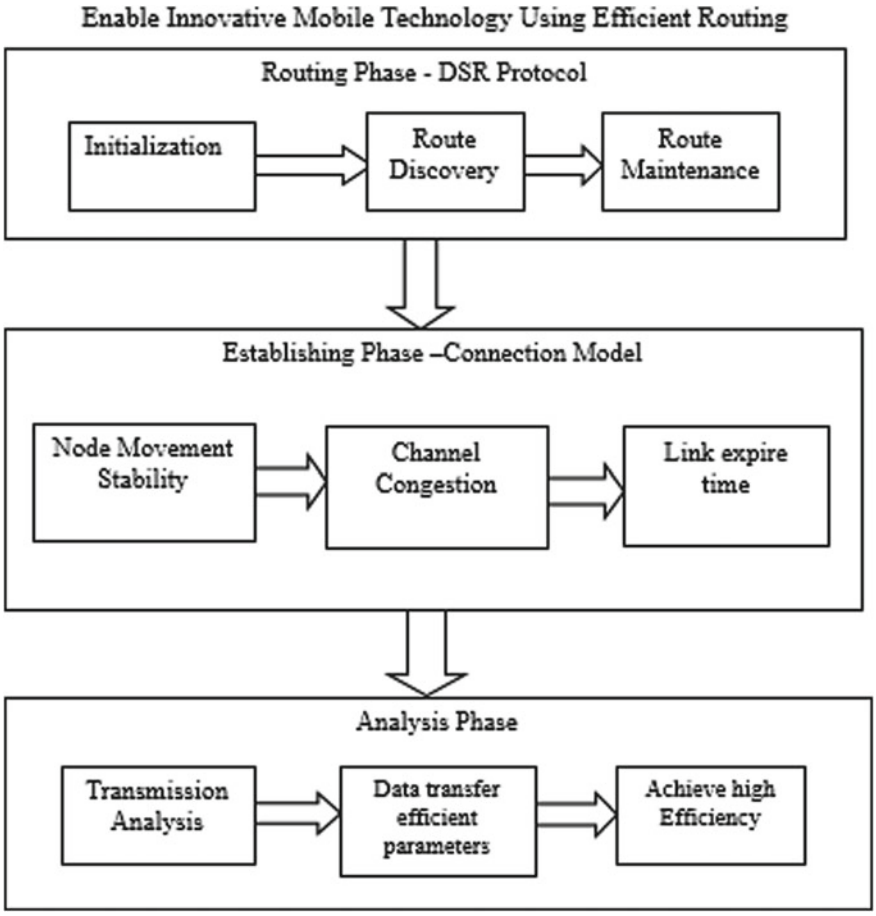

Fig. 1 Architecture design

3 Methodologies

Hub Initialization

This module is used to introduce the center point in network topology. The system topology and geography for the network animator window (nam window) is utilized. The language structure is made for new center points in network animator window. At that point, the hub is made in two kinds like irregular and fixed movements. Dynamic source routing (DSR) is an on-demand responsive routing protocol intended to limit data transfer capacity devoured by control parcels, by disposing of the occasional table top update information necessary in the table-driven proactive methodology. It makes use of source routing as opposed to depending on the routing table at each moderate hub. DSR is beaconless and subsequently does not need intermittent 'hi'

parcel broadcasts. Path development stage builds up a path by overflowing route request (RR) parcels in the system.

Hub Stability

The steady hubs are fundamental in sending gathering to give better parcel delivery administrations. Two measurements are distinguished for hub development steadiness in network: self-dependability and neighbor hubs strength. The means in identifying the security of the hub is given as the following. (1) Entire hubs in MANET locate oneself—development dependability, i.e., hub development with respect to its past position, and (2) discover neighbor hub development security of the considerable number of hubs in MANET by thinking about the neighbor's self-strength.

$$d_i^t = \sqrt{(x_n - x_r)^2 + (y_n - y_r)^2} \tag{1}$$

Congestion Scheduling Model

To demonstrate the blockage issue in MANET, following two models are developed: channel load model and buffer occupancy mode.

Channel Load Model

Overcrowding in a framework is estimated dependent on pace of progress in channel load (CL). It can be spoken where T active and T inactive are active and inactive events of the channel. If channel weight assembles, blockage in the system rises. Consequently, variation in pace of channel burden in a specific time window shows modification in flooding level.

$$\mathrm{CL} = T_{\text{active}}/(T_{\text{active}} + T_{\text{inactive}}) \tag{2}$$

Link Buffer Occupancy (LBO) Model

A hub ought to keep up a normal buffer level to maintain a strategic distance from congestion and continuous connection disappointments. LBO is characterized as the proportion of queue occupancy (QOCC) by a connect to greatest queue size (QSIZE) of the buffer in a certain time window at middle hub.

$$\mathrm{LBO} = \frac{\mathrm{QOCC}}{\mathrm{QSIZE}} \tag{3}$$

Link/Route Scheduling

The link expiration time (LET) model is proposed toward diminishing the information parcels misfortune because of connection disappointments. LET characterizes the lifetime of a connection between transitional hubs. In prevailing protocols, a versatile hub continues to utilize the path until the connections are disconnected. Here, to utilize a proactive strategy for discovering a period of time that adjacent neighbors

stay associated if the speed, bearing, and radio broadcast extent are recognized. Anticipating the LET along every hop on the path will encourage the forecast of route expiration time (RET). The lifetime is characterized as RET for path among customer and server.

3.1 Procedure for Proposed Scheme

Steps for the proposed plan are as per the following.

- Generate specially appointed system with given quantity of hubs.
- Evaluate the neighbor steadiness dependent on self-hub development security and neighbor hub development steadiness.
- Compute interface blockage factor dependent on channel overcrowding and buffer blockage factors. Calculate LET.
- Inform connect information at every hub thinking about their neighbors.
- Establish route discovery process utilizing route request, route reply, and route error and appropriately update RIC.
- Initiate the path(s) between customer to servers and transmit the information parcels.
- Calculate execution constraints of the framework.

4 Results and Discussion

The plans for n-anycast servers are associated with thin and thick method. For thin and thick specialist co-ops, it is seen that the control overhead is decreased plan. For the thin case, the assess of control overhead by shifting the n esteems from 1 to 10, whereas the assess overhead for the thick event by changing n esteems from 11 to 50. The impact of PDR is considered by changing the quantity of hubs, versatility of the hubs, and number of customers. The adaptability in the framework is tried by discovering the PDR with increment in number of hubs from 50 to 250 with static portability of the hub as 5 m/s. From examination outcomes, it is seen the PDR increments reliably with increment in number of hubs also increment in number of servers from 10 to 15. This makes PDR is essentially superior to flooding and DSR. PDR increments as number of server's increment since customer can get associated with some other server even when the associated server has versatility. Comparing PDR and DSR with flooding, there is a noteworthy contrast when the movement rises. If the speed of the hub increments, new route finding is done in PDR for overflowing, whereas DSR causes loss of parcels. Though MQAR plot modifies the transmission way dependent on three models such as stability, congestion, and route expiry models, allows the bundles to move to most extreme degree at whatever point either hub/interface fizzles or hubs move out of coverage. Thus, has larger PDR than different plans. End-to-end delay for differing portability of hubs and number of

hubs is portrayed. If portability speed of the hubs increments, end-to-end delay also increments. This postponement is larger in flooding and DSR as analyzed.

4.1 Performance Analysis

The proposed work is simulated for various wireless network environments to validate its performance. From the simulation results given in Figs. 2, 3, 4, 5, 6, and 7, it is observed that the proposed scheme performs better than traditional flooding,

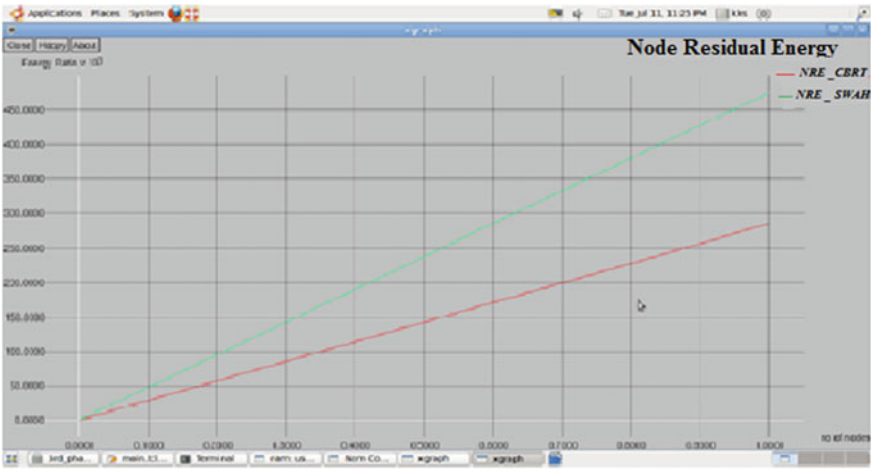

Fig. 2 Node residual energy

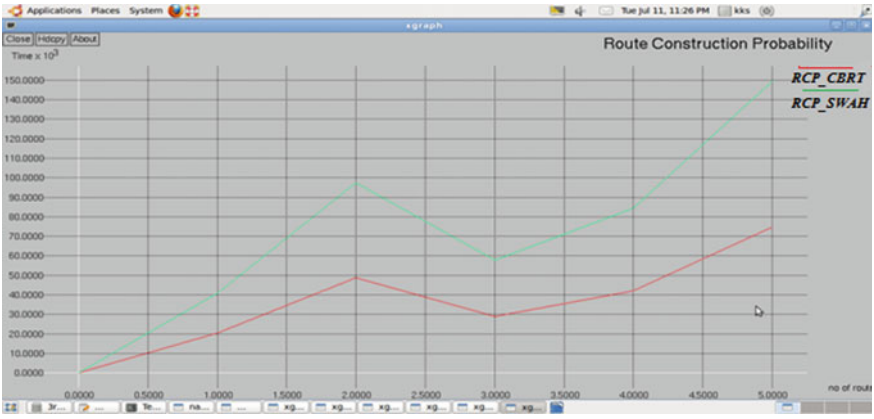

Fig. 3 Route construction probability

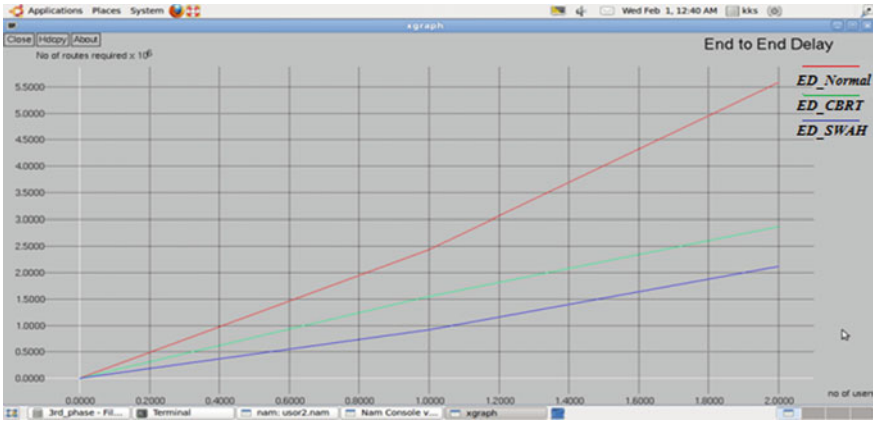

Fig. 4 End-to-end delay

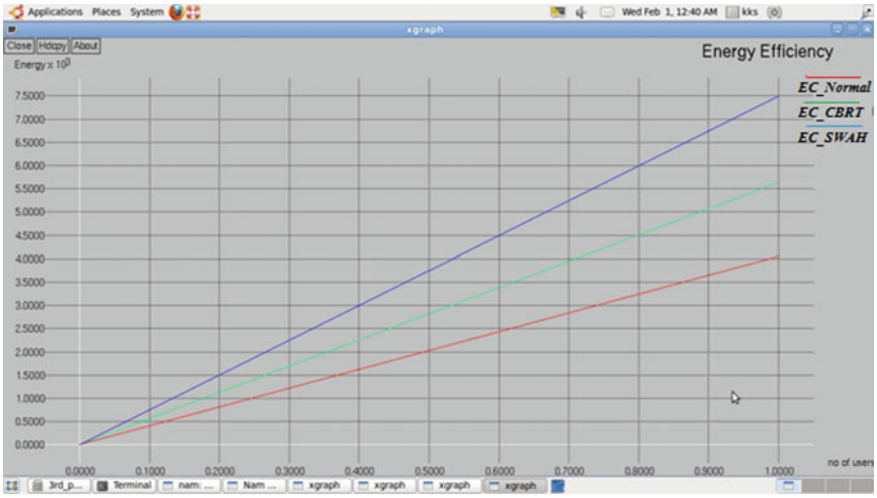

Fig. 5 Energy consumption

DSR, and DIASD scheme in terms of control overhead, packet delivery ratio, and end-to-end delay.

End-to-end delay or one-way delay (OWD) implies the time taken for a group to be transmitted over a framework from source to beneficiary. It is the typical term in IP framework checking, and shifts from round trip time (RTT) in that solitary route in the one bearing from source to receiver is evaluated. In proposed work, the end-to-end delay is diminished to the most extreme. The energy consumption in network varies depending on the protocols used and the number of nodes connected

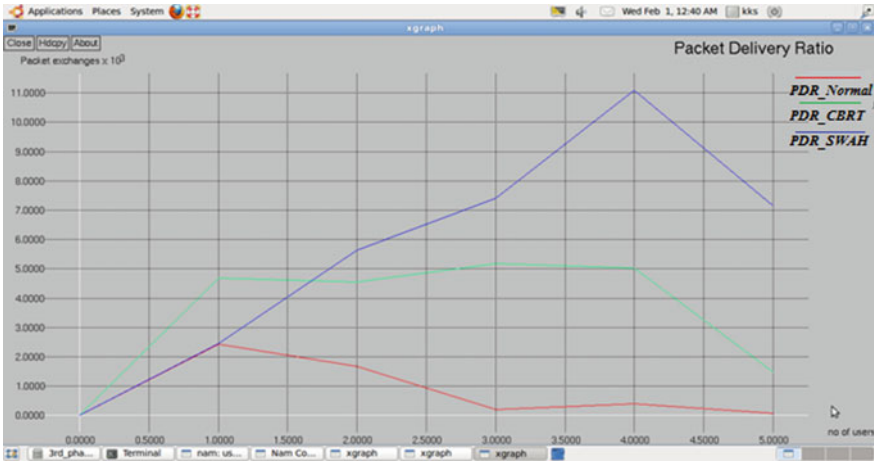

Fig. 6 Packet delivery ratio

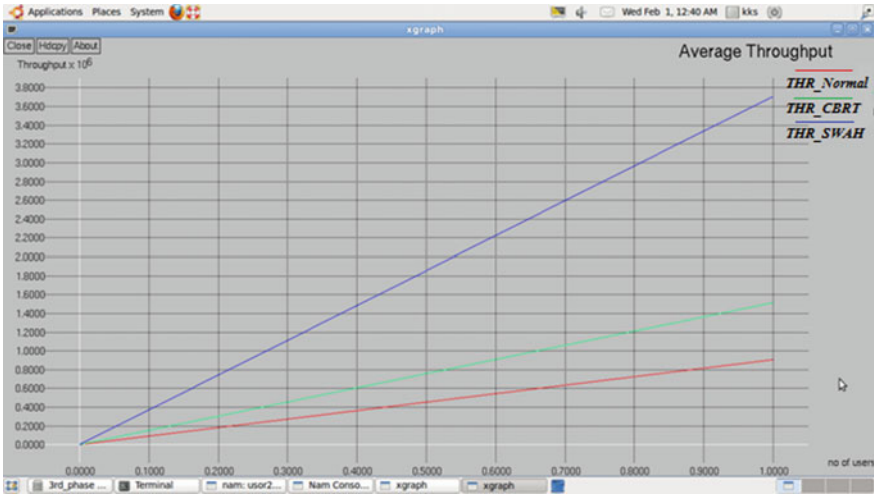

Fig. 7 Average throughput

to the network. Energy efficiency ratio is compared between normal, existing, and proposed work.

Packet delivery ratio is portrayed as the extent of data packages got by the goals to those made by the sources destinations to those created by the sources. Numerically, it tends to be characterized as: PDR $= S1 \div S2$ where $S1$ is the total of information parcels got by every destination and $S2$ is the total of information bundles created by each source. So, the packet delivery ratio is high for the proposed SWAH work. Average throughput is the total payload over the entire session divided by the total

time. Average throughput ratio is compared between normal, existing, and proposed work.

5 Conclusion

Hub's movement constancy, channel weight, hub clog level, and route expiry time are the significant QoS measurements between a few QoS constraints for giving a productive, less overhead QoS support for any cast routing in wireless networks. Here, the versatility and QoS based any cast directing in wireless networks is proposed. The proposed work is reproduced for different wireless networks conditions to approve its presentation. From the simulations, it is seen that the proposed plan performs superior to conventional flooding, DSR, and DIASD plot as far as control overhead, parcel conveyance proportion, and end-to-end delay.

The control overhead of our plan MQAR is decreased contrasted with conventional flooding, DSR, and DIASD plans. MQAR utilizes the ways which fulfill the hub soundness, QoS, and blockage levels and RET; henceforth, breakage of ways for hubs is less. The chose way to a server will be robust and remain for a more extended term without information misfortune. At the point when the quantity of customer's increment, control overhead of three methodologies increment. MQAR performs better contrasted with different plans since it utilizes the sending control component through just steady and non-clog hubs. Subsequently, the quantity of request/reply parcels utilized are decreased. This casing work accomplishes high security, more energy efficiency, high parcel conveyance proportion, less latency, contrasting with past edge works.

References

1. Molnar I (2018) CFS scheduler [Online]. Available: https://people.redhat.com/mingo/cfs-scheduler/sched-design-CFS.txt
2. Parekh AK, Gallager RG (1993) A generalized processor sharing approach to flow control in integrated services networks: the single-node case. IEEE/ACM Trans Netw 1(3):344–357
3. Duda KJ, Cheriton DR (1999) Borrowed-virtual-time (bvt) scheduling: supporting latency-sensitive threads in a general purpose scheduler. In: Proceedings of symposium operation system principles, pp 261–276
4. Johnson D, Hu Y, Maltz D (2007) The dynamic source routing protocol (DSR) for mobile ad hoc networks for IPv4. Internet Requests for Comments, RFC Editor, RFC 4728
5. Yang S, Kiat Yeo C, Sung Lee B (2012) Toward reliable data delivery for highly dynamic mobile ad hoc networks. IEEE Trans Mobile Comput 11(1)
6. Goyal P, Guo X, Vin HM (1996) A hierarchical cpu scheduler for multimedia operating systems. In: Proceedings of USENIX symposium operating system des implementation, pp 107–122
7. Chandra A, Adler M, Goyal P, Shenoy P (2000) Surplus fair scheduling: a proportional-share cpu scheduling algorithm for symmetric multiprocessors. In: Proceedings of USENIX symposium operating systems design implementation, 4 (1–4:14)

8. Baruah SK, Cohen NK, Plaxton CG, Varvel DA (1993) Proportionate progress: a notion of fairness in resource allocation. In: Proceedings of symposium theory computing, pp 345–354
9. Chlamtac I, Conti M, Liu J-N (2003) Mobile ad hoc networking: imperatives and challenges. Ad Hoc Netw 1(1):13–64
10. Wang S, Basalamah A, Min Kim S, Guo S, Tobe Y, He T (2015) Link-correlation-aware opportunistic routing n wireless networks in wireless communications. IEEE Trans 14(1):47–56
11. Broch J, Maltz DA, Johnson DB, Hu Y-C, Jetcheva J (1998) A performance comparison of multi-hop wireless ad hoc network routing protocols. Proc ACM MobiCom 32(3):85–97
12. Luo J, Hu J, Wu D, Li R (2015) Opportunistic routing algorithm for relay node selection in wireless sensor networks. IEEE Trans Indus Inf 11(1):112–121
13. Mauve M, Widmer A, Hartenstein H (2001) A survey on position-based routing in mobile ad hoc networks. IEEE Netw 15(6):30–39
14. Giordano S, Lu W (2001) Challenges in mobile ad hoc networking. IEEE Commun Mag 39(6):129–129
15. Marina MK, Das SR (2001) On-demand multipath distance vector routing in ad hoc networks. In: Proceedings of ninth international conference network protocols (ICNP), pp 14–23
16. Pogkas N, Karastergios GE, Antonopoulos CP, Koubias S, Papadopoulos G (2007) Architecture design and implementation of an ad-hoc network for disaster relief operations. IEEE Trans Industr Inf 3(1):63–72

Harvesting of Electricity from Handloom Weaving Machine Coupled with Dynamo

N. Bhuvanesh, G. Kumaresan, C. Subramaniyan, C. Sasikumar, and R. Mukeshu

Abstract A hand loom is a device used to weave cloth and tapestry. The basic purpose of any loom is to hold the warp threads under tension to facilitate the interweaving of the weft threads. Most of the handloom units run either as sole-proprietors or on partnership basis, and there is a lack among owners about professional outlook in the overall handing of their units. Handloom weaving machine can be coupled to a power generator/dynamo through mechanical linkages. The continuous oscillating motion of to-and-fro moving wood can be used to drive a dynamo, thereby producing electricity. It is an eco-friendly system of generating electricity, which does not harm our society and the environment. The main objective of the work is to couple dynamo to the handloom weaving machine and to produce power/electricity. The movement of to-and-fro moving wood makes the dynamo to rotate, which will be coupled to the handloom weaving machine with the help of mechanical linkages, and the power is transmitted to the dynamo. The power generated from the dynamo can be either stored in a battery or used as a direct power source. Physically challenged people easily operate this machine. Electricity of 60 W per hour of operation can be produced from the handloom weaving machine coupled with dynamo. The efficiency of the proposed machine can be improved by adjusting the gear ratio. The electricity generated depends on the rotation of the dynamo and thereby handloom weaving machine, and it does not cause any harmful effects to the society and to the person who is working on it. One working system of handloom weaving machine can produce minimum power of 60 W per hour of operation. If the proposed technology is used throughout the country in weaving industrial area, then crises of power need will be eradicated to a certain extent.

Keywords Handloom · Power · Dynamo

N. Bhuvanesh (✉) · G. Kumaresan · C. Subramaniyan · C. Sasikumar · R. Mukeshu
Department of Mechanical Engineering, Bannari Amman Institute of Technology, Sathyamangalam, Erode, Tamil Nadu 638401, India
e-mail: bhuvanindian@gmail.com

G. Kumaresan et al. (eds.), *Advances in Materials Research*, Springer Proceedings in Materials 5, https://doi.org/10.1007/978-981-15-8319-3_46

1 Introduction

A hand loom is a device used to weave cloth and tapestry. The basic purpose of any loom is to firmly hold the warp threads under tension to facilitate the interweaving of the weft threads. The hand loom industry has been developing over a period of time, and it is spread throughout the country. Many of handloom proprietors are not aware of the modern technique of coupling dynamo with the handloom. Handloom weaving machine can be coupled to a power generator/dynamo through mechanical linkages. The continuous oscillating motion of to-and-fro moving wood can be used to drive a dynamo, thereby producing electricity. It is an eco-friendly system of generating electricity, which does not harm our society and the environment. The handloom-made products not only emphasize the artistry of the weavers but also the rich look and diversity of the Indian culture. Tamilnadu occupies the place of pride in having the large numbers of handlooms in the country. Handloom weaving is one of the largest economic activities in Tamilnadu. Number of handlooms in Tamilnadu is about 154,509, and number of handloom weavers is about 352,321. All over India, in rural areas, there are about 20.66 lakh looms, and in urban areas there are about 3.11 lakh looms. The number of people engaged in allied activities and allied is around 43.31 lakh people [1, 2]. On an average, number of days worked per weaver per annum is 234 days. In India, 77% are women and 23% male weavers, out of 38.47 lakh adult weavers and allied workers. Among total population of weavers, 10% are scheduled caste weavers, 18% of the weavers are from scheduled tribes, 45% are from other backward classes, and 27% are from other caste. The handloom commodities with the premium India handloom trademark are differentiated from other brand of commodities in terms of quality [3, 4]. The manufactured goods quality is elevated because of appropriate texture and use of high-quality yarns, and threads is dyed with secure non-carcinogenic dyes which are free from banned amines and have good quality fastness property [5, 6].

2 Literature Review

In order to save the culture of handloom in India, we can adopt some change in techniques to those handloom machines to make the people to withhold the culture of handloom techniques [7]. Backer [8] Hazarika et al. (2015) enumerated the literature on technology adoption is huge, studies focused on implementation related issues concerning nonfarm, rural, and informal micro-entrepreneurs in rising economies are little and distant between. In many rural-areas, small-scale and medium-scale firms play important role in development of the country. Bhagavatula et al. [9] investigated the ability to identify opportunities and mobilize resources, by influence of social and human capital of entrepreneurs. Also, the power-generating technology has been included in co-operate to handloom machine to collaborate the modern technology with the traditional one [10, 11]. Chen et al. [12] found that greater advantages

are found in self-charging power textile (SCPT) based on harvesting of energy and storing of energy components for development of electronics that are wearable. A new SCPT has been developed with fabric tribo electric nanogenerator and a woven super capacitor (W-SC) for human motion energy harvesting and storing simultaneously [13, 14].

Goswami et al. [15] found that, in India, 65% of the total handloom households are from northeastern states. Modern techniques incorporate with our traditional machines that must be adopted to safeguard traditional weaving techniques due to less percent of the working looms utilized for commercial purposes, and the handloom weaving industry is overwhelmed with many manifold problems [16, 17].

3 Methodology

A dynamo is an electrical generator which produces direct current using a commutator. For delivering power to industries, dynamos were used as first electrical generators. The disadvantage of a dynamo is its mechanical commutator. This prototype of handloom is coupled to the dynamo. Dynamo works on the principle of Faraday's law. The handloom weaving machine is coupled to power generator/dynamo. The movement of to-and-fro moving wood makes the dynamo to rotate, which will be coupled to the handloom weaving machine with the help of mechanical linkages. The power generated from the dynamo can be either stored in a battery or used as a direct power source. Electricity of 60 W per hour of operation can be produced from the handloom weaving machine coupled with dynamo. The efficiency of the proposed machine can be improved by adjusting the gear ratio. The electricity generated depends on the rotation of the dynamo and thereby handloom weaving machine. One working system of handloom weaving machine can produce minimum power of 60 W per hour of operation. The coupling of dynamo increases the employment for youth generation. In a wooden vertical-shaft looms, heddles are fixed in place in the shaft. The to-and-fro motion of the weaving machine connected to the rotating shaft is again connected to the sprocket and the spur gear of the dynamo. The DC dynamo is connected to the rechargeable unit and the 6 V light. The light source is helpful for the working of the machine in night hours.

4 Results and Discussion

The design calculations of the proposed work handloom weaving machine coupled with dynamo are given below.

Let W_T represent permissible tangential tooth load in Newton

$$W_T = \frac{P}{V} * C_S$$

Rated power, P – 6 W

$$V = \frac{\pi DN}{60}$$

Diameter = 0.05 m, number of revolutions per unit = 65 rpm, and service factor is taken as 1

$$W_{\mathrm{T}} = \frac{6 \times 60}{\pi \times 5 \times 10^{-2} \times 65}$$

$$W_{\mathrm{T}} = \frac{6}{0.170}$$

$$W_{\mathrm{T}} = 35.29\,\mathrm{N}$$

On applying Lewis equation:
Let W_{T} be tangential load

$$W_{\mathrm{T}} = \sigma_0 \times c_v \times b \times \pi \times y' \times m$$

$$\sigma_0 = \text{allowable static loads}$$

$$\sigma_0 = 140\,\mathrm{N/mm^2}$$

b = face width of spur gear.
b = 12.5 mm.
c_{v} = deformation by using Buckingham theorem.
c_{v} = 80.
t_{E} = equivalent teeth

$$t_{\mathrm{E}} = \frac{t_{\mathrm{s}}}{\cos^3\alpha}$$

$$t_{\mathrm{E}} = 30$$

$$y' = 0.154 - \frac{0.192}{t_{\mathrm{E}}}$$

$$y' = 0.154 - 0.0304$$

$$= 0.1236$$

c_{v} = coefficient of velocity factor

$$c_{\mathrm{v}} = \frac{6}{6+v}$$

$$c_{\mathrm{v}} = 0.97244$$

$$W_T = \sigma_0 \times c_v \times b \times \pi \times y' \times m$$

$$W_{\mathrm{T}} = 140 \times 0.97244 \times 12.5 \times 10^3 \times 3.14 \times 8$$

$$W_{\mathrm{T}} = 42.748\mathrm{N}$$

Let W_{D} be dynamic Load.

$$W_{\mathrm{D}} = W_{\mathrm{T}} + W_{\mathrm{I}}$$

$$W_{\mathrm{I}} = \frac{2lv(b.c \pm W_{\mathrm{T}})}{2lv\sqrt{b.c + W_{\mathrm{T}}}}$$

$$W_{\mathrm{D}} = 42.748 + \frac{3.57(43.748)}{3.57(20.916)}$$

$$W_{\mathrm{D}} = 42.748 + 2.0916$$

$$W_{\mathrm{D}} = 44.8396\mathrm{N}$$

Tooth form factor:

$$y_{\mathrm{p}} = 0.175{-}0.0021$$

$$y_{\mathrm{p}} = 0.1582\,\mathrm{m}$$

Static tooth load or endurance strength of the tool:

$$W_{\mathrm{s}} = \sigma_e \times y_p \times b \times \pi \times b \times m$$

$$\sigma_{\mathrm{e}} = 84$$

$$W_{\mathrm{s}} = 84 \times 12.5 \times \pi \times 8 \times 0.1582$$

$$W_{\mathrm{s}} = 4174.7996\ \mathrm{N}$$

Ratio factor:
Let w_w be maximum or limiting load for wear:-

$$w_w = D_P \times b \times Q \times k$$

$$k = 1.4$$

$$Q = \frac{2 \times V.R}{V.R + 1}$$

$$Q = \frac{2 \times 2.5}{3.5}$$

$$Q = 1.428$$

$$w_w = 2 \times 12.5 \times 1.428 \times 1.4$$

$$w_w = 49.98\,\text{N}$$

Therefore, the wear load is not less than the dynamic load. Hence, the proposed gear system can withstand the forces and transfer the rated power. Figure 1 shows the

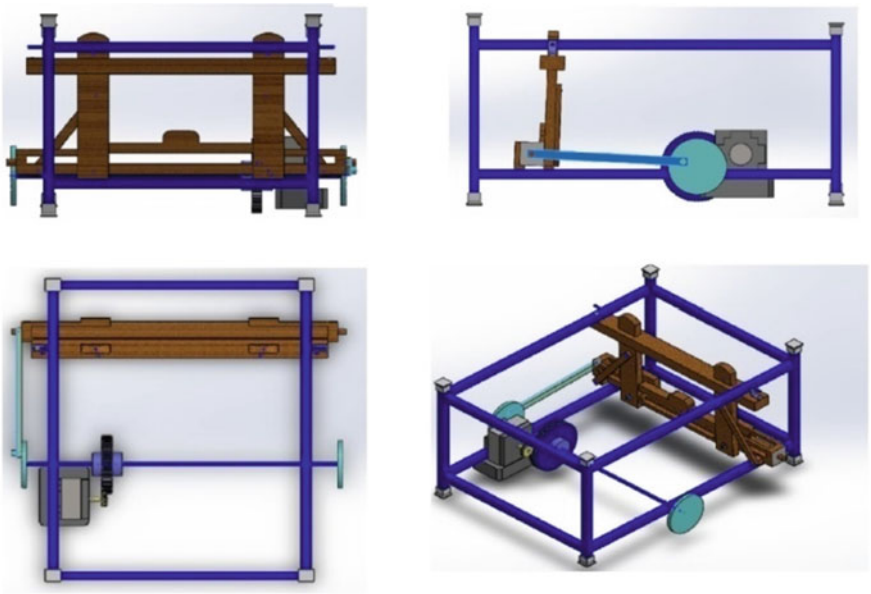

Fig. 1 Developed handloom weaving machine coupled with dynamo

developed handloom weaving machine coupled with dynamo to generate electricity, thereby storing it in a battery or it can be connected to a grid directly.

5 Conclusion

The handloom weaving machine is coupled to a power generator/dynamo. The movement of to-and-fro moving wood makes the dynamo to rotate, coupled to the machine with the help of mechanical linkages, and power is transmitted to gear arrangement system. This makes the dynamo to produce electricity. The power generated from the dynamo can be either stored in a battery or can be directly connected to the grid or can be used as a direct power source. The efficiency of the developed machine can be improved by adjusting the gear ratio. The vibration of handloom leads to the power generation. The rotating shaft connected to the moving wood is the main reason for the power generation. The rotating shaft coupled with the dynamo produces power supply of about 6 V in the showcased prototype. The power storage level is also good and considerable. This operates only on the hands, so that the physically challenged people can use the handloom. Developed handloom weaving machine coupled with dynamo is an eco-friendly system of generating electricity, which does not harm our society and the environment. The generated electricity can be used to power the room where the handloom is installed, it can be either stored in a battery or can be directly connected to the grid to satisfy the domestic power needs. Handloom weaving activity plays an active role in the growth process of the state as well as the nation.

References

1. Baeber EJW (1991) Prehistoric textiles. Princeton University Press. ISBN 0-691-00224-x
2. Collier AM (1970) A handbook of textiles. Pergamen Press, 258. ISBN 0-08-018057-4
3. Collier AM (1974) A handbook of perrgamon Press, p 258. ISBN 0-08-018057-4
4. Burnham DK (1980) Warp and weft a textile terminology royal Ontario museum 0-08-01-018057-4
5. Guest R (1823) The compendious history of cotton—manufacture. Retrieved 2009-02-15
6. Geoffrey T (1993) The last shift: the decline of handloom weaving in nineteenth-century Lancashire Manchester University Press ND, ISDN 0-7190-3725-5
7. Dooley WH (1914) Textiles (Project Gutenber ed.). D.C Heath and Co, Boston, retrieved 30 October 2011
8. Backer P (2005) Technology in the middle ages, history of technology, technology and civilization (tech 198). San Jose State University, USA
9. Bhagavatula S, Elfring T, van Tilburg A, van de Bunt GG (2008) J Bus Venturing 25 (2010):245–260
10. McEwam GF (2006) The incas: new perspective. W.W Norton & Co., New York, p 167; Cartwright, Mark, "Inca Textiles", ancient history encyclopaedia
11. Freethy R (2005) Memories of the Lancashire cotton mills countryside book aspects of local history. Newbury, Berkshire (978-1-84674-104-3)

12. Chen J, Guo H, Pu X, Wang X, Xi Y, Hu C (2018) Traditional weaving craftfor one-piece self-charging power textile for wearable electronics
13. Bell LS (2000) Of silk women, and capital: peasant women's labour in chinese and other third world capitalism. J Women's History 11(4):83
14. Guest R (1823) A compendious history of the cotton-manufacture. Manchester: Author, Printed by Joseph Pratt, Chapel Walks. Retrieved 2011-11-23
15. Goswami K, Hazarika B, Handique K (2017) Asia Pac Manag Rev 22:168–175
16. Crow Foot G (1936–1937) Of the wrap weighted loom. Ann Br Schools Athens 37:36–47
17. Belley R (2005) Chasing the sixpence: the lives of Bradford mill folk, ayr: fort publishing Ltd. SBN 0-9547431-8-0

Removal of Rain Particles from the Single Captured Image

K. P. Sampoornam, S. Saranya, S. Vigneshwaran, J. Roshini Roy, and P. Santhya

Abstract The captured image often suffers from rain or snow due to bad weather. To remove the rain streaks, many methods and algorithm were proposed. However, in this paper, we proposed a novel idea in the restoration part. The first step is to apply filtering techniques on the image and then comes the restoration portion where the new approach is taken that is expectation-maximization algorithm. In this method, the parameter estimation of incomplete data is done by maximum likelihood method.

Keywords Image enhancement · Centroid · Filtering · Backfilling · Clustering

1 Introduction

Nowadays, the vision systems are widely used for various applications such as surveillance, machine vision, and navigation. Sometimes these systems collect data which are mainly affected by dynamic weather such as raindrops or snow. It affects the visual data which reduces the quality performance of the vision systems. Most of the early works are about removing raindrops or snow from the video. But the removal of those from the image is a complex process because the raindrops may have different pattern of streaks and different directions. The snow will be in different sizes. This

K. P. Sampoornam (✉) · S. Saranya · S. Vigneshwaran · J. Roshini Roy · P. Santhya
Department of Electronics and Communication Engineering, Bannari Amman Institute of Technology, Sathyamangalam, Erode, Tamil Nadu 638401, India
e-mail: sampoornam@bitsathy.ac.in

S. Saranya
e-mail: saranya.co19@bitsathy.ac.in

S. Vigneshwaran
e-mail: vigneshwaran.co19@bitsathy.ac.in

J. Roshini Roy
e-mail: roshiniroy.co19@bitsathy.ac.in

P. Santhya
e-mail: santhya.co19@bitsathy.ac.in

G. Kumaresan et al. (eds.), *Advances in Materials Research*, Springer Proceedings in Materials 5, https://doi.org/10.1007/978-981-15-8319-3_47

causes the image blur, and the quality of the image may be reduced. To address these type of problems, many proposed different algorithms for various applications.

In this paper, based on the previous methods and studies, the identification of the raindrops or snow in an image using Gaussian filer which gives the low-frequency components have been analyzed. Using that high-frequency component which contains the rain drops or snowflakes in the image can be obtained. And in the next step, for the obtained low-frequency components, the expectation–maximization algorithm which is used for the restoration process of the removed pixels is applied. This method uses their neighboring values for the restoration process. The neighbor pixel values are summed and averaged. Then, those values are assigned for the lost pixel. The detailed study of this method is explained in this paper which involves the removal of raindrops and snow and its effective restoration process. This method can be effectively used for the raindrops or snowflakes which are smaller in size where the loss of data is less.

2 Literature Review

The downpour/snow expulsion from a solitary shading picture is proposed in [1]. They illustrated a few normal qualities of rain and day off, which two measurements are defined, to be specific, the sensitivity of variance crosswise over color channels (SVCC) and the principal direction of an image patch (PDIP). They created a low-recurrence part utilizing guided filter, while the comparing high-recurrence part is made integral to the low-recurrence part. They separated picture subtleties from the high-recurrence part utilizing three-layer chain of command. Specifically, the first layer is a three-times classification that depends on a prepared word reference (over-complete), the subsequent layer applies another mix of downpour/snow identification and a guided filter, and the third layer uses the SVCC to improve the visual nature of the downpour/snow-evacuated picture.

In [2], the authors analyzed about the imaging system for visual effects of rain. They developed a correlation model to capture the dynamics of rain and a physics-based motion blur model that explains the photometry of rain. In order to remove haze from the single image, the authors in [3] combined dark channel prior with haze imaging model. For distant objects, the original scene is not recovered perfectly. Later, [4] developed geometric and photometric models to analyze the complex effects of rain [5] developed a method for recovering the needed parameter to separate the air light which is scattered by the haze particles toward the camera. Due to bad weather, the light falling on the camera can be completely scattered [5]. To overcome this, [6] presented a method to identify the depth discontinuities and to compute structure of a scene. Description of the splitting of visual system explains the results of a color-matching study in the Great Smoky Mountains National Park. The changes in the colorfulness of the object will affect the optical depth not the hues of objects seen through haze [7].

Kang et al. [8] proposed a solution for removing rain streaks by applying morphological component analysis for image decomposition. In [9], the authors proposed computer vision-based technique for detecting rain drop. They used Gaussian mixture model for separating foreground images from the background images [9]. Further, an algorithm for removing rain streaks of video captured with moving objects is developed [10]. An efficient research direction for effectively detecting outdoor environmental conditions is suggested in [11]. In [12], the authors analyzed about five types of road conditions such as "Dry," "Wet," "Slushy," "Icy," and "Snowy," by adopting image analysis technology.

Textural features can be computed quickly based on relative frequency distribution. This can be used as an additional input for detecting rain drops [13]. An effective algorithm along with classifier can be used to detect motion blur in a single image [14]. In moving objects, synopsis collision can be decreased by calculating time positions and coefficients which reduces the size of an object [15]. By using adaptive non-local means filter, major image details cannot be retrieved, and it does not remove all of the rain drops [16]. In [17], guided image filter is used with dictionary learning and sparse coding where complexity in coding resulted an inefficient removal of rain drops in an image.

3 Overview of Existing and Proposed Method

3.1 Existing Method

In the first step, the dynamic components of the original image can be found out by using windowing techniques. To decompose a rain/snow images into the low-frequency and high-frequency part by using the well-designed filters, the image is enhanced using guided filter. The balance between removing rain/snow components and preserving image's details is improved much in this result. The model-based processing can be applied on the high-frequency part to further extract the image details to be added back into the low-frequency part [1], while the low-frequency part can be made free of rain or snow as much as possible.

In the second step, to obtain the final rain/snow-removed image, the image details can be added back to the low-frequency part. It is difficult to accurately separate rain/snow with other non-rain/snow components by normal detection methods because the location of rain/snow components is random. Some are rain/snow components, and the others are non-rain/snow components. One of the excellent image decomposition method is dictionary learning, which can decompose an image into many components. For factorizing the high-frequency components, we use online dictionary learning method. The problem with a new online optimization algorithm that is based on stochastic approximation is factorized by this method.

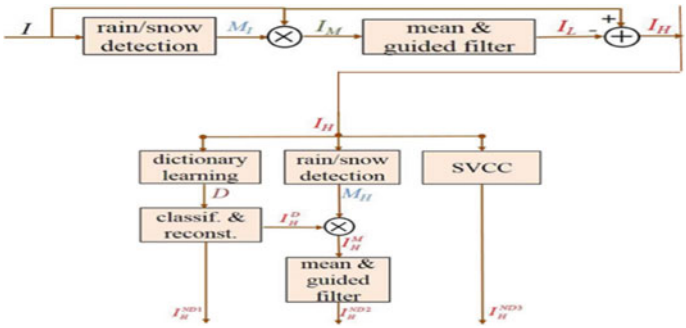

Fig. 1 Rain drop/snow removal using SVCC method

Here, word reference particles representing dynamic segments will have a littler aggregate of pixel shading channel difference. In this manner, the whole of pixel shading channel difference is determined for every lexicon iota.

From that point onward, non-dynamic parts that normally contain shading esteems that are very not quite the same as that of dynamic segments is separated. Be that as it may, non-dynamic parts whose hues are like unique segments would even now stay in the resultant picture.

At that point normal of total flat angle of the pixels, it is taken in these word reference particles in which the pixels with nonzero slope esteems are chosen. The molecules with an enormous mean of total flat slope speak to dynamic particle. At that point, the resultant picture is thresholded to recognize the dynamic parts viably. The principal direction of an image patch (PDIP) of dynamic particles is almost steady and has little fluctuation, and it is found. These three are included, and the powerful identification of downpour/snow is performed.

A minority of non-dynamic subtleties still exist in the past advance. So as to get more picture subtleties, dynamic parts is recognized in high-recurrence segments again by the blend of downpour/snow recognition and a guided filter and utilized the recently determined area guide to fill the gap. The downpour drop-expelled or snow-evacuated results are still somewhat obscured. So as to additionally improve the visual quality, sensitivity of variance of color channel (SVCC) guide of the high-recurrence part is determined and afterward use it to filter the high-recurrence part to get some non-dynamic segments. Finally, all non-dynamic segments are summarized to get the downpour/snow-evacuated picture as appeared in Fig. 1

3.2 Drawbacks of Existing Technology

- The existing work cannot effectively remove the rain drops in the image captured during heavy rain. The enhanced output cannot be expected in this work.
- The complexity in getting the exact output involves much time consuming one

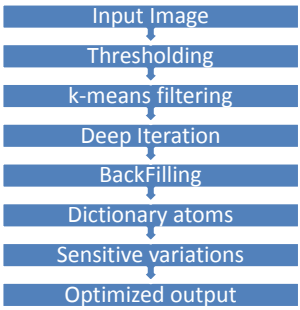

Fig. 2 Flowchart of proposed method

3.3 Proposed System

The image is processed by using threshold technique with appropriate values, which separates high-frequency rain components and low-frequency components that contain image details. Here, *k*-means clustering is used which is an iterative, data-partitioning algorithm that assigns several observations to exactly one of '*k*' clusters defined by centroids, where *k* is chosen before the algorithm starts. *k* value is chosen from 1 to 3 which is used for the iteration. *k* initial cluster centers (centroid) is chosen. Compute point-to-cluster-centroid distances of all observations to each centroid. This algorithm uses batch update which is assigned for each observation to the cluster with the closest centroid. The average of the observations in each cluster is computed to obtain *k* new centroid locations. Repeat steps until cluster assignments do not change, or the maximum number of iterations is reached.

Resulted output is then filtered using 2D order-statistic filtering where the clustered values are replaced by a single value. Then, it undergoes edge detection followed by masking with 5×5 window (most of the rain pixels lie within this window size). The masked image is filtered using Gaussian filter, the image is smoothened using neighboring pixels which blurs the rain drops. The smoothing is repeated for some iteration to get an appropriate result. Then, the morphological operations is applied to fill the gaps where blur pixels are reduced without any noise. This enhances the image quality. Finally, the point-spread function is converted to optical transfer function which is used to increase the pixel intensity. The design flow of this proposed method is shown in Fig. 2

4 Result and Discussion

The image in which the snow/rain streaks to be removed is captured by digital camera. The quality of the image is quite important for the operation to be successful. In the captured image, the coarse location of dynamic components are detected. The dynamic component consists of rain and snow components. From this location, binary

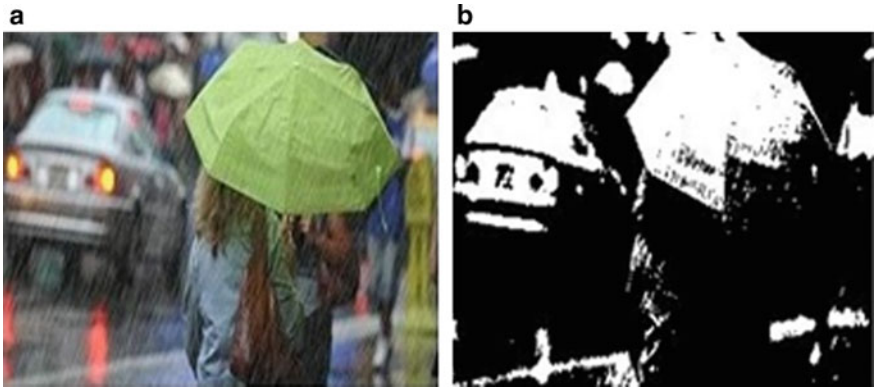

Fig. 3. **a** Input image. **b** Threshold image

location matrix is formed. The MATLAB software is used for implementing all the steps given in Fig. 2

The captured color image is in RGB format as shown in Fig. 3a. This should be converted into gray scale image for easy computation. In order to identify the noise in the image, the threshold is applied. The threshold value normally lies within 100–200 which is fixed by trial and error method. The resultant image is shown in Fig. 3b.

Next, *K*-means clustering algorithm is applied with *K* value which ranges from 1 to 3. The output obtained at this stage is shown in Fig. 4(a–c). The average of the observations in each cluster is calculated to obtain knew centroid locations.

Figure 5 shows the Sobel edge detected image which is used to split the image into layers. The more number of iteration results in finding the depth of the background pixels effectively. In order to remove the variation of noise that occurs in the process, the backfilling process is used. It is based on the discrete cosine transform. The resultant image is compressed to minimize the pixel values which are maximized during the process. Figure 6 shows the image after backfilling operation is completed. Finally, the gradient minimization is used to smoothen the resultant image. The replaced pixel boundaries are reshaped by this process. This will remove the variations in the backfilled pixels to the neighboring pixels which results the clear output image as shown in Fig. 7.

5 Conclusions

This paper proposes the mechanism to remove rain/snow from a single color image. Noise is detected by applying threshold and then by using *k*-means clustering (EM algorithm) followed by edge detection, the image details are restored. Back filling

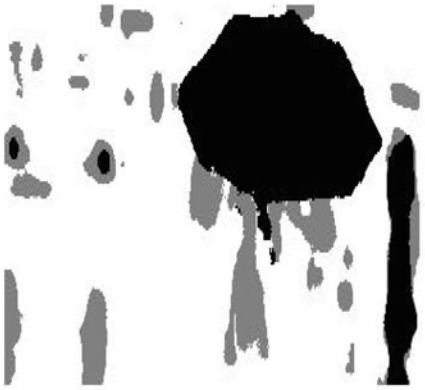

(a) Image 1

(b) Image 2

(c) Image 3

Fig. 4 Cluster images

Fig. 5 Edge detection

Fig. 6 Backfilling

Fig. 7 Output image

technique replaces the rain streaks pixels. This backfilled raindrop borders are identified by dictionary atoms. Further, the image quality is enhanced by smoothing process.

References

1. Wang Y, Liu S, Chen C, Zeng B (2017) A hierarchical approach for rain or snow removing in a single color image. IEEE Trans Image Process 26(8)
2. Garg K, Nayar SK (2004) Detection and removal of rain from videos. In: Proceedings of IEEE conference computer vision pattern recognition (CVPR),vol 2. Washington, pp 528–535
3. He K, Sun J, Tang X (2011) Single image haze removal using dark channel prior. IEEE Trans Pattern Anal Mach Intell 33(12):2341–2353
4. Garg K, Naya SK (2006) Photometric model for raindrops. Columbia University technical report
5. Shwartz S, Namer E, Schechner YY (2006) Blind haze separation Proc IEEE Conf. Comput Vis Pattern Recognit 2:1984–1991
6. Narasimhan SG, Nayar SK (2003) Contrast restoration of weather degraded images, IEEE Trans. Pattern Anal Mach Intell 25(6):713–724
7. Mahadev S, Henry RC (2000) Color perception through atmo-spheric haze. J Opt Soc Am A 17(5)
8. Kang L-W, Lin C-W, Fu Y-H (2012) Automatic single-image-based rain streaks removal via image decomposition. IEEE Trans Image Process 21(4):1742–1755

9. Bossu J, Hautière N, Tarel JP (2011) Rain or snow detection in image sequences through use of a histogram of orientation of streaks Int. J Comput Vis 93(3):348–367
10. Garg K, Nayar S (2006) Photorealistic rendering of rain streaks. ACM Trans Graph 25(3):996–1002
11. Shehata MS, Cai J, Badawy WM, Burr TW, Pervez MS, Johannesson RJ, Radmanesh A (2008) Video -based automatic incident detection for smart roads: the outdoor environmental challenges regarding false alarms. IEEE Trans Intell Transp Syst 9(2):349–360
12. Yamada M, Ueda K, Horiba I, Sugie N (2001) Discrimination of the road condition toward understanding of vehicle driving environments. IEEE Trans Intell Transp Syst 2(1):26–31
13. Haralick RM, Shanmugam K, Dinstein I (1973) Texture features for image classification. IEEE Trans Syst Man Cybern SMC-3(6): 610–621
14. Pang Y, Zhu H, Li X, Pan J (2016) Motion blur detection with an indicator function for surveillance machines. IEEE Trans Ind Electron 63(9):5592–5601
15. Li X, Wang Z, Lu X (2016) Surveillance video synopsis via scaling down objects. IEEE Trans Image Process 25(2):740–755
16. Kim JH, Lee C, Sim JY, Kim CS (2013) Single-image deraining using an adaptive nonlocal means filter. In: 20th IEEE international conference on image processing (ICIP), pp 914–917
17. Chen Chien D-Y, Li CC, Kang LW (2014) Visual depth guided color image rain streaks removal using sparse coding. IEEE Trans Circ Syst Video Technol 24(8): 1430–1455

Effects of Chemical Curing on the Mechanical Properties of Mineral Admixtures Blended Concrete

V. Kannan and N. Karthiga Shenbagam

Abstract In this paper study the experimental investigation of partial replacement of fly ash, lime, metakaolin by the weight of cement. It can increase the strength of concrete. The replacement of pozzolanic material various percentages of 0, 5, 10, 15, 20, 25, 30 by cement content. The preliminary test is conducted in the cementitious material such as fly ash, lime, metakaolin for specific gravity, fineness test, soundness test, and setting time of cement to check that having cementitious properties and then conducted the strength test of harden concrete like compressive strength, flexural strength, and split tensile strength test.

Keywords Cement · Lime · Fly ash · Metakaolin · Water absorption · Compressive strength · Flexural strength

1 Introduction

It is always important to determine the optimal process parameters of any. Nowadays, construction is using concrete as a mixed material of cement, water, sand, and aggregate. Many researches used pozzolanic materials such as silica fume, fly ash, lime, metakaolin (MK), furnace slag, rice husk ash as replacement with the weight of cement materials [1]. The disadvantage of metakaolin decreases the workability of fresh concrete mix [1]. MK is fineness material to get affect the environmental pollutions [1]. MK is partial replacement material of cement in percentage of 0, 5, 10, 15, 20, 25, 30%. So addition of superplasticizers in concrete is carries out to increase the workability of fresh concrete. Fly ash is generated from the power station combustion. Ash is get from the agricultural byproduct. That all above cementitious

V. Kannan
Department of Civil Engineering, Francis Xavier Engineering College, Tirunelveli 627003, India
e-mail: kannanvpandian@gmail.com

N. Karthiga Shenbagam (✉)
Department of Civil Engineering, Bannari Amman Institute of Technology, Sathyamangalam, Erode, Tamil Nadu 638401, India
e-mail: karthis47@gmail.com

G. Kumaresan et al. (eds.), *Advances in Materials Research*, Springer Proceedings in Materials 5, https://doi.org/10.1007/978-981-15-8319-3_48

Table 1 Physical properties of cement (OPC), lime, metakaolin, fly ash and sand

Sl. No.	Materials	Specific gravity	Fineness passing	
			90 mic	75 mic
1	OPC	3.108	–	–
2	Lime	2.31	100	99.8
3	Metakaolin	2.803	100	100
4	Fly ash	2	100	100
5	Fine aggregate	2.32	–	–
6	Coarse aggregate	2.62	–	–

materials can increase the various physical and chemical properties in concrete [1]. Various cementitious properties of material replace by the cement such as fly ash, lime, silica fume, metakaolin (MK), and rice husk ash [2]. These wastes are the reuse of cement replacement material to reduce use of cement content and respectively heat of hydration [2]. The fly ash is a common replacement material of cement productions [2].

Ash is a burning process of electric and power station byproduct [3]. Limestone which is heated at 500–800 °c is generated to the limestone power waste (LPW) [3]. It is a fine natural material, so it causes an environmental pollution and generated a heat of hydration in concrete [3]. When lime is added in cement it will increase the need of water content for workability of fresh concrete. The effect of waste material replacement checks the water absorption, compressive strength, and split tensile strength [3]. The different proportion of rice husk ash is replaced by the weight of cement to test the strength of concrete at 7, 28, and 58 days [4]. Optimum replacement of rice husk ash is 10% the grade of concrete [4–8].

When rice husk ash is added as binder in concrete it tends to reduce the permeability and enhances a very strong bonding between the concrete, when replaced by 10% of cement content and when the particle of Rice husk ash varies between 6–10 μm tends to develop the strength and durability of concrete [8]. Internal curing process of concrete is using PEG 400 to improve the strength high performance of concrete [9, 10]. The internal curing of concrete to reduce the water content and effect of void, and porous nature of concrete is to be supported [11] (Table 1).

1.1 Mix Proportions

The mix proportion of concrete involves constituents as cement, water, lime, fly ash, metakaolin, sand, and aggregates. The cement replacement materials such as lime, fly ash, metakaolin, and mix proportions are generally carried out for optimum percentage of 5, 10, 15, 20, 25, 30% by the weight of cement material. Lime, fly ash, metakaolin, and each material are replaced by the various percent and addition of internal curing materials of polyethylene glycol (PEG 400). The fresh concrete

Table 2 Cement replaced by binary of metakaolin strength at 7 days and 28 days

Grade of concrete	Mix ID	% of fly ash and metakaolin	7 days strength N/mm^2	28 days strength N/mm^2
External curing				
M30	M0	0%	16.5	24
M30	M1	10%	24.5	35.5
M30	M2	20%	21	30.5
M30	M3	30%	15.6	22.6
M30	M4	40%	12	17.4
Internal curing: (*PEG 400*)				
M30	M5	10%	15	21.8
M30	M6	20%	20.1	29.15
M30	M7	30%	15.3	22.2
M30	M8	40%	12.8	18.6

can be properly placed with adequate workability and compacted and achieved the required durability and strength of concrete.

1.2 Experimental Programs

Material Used

The materials used in the concrete as ordinary Portland cement (OPC 53 grade), lime, fly ash, metakaolin, sand, aggregate, portable water, and PEG 400 were added to check the internal curing process. The replacement materials are the preliminary test conducted to check the physical and chemical properties which follow as per the standard methods.

1.3 Compressive Strength of Concrete

See Tables 2, 3, and 4.

1.4 Flexural Strength of Concrete

See Tables 5, 6, and 7

Table 3 Cement replaced by ternary of fly ash, metakaolin strength at 7 days and 28 days

Grade of concrete	Mix ID	% of fly ash and metakaolin	7 days strength	28 days strength
			N/mm^2	N/mm^2
External curing				
M30	M0	0	16.5	24
M30	M1	10	17.1	24.8
M30	M2	20	9.3	13.5
M30	M3	30	6.5	9.43
M30	M4	40	5.4	7.83
Internal curing: (*PEG 400*)				
M30	M5	10	18.1	26.3
M30	M6	20	9.9	14.4
M30	M7	30	8.8	12.8
M30	M8	40	3.3	5

Table 4 Cement replaced by quaternary of lime, fly ash, and metakaolin strength at 7 days and 28 days:

Grade of concrete	Mix ID	% of lime, fly ash and metakaolin	7 days strength	28 days strength
			N/mm^2	N/mm^2
External curing				
M30	M0	0	5	8.9
M30	M1	5	10.25	14
M30	M2	10	8.6	11.1
M30	M3	15	4.7	9.2
M30	M4	20	4.6	8.5
M30	M5	25	4.5	8.3
Internal curing (*PEG 400*)				
M30	M6	5	13.95	18.8
M30	M7	10	9.65	11.3
M30	M8	15	9.5	11
M30	M9	20	5.5	10.8
M30	M10	25	4.2	8

1.5 Split Tensile Strength of Concrete

See Table 8

Table 5 Cement replaced by binary of metakaolin strength at 7 days and 28 days

Grade of concrete	Mix ID	% of metakaolin	7 days strength	28 days strength
			N/mm^2	N/mm^2
External curings				
M30	M0	0	1.27	1.84
M30	M1	10	2.39	3.47
M30	M2	20	1.43	2.07
M30	M3	30	0.95	1.38
M30	M4	40	1.11	1.61
Internal curings (*PEG 400*)				
M30	M5	10	0.89	1.29
M30	M6	20	1.75	2.54
M30	M7	30	0.76	1.1
M30	M8	40	0.86	1.25

Table 6 Cement replaced by ternary of fly ash, metakaolin strength at 7 days and 28 days

Grade of concrete	Mix ID	% of fly ash and metakaolin	7 days strength	28 days strength
			N/mm^2	N/mm^2
External curings				
M30	M0	0	1.27	1.84
M30	M1	10	1.18	1.71
M30	M2	20	1.11	1.61
M30	M3	30	0.8	1.16
M30	M4	40	0.79	1.15
Internal curings (*PEG 400*)				
M30	M5	10	0.86	1.25
M30	M6	20	0.8	1.16
M30	M7	30	0.78	1.14
M30	M8	40	0.48	0.7

2 Results and Discussion

2.1 Compressive Strength of Concrete

The investigation of the test result is compared to conventional concrete. Two types of curing methods are conducted. First one is external curing, and second one is internal curing by using PEG 400. Both types of curing methods conducted various mixing ratios. The size of specimen is 100 × 100 × 100 (mm). The result of the

Table 7 Cement replaced by quaternary of lime, fly ash, and metakaolin strength at 7 days and 28 days

Grade of concrete	Mix ID	% of lime, fly ash and metakaolin	7 days strength	28 days strength
			N/mm^2	N/mm^2
External curing				
M30	M0	0	1.58	1.62
M30	M1	5	1.11	1.43
M30	M2	10	1.03	1.4
M30	M3	15	1.11	1.43
M30	M4	20	0.64	0.89
M30	M5	25	0.6	8
Internal curing (*PEG 400*)				
M30	M6	5	1.19	1.81
M30	M7	10	1.11	1.15
M30	M8	15	0.8	0.89
M30	M9	20	0.6	0.58
M30	M10	25	0.5	0.73

Table 8 Cement replaced by binary of metakaolin strength at 7 days and 28 days

Grade of concrete	Mix ID	% of metakaolin	7 days strength	28 days strength
			N/mm^2	N/mm^2
External curing				
M30	M0	0	1.27	1.84
M30	M1	10	2.39	3.47
M30	M2	20	1.43	2.07
M30	M3	30	0.95	1.38
M30	M4	40	1.11	1.61
Internal curing (*PEG 400*)				
M30	M5	10	0.89	1.29
M30	M6	20	1.75	2.54
M30	M7	30	0.76	1.1
M30	M8	40	0.86	1.25

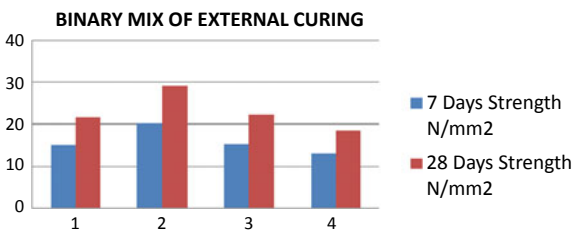

Fig. 1 Binary mix external curing

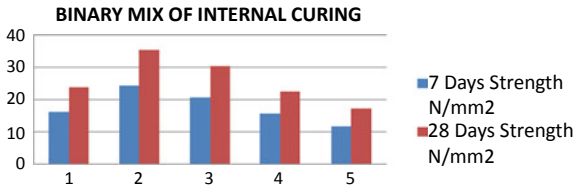

Fig. 2 Binary mix internal curing

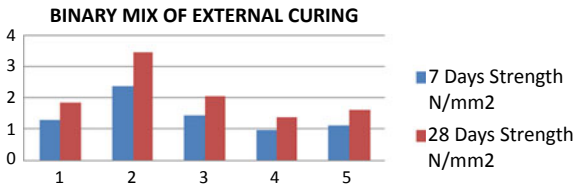

Fig. 3 Binary mix external curing

external and internal curing concrete strength at 7 and 28 days is as shown in Figs. 1 and 2.

2.2 Flexural Strength of Concrete

The various cement are replaced by binary, ternary, and quaternary of lime, fly ash, and metakaolin. The strength attained the conventional concrete. The tested specimen size is 100 mm Ø, 200 mm length of cylinder (Fig. 3).

3 Conclusions

In this research work a detailed study on normal concrete and partial replacement of cementitious material was carried out and the strength of concrete was explained in two ways such as External and Internal Curing of concrete. The replacement materials are such as lime, fly ash, and metakaolin by the cement weight, and it is checked the binary, ternary, and quaternary percentage of replaced to analyze the strength-wise.

MK is binary replaced by the weight of cement to get the result of compressive, flexural, and split tensile strength of external and internal curing (using chemical of PEG400). Fly ash and MK are the ternary replace to known the strength of concrete updated. Lime, fly ash, and MK are quaternary percentage mixed to analyze the strength of concrete (compressive, flexural, and split tensile).

Investigating the curing of concrete is external curing period which is checked at 7 and 28 days. The process of internal curing is conducted by using polyethylene glycol 400 (PEG400) to check the strength of concrete at 7 and 28 days. When the

use of PEG 400 is reducing the water demand of curing, at the same these do not affect the strength of concrete.

References

1. Shatat MR (2013) Hydration behavior and mechanical properties of blended cement containing various amounts of rice husk ash in presence of metakaolin. Faculty of Science Al Azhar University, Assuit, Egypt 23, pp 1–17
2. Sathawanea SH, Vairagadeb VS, Kenec KS (2013) Combine effect of rice husk ash and fly ash on concrete by 30% cement replacement. Procedia Eng (51):35–44
3. Torkaman J, Ashori A, Sadr Momtazi A (2014) Using wood fiber waste, rice husk ash, and limestone powder waste as cement replacement materials for lightweight concrete. Construct Build Mater (50):432–436
4. Kishore R, Bhikshma V, Jeevana Prakash P (2011) Study on strength characteristics of high strength rice husk ash concrete. Procedia Eng (14): 2666–2672
5. Fortin-Smitha J, James Sherwood A, Dranea P, Kretschmann D (2016) Characterization of maple and ash material properties as a function of wood density for bat/ball impact modeling in LS-DYNA. Procedia Eng (147):413–418
6. Siddique R, Utilization of wood ash in concrete manufacturing. Senior Professor of Civil Engineering, Thapar University, Patiala 147004, Punjab, India
7. Auta T*, Hassan AT (2016) Reproductive toxicity of aqueous wood-ash extract of *Azadirachta indica* (neem) on male albino mice. Department of Biological Sciences Federal University Dutsin-Ma, Katsina State, Nigeria 1(1), pp 36–40
8. Horsakulthai V, Phiuvanna S, Kaenbud W (2011) Investigation on the corrosion resistance of bagasse-rice husk-wood ash blended cement concrete by impressed voltage (25):1:54–60
9. Kamala MM, Safana MA, Bashandya AA, Khalilb AM, Experimental investigation on the behavior of normal strength and high strength self-curing self-compacting concrete
10. Mousa MI*, Mahdy MG, Abdel-Reheem AH, Yehia AZ (2014) Mechanical properties of self-curing concrete (SCUC) a Structural Engineering Department, Faculty of Eng. El-Mansoura University, El-Mansoura, Egypt b Ministry of Water Resources and Irrigation, El- Mansoura, Egypt (10)1–10
11. Al Saffar Aymen DM, Al Saad JK, Taye BA, Effect of internal curing on behavior of high performance concrete: an overview. Case Stud Construct Mater (10):1–11

Emulator for Efficiency Enhancement of Heave Type Wave Energy Converter

Nagulan Santhosh, M. Srinivasan, Ragupathy Karu, and Eswaramoorthy Santhosh Kumar

Abstract Over the past decade, power generation based on ocean wave energy has become a significant component in modern renewable energy systems, which has caused a substantial increase in the ocean wave power-based research. As it is complicated to use a real WEC (Wave Energy Converter) for laboratory purposes, development of a replica of a WEC that can be connected and used indoors is imperious. This paper presents the design and development of a heaving type WEC emulator device which is a motor-generator coupled system inbuilt with Pulse Width Modulation (PWM). First, the mathematical model of the heave type WEC emulator is developed and the corresponding hardware is involved. A reactive control for efficiency enhancement for the proposed WEC is implemented in the developed emulator under the regular and irregular wave conditions. The efficiency of the WEC is attained through optimal electrical damping and further, the emulator facility enhances the research potential towards the heaving type WEC.

Keywords Wave energy converter · Renewable energy systems · Pulse width modulation · Emulator · Reactive control

N. Santhosh (✉) · E. Santhosh Kumar
Department of Mechanical Engineering, Bannari Amman Institute of Technology, Sathyamangalam, Erode, Tamil Nadu 638401, India
e-mail: santhoshmech10@gmail.com

E. Santhosh Kumar
e-mail: santhoshmech10@gmail.com

M. Srinivasan
Department of Electrical and Electronics Engineering, Bannari Amman Institute of Technology, Sathyamangalam, Erode, Tamil Nadu 638401, India

R. Karu
Department of Automobile Engineering, Bannari Amman Institute of Technology, Sathyamangalam, Erode, Tamil Nadu 638401, India

G. Kumaresan et al. (eds.), *Advances in Materials Research*, Springer Proceedings in Materials 5, https://doi.org/10.1007/978-981-15-8319-3_49

1 Introduction

The progress of renewable energy technologies has become indispensable in the perspective of today's global environmental concerns. In recent years, various research activities have been put forth in the renewable energy converters and ocean WEC plays a significant contribution. Till date, plenty numbers of concepts are proposed and patented to harvest the energy from the ocean environment [1, 2]. Over 1000 wave energy conversion techniques have been patented in Japan, North America, and Europe. Various wave energy conversion devices based on their working principle were reviewed [5–7]. These devices are measured to be at prototype stage and under extensive development stage. The point absorber is one of the types of WEC which is well known [4]. These point absorbers are generally instigated in the offshore environment. Point absorbers are lesser in dimension when compared to the wavelength and they are constrained to heave motion only. The heave motion which is produced due to the relative motion between the wave and the point absorber is further converted into rotary motion and then fed to conventional generator or implementing the linear generator integrated with the point absorber for direct energy conversion.

For any WEC device to work efficiently in the ocean environment and to extract maximum power, the device has to be controlled efficiently [8, 9]. The controlling means how the dynamics of the WEC are prepared to meet the irregular wave of the ocean [10, 11]. In particular, the non-buoyant typed WEC which is used in this research work performs well when the natural frequency of the device is closed to the frequency of the incident wave. Hence the damping plays a vital strategy in the performance of the WEC. Moreover, if the damping is high, then the motion of the WEC is limited and at the same time if the damping is low then very little amount of energy will be harvested. Therefore, optimal damping is required. In the real sea environment the waves are subject to highly irregular wave conditions which continuously vary in height and frequency and the WEC in order to adopt such a drastic condition the dynamics of the converter have to be actively controlled. Generally, the major improvement is noticed when the WEC is subject to active control of the dynamics. The level of tuning the WEC can vary from tuning the dynamics of the system to a particular sea state to wave-by-wave adoption.

High research facility at the laboratory level or in the onshore is required to enhance the research activity for this type of WEC. As a result, a device that can mimic the functionality of a WEC in a laboratory environment is of most importance. The foremost requirement of such a device, which may be called a WEC emulator, is the ability to produce the same static and dynamic characteristics of a real WEC. Various simulation tools are available to simulate the WEC in various operational wave conditions [15]. These simulation devices can model the real system and have some limitations that only certain properties can be modified and tested and this has high constrains over the research activities on dynamic characteristics. An emulator can overcome these issues by replicating the real hardware system and captures the functional connections between inputs and outputs of the system, based on processes

that are the same as, or similar to, those of that real systems. Emulator model is developed by many researchers for enhancing the research potential of wind turbines [12, 13].

In this research work, this concept is initiated to a WEC such as the development of the emulator for the non-buoyant type WEC and the mathematical model for the same is developed and validated through experimental setup. The dynamic tuning of the system such as the optimal electrical load damping is performed in the emulator and the wave energy extraction efficiency enhancement is observed.

2 Non-Buoyant WEC

The proposed non-buoyant type of WEC is generally a near-shore device to be placed on a rigid platform (see Fig. 1). The general working principle of the proposed innovative concept is published in the previous article [3]. To overview the developed model, the system consists of a straight steel-framed oscillating arm, which is pivoted at its middle. One end of the arm is suspended through a metal rope by a non-floating cylindrical container with open bottom and an air vent is provided at the top (a semi immersed container filled with water) and the other end is provided by a counter mass (metal plates). The arm is coupled with the rotatable shaft at the pivoted point and the whole assembly is mounted on a base plate. Further, the rotatable shaft is connected with a unidirectional gearbox followed by a step-up gearbox and finally the generator.

When the wave crest approaches the semi immersed container, the water level around the container increases, and thus, the container's effective mass gets decreased

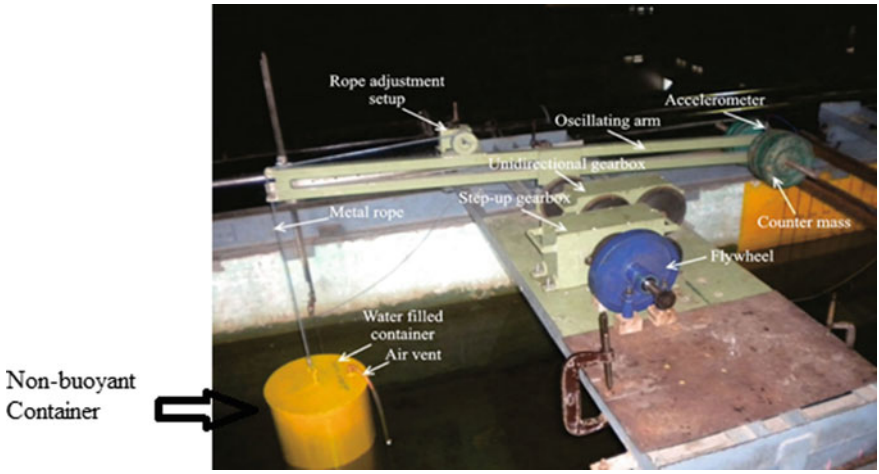

Fig. 1 Experimental system [3]

as a result, the arm becomes unbalanced. An action of balancing this leads the counter mass to pull the container up and the arm oscillates in one direction. When the wave trough approaches the container, the effective mass of the container gets increased due to fall in the water level around the container and thus, it makes the container weight heavy which in turn pulls the counter mass up. This alternating balancing makes the arm to oscillate continuously. This continuous oscillation is transmitted to an input gear of the unidirectional gearbox which is coupled at the center of the oscillating arm. Further, the unidirectional gearbox transmits the low-speed high torque rotation into high-speed rotation through step-up gearbox and it is immediately followed by the generator to convert the rotation into electricity.

3 Reactive Loading Control

To achieve maximum energy extraction from ocean waves, effective control technology has to be implemented, and to attain this, the optimal phase or optimal amplitude or both must be implemented [14]. Among the various control techniques, the reactive control technique seems to be more effective in achieving both the optimal phase and amplitude. But it is intricate to implement the reactive loading control because it has strict constraints and all the constraints are frequency dependent. To overcome this, a control strategy can be adopted in which the control is achieved by adjusting the dynamic parameters of the energy converter such as the spring constant, inertia, and the energy-absorbing damping. Further, this leads to the phase matching between the floating body of the WEC and the incident wave. But, in the real sea environment, it is complex to change the dynamic parameters of the WEC. Instead, it is convenient to tune the damping load which has an impact on the dynamics characteristics of the WEC. In this work, the damping to the WEC means in terms of electrical load.

4 Emulator and Load Model

The reactive control is implemented on WEC in both the regular and irregular wave conditions. Further, the experimental analysis is performed in the emulator which dynamically mimics the non-buoyant WEC. The developed emulator is a DC motor-generator coupled system. A mathematical model is developed for coupled motor-generator system where in load is connected to the generator. Starting with the motor, the output of the motor can be expressed using Kirchoff's voltage law and rotational equation as,

$$V_{\mathrm{a}} = I_{\mathrm{m}}(L_{\mathrm{m}} + R_{\mathrm{m}}) + E_{\mathrm{bemf}} \tag{1}$$

Here, V_a is the motor armature voltage, E_{bemf} is the backemf of the motor, I_m is the motor armature current, R_m is the armature resistance of the motor and L_m is the armature inductance of the motor.

Similarly, the governing equation for the generator is

$$E_g = I_g(R_L + R_g + L_g) \tag{2}$$

The equation for the generator is similar to that of the motor in which parameters are indicated with subscript g, except E_g which is known as an induced emf of the generator and R_L is the resistive load.

Now, the torque of the motor can be derived as,

$$P_m = E_{bemf} I_m \tag{3}$$

Here, P_m is the mechanical power of the motor.

The mechanical power P_m is related to the electromagnetic torque T_m as,

$$P_m = T_m \omega \tag{4}$$

ω is an angular speed in rad/s.

Now, equating Eqs. (3) and (4)

$$E_{bemf} I_m = T_m \omega \tag{5}$$

Further, it can be simplified as,

$$T_m = K_m I_m \tag{6}$$

Here, the torque constant and voltage constant is considered to be equal and denoted as motor constant K_m.

Similarly for the generator, the corresponding torque equation and induced emf is,

$$T_g = K_g I_g \tag{7}$$

and

$$E_g = K_g \omega \tag{8}$$

Let's consider the resistive lamp as the load connected to a DC generator output terminals. At steady-state conditions, Eq. (8) can be rewritten as,

$$E_g = I_g(R_L) \tag{9}$$

Using Eq. (8) and (9) the current flowing through the load can be obtained as,

$$k_g \omega = I_g(R_L) \tag{10}$$

Now, the power intake of the resistance load P_L is given as,

$$P_L = \frac{k_g^2 \omega^2}{R_L} \tag{11}$$

where kg^2 is the generator constant and the above equation gives the relation between the resistance values of the system to that of the system angular speed and further, the optimal resistive load can be obtained from the corresponding angular speed of the system.

5 Hardware Implementation

The emulator is developed with hardware components that are integrated with a software tool scripted in the Java platform. The signal output of the software tool dives the direct current motor that has been inured to operate in a torque control mode with an external analogue voltage signal. The electric power is generated by a rotor induction machine driven by a servo-motor. Table 1 gives the various system components of the emulator setup.

The basic arrangement of the hardware devices and the emulator setup used for the proposed model is shown in the Figs. 2 and 3. Here, the DC power source is provided with 50 V which is supplied to the DC PWM drive. The wave pattern or the corresponding non-buoyant displacement with respect to time is fed to the same via computer interface. The DC PWM drive converts the wave pattern, or the non-buoyant profile into the corresponding PWM duty signal. Further, the duty cycle in terms of voltage is varied from 0 to 100% is supplied to the armature coil of the PMDC motor where the maximum speed of the motor is to be 1750 RPM. PMDC motor rotates with different speed bases in the range of the duty cycle and the motor is coupled to the generator at the help of the shaft, which forms the DC motor/DC

Table 1 System components of the emulator setup

S. No.	Components	Ratings
1	PMDC motor	RPM 1750, power 750 W, input voltage 50 V DC, current 15 A
2	PMDC generator	RPM 1500, power 500w, output voltage 50 V DC, current 10 A
3	Resistive lamp load	Power 400 w, voltage 50 V, DC current 8 A
4	Linear PWM controller (Motor drive)	Power 750 w, Voltage 60 V DC
5	Linear PWM controller (Load controller)	Power 500 w, voltage 60 V DC

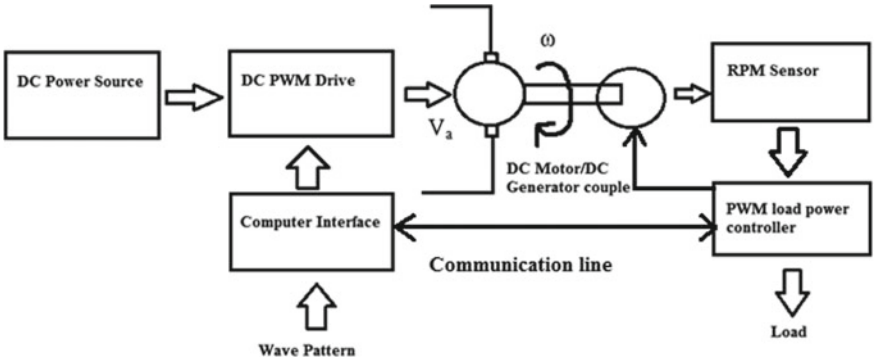

Fig. 2 Hardware devices

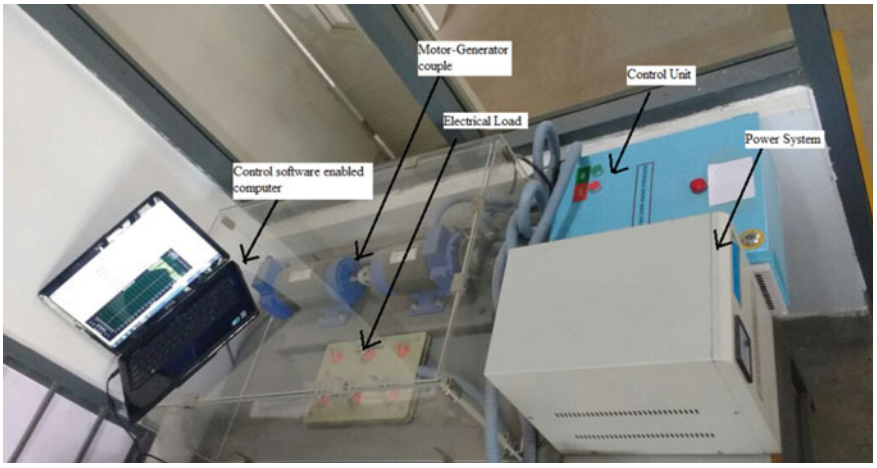

Fig. 3 Emulator setup

generator couple. The installed generator has a maximum capacity of 1500 RPM and maximum power production of 500 W. In the real ocean environment, to generate the power in a batter quality, it is always required to rotate the generator with constant speed. But this is not possible due to variation in the ocean wave and variation in load. This problem is overcome by introducing the reactive control technique where a sensor which monitors the generator shaft speed. If there is a variation in the generator speed due to irregularity in the ocean wave or oscillations in the load, the sensor monitors and sends the information to the load controller. Where the load controller tunes the load accordingly and the optimal load is provided to maintain the generator speed constant.

6 Experimental Investigation in Emulator

The emulator is designed and fabricated in order to conduct analysis for any kind of wave and non-buoyant displacement profile. The modification of the input wave is achieved in the emulator and the corresponding output can be retrieved. These modifications cannot be easily done in the real laboratory scaled WEC. In the emulator, the data set such as the time and corresponding wave is fed to the emulator through the developed software tool.

The time period input and the displacement of the non-buoyant are fed to the software tool and these fed data's can be viewed in the graphical form in the graphical window. Also, the data can be viewed in the right top column of the software tool. The wave data which is fed is lying in both the positive and the negative half cycle, before forming the duty cycle the wave cycle completely transferred to the positive half cycle as shown in Fig. 4. Further, the corresponding duty cycle is formed and fed to the drive.

The control panel of the developed software consists of a number of provisions such as drive duty, drive status, drive current and other parameters modifying facility. After feeding the data, such as the time and the non-buoyant displacement the algorithm finds the duty cycle for the corresponding wave profile. Further, when the motor coupled generator is switched on, the motor runs with respect to the duty cycle provided and in turn drives the generator. The load provided to the generator is tuned accordingly to provide optimal power efficiency.

Fig. 4 Formed duty cycle

7 Results and Discussions

Reactive control of the energy converter is performed for the regular waves in the emulator model. The wave data which is provided to the emulator is a set of different regular waves of amplitude and time period of 20 cm/2.2 s, 25 cm/2.2 s, and 25 cm/2.4 s. Before running the emulator for the given wave conditions the duty cycle and the generator speed are fixed, where these values resemble the values of the flume wave and the laboratory scaled energy converter.

The servo motor rotates as per the duty cycle, which mimics the real wave and further generator is coupled with the motor for power production. A pick-up sensor monitors the generator shaft speed and compare with the set speed and accordingly the load is adjusted such that two-speed value is approximately equal. The power production is recorded and it varies in such a manner that the speed of the generator shaft matches the set speed.

From the above results which are given in Figs. 5, 6 and 7 the electrical load is modified to maintain the set speed, by doing so the quality of power generated is maintained, and also the WEC work in the resonance condition where the frequency of the energy converter is in phase with the ocean wave. The resonance condition of the energy converter is validated in the wave flume experimental setup by providing the optimal load which is obtained from the emulator result. Results are shown in Figs. 9 and 10 where the wave frequency and the non-buoyant frequency match each other and with the phase difference of 180° (Fig. 8).

Generally to obtain the optimal energy from the regular waves, the load conditions are varied to maintain the generator speed constant, but it is not possible for the irregular waves. It is not possible to fix the speed at a constant level in the case of an irregular wave conditions.

Reactive control of the energy converter is performed for the irregular waves in the emulator model. The wave data which is provided to the emulator is a set of different

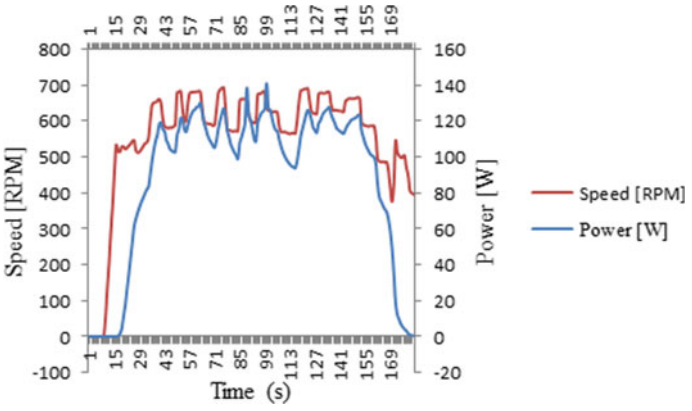

Fig. 5 Power generated for 10 cm 2.2 s wave at 600 RPM set speed

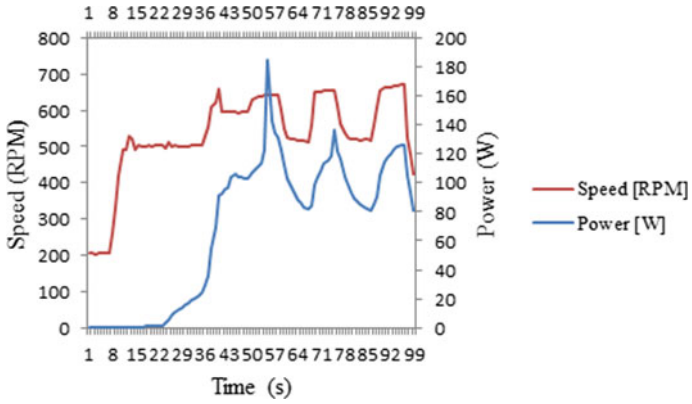

Fig. 6 Power generated for 20 cm 2.2 s wave at 500 RPM set speed

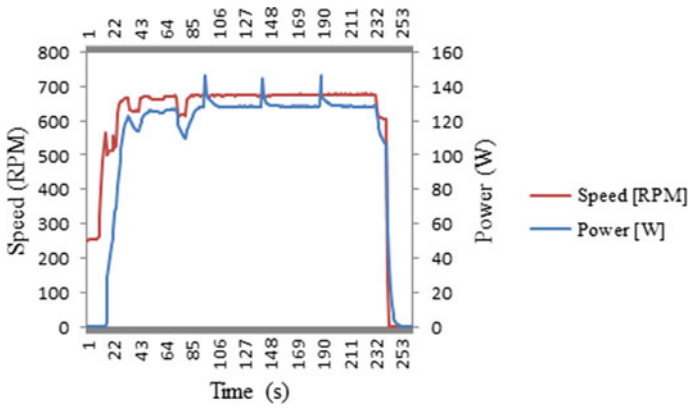

Fig. 7 Power generated for 25 cm 2.2 s wave at 700 RPM set speed

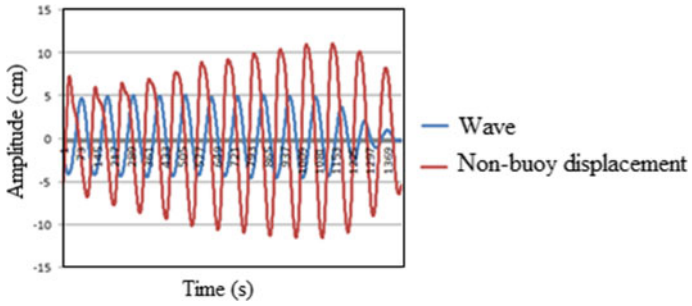

Fig. 8 Undamped WEC for 10 cm wave amplitude and 2.2 s time period

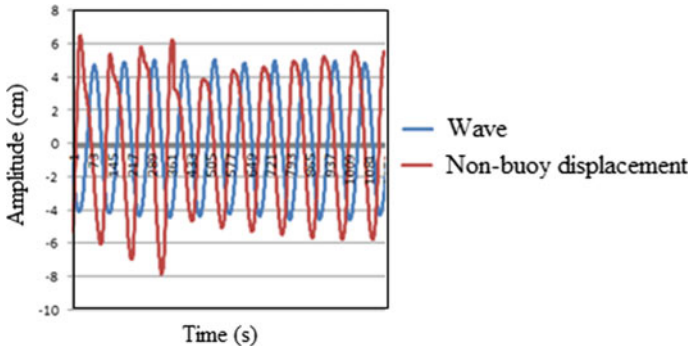

Fig. 9 Damped WEC for 10 cm wave amplitude and 2.2 s time period

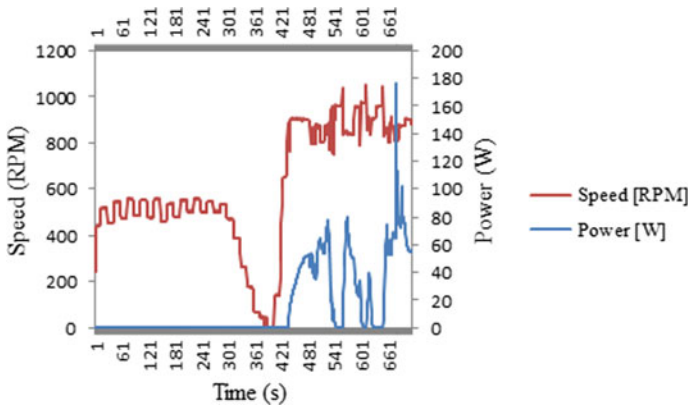

Fig. 10 Power generated for irregular wave I

irregular waves which is a combination of different amplitude and time period. The power which is produced in the irregular wave conditions is discussed.

Figures 10, 11 and 12 shows the production of power in different irregular wave conditions and it is noted that the power production is highly affected in the case of irregular waves. Thus, in order to obtain an optimal energy from the irregular waves along with the reactive control, predicting the incident irregular wave in advance is required. To achieve this an intelligent system has to be incorporated along with the system.

8 Conclusion

The huge research potential is required to carry out the research activities in wave energy conversion. It is intricate and complex to perform any kind of exploration

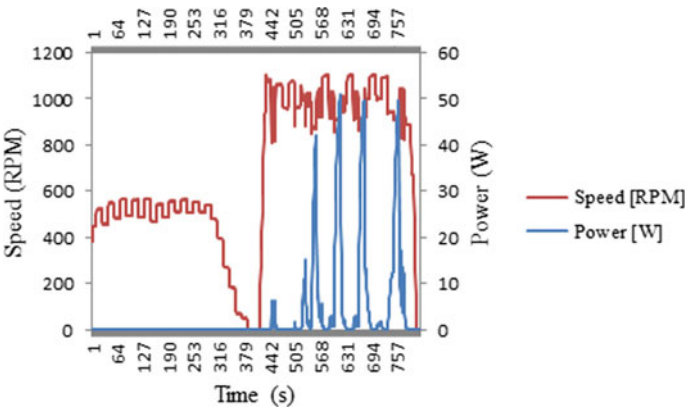

Fig. 11 Power generated for irregular wave II

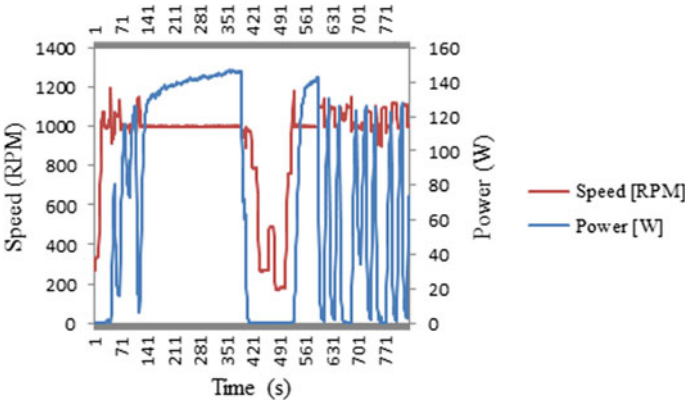

Fig. 12 Power generated for irregular wave III

activity on the WEC in the real shore environment or in the laboratory scaled wave flume. This paper demonstrates an emulator for a particular heave type WEC. The following results are obtained from the development of the emulator model:

- The developed emulator replicated the real hardware system and holds the functional relations between inputs and outputs of the system, based on processes that are the same as, or similar to, those of that real systems.
- It enhances the research potential of the WEC.
- Reactive control is performed in the developed emulator model and the optimal phase matching is obtained to enhance the efficiency of WEC.
- Intelligent systems are required to predict the irregular wave in advance in order to find the optimal parameter (electrical load).

These kinds of WEC emulators reduce the experimental complexity and economic constraints in WEC research. Also, enhance the research potential of the energy converters.

References

1. Ahn K, Truong K, Tien H (2012) An innovative design of wave energy converter. Renew Energy 42:186–194
2. Al-Habaibeh A, Su D, McCague J (2010) An innovative approach for energy generation from waves. Energy Convers Manage 51:1664–1668
3. Amarkarthik A, Chandrasekaran S, Sivakumar K, Sinhmar H (2011) Laboratory experiment on using non-floating body to generate electrical energy from water waves. Front Energy 6(4):361–365
4. Budal K, Falnes J (1980) Interacting point absorbers with controlled motion. In: Power from sea waves (B. Count, ed.). Academic Press, London, pp 381–399
5. Chandrasekaran S, Sinhmar H (2012) Power generation using Mechanical wave energy converter. J Ocean Clim Sci Technol Impacts Ocean Clim Syst 3(1):57–70
6. Drew B, Plummer AR, Sahinkaya MN (2009) A review of wave energy converter technology. J Power Energy 223(8):887–902
7. De O, Falcao AF (2009) Wave energy utilization: a review of the technologies. Renew Sustain Energy Rev 14(3):899–918
8. Erik L (2010) Theoretical and experimental analysis of operational wave energy converters. Ph.D. thesis, Uppsala Universitet, Sweden
9. Falnes J (2007) A review of wave-energy extraction. Mar Struct 20:185–201
10. Lindroth S, Leijon M (2011) Offshore wave power measurements—a review. Renew Sustain Energy Rev 15:4274–4285
11. Mikael E (2009) Modelling and experimental verification of direct drive wave energy conversion. PhD thesis, Uppsala University, Sweden
12. Mohod SW, Aware MV (2011) Laboratory development of wind turbine simulator using variable speed induction motor. Int J Eng Sci Technol 3(5):73–82
13. Santaphon K, Chanrit T (2010) Real-time wind turbine emulator for testing wind energy conversion systems. In: IEEE international energy conference
14. Wanan S, Raymond A, Anthony L (2014) Latching control theory for wave energy conversion. In: 29th international workshop on water waves and floating bodies. Osaka, Japan
15. Yi-Hsiang Y, Michael L, Kelley R, Carlos M (2014) Development and demonstration of the WEC-Sim wave energy converter simulation tool. In: Proceedings of the 2nd marine energy technology symposium

Characterization and Fabrication of ABS and PLA-Based Polymer Matrix Composites Using 3D Printing

Anandha Moorthy Appusamy, E. Prakash, S. Madheswaran, Arunkumar Rajamanickam, Vinoth Kumar Selvakumar, and P. Chandrasekar

Abstract The recent dynamical world cannot imagine the growth without fetching any thought of upgrading in material composite. Numerous studies are taking place in these biodegradable polymer composite materials to attain the required standards. Biodegradable fiber embedded polymer composites have a strong correspondence to change the composite fabricated of plastics. Natural polymer materials have the following pros like low-cost, lightweight, improved strength, easy accessibility, non-toxic, non-abrasive, and decomposable properties. Researchers have extended their proficiency idea in the product design by using raw materials which consist of natural fiber. Natural fibers are stronger and also can be utilized in producing high-end quality viable manufacturing products. The primary intention of the current experimentation is to observe the mechanical performance of Gangura roselle fiber reinforced with thermoplastics composites. Gangura roselle fibers are reinforced in thermoplastics like PLA and ABS to produce composite materials. Later test for mechanical properties of the polymer matrix composite is verified as per different ASTM standards. The outcomes of the testing were plotted in the graph and the properties are observed and their uses in different mechanical applications.

Keywords Natural fiber reinforced Composite · PLA · ABS · Gangura roselle fibers · ASTM

1 Introduction

The day-by-day increasing environmental awareness and public interest, administrations, and the novel ecological guideline, led to the thoughts of environmental responsive raw material. Hence the biodegradable fiber is considered as the environmental responsive materials which have better effects as soon as compared with

A. M. Appusamy (✉) · E. Prakash · S. Madheswaran · A. Rajamanickam · V. K. Selvakumar · P. Chandrasekar
Department of Mechanical Engineering, Bannari Amman Institute of Technology, Sathyamangalam, Erode 638401, India
e-mail: anandhamoorthya@bitsathy.ac.in

G. Kumaresan et al. (eds.), *Advances in Materials Research*, Springer Proceedings in Materials 5, https://doi.org/10.1007/978-981-15-8319-3_50

other polymer materials. Most of the countries have forced industries like aerospace, production and manufacturing, automotive, construction and packaging to search for ecologically responsive alternate materials. During the 90s, the term polymer composite material was stretched out to all frameworks with something like two parts, one of which was natural. Currently, the composite application is thriving. Composites prepared with the addition of bio fibers are the most attractive alternative to solve the environmental issues developed by the industries [1]. Recently the researchers are deeply engaged to find the alternate for monolithic materials to enhance biodegradability and safe ecology.

Sathish Kumar et al. [2] revealed this research paper presents that fiber-reinforced materials are widely utilized for basic appliances because of improved weight-bearing capacities.

Uygunoglu et al. [3] proposed this research paper presents, normal filaments, composites are likewise gotten by expulsion process. These composites show exhibitions that permit their utilization just for brief term.

Velusamy et al. [4] investigation includes, Water absorption behavior and mechanical properties of epoxy composites reinforced by Calotropis Gigantea fiber synthesized using compression molding method.

Joseph et al. [5] has been characterized by the Calotropis Gigantea fiber embedded epoxy composites synthesized by pressure moulding methods. Experimentations were done on specimens with various volume portion (0, 5, 10, 15, 20, 25, and 30%) and fiber length (10, 20 & 30 mm).

2 Materials and Methods

2.1 Manufacturing Method

The specimen preparation involves 3D printing technology. Different kinds of 3D printing technologies are Stereo lithography [SLA], Fused Deposition Modeling [FDM] [6], Selective Laser Sintering [SLS], three-Dimensional Printing [3DP], Electron Beam Melting [EBM]. These materials are easily available in market in the form of filament. The 3D printing technology available [6] for filament type material is Fused Deposition Modeling [FDM] is shown in Figs. 1 and 2.

2.2 Significance of Composite

Normal conventional parts are more weight, more abrasive, non-biodegradable [3]. It doesn't sustain more stress and forces. Manufacturing process is quite complicated. Conventional parts are not so great in providing reinforcement in comparison with polymer matrix composites. There are numerous reasons that conventional parts are

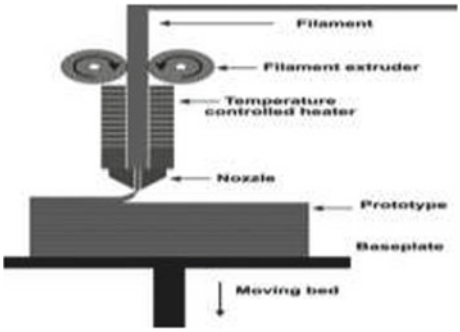

Fig. 1. Fused deposition method

Fig. 2 PLA and ABS Specimens

influenced by heat and fall short in corrosion resistance. Conventional parts are high end in terms of cost. Conventional parts are not so resilient enough like polymer matrix composites. They also wear off easily and have less stiffness.

2.3 Methodology

Initially, collecting the required information about the problem analysis, then investigate for the appropriate system, then the fiber is extracted from the natural source,

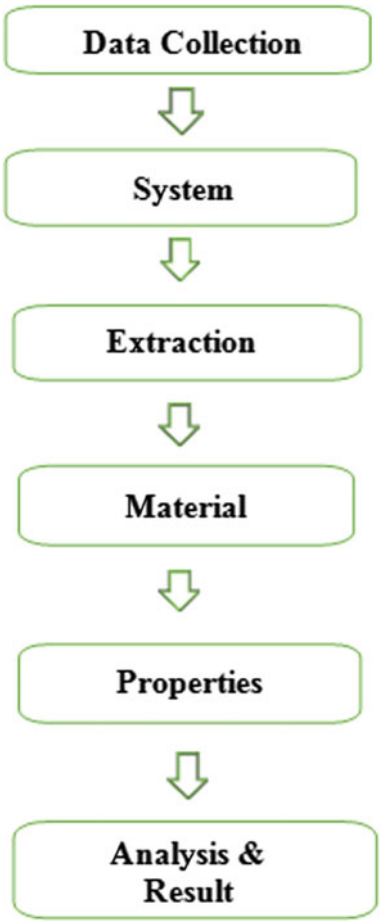

Fig. 3 Experimental procedure

then the suitable reinforcement materials should be selected and check for its properties after preparing the specimen, analyze its mechanical properties and hence plot the results (Fig. 3).

2.4 Matrix Materials

For experimental purpose, Acrylonitrile Butadiene Styrene [ABS] and Poly Lactic Acid [PLA] are selected as matrix material. ABS is an opaque thermoplastic polymer material made from monomers Acrylonitrile Butadiene Styrene. They have high strength, durability, and also cheap [7] and easily available in the market. ABS has a glass transition temperature (solid-state to rubber state) is ($TG = 110$ °C) [7]. PLA is stronger than ABS. PLA is more brittle in nature. PLA reduces the effect of

warping by having a low co-efficient of thermal expansion. PLA does not have health affects even though printed in non-ventilated area [8]. PLA have a glass transition temperature (solid-state to rubber state) is ($TG = 60$ °C).

3 Results and Discussions

3.1 Flexural Test

Flexural test of polymer material gives fatigue load carrying capacity and flexural modulus [2]. Flexural load-carrying capacity at outermost surface of the specimen gives either the tension or compression side and the specimens are shown in Fig. 2. The ASTM standard Fig. 4 for flexural test specimen is D790 [9]. The total no of work piece for flexural test is 4 including the base material and the test is processed Fig. 5 and the reading is plotted. The graph represents the flexural test on PLA and ABS material. The flexural test on the PLA material shows the flexural strength rises till particular load at a certain load the PLA test specimen broke into two pieces while the flexural test on the ABS material withstand load but it does not break into two pieces.

Flexural strength of ABS matrix composites without fiber is shown in Fig. 6. This figure shows the flexural strength of 0° printing orientation. Deflection of the specimen gradually increases with increase in applied load up-to 2 kg, negligible amount of deflection is recorded. The applied load is directly proportional to the defection of the specimen up-to 3 kg. The failure of the specimen is recorded at

Fig. 4 Flexural test specimen [ASTM]

Fig. 5 Flexural test machine

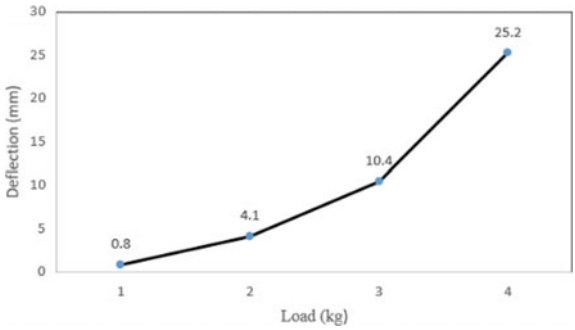

Fig. 6 ABS without fiber

4 kg with three-point bending. Flexural strength of 0° printing orientation specimen reaches a maximum deflection of 25 mm.

Transverse 3-point bending results of ABS with 0° printing orientation shown in Fig. 7. The figure shows the deflection varies with respect to the applied load. Deflection of the specimen gradually increases with increases in the applied load. The maximum bending deflection of the specimen is recorded at 3.9 kg with a deflection of 19 mm before yielding.

Flexural strength of PLA matrix composites without fiber is shown in Fig. 8. This figure shows the flexural strength of 0° printing orientation. Deflection of the

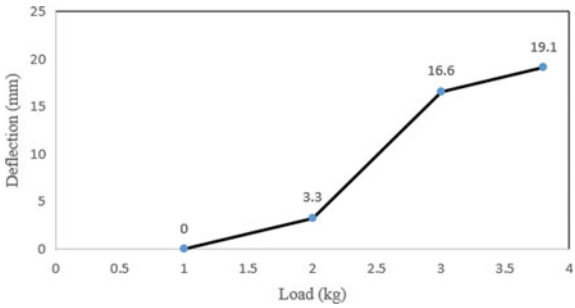

Fig. 7 ABS with fiber

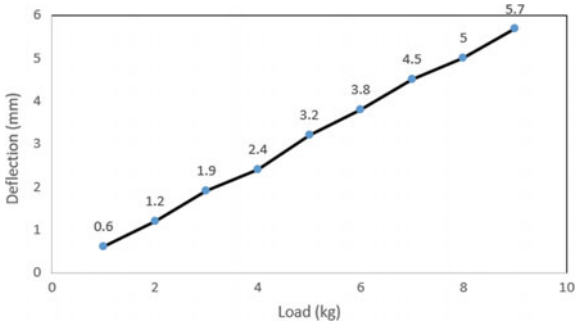

Fig. 8 PLA without fiber

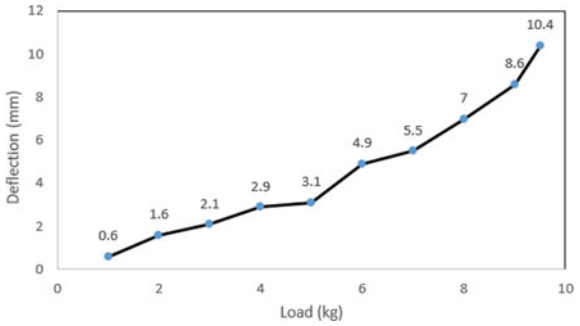

Fig. 9 PLA with fiber

specimen gradually increases with increase in applied load up-to 9 kg, negligible amount of deflection is recorded. The failure of the specimen is recorded at 9 kg with three-point bending. Flexural strength of 0° printing orientation specimen reaches a maximum deflection of 5.9 mm.

Transverse three-point bending results of PLA with 0° printing orientation shown in Fig. 9. The figure shows the deflection varies with respect to the applied load. Deflection of the specimen gradually increases with increases in the applied load up-to 4 kg. The deflection of the specimen increases with increases in the applied load. The maximum bending deflection of the specimen is recorded at 9 kg with a deflection of 10.3 mm before yielding.

3.2 Tensile Test

The most common purpose of the tensile test is check the tensile strength [2] of the specimen using universal tensile test machine Fig. 11. Tensile strength [5] is the material's ability to withstand a pulling force. It is defined in the unit of force per cross-sectional area. The ASTM standard for tensile test specimen is D638 [10] Fig. 10.

Figure 11 shows the schematic view of the tensile test apparatus which gives direct relation between applied load and deflection of the specimen with equal interval. Elongation plot has been generated by the output device. Applied load in *Y* axis and the corresponding deformation plotted in *X* axis.

Tensile strength of ABS matrix composites without fiber is shown in Fig. 12. This figure shows the tensile strength of 0° printing orientation. Elongation of the

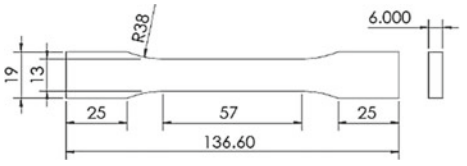

Fig. 10 Tensile test specimen [ASTM]

Fig. 11 Tensile test machine

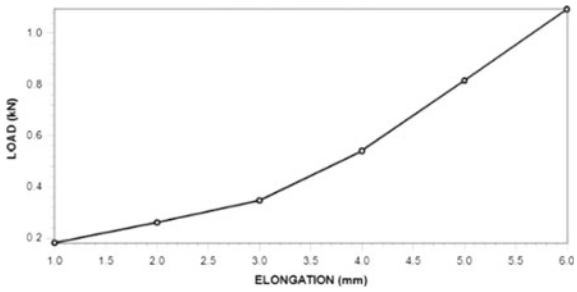

Fig. 12 ABS without fiber

specimen is directly proportional to the applied load up-to 0.2 kN. Elongation of the specimen gradually increases with the increases in the applied load. It reaches a maximum elongation of 11 mm at a weight of 1.4 kN at rupture.

Longitudinal tensile strength results of ABS with 0° printing orientation shown in Fig. 13. The figure shows the elongation varies with respect to the applied load. The elongation of the specimen increases gradually with increases in applied load. It reaches a maximum elongation of 20 mm at a load of 1.4 kN.

Tensile strength of PLA matrix composites without fiber is shown in Fig. 14. This figure shows the tensile strength of 0° printing orientation. Elongation of the specimen is directly proportional to the applied load up-to 2 kg. Elongation of the specimen gradually increases with the increases in the applied load. It reaches a maximum elongation of 6 mm at a weight of 3.9 kg at rupture.

Longitudinal tensile strength results of PLA with 0° printing orientation shown in Fig. 15. The figure shows the elongation varies with respect to the applied load.

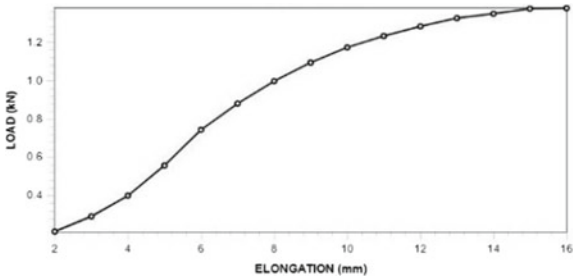

Fig. 13 ABS with fiber

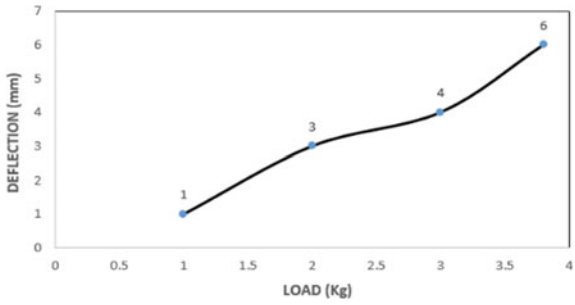

Fig. 14 PLA without fiber

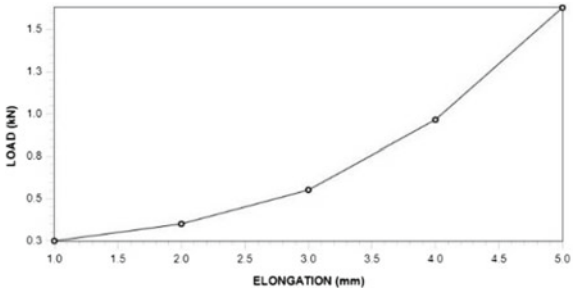

Fig. 15 PLA with fiber

The elongation of the specimen increases gradually with increases in applied load. It reaches a maximum elongation of 6.5 mm at a load of 2.4 kN.

3.3 Hardness Test

Indentation hardness tests are used in mechanical engineering to determine the hardness of a material to deformation. Several such tests exist, wherein the examined material is indented until an impression is formed; these tests can be performed on macroscopic or microscopic scale with the Rockwell hardness tester as shown in Fig. 16. The application of hardness testing enables you to evaluate a material's

Fig. 16 Rockwell testing machine

properties, such as strength, ductility, and wear resistance whether that material is suitable for that high payloads**.** For Rockwell test, two pieces are made one with fiber and one without fiber. The test results are processed and it has been figured out that ABS & PLA material with fiber explaining for results [11].

Hardness result shows that the addition of fiber into the matrix material ultimately improves the hardness of composite specimens [12]. Comparatively, ABS gives better indentation resistance. In Fig. 17 shows 25% of improved hardness in ABS and PLA gives 26% improved hardness.

4 Conclusions

The test results of Gangura roselle fiber reinforced polymer matrix composite specimens were good as compared with base material and other conventional polymers. The polymer matrix composites with Gangura roselle fiber can be a better replacement for the application of conventional parts in automobile field and fit for many

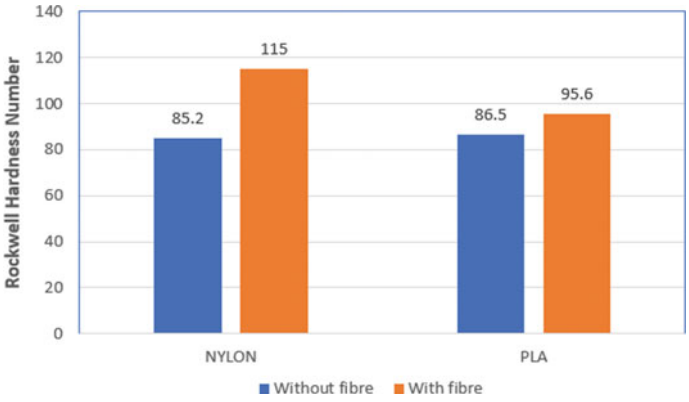

Fig. 17 Rockwell hardness of ABS and PLA

sectors too. The test results also adding evidence that the Gangura roselle fiber reinforced with ABS and PLA exhibits maximum flexural and tensile strength with improved hardness value. The experimentation clearly defines that the strength of the composite mainly depends on fiber volume fraction.

References

1. Wallenberger FT, Weston N (2004) Natural fibers, plastics and composites natural. Materials Source Book from C.H.I.P.S, Texas
2. Sathish Kumar TP (2012) Mechanical properties of randomly oriented snake grass fiber with Gangura and coir fiber-reinforced hybrid composites. J Compos Mater 47(18):2181–2191
3. Uygunoğlu T (2015) Physical and mechanical properties of polymer composites with high content of wastes including boron. J Mater Res 3(25):271–276
4. Velusamy K (2018) The influence of fiber content and length on mechanical and water absorption properties of Calotropis Gigantea fiber reinforced epoxy composites. J Indust Text 4: 15280837 18 763778.
5. Joseph K (1999) A review on sisal fiber reinforced polymer composites. Rev Brasileira de Engenharia Agrıcola e Ambiental 3:367–379
6. Wong KV, Hernandez A (2012) A review of additive manufacturing. 2012, Article ID 208760
7. Angel R, Perez T, Roberson DA, Wicker RB (2014) Fracture surface analysis of 3D-printed tensile specimens of novel ABS-based materials
8. Stephens B, Azimi P, El Orch Z, Ramos T (2013) Ultrafine particle emissions from desktop 3D printers. Atmos Environ 79:334–339
9. Letcher T, Waytashek M, Material property testing of 3D-printed specimen in PLA on an entry-level 3D printer. IMECE2014-39379
10. Standard ASTM, D638 (2010) Standard test methods for tensile properties of plastics. ASTM International, West Conshohocken
11. Bellini A, Gu¨c¸eri S (2003) Mechanical characterization of parts fabricated using fused deposition modeling. Rapid Prototyping J 9(4):252–264

12. Appusamy AM et al (2019) Experimental studies on mechanical properties and characterization of parthenium short fibre reinforced polymer matrix composites. Int J Recent Technol Eng 7(4s):413–416

An Investigation on Wear Process Parameter of Metal Matrix Composite Using Optimization Technique

S. Vignesh Kumar and N. V. Dhandapani

Abstract Aluminium-reinforced with SiC composition was produced by stir casting method, and their wear resistance and friction coefficient are investigated on different load conditions and different reinforcement percentages. Pin-on-disc wear test apparatus is used to study the dry sliding wear properties of single-reinforced composites, and the same was investigated at a constant sliding velocity of 1.05 m/s and sliding distance of 1774 m over different loads of 10, 20 and 30 N for particle weight percentage ranges from 10, 15 and 20%. The reinforcement addition up to a 20% weight reduces the wear rate. As a result, the wear rate of the specimens decreases with the increasing sliding distance, and the wear rate of the specimens increases with increase in load. Vickers hardness is used to measure the hardness of the specimen at room temperature. By increasing in percentage of reinforcements, the hardness of the composite test specimens increases. The uniform distribution of reinforcement in matrix is assessed using scanning electron microscope image. A plan of experiment done through RSM technique is used to conduct experiments based on L_{15} orthogonal array. The optimum wear under the influence of applied load, time and reinforcement percentage was identified by ANOVA and the regression equations.

Keywords Aluminium alloy · Stir casting · Response surface methodology · ANOVA

1 Introduction

For the past few decades, conventional material such as cast iron has played important role in automotive components. Grey cast iron, for instance, is used to produce

S. Vignesh Kumar (✉)
Department of Mechanical Engineering, Bannari Amman Institute of Technology, Sathyamangalam, Erode, Tamil Nadu 638401, India
e-mail: vigneshkumar@bitsathy.ac.in

N. V. Dhandapani
Department of Mechanical Engineering, Karpagam College of Engineering, Coimbatore, Tamil Nadu 641032, India

G. Kumaresan et al. (eds.), *Advances in Materials Research*, Springer Proceedings in Materials 5, https://doi.org/10.1007/978-981-15-8319-3_51

automotive drum and disc brake, motor cylinders and pistons because of its low cost, good rigidity, good wear resistance, compressive strength, etc. However, grey cast iron is not a light material. The high density material will increase the fuel consumption in vehicle. The market price of the petrol is increasing continuously day to day. This study is based on the need to find an alternative material for automobile application. The alternative material should not only be lightweight but also must have properties—high strength, hardness, toughness and wear resistance. The superior properties aluminium-based MMCs make these materials attractive for automotive applications. Al–MMCs specimens with various particle sizes and weight percentage of SiC (10–15 μm) were tested to find the mechanical properties, tribological property and its characterization. By controlling the processing factors as well as the relative amount of the reinforcement material, it is possible to obtain a composite which satisfies the need [1].

2 Experimental Procedure

The production cost in preparing MMCs is high, so it is proposed to select alternate techniques which offer lower cost of production [2, 3]. Stir casting method is used in this study because its reinforcement distribution is uniform that leads to good mechanical and tribological properties and low production cost compared to other techniques as shown in Fig. 1b [4–8]. Pin-on-disc type wear tester as shown in Fig. 1a is used to check the dry sliding wear tests for different factors like load, sliding time and reinforcement percentage as shown in Table 1.

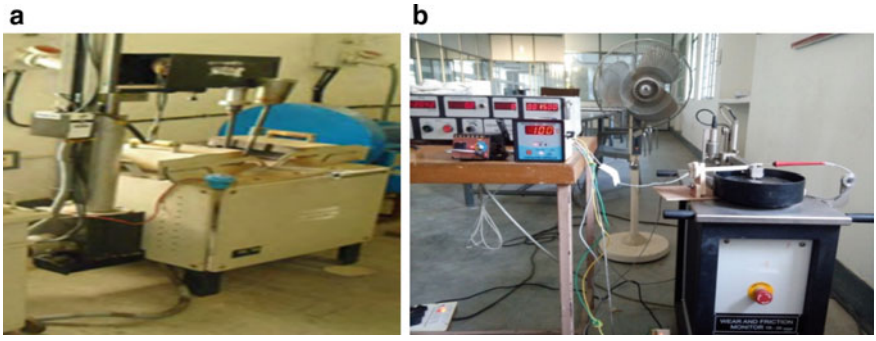

Fig. 1 **a** Stir casting setup. **b** Wear tester

Table 1 Process parameters and levels

Level	Load (N)	Time (min)	Reinforcement (%)
−1	10	5	10
0	20	10	15
+ 1	30	15	20

2.1 Optimization (Response Surface Methodology)

The experiments were conducted based on the standard orthogonal array [9–11]. In this article, an L_{15} orthogonal array was chosen, which has 15 rows corresponding to the number of tests and 03 columns at three levels and three factors, as shown in Table 2. This paper is focused only on response surface method approach by applying L_{15} orthogonal array from the obtained mechanical and tribological result. This approach is capable of determining significant factors which affect the properties of Al-MMC and determine the optimum conditions [9, 10, 12]. The objective of this present study is to optimize the minimum wear rate on Al 6061 metal matrix composite which depends on the process factors such as sliding time, load and percentage of the reinforcements using response surface method. The selected factor parameters for wear processing are (a) load, (b) sliding time and (c) reinforcement percentage of SiC. As the speed is set as constant, it is neglected for process factor. The experiments were conducted based on orthogonal array with level of parameters given in each row (Table 3).

Table 2 L_{15} orthogonal array

Standard order	Run order	Load (N)	Time (min)	Reinforcement (%)
15	1	0	0	0
6	2	1	0	−1
3	3	−1	1	0
14	4	0	0	0
9	5	0	−1	−1
4	6	1	1	0
12	7	0	1	1
5	8	−1	0	−1
1	9	−1	−1	0
13	10	0	0	0
8	11	1	0	1
10	12	0	1	−1
11	13	0	−1	1
7	14	−1	0	1
2	15	1	−1	0

Table 3 Experimental data

Standard order	Run order	Load (N)	Time (min)	Reinforcement (%)	Wear rate (μm)
15	1	20	10	15	199.8
6	2	30	10	10	385.0
3	3	10	15	15	161.1
14	4	20	10	15	199.8
9	5	20	5	10	247
4	6	30	15	15	298.3
12	7	20	15	20	186.6
5	8	10	10	10	230.2
1	9	10	5	15	158
13	10	20	10	15	199.8
8	11	30	10	20	240.2
10	12	20	15	10	289.5
11	13	20	5	20	159.8
7	14	10	10	20	123.1
2	15	30	5	15	278.6

3 Result and Discussion

3.1 Contour Plot of Wear Rate (Akima's Polynomial Method)

With respect to the plan of experiment, the investigated results and calculated values were obtained, and MINITAB® 16 a commercial software for DOE is used to analyse the results. The influence of dominant factors such as load, sliding time and reinforcement percentage was analysed based on contour. In the listed factor, percentage of reinforcement is primary dominating factor on the wear rate followed by load. The influence of conquered process parameters on wear rate is shown graphically in Figs. 2, 3 and 4

Figure 2 clearly shows that increase in percentage of reinforcement leads to less wear rate, where the reinforcement strengthens the material and increase in load tends to gradual increase of wear rate which is suitable for the application. The application like clutch plate requires high friction but less wear rate, so this composition will meet the demand of such application [10, 13–15]. Figure 3 states that increase in sliding time causes increase in wear, but after some duration of continuous operation (increased time), wear rate gets reduced, in which material gets naturally wear up to some extent and fitted for the application. Figure 4 satisfies the basic science concept that at 15 N of load wear rate lies in the range of 150–200 μm, as the load increased from 15 to 30 N, the wear rate also increases to the range of 300–350 μm, so the optimum load and time are chosen based on the application.

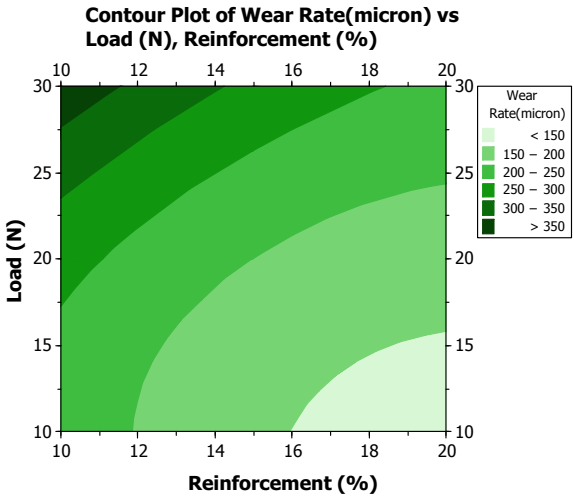

Fig. 2 Contour plot of load (N) versus reinforcement (wt%)

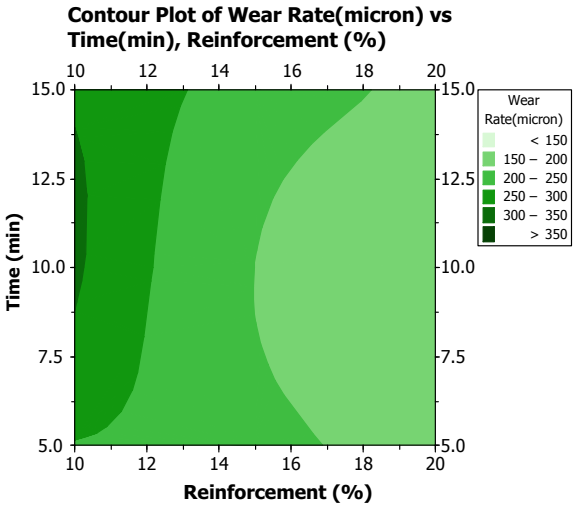

Fig. 3 Contour plot of time (min) versus reinforcement

3.2 Surface Plot of Wear Rate (Akima's Polynomial Method)

The influencing factors like load, sliding time and reinforcement percentage were analysed based on surface plot. The above surface plot graph satisfies the basic science concept. For strengthening the values in three-dimensional form, Figs. 5, 6 and 7 have been included. Among these parameters, percentage of reinforcement is primary dominating factor on the wear rate followed by load.

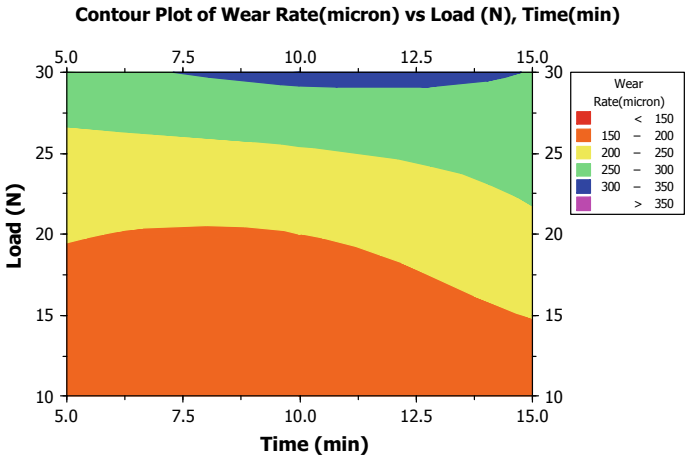

Fig. 4 Contour plot of load (N) versus time (min)

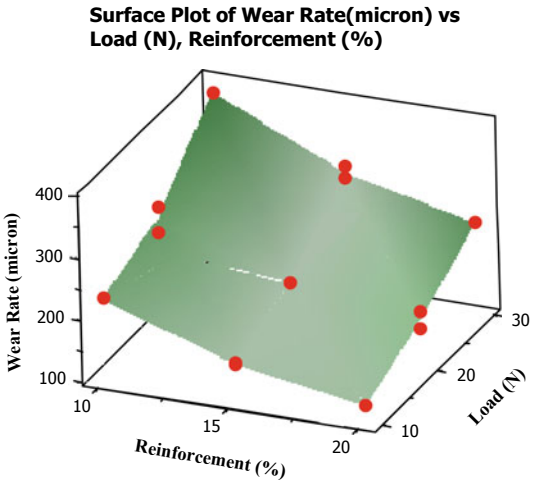

Fig. 5 Surface plot of wear rate (micron) versus load (N) and reinforcement (wt%)

3.3 Residual Plots for Wear Rate

Normality of the Data

This graph shows the residuals on the vertical axis and the independent variable on the horizontal axis. Linear regression model is appropriate for the data if the points in a residual plot are randomly dispersed around the independent variable; otherwise, a nonlinear model is more appropriate. Normality of the data was done by means of normal probability plot. The normal probability plot of the residuals for specific wear rate is shown in Fig. 8.

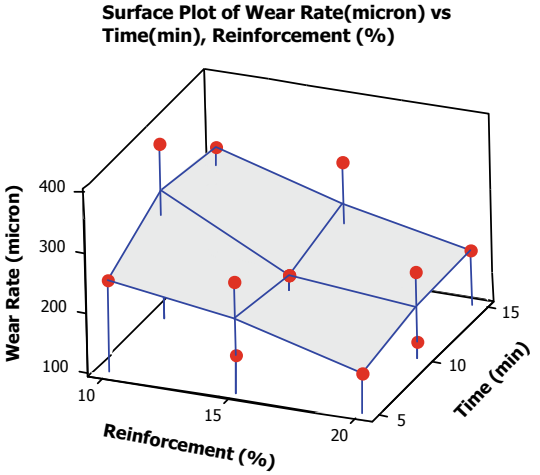

Fig. 6 Surface plot of wear rate (micron) versus time (min) and reinforcement

Fig. 7 Surface plot of wear rate (micron) versus time (min) and load (N)

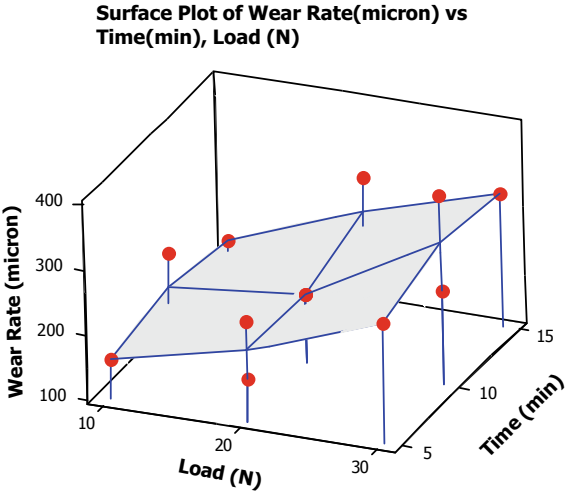

Fig. 8 Normality of wear

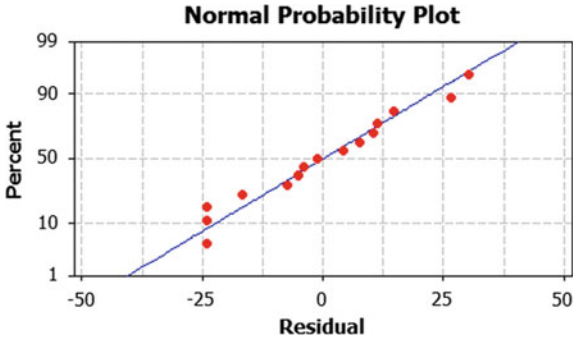

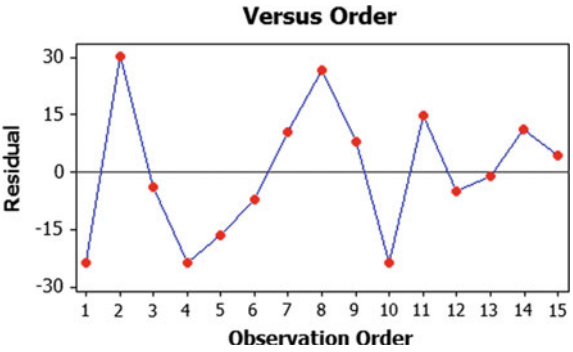

Fig. 9 Residual plot of wear

Table 4 Optimum level process parameter for wear rate

S. No.	Speed (rpm)	Load (N)	Time (Min)	Percentage of reinforcement (wt%)	Wear rate (μm)
1	400	20	15	20	186.6

Independency of the Data

Independency of the data was tested by plotting a graph between the residuals and the observation order. The residual plot for specific wear rate is shown in Fig. 9, which reveals that there was no predictable pattern observed because all the run residues lay on or between the levels of −30 to 30.

Analysis of Variance

Based on the analysis of these experimental results, the optimum conditions resulting in wear rate are shown in Table 4.

Table 5 shows the ANOVA result on the wear rate for SiC-reinforced composite. This analysis is done for 5% significance that is up to a confidence level of 95%. The linear regression model is shown in Eq. (1).

The regression equation is

$$\text{Wear Rate(micron)} = 234 + 6.62\,\text{Load(N)} + 2.30\,\text{Time(min)} - 11.0\,\text{Reinforcement (\%)} \quad (1)$$

$$R - \text{Sq(adj)} = 90.7\%$$

4 Conclusion

- Aluminium alloy with SiC reinforcement was prepared by stir casting setup, and required mechanical and tribological test was conducted.

Table 5 Analysis of variance for wear rate (μm)

Source	DF	Seq SS	Adj SS	Adj MS	F	P
Regression	6	61,039.4	61,039.4	10,173.2	19.05	0.000
Linear	3	60,553.6	60,553.6	20,184.5	37.79	0.000
Load (N)	1	35,072.8	35,072.8	35,072.8	65.66	0.000
Time (min)	1	1060.3	1060.3	1060.3	1.99	0.197
Reinforcement (%)	1	24,420.5	24,420.5	24,420.5	45.72	0.000
Interaction	3	485.8	485.8	161.9	0.30	0.822
Load (N) * time(min)	1	68.9	68.9	68.9	0.13	0.729
Load (N) * reinforcement (%)	1	355.3	355.3	355.3	0.67	0.438
Time (min) * reinforcement (%)	1	61.6	61.6	61.6	0.12	0.743
Residual error	8	4273.2	4273.2	534.2		
Lack-of-fit	6	4273.2	4273.2	712.2		
Pure error	2	0.0	0.0	0.0		
Total	14	65,312.6				

- The obtained result is optimized using RSM technique of L_{15} orthogonal array.
- As per this experiment result, 20% of reinforcement at 20 N of load gives the optimum result in wear which meets the need.
- The contour plot and surface plot show that increase in reinforcement and optimal load has less wear rate over other combinations.
- The dominant parameter in this paper is the load followed by percentage of reinforcement.
- The ANOVA test provides the optimal value which will be suitable for the application.

References

1. Mazahery A, Shabani MO (2011) Mechanical properties of squeeze- cast A356 composites reinforced with B_4C particulates. J Mater Eng Perform. Published online: 12 Feb 2011. https://doi.org/10.1007/s11665-011-9867-6
2. Basavarajappa S, Chandramohan (2005) Wear studies on metal matrix composites: a Taguchi approach. J Mater Sci Technol 21(6)
3. Dharmalingam S, Subramanian R (2010) Analysis of dry sliding friction and wear behavior of aluminium-alumina composites using Taguchi's techniques. J Compos Mater 44(18)
4. Dharmalingam R, Subramanian K, Vinoth S, Anandavel B (2010) Optimization of tribological properties in aluminum hybrid metal matrix composites using Gray-Taguchi method. J Mater Eng Perform. Published online: 21 Dec 2010. https://doi.org/10.1007/s11665-010-9800-4
5. Lee C, Kim YH, Han KS (1992) Wear behaviour of alurninium matrix composite materials. J Mater Sci 27:793–800
6. Benal MM, Shivanand HK (2007) Effects of reinforcements content and ageing durations on wear characteristics of Al (6061) based hybrid composites. Wear 262:759–763

7. Toropova LS, Eskin DG, Kharakterova ML, Dobatkina TV (1998) Advanced aluminum alloys containing scandium:structure and properties. Gordon and Breach Science Publishers, The Netherlands
8. Uvaraja VC (2014) Heat treatment parameters to optimize friction and wear behaviour of novel hybrid aluminium composites using Taguchi technique. Int J Eng Technol 6(2). ISSN 0975-4024
9. Ahamed RA, Asokan P, Aravindan S, Prakash MK (2010) Drilling of hybrid Al-5%SiCp-5%B_4Cp metal matrix composites. Int J Adv Manuf Technol 49:871–877
10. Uvaraja VC, Natarajan N (2012) Optimization on friction and wear process parameters using Taguchi technique. Int J Eng Technol 4(2):694–699
11. Mrówka-Nowotnik G, Sieniawski J, Wierzbiska M (2007) Analysis of intermetallic particles in AlSi1MgMn aluminium alloy. J Achieve Mater Manuf Eng 20:155–158
12. Correia DS, Gonçalves CV, da Cunha Jr SS, Ferraresi VA (2005) Comparison between genetic algorithms and response surface methodology in GMAW welding optimization. J Mater Process Technol 160(1):70–76
13. Vignesh Kumar S, Arivu Y (2015) Experimental investigation on mechanical and tribological behaviour of aluminium metal matrix composite & optimizing the wear characteristic for the application of clutch plate. Int J Innov Res Sci Eng Technol 4(4):207–220
14. Zhang Z, Chen X-G, Charette A (2009) Fluidity and microstructure of an Al–10% B4C composite. J Mater Sci 501:442–492
15. Modi OP (2014) Two-body abrasion of a cast Al–Cu, alloy—Al_2O_3 particle composite: influence of heat treatment and abrasion test parameters. Wear 248:100–111

Experimental Investigation on Tribological Behaviour of Alumina Nano Particles Reinforced with Aluminium Alloy Composite Material

K. Ramachandra Raju, G. Senthilkumar, Y. Arivu, D. Sathya, A. Sathya, and S. Sandeep

Abstract Aluminium alloy LM25 utilization is restricted in many requirements due to less wear resistance and frictional force resistance. In this paper, to enhance its properties for such applications, it is reinforced with nano Alumina (Al_2O_3). A series of LM25 Aluminium alloy with 0, 1, 1.5, 2% weight of nano Al_2O_3 particle were fabricated in liquid process technique using stir casting. The nanoparticles distributed uniformly in the metal by means of enhanced wettability of particles with the matrix LM25 Alloy as confirmed by doing Scanning Electron Microscopy. The tribological behaviour of LM25 Aluminium alloy with nano Al_2O_3 was investigated by pin on disc apparatus. The results show that nano Al_2O_3 particles addition with the LM25 alloy has improved the wear resistance of LM25 Aluminium alloy significantly. Also, friction coefficient can be made as an optimum. A comparison of wear performance and the friction of LM25 Aluminium alloy with metal matrix composite containing 1, 1.5 and 2% by weight was done. Increase in volume percentage of nano Alumina particles reinforcement has reduced the wear and frictional force.

Keywords Stir casting · Al_2O_3 · LM25 al alloy · Volume fraction · Wear rate · Frictional force

1 Introduction

Because of unique mechanical characteristics and low density, Aluminium is selected as the most important material for processing. Also coefficient of thermal expansion is low and high damping capacity is high that makes it useful in aerospace as well as mechanical fields [1]. Even though, its applications have been limited due to low wear resistance and lesser friction coefficient.

K. Ramachandra Raju (✉) · G. Senthilkumar · Y. Arivu · D. Sathya · A. Sathya · S. Sandeep
Department of Mechanical Engineering, Bannari Amman Institute of Technology, Sathyamangalam, Erode, Tamil Nadu 638401, India
e-mail: rajukrc@gmail.com

G. Kumaresan et al. (eds.), *Advances in Materials Research*, Springer Proceedings in Materials 5, https://doi.org/10.1007/978-981-15-8319-3_52

Different authors found that matrix dominated mechanical properties of material composites are improved by reinforcement of ceramic particles [2], for example, mica, alumina trihydrate, SiO_2, $CaCO_3$, glass beads, clay or fly ash. The improvements are increased hardness, strength, stiffness, heat distortion temperature, mold shrinkage, and also additionally processing cost reduced. It depends on preparing method and types [3], and on filler concentration [4, 5], shape, size [6, 7], and packing attributes, particle contents [8] also interfacial bonding with the matrix [9]. Particle size plays a significant role in improving properties of the MMCs, when the particle size is reduced from micro to nanoscale [10]. Nano Alumina are the ceramic particulate reinforcements have the ability to increase wear resistance and frictional resistance. Good fluidity, high strength and stiffness, hard and wear-resistant are the attractive properties of nano alumina particles [11].

In this work, nano Al_2O_3 particles reinforced with LM25 By using Stir casting method aluminum alloy was fabricated. Friction and properties of wear are considered as the critical properties during the selection and application of material [12, 13]. Wear resistance and frictional force resistance was determined by using Pin on disc apparatus. Microscopic visualization was found by using Scanning Electron Microscopy. Cylindrical pins are used for wear test, having diameter 10 mm and height 30 mm. The steel disk is used against which the cylindrical pin slides [14, 15].

2 Material and Methods

2.1 Materials and Stir Casting

In this work, we implemented two types of material i.e., matrix material and reinforcement material. LM25 aluminum alloy composition (% of weight) as shown in Table 1 is preferred for matrix material and nano alumina ($Al_2O_{3)}$ particles supplied by Alfa Aesar, United Kingdom are 40 nm for reinforcement material. The material was casted by using stir casting method.

The following four specimens were prepared

1. Pure LM25 Aluminium alloy
2. LM25 Aluminium alloy with 1% nano alumina ($Al_2O_{3)}$.
3. LM25 Aluminium alloy with 1.5% nano alumina ($Al_2O_{3)}$.
4. LM25 Aluminium alloy with 2% nano alumina ($Al_2O_{3)}$.

Initially, LM25 Al alloy was charged into furnace and heated to approximately 800 °C above the Al alloy liquid temperature. At that point, the mixer was brought

Table 1 Composition of aluminium alloy LM25%Wt

Cu	Si	Mg	Fe	Mn	Ni	Zn	Pb	Sn	Ti	Al
0.2	7.5	0.06	0.5	0.3	0.1	0.1	0.1	0.05	0.2	Balance

Fig. 1 Stir casted solidified sample

into the dissolve gradually down to stir the liquid metal. The particles of the Nano Al_2O_3 were preheated before mixing with the melting of the Al alloy. Once particle feeding is completed, a further 10 min of mixing was done. At that point, the liquid mixture was poured in the pre-heated form situated beneath the heater. The heater had a bottom tapping clause, which allowed heating and stirring to continue even during melt tapping. Cast samples made as shown in Fig. 1 have a diameter of 100 mm and a height of 200 mm.

2.2 Testing

Specimens were prepared by grinding with 220, 320, 600, 800, 1000 and 1200 grit papers respectively for metallographic observation. The polishing was completed on cloth using 3 and 1 μm diamond powder. Such experiments have been used to study the dispersion of the matrix reinforcement particles by scanning electron microscopy (SEM).

The microhardness test specimens were prepared as per ASTM E92 standard. The fabricated composites were machined to the diameter of 20 mm and length as 20 mm. The micro-vickers hardness values of the samples were measured on the polished samples using diamond cone indenter with a load of 100 g and 15 s as a holding time. For harness results, test was repeated three times to obtain a precise average value.

Wear has been defined as the displacement of material caused by hard particles or hard protuberances where these hard particles are forced against and moving along a solid surface. Two body sliding wear tests were carried out on prepared coated specimens. Computerized pin-on-disc wear test machine (Make: DUCOM, Bangalore) was used for these tests. The tangential friction force and wear in microns

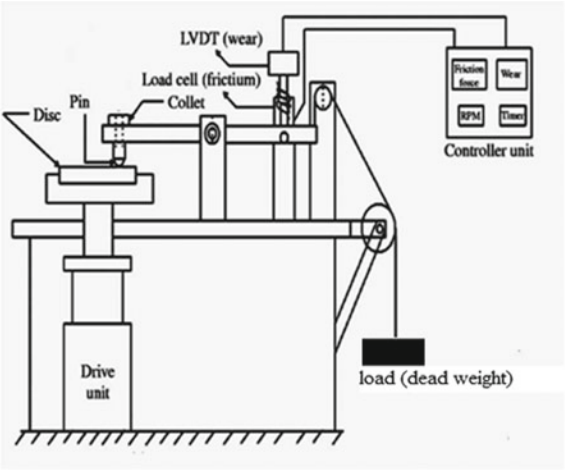

Fig. 2 Pin-on-disc wear testing machine

were monitored with the help of electronic sensors and data acquisition software WINDUCOM 2010. Wear test machine as shown in Fig. 2 was used for these tests.

A cylindrical pin of size 10 mm diameter and 30 mm length as shown in Fig. 3 are prepared from composite casting were loaded through a vertical specimen holder against horizontal rotating disc. Before testing, the flat surface of the specimens was abraded by using 2000 grit paper. The rotating disc was made of carbon steel of diameter 50 mm and hardness of 64 HRC. Wear tests were carried out at room temperature without lubrication for 2 min at a constant sliding velocity. Wear test

Fig. 3 Wear test specimens

parameters are disc speed 200RPM, Sliding distance 500 m and Load 10 N. Wear tests were carried out at room temperature without lubrication as per ASTM G99 standards. The principal objective of investigation was to study the wear rate and frictional force.

3 Result and Discussion

3.1 Micro Structural Visualization

The properties of the MMC s depend not only on the particle-matrix and the fraction of the volume but also on the distribution of strengthening particles and the bonding of the interface between the particle and the matrix. In reality, obtaining a homogeneous distribution is difficult. The process parameters above should therefore be optimized.

The aluminum matrix being very soft, the samples for microscopy are grinding and polishing resulting in the removal of the matrix reinforcement particles as well as marks being left on the surface. The nanocomposite displays a more homogeneous particle distribution and better wettability. The SEM microstructural visualization in Fig. 4 indicates pure LM25 and Figs. 5, 6 and 7 LM25 with Alumina nanoparticles of 1, 1.5 and 2% inferring uniform particle distribution.

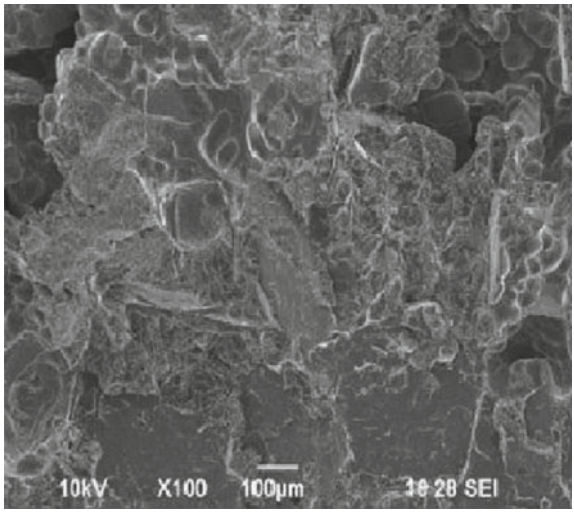

Fig. 4 Pure LM25 Al alloy

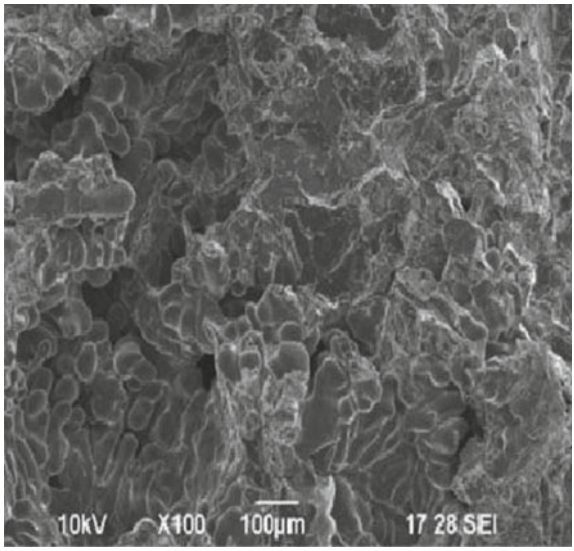

Fig. 5 LM25 Al alloy with 1% nano alumina

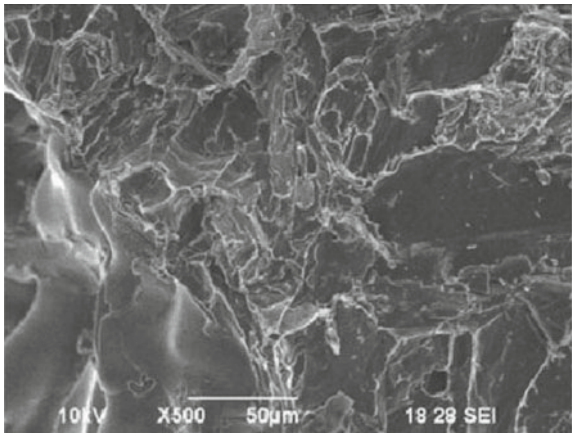

Fig. 6 LM25 Al alloy with 1.5% nano alumina

3.2 Micro Hardness Values

Hardness of the LM25 alloy and effect of reinforced alumina nanoparticles reinforcements are inferred from the Vickers hardness test results shown in Fig. 8. The hardness values of LM 25 are lesser compared to Alumina nanoparticles reinforcements.

The adding of alumina nano reinforcements enhanced the microhardness of composites by virtue of nanoparticles binding the LM25 alloy matrix and improving the hardness. The reinforcement's % increase also had the effect on increase of hardness.

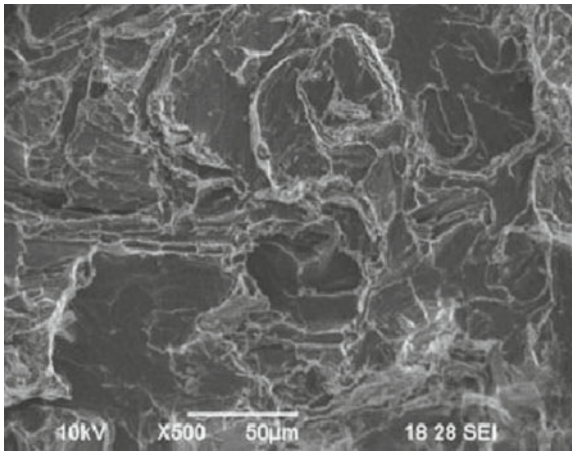

Fig. 7 LM25 Al alloy with 2% nano alumina

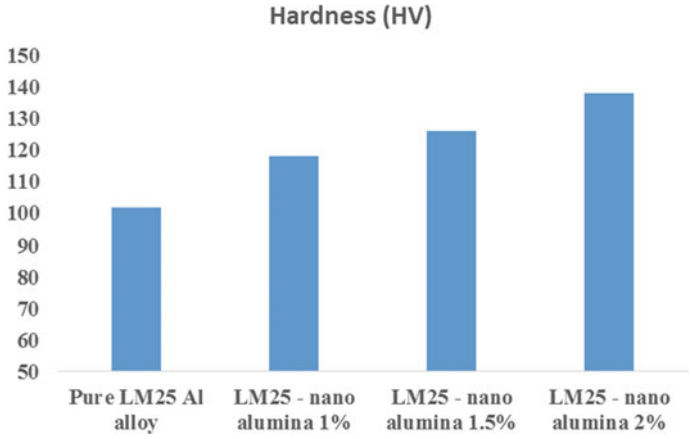

Fig. 8 Microhardness values of specimens LM25, 1, 1.5 and 2% of alumina

Increasing the % of reinforcements in the matrix leads to the increased hardness. Hardness improvement also leads to more effect on tribological behaviour and surface characteristics.

3.3 Tribological Behaviour

The Tribological behaviours wear properties and friction forces of the LM25 Aluminium alloy reinforced with nano alumina specimens were investigated using the graphs, obtained from Pin on disc apparatus as shown in Fig. 9. The composite

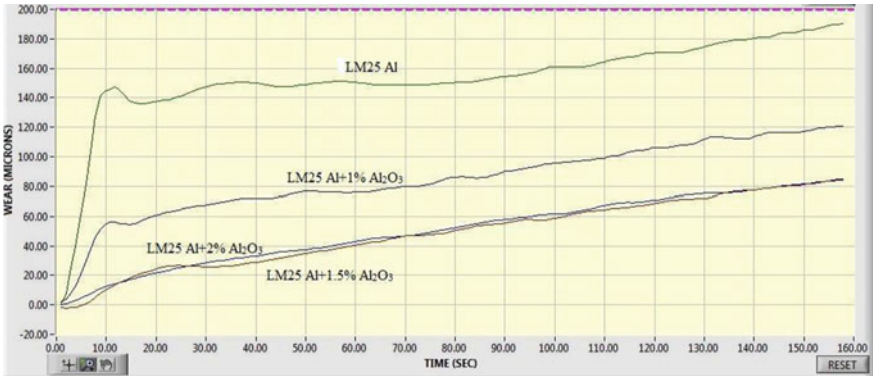

Fig. 9 Comparison of wear behaviour of four specimens

material (LM25 Aluminium alloy + 2% of nano Al_2O_3 shows high resistance to wear compared to other samples tested.

It is obvious from Fig. 10 that LM25 Aluminium alloy + 2% nano Al_2O_3 has less frictional force when compared to other samples and LM25 Aluminium alloy has high frictional force when compared to other samples.

The reduced wear and low frictional force attained by reinforcement of nano Al_2O_3 reveals that the nanoparticles distribution in the LM25 matrix has good bonding of particles of surface structure for smooth motion between bodies. Also, it is inferred that higher the % of reinforcement, better the surface condition for tribological behaviour. Table 2 shows the wear and frictional force for 155 s two-body wear test. Wear and frictional force had the effect of increase of reinforcements of nano Al_2O_3.

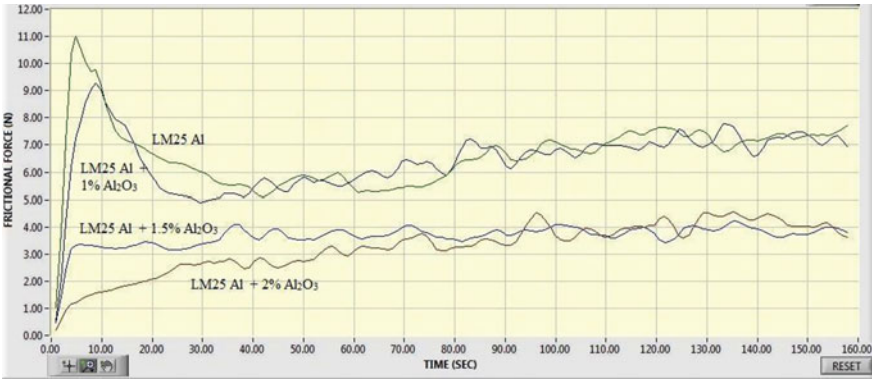

Fig. 10 Comparison of frictional force for different specimens

Table 2 Wear and Frictional force values of specimens

Sl. No.	Specimens	Wear (micro meters)	Frictional force (N)
1	Pure LM25 Al alloy	185	7.5
2	LM25—nano alumina 1%	120	7.0
3	LM25—nano alumina 1.5%	93	3.8
4	LM25—nano alumina 2%	80	4.2

4 Conclusion

The wear properties and friction behaviour of LM25 Aluminium alloy reinforced with nano alumina specimens were investigated by Pin on disc apparatus. The wear level of nano-composite aluminum alloy material decreased with the increase in nano-aluminum added in aluminum alloy LM25. The frictional strength of aluminum alloy material strengthened by nanocomposite decreased as the addition of nano aluminum in alloy LM25 increased. LM25 Aluminium alloy with 2% Al_2O_3 has low wear rate 80 μm and frictional force of 4.2 N. Hence, it is obvious that wear rate gets decreased with the addition of Al_2O_3 and friction coefficient can be made as an optimum one by the addition of nano Al_2O_3 particles.

References

1. Li G (2015) Friction & wear behaviour of nano-Al_2O_3 particles reinforced copper matrix composites. ASME J Tribol 137(1):1–7
2. Harichandran R, Selvakumar N (2016) Effect of nano/micro B4C particles on the mechanical properties of aluminium metal matrix composites fabricated by ultrasonic cavitation assisted solidification process. Arch Civ Mech Eng 16:147–158
3. Ibrahim IA, Mohamed FA, Lavernia EJ (1991) Particulate reinforced metal matrix composites—a review. J Mater Sci 26:1137–1156
4. Kai XZ, Li ZQ, Fan GL (2013) Enhanced strength and ductility in particulate-reinforced aluminum matrix composites fabricated by flake powder metallurgy. Mater Sci Eng 587:46–53
5. Ahmadi A, Toroghinejad MR, Najafizadeh A (2014) Evaluation of microstructure and mechanical properties of Al/Al_2O_3/SiC hybrid composite fabricated by accumulative roll bonding process. Mater Des 53:13–19
6. Suh YS, Joshi SP, Ramesh KT (2009) An enhanced continuum model for size-dependent strengthening and failure of particle reinforced composites. Acta Mater 57:5848–5861
7. Kady OE, Fathy A (2014) Effect of SiC particle size on the physical and mechanical properties of extruded Al matrix nanocomposites. Mater Des 54:348–353
8. Wang Z, Song M, Sun C (2010) Effect of extrusion and particle volume fraction on the mechanical properties of SiC reinforced Al–Cu alloy composites. Mater Sci Eng 527:6537–6542

9. Shorowordi KM, Laoui T, Haseeb ASMA (2003) Microstructure and interface characteristics of B_4C, SiC and Al_2O_3 reinforced Al matrix composites: a comparative study. J Mater Process Technol 142:738–743
10. Tjong SC (2007) Novel nanoparticle-reinforced metal matrix composites with enhanced mechanical properties. Adv Eng Mater 9(8):639–652
11. Zhou G (2009) Fretting behaviour of nano Al_2O_3 reinforced copper matrix composites prepared by co precipitation. Assoc Metallurgical Eng Serb 669(35):718–492
12. Agarwal R (2014) Synthesis and characterization of Al/Al3Fe Nano composite for tribological applications. ASME J Tribol 136(012001):1–9
13. Ahemad J (2013) Development of Al/Sic5%, Al/Sic10%, Al/Sic15%, metal matrix composite and its comparison with aluminium alloy-LM25 on tribological parameters. Int J Emerg Technol Adv Eng 3(9):545–549
14. Suresh SM (2011) Production and characterization of micro and nano Al_2O_3 particle-reinforced LM25 aluminium alloy composites. ARPN J Eng Appl Sci 6(6):94–98
15. Radhika N (2015) Studies on mechanical properties and tribological behaviour of LM25/SiC/Al_2O_3 composites. J Eng Sci Technol 10(2):149–155

Comprehensive Study of Hydrogenated Diamond-Like Carbon Coated AISI 5140 Alloy Steel

R. Sivakumar, P. Senthilkumar, M. Sreenivasan, and Ram Krishna

Abstract The tribological characteristics of a-C:H coating in varying thickness of H-DLC/AISI 5140 steel tribological contact in pin-on-disc tribometer test under dry sliding with diesel fuels used in this work. The influences of load, sliding distance, and sliding velocity on the coated and uncoated counter body friction and wear was investigated with a constant relative humidity of 25% was maintained. The conclusion showed that the a-C:H coating on the substrate offered higher tribological properties than the alternate coating material. The wear and friction coefficient of all substrates and H-DLC coated AISI 5140 steel substrate samples were analyzed then compared. The SEM and AFM instruments are used to study the surface topography and structural properties.

Keywords Friction · Wear · Hydrogenated diamond-like carbon · Pin-on-disc tribometer · Physical vapour deposition

1 Introduction

In internal combustion engines (ICEs), around 40% of power losses due to exhaust heat temperature, cooling the high-temperature components, and frictional losses in the automotive systems at high temperatures and peak load. Among 6–7% of the energy losses are due to friction and wear between valve train components. The flow efficiency and the working of the engine mainly rely on the valve system of the engine [1, 2]. For instance, the wear and resistance loss is significantly higher in valves distinguished to other drive components at high temperature mainly in exhaust valve. The increase in frictional and thermal losses through valve train components

R. Sivakumar (✉) · M. Sreenivasan · R. Krishna
Department of Mechanical Engineering, PACE Institute of Technology and Sciences, Ongole, Andhra Pradesh 523272, India
e-mail: ersivakumar123@gmail.com

P. Senthilkumar
Department of Automobile Engineering, Madras Institute of Technology, Chennai, Tamil Nadu 600044, India

G. Kumaresan et al. (eds.), *Advances in Materials Research*, Springer Proceedings in Materials 5, https://doi.org/10.1007/978-981-15-8319-3_53

can cause regional reduction in the efficiency of ICEs [3]. But diesel engine valves crafted from stainless steel are insufficient to meet the operating circumstances, such as high working temperature strength, friction and wear, corrosion and erosion [1]. Evidently, this sharpens the requirements for decreasing the wear and tear and friction, to stay the emissions low through the span of the engine, and presents a great challenge.

Over the decades, various industrialists and researchers are have become involved regarding enhancing the friction and wear characteristics for promising surface coating applications. A wear study reports that reduction in wear/friction will considerably cut back economic prices in regard to environmental advantages and conjointly improved the service lifetime of the parts [4]. Therefore various surface coatings such as Polytetrafluoroethylene (PTFE) and titanium nitrides for improving lubricity and wear resistance, however, it shows the poor performance [5]. Heat treatment of the ceramic coating results in a crack that shows in poor performance of the parts. Although WC and TiN coatings are noted for their superior hardness in lubricated condition, it offers the frictional coefficient between 0.4 and 0.8 which is comparatively higher in many cases. There are numerous tribology systems that can report a high wear resistance, low friction and superior tribological properties. The use of surface engineering is most generally used route so as to tailor surface structure and other properties of substrate material without changing bulk properties of the materials. The general techniques used for deposition of coating as, chemical vapor deposition/physical vapor deposition (CVD/PVD), radio frequency magnetron sputtering (RFMS) and ion beam deposition. Presently, research work have been concentrated on amorphous carbon [6, 7], carbon nanotubes (CNTs) [8], graphite-like carbon [9] so as to fabricate coatings with superior wear performance and improved durability of the engine parts. Amorphous carbon has superior friction and adhesion resistance with promising function in metal process [10]. The difficult tasks with amorphous coating have poor adhesion and as lead to fast wear by induced stress on extremely fine surfaces [11, 12]. It is even expressed that oxide (SiO_2) layer coating or Si doping can notably increase the DLC film adhesion properties. Hence, for the better adhesiveness among substrate and a-C:H coating with Si layer are incorporated during this study [13]. Even though many methods are used for examining mechanical and physical performance of CNTs/a-C:H coatings but still no customary technique is accessible for scheming tribological properties of coated materials.. To test tribological characteristics of CNTs/DLC, pin on disc (POD) apparatus are used with ambient pressure with appropriate relative humidity and temperature. The important parameters such as load, sliding velocity (SV) and sliding distance (SD) which affected the wear properties are studied. Recently most automotive parts are have been coated with DLC coatings, to increase tribological characteristics. Hence the wear and frictional loss have to be reduced considerably improving the durability of the components and engine performance [14].

In the present study, AISI 5140 low carbon steel used as substrates and H-DLC coating was deposited by the process of physical vapour deposition (PVD).

Table 1 Chemical composition of AISI 5140 steel (wt%)

C	Si	Mn	P	S	Ni	Cr	Mo	Cu	Ti	Co	Al
0.42	0.24	0.71	0.013	0.013	0.058	0.95	0.007	0.016	0.001	0.001	0.023

Tribological characteristics of the coatings were examined by pin-on-disc apparatus; the surface morphology and topography are examined using scanning electron microscope (SEM) and atomic force microscopy (AFM) respectively.

2 Materials and Methods

2.1 Sample Preparation

Here for the analysis, AISI 5140 low carbon alloy steel were chosen as a substrate for Kirloskar single-cylinder ICEs exhaust valve and their chemical structures are obtained using Optical Emission Spectrophotometer (OES) and the weight percentage is presented in Table 1.

2.2 Deposition of Coating

The deposition of a-C:H coating on substrate by sputtering process is shown in Figure 1a. The deposition process is fully automated and process computer is used

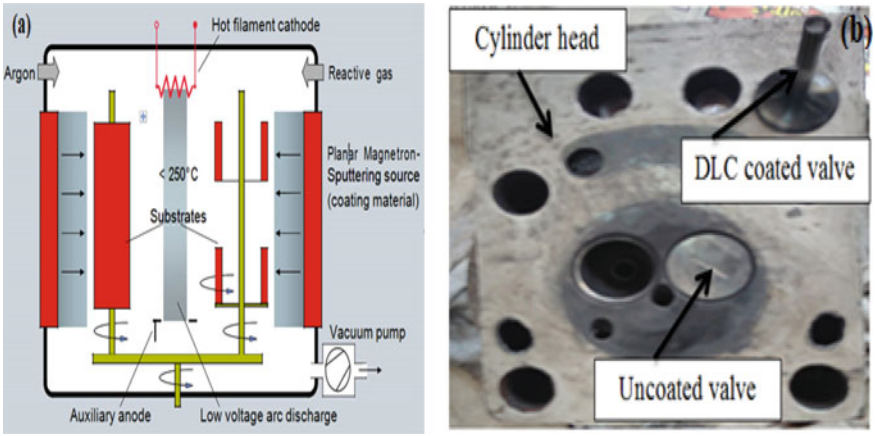

Fig. 1 **a** Schematic representation of sputtering process (*Courtesy* Oerlikon Balzers India Ltd., Bangalore, India). **b** Photographic view of exhaust valves

Table 2 Process parameters of sputtering process

Parameter	Coating	Substrate temperature (°C)	Nitrogen pressure (Pa)	Accelerating voltage (V)	Coating period (Min)
Set value	a-C:H	<250	1.5	110	120

to control the entire deposition system and begins with the substrates were cleaned ultrasonically for 6 min in acetone followed by 6 min of in ethanol and dried with a compressed filtered airflow. The sputtering process parameters are shown in Table 2 and Figure 1b Shows the photographic views of H-DLC coated exhausted valves. The structure and essential feature of the H- DLC coatings were measured by SEM and AFM instruments.

2.3 Characterizations

By using SEM with EDS (Zeiss Evo 18), characterization of coated and uncoated surfaces of AISI 5140 steel was done. Figure 2a displays the homogeneity and surface structure of the substrate and Fig. 2b displays the structure of the H-DLC coated substrates, which displays melted carbon globules, discharged from the cathode at high sliding velocity deposited on the substrate surface, and present as white and droplets spots [15]. Figure 3a, b displays the AFM images of 2D and 3D topography of H-DLC coated steel surface and the vertical deviation shows the surface roughness around 0.33 μm and grain size of 20–30 nm influenced by the substrate heat and bias [16].

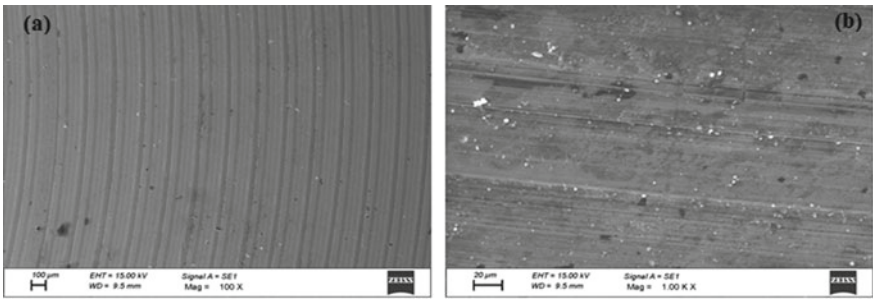

Fig. 2 SEM image of **a** uncoated AISI 5140. **b** H-DLC coated AISI 5140

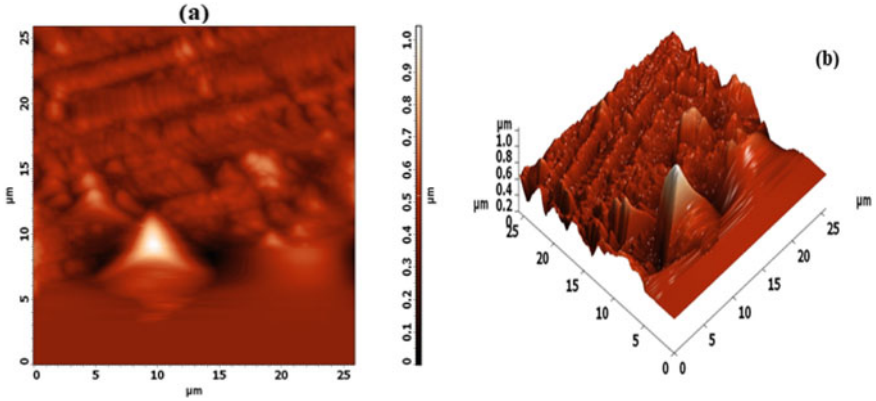

Fig. 3 AFM image of H-DLC coated AISI 5140 steel **a** 2D. **b** 3D topography

2.4 Pin-On-Disc Test

The objective of wear test (Model: ASTM 99, Ducom TR 20) is to find and decide the kind of coating superior for the diesel engine valves that desire less wear, friction and more service life. The performance test is conducted with various thickness of a-C:H coated exhaust valve such as 2, 3, 4, 5, and 6 µm to optimize the most effective coating thickness compared with base engine. Among the five different thickness of coating, 4 µm thickness valve is selected based on the engine performance characteristics at peak loads [17]. In the wear test all the samples were cleaned by ethanol then dried and the test was conducted at the laboratory temperature of 250 °C, the pin is fastened at right angles to the disc surface and also the disc revolves counter the pin with the size of 30 mm × 8 mm in diameter is employed for this study in a dry sliding condition, under a load of 10–30 N, sliding velocity(SV) of 0.5–1.5 m/s and the sliding distance (SD) of 300–900 m. The friction coefficient and were loss were measured by using a load cell and electronic weighing machine, with an accuracy of ±0.0001 gm. The wear loss values have been changed to a specific wear rate (SWR) by using Eq. (1) and also the worn surface structure and wear properties are studied using SEM.

$$\text{specific wear rate} = \frac{\text{wear mass loss}}{(\text{Applied load} * \text{Sliding distance})} (\text{gm/Nm}) \tag{1}$$

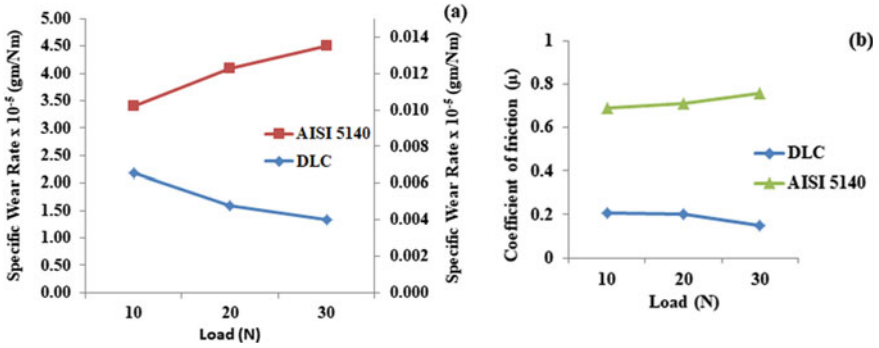

Fig. 4 Load versus. **a** Specific wear rate. **b** Friction coefficient

3 Results and Discussions

3.1 Effect of Load on Friction Coefficient (M) and Specific Wear Rate (SWR)

Figure 4a, b shows effect of load on the SWR and μ of the coated and uncoated substrates. The SWR of the coating decreases with increasing the load, however remains minimal compared to the substrates at all levels. The depth of penetration of the pin will increase in high loads meanwhile metallic element transfer between the contact surfaces, a higher degree of surface softening ends up in the smoothening of the contact surfaces, and ends up in the formation of tiny patches. This implied that the friction and wear rate of the uncoated steel increases, whereas for H-DLC it decreases at all levels [18].

3.2 Effect of Sliding Velocity on Friction Coefficient (M) and Wear Rate

Figure 5a, b shows, increase in SV, the μ and SWR also increased for the substrate due to friction, the micro-thermal softening take place which lessen the bond strength whereas, the a:c:H coating shows decrease in μ and SWR due to its high hardness. Therefore, were observed that increase in the sliding velocity decreases the frictional effect between the coated contact surfaces compared to the uncoated surfaces in dry conditions.

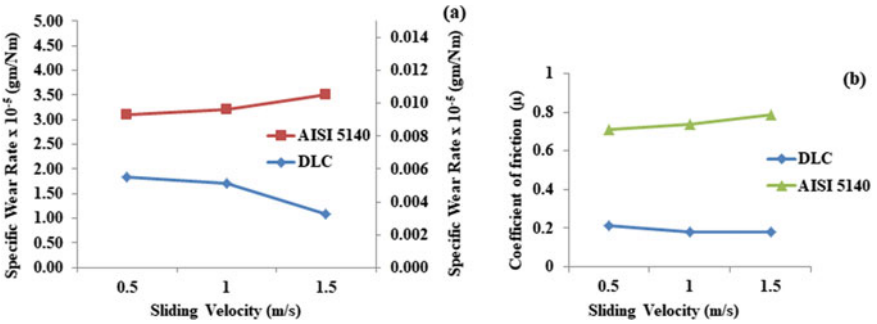

Fig. 5 Sliding speed versus **a** Friction coefficient. **b** Specific wear rate

3.3 Effect of Sliding Distance on Friction Coefficient (M) and Wear Rate

Figure 6a displays the effect of the sliding distance on the specific wear rate and also observed that specific wear rate is decreased as the growth of a transfer film on the counter layer that is generated because of physical variation in sliding. Among these basic impacts, the re-crystallization of the surface will in general be dominating at the contact interface during sliding. The re-crystalized layers keep an eye on re-arrange consequently bringing the basal planes parallel to the top surface of the coating with an enormous decrease in the wear rate [19]. Hence, increment in the sliding distance builds the wear domain, which prompts substantial distortion and temperature ascend in substrate while less in H-DLC coating on AISI 5140 steel because of high hardness and self-lubricating properties. The steady ascent in temperature makes milder the material and tears the surface, anyway at higher sliding distance the tribo layer is shaped, and this immerses the particular wear rate. The μ of coated AISI 5140 steel noticed diminishes pattern inside the scope of 0.15–0.13 because of the improvement of graphite-like lubricious tribolayer contrasted with substrates. As an increasing

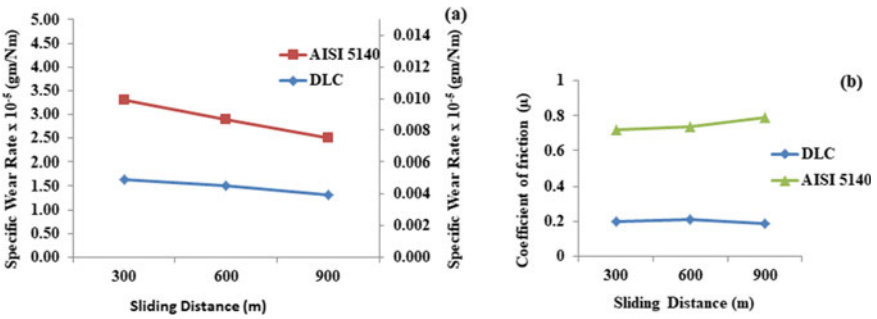

Fig. 6 Shows impact of sliding distance on **a** friction coefficient. **b** Specific wear rate

trend in load, the graphitized tribo layers are self-adjusted and the rubbing was decreased by means of active passivation [20].

3.4 Surface Analysis

Figure 7a, b shows the a-C:H coated substrates were not much affected compared to uncoated substrate. The coating gives better protection from plastic deformation, adhesive wear and ploughing in this manner no material misfortune happens though uncoated steel pin produces extraordinary surface imperfections and over the top wear. The outcome demonstrated that the H-DLC has diminished wear rate [21]. Figure 7a show the SEM appearance of the uncoated valve wear track and surface imperfections are studied in this investigation. The metallic surface is additionally stripped off because of the sliding force on the pin. Figure 7b showed that surface has not experienced any extreme harm and coated surface has better wear resistance. Figure 8a demonstrates the structure analysis of the uncoated steel, demonstrating appearance of abrasion pitting and debris in correlation with the coated substrate appeared in Fig. 8b. This is because of heat delivered in the contact region and coated surface is significantly prone to plastic deformation [22].

Figure 9 and 10 indicates that at 30 N load debris and grooves are occurred for substrates whereas no measurable wear is observed in the a-C:H coated AISI 5140 steel surface But in some case the inner CrN layer is exposed due to excess heat and the result showed the presence of foreign elements like Al, F, Na, Si, Ca. The DLC and Fe particles transfer inhibits the contact between the sliding surfaces; Hence, the a-C:H coating wear resistance had been improved [23].

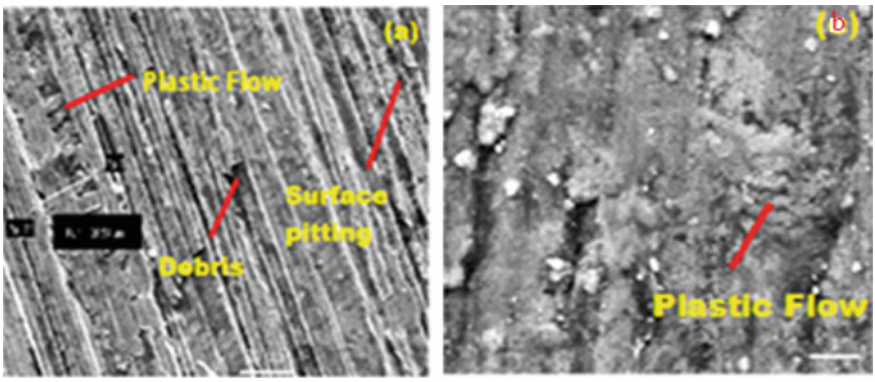

Fig. 7 SEM images of 10 N load, 1.5 m/s SV and 900 m SD of **a** substrate. **b** a-C:H

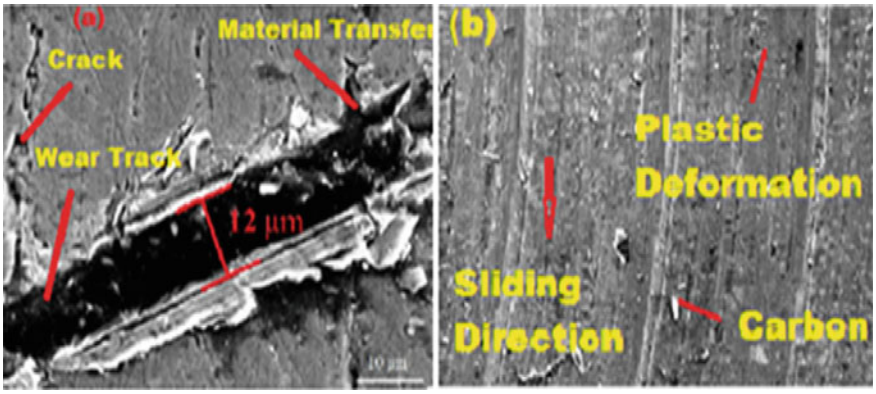

Fig. 8 SEM images of 20 N load 1.5 m/s SV and 900 m SD. **a** Substrates. **b** a-C:H

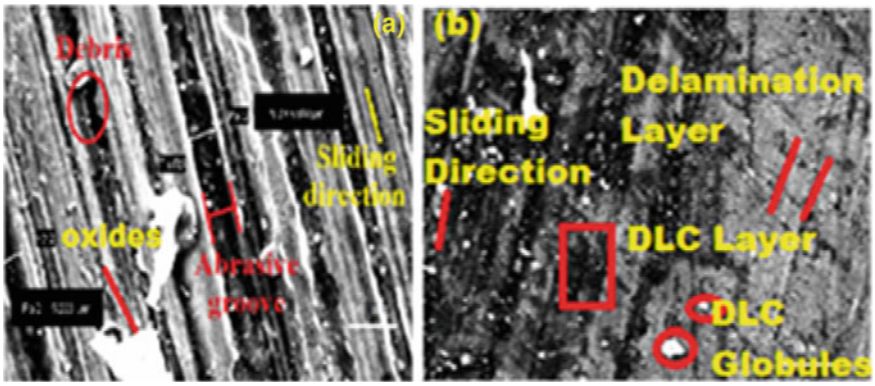

Fig. 9 SEM images of **a** substrate. **b** a-C:H under 30 N loads, SV of 1.5 m/s and 900 m SD

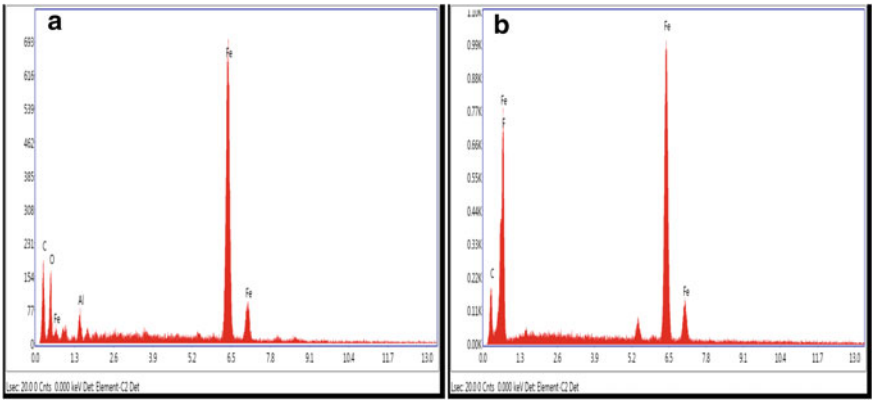

Fig. 10 EDS of **a** substrate. **b** a-C:H

4 Conclusions

The experimental work shows that friction coefficient and wear of the a-C:H film decreased significantly for increasing load and speed compared with uncoated materials, and also increased service life of the engine parts are noticed. The a-C:H coated sample wear rate and friction coefficients are decreased by three times and more than 5 times (SWR of 6.50×10^{-8} gm/Nm for DLC vs. 4.5×10^{-5} gm/Nm for substrate) compared with substrates. From the surface investigation, no quantifiable wear was found in a-C:H coating yet tiny patches were initiated. Finally, H-DLC could be used for larger area such as medical, cutting tools, aerospace, automotive components, etc.

References

1. Forsberg P, Hollman P, Jacobson S (2011) Wear mechanism study of exhaust valve system in modern heavy duty combustion engines. Wear 271:2477–2485
2. Voorwalda HJC, Coisse RC, Cioffi MOH (2011) Fatigue strength of X45CrSi93 stainless steel applied as internal combustion engine valves. Procedia Eng 10:1256–1261
3. Rahmani R, Rahnejat H, Fitzsimons B, Dowson D (2017) The effect of cylinder liner operating temperature on frictional loss and engine emissions in piston ring conjuction. J of App Energy 191:568–581
4. Szeri AZ (1980) Tribology: friction, lubrication, and wear. Tata McGraw-Hill
5. Beresnev VM, Bondar PBO, Lisovenko MO, Abadias G, Chartier GP, Kolesnikov PDA, Borisyuk VN, Mukushev BA, Zhollybekov BR, Andreev AA (2014) Comparison of tribological characteristics of nanostructured TiN, MoN, and TiN/MoN Arc-PVD coatings. J Frict Wear 35(5):374–382
6. Zhang F, Yan M, Lu C, Yin F (2018) Plasma nitriding of 2024 Al alloy deposited with Ti film: effects of N_2–H_2 ratio on microstructure evolution and mechanical properties. Adv Mater Process, 1–13
7. Liu DG, Liu ZL, JQ, Luo M, Wu YC, (2018) Structure and lubricated tribological behavior of silicon incorporated carbon nitride composite films deposited by magnetron sputtering. J Dia Rela Mater 82:115–123
8. Ashkinazi EE, Sedov VS, Petrzhik MI, Sovyk DN, Khomich AA, Ralchenko VG, Vinogradov DV, Tsygankov PA, Ushakova IN, Khomich AV (2017) Effect of crystal structure on the tribological properties of diamond coatings on hard-alloy cutting tools. J Frict Wear 38(3):252–258
9. Ren S, Huang J, Cui M, Pu J, Wang L (2017) Improved adaptability of polyaryl-etherether-ketone with texture pattern and graphite-like carbon film for bio-tribological applications. Appl Surf Sci 400:24–37
10. Zhao R, Steiner J, Andreas K, Merklein M, Tremmel S (2017) Investigation of tribological behaviour of a-C: H coatings for dry deep drawing of aluminium alloys. Tribol Int 118:484–490
11. Lin Y, Zia AW, Po ZZ, Shum W, Li KY (2017) Development of diamond-like carbon (DLC) coatings with alternate soft and hard multilayer architecture for enhancing wear performance at high contact stress. Surfe Coat Tchnol 320:7–12
12. Mano H, Ohana T (2017) Evaluation of anti-adhesion characteristics of diamond-like carbon film using high-frequency, linear-oscillation tribometer.Wear 386:188–194
13. Zhang T, Wan ZX, Ding JC (2018) Microstructure and high-temperature tribological properties of Si-doped hydrogenated diamond-like carbon films. Appl Surf Sci 435:963–973
14. Hoshi M (1984) Reducing friction losses in automobile engines. Tribol Int 17(4):185–189

15. Saravanan I, Perumal A, Vettivel AC, Selvakumar N, Baradeswarn A (2015) Optimizing wear behaviour of TiN coated SS 316L against Ti alloy using response surface methodology. Mat Des 67:469–475
16. Stetsko E, Stetsko YT (2019) Complex method of the composite nanocoatings formation. Adv Thin Films Nanostruct Mater Coat, 179–188
17. Sivakumar ER, Senthilkumar P (2018) Investigation on effect of H-DLC and TiN coated inlet and exhaust valve on performance, emission and combustion characteristics of a diesel engine. Taga J 14:333–346
18. Bull SJ (1995) Tribology of carbon coatings: DLC, diamond and beyond. Dia Related Mater 4:827–836
19. Haque T, Morina A, Neville A, Kapadia R, Arrowsmith S (2009) Effect of oil additives on the durability of hydrogenated DLC coating under boundary lubrication conditions. Wear 266:147–156
20. Erdemir A (2001) The role of hydrogen in tribological properties of diamond-like carbon films. Surf Coat Technol 292:146–147
21. Xiong J, He L (2018) Influence of surface buffer layer thickness and deposition rate on the release rate of silver ions in Ag–TiOx nanocomposites. Adv Mater Process, 75–81
22. Solis J, Zho H, Wang C, Verduzco JA, Bueno AS, Neville A (2016) Tribological performance of an H-DLC coating prepared by PECVD. App Surf Sci 383:222–229
23. Wang X, Song X, Jiang M, Li P, Hua Y, Wang K (2012) Modeling and optimization of laser transmission joining process between PET and 316L stainless steel using response surface methodology. Opt Las Technol 44:656–663

Review on Thermal Energy Storage with Phase Change Materials and Its Applications

Athimoolam Sundaramahalingam, S. Jegadheeswaran, Muthusamy Ponmurugan, and C. Sasikumar

Abstract Thermal energy storage using phase change materials (PCMs) is been of interest among the researchers for the past few decades because of its desirable properties like high storage density, isothermal heat transfer, chemical stability, etc. Although number of works have been done quantitatively, still the implementation of PCM incorporated latent heat thermal energy storage systems (LHTESS) in real-time applications is been limited because of its undesirable characteristics such as poor thermal conductivity, phase segregation, etc. This drives the scientific community to analyze the usage of thermal conductivity enhancers like fins, metal structures, metal balls, porous medium, nanomaterials, etc. with PCMs. This paper provides detailed information on thermal energy storage using phase change materials, heat transfer enhancement techniques and its applications.

Keywords Phase change material (PCM) · Thermal energy storage · Latent heat

1 Introduction

The steady rise in fuel prices and decrease in fossil fuel reserves drives the researchers to take efforts on usage of renewable energy sources effectively. The role of solar energy is vital among all the renewable energy sources because of its plentiful availability in nature. But today's technologists find it challenging to store solar energy and to convert it into useful form. Solar thermal energy storage in the form of latent heat has attracted the researchers because of its high storage capacity, constant temperature heat transfer and good chemical stability [1]. In spite of these advantages, it has practical difficulties for implementation like low thermal conductivity, phase segregation and subcooling of PCMs.

A. Sundaramahalingam (✉) · S. Jegadheeswaran · M. Ponmurugan · C. Sasikumar
Department of Mechanical Engineering, Bannari Amman Institute of Technology, Erode, Tamil Nadu 638401, India
e-mail: sundaraero.89@gmail.com

G. Kumaresan et al. (eds.), *Advances in Materials Research*, Springer Proceedings in Materials 5, https://doi.org/10.1007/978-981-15-8319-3_54

2 Phase Change Materials

Phase change Materials (PCMs)/Latent heat storage materials absorb and release heat by changing its phase so that the thermal energy is retained and released. They could store 5–14 times more energy than sensible heat storage materials of same volume. Even though PCMs are used for wide temperature ranges, these materials must have other suitable thermodynamic, kinetic and chemical properties for their use as latent heat storage materials. In fact, economic conditions and the ease of availability of these resources must also be taken into account [2].

2.1 Properties of PCMs

A good PCM should possess the following thermal, physical, kinetic, chemical and economical requirements [2, 3].

Thermal Properties

1. appropriate melting point
2. good phase change thermal energy storage
3. high thermal conductivity.

Physical Properties

1. high-density
2. little changes in volume during phase change
3. less vapour pressure.

Kinetic Properties

1. little or no sub-cooling during freezing
2. good crystallization properties
3. isothermal melting and solidification
4. phase segregation.

Chemical Properties

1. long-term chemical stability
2. capable of a reversible freezing/melting process
3. no degradation upon thermal cycles
4. corrosive resistance.
5. untoxic
6. no risk of fire

Economical Requirements

1. low price

2. recyclable
3. abundant in nature.

2.2 Classification

According to the change of state, PCMs are broadly classified as solid–solid, solid–liquid, liquid–gas or solid–gas as shown in Fig. 1.

Even though we have many kinds of PCMs, the interest on solid–liquid PCMs is increasing among the researchers due to their high latent heat of fusion and very less changes in volume during melting and solidification. Each PCM group has its own properties, forces and constraints. Table 1 displays the detailed comparison of various PCM classes. And it has been observed that Paraffin and salt hydrates are potential candidate as PCM comparing to the others [4].

Organic Solid–Liquid PCMs

Organic solid–liquid PCMs are further classified as paraffin and non-paraffin (fatty acid, alcohol and glycol). They are congruent, safe and have stable phase change temperatures and good nucleation characteristics.

Paraffin. Paraffin primarily consists of straight chain n-alkanes with a molecular formula of C_nH2_{n+2}. It has certain positive attributes like high latent heat of fusion, no subcooling and phase segregation problems, congruent melting and it is suitable for wide range of temperatures. Although it has various gains, its undesirable

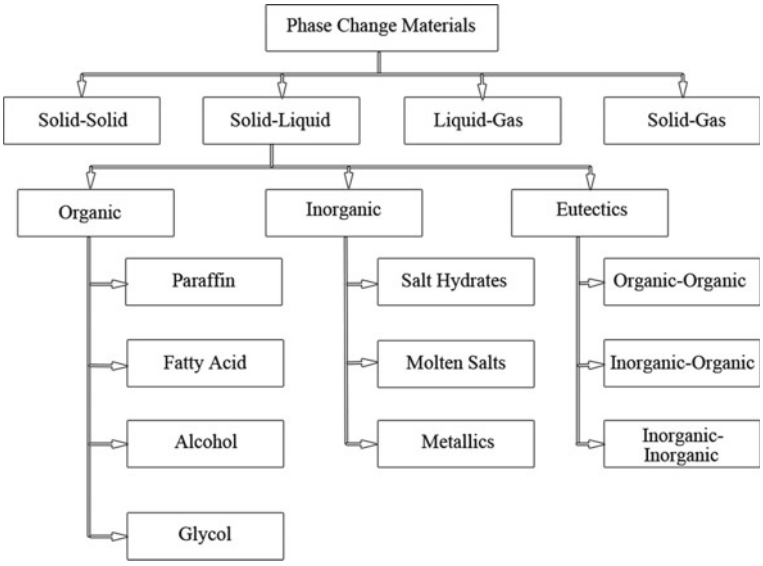

Fig. 1 Classification of phase change materials

Table 1 Comparison of phase change materials

Classification	Organic materials		Inorganic materials			Eutectics
	Paraffins	Fatty acids	Salt hydrates	Molten salts	Metallics	
Key features	1. Wide temperature range availability	1. In comparison to paraffins, every material has its own properties 2. Melts over a wide temperature range	1. Solid at room temperature and begins to dissolve into its own water crystal after reaching its melting point	1. Suitable for high-temperature ranges	1. Increased weight	1. Combination of two or more soluble components 2. Concurrent melting and solidification
Advantages	1. Inexpensive and non-corrosive 2. Suitable for wide temperature ranges 3. No subcooling and phase segregation problems 4. High latent heat of fusion 5. Congruent melting	1. Non-toxic 2. Less corrosive 3. Chemical and thermal stability 4. No subcooling	1. Low thermal resistance 2. High phase change heat 3. Less change in volume upon melting 4. Good storage density	1. Congruent fusion and solidification without separation of materials 2. High energy storage capacity	1. Low thermal resistance 2. Low specific heat 3. High phase change energy 4. Low vapour pressure	1. Sharp melting point 2. High energy storage density
Disadvantages	1. High thermal resistance 2. Medium energy storage density 3. Flammable 4. Incompatible with plastic containers	1. Expensive 2. Flammable	1. Corrosive 2. Subcooling and phase segregation 3. Thermally instable 4. Incongruent melting	1.Corrosive 2. Possess less enthalpy than salt hydrates	1. Expensive 2. Poor phase change heat capacity	1. Expensive 2. Low thermal conductivity 3. Corrosive 4. Thermal instability 5. Subcooling

(continued)

Table 1 (continued)

Classification	Organic materials		Inorganic materials			Eutectics
	Paraffins	Fatty acids	Salt hydrates	Molten salts	Metallics	
Method of improvement	1. Incorporation of fins 2. Addition of high conductive particles 3. Encapsulation 4. Addition of fire retardants	1. Addition of fire retardants 2. Addition of high conductive particles	1. Adding nucleating and thickening agents 2. Thermal conductivity promoters 3. Encapsulation 4. Stirring	1. Adding fillers 2. Adding nano-additives		

attributes (poor thermal conductivity, moderate energy storage capacity, flammability and incompatible with plastic containers) lead to slow melting and solidification rates.

Non-paraffin. The use of organic non-paraffin materials like esters, fatty acids, alcohols and glycol as PCM has also been done by various researchers. This is the largest category of PCMs for thermal energy storage in which the fatty acids ($CH_3(CH_2)_{2n}.COOH$) are protected by the carboxyl group (COOH) at the end. This makes them non-corrosive, non-toxic and chemically stable [5]. Moreover, the higher latent heat of fatty makes them attractive than paraffins.

Inorganic Solid–Liquid PCMs

Inorganic PCMs can also be classified as salt hydrates, molten salts and metallics. These materials possess improved enthalpy for phase changes than organics but the most important drawbacks are oxidation, undercooling, isolation, lack of thermal stability and separation of phases [5].

Salt Hydrates. Salt hydrates are considered as the combination of inorganic salts and water which forms a crystalline solid with chemical formula $AB.nH_2O$. Where A is cation, B is anion and n represents number of water molecules. The hydrate crystals break down at the melting point into anhydrous salt and water. One concern with the salt hydrates is the insufficient amount of water released from crystallization to dissolve all the salts which lead to incongruent melting. This problem could be resolved by (i) addition of chemicals which increases the solubility with more number of water molecules (ii) by mechanical stirring (iii) by adding thickening agents (iv) use of excess water.

Molten salts. Molten salts are inorganic salts with chemical formula X_nY_m and are best suited for high-temperature applications. Where X is cation and Y is anion. The enthalpy of molten salts is lower than salt hydrates and proper selection of high-temperature materials is necessary to withstand the aggressive chemical behaviour of molten salts.

Metallics. This inorganic PCM subgroup involves low fusion metals and metal eutectics. These are fit for elevated temperatures when volume is not a consideration, since it has high latent heat per unit volume. This category of PCMs possesses high conductivity, low specific heat and low vapour pressure.

Eutectics

Eutectics are a mixture of two or more compounds; each melts and freezes during crystallization creating a mixture of the component crystals. The variation may be organic-organic, inorganic-inorganic and inorganic–organic. It possesses concurrent melting and solidification behaviour and high energy storage density.

3 Heat Transfer Enhancement

Fan and Khodadadi [6] classified the thermal conductivity enhancers into two classes: fixed structures and free-form enhancers. The fixed structures possess high thermal conductivities and are available in various forms like fins [7, 8], porous matrices [9], rings [10] and balls [11].

Fins are being used in LHTESS to augment the heat transfer rate by increasing the heat transfer area. Moreover, it is necessary to understand whether or not the existence of fins actually provides significant performance improvements [12]. Lacroix and Benmadda [13] have investigated the mechanism of melting in a rectangular enclosure containing horizontal fins protruding from vertical heated walls. This numerical simulation showed the impact of the presence of fins and its length on melting rate. Shatikian et al. [14] reported that the temperature of fin's surface remains uniform throughout its length for thick fins and in case of thin fins of same length, temperature gradient is felt. In this view, thick fins are preferred than thin fins.

Incorporation of PCM in the voids of metal foam could also substantially improve the conductivity of the PCM, with the cost of reduced heat storage capacity. Aluminium foam [15], copper foam [16], nickel foam [17] and titanium dioxide foam [18] are currently the most commonly reported materials. The other alternative is to use high-conductivity materials that are free-moving. Researchers have long been examining the increase in conductivity of fluids by suspending high-conductivity nano/microparticles. Jegadheeswaran et al. [1] provides extensive information on the effects of nanoparticles on PCM properties through an extensive review of previous findings. The modified thermo-physical properties of PCM enhance the charging and discharging rates of LHTESS. Qu et al. [19] examined the effect of carbon nanoadditives (carbon nanofibres and carbon nanotubes) with paraffin-HDPE phase change material.

Though the metallic nanoparticles Cu [20], Al, Al_2O_3 [21], TiO_2 [22], CuO, ZnO, Y_2O_3 [22] have higher thermal conductivity, their chemical reaction tendency renders them undesirable for certain conditions. On the other hand, non-metallic particles are extremely stable and chemically inert, although they are of poor thermal conductivity. It was recently suggested that the thermal properties of PCMs could be improved by combining a small quantity of metallic nanoparticles with non-metallic nanoparticles [23]. Even though nanoparticles have favourable features, its cost makes them uneconomical which is 25 times more than micron-sized particles. Jegadheeswaran et al. [24] investigated the use of micro size copper particles in hydrated salts over a shell and tube LHTESS and found that microparticles are superior than nanosized particles in solidification.

Apart from the thermal conductivity enhancers, the geometry of the PCM container is also considered as an important factor since it directly influences melting and solidification time. Dhaidan et al. used CuO nanoparticles dispersed n-octadecane as PCM inside an annular container [25] and square container [26] to examine the effect of nanoparticle fraction on melting and recorded an increase in melting rate. Instead of double pipe arrangement [27], shell and tube arrangement [22, 24] provides

higher melting and solidification rate. Mahdi et al. [21] used triplex-tube arrangement with 8 longitudinal copper fins and Al_2O_3 nanoparticles to study the melting behaviour of RT82 PCM. Alizadeh et al. [28] employed similar triplex-tube arrangement with V-shaped fins. Elbahjaoui and El Qarnia [29] investigated the thermal performance of paraffin/Al_2O_3 latent heat storage unit using rectangular channel arrangement.

4 Applications

4.1 Solar Water Heating Systems

Solar water heaters are considered as the handiest alternative for electric and gas water heating systems. However, it requires a thermal storage system that is efficient to store solar energy. This could be done in the form of latent heat by using appropriate phase change materials. PCM installed water tank absorbs more amount of heat than the conventional storage tanks. Another major benefit of this type of storage tank are less fluctuations in temperature of stored water. Hasan et al. [30] examined the use of fatty acids (myrtical acid, palmitic acid and stearic acid) as PCM in solar water heater. Al-Kayiem et al. [31] has carried out a performance assessment of solar flat plate collector using nano copper-paraffin composite at various inclinations. Deng et al. [32] investigated the use of PCM in a mantle on domestic hot water tank to study its thermal performance. Similarly, the thermal stratification of solar water tank have been investigated by Huang et al. [33] using sodium acetate trihydrate as PCM.

4.2 Solar Air Heating Systems

PCM-based solar air heaters are also growing interest among the researchers due to its desirable advantages over the conventional air heaters. Kabeel et al. [34] evaluated the efficiency improvement of plate finned solar air heater using paraffin wax. And the results showed that the PCM enhances the daily efficiency of the device by 10.8–13.6%. An experimental and numerical study was done by Moradi et al. [35] to optimize the flow rate of air, paraffin-PCM amount, PCM thermal conductivity and the test results were well in accordance with the experimental findings.

4.3 Solar Cookers

Solar cooking is one of the solar energy's key applications. But the use of solar cookers is minimal since it could be used only during the sunshine hours. But the

usage and efficiency of these cookers could be increased if the heat energy is stored using PCMs.

4.4 Buildings

PCMs have been used for building applications for thermal energy storage since before 1980. Since some of the PCMs are hazardous in nature, the selection of PCM and fire-retardant additives are important for using it in buildings. These materials have been deployed for use in cooling and heating applications on a variety of places, including Trombe wall [36, 37], shutters [38, 39], wallboards [40, 41], under-floor [42, 43] and roof and ceiling boards [44, 45].

4.5 Off-Peak Electricity Storage

Several attempts were made by researchers to develop PCM storage systems for using it during off-peak electricity. Off-peak electricity can be used to melt the PCMs to store electrical energy as latent heat and it could be utilized by active systems when needed. Thus it helps to reduce the peak load and can therefore reduce electricity generation costs by holding demand almost constant.

4.6 Textiles

Reconfiguration of fabrics by the incorporation of PCMs is an intensively evolved technology. PCM incorporated fabrics increase the thermal resistance, particularly in transient conditions. These materials are found in various applications like sportswear, snowboard gloves, ice climbing, hill climbing, footwear, cycling, running, etc. PCM-containing textiles are known to be used as heat storing elements in buildings for accumulation of hotness/coldness in the form of window blinds and wallpapers, thus increasing thermal comfort in the room [46].

4.7 Photovoltaic (PV)-Thermal

Integration of PV panels and PCMs is quite popular now-a-days for the performance improvement in PV cells [47]. Huang et al. [48] conducted experiments to restrict the surface temperature increase of a PV panel using two PCMs (Rubitherm RT25 & granular GT40). Rubitherm RT25 controlled the PV module's surface temperature substantially and increased the system's electrical conversion efficiency in return. It

has been also suggested about the use of granular GT40 to regulate the PV module's surface temperature, but it is not as effective as RT25.

4.8 Microelectronics

The use of chalcogenide-based PCMs in non-volatile memory devices that can hold stored data even without electrical power, typically used in cell phones, computers, digital cameras and digital music players as secondary storage devices is quite popular. Such glasses switch from an amorphous state to a crystalline state and vice versa [49]. Chalcogenide glasses typically used in non-volatile memory devices are as, Ge–As–Se, Ge–Se–Te, As–Se, As–S, etc. [50]. Due to technological advances, temperature control of electronic devices become more important with extreme drop in circuit size and it could be achieved with the help of PCM-based cooling systems that makes the electronic devices work more efficiently.

5 Conclusion

This review focuses on recent advances in latent heat thermal energy storage materials and its applications. Besides the scope of versatile temperature ranges, PCMs with a higher thermal storage capacity minimize storage tank sizes/volume. Nevertheless, the extensive commercial use of PCMs remains limited and their reliability is less than sensible heat storage materials. Most of the recent works focus on stability, supercooling and reducing costs. The choice of organic, inorganic and Eutectic PCMs depends on the thermal, physical, chemical, kinetic properties and availability besides its latent heat, melting range, storage density, and thermal conductivity. Although inorganic PCMs display high storage density, conductivity and a comparatively greater melting point, they possess corrosiveness and experience supercooling. This work also summarizes the various potential applications for PCMs ranges from hot and cold storage in buildings to thermal storage in protective clothing.

References

1. Jegadheeswaran S, Sundaramahalingam A, Pohekar SD (2019) High-conductivity nanomaterials for enhancing thermal performance of latent heat thermal energy storage systems. J Therm Anal Calorim 3:1137–1166
2. Sharma A, Tyagi VV, Chen CR, Buddhi D (2009) Review on thermal energy storage with phase change materials and applications. Renew Sustain Energy Rev 13:318–345
3. Su W, Darkwa J, Kokogiannakis G (2015) Review of solid-liquid phase change materials and their encapsulation technologies. Renew Sustain Energy Rev 48:373–391

4. Khan Z, Khan Z, Ghafoor A (2016) A review of performance enhancement of PCM based latent heat storage system within the context of materials, thermal stability and compatibility. Energy Convers Manag 115:132–158
5. Giro-Paloma J, Martínez M, Cabeza LF, Fernández AI (2016) Types, methods, techniques, and applications for microencapsulated phase change materials (MPCM): a review. Renew Sustain Energy Rev 53:1059–1075
6. Fan L, Khodadadi JM (2011) Thermal conductivity enhancement of phase change materials for thermal energy storage: a review. Renew Sustain Energy Rev 15:24–46
7. Abdulateef AM, Abdulateef J, Mat S et al (2018) Experimental and numerical study of solidifying phase-change material in a triplex-tube heat exchanger with longitudinal/triangular fins. Int Commun Heat Mass Transf 90:73–84
8. Sathish Kumar TR, Jegadheeswaran S, Chandramohan P (2019) Performance investigation on fin type solar still with paraffin wax as energy storage media. J Therm Anal Calorim 136:101–112
9. Li W, Wan H, Lou H et al (2017) Enhanced thermal management with microencapsulated phase change material particles infiltrated in cellular metal foam. Energy 127:671–679
10. Velraj R, Seeniraj RV, Hafner B et al (1999) Heat transfer enhancement in a latent heat storage system. Sol Energy 65:171–180
11. Ettouney H, Alatiqi I, Al-Sahali M, Al-Hajirie K (2006) Heat transfer enhancement in energy storage in spherical capsules filled with paraffin wax and metal beads. Energy Convers Manag 47:211–228
12. Jegadheeswaran S, Pohekar SD (2009) Performance enhancement in latent heat thermal storage system: a review. Renew Sustain Energy Rev 13:2225–2244
13. Lacroix M, Benmadda M (1997) Numerical simulation of natural convection-dominated melting and solidification from a finned vertical wall. Numer Heat Transf Part Appl 31:71–86
14. Shatikian V, Ziskind G, Letan R (2008) Numerical investigation of a PCM-based heat sink with internal fins: constant heat flux. Int J Heat Mass Transf 51:1488–1493
15. Jiang J, Zhu Y, Ma A et al (2012) Preparation and performances of bulk porous Al foams impregnated with phase-change-materials for thermal storage. Prog Nat Sci Mater Int 22:440–444
16. Liu X, Rao Z (2019) Thermal diffusion and phase transition of n-octadecane as thermal energy storage material on nanoscale copper surface: a molecular dynamics study. J Energy Inst 92:161–176
17. Xiao X, Zhang P, Li M (2014) Effective thermal conductivity of open-cell metal foams impregnated with pure paraffin for latent heat storage. Int J Therm Sci 81:94–105
18. Li Y, Li J, Deng Y et al (2016) Preparation of paraffin/porous TiO_2 foams with enhanced thermal conductivity as PCM, by covering the TiO_2 surface with a carbon layer. Appl Energy 171:37–45
19. Qu Y, Wang S, Tian Y, Zhou D (2019) Comprehensive evaluation of Paraffin-HDPE shape stabilized PCM with hybrid carbon nano-additives. Appl Therm Eng 163:114404
20. Wu SY, Wang H, Xiao S, Zhu DS (2012) An investigation of melting/freezing characteristics of nanoparticle-enhanced phase change materials. J Therm Anal Calorim 110:1127–1131
21. Mahdi JM, Nsofor EC (2017) Melting enhancement in triplex-tube latent thermal energy storage system using nanoparticles-fins combination. Int J Heat Mass Transf 109:417–427
22. Khan Z, Khan ZA, Sewell P (2019) Heat transfer evaluation of metal oxides based nano-PCMs for latent heat storage system application. Int J Heat Mass Transf 144:118619
23. Chamkha AJ, Doostanidezfuli A, Izadpanahi E, Ghalambaz M (2017) Phase-change heat transfer of single/hybrid nanoparticles-enhanced phase-change materials over a heated horizontal cylinder confined in a square cavity. Adv Powder Technol 28:385–397
24. Jegadheeswaran S, Pohekar SD, Kousksou T (2012) Investigations on thermal storage systems containing micron-sized conducting particles dispersed in a phase change material. Mater Renew Sustain Energy 1:0005–0007
25. Dhaidan NS, Khodadadi JM, Al-Hattab TA, Al-Mashat SM (2013a) Experimental and numerical investigation of melting of NePCM inside an annular container under a constant heat flux including the effect of eccentricity. Int J Heat Mass Transf 67:455–468

26. Dhaidan NS, Khodadadi JM, Al-Hattab TA, Al-Mashat SM (2013b) Experimental and numerical investigation of melting of phase change material/nanoparticle suspensions in a square container subjected to a constant heat flux. Int J Heat Mass Transf 66:672–683
27. Ahmad W, Syed KS, Ishaq M et al (2017) Numerical study of conjugate heat transfer in a double-pipe with exponential fins using DGFEM. Appl Therm Eng 111:1184–1201
28. Alizadeh M, Hosseinzadeh K, Shahavi MH, Ganji DD (2019) Solidification acceleration in a triplex-tube latent heat thermal energy storage system using V-shaped fin and nano-enhanced phase change material. Appl Therm Eng 163:114436
29. Elbahjaoui R, El Qarnia H (2017) Transient behavior analysis of the melting of nanoparticle-enhanced phase change material inside a rectangular latent heat storage unit. Appl Therm Eng 112:720–738
30. Hasan A*, Sayignt AA (1994) Some fatty acids as phase-change thermal energy storage materials Renew Energy 4:69–76
31. Al-Kayiem HH, Lin SC (2014) Performance evaluation of a solar water heater integrated with a PCM nanocomposite TES at various inclinations. Sol Energy 109:82–92
32. Deng J, Furbo S, Kong W, Fan J (2018) Thermal performance assessment and improvement of a solar domestic hot water tank with PCM in the mantle. Energy Build 172:10–21
33. Huang H, Wang Z, Zhang H et al (2019) An experimental investigation on thermal stratification characteristics with PCMs in solar water tank. Sol Energy 177:8–21
34. Kabeel AE, Khalil A, Shalaby SM, Zayed ME (2017) Improvement of thermal performance of the finned plate solar air heater by using latent heat thermal storage. Appl Therm Eng 123:546–553
35. Moradi R, Kianifar A, Wongwises S (2017) Optimization of a solar air heater with phase change materials: experimental and numerical study. Exp Therm Fluid Sci 89:41–49
36. Li S, Zhu N, Hu P et al (2019) Numerical study on thermal performance of PCM Trombe Wall. Energy Procedia 158:2441–2447
37. Leang E, Tittelein P, Zalewski L, Lassue S (2017) Numerical study of a composite Trombe solar wall integrating microencapsulated PCM. Energy Procedia 122:1009–1014
38. Silva T, Vicente R, Amaral C, Figueiredo A (2016) Thermal performance of a window shutter containing PCM: numerical validation and experimental analysis. Appl Energy 179:64–84
39. Alawadhi EM (2012) Using phase change materials in window shutter to reduce the solar heat gain. Energy Build 47:421–429
40. Peippo K, Kauranen P, Lund PD (1991) A multicomponent PCM wall optimized for passive solar heating. Energy Build 17:259–270
41. Neeper DA (2000) Thermal dynamics of wallboard with latent heat storage. Sol Energy 68:393–403
42. Athienitis AK, Chen Y (2000) The effect of solar radiation on dynamic thermal performance of floor heating systems. Sol Energy 69:229–237
43. Lin K, Zhang Y, Xu X et al (2004) Modeling and simulation of under-floor electric heating system with shape-stabilized PCM plates. Build Environ 39:1427–1434
44. Lu S, Chen Y, Liu S, Kong X (2016) Experimental research on a novel energy efficiency roof coupled with PCM and cool materials. Energy Build 127:159–169
45. Srinivasan PSS, Ravikumar M (2014) Heat transfer analysis in PCM-filled RCC roof for thermal management. J Mech Sci Technol 28:1073–1078
46. Jaworski M (2019) Mathematical model of heat transfer in PCM incorporated fabrics subjected to different thermal loads. Appl Therm Eng 150:506–511
47. Browne MC, Norton B, McCormack SJ (2015) Phase change materials for photovoltaic thermal management. Renew Sustain Energy Rev 47:762–782
48. Huang MJ, Eames PC, Norton B (2006) Phase change materials for limiting temperature rise in building integrated photovoltaics. Sol Energy 80:1121–1130
49. Atwood G (2008) Phase-change materials for electronic memories. Science (80) 321:210–211
50. Mehta N (2006) Applications of chalcogenide glasses in electronics and optoelectronics: A review. J Sci Ind Res (India) 65:777–786

A Review on Passive Cooling Methods for Green Energy Buildings

Muthusamy Ponmurugan, M. Ravikumar, and Athimoolam Sundaramahalingam

Abstract Due to the population growth, the energy demand for thermal comfort for human increases. The global warming also rises the temperature of the universe. The residential demands for electricity are electric lighting, air-conditioning, and household appliances. Fifty percentage of the power supply is consumed by the building sector in economically developing countries. The natural cooling methods are not supportive to meet the requirement. Heat dissipation, heat reduction, and thermal management are passive cooling techniques. For these, storage of energy is needed and its role is vital in power generation management. The suitable technology is to be selected, and it depends on so many factors. Many investigations have been done to reduce the cooling load of a building through reflective and radiative roofs. It is not easy to adopt a particular technology universally. This review reveals the reducing, modifying heat gains as well as the removing internal heat by considering the factors involved in these. It paves the way to select the appropriate technology that plays a dominant role for the particular requirement.

Keywords Passive cooling · Phase change materials · Coating on ceilings · Cool roof · Thermal storage

1 Introduction

"Buildings are a key driver of energy demand, and developments within the sector such as the growing uptake of air conditioners are having a big impact on energy and environmental trends at the global level," said Dr. Fatih Birol [1], Executive Director of the International Energy Agency (IEA). "If we do not make buildings more efficient, their rising energy use will impact us all, whether it be through access to affordable energy services, poor air quality, or higher energy bills." The building sector includes both residential and commercial. The building sector takes in around

M. Ponmurugan (✉) · M. Ravikumar · A. Sundaramahalingam
Department of Mechanical Engineering, Bannari Amman Institute of Technology, Sathyamanglam, Erode District, Tamil Nadu 638401, India
e-mail: ponmuruganm@bitsathy.ac.in

G. Kumaresan et al. (eds.), *Advances in Materials Research*, Springer Proceedings in Materials 5, https://doi.org/10.1007/978-981-15-8319-3_55

34% of the total energy consumption probably in most countries. The residential demands for electricity are electric lighting, air-conditioning, and household appliances. Fifty percentage of the power supply is consumed by the building sector in economically developing countries. In developed countries, the economic growth leads to the increase of residential demand for electricity. They transform the living standards to a higher level. Cooling technologies for buildings are broadly classified into two types, namely active cooling and passive cooling. Electricity is needed to produce the cooling effect in active cooling method. Natural processes and passive technologies are used in passive cooling method. The advantages of the later method are the absence of power source and low-grade energy usage. Of many alternative energy sources methods, passive cooling method is the best among the existing methods.

2 Classification of Passive Cooling Methods for Green Energy Buildings

There are three ways of cooling the buildings, viz. protecting the entry of solar heat into the building, modulating the heat inside the building, and dissipating the heat from the building. The classification of passive cooling methods for buildings is shown below.

1. Reducing heat gains
   - (i) Microclimate—Vegetation, landscaping, water surfaces
   - (ii) Solar control—Aperture, glazing, shading
2. Modifying heat gains
   - (i) Thermal mass without energy storage
   - (ii) Thermal mass with energy storage by PCM enhanced ventilation/walls/wallboard/roof/
   - (iii) Night ventilation
3. Removing internal heat (heat dissipation technique)
   - (i) Free cooling with thermal energy storage
   - (ii) Natural cooling without thermal energy storage
     - (a) Evaporative cooling
     - (b) Radiative cooling via paints, movable insulation, flat plate air cooler
   - (iii) Natural ventilation without thermal energy storage
     - (a) Single-sided ventilation
     - (b) Wind-driven cross-ceiling
     - (c) Buoyancy-driven stock ventilation through Trombe wall/solar chimney.

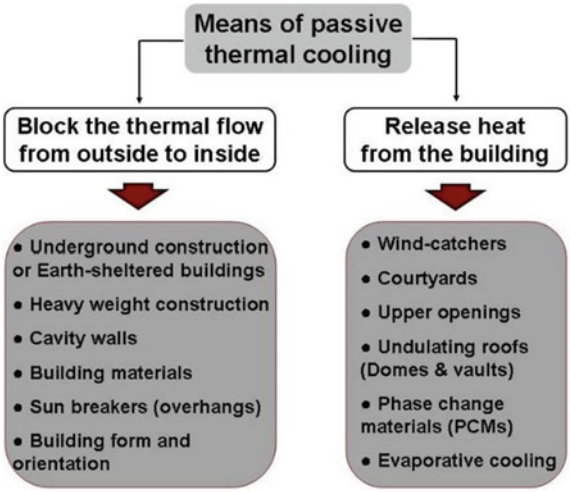

Fig. 1 Means of passive cooling

Heat can be released from buildings through wind-catchers, courtyards, undulating roofs, or by using phase change materials, evaporative cooling. Thermal flow can be blocked to the buildings by some techniques. These are illustrated in Fig. 1. Heat dissipation, heat reduction, and thermal management are passive cooling techniques. For these, storage of energy is needed and its role is vital in power generation management. Energy can be stored either for a short period or for a long period. "Short-term energy storage" is meant for storing the energy for hours, whereas "long-term energy storage" is meant storing the energy for days. But, many energy sources are intermittent in nature. Solar energy is available only during the daytime, and it has to be stored by efficient thermal energy storage to utilize during the night. Many researchers have attempted to utilize the passive cooling technologies in global warming affected countries. But the challenges for achieving this are more [2], and the sustainability is very less in those countries. This work aims at reviewing the various passive cooling methods for the green energy buildings and the challenges to utilize the technologies in hot countries.

3 Passive Cooling Techniques

The passive cooling techniques for heat prevention mainly focus on the reduction of air temperature. This can be approached by radiation loss, conductive loss, reducing the thermal mass, providing microclimate and ground cooling. The buildings are directly in contact with the atmospheric air and the ground (earth). The buildings act as a direct contact earth–air heat exchanger. The vegetation, landscaping, and providing water surfaces are the techniques to provide microclimate. Shading, night sky radiation, aperture, glazing are the other passive cooling techniques. Different

phase change materials are employed in the ceilings, wallboards, roof, and this is one of the effective techniques to reduce the heat gain [3].

3.1 Reducing Heat Gains

Combustion of fuels results in high pollution as the electricity demand has been increasing due to population growth. Maintaining internal air quality (IAQ) standards for air-conditioning engineers has become a challenge in the recent past. The technologies have changed their gears to move to cool materials for roofs as well as walls of the buildings. The materials which have high reflecting and emitting characteristics are needed for this. Synnefa et al. [4] found that the maximum difference between the solar reflectance of a conventional color coating and cool color coating is 0.22 with a corresponding surface temperature difference of 10.28 °C. In ancient days, the solar reflectance was in the range of 0.05–0.25. Nowadays, it has improved a lot around 0.30–0.45 reported by Santamouris and Asimakopoulos DN in their book [5]. Shen et al. [6] studied the impact of reflective coatings on thermal comfort, energy consumption, air temperature, globe temperature, and building surface temperatures experimentally. Packett [7] concluded that by applying two coats, i.e., an appropriate primer and a gloss white acrylic paint, over it will be the most effective solution. Suehrcke et al. [8] suggested using a light or reflective roof color to achieve the efficient heat reduction in the roof. He emphasized that an R-value can be assigned to the reflectivity of a roof surface. Hosseinia et al. [9] found that for the largest energy demand in the world cool roof coating with less insulating material is recommended. They concluded that higher energy saving can be obtained in real life by an application of cool roof in the long term. Gupta et al. [10] conducted experiments on the sites the two office rooms located in the central workshop premises near Katra town in Reasi District of the Indian state of Jammu and Kashmir Katra is located at 32.98 °N, 74.95 °E and has an average elevation of 754 m (2474 ft). They analyzed the heat reduction by cool roof pavements and found that the maximum percentage of heat reduction was 80%. The impact of using cool roof technologies on the thermal comfort of the office buildings were discussed in a report of cool roof kit [11]. Suriya Pradap Singh et al. [12] compared the green roof and white roof and concluded that white roofs are three times more effective than green roofs in cooling down the neighborhood. Cement-based materials in wall and roof ceilings are useful in tropical weathers as they are extremely resistant to hot and cold temperature.

3.2 Modifying Heat Gains

Heat gains can be modified either by free cooling or changing the thermal mass. Phase change materials are incorporated for both methods. Analysis of natural cooling of building with phase change materials by conducting experiments was

done by Srinivasan and Ravikumar [13], Madhumathi and Sundarraja [14], Heier et al. [15] combined the different thermal energy storage techniques for buildings and presented. A study [16] shows that by adopting cool roofs, the consumption of electricity can be decreased by 25%. The methods of modifying heat gains are illustrated in Fig. 2. Pasupathi and Velraj [17] explained the various effects of phase change material in building roof for year round thermal management and applied in residential and commercial establishments [18].

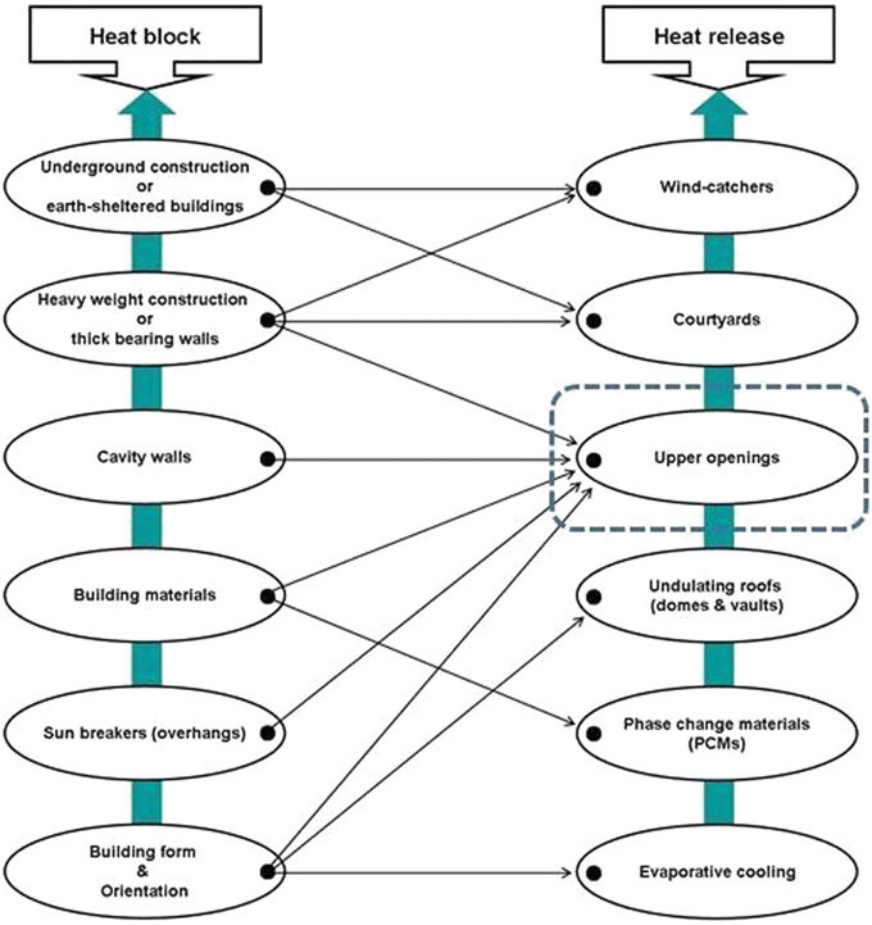

Fig. 2 Ways of modifying heat gains

3.3 Heat Dissipation Technique (Remove Internal Heat)

Radiation means the release of heat in the form of electromagnetic waves. The photons having energy of $E = h\nu$ are released continuously, and there is no zero radiating materials in practice according to third law of thermodynamics. This radiation heat release stops when the system (buildings) and the atmosphere are in equilibrium condition. Heat dissipation techniques are summarized as follows in a line diagram (Fig. 3).

One of the techniques used to reduce heat through roof is nocturnal cooling. Nocturnal cooling systems for space cooling and its challenges are reviewed by Nwaigwe et al. [19], Watson and Chapman [20], emphasized that air is cooled by radiant cooling in two-storeyed buildings using light color coatings with high reflection. Chung et al. [21] analyzed the loads handled, characteristics of load, air systems in different zones and control strategies used in (Fig. 4) thermally activated building systems (TABS).

The envelope's insulation, solar protection, and surface properties are the factors to increase the cooling effect. Givoni [22] concluded that protecting the roof from heat during the daytime is completely different from other approaches such as flat

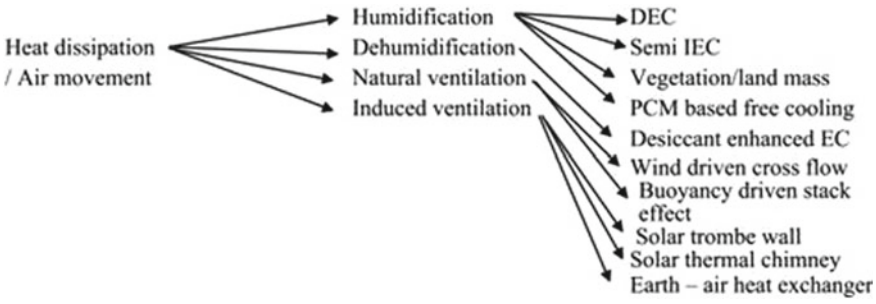

Fig. 3 Heat dissipation techniques

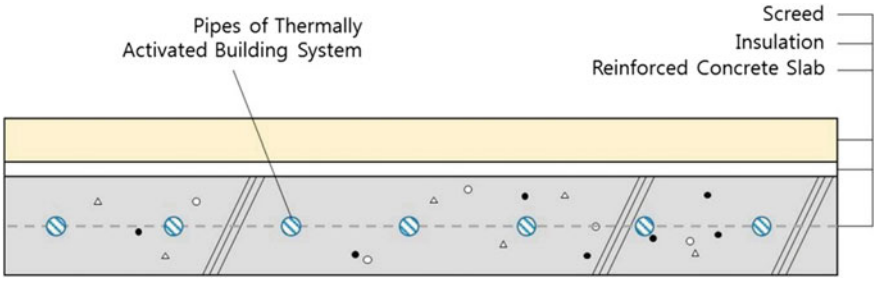

Fig. 4 Section view of the thermally activated building system (TABS)

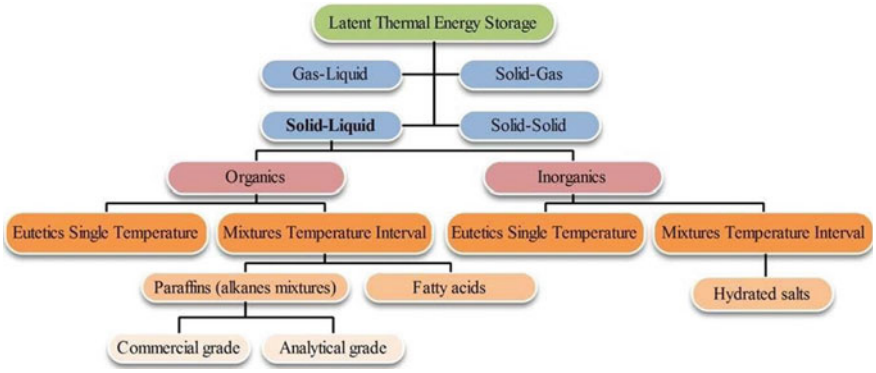

Fig. 5 Classification of latent thermal energy storage

plate air cooler and reflective insulation system. This method provided a cooling effect of 0.266 kWh/m^2 per day [23].

Muscio [24] insisted that when photons from radiation hit a surface of dense material, these photons are neither reflected nor absorbed and found that solar reflectance is associated with the use of flat surface and polish of the surface. Radiative cooling using solar plate collector [25] can be done effectively. Energy can be stored and retrieved for passive cooling. Figure 5 shows the various possible ways of latent heat energy storage systems in practice. Solar control glazing on energy savings is analyzed by Bakker and Visser [26].

4 Conclusion

In this paper, a review of various passive cooling technologies has been done instinct. Due to the population growth, the energy demand for thermal comfort for human increases. The global warming also rises the temperature of the universe. The natural cooling methods are not supportive to meet the requirement. Hence, the appropriate modern passive cooling technology has to be employed for buildings. The various studies show that the suitable technology is to be selected and it depends on so many factors [27–29]. Many investigations [30–32] have been done to reduce the cooling load [33, 34] of a building through reflective and radiative roofs. It is not easy to adopt a particular technology universally. However, the cool roof technology with reflective coating and radiant cooling through with latent heat thermal energy storage materials play a dominant role among these technologies.

References

1. https://news.un.org/en/story/2018/12/1027901
2. Hassana AM, Oh HLS (2016) Challenges of passive cooling techniques in buildings: a critical review for identifying the resilient technique, J Teknol 78(6) 149–162. eISSN 2180–3722
3. Zhang P, Ma Z, Wang R (2010) An overview of phase change material slurries: MPCS and CHS. Renew Sustain Energy Rev 14(2):598–614
4. Synnefa A, Santamouris M, Akbari H (2007) Estimating the effect of using cool coatings on energy loads and thermal comfort in residential buildings in various climatic conditions. Energy Build 39:1167–1174
5. Santamouris M, Asimakopoulos DN (1996) Passive cooling of buildings. James & James, London, pp 598–614
6. Shen H, Hongwei T, Tzempelikos A (2011) The effect of reflective coatings on building surface temperatures, indoor environment and energy consumption. An experimental study. Energy Build 43(2–3):573–580
7. Pockett J (2016) Heat reflecting paints and a review of their advertising material. Sustainable Energy Centre
8. Suehrcke H, Peterson EL, Selby N (2008) Effect of roof solar reflectance on the building heat gain in a hot climate. Energy Build 40:2224–2235
9. Hosseinia M, Leea B, Vakiliniab S (2017) Energy performance of cool roofs under the impact of actual weather data. Energy Build 145:284–292
10. Anand Y, Gupta A, Maini A, Gupta A, Sharma A, Khajuria A, Gupta S, Sharma S, Anand S, Tyagi SK (2014) Comparative thermal analysis of different cool roof materials for minimizing building energy consumption. J Eng Hindawi. Article ID 685640
11. Global Cool Setting Alliances (2012) A Practical guide to cool roofs and cool pavements. www.imaginaryoffice.com
12. Pradap SP, Smayana (2007) Int J Sci Res Dev 4(11) 97–101, ISSN (online): 2321–0613
13. Srinivasan PSS, Ravikumar M (2008) Phase change material as a thermal energy Storage material for cooling of building. J Theoret Appl Inf Technol 4:503–511
14. Madhumathi B, Sundarraja MC (2012) Experimental study of passive cooling of building facade using phase change materials to increase thermal comfort in buildings in hot humid areas. Int J Energy Environ 3(5):739–748
15. Heier J, Bales C, Martin V (2015) Combining thermal energy storage with buildings—a review. Renew Sustain Energy Rev 42(1):305–325
16. Cool roofs mandatory for all new buildings. https://archive.indianexpress.com/news/-cool-roofs-mandatory-for-all-newbuildings/
17. Pasupathy A, Velraj R (2008) Effect of double layer phase change material in building roof for year round thermal management. Energy Build 40:193–203
18. Pasupathy A, Velraj R, Seeniraj RV (2008) Phase change material-based building architecture for thermal management in residential & commercial establishments. Renew Sustain Energy Rev 12:39–64
19. Nwaigwe KN, Okoronkwo CA, Ogueke NV, Anyanwu EE (2010) Review of nocturnal cooling systems. Int J Energy Clean Env 11(1–4):117–143
20. Watson RD, Chapman KS (2002) Radiant heating and cooling handbook. McGraw-Hill, New York
21. Chung WJ, Park SH, Yeo MS, Kim KW (2017) Control of thermally activated building system considering zone load characteristics. Sustainability 9:586
22. Givoni B (1969) Climate and architecture. Elsevier Publishing Company Limited, Amsterdam
23. Givoni B (1994) Passive and low energy cooling of buildings. Vanm Nostrand Reinhold Co., New York
24. Muscio A (2018) The solar reflectance index as a tool to forecast the heat released to the urban environment: potentiality and assessment issues. Climate 6(1):12
25. Erell E, Etzion Y (2000) Radiative cooling of buildings with flat plate solar collectors. Build Environ 35:297–305

26. Bakker LG, Visser H (2005) Impact of solar control glazing on energy and CO_2 savings in Europe, Delft: TNO report 2007-D-R0576/B. CEI UNI ENV 13005
27. Hasan A, Al-Sallal KA, Alnoman H, Rashid Y, Abdelbaqi S (2016) Effect of phase change materials (PCMs) integrated into a concrete block heat gain prevention in a hot climate. Sustainability 8:1009
28. Patel JH, Darji PH, Qureshi MN (2014) Phase change material with thermal energy storage system and its applications: a systematic review. J Eng 9, Article ID 685640 (Hindawi Publishing Corporation)
29. Madhumathi AA, Sundarraja BMC (2012) Experimental study of passive cooling of building facade using phase change materials to increase thermal comfort in buildings in hot humid areas. Int J Energy Env 3(5):739–748
30. Joudi A, Svedung H, Cehlin M, Ronnelid M (2013) Reflective coatings for interior and exterior of buildings and improving thermal performance. Appl Energy 103:562–570
31. Sabzi D, Haseli P, Jafarian M, Karimi G, Taheri M (2015) Investigation of cooling load reduction in buildings by passive cooling options applied on roof, energy and buildings. Energy Build 109:135–142
32. Nicol F (2004) Adaptive thermal comfort standards in the hot humid tropics. Energy Build (Elsevier) 36(7):628–63729
33. Roslan Q, Ibrahim SH, Affandi R, Nawi M, Baharun A (2016) A literature review on the improvement strategies of passive design for the roofing system of the modern house in a hot and humid climate region. Front Archit Res 5:126–133
34. Talebn HM (2014) Using passive cooling strategies to improve thermal performance and reduce energy consumption of residential buildings in U.A.E. buildings. Front Archit Res 3:154–165

Enhancement of Soil Using Pyrolyzed *Cocus nucifera* Midrib Carbon

M. Angelina Thanga Ajisha, Jaslin J. Christopher, A. S. Jebamalar, and I. Regina Mary

Abstract The bearing capacity of the soil can be improved using controlled compaction, proportioning, adding stabilizer, or admixtures which help in enhancing bearing capacity of the soil. In this experimental work, Pyrolyzed *Cocus nucifera* midrib carbon was used to improve the performance of the soil which may be an economical solution of soil stabilization. The black cotton soil was treated with various percentage of Pyrolyzed *Cocus nucifera* midrib carbon (PCMC) (0, 1, 2, 3, 4, 5, 6, 7, 8, and 9% by dry weight of soil). Specific gravity, Atterberg limits, compaction characteristics, and unconfined compressive strength were tested with different percentages of PCMC, which was obtained from *Cocus nucifera.* Significant improvement in index properties, compaction, and strength characteristics was confirmed from the test conducted. The effects of PCMC behavior vary depending upon the quantity of PCMC that was mixed with the black cotton soil sample.

Keywords *Cocus nucifera* midrib · Stabilization · Geotechnical parameters · Black cotton soil

M. Angelina Thanga Ajisha (✉)
Department of Civil Engineering, Francis Xavier Engineering, Tirunelveli, Tamil Nadu 627003, India
e-mail: ajeeshain2010@gmail.com; angelincivil@francisxavier.ac.in

J. J. Christopher
Department of Chemistry, Manonmaniam Sundaranar University Constituent College, Palkulam, Kanyakumari District, Tamil Nadu 629 401, India

A. S. Jebamalar
Department of Physics, Nesamony Memorial Christian College, Marthandam, Kanyakumari District, Tamil Nadu 629 165, India

I. R. Mary
Department of Civil Engineering, Mount Zion College of Engineering and Technology, Pudukkottai, Tamil Nadu 622507, India

G. Kumaresan et al. (eds.), *Advances in Materials Research*, Springer Proceedings in Materials 5, https://doi.org/10.1007/978-981-15-8319-3_56

1 Introduction

Nearly 3% of the total land in the world has black cotton soil (BCS) in which it is found abundance in West Indies, Russia, Asia, Africa, and Australia. In Asia, India has abundance of BCS [1]. This BCS is also named as expansive soil as it contains fine grain soil and also decomposed rock which may expand on the fluctuation of moisture content. When this BCS is straightly imposed on environmental variations and seasonal variations, swelling–shrinkage behavior occurs on the ground surface. BCS has a clay mineral called montmorillonite which is most likely to be in unsaturated form. In BCS, failure happens when the soil contains more monovalent cations which are absorbed into the clay minerals [2]. Swelling or shrinkage due to the changes in water content of black cotton soil is often stated as heaving and also as settlement of lightly loaded geotechnical structures like channel or reservoir lining, railways, pavements, foundations [3].

In order to improve or to stabilize the BCS, many methods are adopted with some additives to the soil. Some of the methods adopted are mechanical and chemical stabilization. Many researches have been undergone with mechanical stabilization which is said to be the economical and easier method of soil stabilization. In this mechanical method, a dynamic force is applied to stabilize the BCS. Applying such forces increase the density of the soil as well reduce the moisture content and too increase the shear strength of the soil and ultimately increase the characteristics of the soil [4].

In chemical stabilization of soil, mixing or injecting of calcium or sodium chloride, fly ash, Portland cement, lime with BCS increase the stability. Apart from the above, a viscoelastic material called bitumen is also used for stabilization. Other than chemicals many researches have been done with nylon fiber, iron residue, aluminum residue, jute, palm fibers, fly ash, coal, etc. In order to increase the strength and durability, waste material is also used like recycled waste which is an attractive method for sustainable development and also economical, reduce environmental pollution which is nowadays more required in our mother earth.

Due to rapid industrialization and comfort life, large quantity of solid waste is generated which is one of the biggest threats in developing countries in order to dispose them. One of the waste material fibers is hence nowadays used in concreter as reinforcement which was found to reduce cracks and also has increased the tensile strength of soil. Likewise, many waste materials are found which may be benefitted to research filed [4].

In this study, a newer material is introduced to stabilize the black cotton soil with various percentage of Pyrolyzed *Cocus nucifera* midrib carbon (PCMC) (0, 1, 2, 3, 4, 5, 6, 7, 8, and 9% by dry weight of soil).

Many researchers have under their research with various wastes which are discussed below. In order to enhance the property of a lean clay, Hanifi Canakci et al. investigated with aluminum beverages can strip to improve the strength and swelling property. Experimental work and its results found that this waste beverage can enhance the compaction characteristics, swelling, and strength properties of clay

[4]. Another waste material from sugarcane, the bagasse fibers were taken by Liet Chi Dang et al. [2] to study the behavior of expansive soil in addition with bagasse fiber. Bagasse fiber of 0.5, 1.0, and 2.0% was mixed randomly with hydrated lime—expansive soil. The experimental results found that the bagasse fiber reinforcement blended with hydrated lime has increased the compressive strength of the expansive soil on the addition of additives and also the prolonged curing time. While increasing hydrated lime, bagasse fiber proportions, and curing period, the linear shrinkage of stabilized expansive soil decreased. Hence, it was proved that combination of hydrated lime and bagasse fiber can stabilize the soil successfully.

Soil stabilization research was investigated using locally available and cheaper material the rice husk ash (RHA), sugarcane bagasse ash (SCBA), and cow dung ash (CDA) by Anjani Kumar Yadav et al. [5]. Partial replacement of soil was done with rice husk ash(RHA), sugarcane bagasse ash (SCBA), and cow dung ash (CDA) by weight in 0, 2.5, 5, 7.5, 10, and 12.5%. The results from the experimentation confirm that there is a drastic improvement in CBR test, UCS test, and also, it was able to control volumetric change. Anjani Kumar Yadav et al. [5] investigated the stabilization of subgrade soil using different types of locally available materials such as rice husk ash(RHA), sugarcane bagasse ash (SCBA), and cow dung ash (CDA). The RHA, SCBA, and CDA were mixed by partial replacement of soil by weight in 0, 2.5, 5, 7.5, 10, and 12.5%. The results showed that there is a significant improvement in CBR, UCS and also able to control the volumetric change.

2 Materials and Methods

2.1 Soil Sample

In this research, the soil used is a black cotton soil (BCS) taken is dark gray in color, which was collected from Manonmaniam Sundaranar University at Tirunelveli District, Tamil Nadu. This soil sample of black cotton soil was collected in sacks and taken to the laboratory. A small quantity of the soil sample was sealed in polythene bag for determining its natural moisture content. The soil was air dried, pulverized, and sieved with 4.75 mm aperture as required for laboratory test. Properties of natural black cotton soil are given in Table 1.

2.2 Pyrolyzed Cocus nucifera *Midrib Carbon (PCMC)*

Pyrolyzed *Cocus nucifera* midrib carbon (PCMC) was obtained locally from Tirunelveli District. It was burnt in Muffle furnace at 600 ºC. Carbon passing through 425 μ sieve was used in this investigation.

Table 1 Black cotton soil characteristics

Property	Value
Percentage passing IS 75 micron sieve	76.9
Liquid limit	50.00%
Plastic limit	17.00%
Plasticity index	33.00%
Shrinkage limit	18.05%
Linear shrinkage	12.64%
Indian standard classification system (ISCS)	CI-CH
AASHTO classification	A-7–6
Maximum dry density (MDD)	1.675 g/cc
Optimum moisture content (OMC)	11.8%
Unconfined compressive strength (UCS)	9.38×10^{-2} N/mm^2
Soaked California bearing ratio (CBR)	3.05%
pH	9.85
Specific gravity	2.33
Coefficient of permeability (k)	1.42×10^{-7} cm/s
Natural moisture content	4%

2.3 Experimental Work

In order to achieve the objectives of the study, a testing program was designed to investigate the behavior of the treated clay soil. The tests included specific gravity, Atterberg limits, maximum dry density, unconfined compressive strength. These tests were performed at different percentages of PCMC mixed with soil sample.

3 Results and Discussion

3.1 Specific Gravity

The specific gravity at no PCMC content was 2.33. Gradual decrease in specific gravity to a minimum value of 1.3 was observed with increasing percentage of PCMC up to 9%. Further addition of PCMC led to decrease in specific gravity. The variation of specific gravity of the samples with the addition of different percentage of PCMC is shown in Fig. 1.

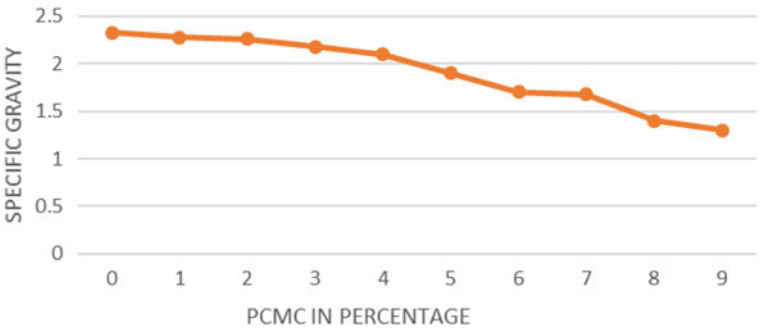

Fig. 1 Specific gravity of BCS with PCMC

3.2 Sieve Analysis

As per Indian Standard Classification System (ISCS), the soil comes under the dual group CI-CH (inorganic clays of medium to high plasticity). As per AASHTO classification system, the soil comes under the group A-7–6.

3.3 Atterberg Limit

3.3.1 Liquid Limit

The liquid limit of the soil sample was carried out using Casagrande apparatus. The liquid limit of the samples was determined and plotted against the PCMC content. The liquid limit of untreated soil was determined as 50%. There was an increase in liquid limit with increase in coconut shell carbon up to 2%. The liquid limit of the soil decreased with increase in coconut shell carbon content up to 8%. After that, there was an increase in liquid limit at 9% carbon content. The effect of PCMC on the liquid limit of the black cotton soil samples is presented in Fig. 2.

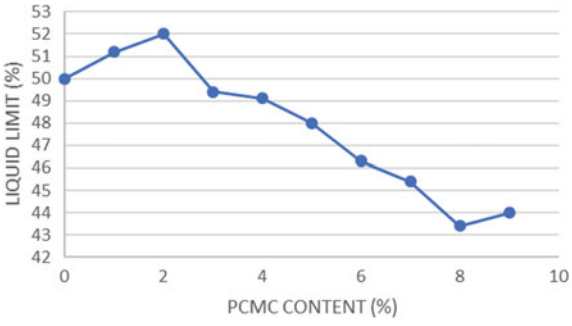

Fig. 2 Liquid limit of BCS with PCMC

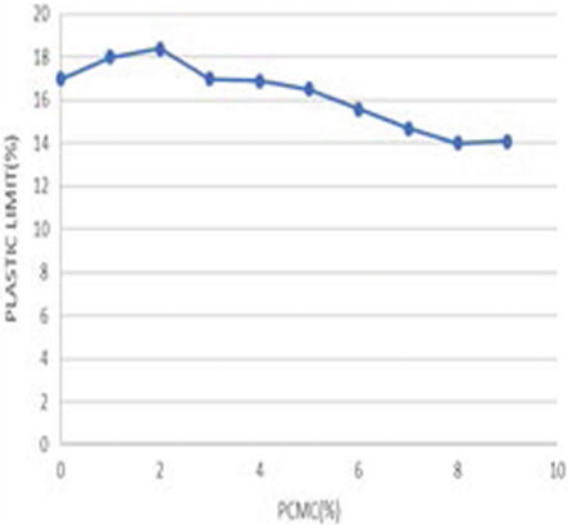

Fig. 3 Plastic limit of BCS with PCMC

3.3.2 Plastic Limit

The plastic limit (PL) test was carried out as per IS:2720 (Part V)-1985. As can be seen from the graph, the addition of PCMC resulted in a decrease in the plastic limit of the treated soil. The plastic limit of untreated soil was 17.00%. There was an increase in plastic limit with increase in Pyrolyzed *Cocus nucifera* carbon up to 2%. As the stabilizer was increased to 9% PCMC, lowest value of 14.00% was observed at 8% PCMC content. A sharp increase in the plastic limit (14.20%) was observed at 9% PCMC content. The effect of PCMC on the plastic limit of the black cotton soil samples is presented in Fig. 3.

3.3.3 Plasticity Index

The addition of PCMC decreases the plasticity index of the soil samples. Plasticity index at no PCMC content was 33.00%. The plasticity index varies from 33% to 29.5%. This shows that the plastic nature of the soil decreases and the stiffness of the soil increases as the PCMC content increases. The effect on the liquid and plastic limit by the addition of PCMC is observed to reflect the trend of variation of plasticity index upon the addition of PCMC in increasing percentages. The variation of plasticity index of the samples with the addition of different percentages of PCMC is shown in Fig. 4.

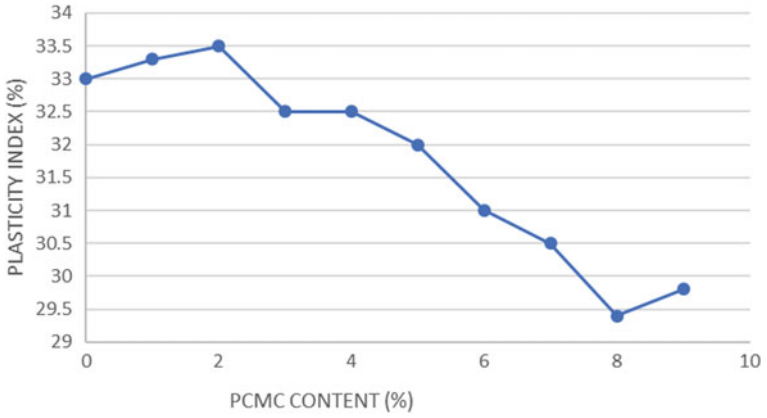

Fig. 4 Plasticity index of BCS with PCMC

3.3.4 Shrinkage Limit

The shrinkage limit of the soil samples was determined as per IS:2720 (Part VI)-1972. It is seen that the shrinkage limits of the samples follow a steady increase with the addition of PCMC in increasing percentages. A value of 18% was recorded for the natural soil. An increase in shrinkage limit to a peak value of 45.1 at 8% PCMC content can be observed with increasing percentages of PCMC [6–8]. A sharp decrease in the shrinkage limit (43%) was observed at 9% PCMC content. The variation of shrinkage limit of the samples with the addition of different percentages of PCMC is shown in Fig. 5.

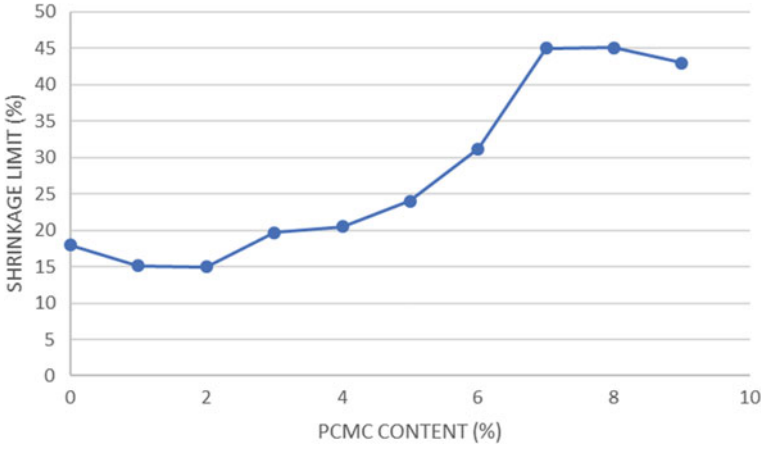

Fig. 5 Shrinkage limit of BCS with PCMC

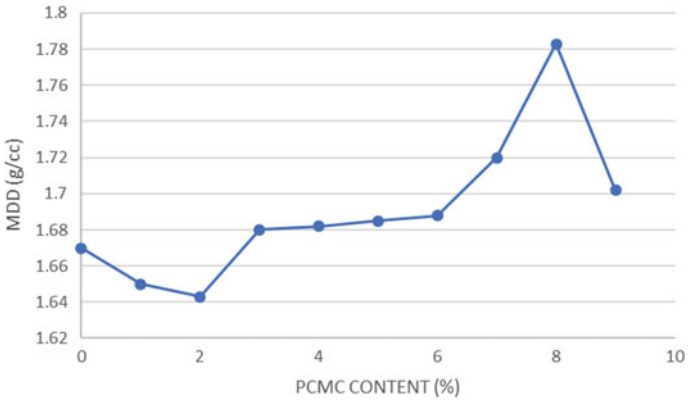

Fig. 6 Variation of MDD with PCMC

3.3.5 Compaction Parameters

Optimum Moisture Content (OMC)

The OMC at no PCMC content was 11.5%. Subsequent increases in OMC reached a value of 13 at 4% Pyrolyzed *Cocus nucifera* midrib carbon. Further addition of *Cocus nucifera* midrib carbon led to sharp reduction in the OMC to 9.9 at 8% PCMC content. Finally increase of optimum moisture content to 10.6% was observed at 9% PCMC content.

Maximum Dry Density

At 0%, Pyrolyzed *Cocus nucifera* midrib carbon content, the maximum dry density was 1.67 g/cc. On the addition of PCMC, a decrease in maximum dry density was observed to a value of 1.682 g/cc at 4% PCMC content. Further increase in PCMC content led to increase in maximum dry density to a peak value of 1.783 g/cc at 8% PCMC. Subsequently increase in *Cocus nucifera* midrib carbon led to reduction in MDD value [9–11]. The effect of PCMC on the maximum dry density of the black cotton soil samples is presented in Fig. 6.

3.3.6 Unconfined Compressive Strength (UCS)

It was observed that the unconfined compressive strength of the soil samples decreased up to 2% with Pyrolyzed *Cocus nucifera* midrib content. The reason for the decrease could be due to the lack of adequate lime in the *Cocus nucifera* midrib carbon which is required for the stabilization of the black cotton soil. However, at 3, 4, 5, 6, 7, and 8% PCMC, there was increased values of UCS recorded. The UCS

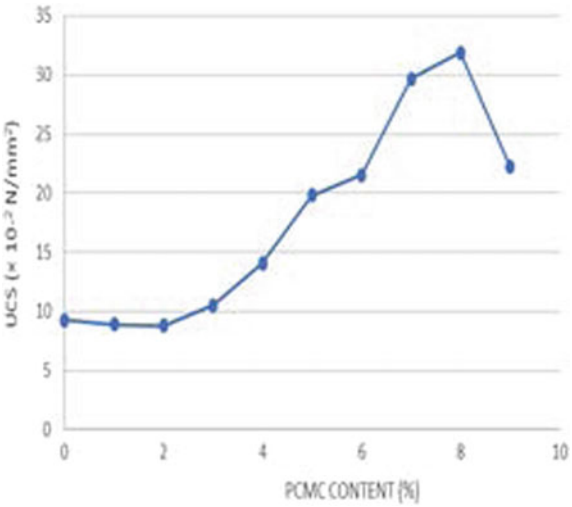

Fig. 7 Variation of first day UCS with PCMC

value at 8% PCMC content was 31.9×10^{-2} N/mm^2 [12–15]. The effect of addition of PCMC to the black cotton soil sample on their UCS values is given in Fig. 7.

4 Conclusion

From the research work, it was found that Pyrolyzed *Cocus nucifera* midribs are a good stabilizer for enhancing the geotechnical characteristics of expansive or the black cotton soil. The compaction, strength characteristics, and also the index properties have significantly improved on the addition of Pyrolyzed *Cocus nucifera* midribs. Decreasing trend of values in liquid limit and plastic limit of the soil on the addition of PCMC indicates a desirable change in the soil with PCMC mix, which gains strength at an early stage than the virgin soil with the change in water content. It was also interesting in noticing that the plasticity index has relatively decreased which is another favorable change as it will increase the workability of the soil. On adding PCMC to the soil, the shrinkage limit of the soil increases and also the compaction parameters increase. On increasing the PCMC, the maximum dry density of the soil with decrease in the corresponding values of optimum moisture content. The research finding shows the increase in unconfined compressive strength of the soil on the addition of PCMC, which confirms the suitability of PCMC for soil stabilization.

References

1. Etim RK, Eberemu AO, Osinubi KJ (2017) Stabilization of black cotton soil with lime and iron ore tailings admixture. Transp Geotechn 10:85–95
2. Dang LC, Fatahi B, Khabbaz H (2016) Behaviour of expansive soils stabilized with hydrated lime and bagasse fibres. Proc. Eng. 143:658–665
3. Ene E, Okagbue C (2009) Some basic geotechnical properties of expansive soil modified using pyroclastic dust. Eng Geol 107:61–65
4. Canakcia H, Celika F, Bizneb MOA, Biznea MOA (2016) Stabilization of clay with using waste beverage can. Proc Eng 161:595–599
5. Yadav AK, Kumar G, Kishor R, Suman SK (2017) Stabilization of alluvial soil for subgrade using rice husk ash, sugarcane bagasse ash and cow dung ash for rural roads. Int J Pavement Res Technol 10:254–261
6. Dang L, Hasan H, Fatahi B, Jones R, Khabbaz H (2016) Enhancing the engineering properties of expansive soil using bagasse ash and hydrated lime. Int J Geomate 11(25):2447–2454
7. Fatahi B, Le T, Fatahi B, Khabbaz H (2013) Shrinkage properties of soft clay treated with cement and geofibers. Geotech Geol Eng 31(5):1421–1435
8. Sharma R, Phanikumar B, Rao B (2008) Engineering behavior of a remolded expansive clay blended with lime, calcium chloride, and rice-husk ash. J Mater Civ Eng 20(8):509–515
9. Afrin H (2017) A review on different types soil stabilization techniques. Int J Transp Eng Technol 3(2):19–24
10. Bell FG (1996) Lime stabilization of clay minerals and soils. Eng Geol 42(4):223–237
11. Pei X, Zhang F, Wu W, Liang S (2015) Physicochemical and index properties of loess stabilized with lime and fly ash piles. Appl Clay Sci 114:77–84
12. Pandian NS (2013) Fly ash characterization with reference to geotechnical applications. J Indian Inst Sci 84(6):189–216
13. Angelina Thanga Ajisha M, Rajagopal K (2013) Characterization and adsorption study using *Cocus nucifera* midribs for fluoride removal. J. Inst. Eng. India Ser. A 94(4):209–217
14. Cokca E (2001) Use of class C fly ashes for the stabilization of an expansive soil. J Geotech Geoenviron Eng 127:568–573
15. IS 2720 (6) (1985) Methods of test for soils, determination of shrinkage factors

Experimental Studies on Milling Parameters for Al6061 Hybrid Metal Matrix Composite

K. Ramachandra Raju, G. Senthilkumar, Y. Arivu, M. Vignesh, D. Thangeswaran, and G. Vivek

Abstract Metal matrix composites (MMC) are extensively utilized in engineering fields of automobile, aerospace, construction and microelectronics. In conjunction with innovations in these advanced materials, machining them to obtain good dimensional accuracy and surface integrity has become a challenge. This work experimentally studies about minimizing force acting on tool by machining the composite material. The alumina refinery residues reinforced with Al6061 are fabricated by stir casting technique and machined in CNC milling machine. The machining parameters like in-feed force, thrust force and cross-feed are studied that lead to the benefit of energy and functional enhancements. The design of experiments was conducted as per L9 orthogonal array and analysed. It was realized from the studies that the effects of most influencing cutting parameters are feed rate, depth of cut and cutting speed in end milling operations.

Keywords End milling · Cutting forces · Stir casting · Effect of cutting parameters · Taguchi L9

1 Introduction

The advancement of high-technology aerospace, automobiles, defence, medical products requires specific materials related to the specific features provided with unique designs. Composite fabrication for the desired application is the need of the hour in order to get energy efficient, economical, reliable and high performance of products at critical operating conditions. The most important motivation is to take of particular properties advantage of the constituent materials in order to meet development of composites for specific demands [1]. The matrix provides high thermal conductivity, corrosion resistance, toughness and properties of melting point.

K. Ramachandra Raju (✉) · G. Senthilkumar · Y. Arivu · M. Vignesh · D. Thangeswaran · G. Vivek
Department of Mechanical Engineering, Bannari Amman Institute of Technology, Sathyamangalam, Erode District, Tamil Nadu 638401, India
e-mail: rajukrc@gmail.com

G. Kumaresan et al. (eds.), *Advances in Materials Research*, Springer Proceedings in Materials 5, https://doi.org/10.1007/978-981-15-8319-3_57

Aluminium is the base alloy which is widely selected for composites of metal matrix in many applications [2]; by virtue of its higher ratio of strength to weight, resistance to environment and higher stiffness. But, aluminium is having poor wear resistance; predominantly at partial lubricating conditions at boundary, thermally unstable at elevated temperatures. The ceramic particle reinforcements are good in improving the properties of hardness, thermal stability, wear resistance, strength and friction. Owing to the (Fe, Cu and Al) matrix materials, B4C, SiC and Al_2O_3 are widely used ceramic particles due to easy availability [3]. In liquid state process, the method of stir casting is the correct method for particulate reinforcement for the composites fabrication [4–6]; among the different technologies involved [7]. The microstructure and properties of composites are influenced by the particulates content, size, interface, homogeneity, process parameters, etc.

The solid lubricant effects, speed at sliding and the tribological load behaviour of reinforced composites of silica reveal that MoS_2 reinforcement has the highest hardness, density and effective lubrication. Solid lubricants are contributing effectively to reduce the wear rate [8]. Graphite reinforcement provides higher braking performance. (K2TiF6) Potassium hexafluoro titanate flux quantity is equal to boron carbide for wettability development [9] of boron carbide with below 850 °C of aluminium alloy which shows that 10 weight percent of B4C and 5 wt% of graphite 7075 hybrid composite has high hardness with better elongation in % than alloy 6061 and its hybrid composite; RSM analysis shows that minimum wear rate was obtained for the combination of (10 N) load applied, (0.8 m/s) sliding speed and (2000 m) sliding distance for hybrid composite 7075 when it is differentiated to the base alloys and hybrid composite 6061.

Mechanical behaviour of combinations of aluminium—alumina of 3%—boron carbide of 2%, aluminium—alumina of 2%—boron carbide of 3%, and aluminium LM25 stir casting indicate that tensile strength is higher with alumina 3% reinforced, flexural strength higher with aluminium LM25, hardness higher with boron carbide 3% level samples [10]. ADC12 aluminium alloy with zirconium silicate ($ZrSiO_4$) and silicon carbide particles by variations (9 + 3) %, (6 + 6) %, (3 + 9) % by stir casting technique shows that (6 + 6) wt% combination is optimum results of microhardness and tensile strength [11]. Aluminium 6063 hybrid composite is then reinforced with graphite and silicon carbide. Other reinforced with SiC, B_4C by stir casting technique shows that hardness strength of tensile and flexural is increased in the particulates than the SiC and graphite-reinforced composite [12]. Alumina had a greater effect on the wear and graphite improved the wear resistance of composites as primary and secondary reinforcements, respectively. It forms a layer between pin and counter face which is protective [13]. LM6 alloy with boron carbide 0, 2.5, 5 and 7.5 wt% of reinforcement levels discloses that B4C particles are uniformly distributed in matrix aluminium which increases hardness and tensile strength and also increase of its wt% decreases the density of the composite [14]. It is found that the desirability analysis yielded good results in optimal input conditions finding [15, 16]. Machining of Al6351/20% Al2O3 composite using μWEDM process using response surface methodology shows the surface roughness values from the experimental domain and predicted values matched well demonstrating a better model fitness and adequacy

and desirability analysis in identifying the optimal machining parameter combination shows that the enhanced capacitance was found to produce a better surface finish [17], while a lower level of feed and voltage was observed to produce similar results.

The demand for the new materials is prevalent in fast growing economy and social transformations. The international reputed survey agency of McKinsey and Company reported that great potential for lightweight aluminium and carbon fibre indicating cumulative annual growth rate of 6% and 17%, respectively. On the other hand, steel and high-strength steel have very slow growth rate of 1–3% only [18].

Though some of the components made of composites have reached the demonstration stage and have many barriers to occupy before widespread application expected [19]. A step-by-step process gain of composite experience from 1980 in primary structures, composite structure/structure weight (%) reduces operational cost, reduces impact in global environment, improves the comfort of passenger by cabin pressure at higher, reduction of weight fuel, reduction of cost and impact in environmental reduction, corrosion-free and fatigue, reduces costs in maintenance of a great deal of benefits to the industry and product are being realized by airbus [20]. Cylinder space tightening has resulted in the reduction of overall length and weight savings of the engine by using MMC engine blocks in vehicles Accord, Ascot, Innova and the S2000 models. Honda has also developed a high-pressure die casting for manufacturing the MMC engine blocks which reduces process cost [21].

The reinforcement modifies the microstructure and refines the grain growth of the composites. Small-size particles are the best with increasing percentage quantity. Reinforcement's percentage reduces the wear rate. These composites will suffer a great loss in toughness and ductility due non-deformable ceramic particulates which decrease their applications to a certain extent. Hence, instead of going on increasing the wt% of single reinforcement, there is a need of optimizing the properties of composites by hybridization.

There is a vast potential opportunity for the researchers still left to improve or increase the mechanical properties, thermal stability and tribology properties of aluminium composites to suit specific application fields by varying parameters associated with reinforcement particle size, adding different reinforcements. Though some of the components made of composites have reached the demonstration stage and have many barriers to occupy before widespread application expected. A step-by-step process gain of composite experience from 1980 in primary structures, composite structure/structure weight (%) and changing ratio of them, selecting the fabrication technique. Great deal of property enhancement by processing through strengthening mechanism such as precipitation hardening, age hardening, strain hardening, cold working, grain refinement, etc., can be obtained.

Machinability of Al/SiCp composite using rhombic tool on turning operation. Using the SEM micrograph, the built-up edge (BUE) and chip formation were examined to provide an economic machining solution through their work [22]. Cutting force is obtained through conventional turning and ultrasonic vibration turning using PCD turning tool; he concluded that high depth of cuts and low speed reduces cutting speed [23]. Process parameters for turning thin wall Al/SiC composites using coarse grade PCD insert under different condition of cutting. By employing ANOVA table,

Table 1 Composition of aluminium 6061 alloy in weight %

Mg	Si	Cu	Zn	Ti	Mn	Cr	Al
0.85	0.68	0.22	0.07	0.05	0.32	0.06	Balance

the machining conditions were optimized for low surface roughness. The process parameters on tool flank and surface roughness were also described by them [24].

This provides the background for the present work of 6061 with alumina refinery residues reinforcements through stir casting process and study of the cutting forces in end milling operations which has the overall effect on total power consumption and need of optimal machine design for economic advantage. The influence of alumina refinery residues reinforcements in microstructure makes it suitable for specific applications in automotive field as an alternate to steel material and which could lead to more benefits in environment.

2 Materials and Methods

2.1 Materials

The materials used in this study are 6xxx series aluminium alloy 6061 containing approximately the proportions needed for magnesium silicide (Mg 0.8Si 0.68) formation, making them heat treatable. Although not as strong as most 2xxx and 7xxx alloys, 6xxx series aluminium alloys have superior formability, weldability, machinability and relatively good resistance to corrosion, with 3 weight % of alumina refinery residues reinforced with Al6061. Aluminium 6061 alloy composition is shown in Table 1.

2.2 Stir Casting

The aluminium alloy 6061 ingots cut into slices of 10–15 mm thickness were fed into the crucible as per experimental plan and melted by heating in the induction furnace at the temperature of 850 °C for 2–3 h. It is above its liquidus temperature done to covert the form into liquid state which is (600 ℃). The silicon carbide and boron carbide particles in their right proportion as per experimental plan were preheated to 200 °C to make their surface oxidized. Precoated die was preheated to 200 °C for proper solidification.

During the reheating process of aluminium alloy at 750 ℃, stirring is done with stirrer, speed at 400 rpm. Then, the reinforcement powders are added to furnace with liquid aluminium alloy. (K2TiF6) Potassium hexafluoro titanate flux quantity equal to boron carbide added after preheating it for 200 °C to improve wettability of boron

Fig. 1 Stir casting setup and sample

carbide with aluminium alloy at below 850 °C. Argon gas was passed into the molten metal to remove the soluble gases present in liquid state metal. Stirring of the molten metal is carried out for 10 min duration. Samples were made by pouring the melt into the die and solidified as shown in Fig. 3.

The stir caster was mounted on the furnace with the help of links. The stirrer is used to agitate the liquid metal. The stirrer positioned such that 35% of material to be below the stirrer and 65% of material above the stirrer. Figure 1 represents cast composite from the stir casting setup. The molten composite is poured inside the die cavity which has graphite coating and the open view of the mould cavity.

2.3 Optical Microscopic Test

Microstructure of the composite materials is studied on the prepared surface or thin foil of material. The microstructure of a material (which can be broadly classified into metallic, polymeric, ceramic and composite) can strongly influence physical properties such as strength, toughness, ductility, hardness, corrosion resistance, high/low temperature behaviour, wear resistance and so on, which in turn govern the application of these materials in industrial practice.

The samples were ground with 240, 320, 400, 600 and 800—grit silicon carbide paper and polished with 5 and 2 micron diamond paste on velvet cloth. They were

Fig. 2 End milling setup in LMW JV 55 CNC

rinsed in demineralized H_2O. The specimens were placed in desiccators before use. It was then dipped in aqueous solution of sodium hydroxide and then dropped in the etchant (11c Beraha) until bluish brown colour appears. Later, the sample is dried to remove moisture if any present and then placed under the optical microscope (× 500) for observation.

2.4 Machining

Unwanted piece of metal work removed in the form of chips is called machining. The method of machining will form the work piece desired and usually done with machine and cutting tools [25]. Machinability studies have acquired greater importance in the area of composite.

End milling is commonly utilized in automobile and aerospace industries where quality is an important factor in manufacturing of slots, pockets and moulds/dies. End mills are used in milling applications like profile milling, tracer milling, face milling and plunging. The end mills are used for light operations like cutting slots, precise machining of holes, producing narrow flat surfaces and for profile milling operations [26]. Machining is done using CNC vertical machining centre which makes LMW model JV55 (Figs. 2 and 3).

2.5 Milling Tool Force Measurement

Milling tool force dynamometer is used in this work. It is most suitable in force calculation on a milling operation during end milling operation. The system displays an indicated force in X, Y and Z directions on a end milling cutter during the milling operation. It comprises tri-axial piezo-electric measuring sensor. The signal from

Fig. 3 Tool cutting force digital display unit

the sensor is transmitted to the signal conditioner which in turn sends those to communication card to the digital display unit.

The milling tool force dynamometer can be mounted on the table of milling machine, and any component can be fixed over the dynamometer. Slots are provided to mount the dynamometer to milling machine. Holes have been provided on the milling dynamometer to enable any type of components to be fixed on it. The output terminals are provided for the force in X, Y and Z-direction acting on the workpiece.

2.6 Design of Experiment

Experimental design is a systematic method for obtaining the most reliable results with minimal wastage of time/money and refining the procedures and identifying the most important factors that can require various experiments. Using MINITAB 17 software, Taguchi L9 nine experiments were planned with varied cutting parameters in the cast composite specimen. Figure 2 shows computer numerical control vertical milling centre used for machining such as slots, profile and present work involves taking a slot (Figs. 4 and 5; Table 2).

3 Result and Analysis

3.1 Macroscopic Structure

As shown in Fig. 6, it is clearly seen that alumina refinery residues particles distribute more uniformly in the matrix and the agglomerates and coarse alumina refinery residues blocks are not present. This indicates the clear formation of alumina refinery residues particles from the reaction. It exhibits preferred particulate features and

Fig. 4 End milling forces

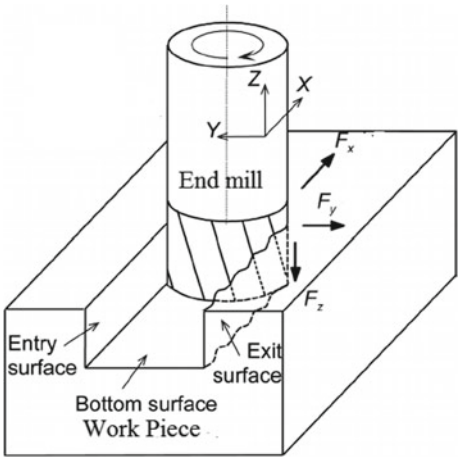

Fig. 5 End milled sample

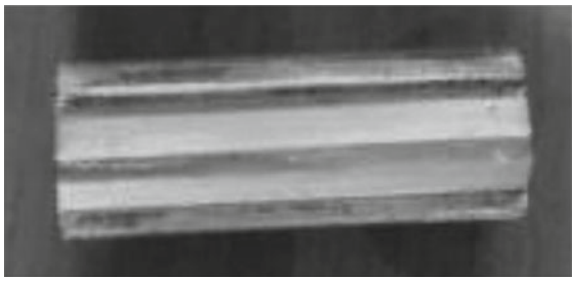

Table 2 Design of experiments

Factors/levels	−1	0	1
Speed (rpm)	1500	2000	2500
Feed (mm/min)	0.1	0.2	0.3
Depth of cut (mm)	1	1.5	2

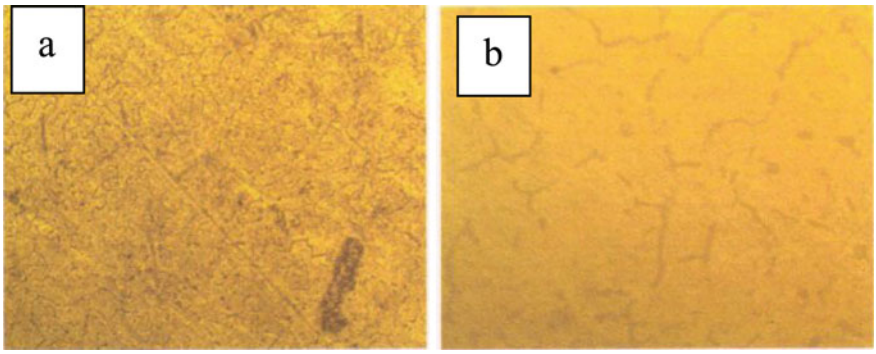

Fig. 6 Microscopic images of Al6061 with 3 wt% of alumina refinery residues at **a** 100× and **b** 400

Table 3 End milling cutting forces SN ratio and means

Ex. No.	Speed	Feed	Depth of cut	*Fx*			*Fy*			*Fz*		
				Fx N	SNR	Mean	*Fy* N	SNR	Mean	*Fz* N	SNR	Mean
1	−1	−1	−1	216	−46.7	215.6	146	−43.3	145.8	38	−31.6	37.8
2	−1	0	0	237	−47.5	236.5	151	−43.6	151.2	46	−33.3	46.2
3	−1	1	1	348	−50.8	347.6	207	−46.3	207.4	59	−35.4	58.8
4	0	−1	0	176	−44.9	176.0	132	−42.4	131.8	40	−32.0	39.9
5	0	0	1	242	−47.7	242.0	168	−44.5	168.5	45	−33.1	45.2
6	0	1	−1	274	−48.8	273.9	156	−43.8	155.5	50	−34.1	50.4
7	1	−1	1	218	−46.8	217.8	141	−43.0	141.5	40	−32.0	39.9
8	1	0	−1	187	−45.4	187.0	148	−43.4	148.0	45	−33.1	45.2
9	1	1	0	253	−48.1	253.0	172	−44.7	171.7	56	−34.9	55.7

more homogeneous distribution of alumina refinery residues particles. This would be beneficial for smooth machining and reduction of cutting forces.

3.2 Milling Tool Cutting Forces Analysis

The experimental data were reported in Table 3 for means and S/N ratio of the cutting force *Fx*, *Fy*, *Fz*.

The analyses of the experimental data are carried using the MINITAB 17 software especially used for design of experiment applications (Table 4).

We observe that the plot for speed, feed and depth of cut to SN ratios, the effective speed is 1500 rpm, Effective feed is 0.3 mm/min and effective depth of cut 2 mm.

From Table 5, we can infer that speed is of prime consideration to minimize the cutting force to certain extent followed by feed and depth of cut.

Taguchi Analysis: *Fz* (*N*) versus Speed, Feed, Depth of cut

Figures 7, 8, 9, 10, 11 and 12 shows the main effects plot for S/N ratios and means. The level of a factor with the highest S/N ratio was the optimum level for responses

Table 4 Response table for signal-to-noise ratios (smaller is better) and means for *Fx*

Level	*Fx* signal to noise ratios			*Fx* means		
	Speed	Feed	Depth of cut	Speed	Feed	Depth of cut
−1	−48.23	−46.11	−46.95	266.6	203.1	225.5
0	−47.11	−46.86	−46.32	230.6	221.8	221.8
1	−46.75	−49.21	−48.42	219.3	291.5	269.1
Delta	1.57	3.10	1.60	47.3	88.4	47.3
Rank	3	1	2	3	1	2

Table 5 Response table for signal-to-noise ratios (smaller is better) and means for *Fy*

Level	Signal-to-noise ratios			Means		
	Speed	Feed	Depth of cut	Speed	Feed	Depth of cut
−1	−44.4	−42.89	−43.5	168.1	139.7	149.8
0	−43.59	−43.84	−43.56	151.9	155.9	151.6
1	−43.7	−44.96	−44.63	153.7	178.2	172.4
Delta	0.81	2.06	1.12	16.2	38.5	22.7
Rank	3	1	2	3	1	2

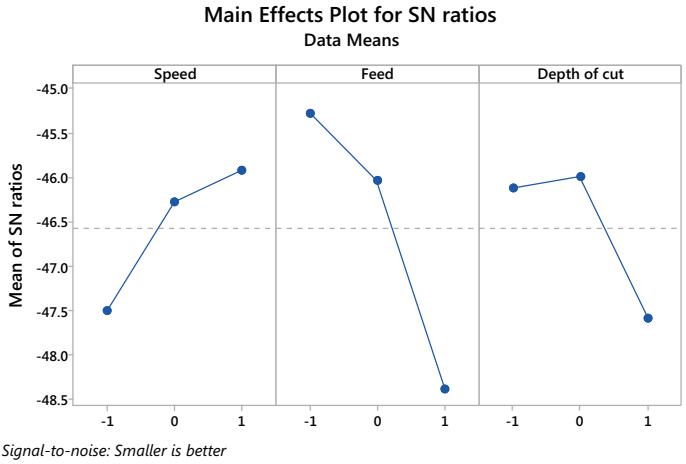

Fig. 7 SN ratio for *Fx* (*N*)

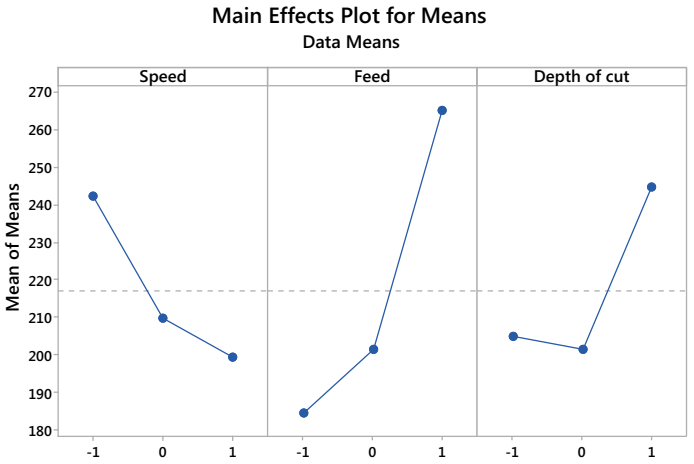

Fig. 8 Means plot for *Fx* (*N*)

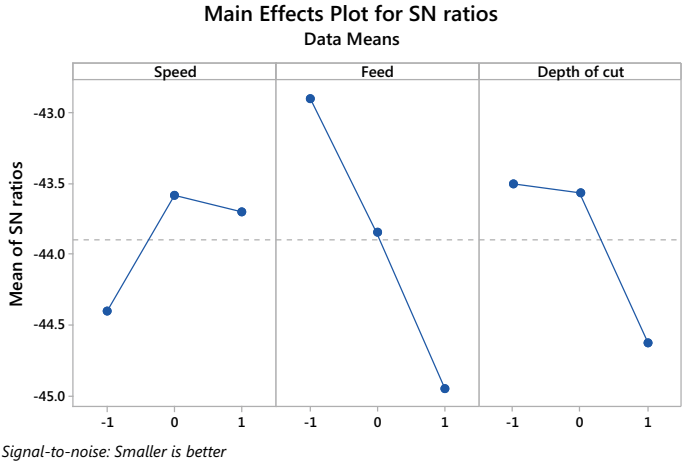

Fig. 9 SN Ratio for *Fy* (*N*)

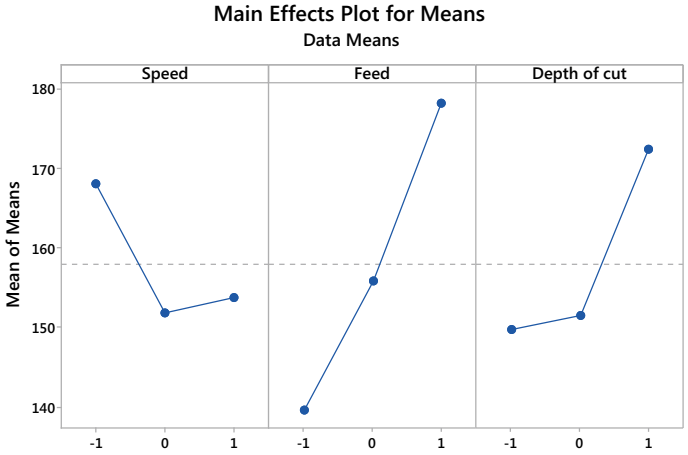

Fig. 10 Means plot for *Fy* (*N*)

measured. From the S/N ratio analysis in Figs. 1, 2 and 3, the optimal machining conditions were 400 mm/min feed rate (level 1), 2600 rpm spindle speed (level 3) and 0.7 mm depth of cut (level 1) for cutting force *Fx*, *Fy* and *Fz*.

Main effects are feed, depth of cut, and cutting speed as per the response Tables 4, 5 and 6 for forces *Fx*, *Fy* and *Fz*.

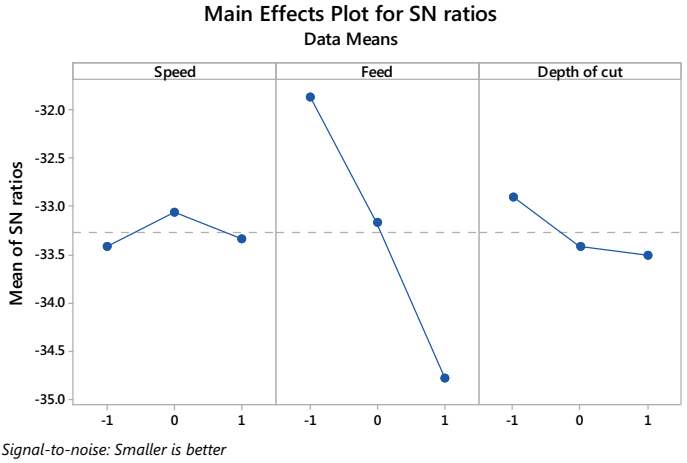

Fig. 11 SN ratio for *Fy* (*N*)

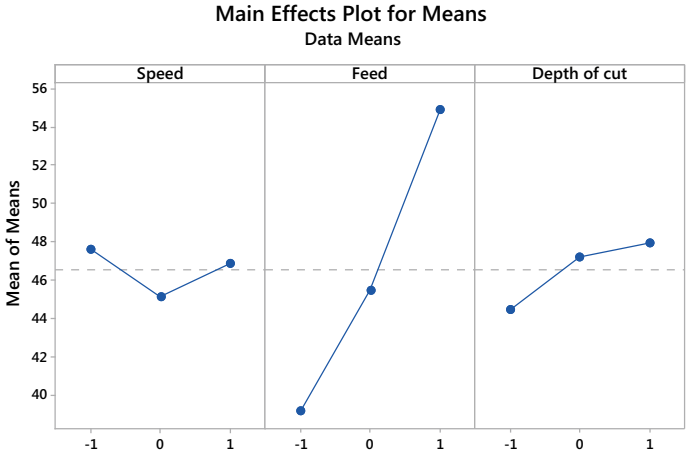

Fig. 12 Means plot for *Fy* (*N*)

Table 6 Response table for signal-to-noise ratios (smaller is better) and means for *Fz*

Level	Signal-to-noise ratios			Means		
	Speed	Feed	Depth of cut	Speed	Feed	Depth of cut
−1	−33.41	−31.86	−32.86	47.6	39.2	44.5
0	−33.05	−33.16	−33.41	45.2	45.5	47.3
1	−33.34	−34.78	−33.5	46.9	55.0	48.0
Delta	0.36	2.92	0.60	2.5	15.8	3.5
Rank	3	1	2	3	1	2

4 Conclusion

Thus, the alumina refinery residue-reinforced Al6061 hybrid metal matrix composite plate is subjected to milling operation in a vertical machining centre. The forces acting on the tool are measured using a tool force dynamometer, and the readings were noted down with the help of a digital force indicator. When compared to the previous studies done on the aluminium-based hybrid metal matrix composite [1], the alumina refinery residue-reinforced hybrid metal matrix composite results in less force on the tool while milling. Thus, the machinability of this composite will be comparatively low.

References

1. Alam MT, Ansari AH (2014) Characterisation and behaviour of aluminium-silicon carbide composite casting. Indian Foundry J 60(11):36–42. ISSN 0379-5466
2. Harris SJ (1998) Cast metal matrix composites. Mater Sci Technol 4(3):231–239
3. Nosonovsky M, Rohatgi PK (2012) Biomimetics in materials science: self-healing, self-lubricating, and self-cleaning materials. In: Springer series in materials science, vol 152, New York, pp 95–236
4. Winkler PJ (2000) Materials for transportation technology. Wiley-VCH
5. Ray N, Kerketta DK (2010) Some studies on aluminium matrix in situ composites produced by stir casting method. ME thesis. NIT Rourkela
6. Ibrahim IA, Mohamed FA, Lavernia EJ (1991) Metal matrix composites a review. J Mater Sci 26:1137–1157
7. Rosso M (2006) Ceramic and metal matrix composites: routes and properties. J Mater Process Technol 175(1–3):364–375
8. Ram Prabhu T (2015) Effects of solid lubricants, load, and sliding speed on the tribological behavior of silica reinforced composites using design of experiments. Mater Des 77:149–160
9. Baradeswaran A, Vettivel SC, Elaya Perumal A, Selvakumar N, Franklin Issac R (2014) Experimental investigation on mechanical behaviour, modeling and optimization of wear parameters of B4C and graphite reinforced aluminium hybrid composites. Mater Des 63:620–632
10. Vijaya Ramnath B, Elanchezhian C, Jaivignesh M, Rajesh S, Parswajinan C, Siddique Ahmed Ghias A (2014) Evaluation of mechanical properties of aluminium alloy, alumina boron carbide metal matrix composites. Mater Des 58:332–338
11. Patel SK, Kumar R, Nateriya R (2014) Microstructural analysis, micro hardness and tensile strength of silicon carbide and zirconium silicate dual reinforced particle ADC-12 alloy composite. Int J Appl Sci Eng Res 3(3):723–733
12. Kumar D, Singh J (2014) Comparative investigation of mechanical properties of aluminium based hybrid metal matrix composites. Int J Eng Res Appl, National Conference on Advances in Engineering and Technology. ISSN 2248-9622, 5–9. http://www.ijera.com/special_issue/AET_Mar_2014/ME/B0509.pdf
13. Maheswaran P, Thomas Renald CJ (2014) Investigation on wear behavior of Al6061–Al_2O_3—graphite hybrid metal matrix composites using artificial neural network. Int J Curr Eng Technol, E-ISSN 2277 – 4106, P-ISSN 2347 - 5161, 363–367. http://inpressco.com/wp-content/uploads/2014/02/Paper66363-367.pdf
14. Rama Rao S, Padmanabhan G (2012) Fabrication and mechanical properties of aluminium—boron carbide composites. Int J Mater Biomater Appl, ISSN 2249-9679, 15–18
15. Dhaval JP, Jayvadan KP, Vikram MP, Rishad RJ, Ritu DP (2010) Optimization of formulation parameters on famotidine nanosuspension using factorial design andthe desirability function.

Int J Pharm Tech Vol.2, No.1:155–161. http://sphinxsai.com/sphinxsaiVol_2No.1/PharmTech_Vol_2No.1/PharmTech_Vol_2No.1PDF/PT=25%20(155-161).pdf
16. Khushbu SP, Vadalia KR, Patel JK (2014) Development and evaluation of in situ gelling system for treatment of periodontitis. Int J Pharm Tech 6(7):2102–2112
17. Adalarasan R, Santhanakumar M (2014–2015) Response surface methodology and desirability analysis for optimizing μ WEDM parameters for Al6351/20%Al_2O_3 composite. Int J Chem Tech Res 7(6):2625–2631
18. Heuss R, Müller N, van Sintern W, Starke A, Tschiesner A (2012) Advanced industries light weight, heavy impact, McKinsey - Berlin Article pp 1–24. https://www.mckinsey.com/~/media/mckinsey/dotcom/client_service/automotive%2520and%2520assembly/pdfs/lightweight_heavy_impact.ashx
19. Rohatgi P (1991) Cast aluminum matrix composites for automotive applications—potential applications of metal matrix composites, JOM 43, 10–15. https://doi.org/10.1007/BF03220538
20. Hellard G (2013) Composites in airbus a long story of innovations and experiences composites in Global Investor Forum by Dr Roland Thévenin _V51PR _v1 1, 1–26. https://docplayer.net/25342669-Composites-in-airbus-a-long-story-of-innovations-and-experiences-presented-by-guy-hellard.html
21. Rajan TPD, Pai BC (2014) New directions in development and applications of cast metal matrix composites. Indian Found J 60(11):22–30. ISSN 0379-5466
22. Manna A, Bhattacharayya B (2003) A study on machinability of Al/SiC–MMC. J Mater Process Technol 140:711–716
23. Liu CS, Zhao B, Gao GF, Jiao F (2002) Research on the characteristics of the cutting force in the vibration cutting of a particle reinforced metal matrix composites SiCp/Al 129(1–3):196–199
24. Muthukrishnan N, Paulo Davim J (2009) Optimization of machining parameters of Al/SiC-MMC with ANOVA and ANN analysis. J Mater Process Technol 209:225–232
25. Arokiadass R, Palaniradja K, Alagumoorthi N (2011) Surface roughness prediction model in end milling of Al/SiCp MMC by carbide tools. Int J Eng Sci Technol 3(6):78–87
26. Divya Theja K, Harinath Gowd G, Kareemulla S (2013) Prediction and optimization of end milling process parameters using artificial neural networks. Int J Emerg Technol Adv Eng 3(9):117–122

Experimental Studies on Mechanical Behaviour of Polylactide (PLA) Matrix—Aluminium Oxide (Al_2O_3) Particles Reinforced Composites

R. Girimurugan, M. Vairavel, A. Anandha Moorthy, E. Prakash, and S. Madheswaran

Abstract In the recent years, research focuses on metal powder reinforced polymer matrix composites that are significantly increased to develop the high strength, lightweight, high stiffness, low-cost composites and the replacement of the conventional materials for commercial applications like aircraft, automobiles and so on. Abundant researcher's investigation is focusing on the usage of polymeric materials as matrix materials and metallic powders as reinforcement to develop various varieties of polymeric material-based composites. This research work is focused on the mechanical behaviour of aluminium oxide (Al_2O_3) particles which are reinforced with polylactide (PLA) in different concentration ratios (0/100, 5/95, 10/90, 15/85, 20/80, 25/75 and 30/70) by weight percentage. The required specimens with ASTM standards are taken over from the polymer-based composite panel using the water jet machining process. The mechanical properties of the well-prepared PLA-based composites are evaluated under the standard testing methods, and the test outcomes reveal that the increasing weight percentages of the Al_2O_3 particles with PLA are enhancing the mechanical properties of the composites significantly.

Keywords Mechanical behaviour · Experimental studies · Polylactide (PLA)—aluminium oxide (Al_2O_3) particles · Composites

R. Girimurugan (✉)
Department of Mechanical Engineering, Nandha College of Technology, Erode, Tamil Nadu, India
e-mail: dr.r.girimurugan@gmail.com

M. Vairavel
Department of Mechanical Engineering and Science, Vels Institute of Technology and Advanced Studies, Chennai, Tamil Nadu, India

A. A. Moorthy · E. Prakash · S. Madheswaran
Department of Mechanical Engineering, Bannari Amman Institute of Technology, Sathyamangalam, Erode District, Tamil Nadu 638401, India

G. Kumaresan et al. (eds.), *Advances in Materials Research*, Springer Proceedings in Materials 5, https://doi.org/10.1007/978-981-15-8319-3_58

1 Introduction

Recent increasing production of biodegradable plastic materials has raised environmental concerns about the large-scale production of nonbiodegradable and nonrecyclable petroleum-based polymers. Polylactic acid (PLA) is a widely utilized biodegradable polymer because of its good mechanical properties, high stiffness, high transparency, excellent printability and good processability [1, 2]. Polylactic acid or polylactide (PLA), a eco-friendly polyester formed from renewable resources, is used for a variety of applications (biomedical, packaging, textile fibres and technical items). Owed to its intrinsic properties, PLA has a key point in the market of biopolymers, being one of the largest parts shows potential for extra developments [3]. Different studies showed that polylactide (PLA) is one of the most promising biopolymers due to its good mechanical properties and biodegradability [4]. In recent times, the adding up of Al_2O_3 particles reinforcements are to be found high to enhance some mechanical properties of the polymer matrix composites significantly [5, 6]. Doping of Al_2O_3 particles with polylactide in very small concentrations is significantly improved the tensile strength, Young's modulus and ductility of the polymer matrix composites [7]. Crystallization rate of PLA was affected by the inclusion of reinforcement particles (nano-Al_2O_3) with PLA composites. The XRD results also confirmed that the crystal formation is very clear in the PLA/nano-Al_2O_3 composites due to the addition of the reinforcement particles (nano-Al_2O_3). The inclusion of nano-Al_2O_3 particles increases the crystallinity and leads to an improvement of the storage modulus [8]. Processing polymer composites with inorganic/organic nanoparticles or blending with other polymers offer a great opportunity to enhance the physical, thermal and mechanical properties of neat polymers [9–12]. The effectiveness of fillers with nanometric dimensions strongly depends on their shape, particle size, aggregate size, surface characteristics and degree of dispersion. According to classical composite theory, improved interfacial bonding between the polymer matrix and filler particles leads to enhanced practical properties of the composites. PLA composites have been reported with various nanoparticles, including carbon nanotubes, layered silicates or clays, silica, graphite, magnesium oxide, etc. [13]. Polymer–alumina associations have interesting applications owing to their mutual interaction through polar coupling and hydrogen bonding, which provide good adhesion between the ceramic and polymeric components. This is of practical interest in the case of polymeric system such as polylactic acid (PLA). These polymers contain carboxylic ester groups in their structures, which could give rise to strong interactions with alumina particles [14]. The composites which are made by using the PLA/nano-Al_2O_3 particles became highly rigid, exhibiting a high modulus with an increase in the reinforcement weight percentage with PLA matrix [15]. So in this experimental studies, PLA has taken as a matrix material and aluminium oxide (Al_2O_3) particles are taken as reinforcement material to prepare the composites with seven different weight percentages of PLA and Al_2O_3 particles.

2 Materials and Methods

The PLA which is used in this experimental study is a commercial grade (L99L—GBP30), obtained from Covai Seenu and Company Ltd., Coimbatore, Tamil Nadu, India. It had a density of 1.25 ± 0.05 g/cm^3; weight average molecular weight $M_W =$ 187 kg/mol; density = 1.58 g/cm^3; glass transition temperature, T_g, is approximately 60–63 °C; and melting temperature, Tm, is around 179–180 °C. The aluminium oxide (Al_2O_3) which is used in this research is procured from Totale Refractories, Chennai, Tamil Nadu, India, which is containing 65% of pure Al_2O_3 particles remaining 35% significantly lower levels of common impurities such as iron, sodium and silica. PLA pellets and Al_2O_3 in different weight percentage of 0, 5, 10, 15, 20, 25 and 30 were mixed. The mixtures of PLA pellets and Al_2O_3 were melted and blended inside the roto-thermo heating come blending machine at a rotational speed of 175 rpm, at a temperature of 200 °C at an interval of 10 min. The well-blended composites were taken over into a compression moulding machine at 180 °C, and the compressed composite mats are allowed to cool at room temperature. The weight percentage of Al_2O_3 reinforcement materials with PLA matrix composites of 0, 5, 10, 15, 20, 25 and 30 were likewise abridged as Sample-S1, S2, S3, S4, S5, S6 and S7 respectively. The required test specimen with ASTM statndards is cutout from the well-prepared composite mats using water jet machining process (Tables 1 and 2; Fig. 1).

An ASTM D638 standard is adopted to evaluate the various tensile properties of polylactide (PLA)—aluminium oxide (Al_2O_3) composites. A typical tension test is carried in computerized universal testing machine. The test specimen with 165 mm gauge length, 13 mm width and 10 mm thickness has positioned among the jaws of the universal testing machine and rate of load is kept constant at 3 mm/min. The different tensile properties like tensile load, tensile stress and tensile strain are estimated. The compressive properties of the polylactide (PLA)—aluminium oxide (Al_2O_3) composites are calculated using the ASTM standard D3410, and the test specimen with 155 mm gage length, 25 mm width and 5 mm thickness has located

Table 1 Chemical composition of reinforcement material (aluminium oxide—Al_2O_3)

S. No.	Compound/element	Percentage of compound/element (w/w)
1	Al_2O_3	64.8
2	CaO	0.93
3	SiO_2	4.0
4	Fe_2O_3	1.5
5	MgO	3.2
6	Na_2O	2.75
7	K_2O	0.51
8	Cl	3.9
9	C	1.25
10	S	0.22

Table 2 Composition of matrix, reinforcement materials and specimen description

S. No.	Weight % of matrix material (polylactide—PLA) (%)	Weight % of reinforcement material (aluminium oxide—Al_2O_3) (%)	Specimen description
1	100	0	Sample-S1
2	95	5	Sample-S2
3	90	10	Sample-S3
4	85	15	Sample-S4
5	80	20	Sample-S5
6	75	25	Sample-S6
7	70	30	Sample-S7

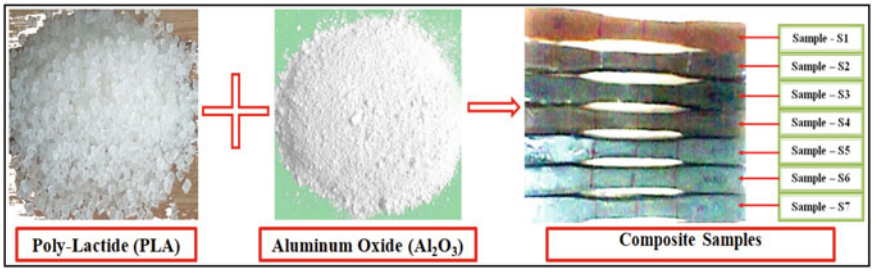

Fig. 1 Materials and composite specimens

in the grips of the computerized universal testing machine. The load rate is kept constant at 5 mm/min. The surface hardness of the polylactide (PLA)—aluminium oxide (Al_2O_3) composites is determined using the ASTM standard D785, and the test specimen with 50 mm width, 50 mm breadth and 5 mm thickness has kept on the test table in the Rockwell hardness tester. According to specimen composition, the load was applied on the surface of the specimens and the corresponding readings were noted directly from the dial which is available in the Rockwell hardness tester.

3 Results and Discussions

The different mechanical test results which are obtained from the Computerized Universal Testing Machine (UTM) and Rockwell hardness tester are depicted in Figs. 2, 3, 4 and 5. The particular mechanical properties of the PLA/Al_2O_3 composites are superiorly influenced by the weight percentage of the aluminium oxide (Al_2O_3) particles with polylactide (PLA). The tensile and compressive load of the composite specimens which are made from PLA/Al_2O_3 are improved considerably with the additional weight percentage of Al_2O_3 particles and reduced correspondingly to the

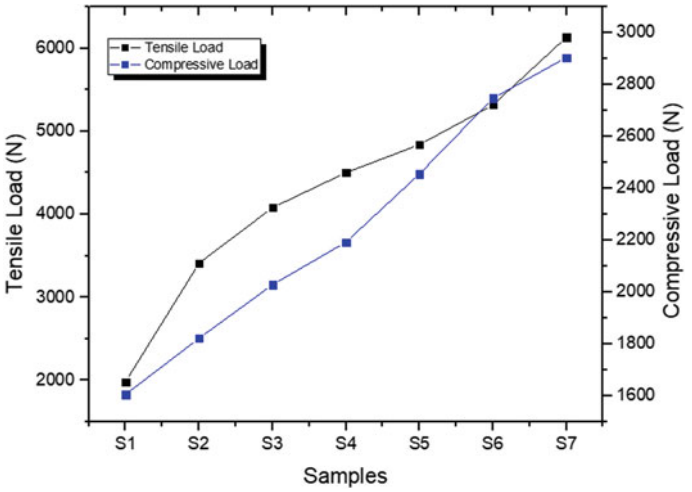

Fig. 2 Variation of maximum tensile and compressive load on PLA/Al_2O_3 composites

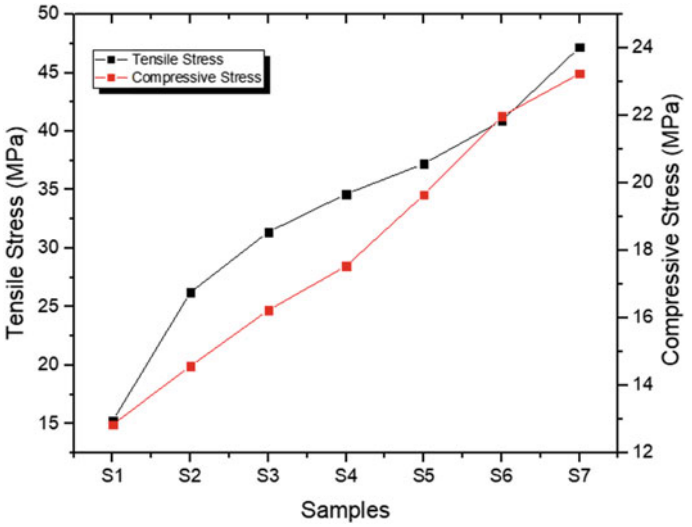

Fig. 3 Variation of tensile and compressive stress on PLA/Al_2O_3 composites

increasing weight percentage of PLA. The enhancement of mechanical properties of these composite specimens was owed to the elevated weight percentage of Al_2O_3 particles, superior interfacing and stress shifting between the reinforcement material (i.e. Al_2O_3 particles) to the matrix material (i.e. PLA).

The tensile and compression test results which are obtained experimentally from universal testing machine are shown in Figs. 2, 3 and 4. The maximum tensile

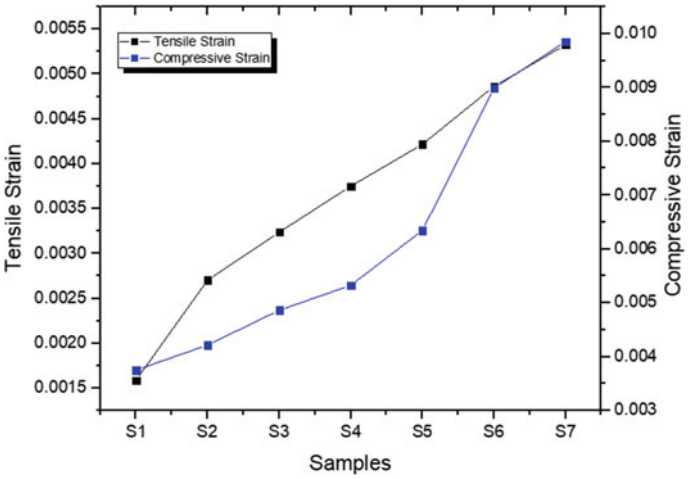

Fig. 4 Variation of maximum tensile and compressive load on PLA/Al_2O_3 composites

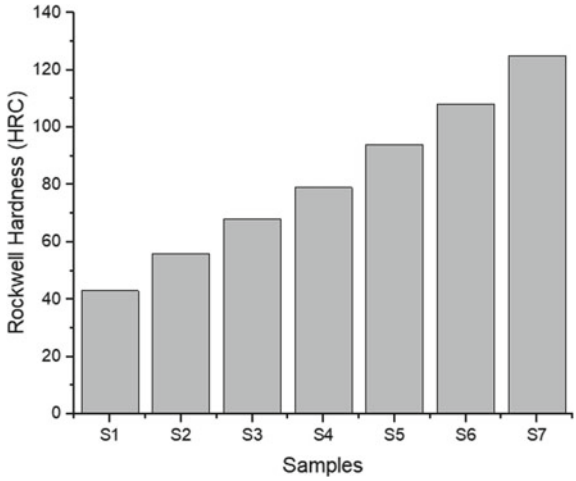

Fig. 5 Variation of Rockwell hardness on PLA/Al_2O_3 composites

and compressive load of the PLA/Al_2O_3 composites which are obtained from the tensile and compressive test are in the range of 6133 and 2905 N correspondingly. The minimum tensile and compressive load of the PLA/Al_2O_3 composites which are obtained from the tensile and compression test are in the range of 1981 and 1606 N correspondingly. Along with the seven PLA/Al_2O_3 composites specimens, the highest tensile and compressive load of 6133 N and 2905 N are noted from the specimen S7 (70% PLA, 30% Al_2O_3 particles), the lowest tensile and compressive load of 3048 N and 2826 N are identified from the specimen S1 (100% PLA, 0% Al_2O_3 particles), respectively. The maximum tensile and compressive stress of the

PLA/Al_2O_3 composites which are obtained from the tensile and compressive test are in the range of 47.177 and 23.238 MPa correspondingly.

The minimum tensile and compressive stress of the PLA/Al_2O_3 composites which are obtained from the tensile and compressive test are in the range of 15.242 and 12.846 MPa correspondingly. Along with the seven PLA/Al_2O_3 composites specimens, the highest tensile and compressive stress of 47.177 and 23.238 MPa are noted from the specimen S7 (70% PLA, 30% Al_2O_3 particles), the lowest tensile and compressive stress of 15.242 and 12.846 MPa are identified from the specimen S1 (100% PLA, 0% Al_2O_3 particles), respectively. The maximum tensile and compressive strain of the PLA/Al_2O_3 composites are in the range of 0.0053257 and 0.0098543, respectively. The minimum tensile and compressive strain of the PLA/Al_2O_3 composites are in the range of 0.0015874 and 0.0037514, respectively.

Along with the seven PLA/Al_2O_3 composites specimens, the highest tensile and compressive strain of 0.0053257 and 0.0098543 are noted from the specimen S7 (70% PLA, 30% Al_2O_3 particles), the lowest tensile and compressive strain of 0.0015874 and 0.0037514 are identified from the specimen S1 (100% PLA, 0% Al_2O_3 particles), respectively. The maximum and minimum values of Rockwell hardness (HRC) of the PLA/Al_2O_3 composites are in the range of 43 HRC and 125 HRC, respectively. Along with the seven PLA/Al_2O_3 composites specimens, the highest (125 HRC) and lowest values (43 HRC) of Rockwell hardness are noted from the specimen S7 (70% PLA, 30% Al_2O_3 particles) and S1 (100% PLA, 0% Al_2O_3 particles), respectively. The X-ray diffraction (XRD) pattern of PLA/Al_2O_3 composites (70% PLA, 30% Al_2O_3 particles) is shown in Fig. 6 that shows the stages that exist in alloy and are largely aluminium and Al_2O_3 in the PLA/Al_2O_3 composites. Similarly, the scanning electron microscope (SEM) image of the better composite sample (30% Al_2O_3/70% PLA) is shown in Fig. 7.

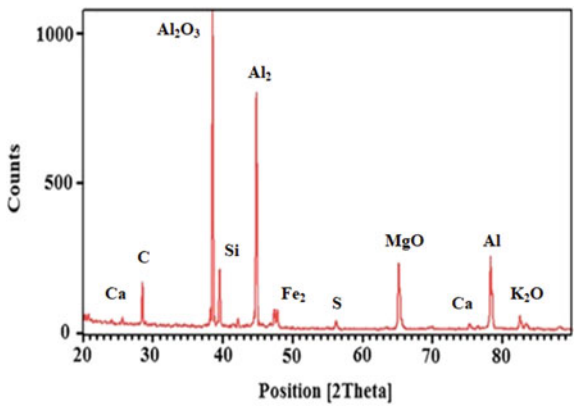

Fig. 6 X-ray diffraction pattern of PLA/Al_2O_3 composites (70 wt% of PLA/30 wt% of Al_2O_3 particles)

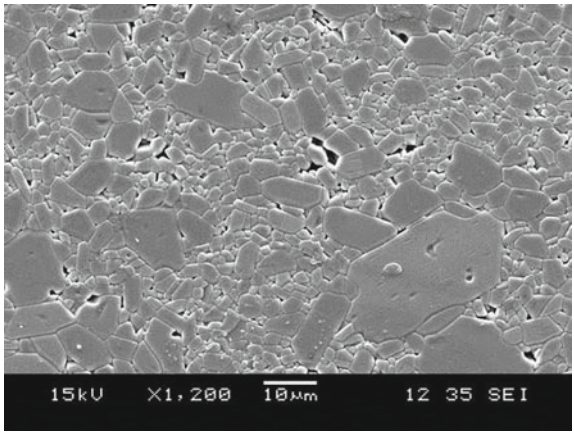

Fig. 7 Scanning electron microscope (SEM) image of PLA/Al_2O_3 composites (70 wt% of PLA/30 wt% of Al_2O_3 particles)

4 Conclusions

The experimental result shows that a helpful polymer–metal composite with reasonable strength might be successfully developed using aluminium oxide (Al_2O_3) particles as reinforcement material and polylactide (PLA) as matrix material. The combinations of PLA/Al_2O_3 composites are get hold of well mechanical properties with respect to the increasing % of reinforcement with matrix material. It was noted that the several mechanical properties like tensile load, compressive load, tensile stress, compressive stress, tensile strain, compressive strain and hardness were superior, when the aluminium oxide (Al_2O_3) particles weight percentage with PLA were raised from 0 to 30%. The maximum tensile load, tensile stress, tensile strain, compressive load, compressive stress, compressive strain and hardness are noted for the Al_2O_3 composites having 30% of reinforcement particles and 70% of matrix material. Nevertheless, there is a requisite to do a supplementary research work that should be done on the interaction optimization between the reinforcement and matrix to attain the most excellent mechanical performance composites. It is suggested that the composites which are developed from the aluminium oxide (Al_2O_3) particles and polylactide (PLA) be capable of a substitute for some steel materials due to the superior mechanical properties.

References

1. Yin HY, Wei XF, Bao RY, Dong QX, Liu ZY, Yang W, Xie BH, Yang MB (2015) Enantiomeric poly (d-lactide) with a higher melting point served as a significant nucleating agent for poly(l-lactide). Cryst Eng Commun 17:4334–4342
2. Park SH, Lee SG, Kim SH (2013) Isothermal crystallization behavior and mechanical properties of polylactide/carbon nanotube nanocomposites. Compos Part A 46:11–18

3. Murariu M, Dubois P (2018) PLA composites: from production to properties. Adv Drug Deliv Rev 107:17–46
4. Srivatsan TS (1996) Microstructure, tensile properties and fracture behaviour of Al_2O_3 particulate-reinforced aluminium alloy metal matrix composites. J Mater Sci 31:1375–1388
5. Kim HH, Babu JSS, Kang CG (2014) Hot extrusion of A356 aluminium metal matrix composite with carbon nanotube/Al_2O_3 hybrid reinforcement. Metall Mater Trans A 45:2636–2645
6. Siengchin S, Pohl T, Medina L, Mitschang P (2013) Structure and properties of flax/polylactide/alumina nanocomposites. J Reinf Plast Compos 32(1):23–33
7. Lobo AG, Sarojini BK, Thomas S, Aman A, Nawaz M, Mujeeb A (2018) An experimental and theoretical study on the effect of microstructure on the tensile behavior of polylactide nano composites. In: Antony K, Paulo Davim J (eds) Advanced manufacturing and materials science. Lecture notes on multidisciplinary industrial engineering. Springer, Cham, pp 337–348
8. Lule Z, Kim J (2019) Nonisothermal crystallization of surface-treated alumina and aluminium nitride-filled polylactic acid hybrid composites. Polymers 11:2–12
9. Nijenhuis AJ, Colstee E, Grijpma DW, Pennings AJ (1996) High molecular weight poly (l-lactide) and poly (ethylene oxide) blends: thermal characterization and physical properties. Polymer 37:5849–5857
10. Liu M, Pu M, Ma H (2012) Preparation structure and thermal properties of polylactide/speiolite nanocomposites with and without organic modifiers. Compos Sci Technol 72:1508–1514
11. Najafi N, Heuzey MC, Carreau PJ (2012) Polylactide (PLA)-clay nanocomposites prepared by melt compounding in the presence of a chain extender. Compos Sci Technol 72:608–615
12. Zhang MQ, Rong MZ, Ruan WH (2009) Nano and micro mechanics of polymer blends and composites. Hanser Publishers 4:425–470
13. Das K, Ray SS, Chapple S, Wesley-Smith J (2013) Mechanical, thermal, and fire properties of biodegradable polylactide/boehmite alumina composites. Ind Eng Chem Res A-I 52(18):6083–6091
14. Papirer E, Perrin JM, Nanse G, Ftoux P (1994) Adsorption of poly (methylmethacrylate) on an a-alumina: evidence of formation of surface carboxylate bonds. Eur Polymer J 30:985–991
15. Lule Z, Kim J (2019) Thermally conductive and highly rigid polylactic acid (PLA) hybrid composite filled with surface treated alumina/nano-sized aluminium nitride. Compos Part A 124:01–08

The Effect of Mg and Mn Addition on Hardness, Tensile and Wear Properties of LM6 Aluminum Alloy

S. Manojkumar, M. Kumar, M. Ananth, G. Mageshwaran, and P. Hariprakash

Abstract Aluminum and its alloys have become inevitable in the modern world. Today, aluminum has become the most preferred material by the engineers due to its peculiar properties such as light, strong, resilient, ductile at low temperature, high-strength to weight ratio and corrosion resistance. Aluminum has approximately 1/3rd of the weight of iron, copper, brass or steel. Aluminum alloys are widely used in modern aircraft industries and in various other transportation industries because of its improved properties. Among all series of Al alloys, aluminum-silicon alloy is widely used in the automotive industry because of its good castability, low cost and superior mechanical properties. In this study, the aluminum LM6 is alloyed with magnesium and manganese in three aspects i.e. LM6 aluminum alloy is added with 5 wt% magnesium as first specimen, LM6 aluminum alloy with 5 wt% manganese as second and LM6 aluminum alloy with both manganese (5 wt%) and magnesium (5 wt%) as third specimen was synthesized by stir casting method. The effect of Mg and Mn reinforcement with LM6 aluminum alloy on its hardness, tensile properties and wear loss were investigated.

Keywords LM6 · Mg · Mn · Hardness · Tensile strength · Wear loss first section

1 Introduction

LM6 aluminum alloy is mostly used in the automobile sector because of its good castability, low cost and excellent mechanical properties and the properties of the LM6 alloy can be enhanced through proper heat treatment [1–4]. Manganese (Mn) is an important element in aluminum–silicon (Al–Si) casting alloy to establish the mechanical properties of the alloy. Addition of 0.2 wt% of Mn in Al–Si alloy which converts iron platelet phases into star-like intermetallics. The tensile property of the alloy mostly depends on the dimensions of the intermetallics. The increase in Mn/Fe

S. Manojkumar (✉) · M. Kumar · M. Ananth · G. Mageshwaran · P. Hariprakash
Department of Mechanical Engineering, Bannari Amman Institute of Technology, Sathyamangalam, Erode District, Tamil Nadu 638401, India
e-mail: mjoeaccet24@gmail.com

G. Kumaresan et al. (eds.), *Advances in Materials Research*, Springer Proceedings in Materials 5, https://doi.org/10.1007/978-981-15-8319-3_59

ratio does not show shows as much improvement in the tensile property of the alloy. The reduction in the Magnesium (Mg) in the Al–Si alloy results in the decrease in the yield stress, ultimate strength, hardness and also increase in the elongation of the fracture [1, 5].

Addition of Mn changes the morphology of β-Al_5FeSi needle-like structure into Chinese script like morphology which increases the overall tensile and fatigue properties [6]. Increase in the Mg content in the Al–Si–Mg alloys leads to raising the tensile properties of the alloy by 10 MPa and small decrease in the ductility. The increase in the Mg content forms a large volume fraction of the π-$Al_8Mg_3FeSi_6$ in the alloy which is the main phenomena in the effect of strength and ductility [7].

Adding Mg content in the AA2219 aluminum alloy along with Sc (Scandium) promotes the formation of nucleation rate of the Al_3Sc which will lead to an increase in the improved high-temperature stability of the alloy [8]. The formation of Mg_2Si found in Al–Si alloy while adding Mg content in the alloy, this increase in the Mg content in the alloy leads to an increase in the hardness of the alloy. As well as the increase in the Mg content in the alloy shows the improvement in the tensile strength of the alloy and the percentage of elongation values decreased [9]. In A356 alloy, decrease in the grain coarsening rate of globular α-Al in the isothermal heating while adding magnesium in the semi-solid condition. Large Chinese script Mg_2Si intermetallic compound is formed which increases the tensile properties of the alloy [10]. In die-cast 380 alloys, the increase in Mg content from 0.06 to 55%, leads to formation of π-$Al_8Mg_3FeSi_6$ and Q-$Al_5Cu_2Mg_8Si_6$ phases from 0.8% to 1.7%. Tensile strength is maximum at 0.3% of Mg, further increase Mg content leads to the decrease in the tensile strength, because of the formation of the insoluble intermetallic [11].

The current study aims to study the influence of Mg and Mn inclusion in LM6 aluminum alloy on its hardness, tensile strength and wear loss.

2 Experimental Details

The chemical elements present in LM6 aluminum alloy is given in Table 1. There are three alloys prepared with varying percentage of Mg and Mn content. The melting temperature for the proposed alloys was maintained at 750 ± 20 °C. The alloys were prepared using stir casting method, as follows: LM6 + 5 wt% Mg, LM6 + 5 wt% Mn and LM6 + 5 wt% Mg + 5 wt% Mn.

The molten metal was poured into the die to get the desired LM6 alloy which is shown in Fig. 1a. Subsequently, the specimens are machined and subjected to the

Table 1 Chemical composition of LM6

Elements	Cu	Fe	Mg	Mn	Ni	Pb	Si	Al
Percentage (%)	0.10	0.60	0.10	0.50	0.10	0.10	10–13	Remaining

Fig. 1 **a** Casted LM6 alloy. **b** Tensile testing machine

hardness, tensile, and wear testing. Hardness test was performed in the specimen to measure the hardness of the alloy using Rockwell B-scale. Hardness values are calculated with an average of five readings in each specimen. Later, for the tensile testing, the specimen is machined as per ASTM E-8 standard and testing was done in the tensile test machine to measure the tensile strength of the alloy which was shown in Fig. 1b.

Next, the specimen was subjected to the wear test in the computerized pin on disk tribometer to measure the wear resistance of the alloy. The specimens were prepared as per ASTM standard ASTM G99-05 having dimension of circular cross-section with 10 mm diameter and 30 mm in length. The pin is placed against the EN 31 hardened steel disc of 60 HRC. The rotating steel disc has 165 mm diameter and of 8 mm thickness. The dry sliding friction and wear tests were carried out for the loads of 10 and 15 N for the sliding speed ranges from 250 to 750 rpm with an increment of 250 rpm, and for a sliding distance of 1000 m. Before and after each test trial, the specimen surfaces were cleaned with acetone to remove the foreign particles. The pin was weighed before and after each test using weighing apparatus having an accuracy of 0.001 g. The wear loss (μm) is measured by the instrument and the data are noted down. All the experiment trails were conducted at room temperature.

3 Results and Discussion

3.1 Hardness Test

Hardness values of the produced alloys with Mg and Mn are shown in Table 2 and Fig. 2. Figure 2 shows that the average hardness values of the LM6 alloy show higher when compare the LM6 alloyed with Mg and LM6 alloyed with Mn. The Mg 5 wt%

Table 2 Rockwell hardness of the alloys

Specimen	Average hardness value (HRB)
LM6	53.5
LM6 + Mg	44
LM6 + Mn	49.5
LM6 + Mg + Mn	55.5

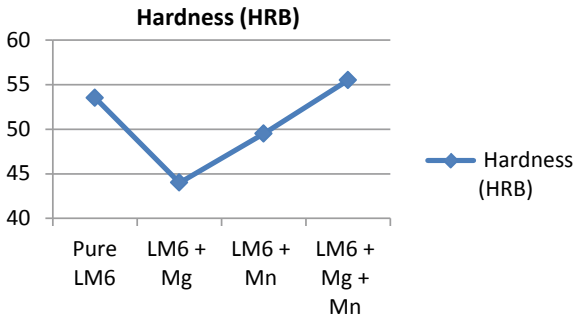

Fig. 2 Average hardness values of LM6 alloys

added in the LM6 alloy reduces the hardness of the alloy and then Mn 5 wt% addition also shows the slight reduction in the LM6 alloy. Mg content 0.25–0.39 wt% will show the significant increase in the harness alloy and then similarly the Mn addition does not significantly affects the alloy [1].

3.2 Tensile Test

The samples tensile tests results are shown in Table 3 and Fig. 3. Tensile test results indicate that decrease in the ultimate strength (UTS), yield strength (YS) and % elongation (e). Magnesium addition from 0.25 to 0.4 wt% allowing to improve tensile strength, yield strength and decrease in the ductility [1]. The results show that there was a decrease in the tensile properties of the alloy may be the presence of intermetallics in the alloy.

Table 3 Tensile test results of the samples

Alloy type	UTS (MPa)	YS (MPa)	% Elongation
Pure LM6	226	214	9.901
LM6 + Mg	179	171	1.818
LM6 + Mn	200	167	1.818
LM6 + Mg + Mn	135	35	1.818

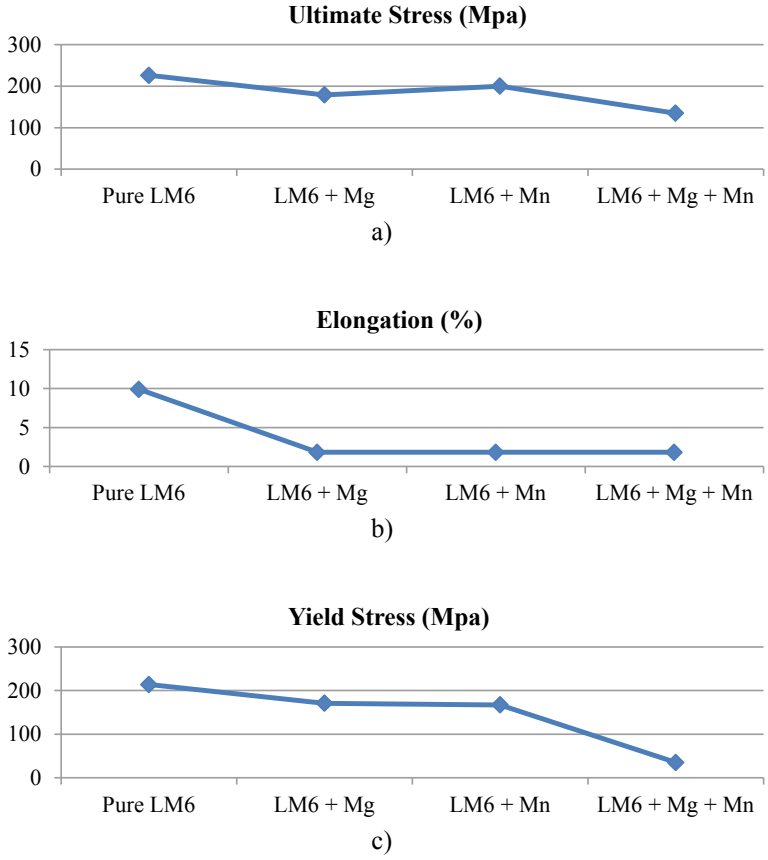

Fig. 3 Effect of Mg and Mn on the tensile properties **a** Ultimate stress **b** % of Elongation **c** Yield stress

3.3 Wear Test

The wear behavior of the LM6 alloy with Mg, Mn and Mg + Mn shown in Table 4. The wear loss was calculated by varying load, sliding speed with constant sliding distance. It was observed that the wear loss is maximum at 500 rpm sliding speed at 1 kg load for pure LM6 alloy. Similarly LM6 + Mg + Mn, the wear loss is maximum at 500 rpm sliding speed at 1 kg load. And then LM6 + Mn, the wear loss is maximum at 15 N load at 500 rpm sliding speed. In LM6 + Mg alloy, the wear loss was maximum at 1.5 kg at 750 rpm sliding speed. The wear loss was observed minimum for LM6 + Mn alloy 1.5 kg at 250 rpm sliding speed. The reason for that minimum wear loss may be the formation of compounds with iron; it tends to lead the morphology dendrites to form into Chinese script morphology.

Table 4 Wear test results

S. No.	Alloy type	Load (N)	Speed (RPM)	Mass before (g)	Mass after (g)	Time (min)	Wear loss (microns)
1	LM6	10	250	6.390	6.386	5	127
2	LM6	10	500	6.386	6.382	5	454
3	LM6	10	750	6.382	6.381	5	134
4	LM6	15	250	6.381	6.379	5	50
5	LM6	15	500	6.379	6.377	5	212
6	LM6	15	750	6.377	6.370	5	8
7	LM6 + Mn	10	250	6.399	6.395	5	176
8	LM6 + Mn	10	500	6.395	6.384	5	11
9	LM6 + Mn	10	750	6.384	6.383	5	80
10	LM6 + Mn	15	250	6.383	6.382	5	7
11	LM6 + Mn	15	500	6.382	6.381	5	124
12	LM6 + Mn	15	750	6.381	6.376	5	28
13	LM6 + Mg	10	250	5.805	5.803	5	96
14	LM6 + Mg	10	500	5.803	5.802	5	91
15	LM6 + Mg	10	750	5.802	5.801	5	130
16	LM6 + Mg	15	250	5.801	5.798	5	111
17	LM6 + Mg	15	500	5.798	5.795	5	75
18	LM6 + Mg	15	750	5.795	5.791	5	241
19	LM6 + Mn + Mg	10	250	6.352	6.344	5	200
20	LM6 + Mn + Mg	10	500	6.344	6.342	5	221
21	LM6 + Mn + Mg	10	750	6.342	6.341	5	47
22	LM6 + Mn + Mg	15	250	6.341	6.340	5	69
23	LM6 + Mn + Mg	15	500	6.340	6.339	5	74

(continued)

Table 4 (continued)

S. No.	Alloy type	Load (N)	Speed (RPM)	Mass before (g)	Mass after (g)	Time (min)	Wear loss (microns)
24	LM6 + Mn + Mg	15	750	6.339	6.336	5	33

4 Conclusion

From the experimental study, the effect of Mg and Mn addition on hardness, tensile strength and wear behavior of LM 6 was investigated the following conclusions are drawn:

- Addition of the 5 wt% Mg with LM6 and 5 wt% Mn with LM6 decrease the hardness of the LM6 alloy. However, the addition of both Mg 5 wt% and Mn 5 wt% to the LM6 which leads to an increase the hardness by 4% than base alloy.
- The tensile properties of produced alloys show decreased tensile properties while adding with Mg, Mn and Mg + Mn to the LM6 alloy. The higher amount (5 wt%) of the Mg and Mn leads to an decrease in the tensile properties of the alloy due to the formation of intermetallic compounds which reduces the ductility of fabricated alloys.
- The addition of both Mg and Mn has significant effect on wear loss. The results show minimum wear loss was observed at 5 wt% of Mg and 5 wt% of Mn to the LM6 aluminum alloy. This is due to the formation of hard interface at the surface that reduces wear loss in the alloy.

References

1. Fortini A, Merlin M, Fabbri E, Pirletti S, Garagnani GL (2016) On the influence of Mn and Mg additions on tensile properties, microstructure and quality index of the A356 aluminum foundry alloy. Proc Struct Integrity 2:2238–2245
2. Ravi Kumar V, Suresh R, Prakash Rao CR, Ravi Kumar DV, Bharat V (2019) Effect of heat treatment on tensile and corrosion properties of LM6 hybrid metal matrix composite reinforced with cenosphere and red mud. J Min Mater Charact Eng 7:1–17
3. . Ervina Efzan MN, Siti Syazwani N, Abdullah MMAB (2016) Microstructure and mechanical properties of fly ash particulate reinforced in LM6 for energy enhancement in automotive applications. In IOP conference series: materials science and engineering, vol 133, p 012046. https://doi.org/10.1088/1757-899X/133/1/012046
4. Shivaramu HT, Umashankar KS, Prashantha DA (2018) Wear characteristics comparison of cast and powder metallurgy based Al and Al–Si alloy [LM6]. Mater Today Proc 5:8138–8146
5. Shabestari SG (2004) The effect of iron and manganese on the formation of intermetalliccompounds in aluminum–silicon alloys. Mater Sci Eng A 383:289–298
6. Ceschini L, Boromei I, Morri A, Seifeddine S, Svensson IL (2009) Microstructure, tensile and fatigue properties of the Al–10%Si–2%Cu alloy with different Fe and Mn content cast under controlled conditions. J Mater Process Technol 209:5669–5679

7. Ibrahim MF, Alkahtan SA, Abuhasel KhA, Samuel FH (2015) Effect of intermetallics on the microstructure and tensile properties of aluminum based alloys: role of Sr, Mg and Be addition. Mater Des 86:30–40
8. Naga Raju P, Srinivasa Rao K, Reddy GM, Kamaraj M, Prasad Rao K (2007) Microstructure and high temperature stability of age hardenable AA2219 aluminium alloy modified by Sc, Mg and Zr additions. Mater Sci Eng A 464:192–201
9. Yildirim M, Özyürek D (2013) The effects of Mg amount on the microstructure and mechanical properties of Al–Si–Mg alloys. Mater Des 51:767–774
10. Abedi M, Shahmiri BA, Esgandari BN (2013) Microstructural evolution during partial remelting of Al–Si alloys containing different amounts of magnesium. J Mater Sci Technol 29(10):971–978
11. Morin S, Elgallad EM, Doty HW, Valtierra S, Samuel FH (2016) Effect of Mg content and heat treatment on the mechanical properties of low pressure die-cast 380 alloy. Adv Mater Sci Eng, 12. Article ID 7841380

Investigation of Geopolymer Concrete with Ceramic Waste as a Partial Replacement of Coarse Aggregate

V. Vignesh Prabu, S. Velmurugan, and O. P. Deepak

Abstract The study focuses on analyzing the compressive strength in usage of ceramic waste material as partial replacement of coarse aggregates. Concrete cubes were prepared for 5, 10, 15, 20 and 25% replacements and tested for optimum content for two grades of concrete mixes (G30 and G50). The optimum content of ceramic waste was found to be 15 and 20% by weight of coarse aggregates for G30 and G50, respectively. The compressive strength of the concrete waste containing geopolymer concrete was compared with control mix concrete and was found to have an increment of 13.5% in compressive strength comparatively. Also, it was observed that the compressive of the geopolymer concrete increased up to certain replacements with the increase in the percentage of waste materials, and it is found suitable to use the ceramic industrial waste for the concrete.

Keywords Ceramic waste · Compressive strength · Geopolymer concrete

1 Introduction

The demand for concrete as a material of construction will surge as the demand for infrastructure expansion rises, principally in countries such as China and India. So as to encounter this demand, the manufacture of Portland cement must increases. Furthermore, Portland cement is also among the most energy-exhaustive construction materials followed by aluminum and steel. In contrast, fly ash is available lavishly across the world. In 2001, the fly ash production in USA was roughly 68 million tons, but only 32% was used in various applications, such as in concrete, structural fills, and wastes stabilization. So many benefits are there in using fly ash as a substitute for Portland cement, especially to overcome the hike in the need for concrete required for construction developments. As silicon and aluminum are the key ingredients, fly ash is having high potential as a cement replacement material in concrete. The

V. Vignesh Prabu (✉) · S. Velmurugan · O. P. Deepak
Department of Civil Engineering, Bannari Amman Institute of Technology, Sathyamangalam, Erode District, Tamil Nadu 638401, India
e-mail: vigneshprabu@bitsathy.ac.in

G. Kumaresan et al. (eds.), *Advances in Materials Research*, Springer Proceedings in Materials 5, https://doi.org/10.1007/978-981-15-8319-3_60

replacement of Portland cement as concrete binder, activation of fly ash is needed by making use of alkaline solutions as activator.

1.1 Geopolymer Concrete

In geopolymer, the process of polymerization comprises a chemical reaction with highly alkaline circumstances for Al-Si minerals, yielding polymeric bonds, and it generates a lot of heat during chemical reaction. The chemical composition of geopolymer resembles to that of zeolites; however it shows an amorphous microstructure [1]. The structural prototype of geopolymer material is running under investigation, hence the precise mechanism by which geopolymer setting and hardening is happening, still not clear. The geopolymerisation process consists of dissolution, transportation, orientation and polycondensation and takes place through an exothermic progression. The strength of geopolymer depends on the nature of source materials. Geopolymer made from calcined source materials, such as metakaolin (calcined kaolin), fly ash and slag, yields higher compressive strength when compared to those made from non-calcined materials, such as kaolin clay [2]. The source material used for geopolymerisation can be a single material or a combination of many types of materials.

A grouping of sodium or potassium silicate and sodium or potassium hydroxide has been widely used as the alkaline activator from a long time, with the activator liquid-to-source material ratio by mass in the range of 0.25–0.30. Because heat is a reaction accelerator, curing of fresh geopolymer is carried out mostly at an elevated temperature. Daniel and Jay Sanjayan [3] state that when curing is done at elevated temperatures, care must be taken to minimize the loss of water. However, curing at room temperature has successfully been carried out by using calcined source material of pure geological origin, such as metakaolin and GGBFS.

1.2 Application of Geopolymer

The geopolymer material can be used in various applications, such as fiber composites, automotive and aerospace industries, nonferrous foundries and metallurgy, civil engineering, cements and concretes, ceramics and plastics industries, waste management, art and decoration, retrofit of buildings, depending on the chemical composition of the source materials and the activators [4].

1.3 Ceramaic Waste

In the production plants as well as at construction sites, a lot of ceramic waste is generated which is a concern of disposal and spoils the aesthetic of the surroundings. Ceramic waste is having properties like fire resistance, high rigidity, density, low porosity, high breaking strength, corrosion resistance and acid resistance. In an effort to use the ceramic waste in large volume, research is being carried out for its possible large-scale utilization in making concrete as partial replacement of coarse aggregate in geopolyer concrete [5]. In the present study, coarse aggregate is partially replaced by ceramic waste in geopolymer concrete, and its compressive strength was investigated.

2 Experimental Investigation

In the investigation, the geopolymer concrete cubes were cast of two grades G30 and G50, the coarse aggregate is partially replaced by ceramic waste, and their compressive strength was investigated compared to the conventional concrete.

2.1 Materials

The following materials used for the current study: Fly ash, ground granulated blast furnace slag, fine aggregates, coarse aggregates, sodium hydroxide, sodium silicate, ceramic waste, water and super-plasticizers are the materials used in the current study. The coarse aggregates were crushed to the angular size of 10–20 mm. The specific gravity of the aggregates of course aggregate is 2.79, and fineness modulus is 7.12. The fine aggregate (river sand) used consists of zone II, specific gravity was 2.61, and its fineness modulus is 3.55. Low calcium class F fly ash was used. The specific gravity of fly ash is 2.64 with fineness of 380 m^2/kg. The specific gravity of ceramic waste is 2.68, and for GGBFS, it is 2.86 with fineness of 400 m^2/kg. Super-plasticizer was used to improve the workability of concrete. Super-plasticizer content was 1% by weight of binding material, and it was added to improve the workability of concrete. The super-plasticizer used was Naphthalene-based Conplast SP-430.

2.2 Properties of Ingredients

Test data for materials.

i. Ratio of Na_2SiO_3 to NaOH: 2.5
ii. Ratio of water to geopolymer solid: 0.26

Table 1 Quantity of materials

Material	Quantity (kg/m^3) G30		Quantity (kg/m^3) G50
Fly ash	190		240
GGBFS	190		240
NaOH	48.95		61.72
Na_2SiO_3	122		154.28
Coarse aggregate	20 mm	775	763
	12.5 mm	520	515
Fine aggregate	555		510
Water	38		14.4
Super plasticizer	3.8[a]		4.8[a]

[a]**Super-plasticizer** content is adopted as 1% of the binding material (i.e., fly ash and GGBFS) as per the literature and the workability requirements

iii. Molarity of NaOH: 12 M (Table 1).

2.3 Mix Proportions

See Tables 2 and 3.

3 Testing of Specimens

As per IS 516 (1959), compression testing machine was used to test the cubes of concrete. Concrete cubes were placed centrally on the CTM, and load was gradually applied [6] (Figs. 1 and 2).

Table 2 Mix proportion for G30 for cubes

Mix designation	% of ceramic waste	Fly ash + GGBFS (kg/m^3)	FA (kg/m^3)	CA (kg/m^3)	Ceramic waste (kg/m^3)	Alkaline Solution (kg/m^3)	Number of cubes
GCK	Control	380	555	1294	–	171	3
GC5	5	380	555	1229.6	64.7	171	3
GC10	10	380	555	1164.6	129.4	171	3
GC15	15	380	555	1099.9	194.1	171	3
GC20	20	380	555	1035.2	258.8	171	3
GC25	25	380	555	970.5	323.5	171	3

Table 3 Mix proportion for G50 for cubes

Mix designation	% of ceramic waste	Flyash + GGBFS (kg/m^3)	FA (kg/m^3)	CA (kg/m^3)	Ceramic waste (kg/m^3)	Alkaline solution (kg/m^3)	Number of cubes
GHK	–	480	510	1278	–	216	3
GH5	5	480	510	1214.1	63.9	216	3
GH10	10	480	510	1150.2	127.8	216	3
GH15	15	480	510	1086.3	191.7	216	3
GH20	20	480	510	1022.4	255.6	216	3
GH25	25	480	510	958.5	318.75	216	3

Fig. 1 Specimen before testing

Fig. 2 Specimen after testing

Table 4 Compressive strength at 7 and 28 days

% Replacement	Compressive strength (N/mm^2)			
	G30		G50	
	7 days	28 days	7 days	28 days
Control mix	26.12	44.36	37.59	65.61
5	27.46	46.32	39.58	68.72
10	28.21	47.51	40.36	69.07
15	29.34	49.28	42.04	71.23
20	28.77	48.11	43.57	72.69
25	28.41	47.82	41.80	70.63

4 Results and Discussion

4.1 Compressive Strength

Compression test according to IS: 516 (1959) was carried out on cubes to determine the compressive strength after 7 days and 28 days of standard curing [6]. The compressive strength for both grades of concrete is given in Table 4.

5 Conclusions

Based on the experimental investigations, the following conclusions are drawn.

1. Utilization of ceramic waste in geopolymer concrete is found to be useful as it improves compressive strength of the concrete.
2. It was observed that as the ceramic waste content increased, the compressive strength increased up to 15% for G30 and 20% for G50 and then decreased continuously, when compared with the control geopolymer concrete.
3. As the geopolymer concrete made with fresh ceramic waste partially as a coarse aggregate is more cohesive and workable than conventional geopolymer concrete and this is due to the lower water absorption and smooth surface texture of the ceramic waste coarse aggregate
4. It is observed that the geopolymer concrete made with ceramic tiles partially as coarse aggregate shows 11.09% and 10.79% more strength than the control mix geopolymer concrete of grade G30 and G50, respectively.

References

1. Aleem A, Arumairaj PD (2012) Optimum mix for the geopolymer concrete. Ind J Sci Technol 5(3):1–3
2. Adak D, Sarkarand M, Mandal S (2014) Effect of nano-silica on strength and durability of fly ash based geopolymer mortar. Constr Build Mater 70:453–459
3. Daniel LYK, Jay Sanjayan G (2010) Effect of elevated temperatures on geopolymer paste, mortar and concrete. Cem Concr Res 40:334–339
4. Anuradha R, Sreevidya V, Venkatasubramani R, Rangan BV (2012) Modified guidelines for geopolymer concrete mix design using Indian standard. Asian J Civ Eng 13:353–364
5. Albitar M, Mohammed Ali MS, Visintin P (2017) Durability evaluation of geopolymer and conventional concretes. Construct Build Mater 136:374–385
6. IS 516: 1959 Indian standard methods of tests for strength of concrete

Numerical Investigation on Cold-Formed Steel Web Stiffened Lipped Channel Columns Subjected to Local-Distortional Interaction Mode Buckling

O. P. Deepak and P. Aravinth

Abstract This paper describes the numerical investigation carried out on cold-formed steel fixed-ended web stiffened lipped channel (WSLC) column sections undergoing local-distortional interaction mode buckling. The ultimate strength erosion caused by L–D interaction are presented. The sections failing due to L–D interaction are identified by "trial and error method" from GBTul. The column sections are carefully selected to ensure that would be fairly high level of L–D interaction by the ratio ($P_{crl}/P_{crd} = 0.8–1.2$). The elastic buckling analysis is performed predicting the section properties and length of the columns by using GBTul software. Finite Element Models were developed by using ABAQUS and comparative study on load results was made with DSM (direct strength method), NLD, NLD, MNLD approaches and whether they are capable of predicting them efficiently. The parametric studies on the identified sections are presented.

Keywords Web stiffened lipped channel columns · ABAQUS · Finite element analysis · Interactive buckling · Gbtul · Numerical simulations · Direct strength method

1 Introduction

Cold-formed steel sections (CFS) are widely used in construction field, popular due to its high strength to weight ratio, easy erection economical aspect, uniform quality throughout the section and easy handling and transportation, etc., Cold-formed channels are usually used as compression members like wall studs and chord members of roof trusses in steel framed residential and commercial buildings. It is found that the commonly used column geometries undergo three modes of failures such as local, distortional, and global buckling. The major impact in the failure is when the combination of the above-mentioned mode interactions. The local distortional

O. P. Deepak (✉) · P. Aravinth
Department of Civil Engineering, Bannari Amman Institute of Technology, Sathyamanglam, Erode District, Tamil Nadu 638401, India
e-mail: deepak@bitsathy.ac.in

G. Kumaresan et al. (eds.), *Advances in Materials Research*, Springer Proceedings in Materials 5, https://doi.org/10.1007/978-981-15-8319-3_61

interaction buckling of cold-formed steel thin-walled sections was reported first by Kwon and Hancock. To avoid buckling and enhance the strength of the sections various stiffeners are used.

The influence of L–D interaction in the behavior and design of CFS web stiffened lipped channel columns were numerically analyzed by Martins et al. [1]. Through this study, found that the NDL estimates were good in the quality and reliable but the MNDL approach does not seem to be satisfactory to the experimental failure loads. Dinis et al. [2] done a profound study on the behavior and interactive mode failure pattern of the web stiffened lipped channel columns. This study had a major contribution towards the interactive failure modes that were actually triggered by the flange and web portions. The experimental and numerical investigation of the sections was performed with finite element software (ABAQUS) and behavior of both the results compared preferably, showed fair bond in accordance. The obtained results were validated against the direct strength approach methods and a new approach was developed with context of the existing works performed, literally approach given in this study was a combination of earlier interactive approach design considerations. The proposed approach showed moreover similar results comparable with numerical and experimental findings. He et al. [3] contributed towards experimental study on the post-buckling behavior of web stiffened lipped channel columns with the fixed ended boundary involving the interactive failure of local-distortional and distortional-local modes. The yielded results from experiments concerning interactive failures were compared with the DSM based approaches and were found unsafe by the dissimilar values of ultimate strengths. Eminent study showed the liable parallel results when done NLD and NDL approaches. In this study, lips functionality that decided the failure interaction either L–D or D–L modes are noted, and importance of their behavior was seen through. Martins et al. [1] studied the interactive behavior of local and distortional buckling on the web stiffened lipped channel sections. This study shows the efficient role of the GBTul software analysis for finding the critical load and finite element analysis using ABAQUS software. The numerical investigated results were checked for the relevance against various DSM predictions or approaches. This study found the profound work to hold good evidence with NDL approach and simultaneously the MNDL approach could not be as effective. Landesmann et al. [4] experimented with lipped channel columns distortional buckling and failure mode with ‘V’ shaped stiffeners provided over both flanges and the web portion. And essentially concluded the presence of stiffeners highly influenced and modified the ultimate strengths and behavior of the sections chosen. The numerical analysis was performed by ANSYS and the results agreed to concern with the experimental specimens. This study concluded to have an important note on the web to lip width ratio should be a salient criterion in developing a new design approach for the buckling effects. Zhou et al. [5] done experimental and shell finite element analysis of the web stiffened lipped channels with including the batten sheets across connecting two edges of the lips of open cross-section sides. Inclusive of the batten sheets would significantly effect and increase the ultimate strength of the columns. The distortional buckling occurring in the columns was effectively delayed and in some occurrence it could even excluded from happening by the presence of batten

sheets. The ultimate strength was possibly to double by the inclusion of batten sheets at specified intervals effectively for long columns. Influence on ultimate strength of CFS lipped channel columns subjected to interaction on distortional global buckling was investigated by Anbarasu [6]. From the study, found that the relationship between the ultimate strength found through finite element analysis and the ultimate resistance predicted by DSM approach is found to be almost linear $P_{\text{fea}} = 0.866P_{\text{dsm}}$. This paper reports about the local distortional mode interactive failures of web stiffened lipped channel CFS sections. It was absolutely found that the L–D interaction effects occur once when the proportion between distortional and local buckling loads is either (i) ratio close of 1.0 (at least between 0.8 and 1.2), which corresponds to "true L–D interaction", (ii) above 1.0 (conceivably by a wide margin), provided that the squash load exceeds the distortional buckling load by huge amount allowing for the occurrence of development of significant L–D interaction effects before failure occur, which corresponds to "L–D interaction due to a secondary (distortional) bifurcation". Considerable amount of research work has been devoted to investigate local–distortional (L–D) interaction in cold-formed steel thin-walled columns – this work involves mostly lipped channel columns and comprises numerical analysis and design proposals. The ABAQUS shell finite element analysis is used for numerical investigation, in order to sketch the post-buckling behavior and strength of WSLC columns experiencing marginal L–D interaction effects. The FEA results discuss about the (i) ultimate strengths, (ii) post-buckling behavior and (iii) failure mechanisms of WSLC columns selected to undergoing L–D interaction. A good review is given to comparing the ultimate strength results of L–D interactions in WSLC columns with the DSM design considerations.

2 Methodology

2.1 Column Geometry

The selection of the column geometry was achieved through trial-and-error buckling analysis sequences, carried out in the code GBTUL. The various column geometries identified by conducting iterative buckling analysis in an open-source GBTUL program. GBTUL is free software programs that execute elastic buckling (bifurcation) and vibration analysis of prismatic thin-walled members. GBTUL V2.06 is used for the buckling analysis. Web stiffened lipped channel column sections are chosen carefully so that it undergoes L–D interactive modes. To ensure the interactive mode failure of local and distortional buckling numerous buckling analysis is performed. The software shows elastic buckling loads of local, distortional, global buckling with corresponding to the deformable modes.

2.2 Finite Element Modelling

The finite element nonlinear analysis program ABAQUS was used to simulate the experimental behavior of fixed-ended cold-formed web stiffened lipped channel columns. The sections are modeled based on the centerline measurements of the cross-sections. ABAQUS V6.14 [7] is used for numerical analysis of the identified sections. The geometric and material non-linearity is used and sections are modeled on the elastic strain hardening behavior. Linear analysis is carried out for determining the buckling mode shapes. Post buckling analysis of the sections is then carried estimating the ultimate strength and to study the load versus end shortening characteristics. S4R5 shell elements are used which is usually a four-node doubly curved shell element with reduced integrations with 5 degrees of freedom per node. Mesh size is chosen as 1(length to width ratio) based on the previously done investigations. The column ends are tie constrained to inner face of the solid plates (deformable solid plate element C3D8R). The solid plates are set to fixed with the boundary conditions and only the top plate is allowed for longitudinal displacement. Compressive static load of 1 N/mm^2 is applied on the top plate of the column. Linear buckling analysis the isotropic and homogeneous material is chosen with elastic modulus of 210 GPa and Poisson ratio of 0.3. For the nonlinear buckling analysis plastic properties are given in addition. the results determined were obtained using the finite element code ABAQUS with fine mesh discretization using 4-node iso-parametric shell elements To assess the accuracy of adopted finite element modeling method in this study, linear buckling and non-linear post-buckling analysis are carried out for a section. The geometric imperfection value of 0.1 T (T-thickness of the section considered) is carried throughout the analysis. The comparison shows the present model can fairly simulate the critical buckling stresses, failure load, and failure mode reported by He et al. [3] (Tables 1 and 2).

Table 1 Comparison of present FEA with Ziqi et. al

	b_w	b_f	b_l	d_1	d_2	T	L	F_{crd}	F_{crl}	F_u
Ziqi He et al	163.2	123.2	16.5	10.4	20.4	1.47	1501.8	136.2	128.6	97.1
Present work	163.2	123.2	16.5	10.4	20.4	1.47	1501.8	139.69	139.69	97.67
Ratio (Ziqi He/present work)								0.975	0.92	0.99

Table 2 Specimen name, cross-sectional details, thickness and length (in mm), area (mm^2), critical buckling stresses (in MPa), and critical stress ratios

Specimen	b_w	b_f	b_l	d_1	d_2	T	L	Area	F_{crl}	F_{crd}	F_{crd}/F_{crl}
S1	170	110	20	10	20	1.5	1000	657.42	281.02	282.32	1.00
S2	180	120	20	10	20	1	1000	468.28	66.63	199.60	2.99
S3	200	140	20	10	20	1	1000	528.28	49.53	165.44	3.33

3 Results and Discussions

3.1 Post-Buckling Analysis

The ultimate strength behavior and occurrence of L–D interaction in the sections and failure modes are discussed below.

3.1.1 Section S1

The section S1-250 fails by L–D interaction, the local buckling with four half waves on either side of the flange occurs at 65.13 kN (Fig. 1a shows emergence of local buckling S1-250) and three half waves local buckling occurring in the web portion at both ends of the column section. Further, on deforming interacts with distortional buckling at 92.25 kN (Fig. 1b shows L–D interaction in S1-250) with deviating outwards and reaches the ultimate load at 100.33 kN and fails literally. S1-350 starts deforming with occurrence local buckling at 65.13 kN and L–D interaction occurs at 93.67 kN and fails at 118.24 kN and the failure behavior is same as that of the S1-250 section. S1-550 varies from the previous discussed section with local buckling occur at 68.31 kN and prolongs to interact with distortional buckling at 101.83 kN and fails immediately at 134.51 kN by L–D interaction. This sections half-wave behavior is same as previously section but fails by flanges deforming inwards. S1-800 shows six half wave local buckling on the flanges at one side at 87.64 kN and the local buckling at other side occurs at 107.07 kN and L–D interaction takes place at 122.76 kN and the ultimate failure occurs at 135.89 kN.

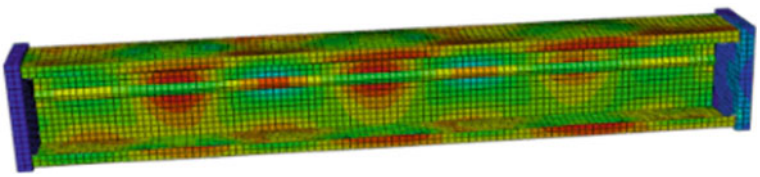

Fig. 1 Emergence of local buckling S1-250

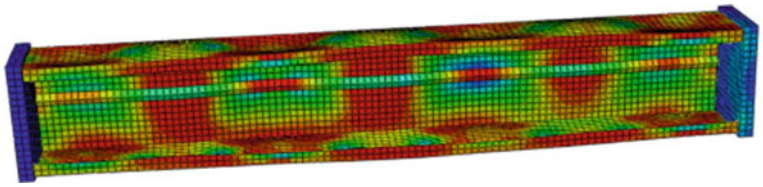

Fig. 2 L–D interaction in S1-250

3.1.2 Section S2

S2-250 shows four half-wave local buckling at 34.48 kN and interaction takes place at 52.15 kN (Fig. 2a shows emergence of local buckling S2-350) and undergoes for a little displacement and it reaches the ultimate load failing at 54.47 kN. Two half-wave local buckling on web portion occurs at 52.15 kN (Fig. 2b shows L–D interaction in S2-350) just before the failure the section fails L–D interaction and flange buckling inwards. Five half-wave buckling occurs at either sides of the flanges at 26.35 kN, five half-wave occurs at web portion at 47.97 kN of S2-350 and by then interacts with distortional mode at 54.42 kN and fails simultaneously. Similar interaction is found on the S2-550 with moreover same half wave buckling effects with first occurrence of local buckling on the flanges at 31.67 kN interacting with distortional at 55 kN and fails by L–D interaction at 62.14 kN. S2-800 shows similar half-wave buckling effects on the flanges at 31.67 kN but not similar as in the web portion two half-wave local buckling occurs at 51.32 kN and interaction takes place at 55 kN and reaches the ultimate load capacity at 64.17 kN.

3.1.3 Section S3

S3-250 shows emergence of the local buckling on the flanges with three half-wave occurring at one side and four half waves on either side of the section at 29.94 kN. The section goes on deformation and interacts with distortional at 45.64 kN and fails at 51.43 kN with occurrence of two half-waves on the web. Four half wave local buckling occurs on the either side of S3-350 at 33.39 kN and one half-wave local buckling on the web at 47.19 kN and interacts with the distortional simultaneously and ultimate reaches to 56.05 kN. S3-550 goes with occurrence of six half-wave on one side and four half-wave at other experiencing local buckling at 28.14 kN (Fig. 3a shows emergence of local buckling S3-550) and L–D interaction occurs at 48.723 kN and failure occurs at the ultimate load of 57.39 kN (Fig. 3b shows L–D interaction in S3-550) with two half-wave local buckling on the web. Four half-wave local buckling occurs at flanges and two half-waves local buckling on the web at the same time at 45.52 kN of the section S3-800 and the distortional interaction takes place at 49.03 kN and L–D failure occurs at 63.71 kN reaching its ultimate strengths (Figs. 4, 5, 6, 7 and 8).

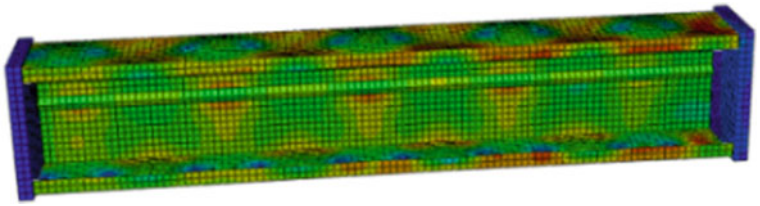

Fig. 3 Emergence of local buckling S2-350

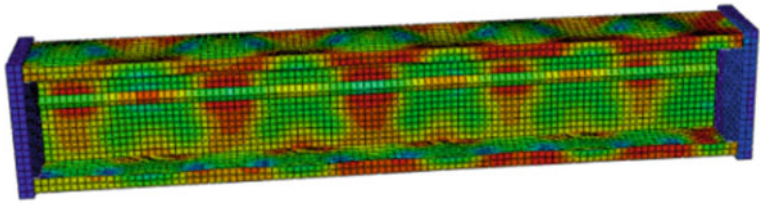

Fig. 4 L–D interaction in S2-350

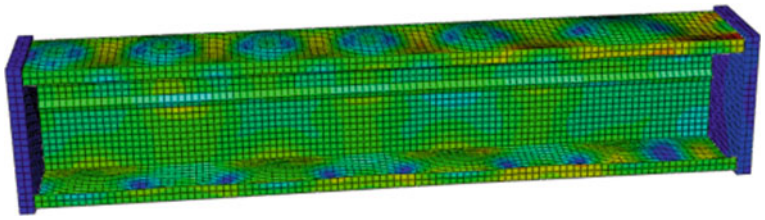

Fig. 5 Emergence of local buckling S3-550

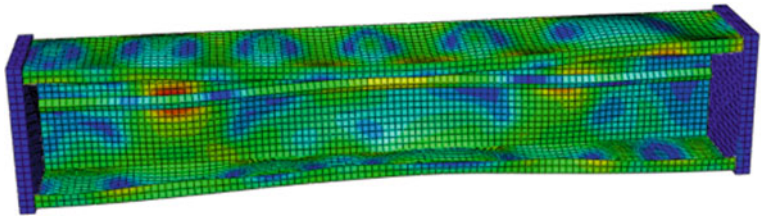

Fig. 6 L–D interaction in S3-550

3.2 Direct Strength Method

The specifications AISI S-100 and AS/NZ 4600 provide effective width method (EWM) and direct strength method (DSM) based design procedures for design of

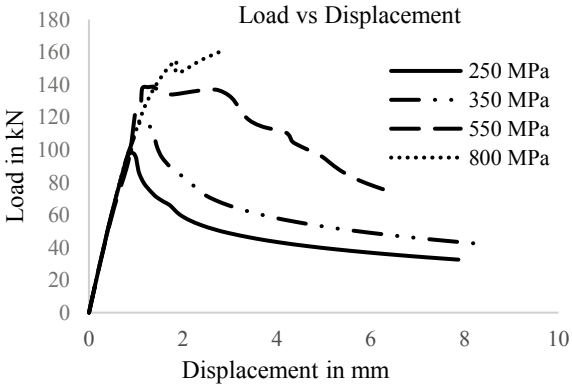

Fig. 7 Comparison of load versus displacement of various yield stresses of the section S1

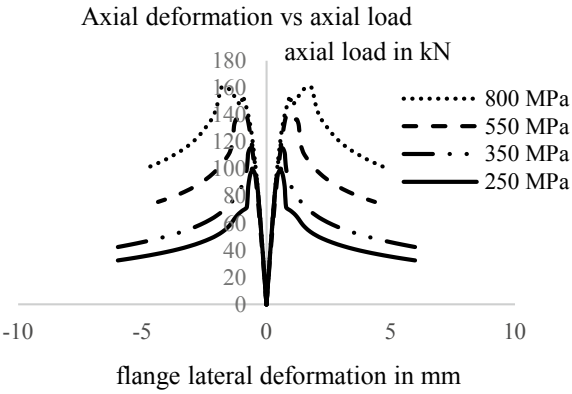

Fig. 8 Comparison flange lateral displacement versus axial load of the section S1

cold-formed steel structural members. The DSM based design eradicates the limitations that the traditional EWM have like complex effective width calculations and unaccountability of web-flange juncture rotational stiffness for distortional buckling. The DSM based design was first proposed by Schafer and Pekoz (1998), it adopts Winter type strength curves to predict the nominal strength for columns and beams that fail after L, D, G (flexural, torsional and flexural–torsional) and L–G mode buckling. The DSM strength curves are developed based on the elastic buckling stresses obtained from finite strip analysis program and column strength data obtained from various experimental tests. The DSM design of cold-formed steel members under compression and bending depends only on the elastic buckling stress and the yield stress values. The AISI S-100specification provides limitations to use DSM design for members based on the cross sectional shape and dimensions. The column sections investigated in this paper have cross-sectional shape and dimensions within the specified limits and belongs to re-qualified columns category as per AISI S-100 for which DSM design can be conveniently adopted. All the column sections considered in this study have fixed ended boundary conditions and so the shift of effective centroid due

to local buckling is neglected. As the equation prescribed by AISI to predict column nominal strength for local buckling includes L-G interaction mode buckling, the same equation is refined as given in Eq. (1) to calculate the column nominal strength for local buckling alone. The equation to predict column strength for distortional buckling as prescribed by AISI is given in Eq. (2).

for $\lambda_l \leq 0.776$.

$P_{nl} = P_y$.

for $\lambda_l > 0.776$

$$P_{nl} = \left[1 - 0.15\left(\frac{P_{crl}}{P_y}\right)^{0.4}\right]\left(\frac{P_{crl}}{P_y}\right)^{0.4} P_y \tag{1}$$

$$P_{nd} = \left[1 - 0.25\left(\frac{P_{crd}}{P_y}\right)^{0.6}\right]\left(\frac{P_{crd}}{P_y}\right)^{0.6} P_y \tag{2}$$

where

$\lambda_l = \sqrt{\frac{P_y}{P_{crl}}}$ (non-dimensional local slenderness ratio).
P_{crl} = Critical elastic local column buckling load.
P_y = Column squash load.
P_{nl} = Nominal strength of column for local buckling.
$\lambda_d = \sqrt{\frac{P_y}{P_{crd}}}$ (non-dimensional distortional slenderness ratio).
P_{crd} = Critical elastic distortional column buckling load.
P_{nd} = Nominal strength of column for distortional buckling.

As the design specifications AISI S-100 and AS/NZ4600 do not provide DSM column strength curve for columns failing under L–D interaction mode buckling phenomenon, the DSM based design procedures available from literature which includes interactive L–D mode buckling failure are used to calculate the nominal strength of the columns. Schafer (2002) suggested EWM and DSM based strength equations to include the various interactive modes buckling failure. Amongst them, the DSM based strength equation for columns failing after L–D interaction mode given in Eqs is adopted to calculate the nominal strength of the columns. Kwon et al. (2009) based on their experimental tests results modified the nominal strength equation for medium-strength cold-formed steel columns failing after L–D interaction mode buckling. The modified equation is given in Eqs. (3) and (4).

for $\lambda_{ld} \leq 0.776$.

$P_{nld} = P_{nd}$.

for $\lambda_{ld} > 0.776$

$$P_{nld} = \left[1 - 0.15\left(\frac{P_{crl}}{P_{nd}}\right)^{0.4}\right]\left(\frac{P_{crl}}{P_{nd}}\right)^{0.4} P_{nd} \tag{3}$$

$$P_{mnld} = \left[1 - 0.2\left(\frac{P_{crl}}{P_{nd}}\right)^{0.4}\right]\left(\frac{P_{crl}}{P_{nd}}\right)^{0.4} P_{nd} \tag{4}$$

where

$\lambda_{ld} = \sqrt{\frac{P_{nd}}{P_{crl}}}$
P_{crl}= critical elastic local column buckling load.
P_{nd}= nominal strength of column for distortional buckling computed by equations.
P_{nld}= nominal strength of column for L–D interaction mode buckling.
P_{mnld}= modified nominal strength of column for L–D interaction mode buckling.

The DSM based column strength equation (NDL approach) to cater the L–D interaction mode buckling is proposed by Silvestre et al. (2009) based on numerical investigation of simply supported columns. The DSM based NDL approach column strength equations are given in Eq. (4). Silvestre et al. (2012) based on their numerical investigation of fixed ended lipped channel columns modified the DSM based NDL approach. The DSM based column strength Eq. (5), includes the column strength eroded by L–D interaction mode buckling, proposed based on the experimental and numerical investigations conducted mostly on lipped channel and web stiffened lipped channel column sections. Recently, Dinis et al. [8], Martins et al. (2015) and Martins et al. [1] accessed the accuracy of strength predicted by NDL and modified NDL approaches based on experimental tests (rack and lipped channel column sections) and numerical investigations (lipped channel, web stiffened lipped channel, rack, Zed, hat column sections). As mentioned earlier, the DSM strength curves are explicit, as the column strengths are arrived purely on the basis of yield and critical buckling stresses of the column section.

The literature studies concerning L–D interaction buckling failure insists that the column sections investigated do not cover the entire possible ranges of the strength-related parametric ratios and cross-sectional shapes, hence the explicit nature of the proposed [14].

DSM column strength curves [15] need to be assessed by conducting further studies (both experimental and numerical investigations) on a large amount of column sections that cover wide ranges of strength related parametric ratios and various cross-sectional shapes.

$$P_{ndl} = \left[1 - 0.25\left(\frac{P_{crd}}{P_{nl}}\right)^{0.6}\right]\left(\frac{P_{crl}}{P_{nl}}\right)^{0.6} P_{nl} \tag{5}$$

where

$\lambda_{dl} = \sqrt{\frac{P_{nl}}{P_{crd}}}$ (non-dimensional D-L slenderness ratio).

P_{crd}= critical elastic distortional column buckling load.
P_{nl}= nominal strength of column for local buckling.
P_{ndl}= nominal strength of column for D-L interaction mode buckling (Tables 3 and 4).

4 Conclusions

Numerical investigation on the post-buckling behavior, ultimate strength, and comparison of ultimate strengths obtained by software with DSM design of fixed-ended cold-formed steel web-stiffened lipped channel columns with L–D interaction buckling is reported. The results obtained by numerical simulation with the software are compared against the various approaches. The sections provided in the article falls in L–D interactions and the failure occurs by the same effect. The current DSM approach highly deviates from the numerical results obtained by ABAQUS overestimating the ultimate strengths and a better method to be recommended for the sections failing by L–D interaction effects. $P_{nld,}$ P_{ndl} and P_{mnld} approach results come nearby giving moreover similar strength results. The above-mentioned approach shows far better results with the numerical results comparable to P_{nd}, P_{nl} approaches.

Table 3 Column strength predicted by DSM equations

Specimen	F_y (MPa)	P_y (kN)	P_{crl} (kN)	P_{crd} (kN)	λ_l	λ_d	λ_{ld}	λ_{dl}	P_{nl} (kN)	P_{nd} (kN)	P_{nld} (kN)	P_{ndl} (kN)	P_{mnld} (kN)
S1	250	164.35	184.75	185.61	1.16	1.16	0.84	0.88	129.25	100.33	145.16	123.30	119.49
	350	230.09	184.75	185.61	1.37	1.38	0.92	0.99	157.82	118.24	181.80	141.23	137.48
	550	361.58	184.75	185.61	1.72	1.73	1.04	1.15	201.74	138.74	244.72	166.56	163.41
	800	525.94	184.75	185.61	2.08	2.08	1.15	1.30	243.86	159.91	311.93	188.94	186.62
S2	250	117.07	31.20	93.47	2.83	1.64	1.60	0.82	79.94	57.07	62.89	49.22	54.47
	350	163.89	31.20	93.47	3.34	1.94	1.76	0.91	96.13	64.26	77.89	55.43	62.66
	550	257.55	31.20	93.47	4.19	2.43	1.97	1.05	121.12	66.53	103.58	64.27	74.50
	800	374.62	31.20	93.47	5.06	2.93	2.16	1.18	145.17	75.76	130.93	72.12	85.11
S3	250	132.07	26.17	87.40	3.09	1.69	1.78	0.85	82.97	51.43	63.69	47.35	53.73
	350	184.89	26.17	87.40	3.66	2.00	1.95	0.95	99.14	56.05	78.78	53.07	61.54
	550	290.55	26.17	87.40	4.58	2.51	2.18	1.09	124.13	60.87	104.58	61.24	72.82
	800	422.62	26.17	87.40	5.53	3.03	2.38	1.23	148.23	62.92	132.05	68.52	82.97

Table 4 Proportion of numerical results (FEA P_u) with P_{nl}, P_{nd}, P_{nld}, P_{ndl}, P_{mnld} approaches

Specimen	F_y (MPa)	Failure mode	FEA P_u	P_{nl}/FEA P_u	P_{nd}/FEA P_u	P_{nld}/FEA P_u	P_{ndl}/FEA P_u	P_{mnld}/FEA P_u
S1	250	L–D	100.33	1.45	1.29	1.23	1.19	1.14
	350	L–D	118.24	1.54	1.33	1.19	1.16	1.12
	550	L–D	138.74	1.76	1.45	1.20	1.18	1.13
	800	L–D	159.89	1.95	1.52	1.18	1.17	1.12
S2	250	L–D	57.07	1.10	1.40	0.86	0.95	0.83
	350	L–D	64.26	1.21	1.50	0.86	0.98	0.83
	550	L–D	66.53	1.56	1.82	0.97	1.12	0.94
	800	L–D	75.76	1.73	1.92	0.95	1.12	0.92
S3	250	L–D	51.43	1.24	1.61	0.92	1.04	0.89
	350	L–D	56.05	1.41	1.77	0.95	1.10	0.92
	550	L–D	60.87	1.72	2.04	1.01	1.20	0.98
	800	L–D	62.92	2.10	2.36	1.09	1.32	1.06
Mean				1.56	1.67	1.03	1.13	0.99
SD				0.30	0.32	0.14	0.10	0.12

References

1. Martins AD, Dinis PB, Camotim D (2016) On the influence of local-distortional interaction in the behaviour and design of cold formed steel web-stiffened lipped channel columns. Thin Wall Struct 101:181–204
2. Dinis PB, Young B, Camotim D (2014) Strength, interactive failure and design of web-stiffened lipped channel columns exhibiting distortional buckling. Thin Wall Struct 81:195–209
3. He Z, Zhou X, Liu Z, Chen M (2014) Post-buckling behaviour and DSM design of web-stiffened lipped channel columns with distortional and local mode interaction. Thin Wall Struct 84:189–203
4. Landesmann A, Camotim D, Garcia R (2016) Web/flange-stiffened lipped channel columns buckling and failing in distortional modes. Thin Wall Struct 105:248–265
5. Zhoua X, Chena M (2018) Experimental investigation and finite element analysis of web-stiffened cold-formed lipped channel columns with batten sheets. Thin Wall Struct 125:38–50
6. Anbarasu M, Sukumar S (2014) Local/distortional/global buckling mode interaction on thin walled lipped channel columns. Lat Am J Solids Struct 11:1363–1375
7. ABAQUS (Computer Software), ABAQUS standard user's manual, version 6.14. Dassault Systèmes Simulia, Providence, RI
8. Dinis PB, Young B, Camotim D (2014) Local–distortional interaction in cold-formed steel rack-section columns. Thin Wall Struct 81:185–194
9. Martins AD, Dinis PB, Camotim D, Providência P (2015) On the relevance of local-distortional interaction effects in the behaviour and design of cold-formed steel columns. Computational Structures 160: 57-89
10. Schafer BW (2002) Local, distortional and Euler buckling of thin-walled column. Journal of Structural Engineering 128(3): 289-299
11. Schafer BW, Peköz T (1998) Computational modelling of cold-formed steel: characterizing geometric imperfections and residual stresses. Journal of Construction Steel Research 47:193-210

12. Kwon YB, Kim BS, Hancock GJ (2009) Compression tests of high strength cold-formed steel channels with buckling interaction. Journal of Constructional Steel Research 65:278-289
13. Silvestre N, Camotim D, Dinis PB (2009) Direct strength prediction of lipped channel columns experiencing local-plate/distortional interaction. Advanced Steel Construction 5(1): 49-71
14. Muthuraj H, Sekar SK, Mahendran M, Deepak OP (2017) Post buckling mechanics and strength of cold-formed steel columns exhibiting local-distortional interaction mode failure. Struct Eng Mech 64(5):621–640
15. Silvestre N, Camotim D, Dinis PB (2012) Post-buckling behaviour and direct strength design of lipped channel columns experiencing local/distortional interaction, Journal of Construction Steel Research 73:12-30

Experimental Investigations on Mechanical Properties and Morphological Analysis of Carbon Steel Grade III Leaf Spring Steel

A. Anandha Moorthy, E. Prakash, S. Madheswaran, C. Sasikumar, M. Vairavel, and R. Girimurugan

Abstract An attempt has been made to explore some mechanical properties of the leaf spring steel material experimentally under stress-relieved cum shot penned and shot penned cum sandblasted process. Effects of different mechanical treatment process on mechanical characteristics of the leaf spring steel like surface hardness, ultimate tensile strength and percentage of elongation were represented. A typical morphological analysis also carried out to establish the microstructural changes in the leaf spring steel material causes by mechanical treatments. The outcomes of this research are exposed that the good improvement in mechanical properties of the leaf spring steel material in shot penned cum sandblasted process. The experimental results show that the percentage of elongation is very less in shot penned cum sandblasted processed leaf spring steel material due to the higher surface hardness. After the mechanical treatment, the morphological analysis revealed that the huge significant effect in the microstructures of leaf spring steel material due to the shot penned cum sandblasted process.

Keywords Carbon steel · Morphological analysis · Spring steel · Shot peening

1 Introduction

Heat treatment is a significant process to the automotive parts, as the mechanical properties of metals can be enhanced by different behaviour throughout the process [1–3]. There are different methods to perform heat treatment, such as shot blasting,

A. Anandha Moorthy (✉) · E. Prakash · S. Madheswaran · C. Sasikumar
Department of Mechanical Engineering, Bannari Amman Institute of Technology, Sathyamangalam, Erode District, Tamil Nadu 638401, India
e-mail: anandhamoorthya@bitsathy.ac.in

M. Vairavel
Department of Mechanical Engineering, Annapoorna Engineering College, Salem, Tamil Nadu, India

R. Girimurugan
Department of Mechanical Engineering, Nandha College of Technology, Erode, Tamil Nadu, India

G. Kumaresan et al. (eds.), *Advances in Materials Research*, Springer Proceedings in Materials 5, https://doi.org/10.1007/978-981-15-8319-3_62

shot penning. The heat treatment of automobile parts plays a major role to enhance the fatigue life of parts [4, 5]. Carburizing is a process which has a phase transformation at cooling the substrate. Since this method is held at temperature which was the steady phase of the steel that is austenite [6]. Now, the carbon content of the steel surface is improved at phase conversion of the austenite into martensite which is the phase that was having higher hardness and the wear resistance. The salt mixtures formerly add 60–70% by weight NaCN and 30–40% KCN with a few percents of carbonates Na_2CO_3 and cyanates NaCNO [7, 8]. At operation, a required level of cyanate should be 45%. During the process, a chemical reaction is taking place. Salt bath process led to an outer surface compound layer of g-nitride (Fe_4N) and e-nitride (Fe_3N) which are not as brittle as z-nitride (Fe_2N) and are used to enhance the wear resistance, the friction properties and the resistance to corrosive of the steel surface [9]. The formation of these layers is due to the reaction between oxygen-saturated cyanates which are active compounds that were formed by aeration of the bath which oxidized the cyanides and the steel surface [10]. A various advanced methodologies have been established to improve the fatigue life of components, like surface engineering, heat treatment, alloying additions, surface coating, etc., and the shot blasting is a surface treatment process which attacks with millions of microshot with a controlled process can be greatly their surfaces to make compressive residual stresses [11]. The functional life of elements like engines, dynamic elements in machines, cams, shafts and leaf springs dies can be improved by this procedure. Shot blasting consists of an aggressive surface of a substance with different types of shots. Generally, this is performed to report a specific exterior part to the parts being shot blasted, like the rolls utilized to generate a two-dimensional finish [12]. Shot blasting is a methodology utilized to wash, reinforce (peen) or refine the metal. The shot could be sand, tiny steel balls of different widths, particles of SiC and so on. The residual compressive stresses were produced by this procedure into the film structure; therefore, the hardness of coating and brittleness was improved [13–16]. There are two technologies used: wheel blasting and the other is air blasting. Specific wheel blast machineries force plastic abrasive in a cryogenic space and are generally utilized for deflating the elements of rubber and plastic. Sandblasting is a procedure of utilizing compressed air to force abrasive grit at an elevated velocity on the parts to eliminate the oxide layer or any additional impurities from the exterior part of a material [17, 18]. As per the impacting influence of the abrasive sand, the exterior part of the component is washed completely, and consequently, the characteristics of surface and the mechanical performance are improved. Silica, which is also referred to as quartz, is the most general category of sandblasting grit. It is virtuous for sandblasting since the particulate matters are even in size, and it approximately microscopic sharp edges of the specific particle make it very efficient for eliminating material from the material being sandblasted.

2 Materials and Methods

In this study, a carbon steel grade III leaf spring Steel was utilized as test material and the chemical composition of the material is listed in Table 1. According ISO, sample to be utilized for plate, bars and Sects. (5 mm thickness, 150 mm width and 300 mm length). Forming, machining and drawing stimulate stresses in materials. A stress relief operation is in general used to eliminate internal residual stresses that include in the material. These stresses can source cracking, distortion and fatigue failures. The stress relief process is carried by heating process in an induction furnace at 230 °C, and time duration of 30 min to attain the desired properties. Shot peening of entire specimens was performed in similar resources equipped with rotating drum. As soon as the procedure was submitted, the specimens are moved. The resources 'hot spot' was defined to be similar for entire circumstances. A single pass was utilized for entire specimen machine functional current; turbine rotational velocity and shot media phase in the basin were kept fixed in entire situations; to warrant that entire procedure terms are similar, apart from the thickness of the shot media. An image analyzer was utilized to define the shot peening coverage and was quantified to be over 100% in entire situations, and this value was achieved previously in the initial peening. The exact coverage was not quantified, but subsequently entire shot peening circumstances are continuous; it is expected that specimen coverage is also continuous.

In SEM, X-rays were produced in two stage. In the initial stage, the specimens were stroke by the electron beam, and the portion of its energy is transferred into the particles of the sample. The electrons of the atom utilize this energy and to 'jump' with an energy shell with greater energy or being beaten from the particle. If this changeover happens, the electron leaving a hole. The positive charge is present in holes. In the second stage, the positively charged holes attracting negatively charged electrons from the greater-energy shells. When there is an electron from this greater-energy shell filled up a hole of the lower-energy shell, the energy disparity of this change can be distributed as an X-ray. This X-ray encompasses energy that is typical of the energy variance among those two shells. This will depend on the atomic number, which is an exclusive feature of each component. In this method, X-rays are a 'fingerprint' of every single element and could be utilized to distinguish the category of elements that occur in a specimen. The microstructure description was performed on specimen that was cutting by utilizing an optical microscope from the as-received stock of the titanium alloy. The models were placed in Bakelite and at that time damp ground on gradually better grades of SiC-saturated emery paper by means of abundant amounts of water both as a coolant and lubricant. Then, the ground specimen was automatically polished by utilizing a five micron diamond solution. Well

Table 1 Chemical composition (wt%) of work material

C	Si	Mn	Cr	Ni
1.20%	1.44%	1.54%	23.20%	1.38%

refining to an accurate mirror-like finishing of the exterior was attained by utilizing the one-micron diamond solution as the lubricant. The refined specimen of every single positioning was engraved by utilizing a reagent that is a combination of 70 ml of water (H_2O), 20 ml of hydrofluoric acid (HF) and 10 ml of nitric acid (HNO_3). The etched part of the refined specimens was detected in an optical electron microscope and imaged by utilizing a typical optimistic field illumination methodology. The mechanical characteristics of hardness of the material are suitably dissimilar as the resistance attainable by the material to a slash, stable distortion and fracture was studied by utilizing a Vickers hardness tester. The hardness test is a modest, informal and non-destructive technique which is vital and normally utilized for evaluating the mechanical characteristics of metals, their alloy parts and also for merged materials. The Nikon microscope was utilized to measure the measurements of Vickers Hardness (HV) with clemex image analyzer by utilizing a 150 gm of indentation load for 25 s of dwell time through Vickers tool indenter. The indenter (which is produced with diamond) has a pyramidal geometry with square base with a 250° of inclined angle. The machine creates an impression or indent, on the exterior part of the specimen whose transverse dimension was calculated through an optical microscope with low resolution. The number of Vickers Hardness (HV) is the proportion of load applied to the exterior part of the indent.

3 Result and Discussion

Various mechanical properties of the untreated, stress-relieved cum shot penned and shot penned cum sandblasted leaf spring steels are shown in Fig. 1 and 2. From figure, it was understood that the Vickers hardness and ultimate tensile strength (UTS) of the leaf steel were improved for both the stress-relieving cum shot penning and shot penning cum sandblasting process. It was found that the ultimate tensile strength of the leaf spring steel is improved in shot penned cum sandblasted process. The improvement in the hardness of the material is sophisticated in the shot penning cum sandblasted materials. Unlikely, the percentage of elongation is very less in shot penned cum sandblasted processed leaf spring steel and very high in untreated leaf spring steel. The ultimate tensile strength (UTS) for every single material was computed according to the examination of calculated Vickers Hardness (VH) values. From the past literature, the relationship of UTS was expressed as UTS $= 9.81[H/2.9][n/0.217]n$ ($n =$ Strain hardening index, $n = 0.20$ for medium carbon steel, $H =$ Vickers hardness). The microstructures of stress-relieved cum shot penned and shot penned cum sandblasted leaf spring steels are shown in Fig. 3. As sample shows well distinct strain-induced elongated fine grains of pearlite with traces of ferrite. Also, there is no rupturing of grains or no alignment of grains along the particular direction [19]. The microstructure was found to be quite uniform. The microstructure of the untreated specimen mixture of pearlite (black) and ferrite (white), while the morphology of the shot penned sample is demonstrated in Fig. 3.

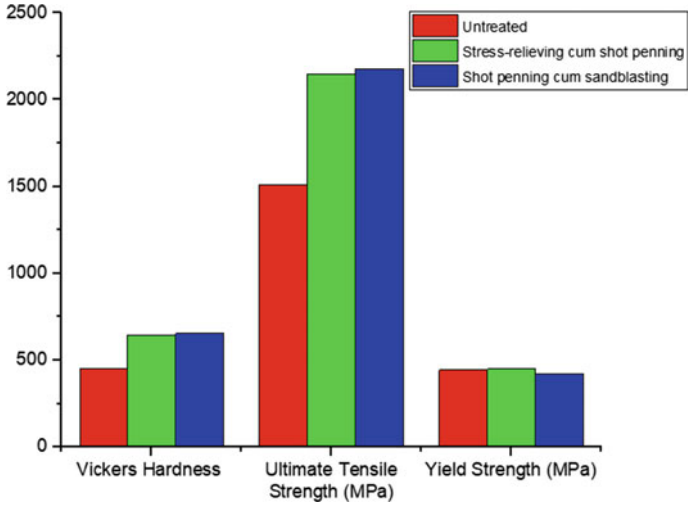

Fig. 1 Effect of mechanical treatment process on various mechanical properties for carbon steel grade III leaf spring steel

Fig. 2 Effect of mechanical treatment process on elongation percentage for carbon steel grade III leaf spring steel

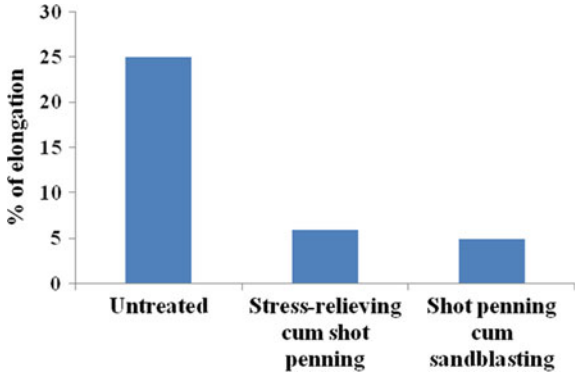

From figure, it was understood that the ferrite grains had experienced comprehensive shot penning diameter of 1 mm with 10 min, and the distorted structure was fully normalized and the final microstructure consisted well distinct strain-induced elongated fine grains of pearlite with traces of ferrite. Summary of microstructure of untreated and treated carbon steel grade III leaf spring steel material is listed in Table 2.

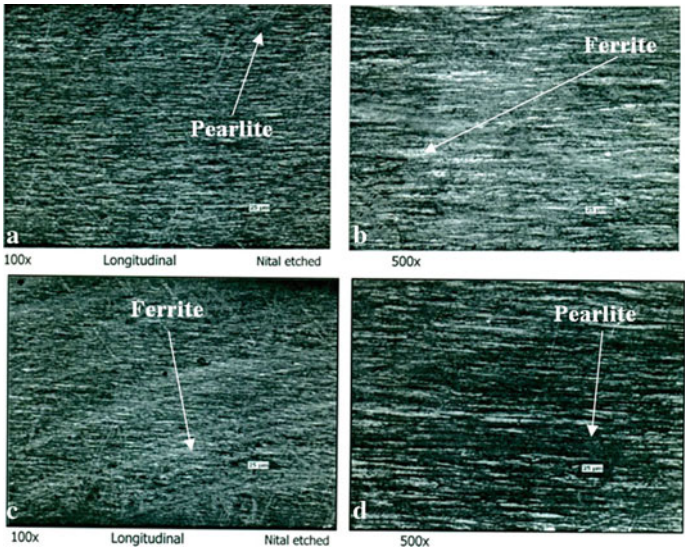

Fig. 3 **a**, **b** Microstructure of carbon steel grade III leaf spring steel after stress-relieving cum shot penning process at 100× magnification and 500× magnification. **c**, **d** Microstructure of carbon steel grade III leaf spring steel after shot penning cum sandblasting process at 100× magnifications and 500× magnification.

Table 2 Summary of microstructure of untreated and treated carbon steel grade III leaf spring steel material

Treatment type	Established microstructure
Untreated sample	Ferrite and pearlite matrix
Stress-relieving cum shot penning	Coarse grains of pearlite with traces of ferrite
Shot penning cum sandblasting	Fine grains of pearlite with traces of ferrite

4 Conclusions

Mechanical properties and microstructure of carbon steel grade III- leaf spring steel were examined from its sample by means of different treatment process. The subsequent points were demonstrated from this research. Both stress-relieved shot penned and shot penned cum shot blasted might expose the greater ultimate tensile strength and hardness than untreated leaf spring steel material. In the sample, hardness was improved by the shot penned cum sandblasted process according to the improved shot energy. Both stress-relieved cum shot penned and shot penned cum sandblasted processed leaf spring steels having low elongation due to higher surface hardness. The microstructure of all the process sample having fine grains of pearlite with traces of ferrite. The results of the study have demonstrated a major consequence for the

development of a new method of treatment of leaf spring made of carbon steel grade III with the aim of increasing their service life and reliability.

References

1. Aggarwal ML, Agrawal VP, Khan RA (2006) A stress approach model for predictions of fatigue life by shot peening of EN45A spring steel. Int J Fatigue 28(12):1845–1853
2. AlMangour B, Yang J-M (2016) Improving the surface quality and mechanical properties by shot-peening of 17–4 stainless steel fabricated by additive manufacturing. Mater Des 110:914–924
3. Arora VK, Bhushan G, Aggarwal ML (2017) Enhancement of fatigue life of multi-leaf spring by parameter optimization using RSM. J Braz Soc Mech Sci Eng 39(4):1333–1349
4. Ayada M et al (2009) Leaf spring material and manufacturing method thereof. U.S. patent application no. 12/324,586
5. Fragoudakis R et al (2013) Fatigue assessment and failure analysis of shot-peened leaf springs. Fatigue Fract Eng Mater Struct 36(2):92–101
6. Ganesh P et al (2012) Studies on laser peening of spring steel for automotive applications. Opt Lasers Eng 50(5):678–686
7. Giannakis E, Malikoutsakis M, Savaidis G (2016) Fatigue design of leaf springs for new generation trucks. In: IOP conference series: materials science and engineering
8. Jadhav Mahesh V et al (2012) Performance analysis of two mono leaf spring used for maruti 800 vehicle. Int J Innov Technol Explor Eng (IJITEE) 2(1):65–67 ISSN: 2278-3075
9. Dewanji P (2016) Design and analysis of composite leaf spring. Int J Mech Eng Technol (IJMET) 7(5):177–183. ISSN 0976–6340
10. Landgraf RW, Francis RC (1979) Material and processing effects on fatigue performance of leaf springs. SAE Trans 1(1):1–12. ISSN: 0148–7191
11. Kadziela B. (2015) Validation and optimization of the leaf spring multibody numerical model. Arch Appl Mech 85 (1):1899–1914
12. Mattson RL, Coleman Jr WS (1954) Effect of shot-peening variables and residual stresses on the fatigue life of leaf-spring specimens. SAE Trans 62:546–556
13. Palacios M et al (2014) Influence of severe shot peening on wear behaviour of an aluminium alloy. Fatigue Fract Eng Mater Struct 37(7):821–829
14. Raghavedra M et al (2012) Modeling and analysis of laminated composite leaf spring under the static load condition by using FEA. Int J Mod Eng Res (IJMER) 2(4):1875–1879
15. Shokrieh MM, Rezaei D (2003) Analysis and optimization of a composite leaf spring. Compos Struct 60(3):317–325
16. Tanabe K, Seino T, Kajio Y (1982) Characteristics of carbon/glass fiber reinforced plastic leaf spring. SAE Trans 91(2):1628–1636
17. Wilson W, Farrell B (2017) Leaf spring and method of manufacture thereof having sections with different levels of through hardness. U.S. patent no. US9573432B2
18. Gonçalves LA (2020) Theoretical and experimental investigation of performance characteristics and design aspects of cross-spring pivots. Int J Solid Struct 185–186:240–256
19. Anandha Morrthy Appusamy et al (2019) Design and dynamic analysis of active suspension system for alterin vehicle. Int J Mech Prod Eng Res Develop 9(1):14–19. ISSN: 2249–6890

Degassing of Aluminum Metals and Its Alloys in Non-ferrous Foundry

Bhaskar M. Reddy and Tamilselvam Nallusamy

Abstract In non-ferrous foundry, casting defects like microporosity and pin-hole porosity are due to expel of dissolved gases like hydrogen during solidification of castings from liquid stage to solid stage. These porosity defects significantly affect the strength and pressure tightness of the aluminum components. For a sound casting, the amount of dissolved gases present in the molten aluminum metal should be less. Degassing is a perfect process for removing dissolved gases from molten aluminum metal and its alloys. In this research, degassing of LM13, LM25, LM28, L99, and L155 was performed by passing nitrogen gas into rotary degassing chamber at different treatment time. The amount of H_2 ml/100 g available in the aluminum alloys was measured after degassing by hydrogen gas analyzer and compared with the minimal value. Nitrogen degassing reduced the quantity of H_2 ml/100 g less than the minimal value and made the aluminum alloys defect free.

Keywords Degassing · Pressure die casting · Casting defects · Porosity · Aluminum melting and non-ferrous foundry

1 Introduction

Aluminum metals and alloys are melted in different types of furnaces for casting purposes. The input raw materials to the melting furnaces are the virgin ingots, scrap, runners, risers, and foundry returns. There are different types of die casting process such as gravity die casting, high pressure die casting, low pressure die casting, which are widely used in non-ferrous casting industry [1–4]. Gravity die casting (GDC) is a process in which aluminum alloy is melted in the melting furnace, and the molten metal is transferred through the ladle and poured into the metallic mold. Here, the cavity/mold is filled up under gravitational force of liquid metal and hence, the name

B. M. Reddy (✉) · T. Nallusamy
Department of Aeronautical Engineering, MVJ College of Engineering (Autonomous), Bangalore, Karnataka 560067, India
e-mail: mbhaskar0210@gmail.com

G. Kumaresan et al. (eds.), *Advances in Materials Research*, Springer Proceedings in Materials 5, https://doi.org/10.1007/978-981-15-8319-3_63

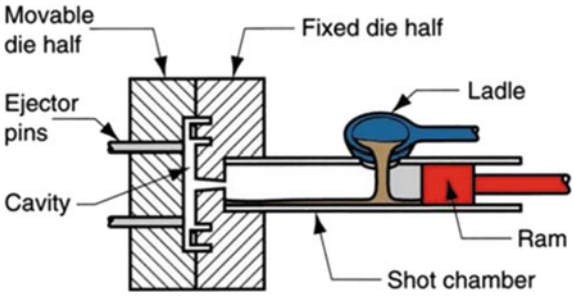

Fig. 1 High pressure die casting

gravity die casting. After the solidification of metal, the casting is removed from the mold for further operations like cleaning, inspection, machining, etc.

Gravity die casting is widely used for casting medium and large size castings such as fly wheels, cylinder heads, engine blocks, housings. The production rate of gravity die casting process is low, and the wall thickness must be sufficiently large enough for filling up of the cavity.

High pressure die casting process is a process in which aluminum alloy is melted in the crucible furnace, and the liquid metal is poured in to shot sleeve by manual or auto ladle [5]. The metal is injected into the metallic mold cavity with high velocity and pressure. The pressure range in the order of 1000–1200 bars and hence the name high pressure die casting process (Fig. 1). The cavity is filled up with in fraction of seconds. The solidification time required is 3–30 s depending upon the size of the casting. The strength and surface finish of the casting are high compared to gravity die casting process. The initial cost of the machine and die is very high which can be compensated with high production rate [6–8]. HPDC is widely used for production of automobile engine components. Casting defects like gas entrapment porosity, pin-hole porosity, microporosity, and shrinkage porosity is common in high pressure die casting process.

In low pressure die casting process (LPDC), liquid metal is flows through the cast iron or ceramic tube which is fitted to bottom of the die, and the tube is immersed in the molten metal in the holding furnace [9]. By pressurizing the holding furnace with air, argon, or nitrogen under low pressure, the molten metal rises through the ceramic or cast iron tube and fills with the die cavity under low pressure of 0.3 bars (Fig. 2). After solidification of metal in the die, the furnace chamber is depressurized, and the die is opened along with casting [10–13]. The casting is released from the upper die with the help of ejector mechanism. The casting is subjected further operations like cleaning, inspection, machining, plating, painting, etc., low pressure die casting widely used for casting alloys wheels, clutch plates, fly wheels, engine cylinder heads, cylinder covers, and transmission cases. Here, also the defects like pin-hole porosity, microporosity, shrinkage porosity, cold shuts are quite common [14].

Degassing process is very important process in today's aluminum foundry to get sound castings that are subjected to fluid pressure tightness and strength in automobile and aerospace industries. In this paper, various methods like gravity die casting (GDC), high pressure die casting (HPDC), and low pressure die casting (LPDC)

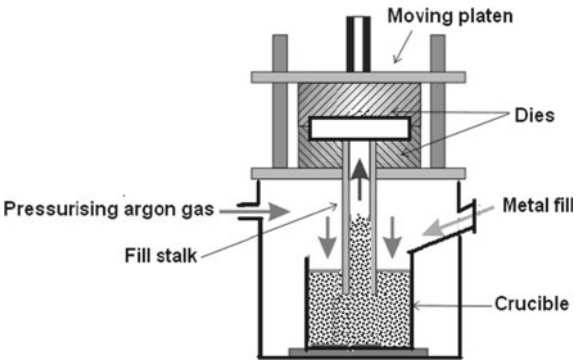

Fig. 2 Low pressure die casting

to reduce and control the dissolved gases in the molten aluminum before casting processes are discussed.

Successful casting of aluminum alloys requires greater attention in melting of metal and its alloys. The common furnaces used for melting alloys are liquid fired, gas fired, electrical coil heater type, or induction furnaces. Molten metal easily absorbs hydrogen from atmosphere, moisture-contained scraps, wet scraps, or moisture-contained refractory linings [13]. The solubility limit of hydrogen in solid aluminum alloys is very low so that the dissolved hydrogen gas is readily expelled from the molten aluminum in the form of gas bubbles, macro porosity, and microporosity as the alloy freezes. To achieve sound, high integrity, defect free castings, degassing of molten aluminum alloys is highly essential before casting process [15].

The maximum solubility limit of hydrogen in molten aluminum is as high as 0.6 ml H_2/100 g. This can be reduced to 0.2–0.3 ml H_2/100 g with careful attention and best melting practices. The degassing process entails successfully passing gases like chlorine, argon, or nitrogen over the melt in order to weaken hydrogen quantity approximately 0.1 ml/100 g. For several years, making use of chlorine gas by plunging hexachloroethane degasser tablets through the melt is usual practice. Use of these degasser tablets is prohibited in European countries with effect from April 1, 1998 due to environmental and health issue to the work men in foundries [16]. The liquid and solid solubility limit of H_2 is different for different alloy series. For example, Al–Cu–Ni alloy have nil porosity at 0.32 ml H_2/100 g for low silicon. Whereas high-silicon Al–Cu–Mn alloy is free from porosity at 0.12 ml H_2/100 g. In aluminum foundry's tablet type, degassing is replaced by argon or nitrogen gas degassing by passing gas through specially designed graphite rotary impeller immersed in the ladle or furnace which contains molten metal [17]. This rotary impeller rotates at the base of melt and ensures even distribution of nitrogen gas which results in effective expel of hydrogen gas.

The hydrogen in liquid metal comes from sources such as melting wet scrap, dirty or damp foundry tools, damp fluxes, damp refractory, and crucible linings, water vapor in burner fuels and moisture from atmosphere. The graph shows relationship between temperatures of melt versus hydrogen content is shown in Fig. 3 [18]. To reduce H_2 pickup; crucible, foundry tools, refractories, wet scrap, oil scrap, and

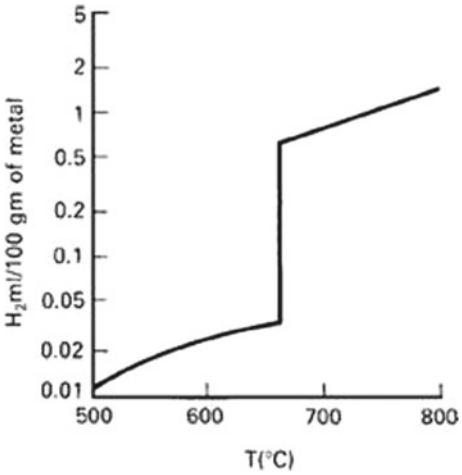

Fig. 3 Relationship between temperatures of melt versus hydrogen content [18]

ingots are thoroughly preheated to remove moisture. The melt temperature is kept at low temperature since more H_2 gets dissolved at high temperature of melts. The excess hydrogen in the combustion products avoided by slight oxidation of burner fuels. The amount of hydrogen gas content can be measured by using hydrogen gas analyzer device [19].

Various methods are available to reduce and control the dissolved gases in the molten aluminum before casting processes like gravity die casting (GDC), high pressure die casting (HPDC), and low pressure die casting (LPDC). It also reveals the sources for causing the gases dissolved in melting of aluminum metal and alloys in aluminum melting and casting foundry. In this research, degassing of LM13, LM25, LM28, L99, and L155 was performed by passing nitrogen gas through rotary impeller at different treatment time and ladle size. The quantity of H_2 ml/100 g present in the LM13, LM25, LM28, L99, and L155 alloys was measured before and after passing nitrogen gas inside the chamber and compared with the minimal value. Porosity free castings can be produced with minimal hydrogen content of 0.15 ml H_2/100 g. Anything higher than 0.15 ml H_2/100 g results in microporosity and pin-hole porosity in the castings.

2 Experimentation and Results

The equipment consists motor for rotating the specially designed graphite rotary impeller, inert gas cylinder supply, and a mechanism to lower down the rotary impeller and to take up the rotary impeller from the base of the molten metal (Fig. 4).

For effective degassing, it is essentially a very fine stream of bubbles of dry inert gases like argon or nitrogen which is generated at the bottom of molten metal and is dispersed thorough out the metal. The temperature level of the liquefied metal

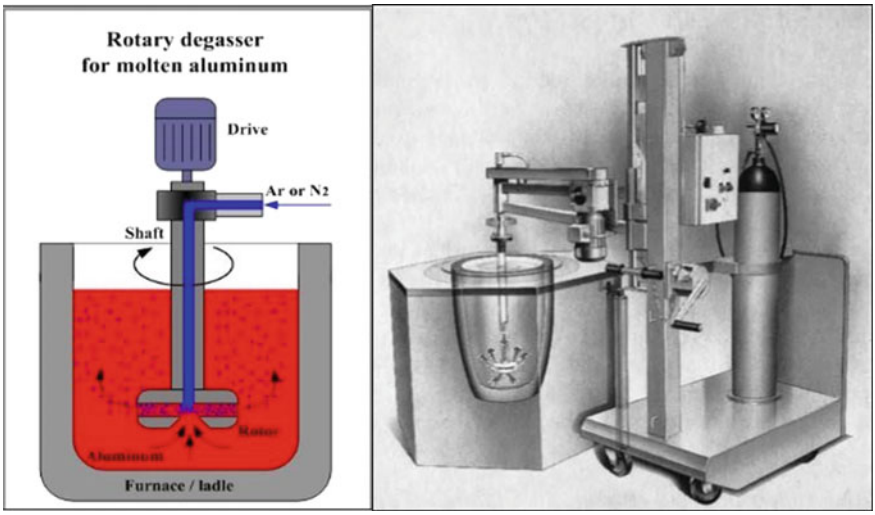

Fig. 4 Rotary degassing mechanism

must be maintained as low as possible throughout the degassing process [17]. The solubility limit of hydrogen is low at low temperature and vice versa. The operation is started by slowly dipping down the rotary impeller to the base of the melt and switching on motor and inert gas flow through the impeller. The rotational speed of rotor is around 250–300 rpm, and this produces fine stream of inert gas bubbles though out the melt [20]. The fine stream of bubbles rises through the melt and takes away the dissolved hydrogen gases from the melt to the atmosphere as the bubbles reaches the surface of the melt. The rising bubbles also take away the inclusions from the melt to the surface, and it can be skimmed off (Fig. 5).

The equipment is designed as fixed degassing unit or mobile degassing unit based on the service requirement. The mobile degassing unit is pushed around the shop floor

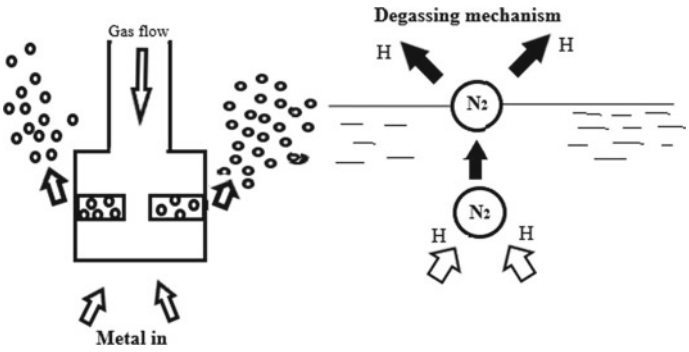

Fig. 5 Bubble formation, degassing mechanism

Table 1 Typical analysis results of degassing of aluminum alloys

S. No.	Alloy	Ladle size (Kg)	Treatment time (min)	Hydrogen content (ml/100 g)		
				Before	After	Minimal [22]
1	LM 13: Al-Si12Cu1Mg1	250	5	0.29	0.19	0.15
2	LM 25: Al-Si7Mg0.5	250	6	0.41	0.14	0.15
3	LM 28: Al-Si8Cu1.5Mg1Ni1	250	10	0.29	0.19	0.15
4	L99: Al-Si7Mg0.3	250	7	0.24	0.12	0.15
5	L155: Al-Cu4Si1	90	15	0.23	0.11	0.15

and brought near to the furnace. The arm swung over the furnace, and the impeller is lowered to the center and at bottom of the melt. The degassing operation is carried out by switching on motor and inert gas. The treatment time, gas flow, rotational speed are preset for given melt capacity, and the process is completed within 3–7 min. After degassing, the impeller is raised from the melt, and the unit is take away from the furnace. All the slag and inclusions collected at the top of melt is skimmed off, and the metal is ready for casting process (Fig. 5). The graphite rotor has life of 100–150 metal treatments based on the temperature of the melt. Melts of 500–1000 kg can be treated within time span of 1.5–6 min with inert gas flow ranging from 6 to 18 L/min [21]. Foseco manufacturing and supplying both fixed and mobile degassing units to aluminum foundries in India and abroad. The results of typical analysis of degassing of aluminum alloys displayed in Table 1. The degassing is widely used in gravity die casting, high pressure die casting, and low pressure die casting units [22]. After degassing operation, the hydrogen content is significantly reduced and results in porosity a free casting which improves strength and pressure tightness of the aluminum castings.

3 Results and Conclusion

Casting defects like microporosity, pin-hole porosity are due to expel of dissolved hydrogen gases during solidification of castings from liquid state to molten state. These defects can be reduced by degassing of aluminum melt by with inert gases like argon or nitrogen gas with help of degassing equipment. The time duration of degassing process greatly influences the solubility concentrations of dissolved hydrogen gases in the melt. High degassing time results in fewer amounts of dissolved gases in the melt. This results in porosity free castings. This research paper also gives the hydrogen content before degassing and after degassing for different alloys. Porosity free castings can be produced with minimal hydrogen content of 0.15 ml H_2/100 g.

Anything higher than 0.15 ml H_2/100 g results in microporosity and pin-hole porosity in the castings.

Acknowledgements The author acknowledges Sundaram Clayton foundry, sun beam foundry, Amtech auto limited, NSSL foundry, and MVJ College of Engineering for their support extended during the course of this research work.

References

1. Dong X et al (2019) High strength and ductility aluminium alloy processed by high pressure die casting. J Alloy Compd 773:86–96
2. Zhang Y et al (2019) Improve mechanical properties of high pressure die cast Al_9Si_3Cu alloy via dislocation enhanced precipitation. J Alloy Compd 785:1015–1022
3. Jiao X et al (2019) Characterization of high-pressure die-cast hypereutectic Al–Si alloys based on microstructural distribution and fracture morphology. J Mater Sci Technol 35(6):1099–1107
4. Liu T et al (2019) The combined effects of Sr additions and heat treatment on the microstructure and mechanical properties of high pressure die cast A383 alloy. Mater Sci Eng A 756:373–380
5. Bach L et al (2019) A study on Mg and AlN composite in microstructural and electrochemical characterizations of extruded aluminum alloy. Compos B Eng 156:332–343
6. Chen G et al (2019) Ultrasonic assisted squeeze casting of a wrought aluminum alloy. J Mater Process Technol 266:19–25
7. Yuan D et al (2019) Development of high strength and toughness nano-SiCp/A356 composites with ultrasonic vibration and squeeze casting. J Mater Process Technol 269:1–9
8. Chong L et al (2019) Influence of high pressure and manganese addition on Fe-rich phases and mechanical properties of hypereutectic Al–Si alloy with rheo-squeeze casting. Trans Nonferrous Metal Soc China 29(2):253–262
9. Eskin DG, Al-Helal K, Tzanakis I (2015) Application of a plate sonotrode to ultrasonic degassing of aluminum melt: acoustic measurements and feasibility study. J Mater Process Technol 222:148–154
10. Fritzsche A et al (2018) Improved degassing in laser beam welding of aluminum die casting by an electromagnetic field. J Mater Process Technol 253:51–56
11. Tzanakis I et al (2015) In situ synchrotron radiography and spectrum analysis of transient cavitation bubbles in molten aluminium alloy. Phys Proc 70:841–845
12. Tzanakis I et al (2015) In situ observation and analysis of ultrasonic capillary effect in molten aluminium. Ultrason Sonochem 27:72–80
13. Liu X et al (2015) Study on hydrogen removal of AZ91 alloys using ultrasonic argon degassing process. Ultrason Sonochem 26:73–80
14. Haghayeghi R, Bahai H, Kapranos P (2012) Effect of ultrasonic argon degassing on dissolved hydrogen in aluminium alloy. Mater Lett 82:230–232
15. Mancilla E et al (2017) Comparison of the hydrodynamic performance of rotor-injector devices in a water physical model of an aluminum degassing ladle. Chem Eng Res Des 118:158–169
16. Puga H et al (2009) The influence of processing parameters on the ultrasonic degassing of molten $AlSi_9Cu_3$ aluminium alloy. Mater Lett 63(9–10):806–808
17. Ren Y et al (2014) Degassing of aluminum alloys via the electromagnetic directional solidification. Vacuum 109:82–85
18. Uludağ M et al (2018) The effects of degassing, grain refinement & Sr-addition on melt quality-hot tear sensitivity relationships in cast A380 aluminum alloy. Eng Fail Anal 90:90–102
19. Xu H, Han Q, Meek TT (2008) Effects of ultrasonic vibration on degassing of aluminum alloys. Mater Sci Eng A 473(1–2):96–104

20. Shusen W et al (2012) Degassing effect of ultrasonic vibration in molten melt and semi-solid slurry of–Al-Si alloys. China Foundry 9(3):201–206
21. Zhao L et al (2012) Degassing of aluminum alloys during re-melting. Mater Lett 66(1):328–331
22. Zeng J, Gu P, Wang Y (2012) Investigation of Inner Vacuum Sucking method for degassing of molten aluminum. Mater Sci Eng B 177(19):1717–1720

Design and Fabrication of Hybrid Mobility Scooter

N. Ramachandran, R. Sivasubramanian, R. Palanivel, P. Nishanth Kalathil, and B. Nirmal

Abstract The concept of design and fabrication of hybrid vehicle was mainly intended for differently abled people and the elderly. It is a vehicle which is solar powered by solar and electrical energy. This vehicle is an electric vehicle powered by solar energy obtained from solar panels on the surface of the vehicle. Solar vehicles are not practical day-to-day transportation devices at present, but are used as primary demonstration vehicle and for engineering exercises. The battery is the energy storage device which can store charge from single-phase 230 V wall socket or through the solar panel. A BLDC motor is the prime mover, and it drives the vehicle with the support of two wheels. This vehicle has the capability to carry weights up to limits of 150 kg and can travel at speeds of 40 km/h. It is designed as user-friendly which is free from pollution, and it is different from conventional vehicles. Our main motto is to fabricate a vehicle which supports differently abled and elder people at the lowest cost possible.

Keywords Hybrid · Cost efficient and user-friendly

1 Introduction

Most of the vehicles in the market today cause pollution, and fuel cost is also increasing day by day. In order to compensate the fluctuation of the fuel cost and the increasing levels of pollution, a sustainable mean of transport is required. This vehicle is for a single person who has difficulty in going places such as differently abled or elder people. A person with such difficulties will be able to drive the vehicle without any dependencies. In order to reduce pollution and help these cases, this vehicle is a feasible solution [1].

N. Ramachandran (✉) · R. Sivasubramanian · R. Palanivel · P. Nishanth Kalathil · B. Nirmal
Sri Krishna College of Engineering and Technology, Coimbatore 641008, India
e-mail: ramachandrann@skcet.ac.in

G. Kumaresan et al. (eds.), *Advances in Materials Research*, Springer Proceedings in Materials 5, https://doi.org/10.1007/978-981-15-8319-3_64

2 Objectives

- It should be simple and easy to use.
- It should be durable and safe.
- It should be comfortable.
- It should be affordable.
- It should have low maintenance.
- It should have proper operating capabilities.

3 Components Used

The components used in fabricating of said vehicle are explained below.

3.1 Chassis

A chassis is the basic component of a vehicle on which other parts and subsystems are fixed. It can also be called the backbone for any vehicle. The supreme objective of a chassis is to provide support to the vehicle's parts and body. It is meant to absorb all loads acting on the vehicle while at rest or in motion with absolutely no deformation or failure [2].

3.2 BLDC Motor

Brushless DC motors are highly efficient motors which are used for a variety of applications. The reasons for their extensive use are good torque, efficiency, silent operation and durability. The two distributions of the windings are sinusoidal and distributed [3]. A distributed winding has a trapezoidal back EMF, and a sinusoidal winding would have a sinusoidal back EMF. The commutation of a BLDC motor is controlled by electrical signals. In order to make sure, the motor controller energizes coils in a correct order; implementation of Hall sensors helps in determining the way the rotor is positioned [4].

3.3 Lead–Acid Battery

Lead–acid batteries are the common large-capacity rechargeable batteries. They are very popular because they are dependable and inexpensive on a cost-per-watt basis. There are other batteries that deliver bulk power as cheaply as lead–acid, and this

makes the battery cost-effective for automobiles, electrical vehicles, forklifts, marine and uninterruptible power supplies (UPSs) [5].

3.4 Controller

The DRV8307 is a three half-bridge pre-driver which drives six *N*-type MOSFETs 30 mA with single power supply. Aimed at censored three-phase brushless DC motors, the DRV8307 is driven by a single PWM input and supports integrated commutation logic with all three Hall sensor inputs [6]. A separate 5-V regulator is included to be used to power Hall effect sensors and for external components also. The DRV8307 normally includes a current sense input for current limiting and protection. The current limit should be set by adjusting the value of RISENSE sense resistor [7]. Motor operation is controlled by the ENABLE terminal. If the ENABLE terminal is set high and motor rotation has stopped, the device enters into a low-power standby state, thereby conservation of overall system power during periods of inactivity [8]. Protection features are included in the DRV8307 device such as locked rotor detection, overcurrent and over-temperature protection and under-voltage lockout to bolster overall system robustness and reliability [9].

3.5 Solar Panel

Solar energy from the sun's rays is converted into electric energy by photovoltaic cells present in the solar panel using photovoltaic effect. The photovoltaic cells are crystalline silicon structures of very thin cross section. Photovoltaic cells are fragile and should be kept safe from any sort of physical damage and moisture [10]. The cells are available in rigid and semiflexible types. The connection between consecutive cells is always done in series. The photovoltaic cells use MC4-type connectors to create an all-weather usable circuit completing the system. All connections within the modules are in series in order to achieve required output voltage. Magnetic or non-magnetic conduction materials present in wires are used to remove current passing through the cells [11].

3.6 Accelerator

The accelerator operates exactly as a motorcycle throttle. As the accelerator is twisted, according to the signals sent from the accelerator the motor rotates and moves the vehicle forward. These are very easy to use. To use the accelerator, the user holds the throttle and turns it anticlockwise [12]. The accelerator is connected to a controller.

The speed of the motor is directly proportional to the amount of twist on the electric throttle. Care must be taken while operation as throttle is sensitive [13].

3.7 Solar Panel Mounts

Solar panels include bracket to be fixed onto any existing structure since this is a new design, mounts of the solar panel and structures to mount them on to the vehicle were custom designed and fabricated to suit our requirements. These mounts were designed in such a way that the panel acts as a roof of the vehicle while being mounted in such a manner that it has maximum exposure to sunlight whenever available. The mounts are designed to act as an extra safety measure in case of any impact.

3.8 Driving Wheel and Balancing Wheels

The vehicle is a three wheeler; hence, one is for driving and two balancing wheels. The driving wheel houses the BLDC motor inside its hub and is mounted at the front in order to achieve better starting torque as it is easier to pull rather push a load. The driving wheel has a diameter of 450 mm. In the rear, two wheels are positioned at two ends of the chassis of 210-mm diameter each [14].

3.9 Suspension

The vehicle was designed for outdoor travel on the streets and roads. This means the vehicle will endure bumps and potholes while driving in order to minimize this impact on the driver coil over suspensions are used on all three wheels on the vehicle the front uses tube forks with shock absorbers, while the rear two wheels each have their own coil spring shock absorbers. The front and the rear suspension setups work in tandem to improve riding comfort and stability [15].

4 Fabrication Methodology and Material Selection

4.1 Fabrication Methodology

The methodology used for fabricating hybrid mobility scooter is shown in Fig. 1.

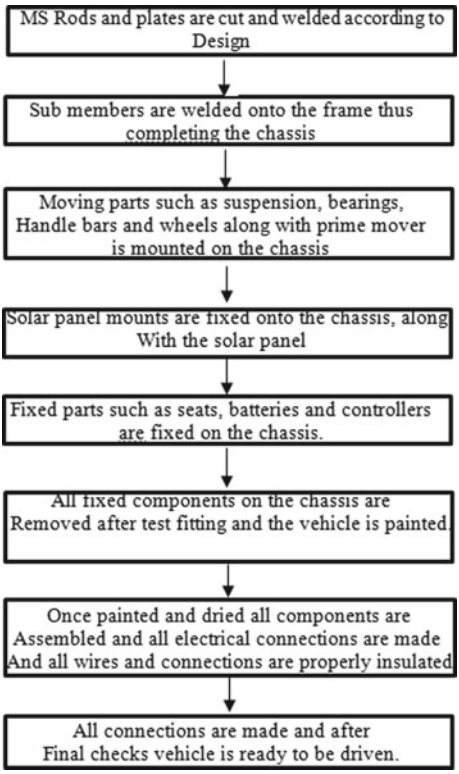

Fig. 1 Fabrication methodology

4.2 Selection of Materials

The material chosen should have the required characteristics for the design. The different criteria which were up to the mark are: strength, shelf life, rigidity and so on. Exclude these external factors such as availability, cost, machinability and fabrication costs, which in most cases are decisive factors while choosing materials (Table 1).

5 Parts Fabricated

5.1 Chassis

The chassis is fabricated with stainless steel hollow circular members. The procedure commences with modifying the rods and plates into required lengths, and then bent to actual design angles. To fasten the frame and other components, drilling is done according to the design. Arc welding is done to join the members and plates

Table 1 Bill of materials

Part name	Material	Quantity
210-mm tire and tube	Rubber	2
450-mm tire and tube	Rubber	1
BLDC motor with wheel hub	–	1
Solar panel—75 W	Aluminum	1
Wheel rims	Zinc-coated Mild steel	2
Bearing	Alloy steel	6
Suspension	Alloy steel	3
Swing arm	Mild steel	1
12 v, 7AMPH battery	–	4
Controller	Plastic	1
Seat	Plastic	1
Twist throttle	Plastic	1
Screw	Steel	As req
Nut	Steel	As req
Washer	Steel	As req
Bolt	Steel	As req
Panel mounts	Mild steel	4

together. Bushes are made up of hollow mild steel cylindrical members. Small and equal lengths of the members are cut and converted into bushes for required use by operations like milling, boring, drilling, reaming, etc. Arc welding is performed to join all separately fabricated components together, thus finally completing the chassis.

5.2 Solar Panel Mounts

They are mild steel rods of L-cross section which is cut into required length and then bent to the required angle at which the solar panel should be. Once bent, holes are drilled of required diameter and fastened into the vehicle base using fasteners.

5.3 Housing Unit

The housing unit consists of the power pack, the controller, the charging and discharging circuit, the solar circuit, and all necessary wiring. The housing unit was fabricated using stainless steel plates by cutting the plates using gas cutting machine

according to the design and then welded in the shape of a rectangular box on the base below the passenger seat using arc welding.

5.4 Storage Bay

It is made up of high-grade steel. It is attached to the vehicle to carry everyday necessities of the user around along with extras such as groceries and pets; it is made of high-grade steel and in the form of a basket usually found on cycles. It was fabricated by cutting and welding pieces of different length steel rods of small diameter to form a skeleton; then, a wire mesh of aluminum was wrapped on 3 sides leaving the top open and welded to the skeleton, thus forming the storage bay.

5.5 Handle Bar

It is constructed using stainless steel members. Its primary function is to maneuver the vehicle. It is fabricated as a single hollow rod with a T-shaped extension for mounting the handle bar onto the steering column bearing of the vehicle.

6 Working Principle

The working principle of "design and fabrication of hybrid mobility scooter" is as follows: The vehicle is driven by means of motor. Here, the motor is the prime mover. The brushless direct current (BLDC) motor is used. The prime mover is supplied power from a 42-V lead–acid battery, and the circuit is controlled by a controller. The lead–acid battery is a secondary battery, and it is able to sustain to the vehicle for speeds up to 40 kmph. While running of vehicle on roads, it obtains charge from the solar panel and the charge generated is controlled by the charge controller. The battery and controller setup is placed in the housing unit. The key is turned, and the supply passes from the battery to the BLDC motor through the controller. BLDC is prime mover which operates by minimum resistance path and through which high initial torque can be obtained. Once the key on the circuit is closed and current flows from the battery to the BLDC motor via the controller. The controller varies the current flowing to the BLDC based on signals sent to it by the twist throttle in the right-hand side of the handle bar. The rear wheels are the supporting wheels for the chassis, and the suspension is provided for both the wheels. The front wheel has the prime mover and the braking inside the wheel hub. Braking system uses drum brakes with shoes for easy maintenance and dependability (Figs. 2 and 3).

Fig. 2 Front view of hybrid vehicle

Fig. 3 Rear view of hybrid vehicle

7 Applications

It can be used by all people for everyday commutes. It can be used to help people with walking difficulties to move around. It can be used in crowded cities to avoid traffic congestions and to avoid pollution.

8 Conclusion

As described in the above note, the hybrid mobility scooter is a vehicle which can help people with moving challenges and suit their individual needs without extensive modification.

References

1. Pop CV, Fodorean D (2016) Modelling of an in-wheel motor with integrated magnetic gear for electric vehicle applications. In: 2016 international conference and exposition on electrical and power engineering (EPE), pp 240–244
2. Tousi S, Bajaj AK, Soedel W (1988) On the stability of a flexible vehicle controlled by a human pilot. Veh Syst Dyn 17:37–56
3. Cooper RA (1993) Stability of a wheelchair controlled by a human pilot. IEEE Trans Rehabil Eng 1(4):193–206
4. Cooper RA (1995) Intelligent control of power wheelchairs. IEEE Eng Med Biol Mag 14(4):423–431
5. Bourhis G, Horn O, Habert O, Pruski A (2001) An autonomous vehicle for people with motor disabilities. IEEE Robot Autom Mag 8(1):20–28
6. Ramachandran N, Sivakumar S, Sivasundar S (2019) Design and fabrication of stair climbing load carrier. Int J Innov Technol Explor Eng (IJITEE) 8(4):01–05
7. Song B-M, Choi J-Y (2011) A low-speed high-torque permanent magnet motor for electric scooters. In: 2011 IEEE vehicle power and propulsion conference, pp 1–6
8. Ravi N, Ekram S, Mahajan D (2006) Design and development of an in-wheel brushless D.C. motor drive for an electric scooter. In: PEDES 2006 international conference on power electronics drives and energy systems, pp 1–4
9. Nguyen C-L, Lee H-H (2012) AC voltage sensorless control of battery charger system in electric vehicle applications. In: IPEC 2012 conference on power & energy, pp 515–520
10. Azidin FA, Hannan MA (2012) Harvesting solar and energy management system for Light Electric Vehicles (LEVs). In: 2012 international conference on renewable energy research and applications (ICRERA), pp 1–6
11. Onar OC, Khaligh A (2010) Grid interactions and stability analysis of distribution power network with high penetration of plug-in hybrid electric vehicles. In: 2010 twenty-fifth annual applied IEEE power electronics conference and exposition (APEC), pp 1755–1762
12. Dusmez S, Khaligh A (2012) A novel low cost integrated on-board charger topology for electric vehicles and plug-in hybrid electric vehicles. In: 2012 twenty-seventh annual IEEE applied power electronics conference and exposition (APEC), pp 2611–2616
13. Dahan N, Peretz MM, Zeltser I (2017) Cell-level hybrid architectures for active balancing of serially-connected batteries. In: 2017 IEEE applied power electronics conference and exposition (APEC), pp 2382–2389

14. Shahid A (2014) Simulation based analysis of regenerative DC motor drives for vehicular power systems. In: 2014 IEEE PES Asia-Pacific power and energy engineering conference (APPEEC), pp 1–6
15. Murcia E, Ramirez C, García H, León N (2014) Optimization of energy distribution for sun-powered thermo-HEV prototype. Energy Proc 57:920

Optimization of Process Parameters to Reduce the Green Sand Casting Defects

M. Nandagopal, K. Sivakumar, M. Sengottuvelan, and S. Velmurugan

Abstract In this work, the mold-related sand casting defects are minimized by using the Taquchi optimization technique. The parameters considered are water content percentage, green compression strength (GCS), hardness of the mold, and molding sand particle size. The L9 orthogonal array is used to conduct the experiments. The outcome of this work leads to the sand casting foundry men to select the suitable level of process parameters to produce good quality castings. The improvement expected is around 8–10% reduction in mold-related casting defects.

Keywords Sand mold · Casting defects · Sand casting and Taguchi technique

1 Introduction

Green sand casting is one of the most widely used manufacturing processes. Depending upon the requirements, casting having various complex shapes and sizes can be easily manufactured in sand casting process. The steps involved in the sand casting process are pattern making, mold and core preparation, melting and pouring of the molten metal, and fettling. The major causes of casting rejections are due to improper design of gating system, poor mold quality, and improper fettling of the castings.

The quality of the products is more important in all manufacturing processes. The casting rejection is more in sand casting process due to more process parameters. In sand casting foundries, the total casting rejection rate is around 7–8%. The 35–50% of the total casting rejections is only due to the poor condition of the mold. The mold-related casting defects are occurring due to improper sand properties and mold preparation. Many researches optimized the foundry process parameters, and their result shows that the poor quality of the casting is due the uncontrollable mold preparation process variables.

M. Nandagopal (✉) · K. Sivakumar · M. Sengottuvelan · S. Velmurugan
Department of Mechanical Engineering, Bannari Amman Institute of Technology, Sathyamanglam, Erode District, Tamil Nadu 638401, India
e-mail: gopalnanda07@gmail.com

G. Kumaresan et al. (eds.), *Advances in Materials Research*, Springer Proceedings in Materials 5, https://doi.org/10.1007/978-981-15-8319-3_65

Many researches were carried out to improve the quality of the sand casting by using optimization techniques, casting analysis software, and quality control tools [1] such as Ishikawa diagram, Pareto-Lorenzo's analysis. Apart from sand casting process parameters optimization, many researchers tried to optimize the process parameters of the other casting process like pressure die casting, centrifugal casting, and investment casting [2, 3]. The sand casting process parameters such as compression strength, moisture, permeability, mold hardness, solidification time, metal temperature, filling time, and sand particle size are optimized using Taguchi optimization technique [4–7].

The sand casting defects are analyzed by using other methods such as non-destructive testing and the genetic algorithm optimization technique [8, 9]. Apart from process parameters, cast iron chemical composition also optimized by few researchers [10]. The most commonly occurring sand casting defects such as blow-holes, porosity, shrinkage, hot tear, and lumps are analyzed by many researchers [11, 12]. Case study researches [13, 14] were also carried out to improve the quality of the cast iron cylinder block and housing. The optimization techniques are also used to optimizing cutting conditions in single pass face milling for minimum cutting energy, time, cost, and surface roughness [15].

The literature review results show that nearly 40–50% of the casting defects are occurring only due to the poor quality of the mold. The most commonly occurring defects are shown in Fig. 1. Hence in this work, the process parameters influencing the quality of the molds are considered for optimization. Taguchi optimization is a very useful problem-solving technique to improve the casting quality and productivity. The process parameters such as water content percentage, GCS, hardness of the mold, and molding sand practical size are optimized in this work by using the Taguchi optimization technique.

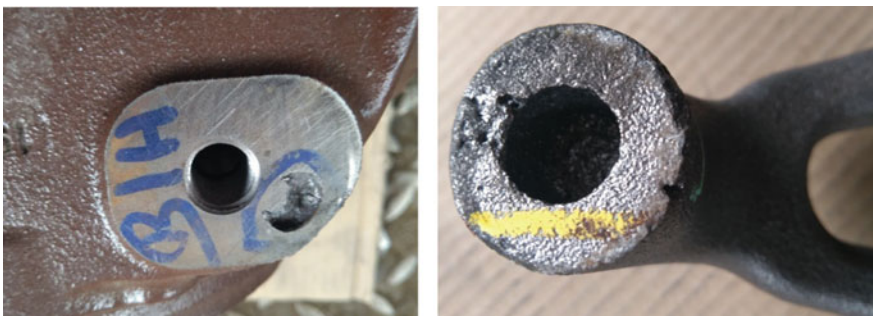

Fig. 1 Casting defects

2 Methodology and Experimentation

The objective of this paper is to optimize the sand casting major process parameters such as water content percentage, GCS, hardness of the mold, and molding sand practical size. The experiments for the optimization of sand casting process parameters are carried out in a jobbing foundry in South India. The Taguchi optimization technique and L9 orthogonal array are selected for this work. The methodology of the work is shown in Fig. 2. Based on standards, significant interactions, and foundry men past experiences, three levels are selected for each process parameters. The parameters, along with their ranges, are given in Table 1.

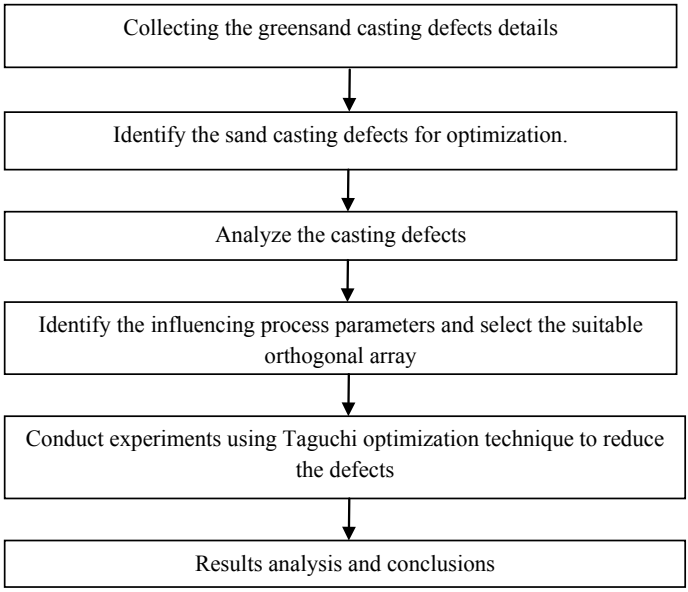

Fig. 2 Methodology

Table 1 Range and levels of process parameters

Parameter	Range	Level 1	Level 2	Level 3
Water content (%)	3.0–4.0	3.0	3.5	4.0
GCS (g/cm^2)	1250–1650	1250	1450	1650
Molding sand particle size (AFS number)	50–60	50	55	60
Hardness of the mold (number)	60–80	60	70	80

Table 2 Experimental array

Trail number	Water content (%)	GCS (g/cm^2)	Molding sand particle size (AFS number)	Hardness of the mold (number)
1	3.0	1250	50	60
2	3.0	1450	55	70
3	3.0	1650	60	80
4	3.5	1450	55	80
5	3.5	1650	60	60
6	3.5	1250	50	70
7	4.0	1650	60	70
8	4.0	1250	50	80
9	4.0	1450	55	60

2.1 Quality Characteristics

The most commonly occurring sand casting defects due to poor quality of mold are monitored and recorded. The objective function is (Eq. (1))

$$\text{Smaller is better} = -10^{*} \log 10 \left(\text{sum}\left(Y^{**}2/n\right)\right) \tag{1}$$

The experimental array detail is shown in Table 2.

2.2 Experiment Results and S/N Ratios

The experiments are conducted three times for the same set of parameters. The casting defects occurring in each trial conditions are recorded. The average casting defects and S/N ratio are calculated using Eq. (2) and shown in Table 3. The molds prepared for the experiments are shown in Figs. 3 and 4.

$$\begin{aligned} \eta &= -10 \log\left[\left(\varepsilon_y^{2i}\right)/3\right] \\ &= -10 \log\left[\left(6.1^2 + 5.2^2 + 6.8^2/3\right)\right] \\ &= -15.56 \end{aligned} \tag{2}$$

Table 3 Experimental results and S/N ratio

Trial number	Experimentation results—percentage of defects				Average value	S/N ratio
	1	2	3	Total		
1	6.1	5.2	6.8	18.1	6.033	15.560
2	5.2	4.4	5.2	14.8	4.933	13.888
3	7.3	5.8	7.6	20.7	6.900	16.833
4	3.9	3.4	3.1	10.4	3.467	10.840
5	6.4	4.8	7.4	18.6	6.200	15.975
6	7.2	6.7	6.1	20.0	6.667	16.500
7	6.8	4.3	6.2	17.3	5.767	15.364
8	3.2	7.3	4.7	15.2	5.067	14.555
9	3.1	3.9	2.7	9.7	3.233	10.294

Fig. 3 Experimental molds

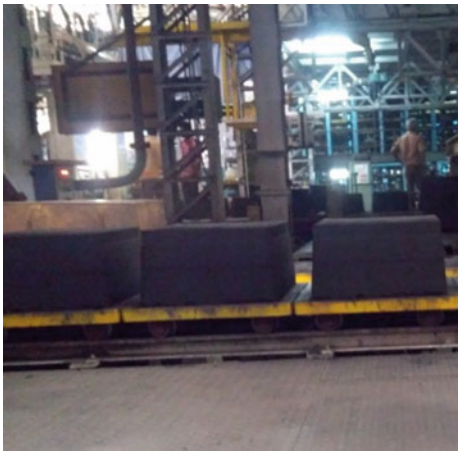

3 Conclusion

The literature review shows that nearly 40–50% of the casting defects are occurring only due to the poor quality of the mold. Hence in this work, four important sand casting process parameters are optimized to improve the mold quality using Taguchi optimization technique. The Taguchi optimization results show that the optimal condition of the process parameters is

Water content—level 2–3.5%
GCS—level 2–1450 (g/cm^2)
Molding Sand Particle Size—level 1–50 (AFS Number)
Hardness of the mold—level 3–80 (Number).

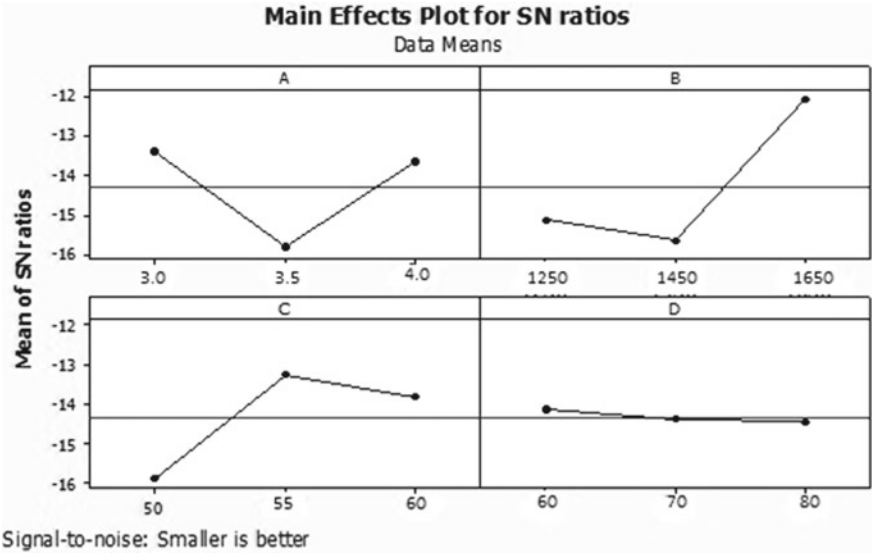

Fig. 4 SN ratio plot

From the above-optimized value, the improvement expected is 8–10% reduction in mold-related casting defects. The optimized process parameters not only reduce the casting defects, also improve the casting surface finish, dimensional accuracy, and castings rework.

References

1. Siekański K, Borkowsk S (2003) Analysis of foundry defects and preventive activities for quality improvement of castings. Metalurgija 42:57–59
2. Kaewkongkha P, Sitcharoen ST (2015) Investigation of factors affecting the blow holes in die casting process. IOSR J Eng 05(06):47–51
3. Suryawanshi A, Chandra H, Shekhar S (2015) Optimization to improve the quality of centrifugal casting by grey fuzzy method. Int J Adv Eng Res 4(2):164–166
4. Saravanakumar M, Jeyaprakash K (2015) Optimization of casting process parameters using Taguchi analysis. Int J Mech Eng Res 5:134–136
5. Sathishkumar AK, Gupta PC (2012) Optimization of process parameters of pressure die casting using Taguchi methodology. Int J Ind Manuf Eng 6(8):1484–1488
6. Upadhye RA, Keswa IP (2012) Optimization of sand casting process parameter using Taguchi method in foundry. Int J Eng Res Technol 1(7):1–11
7. Senthilkumar B, Ponnambalam SG, Jawahar N (2009) Process factor optimization for controlling pull down defects in iron casting. J Mater Process Technol 209(1):554–560
8. Saravana Kumar V, Dharmalingam, Pandyrajan R (2015) Defect analysis in a casting component and measures to mitigate it using non-destructive testing and genetic algorithm. Int J Adv Eng Res Appl 1(2):56–62
9. Wisam M, Jadayil A (2011) Studying the effects of varying the pouring rate on the casting defects using non-destructive testing techniques. Jordon J Mech Indu Eng 5:521–526

10. Crisan A, Munteanu SI, Ciobanu I, Riposan I (2008) Optimization of the chemical composition of cast iron used for casting ball bearing grinding disks. Tsinghua Sci Technol 13(2):164–169
11. Juriani A (2015) Casting defects analysis in foundry and their remedial measures with industrial case studies. J Mech Civ Eng 6(1):43–54
12. Kumar S, Satssangi PS, Prajapati DR (2011) Six sigma an excellent tool for process improvements—a case study. Int J Sci Eng Res 2(9):1–10
13. Latte MR, Chougule PD (2017) Blow-hole defect analysis of cylinder block—a case study. Int J Eng Res Technol 10(1):626–631
14. Shivappa DN, Rohit A (2012) Bhattacharya analysis of casting defects and identification of remedial measures—a diagnostic study. Int J Eng Invent 1:1–5
15. Jdidia AB, Hentati T, Bellacicco A, Khabou MT, Rivier A, Haddar M (2019) Optimizing cutting conditions in single pass face milling for minimum cutting energy, time, cost, and surface roughness. In: Lecture notes on mechanical engineering book series, pp 214–222

Optimization of Welding Parameters in CMT Welding of Al 5083

S. Suryaprakash, S. Vishal, M. Sethu Raman, S. Rajendra Kumar, M. Umar, and T. Deepan Bharathi Kannan

Abstract In this article, an attempt is made to identify the optimized parameter combination in cold metal transfer (CMT) welding of aluminium 5083 using technique for order of preference by similarity to ideal solution (TOPSIS) optimization technique. Welding was carried out based on L9 Taguchi array with current (*A*), welding speed (*B*), and frequency (*C*) as input parameters. The quality of weld was assessed by measuring the depth of penetration, bead width, reinforcement and heat affected zone (HAZ) width. From the TOPSIS optimization method, it was identified that A1B2C3 as the optimized parameter combination. Analysis of variance (ANOVA) was used to identify most influential factor on the overall objective function and it was found that welding speed controlled the weld geometry to the maximum extent.

Keywords Cold metal transfer welding process · Al5083 · Technique for order of preference by similarity to ideal solution · Analysis of variance

1 Introduction

Aluminium 5083 alloys have wide range of industrial applications and play a major role in all industries due its high strength-to-weight ratio and lesser density. Al 5083 also has very good structural integrity despite its lesser weight. Al 5083 are highly preferred in the manufacture of automotive components, ship building, and aerospace components due to its high corrosion resistance and good formability [1]. In the process of manufacturing industrial components using Al alloy 5083, welding

S. Suryaprakash · S. Vishal · M. Sethu Raman · S. Rajendra Kumar · T. Deepan Bharathi Kannan (✉)
Department of Mechanical Engineering, SRM Institute of Science and Technology, Kattankulathur, Chengalpattu, Tamil Nadu 603203, India
e-mail: tdbk23@gmail.com

M. Umar
Department of Production Engineering, National Institute of Technology Trichy, Trichy, Tamil Nadu 620015, India

G. Kumaresan et al. (eds.), *Advances in Materials Research*, Springer Proceedings in Materials 5, https://doi.org/10.1007/978-981-15-8319-3_66

is preferred in the areas of complicated shapes. Till now, welding of Al 5083 is explored using tungsten inert gas welding [2], laser beam welding [3] and also using solid-state welding process such as friction stir welding processes [4].The main problems associated with welding of Al 5083 are the formation of hot cracks and reduction in the properties that was obtained through work hardening [5]. Excessive heat input supplied during the conventional arc welding process is one of the major reasons for the weld property reduction. One of the ideal options to reduce the heat input is the usage of advanced arc welding processes such as pulsed TIG welding and CMT welding processes [6].

Fronius of Austria developed CMT process in the year 2004 as an advanced version of metal inert gas welding process which has the capability to weld at lower heat input, with controlled metal deposition. CMT welding process is preferred for both similar and dissimilar weldings. CMT welding process works under short-circuit mode and at low current, voltage ranges. The quality of the CMT weld mainly depends on the parameters such welding speed, current, frequency, and the filler wire feed rate [7]. Owing to the process nature of CMT, it would be an ideal option for joining Al alloys. Gungor et al. [8] welded Al 5083 using CMT process and the authors were able to obtain weld with good joint efficiency even at higher welding speed. One of the main challenges in the application of new processes to any material is the identification of optimized parameters. Identification of optimized parameters by trial and error method is time consuming and laborious. Multi-objective optimization technique would come in handy for the identification of optimized parameters in any manufacturing processes. Grey relational analysis (GRA), TOPSIS are some of the few examples of multi-objective techniques which are widely preferred in the manufacturing processes. TOPSIS is a multi-criteria decision-making analysis which was developed by Ching-Lai Hwang and Yoon in the year 1981 [9] and further developed by Yoon in year 1987 [10]. Deepan Bharathi Kannan et al. [11] successfully used TOPSIS optimization techniques for identifying the optimized parameters in laser welding of NiTinol shape memory alloys. Mahidhar et al. [12] successfully determined the optimized parameters in laser welding of Hastelloy C-276. Sampreet et al. [13] welded Ti-6Al-4V using Nd: YAG laser welding process and successfully found the optimized parameters using TOPSIS Optimization. Laser power was found to be the most influential parameter on the overall weld quality. Srirangan et al. [14] welded Incoloy 800HT using gas tungsten arc welding and found using TOPSIS that optimized parameter was within the L9 taguchi array. The authors recommended the usage of TOPSIS for all the manufacturing processes owing to its simplicity. Sudhagar et al. [15] compared the results of TOPSIS and GRA in friction stir welding process. The authors found that the optimized parameter combination identified by both GRA and TOPSIS was same.

From the above literatures, it is understood that only few works are explored in the CMT welding of Al 5083 alloys. It is also understood that TOPSIS is one of the ideal multi-objective optimization techniques for identifying the optimized parameters in any manufacturing processes. No visible literatures related to the optimization of welding parameters in CMT welding of Al 5083 were found. Hence, in this work,

an attempt is made to weld Al 5083 using CMT welding process and use TOPSIS for identifying the optimized welding parameters.

2 Materials and Methods

2.1 Experimentation

Al 5083 plates of thickness 3 mm was used in this work and the chemical composition of the same is presented in Table 1.

Butt joints were made using CMT welding machine and the picture of the welding is depicted in Fig. 1.

Three levels of current, welding speed, and frequency were used in this work and the corresponding values are presented in Table 2.

Table 1 Material composition

Elements	Si	Fe	Cu	Mn	Mg	Cr	Ni	Zn	Ti	Al
Composition	0.12	0.4	0.02	0.94	4.57	0.06	0.01	0.02	0.027	Bal.

Fig. 1 CMT 6-axis machine

Table 2 Levels of input parameters

A (A)	*B* (mm/min)	*C* (Hz)
60	200	0.5
65	225	1
70	250	1.5

Table 3 Input and output parameters

A (A)	*B* (mm/min)	*C* (Hz)	Depth of penetration (mm)	Reinforcement size (mm)	Bead width (mm)	Heat affected zone (mm)
60	200	0.5	4.295	1.895	6.474	0.884
60	225	1	4.239	2.41	6.427	0.889
60	250	1.5	3.815	2.52	5.858	0.915
65	200	1	3.672	2.552	7.690	0.799
65	225	1.5	4.387	2.293	6.877	0.679
65	250	0.5	3.63	2.017	6.983	1.255
70	200	1.5	3.991	2.139	8.156	0.835
70	225	0.5	4.248	2.071	8.442	0.826
70	250	1	3.861	2.165	6.809	1.017

ER5356 wire of diameter 1.2 mm was used as filler wire and the wire feed rate was maintained at 1600 mm/minute. Argon gas at a constant flow rate of 14.6 L/min was used as shielding gas. The input parameters along with the output parameters obtained in this work are presented in Table 3.

For micro-analysis and macro-analysis, the specimens were polished in two stages: rough and fine polishing; rough polishing was done by using emery seats of different grit sizes such as 400, 600, 800, 1000, 1200, 1500, 2000. The rough-polished specimens were fine polished using hiffin spray and diamond paste. Followed by fine polishing, Keller's reagent which is the mixture of 6 ml HNO_3 and 2 ml HF with 92 ml deionized water was used as etchant. The etching separated the welded and base surface for easy identification of the surfaces.

The etched surfaces were then observed using 2D OLM-vision machine for macro-analysis to find the depth of penetration, bead width, reinforcement and heat affected zone width. The microstructure of the optimized weld was taken using upright optical microscope.

2.2 TOPSIS

TOPSIS is multi-criteria decision making method used to solve decision-making problems. It gives a solution closer to the ideal solution based on the parameters we get based on experiment done and farther to the less ideal or negative ideal solution.

3 Result and Discussion

3.1 Optimization Technique

The steps involved in TOPSIS analysis are as follows:

Step 1: The first step involves the normalization of the attributes.
The formula for calculating the normalized values is given by Eq. (1)

$$N_{xy} = A_{xy} / \left(\sum A_{xy}^2 \right) \quad \text{where } x = 1 \ldots n; \quad y = 1 \ldots m \tag{1}$$

Step 2: The weights are allocated based on the importance given to each output parameters. In this work, equal weights are given to all the output parameters and hence the weight is chosen as 0.25.
Step 3: Weighted normalized values are calculated by multiplying each column of normalized attributes with their respective weights. The weighted normalized values are calculated using Eq. (2)

$$P_{xy} = Q_y R_{xy} \tag{2}$$

Normalized and Weighted Normalized values are calculated and the corresponding values are presented in Fig. 2.
Step 4: Determination of positive ideal and less ideal solutions based on the weighted normalized table values where Z^+ is idealized values and Z^- is negative idealized values which are found using Eqs. (3) and (4), respectively

$$Q^+ =, \left\{ Z_1^+, \ldots, Z_x^+ \right\} \quad \text{where } Z_y^+ = \{\max(Z_{XY}) \text{ if } y \in Y; \ \min(Z_{XY}) \text{ if } y \in Y'\} \tag{3}$$

$$Q^- = \left\{ Z_1^-, \ldots, Z_x^- \right\} \quad \text{where } Z_y^- = \{\max(Z_{XY}) \text{ if } y \in Y; \ \min(Z_{XY}) \text{ if } y \in Y'\} \tag{4}$$

The positive ideal and negative ideal values after calculation are given in Table 4.
Step 5: This step helps in determining the separation from the ideal value.
The separation from the ideal alternative is given by Eq. (5)

$$B_x^+ = \left[\Sigma \left(Z_y^+ - Z_{xy}^+ \right) 2 \right]^{0.5} \quad \text{where } x = 1, \ldots, n \tag{5}$$

Similarly, the separation from the negative ideal alternative given by Eq. (6)

$$B_x^- = \left[\Sigma \left(Z_y' - Z_{xy}' \right) 2 \right]^{0.5} \quad \text{where } x = 1, \ldots, n \tag{6}$$

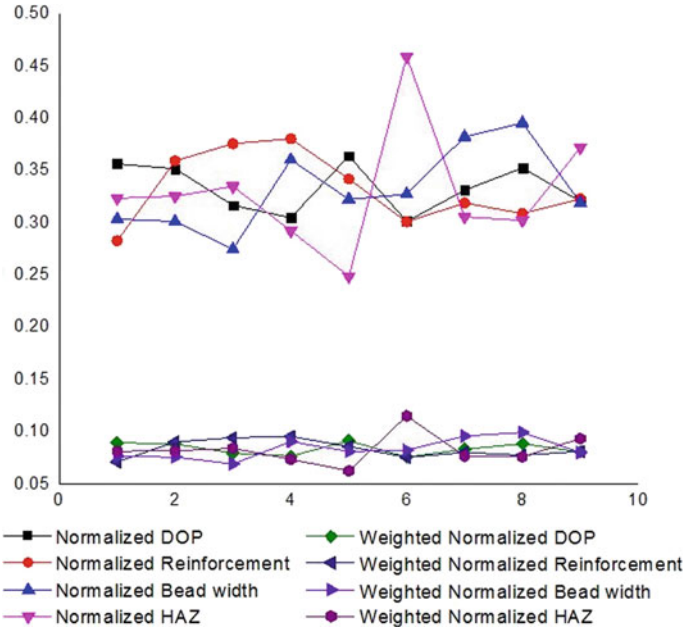

Fig. 2 Relation between normalized and weighted normalized matrix

Table 4 Positive ideal and negative ideal values

Z^+	0.090843	0.070512919	0.0685156	0.061995
Z^-	0.075168	0.094959878	0.0987383	0.114586

The values which are obtained from these equations are tabulated and presented in Table 5

Table 5 Separation measure

B^+	B^-
0.020147	0.049644
0.028081	0.043117
0.033845	0.043511
0.037364	0.042562
0.019010	0.058647
0.056615	0.026220
0.032787	0.042116
0.033834	0.044926
0.035996	0.032669

Table 6 Relative closeness value

V_X	Rank
0.711327	2
0.605591	3
0.562478	5
0.532521	7
0.755207	**1**
0.316533	9
0.562276	6
0.570415	4
0.475773	8

Step 6: Calculation of relative closeness and the same is calculated using Eq. (7) and tabulated in Table 6

$$V_X = B_X^- / \left(B_{X+}^+ B_X^-\right) \tag{7}$$

From Table 6, it is understood that experiment number 5 has the highest relative closeness value. The graph showing the relative closeness value with respective the closeness value is shown in Fig. 3.

Mean response table values were calculated based on relative closeness value and the same is presented in Table 7.

From Table 7, it can be inferred that AlB2C3 as the optimized parameter combination. The optimized parameter combination does not come inside the L9 combination. Hence, confirmation test is done based on the optimized parameter combinations in order check the prediction accuracy of the TOPSIS technique.

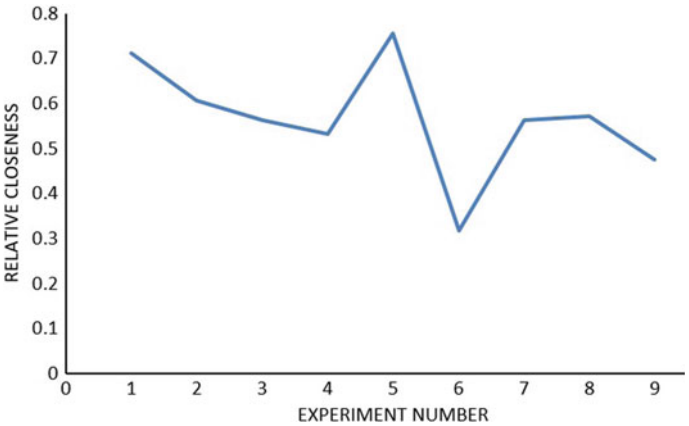

Fig. 3 Experiment number versus relative closeness

Table 7 Response table

Symbol	Input parameters	1	2	3	Optimum level	Max–Min	Rank
A	Current	**0.62647**	0.53475	0.53615	**A1**	0.09031‘	3
B	Speed	0.60204	**0.64374**	0.53795	**B2**	0.17214	1
C	Frequency	0.53276	0.53796	**0.62665**	**C3**	0.09390	2

Table 8 Initial and optimal values comparison

Setting level	Initial value	Optimized parameters	
		Prediction	Experiment
	A1B1C1	A3B1C2	A3B1C2
Depth of penetration	4.387	–	4.8
Reinforcement	2.293	–	2.18
Bead width	6.877	–	6.69
HAZ	0.679	–	0.58
Closeness value	0.7552	0.7653	0.7879

3.2 Confirmation Test

The predicted relative closeness value of the optimized parameter combination is calculated using Eq. (8)

$$E = E_x + \sum_{X=1}^{Y} (E_z - E_x) \tag{8}$$

where E_q is the average of the closeness values, E_z is the values of the optimized repose matrix values, and y is the number of parameters used for welding. The comparison between the initial and optimum values is done and tabulated in Table 8.

The predicted and confirmation test relative closeness values are good in agreement with each other and the percentage difference was found to 2.95% only.

3.3 Anova

Anova was used to find the most influencing parameter on the overall objective function. The values that are obtained from ANOVA are tabulated in Table 9.

From Table 9, it could be observed that welding speed is the most influencing parameter on the overall objective function followed by equal importance for both current and frequency.

Table 9 Significance of the parameters from ANOVA

Source	DF	Adj SS	Adj MS	*F*-value	*P*-value
A	2	0.01657	0.008284	0.47	0.682
B	2	0.06129	0.030646	1.73	0.366
C	2	0.01671	0.008355	0.47	0.680
Error	2	0.035446	0.017729		
Total	8	0.13003			

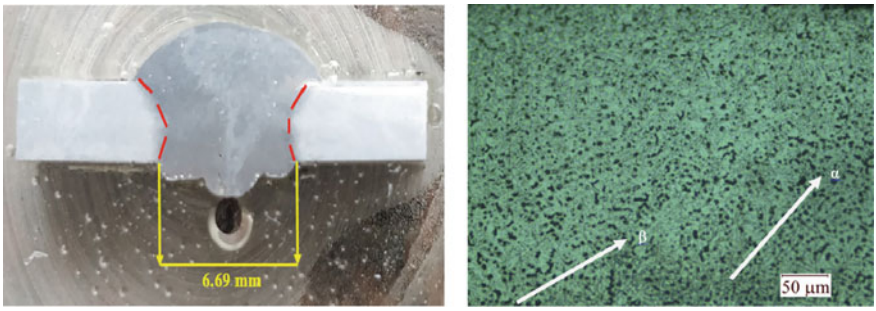

Fig. 4 Optimized weld macro- and microstructure

3.4 Metallurgical Aspects of the Optimized Weld

The macrostructure and microstructure obtained after welding the specimen is given in Fig. 4, respectively.

The microstructure of the optimized weld contained main matrix (α) and Al_3Mg_2 (β). β phase was found to be evenly distributed. The presence of uniformly distributed β phase particles acts as a hindrance during plastic deformation and hence improves mechanical properties of the weld joint. Optimized weld was free from defects such as porosity due to the proper shielding from atmospheric contaminations.

4 Conclusions

Al 5083 plates were successfully welded using CMT welding process and the following observations were made.

The full penetration was seen in all the nine welding trials. TOPSIS optimization technique was successfully used for predicting the optimized parameter combination.

The optimized parameter was outside L9 Taguchi array and the confirmation test was performed. The predicted and confirmation test results were in good agreement.

Welding speed was found to be the most influencing factor on the overall multi-objective function. Microstructure of the optimized revealed the presence of α and β phases.

Acknowledgements The Authors of this article would like to extend their sincere thanks to **Dr. N. Siva shangmugam, Laboratory incharge, Materials Joining and Testing Laboratory, Department of Mechanical Engineering, NIT Trichy** for providing the CMT Machine to carry out the welding trials.

References

1. Madhavan S, Kamaraj ML, Srinivasa Vijayaraghavan Rao K (2016) Microstructure and mechanical properties of aluminium/steel dissimilar weldments: effect of heat input. J Mater Sci Technol 0267–0836: 1743–2847
2. Singh SK, Tiwari RM, Kumar A, Kumar S, Murtaza Q, Kumar S (2018) Mechanical Properties and Microstructural of Al-5083 by TIG. Mater Tod Proc 5:819–822
3. Sánchez Amaya JM, Delgado T, González-Rovira L, Botana FJ (2009) Laser welding of aluminium alloys 5083 and 6082 under conduction regime. Appl Surf Sci 255:9512–9521
4. Msomi V, Mbana N, Mabuwa S, Microstructural analysis of the friction stir welding 1050-H14 and 5083-H111 aluminium alloys. Mater Tod Proc. https://doi.org/10.1016/j.matpr.2019.10.038
5. Umar M, Sathiya P (2018) Effects of pulse duration on corrosion and impression creep properties of AA5083-H111 Al–Mg alloy weldments processed by P-GTAW. Adv Eng Mater 171147:1–10
6. Pavan Kumar N, Arungalai Vendan S, Siva Shanmugam N (2015) Investigation on the parametric effects of cold metal transfer process on the microstructural aspects in AA6061. J Alloy Compd S0925–8388:31422–5
7. Pickin CG, Williams SW, Lunt M (2011) Characterization of cold metal transfer (CMT) process and its application for low dilution cladding. J Mater Process Tech 211:496–502
8. Gungor B, Kaluc E, Taban E, Aydin SIK (2014) Mechanical and microstructure properties of robotics cold metal transfer (CMT) welded 5083–H111 and 6082–T651 aluminium alloys. Mater Tod Proc 54:207–211
9. Hwang CL, Yoon K, Methods for multi attribute decision making. Lect Notes Econ Math 58–191
10. Yoon K (1987) A reconciliation among discrete compromise solutions. JORS 38(3):277–286
11. Deepan Bharathi Kannan T, Shegokar AR, Sathiya P, Ramesh T (2017) Parameter design and analysis in laser welding of NiTinol shape memory alloy. Mater Tod Proc 4:8883–8891
12. Mahidhar V, Sampreet KR, Kannan R, Deepan Bharathi Kannan T (2019) Parameter optimization in laser welding of Hastelloy C-276 using TOPSIS. Mater Tod Proc. https://doi.org/https://doi.org/10.1016/j.matpr.2019.06.722
13. Sampreet KR, Mahidhar V, Kannan R, Arunagiri, Deepan Bharathi Kannan T (2020) Optimization of parameters in Nd:YAG laser welding of Ti-6Al-4V using TOPSIS. Mater Tod Proc https://doi.org/https://doi.org/10.1016/j.matpr.2019.05.401
14. Srirangan AK, Sathiya P (2017) Optimisation of process parameters for gas tungsten arc welding of Incoloy 800HT using TOPSIS. Mater Tod Proc 4:2031–2039
15. Sudhagar S, Sakthivel M, Mathew PJ, Daniel SAA (2017) A multi criteria decision making approach for process improvement in friction stir welding of aluminium alloy. Measurement 108:1–8

Effect of Cyclic Annealing on the Grain Size of Low-Carbon Steel: An Image-Processing Approach

K. Gajalakshmi and S. Saravanan

Abstract In this study, low carbon steel (LCS) plates are subjected to cyclic annealing (repeated heating above 910 °C for 30 min followed by furnace cooling), and the variation in microstructure, number of grains and its average size, is determined. The number of grains increases with the annealing cycle, as the grains splits to form newer grains. Similarly, the pearlite concentration, in the low-carbon steel, augments with the annealing cycle. Further, an attempt is made to automatically count the number of grains in the cyclic annealed LCS microstructure by employing image-processing techniques, viz. Canny edge detection and Otsu threshold. The coding for the image-processing algorithms was developed in MATLAB platform. The deviation in the number of grains between the proposed image-processing method and the manual three-circle method is less than 10%. Of the two image-processing methods, Canny edge detection achieves a closer prediction (less than 2%).

Keywords Cyclic annealing · Grain size measurement · Image processing

1 Introduction

Low-carbon steel UNS 10180 (LCS) is extensively employed in water, air and moderate-temperature industrial environments, in the form of plates and tubes. During operation, LCS sheet and pipes are often subjected to repeated heating and cooling, thereby a systematic change in the grain boundaries and the average size of grains results. This behavior influences the mechanical and corrosion properties of the low-carbon steel [1, 2]. Sahay et al. while attempting short duration cyclic annealing (5 min) reported the acceleration of bainite grains in 1080 steel [3]. Likewise, Saha et al. reported the variation in microstructure and mechanical properties

K. Gajalakshmi
Shree Raghavendra Arts and Science College, Kilmoongiladi, Tamil Nadu, India

S. Saravanan (✉)
Department of Mechanical Engineering, Annamalai University, Annamalai Nagar, Chidambaram, Tamil Nadu 608002 , India
e-mail: ssvcdm@gmail.com

G. Kumaresan et al. (eds.), *Advances in Materials Research*, Springer Proceedings in Materials 5, https://doi.org/10.1007/978-981-15-8319-3_67

Table 1 Chemical composition (wt%) of low-carbon steel UNS G10180

Specimen	Cu	C	Si	Mn	P	S	Fe
UNS G10800	0.6	0.2	0.6	0.6	0.04	0.50	Bal

of low–, medium- and high-carbon steel during cyclic annealing [2, 4, 5]. In another study, Lu et al. attempted cyclic annealing of medium-carbon steel up to 12 cycles, and concluded that the strength of the steel reduces after 5 cycles [6]. Recently, Zhai et al. attempted cyclic annealing of amorphous alloys and reported deterioration of magnetic properties at higher annealing cycles [7]. In a different attempt, Mandal et al. concluded that the wear behavior and strength characteristics of cyclic annealed white iron samples are higher than continuous annealing samples [8].

With respect to the grain size measurement in metals, metallurgists manually determine the average size of grain by various methods, viz. intercept, planimetric and three-circle method [9, 10]. Manual grain size measuring methods consider the grains prevailing in a particular region or grains intersecting a rectangle or a circle of known radius, ignoring the other section of the microstructure. Further, the accuracy of the manual grain size measurement depends on many factors, viz. surface irregularities, lighting condition, ability of the microscope and external factors, viz. visual condition, tiredness, distraction, bias or perception of the human analyst [11]. The observations of analyst vary as some of the grain boundaries are not closed, while few boundaries are separated, leading to incorrect measurement and a decline in the accuracy of the grain size measurement [12]. In this context, Baretto et al. employed image-processing (Otsu) technique to count the number of grains in a particular region of microstructure [11]. On the other hand, Gajalakshmi et al. recommended Canny edge detection technique for the counting of grains in a whole microstructure [13]. Recently, Banergee et al. employed Canny edge detection method to detect edges in a metallic microstructure, thereby counted the number of grains and correlated with image J software [14].

Though few researchers studied the effect of cyclic annealing and grain size measurement in metallic microstructure separately, studies on the variation of microstructure after cyclic annealing and the subsequent grain size measurement in low-carbon steel are scarce. Hence in this study, LCS plates are subjected to four cycles of annealing, and the variation in microstructure and the number of grains is determined by manual three-circle method. In addition, image-processing techniques, viz. Otsu and Canny edge detection, are implemented, in a MATLAB platform, to automatically count the number of grains after each annealing cycle, correlated with the manual three-circle method, and the results are reported.

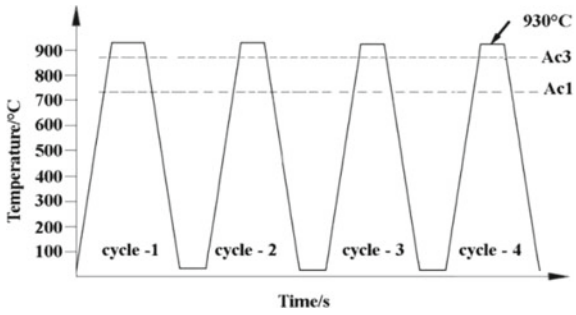

Fig. 1 Cyclic annealing

2 Cyclic Annealing

Low-carbon steel plates (chemical composition given in Table 1), having dimensions $140 \times 40 \times 5\ mm^3$ were subjected to cyclic annealing varying from one to four cycles (Fig. 1). Each cycle consists of heating the alloy at 930 °C (above Ac3 temperature) for 30 min, in an INDFUR furnace, followed by furnace cooling to atmospheric temperature. The as-received and cyclic annealed microstructure (100×) are determined in a VERSAMAT–3 optical microscope equipped with Clemex image-analyzing system following standard metallographic procedures, viz. grinding, polishing and etching (4 ml nitric acid, 100 ml ethanol).

3 Proposed Methodology

The determination of the number of grains and the average grain size in a cyclic annealed LCS microstructure is attained by following the steps detailed in Fig. 2. Initially, each input microstructure image is converted into a grayscale image representing only an amount of light, as processing of color microstructure is complicated due to variation in color levels of each pixel.

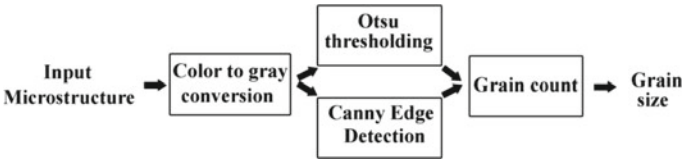

Fig. 2 Proposed methodology

3.1 Otsu Method

The input gray image is processed, and a histogram is generated based on the mean and variance of the intensity of neighboring eight pixels. Subsequently, the gray image is thresholded to identify the vanished grain boundaries and threshold, a specific value of intensity determined from the histogram. The underlying mathematical expressions are given by [15]

$$\sigma_w^2(T) = n_B(T)\sigma_B^2(T) + n_o(T)\sigma_o^2(T) \tag{1}$$

where

$$n_B(T) = \sum_{i=0}^{T-1} p(i) \tag{2}$$

$$n_o(T) = \sum_{i=T}^{N-1} p(i) \tag{3}$$

'T' is the threshold value, $P(i)$ represent the number of pixels with gray value 'i' in the image and $\sigma o\ (T)$ and $\sigma B\ (T)$ are the variance of the pixels in the foreground and background, respectively. Thresholding of the input image is achieved by (a) separating pixels into two classes (foreground and background) based on the threshold; (b) calculating the mean of pixels in both classes, (c) determining the difference between the means and square the difference; and finally (d) multiplying the obtained value by the number of pixels in both classes [16]. The pixels having the intensity greater than threshold value are grouped into one class, and the remaining pixels with lower intensity are grouped as another.

3.2 Canny Edge Detection

Canny edge detector method, a standard edge detection method, provides a balance between noise and edge detection. It is implemented in three steps, viz. good localization, detection and minimum response. Good localization indicates the closer possible detection of edges in the real image, while a good detection means plotting of possible real edges without missing the actual edges. The final pace, i.e., minimum response, indicates the marking of correct edges in a single response, devoid of creating false edges [17]. The Canny edge detector initially smoothes the input image, to eliminate the noise, by applying the Gaussian filter having a kernel size $(2k + 1) \times (2k + 1)$, given by [13, 17]

$$H_{ij} = \frac{1}{2\pi\sigma^2} \exp\left(-\frac{(i-(k+1))^2 + (j-(k+1))^2}{2\sigma^2}\right); \quad 1 \le i,\ j \le (2k+1) \tag{4}$$

Up next, the image gradient is determined to highlight the regions with higher spatial derivatives. Subsequently, the Canny algorithm employs various filters to detect horizontal, vertical and diagonal edges of the blurred image. The value in terms of the first derivative in horizontal (Gx) and vertical direction (Gy), respectively, is determined by

$$G = \sqrt{G_x^2 + G_y^2} \tag{5}$$

The edge direction angle is rounded to one of four angles representing vertical, horizontal and the two diagonals (0°, 45°, 90° and 135°). An edge direction falling in each color region will be set to a specific angle values, for instance θ in [0°, 22.5°] or [157.5°, 180°] maps to 0°. After identification of edges in the image, direction (Θ) is identified by the relation

$$\Theta = a\tan 2(G_y, G_x) \tag{6}$$

where 'G' is computed by the hypot function, and 'atan2' is the arc tangent function with two arguments. Finally, the regions holding higher magnitude (above threshold value) are marked as edges, while the other regions having lower magnitude are considered as non-edges.

4 Results and Discussion

4.1 Microstructure Variation

The optical microstructures of the as-received specimen (0 cycle) and different (1–4) cyclic annealed LCS specimens (Fig. 3) feature the presence of ferrite grains and pearlite (visible as dark color). The grain boundaries are irregular in nature and the number of grains increases with annealing cycles, with a reduced average grain size, consistent with earlier researchers [2–5]. With increasing annealing cycle, the concentration of pearlite increases as well.

The microstructure of the as-received specimen (Fig. 3a: 0-cycle), prior to annealing comprises coarse proeutectoid ferrite and pearlite primarily at the grain boundaries. The as-received specimen contains 75% ferrite and 25% pearlite, consistent with Fe–Fe_3C phase diagram. The average size of the LCS grains, by manual three-circle method, is determined by placing three equally spaced concentric circles, having a total circumference of 500 mm on the microstructure. Subsequently, the

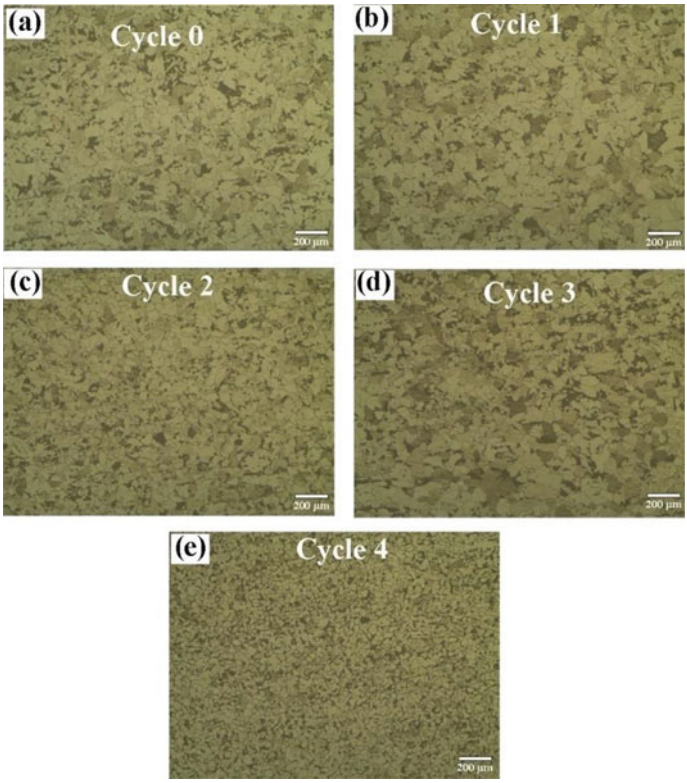

Fig. 3 **a–e** Optical microstructure of LCS subjected to various annealing cycles

number of grain boundaries intersecting the concentric circles is counted and divided by the magnification of the microscope to obtain the average grain size.

On execution of the initial heat treatment cycle (Fig. 3b), proeutectoid ferrite and the ferrite concentration in pearlite transforms into austenite, which is diffusion less in nature [2]. As the heat treatment temperature is above Ac3 temperature, the polymorphic transformation of α iron to γ-iron is probable [6]. Hence, the proeutectoid ferrite begins to transform to austenite at high-energy locations, viz. ferrite, ferrite boundaries and pearlite interfaces, leading to a increase in pearlite concentration of 31%. Gaude-Fugarolas and Bhadeshia [18] opined that the pearlite interface and ferrite grains are the probable locations for austenitization, as the cementite decomposition yields carbon to the transformation front lowering the transformation temperature. However on the pearlite region, austenitization commences on the interface of ferrite–cementite lamellae. In this case, the ferrite transforms in to austenite quite rapidly; however, the dissolution of cementite into austenite is diffusion-controlled slow process [19] and is probable due to furnace cooling which provides sufficient duration for the dissolution. Hence, it is observed that the implementation of heat treatment (930 °C for 30 min) promotes a microstructure having fine austenite and

cementite grains embedded in austenite. In addition, fine grains are evolved from the austenite grains, during cooling, which lead to the grain size reduction, detailed in the next section.

The second annealing cycle microstructure (Fig. 3c) is similar to the previous case, except the formation of smaller grains and thicker cementite grains. The thicker cementite grains enhance the pearlite concentration to 35%, attributed by the diffusion of additional carbon across the grain boundaries, created during the first cycle of annealing. In the next cyclic annealing cycles (3rd and 4th cycles), cementite lamellae dissolve in austenite leading to enhanced carbon diffusion across the boundaries. The cementite lamellae of pearlite are rapidly dissolved in austenite, and carbon diffusion is amplified, leading to increase in the concentration of pearlite (38%), as shown in Fig. 3d, e. It is inferred from the microscopic study that the execution of cyclic annealing reduces the grain size and promoting the nucleation of finer austenite grains (Fig. 3b–e) at the grain boundaries. However, the concentration of pearlite increases with the annealing cycle. The variation in grain size due to cyclic annealing in LCS is determined by image-processing techniques, detailed in the next section.

4.2 Grain Size Measurement by Image Processing

The optical microstructure, Otsu threshold and Canny edge detected images of LCS, subjected to various annealing cycles, are shown in Fig. 4a–o. In Otsu images as shown in Fig. 4b, e, h, k, n, the closed grain boundaries are automatically counted by differentiating black and white, based on their pixel intensity. The unconnected and the grains prevailing in the periphery are closed by implementing connected component algorithm. However, in canny edge detected images, grain boundaries are detected and highlighted in white color, while the inner sections of the grain are visible as black Fig. 4c, f, i, l, o. It is observed that the number of grain increases with the annealing cycles due to the formation of new smaller grains across the boundaries, consistent with the findings of Saha et al. [4].

The optical microstructure, Otsu and Canny edge detected images of LCS after the first cycle of annealing are shown in Fig. 4d–f, respectively. When analyzing the input microstructure (Fig. 4d), Otsu threshold algorithm generates a histogram based on the intensity of neighboring 8 pixels (Fig. 5), thereby a threshold (132) value is determined. The grains having intensity higher than the threshold is labeled as white, remaining as black (Fig. 4e). Finally, the white and black are counted to determine the total number of grains (1054) prevailing in the microstructure. While implementing the Canny edge detection technique on the same input image (Fig. 4d), grain boundaries are identified (Fig. 4f) and thereby, the quantity of grains (1108) is automatically counted. Post the first cycle of annealing, both Otsu and Canny edge detection methods show a nearly 20% increase in the number of grains, than the 0-cycle annealing condition (Fig. 4a–c: Otsu: 820; Canny edge detection: 910). The increase in the number of grains is attributed by the formation of new grains across the boundaries, consistent with the reports of Offerman et al. [20].

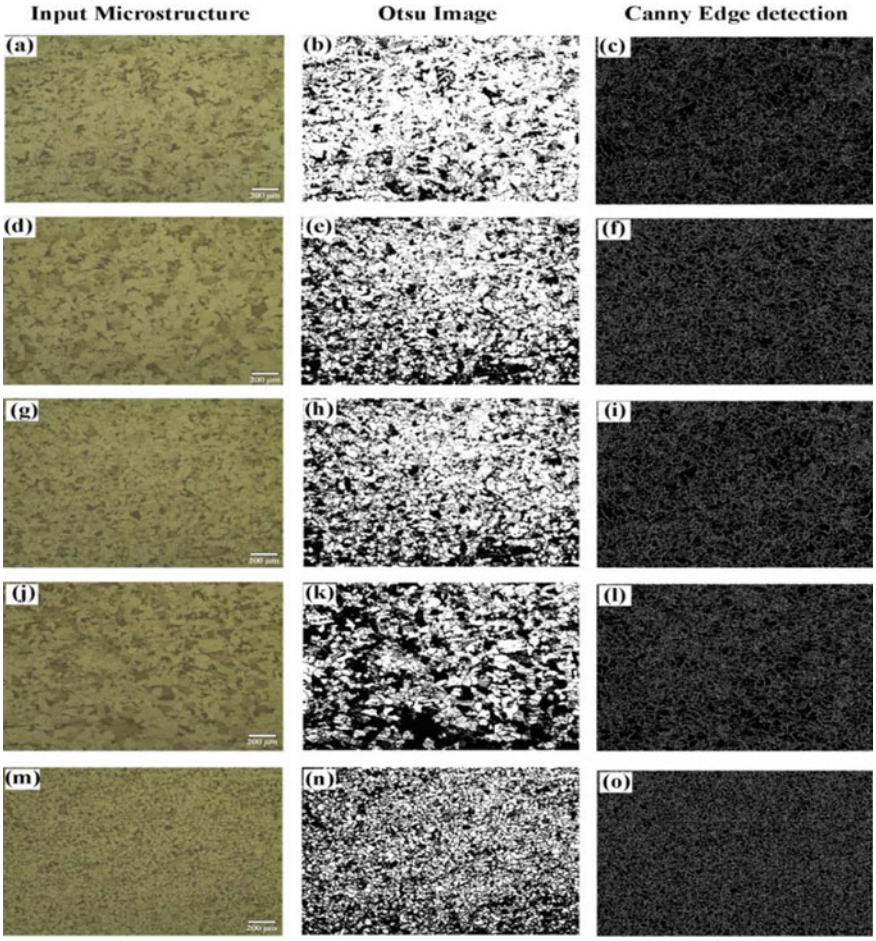

Fig. 4 Optical, Otsu and Canny images **a–c** 0th cycle **d–f** 1st cycle **g–i** 2nd cycle **j–l** 3rd cycle **m–o** 4th cycle

The second cycle of annealing further divide the grain boundaries, thereby newer grains with smaller cross sectional area are formed (Fig. 4g). Post the second cycle of annealing, Otsu algorithm determines 1594 closed grains (Fig. 4h), while Canny algorithm which highlights the grain boundaries, thereby 1765 grains are identified in the same microstructure (Fig. 4i). The enhancement in the number of grains reduces the average grain size, determined by [21, 22].

$$\text{Average size (A)} = \text{Total area/Total number of grains} \tag{7}$$

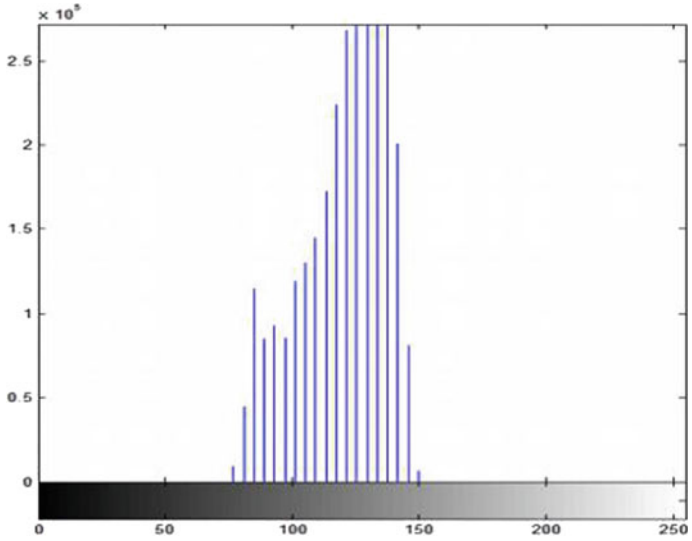

Fig. 5 Histogram

The average size of grain, after second cycle of annealing, by Otsu algorithm and Canny edge detection technique reduces to 0.0025 mm^2 and 0.0022 mm^2, respectively. According to Mohammed et al., metals having small grains exhibit higher mechanical strength [22]. For metals having a larger grain size, even a low magnitude of stress causes the grain boundary to collapse thereby the strength of the metal gets reduced [23, 24]

Subsequent to the third cycle of annealing, number of grains in the microstructure further increases to 2116 (Fig. 4k: Otsu), with an average grain size of 0.00189 mm^2 and 2285 (Fig. 4l: Canny) having an average grain size of 0.0017 mm^2, respectively. The transformation temperature and cooling rate during the cyclic heat treatment contribute to the enhancement in the number of grains and a decline in the grain size [4, 25]. Finally, the highest number of grains with the smallest average grain size is obtained after the fourth annealing cycle (Fig. 4n: Otsu: 3557: grain size: 0.00112 mm^2; Fig. 6o: Canny: 3758, grain size: 0.0010 mm^2). Hence, it is inferred that the number of grains increases with annealing cycle, and consequently the average size of grain reduces. The number of grains in Canny edge detection technique is 5–10% higher than Otsu technique for all attempted conditions, as the grain boundaries are detected more precisely by the Canny technique. In contrast, the Otsu technique presumes few of the unclosed boundaries as single grain and fails to count the grains. It is concluded that the Canny edge detection technique is suitable for counting grains in a cyclic annealed LCS microstructure than Otsu threshold method.

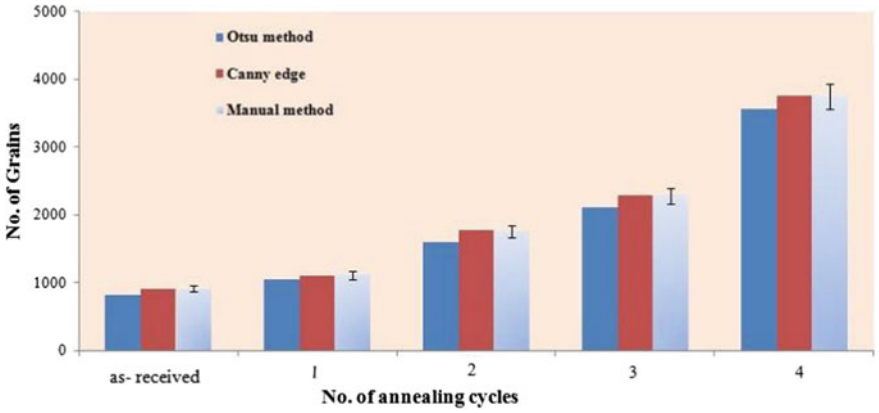

Fig. 6 Comparison of results

4.3 Comparison of Results

The total number of grains in the as-received (0 cycle) and cyclic annealed LCS (1–4 cycles), by Otsu, Canny and the manual method is shown in Fig. 6. The deviation between the Otsu method and Canny edge detection method with manual method is less than 10 and 2%, respectively. Further, the deviation between the Canny and Otsu method ranges between 5 and 10%. According to Gajalakshmi et al., the deviation between actual and predicted should be less than or equal to 10%; hence, the results are acceptable [26]. Hence, it is inferred that Canny edge detection technique determines the number of grains more preciously than Otsu technique.

5 Conclusion

A image processing approach for the counting the number grains and measurement of grain size in a metallic microstructure subjected to cyclic annealing was attempted, and the salient conclusions of this experimental study are

1. The quantity of grains in microstructure increases with annealing cycle, due to the formation of newer grains across the boundary.
2. The concentration of pearlite grain increase with annealing cycles.
3. Image-processing technique is very effective in microstructure analysis.
4. Canny edge detection technique identifies the grain boundaries more preciously.
5. The deviation between Canny edge detection and Otsu technique with manual method is less than 10%.

References

1. Fayorni OSI, Kanyane LR, Popoola API, Oyedepo SO (2018) Electrolytic deposition of super-smart composite coating of Zn–V_2O_5–NbO_2 on low carbon steel for defence application. Def Technol 14(5):446–450
2. Saha A, Mondal DK, Biswas K, Maity J (2012) Microstructural modifications and changes in mechanical properties during cyclic heat treatment of 0.16% carbon steel. Mater Sci Eng A Struct 534:465–475
3. Sahay SS, Malhotra CP, Kolkhed AM (2003) Accelerated grain growth behavior during cyclic annealing. Acta Mater 51(2):339–346
4. Saha A, Mondal DK, Maity J (2010) Effect of cyclic heat treatment on microstructure and mechanical properties of 0.6 wt% carbon steel. Mater Sci Eng A Struct A 527(16–17):4001–4007
5. Saha A, Mondal DK, Biswas K, Maity J (2012) Development of high strength ductile hypereutectoid steel by cyclic heat treatment process. Mater Sci Eng A Struct A 541:204–215
6. Lü ZQ, Zhang HF, Meng Q, Wang ZH, Fu WT (2016) Effect of cyclic annealing on microstructure and mechanical properties of medium carbon steel. J Iron Steel Res Int 23(2):145–150
7. Zhai XB, Zhu L, Zheng H, Dai YD, Chen JK, Wang YG, Pan FM (2018) Optimization of crystallization, microstructure and soft magnetic properties of Fe–B–Cu alloys by rapid cyclic annealing. J Alloy Compd 768:591–597
8. Mandal SS, Ghosh KS, Mondal DK (2017) Microstructure, mechanical and abrasive wear behavior of 8.0 wt pct Cr white iron subjected to continuous and cyclic annealing treatment. Metall Mater Trans A 48(7):3432–3444
9. ASTM Standard E112-10 (2010) Standard test method for determining average grain size
10. Reiter J, Bernhard C, Presslinger H (2008) Austenite grain size in the continuous casting process: metallographic methods and evaluation. Mater Charact 59(6):737–746
11. Peregrina-Barreto H, Terol-Villalobos IR, Rangel-Magdaleno JJ, Herrera-Navarro AM, Morales Hernández LA, Manríquez-Guerrero F (2013) Automatic grain size determination in microstructures using image processing. Measurement 46(1):249–258
12. Yang W, Lee WB (1993) Grain boundary engineering and related topics. In: Meso-plasticity and its applications. Springer, Berlin
13. Gajalakshmi K, Palanivel S, Nalini NJ, Saravanan S, Raghukandan K (2017) Grain size measurement in optical microstructure using support vector regression. Optik 138:320–327
14. Banerjee S, Chakraborti PC, Saha SK (2019) An automated methodology for grain segmentation and grain size measurement from optical micrographs. Measurement 140:142–150
15. Ng HF (2006) Automatic thresholding for defect detection. Pattern Recogn Lett 27(14):1644–1649
16. Parker JR (2011) Algorithms for image processing and computer vision. Wiley, Indianapolis
17. Ding L, Goshtasby A (2001) On the Canny edge detector. Pattern Recogn 34(3):721–725
18. Gaude-Fugarolas D, Bhadeshia HKDH (2003) J Mater Sci 38(6):1195–1201
19. Luo H, Shi J, Wang C, Cao W, Sun X, Dong H (2011) Experimental and numerical analysis on formation of stable austenite during the intercritical annealing of 5Mn steel. Acta Mater 59(10):4002–4014
20. Offerman SE, Van Dijk NH, Sietsma J, Grigull S, Lauridsen EM, Margulies L, Poulsen HF, Rekveld MT, Van der Zwaag S (2002) Grain nucleation and growth during phase transformations. Science 298(5595):1003–1005
21. Santofimia MJ, Zhao L, Sietsma J (2009) Microstructural evolution of low-carbon steel during application of quenching and partitioning heat treatments after partial austenitization. Metall Mater Trans A 40(1):46–57
22. Mohamed FA (2003) A dislocation model for the minimum grain size obtainable by milling. Acta Mater 51(14):4107–4119
23. Legros M, Gianola DS, Hemker KJ (2008) In situ TEM observations of fast grain-boundary motion in stressed nanocrystalline aluminum films. Acta Mater 56(14):3380–3393

24. Yoshinaga N, Kawata H, Hikida K (2018) Recent topics on development of automotive high-strength sheet steels. In: Advanced high strength steel. Lecture notes in mechnical engineering 21–26.
25. Bai XM, Voter AF, Hoagland RG, Nastasi M, Uberuaga BP (2010) Efficient annealing of radiation damage near grain boundaries via interstitial emission. Science 327(5973):1631–1634
26. Gajalakshmi K, Palanivel S, Nalini NJ, Saravanan S (2018) Automatic classification of cast iron grades using support vector machine. Optik 157:724–732

Assessment of Start-Up Agility Using Multi-grade Fuzzy and Importance Performance Analysis

Edrion Chacko and M. Suresh

Abstract The aim of these papers is to report a study that has been carried out for assessing agility of start-up using multi-grade fuzzy approach and classifying the attributes based on Importance Performance Analysis (IPA). Agility refers to the ability of an organisation to positively adapt to the changing business environment. An agility assessment model was developed using multi-grade fuzzy. The model was applied to the data gathered from a start-up to identify its agility index. The study revealed that the start-up is agile but still there are still scopes for improvement. The areas for improvement were analysed through IPA model. The proposed framework helps for growing start-up companies to evaluate their agility index and focus on the weaker attributes to improve the agility level in their practice.

Keywords Agile · Agility assessment · Agility in start-ups · Multi-grade fuzzy · Importance performance analysis

1 Introduction

Advancement in information and technologies have resulted in the blooming of large number of start-ups in various sector in recent years. It has become a recent phenomenon where people shift from job seekers to job creators. Ground-breaking innovations caused start-ups coming up in higher rates in every part of the world. Various government bodies have been taking up actions to drive up the start-up ecosystem.

According to a recent report by IBM Institute for Business Value and Oxford Economics, 90% of start-ups in India fail within five years [1]. The number of

E. Chacko (✉) · M. Suresh (✉)
Amrita School of Business, Amrita Vishwa Vidyapeetham, Coimbatore, India
e-mail: edrionchacko@gmail.com

M. Suresh
e-mail: drsureshcontact@gmail.com

G. Kumaresan et al. (eds.), *Advances in Materials Research*, Springer Proceedings in Materials 5, https://doi.org/10.1007/978-981-15-8319-3_68

start-ups that are coming up and the number of start-ups that fail are highly correlated. Amidst of various supporting schemes provided to support start-ups both in terms of finance and resources, they fail to meet success. There are multiple reasons contributing to the failure of start-ups which limelight to the question of start-up agility. Agility is the ability of an organisation to positively respond to the changes in business environment. Unceasingly updating technologies and innovations call for start-ups to adopt agile practices. In order to survive in this dynamic business environment, it is high time for start-ups to embrace agility.

2 Literature Review

Muduli et al. [2] proposed employee involvement can improve organisational performance. Sherehiy and Karwowski [3] explained autonomy as an important predictor of workforce agility. The study explained if management is responsive then the employees are more likely to be adaptive and flexible. Sherehiy et al. [4] proposed workforce agility as an important characteristic of agility that can be applied to all aspects of enterprise. The paper explains adaptability, flexibility and agility as the concepts needed for organisations to respond to changes. Nguyen-Duc et al. [5] suggested strategy, personnel, artifact and resources as tactics that will enable start-ups to achieve agility in its early stage. Patil and Suresh [6] explains innovation as the tool to react to business changes and rebound easily. The study also proposes collaboration within employees can help in exchanging expertise and thus faster execution. Shinwon et al. [7] proposed employees should be trained on new technologies and skillsets and put them into action. Olugbola [8] highlighted training has a positive influence on developing entrepreneurial ability and motivation. Patten et al. [9] suggests that anticipation, agility and adaptability can improve the capability of organisations to support agile enterprise. It is the primary step towards agile, anticipating what might happen in future and preparing accordingly to respond to the opportunities and challenges.

Lin et al. [10] used fuzzy logic approach to develop a framework to measure agility index. The study presented unprecedented application of fuzzy logic by illustrating a rational structure to review the imprecise phenomena in agility evaluation. Vinodh and Devadasan [11] used fuzzy logic to develop agility index measurement model. The paper discussed the obstacles for attaining agility in manufacturing organisation based on a twenty-criteria model comprehended with fuzzy logic. The study identified agility index that helped to identify the gaps and propose scopes for improvement. Nallusamy et al. [12] used multi-grade fuzzy approach to measure environmental sustainability. The study proposed a model to measure environmental sustainability index and identify prospect for improvement. Vimal et al. [13] proposed fuzzy logic to assess the sustainability of process orientation in organisations. The model calculated process sustainability index and observed the obstacles to achieve sustainability improvement.

Based on the literature review it was figured out that no research was reported on assessment of start-up agility using multi-grade fuzzy logic and Important Performance Analysis (IPA) model. In this context, this research study has been initiated.

3 Conceptual Model for Assessing Start-Up Agility

The conceptual model for assessing agility of Start-ups is shown in Table 1. This conceptual model was derived based on three aspects of start-up agility namely Organisation [14], Technology [15] and Strategy [11]. The model consists of three levels. The first level is the enabler, second level shows the criteria and the third level includes the respective attributes. As a sample, the enabler organisation has two criteria namely management and flexibility. The criteria management has three attributes namely flat organisational structure, employee involvement and autonomy and responding to changes in business.

Table 1 Conceptual model for assessing start-up agility

Enablers	Criteria	Attributes
Organisation (I_1)	Management (I_{11})	Flat organisational structure (I_{111})
		Employee involvement and autonomy (I_{112})
		Responding to changes in business (I_{113})
	Flexibility (I_{12})	Multi-skilled employee (I_{121})
		Positively adapt to changes (I_{122})
Technology (I_2)	Innovation (I_{21})	Using latest technologies (I_{211})
		Efficient methodology (I_{212})
	Artifacts (I_{22})	Developing new product or model (I_{221})
		Upgrading existing systems (I_{222})
Strategy (I_3)	Training (I_{31})	Cross learning in organisation (I_{311})
		Training new skill set and technologies (I_{312})
	Collaboration (I_{32})	Team working (I_{321})
		Collaborating outside organisation (I_{322})
	Anticipation (I_{33})	Tracking changes in business (I_{331})
		Forecasting opportunities and challenges (I_{332})

4 Research Methodology

Literature review on agility assessment was initiated to identify the relevant criteria based on which the conceptual model was developed. The weightage for calculating the start-up agility based on the developed conceptual model is done through expert opinion. After which a suitable start-up was identified for conducting the case study. The proprietors and employees of the start-up were interviewed to assess the agility in that start-up. Based on the rating assessment and weightages by expert's agility is measured followed by IPA analysis and discerning attributes for improvement to achieve agility.

5 Case Study

5.1 About Case Company

The study is carried out in one case start-up from India (hereafter referred to as ABC start-up). ABC start-up is an IT consulting and services firm specialising in online digital marketing, corporate branding, interior branding, social media promotions and search engine optimisation. The company aims to achieve enviable loyal customers in its focus segments.

5.2 Assessment of Agility Using Fuzzy Logic

The agility of a start-up is denoted by I. It is the product of mean weightage of the expert opinions represented by W and the overall rating factor R. The equation for agility is given by $I = W * R$. Since the calculation of agility factor includes fuzzy determination the assessment is categorised into five grades, $I = (10, 8, 6, 4, 2)$ where the range 8–10 represents that the start-up is 'extremely agile', 6–8 represents 'agile', 4–6 represents 'moderately agile', 2–4 represents 'non-agile' and 0–2 represents 'extremely non-agile'. Five experts contributed to the discussion meeting for weightage of agile enablers, criteria and attributes for IT-based start-ups. Five experts from case company participated in the evaluation for agility assessment. The mean normalised weightage of the experts' opinions and the attributes rating is shown in Table 2.

5.2.1 Primary Assessment Calculation

The calculation applied for the criteria 'Management' is as shown as follows. The weightage related to the criteria 'Management' $W_{11} = (0.34, 0.31, 0.35)$. Rating

Table 2 Single-factor rating and weightage by experts

I_i	I_{ij}	I_{ijk}	R_1	R_2	R_3	R_4	R_5	W_{ij}	W_i	W
I_1	I_{11}	I_{111}	7	9	9	8	8	0.34	0.56	0.32
		I_{112}	6	6	6	5	6	0.31		
		I_{113}	7	8	8	9	8	0.35		
	I_{12}	I_{121}	8	9	8	8	9	0.45	0.44	
		I_{122}	8	9	9	6	7	0.55		
I_2	I_{21}	I_{211}	8	9	7	8	9	0.43	0.49	0.34
		I_{212}	8	7	7	6	7	0.57		
	I_{22}	I_{221}	6	6	6	7	6	0.52	0.51	
		I_{222}	7	8	8	7	8	0.48		
I_3	I_{31}	I_{311}	8	9	10	7	10	0.56	0.33	0.35
		I_{312}	6	6	6	7	7	0.44		
	I_{32}	I_{321}	9	9	10	9	10	0.57	0.32	
		I_{322}	8	8	9	7	9	0.43		
	I_{33}	I_{331}	8	7	7	9	8	0.49	0.35	
		I_{332}	7	7	8	7	8	0.51		

vector related to the criteria 'Management' is given by

$$R_{11} = \begin{bmatrix} 7 & 9 & 9 & 8 & 8 \\ 6 & 6 & 6 & 5 & 6 \\ 7 & 8 & 8 & 9 & 8 \end{bmatrix}$$

Index for the criteria 'Management' is calculated as [16]

$$I_{11}{=}W_{11} * R_{11}$$
$$I_{11} = (6.69,\ 7.71,\ 7.71,\ 7.42,\ 7.38)$$

Similarly, using the same concept, the index for the other agile criteria is also computed.

$$I_{12} = (8,\ 9,\ 8.55,\ 6.89,\ 7.89)$$
$$I_{21} = (8,\ 7.85,\ 7,\ 6.85,\ 7.85)$$
$$I_{22} = (6.48,\ 6.96,\ 6.96,\ 7,\ 6.96)$$
$$I_{31} = (7.123,\ 7.7,\ 8.25,\ 7,\ 8.69)$$
$$I_{32} = (8.57,\ 8.57,\ 9.57,\ 8.13,\ 9.57)$$
$$I_{33} = (7.49,\ 7,\ 7.50,\ 7.99,\ 8)$$

5.2.2 Secondary Assessment Calculation

The calculation applied for the enabler 'Organisation' is as shown as follows. The weightage related to the enabler 'Organisation' $W_1 = (0.56, 0.44)$. Rating vector related to the criteria 'Management' is given by

$$R_1 = \begin{bmatrix} 6.69 & 7.71 & 7.71 & 7.42 & 7.38 \\ 8 & 9 & 8.55 & 6.89 & 7.89 \end{bmatrix}$$

Index for the criteria 'Management' is calculated as [17]

$$I_1 = W_1 * R_1$$
$$I_1 = (7.26,\ 8.28,\ 8.08,\ 7.19,\ 7.60)$$

Similarly using the same concept, the index for the other agile enablers are also computed.

$$I_2 = (7.22,\ 7.40,\ 6.98,\ 6.93,\ 7.40)$$
$$I_3 = (7.72,\ 7.73,\ 8.41,\ 7.71,\ 8.73)$$

5.2.3 Tertiary Assessment Calculation

The calculation applied for finding the value of agile index of ABC is as follows. Overall weight $W = (0.32, 0.34, 0.35)$. Overall rating vector is given by R

$$R = \begin{bmatrix} 7.26 & 8.28 & 8.08 & 7.19 & 7.60 \\ 7.22 & 7.40 & 6.98 & 6.93 & 7.40 \\ 7.72 & 7.73 & 8.41 & 7.71 & 8.73 \end{bmatrix}$$

Agility index I = W * R

$$I = (7.41,\ 7.79,\ 7.82,\ 7.28,\ 7.92)$$
$$I = (7.41 + 7.79 + 7.82 + 7.28 + 7.92)/5$$
$$I = 7.6$$

5.3 Classification of Agile Attributes Using IPA

IPA model is used to measure the agility of start-ups. IPA relates the mean weightage of the expert opinion to the rating assessment of start-up. IPA model is graphically represented in a framework distinguished by four zones [18]. The four zones and the inference of IPA is described in Table 3. The zones of the IPA framework correspond to the average of the mean weightage of expert opinion and the average of the mean assessment rating [19].

6 Results and Discussions

Based on the assessment of agility, agility index for the start-up ABC was computed to be 7.6. It comes in scale 6–8 which indicates that the start-up ABC is agile. Scale 8–10 is the range of extremely agile. This conveys that ABC has not achieved high level of agility and still there are scopes for improvements.

Improvement Performance Analysis (IPA) was done to identify the obstacles achieving high level of agility. The IPA model mentioned in Fig. 1 presented the attributes that need to be focused. Developing new products or models, use of efficient methodologies, forecasting opportunities and challenges in business environment and tracking changes in the business are the areas to be concentrated for improvement. Performance of ABC in these attributes is fairly low and requires action to be taken. Responding to changes in business, cross learning in organisation and team working are the areas which are perceived to be important where

Table 3 Zones and inference of IPA model

Zones	Inference
Zone 1 focus area	This is the area of highest priority. Experts assessed the attributes in this area as highly important ones. But the performance of the company is low in this region. This indicates that the improvement actions should be more focused on the attributes present in this region
Zone 2 preserve area	Attributes in this zone are also assessed as highly important ones by the experts. In this region, the Start-up is also doing a fairly good job. This supports the company to maintain its performance in these attributes
Zone 3 low-priority area	This zone is analysed as the area of lower weightage by the experts. Even though the performance of Start-up's is low in this region, it does not disturb the company's overall performance. Less priority is needed on the attributes present in this zone
Zone 4 unmerited area	The performance of Start-up on the attributes in this zone is high, but these attributes are assessed as of lower importance by experts. Start-ups should focus less on this area. Managers should rethink about the resource allocation and prioritise the attributes in this region

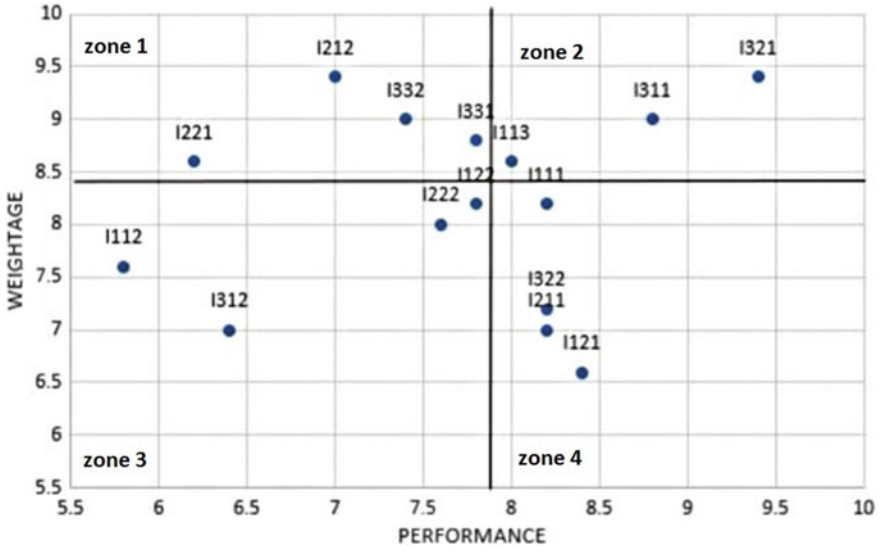

Fig. 1 IPA for startup agility assessment

ABC keeps a quality work. Employee involvement and autonomy, training new skills and technologies, upgrading existing systems and positively adapting to changes are some areas where the performance of the start-up ABC is low, but it is identified as a region of lower importance. This indicates that the low performance in these attributes won't have much effect on company's overall performance. Flat organisational structure, collaboration with outside organisation, using latest technologies and upholding multi-skilled employees are the areas where the performance of the company is higher than needed. Manager's may reconsider about resource allocation on the attributes in this region and may focus more on other attributes that need improvement.

6.1 Improvement Proposal for the Weaker Attributes

1. Developing new product or model: In this age of agility, driven by technology and innovation new service or product development has become the lifelines of any start-up. So, it is important to identify the needs of the targeted customer segment and cater to the product or service depending on the customer demand. The new product or should be able to deliver value to customers and able to make customer delight.
2. Efficient methodologies: Use of efficient methodologies are vital for the success of start-ups. Efficiency is important to save both time and money as well as for proper use of resources. This can be achieved through focusing more on the areas

where the performance of company is low by matching the proper skill sets to meet these tasks and keeping the goals of the start-up focused and clear.
3. Forecasting opportunities and challenges: It is important for the success of start-ups to forecast the challenges and opportunities as the pace of change in technology and innovation takes place at a higher rate. This can be done through keeping note of the updating technologies, understanding the changing preferences of the customer segment and analysing the economic conditions.
4. Tracking changes in business: Business is a dynamic environment that is directly affected by external as well as internal environmental conditions. However, the internal factors are under the control of managers, the external factors are beyond their control. So, to sustain in the competitive circumstance managers should keep track of the surrounding changes and adapt accordingly.

7 Managerial Implications

The methodology for assessing agility index proposed in this study enables the start-ups to measure its agility level. Apart from calculating agility index, the study helps the managers to identify obstacles for agility improvement and the areas to be concentrated. The managers can use this model to prioritise the attributes to achieve agility in their organisation. This research is a useful resource for industry persons as it constitutes the inputs from industry experts. In this context modern managers can focus their start-up's to be successful in ensuring agile practices by using this methodology.

8 Conclusion

The prime focus of this research is to assess the agility level of start-ups. Agility refers to the ability of a firm to positively adapt to the dynamic business environment. This study proposes a model to measure the agility index of start-ups. The model was developed using multi-grade fuzzy approach that incorporated the opinions of the industry experts. The paper discusses the case study of a start-up whose agility index is measured using the developed conceptual model. IPA is used to find the obstacles for the agility enhancement of start-up. On improvement of the weaker attributes start-up can improve its agility level to attain competitive advantage. The model can be further developed by incorporating enablers that are not addressed in this study. The case study has been carried out in a single start-up that is into IT consulting and services. Further study can be extended to various start-ups in different segments to make the conceptual model more generic and validated.

Compliance with Ethical Standards Conflict of Interest The authors declare that there is no conflict of interest in publishing this paper. The authors states the clarification of the anonymization of the data collection or for questionnaires (if any).

References

1. Business Line (2017) 90% start-ups in India fail within 5 years: IBM, https://www.thehindubusinessline.com/info-tech/90-startups-in-india-fail-within-5-years-ibm/article9704251.ece. Assessed on 1 Nov 2019
2. Muduli A, Verma S, Datta SK (2016) High performance work system in India: examining the role of employee engagement. J Asia Pac Bus 17(2):130–150
3. Sherehiy B, Karwowski W (2014) The relationship between work organization and workforce agility in small manufacturing enterprises. Int J Ind Ergon 44(3):466–473
4. Sherehiy B, Karwowski W, Layer JK (2007) A review of enterprise agility: concepts, frameworks, and attributes. Int J Ind Ergon 37(5):445–460
5. Nguyen-Duc A, Weng X, Abrahamsson P (2018) A preliminary study of agility in business and production: cases of early-stage hardware startups. In: Proceedings of the 12th ACM/IEEE international symposium on empirical software engineering and measurement. ACM, Oct 2018, p 51
6. Patil M, Suresh M (2019) Modelling the enablers of workforce agility in IoT projects: a TISM approach. Glob J Flex Syst Manag 20(2):157–175
7. Shinwon S, Sunguk P, Mihyun G, Namgyu K, Sunguk L (2015) Key factors of change readiness for the success of management innovation in manufacturing industry. Int J u e-Serv Sci Technol 8(10):179–192
8. Olugbola SA (2017) Exploring entrepreneurial readiness of youth and startup success components: entrepreneurship training as a moderator. J Innov Knowl 2(3):155–171
9. Patten K, Whitworth B, Fjermestad J, Mahindra E (2005) Leading IT flexibility: anticipation, agility and adaptability. In: AMCIS 2005 proceedings, p 361
10. Lin CT, Chiu H, Tseng YH (2006) Agility evaluation using fuzzy logic. Int J Prod Econ 101(2):353–368
11. Vinodh S, Devadasan SR (2011) Twenty criteria based agility assessment using fuzzy logic approach. Int J Adv Manufact Technol 54(9–12):1219–1231
12. Nallusamy S, Ganesan M, Balakannan K, Shankar C (2016) Environmental sustainability evaluation for an automobile manufacturing industry using multi-grade fuzzy approach. Int J Eng Res Afr 19:123–129 (Trans Tech Publications)
13. Vimal KEK, Vinodh S, Muralidharan R (2015) An approach for evaluation of process sustainability using multi-grade fuzzy method. Int J Sustain Eng 8(1):40–54
14. Patri R, Suresh M (2019) Agility in healthcare services: a systematic literature exploration. Int J Serv Operat Manag 32(3):387–404
15. Suresh M, Patri R (2017) Agility assessment using fuzzy logic approach: a case of healthcare dispensary. BMC Health Serv Res 17(1):394
16. Ganesh J, Suresh M (2016) Safety practice level assessment using multigrade fuzzy approach: a case of Indian manufacturing company. In: 2016 IEEE international conference on computational intelligence and computing research (ICCIC). IEEE, Dec 2016, pp 1–5
17. Sridharan V, Suresh M (2016) Environmental sustainability assessment using multigrade fuzzy—a case of two Indian colleges. In: 2016 IEEE international conference on computational intelligence and computing research (ICCIC). IEEE, Dec 2016, pp 1–4
18. Hemmington N, Kim PB, Wang C (2018) Benchmarking hotel service quality using two-dimensional importance-performance benchmark vectors (IPBV). J Serv Theory Pract 28(1):2–25
19. Feng M, Mangan J, Wong C, Xu M, Lalwani C (2014) Investigating the different approaches to importance–performance analysis. Serv Ind J 34(12):1021–1041

Design and Analysis of Pre-engineered Buildings Using Staad Pro

C. Kavitha, S. Suryaprakash, N. Lavanya, and S. Durgadevi

Abstract Pre-engineered building (PEB) has greater advantages in long-span structures. In this paper, pre-engineered industrial building of 30 mspan and 10 m eave height with slope of 10° has analyzed and designed using staad pro to understand the behavior of structure and to achieve the economy in steel design by reducing the material quantity as well as number of purlins and saving in erection time and construction time. Designs are done as per IS 800-2007 codes. Load is considered in modeling which are dead load, live load, wind load, and earthquake loads. Results are observed for base reaction, column moment, rafter moment, and displacement. From the parametric study, the PEB is fabricated in a factory and then it is erected at site as per the requirement.

Keywords Steel design · Moment reaction · Staad pro

1 Introduction

Pre-engineered building came into existence in 1960. Pebs are used for making construction materials in a variety of shapes. This type of construction is usually fabricated in site, and then they are transported to site [1]. Structural steel shapes like I-beams have high moments of area, which means they are very stiff with respect to their cross-sectional area and thus can support a high load without excessive sagging and requires no support conditions [2]. Because of its behavior and structural aspects, it possesses integrity and also pleasing appearance and better aesthetic view with minimum quantity of steel requirements resulting in economy [3].

Usually, peb columns and beams are not available in standard shapes, and they are just plate girders which are welded together to form members of different sizes to provide stiffness [4]. Nowadays, cold-formed Z- and C-shaped members are used as secondary structural elements to fasten and support the external cladding [5].

C. Kavitha (✉) · S. Suryaprakash · N. Lavanya · S. Durgadevi
Department of Civil Engineering, Bannari Amman Institute of Technology, Sathyamangalam, Erode District, Tamil Nadu 638401, India
e-mail: civil.kavii@gmail.com

G. Kumaresan et al. (eds.), *Advances in Materials Research*, Springer Proceedings in Materials 5, https://doi.org/10.1007/978-981-15-8319-3_69

Pre-engineered buildings can be adapted to suit a wide variety of structural applications; the greatest economy will be realized when utilizing standard details [6]. An efficiently designed pre-engineered building can be lighter than the conventional steel buildings by up to 30% [7, 8]. Lighter weight results into less steel and great savings in structural framework. Pre-engineered buildings have bolted connections and hence can also be reused after dismantling and act as a roller support and provide lateral resistance to earthquakes [9, 10]. Thus, pre-engineered buildings can be shifted and/or expanded as in case of heavy loading conditions. Mezzanine floors are new technologies in which multi-stories can also be constructed using pre-engineered buildings.

2 Experimental Procedures Building

2.1 Description Details

Large industrial warehouse is been designed with span conditions 30 m × 30 m.

Structure	Industrial warehouse
Location	Coimbatore
Eave Height	10 m
Slope of Rafter	5.71°
Bay spacing	5 m
Wind speed	44.85 m/s
Terrain category	Category 2 (Open terrain with well-scattered obstructions)
Importance factor	1.15 (Industrial Building).

2.2 Structural Drawings Using Staad Pro

They are designed using staad pro software, where all the inputs are computed as per given details. First modeling of the structure has been complete. Then various combinations of load acting on the structures are imposed on structure using loads and definition methods [11]. Then post-processing methods are done to verify the output. Followed by output steel design is achieved and quantities of steel requirements a redetermined. To ensure economical purposes, unity check is also carried out to cross-verify shear and moment safety and reduce over unnecessary weights, so that overall economy can be achieved [12].

2.3 Design of Primary and Secondary Sections

There are different kinds of tapered members which are designed using staad pro, and their properties after deigned are listed below. The purlin used is cold-formed C sections with lips, and other cladding materials are to used to finalize the structure [9]. The cold-formed purlins are used to reduce the total weight of the structure, and wind bracing is used to hold to provide resistance. In normal CSB buildings, the purlins weight is associated with 28% of total weight and cold-formed structures are light in weight and resulting in economy and faster constructions (Table 1).

Load Combinations Considered

- 1.5 (Dead load live load)
- 1.5 (Dead load + wind load along + x) + 0.5 cpi
- 1.5 (Dead load + wind load along $-x$) + 0.5 cpi
- 1.5 (Dead load + wind load along + Z) + 0.5 cpi
- 1.5 (Dead load + wind load along $+x$) + 0.5 cpi
- 1.5 (Dead load + wind load along $-x$) −0.5 cpi
- 1.5 (Dead load + wind load along $+Z$) −0.5 cpi
- 1.5 (Dead load + wind load along $-Z$) −0.5 cpi
- 1.5 (Dead load + wind load along $-Z$) −0.5 cpi
- Earthquake load along + x
- Earthquake load along $-x$
- Earthquake load along + z
- Earthquake load along –z.

Table 1 Properties of member

Members	Column (M)	Rafter 2 (M)	Rafter 3 (M)	Rafter 4 (M)	Column 5 (M)
f1 (depth @ start node)	0.4	0.8	0.275	0.35	0.6
f2 (thickness of web)	0.012	0.016	0.016	0.016	012
f3 (depth @ end node)	0.6	0.275	0.275	0.6	0.8
f4 (width of top flange)	0.25	0.25	0.25	0.2	0.25
f5 (thickness of top flange)	0.025	0.02	0.02	0.02	0.025
f6 (width of bottom flange)	0.25	0.25	0.25	0.2	0.25
f7 (thickness of bottom flange)	0.025	0.02	0.02	0.02	0.025

Table 2 Length and weight of each member

Profile	Length (mm)	Weight (N)
Tapered member 1	69,999	96,254
Tapered member 2	71,386	98,490
Tapered member 3	71,386	75,457
Tapered member 4	71,386	82,038
Tapered member 5	69,999	109,160
Cold-formed purlins	210,000	34,105
Cross-bracings	48,000	248,010
Gable columns	44,000	179,754
Tie rods	59,999	25,073

Total weight: 948,346 N

3 Results and Discussion

3.1 Steel Takeoff

This steel takeoff helps in determining the total requirement of steel used in building as per different specifications (Table 2).

Area-to-Weight Ratio
For an industrial area of 900 m^2, the required quantity of steel is determined using staad pro. The area-to-weight ratio of the industrial warehouse upto eave height of 10 m is listed below.

Area—900 m^2
Required quantity of steel in kg—96671.3
Area-to-weight ratio—107.5.

4 Conclusion

Thus by using PEB roof structures, the dead weights are greatly reduced and for especially for long-span structures the weight in rafters are considerably reduced because these are designed using point of contra flexure and quantities of steel are considerably used. Usage of pre-engineered building structures is faster in construction, and they are fabricated in factory and are assembled in site. The overall economy is achieved to about 30%.

References

1. Ley J (2003) An environmental and material flow analysis of the UK steel construction sector. Doctor of engineering thesis. University of Wales
2. Hicks SJ, Lawson RM, Rackham JW, Fordham P (2004) Comparative structure cost of modern commercial buildings, 2nd edn. The Steel Construction Institute
3. Bui N, Mershbrock C, Munkold BE (2016) A review of building information modelling for construction in developing countries. Procedia Eng 164:487–494
4. Meera CM (2013) Pre engineered building design of an industrial warehouse. Int J Eng Sci Emerg Technol 5(2):1484–1488
5. Rao P (2014) Comparative study of pre engineered and conventional industrial building. Int J Eng Trends Technol 9(1):1–6
6. Kulkarni AV (2013) Analysis and design of pre engineered buildings and conventional frames. IOSR J Mech Civ Eng 5(1):32–43
7. Bhojkar M (2014) Comparison of pre engineering building and steel building with cost and time effectiveness. Int J Innov Sci Eng Technol 1(10):487–490
8. Chavan VB (2014) Economic evaluation of open and hollow structural sections in industrial trusses. ACI Struct J 3(2):9554–9565 ((6) Design of Steel Structures by N. Subramanian)
9. Parikh S (2013) Design of steel compression members (According To Is: 800). Int J Eng Res Technol (IJERT) 2(11):1411–1417
10. Firoz S, Sarath Chandra Kumar B, Kanakambara Rao S (2012) Design concept of pre engineered building. Int J Eng Res Appl 2(2):267–272
11. Snyman JA (2005) Practical mathematical optimization: an introduction to basic optimization theory and classical and new gradient-based algorithms. Springer Publishing. ISBN 0-387-24348-8
12. Sacks R, Barak R (2007) Impact of three-dimensional parametric modeling of buildings on productivity in structural engineering practice. Faculty of Civil and Environmental Engineering, Technion-Israel Institute of Technology, Israel, Elsevier (Science Direct)

Effect of Compression Ratio on the Performance, Emission, and Combustion Characteristics of C.I. Engine Using Waste Cooking Oil and Its Emulsion as Fuel

Selvakumar Raja, Jaikumar Mayakrishnan, Sasikumar Nandagopal, and Sangeethkumar Elumalai

Abstract Increase in the use of fossil fuel results in the depletion of underground reserves and responsible for increase in pollution. This demand for an alternate fuel resources which provide performances close to fossil fuels with less emissions. Waste Cooking Oil (WCO) is found as one such alternate fuel which possesses properties close to diesel fuel. In addition, ease of availability, non-toxicity, and biodegradability makes WCO a more desiring alternate fuel source. This work aims to focus on studying the performance, emission, and combustion properties of WCO in Compression Ignition (CI) engine. In this first phase of the work, neat diesel and WCO were tested in a single-cylinder water cooled diesel engine at different load conditions. In the second phase, WCO was converted in to its emulsion and tested in the test engine. Finally, the test engine was operated with above mentioned said fuels at two different compression ratio (i.e., 17.5:1 and 18:1), and results were compared. It comes to know that compression ratio is a strong function of performance, emission, and combustion characteristics of the test engine operated with different test fuels. It is concluded that the WCO and its emulsion give trade-off between brake thermal efficiency and oxides of nitrogen (NO_x).

Keywords Fossil fuels · Waste cooking oil · Compression ratio

1 Introduction

The importance of alternative fuels comes to limelight as the fossil fuel reserves are depleting at larger rate. In addition, talks over climatic change also increases the need of finding a suitable alternative for fossil-based energy resources. Past research on alternate fuels over three decades claims different types of alternate fuels for day-to-day application but the main challenge remains on effective utilization of

S. Raja (✉) · J. Mayakrishnan · S. Nandagopal · S. Elumalai
Department of Automobile Engineering, Hindustan Institute of Technology and Science, Chennai, Tamil Nadu 603103, India
e-mail: rselvak@hindustanuniv.ac.in

G. Kumaresan et al. (eds.), *Advances in Materials Research*, Springer Proceedings in Materials 5, https://doi.org/10.1007/978-981-15-8319-3_70

those alternate fuels in existing engine. The properties of vegetable oil were closer to the diesel fuel. It can be due to the presence of triglycerides, try-glycerol ester of various fatty acids with glycerol in chemical composition of vegetable oil. The energy content of vegetable oil is also found to be almost close to the diesel fuel.

Vegetable oils like maua oil, rice bran oil, jatropha oil, and neem oil, etc., were some of the notable vegetable oil utilized in diesel engines. WCO is also one such resources from vegetable oil family. It comes to know that generation of WCO is quite increasing in recent times due to the increase in restaurants as a result of urbanization and change in people's food habit. It was also observed that disposal of such oil was highly challenging task as it spoils both human health as well as environment [1]. The possibility of waste oils as alternative fuel for diesel engine and identified that higher viscous nature of WCO needs to be addressed as it results in poor spraying behavior [2]. The use of emulsion, water induction for controlling diesel engine emissions it was observed from a study that the smoke emission of engine reduced operated with emulsified form of WCO fuel (WCOE). [3]. Another investigation reported that utilization of emulsified fuel increased peak pressure of the engine owing to the secondary atomization of injected fuel. Study also reported reduced part-load performance with emulsified fuel [4].

The advantage of emulsified fuel was to reduce the effort of ignition continued burning nature at low-temperature environments [5]. A study revealed that emulsified fuels prepared from equal proportions of used frying oil, and gas oil showed reduced NO_x concentration and smoke density without failing BSFC at rated output. [6]. It is stated that emulsions of animal fat with methanol or ethanol apply for maximum pressure and maximum rate of pressure rise as compared with neat animal fat [7]. The compression ratio is a strong function of BTE. Increased in compression ratio, eventually increases the pressure and temperature, helps to ensure effective utilization of injected fuel and increase the BTE [8].

This is clear from the literature that WCO has wide range of scope to utilize as fuel for CI engine. However, it requires modification in the fuel as well as engine level for optimized performance and emission behavior. In this study, an attempt was made to study the effect of engine as well as fuel level modification of a compression ignition engine operated with WCO. The study gives a brief idea about the influence of WCO on fuel injection and course of combustion. It was found that ignition delay of injected fuel increases as the load increases. Emissions like HC and CO have also increased with the amount of WCO; however, NO_x emission was on the lower side. Usage of emulsified fuels was also found be gaining lots of attention in recent days. The addition of water and surfactant in the form of emulsion with bio oil is understood to improve the combustion and performance characteristics of CI engines. Bio oil emulsions resulted in considerable reduction in the concentration of pollutants as well. Particularly, the concentration of oxide of nitrogen emission showed a important reduction with emulsions of bio oil due to reduced cycle temperature.

2 Materials and Methods

2.1 Fuel Preparation

The Waste Cooking Oil (WCO) was collected and filtered for removing the minute food particles and dust. The Waste Cooking Oil Emulsion (WCOE) prepared from a dispersion of two non-miscible fluids. SPAN80 was chosen as surfactant to reduce the surface tension of emulsion. Ethanol is chosen as a co-surfactant to reduce the viscosity of the emulsion. Waste Cooking Oil Emulsion (WCOE) was prepared by mixing water, neat WCO, SPAN 80, and ethanol. Initially, ternary diagrams given in Fig. 1 were drawn to prepare and identify the sample which was stable in nature over a period of time. 20 samples were made and found a sample with a 90% WCO, 3% water, 5% ethanol, and 2% Span80 by volume appeared to be more stable for two weeks. The important properties of WCO and WCOE were tested in the laboratory. Important properties of the test fuels are listed in Table 1.

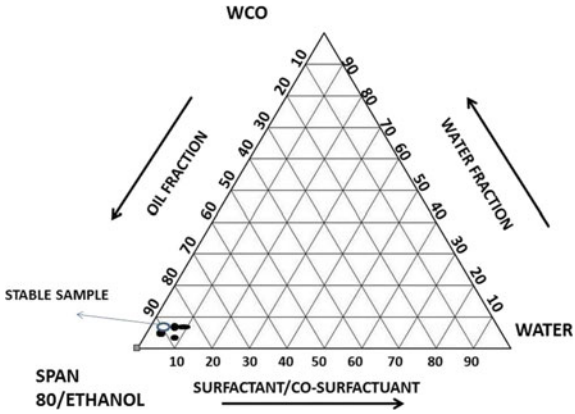

Fig. 1 Ternary diagram

Table 1 Properties of the fuels

Properties	Diesel	Waste cooking oil (WCO)	Waste cooking oil emulsion (WCOE)	ASTM standard
Density at 15 °C	818 kg/m^3	880.7 kg/m^3	925.8 kg/m^3	D1298
Kinematic viscosity at 40 °C	2.95 cst	5.12 cst	1.27 cst	D445
Cetane number Flash point (°C)	43	39	41	D613
Gross calorific value	45,325 kJ/kg	38,740 kJ/kg	36,195 kJ/kg	D5865

2.2 Experimental Setup

A single cylinder, four stroke, constant speed, direct injection, and water cooled diesel engine has been selected to conduct experiments and study the performance, emission, and combustion characteristics. Detailed specification of the test engine is given in Table 2. The schematic diagram of the developed engine set up is given in Fig. 2. Engine was connected to an eddy current dynamometer for applying load on the engine. A burette and stop clock were used to measure the fuel consumption. Engine is initially operated with standard CR 17.5:1, and injection timing is 23° BTDC. AVL 444 N Di Gas analyzers and AVL 437C smoke meter were used to measure the tail pipe emission. Piezoelectric pressure transducer and crank angle encoder were used to measure the in-cylinder pressure. Maximum load calculation was carried out for smooth operation of the engine. The uncertainty of the measured instruments is listed in Table 3.

Table 2 Engine specification

Make	Kirloskar/240PE
Type	Single cylinder, four stroke CI engine
Cubic capacity	661 cc
Bore × Stroke	87.5 mm × 110 mm
Compression ratio	17.5:1
Power rating	3.54 kW
Rated speed	1500 rpm
Loading device	Eddy current dynamometer
Standard injection timing	23°BTDC

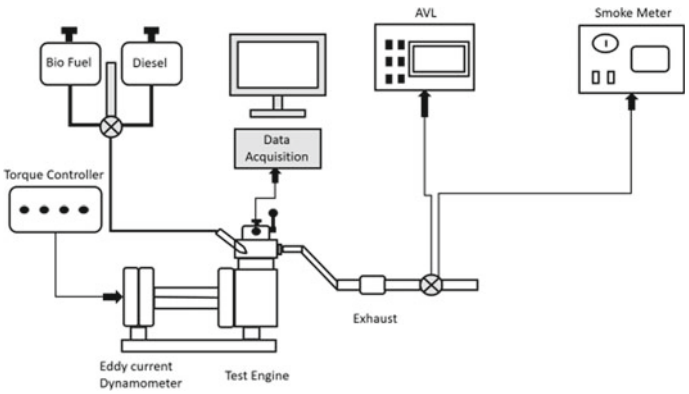

Fig. 2 Experimental setup

Table 3 Uncertainty of the instruments

Particulars	Uncertainty percentage (%)
Pressure (bar)	±0.50
Brake thermal efficiency	±0.05
Engine speed (rpm)	±1.50
NO (ppm)	±2.80
Brake power (W)	±1.20
HC (ppm)	±0.60
CO (ppm)	±0.70

3 Result and Discussion

3.1 Brake Specific Fuel Consumption (BSFC)

Figure 3 shows the Brake Specific Fuel Consumption (BSFC) of test fuels at different load conditions. The diesel fuel has least BSFC as compared to other test fuels. On the same hand, utilization of WCO in the test engine experienced highest BSFC of all test fuels. It can be due to the lower energy content of the WCO which demands higher fuels consumption for produced same power output as compared to diesel [9–12]. However, on increasing the CR, slight decrease in the BSFC was noticed with waste cooking oil at all the brake power.

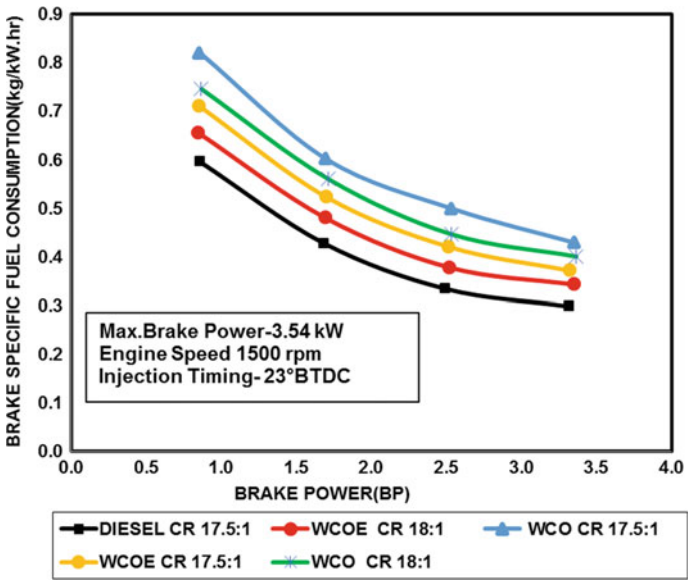

Fig. 3 Brake power versus brake specific fuel consumption

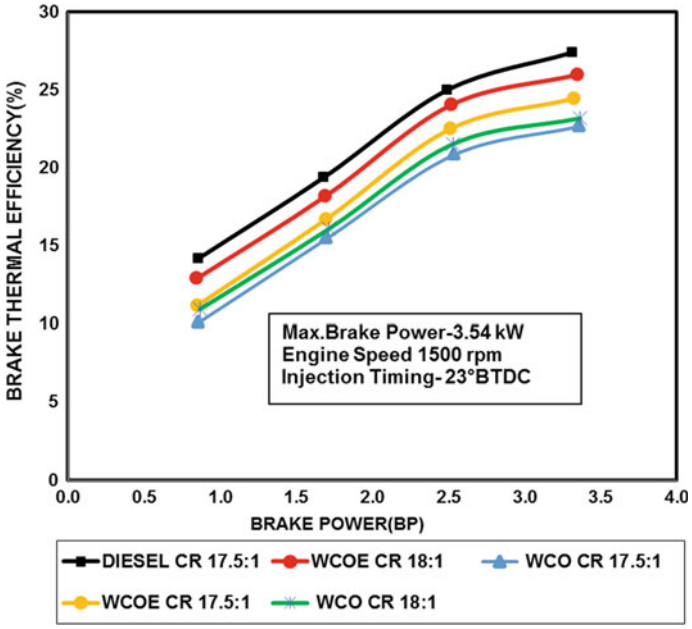

Fig. 4 Brake power versus brake thermal efficiency

3.2 Brake Thermal Efficiency (BTE)

Figure 4 shows the variation in BTE of test fuels at various load conditions. It comes to know from the plot, diesel fuel experienced highest BTE as compared to other test fuels. From the graph that, utilization of neat form of waste cooking oil in test engine decreased the BTE. Maximum BTE observed with 22.6% at maximum brake-power of the test engine with WCO. Decrease in the BTE with neat from of WCO is mainly due to the slow burning nature of injected high viscous WCO [13–15]. However, improvement in the BTE was observed when WCO was used in the test engine operated at higher CR (i.e., 18:1). On the other hand, emulsified from of WCO also resulted in significant increase in the BTE even at the standard CR of 17.5:1. Maximum BTE with WCOE was observed as 24.4% at maximum brake power of the test engine. Further increase in the BTE was observed with WCOE when it was utilized in the test engine at higher CR.

3.3 Unburned Hydrocarbon (UHC) Emission

Figure 5 shows the variation of UHC emission of test fuels at different load conditions; it is observed that emulsified from of WCO was producing high-hydrocarbon

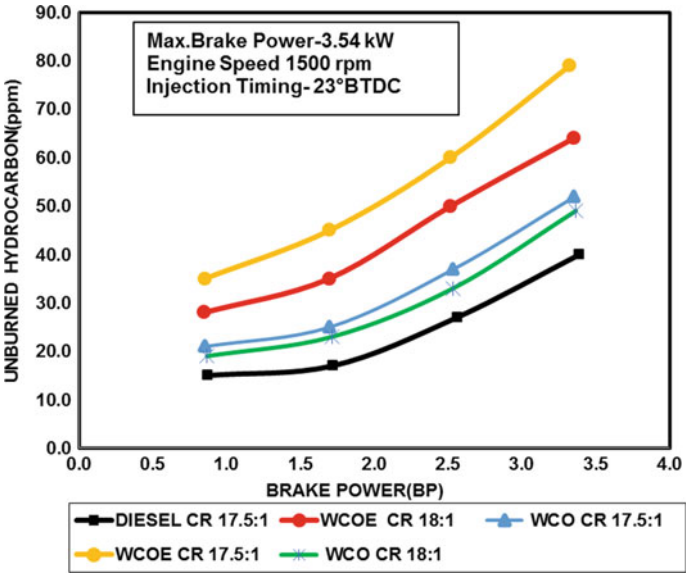

Fig. 5 Brake power versus unburned hydrocarbon

emission as compared with other test fuels at various power output. Maximum UHC emission observed with WCOE was noted as 79 ppm at maximum brake power where as it was only around 52 ppm with WCO at same power output. Main reason for the contrasting result is low-temperature combustion associated with WCOE [15].

3.4 Smoke Emission

Difference of smoke emission of test engine shows in Fig. 6. The diesel fuel shows least smoke emission as compared with other test fuels at all the power outputs. Usage of neat form of WCO resulted in highest smoke emission at all the load condition. It can be due to the poor atomization characteristics of injected WCO which consequences in large size fuels droplets, resulted in poor burning of injected fuel and increase the smoke level in the tail pipe. However, on operating the same fuel with higher CR ended up with reduced smoke emission [4]. Smoke emission was observed as 47 ppm with WCOE at peak power output. Further reduction in the smoke emission is observed when emulsified fuel was utilized. The smoke emission was reduced to 38% with WCOE at CR of 18:1. This could be due to microexplosion which is responsible for secondary atomization and reduce the smoke level.

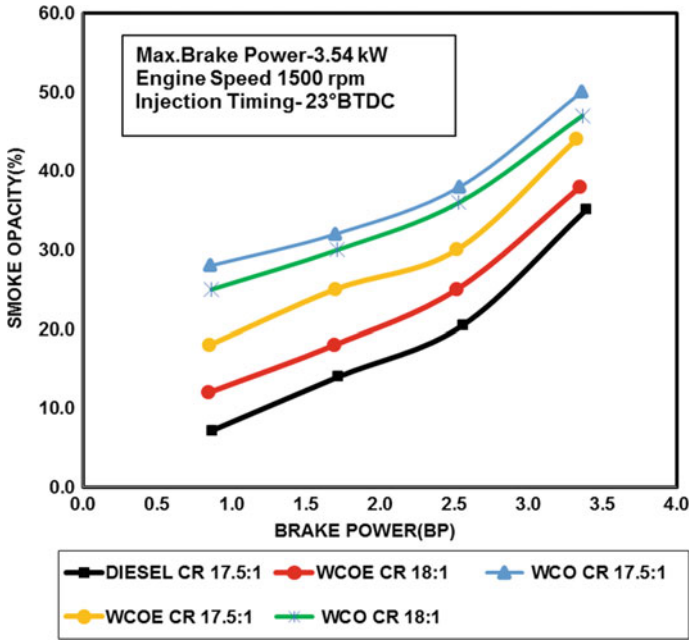

Fig. 6 Brake power versus smoke opacity

3.5 *Oxides of Nitrogen Emission (NO_x)*

Variation of NO_x emission of test fuels at different load conditions is shown in Fig. 7. The increases of the in-cylinder temperature of the CI engine which leads to produce the NO_x emission. It is very clear diesel fuel experienced highest NO_x emission as compared to all other test fuels at all the load conditions. However, direct usage of the WCO in the unmodified test engine resulted in reduced NO_x emission. Minimal NO_x emission noticed with the waste cooking oil at maximum power output was 830 ppm but the diesel fuel gives 980 ppm at same power output.

3.6 *Heat Release Rate*

Figure 8 shows the variation of heat release rate of test fuels at peak load conditions. It is clear from the plot, diesel fuel experienced highest heat release rate among all other test fuels. It is mainly due to the higher energy content of the injected fuel. On the other hand, straight form of WCO resulted in lowest heat release rate. It is generally due to the slow burning of injected WCO [16–18]. This increase the overall combustion duration and reduce the BTE as seen in Figure (BTE). It is also observed that shift in the occurrence of peak heat release rate with WCO and

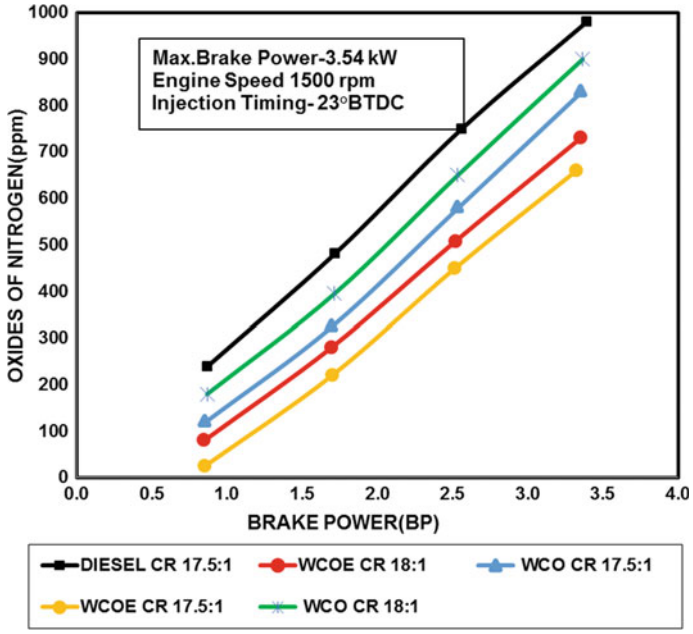

Fig. 7 Brake power versus oxides of nitrogen

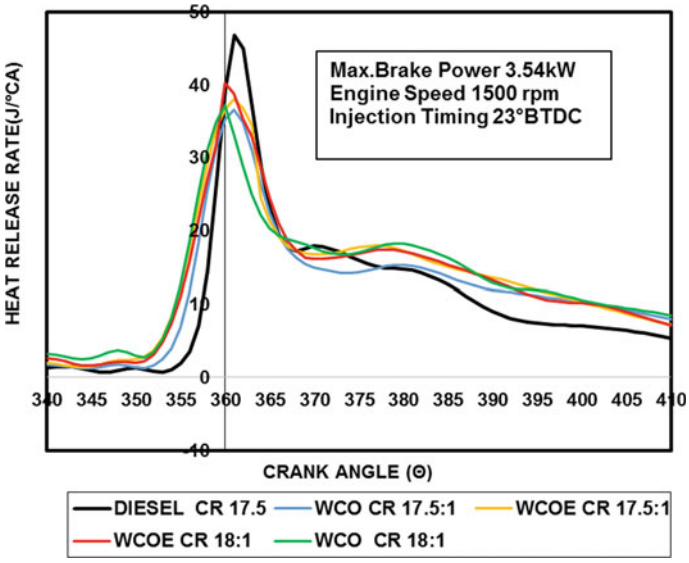

Fig. 8 Crank angle versus heat release

prolonged diffusion combustion phase which is clear indication of increased smoke emission as seen in Fig. 6.

4 Conclusion

Below conclusion was drawn from the above experimental work,

- It comes to know that compression ratio is the strong function of performance, combustion, and emission characteristics of the test engine. It is also proved that both fuel and engine level modifications are mandate for the use of alternate fuels in CI engine.
- Utilization of neat form of WCO in unmodified CI engine reported for inferior performance and emission characteristics. BTE, NO_x and smoke emissions with WCO were observed as 22.6%, 50%, and 830 ppm, respectively, at max. brake power.
- Increase of CR has of the test engine which has increased the BTE to 24.6% with WCO at same above mentioned power output with a slight increase in NO_x emission. At the same time, it is also observed with increase in CR all the carbon-based emissions with WCO were reduced as compared with the previous case.
- Utilization of emulsified fuels ended up with simultaneous reduction of NO_x and smoke emission to a minimal value of 660 ppm and 44%, respectively, with significant improvement in the BTE as well. Further improvement in the BTE was obtained with WCOE as the CR was increased at a penalty of increased NO_x emission.

Acknowledgements Authors like to acknowledge Hindustan Institute of Technology and Science, Rajiv Gandhi Salai, Padur, Chennai, Tamil Nadu, India for interminable support and encouragement. Authors extent their thankfulness to Dr. M. Senthilkumar, Professor and Head, Department of Automobile Engineering, MIT, Anna University, Chennai for their valuable guidance.

References

1. Senthil Kumar M, Bellettre J, Tazerout M (2009) The use of biofuel emulsions as fuel for diesel engines: a review. Proc Inst Mech Eng Part A J Power Energy 223(7):729–742
2. Naima K, Liazid A (2013) Waste oils as alternative fuel for diesel engine: a review. J Petrol Technol Altern Fuels 4(3):30–43
3. Nazha MAA, Rajakaruna H, Wagstaff SA (2001) The use of emulsion, water induction and EGR for controlling diesel engine emissions. SAE Trans 1205–1211
4. Raja S, Mayakrishnan J, Nandagopal S, Elumalai S, Velmurugan R (2018) Comparative study on smoke emission control strategies of a variable compression ratio engine fueled with waste cooking oil. No. 2018-01-0908. SAE technical paper

5. Crookes RJ, Kiannejad F, Nazha MAA (1997) Systematic assessment of combustion characteristics of biofuels and emulsions with water for use as diesel engine fuels. Energy Conver Manag 38(15–17):1785–1795
6. Yoshimoto Y, Onodera M, Tamaki H (1999) Reduction of NO_x, smoke, and BSFC in a diesel engine fueled by biodiesel emulsion with used frying oil. SAE Trans 1913–1920
7. Senthil Kumar M, Kerihuel A, Bellettre J, Tazerout M (2006) A comparative study of different methods of using animal fat as a fuel in a compression ignition engine. J Eng Gas Turbines Power 128(4):907–914
8. Muralidharan K, Vasudevan D (2011) Performance, emission and combustion characteristics of a variable compression ratio engine using methyl esters of waste cooking oil and diesel blends. Appl Energy 88(11):3959–3968
9. EL-Kassaby M, Nemitallah MA (2013) Studying the effect of compression ratio on an engine fueled with waste oil produced biodiesel/diesel fuel. Alex Eng J 52(1):1–11
10. Mayakrishnan J, Nandagopal S, Sathiyaseelan V, Raja S (2018) Canola oil as a fuel for compression ignition engine—an experimental investigation. No. 2018-01-0910. SAE technical paper
11. Senthil Kumar M, Jaikumar M (2014) A comprehensive study on performance, emission and combustion behavior of a compression ignition engine fuelled with WCO (waste cooking oil) emulsion as fuel. J Energy Inst 87(3):263–271
12. Kerihuel A, Senthil Kumar M, Bellettre J, Tazerout M (1729) Experimental investgations on a compression ignition engine using animal fat emulsions as fuel with water and methanol. Society of automotive engineers paper 2005-01
13. Senthil Kumar M, Ramesh A, Nagalingam B (2001) Experimental Investigations on a Jatropha oil methanol dual fuel engine. No. 2001-01-0153. SAE technical paper
14. Masimalai S, Mayakrishnan J, Ganesan N (2017) A comprehensive assessment on combined effect of thermal barrier coating and emulsification techniques on engine behavior of a Mahua oil based diesel engine. SAE technical paper 2017-01-0873. https://doi.org/10.4271/2017-01-0873
15. Masimalai SK, Mayakrishnan JK (2017) A comparative study on different methods of using waste cooking oil as fuel in a compression ignition engine. No. 2017-01-0876. SAE technical paper
16. Kulkarni HB, Kubade PR (2020) Performance optimization of VCR diesel engine using soybean oil-based biodiesel. In: Vijayaraghavan L, Reddy K, Jameel Basha S (eds) Emerging trends in mechanical engineering. Lecture notes in mechanical engineering. Springer, Singapore
17. Roy SK, Mohanty AR (2020) Combustion detection in IC engine by analysis of instantaneous angular acceleration. In: Biswal B, Sarkar B, Mahanta P (eds) Advances in mechanical engineering. Lecture notes in mechanical engineering. Springer, Singapore
18. Dabas N, Dubey V, Chhabra M, Dwivedi G (2019) Performance analysis of an IC engine using methanol, ethanol, and its blend with gasoline and diesel as a fuel. In: Saha P, Subbarao P, Sikarwar B (eds) Advances in fluid and thermal engineering. Lecture notes in mechanical engineering. Springer, Singapore

Agile Practices in Human Resource Management

R. Kavitha and M. Suresh

Abstract The agile approach gives scope for managing work as small consumable teams and enables incremental, value-based developments for quicker customer delivery. The concept of agility is transcribed into support functions of the organization basically into Human Resources (HR) as it is the driver and enabler of agile culture in the organization. This paper is the literature review on agility within the HR department and the HR processes. This paper looked at information available in the blogs, columns and few research papers from industry and HR thought leaders. The concepts, practices and experiments with Agile HRM from industry have been collated and presented based on which a model has been constructed.

Keywords Agile HRM · Agility · Agile practices · Agile organizations · Human resources

1 Introduction

Agile HRM is the popular trend in Human Resources (HR) domain. Agility is the software development model that has been off late adopted in all support functions as it offers empowerment for individuals and offers new levels of flexibility. With agility gaining insight into HR, HR department in organizations have to adapt to new paradigm and rethink the processes that they have been handling for decades.

There has been no definite definition for Agile HRM but there have been efforts by practioners to get to the closest definition. Agile HR is “Designing HR to support and organization that works according to agile methodologies. Designing the people practices to support agile ways and methodologies of working, the agile organization model and the agile cycles”. Agile HR also defined as "Organizations where the cross-functional teams that use agile methodologies help HR for stepwise incremental development by following the values like agilemanifesto.org and the

R. Kavitha · M. Suresh (✉)
Amrita School of Business, Amrita Vishwa Vidyapeetham, Coimbatore, India
e-mail: drsureshcontact@gmail.com

G. Kumaresan et al. (eds.), *Advances in Materials Research*, Springer Proceedings in Materials 5, https://doi.org/10.1007/978-981-15-8319-3_71

agilehrmanifesto.com in all the processes" [1]. "Agile HR" means looking ahead [2].

Agile is not a technical jargon anymore. Agile has penetrated into other areas and functions, from product development to manufacturing to marketing. It is now transforming the way in which organizations manage to hire and develop their workforce [3]. It is the capability of HR, functionally increasing its responsiveness effectively to changes in employee expectations, workplace disruptions and business requirements [4]. An agile HR approach is to evolve to an entire new degree of responsiveness in an organization. In an agile environment, it is pertinent for HR to help manage change within the organization.

Adaptation of HR to various new techniques and methods that can be responsive in functional areas like manpower planning and organizational management, revamping the HR policies, procedures, systems and programmes [5]. Agile-driven human resource approach is an exit from traditional human resource management approach which is predominantly plan-driven. In summary, agility of HR will drive the organization to endure a confirming paradigm where HR can learn and replicate the practices of agile software project management [6].

Agile transformations in an organization influence the teams' organization and management, capability building required for those teams are diagnosed, and organizational talents are managed accordingly. Whether the teams in the organization use SAFe(R), Less, Scrum, Kanban, XP, Scrum waterfall method, understanding the context to design is most important. Every organization has its own business situations, legal constraints and culture; hence, Agile HR cannot be designed commonly to suit all.

In an agile organization, HR provides the people services with greater responsiveness in the processes like hiring, professional development and performance management. The scales of responsiveness cater to the evolving culture and work style of the organizational changes [7]. HR's role is just not to on board the transformation process, but also be a transformation driver and enabler.

With agile processes influence and impact the organizations, there is a limited published literature on methods to enable integration of HR and the other support functions to the product development process and increasing the agility at work.

2 Bridging and Integration

It is essential that leadership teams in business begin to identify the concepts of agility that could help manage HR's business operations. The focus in HR operations would be on teams handling recruiting, training and development, communications and compliance. Rather than operating as a one whole unit, HR has to redesign itself as small teams through agile concepts—prioritizing for value and maximizing flow. With the IT business successfully adopting agile play book, it is time for people management team to replicate the model for overhauling its operations.

HR operations impact every employee of an organization in all the possible aspects. The transformation of HR to agility throws many challenges as its complex and extensive. The pioneers in the tech who have adopted agile techniques in their software processes are way ahead of others. The HR function requires re-skilling with more expertise in IT support and tools. Industry needs a future workforce which is skilled and responsive. Hence, there is a need for HR function to go agile to support the future workforce.

The "Agile Model of HR" conditions that HR department should do away with controls and standards implementation and focus and drive execution. The focus has to be to facilitate and improve agility in the organization.

Below given are examples of few Agile HR strategies [8]:

- Training leaders at all levels of the company to act as coaches and not just be managers.
- Planning and dividing the organization into small, high-performance teams that are independently set and achieve their targets.
- Create a scope for customer interactions internally and with all the other stakeholders in the organization.
- Deliver alignment to create a strong, focus-minded value systems.
- Create systems with information transparency about the organizational goals, information on who is working on what projects, who are the experts?
- Building a learning culture at all levels and focusing on continuous learning.
- Encourage people to give direct feedback to each other.
- Hiring and promoting experts/specialists, not just managers.
- Employing strategies to build a strong employment brand that attracts the right talent.
- Implement systems for engagement and not dwell into practices of collaboration, information-sharing, project management.

HR traditionally has been a function that revolves around managing people and policies. While the agile frameworks actually may not directly impact the way everyday processes of the HR department are handled but it will definitely impact HR department if their company goes Agile. In most of the successful industry transformations, HR has played the role of driver of the change and a pivotal hub for driving organizational change to success.

Going agile turns the HR into an aware, responsive team that evolves the organization to be agile and drives its culture on a daily basis. The ability of HR to flex and flow with demand, by serving its customers better, and the enterprise is a form of Agile HRM. Agile HRM is finding the minimal process route to drive or transform operations from point A to point B. With latest generation cloud-based HR solutions available, aiming towards the agile approach will be the next wave in HR transformation. Enriching and expanding agility to meet the challenges and needs should the primary angle in HR radar.

HR agility becomes imperative in organizations that are adapting to agile culture and hire agile workforce.

The talent report from Randstad Source right offers guidance to HR in maximizing an agile workforce [9]:

- Investing in appropriate tools—Organizations should have a platform for performance measurement of all their workers to enable better management.
- Following the attraction strategies—Tailor the employer branding to appeal to the best available talent pool.
- Keeping up compliance—To stay and follow compliance may be a challenge where there is increasing contractual, independent and temporary workers. Employers have to understand legalities with each category of worker.
- Building an integrated talent model—A cohesive methodology to incorporate flexible workers into the mainstream workforce will be the strategy in optimizing talent management.

The four values of agile development—adaptability, transparency, simplicity and unity can be applied easily to the HR practices. Incorporating these can help improve HR service delivery [5].

3 Alignment Areas

Alignment of human resource activities and the future needs of the business is the rule; in strategizing growth and sustainability of most of the organizations, Agility in the context of HR means driving the HR practices that creates adaptability, develops competitive advantage, brings in innovation, collaboration and speed in managing the projects. Organizations are radically changing their approach on managing performance and evaluating talent, developing the skills that emphasize and develop radical approaches in recruitment and rewards, and the ways to facilitate learning.

4 Talent Acquisition and Management

Agility in talent management is the new requirement for HR leaders. Agile talent acquisition (TA) is the next generation framework, and operating model for recruiting in the digital era applying the incremental and iterative work cycle and framework from agile can add value to talent acquisition in a multitude of ways [10]:

- Increase speed and efficiency
- Enhance the quality of an organization's talent pool
- Reduce wasted cost and resources
- Decrease cycle time
- Increase predictability
- Prioritize to deliver the highest value first
- Improve the experience of candidates and hiring managers.

Infusing Agile into an organization's talent acquisition and recruiting functions needs to be coupled with an assessment of skills and a review of the pre-existing perceptions and expectations of the business [10].

HR needs to have more flex and flow in organizations. To meet the current needs and drive the organization strategically HR should re-design, expand or eliminate the roles. HR has to develop strategies to identify people that are open and can adapt swiftly, who can be resourceful, who can be resilient to changes, who can remain rational in uncertain situations and who can perform under pressure and any circumstances. These are the capabilities that are essence of agility which has to be identified and nurtured.

HR has to devise and align its strategies to identify and track the candidates who can survive in an agile work environment. GE, IBM and Cisco are working with the vendors to create software's that do this.

5 Performance Appraisal

The core competitive advantage of any business lies in its performance management system (PMS). An organization can become agile and responsive, with a flexible PMS that ensures sustained business performance that results from continuous performance of employees. The compensation and reward system in an organization should also be flexible and aligned to the flexible PMS.

In agile organizations where individuals work on short-term projects of various lengths, yearly performance feedback from one boss, looks archaic. In agile organization, the focus will be on delivering continuous feedback so that teams become swifter and "course-correct" mistakes, enhance performance and learn through continual iterations. These are the key agile principles.

The appraisal processes should be tailored to cater the groups' needs. The new norm of continual and instant feedback should be enabled through technology HR that requires a paradigm shift towards planning and enabling a PMS that supports agility.

6 Learning and Development

HR has to completely revamp its training and development process. Traditional, L and D approach was focussed on successional planning where the archetype top-down approach and long-term planning was the best practice. In agile environment, cross-training on various tools and practices, inter-departmental skill sharing is the standard.

HR has to create an inventory matrix of the available skills and the needed skills, bridge the gap between knowledge and expertise to build the capabilities critical to

the organization's future. The focus should be to identify and grow leaders from all levels of the organization to act as coaches and not just be the managers.

To create an effective learning strategy, it should reflect the essence of the organizations strategy with particular attention around how to engage talent. The 4C's model covered in learning strategy for the C suite includes: capability; capacity; compliance and culture. Implementation of learning has to focus on the capability development that leverages a robust framework. A library that can provide accessible on-line and off-line content should be created [11].

Agile HRM should accentuate towards newer approaches that utilizes data analysis for identifying the skills required for niche jobs and for career advancements. It should sensitize employees about the individual training needs and futuristic jobs, based on the individual experience and interest [12]. By combining a neuroscientific approach through short games based on "behaviours and traits", making the players determine internal traits and behaviours as part of best practice they would like to cultivate, attract or avoid. HR has to focus on developing individualized training suites for employees as a part of its agile transformation.

7 Compensation

Pay in agile context is changing as well. In an agile work culture, compensation has to reinforce and reinstate in individuals the agile values of learning and knowledge sharing. Pay structuring should reflect individuals' impact on the business. The compensation system should adequately address the needs of the employee and the business. It should have multiple components to cater individual choice and needs. The flexible compensation system should support and align with business fluctuations and should also cater to the needs of employees [11].

8 Building High-Performance Team

The strength of agile transformation is on its small self-managed teams. The self-managed teams have to focus on creating customer delight, bring a culture of building value and innovation in the products and services and build a bold and complementing vision for people management. Agile transformation does not just mean improvements in HR process, but requires a fundamental shift in the kind of management [13].

Organizations are now organizing their work around the projects by organizing into small, high-performance teams that set flexible own targets. Agile teams usually create, execute and review their goals and tasks with scrums. Scrums help to adapt quickly to new information that it comes in and redesign. These teams track their progress effectively, identify obstacles quickly, assess their leadership diligently and

generate performance improvement insights. A multi-directional, multi-level feedback are required to be in practice among peers, and decisions have to be made upfront. Managers should be responsive and sensitive to manage the complex team dynamics. Reaching the "more Agile" vision becomes essential to a HR team that has turned Agile.

9 The Agile HRM Model

The aim of this paper is to put into perspective the functional areas within HR that needs attention into evolving as an agile HR operation. The model for Agile HRM shows the need for self-managed smaller teams enabled with technology that can cater to individual HR functions. These functions individually have their own capabilities, boundaries and functionalities. They holistically make an Agile HRM but are intrinsically linked to one another.

This model is an output of the literature review on Agile HR practices and experiments carried out by consultants in organizations. Based on the understanding from various sources of information, the model was developed to collate and establish relationships in building a framework of one HR.

Technology should drive the processes, and the process has to align with each other on a technology enabled platform. Flexibility and adaptability with scope for iterations should be the focus of one HR (Fig. 1).

10 Conclusion

HR has not changed much in recent decades when compared to the line operating system it supports. But now as the operating levels are turning agile, the pressure is on for HR to move away from old practices that are redundant. To cope with the changing competition, the organization needs to have agile workforce [14]. The readiness for change is necessary for workforce [15]. The HR function will also require re-skilling. With cloud technology and the performance data generated by the new apps, HR requires more expertise in IT skills and deeper knowledge about people management skills in teams. It is essential to the new world HR that has to undergo transformation to become more agile itself and also catalyze the organization to become agile. The role of HR as an agile driver and enabler is expanding, and HR function needs to transform itself to meet the new norms of business. More academic research in this area can provide insights towards model development and methods of scaling effectiveness.

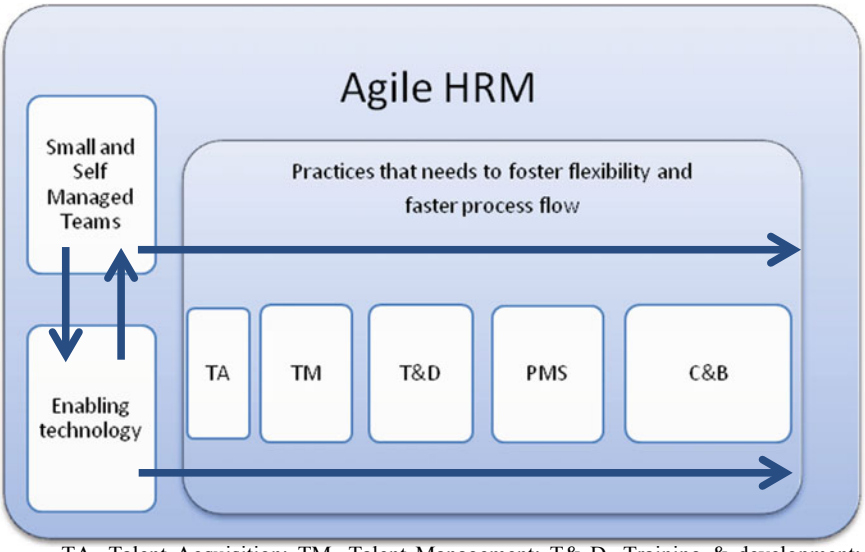

TA- Talent Acquisition; TM- Talent Management; T& D- Training & development; PMS- Performance Management systems; C&B- Compensation and Benefits

Fig. 1 One HR—a unified model for agile HRM

References

1. Hellstorm R (2016)The best definition of #AGILEHR (so far). https://peoplegeeks.net/2016/09/the-best-definition-of-agile-hr-so-far/. Accessed on 1 Nov 2018
2. Haberman M (2017) "Agile HR" means looking ahead. https://workology.com/agile-hr-means-looking-ahead/#comments. Accessed on 1 Nov 2018
3. Cappelli P, Tavis A (2018) HR goes agile. Harv Bus Rev 96(2):46–52
4. Tarken W (2016)What is HR agility? what's your definition? 5 July 2016. https://www.linkedin.com/pulse/what-hr-agility-whats-your-definition-wayne-tarken-csm-sphr/. Accessed on 1 Nov 2018
5. Kreissl B (2012) What is agile human resources? Learning from agile software development methodologies. https://www.hrreporter.com/columnist/hr-policies-practices/archive/2012/04/24/what-is-agile-human-resources/. Accessed on 1 Nov 2018
6. Huzooree G, Ramdoo VD (2015) Review of effective human resource management techniques in agile software project management. Int J Comput Appl 114(5):10–15
7. Gothelf J (2017) How HR can become agile (and why it needs to). https://hbr.org/2017/06/how-hr-can-become-agile-and-why-it-needs-to. Accessed on 1 Nov 2018
8. Srivastava R (2017) An agile approach takes HR to a whole new level of responsiveness, #StrategicHR, Mar 2017. https://www.peoplematters.in/article/strategic-hr/an-agile-approach-takes-hr-to-a-whole-new-level-of-responsiveness-15119. Accessed on 1 Nov 2018
9. Gaul P (2017) Highly agile workforce requires change in talent development**,** June 2017. https://www.td.org/magazines/td-magazine/highly-agile-workforce-requires-change-in-talent-development. Accessed on 1 Nov 2018
10. Putterman D (2018) Agile TA: the next generation operating model for talent acquisition, 18 Apr 2018. https://www.linkedin.com/pulse/agileta-next-generation-operating-model-talent-dave-putterman. Accessed on 1 Nov 2018

11. Srivastava P (2016) Flexible HR to cater to VUCA times. Glob J Flex Syst Manag 17(1):105–108
12. Fletcher A (2017) The demand for an agile, innovative workforce. Train Dev 44(4):28
13. Denning S (2018) The emergence of agile people management. Strat Leadersh 46(4):3–10
14. Patil M, Suresh M (2019) Modelling the enablers of workforce agility in IoT projects: a TISM approach. Glob J Flex Syst Manag 20(2):157–175
15. Vaishnavi V, Suresh M, Dutta P (2019) Modelling the readiness factors for agility in healthcare organization: a TISM approach. Benchmark Int J 26(7):2372–2400

Assessment of Organizational Agility Using Multi-grade Fuzzy: A Case of Adhesives Manufacturing Organization

Aravind Hariharan and M. Suresh

Abstract Ability of the technology, people, processes, work, production, logistics, safety and support functions of an organization to respond to crisis situations, adapt to changes in the market and use the change as a competitive advantage as quick as possible before the competitors respond is termed as organizational agility. The more it is, the more agile the organization is, which clearly means that the organization can sustain in the long-run. This paper attempts to develop an assessment framework for organizational agility using Multi-grade Fuzzy (MGF) approach. The framework has been applied to the Adhesives Manufacturing Organization (AMO). The agile attributes are classified based on Importance-Performance Analysis (IPA). The study indicates that the case organization become 'agile' but has scope for improvement. The case organizations' weaker attributes are identified through IPA method and appropriate suggestions have been provided that for improvement.

Keywords Organizational agility · Manufacturing organization · Agile systems · Multi-grade fuzzy · Importance performance analysis

1 Introduction

The Adhesives and Sealants market in India is consolidated, with the major players at the top of the Industry with more than 80% market share in that sector. In such a market, competition among the players who try to capture the remaining share in the market is cut-throat. In a market where competitors can innovate their processes, take strategic decisions to change the product line, strategic price changes, improve quality, take cost-cutting measures etc., organizational agility plays a significant role in the survival and growth of the organizations.

Changes are going to be certain and the resilience of the organization is of utmost importance. The organizations must be able to use the impact for its betterment and come up steadier and stronger. Assessment of organizational agility will help

A. Hariharan · M. Suresh (✉)
Amrita School of Business, Amrita Vishwa Vidyapeetham, Coimbatore, India
e-mail: drsureshcontact@gmail.com

G. Kumaresan et al. (eds.), *Advances in Materials Research*, Springer Proceedings in Materials 5, https://doi.org/10.1007/978-981-15-8319-3_72

the organization to find the agility level and identify the weaker attributes of that organization. Assessment helps the organization to improve agility level from current stage to future stage. To ensure the organization is agile enough for its survival and there-by enabling it to thrive in a competitive environment without the fear of succumbing to market pressures and crisis.

2 Literature Review

Ability of the technology, people, processes, work, production, logistics, safety and support functions of an organization to respond to crisis situations, adapt to changes in the market and use the change as a competitive advantage as quick as possible before the competitors respond is termed as organizational agility. The more it is, the more agile the organization is, which clearly means that the organization can sustain in the long-run. Gunasekaran [1] developed agile implementation framework and indentified key agile enablers for manufacturing organizations. Dahmardeh and Banihashemi [2] proposed that the crucial concepts of agile manufacturing are responding to changes and using them for benefit through tactical utilization of manufacturing and managerial methods. Yusuf et al. [3] formulated that the fundamental aspect of agile paradigm is to achieve competitive advantages in cohesion and without trade-offs. Surbakti et al. [4] presents organizational agility based on Goldman model with attributes such as people, organization, cooperation and customer satisfaction to assess the level of its agility [5] reasoned that people have been overlooked in the field of organizational agility because new organizational relationships and forms openly resist description with traditional words, phrases and concepts [6] used the fuzzy logic framework and proposed that an agile enterprise's foundation lies in integration of people, business processes and information technologies [7] used multi-grade fuzzy framework to propose that the contemporary organization can use sustainability assessment to survive in the market with cut-throat competition and achieve high status [8] applied fuzzy logic framework to evaluate organizational agility.

3 Conceptual Model for Assessing Organizational Agility

In order to assess the organizational agility of a case organization, literature review was initiated to find the criteria and attributes that are relevant to organizational agility. Based on these, identified factors, the conceptual model was developed. The conceptual model for assessing organizational agility is shown in Table 1. This conceptual model was derived based on three aspects of agility namely technology agility [9], operational agility [10–12] and management agility [13–16]. The model consists of three levels. The first level is the enabler, second level shows the criteria and the third level includes the respective attributes.

Table 1 Conceptual model for assessing organizational agility

Enabler	Criteria	Attributes
Technology agility (I_1)	IT integration (I_{11})	IT application to eliminate paperwork (I_{111})
		IT utilities (I_{112})
	Product development (I_{12})	Management support for new product development (I_{121})
		Concurrent product development (I_{122})
		Design for Producibility (I_{123})
		New product development team (I_{124})
Operational agility (I_2)	Workforce (I_{21})	Workplace spirituality (I_{211})
		Multi-skilled workforce (I_{212})
		Implementing job rotation (I_{213})
	Process (I_{22})	Readiness for process change (I_{221})
		Total productive maintenance (I_{222})
		Process waste elimination (I_{223})
		Maximum utilization of available equipment (I_{224})
	Flexibility (I_{23})	Flexible inventory systems (I_{231})
		Flexible production capacity (I_{232})
		Flexible automation (I_{233})
		Variety of products (I_{234})
Management agility (I_3)	Devolution of authority (I_{31})	Training to create self-managed teams (I_{311})
		Clear definition of personnel's responsibility and authority (I_{312})
	Organizational structure (I_{32})	Interchange-ability of personnel (I_{321})
		Team oriented organizational structure (I_{322})
		Positive organizational culture (I_{323})
		Smooth information flow (I_{324})
	Nature of management (I_{33})	Participative management style (I_{331})
		Transparency in information sharing (I_{332})
		Rapid evaluation and implementation of employee suggestions (I_{333})

4 Case Study

The company in which the study is carried out is an Adhesives Making Organization (AMO) located in India. AMO makes different types of adhesives and sealants for different small and medium-scale industries depending upon their requirement. The company's goal is to expand its horizons and increase its market share.

4.1 Assessment of Agility Using Multi-grade Fuzzy

Organizational Agility is denoted by 'I'. It is the product of mean weightage of the expert opinions denoted by 'W' and the overall rating factor denoted by 'R'. The equation for agility is as follows; $I = W * R$ [17, 18].

Since the calculation of agility factor includes fuzzy determination, the assessment is classified into five grades, $I = (10, 8, 6, 4, 2)$. where the range 0–2 represents that the organization is 'extremely non-agile', 2–4 represents 'non-agile', 4–6 represents 'moderately agile', 6–8 represents 'agile' and 8–10 represents 'extremely agile'. For the discussion of assessment of organizational agility, five experts from case organization were contributed for ratings. Five experts from various organizations contributed to the weightage of the enablers (W_i), criteria (W_{ij}) and attributes (W_{ijk}). The factor rating and the mean normalized weightage of the experts' opinions are captured in Table 2.

4.1.1 Primary Assessment Calculation

The calculation applied for the criteria 'IT Integration' is as shown as follows.

The weightage related to the criteria 'IT Integration' $W_{11} = (0.507692, 0.492308)$.

Rating vector related to the criteria 'IT Integration' is given by

$$R_{11} = \begin{bmatrix} 6 & 7 & 8 & 6 & 6 \\ 5 & 7 & 7 & 6 & 7 \end{bmatrix}$$

Index for the criteria 'IT Integration' is calculated as [19]

$$I_{11} = W_{11} * R_{11}$$
$$I_{11} = (5.507692,\ 7,\ 7.507692,\ 6,\ 6.492308)$$

Similarly using the same concept, the index for the other agile criteria is also computed.

$$I_{12} = (6.745762,\ 5.559322,\ 6.694914,\ 5.661018,\ 5.677966)$$
$$I_{21} = (6.234044,\ 6.425533,\ 7.904256,\ 5.648937,\ 6.319150)$$

Table 2 Rating and weightage by experts

I_i	I_{ij}	I_{ijk}	R_1	R_2	R_3	R_4	R_5	W_{ijk}	W_{ij}	W_i
I_1	I_{11}	I_{111}	6	7	8	6	6	0.50	0.50	0.29
		I_{112}	5	7	7	6	7	0.49		
	I_{12}	I_{121}	8	6	7	4	5	0.25	0.49	0.33
		I_{122}	4	5	4	5	4	0.18		
		I_{123}	8	6	7	8	7	0.30		
		I_{124}	6	5	8	5	6	0.25		
I_2	I_{21}	I_{211}	4	7	6	3	4	0.25	0.34	
		I_{212}	7	8	9	7	8	0.41		
		I_{213}	7	4	8	6	6	0.32		
	I_{22}	I_{221}	8	8	8	7	9	0.27	0.31	
		I_{222}	6	5	7	7	6	0.21		
		I_{223}	7	6	7	8	8	0.25		
		I_{224}	9	7	6	8	6	0.25		
	I_{23}	I_{231}	8	5	5	6	7	0.248	0.33	
		I_{232}	7	5	7	7	6	0.256		
		I_{233}	7	5	8	6	6	0.256		
		I_{234}	5	4	6	8	7	0.24		
I_3	I_{31}	I_{311}	6	7	7	6	9	0.47	0.30	0.37
		I_{312}	6	8	8	9	8	0.52		
	I_{32}	I_{321}	6	5	9	7	8	0.23	0.34	
		I_{322}	8	7	9	6	7	0.25		
		I_{323}	8	9	8	6	9	0.27		
		I_{324}	7	6	7	8	6	0.23		
	I_{33}	I_{331}	8	6	6	4	5	0.34	0.35	
		I_{332}	7	5	6	4	7	0.34		
		I_{333}	5	4	4	5	8	0.30		

$$I_{22} = (7.566426,\ 6.594399,\ 7.027965,\ 7.503489,\ 7.342650)$$
$$I_{23} = (6.768,\ 4.76,\ 6.52,\ 6.736,\ 6.488)$$
$$I_{31} = (6,\ 7.527027,\ 7.527027,\ 7.581081,\ 8.472973)$$
$$I_{32} = (7.287679,\ 6.835624,\ 8.260282,\ 6.705486,\ 7.554802)$$
$$I_{33} = (6.726190,\ 5.035714,\ 5.380952,\ 4.309524,\ 6.619048)$$

4.1.2 Secondary Assessment Calculation

The calculation applied for the enabler 'Technology Agility' is shown as follows.

The weightage related to the enabler 'Technology Agility' $W_1 = (0.506494, 0.493506)$.

Rating vector related to the criteria 'Technology Agility' is given by

$$R_1 = \begin{bmatrix} 5.507692 & 7 & 7.507692 & 6 & 6.492308 \\ 6.745762 & 5.559322 & 6.694914 & 5.661018 & 5.677966 \end{bmatrix}$$

Index for the criteria 'Technology Agility' is calculated as

$$I_1 = W_1 * R_1$$
$$I_1 = (6.118686,\ 6.289016,\ 7.106581,\ 5.83271,\ 6.090425)$$

Similarly using the same concept, the index for the other agility enablers is also computed.

$$I_2 = (6.833405,\ 5.914211,\ 7.160011,\ 6.599702,\ 6.697793)$$
$$I_3 = (6.695968,\ 6.414997,\ 7.024017,\ 6.131855,\ 7.507257)$$

4.1.3 Tertiary Assessment Calculation

The calculation applied for finding the value of organizational agility index of AMO is as follows.

Overall weight $W = (0.297520661, 0.330578512, 0.371900826)$.

Overall rating vector is given by R

$$R = \begin{bmatrix} 6.118686 & 6.289016 & 7.106581 & 5.83271 & 6.090425 \\ 6.833405 & 5.914211 & 7.160011 & 6.599702 & 6.697793 \\ 6.695968 & 6.414997 & 7.024017 & 6.131855 & 7.507257 \end{bmatrix}$$

Agile index $I = W * R$

$$I = (6.569654,\ 6.211972,\ 7.093545,\ 6.197519,\ 6.818135)$$
$$I = (6.569654 + 6.211972 + 7.093545 + 6.197519 + 6.818135)/5$$
$$I = 6.578165$$

4.2 Importance Performance Analysis

IPA approach is used to classify the attributes of organizational agility. IPA approach is graphically represented by four quadrants [20]. These quadrants are splits based on the average of the mean weightage of experts' opinion and the average of the mean assessment rating of attributes [21]. The four quadrants and the inference of IPA is described in Table 3.

5 Results and Discussions

Agility Index of AMO was computed to be 6.578165. It means that the organizational agility of AMO falls in the category of 6–8, which proves that the organization is 'agile'. AMO is an agile organization but there is skill scope for improving its organizational agility to reach the category of 8–10 which will make the organization, 'highly agile'.

In the IPA the attributes were placed in four quadrants according to the expert weightage and performance and it was found that majority of the attributes are considered significant and weighed high by the experts. IT utilities, management support for new product development, concurrent product development, new product development team, implementing job rotation, total productive maintenance, participative management style, transparency in information sharing and rapid evaluation and implementation of employee suggestions were the attributes where AMO needs to improve its performance. These attributes lie in the quadrant-I.

Table 3 Quadrants and inference of IPA

Quadrants	Inference
Quadrant-I improve performance	This is the area that is categorized as most significant by experts but performance is not up to the mark here. If the performance is improved in these attributes, organizational agility will definitely be high
Quadrant-II maintain and retain	This area also falls under the categorization of most significant according to experts, and AMO's performance in these attributes is already very well. AMO should try to maintain and retain this
Quadrant-III not very significant	Neither this area is significant according to experts nor is the performance high. This area need not be under high priority
Quadrant-IV excess performance	This area is not very significant according to experts. But the performance is high. AMO can divert resources and efforts from this area and focus on quadrant-I for better results concerning Organizational Agility

IT Application to eliminate paperwork, design for producibility, multi-skilled workforce, readiness for process change, maximum utilization of available equipment, training to create self-managed teams, interchange-ability of personnel and team-oriented organizational structure are the attributes where AMO is doing well and has to maintain and retain it. These attributes lie in the quadrant-II.

Process waste elimination, Clear definition of personnel's responsibility and authority, Positive organizational culture and Smooth information flow are the attributes which are not very significant but AMO has high performance in these agile factors. If AMO can channel its efforts from quadrant-IV to quadrant-II it can improve its organizational agility significantly.

Workplace spirituality, flexible inventory systems, flexible production capacity, flexible automation and variety of products are the attributes which are regarded not-very-significant and AMO's performance is also not very high. This is quadrant-III and much focus is not required here.

5.1 Improvement Proposal for the Weaker Attributes

Adapt to the changing market: Instead of developing all the attributes in one go, AMO can see which attributes contribute the most towards organizational agility in the current market conditions and focus on development to those attributes.

Channelizing the efforts and resources: In quadrant-IV, attributes are not very significant for organizational agility. The AMO can channel the effort and resources away from these attributes and concentrate on the development of crucial attributes for organizational agility.

Cost–Benefit Analysis: AMO can perform a cost–benefit analysis to identify the attributes where performance can be increased with comparatively lesser cost but which contributes the most to the organizational agility.

6 Conclusion

This paper focuses on assessment of organizational agility in an AMO. The methodology used was multi-grade fuzzy approach. The attributes that contribute to organizational agility, were rated by staff members of AMO and expert opinions was taken to measure the importance of the attributes. The case AMO's organizational agility falls in the category of 'Agile'. IPA approach was used to segregate the attributes into four quadrants and making the AMO aware of the actions needed/not needed to increase the strength of the attribute, ultimately increasing the organizational agility. This study can also be expanded to other organizations in Adhesives and Sealants industries sector.

References

1. Gunasekaran A (1998) Agile manufacturing: enablers and an implementation framework. Int J Prod Res 36(5):1223–1247
2. Dahmardeh N, Banihashemi SA (2010) Organizational agility and agile manufacturing. Eur J Econ Financ Administr Sci 27:178–184
3. Yusuf YY, Sarhadi M, Gunasekaran A (1999) Agile manufacturing: the drivers, concepts and attributes. Int J Prod Econ 62(1–2):33–43
4. Surbakti E, Azwir HH, Taslim A (2018) Application of fuzzy logic and importance performance analysis in assessing organizational agility of PT. IF heavy equipment distributor. J Adv Res Dynam Control Syst 11(05):319–331
5. Crocitto M, Youssef M (2003) The human side of organizational agility. Ind Manag Data Syst 103(6):388–397
6. Lin CT, Chiu H, Tseng YH (2006) Agility evaluation using fuzzy logic. Int J Prod Econ 101(2):353–368
7. Vinodh S (2011) Assessment of sustainability using multi-grade fuzzy approach. Clean Technol Environ Policy 13(3):509–515
8. Yaghoubi NM, Kord B, Azadikhah O (2011) Assessing organizational agility via fuzzy logic. Int Bus Res 4(3):135–144
9. Suresh M, Patri R (2017) Agility assessment using fuzzy logic approach: a case of healthcare dispensary. BMC Health Serv Res 17(1):394
10. Suresh M, Ganesh S, Raman R (2019) Modelling the factors of agility of humanitarian operations. Int J Agile Syst Manag 12(2):108–123
11. Patri R, Suresh M (2017) Modelling the enablers of agile performance in healthcare organization: a TISM approach. Glob J Flex Syst Manag 18(3):251–272
12. Patil M, Suresh M (2019) Modelling the enablers of workforce agility in IoT projects: a TISM approach. Glob J Flex Syst Manag 20(2):157–175
13. Vinodh S, Kumar VU, Girubha RJ (2012) Thirty-criteria-based agility assessment: a case study in an Indian pump manufacturing organisation. Int J Adv Manufact Technol 63(9–12):915–929
14. Gayathri K, Suresh M (2018) Modelling the factors of agile practices in project management: a case of illumination project organization. Int J Eng Technol 7(2.33):541–547
15. Vaishnavi V, Suresh M, Dutta P (2019) Modelling the readiness factors for agility in healthcare organization: a TISM approach. Benchmark Int J 26(7): 2372–2400
16. Patri R, Suresh M (2019) Agility in healthcare services: a systematic literature exploration. Int J Serv Oper Manag 32(3):387–404
17. Vinodh S, Prasanna M (2011) Evaluation of agility in supply chains using multi-grade fuzzy approach. Int J Prod Res 49(17):5263–5276
18. Ganesh J, Suresh M (2016) Safety practice level assessment using multigrade fuzzy approach: a case of Indian manufacturing company. In: 2016 IEEE international conference on computational intelligence and computing research (ICCIC). IEEE, Dec 2016, pp 1–5
19. Sridharan V, Suresh M (2016) Environmental sustainability assessment using multigrade fuzzy—a case of two Indian colleges. In: 2016 IEEE international conference on computational intelligence and computing research (ICCIC). IEEE, Dec 2016, pp 1–4
20. Deng WJ (2008) Fuzzy importance-performance analysis for determining critical service attributes. Int J Serv Ind Manag 19(2):252–270
21. Feng M, Mangan J, Wong C, Xu M, Lalwani C (2014) Investigating the different approaches to importance–performance analysis. Serv Ind J 34(12):1021–1041

Advertising Media Selection Framework Using Fuzzy VIKOR Approach: A Case of New Insurance Product

M. Suresh and Deepak Joshy

Abstract Appropriate advertising strategies or media determine the potential customer reach, adaptability and acceptability, and help the brand image to attain competitive advantage. The selection of the advertising media is a challenging task, and furthermore, the complexity increases when it comes to the promotion of new product to the market. In this paper, an attempt has been made to develop a framework for the selection of suitable advertising media for the release of a new insurance product using fuzzy VIKOR (meaning is multicriteria optimization and compromise solution) method. The case of this new insurance product is presented to exhibit the applicability of the fuzzy VIKOR method. The result of this study shows that it could be applied in new product promotion stage to accelerate a customer's purchase intention through appropriate media mix.

Keywords Fuzzy VIKOR · Media selection · Advertising media · Advertising strategies · Insurance products

1 Introduction

There are several works which have analysed the importance of advertising. Still, advertisers are in a dilemma whether to have a soft-sell or hard-sell approach in various media to promote goods or services through advertisements. India is one of the emerging economies in the global market, and particularly after the 1990s, India's growth in the consumer market is tremendous. As the second highest populated country, India is a target market for producers worldwide. The main tool which assists any manufacturer to reach his customers is advertising. These days, we see advertisements for anything and everything from a bar of soap to a cup of tea. But the

M. Suresh (✉) · D. Joshy
Amrita School of Business, Amrita Vishwa Vidyapeetham, Coimbatore, India
e-mail: drsureshcontact@gmail.com

D. Joshy
e-mail: deepakjoshy007@gmail.com

G. Kumaresan et al. (eds.), *Advances in Materials Research*, Springer Proceedings in Materials 5, https://doi.org/10.1007/978-981-15-8319-3_73

question remains, do these advertisements fulfil what they are aimed at? Do they use the right kind of appeal? Through which medium should they advertise their product? Are they really effective? To what extent do these advertisements drive a consumer to purchase a product? Thus, any advertisement should accomplish its objectives while simultaneously adhering to the social and cultural diversity of India. In this paper, a selection of advertisement media in television, radio, newspaper/magazine, outdoor and Internet advertising have been studied through literatures, and an attempt has been made to develop a framework for media selection. A case of selection of a suitable medium of advertising for an insurance product is presented in this paper.

2 Literature Review

The literature has been reviewed from the perspective of various advertising media and media mix strategies. Wysong and Beldona [1] have studied the billboard advertising media and its effective reach to targeted audiences. Jackson et al. [2] discussed sport advertising with reference to the cross-cultural differences. Jackson [3] has studied the relationship between advertising and sales income. Smith [4] has discussed the significance of Advergames strategy. Barnes and Hair [5] have discussed the advertising paradigm shifts from the banners to Internet media and its futuristic direction. Also, they studied the chronology of Internet adverting media strategy from 1994 to 2007. Chtourou et al. [6] have studied the effects of advertising through the animation in the internet media. Walsh [7] has studied the avoidance behaviour of Internet advertisements. Coyle et al. [8] studied the effectiveness of word-of-mouth marketing. Drossos et al. [9] have extensively studied the factors influencing Internet advertising and related efficiency in the perceptions of advertising agencies. Pan et al. [10] have studied the inter-relations between mass media advertising and its impacts on revenue generation in the airline industry. They have also proposed a network optimization model for advertising revenue management. Rehman and Vaish [11] have studied the blend of various traditional and new media advertising practices to achieve the media effectiveness and adaptability. Aouni et al. [12] have applied a stochastic goal programming model for selection of suitable media. Dasgupta and Gupta [13] have analysed the critical success factors in experimental markets and a related case study is presented based on seventeen Indian restaurants. Kamal and Chu [14] have studied social media usage in young customers in Dubai and have also examined adverting behaviours in social media. Raj et al. [15] have studied the performance evolution of Adstock models in the consumer packaged goods industry. Adzharuddin [16] has conducted an extensive literature review on the new and traditional advertising media mixes. Azadi et al. [17] have developed a neutral data envelopment analysis model for media selection. Cader and Al Tenaiji [18] have conducted a survey for social media marketing in UAE. Lohtia et al. [19] have studied the presence of impacts of advertising and blogger trustworthiness. Rau et al. [20] have studied mobile media advertising and have extensively identified the critical factors influencing the customers to the avoidance

of this media advertisement. Nilakantan [21] has studied the strategy of television advertisements. Olga and Raj [22] studied the linkages between tourism promotion adverting through social media and the changes of consumer behaviours regarding the tourism destinations. Park and Ohm [23] have studied the impacts of customer attitudes and purchase intentions on mobile advertisements. Qureshi [24] has analysed the advertising expenditure with respect to various media and also studied the valuation effects in different media in UK firms.

Selecting the right media to advertise a product is extremely important in the promotion of their product and thereby overall business. It is not necessary that all advertisements should represent details which help consumers to choose a product. There are several researches that focused on the criteria that should be considered while evaluating advertisement effectiveness. Criterion of this sense includes educational level [25–27] and user-friendliness design [28]. This paper considers the following media, viz. newspapers, television, Internet, radio, outdoor advertising, i.e. these were the media adopted for this study based on the literature survey [29–31].

3 Case Study

The case study has been piloted in a new life insurance product advertisement. There exists a necessity to select the best advertising medium for a new insurance product among the available alternatives. A new insurance product is selected as the case study because the importance of having insurance is immense. Also, we will get to know the best medium to advertise a new insurance product. It has the double benefits of saving and security. Life is full of uncertainties so we can protect it from any unforeseen events that may happen. It also acts as a safe and profitable long-term investment which has tax benefits and generates income through annuities, dividends, etc. In most of the developed foreign countries, insurance is a must. All classes of people can benefit from having insurance coverage. Table 1 depicts the advertising media selection factors.

In this study, best advertising strategy for a life insurance product is found out using the fuzzy VIKOR model of multicriteria decision-making methods. The key benefit of the VIKOR method is that it emphasizes on classification and assortment from a set of alternatives in the presence of differing criteria. It introduces the ranking index based on the particular degree of closeness to the best solution as well. The alternatives for advertisements are television ad (A_1), radio ad (A_2), Internet ad (A_3), newspaper/magazine ad (A_4) and outdoor ads (A_5). Based on the evaluation, criterion optimization directions are determined. Based on the feedback collected from the five decision-makers, the best advertising medium has been found out. The decision-makers include southern head of a public sector insurance company; two postgraduate students in advertising and media studies and another two experts in the insurance field. Here, the weights of various criteria and the ratings are considered as linguistic variables as it can assess the independent opinion of decision-makers. The linguistic

Table 1 Factors influencing the advertising media selection

Criteria	Attributes of the criteria
Audience fit (C_1)	**Age**: Feel good effect, visual imagery based on age, ageing and emotional, older and rational; ageing and interest towards ads
	Gender: Usual perception that females are more likely to perceive soft-sell. Cross-cultural differences, intention to purchase
	Educational Background: Less educated more likely to believe TV ads. Knowledge that holds is important
Advertisement irritation (C_2)	Younger people less irritated, depends on interaction, time spent in watching ads
Purchase intention (C_3)	Credibility of the ads, the appeal that the ad creates, how well the message is conveyed
Advertisement believability (C_4)	Easiness to understand, matching requirements, creating a favourable image, trustworthy, exaggeration etc
Product brand (C_5)	Mentioning brand or product, placement of brand and awareness
Time of advertisement (C_6)	Geographical and cultural differences, prime time ads, max reach of ads through proper time and location
Cultural differences (C_7)	Different countries different perceptions, emotions, beliefs, etc.
Cost of advertising (C_8)	Amount spent: prime time ads, location, size of ads, etc.
Coverage (C_9)	Selectivity, pass along frequency range, target reach, etc.

variables and their fuzzy numbers are shown in Table 2. The fuzzy VIKOR approach is adopted from [32] and [33] for selection of the advertising media.

Five decision-makers D1 to D5 have given weights for each criterion. They have used the linguistic variables to give weights to understand the importance of the criteria. The respective weights of the criteria by the decision-makers are shown in Table 3.

Also another five decision-makers have given ratings for the five alternatives with respective to each criterion using the linguistic rating variables, and it is shown in

Table 2 Linguistic variables for significance of every criterion [34]

Linguistic variable	Fuzzy number
Very poor (VP)	(0.0, 0.0, 0.1, 0.2)
Poor (P)	(0.1, 0.2, 0.2, 0.3)
Medium poor (MP)	(0.2, 0.3, 0.4, 0.5)
Fair (F)	(0.4, 0.5,0.5, 0.6)
Medium good (MG)	(0.5, 0.6, 0.7, 0.8)
Good (G)	(0.7, 0.8, 0.8, 0.9)
Very good (VG)	(0.8, 0.9, 1.0, 1.0)

Table 3 Weights of the criteria provided by decision-makers

Criteria	Decision-makers				
	D_1	D_2	D_3	D_4	D_5
C_1	G	G	VG	VG	VG
C_2	F	MP	G	VG	F
C_3	G	VG	VG	VG	G
C_4	G	G	MG	VG	F
C_5	G	VG	MG	G	G
C_6	VG	VG	G	F	VG
C_7	G	G	VG	G	G
C_8	MG	G	MG	VG	MG
C_9	G	G	G	VG	G

Table 4. The decision-maker's judgements are analysed to get the aggregated fuzzy weight of each criterion, and fuzzy decision matrix was constructed using aggregated fuzzy ratings of alternatives [32]. Aggregated fuzzy ratings $b_{ij} = \{b_{ij1}, b_{ij2}, b_{ij3}, b_{ij4}\}$.

The fuzzy decision matrix is constructed, and then, it is defuzzified and fuzzy weight of each criterion is converted into crisp values using centre of average defuzzification relation [33]. The values of S, R and Q are calculated for all alternatives and presented in Table 5.

4 Results and Discussions

According to the results from fuzzy VIKOR analysis of selecting the best alternative (smallest Q value is the best ranking) for the advertisement of an insurance product, it is shown that advertising in television (A_1) has got more effect on consumers followed by newspaper/magazine advertisements (A_4), radio ads (A_2), Internet ads (A_3) and outdoor ads (A_5) respectively. According to the results, the top two alternatives can send custom-made messages to narrowly defined and segmented target audiences, which show their efficiency. The main limitation of this research is the lack of broader variety of products and the cross-cultural validation for greater generalizability.

5 Conclusion

Different products are bought and used up for diverse reasons, and hence, the objectives related to endorsing the goods may be different from those associated with promoting another product. Product life cycle is an important factor that which affects the strategy of advertising a particular product. The advertising objective at the time

Table 4 Rating of five alternatives by decision-makers under the criteria

Decision-makers	Alternative	C_1	C_2	C_3	C_4	C_5	C_6	C_7	C_8	C_9
K_1	A_1	G	MG	G	VG	G	VG	G	G	G
	A_2	G	F	G	G	G	G	G	MG	MG
	A_3	G	F	G	VG	G	G	MG	F	VG
	A_4	G	MG	G	G	G	MG	G	MG	G
	A_5	G	MP	MG	G	G	F	G	G	MG
K_2	A_1	VG	F	VG	G	F	VG	VG	MG	VG
	A_2	G	MG	G	VG	G	VG	G	P	G
	A_3	MG	F	F	MP	P	VP	MP	P	F
	A_4	VG	F	G	G	MG	F	VG	F	MG
	A_5	F	P	F	MP	P	F	VG	MG	MP
K_3	A_1	G	G	VG	G	G	VG	MG	G	VG
	A_2	G	MG	G	F	G	F	P	G	G
	A_3	MG	MP	G	G	MP	MG	P	MG	MG
	A_4	G	F	G	G	MG	G	MG	MG	G
	A_5	MP	G	MG	G	F	P	P	F	G
K_4	A_1	VG	VG	VG	VG	VG	VG	VG	VG	VG
	A_2	MG	G	MG	F	VG	G	VG	MG	MP
	A_3	VG	G	MG	G	VG	P	VG	MG	G
	A_4	G	MG	G	F	VG	P	VG	F	G
	A_5	MG	MP	MP	F	VG	VP	VG	F	MG
K_5	A_1	G	G	G	G	VG	VG	F	G	G
	A_2	P	VP	MG	MG	MG	P	P	MG	F
	A_3	MG	MG	MG	G	MP	MP	F	MG	MG
	A_4	G	MG	MG	G	F	F	F	MG	G
	A_5	MG	MG	MG	MG	G	G	VP	VG	G

Table 5 Values of S, R and Q for all alternatives

	A_1	A_2	A_3	A_4	A_5
S	0.082	4.93	5.39	2.87	6.25
R	0.082	0.85	0.84	0.63	0.87
Q	0.00	0.88	0.91	0.57	1.00

of the introduction of the product will be to build awareness, whereas during the growth and maturity of the product, it will be to generate further interest. Publicizing as well as communicating objectives will vary from the time before the launch to the time at which the end of the particular product in the market occurs. Certain media will be more effective in promoting certain products; everything won't go in a single

method of advertising. So in all these cases, different mediums of advertising have their own importance. Some advertisements can easily create brand awareness, while some other can certainly affect the building of customer loyalty and so on. Different ways of advertising in different mediums have their own importance in the promotion, life cycle, etc. of a particular product. There are indeed an extensive group of customized market segments, so it is important for one to know about the segments and strategies that can be implemented in different market segments before planning of promotion of a product. This research represents the selection of the best medium of advertising before the plan to promote their product in the market is made. In summary, the effectiveness of advertising in different mediums was measured for an insurance product, and the best alternative was found out. Fuzzy VIKOR analysis is a significant and manageable instrument that can be effectively employed by marketing specialists when considering the issue of which mass media will be the most fitting for promotion of a specific product.

References

1. Wysong S, Beldona S (2004) When should a firm use billboard advertising? A conceptual look at differing levels of recall. J Int Bus Entrepreneurship Dev 2(2):91–98
2. Jackson SJ, Brandl-Bredenbeck HP, John A (2005) Lost in translation: cultural differences in the interpretation of violence in sport advertising. Int J Sport Manage Mark 1(1):155–168
3. Mangani A (2007) The optimal ratio between advertising and sales income. Int J Revenue Manage 1(1):65–78
4. Smith AD (2007) Exploring advergaming and its online advertising implications. Int J Bus Inf Sys 2(3):298–311
5. Barnes S, Hair N (2009) From banners to youtube: using the rear-view mirror to look at the future of internet advertising. Int J Int Mark Adv 5(3):223–239
6. Chtourou MS, Choura Abida F (2010) What makes one animation more effective than another? An exploratory study of the characteristics and effects of animation in internet advertising. Int J Int Mark Adv 6(2):107–126
7. Walsh MF (2010) New insights into what drives internet advertising avoidance behaviour: the role of locus of control. Int J Internet Mark Advertising 6(2):127–141
8. Coyle JR, Smith T, Lightfoot E, Neace W, Platt G (2011) 'Click here to share with a friend': a uses and gratifications approach to word-of-mouth marketing effectiveness. Int J Electron Mark Retailing 4(4):225–247
9. Drossos DA, Fouskas KG, Kokkinaki F, Papakyriakopoulos D (2011) Advertising on the internet: perceptions of advertising agencies and marketing managers. Int J Internet Mark Advertising 6(3):244–264
10. Pan K, Leung SCH, Xiao D (2011) A linear programming model to revenue management for advertising in mass media. Int J Revenue Manage 5(2–3):145–156
11. Rehman V, Vaish A (2011) Media mix: a pragmatic solution for advertising complexities. Int J Manage Pract 4(4):345–359
12. Aouni B, Colapinto C, La Torre D (2012) Stochastic goal programming model and satisfaction functions for media selection and planning problem. Int J Multicriteria Decis Making 9 2(4):391–407
13. Dasgupta S, Gupta S (2011) Critical success factors for experiential marketing: evidences from the Indian hospitality industry. PRIMA: Pract Res Mark 1(2):8–19

14. Kamal S, Chu SC (2012) Beliefs, attitudes, and behaviours toward advertising on social media in the Middle East: a study of young consumers in Dubai, United Arab Emirates. Int J Internet Mark Advertising 7(3):237–259
15. Raj KAAD, Kanagasabapathi B, Shrivastava S, Krishnan K, Shah M (2012) Performance evaluation of Adstock models using market drivers in the consumer packaged goods (CPG) industry. Int J Electron Mark Retailing 5(2):173–186
16. Adzharuddin, N. A. (2013). Marketing mix through the integration of new and traditional media: a review of recent literature. Int J Soc Entrepreneurship Innov 2 2(1):3–10
17. Azadi M, Saen RF, Momeni E (2013) Developing a new neutral DEA model for media selection in the existence of imprecise data. Int J Oper Res 18(1):16–34
18. Cader Y, Al Tenaiji AA (2013) Social media marketing. Int J Soc Entrepreneurship Innov 2(6):546–560
19. Lohtia R, Donthu N, Guillory MD (2013) The impact of advertising, trustworthiness, and valence on the effectiveness of blogs. Int J Electron Mark Retailing 5(4):317–339
20. Rau PLP, Liao Q, Chen C (2013) Factors influencing mobile advertising avoidance. Int J Mobile Commun 11(2):123–139
21. Nilakantan R (2014) Advertising, programme choice, and competition concerns in a mixed duopoly television broadcast industry. Int J Econ Bus Res 8(3):309–323
22. Olga LP, Raj R (2013) Evolution of Social Media and Consumer Behavior Changes in Tourism Destination Promotion. Int J Sales Retailing Mark 2(2):31–39
23. Park E, Ohm J (2014) The impacts of media type, placement and exposure type on attitudes towards advertisements on mobile devices. Int J Mobile Commun 12(2):160–176
24. Qureshi MI (2015) Valuation of various media advertising expenditures-UK perspective. Int J Acc Auditing Perform Eval 11(1):1–13
25. Fraenkel JR, Wallen NE, Hyun HH (2011) How to design and evaluate research in education. McGraw-Hill, New York
26. Strasser AA, Tang KZ, Romer D, Jepson C, Cappella JN (2012) Graphic warning labels in cigarette advertisements: recall and viewing patterns. Am J Prev Med 43(1):41–47
27. Brown RS (1978) Estimating advantages to large-scale advertising. Rev Econ Stat 428–437
28. Kim J, McMillan SJ (2008) Evaluation of internet advertising research: a bibliometric analysis of citations from key sources. J Adv 37(1):99–112
29. Johar GV, Sengupta J, Aaker JL (2005) Two roads to updating brand personality impressions: trait versus evaluative inferencing. J Mark Res 42(4):458–469
30. Keller KL, Lehmann DR (2006) Brands and branding: Research findings and future priorities. Mark Sci 25(6):740–759
31. Krugman HE (1965) The impact of television advertising: learning without involvement. Pub Opin Q 29(3):349–356
32. Opricovic S, Tzeng GH (2004) Compromise solution by MCDM methods: a comparative analysis of VIKOR and TOPSIS. Eur J Oper Res 156(2):445–455
33. Vinodh S, Varadharajan AR, Subramanian A (2013) Application of fuzzy VIKOR for concept selection in an agile environment. Int J Adv Manuf Technol 65(5–8):825–832
34. Vinodh S, Nagaraj S, Girubha J (2014) Application of Fuzzy VIKOR for selection of rapid prototyping technologies in an agile environment. Rapid Prototyping J 20(6):523–532

Modelling the Factors of Store Environment on Impulse Buying Behavior Using TISM

M. Suresh and R. Dev Abhishek

Abstract The paper aims at identifying and studying all the major factors of the store environment that affect the impulse buying behavior of customers in Indian supermarkets, using the total interpretive structural modelling (TISM) technique. This paper also describes the network of relationships among various factors along with their positions of importance in causing impulse buying behavior, using analyses of their dependent and driving power. Lighting, merchandizing display, temperature, scent, and music are found to be the most important driving factors of the store environment that influence impulse buying behavior. The dependent factors are found to be degree of socialization, layout, and in-store promotional activities. Managers would do well to focus more on the driving factors to drive impulse buying behavior. Understanding the impact of the driving factors upon the dependent factors is also a key in executing an impulse buying strategy.

Keywords Impulse buying behavior · Store environment · Super markets · Total interpretive structural modelling

1 Introduction

Impulse buying behavior has been one of the most extensively researched topics in literature. One of the early researchers of impulse buying [1] defined the term as purchases made in an unplanned manner, as a response to stimuli. Stern [2] added another dimension to impulse buying, saying it could be planned as well, as in the shopper comes to the store planning to buy on impulse, contingent on stimuli. After [2], literature has focused on the impact of various internal and external stimuli such

M. Suresh (✉) · R. D. Abhishek
Amrita School of Business, Amrita Vishwa Vidyapeetham, Coimbatore, India
e-mail: drsureshcontact@gmail.com

R. D. Abhishek
e-mail: radhakrishnandevabhishek@gmail.com

G. Kumaresan et al. (eds.), *Advances in Materials Research*, Springer Proceedings in Materials 5, https://doi.org/10.1007/978-981-15-8319-3_74

as those based on the personal characteristics of the buyer such as shopping enjoyment tendency, situational factors such as money availability [3] and characteristics of the external environment such as lighting [4]. Mattila and Wirtz [5] have emphatically asserted that the store environment must be as stimulating as the degree of impulsiveness one would want the incoming customers to possess. Chang et al. [6] also have corroborated on this and agreed that a customer would be more inclined to buy on impulse when in a positive state of mind influenced by carefully manipulated stimuli in the store environment. In fact, [7] have dealt with four environmental factors that influence impulse buying in an Indian context. It has thus become clear that identifying the degree of importance of various store environment factors, in reference to their influence on impulse buying behavior has become crucial. This study takes into consideration all the major store environment factors that may have an impact on impulse buying behavior.

2 Literature Review

Reviewing literature from various sources with regard to impulse buying behavior has helped in identifying the ten factors used for this study. The literature review for each of the factors has been detailed below.

2.1 Lighting in the Store Environment

The first factor refers to the quantum and genre of lighting in the store environment that helps customers optimally view the layout, products, and other nuances of the supermarket [4, 7].

2.2 Layout of Products in the Store

Layout of products in a store refers to the arrangement of products in a particular way so as to accommodate a spacious, comfortable platform for customers to view and buy products from. A spacious layout can put the customers' mind at ease and shop at their own pace, thus making them comfortable enough to shop impulsively [7, 8].

2.3 Music Played in the Background

Music is one of the most studied aspects of the store environment that can influence impulse buying decisions [9, 10].

2.4 Merchandizing Display

Merchandizing display refers to the degree of attractiveness of the products in display at the supermarket. Customers would feel more enticed about after viewing the visually appealing products and that excitement could translate to making impulse purchases [11, 12].

2.5 Temperature of the Store Environment

The in-store temperature stands for how comfortable the customers feel inside the store with reference to the levels of internal climate they feel in their bodies in response to the external climate present in the store environment [13, 14].

2.6 Employee Friendliness

Employee friendliness corresponds to how friendly the employees are toward the customers visiting the store. Friendlier employees make the customers stay for a longer period of time in the store, and thus invoke the possibility of impulse purchases [5, 15].

2.7 Degree of Socialization Involved While Shopping

Degree of socialization refers to the impact of the surrounding social group upon the immediate shopping environment of the customer. This social group can have a significant bearing on the impulse buying behavior of the customers [16, 17].

2.8 Crowding of a Store

Crowding means a large number of people in the store. When a large number of people are in the supermarket, customers may look to get done with their shopping and leave the store soon enough, thus not giving themselves enough time to engage in impulse buying behavior [10, 15].

2.9 Scent in the Store

Scent means the smell that can be sensed by the shoppers when they are inside the supermarket. This scent, when found appealing by the customers, can relax them and cause them to engage in impulse buying behavior [14, 18].

2.10 In-Store Promotional Activities

The in-store promotional activities correspond to those activities that are aimed at delivering or pitching a product or service through aesthetically designed activities that may appeal to the senses of customers so that they may go ahead and buy that particular product or service, or at the very least cause them to get interested about it [1, 19].

3 Methodology

The TISM technique is a modified and upgraded version of the ISM approach, and over the years has found use in a diverse stream of applications [20–26]. TISM requires the successful implementation of the following steps [27–30] in order to be useful for analysis and practical implications:

Identify and define the factors: Ten factors are identified from literature and all of these are corroborated upon by experts, who incidentally also have taken up the questionnaire survey. Impulse buying behavior has vast literature. The ten factors can be glimpsed as part of Table 1 along with sources.

Initial Reachability Matrix (IRM): To arrive at the reachability matrix in its initial form, it is necessary to first arrive at contextual relationships among various factors. To aggregate the 25 responses of individual experts and customers, mode is used as a method of compilation. The IRM for impulse buying behavior in supermarket is depicted in Table 2.

Table 1 Factors identified in the store environment

Factors	References	Factors	References
Lighting (F1)	[4, 7]	Employee friendliness (F6)	[5, 15]
Layout (F2)	[7, 8]	Degree of socialization (F7)	[16, 17]
Music (F3)	[9, 10]	Crowding (F8)	[10, 15]
Merchandizing display (F4)	[11, 12]	Scent (F9)	[14, 18]
Temperature (F5)	[13, 14]	In-store promotional activities (F10)	[1, 19]

Table 2 IRM for store environment on impulse buying behavior

	F1	F2	F3	F4	F5	F6	F7	F8	F9	F10
F1	1	1	1	1	0	0	0	0	0	1
F2	0	1	0	0	0	0	0	0	0	1
F3	0	0	1	0	0	1	1	1	0	0
F4	0	1	1	1	0	0	1	1	0	1
F5	0	0	0	0	1	1	0	1	0	0
F6	0	0	0	0	0	1	1	1	0	1
F7	0	1	0	0	0	0	1	0	0	1
F8	0	1	0	0	0	1	0	1	0	1
F9	0	0	0	0	0	1	1	1	1	1
F10	0	0	0	0	0	0	0	0	0	1

Use transitivity check to design the final reachability matrix (FRM): A process called the transitivity check is used to arrive at the final reachability matrix. If $K = L$ and $L = M$; then $K = M$. The FRM depicts in Table 3.

Splitting up the reachability matrix into partitions: In this step, the reachability matrix is partitioned into three sets, viz. reachability set, antecedent set, and intersection set.

Interaction matrix: The interaction matrix is designed using the direct links as well as the transitive links that are significant.

Using the digraph to create the TISM technique: At the final level, an entity known as the digraph is created. The model prepared using the TISM approach is shown in Fig. 1.

Table 3 FRM for store environment on impulse buying behavior

	F1	F2	F3	F4	F5	F6	F7	F8	F9	F10	Driving power	MICMAC rank
F1	1	1	1	1	0	1*	1*	1*	0	1	8	1
F2	0	1	0	0	0	0	0	0	0	1	2	7
F3	0	1*	1	0	0	1	1	1	0	1*	6	4
F4	0	1	1	1	0	1*	1	1	0	1	7	3
F5	0	1*	0	0	1	1	1*	1	0	1*	6	2
F6	0	1*	0	0	0	1	1	1	0	1	5	5
F7	0	1	0	0	0	0	1	0	0	1	3	6
F8	0	1	0	0	0	1	1*	1	0	1	5	5
F9	0	1*	0	0	0	1	1	1	1	1	6	2
F10	0	0	0	0	0	0	0	0	0	1	1	8
Dependence	1	9	3	2	1	7	8	7	1	10		

*indicates transitive links

4 Results and Discussions

4.1 Interpretive Interaction of the TISM Model

According Fig. 1 demonstrates the results of the TISM analysis of the factors in the supermarket environment that influence impulse buying behavior in supermarkets. The model describes seven levels of factors. Interpretive interactions between the factors are as follows:

F1 to F2: The layout of products may be adjusted to suit the lighting system put in place, for the ease of movement and viewing of the customers.

F1 to F3: If the music is not played in tune with the aesthetic appeal created by the lighting system in place, then it may not appeal to the customer's senses.

F1 to F4: Products may appear more attractive under the right kind of lighting. On the contrary, bad lighting can ruin the aesthetic appeal of a product.

F1 to F10: The right kind of lighting can augment the in-store promotional activities by highlighting the visual appeal of the activity in the customer's eyes.

F2 to F10: The layout of products in the supermarket can make it physically easy for in-store promotional activities to be carried out.

F3 to F6: The mood of employees working in 12-h shifts may change as a result of the pleasantness of music.

F3 to F7: Older people may not prefer supermarkets with loud/rock music.

F3 to F8: Unappealing and loud music can drive out customers.

F4 to F2: The layout must be adjusted to accommodate the diverse degrees of attractiveness of products so as to obtain the right kind of appeal.

F4 to F3: Supermarkets with more attractive merchandizing displays tend to back up their displays with more exotic music.

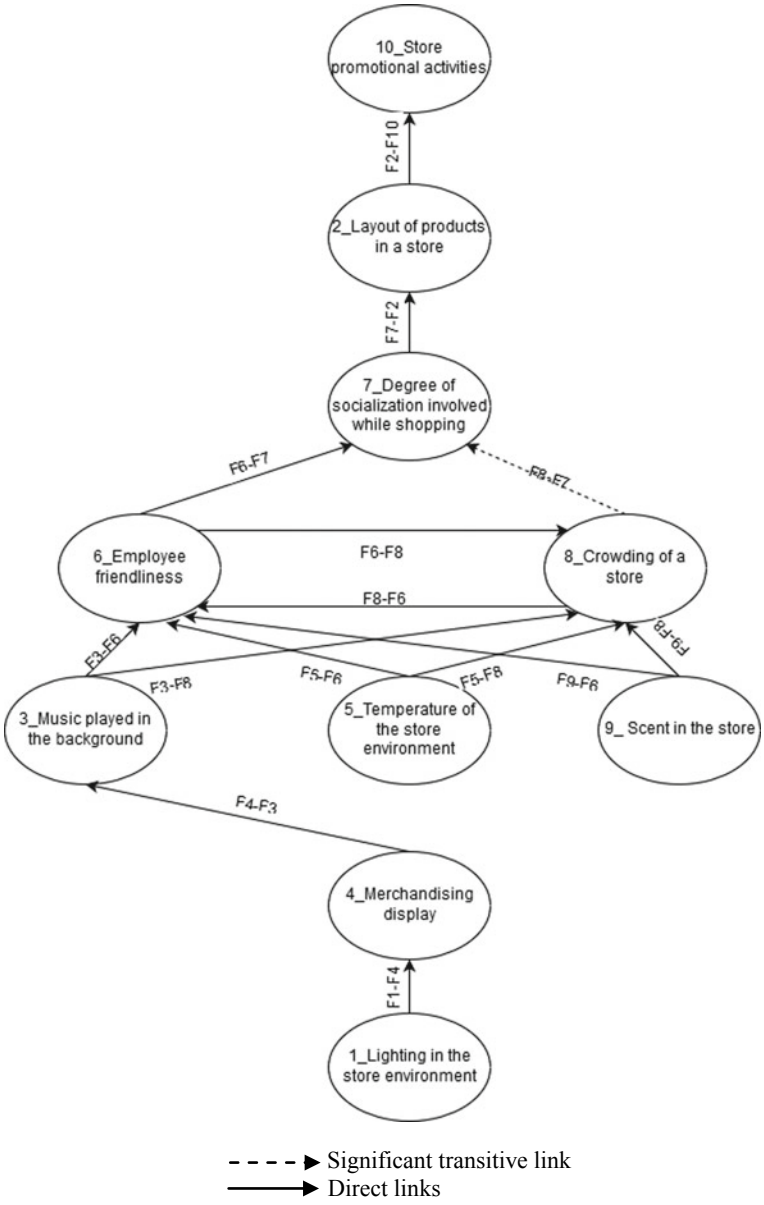

Fig. 1 TISM Model for impulse buying factors

F4 to F7: The attractiveness of merchandizing display may influence customers to bring along younger companions to visit the supermarket.

F4 to F8: Visually appealing merchandize can bring more customers into the supermarket.

F4 to F10: The visual appeal of merchandizing display may make for aesthetic viewership and positive acknowledgement of in-store promotional activities.

F5 to F6: Extreme temperatures can create an unpleasant working environment, leading to less friendlier employees.

F5 to F8: Extreme temperatures may make the customers feel uncomfortable.

F6 to F7: Supermarkets with more friendly employees may make it an attractive option to take kids and older people along.

F6 to F8: Employee friendliness may cause the inflow of customers to increase as a result of pleasant shopping experiences.

F6 to F10: Customers are likelier to pay heed to in-store promotional activities if they are delivered by friendlier employees who create pleasant shopping experiences for them.

F7 to F2: Bringing along hyperactive companions like kids may be feasible only if the layout is designed appropriately.

F7 to F10: The age-related demography of the customers visiting the supermarket may affect the genre of in-store promotional activities put in place.

F8 to F2: The degree of crowding in a supermarket may force the supermarkets to alter the layout appropriately so as to accommodate the crowd.

F8 to F6: Employees who work on long shifts may not be too high in spirits after/while attending to a large crowd.

F8 to F7 (Significant transitive link): The degree of how crowded a supermarket is may affect the likelihood of customers bringing along companions who are very young/old, owing to their special requirements of care.

F8 to F10: The crowding that happens in a supermarket may make it more difficult for the in-store promotional activities to happen owing to diverted resources.

F9 to F6: Employees may not be able to exercise friendliness in a foul-smelling environment, as a result of their dampened moods.

F9 to F7: Supermarkets with dense/pungent smells may not be preferable for taking older people along.

F9 to F8: The pleasantness of scent inside the supermarket can influence more people to visit the supermarket.

F9 to F10: Good scent can accentuate the positive aspects of in-store promotional activities by creating a sensually appealing experience for the customers.

4.2 MICMAC Analysis of the Store Environment

MICMAC refers to 'Matrix Impact Cross Multiplication Applied to Classification.' It classifies the given factors into four different zones: the first zone comprises the autonomous factors; the second zone comprises dependent factors; the third includes

the linkage factors; and the fourth zone comprises the independent/key /driving factors [31–37]. It defines the relationships between various factors and gives them a rank.

This present study has found no relevant autonomous factors, i.e., factors that have both less driving and dependent power. It only comprises the driving, linkage, and dependent factors. The driving factors are found to be factors 1, 4 5, 9, and 3. This being the case, and the significance of the driving factors becomes even more crucial. The linkage factors are found to be 6 and 8. These factors have both high dependent and driving power. The dependent factors are 7, 2, and 10. These factors depend on the driving factors to establish a significant amount of presence.

The ranking as per the MICMAC analysis for the ten factors considered for the study of impulse buying behavior in supermarkets is depicted in Table-3. The MICMAC rank computes extremely critical ratios by dividing the driving power by the dependence [38–41] of each factor. The MICMAC ranks show the importance of each factor in the entire system of the chosen store environment factors with reference to impulse buying behavior in supermarkets. Factor 1, corresponding to lighting, is clearly the most important factor according to the MICMAC analysis. It is the foremost driver in the system of chosen factors. Apart from factor 1, the factors 4, 5, 9, and 3 are also found to be ranked at the top so as to indicate criticality and importance in driving the entire system. Factor 4 refers to merchandizing display which refers to the attractiveness of the products; factor 5 stands for the in-store temperature; factor 9 refers to the scent in the store environment; and factor 3 refers to the music being played out at the background. Managers in supermarkets can leverage these driving factors to influence impulse buying behavior.

5 Conclusion

This paper has identified ten major factors of the store environment in a supermarket, which are responsible for customers' impulse buying behavior. TISM model formulated through the approaches provide an insight as to which factors drive the entire system of chosen factors relating to customer impulse buying behavior. As per the TISM model developed using the chosen ten factors, managers in supermarkets can use the factors in various manners to elicit various intensities of impulse buying behavior on the part of customers. The driving factors of the model from the in-store environment, instrumental in controlling the entire system of chosen factors, are found out to be lighting, merchandizing display, temperature, scent, and music. The linkage factors are employee friendliness and crowding. The dependent factors are degree of socialization, layout, and in-store promotional activities. Managers in supermarkets can use this framework as a model, on which to base their actions with regard to the importance they place on each factor, when they decide to act on improving customer impulse buying behavior. After all, every supermarket has its own nuances with regards to the intensities of application of the ten chosen factors. It

is also important to note that the ten factors chosen for this study are not an exhaustive list of the possible in-store environmental factors.

References

1. Applebaum W (1951) Studying customer behavior in retail stores. J Mark 16(2):172–178
2. Stern H (1962) The significance of impulse buying today. J Mark 26(2):59–62
3. Beatty SE, Ferrell ME (1998) Impulse buying: modeling its precursors. J Retail 74(2):169–191
4. Parsad C, Prashar S, Sahay V (2017) Impact of impulsive personality traits and store environment on impulse buying behaviour. J Bus Manage 23(1/2):1–24
5. Mattila AS, Wirtz J (2008) The role of store environmental stimulation and social factors on impulse purchasing. J Serv Mark 22(7):562–567
6. Chang HJ, Eckman M, Yan RN (2011) Application of the Stimulus-Organism-Response model to the retail environment: the role of hedonic motivation in impulse buying behavior. Int Rev Retail Distrib Consum Res 21(3):233–249
7. Mohan G, Sivakumaran B, Sharma P (2013) Impact of store environment on impulse buying behavior. Eur J Mark 47(10):1711–1732
8. Gupta S, Heng X, Sahu V (2009) Impact of store size on impulse purchase. IUP J Mark Manage 8(1):7–22
9. Yalch R, Spangenberg E (1990) Effects of store music on shopping behavior. J Consum Mark 7(2):55–63
10. Mattila AS, Wirtz J (2001) Congruency of scent and music as a driver of in-store evaluations and behavior. J Retail 77(2):273–289
11. Peck J, Childers TL (2006) If I touch it I have to have it: individual and environmental influences on impulse purchasing. J Bus Res 59(6):765–769
12. Hulten P, Vanyushyn V (2011) Impulse purchases of groceries in France and Sweden. J Consum Mark 28(5):376–384
13. Sherman E, Mathur A, Smith RB (1997) Store environment and consumer purchase behavior: mediating role of consumer emotions. Psychol Market 14(4):361–378
14. Cho J, Ching GS, Luong TH (2014) Impulse buying behavior of Vietnamese consumers in supermarket setting. Int J Res Stud Manage 3(2):33–50
15. Xu Y (2007) Impact of store environment on adult generation Y consumers' impulse buying. J Shop Center Res 14(1):39–56
16. Luo X (2005) How does shopping with others influence impulsive purchasing? J Consum Psychol 15(4):288–294
17. Prashar S, Parsad C, Tata SV, Sahay V (2015) Impulsive buying structure in retailing: an interpretive Structural modeling approach. J Mark Anal 3(4):215–233
18. Spangenberg ER, Crowley AE, Henderson PW (1996) Improving the store environment: do olfactory cues affect evaluations and behaviours? J Mark 60(2):67–80
19. Dholakia UM (2000) Temptation and resistance: an integrated model of consumption impulse formation and enactment. Psychol Mark 17(11):955–982
20. Gayathri K, Suresh M (2018) Modelling the factors of agile practices in project management A case of illumination project organization. Int J Eng Technol (UAE) 7(2.33):541–547
21. Sankar, H., & Suresh, M.(2018). Modelling the factors of workplace spirituality in healthcare organization. Int J Eng Technol (UAE) 7(2.33):786–790
22. Keerthanaa P, Suresh M (2018) Informal learning in work place: a case of caregivers. Int J Eng Technol (UAE) 7(2.33):791–795
23. Gautham GR, Suresh M, Ranganathan R (2018) Factors affecting human performance in lathe machine shop operations. Int J Eng Technol (UAE) 7(2.33):882–885
24. Haresh B, Suresh M, Ranganathan R (2018) Factors influencing success of new product launch: a case of SME stationery industry in India. Int J Eng Technol (UAE) 7(2.33):902–906

25. Jeevan S, Suresh M, Ranganathan R (2018) Risk factors influencing humanitarian operations: a case of temple cart festival. Int J Eng Technol (UAE) 7(2.33):946–949
26. Aarthi N, Suresh M (2018) Factors influencing people to approach micro finance institutions in India. Int J Eng Technol (UAE) 7(2.33):978–981
27. Patri R, Suresh M (2017) Modelling the enablers of agile performance in healthcare organization: a TISM approach. Glob J Flex Syst Manage 18(3):251–272
28. Patil M, Suresh M (2019) Modelling the enablers of workforce agility in IoT projects: a TISM approach. Glob J Flex Syst Manage 20(2):157–175
29. Vaishnavi V, Suresh M, Dutta P (2019a) A study on the influence of factors associated with organizational readiness for change in healthcare organizations using TISM. Benchmark Int J 26(4):1290–1313
30. Vaishnavi V, Suresh M, Dutta P (2019b) Modelling the readiness factors for agility in healthcare organization: a TISM approach. Benchmark Int J 26(7):2372–2400
31. Patri R, Suresh M (2018) Factors influencing lean implementation in healthcare organizations: an ISM approach. Int J Healthc Manageme 11(1):25–37
32. Amrita VV, Suresh M (2016) Factors influencing lean practices in Super market services using interpretive structural modeling. In: 2016 IEEE international conference on computational intelligence and computing research (ICCIC). IEEE, pp 1–5
33. Keerthana S, Suresh M (2016) Drivers influencing lean practices in street food vending process. In: 2016 IEEE international conference on computational intelligence and computing research (ICCIC). IEEE, pp 1–5
34. Renganath, K., & Suresh, M. (2016, December). Analyzing the drivers for safety practices using interpretive structural modeling: a case of Indian manufacturing firms. In: 2016 IEEE international conference on computational intelligence and computing research (ICCIC). IEEE, pp 1–6
35. Abinaya R, Suresh M (2016) Analyzing the drivers for lean practices of commercial banking using interpretive structural modelling. In: 2016 IEEE international conference on computational intelligence and computing research (ICCIC). IEEE, pp 1–4
36. Venkatesh AB, Suresh M (2016). Factors influencing Indian tourism promotion in social media. In: 2016 IEEE international conference on computational intelligence and computing research (ICCIC). IEEE, pp 1–5
37. Sudharsan TM, Suresh M (2016). Factors influencing purchase decision of solar lanterns by street vendors. In: 2016 IEEE international conference on computational intelligence and computing research (ICCIC). IEEE, pp 1–4
38. Miruthu Bashini R, Suresh M (2018) Modelling the ergonomics factors affecting the work system in hospital: an ISM approach. Int J Pure Appl Mathem 119(7):183–198
39. T Shiyam Sundar, M Suresh, R Raghu Raman (2018) Modelling the ergonomics factors affecting the work system in hospital: an ISM approach. Int J Pure Appl Math 119(7):107–125
40. Suresh M, Ganesh S, Raman R (2019) Modelling the factors of agility of humanitarian operations. Int J Agile Syst Manage 12(2):108–123
41. Suresh M, Mahadevan G, Abhishek RD (2019) Modelling the factors influencing the service quality in supermarkets. Int J Syst Assur Eng Manage 1–13. doi: https://doi.org/10.1007/s13198-019-00897-4

Modelling the Factors of Environmental Sustainability in Healthcare Dispensaries

M. Suresh and S. V. Krishnan

Abstract Sustaining the environment as it is in which we are living has become a challenging task to the mankind. Dispensary still acts as primary health centre (PHC) in many parts of India. In this paper, interpretive structural modelling (ISM) approach has been used to identify the interrelationship between the factors and identifying key/triggering factors using MICMAC analysis. This framework helps to the administrators to enrich the environmental sustainability practices in their dispensaries. This study results indicates that standard operating procedure is the key influencing factor followed by management of hazardous substances and resource usage for maintaining environmental sustainability in dispensaries.

Keywords Environmental sustainability · Healthcare · Dispensary · Primary healthcare · Interpretive structural modelling

1 Introduction

People's longevity and increasing scale of global population are no secrets in today's world. In fact, according to the report by the United Nations projects, the earth will be filled by more than 10 billion people by the year 2100 [1]. The increase in population is directly proportional to the increase in the use of natural resources, which ultimately would lead to a saturation point. This increase in the population and utilization of resources are one of the main reasons why environmental sustainable development is very important, and through such development we can conserve something for our future generations.

The mankind will be forced to seek the hospital or dispensary, if they do not take care of the environment. The overall value of Indian healthcare market around US$ 100 billion, and by 2020, it is expected to be around US$ 280 billion [2]. There are many environmental sustainability projects undertaken around the world but it

M. Suresh (✉) · S. V. Krishnan
Amrita School of Business, Amrita Vishwa Vidyapeetham, Coimbatore, India
e-mail: drsureshcontact@gmail.com

G. Kumaresan et al. (eds.), *Advances in Materials Research*, Springer Proceedings in Materials 5, https://doi.org/10.1007/978-981-15-8319-3_75

would be more effective if it started from our end. This paper helps in identifying the factors which can influence the environmental sustainability in a dispensary.

The interrelationship between these factors and the order of influence between each factor can be found with the help of the interpretive structural modelling (ISM) approach and used MICMAC analysis for categorizing the factors. This study will help in identifying the key factors that play a major role in determining environmental sustainability in dispensary.

2 Literature Review

The literature review is classified into two parts: environmental sustainability practice and ISM approach. The first part is about the environmental sustainability practice followed around the world and the second part is about the ISM approach and its application on various fields.

2.1 Literature Review on Environmental Sustainability

Sustainability is considered as one of the most important tools of survival in this competitive business world [3]. Ljungberg [4] discussed four complications such as pollution, over consumption, resource consumption and overpopulation as the reasons for the state of being unsustainable. Sangeeth Kumar and Gokulachandran [5] studied cleaner production strategies based on environmental sustainability, maximization of waste reduction, recycling and reuse in cleaning equipment manufacturing company. Vinodh et al. [6] discussed the sustainability valuation has become an important tool to move in the direction of sustainability. Cui et al. [7] applied environmental sustainability index to measure the sustainable development of Shandong province in China. Hai et al. [8] analysed the sustainable development of health and environmental sustainability in Vietnam.

2.2 Literature Review on ISM Approach

Jain and Banwet [9] applied ISM for the analysing critical factors in telecom operator space. Mahajan [10] applied ISM for analysing quality factors of management education in India. Bag [11] identified the interrelationship between the factors of flexible manufacturing system using ISM approach. Mandal and Deshmukh [12] applied ISM approach to determine key enablers for vendor selection process. Kumari et al. [13] applied ISM for analysing the rural marketing barriers.

Meena and Thakkar [14] developed a balanced scorecard for healthcare system with the help of ISM and analytic network process. Sharma and Singh [15] used ISM

as a tool to identify barriers in knowledge sharing of an organization. Satapathy et al. [16] applied ISM for analysing service quality factors of e-electricity utility service. Azar and Bayat [17] applied ISM for process orientation factors. Sarkar and Panchal [18] developed a project risk management framework using ISM.

3 Research Methodology

Preserving the environment and sustaining it for the future generations has become important to the mankind. Thus, the responsibility lies with each and every one of us and also on all organizations to maintain the environmental sustainability for a better future. This paper focuses on the identification of environmental sustainability factors which influence the day-to-day dispensary operations and analysing the relationship between the factors using ISM. The various factors that influence environmental sustainability in hospitals are identified by the study of published works in this area. The identified factors are shortlisted with the help of experts based on the impact of environmental sustainability of dispensary. The experts are doctors and nurses of selected dispensaries located in Tamil Nadu, India.

ISM method involves the following steps:

1. Identification of factors that will affect the environmental sustainability in dispensaries (Table 1).
2. 2. Self-Structural Interaction Matrix (SSIM): It is prepared based on the contextual relationship between the pair of factors [19–22] and it is shown below:
   Example: Relationship between the factors *x* and *y* ?
   Option-1: V: *x* influences *y.*
   Option-2: A: *y* influences *x.*
   Option-3: X: mutual relationship between *x and y.*
   Option-4: O: no relationship between *x and y.*
   SSIM is developed based on the consensus of the 23 experts' opinions, and it is shown in Table 2.
3. Initial Reachability Matrix (IRM): It is developed from SSIM [23–26]. The IRM has been shown in Table 3.
4. Final Reachability Matrix (FRM): It is developed from IRM through transitivity analysis which follows that if F = G, G = H, then F = H [27–30]. The FRM has been shown in Table 4.
5. Partition of the FRM: The FRM is then partitioned into different levels [31, 32], and the MICMAC ranks are captured in Table 4.

Table 1 Identified factors for environmental sustainability

Factors	Definition	References
Waste management system (T1)	Establish and practice an appropriate waste collection system for waste disposal	[33]
Management of hazardous substances (T2)	Establish hazardous waste collection system and safe handling practices	[33]
Energy conservation (T3)	Knowledge of energy consumption and efficient use of practice	[33]
Green image (T4)	Maximum use of eco-friendly products to maintain the green image	[33]
Recyclability (T5)	Ability to recycle products/processes, waste and materials to reduce resource consumption	[33]
Resource usage (T6)	Make the most efficient use of available resources and utilize natural resources	[33]
Standard operating procedure (T7)	Certain procedures followed in dispensary for various treatments	[34]
Reducing Air pollution (T8)	Air pollution that may be caused by using various equipment and chemicals in dispensary. Try to avoid or minimize the air pollution in dispensary	[35]
Renewable energy (T9)	Percentage of renewable energy used when compared to total energy utilized	[36]
Green building initiatives (T10)	The initiative taken in a dispensary in order to maintain a green environment	[37]

Table 2 SSIM for environmental sustainability

Factors	T1	T2	T3	T4	T5	T6	T7	T8	T9	T10
T1	1	A	O	V	A	A	O	A	O	V
T2		1	O	V	O	O	A	V	O	V
T3			1	O	O	A	A	O	V	O
T4				1	A	O	O	A	X	V
T5					1	O	A	O	O	O
T6						1	A	O	O	O
T7							1	O	O	O
T8								1	O	V
T9									1	V
T10										1

Table 3 IRM for environment sustainability

Factors	T1	T2	T3	T4	T5	T6	T7	T8	T9	T10
T1	1	0	0	1	0	0	0	0	0	1
T2	1	1	0	1	0	0	0	1	0	1
T3	0	0	1	0	0	0	0	0	1	0
T4	0	0	0	1	0	0	0	0	1	1
T5	1	0	0	1	1	0	0	0	0	0
T6	1	0	1	0	0	1	0	0	0	0
T7	0	1	1	0	1	1	1	0	0	0
T8	1	0	0	1	0	0	0	1	0	1
T9	0	0	0	1	0	0	0	0	1	1
T10	0	0	0	0	0	0	0	0	0	1

Table 4 FRM for environment sustainability

Factors	T1	T2	T3	T4	T5	T6	T7	T8	T9	T10	Driving Power	MICMAC rank
T1	1	0	0	1	0	0	0	0	*1*	1	4	6
T2	1	1	0	1	0	0	0	1	*1*	1	6	2
T3	0	0	1	*1*	0	0	0	0	1	*1*	4	5
T4	0	0	0	1	0	0	0	0	1	1	3	7
T5	1	0	0	1	1	0	0	0	*1*	*1*	5	3
T6	1	0	1	*1*	0	1	0	0	*1*	*1*	6	2
T7	*1*	1	1	*1*	1	1	1	*1*	*1*	*1*	10	1
T8	1	0	0	1	0	0	0	1	*1*	1	5	4
T9	0	0	0	1	0	0	0	0	1	1	3	7
T10	0	0	0	0	0	0	0	0	0	1	1	8
Dependence	6	2	3	9	2	2	1	3	9	10		

1 indicates transitive links

4 Results and Discussions

The ISM digraph is obtained from the final FRM, and it depicts in Fig. 1. The digraph is a visual representation of the various relationships between the factors and the levels at which they are positioned. Top level indicates level-1, and bottom level indicates least level.

Group I:

Autonomous factors: These factors have weak driving power and weak dependence power [38, 39]. In this case, autonomous factors are recyclability (T5), energy conservation (T3) and reducing air pollution (T8).

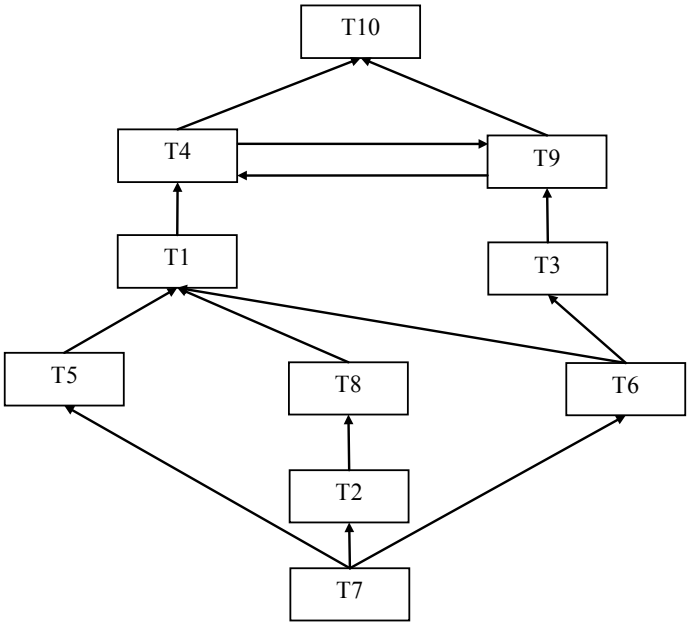

Fig. 1 ISM for the environmental sustainability factors

Group II:

Dependence factors: These factors have weak driving power and strong dependence power [40, 41]. In this group we have four factors, waste management system (T1), green image (T4), renewable energy (T9) and green building initiatives (T10).

Group III:

Linkage factors: These factors have strong driving power as well as strong dependence power [42, 43]. The absence of linkage factors in this study indicates that all the key factors are directly impacts on dependent factors.

Group IV:

Driving factors: These factors also called key or triggering factors. These factors have strong driving power and weak dependence power [44, 45]. In this group, we have three factors, management of hazardous substances (T2), resource usage (T6) and standard operating procedure (T7).

The MICMAC rank is calculated through driving power divided by dependence. It depicts in Table 4. This rank 1 factor indicates highest priority, and rank 8 indicates least priority and appropriately given importance to the improvement of environmental sustainability practices in dispensaries.

5 Conclusion

In the dynamic environment, implementation of environmental sustainability practices in our everyday business or process has become necessary in order to conserve the environment for our future generations. This model enables managers to identify key factors in the implementation of environmental sustainability in dispensary. These factors are to be considered for the successful implementation of environmental sustainability in dispensary. This study focuses on ten major identified factors using the ISM approach. The MICMAC analysis provides the classification of factors. This gives a direction to the dispensaries for concentrating on the important factors required for the implementation, and the dispensaries will be able to prepare their own action plan in maintaining environmental sustainability successfully.

In the current study, green building initiatives have been inferred as the most dependent factor. The other factors have been distributed at various levels in the order as: green image and renewable energy at level–2, waste management system and energy conservation at level–3, recyclability, resource usage and reducing air pollution at level-4, management for hazardous substances at level-5 and standard operating procedure at level-6. This ISM model was developed based on the experts' opinions of the particular region. Future work could be extended to the opinion of different regional experts and investigates the barriers to successful implementation of environmental sustainability in dispensary. The structural equation modelling can be applied for statistical validation of this model.

References

1. Fengler W, Samir KC (2015) https://www.brookings.edu/blog/future-development/2015/09/04/will-the-world-reach-10-billion-people/. Accessed on 16 Feb 2017
2. India brand equity foundation, Sectoral Report: Healthcare Industry in India (2017) https://www.ibef.org/industry/healthcare-india.aspx/. Accessed on 16 Feb 2017
3. Bevilacqua M, Ciarapica FE, Giacchetta G (2007) Development of a sustainable product lifecycle in manufacturing firms: a case study. Int J Prod Res 45(18–19):4073–4098
4. Ljungberg LY (2007) Materials selection and design for development of sustainable products. Mater Des 28(2):466–479
5. Sangeeth Kumar KS, Gokulachandran J (2015) Implementation of cleaner production strategies in a manufacturing industry. Int J Appl Eng Res 10(7):17291–17302
6. Vinodh S, Jayakrishna K, Kumar V, Dutta R (2014) Development of decision support system for sustainability evaluation: a case study. Clean Technol Environ Policy 16(1):163–174
7. Cui Y, Hens L, Zhu Y, Zhao J (2004) Environmental sustainability index of Shandong province, China. Int J Sustain Dev World Ecol 11(3):227–233
8. Hai LT, Hai PH, Hens L (2009) Health and environmental sustainability indicators in Quang Tri Province, Vietnam. Int J Sustain Dev World Ecol 16(2):77–86
9. Jain D, Banwet DK (2013) Modelling critical elements of selection for strategic alliance partner for network managed services using interpretive structural modelling (ISM). J Model Manage 8(3):290–304
10. Mahajan R, Agrawal R, Sharma V, Nangia V (2014) Factors affecting quality of management education in India: an interpretive structural modelling approach. Int J Educ Manage 28(4):379–399

11. Bag S (2014) Modeling the enablers of flexible manufacturing systems using interpretive structural modeling. J Suppl Chain Manage Syst 3(3)
12. Mandal A, Deshmukh SG (1994) Vendor selection using interpretive structural modelling (ISM). Int J Oper Product Manage 14(6):52–59
13. Kumari P, Gupta N, Sindhu S (2014) Modeling the barriers to rural marketing using the interpretive structural modeling approach. IUP J Market Manage 13(3):7
14. Meena K, Thakkar J (2014) Development of balanced scorecard for healthcare using interpretive structural modeling and analytic network process. J Adv Manage Res 11(3):232–256
15. Sharma BP, Singh MD (2012) Knowledge sharing barriers: an approach of interpretive structural modeling. IUP J Knowl Manage 10(3):35
16. Satapathy S, Patel SK, Biswas A, Mishra P (2012) Interpretive structural modeling for E-electricity utility service. Serv Bus 6(3):349–367
17. Azar A, Bayat K (2013) Designing a model for" Business process-orientation" using interpretive structural modeling approach (ISM). Afr J Bus Manage 7(26):2558
18. Sarkar D, Panchal S (2015) Integrated interpretive structural modeling and fuzzy approach for project risk management of ports. Int J Constr Project Manage 7(1):17
19. Gayathri K, Suresh M (2018) Modelling the factors of agile practices in project management: a case of illumination project organization. Int J Eng Technol (UAE) 7(2.33):541–547
20. Sankar H, Suresh M (2018) Modelling the factors of workplace spirituality in healthcare organization. Int J Eng Technol (UAE) 7(2.33):786–790
21. Keerthanaa P, Suresh M (2018) Informal learning in work place: a case of caregivers. Int J Eng Technol (UAE) 7(2.33):791–795
22. Gautham GR, Suresh M, Ranganathan R (2018) Factors affecting human performance in lathe machine shop operations. Int J Eng Technol (UAE) 7(2.33):882–885
23. Keerthana S, Suresh M (2016) Drivers influencing lean practices in street food vending process. In: 2016 IEEE international conference on computational intelligence and computing research (ICCIC) (pp 1–5). IEEE
24. Haresh B, Suresh M, Ranganathan R (2018) Factors influencing success of new product launch: a case of SME stationery industry in India. Int J Eng Technol (UAE) 7(2.33):902–906
25. Jeevan S, Suresh M, Ranganathan R (2018) Risk factors influencing humanitarian operations: a case of temple cart festival. Int J Eng Technol (UAE) 7(2.33):946–949
26. Aarthi N, Suresh M (2018) Factors influencing people to approach micro finance institutions in India. Int J Eng Technol (UAE) 7(2.33):978–981
27. Amrita VV, Suresh M (2016) Factors influencing lean practices in Super market services using interpretive structural modeling. In 2016 IEEE international conference on computational intelligence and computing research (ICCIC) (pp 1–5). IEEE
28. Renganath K, Suresh M (2016) Analyzing the drivers for safety practices using interpretive structural modeling: a case of Indian manufacturing firms. In 2016 IEEE International Conference on Computational Intelligence and Computing Research (ICCIC), pp 1–6. IEEE
29. Abinaya R, Suresh M (2016) Analyzing the drivers for lean practices of commercial banking using interpretive structural modelling. In: 2016 IEEE international conference on computational intelligence and computing research (ICCIC), pp 1–4. IEEE
30. Patri R, Suresh M (2018) Factors influencing lean implementation in healthcare organizations: an ISM approach. Int J Healthcare Manage 11(1):25–37
31. Venkatesh AB, Suresh M (2016) Factors influencing Indian tourism promotion in social media. In: 2016 IEEE International Conference on Computational Intelligence and Computing Research (ICCIC), pp 1–5. IEEE
32. Sudharsan TM, Suresh M (2016) Factors influencing purchase decision of solar lanterns by street vendors. In 2016 IEEE international conference on computational intelligence and computing research (ICCIC), pp 1–4. IEEE
33. Vimal KEK, Vinodh S, Muralidharan R (2015) An approach for evaluation of process sustainability using multi-grade fuzzy method. Int J Sustain Eng 8(1):40–54
34. Gopal PRC, Thakkar J (2015) Development of composite sustainable supply chain performance index for the automobile industry. Int J Sustain Eng 8(6):366–385

35. Wier M, Christoffersen LB, Jensen TS, Pedersen OG, Keiding H, Munksgaard J (2005) Evaluating sustainability of household consumption—using DEA to assess environmental performance. Econ Syst Res 17(4):425–447
36. Kaivo-oja J, Panula-Ontto J, Vehmas J, Luukkanen J (2014) Relationships of the dimensions of sustainability as measured by the sustainable society index framework. Int J Sustain Dev World Ecol 21(1):39–45
37. Harik R, El Hachem W, Medini K, Bernard A (2015) Towards a holistic sustainability index for measuring sustainability of manufacturing companies. Int J Prod Res 53(13):4117–4139
38. Patri R, Suresh M (2017) Modelling the enablers of agile performance in healthcare organization: a TISM approach. Glob J Flexib Syst Manage 18(3):251–272
39. Suresh M, Ganesh S, Raman R (2019) Modelling the factors of agility of humanitarian operations. Int J Agile Syst Manage 12(2):108–123
40. Suresh M, Mahadevan G, Abhishek RD (2019) Modelling the factors influencing the service quality in supermarkets. Int J Syst Assur Eng Manage. https://doi.org/10.1007/s13198-019-00897-4
41. Patil M, Suresh M (2019) Modelling the enablers of workforce agility in IoT projects: a TISM approach. Glob J Flexib Syst Manage 20(2):157–175
42. Miruthu Bashini R, Suresh M (2018) Modelling the ergonomics factors affecting the work system in hospital: an ISM approach. Int J Pure Appl Math 119(7):183–198
43. Vaishnavi V, Suresh M, Dutta P (2019a). A study on the influence of factors associated with organizational readiness for change in healthcare organizations using TISM. Benchmark Int J 26(4):1290–1313
44. Shiyam Sundar T, Suresh M, Raghu Raman R (2018) Modelling the ergonomics factors affecting the work system in hospital: an ISM approach. Int J Pure Appl Math 119(7):107–125
45. Vaishnavi V, Suresh M, Dutta P (2019b) Modelling the readiness factors for agility in healthcare organization: a TISM approach. Benchmark Int J 26(7):2372–2400

Manufacturing Flexibility Assessment Using Multi-Grade Fuzzy: A Case of Garment Industry

R. Sowmiyaa Sri and M. Suresh

Abstract Flexibility in manufacturing is an effective way of confronting the uncertainties of the rapidly changing environment. The paper develops a conceptual framework for assessing the manufacturing flexibility level of a garment industry using multi-grade fuzzy approach. Flexibility is the ability and willingness to change or compromise to perform better. The flexibility attributes are classified based on importance-performance analysis (IPA). The study indicates that the case industry has become 'flexible' but has scope for improvement. Using this framework, the company can better evaluate its manufacturing flexibility and the areas that the company needs to focus on to improve its flexibility.

Keywords Manufacturing flexibility · Flexibility in garment industry · Production flexibility · Multi-grade fuzzy · Importance-performance analysis

1 Introduction

As globalisation increases, market competitive pressure increases. The ability to compete is an essential requirement for organisation's survival in the manufacturing industry. The evolving market needs cause constant changes in the product life cycle, setup times and cost–benefits. Flexibility in manufacturing is an effective way of confronting the uncertainties of this rapidly changing environment. Flexibility is the ability of the manufacturing firm to adapt to changes and the uncertainties associated with them. The aim of the study is to first find the enablers, criteria, and attributes that affect the manufacturing flexibility and assess them using multi-grade fuzzy approach and identify the weaker attributes that the firm must work on to increase its flexibility index. A case of a garment industry is taken for assessing the flexibility. Garment

R. S. Sri · M. Suresh (✉)
Amrita School of Business, Amrita Vishwa Vidyapeetham, Coimbatore, India
e-mail: drsureshcontact@gmail.com

R. S. Sri
e-mail: sowmy.rr@gmail.com

G. Kumaresan et al. (eds.), *Advances in Materials Research*, Springer Proceedings in Materials 5, https://doi.org/10.1007/978-981-15-8319-3_76

industry is taken because most garment manufacturing units work only toward quality and not flexibility. They still follow the traditional method and are not yet digitised completely. In this paper, six enablers of flexibility are discussed viz. product, process, strategy, technology, workforce, and customer–supplier management.

2 Literature Review

According to [1], flexibility refers to the firm's capability to make intentional changes, respond to anticipated changes and adjust to the consequences of these changes. Das and Caprihan [2] refers manufacturing flexibility as the system's ability to adapt to consumer demand and market conditions. Normally, computing an accurate estimate of the flexibility for an organisation is difficult due to varying contribution levels of underlying elements. [3] describes product flexibility as the flexibility of the introduction of new products and modification of the existing products like making design changes and adding value to the product. The number of new products produced per year, the time required to produce those new products, the cost of producing new products, etc., come under product flexibility. As per [4], the range of volumes can be produced, and time and cost required for changing the required quantity come under volume flexibility. Expansion flexibility is the additional capital required for increasing the plant capacity with small marginal investments [5]. Process flexibility is the ability to produce a new set of part patterns with different batch sizes [6]. Rerouting, transfer speed, and substitutivity are the factors that come under process flexibility [7].

Based on the literature review, it was found that no research has been reported on the evaluation of manufacturing flexibility in a garment industry using a multi-grade fuzzy and IPA. This study has for the first time developed the manufacturing flexibility assessment framework for the garment industry using multi-grade fuzzy and IPAs.

3 Conceptual Model for Assessing Manufacturing Flexibility

A conceptual model has been developed to estimate the manufacturing flexibility of a garment industry and is shown in Table 1. This conceptual model is derived from the literature review and experts' opinion. The multi-grade fuzzy logic approach has three levels. The first level consists of six enablers, the second level has the criteria, and the third level consists of the various attributes corresponding to each criterion.

Table 1 Conceptual model to assess manufacturing flexibility in a garment industry

Enablers	Criteria	Attributes
Product flexibility (I_1)	Customisation (I_{11})	New product introduction (I_{111})
		Response to changing market requirement (I_{112})
		Value addition to products (I_{113})
	Volume (I_{12})	Range of volume (I_{121})
		Time required to increase or decrease the output (I_{122})
		Cost required to increase or decrease the volume of output (I_{123})
Process flexibility (I_2)	Material handling flexibility (I_{21})	Rerouting (I_{211})
		Transfer speed (I_{212})
		Substitutability (I_{213})
	Expansion flexibility (I_{22})	Modularity index (I_{221})
		Expansion ability (I_{222})
Workforce flexibility (I_3)	Human knowledge and skills (I_{31})	Multi-skilled and flexible people (I_{311})
		Job rotation system (I_{312})
		Training and workforce skill update (I_{313})
	Team work (I_{32})	Cross-functional team (I_{321})
		Empowerment and centralised decision making (I_{322})
Technology flexibility (I_4)	IT integration (I_{41})	Online order tracking (I_{411})
		E-bills (I_{412})
		Paperless work (I_{413})
	Manufacturing setup (I_{42})	Less time for changing manufacturing setups(I_{421})
		Automated tools for reducing repeated work (I_{422})
		Upgradation of machines (I_{423})
Customer and supplier management (I_5)	Supplier (I_{51})	Delivery of multiple kinds of materials as per the requirements (I_{511})
		Involvement of suppliers (I_{512})
	Customer requirement and feedback (I_{52})	Communication media to collect the customer responses (I_{521})
		Effective system for handling customer complaints (I_{522})

(continued)

Table 1 (continued)

Enablers	Criteria	Attributes
		Empowerment of personnel to resolve customer problems (I_{523})
Strategy flexibility (I_6)	Quality (I_{61})	Products exceeding customer's expectations (I_{611})
		*I*nnovation in product design (I_{612})
		Survey/feedbacks to ensure quality status (I_{613})
	Time management (I_{62})	Scheduled activities (I_{621})
		Effective and immediate communication—information flow on time (I_{622})
		Adoption of time compression technologies (I_{623})

4 Research Methodology

The literature review on manufacturing flexibility was conducted to identify the relevant enablers, criteria, and attributes. A garment industry was chosen, and employees in the managerial level or above were interviewed to rate the attributes. The weightage for calculating the manufacturing flexibility based on the conceptual model developed is done by collecting data from experts in various garment industries.

4.1 About Case Company

The study was done in one garment manufacturing unit from Tirupur, Tamil Nadu, India (hereafter referred to as *XYZ* Garments). *XYZ* Garments are hosiery garment manufacturer with inbound printing and embroidery services. *XYZ* is specialised in manufacturing *t*-shirts for multiple international brands. Knitting and dyeing are outsourced, whereas all other processes like cutting, ironing, packing, and stitching are done within that company. The company aims to expand further and double the turnover.

4.2 Assessment of Flexibility Using Multi-grade Fuzzy

The manufacturing flexibility is denoted by I. It is the product of mean normalised weightage of the expert opinions represented by W and the overall rating factor R [8–12]. The equation for flexibility is given by $I = W*R$.

Regarding the weightage of the enablers, criteria, attributes, and case company attributes, ratings are captured using the following scale (Table 2):

Calculating flexibility factor includes fuzzy determination, and hence, the assessment is categorised into five grades, $I = (10, 8, 6, 4, 2)$ where the range 8–10 represents that the garment industry is 'extremely flexible', 6–8 represents 'flexible', 4–6 represents 'moderately flexible', 2–4 represents 'non-flexible', and 0–2 represents 'extremely non-flexible'. Five experts were interviewed for the assessment of manufacturing flexibility in the *XYZ* garment industry. Five experts from five different garment industries contributed to the discussion meeting for weightage of flexibility enablers, criteria, and attributes. Experts' opinions mean normalised weightage of enablers, criteria, and attributes, and the attribute ratings are captured in Table 3.

4.2.1 Primary-Level Assessment Calculation

The calculations that were applied for the criteria 'customisation' are shown below:

The weightage corresponds to the criteria 'customisation' $W_{11} = (0.32, 0.36, 0.32)$. Rating vector for the criteria 'customisation' is given by

$$R_{11} = \begin{bmatrix} 7 & 8 & 8 & 8 & 8 \\ 9 & 8 & 8 & 9 & 9 \\ 8 & 8 & 8 & 7 & 8 \end{bmatrix}$$

Index calculation for the criteria 'customisation' is $I_{11} = W_{11} * R_{11}$.

$I_{11} = (8.0, 8, 8, 8.0, 8.36)$.

Similarly, the index for other manufacturing flexibility criteria is computed.

Table 2 Weightage and rating scale for enablers, criteria, and attributes

Scores	Level
0–2	Very low
2.01–4	Fair
4.01–6	Normal
6.01–8	Good
8.01–10	Excellent

Table 3 Factor ratings and expert weightages

I_i	I_{ij}	I_{ijk}	R_1	R_2	R_3	R_4	R_5	W_{ij}	W_i	W
I_1	I_{11}	I_{111}	7	8	8	8	8	0.32	0.51	0.19
		I_{112}	9	8	8	9	9	0.36		
		I_{113}	8	8	8	7	8	0.32		
	I_{12}	I_{121}	8	9	10	8	9	0.35	0.49	
		I_{122}	8	9	10	8	9	0.34		
		I_{123}	7	8	9	8	7	0.30		
I_2	I_{21}	I_{211}	7	9	8	7	6	0.31	0.55	0.16
		1_{212}	9	8	7	8	8	0.34		
		I_{213}	9	8	8	9	9	0.35		
	I_{22}	I_{221}	7	7	6	7	7	0.49	0.45	
		I_{222}	7	8	6	7	6	0.51		
I_3	I_{31}	I_{311}	8	9	8	8	9	0.31	0.49	0.17
		I_{312}	9	8	7	9	9	0.34		
		I_{313}	9	8	8	9	9	0.35		
	I_{32}	I_{321}	9	8	7	8	9	0.50	0.51	
		I_{322}	8	7	7	8	7	0.49		
I_4	I_{41}	I_{411}	6	7	6	5	6	0.29	0.47	0.15
		I_{412}	8	6	7	8	7	0.35		
		I_{413}	7	8	6	7	7	0.35		
	I_{42}	I_{421}	8	8	7	8	7	0.3	0.53	
		I_{422}	8	8	9	8	7	0.35		
		I_{423}	9	8	9	7	8	0.35		
I_5	I_{51}	I_{511}	9	8	8	8	9	0.51	0.50	0.17
		I_{512}	8	9	9	8	8	0.49		
	I_{52}	I_{521}	8	8	9	8	8	0.32	0.49	
		I_{522}	8	9	8	9	8	0.33		
		I_{523}	8	9	8	7	9	0.34		
I_6	I_{61}	I_{611}	9	8	8	7	9	0.35	0.51	0.16
		I_{612}	8	7	8	7	7	0.35		
		I_{613}	8	9	8	8	7	0.30		
	I_{62}	I_{621}	7	8	9	9	8	0.34	0.49	
		I_{622}	8	8	9	8	8	0.34		
		I_{623}	8	7	7	8	8	0.33		

4.2.2 Secondary-Level Assessment Calculation

The calculations that were applied for the enabler 'product flexibility' is shown below: the weightage corresponds to the enabler 'product flexibility' $W_1 = (0.51, 0.49)$. Rating vector corresponding to the criteria 'product flexibility' is obtained from primary-level assessment results.

Index calculation for the enabler 'product flexibility' is $I_1 = W_1 * R_1$.

$I_1 = (7.87, 8.34, 8.829, 8.02, 8.38)$.

Similarly using the same concept, the index for the other flexibility enablers is also computed.

4.2.3 Tertiary-Level Assessment Calculation

The calculation to find the manufacturing flexibility index of case *XYZ* Garment industry is as follows: Overall weightage $W = (0.187, 0.159, 0.167, 0.151, 0.171, 0.163)$.

Overall rating vector is given by R which is obtained from results of secondary-level assessment calculations.

$$\text{Flexibility index } I = W * R$$

$$I = (8.04, 8.03, 7.88, 7.85, 7.92)$$
$$I = (8.04 + 8.03 + 7.88 + 7.85 + 7.92)/5$$
$$I = 7.94$$

4.3 Classification of Flexibility Attributes Using IPA

IPA approach helps us to measure the manufacturing flexibility in the case garment industry. IPA shows the relation between the average weightage of the expert opinions and the rating assessment of the chosen garment industry. IPA model is graphically depicted using a framework separated by four regions [13, 14]. The four regions and their conjectures are explained in Table 4. Also, the case industry flexibility attributes are classified into four regions and shown in Table 4.

5 Results and Discussions

Based on the assessment model, the manufacturing flexibility index for the *XYZ* Garment Industry is valued at 7.94. It comes under the scale range 6–8, which means

Table 4 Regions and conjectures of IPA

Region	Conjecture
Region 1: Areas for improvement	This is the highly perceived area for improvements. The attributes in this region are weighted high by experts, but the garment industry performance is lesser comparatively. This shows that all attributes in this region should be given importance and focused I_{612}, I_{111}, I_{113}
Region 2: Highly performing area	Attributes in this region are weighted high by the experts, and the organisation is also performing well in these factors. This is the highly performing region, and the same should be maintained I_{112}, I_{121}, I_{122}, I_{213}, I_{311}, I_{312}, I_{313}, I_{422}, I_{423}, I_{511}, I_{512}, I_{521}, I_{522}, I_{523}, I_{611}, I_{621}, I_{622}
Region 3: Low-priority area	Attributes in this region are analysed as lower weightage by the experts. Despite the organisation's low performance in this region, it will not disturb the organisation's overall performance. Less priority is enough for the attributes in this region I_{123}, I_{211}, I_{212}, I_{221}, I_{222}, I_{322}, I_{411}, I_{412}, I_{413}, I_{421}, I_{613}, I_{623}
Region 4: Overkill	The garment industry's performance on the attributes in this region is very high, but these attributes are given lower weightage by the experts. The organisation should reduce focus on this area, and the management should re-consider the resource allocation and prioritise the factors for improvement I_{321}

that the *XYZ* Garment Industry is 'flexible'. For extreme flexible, the scale range is 8–10. Thus, we conclude that *XYZ* has further scope to improve the flexibility index and move into the 'extremely flexible' category.

IPA is done to identify the focus areas for achieving high level of manufacturing flexibility. It helped identify the attributes that need to be focused on. New product introduction, value addition to products, and innovation in product design are the areas that need to be focused on for improvement. Performances of the above attributes are comparatively low and require immediate actions to be taken by the case industry. Responding to changing marketing conditions, flexibility in the range of volume manufactured, the time required to cope up with this volume change, workforce skill and training, job rotation techniques, handling customer complaints, and resolving them are the areas where case industry is performing really well. Expansion ability, centralised decision making, online order tracking, paperless work, and adoption of time compression technologies are areas where case industry performs low, but these also have low weightage. Hence, these low performing attributes will not have much impact on overall flexibility. Cross-functional team is the areas where the case industry's performance is higher than needed. Managers may reconsider the resource allocation on the attributes in this region and may focus more on other attributes that need improvement.

5.1 Improvement Proposal for the Weaker Attributes

1. *Innovation in product design*: In this current technology-driven world, in order to compete, firms have to constantly innovate new service or product. Hence, it is important to identify customer needs and satisfy the customer demand with the new product features.
2. *Value-addition to products*: Every customer wants value addition to their product. With respect to garments, the value can be in terms of quality of the material, organic/eco-friendly fabric and attractive and trending designs at affordable prices. The organisation should rightly identify the values it can provide and maintain the competitive advantage.
3. *New Product Introduction*: If the firm is manufacturing only t-shirts, it should be ready to add products to its product line like shorts, pants, jackets, etc. They should have the resource and capacity to add new products.

6 Managerial Implications

The framework proposed in this study helps the garment manufacturing units to measure its manufacturing flexibility index. This study helps top management to identify their weak attributes and identify areas of improvement. The management team will use this framework to focus on the weaker attributes that will drive significant changes in their company's manufacturing flexibility and lead them to maintain competitive advantage.

7 Conclusion

The main focus of this paper is to assess the manufacturing flexibility in garment industry. Flexibility refers to the ability of a firm to continuously change and adapt according to the customer needs and market trends. This research has proposed a framework to measure the manufacturing flexibility index of garment industry. This conceptual model developed using multi-grade fuzzy approach. The case *XYZ* industry comes under the category of 'flexible' but there is still scope to achieve 'extremely flexible'. IPA is used to identify areas of improvement and areas where more resources are used and how these inferences can help an industry improve its flexibility index. This framework was limited to garment industry particularly *t*-shirts manufacturing. The scope of this framework can be further expanded by incorporating additional flexibility attributes related to the textile or clothing, spinning mills and dyeing industries.

Compliance with Ethical Standards Conflict of Interest The authors declare that there is no conflict of interest in publishing this paper. The authors state the clarification of the anonymisation of the data collection or for questionnaires (if any).

References

1. Bahrami H (1992) The emerging flexible organization: perspectives from Silicon Valley. California Manage Rev 34(4):33–52
2. Das A, Caprihan R (2008) A rule-based fuzzy-logic approach for the measurement of manufacturing flexibility. Int J Adv Manuf Technol 38(11–12):1098–1113
3. Ettlie JE, Penner-Hahn JD (1994) Flexibility ratios and manufacturing strategy. Manage Sci 40(11):1444–1454
4. Browne J, Dubois D, Rathmill K, Sethi SP, Stecke KE (1984) Classification of flexible manufacturing systems. the FMS Mag 2(2):114–117
5. Stecke K, Raman N (1986) Production flexibilities and their impact on manufacturing strategy. Working paper #484, Graduate School of Business Administration, The University of Michigan, Ann Arbor, MI
6. Brill PH, Mandelbaum M (1989) On measures of flexibility in manufacturing systems. Int J Prod Res 27(5):747–756
7. Ansari SR, Mittal PK (2010) Multi-criteria decision making using fuzzy logic approach for evaluating the manufacturing flexibility. J Eng Technol Res 2(12):237–244
8. Vinodh S, Devadasan SR, Vasudeva Reddy B, Ravichand K (2010) Agility index measurement using multi-grade fuzzy approach integrated in a 20 criteria agile model. Int J Prod Res 48(23):7159–7176
9. Vinodh S, Chintha SK (2011) Leanness assessment using multi-grade fuzzy approach. Int J Prod Res 49(2):431–445
10. Vinodh S, Prasanna M (2011) Evaluation of agility in supply chains using multi-grade fuzzy approach. Int J Prod Res 49(17):5263–5276
11. Ganesh J, Suresh M (2016) Safety practice level assessment using multigrade fuzzy approach: a case of Indian manufacturing company. In 2016 IEEE international conference on computational intelligence and computing research (ICCIC). IEEE pp 1–5
12. Sridharan V, Suresh M (2016) Environmental sustainability assessment using multigrade fuzzy—A case of two Indian colleges. In: 2016 IEEE international conference on computational intelligence and computing research (ICCIC). IEEE pp 1–4
13. Deng WJ (2008) Fuzzy importance-performance analysis for determining critical service attributes. Int J Serv Indus Manage 19(2):252–270
14. Feng M, Mangan J, Wong C, Xu M, Lalwani C (2014) Investigating the different approaches to importance–performance analysis. Serv Ind J 34(12):1021–1041

Leanness Assessment Using Multi-grade Fuzzy: A Case of Textile Manufacturing Company

S. Sreedharshini and M. Suresh

Abstract Lean practices are implemented in many small businesses to improve productivity and increase profitability. This article discusses the assessment of leanness level in a small-scale textile Tape Manufacturing Company (TMC) using a multi-grade fuzzy (MGF) approach. This approach has a unique advantage of being concise and avoids bias in computation. The lean enablers, criteria and attributes are identified through literature review and expert opinions. The weaker attributes are identified through importance performance analysis (IPA). The results found that the weak attributes of the case company were smooth information flow, managerial engagement, consistent operating practice, information transparency and layout. The proposed framework helps for small-scale tape manufacturing companies to evaluate their leanness level and focuses on weak attributes to improve leanness.

Keywords Leanness · Lean assessment · Small-scale manufacturing · Importance performance analysis · Textile · Multi-grade fuzzy

1 Introduction

Lean is now implemented in many small-scale manufacturing industries in India, but it is not as effective as it is implemented and used in large-scale industries. Many companies claim that they are lean practitioners but in reality they are not an effective lean practitioner. Some of the small-scale industries are not aware of most of the lean concepts. Waste can be eliminated from their systems by effectively implying and practicing lean concepts.

S. Sreedharshini (✉) · M. Suresh (✉)
Amrita School of Business, Amrita Vishwa Vidyapeetham, Coimbatore, India
e-mail: dharshudharsh00@gmail.com

M. Suresh
e-mail: drsureshcontact@gmail.com

G. Kumaresan et al. (eds.), *Advances in Materials Research*, Springer Proceedings in Materials 5, https://doi.org/10.1007/978-981-15-8319-3_77

There are other types of small-scale businesses that are unwittingly running lean practices in their company. Therefore, to understand the effectiveness of lean practice in the organization, specific industry-related lean attributes are identified and evaluated. This paper focuses on developing a framework for calculating leanness level in the organization and simplifying the calculation using the MGF approach.

2 Literature Review

Vinodh and Vimal [1] developed leanness assessment model using fuzzy logic approach for manufacturing industry. Rakhmanhuda and Karningsih [2] developed a lean assessment framework. The concept of continuous improvement and lean can be used as a solution in solving global challenges such as cost-effectiveness, lead time, quality and safety. Leanness in both quantitative approach and the qualitative approach is assessed. In quantitative approach, it measures the application of lean in accordance with the implemented results and objectives. In qualitative approach, it reflects the stakeholder's perception. Bidhendi et al. [3] developed weighted leanness assessment framework. Leanness index provides a direction to eliminate or at least reduce manufacturing wastes during the implementation of lean strategies toward continuous improvement. To measure the leanness level of an organization more accurately, quantitative methods have been developed using lean performance metrics. Vidyadhar et al. [4] developed leanness assessment framework for SMEs using fuzzy logic approach. Vinodh and Balaji [5] developed a decision support system using fuzzy logic approach for leanness assessment in manufacturing industry. Narayanamurthy et al. [6] developed an assessment framework for readiness for lean implementation in healthcare settings using fuzzy logic approach. Vimal and Vinodh [7] developed leanness assessment framework using if–then rules for manufacturing organizations.

3 Conceptual Model for Assessing Leanness

The enablers, criteria and attributes are identified using literature review and expert opinion in the field. In this framework, four enablers, nine criteria and twenty-nine attributes are identified to evaluate the leanness level of the case TMC and it is depicted in Table 1. This conceptual model was derived based on four aspects of leanness, namely management responsibility [8–10], overall equipment effectiveness [11], wastage elimination [12–15] and manufacturing leanness [1].

Five experts from a different TMC contributed to the discussion meeting for weightage of lean enablers, criteria and attributes. Five experts from case TMC participated in the evaluation for leanness assessment.

Table 1 Conceptual model for leanness assessment

Enablers	Criteria	Attributes
Management responsibility (L_1)	Nature of management (L_{11})	Smooth information flow (L_{111})
		Management involvement (L_{112})
		Standard operating procedure (SOP) (L_{113})
	Organization culture (L_{12})	Information transparency (L_{121})
		Resistance to change (L_{122})
		Cleanliness (L_{123})
		Job security (L_{124})
		Team working skills (L_{125})
Overall equipment effectiveness (L_2)	Availability (L_{21})	Downtime (L_{211})
		Instantaneous availability (L_{212})
	Performance (L_{22})	Machine utilization (L_{221})
		Production speed (L_{222})
	Quality (L_{23})	Defect rate (L_{231})
		Customer satisfaction (L_{232})
		Rework (L_{233})
Wastage elimination(L_3)	Cost (L_{31})	Inventory cost (L_{311})
		Overproduction (L_{312})
		Scrap sales (L_{313})
		Transportation cost (L_{314})
	Time (L_{32})	Setup time (L_{321})
		Non-value-added time (L_{322})
		SMED (L_{323})
Manufacturing leanness (L_4)	Standardization (L_{41})	Process flow standardization (L_{411})
		IT communication (L_{412})
		Standardization of components (L_{413})
		Layout (L_{414})
	Pull production (L_{42})	Demand-driven production (L_{421})
		WIP reduction (L_{422})
		JIT delivery (L_{423})

4 Case Study

This organization is a private textile tape manufacturing organization, which manufactures cotton tapes, webbing tapes, twill tapes, etc., operated in a small town from Tamil Nadu, India. Cotton yarn is purchased from spinning mills. First process of

manufacturing is stated by converting cotton yarn into warp using warping machine. This warp is loaded to shuttle loom machine or needle loom machine. There are almost 60 shuttle looms involved in the process and 10 needle looms.

Needle looms are modern machines that run at a rate five times faster than shuttle looms. This is an important process for the company to convert the warp into tapes. Then, the tapes are sent to the packaging.

4.1 Assessment of Leanness Using Multi-grade Fuzzy

This framework helps the managers of the TMC by answering the following research questions (RQ):

RQ 1: How to measure leanness levels in Textile Manufacturing Company?

RQ 2: What are the attributes that influence leanness in Textile Manufacturing Company?

RQ3: How to address those weaker attributes to enhance leanness level?

Regarding the weightage of the enablers, criteria, attributes and case, company attribute ratings are captured using the following scale (Table 2):

The rating and weightage are collected from the experts in manufacturing firms. Among the collected data, the ratings for negative attributes (minimum is best) are collected in the reverse order of scale. The mean normalized weightage of the experts' opinions and the attribute ratings are shown in Table 3.

4.1.1 Primary Assessment Calculation

The primary assessment calculation is performed by using the below-mentioned formula. The calculation is performed using data collected for rating and the weightage calculated from the mean of the attributes.

$R_{11} * W_{11} = L_{11}$ [16–18].

Table 2 Importance and rating scale

Scores	Level	Grades
0–2	Very low	Extremely non-lean
2.01–4	Fair	Non-Lean
4.01–6	Normal	Moderately lean
6.01–8	Good	Lean
8.01–10	Excellent	Extremely lean

Table 3 Rating and weightage by experts

LA_{ijk}	E1	E2	E3	E4	E5	W_{ij}	W_i	W
LA_{111}	8	7	7	9	8	0.330508475	0.4878	0.2704
LA_{112}	9	7	6	8	7	0.338983051		
LA_{113}	7	8	8	9	7	0.330508475		
LA_{121}	8	8	7	7	8	0.213903743	0.5122	
LA_{122}	7	6	7	7	8	0.14973262		
LA_{123}	6	8	5	9	7	0.197860963		
LA_{124}	8	8	8	8	9	0.22459893		
LA_{125}	8	9	7	8	9	0.213903743		
LA_{211}	10	9	8	10	9	0.535211268	0.32	0.2453
LA_{212}	6	7	6	9	7	0.464788732		
LA_{221}	10	10	9	8	9	0.548780488	0.328	
LA_{222}	9	10	5	9	8	0.451219512		
LA_{231}	9	9	6	9	8	0.294117647	0.352	
LA_{232}	9	10	7	9	9	0.344537815		
LA_{233}	10	5	9	10	8	0.361344538		
LA_{311}	4	7	4	8	6	0.2265625	0.494	0.2327
LA_{312}	5	5	5	6	6	0.2109375		
LA_{313}	10	7	8	9	8	0.2890625		
LA_{314}	8	9	3	8	9	0.2734375		
LA_{321}	4	7	7	9	7	0.329545455	0.506	
LA_{322}	10	7	8	9	8	0.375		
LA_{323}	8	9	3	8	9	0.295454545		
LA_{411}	10	9	8	9	9	0.252941176	0.5059	0.2516
LA_{412}	8	9	8	8	9	0.247058824		
LA_{413}	10	10	9	9	8	0.258823529		
LA_{414}	8	7	7	7	8	0.241176471		
LA_{421}	9	8	6	9	8	0.371681416	0.4941	
LA_{422}	7	7	6	8	7	0.327433628		
LA_{423}	9	10	7	7	9	0.300884956		

4.1.2 Secondary Assessment Calculation

The secondary assessment calculation is performed by applying the results from the primary assessment calculation and using the weightage calculated for criteria of the data collected.

4.1.3 Tertiary Assessment Calculation

The tertiary assessment calculation is performed by applying the results from the secondary assessment calculation and using the weightage calculated for enablers of the data collected.

Leanness index is found by calculating the average of the resultant matrix. Thus, the average of L is found to be around 7.9; hence, the TMC is 'lean.'

4.2 Classification of Lean Attributes Using IPA

The mean of the attribute rating is taken as performance which is the X-axis, and the weightage of the attributes is taken as the weightage which is in the Y-axis [19]. The data are plotted in a scattered plot graph, and the average of both the performance and the weightage is marked using a line in the graph, to section it into four quadrants [20]. The four quadrants and the inference of IPA are described in Table 4. The attributes are classified using IPA, and it is depicted in Fig. 1.

5 Results and Discussion

The case TMC leanness level L is found to be around 7.9, which lies in the scale of 6–8 and which proves that the organization is 'lean.' Case TMC is a lean organization, but there is still scope for improving its leanness to reach the category of 8–10 which will make the organization 'extremely lean.'

5.1 Improvement Proposal for Weaker Attributes

The weaker attributes are identified using the IPA. The attributes falling in the quadrant-1 are weaker attributes, and these attributes deserve more attention. Some suggestions for improvements have been identified and recommended in Table 5.

6 Conclusion

The main focus of the paper is assessment of leanness level in the case TMC. Lean implies more efficiency by reducing wastage and improving the ease of process flow. A multi-grade fuzzy approach is used to create this framework, and IPA is used to identify weak attributes. Also, suggestions are provided to improve weaker attributes and gain competitive advantage. The case TMC comes under the category of 'lean,'

Table 4 Inference of IPA

Quadrants–Inference	Attributes in the quadrant
Q1—The performance of the attributes in this quadrant is not appreciable, and it is high weightage area where these attributes should be focused more	L112, L121, L414, L111, L113
Q2—The performance of the attributes in this quadrant is good, and the weightage of these attribute is also high; hence, this should be maintained for a longer period	L421, L124, L125, L233, L412, L322, L232, L231, L211, L413, L221, L411
Q3—The performance of the attributes in this quadrant is not good, and it is not important to improve it	L422, L123, L321, L212, L122, L323, L312, L311
Q4—The performance of the attributes lying in this quadrant is good, but the weightage is low; hence, it is not important to maintain it	L222, L314, L423, L313

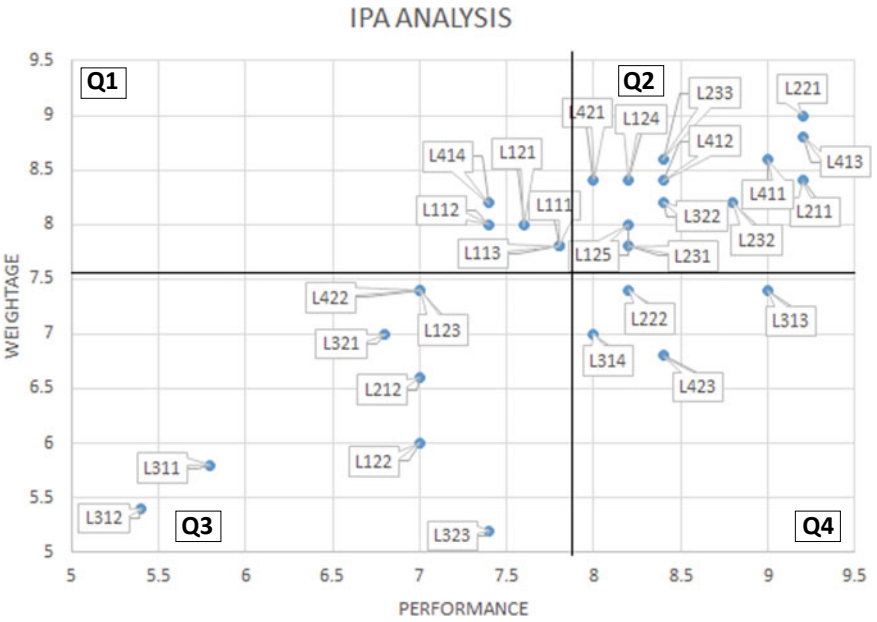

Fig. 1 IPA for leanness assessment

Table 5 Weaker attributes identified

Weaker attributes	Improvement suggestions
Management involvement (L_{112})	The management involvement is found to be low in this organization, where it is very important to improve the involvement of the management. The management should then and there follow up the flow of processes and encourage employees
Information transparency (L_{121})	The information transparency should be improved. It helps to build trust in the views of the employees of the organization which increases the profitability of the company
Layout (L_{414})	The layout of the manufacturing unit is not very appreciable, and an effective layout must be built either with the help of internal/external consultants or by taking time studies
Smooth information flow (L_{111})	The smooth information flow helps the employees and the managers to take right action at right time. A proper and efficient communication channel could be set up to enhance the smooth flow of information
SOP (L_{113})	Standard operation procedure is very important for a company to set up and follow. SOP could improve the efficiency and flow of materials and information of the company. Employees should be encouraged to follow the SOP

but there is still scope to achieve 'extremely lean.' The scope of this framework can be further expanded by incorporating additional lean attributes related to the textile processing industries. Although this framework is well suited to TMC, it can also be used to evaluate the leanness level of other clothing or garment industries by slightly changing the attributes used in this framework.

Compliance with Ethical Standards' Conflict of Interest The authors declare that there is no conflict of interest in publishing this paper. The authors state the clarification of the anonymization of the data collection or for questionnaires (if any).

References

1. Vinodh S, Vimal KEK (2012) Thirty criteria based leanness assessment using fuzzy logic approach. Int J Adv Manuf Technol 60(9–12):1185–1195
2. Rakhmanhuda I, Karningsih PD (2018) Development lean assessment indicator: a case study. In MATEC web of conferences, vol 204, p 03018. EDP Sciences
3. Bidhendi SS, Goh S, Wandel A (2019) Development of a weighted leanness measurement method in modular construction companies. J Ind Eng Int 1–23
4. Vidyadhar R, Sudeep Kumar R, Vinodh S, Antony J (2016) Application of fuzzy logic for leanness assessment in SMEs: a case study. J Eng Des Technol 14(1):78–103
5. Vinodh S, Balaji SR (2011) Fuzzy logic based leanness assessment and its decision support system. Int J Prod Res 49(13):4027–4041
6. Narayanamurthy G, Gurumurthy A, Subramanian N, Moser R (2018) Assessing the readiness to implement lean in healthcare institutions—a case study. Int J Prod Econ 197:123–142
7. Vimal KEK, Vinodh S (2012) Leanness evaluation using IF–THEN rules. Int J Adv Manuf Technol 63(1–4):407–413
8. Madhan K, Suresh M (2016) Leanness assessment using fuzzy logic approach: a case of Indian cooperative bank. In 2016 international conference on advanced communication control and computing technologies (ICACCCT), pp 341–346. IEEE
9. Patri R, Suresh M (2018) Factors influencing lean implementation in healthcare organizations: an ISM approach. Int J Healthc Manage 11(1):25–37
10. Narayanamurthy G, Gurumurthy A (2016) Leanness assessment: a literature review. Int J Oper Prod Manage 36(10):1115–1160
11. Domingo R, Aguado S (2015) Overall environmental equipment effectiveness as a metric of a lean and green manufacturing system. Sustainability 7(7):9031–9047
12. Keerthana S, Suresh M (2016) Drivers influencing lean practices in street food vending process. In 2016 IEEE international conference on computational intelligence and computing research (ICCIC), pp 1–5. IEEE.
13. Amrita VV, Suresh M (2016) Factors influencing lean practices in Super market services using interpretive structural modeling. In: 2016 IEEE international conference on computational intelligence and computing research (ICCIC) (pp 1–5). IEEE
14. Abinaya R, Suresh M (2016) Analyzing the drivers for lean practices of commercial banking using interpretive structural modelling. In 2016 IEEE international conference on computational intelligence and computing research (ICCIC), pp 1–4. IEEE
15. Vignesh V, Suresh M, Aramvalarthan S (2016, September) Lean in service industries: a literature review. In IOP conference series: materials science and engineering, vol 149, No 1, p 012008. IOP Publishing
16. Vinodh S (2011) Assessment of sustainability using multi-grade fuzzy approach. Clean Technol Environ Policy 13(3):509–515

17. Ganesh J, Suresh M (2016) Safety practice level assessment using multigrade fuzzy approach: a case of Indian manufacturing company. In 2016 IEEE international conference on computational intelligence and computing research (ICCIC) (pp 1–5). IEEE
18. Sridharan V, Suresh M (2016) Environmental sustainability assessment using multigrade fuzzy—a case of two Indian colleges. In: 2016 IEEE international conference on computational intelligence and computing research (ICCIC), pp 1–4. IEEE
19. Deng WJ (2008) Fuzzy importance-performance analysis for determining critical service attributes. Int J Serv Indus Manage 19(2):252–270
20. Feng M, Mangan J, Wong C, Xu M, Lalwani C (2014) Investigating the different approaches to importance–performance analysis. Serv Ind J 34(12):1021–1041

Pairwise Nonparametric Model Analyzed Advanced ICT Skills and Adaption of E-Health Solution in India

K. Ravichandran

Abstract The information and communication technology (ICT) in health will create a distinct world of all told level. The transformation of the health system has narrowly targeted on the activity of diseases in hospitals by health professionals. There is a system targeted on keeping public health by providing them with data to require care of their health, whenever the requirement arises, and where they will be available. Hospital administrators and their staff need to properly manage ICT e-health skills with the mind-set that it can improve quality, strengthen processes and create its additional economy. The public health service of the government has bowed down and collapsed. In the vast world, increasing population density, lack of transportation and the resulting hardship, illiteracy, poverty, poor environmental pollution, poor health, lack of funding and poor eating habits are all contributing factors to the decline in healthcare services. This paper discusses the challenges and opportunities in ICT implementation during a healthcare specific to the Indian scenario with pairwise nonparametric model analyzed advanced ICT skills and adaption of e-health and solution of India.

Keywords Information and communication technology—ICT · E-health and nonparametric model

1 Introduction

India is that the most populous settled country within the world, and it has one-fourth billion population tending access between urban and rural regions [1, 2]. Indian health services are often very favourable to urban people. Unfortunately, only one-third of the total population has access to proper health care, especially the 700 million people who do not have access to accurate medical care. The main reason for this is that 18% of medical professionals are willing to work in urban areas for more

K. Ravichandran (✉)
Department of Visual Communication and Animation, Dr. MGR Educational and Research Institute, Chennai 600095, Tamil Nadu, India
e-mail: ravi.news10@yahoo.com

G. Kumaresan et al. (eds.), *Advances in Materials Research*, Springer Proceedings in Materials 5, https://doi.org/10.1007/978-981-15-8319-3_78

money and luxury facilities [3]. Nearly, one million Indians die each year without inadequate tending facilities [4]. "E-health is a rising field inside the convergence of medicinal data preparing, general well-being and business, bearing on well-being administrations and the information conveyed or improved through the web and associated innovations" [5]. Overburdened and folded public healthcare system is additionally taking the ICT components of the country [6]. The prime objectives are ICT with Internet service area unit essential for medical professionals, and a body supported members and patients to prepare, share and access medical services [7].

Increasing health care not only enhances the information and skills of medical professionals but also empowers ICTs to provide individuals with the information they need to create intellectual needs for a way to live healthier [8]. As an alternative to human activities, ICT provides vital health information, health awareness and counselling to the general public [9].

Evidence-based clinical practice needs sufficient knowledge on the latest development in medical science [10, 11]. Automated information management tools like the Internet, web-based libraries, electronic medical record (EMR), electronic health record (EHR) and computerized prescriptions are important components. Quality assurance (QA) is analyzed by total quality management (TQM) through the computerization of hospitals, so that all processes, including pharmacy, finance and procurement division [12], are audited, including medical and nursing. Computerization can help inventory and administration machinery, and accurately detect the budget, time and human error [13]. India faces many difficulties inside the improvement of compelling e-health arrangements simply like the inactivity of antiquated plans and ways that of getting things done [14]. There are various questions about the way to properly modify the health system that technical standard area unit has to be adopted for the current level of technology [15, 16].

2 Objective of the Study

- The objective is to study the ICT skills in the health sector and challenges of implementation healthcare system in India.

3 Materials and Methods

Essential information was gathered dependent on the overall population view of the elements concerning model once a few adjustments. This investigation of data gathered 300 samples from doctors, patients, students and IT experts from numerous spots like city town in India. Supposition concerning medical help quality was evoked from the point of cutting-edge ICT abilities in the therapeutic segment toward to support rustic health objective. The research factors of Basic ICT—e-health, Advanced ICT—e-health, Advanced mobile e-health skill, Perceive easy to use, Behavioral

adoption, and E-health information usage has been determined by the Technology Adoption Model (TAM).

4 Results and Discussion

The results analyzed nonparametric models. Based on the survey conducted, the participants like doctors, nurse, laboratory technicians and patients belong to metropolitan cities in India. In total, 328 public participated in the study. Following knowledge screening, a final sample of three hundred was achieved. A total of 300 samples had been taken for this research: 108 were women (36%) and 192 were men (64%). In particular, 3% are between the ages of 25 and 30, 30.3% are between the ages of 26 and 35, 20% are between the ages of 36 and 45 and 19.3% are over the age of 45. In terms of educational qualification, HSc is 24.7%, UG graduates 25.7%, PG graduates 33.3% and professional graduates 16.3%. On the marital status, 60.3% are married and 39.7% are unmarried. In terms of various occupations, the working in the public sector is -45%, the private sector is -25.7%, the self-employed are -20.7% and the others are 20.3%.

Tests like Kruskal–Wallis involve quite a pair of samples. They take a glance at all sample units of measurement from populations with similar characteristics. This characteristic might even be the distribution, mean or median counting on the hypotheses. Denote the null hypothesis. Once this overall hypothesis is rejected at the user-specified significance level (using two-sided p-values apart from the Jonckheere–Terpstra taking a glance at here), we have got a bent to possibly wish to know where is the variation unit of measurement among the populations. The multiple comparison procedure units of measurement have been thought to answer this research question. Particularly, pairwise multiple comparisons and a stepwise reduction procedure have taken for multiple comparison analyses. The Pairwise Multiple Comparisons have all come-at-able combine wise hypotheses like for unit of measurement tested.

Basic ICT with e-health centers comprehend quality tending, just as access to protection care as easy to use by weak customer with low negotiation power. Doctors and attendants accept their aptitudes to work with computers. Advanced computer usage in the medical sector provides healthcare information and improves public health. In Fig. 1, if the adjusted p-value is larger than one, it will be significant. The two-sided p-value area unit is important with the yellow line.

In Fig. 2, if the adjusted p-value is bigger than 1, the two-sided p-values are significant with the yellow line. Advanced ICT–e-health perceives all the equipment of ECG level, blood pressure level and other medical measurements that should have connected to the cloud for using the public utility. Public health is easy to use by e-health, which is an effective solution to improve access to health care for people in rural areas. E-health centers receive quality health care, including access to preventative care and medical record on the cloud, and the doctor can see it and give me medication, anywhere in the world or anywhere in the city, to motivate public

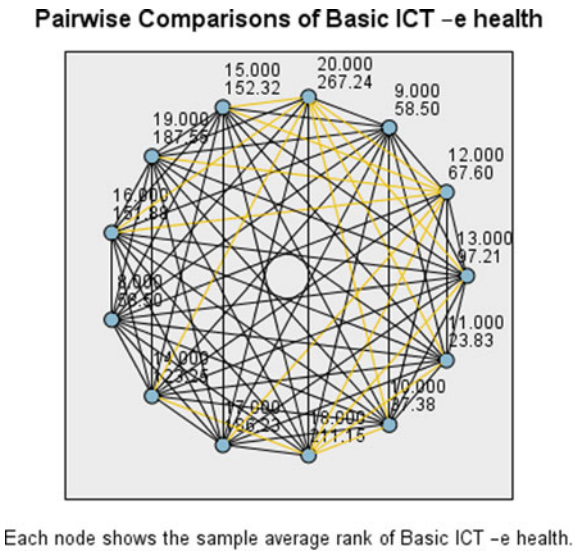

Fig. 1 Basic ICT–e-health

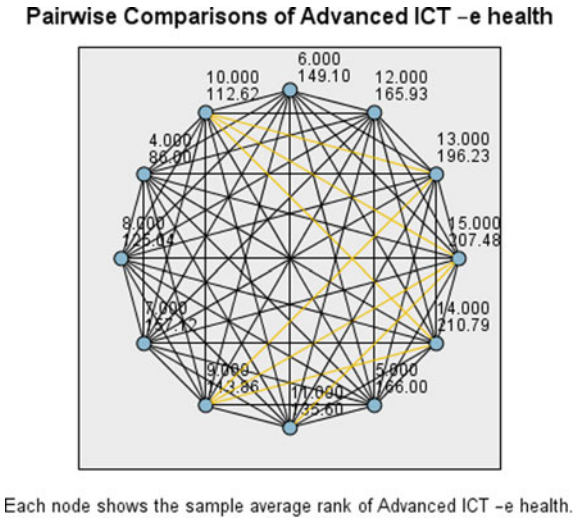

Fig. 2 Advanced ICT–e-health

health system (PHS) with competition and weak customers with low bargaining power.

In Fig. 3, if the adjusted p-value is larger than one, the two-sided p-value area unit is important with the yellow line. Advanced mobile e-health skill comprehends e-health centers get quality tending. ICT helps in therapeutic and nursing instruction, and health care data improve to open.

In Fig. 4, if the adjusted p-value is larger than one, it is set to one. The calculation of the two-sided p-value area unit is important with the yellow line. Perceive easy

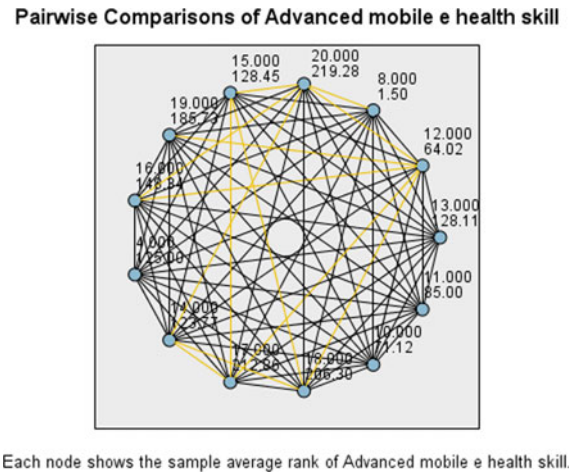

Fig. 3 Advanced mobile e-health skill

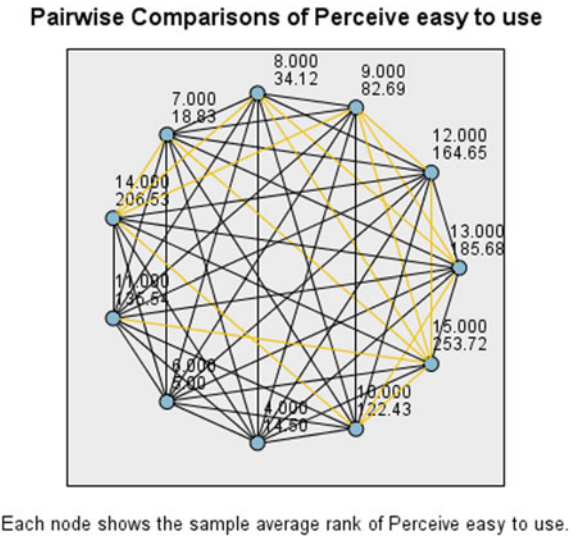

Fig. 4 Perceive simple to use understand

to use, all the instrumentation of ECG graph, blood pressure level, and alternative medical measures—connected to cloud exploitation the computer as simple to use. E-health is a good answer to boost access to tending for individuals in rural areas, as the e-health centers receive quality tending, as well as access to preventative care. Medical records on the cloud and therefore the doctor will see it and provides the medication, anywhere within the world or anywhere within the town, to motivate public health system (PHS).

In Fig. 5, if the adjusted p-value is larger than one, it is set to one. The calculations of the two-sided p-value area unit are important with the yellow line. Behavioral

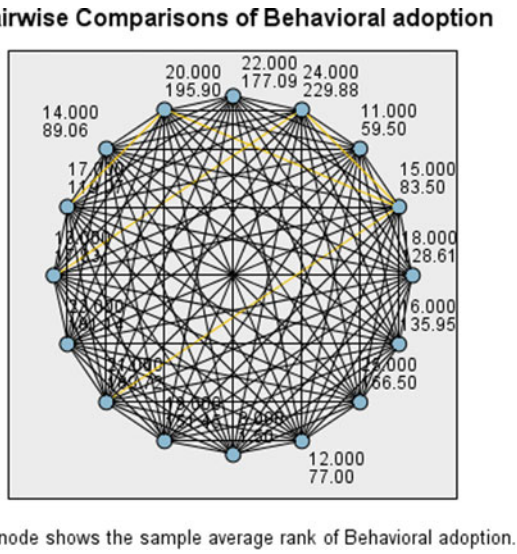

Fig. 5 Behavioral adoption

adoption understands all the instrumentation. The computer is as simple to use by e-health centers and receive quality tending, as well as access the preventative care and medical history on the cloud. In Fig. 6, if the adjusted p-value is larger than one, it is set to one. The calculation of the two-sided p-value area unit is important with a yellow line. E-health data usage understands to access anyplace within the world and to avoid medical errors. This study has been analyzed by the technology adoption model which affirmed that the impression of basic use and utility of e-health had the most grounded effect on patients. Basic fundamental ICT ability region unit is

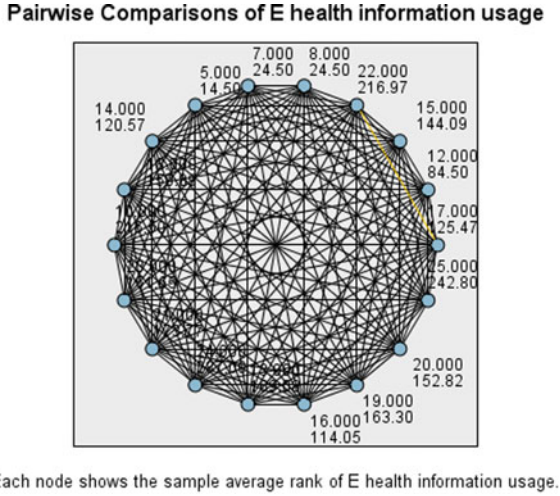

Fig. 6 E-health information usage

appallingly intensely identified with cutting-edge e-health and also with cutting-edge ICT aptitudes. The model furthermore builds up that to a lesser degree essential ICT abilities assume an immediate job in their goal to receive. Propelled e-well-being abilities were appeared to intervene in the job of apparent straightforward use and utility on the aim of researchers to receive e-health. This implies e-health innovation can impact their impression of public health. Indian Vice President Venkaiah Naidu [17] said that the Indian nation faces many challenges in the healthcare sector and the lack of adequate medical infrastructure in rural areas is a challenge. It is necessary for the government to work with the private sector to reach the rural areas with modern health facilities. He also said there was a shortage of qualified physicians and concerned about setting up of technologically advanced ICT primary and secondary health centers.

5 Conclusions

ICT will bolster upgrades inside the nature of social insurance by serving to extend the capabilities and abilities of well-being and therapeutic experts and in this way improve the conveyance of well-being administrations. However, access to data might not be adequate in and of itself. Health professionals ought to gain an understanding of a way to appraise, interpret and apply the data to their specific applications. ICT can even be instrumental in serving the general public to become additionally enlightened concerning their health and the way to be healthy, although till a larger share of the population is online and technologically literate, low-tech solution area unit probably to be more practical. At long last, information and communication technologies will assume a solid job in raising the intensity of well-being administrations. Through Computer-based records in the cloud and option innovative framework building, human services foundations will higher oversee and offer information along these lines raising the intensity of the wellbeing framework as a full. Computer-based logs play an important role in creating a cloud and custom innovative architecture. Such high-quality facilities are helping to possible to fully elevate the welfare of health structure in human society.

Acknowledgements This paper and the research behind it would not have been possible without the exceptional support of President of the Doctors' Association for Social Equality, G.R Raveendranath. His enthusiasm, knowledge and exacting attention to detail have been an inspiration and kept my work to the final draft of this paper.

References

1. Martin PL, Zürcher G (2008) Managing migration: the global challenge, vol 63, No 1. Population Reference Bureau, Washington, DC

2. Hardoy JE, Satterthwaite D (2019) Urban change in the Third World: are recent trends a useful pointer to the living city. Towards Sustain Future 2:75
3. Cousins S (2019) A woman's worth: health, stigma and discrimination in India. Sage Publications Pvt. Limited, Thousand Oaks
4. Lohia N, Prashar M, Singh S, Bhatnagar S, Viswanath S, Anand S, Ranjan R (2019) Epidemiological and survival trends in patients of cancer of uterine cervix treated with definitive concurrent chemoradiotherapy: observations from a north indian hospital-based cancer registry. Ind J Gynecol Oncol 17(2):44
5. Suguna SK, Kumar SN (2019) Application of cloud computing and internet of things to improve supply chain processes. In edge computing, pp 145–170. Springer, Cham
6. Tripathi VVR, Tripathi A, Jaiswal S (2019) Health welfare system in modern India revitalizing Indian Healthcare-Its potential and challenges. ZENITH Int J Multidiscipl Res 9(2):178–193
7. Darwish A, Hassanien AE, Elhoseny M, Sangaiah AK, Muhammad K (2019) The impact of the hybrid platform of internet of things and cloud computing on healthcare systems: opportunities, challenges, and open problems. J Ambient Intel Humanized Comput 10(10):4151–4166
8. Lokshina I, Lanting C (2019) A qualitative evaluation of IoT-driven eHealth: know-ledge management, business models and opportunities, deployment and evolution. In data-centric business and applications, pp 23–52. Springer, Cham
9. Syed L, Jabeen S, Manimala S, Alsaeedi A (2019) Smart healthcare framework for ambient assisted living using IoMT and big data analytics techniques. Future Gener Comput Syst 101:136–151
10. Al Saif AN, Johnson JM, Munir S, Ammal K, Forgrave D (2019) Effectiveness of journal clubs in translating knowledge into practice: a literature review. J Nurs Educ Pract 9(5)
11. Walker HM (2004) Commentary: use of evidence-based interventions in schools: where we've been, where we are, and where we need to go. School Psychol Rev 33(3):398–407
12. Mahapatra SC, Das RK, Patra MR (2011) Current e-governance scenario in healthcare sector of India. E-Governance Scenario in Healthcare Sector of India, pp 121–7
13. Rosenthal U, Kouzmin A (1997) Crises and crisis management: toward comprehensive government decision making. J Publ Adm Res Theor 7(2):277–304
14. Hill JW, Aneiros AN, Hogan PR (2010) Law and the healthcare crisis: the impact of medical malpractice and payment systems on physician compensation and workload as antecedents of physician shortages-analysis, implications, and reform solutions. U. Ill. JL Tech. & Pol'y, 91
15. Bashshur RL, Reardon TG, Shannon GW (2000) Telemedicine: a new health care delivery system. Annu Rev Public Health 21(1):613–637
16. Koschan A, Li S, Visich JK, Khumawala BM, Zhang C (2006) Radio frequency identification technology: applications, technical challenges and strategies. Sensor Review
17. Speech of Hon'ble Vice President, Shri M Venkaiah Naidu at Inauguration of MGM Healthcare, Posted On: 14 Jul 2019 by PIB Chennai. https://pib.gov.in/PressReleasePage.aspx?PRID=1578667

Modelling of Surface Roughness in Wire-EDM Using Response Surface Methodology Technique

P. Mathan Kumar, D. Dinesh, G. Sundarraju, S. Madheswaran, and K. Perumal

Abstract Wire EDM is one of the most important and useful machining process in metal cutting industry due to its minimum heat-affected zone (HAZ) ability near the machined surface. Surface finish of the machined surface in Wire EDM mainly depends on the input parameter such as pulse current, voltage, pulse on time, wire feed and type of dielectric medium. In this current work, surface roughness was taken as a response characteristics for the analyses and further optimized with selected input process parameter. Response surface methodology centre composite second-order rotatable design was used to design the experiments. The selected process parameters for this current study were pulse on time, pulse off time, flushing pressure, wire tension, servo voltage and wire feed rate. The regression model for surface roughness was established with inclusion of all the input process parameter. Optimized values were predicted using genetic algorithms. Finally, predicted optimized value is compared with experimental value, and the closeness with obtained experimental value is stated interns of percentage.

Keywords Wire electric discharge machining · Surface roughness · ANOVA

1 Introduction

Wire electrical discharge machining (WEDM) is been widely used in die-making industry, aerospace, medical and practically machine any electrically conductive material. It is an unconventional machining process which uses continuously feeding electrically conductive electrode wire to cut the work piece based on the written programme. Wire electrical discharge machine commonly called as WEDM, and the conductive wire is fed against the work piece [1]. Majhi et al. [2] have made

P. Mathan Kumar (✉) · D. Dinesh · G. Sundarraju · S. Madheswaran
Department of Mechanical Engineering, Bannari Amman Institute of Technology, Sathyamangalam, India
e-mail: mathankumarp@bitsathy.ac.in

K. Perumal
Department of Mechanical Engineering, KSR College of Engineering, Tiruchengode, India

G. Kumaresan et al. (eds.), *Advances in Materials Research*, Springer Proceedings in Materials 5, https://doi.org/10.1007/978-981-15-8319-3_79

an attempt to determine the optimal process parameters MRR, SR and TWR for EDM process. Kumar and Kumar [3] have modelled and optimized the WEDM for the selected input process parameter. To figure out optimum surface roughness (SR), they selected the input process parameters like pulse on time, pulse off time, wire speed and wire feed. Taguchi techniques was effectively used for optimization of minimizing the SR. Pasam et al. [4] conducted an experiment in WEDM to determine the relation among the responses characteristics and its input process parameter. From the study, they concluded that metal removal rate, surface finish and kerf width are most important responses to study in WEDM. Lal et al. [5] used Taguchi-based gray relational analysis, to find the optimal input process parameter setting for machining composite material using molybdenum wire as an electrode with a diameter of 0.18 mm. Shivade and Shinde [6] have used same technique to optimize the D3 tool steel material. Jaganathan et al. [7] have optimized the wire-EDM input process parameter and output responses characteristics such as material removal rate and surface finish for EN31 using Taguchi L27 orthogonal array (OA). Pradhan [8] had run the experiment using Taguchi method and response surface methodology for designing the experiment and to estimate the optimum machining condition within the input process parameter range. Sinha et al. [9] have applied Taguchi method for single objective optimization and principal component analysis (PCA) been used for multi-objective optimization. Huang and Liao [10] applied grey relational analyses for optimizing the input process parametr in the WEDM.

The main focus on this paper is to analyse the effect of selected input process parameter on the surface roughness.

2 Experimentation

The experiment was conducted on ELEKTRA SPRINTCUT 734 four axes WEDM machine tool. High-carbon high-chromium die steel (HCHCR) was used as a work piece. The composition of high-carbon high-chromium die steel (HCHCR) work material used is given in Table 1. Molybdenum wire of 0.18 mm diameter was used an electrode material for all the run.

The photographic view of the molybdenum wire electrode is shown in Fig. 1. The other fixed parameter details is given in Table 2. The selected input process parameters (are pulse on time, pulse off time, servo voltage and wire feed) and their range with coded value are given in Table 3. The SR was measured by using Mitutoyo-SJ-201P surface tester on the work piece at four different spot after machining. 4 mm is chosen as an evaluation length for the measurement. The average value is taken for

Table 1 Chemical composition of high-carbon high-chromium die steel (HCHCR) (wt%)

C	Cr	Si	V	Mn	Mo
1.54	12	0.32	0.91	0.34	0.76

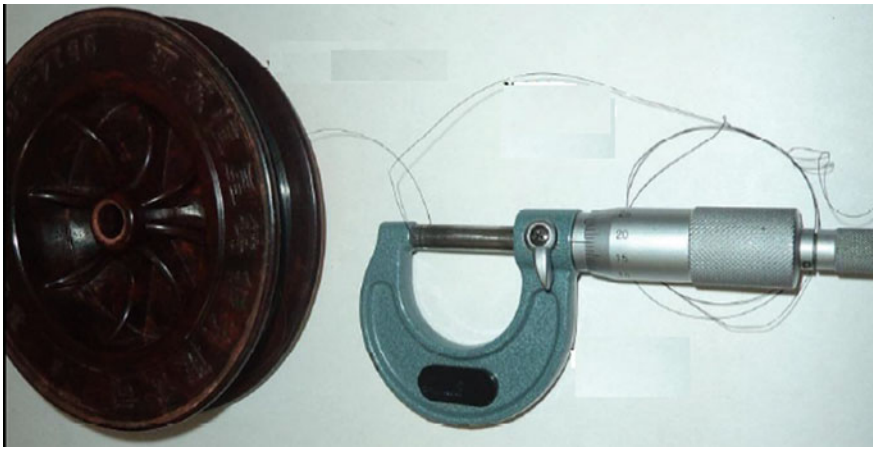

Fig. 1 Molybdenum wire electrode

Table 2 Fixed parameters

S. no.	Fixed parameter	Set value
1	Wire material	Molybdenum wire of diameter of 0.25 mm
2	Peak current	230 Amps
3	Pulse in peak voltage	2
4	Servo feed setting	250

Table 3 Input variable and their levels

Variables	Symbol	Levels				
		−2	−1	0	1	2
Pulse on time—Ton (μs)	A	105	110	115	120	120
Pulse off time—T-off (μs)	B	35	40	45	55	10
Servo voltage—Sv (volt)	C	10	15	20	25	30
Wire feed rate—Wf (m/min)	D	4	6	8	10	12

the analysis. Initially, number of trial runs have been conducted to fix range of input process parameter range for design of experiment. The resolution of the Mitutoyo-SJ-201P machine is 0.01 mm. The surface roughness tester machine which used for this study is shown in Fig. 2.

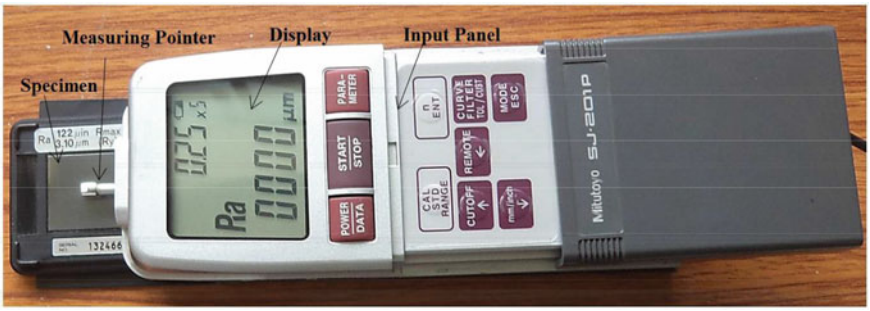

Fig. 2 Surface roughness tester

3 Developing the Design Matrix

Response surface methodology was used for to design the experiment. This is used for experimental modelling of polynomials as limited approximations to get exact input and output interaction. Centre composite second-order routable design was selected for record the readings. This is an effective technique comprises of two subset points, first one which approximate linear and two factor interaction effects and second subset create curvature effect. It is effective method to predict the interaction and required minimal runs to predict errors. It comprises of 16 corner points, 8 axial points and 6 central points. The design is given in Table 4. Accordingly, the 30 experimental runs were conducted to evaluate the linear quadratic and two-way interactive effect of the WEDM variable on the responses.

4 Development of Mathematical Models

Using the experimental result which is obtained from the central composite-rotatable design of experiments and applying regression analysis, the modelling of the selected response with a small quantity of independent input process parameter can be gained. The response surface exists expressed as follows.

$$y = a_0 + \sum_{i=1}^{n} a_i x_i + \sum_{i=1}^{n} a_{ii} x_i^2 + \sum_{i<j}^{n} a_{ij} x_i x_j + \varepsilon \tag{1}$$

In this equation,

y—the corresponding response surface,

x_i and x_j—the coded values of input variables and the coefficients

a_i, a_{ii} and a_{ij}—the linear terms, quadratic terms and interaction effects, respectively.

Table 4 Design of experiments

Run	Ton	Toff	Sv	Wf	SR (μm)
1	2	0	0	0	3.411
2	1	1	−1	1	3.32
3	−1	1	1	−1	2.91
4	−1	1	−1	−1	2.89
5	−1	−1	1	−1	2.89
6	−2	0	0	0	2.82
7	1	1	1	−1	3.32
8	1	1	−1	−1	3.29
9	1	−1	−1	−1	3.252
10	1	1	1	1	3.25
11	0	0	0	−2	3.087
12	0	0	0	2	3.05
13	0	0	0	0	3.04
14	0	0	0	0	3.04
15	0	0	0	0	3.04
16	−1	1	−1	1	3.02
17	−1	1	1	1	3.011
18	−1	−1	1	1	3.01
19	−1	−1	−1	1	2.991
20	−1	−1	−1	−1	2.95
21	0	0	0	0	3.141
22	0	0	2	0	3.11
23	0	0	0	0	3.11
24	0	0	0	0	3.11
25	0	2	0	0	3.11
26	1	−1	−1	1	3.218
27	1	−1	1	−1	3.191
28	1	−1	1	1	3.19
29	0	−2	0	0	3.159
30	0	0	−2	0	3.152

4.1 Developing the Final Model

As determined by the procedures, the final mathematical models in terms of process parameter are given below:

$$\mathrm{SR} = +3.10 + 0.15 * \mathrm{A} + 9.208\mathrm{E} - 003 * \mathrm{B} - 0.010 * \mathrm{C} + 0.010 * \mathrm{D}$$

Table 5 ANOVA for SR

Source	Sum of square	df	Mean square	*F* value	*p*-value Prob > *F*	
Model	0.55	10	0.055	30.13	<0.0001	Significant
A-A	0.52	1	0.52	285.32	<0.0001	
B-B	2.04E−03	1	2.04E−03	1.11	0.305	
C-C	2.46E−03	1	2.46E−03	1.34	0.2608	
D-D	2.46E−03	1	2.46E−03	1.34	0.2608	
AB	7.18E−03	1	7.18E−03	3.92	0.0623	
AC	6.13E−04	1	6.13E−04	0.33	0.5698	
AD	0.014	1	0.014	7.44	0.0133	
BC	6.38E−04	1	6.38E−04	0.35	0.5621	
BD	2.64E−04	1	2.64E−04	0.14	0.7083	
CD	1.81E−05	1	1.81E−05	9.86E−03	0.9219	
Residual	0.035	19	1.83E−03			
Lack of fit	0.024	14	1.75E−03	0.85	0.6331	Not significant
Pure error	0.01	5	2.06E−03			
Cor total	0.59	29				

$$+ 0.021 * \mathrm{A} * \mathrm{B} - 6.187\mathrm{E} - 003 * \mathrm{A} * \mathrm{C}$$
$$- 0.029 * \mathrm{A} * \mathrm{D} + 6.313\mathrm{E} - 003 * \mathrm{B} * \mathrm{C}$$
$$+ 4.062\mathrm{E} - 003 * \mathrm{B} * \mathrm{D} - 1.062\mathrm{E} - 003 * \mathrm{C} * \mathrm{D} \quad (2)$$

Adequacy of the developed model is checked using ANOVA technique. ANOVA result is given in Table 5. It found that model is significant, and lack of fit is not significant. F ratio was greater than the tabulated values at 95% confidence level. R^2 and adjusted R^2 values are 91.49 and 89.27%, respectively.

5 Confirmation Experiments

In order to verify the developed surface roughness regression model, confirmation experiment was conducted. One set of values of input process parameter (pulse on time, pulse off time, servo voltage and wire feed) is taken to feed in the developed equation. The experiment was conducted for the same reading. The experiment values were compared with predicted value. The errors values are in satisfactory level. The comparison value is given in Table 6.

Table 6 Optimum process parameter

Process parameter				SR (μm)		Error
Ton	Toff	Sv	Wf	Predicted	Experimental	
120	55	10	10	3.31	3.24	2.16%

6 Effect of Working Parameters on the Surface Roughness

Figure 3 shows the relationship between pulse on time and pulse off time while keeping other two parameter as a constant (servo voltage and wire feed). From the graph, it observed that an increase in pulse current leads to increase in surface roughness value. It is due to supplying of electrical energy for longer duration which will produce cracks and void on the machined surface. While considering the pulse off time in the graph, it found that increase in pulse off time would reduce the surface roughness. This is due to allowing the time for reaching fresh dielectric medium on the surface which having minimum carbon content [11, 12].

Figure 4 shows the variation of surface roughness with respect to the servo voltage and wire feed. From the shown graph, it was noticed that increase in wire feed would increase the surface roughness. This is due to increase in wire speed which increases the number of spark with respect to time [13]. This makes the work surface more voids on the side. In other aspect of the graph, increase in servo voltage would reduce the surface roughness. This is due to voltage which has inverse relationship with pulse current, so that surface roughness getting reduced [14, 15].

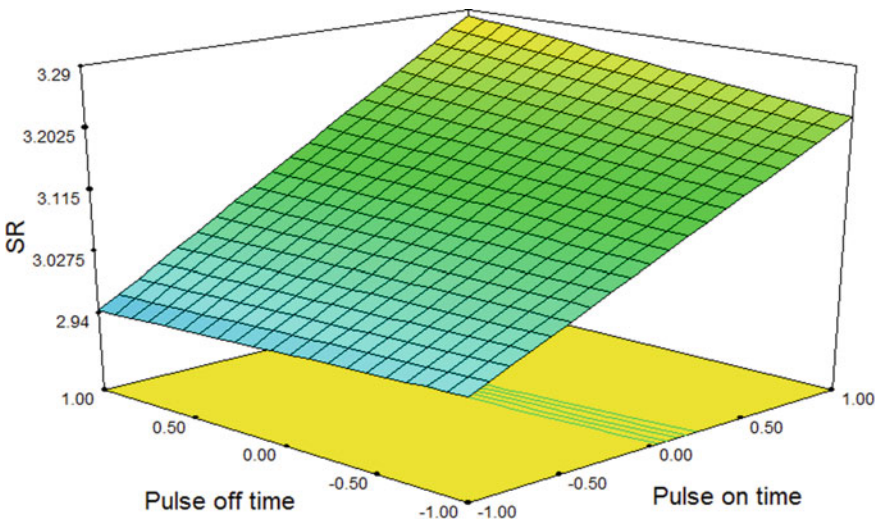

Fig. 3 SR versus pulse on time and pulse off time

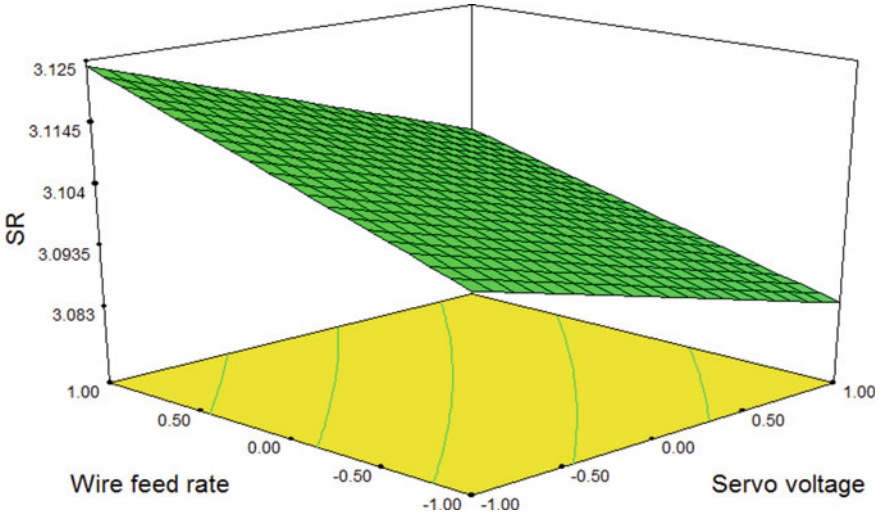

Fig. 4 SR versus servo voltage and wire feed rate

7 Conclusion

In this study, influences of process parameter on surface roughness were investigated, and following conclusion was made:

(i) Wire cut electric discharge machining process has showed its adequacy to machine high-carbon high-chromium die steel (HCHCR) work material under acceptable surface finish (Ra) of 3.41 μm.
(ii) The investigation of the selected response (surface roughness) using response surface methodology—CCD method—has the advantage of explaining the effect of each input parameter on the value of the resultant response characteristics.
(iii) The list of 30 different input process parametric combinations will act as technical information for effective machining of high-carbon high-chromium die steel (HCHCR) work material.
(iv) ANOVA results show that model is significant, and pulse on time has a significant effect on surface roughness rather than a other parameter.

References

1. Ho KH, Newman ST, Rahimifard S, Allen R (2004) State of art in wire electric discharge machining (WEDM). Int J Mach Tools Manuf 44(13):1247–1259

2. Majhi SK, Pradhan MK (2013) Soni H "Application of integrated RSM-Grey-entropy analysis for optimization of EDM parameters. In: Proceedings of the international conference on advanced research in mechanical engineering, Coimbatore. ISBN: 978-93-83060-03-0
3. Kumar K, Kumar RR (2015) Modelling and optimization of WEDM. Int J Mod Eng Res 3(3):1645–1648
4. Pasam VK, Battula SB, Valli MP, Swapna M (2010) Optimizing surface finish in WEDM using the Taguchi parameter design method. J Braz Soc Mech Sci Eng 32(2):155–166
5. Lal S, Kumar S, Khan ZA, Siddiquee AN (2015) Multi-response optimization of wire electrical discharge machining process parameters for Al7075/Al2O3/SiC hybrid composite using Taguchi-based Grey relational analysis. J Eng Manuf 229(2):229–237
6. Shivade AS, Shinde VD (2014) Multi-objective optimization in WEDM of D3 tool steel using integrated approach of Taguchimethod & Grey relational analysis. J Ind Eng Int 10(2):140–149
7. Jaganathan P, Kumar N, Sivasubramanian R (2012) Optimization of WEDM parameters using Taguchi method. Int J Sci Res 5(6):1–4
8. Pradhan MK (2013) Estimating the effect of process parameters on surface integrity of EDM AISI D2 tool steel by response surface methodology coupled with Grey relation analysis. Int J Adv Manuf Technol 67(11):2051–2062
9. Sinha P, Kumar R, Singh GK, Thomas D, Srivastava T (2015) Optimization of wire EDM of AISI D3 tool steel using orthogonal array with principal component analysis. Mater Today Proc 2(5):2512–2521
10. Huang JT, Liao YS (2013) Optimization of machining parameters of Wire-EDM based on Grey relational and statistical analyses. Int J Prod Res 41(8):1707–1720
11. Phillip K, Vain VK, Lal GK (1993) Experimental investigations into electric discharge machining with rotating disk electrode. Precision Eng 2(15):6–15
12. Tsai HC, Yan BH, Huang FH (2003) EDM performance of Cr/Cu based composite electrodes. Int J Machine Tools Manuf 3(43):245–252
13. Ramakrishnana R, Karunamoorthyb L (2008) Modeling and multi-response optimization of inconel 718 on machining of CNC WEDM process. J Mater Process Technol 207:343–349
14. Tsai TC, Horng JT, Liu NM, Chou CC, Chiang KT (2008) The effect of heterogeneous second phase on the machinability evaluation of spheroidal graphite cast irons in the WEDM process. Mater Des 29:1762–1767
15. Sarkar S, Mitra S, Bhattacharyya B (2008) Modeling and optimization of wire electrical discharge machining of TiAl intrim cutting operation. J Mater Process Technol 205:376–387

Experimental Investigation on Mechanical Properties of TIG Welded Dissimilar AISI 304L and AISI 316L Stainless Steel

A. Ramakrishnan, T. Ramesh Kumar, G. Rajamurugan, V. D. Tamilarasan, and M. Vijayakumar

Abstract The practice of stainless steel in the industry is persisting in growing regularly. Investigators conducted different experiments for various grades of steels. The use of austenitic stainless steel (304L) and stainless steel (316L) has been increased noticeably in building up of railway wagons and modern boilers where corrosion resistance areas and mechanical properties like tensile strength, toughness, hardness, etc., of the welded zone plays a major role. The objective of the present paper is to investigate the mechanical properties on dissimilar metal of austenitic stainless dteel (304) and stainless steel (316) joining under TIG welding process. Single V-groove butt welding process was carried out using gas tungsten arc welding (GTA) and shielded metal arc welding (SMAW). The experiment was conducted with identical parameters such as current, gas flow rate, and nozzle-to-plate distance, and their effects were investigated. ASTM standards are adopted for the weld specimens, and the results have been discussed.

Keywords TIG · Stainless steel · Tensile · Hardness and impact

1 Introduction

Steel plays a major role in pharmaceutical, food, biotechnology, construction industries, etc. The structures and pipelines are exposed to pressure, temperature, corrosion, etc., which should possess good weldability. There are different grades of steels, where austenitic stainless steel plays a major role in railway wagon construction.

A. Ramakrishnan (✉) · T. Ramesh Kumar · V. D. Tamilarasan
Department of Mechanical Engineering, Bannari Amman Institute of Technology, Sathyamangalam 638401, Tamil Nadu, India
e-mail: ramakrishnana@bitsathy.ac.in

G. Rajamurugan
Department of Mechanical Engineering, Vellore Institute of Technology, Vellore 632014, India

M. Vijayakumar
Mechanical Engineering, PSN College of Engineering and Technology, Tirunelveli, Tamil Nadu 627152, India

G. Kumaresan et al. (eds.), *Advances in Materials Research*, Springer Proceedings in Materials 5, https://doi.org/10.1007/978-981-15-8319-3_80

The construction of railway wagon consists of different grades of austenitic stainless steel. The permanent joint is done using dissimilar welding process. Controlling the composition in the welded metal is important. Narrow controlling of weld metal composition leads to avoid weld defects like hot cracking and different phase formation. In this work, experimental investigation of mechanical properties of 304 stainless steel and 316 stainless steel dissimilar weld is done. The parameters for this study are taken from the past literature. The author aims to report a novel technology on tungsten inert gas welding. The study finds that the technology provides considerable cost cut off to the user. The welding technique provides improved quality of their product and reduces their cost [1]. The primary requirement is to develop strong high temperature materials. This articles reviews the operational experiences, potential benefits of the present scenario, and the development in materials that require focused attention, in respect to power plants with super critical steam conditions [2]. 6 mm thick modified X2CrNi12 stainless steel is welded using gas metal arc welding and tested for microstructural, toughness properties, and mechanical properties for two different heat inputs. Results reveal that impact toughness is improved due to refinement of grain size. Tensile properties or bend properties does not get affected due to coarsening of gains, but the HAZ impact toughness at sub-zero temperatures reduces generally, and this depends on the amount of courser grain structures and eventual precipitates present [3]. Shielded metal arc welding and gas tungsten arc welding are used to join AISI 201 and AISI 304 dissimilar weld joint. Tensile strength and microhardness of the dissimilar weld joints were obtained along with the microstructure [4]. Three level of speeds are fixed to weld 201 stainless steel sheet using gas tungsten arc welding process. The welded specimens were tested for microstructure, mechanical properties, and corrosion. Higher speed is preferred for welding 201 stainless steel which possess good mechanical, microstructural, and corrosion properties [5].

304 stainless steel base material welded using gas tungsten arc welding with three level of heat input parameters low, medium, and high [6]. The effect on microstructure of the material due to arc energy produced at different levels of heat input is discussed, and tensile properties are tested [7]. Different grades of mild steel and stainless steel dissimilar joints are welded using TIG and MIG where better properties are obtained in TIG welded dissimilar joint compared with MIG. 316 stainless steel is welded using three different parameters at three levels; gray-based Taguchi method is used to optimize the parameters to obtained optimum values [8] (Table 1).

Table 1 Welding process parameters

Parameters	Unit	Samples		
		1	2	3
Current	A	60	80	100
Gas flow rate	L/min	4	5	6
Nozzle-to-plate distance	Mm	9	12	15

Fig. 1 Universal testing machine

2 Welding Procedure Specifications

The shielding gas used for this welding process is argon. The filler rod ER304L holds good for this base metal combination. Gas flow rate is decided to flow from 4 to 6 L/m. The class diameter range is kept constant at 1.6 mm, and the voltage is varied from 10 to 12 V. The welding polarity is DCEN—direct current electrode negative with medium heat input.

3 Testing Methods

3.1 Tensile Test

This dissimilar welding specimen is experimented for its tensile strength using universal testing machine (UTM) as per ASTM standards. The test was done using UTM (Tinius Olsen H10KS) that is shown in Fig. 1. Electrodischarge machining was used to cut the specimen to the required dimension. A constant strain rate of 2 mm/min was maintained. The tensile test specimen is shown in Fig. 2.

3.2 Effect of Weld on Tensile Test

Table 2 shows the test results of different welded samples. The best result is obtained from the sample no. 2 such that the specifications are 80 A current, 5 L/min of gas flow rate, and 12 mm nozzle-to-plate distance. The worst result can be obtained from sample no. 1; thus, the specifications are 60 A current, 4 L/min of gas flow rate, and 9 mm nozzle-to-plate distance.

Fig. 2 Tensile test sample

Table 2 Mechanical properties of 304 and 316 TIG welded joint

Specimen	Yield load, N/mm^2	Yield strength, N/mm^2	Tensile load, KN	Tensile strength	Initial gauge length, mm	Final gauge length	% Elongation
1	44.24	323.68	58.76	449.04	101.61	106.79	5.11
2	47.90	384.54	60.23	50.61	101.82	108.83	7.01
3	46.07	372.37	59.81	486.2	101.15	107.37	5.83

Fig. 3 Tensile strength

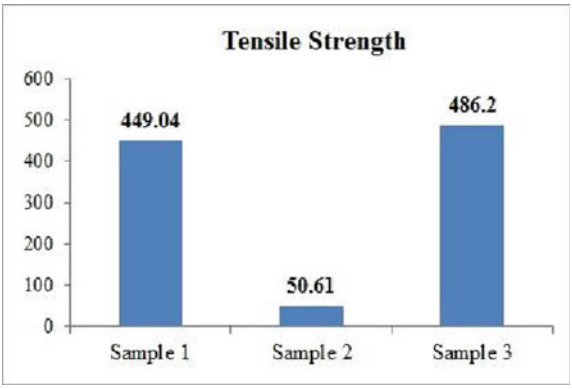

The obtained test results of tensile strength and percentage of elongation are shown in Figs. 3 and 4.

3.3 Effect of Weld on Hardness Test

From Fig. 5, it shows that sample no. 2 gives the higher hardness value when compared with other two specimens. So it clearly shows that the combination of

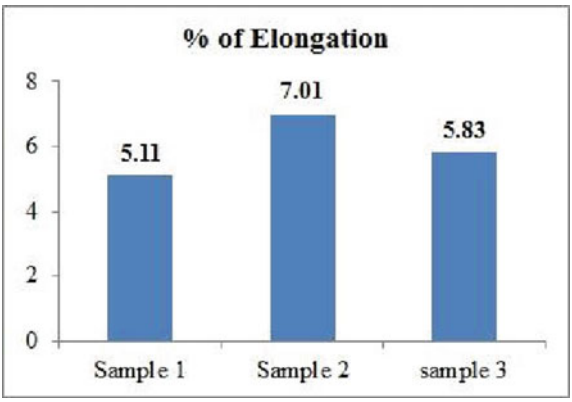

Fig. 4 Percentage of elongation

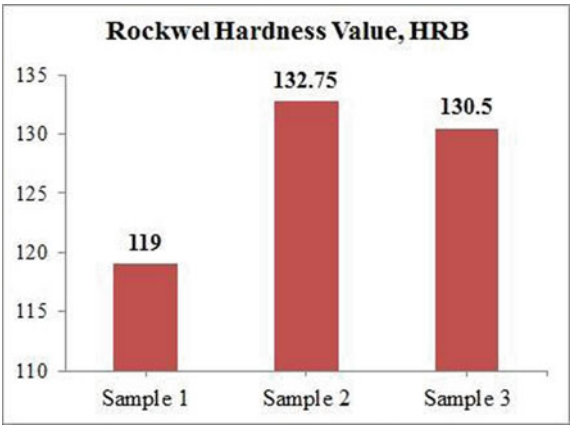

Fig. 5 Rockwell hardness value

80 A current, 4 L/min of gas flow rate, and 9 mm nozzle-to-plate distance gives the higher hardness value.

4 Impact Test

Charpy V notch test is conducted to determine the impact or toughness values. The amount of energy rapt by the material during fracture of welded joint. The toughness value will change because of the effect of heat input given to the base metal for making the permanent joint. This will affect the performance of the welded joint.

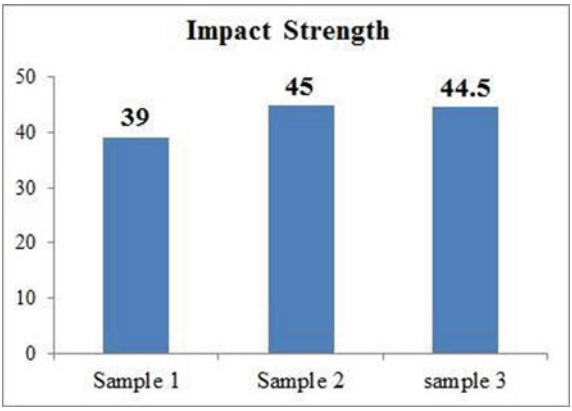

Fig. 6 Impact strength

4.1 Effect of Weld on Impact Test

From Fig. 6, it is observed that the value of energy under toughness region for the samples is 39 Joules, 45 Joules, and 44.5 Joules. From the obtained values, it is clear that the sample no. 2 with specifications of 80 A current, 4 l/min of gas flow rate, and 9 mm nozzle-to-plate distance gives the higher impact strength.

5 Conclusions

The welding of two dissimilar austenitic stainless steels 304L and 316L is successfully carried out. ER304L is the filler rod used to perform welding. The mechanical properties were examined. It is found that the sample no. 2 gives the high tensile strength, hardness value, and impact strength. The welding specifications are 80 A current, 4 L/min of gas flow rate, and 9 mm nozzle-to-plate distance. It is observed that sample no. 2 posses higher hardness value compared to other samples.

References

1. Wilson M (2007) TIP TIG: New technology for welding. Industr Rob Int J 34(6):462–466
2. Kulvirsingh (2006) Advances in materials for advanced steam cycle power plants. BHEL J 27(2):1–19
3. Taban E, Deleu E, Dhooge A, Kaluc E (2007) Gas metal arc welding of modified X2CrNi12 ferritic stainless steel. Instit Mater Mach Mechan 45(2):67–74
4. Vashishtha H, Taiwade RV, Sharma S, Patil AP (2017) Effect of welding processes on microstructural and mechanical properties of dissimilar weldments between conventional austenitic and high nitrogen austenitic stainless steels. J Manuf Process 25:49–29

5. Wichan Chuaiphan, Loeshpahn Srijaroenpramong.: Effect of Welding Speed on Microstructures, Mechanical Properties and Corrosion Behavior of GTA-Welded AISI 201 Stainless Steel Sheets. Journal of Materials Processing Technology 214(2) 402–408 (2014)
6. Kumar S, Shahi AS (2011) Effect of heat input on the microstructure and mechanical properties of gas tungsten arc welded AISI 304 stainless steel joints. Mater Des 32(6):3617–3623
7. Mishra RR, Tiwari VK, Rajesha S (2014) A study of tensile strength of MIG and TIG welded dissimilar joints of mild steel and stainless steel. Int J Adv Mater Sci Eng 3(2):23–32
8. Ghosh N, Pal PK, Nandi G. Parametric optimization of MIG welding on 316L austenitic stainless steel by grey-based Taguchi method. Procedia Technol 25:103

Modelling of Factors Influencing Saving Behaviour of Women in India: An Interpretive Structural Modelling

M. Suresh, D. Sangeetha, and Sumathi Kumaraswamy

Abstract Saving is the amount of money left over after personal consumption for a time period, which can be further turned into income. This paper focuses on saving behaviour of women and emphasis on why do women save and which factors influence their saving. The purpose of this paper is to identify the variables that influence saving behaviour of women in India. An Interpretive Structural Modelling (ISM) has been applied to find key factors influencing women's saving behaviour in India. ISM approach is used to recognize the relationship between each factor and identify the dependence and the driving power of these factors. Finally, this paper concludes with the most influential factors GDP per capita growth, interest rate, inflation rate and bank density which influences women's saving behaviour.

Keywords Interpretive structural modelling · Saving behaviour · Womens saving · Saving influencing factors · Saving systems

1 Introduction

Savings are one of the crucial parts of economic activity. The economic impact is based on how much a consumer spends and how much a consumer saves. Various saving motives and the differences in individual preferences and characteristics of households affecting the saving motives and perceived liquidity constraints across 15 countries in the Euro-zone have been discussed by Blanc et al. [1]. The authors have observed that both household's characteristics and institutional macro-economic variables are significant. The cross-country data analysis had also helped in analysing how country-specific institutional settings affect saving behaviour. Choi et al. [2] have considered how precautionary saving, i.e., saving for future expenses or unexpected

M. Suresh (✉) · D. Sangeetha
Amrita School of Business, Amrita Vishwa Vidyapeetham, Coimbatore, India
e-mail: drsureshcontact@gmail.com

S. Kumaraswamy (✉)
College of Business Administration, University of Bahrain, Zallaq, Kingdom of Bahrain
e-mail: sumathik151@gmail.com

G. Kumaresan et al. (eds.), *Advances in Materials Research*, Springer Proceedings in Materials 5, https://doi.org/10.1007/978-981-15-8319-3_81

future situations, influences savings in China and saving of United States being the world's two largest economies. In this study, discuss the variables that influence the women in India to save. This paper helps in understanding the driving factor for saving based on characteristics related to household as well as economy according to women in India. ISM approach is used to identify the interrelationships between factors.

2 Literature Review

Kibet et al. [3] identifies factors that directs savings of the farmers, teachers and entrepreneurs in seven rural divisions of Nakuru District, Kenya. Study for the result directed that educational qualification, income, gender, nature of profession influences the saving behaviour positively while age, loan amount, dependency ratio influences negatively. Ismail and Rashid [4] analysed the influence of demographic and socio-economic variables with saving of the household's for short term and long term in Pakistan for 1975–2011 using time series data analysis and error correction model. Athukorala and Sen [5] analysed factors influencing the rate of private saving in India for the period 1954–98. Analysis shows that growth of per capita income, inflation rate, spread of banking facilities and real interest rate does positive impact on domestic saving. Niculescu-Aron and Mihaescu [6] analyses the saving behaviour in the Eastern and Central Europe households. The study shows following results: GDP growth influences the saving negatively, interest rate and inflation does not majorly impact savings. Though crisis impact saving behaviour but they aren't fixed. Agrawal et al. [7] have analysed the behaviour of saving in five of the South Asian countries which are Sri Lanka, India, Bangladesh, Pakistan and Nepal. Their findings suggest that access to banking facilities and income per capita positively affect the savings, while availability of foreign savings and dependency ratio impact negatively on savings rate.

Kapounek et al. [8] identified the psychological and economic factors prompting the households behaviour of saving in Eastern Union Countries for the period of 2004 to 2014. Using empirical study authors found that the saving manners of households are more unreasonable especially in the course of financial crisis and economic downturn. Horioka and Terada-Hagiwara [9] analyses the factors of trends in rate of household saving in 12 developing countries in Asia using random effect and fixed effect model for 2001 to 2007. The result of the study includes: income impacts saving negatively for lower income and positively as income rises; credit negatively impacts saving rate and real per capita GDP impacts positively. Umar et al. [10] analyses the influence of socioeconomic variables in saving behaviour of farmers in Gwaram LGA, Nigeria using multiple regression models and descriptive statistics. The authors have considered factors including age, number of years of farming experience, farm size, annual revenue, household size, cost of production, uncertainty in price, financial institutions and found years of education, farm size, annual revenue,

age as significant variables. Pryor [11] examines shift in demographic composition of the population becoming the cause for the decline in personal saving in the future.

The main objective of the paper has been converted into the following Research Questions (RQ):

RQ1: What are the major factors that influencing women's' saving behaviour in India?

RQ2: What is the relationship among these saving behaviour factors?

RQ3: Can these factors be ranked according to priority?

3 Methodology

ISM approach has been applied in diverse fields [12–17]. The following steps are adopted [18] for the successful application of the ISM model:

Table 1 Identified factors influencing women's saving behaviour in India

S. No	Factor	Definition	Reference
1	Expected savings (ES)	Over the next 12 months, how likely is it that you save any money?	[8]
2	GDP per capita growth	long-term and short-term relationship of GDP per capita growth and saving	[4]
3	Annual income	households' average net income at constant prices;	[6]
4	Level of education	Educational qualifications viz. primary, secondary, undergraduate, postgraduate	[10]
5	Age	Age group respondents belong to and years left for retirement	[11]
6	Household size	number of person per household	[10]
7	Dependency Ratio	the ratio of no of unemployed persons in the house to the household size	[9]
8	Interest rate	the relevant rate of real return for most households and even firms in developing countries(real interest rate on bank deposits)	[7]
9	Type of occupation	Teacher/business person/others	[3]
10	Credit access	credit access is normal monthly expenses on loan repayment	[3]
11	Inflation rate	The rate of inflation	[5]
12	Bank density	Population per bank branch	[5]

Table 2 SSIM for factor influencing women's saving behaviour

	F1	F2	F3	F4	F5	F6	F7	F8	F9	F10	F11	F12
F1	1	O	A	A	A	A	A	A	A	A	A	O
F2		1	O	O	O	O	O	A	O	O	X	V
F3			1	X	A	O	A	A	A	V	O	O
F4				1	O	O	O	O	V	O	O	O
F5					1	O	O	O	O	V	O	O
F6						1	V	A	O	O	O	O
F7							1	O	O	V	O	O
F8								1	O	O	X	X
F9									1	O	O	O
F10										1	O	A
F11											1	V
F12												1

1. Factors were identified based on literature review. Table 1 depicts the identified factors related to saving behaviour of women in India. The data was collected for these factors from 20 women in India.
2. Self-Structured Interaction Matrix (SSIM) is created to depict the contextual relationship between two factors [19–22] and it is represented as follows:
   Example: Relationship between the factors x and y ?
   Option-1: V: x influences y.
   Option-2: A: y influences x.
   Option-3: X: mutual relationship between x *and* y.
   Option-4: O: no relationship between x *and* y.
   The pair wise comparisons of factors are taken from opinions of 20 women's. The highest mode of opinion is selected from the opinions of all experts. The SSIM is depicted in Table 2.
3. The Initial Reachability Matrix (IRM) is created using the SSIM [23–25] and its shown in Table 3.
4. Final Reachability Matrix (FRM) is obtained by transitivity analysis from IRM [26, 27]. Transitivity analysis which follows
   First Level transitivity (for 1*): if $J = K; K = L;$ then $J = L$.
   Second Level transitivity (for 1**): if $J = K; K = L; L = M$ then $J = M$.
   Third Level transitivity (for 1***): if $J = K; K = L; L = M; M = N$ then $J = N$.
   FRM for factors influencing women's saving behaviour is shown in Table 4.
5. Partition of the FRM: The FRM is then partitioned into different levels [28, 29].

Table 3 IRM for factor influencing women's saving behaviour

	F1	F2	F3	F4	F5	F6	F7	F8	F9	F10	F11	F12
F1	1	0	0	0	0	0	0	0	0	0	0	0
F2	0	1	0	0	0	0	0	0	0	0	1	1
F3	1	0	1	1	0	0	0	0	0	1	0	0
F4	1	0	1	1	0	0	0	0	1	0	0	0
F5	1	0	1	0	1	0	0	0	0	1	0	0
F6	1	0	0	0	0	1	1	0	0	0	0	0
F7	1	0	1	0	0	0	1	0	0	1	0	0
F8	1	1	1	0	0	1	0	1	0	0	1	1
F9	1	0	1	0	0	0	0	0	1	0	0	0
F10	1	0	0	0	0	0	0	0	0	1	0	0
F11	1	1	0	0	0	0	0	1	0	0	1	1
F12	0	0	0	0	0	0	0	1	0	1	0	1

4 Results and Analysis

Directed graph (Digraph) is prepared from level partition and FRM. The digraph is a visual representation of the various relationships between the factors and the levels in which they are positioned. Factor at top of the digraph is first level and factors at bottom level are sixth level. Figure 1 represents the ISM model.

The key factors are 2, 8, 11 and 12 and these factors are influencing a major role in saving behaviour of women.

F2 influences F11: GDP growth is a result of increase in production which implies increase in employment, hence increased money in an economy, i.e. leading to increase in inflation rate.

F2 influences F12: During increasing GDP growth there is an increase in employment which leads to increase in bank users.

F8 influences F2: Increase in interest rate increases the tendency to save and decreases the tendency to borrow. Similarly, decrease in interest rate decreases the tendency to save and increases tendency to borrow leading to more investments and more spending hence increase in economy growth.

F8 influences F6: Increases in interest rate attract more savers leading to increase in number of bank users. Similarly Decrease in interest rate attracts more borrowers leading to increase in number of bank users.

F8 influences F11: Decrease in the interest rate attracts more borrowers leading to increase in investment and spending, which increases the demand for products. Hence result in increase in inflation rate. Similarly, increase in interest rate decreases inflation rate.

Table 4 FRM for factor influencing women's saving behaviour

	F1	F2	F3	F4	F5	F6	F7	F8	F9	F10	F11	F12	Driving power	MICMAC rank
F1	1	0	0	0	0	0	0	0	0	0	0	0	1	7
F2	1*	1	1**	1***	0	1**	1***	1*	1***	1*	1	1	11	2
F3	1	0	1	1	0	0	0	0	1*	1	0	0	5	5
F4	1	0	1	1	0	0	0	0	1	1**	0	0	5	5
F5	1	0	1	1*	1	0	0	0	1**	1	0	0	6	1
F6	1	0	1*	1**	0	1	1	0	1***	1*	0	0	7	3
F7	1	0	1	1*	0	0	1	0	1**	1	0	0	6	4
F8	1	1	1	1*	0	1	1*	1	1**	1*	1	1	11	2
F9	1	0	1	1*	0	0	0	0	1	1*	0	0	5	5
F10	1	0	0	0	0	0	0	0	0	1	0	0	2	6
F11	1	1	1*	1**	0	1*	1**	1	1***	1*	1	1	11	2
F12	1*	1*	1*	1**	0	1*	1**	1	1***	1	1*	1	11	2
Dependence	12	4	10	10	1	5	6	4	10	11	4	4		

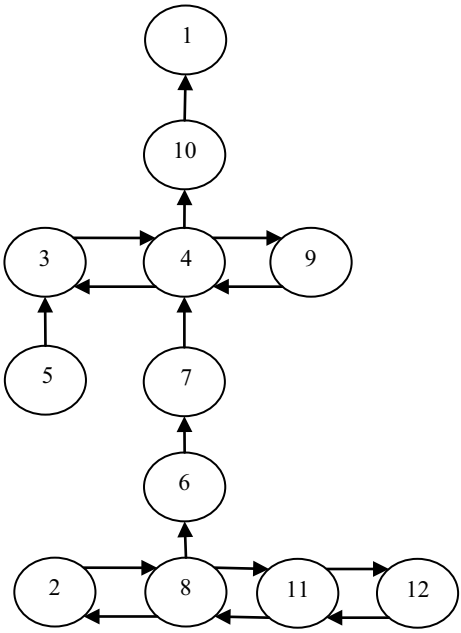

Fig. 1 ISM Model for factors influencing saving behaviour of women

F8 influences F12: Decrease or Increase in interest rate influences rise in number of bank users thus leading to increase in need of banks in a region.

F11 influences F2: During a controlled inflation, employment increases, consumers have more money to buy goods and services leading to economy growth.

F11 influences F8: During a high inflation, interest rate will increase because increase in interest rate reduces the tendency to borrow and increase the tendency to save. Resulting in decrease in the amount of money circulated in the economy and fall in demands of goods and service leading to decrease in inflation. Similarly during a low inflation, there is a decrease in interest rate.

F11 influences F12: During a controlled inflation, employment increases, leading to increase in number of bank users, hence increasing the number of banks needed in a region.

F12 influences F8: When there is an increase in Bank density, Customers are attracted to save leading to increase in supply of money.

5 MICMAC Analysis

MICMAC analysis includes the development of MICMAC Rank and MICMAC graph. Factors are broadly classified into four zones based on the dependence and

the driving power, namely, autonomous factors, dependent factors, linkage factors and independent factor [30–33]. The factors can be explained as below:

1. *Autonomous factors*: Factors that have weak dependence power and weak driving power are known as autonomous factors. Factors F5, F6 and F7 are autonomous factors.
2. *Dependent factors*: Factors that have a strong dependence power, but weak driving power are known as dependent factors. Factors F1, F3, F4, F9 and F10 are dependent factors.
3. *Linkage factors*: Factors that have a strong dependence power and strong driving power are known as linkage factors. This study has no linkage factors.
4. *Driving factors*: Factors that have a strong driving power, but weak dependence power are known as driving factors or independent factors. Factors F2, F8, F11 and F12 are the driving factors in this study.

Table 4 shows the MICMAC Rank for each factor where Rank 1 denotes the most important factor and Rank 7 denotes the least crucial factors among the factors. Age is the most critical factor influencing saving behaviour of women in India. Saving behaviour of women changes according to their age.

6 Conclusion

This paper gives insight on why do women's save and which factor influences the most to save and how each factor influences each other. The usage of ISM approach has been useful in identifying the most momentous variables and finding the relationship between the variables. In this study, the key factors are rate of interest, GDP per capita growth, rate of inflation and bank density which influences women's saving behaviour in India.

References

1. Blanc JL, Porpiglia A, Teppa F, Zhu J, Ziegelmeyer M (2014) Household saving behaviour and credit constraints in the Euro area. Discussion Paper Deutsche Bundesbank No 16/2014
2. Choi H, Lugauer S, Mark NC (2017) Precautionary saving of Chinese and US households. J Money Credit Banking 49(4):635–661
3. Kibet LK, Mutai BK, Ouma DE, Ouma SA, Owuor G (2009) Determinants of household saving: Case study of smallholder farmers, entrepreneurs and teachers in rural areas of Kenya. J Dev Agric Econ 1(7):137–143
4. Ismail A, Rashid K (2013) Determinants of household saving: Cointegrated evidence from Pakistan (1975–2011). Econ Model 32:524–531
5. Athukorala PC, Sen K (2004) The determinants of private saving in India. World Dev 32(3):491–503
6. Niculescu-Aron I, Mihaescu C (2014) Modelling the impact of economic, demographic and social determinants on household saving rate in the former socialist countries (Central and Eastern Europe). Procedia Econ Finance 10:104–113

7. Agrawal P, Sahoo P, Dash RK (2009) Savings behaviour in South Asia. J Policy Model 31(2):208–224
8. Kapounek S, Korab P, Deltuvaite V (2016) (Ir) rational Households' Saving Behavior? An Empirical Investigation. Procedia Econ Finan 39:625–633
9. Horioka CY, Terada-Hagiwara A (2012) The determinants and long-term projections of saving rates in Developing Asia. Jpn World Econ 24(2):128–137
10. Umar S, Muhammed H, Nasir N, Dodo FA (2014) Analysis of socioeconomic factors influencing saving among rural smallhoder farmers in Gwaram LGA, Jigawa State, Nigeria. J Educ Soc Res 4(5):99
11. Pryor FL (2003) Demographic effects on personal saving in the future. Southern Econ J 541–559
12. Amrita VV, Suresh M (2016, December) Factors influencing lean practices in Super market services using interpretive structural modeling. In: 2016 IEEE international conference on computational intelligence and computing research (ICCIC), pp 1–5. IEEE
13. Keerthana S, Suresh M (2016, December) Drivers influencing lean practices in street food vending process. In: 2016 IEEE international conference on computational intelligence and computing research (ICCIC), pp 1–5. IEEE
14. Renganath K, Suresh M (2016, December) Analyzing the drivers for safety practices using interpretive structural modeling: a case of Indian manufacturing firms. In: 2016 IEEE international conference on computational intelligence and computing research (ICCIC), pp 1–6. IEEE
15. Abinaya R, Suresh M (2016, December) Analyzing the drivers for lean practices of commercial banking using interpretive structural modelling. In: 2016 IEEE international conference on computational intelligence and computing research (ICCIC), pp 1–4. IEEE
16. Venkatesh AB, Suresh M (2016, December) Factors influencing Indian tourism promotion in social media. In: 2016 IEEE international conference on computational intelligence and computing research (ICCIC), pp 1–5. IEEE.
17. Sudharsan TM, Suresh M (2016, December) Factors influencing purchase decision of solar lanterns by street vendors. In: 2016 IEEE international conference on computational intelligence and computing research (ICCIC), pp 1–4. IEEE
18. Suresh M, Mahadevan G, Abhishek RD (2019) Modelling the factors influencing the service quality in supermarkets. Int J Syst Assur Eng Manage. https://doi.org/10.1007/s13198-019-00897-4
19. Gayathri K, Suresh M (2018) Modelling the factors of agile practices in project management: a case of illumination project organization. Int J Eng Technol (UAE) 7(2.33):541–547
20. Sankar H, Suresh M (2018) Modelling the factors of workplace spirituality in healthcare organization. Int J Eng Technol (UAE) 7(2.33):786–790
21. Keerthanaa P, Suresh M (2018) Informal learning in work place: a case of caregivers. Int J Eng Technol (UAE) 7(2.33):791–795
22. Jeevan S, Suresh M, Ranganathan R (2018) Risk factors influencing humanitarian operations: a case of temple cart festival. Int J Eng Technol (UAE) 7(2.33):946–949
23. Gautham GR, Suresh M, Ranganathan R (2018) Factors affecting human performance in lathe machine shop operations. Int J Eng Technol (UAE) 7(2.33):882–885
24. Haresh B, Suresh M, Ranganathan R (2018) Factors influencing success of new product launch: a case of SME stationery industry in India. Int J Eng Technol (UAE) 7(2.33):902–906
25. Aarthi N, Suresh M (2018) Factors influencing people to approach micro finance institutions in India. Int J Eng Technol (UAE) 7(2.33):978–981
26. Miruthu Bashini R, Suresh M (2018) Modelling the ergonomics factors affecting the work system in hospital: an ISM approach. Int J Pure Appl Math 119(7):183–198
27. Shiyam Sundar T, Suresh M, Raghu Raman R (2018) Modelling the ergonomics factors affecting the work system in hospital: an ISM approach. Int J Pure Appl Math 119(7):107–125
28. Suresh M, Ganesh S, Raman R (2019) Modelling the factors of agility of humanitarian operations. Int J Agile Syst Manage 12(2):108–123
29. Patri R, Suresh M (2018) Factors influencing lean implementation in healthcare organizations: an ISM approach. Int J Healthcare Manage 11(1):25–37

30. Patri R, Suresh M (2017) Modelling the enablers of agile performance in healthcare organization: a TISM approach. Global J Flexib Syst Manage 18(3):251–272
31. Vaishnavi V, Suresh M, Dutta P (2019a) A study on the influence of factors associated with organizational readiness for change in healthcare organizations using TISM. Benchmarking Int J 26(4):1290–1313
32. Vaishnavi V, Suresh M, Dutta P (2019b) Modelling the readiness factors for agility in healthcare organization: a TISM approach. Benchmarking Int J 26(7):2372–2400
33. Patil M, Suresh M (2019) Modelling the enablers of workforce agility in IoT projects: a TISM approach. Glob J Flexib Syst Manage 20(2):157–175

Modelling the Factors of Job Stress in Audit Firms: A TISM Approach

M. Suresh, R. Srividya, and Sumathi Kumaraswamy

Abstract The purpose of the paper is to identify and categorise the factors causing stress in audit firms using total interpretive structural modelling (TISM) approach. The awareness about these factors would help audit firms in understanding the stress factors and help them in deciding the specific aspects to concentrate on in order to improve their efficiency. This paper also studies the interrelationship among the factors and helps to establish a hierarchy among them using their dependence and driving power. Furthermore, this is the first attempt made to understand these stress factors and their relative significance using TISM approach. Role conflict pressure and role ambiguity pressure are the major driving factors of stress in audit firms. The focus on reducing those pressures would go a long way in reducing the overall stress in the audit firms.

Keywords Audit firms · Stress factors · Occupational stress · Job stress · Total interpretive structural modelling

1 Introduction

Occupational stress has been described as a response to environmental pressures. There are several factors which cause occupational stress in people. Xu [1] has defined stress as a "series of physiological, psychological and behavioural responses due to the continuing effects of one or more stressors on individuals in an organisation". Colligan and Higgins [2] have defined workplace stress as the change in an employee's state, either physical or mental, in response to challenging work places. When the pressure is more than a person's ability to cope up with, he or she undergoes stress.

M. Suresh (✉) · R. Srividya
Amrita School of Business, Amrita Vishwa Vidyapeetham, Coimbatore, India
e-mail: drsureshcontact@gmail.com

S. Kumaraswamy (✉)
College of Business Administration, University of Bahrain, Zallaq, Kingdom of Bahrain
e-mail: sumathik151@gmail.com

G. Kumaresan et al. (eds.), *Advances in Materials Research*, Springer Proceedings in Materials 5, https://doi.org/10.1007/978-981-15-8319-3_82

Stress is common particularly in the healthcare sector, including the nursing profession. Since it is in direct contact with illness and suffering regularly, occupational stress is very high for people in this profession [3]. Another segment which faces stress in healthcare industry is communication profession. In healthcare sector, the communication professionals are responsible for both internal and external communication on behalf of the organisation. Communication professionals need to understand the macro-environment of the organisation in order to cater to the needs of various stakeholders [4]. Other stressful areas include academic staff who generally face stress in the form of heavy workloads, the amount of paperwork, and the relationships with various students [5].

2 Literature Review

However, stress has been frequently identified with the auditing profession. While exploring the literature, several studies have dealt with stress factors in audit and public accounting firms. As auditors interact with a number of people, both internal and external, they are exposed to a lot of stress associated with their position [6]. From literature, it is clear that there are many critical factors that induce stress in an auditing firm. De Zoort and Lord [7] have provided a comprehensive framework for pressure effects in accounting. They have proposed that feedback pressure, social influence pressures, workload pressure, client and litigation pressure are the major pressures faced by a public accounting firm. Time constraints and competitive business environment, which, in turn, affect client retention, are environmental pressures faced by the firms. Role characteristic pressures like role ambiguity and role conflict that can create stress and affect professional attitude are also elaborated.

Smith and Emerson [8] have studied audit quality in the role stress model. The study has proposed that audit quality may be reduced due to role stressors such as work overload, role ambiguity and role conflict. It is stated that auditors face stress from the quantity of work and the limited time allotted to complete it. The role ambiguity and role conflict, dealt with by [7], also play a major role in influencing audit quality and auditor performance. Yan and Xie [9] have further expanded on these factors. They have stated that work stress is caused by the combined effects of work demand, time limitation pressure, cost control and legal risks and responsibilities. Bowrin and King [10] also have studied the relationship among time pressure, task complexity and audit effectiveness. The study has defined time pressure as one's perception of whether he or she could complete a task on time, given that time is a critical requirement of the job.

A study by [6] has identified the relationship between role stressors and job satisfaction and performance of external auditors. It has expanded the research on this area by examining the moderating effect of the Type A behaviour pattern on the role stressors—role ambiguity and role conflict. People who exhibit Type A behaviour patterns tend to be more competitive and aggressive. It is identified that role ambiguity and role conflict negatively affect auditors' job satisfaction and performance. Similarly,

a study by [11] also has dealt with role stressors and their impacts upon auditors. However, this study has focused on the internal auditors, rather than the external auditors. It has explored the determinants and consequences of the role stressors on the local government internal auditors. This study has obtained a slightly different result, i.e., role conflict has a positive impact while role ambiguity has a negative impact upon the job performance.

Many researchers have studied stress factors in workplace. However, none of them have developed a framework for analysing stress factors in audit firms. This gap leads to the study of factors relating to stress in audit firms and that would be a motivation for this paper. The main objective of the paper has been converted into the following research questions (RQ):

RQ1: What are the factors that cause stress in audit firms?

RQ2: What is the relationship among these stress factors in auditing firms?

RQ3: Can these factors be ranked according to priority?

3 Methodology

To establish the interrelationship among the variables, the stress factors in audit firms are identified, and TISM is employed. Sage [12] has described 'interpretive structural modelling' (ISM) as a technique which is used to identify the relationship among various factors in a problem and to help in identifying the contextual relationship between the variables [13–15]. Sushil [16] has introduced TISM as an extension of the ISM. While similar to ISM, TISM is more advanced and unique as it provides interpretation of the links in the hierarchical structure, which helps in providing direction to this complex model.

TISM approach has been applied in diverse fields [17–21]. The following steps are adopted [20] for the successful application of the TISM model:

1. *Identify and define the factors*: The first step involves the identification of the factors which causes stress in audit firms. Thus, the factors causing stress in audit firms have been identified, and expert opinion has been obtained from practicing auditors for the same. Literature review has helped in identifying and defining the stress factors used in this study. The factors are listed in Table 1.
2. *Establishing the contextual relationships*: To arrive at the initial reachability matrix (IRM), contextual relationships between the factors have to be established. For this study, 20 responses have been collected, and the respondents include senior auditors and auditing staff members from audit firms in India. Table 2 contains the IRM.
3. *Interpretation of the relationship between the factors*: In the TISM approach, this step answers the question of 'how', and tries to understand how factor 1 influences factor 2.

Table 1 Factors identified for stress in audit firms

Factors	Definition	Reference/expert opinion
Workload pressure (F1)	Workload pressure is the pressure caused due to carrying on high-intensity workload which leads to auditor burnout	[7–9]
Time limitation (F2)	Time limitation pressure arises when auditors have to complete tasks within specified deadlines and issue an audit report	[7, 9, 10]
Legal risks and responsibilities (F3)	With gradual improvement in laws and regulations, auditors are held responsible by the law for any default like carrying out an improper audit	[7, 9]
Role conflict (F4)	Role conflict is one of the role characteristic pressures. It arises when two or more conflicting demands are placed upon a person	[6–8, 11]
Client retention (F5)	Client retention is the pressure associated with retaining clients when clients are faced with multiple choices as to their choice of auditors	[7]
Task complexity (F6)	Task complexity is the auditors' perception of the complexity of thought process required to complete each task	[10]
Lack of awareness among clients (F7)	Lack of awareness refers to incomplete knowledge among clients about various legal provisions	Expert opinion
Constant changes in law (F8)	Constant changes in law refers to the pressure of keeping abreast of the constant and frequent changes in legal provisions and compliance requirements such as different types of reporting and accounting standards	Expert opinion
Role ambiguity(F9)	Role ambiguity arises from not being aware of one's exact role and its expectations	[6–8, 11]

(continued)

Table 1 (continued)

Factors	Definition	Reference/expert opinion
Dealing with difficult people (F10)	Dealing with difficult people is the pressure of dealing with uncooperative clients who do not provide assistance or support to the auditors in completing their work	Expert opinion

Table 2 IRM for stress factor analysis

	F1	F2	F3	F4	F5	F6	F7	F8	F9	F10
F1	1	1	1	0	0	0	0	0	0	0
F2	1	1	1	0	0	0	0	0	0	0
F3	0	0	1	0	1	0	0	0	0	0
F4	1	0	0	1	0	1	0	0	1	0
F5	0	0	0	0	1	0	0	0	0	0
F6	1	1	0	0	0	1	0	0	0	0
F7	0	0	1	0	0	0	1	0	0	0
F8	0	0	1	0	0	0	1	1	0	0
F9	1	1	0	1	1	1	0	0	1	1
F10	1	1	0	0	0	1	0	0	0	1

4. *Developing the final reachability matrix (FRM) after checking for transitivity*: A transitivity check must be done before arriving at the FRM. Transitivity check must be done on all the entries with '0' in the IRM. 1* or 1** signifies the presence of transitivity, and the lack of it means that the original value of '0' can be retained. 1* implies first-level transitivity, wherein if $P = Q$ and $Q = R$, then $P = R$. 1** implies second-level transitivity, wherein if $P = Q$, $Q = R$, and $R = S$, then $P = S$. Table 3 contains the FRM.
5. *Partition of the factors from FRM into levels*: The FRM is divided into three categories, namely reachability set, antecedent set and interaction set. Beginning from level 1, factors of each level are extracted by way of repeated iterations, and this process is continued until the partitioned reachability matrix is arrived at.
6. *Designing the interaction matrix*: Direct and significant transitive links are used to design the interaction matrix.
7. *Creating the digraph and the TISM model*: The digraph, also known as directed graph, is created by using data from the interaction matrix and the level partitions.

In the digraph, factors at the top of the model are called first-level factors, and subsequent levels are ranked in ascending order. Further, using the digraph and the interpretive interaction matrix, the TISM model is developed. The TISM model is

Table 3 FRM for stress factor analysis

	F1	F2	F3	F4	F5	F6	F7	F8	F9	F10	Driving power	MICMAC rank
F1	1	1	1	0	1*	0	0	0	0	0	4	5
F2	1	1	1	0	1*	0	0	0	0	0	4	5
F3	0	0	1	0	1	0	0	0	0	0	2	6
F4	1	1*	1*	1	1*	1	0	0	1	1*	8	1
F5	0	0	0	0	1	0	0	0	0	0	1	7
F6	1	1	1*	0	1**	1	0	0	0	0	5	4
F7	0	0	1	0	1*	0	1	0	0	0	3	3
F8	0	0	1	0	1*	0	1	1	0	0	4	1
F9	1	1	1*	1	1	1	0	0	1	1	8	1
F10	1	1	1*	0	1**	1	0	0	0	1	6	2
Dependence	6	6	9	2	10	4	2	1	2	3		

*, ** represent transitive links

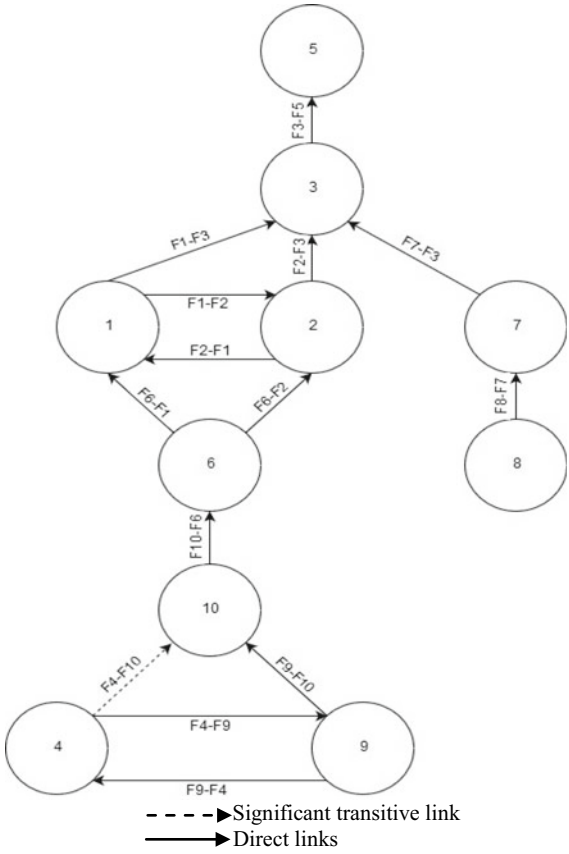

Fig. 1 TISM model for stress in audit firms

shown in Fig. 1, while the reasons behind the direct and the significant transitive links are discussed in Sect. 4.

4 Results and Discussions

4.1 Interpretive Interaction of the TISM Model

Figure 1 shows the results of the TISM analysis of stress factors in audit firms. Six levels of factors are described in the model. Interpretive interactions between the factors are as follows:

F1 to F2: Workload pressure and time limitation pressure are inversely proportional to each other. Defined audit practices cannot be skipped; thus, the pressure increases.

F1 to F3: With increasing workload pressure, the legal risks associated with it increases.

F2 to F1: Workload pressure increases because of time limitation since clients approach the auditors close to the due dates for statutory compliances.

F2 to F3: Due to limited availability of time, a person may file incorrect returns or do an improper audit which increases legal risks.

F3 to F5: Legal risks influence client retention since clients who are not compliant to law can cause problems for the firm.

F4 to F1: Role conflict would end up increasing the workload pressure of the overall team involved.

F4 to F6: It becomes harder for the auditor to complete the task, due to internal or external conflict.

F4 to F9: Role conflict can lead to lack of clarity about performance expectations and create role ambiguity.

F4 to F10 (Significant transitive link): Role conflict makes it harder to deal with non-cooperative clients.

F6 to F1: Pressure increases as the complexity of the task demands more time than usual.

F6 to F2: Task complexity augments the time limitation pressure. Completing vast fields of audit in a limited time period increases time limitation pressure.

F7 to F3: Lack of awareness of the clients regarding the entire process could lead to legal risks like not meeting deadlines.

F8 to F3: If the constant changes in laws are not followed regularly, chances of failing to meet legal norms are high.

F8 to F7: If the clients do not keep themselves updated with the latest changes from the right sources, it affects their awareness levels.

F9 to F1: An employee may not be clear in what he or she does which increases the work pressure.

F9 to F2: Role ambiguity leads to limited time availability since work is not done at full efficiency.

F9 to F4: Ambiguous roles and expectations cause/increase role conflict.

F9 to F5: Role ambiguity might lead to inefficient work and result in the client becoming dissatisfied.

F9 to F6: Lack of clarity about performance expectations increases the task complexity.

F9 to F10: Lack of clarity about specific roles aggravates the pressure of dealing with difficult clients.

F10 to F1: Difficult clients may be uncooperative, and this increases the existing workload pressure.

F10 to F2: Non-cooperative clients may not give the requisite data on time, increasing the time limitation pressure.

F10 to F6: The task becomes more complex since there is no cooperation from the client.

4.2 Matrix Impact Cross Multiplication Applied to Classification Analysis

MICMAC stands for 'matrix impact cross-multiplication applied to classification'. It involves classifying the factors into four different zones, namely driving factors, autonomous factors, dependent factors and linkage factors [22–24]. The factors can be explained as below:

Autonomous factors: Factors that have weak dependence power and weak driving power are known as autonomous factors [25–27]. These factors are disengaged from the system. In the present study, factors 6, 7 and 8 are autonomous factors.

Dependent factors: Factors that have a strong dependence power but weak driving power are known as dependent factors [28–30]. Factors 1, 2, 3 and 5 are dependent factors.

Linkage factors: Factors that have a strong dependence power and strong driving power are known as linkage factors [31, 32]. They establish the connection between the dependence and the driving factors. This study has no linkage factors.

Driving factors: Factors that have a strong driving power but weak dependence power are known as driving factors or independent factors [33, 34]. They form the base for the rest of the factors. Factors 4, 9 and 10 are the driving factors in this study.

As per the MICMAC analysis, the factors causing stress in audit firms are ranked in Table 3. The MICMAC ranks are calculated by dividing the driving power by the dependence of the factors [35, 36]. This rank shows the significance of each factor in the system based on its rank. The higher the rank, the higher the factor's importance in the model. The role conflict pressure, role ambiguity pressure and the pressure of keeping up with the constant changes in law are the most important factors. Other factors which are important in the model, as per MICMAC ranking, are the pressures associated with dealing with difficult people and those caused by lack of awareness among clients. Awareness about these rankings would provide audit firms a point of focus in order to reduce the overall stress to senior auditors and auditing staff members.

5 Managerial Implications

Using the TISM approach, audit firms can understand the factors that cause stress in audit firms and the extent of pressure each factor has in the overall system. Instead of taking decisions based on instincts, auditors can take decisions on a scientific basis using this model. The TISM framework shows which factors are causing more stress and are a drain on the firm's resources. For instance, it is found that pressure caused as a result of role conflict and role ambiguity affects most of the stress factors in the model as well as putting pressure directly on the auditors to a large extent. Clear job roles and expectations, and a well-defined set of tasks and performance metrics, with a focus on reducing the role conflict and role ambiguity, would result in lesser dissatisfaction among the employees. A thorough understanding of these factors in the TISM model can help auditors to reduce the stress for themselves as well as the auditing staff members and help achieve a conducive work environment. More productive and efficient work standards can be achieved since the factors causing stress can be eliminated or reduced to an extent.

6 Conclusion

The research done on stress factors in audit firms has been vast, but there has been no research done in this field to understand how the multiple stress factors interact with each other in addition to affecting the overall organisation. The current study has been an effort to identify such a framework which would help the auditors to better manage their resources and create a prolific work environment, benefitting both the employees and the clients of the firm.

The study has identified ten factors which cause stress in audit firms through literature review and by way of obtaining expert opinions from auditors. TISM is suggested to be used in order to list the stress factors in audit firms and to identify the interrelationship among them. The factors are then ranked according to their order of importance, and a hierarchy is established using MICMAC analysis. It is found out that role conflict pressure and role ambiguity pressure are the major driving factors in the model. This model can be used by audit firms to understand, scientifically, which factors are causing a drain on the firm's resources, and it can then be used to take corrective action in order to minimise or eliminate the stress caused to the employees.

Moreover, this study has taken only ten major factors into consideration, whereas there may be many more factors which cause stress in audit firms. Integrating those factors in the proposed framework and expanding the framework can be one area of future research.

References

1. Xu C (1999) Work stress system: mechanism, handling and management. J Zhejiang Normal Univ Soc Sci 5:69–73
2. Colligan TW, Higgins EM (2006) Workplace stress: etiology and consequences. J Workplace Behav Health 21(2):89–97
3. Yuwanich N, Sandmark H, Akhavan S (2016) Emergency department nurses' experiences of occupational stress: a qualitative study from a public hospital in Bangkok, Thailand. Work53(4):885–897
4. Gilstrap CM, Bernier D (2017) Dealing with the demands: strategies healthcare communication professionals use to cope with workplace stress. Qualit Res Rep Commun 18(1):73–81
5. Zakrizevska M, Bulatova J (2015) Occupational stress and professional deformation among university academic staff. J Bus Manage 9:20–27
6. Fisher RT (2001) Role stress, the type A behavior pattern, and external auditor job satisfaction and performance. Behav Res Account 13(1):143–170
7. DeZoort FT, Lord AT (1997) A review and synthesis of pressure effects research in accounting. J Account Lit 16:28–85
8. Smith KJ, Emerson DJ (2017) An analysis of the relation between resilience and reduced audit quality within the role stress paradigm. Adv Account 37:1–14
9. Yan H, Xie S (2016) How does auditors' work stress affect audit quality? Empirical evidence from the Chinese stock market. China J Account Res 9(4):305–319
10. Bowrin AR, King J (2010) Time pressure, task complexity, and audit effectiveness. Manag Audit J 25(2):160–181
11. Novriansa A, Riyanto B (2016) Role conflict and role ambiguity on local government internal auditors: the determinant and impacts. J Indonesian Econ Bus 31(1):63–80
12. Sage AP (1977) Interpretive structural modeling: methodology for large-scale systems, pp 91–164. McGraw-Hill, New York
13. Gayathri K, Suresh M (2018) Modelling the factors of agile practices in project management: a case of illumination project organization. Int J Eng Technol (UAE) 7(2.33):541–547
14. Sankar H, Suresh M (2018) Modelling the factors of workplace spirituality in healthcare organization. Int J Eng Technol (UAE) 7(2.33):786–790
15. Keerthanaa P, Suresh M (2018) Informal learning in work place: a case of caregivers. Int J Eng Technol (UAE) 7(2.33):791–795

16. Sushil S (2012) Interpreting the interpretive structural model. Glob J Flex Syst Manage 13(2):87–106
17. Balaji M, Arshinder K (2016) Modeling the causes of food wastage in Indian perishable food supply chain. Resour Conserv Recycl 114:153–167
18. Patri R, Suresh M (2017) Modelling the enablers of agile performance in healthcare organization: A TISM approach. Glob J Flexib Syst Manage 18(3):251–272
19. Vaishnavi V, Suresh M, Dutta P (2019a) A study on the influence of factors associated with organizational readiness for change in healthcare organizations using TISM. Benchmarking Int J 26(4):1290–1313
20. Vaishnavi V, Suresh M, Dutta P (2019b) Modelling the readiness factors for agility in healthcare organization: a TISM approach. Benchmarking Int J 26(7):2372–2400
21. Patil M, Suresh M (2019) Modelling the enablers of workforce agility in IoT projects: a TISM approach. Glob J Flexib Syst Manage 20(2):157–175
22. Amrita VV, Suresh M (2016, December) Factors influencing lean practices in Super market services using interpretive structural modeling. In: 2016 IEEE international conference on computational intelligence and computing research (ICCIC), pp 1–5. IEEE
23. Keerthana S, Suresh M (2016, December) Drivers influencing lean practices in street food vending process. In: 2016 IEEE international conference on computational intelligence and computing research (ICCIC), pp 1–5. IEEE
24. Renganath K, Suresh M (2016, December) Analyzing the drivers for safety practices using interpretive structural modeling: A case of Indian manufacturing firms. In: 2016 IEEE international conference on computational intelligence and computing research (ICCIC), pp 1–6. IEEE
25. Abinaya R, Suresh M (2016, December) Analyzing the drivers for lean practices of commercial banking using interpretive structural modelling. In: 2016 IEEE international conference on computational intelligence and computing research (ICCIC), pp 1–4. IEEE
26. Suresh M, Ganesh S, Raman R (2019) Modelling the factors of agility of humanitarian operations. Int J Agile Syst Manage 12(2):108–123
27. Venkatesh AB, Suresh M (2016, December) Factors influencing Indian tourism promotion in social media. In: 2016 IEEE international conference on computational intelligence and computing research (ICCIC), pp 1–5. IEEE
28. Sudharsan TM, Suresh M (2016, December) Factors influencing purchase decision of solar lanterns by street vendors. In: 2016 IEEE international conference on computational intelligence and computing research (ICCIC), pp 1–4. IEEE
29. Miruthu Bashini R, Suresh M (2018) Modelling the ergonomics factors affecting the work system in hospital: an ISM approach. Int J Pure Appl Math 119(7):183–198
30. Shiyam Sundar T, Suresh M, Raghu Raman R (2018) Modelling the ergonomics factors affecting the work system in hospital: an ISM approach. Int J Pure Appl Math 119(7):107–125
31. Gautham GR, Suresh M, Ranganathan R (2018) Factors affecting human performance in lathe machine shop operations. Int J Eng Technol (UAE) 7(2.33):882–885
32. Haresh B, Suresh M, Ranganathan R (2018) Factors influencing success of new product launch: a case of SME stationery industry in India. Int J Eng Technol (UAE) 7(2.33):902–906
33. Jeevan S, Suresh M, Ranganathan R (2018) Risk factors influencing humanitarian operations: a case of temple cart festival. Int J Eng Technol (UAE) 7(2.33):946–949
34. Aarthi N, Suresh M (2018) Factors influencing people to approach micro finance institutions in India. Int J Eng Techno (UAE) 7(2.33):978–981
35. Patri R, Suresh M (2018) Factors influencing lean implementation in healthcare organizations: an ISM approach. Int J Healthcare Manage 11(1):25–37
36. Suresh M, Mahadevan G, Abhishek RD (2019) Modelling the factors influencing the service quality in supermarkets. Int J Syst Assur Eng Manage. https://doi.org/10.1007/s13198-019-00897-4

Performance Analysis of Flat-Plate Solar Collector Using Tungsten Trioxide Nanofluid

J. Vinoth Kumar, A. Amarkarthik, R. Harish, S. Mugundan, and R. R. Suriyaa

Abstract An experimental study was performed to investigate the performance of flat-plate solar collector using water and WO_3 nanofluid as working fluids. Analysis and comparison were carried out for energy efficiency, entropy generation, exergy destruction, and exergy efficiency. WO_3 nanofluid exhibited 13.49% higher efficiency when compared to water on operation with flat-plate solar collector. The entropy generation was minimum for 0.0667 vol.% WO_3 nanofluid and maximum for water. The flat-plate collector exhibited improved exergy efficiency 24.63, 34.83, and 57.39% for 0.0167 vol.% WO3, 0.0334 vol.% WO_3, and 0.0667 vol.% WO_3 nanofluid on comparison with water. The solar collector indicates the highest exergy efficiency for 0.0667 vol.% WO_3 nanofluid. On experimentation, solar flat collector exhibited the use of WO_3 nanofluid could improve the thermal efficiency, and maximum performance was attained for the use of 0.0667 vol.% WO_3 nanofluid.

Keywords Flat-plate solar collector (FPSC) · Nanofluid · Thermal efficiency · Entropy generation · Exergy · Entropy

1 Introduction

In modern era, meeting the energy needs by renewable energy is challenge due to restricted conventional energy resources. The likely of renewable energy resources in fulfilling the requirement of clean energy has become vital [1]. Improvement in renewable energy efficient systems utilizing potent materials has been foremost issue for researchers and engineers. Among the available solar collectors, flat-plate solar collectors offers minimal cost, a reduced amount of maintenance and uncomplicated design hence been incorporated for solar energy-based water heater [2]. Many studies are carried out on change in collector structure and change of working fluids to improve the systems efficiency.

J. Vinoth Kumar (✉) · A. Amarkarthik · R. Harish · S. Mugundan · R. R. Suriyaa
Department of Mechanical Engineering, Bannari Amman Institute of Technology, Sathyamangalam, Erode 638401, Tamil Nadu, India
e-mail: vinothmech1809@gmail.com

G. Kumaresan et al. (eds.), *Advances in Materials Research*, Springer Proceedings in Materials 5, https://doi.org/10.1007/978-981-15-8319-3_83

Flat-plate solar collectors (FPSCs) are ease in design, low cost, and offer minimal maintenance on comparison with other types of collectors. Flat-plate solar collectors are mostly used for heating of water by absorbing solar energy. Performance improvement in working fluid such as addition of high thermal conductivity nanoparticles to working fluid was first initiated by Choi et al. [3]. Nanofluid is a kind of heat transfer fluid suspending small quantity of nanosized particles in the range between 1 and 100 nm which results in improved heat transfer properties [4]. An thermal efficiency enhancement of 28.3% for FPSCs with Al_2O_3/water nanofluid for volume flow rate 2 l/min and particle size 15 nm was investigated by Yousefiet al. [5]. Zamzamian et al. [6] investigated the outcome of Cu nanoparticle on FPSC for various volume flow rate and mass fractions of nanoparticle resulted an optimum point of 0.3 wt.% Cu nanofluid at 1.5 l/min. Verma et al. [7] tested the performance of FPSCs for MgO/water working fluid having particle size 40 nm, particle volume concentration (0.25–1.5%), and volume flow rate (0.5–2.5 lpm). Sharafeldin et al. [8] investigated the effect of WO3/water nanofluid in FPSCs efficiency and found maximum efficiency enhancement of 13.48% for 0.0667% volume fraction of nanoparticle and 0.0195 kg/s mass flow rate on comparison with water. Shojaeizadeh et al. [9] carried out exergy analysis on FPSCs with Al_2O_3/water nanofluid and found 1% increase in exergy efficiency for corresponding 68% decreased mass flow rate and 2% decreased collector inlet temperature.

Tonga et al. [10] performed an experimental investigation of the thermal efficiency, entropy generation, and exergy efficiency of a FPSC for the concentration and mass flow of Al_2O_3 and CuO based on water. Evolved an improved thermal efficiency of 21.9% for FPSC using Al_2O_3 nanofluid on comparison with water. On comparison with water, the exergy efficiency using 0.5 vol.% CuO and 1 vol.% Al_2O_3 nanofluid increased by 49.6 and 56.9%.

2 Analysis of Energy and Exergy for Solar Collector

2.1 Analysis of Energy

Calculation of valuable heat from solar collector is obtained by using Eq. (1)

$$Q_u = \dot{m} c_p \, (T_o - T_i) \tag{1}$$

The nanofluid's specific heat capacity can be calculated by using Eq. (2) [11]

$$c_{p,nf} = \frac{(1-\varphi)\rho_{bf} c_{p,bf} + \varphi \rho_n c_{p,n}}{(1-\varphi)\rho_{bf} + \varphi \rho_n} \tag{2}$$

The density of nanofluid is calculated from the following Eq. (3) [12]

$$\rho_{nf} = (1-\varphi)\rho_{bf} + \varphi\rho_n \tag{3}$$

The efficiency of energy for solar collector (i.e., ratio of gained valuable energy to absorber received solar energy) can be found by using Eq. (4)

$$\eta = \frac{Q_u}{A_c G_T} \tag{4}$$

2.2 Analysis of Exergy

Exergy is the measurable usefulness of energy. Under state condition of open system, exergy balance is expressed by Eq. (5)

$$\dot{E}\, x_{\text{heat}} - \dot{E}\, x_{\text{work}} - \dot{E}\, x_{\text{mass,in}} - \dot{E}\, x_{\text{mass,out}} = \dot{E}\, x_{\text{dest}} \tag{5}$$

Here, exergy by heat, work, and mass are represented at left side and exergy destruction indicated in right side. The solar radiation exergy $\dot{E}\, x_{\text{heat}}$ is expressed by Eq. (6)

$$\dot{E}\, x_{\text{heat}} = \left(1 - \frac{T_a}{T_{\text{sol}}}\right)\dot{Q}_{\text{sol}} \tag{6}$$

where T_{sol} the apparent sun surface temperature assumed to be 4500 K for this study [13].

$\dot{Q}_{\text{sol}}$ is calculated by Eq. (7)

$$\dot{Q}_{\text{sol}} = G(\tau\alpha)A_c \tag{7}$$

The inlet and outlet exergy flow of the collector is expressed by Eqs. (8) and (9).[14].

$$\dot{E}\, x_{\text{mass,in}} = \dot{m}\,[(h_i - h_a) - T_a(s_i - s_a)] \tag{8}$$

$$\dot{E}\, x_{\text{mass,out}} = \dot{m}\,[(h_o - h_a) - T_a(s_o - s_a)] \tag{9}$$

Substitution of Eqs. 6–9 in Eq. 5 yields Eq. (10)

$$\left(1 - \frac{T_a}{T_{\text{sol}}}\right)\dot{Q}_{\text{sol}} - \dot{m}\, c_p(T_o - T_i) + \dot{m}\, c_{p,avg} T_a \ln\left(\frac{T_o}{T_i}\right) - \dot{m}\,\frac{\Delta p}{\rho} = \dot{E}\, x_{\text{dest}} \tag{10}$$

The exergy destruction $\dot{E}\ x_{\text{dest}}$ is expressed by Eq. (11).

$$\dot{E}\ x_{\text{dest}} = T_a \dot{S}_{\text{gen}} \tag{11}$$

For solar collector, the entropy generation is evaluated using Eq. (12) [15]

$$\dot{S}_{\text{gen}} = \dot{m}\ c_p \ln\left(\frac{T_o}{T_i}\right) - \frac{\dot{Q}_{sol}}{T_s} + \frac{\dot{Q}_o}{T_a} \tag{12}$$

The heat loss to atmosphere $\dot{Q}_o$ is expressed by Eq. (13).

$$\dot{Q}_o = \dot{Q}_{\text{sol}} - \dot{m}\ c_p (T_o - T_i) \tag{13}$$

The exergy efficiency (i.e., the ratio of effective exergy yield to the exergy input) is evaluated using Eq. (14).

$$\eta_{ex} = 1 - \frac{\dot{E}\ x_{dest}}{\left[1 - \left(\frac{T_a}{T_{sol}}\right)\right]\dot{Q}_{sol}} \tag{14}$$

3 Preparation of Nanofluid and Experimentation

3.1 WO_3 Nanofluid Synthesis

All chemicals substances were used as received without extra processing and of diagnostic grade. WO_3 nanoparticle were purchased from supplier: Nano Research labs, Jharkhand, India. The size of nanoparticle is of the range 40–50 nm and purity of 99.9%. Two-step method (due to its ease of preparation) is used to prepare nanofluid. Initially, WO_3 nanoparticles are grinded by a mortar to prevent or minimize agglomeration. Later, WO_3 nanoparticles are added to the distilled water by appropriate mass fraction, and the mixture is manually agitated for not less than 10 min. The prepared mixture is positioned in the ultrasonic bath (ANALAB, India) under sonication with a frequency of 30 kHz, 1000 watts power for a period of 4 h. Three different nanofluids of 0.0166, 0.0334, and 0.06667% volume concentration are synthesized. Finally, testing the stability of nanofluid is carried out using zeta potential analyzer.

Table 1 Specifications of the flat-plate solar collector

Specification	Flat-plate solar collector
Dimension	2000 mm × 1000 mm × 80 mm (L × W × H)
Aperture area	1.51 m^2
Weight	34 kg
Cover material	3.8 mm tempered texture glass
Cover thickness	3 mm
Absorber material	Copper
Absorber thickness	0.25 mm
Emissivity of absorber plate	0.95
Fluid capacity	2 L
Thermal insulation thickness	50 mm
Insulation material	Glass wool
Collector tilt angle	15°

3.2 Experimentation

The experiment was conducted in Salem, India (Latitude: 11.66°, longitude: 78.14°), and data are recorded between 10.00 am to 4.30 pm. The circulation of working fluid into the flat-plate solar collector is done through pump (500 W). On circulation, the working fluid enters the FPSC initially, and then, it enters a tank of 150 L capacity and continues the process. The constant temperature bath is utilized to cool the heat gain obtained from solar collector. Three-way valve is used to adjust flow rate, rotameter for desired flow rate upto 4 l/min, and pressure indicator for water and nanofluid. Specification of flat-plate solar collector is given in Table 1. Schematic layout of experiment apparatus is showed in Fig. 1.

4 Results and Discussions

4.1 Thermal Efficiency Analysis for FPSC According to Concentration of WO_3 Nanofluid

The performance of FPSC was investigated experimentally for WO_3 nanofluid as operational fluid for different concentration (0.0167, 0.0334, and 0.0667 vol.%) and at mass flow rate of 0.0167 kg/s. These results were compared with the output obtained from water as working fluid in FPSC. Figure 2 displays the change in efficiency for FPSC according to concentration of nanofluid and water. On comparison, it was conforming the improvement of efficiency for FPSC incorporating nanofluid than to water as operational fluid. The maximum efficiency of 60.9% was achieved in FPSC

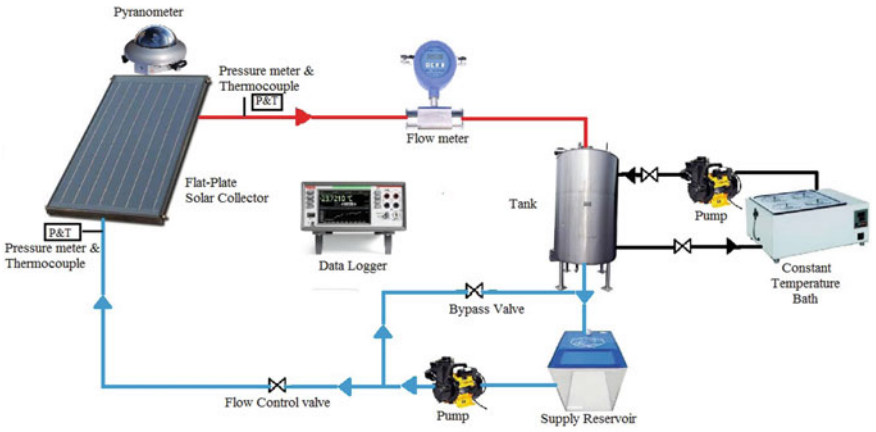

Fig. 1 Experimental setup schematic layout

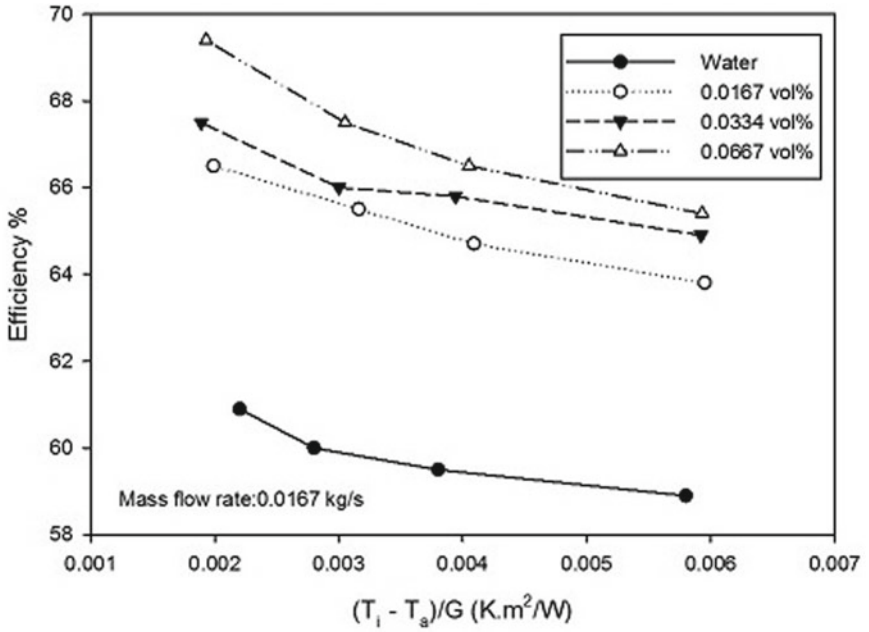

Fig. 2 Efficiency variation of FPSC on the concentration of the WO_3 nanofluids

for water as operational fluid. On other hand, the maximum efficiency of FPSC was 66.5, 67.5, and 69.4 for WO_3 nanofluid of 0.0167, 0.0334, and 0.0667 vol.%. The highest efficiency of 69.4% is achieved for WO_3 nanofluid of 0.0667 vol.%. The increase in efficiency for 0.0667 vol.%—WO_3 nanofluid was 13.95% on comparison

with water. For WO_3 nanofluid of 0.0167 and 0.0334 vol.% in SFPC, the efficiency increased by 9.19 and 10.83% on comparison with water as operational fluid.

This is mainly due to increase of thermal conductivity but also decreases dispersion stability. Thus, the concentration addition are taken as per optimum dispersion stability. Another important factor to be taken for consideration is pressure drop, which imparts in efficiency of FPSC. Here, the variation of pressure drop was found to be of negligible variance in accordance with of water, so the pressure drop been found almost similar for water and nanofluid of different nanofluid concentration.

4.2 Exergy Analysis for FPSC According to Concentration of WO_3 Nanofluid

Figure 3 displays the generation of entropy, and Fig. 4 shows the destruction of exergy for FPSC with respect to solar radiation for the usage of water and the WO_3 nanofluid in the FPSC. Increase in the entropy generation (Sgen) of the FPSC using water and the WO_3 nanofluid was noticed for the increase in the solar radiation. The generation of entropy ($S^{\cdot}gen$) for WO_3 nanofluid was minimal than that for the water. For the aggregate of solar radiation 650 W/m^2, entropy generation (Sgen) was least for WO_3 nanofluid of 0.0667 vol.% of value 2.269 W/K and extreme for

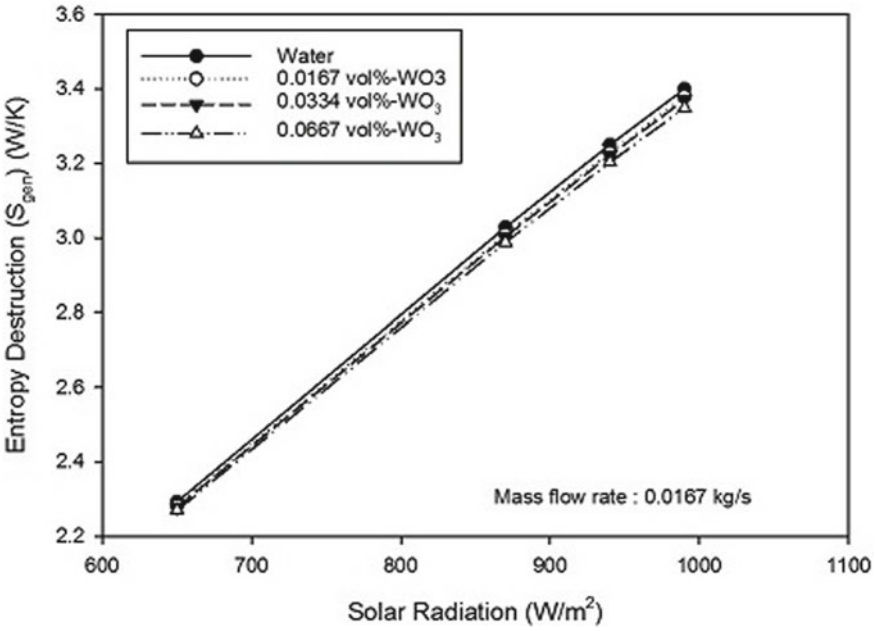

Fig. 3 Entropy generation in FPSC based on variation with solar radiation

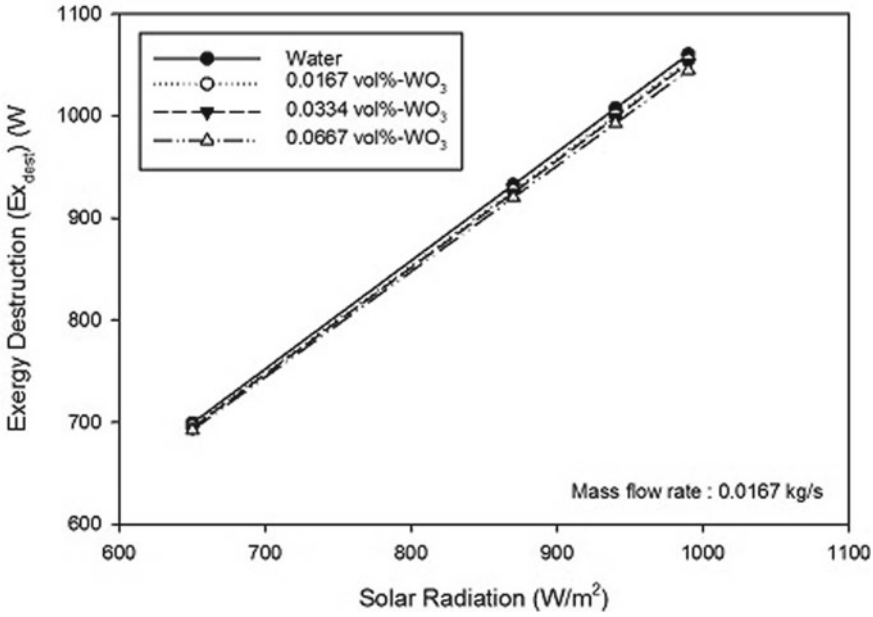

Fig. 4 Exergy destruction in FPSC based on variation with solar radiation

water at the value 2.292 W/K. Next for the aggregate of solar radiation 870 W/m^2, entropy generation (Sgen) was least for WO_3 nanofluid of 0.0667 vol.% of value 2.988 W/K and extreme for water at the value 3.028 W/K. Then, for the aggregate of solar radiation 940 W/m^2, entropy generation (Sgen) was least for WO_3 nanofluid of 0.0667 vol.% of value 3.203 W/K and extreme for water at the value 3.25 W/K. Lastly for the aggregate of solar radiation 990 W/m^2, entropy generation (Sgen) was least for WO_3 nanofluid of 0.0667 vol.% of value 3.348 W/K and extreme for water at the value 3.399 W/K. Thus, it makes a conclusion that generation of entropy increases with increase in solar radiation and increase of volume concentration of nanoparticle tends to decrease the entropy generation for a particular solar radiation intensity.

Exergy destruction in FPSC was found to increase with in solar radiation intensity, and at the mean time, exergy destruction value decreased with addition of nanoparticles for appropriate solar radiation intensity. For solar radiation of 650 W/m^2, exergy destruction in FPSC was found to be of value 699.08, 696.04, 694.61, and 692.29 W for water, 0.0167 vol.% WO_3 nanofluid, 0.0334 vol.% WO_3 nanofluid, and 0.0667 vol.% WO_3 nanofluid. For solar radiation of 870 W/m^2, exergy destruction in FPSC was found to be of value 932.64, 927.07, 924.84, and 920.32 W for water, 0.0167 vol.% WO_3 nanofluid, 0.0334 vol.% WO_3 nanofluid, and 0.0667 vol.% WO_3 nanofluid. For solar radiation of 940 W/m^2, exergy destruction in FPSC was found to be of value 1007.59, 1000.88, 998.48, and 992.95 W for water, 0.0167 vol.% WO_3 nanofluid, 0.0334 vol.% WO_3 nanofluid, and 0.0667 vol.% WO_3 nanofluid. For solar radiation of 990 W/m^2, exergy destruction in FPSC was found to be of value 1060.56,

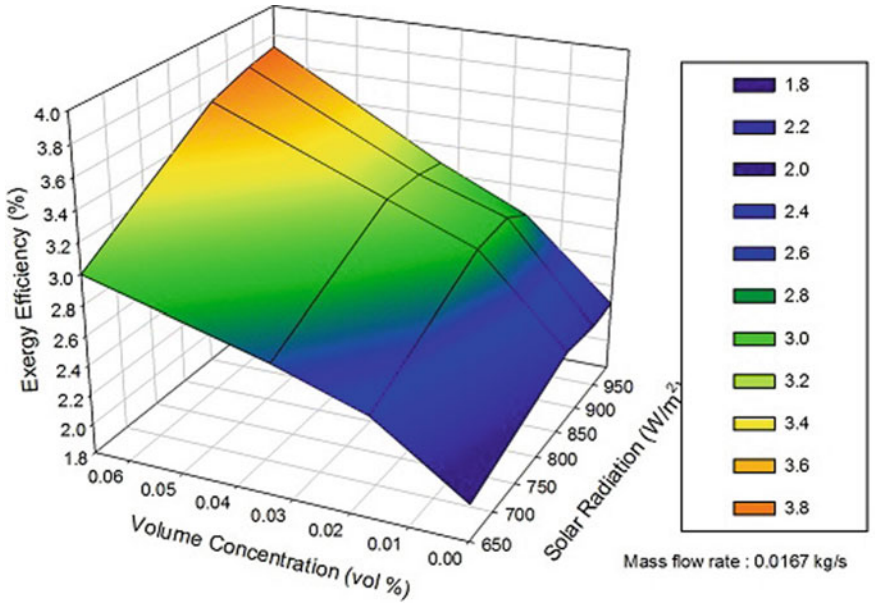

Fig. 5 Entropy efficiency of FPSC using WO_3 nanofluid

1054.79, 1051.85, and 1044.82 W for water, 0.0167 vol.% WO_3 nanofluid, 0.0334 vol.% WO_3 nanofluid, and 0.0667 vol.% WO_3 nanofluid.

Figure 5 displays the change of exergic efficiency with respect to change in volume concentration of nanofluid and change in solar radiation intensity. Exergy efficiency for FPSC was also found to increase with increase in solar radiation. For addition of nanoparticles, exergy efficiency for FPSC increases with increase concentration of nanoparticles. Exergy efficiency was minimal for water at the value 2.0457% for 650 W/m^2 solar radiation and maximum for 0.0667 vol.% WO_3 nanofluid at the value 3.718% for solar radiation of 990 W/m^2.

5 Conclusions

Experimental investigation was done on FPSC using water and WO_3 nanofluid as working fluids. For solar radiation 990 W/m^2, entropy generation was maximum for water at the value 3.39 W/K and minimal at 3.34 W/K. The flat-plate collector exhibited improved exergy efficiency 24.63, 34.83, and 57.39% for 0.0167 vol.% WO_3, 0.0334 vol.% WO_3, and 0.0667 vol.% WO_3 nanofluid on comparison with water. Thus, for increase in concentration of nanoparticles upto 0.0667%, energy efficiency as well as exergy efficiency was found to increase with solar radiation intensity.

References

1. Bellos E, Tzivanidis C (2017) Parametric investigation of nanofluids utilization in parabolic trough collectors. Therm Sci Eng Prog 2:71e79. https://doi.org/https://doi.org/10.1016/j.tsep.2017.05.001
2. Kolagirau S (2004) Solar thermal collectors and applications. Prog Energy Combust Sci 231–95
3. Choi DASS, Wang HP (1995) Enhancing thermal conductivity of fluids with nanoparticles in development and applications of non-newtonian flows. ASME, New York
4. Eastman JA, Choi SUS, Li S, Yu W, Thompson LJ (2001) Anomalously increased effective thermal conductivities of ethylene glycol-based nanofluids containing copper nanoparticles. Appl Phys Lett 78:718e720. https://doi.org/https://doi.org/10.1063/1.1341218
5. Yousefi T, Veysi F, Shojaeizadeh E, Zinadini S (2012) An experimental investigation on the effect of Al_2O_3-H_2O nanofluid on the efficiency of flat-plate solar collectors. Renew Energy 39:293–298
6. Zamzamian A, KeyanpourRad M, KianiNeyestani M, Jamal-Abad MT (2014) An experimental study on the effect of Cu-synthesized/EG nanofluid on the efficiency of flat-plate solar collectors. Renew Energy 71:658–664
7. Sujit Kumar Verma (2016) Arun Kumar Tiwari, Durg Singh Chauhan, Performance augmentation in flat plate solar collector using MgO/water nanofluid. Energy Convers Manage 124:607–617
8. Sharafeldin MA, Gróf G, Mahian O (2017) Experimental study on the performance of a flat-plate collector using WO_3/water nanofluids. Energy 141:2436–2444
9. Shojaeizadeh FV, Kamandi A (2015) Exergy efficiency investigation and optimization of an Al_2O_3-water nanofluid based flat-plate solar collector. Energy and Buildings. https://doi.org/10.1016/j.enbuild.2015.04.048
10. Tonga Y, Lee H, Kangc W, Cho H (2019) Energy and exergy comparison of a flat-plate solar collector using water, Al_2O_3 nanofluid, and CuO nanofluid. Appl Therm Eng 159:113959
11. Sundar LS, Sharma KV (2008) Thermal conductivity enhancement of nanoparticles in distilled water. Int J Nanopart 1:66–77
12. Pak BC, Cho YI (1998) Hydrodynamic and heat transfer study of dispersed fluids with submicron metallic oxide particles. J Therm Energy Gener Transp Storage Convers 11:151–170
13. Jafarkazemi F, Ahmadifard E (2013) Energetic and exegetic evaluation of flat plate solar collectors. Renew Energy 56:55–63
14. Bejan AE (1988) Thermodynamics. Wiley Interscience, New York
15. Bejan (1995) Entropy generation minimization, the method of thermodynamic optimization of finite-size systems and finite-time processes. CRC Press, Boca Ratonm

Investigation on Characteristics of Stir-Casted Aluminum Matrix Composites—A Review

P. Raghuvaran, M. Suresh, J. Baskaran, S. Arun Prasadh, M. K. Charan, and T. Dhananjayan

Abstract Composites made of aluminum matrix are fabricated mostly by stir casting method because of its advantages given to the components made. Researches on this area are compiled in this study. For better understanding, the study was further extended by showing the results of few composites magnesium matrix composites. Results, because varying reinforcements and their percentage to the matrix material, are shown in this study. Better bonding of reinforcements are achieved by fabricating at right percentage of mix, pouring temperature, preheating temperature of die and more which plays a key role in resulting characteristics of materials made. Components fabricated must be ensured for having less porosity, better bonding and uniform distribution of reinforcement with matrix so as to attain better results. Mechanical properties and microstructures analyzed in various articles to ensure the attainment of these characteristics in fabricated components are shown.

Keywords Aluminum · Composites · Stir casting · Mechanical properties · Review

1 Introduction

For manufacture of metal matrix composites with discontinuous particles, stir casting is a good old technique followed over decades. Strength to-wear ratio and wear resistance of such materials will be enhanced by using reinforcements like Al2O3, SiC, etc. Aluminum matrix composites are produced by stir casting technique, and

P. Raghuvaran (✉) · J. Baskaran · M. K. Charan · T. Dhananjayan
Department of Mechanical Engineering, Sri Krishna College of Engineering and Technology, Coimbatore 641008, India
e-mail: ragumechanical@gmail.com

M. Suresh
Department of Robotics and Automation Engineering, PSG College of Technology, Coimbatore 641004, India

S. Arun Prasadh
Supply Chain Management and Purchasing, SKEMA Business School, Lille, France

G. Kumaresan et al. (eds.), *Advances in Materials Research*, Springer Proceedings in Materials 5, https://doi.org/10.1007/978-981-15-8319-3_84

the resulting microstructure and properties depend on various parameters. Interfacial bonding of metal to reinforcement is an important factor among them. It can be achieved by selecting proper stirring speed of reinforcement into the aluminum melt and correct pouring temperature.

1.1 Aluminum and Aluminum Matrix Composites

Aluminum is a lightweight, soft and ductile material having remarkable resistance to corrosion which makes it to employ for aerospace, building and engine casings. Some of the composites made of aluminum are given in this study.

Automobile industries, aerospace and military applications prefer aluminum matrix composites (AMCs) nowadays rather than conventional materials because of the properties resulting like good wear resistance, high temperature resistance with less weight and more. AMCs have better wear resistance and high strength-to-weight ratio than aluminum alloy. Less dense, high electric resistive and low thermal conductive insulating materials are made with aluminum composites by having fly ash as reinforcement. Reinforcing particles are injected into metal liquid to form casting. For mass production, casting can be better chosen since it is less expensive. Best properties can be achieved if uniform distribution of particulates is achieved. It may be affected because of poor wettability and segregation of particles at the bottom of matrix material.

For manufacture of metal matrix composites with discontinuous particles, stir casting is a good old technique followed over decades. Strength-to-wear ratio and wear resistance of such materials will be enhanced by using reinforcements like Al_2O_3, SiC, etc. Aluminum matrix composites are produced by stir casting technique, and the resulting microstructure and properties depend on various parameters. Interfacial bonding of metal to reinforcement is an important factor among them. It can be achieved by selecting proper stirring speed of reinforcement into the aluminum melt and correct pouring temperature.

1.2 Metal Matrix Composites (MMC)

Physically or chemically distinct phases of two or more numbers constitute a material called composite. Characteristics of composites are superior to that of the individual components [1]. Structural engineering materials, nowadays, use MMCs and gained increasing interest in recent years [2]. They are used for replacing steels possessing toughness and high strength at increased temperatures along with low density. Better bonding of matrix and reinforcements makes MMCs to withstand compressive and tensile stresses as load applied on them gets shifted and well distributed to reinforcement material from ductile matrix. MMC with aluminum as matrix material is one of the key areas in research in the field of material processing for the past few

decades having silicon carbide (SiC) as reinforcements to get a lightweight material with high strength and stiffness [3]. Most of the industries prefer aluminum composites among all the materials because of its eminent properties like lightweight, good thermal properties and high strength to composites using SiC, carbon and boron carbide (B_4C) as reinforcements.

Good wear resistance, damping capacity, high specific strength and specific modulus are possessed by metal matrix composites (MMCs) than that of non-reinforced alloy [4]. In achieving good combination of stiffness, strength, density and toughness, there are many limitations in conventional monolithic materials. Composites are capable enough to overcome these limitations and to meet increasing demand of recent days.

1.3 Aluminum Metal Matrix Composites (AMMCs)

Improved hardness, 0.2% yield stress (YS), ultimate tensile stress (UTS), mechanical properties, good machinability, low coefficient of thermal expansion (CTE) and lightweight are some significant properties of aluminum metal matrix composites (AMMCs) which gained attention of researchers in recent years [5]. Results of which are usage of AMMCs for making airframe components in aerospace, engine pistons in automobile and integrated circuit frame mounting components in electronic industries.

Manufacturing of AMMCs use stir casting (vortex technique) as a method since it is economic. As said earlier, it is flexible, simple and suitable for mass production. It is also a best chosen method for manufacturing components which are larger in size. The method of stir casting has some fewer limitations to overcome like porosity and non-uniform distribution of reinforcement with matrix material which need to be overcome for achieve better results.

2 Materials and Methods

Researches of various authors given below are ordered like aluminum composites with titanium diboride (TiB2) as reinforcement [6], aluminum composites with titanium carbide (TiC) as reinforcement [7], Zn-27Al composites with rice husk ash (RHA), silicon carbide (SiC), and graphite (Cg) as reinforcements [8], aluminum composites with nano-magnesium oxide (MgO) as reinforcement [9], aluminum or magnesium composites with silicon carbide as reinforcement [10–21].

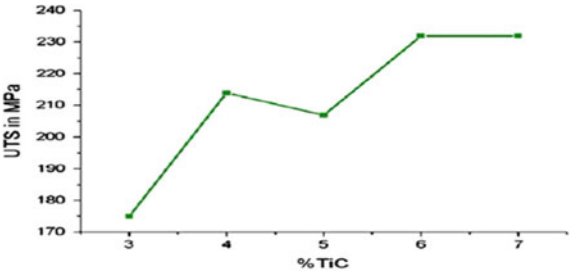

Fig. 1 Effect of TiC addition on tensile strength of AMMC

2.1 Titanium

Composites have many applications in aerospace, automotive and structural components, said by S. Suresh et al. [6]. Keeping other parameters unvarying, the experiment is done on Al6061 MMC using varying weight fraction of TiB_2. Microscopic examination is done to analyze the mechanism of wear and found that wear resistance of composite samples increased on addition of TiB_2. Hardness, tensile strength and wear resistance of the samples are also experimented and found for varying percentage of reinforcements.

Gopalakrishnan et al. produced cost-efficient MMCs for improved specific strength; wear resistance and high-temperature applications [7]. Enhanced stir casting method was used to produce different volume fraction of Al-TiC composites in an argon atmosphere. It was found that increase in percentage of TiC addition improved the specific strength of the composite produced. Variation in ultimate tensile strength (UTS) was observed during the experiment, and the data has been plotted in graph and is shown in Fig. 1.

2.2 Zinc

Mechanical properties of Zn-27Al and its microstructure have been discussed by Alaneme et al. [8] with rice husk ash, silicon carbide and graphite as reinforcements. They used stir casting process to produce different composites of Zn-27Al of varied weight ratios. In order to characterize the composites produced, hardness test, tensile test, fracture toughness test and microstructure examination were done. Fine dispersion of the reinforced particles with dendritic structured Zn-27Al alloy matrix is shown in microstructure evaluation. Hardness, tensile strength, yield strength and fracture toughness variations with change in percentage weight of reinforcements are examined.

2.3 Magnesium

Abdizadeh et al. used A356 aluminum alloy and nanoparticles of MgO (1.5, 2.5 and 5% vol.%) to fabricate Al-Nano MgO composites by powder metallurgy (PM) and stir casting and methods [9]. Casted samples are less porous and resulted in high-density composites than that of PM-made composites. Also, it was found that casting method represented more homogeneous data values of mechanical properties compared to the powder metallurgy method. Compared to PM method, casting represented more homogeneous of mechanical properties.

2.4 Silicon Carbide

Poddar et al. [10] used stir casting method and manufactured Mg and Mg-alloy (AZ91D) composites reinforced using 15 vol% silicon carbide (SiC) particulates. Uniform particle distribution is achieved, and mechanical properties were studied. When compared to monolithic alloys, AZ91D alloy composite exhibited an increase in hardness and modulus and decrease in ductility. Their results show that 680 °C is the optimum holding and stirring temperature of the melt to reduce porosity in cast samples. Aravindan et al. used silicon carbide particle and two-step stir casting process for fabrication of magnesium alloy composites [11]. Mechanical and physical properties of the composites were evaluated for samples under as cast and T6 heat-treated conditions. Mechanical properties decreased on increasing size of the particles and increased on increasing particles of SiC. The result was compared under standard theoretical models and was found that the mechanical properties of composites increased with increasing SiC particles and decreased with increasing particle size. Wang et al. fabricated AZ91 magnesium matrix composite reinforced with 10 vol.% SiC particulate by stir casting technique and discussed its deformation behavior [12]. The experiment was varied from 250 to 400 °C to determine the stress variations. Peak stresses and flow stresses decrease on increase in temperature. The extent of dynamic recrystallization (DRX), on temperature reduction, becomes less. Afshin Matin et al. [13] worked on pure magnesium and AZ80 nanocomposites using stir casting method. By adding different nano-SiC particles homogenously at different weight %, he evaluated the microstructure and mechanical properties at room temperature. It was found that the grain size of the magnesium matrix got reduced significantly because of the addition of SiC nanoparticles. Ductility and tensile strength increased on increasing the content of SiC but lead to reduction in formability and strength beyond the optimum level because of agglomeration of SiC particles. Compressive stress–strain curves are used for analyzing the material hardening behavior. Wang et al. [14] fabricated Mg–Zn–Ca composites with SiCp (5, 10 and 15 vol.%) as reinforcements and achieved uniform particle distribution. Size of SiCp influenced the mechanical properties of the composites at a major extent.

Superior strength of Al2014 matrix was achieved by Zhang et al. [15] on investigating the tensile properties at elevated temperatures of nano-SiCp/Al2014 composites. Without sacrificing ductility, the tensile strength of Al2014 alloy got improved by nano SiCp at 493 K.

Various amounts of SiC particles are used by Jabeen Moses et al. [16] to fabricate AMC using aluminum alloy as matrix material. SiC particles are added into the vortex of aluminum melt formed during stirring and allowed to solidify in a permanent mold. Uniform distribution of SiC particles in aluminum matrix is examined using optical and scanning electron microscope, and particle clusters of SiC are seen in a few places. Better bonding between matrix and reinforcement resulted in the casted material which further gave better microhardness and ultimate tensile strength in the AMCs. Appreciable results were obtained by Dwivedi et al. [17] on testing the samples with different reinforcement weight percentage of A356/SiC samples during hardness, tensile, impact and fatigue tests. Uniform distribution and porosity got exposed during microstructural analysis. Samples with 5% reinforcement exhibited less porosity. Electromagnetic stir casting yielded samples with good mechanical properties on increasing the percentage of reinforcement. With the aid of stir casting, Tony Thomas et al. [18] conducted an experiment with an objective to create MMC using aluminum alloy (LM6)–SiC. Tests on specimens made are utilized for finding the significance of stirrer and feeder.

Maurya et al. [19] investigated the effect of adding SiC particles at various weight fractions to Al6061 alloy ranging from 2 to 8 wt.% made by electromagnetic stir casting technique. Images of scanning electronic microscope (SEM) ensured uniform dispersion of particles into the reinforcement. Mechanical properties of the composites are quite higher than that of Al6061 alone. Saenpong et al. [20] produced A356 matrix composites by semi-solid stir casting method and investigated the hardness variations because of varying particle size and weight percent. Highest hardness was found to be in T6 heat-treated composite having particle SiC particle size of 100 micrometer and weight percentage of 10.

Suresh et al. [21] done a research on tribological behavior of Al7075 and nano-SiC particles. Varying weight percentages of SiC particles are used to form the composite. Wear rate of the composites is found to be less than the Al7075 alloy with increasing SiC percentage.

3 Conclusion

Researches carried out in stir-casted aluminum matrix composites were elaborately discussed in this article. The reviews show a clear picture that the properties of resulting composite samples are influenced by varying parameters like volume or weight percentage of the particles, size of reinforcing particle, holding temperature of the melt and time of holding. In addition to these factors, optimum stirring speed of melt and addition of reinforcement after the formation of vortex in melt lead to uniform dispersion of particles to the melt. For better understanding, a brief summary

of observations made from each papers is given in Table 1. Mechanical properties of the composite samples are greatly influenced by homogeneous dispersion of particles in the matrix. Less porous material can be made if dispersion of particles in the melt is uniform throughout. Wear resistance of the material increases with increasing the

Table 1 Observations from each paper

S. No./Reference No.	Author(s)	Paper title	Observations
[1]	Dinesh Pargunde et al.	Fabrication of metal matrix composite by stir casting method	Better characteristics of composites than separate materials
[2]	Jasmi Hashim	The production of metal matrix composite using the stir casting technique	Structural materials are made from composites
[3]	Sozhamannan G. G. et al.	Effect of Processing Parameters on Metal Matrix Composites: Stir Casting Process	High strength and stiffness results in composites made with SiC as reinforcement
[4]	Sudipt Kumar et al.	Production and characterization of Aluminum–Fly ash composite using stir casting method	Wear resistance and other mechanical properties improved
[5]	Shahin Soltani et al.	Stir casting process for manufacture of Al–SiC composites	Composites are attracted by researchers because of improved mechanical properties
[6]	Suresh S. et al.	Process development in stir casting and investigation on microstructures and wear behavior of TiB2 on Al6061 MMC	Composites are used extensively in aerospace, automotive and structural components
[7]	Gopalakrishnan S. et al.	Production and wear characterization of AA 6061 matrix titanium carbide particulate reinforced composite by enhanced stir casting method	Al-TiC composites fabricated in argon atmosphere Specific strength of composites enhanced
[8]	Kenneth Kanayo Alaneme et al.	Microstructure and mechanical behaviour of stir-cast Zn–27Al based composites reinforced with rice husk ash, silicon carbide, and graphite	Uniform dispersion of reinforcements observed in resulting material Homogeneous dispersion improved mechanical properties of composites manufactured

(continued)

Table 1 (continued)

S. No./Reference No.	Author(s)	Paper title	Observations
[9]	Hossein Abdizadeh et al.	Investigation of microstructure and mechanical properties of Nano MgO reinforced Al composites manufactured by stir casting and powder metallurgy methods: A comparative study	Al-Nano MgO composites are made by PM and stir casting methods Stir-casted composites are found to be less porous and high dense
[10]	Palash Poddar et al.	Processing and mechanical properties of SiC reinforced cast magnesium matrix composites by stir casting process	Mg-SiC composites yielded increase in hardness and modulus and decrease in ductility Optimum holding and stirring temperature was identified as 680 °C
[11]	Aravindan S. et al.	Evaluation of physical and mechanical properties of AZ91D/SiC composites by two step stir casting process	Mechanical properties were evaluated at T6 heat-treated conditions of composites made by two-step stir casting process Increment in particle size decreased the resulting properties
[12]	Wang X. J. et al.	Hot deformation behaviour of SiC_p/AZ91 magnesium matrix composite fabricated by stir casting	Mg-10%SiC composites are made by stir casting with temperature range of 250–400 °C Peak stresses and flow stresses decreased on increase in temperature
[13]	Afshin Matin et al.	Microstructure and mechanical properties of Mg/SiC and AZ80/SiC Nano-composites fabricated through stir casting method	Ductility and tensile strength increased on increasing the content of SiC but lead to reduction in formability and strength beyond the optimum level because of agglomeration of SiC particles
[14]	Wang X. J. et al.	Microstructure and mechanical properties of SiCp/Mg Zn Ca composites fabricated by stir casting	Size of SiCp influenced the mechanical properties of the composites at a major extent

(continued)

Table 1 (continued)

S. No./Reference No.	Author(s)	Paper title	Observations
[15]	Long-Jiang Zhang et al.	High strength and good ductility at elevated temperature of Nano-SiCp/Al2014 composites fabricated by semi-solid stir casting combined with hot extrusion	Tensile strength of Al2014 alloy got improved by adding nano-SiCp at 493 K, without sacrificing ductility
[16]	Jebeen Moses J. et al.	Characterization of silicon carbide particulate reinforced AA6061 aluminum alloy composites produced via stir casting	Uniform distribution of SiC particles in matrix was observed Microhardness of composite increased
[17]	Shashi Prakash Dwivedi	Microstructure and mechanical properties of A356/SiC composites fabricated by electromagnetic stir casting	A356/5%SiC composites exhibited less porosity
[18]	Tony Thomas A. et al.	Development of Feeding and Stirring Mechanism for Stir Casting of Aluminium Matrix Composites	Significance of stirrer and feeder was analyzed by testing composite specimens
[19]	Manish Maurya et al.	Effect of SiC reinforced particle parameters in the development of aluminium based metal matrix composite	Al6061/SiC (2–8 wt%) composites are fabricated by electromagnetic stir casting method Mechanical properties of composites improved
[20]	Saenpong P. et al.	Effect of Particle Size and Weight Percent of SiC Particles on Microstructure and Hardness of A356-SiC Composites Produced by Semi-Solid Stir Casting	Hardness variations, because of varying particle size and weight percent, were investigated Highest hardness was found to be in T6 heat-treated composite having particle SiC particle size of 100 micro meter and 10 wt.%

(continued)

Table 1 (continued)

S. No./Reference No.	Author(s)	Paper title	Observations
[21]	Suresh S. et al.	Tribological Behavior of Al 7075/SiC Metal Matrix Nano-composite by Stir Casting Method	Increasing SiC % reduced wear properties of composite

proportion of SiC particles thus giving a harder material. Thermal and corrosion resistance properties of aluminum composites are analyzed by researchers only to a limited extent.

References

1. Pargunde D, Tambuskar D, Kulkarni SS (2013) Fabrication of metal matrix composite by stir casting method. Int J Adv Eng Res Stud 2(4):49–51
2. Hashim J (1999) The production of metal matrix composite using the stir casting technique. PhD Thesis, Dublin City University
3. Sozhamannan GG, Balasivanandha Prabu S, Venkatagalapathy VSK (2012) Effect of processing paramters on metal matrix composites: stir casting process. J Surf Eng Mater Adv Technol 2:11–15
4. Kumar S, Ananda Theerthan J (2008) Production and characterization of Aluminum–Fly ash composite using stir casting method. Department of Metallurgical & Materials Engineering National Institute of Technology, Rourkela
5. Soltani S, Khosroshahi RA, Mousavian RT, Jiang Z-Y, Boostani AF, Brabazon D (2015) Stir casting process for manufacture of Al–SiC composites. Rare Met 36(7):581–590
6. Suresh S, Shenbaga Vinayaga Moorthi N (2013) Process development in stir casting and investigation on microstructures and wear behavior of TiB2 on Al6061 MMC. Procedia Eng 64:1183–1190
7. Gopalakrishnan S, Murugan N (2012) Production and wear characterization of AA 6061 matrix titanium carbide particulate reinforced composite by enhanced stir casting method. Composites: Part B 43(2):302–308
8. Alaneme KK, Ajayi OJ (2017) Microstructure and mechanical behaviour of stir-cast Zn–27Al based composites reinforced with rice husk ash, silicon carbide, and graphite. J King Saud Univ Eng Sci 29(2):172–177
9. Abdizadeh H, Ebrahimifard R, Baghchesara MA (2014) Investigation of microstructure and mechanical properties of Nano MgO reinforced Al composites manufactured by stir casting and powder metallurgy methods: a comparative study. Composites: Part B 56:217–221
10. Poddar P, Srivastava VC, De PK, Sahoo KL (2007) Processing and mechanical properties of SiC reinforced cast magnesium matrix composites by stir casting process. Mater Sci Eng 460–461:357–364
11. Aravindan S, Rao PV, Ponappa K (2015) Evaluation of physical and mechanical properties of AZ91D/SiC composites by two step stir casting process. J Magnesium Alloys 3(1):52–62
12. Wang XJ, Hu XS, Wu K, Deng KK, Gan WM, Wang CY, Zheng MY (2008) Hot deformation behaviour of SiC_p/AZ91 magnesium matrix composite fabricated by stir casting. Mater Sci Eng 492(1–2):481–485
13. Matin A, Saniee FF, Abedi HR (2015) Microstructure and mechanical properties of Mg/SiC and AZ80/SiC Nano-composites fabricated through stir casting method. Mater Sci Eng 625:81–88
14. Wang XJ, Nie KB, Sa XJ, Hu XS, Wu K, Zheng MY (2012) Microstructure and mechanical properties of SiCp/Mg Zn Ca composites fabricated by stir casting. Mater Sci Eng 534:60–67

15. Zhang L-J, Qiun F, Wang J-G, Jiang Q-C(2015) High strength and good ductility at elevated temperature of Nano-SiCp/Al2014 composites fabricated by semi-solid stir casting combined with hot extrusion. Mater Sci Eng 626:338–341
16. Jebeen Moses J, Dinaharan I, Joseph Sekhar S (2014) Characterization of silicon carbide particulate reinforced AA6061 aluminum alloy composites produced via stir casting. Procedia Mater Sci 5:106–112
17. Dwivedi SP, Sharma S, Mishra RK (2014) Microstructure and mechanical properties of A356/SiC composites fabricated by electromagnetic stir casting. Procedia Mater Sci 6:1524–1532
18. Tony Thomas A, Parameshwaran R, Muthukrishnan A, Arvind Kumaran M (2014) Development of feeding and stirring mechanism for stir casting of aluminium matrix composites. Procedia Mater Sci 5:118–1191
19. Maurya M, Maurya NK, Bajpai V (2019) Effect of SiC reinforced particle parameters in the development of aluminium based metal matrix composite. Evergreen Joint J Novel Carbon Resour Sci Green Asia Strategy 6(3):200–206
20. Saenpong P, Talangkun S, Sanyajivin S, Kapranos P (2019) Effect of particle size and weight percent of SiC particles on microstructure and hardness of A356-SiC composites produced by semi-solid stir casting. Solid State Phenom 285:296–301
21. Suresh S, Gowd GH, Deva Kumar MLS (2019) Tribological behavior of Al 7075/SiC metal matrix nano-composite by stir casting method. J Instit Eng (India): Ser D 100(1):97–103

Mechanical Behavior Investigation of Copper-Added A356 Alloy

J. Baskaran, M. Suresh, P. Raghuvaran, V. K. Dharsan, A. Afesul Gayoom, and S. Dharaneetharan

Abstract The use of aluminum and its alloys has grown dramatically due to the demand for increased performance and fuel economy. Cast aluminum alloys are lightweight and can be cast into complex shapes, and thus, they have attracted significant attention as potential replacements for cast iron and steel in bulky components. Compared to other aluminum alloys, refined A356 alloy is particularly attractive for various automotive applications. Grain refinement of aluminum gives a number of technical advantages, including reduced cracking, better homogeneity, better mechanical deformation characteristics and improved mechanical properties. Microstructural study is carried out to analyze the mechanical properties of the composite. In the present work, cast A356 alloy with added copper was studied with their unique mechanical behavior and microstructure. This is carried out in both normal as cast condition and heat-treated condition, and properties are investigated.

Keywords Grain refinement · Homogeneity · Heat treated

1 Introduction

Aluminum and its alloys provide a unique combination of properties making them most economical and attractive materials for a wide range of applications. They have high strength-to-weight ratio. Al-Si alloys are broadly classified into hypo- and hyper-eutectic alloys depending on the Si content. In all the hypoeutectic cast alloys, Al-7Si-0.3 Mg finds widespread applications in automotive and general engineering industries. Castings with complicated shapes and thin walls are cast by the die casting process, where permanent molds are used.

J. Baskaran (✉) · P. Raghuvaran · V. K. Dharsan · A. Afesul Gayoom · S. Dharaneetharan
Department of Mechanical Engineering, Sri Krishna College of Engineering and Technology, Coimbatore 641008, Tamil Nadu, India
e-mail: baskaranmfgresearch@gmail.com

M. Suresh
Department of Robotics and Automation Engineering, PSG College of Technology, Coimbatore 641004, Tamil Nadu, India

G. Kumaresan et al. (eds.), *Advances in Materials Research*, Springer Proceedings in Materials 5, https://doi.org/10.1007/978-981-15-8319-3_85

This research paper investigates the addition of copper with the source alloy A356. Mechanical properties of this alloy vary with addition of copper considerably. Silicon (Si) is added as one of the most important alloy elements in aluminum cast alloys. Individually, it gives considerable strength to the aluminum alloys. The combination of silicon and magnesium forms Mg_2Si, which gives very good strengthening mechanism [1]. In order to get good machinability thru generation small cutting chips, copper plays a vital role in aluminum matrix. To refine the aluminum in the grain boundaries, alloys such as titanium (Ti) and boron (B) are used [2]. In cast and wrought aluminum alloys, grain refinement plays an important vital role [3]. Generation of intermetallic compounds such as Al_2Cu or Al_2Cu phases is achieved in the grain boundaries with increasing the percentage of copper [6]. Copper is used in this tertiary eutectic system in different wt. % in A356 aluminum alloy [4]. A356 alloys are found to provide good results since they have excellent casting characteristics [5].

Precipitation-hardening (heat-treatment) process is used to improve the strength and other properties of all the aluminum alloys. Most commonly, aluminum alloys may undergone T6 heat treatment to achieve superior properties of strength and ductility [2].

2 Experimental Procedure

2.1 Experimentation

In the present research, 10 kg of master alloys of A356 and required alloys had taken and cleaned. They are preheated before melting in the furnace. After degassing had been done for a period of 60–90 min, gravity casting was carried out in permanent mold filled with molten metal as shown in Fig. 1.

The T6 heat treatment was carried out for a total of 16 h with the first 10 h as solution treatment at 535 °C and the remaining 6 h of aging at 160 °C followed by water quenching.

The cast test specimen is a rectangular bar of dimension of 25 × 70 × 130 mm. The bars were machined into Ø6 mm × 25 mm gage length for the preparation of tensile test specimen, as ASTM E8 standard for the mechanical properties study. An INSTRON Universal Testing Machine (Model 1195-5500R) with Blue Hill software V 1.4 was used for tensile testing.

The quality of the polishing influences the development of the true microstructure. HF 5% + 95% of distilled water is used in study. It is used for constituent identification in cast alloys, especially those containing Si.

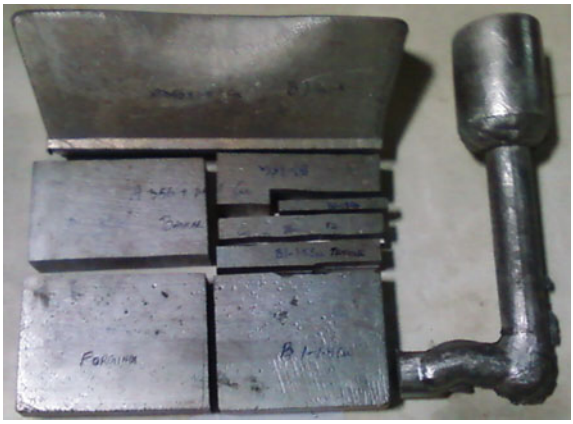

Fig. 1 As Cast specimen

3 Results and Discussion

3.1 Optical Image Analysis

The microstructure and properties of aluminium castings are defined by various parameters like mixture of alloy and metal solidification rate; the microstructure evolves during solidification and its resultant effect on the microstructural features such as dendrite arm spacing, size and defects like porosity.

Figure 2 i, ii. depicts the unreinforced copper. A fine spheroidized particle of silicon is generated after T6 heat treatment from the previous eutectic phase throughout the Al matrix. Sharp silicon needles are disappeared, and new grains are formed and also variation in the grains length is observed.

Figure 2 iii, iv. shows the 0.5% Cu content; the count of silicon particles is increased considerably, and its transformed spherical form improves the mechanical properties. Initially, added copper with primary components causes ternary eutectic reaction at about 520 °C. Next to that coefficient of hydrogen activity is reduced with the steep rise of copper content consequently solubility of hydrogen was decreased.

Figure 2 v, vi. are clearly observed that clear precipitation of intermetallic particles (Al_2Cu) at the grain boundaries with increment of 1% copper addition with the source alloy as ternary component. Secondary dendritic arm spacing size is reduced in the casting microstructure. It would improve the overall mechanical properties of the alloy due to the new generation of secondary phase and reduction in silicon particle size.

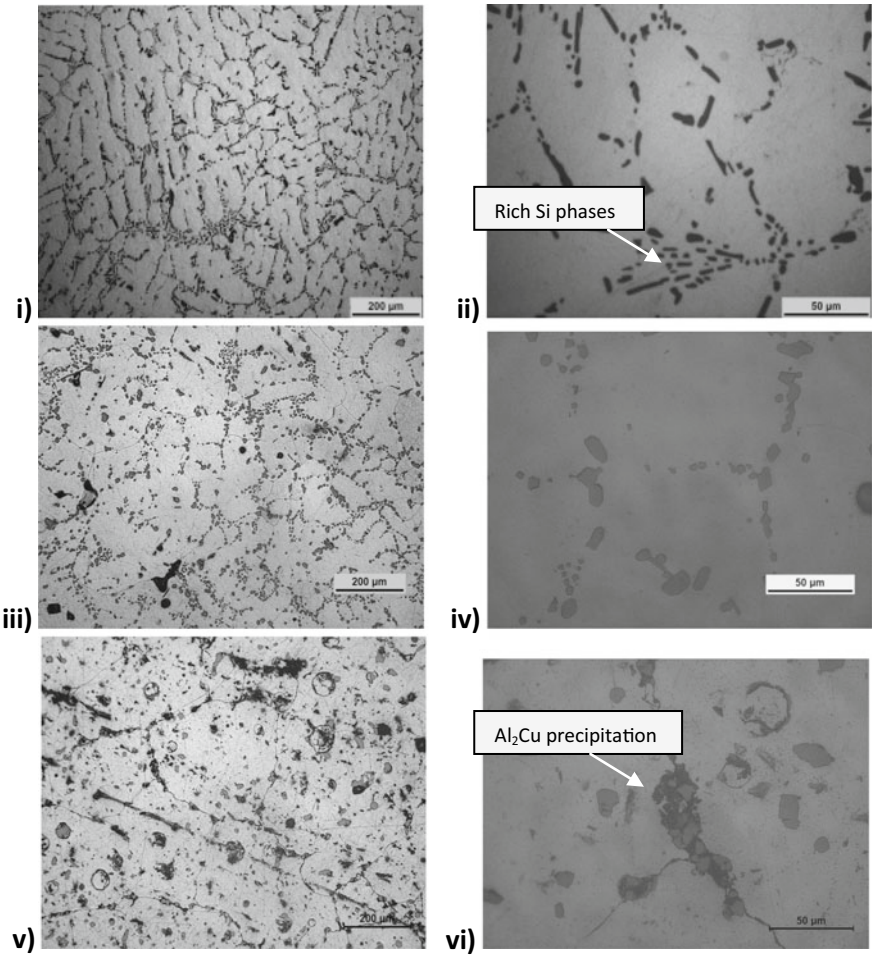

Fig. 2 Optical micrographs of tempered A356 alloy (i, ii—0% Cu, iii, iv—0.5% Cu, v, vi—1% Cu)

3.2 Mechanical Testing Result

See Fig. 3.

4 Conclusions

The current work aimed at the enrichment of mechanical behavior of A356 alloy by the uniformed increment wt% of copper. Based on the obtained result as shown in

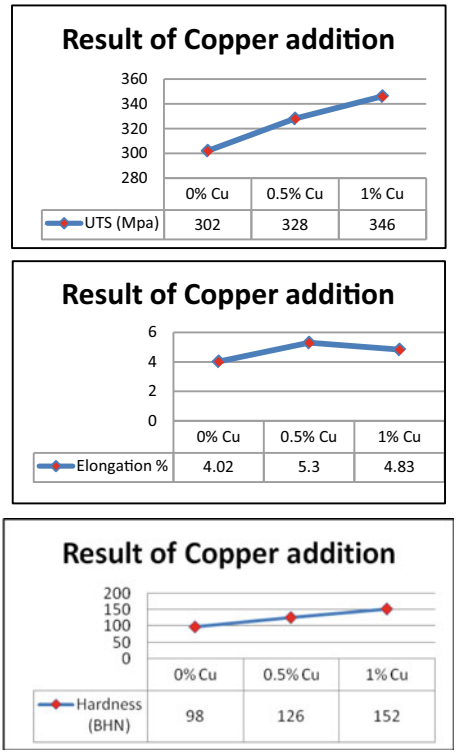

Fig. 3 Mechanical properties of A356 alloy

Fig. 3, the alloy was most advisable one in the field of automobile sectors due to their excellent combination of properties.

- Addition of Cu to A356 results in fine and dispersed silicon phase conversion of coarse α-Al dendritic structure to equiaxed structure. This may be due to Al_2Cu intermetallic particles which lead to adequate α-Al dendrites.
- Dendrite arm spacing also decreases which makes the microstructure finer resulting improved mechanical properties,
- Addition of copper was improved the percentage of elongation and hardness value (75%) at first, but further addition the values was changed drastically.
- A fine Al_2Cu precipitate caused by the increment of copper which influences much improvement in both the tensile and hardness values.

References

1. Kashyap KT, Chandrasekhar T (2001) Effects and mechanisms of grain refinement in aluminium alloys. Bull Mater Sci 24(4):345–353

2. Mallapura DG, Rajendra Udupaa K, Kori SA (2011) Studies on the influence of grain refining and modification on microstructure and mechanical properties of forged A356 alloy. Mater Sci Eng 528:4747–4752 (2011)
3. Peng J-h, Tang X-l, He J-t, Xu D-y (2011) Effect of heat treatment on microstructure and tensile properties of A356 alloys. Trans Nonferrous Mater Soc China
4. Forcellese FG (2000) Warm forging of aluminium alloys: a new approach for time compression of the forging sequence. Int J Mach Tools Manuf 40:1285–1297
5. Lee K, Kwon YN, Lee S (2008) Effects of eutectic silicon particles on tensile properties and fracture toughness of A356 aluminum alloys fabricated by low-pressure-casting, casting-forging, and squeeze-casting processes". J Alloy Compd 461:532–541
6. Lee K, Kwon YN, Lee S (2008) Correlation of microstructure with mechanical properties and fracture toughness of A356 aluminum alloys fabricated by low-pressure-casting, rheo-casting, and casting-forging processes. Eng Fract Mech 75:4200–4216
7. Zhu M, Jian Z, Yang G, Zhou Y (2012) Effects of T6 heat treatment on the microstructure, tensile properties, and fracture behavior of the modified A356 alloys. Mater Des 36:243–249
8. Zhang LY, Jiang YH, Ma Z, Shan SF, Jia YZ, Fan CZ, Wang WK (2008) Effect of cooling rate on solidified microstructure and mechanical properties of aluminium-A356 alloy. J Mater Process Technol 207:107–111
9. Suresh M, Narasimharaj V, Arul Navalan GK, Chandra Bose V (2014) Effect of orientations of an irregular part in vibratory part feeders. Int J Adv Manuf Technol Appl Mechan Mater 550:3–13
10. Baskaran J, Raghuvaran P, Ramakrishnan C, Renga Prasad A, Monish Kumar R (2019) Investigation on the influence of heat treatment of mechanical behavior enhancement of A356 alloy. Int J Mechan Eng Technol 10(03):1088–1093
11. Samson Jerold Samuel C, Ramesh A, Kirubaharan K, Kamal Shankar S, Prabu G (2018) Effect of copper coating and reinforcement orientation on mechanical properties of LM6 aluminium alloy composites reinforced with steel mesh by squeeze casting. Trans Ind Inst Met 71(5):1041–1048
12. Kuppuraj S, Ranganathan S, Aruchamy S, Gopal S (2019) Investigation of dry sliding wear behavior of AA8011 reinforced with zirconium oxide and aluminium oxide hybrid composites processed through multi-direction forging. SAE Technical Paper 2019-28-0057
13. Soundararajan R, Ramesh A, Mohanraj N, Parthasarathi N (2016) An investigation of material removal rate and surface roughness of squeeze casted A413 alloy on WEDM by multi response optimization using RSM. J Alloy Compd 685:533–545
14. Samson Jerold Samuel C, Arthanari R (2018) Optimisation of dry sliding wear parameters of squeeze cast AA336 aluminium alloy–copper coated steel wires reinforced composites by response surface methodology. J Metal Casting 1–13
15. Samson Jerold Samuel C, Arthanari R (2018) Investigation on mechanical properties and tribological behaviour of stir cast LM13 aluminium alloy based particulate hybrid composites. Mater Sci Eng Technol

Review on Manufacturing and Development of Ni-Ti Shape Memory Alloys

M. Sureshkumar and S. Madan Mohan

Abstract The recent trends in shape memory alloy application in various fields are increased to large in number and which requires some specific properties for a particular area of applications. This shape memory alloy has a unique property to memorize or to regain its previous form when particular alloy subjected to thermal or electrical stimulus. Different manufacturing process exhibit various chemical and mechanical properties. This study presents various strength and limitation of different manufacturing process involved in manufacturing of nitinol, historical overview, and recent advance technology and new application of shape memory alloy particularly in aerospace, automobile, robotics and biomedical.

Keywords Nitinol · Shape memory alloys · Additive manufacturing · Manufacturing of nitinol · Application of shape memory alloys

1 Introduction

Nitinol (Nickel Titanium Naval Ordinance Laboratory) is a shape memory alloy (SMA) that has named after its chemical composition and laboratory where it was discovered [1]. Shape memory alloy is mainly classified into two types. One-way shape memory alloy which will exhibit its shape memory effect only when heating the alloy and two-way shape memory alloy which exhibits its character while heating and cooling. Due to its shape memory effect, fatigue resistance, good damping properties and super elasticity have increased its application in various fields mainly in medical application [2]. In 1959, nitinol was discovered by William J.Buehler of the Naval Ordinance Laboratory. This was discovered while trying to develop an impact, fatigue and heat resistance alloy to use as the nose cone of the navy missile [1, 3].

M. Sureshkumar (✉) · S. Madan Mohan
Department of Mechanical Engineering, Bannari Amman Institute of Technology, Sathyamangalam, Erode 638401, Tamil Nadu, India
e-mail: sureshkumar.myil@gmail.com

G. Kumaresan et al. (eds.), *Advances in Materials Research*, Springer Proceedings in Materials 5, https://doi.org/10.1007/978-981-15-8319-3_86

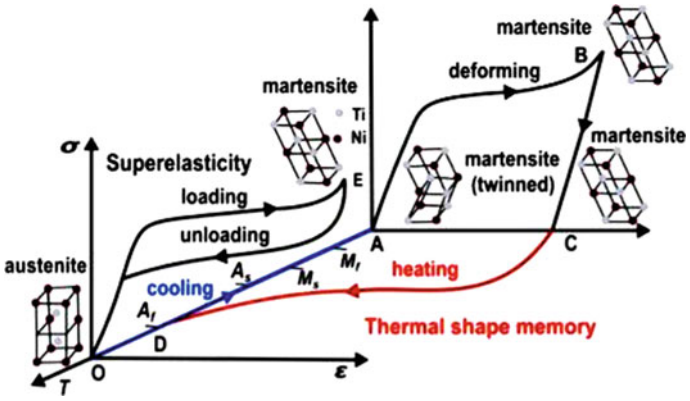

Fig. 1 Stress–strain temperature diagram for nitinol [4]

1.1 Properties of Nitinol

The shape memory alloy exhibits two-phase changes, namely martensite phase which is in the low temperature and austenite phase which will be high-temperature state. Nitinol has mainly two special properties shape memory effect which is thermally induced and superelasticity which is mechanically induced. The shape memory effect can be attained by the following process; initially, the alloy will be in the martensite state which is twinned state, on applying the load its deformed as it will be in the same martensite deformed state, and then by applying the high temperature, it will be changed to austenite state and cooling back the alloy result in phase transformation to martensite. The superelasticity property can be achieved by applying the load on the austenite state at constant temperature; this leads to change of phase to martensite state and again removing the load then phase changed to austenite state. As show in (see Fig. 1), Nitinol in an austenite state at origin point O is cooled along the path OA with no applied stress and which passes through transformation points Af (Austenite finish), As (Austenite start), Ms (Martensite start) and last Mf (Martensite finish) in a twinned state. The deformation process will be through detwinning and reorientation occurs from point A to B with elastic unloading from point B to C [4].

1.2 Nickel–Titanium Ratio Significance

The main key point to manufacture nitinol will be Ni–Ti ratio; if it varies with ratio, then there will be variation in the number of electrons available for bonding. Due to this variation the behavior in transformation temperature can be seen in the resulting material, which shows some deviation in nitinol super elasticity and shape memory effect properties. Various studies have shown that transformation temperature are very sensitive to the ratio of nickel (Ni) and titanium(Ti), if an alloy composition

shift of 1% can result in 100 °C change in alloy transformation temperature [5]. The nitinol with rich nickel has more superelasticity property, and studies have shown that when nitiol with 60% of nickel, the alloy has a low shape memory effect; this can be increased by heat treatment [6, 7].

2 Manufacturing of Nitinol

This section covers different manufacturing process of nitinol, highlighting their strengths, limitations in particular manufacturing process, significance and suitability for particular application.

2.1 Casting/melting Process

Casting process is the most conventional process for manufacturing of nitinol. Casting of nitinol involves molten nitinol composition of nickel and titanium which are more reactive. So this process should be done in vacuum. The main casting process for nitinol will be vacuum induction melting (VIM), vacuum arc remelting (VAR), electron beam melting (EBM), plasma arc melting (PAM); these four methods are widely used for casting nitinol.

Vacuum Induction Melting. The induction melting process will be carried out in the vacuum condition. The process will be done with the graphite crucible placed in the steel shell. The material in the crucible will melt when electrical eddy current is introduced in the graphite crucible. An electrodynamic force will help in mixing and stirring of the melt. This process has major strengths like easy operation, handling due to easy construction of crucible, inexpensive due to graphite and chemical melt homogeneity will be good. The limitations will be high processing cost, carbon particles present in the melt due to increase in concentration of Ni, which will result in decrease in transformation temperature [6, 8, 9].

Vacuum Arc Melting. A consumable or non-consumable electrodes is continuously remelted using an arc in a vacuum environment. This process will result in high purity and therefore used to improve the structure of the vacuum arc melting ingots. This process does not need any crucible and provides higher purity compare to any other method of manufacturing. If any leak in the vacuum make result in carbon and oxygen pickup in the melt [9, 10].

Plasma Arc Melting. The process will be carried out in the argon burner by screwing the input material elements which is placed in the copper water-cooled crystallizer. This method prevents the contamination due to use of graphite crucible with vacuum induction furnaces [12]. Due to quick heat transfer, the melting process will be quick. This process results in less chemical homogeneity and results in variation in the property of shape memory alloy.

Electron Beam Melting. This process will be carried out in the vacuum with higher pressure compared to the vacuum induction melting environment pressure. This process will produce circular shape ingot in the vacuum induction furnace by electron heating. Due to elimination of the graphite crucible, the contamination will be controlled and carbon content will be 4–10 times lower than the vacuum induction melting process [8, 11].

2.2 Powder Metallurgy Process

Powder metallurgy process mainly includes conventional metallurgy process and additive manufacturing process [12]. In this conventional powder metallurgy process includes conventional sintering (CS), hot isostatic pressing (HIP), spark plasma sintering (SPS), metal injection molding (MIM). On the other hand, additive manufacturing includes selective laser melting (SLM), laser engineered net shaping (LENS) and selective laser sintering (SLS).

Conventional Sintering. Conventional sintering process which is low cost, good precision, easy operation and inexpensive compared to casting process. The material wastage will be reduced in the conventional sintering process by using required quantity of powder. The limitation are poor mechanical properties and long heating time due to sintering process. This process is unsuccessful in producing high density parts [13, 14].

Hot Isostatic Pressing. Only the required and efficient materials are used for manufacturing; this process shows good homogeneity and pore size compare to conventional sintering process. This process can be used to produce high-density quality product with good mechanical property. Due to presence of inert gas may cause porosities defect, and this process can be carried out for low production rate [14, 15, 23].

Spark Plasma Sintering. The plasma sintering is the easy operation process for manufacturing of nitinol. This process provides high density sintering of metal powder with low temperature with consume less time for process. This gives a high-quality product with proper shape memory effect and characters. This manufacturing process requires costly DC generator and limited to manufacturing of simple shapes [16, 17].

Metal Injection Molding. This process is suitable for manufacturing net shape products. This offer high geometric precision and cost effective for high volume production. Various shape and size products can be made using this metal injection molding. Density of finished product can be attained up to 98%. This process is expensive due to costly tooling. There will be high amount of impurity phases in metal injection molding [18].

Table 1 Important parameters

Manufacturing methods	Important parameter	References
Vacuum induction melting	Low purity in induction melting	[6, 8, 9]
Electron beam melting	Vacuum environment contamination eliminated	[8, 11]
Vacuum arc melting	High purity due to arc melting in vacuum, crucible not required	[9, 10]
Conventional sintering	Poor mechanical property and long heating time	[13, 14]
Hot isostatic pressing	High density and good mechanical property compare to conventional	[14, 15, 23]
Metal injection sintering	High geometric precision and cost effective for mass production	[18]
Spark plasma sintering	High-density material sintering and costly due to DC supply	[16, 17]
Selective laser sintering	Good homogeneity and poor surface finish	[19, 20]
LENS	Highly dense and good microstructure, slow process	[21]
Selective laser melting	High dense of nitinol up to 97% and energy consumption will be high	[22, 23]

2.3 Additive Manufacturing Process

Selective Laser Sintering. This laser sintering process exhibits good homogeneity and porosity. Due of usage of the laser source, the shape control will be maintained. This process is expensive due to machine cost and poor surface finish; sometimes, the traces of nickel oxides can be found [19, 20].

Laser Engineered Net Shaping. LENS process can able to produce highly pure and good chemical homogeneity product as a resultant. This product will have highly dense and good microstructure. This process has poor surface finish and slow production speed. For this process, the material should be powder [21].

Selective Laser Melting. The parts which are produced in this process will not be having distinct melt or binder from layer to layer. Different scan patterns are possible in the laser melting process. The dense nitinol part up to 97% is achievable in the selective laser melting. There will not be requirement of any postprocessing. The limitations of this process will be more expensive and consumes lot of energy for production [22, 23] (Table 1).

3 Future Scope

There are many application of shape memory alloy in the recent trend technology. In upcoming days, various shape memory materials can be fabricated and applied

in different fields for various usages. Mainly shape memory alloys are used in the medical application for surgery and transplant of bone, and this area gives various openings of researches to apply their shape memory concept in fabricating different components. Automotive industry from passenger car and to the flight, this shape memory alloy helps in efficient working of vehicle and to various advantages in vehicle dynamics are achieved. This shape memory alloy gives various opportunities in civil structure designing and aircraft designing to build an efficient system. Due to their transitional material property, this will provide a various scope to researchers.

4 Summary

This paper gives the comparison data for manufacturing and processing the nitinol in various methods. Different factors have been considered in the comparison which includes strength, limitation and suitability for particular application that provides a quick guide for process selection for nitinol. From the review, it is clear that the chosen manufacturing process or method has the potential to not only define the final product or alloy, it can affect the economic feasibility of manufacturing nitinol in various chemical and mechanical properties. The manufacturing process can be selected based on the application and property required at the end product; for example, in medical application, the nitinol should have some standards for medical devices; mainly, their chemical composition in casting process the vacuum arc melting process provides good properties for medical application [24, 25], and on the other hand, in powder process, mainly in additive manufacturing, the selective laser melting provides more advantage for particular application. This paper will give the right manufacturing process or method for researchers and industrial people interested in manufacturing of nitinol.

References

1. Kauffman GB,Mayo I (1996) The story of nitinol: the serendipitous discovery of the memory metal and its applications. Springer, New York, vol 2, pp 1–21
2. Kapoor D (2017) Nitinol for medical applications: a brief introduction to the properties and processing of nickel titanium shape memory alloys and their use in stents. Johnson Matthey Technol Rev 66–76
3. Wei ZG, Sandstrom R, Miyazaki S (1998) Review Shape-memory materials and hybrid composites for smart systems. J Mater Sci 3743–3762
4. Guo Y, Klink A, Chenhao, Snynder J (2013) Machinability and surface integrity of nitinol and shape memory alloy. CIRP-957, pp 1–4
5. Ming H (2002) Yu, Fabrication of nitinol and components. Mater Sci Forum 394–395:285–292
6. Kocich R,Szurman I, Kursa M (2013) The methods of preparation of Ti-Ni-X alloys and their forming, shape memory alloys—processing, characterization and applications, Intech Open Science and Open Mind, Chapter 2, pp 27–52
7. Hodgson D, Russell S (2000) Nitinol melting, manufacture and fabrication. Min Lnvas Ther Allied Techno 9(2):61–66

8. Otubo J, Rigo OD, Moura Neto C, Mei PR (2006) The effect of vacuum induction melting and electron beam melting techniques on the purity of NiTi shape memory alloys. Mater Sci Eng 438:679–682
9. Frenzel J, Neuking K, Eggeler G (2004) Induction melting of NiTi shape memory alloys—the influence of the commercial crucible graphite on alloy quality. Mat-wiss U Werkstofftech 35(5):352–358
10. Launey M, Robertson SW, Vien L, Senthilnathan K, Chintanalli P, Pelton AR (2014) Influence of microstructural purity on the bending fatigue behaviour of VAR-melted superelastic Nitinol. J Mechan Behav Biomed Mater 34:181–186
11. Otuboab J,Rigob OD, de Moura Netoa C, Kaufmanc MJ, Meib PR (2004) Low carbon content NiTi shape memory alloy produced by electron beam melting. Mater Res 7(2):263–267
12. Tuissi A, Rondelli G, Bassani P (2015) Plasma arc melting (PAM) and corrosion resistance of pure NiTi shape memory alloys. Shap Mem Superelasticity ASM International, Cleveland
13. Novak P, Moravec H, Salvetr P, Prusa F, Drahokoupil J, Kopecek J, Karlik M (2016) Preparation of nitinol by non-conventional powder metallurgy techniques. Mater Sci Technol 31:1886–1893
14. Elahinia MH, Hashemi M, Tabesh M, Bhaduri SB (2012) Manufacturing and processing of NiTi implants: a review. Elsevier Progr Mater Sci 57:911–946
15. Stanford MK (2012) Thermophysical properties of 60-NITINOL for mechanical component applications. NASA/TM pp 1–6
16. Shearwood C, Luo JK, Flewitt AJ, Milne WI (2006) Spark plasma sintering of TiNi nano-powders for biological application. IOP Publishing Ltd 17:5293–5298
17. Butler J, Tiernan P, Gandhi AA, McNamara K, Tofail SAM (2011) Production of nitinol wire from elemental nickel and titanium powders through spark plasma sintering and extrusion. JMEPEG 20:757–761
18. Schuller E, Krone L, Bram M, Buchkremer HP, Stover D (2005) Metal injection molding of shape memory alloys using prealloyed NiTi powders. J Mater Sci 40:4231–4238
19. Shishkovskya V, Kuznetsov MV, Morozovc YuG (2010) Porous titanium and nitinol implants synthesized by SHS/SLS: microstructural and histomorphological analyses of tissue reactions. Int J Self Propag High Temp Synth 19(2):157–167
20. Shishkovski V, Yadroitsev A, Smurov Yu (2011) Selective laser Sintering/melting of nitinol–hydroxyapatite composite for medical applications. Powder Metall Met Ceram 50:275–283
21. Vamsi Krishna B, Bose S, Bandyopadhyay A (2008) Fabrication of porous NiTi shape memory alloy structures using laser engineered net shaping. Wiley Periodicals Inc. pp 481–490
22. Shishkovsky, Yadroitsev, Smurov (2012) Direct selective laser melting of nitinol powder. Physics Procedia 39:447–454
23. Shiva S, Palani IA, Mishra SK, Paul CP, Kukreja IM (2015) Investigations on the influence of composition in the development of NiTi shape memory alloy using laser based additive manufacturing, optics and laser technology 69:44–51
24. Morgan W, Dicello G (2008) Carbon and oxygen level in Nitinol alloy and implications for medical device manufacturing and durability, shape memory alloy and super elastic technology, pp 821–828
25. Jani JM, Leary M, Subic A, Gibson MA (2014) A review of shape memory alloy research, applications and opportunities. Elsevier Mater Des 56:1078–1113

Kinematic and Dynamic Modelling and PID Control of Three Degree-of-Freedom Robotic Arm

K. Renuka, N. Bhuvanesh, and J. Reena Catherine

Abstract Robots have become very common in the manufacturing environment, allowing tasks ranging from the most repetitive to the most complex to be automated. In this paper model and control, a robotic system through the use of a 3DOF articulated robotic arm is done. In the design, manipulator kinematics and dynamics play a vibrant role. The kinematic model is obtained by relating the end effector's position and orientation. Manipulator dynamics gives the relationship between joint actuator torques and motion of links. The control of the robot requires the knowledge of the mathematical model and is obtained from basic physical laws governing robot dynamics. Both linear control schemes and nonlinear controllers can be employed for the manipulator control, and here control is done using PID controller.

Keywords Articulated robot · Links · Manipulator · Joints · Position · Orientation · Transformation matrices

1 Introduction

Robotics, an interdisciplinary branch of engineering and science, deals with its design, construction and operation, and uses computer systems for control, sensory feedback and information processing [1]. A robot consists of electronic, electrical or mechanical units and also a self-controlled device, which replaces human in wide areas. A device used to handle materials without direct contact is said to be a robotic

K. Renuka (✉) · J. Reena Catherine
Department of Electrical and Electronics Engineering, Bannari Amman Institute of Technology, Sathyamangalam, Erode 638401, Tamil Nadu, India
e-mail: renukak@bitsathy.ac.in

J. Reena Catherine
e-mail: reenacatherinej@bitsathy.ac.in

N. Bhuvanesh
Department of Mechanical Engineering, Bannari Amman Institute of Technology, Sathyamangalam, Erode 638401, Tamil Nadu, India
e-mail: bhuvaneshn@bitsathy.ac.in

G. Kumaresan et al. (eds.), *Advances in Materials Research*, Springer Proceedings in Materials 5, https://doi.org/10.1007/978-981-15-8319-3_87

manipulator. Initially, they were automated to perform a sequence of movements, such as moving from one location to another and closing a gripper, and they did not have any external sensing capabilities. Some complicated applications require not only movement but also some external sensing like vision or force sensing, due to the robot's amplified interaction with its surrounding [2]. Robot application areas include underwater and global exploration, satellite retrieval and repair, explosive device resolving and radioactive work where human intervention is adverse and unfeasible. Robot manipulators are defined by the nature of their movement and are made up of joint-connected links. Joints are usually revolute (R) or prismatic (P). A revolute joint allows relative rotation between two joints and is like a hinge. A prismatic joint allows for linear relative motion between two connections [3].

Robot manipulators can be classified by their power source, kinematic structure, intended area of application or control method. Robots are supplied with hydraulic, electrical or pneumatic control. Hydraulic robots are used to lift heavy loads. Electrically driven robots are popular since they are cheap, clean and quiet. Small, electrically driven assembly robots are either revolute or SCARA in design. The areas of application of non-assembly robots are machine loading and unloading, welding, spray painting and material handling. Robots are classified as servo and non-servo robots according to the control method. A robotic arm comprises linkages and joints that are capable of movement [4]. Robotic system components include power supply, motor actuators, controller, sensors and radio communication module for radio. Sensors gather information about the robot and its surroundings. Actuator provides the required forces to move the mechanical structure. The effective performance of a robot depends upon the proper selection of the actuator. It can be either electrical or mechanical. The basic actuators used for controlling motion are air motors, hydraulic motors, stepper motors and servo motors. Stepper motors are best suited for open-loop systems, and servo motors perform best in closed-loop applications. The controller circuit provides the actuator with the necessary input to achieve the desired position, power, speed, etc. Robots can withstand harsh conditions like extreme temperature and high levels of radiation. Space robots perform actions such as positioning of instrument to take measurements, collect samples, assemble a structure and so on.

In this paper, 3DOF articulated robot arm is modelled using kinematics and dynamic modelling and the control is done using PID controller and is organized as follows. Section 2 describes about the robot modelling and control. Section 3 presents the results and discussion of the robot. Finally, Sect. 4 presents the conclusion of this paper.

2 Modelling and Control of a Manipulator

2.1 Kinematic Modelling of the Robotic Arm

The location of objects in three dimensions is concerned in the study of robotics. The artefacts are the manipulator's links, the tools and parts it deals with and other objects in the manipulator's surroundings. Attributes describe these objects are position and orientation. It offers information necessary to determine the position of the manipulator's hand. To describe these attributes of a body in space, a coordinate system or frame is always attached rigidly to the object. With respect to some reference coordinate system, the position and orientation of this frame are described. The depiction of a point in space is altered from one frame to another frame and is referred as mapping [5]. It is to be noted that mapping alters only the depiction of the point and not the point itself. In general, consider two frames, frame {1} and frame {2}. Frame {2} is translated and rotated with respect to frame {1} as shown in Fig. 1. The distance between the two origins is D_2^1. To describe both the position and orientation of frame {2} with respect to frame {1} or with any frame with respect to another frame, homogeneous transformation matrix is found. It is denoted by T and is a 4 × 4 matrix.

$$T = \begin{bmatrix} \text{Rotation matrix}(3 \times 3) & \text{Translation vector}(3 \times 1) \\ \text{Perspective transformation matrix}(1 \times 3) & \text{scale factor}(1 \times 1) \end{bmatrix}$$

In vision systems, perspective transformation matrix is useful and is set to zero vector when no perspective views are involved. For robotics study, the scale factor used is 1 [6].

The orientation of frame {2} is determined by the rotation of one of the three principal axes of frame {1}, and let us consider the rotation of frame {2} with respect to frame {1} by angle θ about the z-axis of frame {1}; then, the fundamental

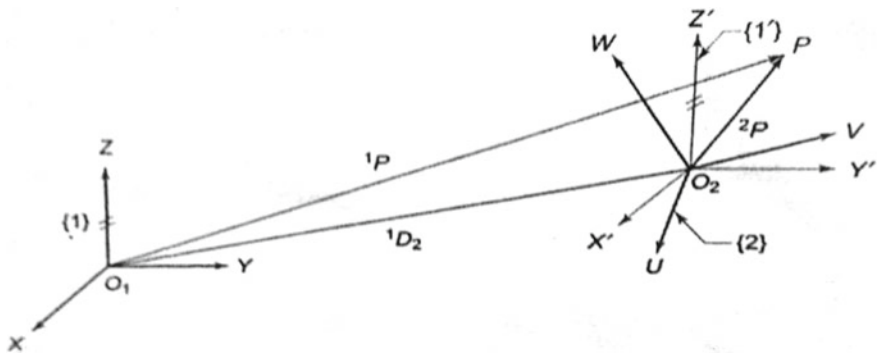

Fig. 1 Mapping between two frames—translated and rotated with respect to each other

rotation matrix is given by Eq. (1) and is denoted as $R_z(\theta)$.

$$R_z(\theta) = \begin{pmatrix} \cos\theta & -\sin\theta & 0 \\ \sin\theta & \cos\theta & 0 \\ 0 & 0 & 1 \end{pmatrix} \tag{1}$$

Similarly, rotation matrix for rotation about x-axis is given by Eq. (2) and is denoted as $R_x(\theta)$.

$$R_x(\theta) = \begin{pmatrix} 1 & 0 & 0 \\ 0 & \cos\theta & -\sin\theta \\ 0 & \sin\theta & \cos\theta \end{pmatrix} \tag{2}$$

Rotation matrix for rotation about y-axis is given by Eq. (3) and is denoted as $R_y(\theta)$.

$$R_y(\theta) = \begin{pmatrix} \cos\theta & 0 & \sin\theta \\ 0 & 1 & 0 \\ -\sin\theta & 0 & \cos\theta \end{pmatrix} \tag{3}$$

If the tool moves from one point to another, the transformation occurs along a vector with components a, b and c. This transformation is given by Eq. (4)

$$\text{Trans}\ (a, b, c) = \begin{pmatrix} 1 & 0 & 0 & a \\ 0 & 1 & 0 & b \\ 0 & 0 & 1 & c \\ 0 & 0 & 0 & 1 \end{pmatrix} \tag{4}$$

Each link in the manipulator is connected to two other links with joints at either end, except the base (first link) or the end effector (last link) which have only one joint. The definition of a manipulator with the joint link parameters for each link and a procedure for assigning right-handed orthonormal coordinate frames, one to each link in an open kinematic chain, was proposed by Denavit and Hartenberg and is known as Denavit–Hartenberg (DH) notation [5]. An n-DOF manipulator has (n + 1) frames with base frame as frame {0} and acts as the reference inertial frame and frame {n} being the tool frame. The composite transformation matrix, which describes frame {i} with respect to frame {$i - 1$}, is obtained using Eq. (5).

$$i - 1_{T_i} = \text{Rot}(z, \theta_i) * \text{Trans}(0, 0, d_i) * \text{Trans}(a_i, 0, 0) * \text{Rot}(x, \alpha_i) \tag{5}$$

$$i-1_{T_i} = \begin{pmatrix} \cos\theta_i & -\sin\theta_i \cos\alpha_i & \sin\theta_i \sin\alpha_i & a_i \cos\theta_i \\ \sin\theta_i & \cos\theta_i \cos\alpha_i & -\cos\theta_i \sin\alpha_i & a_i \sin\theta_i \\ 0 & \sin\alpha_i & \cos\alpha_i & d_i \\ 0 & 0 & 0 & 1 \end{pmatrix} \tag{6}$$

The tool frame can be translated and rotated with respect to the base frame. The transformation between these two frames is the transformation matrix (T) of the end effector and is given by

$$T = 0_{T_n} = 0_{T_1} 1_{T_2} \ldots i-1_{T_i} \tag{7}$$

Kinematic modelling is done to analyse the relationship between the end effector's position and orientation and the joint variables. The position and orientation of the end effector should be controlled in 3D space so that it follows a defined trajectory or manipulate objects in the workspace. The kinematic modelling is split into two parts:

- The problem of finding the position and orientation of the end–effector with respect to a known reference with the given set of joint link parameters for an n–DOF manipulator is mentioned as direct kinematics or forward kinematics [7].
- For a given position and orientation of the end effector with respect to the reference frame, it is necessary to find a set of joint variables that would bring the end effector in the desired position and the orientation and is stated as inverse kinematics. It determines all possible set of joint variables to achieve the specified position.

In the robot manipulator's position control, direct and inverse kinematics is of utmost importance. The inverse kinematics is difficult when compared to direct kinematics because no systematic procedures exist for its solution. Inverse model of every manipulator has to be done separately. Inverse kinematics solution is found by solving nonlinear simultaneous equations which involves transcendental functions. The numbers of simultaneous solutions sometimes are more than the number of unknowns and make some of the equations mutually dependent. The conditions for existence of inverse kinematic solutions should be examined. The workspace of the manipulator is the volume of space in which the manipulator is able to locate its end effector [5]. Reachable workspace is the region that can be reached by the origin of the end effector frame with at least one orientation. The space where the end effector touches every point from all orientations is known as dextrous workspace. If the chosen point P lies outside the reachable workspace, then no solution exists. The existence of multiple solutions is a common situation met in solving inverse kinematics problem. From those multiple solutions, the robot system should be capable to choose one probably the best solution. Two approaches are there to solve the inverse problem: closed-form solutions and numerical solutions. Newton–Raphson method is the iterative algorithm used in numerical methods, and they are computationally difficult and sluggish compared to closed-form methods [8].

2.2 Dynamic Modelling of the Robotic Arm

In kinematics, the forces required to cause the motion are not considered. Position and orientation vary with time and are termed as the dynamic behaviour of the manipulator. In dynamics, the equations of motion for a manipulator are considered which arises from the torques applied by the actuators or the external forces applied to the manipulator. Each joint has a motor for providing input torque. Torques are applied at the joints to balance out the internal and external forces such as inertial, Coriolis, frictional, load and gravitational forces. The serial link manipulator is an intricate dynamic system which can be systematically modelled using Lagrangian mechanics [5]. There are two main dynamic modelling approaches, namely Lagrange–Euler (energy-based) and Newton–Euler (force balance) that can be analytically applied to develop the manipulator equations of motion. Assuming no backlash and friction between the joints, a set of second-order nonlinear differential equations, consisting of inertial loading and coupling reaction forces, are obtained. The Lagrangian L is a scalar function which is defined as the difference between the total kinetic energy K and the total potential energy P of a mechanical system.

$$L = K - P \tag{8}$$

Using Euler–Lagrange formulation, the torque required at the joint to produce desired dynamics is found using Eq. (9).

$$\tau_i = \frac{\mathrm{d}}{\mathrm{d}t}\left(\frac{\partial L}{\partial \dot{q}_i}\right) - \frac{\partial L}{\partial \dot{q}_i} \text{ for } i = 1,2,\ldots,n \tag{9}$$

The formulation is a methodical procedure to obtain the dynamic model of an n-DOF manipulator. Relationship between the joint positions, velocities, accelerations and the torques applied to the manipulator is obtained using dynamic modelling. The following steps are carried out in deriving equations of motion using Lagrange–Euler formulation [9]. The link transformation matrices T obtained from the kinematic modelling are used. The link velocity and inertia tensors are obtained [5]. They are used in kinetic energy computation. Subsequently, potential energy is computed and Lagrangian is formed to get the dynamic model.

The link velocity is required for computing the kinetic energy of a link of an n-DOF manipulator [10]. The velocity of a point in the manipulator with respect to the base frame coordinates is obtained using Eq. (10).

$$v_i^0 = \sum_{j=1}^{i} \frac{\partial^0 T_i}{\partial q_i} \dot{q}_i \tag{10}$$

The transformation matrix T_i^0 involves complex trigonometric terms, and partial derivative with respect to $\dot{q}_i$ involves complex computation. To simplify the computation of partial derivative of the homogeneous transformation matrix T, the following steps are done. The transformation matrix $i-1_{T_i}$ for link i given by Eq. (6) for a rotary joint considered.

$$i-1_{T_i} = \begin{pmatrix} \cos\theta_i & -\sin\theta_i \cos\alpha_i & \sin\theta_i \sin\alpha_i & a_i \cos\theta_i \\ \sin\theta_i & \cos\theta_i \cos\alpha_i & -\cos\theta_i \sin\alpha_i & a_i \sin\theta_i \\ 0 & \sin\alpha_i & \cos\alpha_i & d_i \\ 0 & 0 & 0 & 1 \end{pmatrix} \tag{11}$$

The partial derivative of the transformation matrix $i-1_{T_i}$ with respect to θ_i is

$$\frac{\partial^{i-1}T_i}{\partial\theta_i} = \begin{pmatrix} -\sin\theta_i & -\cos\theta_i \cos\alpha_i & \cos\theta_i \sin\alpha_i & -a_i \sin\theta_i \\ \cos\theta_i & -\sin\theta_i \cos\alpha_i & \sin\theta_i \sin\alpha_i & a_i \cos\theta_i \\ 0 & 0 & 0 & 0 \\ 0 & 0 & 0 & 1 \end{pmatrix} \tag{12}$$

Comparing Eqs. (11) and (12), it gives a pattern. The pattern observed is

- Interchange row 1 with row 2.
- Change the sign of row 1.
- Make row 3 and row 4 zero.

The above steps are used in obtaining the partial derivative of $i-1_{T_i}$ with respect to θ_i without actually differentiating the terms. The above result can be deduced using matrix operations, which is more convenient while performing operations using a computer. Mathematically, the above result is obtained using a 4×4 matrix Q_i defined as

$$Q_i = \begin{pmatrix} 0 & -1 & 0 & 0 \\ 1 & 0 & 0 & 0 \\ 0 & 0 & 0 & 0 \\ 0 & 0 & 0 & 0 \end{pmatrix} \text{(For revolute joint)} \tag{13}$$

Premultiplying $i-1_{T_i}$ with Q_i, we get Eq. (14)

$$Q_i * i-1_{T_i} = \begin{pmatrix} -\sin\theta_i & -\cos\theta_i \cos\alpha_i & \cos\theta_i \sin\alpha_i & -a_i \sin\theta_i \\ \cos\theta_i & -\sin\theta_i \cos\alpha_i & \sin\theta_i \sin\alpha_i & a_i \cos\theta_i \\ 0 & 0 & 0 & 0 \\ 0 & 0 & 0 & 1 \end{pmatrix} \tag{14}$$

The result is same as Eq. (12). Hence,

$$\frac{\partial^{i-1} T_i}{\partial \theta_i} = Q \underset{i}{*} i - 1_{T_i} \tag{15}$$

For prismatic joint Q_i defined as

$$Q_i = \begin{pmatrix} 0 & 0 & 0 & 0 \\ 0 & 0 & 0 & 0 \\ 0 & 0 & 0 & 1 \\ 0 & 0 & 0 & 0 \end{pmatrix} \tag{16}$$

During motion of the link, inertia forces are contributed by the mass of the link. Rotational inertia is represented by a tensor [5]. It is a 4×4 symmetric matrix defined as

$$I_i = \begin{bmatrix} \int x_i^2 dm_i & \int x_i y_i dm_i & \int x_i z_i dm_i & \int x_i dm_i \\ \int x_i y_i dm_i & \int y_i^2 dm_i & \int y_i z_i dm_i & \int y_i dm_i \\ \int x_i z_i dm_i & \int y_i z_i dm_i & \int z_i^2 dm_i & \int z_i dm_i \\ \int x_i dm_i & \int y_i dm_i & \int z_i dm_i & \int dm_i \end{bmatrix} \tag{17}$$

where dm_i is the mass of the element on link located at $r_i^i = \begin{pmatrix} x_i & y_i & z_i & 1 \end{pmatrix}^{\mathrm{T}}$. Moments of inertia are diagonal elements, and inertial products are off diagonal elements. I_i is expressed as

$$I_i = \begin{bmatrix} \frac{1}{2}(-I_{xx} + I_{yy} + I_{zz}) & I_{xy} & I_{xz} & m_i \bar{x}_i \\ I_{xy} & \frac{1}{2}(I_{xx} - I_{yy} + I_{zz}) & I_{yz} & m_i \bar{y}_i \\ I_{xz} & I_{yz} & \frac{1}{2}(I_{xx} + I_{yy} - I_{zz}) & m_i \bar{z}_i \\ m_i \bar{x}_i & m_i y_i & m_i z_i & m_i \end{bmatrix} \tag{18}$$

where m_i is the mass of the link and $r_i^i = \begin{pmatrix} x_i & y_i & z_i & 1 \end{pmatrix}^{\mathrm{T}}$ is its centre of mass.

The total kinetic energy for n-DOF manipulator is given by

$$K = \frac{1}{2} \sum_{i=1}^{n} \sum_{j=1}^{i} \sum_{k=1}^{i} T_r \Big[({}^0T_{j-1} Q_j {}^{j-1}T_i) I_i ({}^0T_{k-1} Q_k {}^{k-1}T_i)^T \Big] \dot{q}_j \dot{q}_k \tag{19}$$

It is a scalar and depends on the position and speed of the joint (q,$\dot{q}$).

Sum of the potential energy of the individual links gives the total potential energy as given below

$$P = \sum_{i=1}^{n} P_i = -\sum_{i=1}^{n} m_i g {}^0T_i {}^i\bar{r}_i \tag{20}$$

where ${}^{i}\bar{r}_i$ represent the centre of mass of link i. The acceleration due to gravity $g = \begin{bmatrix} g_x & g_y & g_z & 0 \end{bmatrix}^T$ is a 4×1 gravity vector with respect to the base frame. The negative sign specifies that work is done on the system to raise the link i against gravity. Potential energy is a scalar, and it depends on joint displacement q.

The Lagrangian $L = K - P$ is given by using Eqs. (19) and (20).

$$L = \frac{1}{2}\sum_{i=1}^{n}\sum_{j=1}^{i}\sum_{k=1}^{i} Tr\left[{}^{0}T_{j-1}Q_j{}^{j-1}T_i)I_i({}^{0}T_{k-1}Q_k{}^{k-1}T_i)^T\right]\dot{q}_j\dot{q}_k + \sum_{i=1}^{n} m_i g {}^{0}T_i {}^{i}\bar{r}_i \tag{21}$$

The torque τ_i of the actuator drives link i of the manipulator at joint i is given below

$$\tau_i = \frac{d}{dt}\left(\frac{\partial L}{\partial \dot{q}_i}\right) - \frac{\partial L}{\partial \dot{q}_i} \tag{22}$$

By substituting L and differentiating, torque τ_i is obtained which is applied to link i of n-DOF manipulator.

$$\tau_i = \sum_{j=1}^{n} M_{ij}(q)\ddot{q}_j + \sum_{j=1}^{n}\sum_{k=1}^{n} h_{ijk}\dot{q}_j\dot{q}_k + G_i \text{ for } i = 1, 2, \ldots, n \tag{23}$$

where

$$M_{ij} = \sum_{p=\max(i,j)}^{n} Tr\left[d_{pj} I_p d_{pi}^T\right] \tag{24}$$

$$h_{ijk} = \sum_{p=\max(i,j,k)}^{n} Tr\left[\frac{\partial (d_{pk})}{\partial q_p} I_p d_{pi}^T\right] \tag{25}$$

$$G_i = \sum_{p=i}^{n} m_p g d_{pi}{}^{p}\bar{r}_p \tag{26}$$

and

$$d_{ij} = \begin{cases} {}^{0}T_{j-1}Q_j{}^{j-1}T_i & \text{for } j \le i \\ 0 & \text{for } j > i \end{cases} \tag{27}$$

and

$$\frac{\partial d_{ij}}{\partial q_k} = \begin{cases} {}^0T_{j-1}Q_j{}^{j-1}T_{k-1}Q_k{}^{k-1}T_i & \text{for } i \geq k \geq j \\ {}^0T_{k-1}Q_k{}^{k-1}T_{j-1}Q_j{}^{j-1}T_i & \text{for } ri \geq j \geq k \\ 0 & \text{for } i <; j \text{ or } i < k \end{cases} \tag{28}$$

The dynamic model is a set of n nonlinear and coupled second-order ODE, and Eq. (23) is the dynamic model for n-links of the n-DOF manipulator. These equations are the manipulator's dynamic equations of motion. The physical significance of various terms in Eqs. (23)–(28) is described as follows.

- Inertia is represented by the coefficients of the $\ddot{q}_j$ terms in the above equation. Acceleration of joint i causes a torque at joint i and is known as the effective inertia, denoted as M_{ii}. Acceleration of joint i causes a torque at joint j and is known as the coupling inertia, denoted as M_{ij}. Inertia loading of the actuator is represented by the coefficients of M_{ij} and is related to the acceleration of the joint.
- The coefficient h_{ijk} denotes the velocity-induced reaction torque at joint i. From Eq. 25 , a term of the form $h_{ijj}\dot{q}_j^2$ is the centrifugal force that acts at joint i due to the velocity at joint j and a term of the form $h_{ijk}\dot{q}_j\dot{q}_k$ is called Coriolis force that acts at joint i due to the velocities at joint j and k.
- q_i = joint displacement for joint i.
- $\dot{q}_i$ = velocity of joint i.
- $\ddot{q}_i$ = acceleration of joint i.
- The terms d_{ij} determine the position and orientation of frame $\{i\}$ relative to the base coordinate frame as q_j changes.

The computation of these matrices is very much intensive and is done using MATLAB code, and the actuator torques are found using the Lagrange–Euler model algorithm.

2.3 Control of the Manipulator Joints

A robot carries out the specified task by moving its end effector accurately and repeatedly. The manipulator control system accepts the joint location time history as input and causes it to track the commanded trajectory. For control, knowledge of the mathematical model is required and is obtained from basic physical laws governing robot dynamics. The robot should be able to control its movement and control the force that it exerts on the environment. The manipulator's individual joints are operated and guided by an actuator that applies a force or torque which causes the link to move. Manipulator's control system helps to achieve the specified end effector motion [11]. Each joint in the manipulator can be controlled independently using a simple control system, which produces a joint actuator force or torque proportional to the required change in the joint variable. In case of open-loop control, the actuator torque is directly computed from the dynamic model of the manipulator. In dynamic modelling, accurate computation of the parameters is difficult because it does not

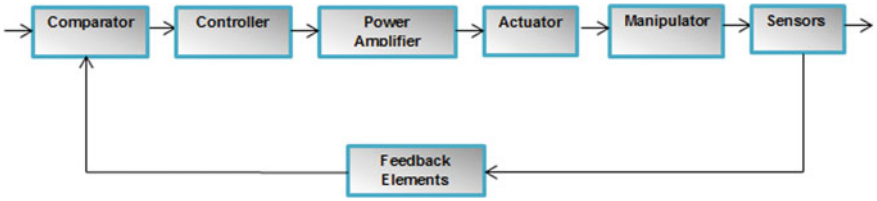

Fig. 2 General block diagram for manipulator control system

include the effects of friction, backlash and so on at the joints. These effects are highly nonlinear and difficult to model. Because of all these complications, open-loop control has limited trajectory tracking capabilities [12]. These limitations are overcome by using a closed-loop control scheme as shown in Fig. 2.

Sensors such as encoders and tachometers mounted at the joints measure the actual joint positions and velocities at every instant of time. These are useful in computing the error between the desired and actual positions and velocities. Amplifiers boost and transform small command signals so that it can actuate the joint actuator. The control schemes are classified as either linear or nonlinear depending upon the control law employed to compute the joint torques [13]. The manipulator dynamic model is highly nonlinear, hence the linear control technique is an approximation method, and for this manipulator joint should be modelled as linear second-order system. Each joint has a single input and a single output. The n-DOF manipulator is therefore modelled as a linear n-independent second-order system and is operated by n-independent SISO control systems [14]. Individual joints of the manipulator can be controlled by using linear control schemes such as PID controller. The integral term used in this controller eliminates the steady-state error. The block diagram of PID control scheme is shown in Fig. 3.

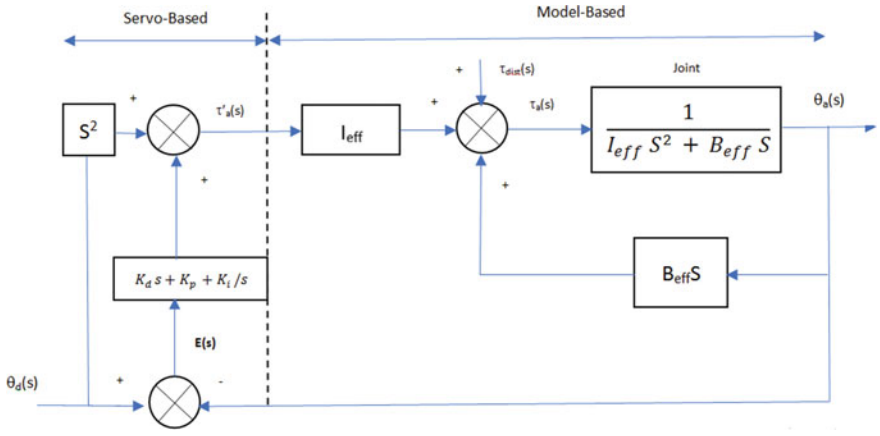

Fig. 3 PID control scheme

The model-based portion of the PID controller is

$$t_a(s) = I_{\text{eff}} t_a'(s) + B_{\text{eff}} s q_a(s) \tag{29}$$

The servo portion includes position, derivative and integral components of the servo error. The PID servo law is given by

$$\tau'_a(s) = s^2{}_d(s) + K_d s_a(s) + K_{pa}(s) + \frac{K_{ia}(s)}{s} \tag{30}$$

The error dynamics for the controller is given by

$$s^2 E(s) + K_d s E(s) + K_p E(s) + \frac{K_l}{s} E(s) = 0 \tag{31}$$

A step function of constant magnitude, $\tau_{\text{dist}}(s) = K/s$, is given as the disturbance, and the error dynamics is

$$s^2 E(s) + K_d s E(s) + K_p E(s) + \frac{K_l}{s} E(s) = \frac{K}{s} \tag{32}$$

or.

$$E(s) = \frac{K}{s^3 + K_d s^2 + K_p s + K_i} \tag{33}$$

The steady-state error for the PID controller in the presence of a disturbance is

$$e_{\text{ss}} = \lim_{s \to 0} s E(s) = \lim_{s \to 0} \frac{sK}{s^3 + K_d s^2 + K_p s + K_i} \tag{34}$$

Simplifying, it gives $e_{ss} = 0$. Even in the presence of disturbance, the PID controller causes the manipulator to reach the desired position.

PID controller is a very simple and easy technique to control the robot's joints. Linear control schemes can be used in controlling the manipulator joint, and nonlinear control techniques are much useful in controlling the manipulator. The nonlinear schemes employ nonlinear feedback to linearize the manipulator dynamics [15]. Methods such as computed torque control, force control, impedance control, robust and adaptive control are more complex control approaches for the manipulator control.

3 Results and Discussion

3.1 Forward Kinematics Using RoboAnalyzer

RoboAnalyzer is a 3D model-based software to learn DH parameters, kinematics and dynamics of robots, allows 3D animation and plots graph as output. To obtain the transformation matrices of the robot, its modified DH parameters are first entered as shown in Table 1.

The modified DH parameters shown in Table 1 are entered in the DH parameter column of the RoboAnalyzer software as shown in Fig. 4. After entering the DH parameters, the robot 3D model appears as shown in Fig. 4

By selecting the Link Config tab, the transformation matrix between the frames can be found for joint angles that are given in the initial value column of the DH parameter table. The end effector matrix is obtained by selecting the EE Config tab as shown in Fig. 5.

Table 1 Modified DH parameters of the robotic manipulator

Joints	Joint angle (θ)	Link twist (α)	Link length (a) in mm	Link offset (d) in mm
1	θ_1	0	0	0
2	θ_2	90	L1	D1
3	θ_3	90	D2	L2

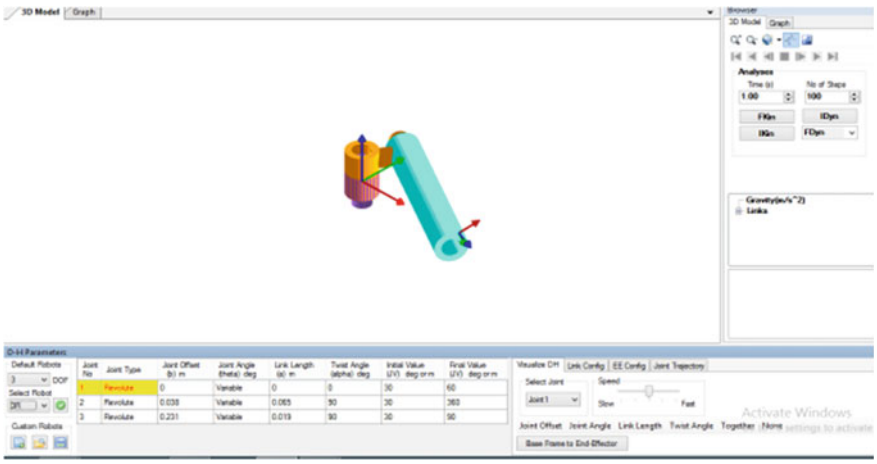

Fig. 4 Robot model and its kinematics using RoboAnalyzer

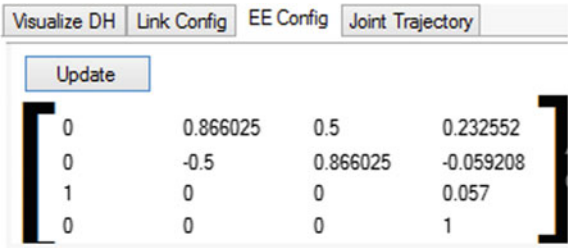

Fig. 5 End effector matrix of the manipulator

3.2 Dynamics of Manipulators Using MATLAB

The equations of motion of a 2DOF RR non-planar manipulator are determined according to the Lagrange–Euler dynamic algorithm for the DH parameter values mentioned in Table 1, it is done using MATLAB, and the corresponding joint torques are found to be as given below.

$$t_1 = 0.0037,\ t_2 = 0.0036$$

The complete dynamic model is obtained using Eqs. (8)–(28) as discussed in Sect. 3.

3.3 Control of Manipulator Joint Using PID Controller

By using PID controller, the joints of the robot arm can be controlled independently. The Simulink model as discussed in Section IV is used. Here, the input given is step input. The reference position of the joint of the manipulator is set as 0.3. The desired response of joint with the help of PID controller is shown in Fig. 6. And its performance is appreciable. The appropriate controller gain values are found by auto-tuning of the controller. The manipulator joint transfer function is found for which the controller is designed.

$$\frac{\tau_a(s)}{\theta_a(s)} = \frac{100}{s(s+4)}$$

Thus, the control of the manipulator joint is done using PID controller which is very simple and easy to implement in controlling the joints of the manipulator.

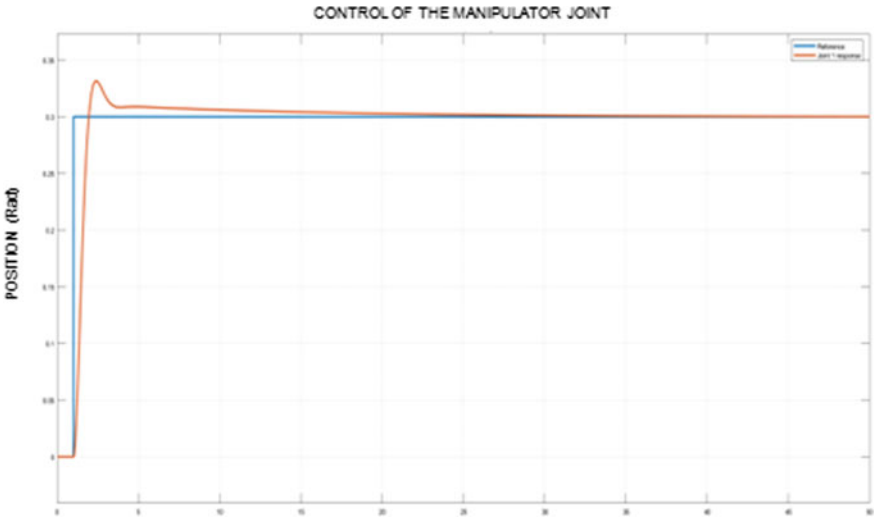

Fig. 6 Response of the joint with PID

4 Conclusion and Future Work

Robots are broadly used in places where there is a necessity for enhanced use of tools and for data collection in human inaccessible areas. This project is about both kinematic and dynamic modelling of 3DOF manipulator, and it is done using MATLAB and RoboAnalyzer software. The kinematics modelling that helps in finding the position and orientation of the manipulator's end effector with respect to the base frame is done. Dynamics helps in finding the input torque for actuating the joints. PID controller is used to control the manipulator joints independently. The control of the manipulator joints is done using Simulink in MATLAB. The work is mainly focussed on the modelling of robot arm, and control is done only for the manipulator joints. When the number of joints of the robot arm increases, the complexity also increases and PID controller will not be efficient and in that case nonlinear control techniques are used in controlling the robot arm. In future, this work can be extended by implementing nonlinear control schemes for the robot manipulator control. Nonlinear control system techniques provide more accurate results because it uses the exact dynamic model of the manipulator. It delivers greater trajectory tracking performance than the linear controllers. Some of the nonlinear control techniques such as computed torque control, force control and feedback linearization method provide result superior to PID control.

References

1. Craig JJ (2005) Introduction to robotics: mechanics and control. Pearson Education, London
2. Okubanjo A, Oluwadamilola O, Martins O, Olaluwoye O (2017) Modeling of 2-DOF robot arm and control. Futo J Ser 3(2):80–92
3. Shrivastava S, Gupta E (2017) Forward kinematics of articulated robotic arm. Int J Res Sci Innov 4(8):78–82
4. Spong MW, Vidhyasagar M (2004) Robot dynamics and control. Wiley, Hoboken
5. Mittal RK, Nagrath IJ (2003) Robotics and control. Tata McGraw Hill, New York
6. Hossein Sadegh L, Zarabadipour H (2014) Modeling, simulation and position control of 3DOF articulated manipulator. Indonesian J Electr Eng Inf 2(3):132–140
7. Mustafa AM, Al-Saif A (2014) Modelling, simulation and control of 2-R robot. Glob J Res Eng Rob Nano-Tech 14(1):49–54.
8. Salem FA (2014) Modelling, simulation and control issues for a robot ARM. Int J Intel Syst Appl 6(4):26–39
9. Siciliano B, Sciavicco L, Villani L, Oriolo G (2009) Robotics: modelling, planning and control. Springer, Berlin
10. Al-Qahtani HM, Mohammed AA, Sunar M (2017) Dynamics and control of a robotic arm having four links. Arab J Sci Eng 42(5):1841–1852
11. Agrawal R, Kabiraj K, Singh R (2012) Modeling a controller for an articulated robotic arm. Intel Control Automat 5(3):207–210
12. Salih TA, Yehea OI (2011) A novel control system for robotics devices. J Theor Appl Format Technol 28(1):48–53
13. Rogers JR (2009) Low-cost teleoperable robotic arm. Mechatronics 19(5):774–779
14. de Silva CW (1995) Applications of fuzzy logic in the control of robotic manipulators. Fuzzy Sets Syst 70(2–3):223–234
15. Walker MW (1988) Manipulator kinematics and the epsilon algebra. IEEE J Robot Autom 4(2):186–192

Investigation on Normal Hard Turning of AISI 4340 Steel

N. Jayakumar, G. Senthilkumar, M. Vignesh, and V. Gokul

Abstract The turning of hardened steel is the current problem with required minimum machining force and surface roughness. In this investigation on normal defect hard turning AISI 4340 steel has been used, because of it is medium carbon (0.4% C) high strength martensitic steel. This material is more important in the critical applications like aerospace and automotive transmissions. To machine a ferrous alloy which is over 45 HRC, the hard turning process has been used to remove the material which has single-point cutting tool at high speeds. For processing hard steel, it involves a traditional approach, and those operations were consumed significant amount of cost and time. When it is compared with hard turning (HT), it reduces the annealing and grinding requirements. Still researchers are finding the best combination of inserts in HT where tool life plays significant role due to its cost and obtaining better surface finish. To discover the best ideal parameters for normal hard turning process by considering the cutting speed, feed rate, and depth of cut as input parameters using L9 orthogonal array in Taguchi method and Grey relational analysis for ANOVA. Normal HT was performed on hardened AISI 4340 steel and obtained the results. The optimal setting for this normal HT with consideration of machining force & surface roughness to the level of factors applying Grey relation grade is speed—900 rpm, feed—0.05 mm/rev, and depth of cut—0.5 mm.

Keywords Normal hard turning (HT) · Cutting speed · Feed rate · Depth of cut · Tool wear · Surface roughness

1 Introduction

The method of removing materials to obtain definite shape is known as machining. The engineering components like gears, bearings, clutches, shafts, nuts, screws, etc., are always should have form and dimensional accuracy with good surface finish.

N. Jayakumar (✉) · G. Senthilkumar · M. Vignesh · V. Gokul
Department of Mechanical Engineering, Bannari Amman Institute of Technology, Sathyamangalam, Erode 638401, Tamil Nadu, India
e-mail: jayakumar@bitsathy.ac.in

G. Kumaresan et al. (eds.), *Advances in Materials Research*, Springer Proceedings in Materials 5, https://doi.org/10.1007/978-981-15-8319-3_88

Processes like casting, forging, etc., generally cannot provide the desired accuracy. For those parts which need to be finished with accuracy, semi-finishing and finishing process are carried out by machining. The basic finishing process is grinding.

HT is a significant procedure since all producers are persistently looking for approaches to make their parts with lower cost, more excellent, fast arrangements, lower investment, and littler tooling stock while dispensing with non-esteem included activities. HT is a reasonable procedure that has genuine and quantifiable financial and quality advantages.

HT process was studied for selecting the tool material, cutting parameters, and cutting edge geometry affecting the efficiency in the way of tool forces, white layer and surface integrities. Most of the research work in hard turning process has been used without cooling. No other works addressing the radial force dominance [1].

In this paper it uncovers that impact in workpiece hardness, cutting parameters, coating method with different aspects of machinability like tool life, surface roughness, and cutting force additionally chip morphology while turning the hardened AISI 4340 steel at various degree of hardness. Finally, it was found that the CVD tool gives the best performance for the cutting speed 300 and 180 m/min for different hardness of the workpiece 35 and 45 HRC. But PVD-coated tool gives the upper limit as 200 m/min [2].

The paper work reveals the optimization of cutting parameters in HT of AISI 4340 steel. The selected parameters are cutting speed, feed, and depth of cut on surface roughness. The optimal parameters have been selected as cutting speed (180 m/min), feed (0.125 mm/rev), and depth of cut (0.8 mm) using Taguchi analysis with signal-to-noise ratio. The feed has most significant and doc is minimum significant [3].

During machining the hard steels, the machining force should be minimum to attain the better surface roughness. To perform better machining, the cutting speed, feed, and depth of cut should be chosen optimal value. While calculating the machining force, it includes the cutting force, thrust force, and feed force. Each and every input parameters plays a significant role in the tool wear and tool life.

2 Experimental Details

2.1 Work Material Specification

AISI 4340 steel shaft of diameter 44 mm and length 380 mm is considered for experimentation as shown in Fig. 1. Centre drill is made on the sides of the rod. AISI 4340 steel chemical composition is Fe 95.73%, C 0.399%, Si 0.302, Mn 0.639%, P 0.012%, S 0.011%, Cr 1.034%, Mo 0.254%, Ni 1.524%, Al 0.020%, Cu 0.058% Ti 0.014%, V 0.005%, W 0.001%, Pb 0.001.

Fig. 1 Work piece

Table 1 Specification of the lathe

Model	Turnmaster-35
Spindle motor	3HP/22 Kw
Feed motor	1HP/DC
Distance between centres	800 mm
Height of centre	175 mm
Maximum speed	1500 rpm

2.2 Machine and Equipment's Used

See Table 1 and Fig. 2 for specification of the lathe & experimental setup.

2.3 Kistler Multicomponent Tool Dynamometer

See Figs. 3 and 4 piezoelectric tool dynamometer and turning insert

2.4 Cutting Tool

- Material selected-cubic boron nitride (CBN KBN10M)
- Designation-CNGA120408S01225ME
- Make-Kyocera
- Megacoat CBN tool is used as insert for machining for hardened AISI 4340 steel. It has TiC coat which acts as flank wear resistance.

Advantages

- Smaller-scale grain CBN tool with imaginative structure scattering.
- Hard-bonded phase (TiC) + MEGACOAT
- Because of its high wear resistant, heat resistant, and pit wear counteractive action execution, it is reasonable for high speed cutting of hardened material.

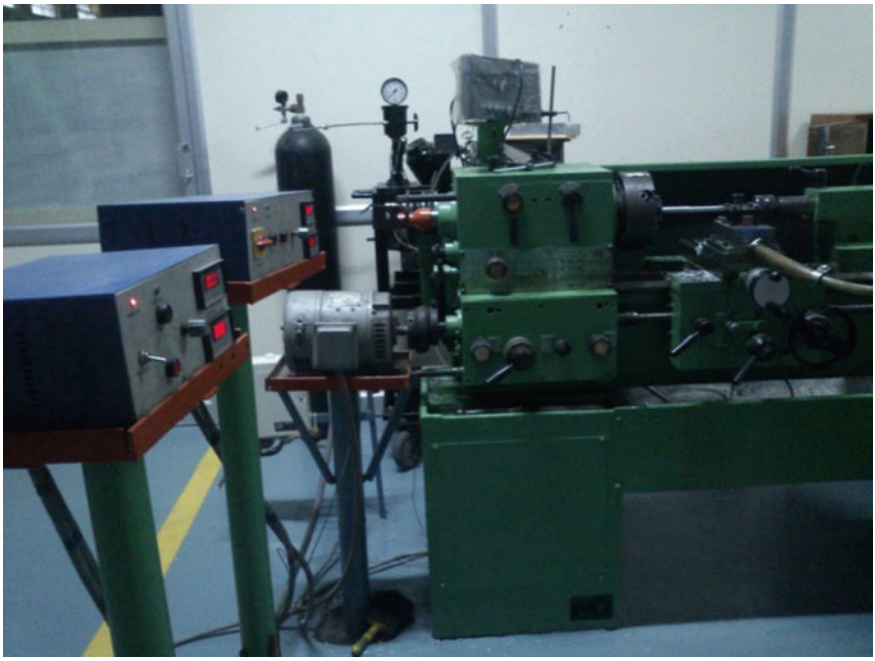

Fig. 2 Experimental setup (centre lathe)

3 Work Piece Preparation

3.1 Hardening

To improve the hardness, the work pieces are heat treated. It is medium carbon steel which is heated above its upper critical temperature at 870 °C and soaked for half an hour. Then, it is quenched in quenching oil. The hardness of material is increased to 48 HRC (Table 2 and Fig. 5) after workpiece hardening.

4 Process Variables and Their Limits

The working ranges of the parameters were selected for design of experiment is based on Taguchi's L9 Orthogonal Array (OA) design. The process variables of this experimental study are cutting speed, depth of cut and feed rate have been selected.

The process variables with their notations and units are listed in (Tables 3 for Orthogonal Array and Table 4 Input Combinations).

Fig. 3 Piezoelectric tool dynamometer

Fig. 4 Turning insert

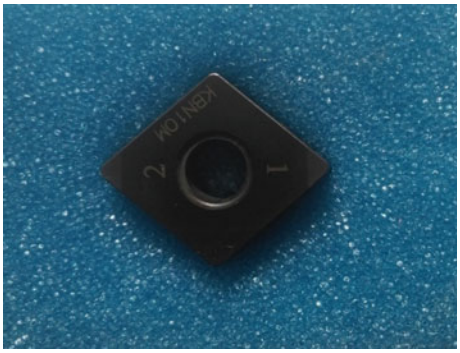

Table 2 Process variables and limits

Levels	Cutting speed (rpm)	Feed (mm/min)	Depth of cut (mm)
Level 1	500	0.05	0.5
Level 2	700	0.07	0.6
Level 3	900	0.09	0.7

Fig. 5 Work piece after hardening

Table 3 Taguchi's L9 Orthogonal Array (OA)

S. No.	A	B	C
1	1	1	1
2	1	2	2
3	1	3	3
4	2	1	2
5	2	2	3
6	2	3	1
7	3	1	3
8	3	2	1
9	3	3	2

Table 4 Input combinations

S.No	Speed (rpm)	Feed (mm/min)	Depth of cut (mm)
1	500	0.05	0.5
2	500	0.07	0.6
3	500	0.09	0.7
4	700	0.05	0.6
5	700	0.07	0.7
6	700	0.09	0.5
7	900	0.05	0.7
8	900	0.07	0.5
9	900	0.09	0.6

4.1 Design of Experiment

To lessen the quantity of analyses, in light of Taguchi strategy and L9 symmetrical cluster were used and the structure of analysis was directed. Investigations have been finished using Taguchi's L9 Orthogonal Array (OA) exploratory plan in these nine (9) mixes of cutting speed (rpm), feed (mm), and depth of cut (mm). It thinks about

three process parameters (without connection) to be changed in three discrete levels. A-Cutting speed (rpm), B-Feed (mm/min), and C-Depth of cut (mm).

Grey Relational Analysis

For machining force and surface roughness, smaller is better (SB),

$$x_i(k) = \frac{\min x_i^o(k) - x_i^o(k)}{\max x_i^o(k) - \min x_i^o(k)}$$

where $x_i(k)$ is the generating value of Grey relational analysis, $minx_i^o(k)$ is the minimum value of $x_i^o(k)$ $\max x_i^o(k)$ is the maximum value of $x_i^o(k)$.

The Grey relational coefficients are calculated by following equation

$$\xi_i(k) = \frac{\Delta_{\min} + \zeta \Delta_{\max}}{\Delta_{oi}(k) + \zeta \Delta_{\max}}$$

where ζ is the distinctive coefficient, $\zeta \in [0,1]$

0.5 is the most suitable value.

Grey relational grades are obtained by following formula

$$\gamma_i = \frac{1}{n} \sum_{k=i}^{n} \xi_i(k)$$

where$\xi_i(k)$ is the Grey relational coefficients.

4.2 Turning Operation

The hard turning is carried out for following input parameter using above experimental setups. Work piece is machined for this experiment without using coolant. There were no built up edges during machining. Tool holder was placed above the Kistler dynamometer to measure the machining force. Turning carried out for combinations as shown in (Table 4) for available length and is sufficient to measure machining force and surface roughness (Fig. 6 for turning operation).

Some of the following assumptions were made during turning operation.

1. Throughout the length of the workpiece, the hardness is same.
2. Vibration is negligible.

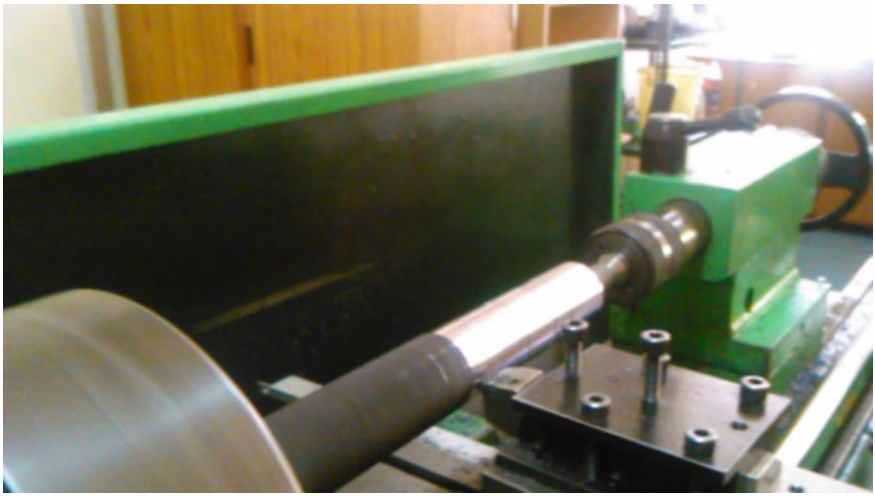

Fig. 6 Turning operation

5 Results and Discussion

5.1 Normal Hard Turning and Machining Force

Machining force: $\text{Fm} = \sqrt{Fc^2 + Ft^2 + Fr^2}$

Where *Fc*: Cutting force, *Ft*: Thrust or radial force and *Fr*: Feed force (Table 5).

Table 5 Force measured from dynamometer and machining force for normal hard turning

Speed (rpm)	Feed (mm/min)	Depth of cut (mm)	Feed force Fr (N)	Thrust force Ft (N)	Cutting force Fc (N)	Machining force (N)	SNRA
500	0.05	0.5	96.21	130.1	101.6	191.0626444	−45.6235
500	0.07	0.6	204.3	198.3	227.2	364.2543342	−51.2281
500	0.09	0.7	277	251.4	299.5	479.1985079	−53.6103
700	0.05	0.6	132	147.2	133.4	238.5107964	−47.5502
700	0.07	0.7	187.5	224.8	198.1	353.4613133	−50.9668
700	0.09	0.5	121.9	185.9	152.7	269.6955877	−48.6175
900	0.05	0.7	141.8	147.1	157.6	258.0376135	−48.2337
900	0.07	0.5	103.3	151.9	120	219.4185498	−46.8255
900	0.09	0.6	180	216.4	175.3	331.6007388	−50.4123

Table 6 Signal-to-noise ratios (smaller the better) response table

Level	Cutting speed (rpm)	Feed rate (mm/rev)	Doc (mm)
1	−50.15	−47.14	−47.02
2	−49.04	−49.67	−49.73
3	−48.49	−50.88	−50.94
Delta	1.66	3.74	3.91
Rank	3	2	1

5.1.1 Machining Force

Then regression is dependence of a variable on one or more other variables. The multiple linear regression equation is the number of independent variable on the right side of the linear equation more the one. Regression equation strength for the experiment is 93.5%.

The regression equation is

$$\text{Machining Force} = -208 - 0.188\ \text{Speed} + 3274\ \text{Feed} + 684\ \text{Depth of cut}$$

Characteristic of machining force is smaller the better.

$$\text{S/N} = -10\ \log 10\ \text{sum}\ (Y2/n).$$

Signal-to-Noise Ratio and Data Mean

The factors are classified into control factors and noise factors. The DOE for obtaining graph for signal-to-noise ratio and data mean for the obtained results. In the response table for the signal-to-noise ratio and data mean, the ranking of respective input parameters are obtained as follows (Table 6).

The most influencing parameter to get better machining force is depth of cut, succeed by feed rate, and cutting speed.

Graph from Figs. 7 and 8 shows that machining force will decrease with increase in speed and decrease in feed and depth of cut. From analysis and experiment, smaller machining force is obtained at cutting speed (500 rpm), feed rate (0.05 mm/rev), and depth of cut (0.5 mm).

5.1.2 Surface Roughness

Then regression is dependence of a variable on one or more other variables. The regression equation strength for the experiment is 96.5% (Table 7).

The regression equation is:

$$\text{Ra} = 0.597 - 0.000329\ \text{Speed} + 5.00\ \text{Feed} + 0.242\ \text{Depth of cut}$$

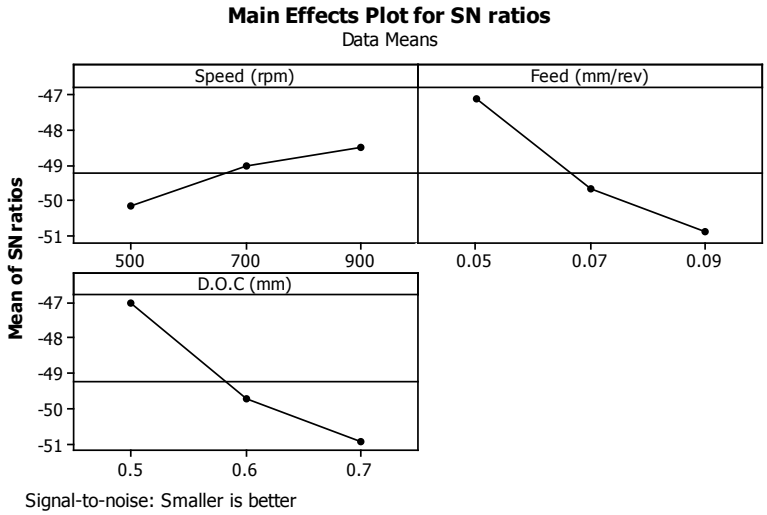

Fig. 7 SN ratio plot for machining force

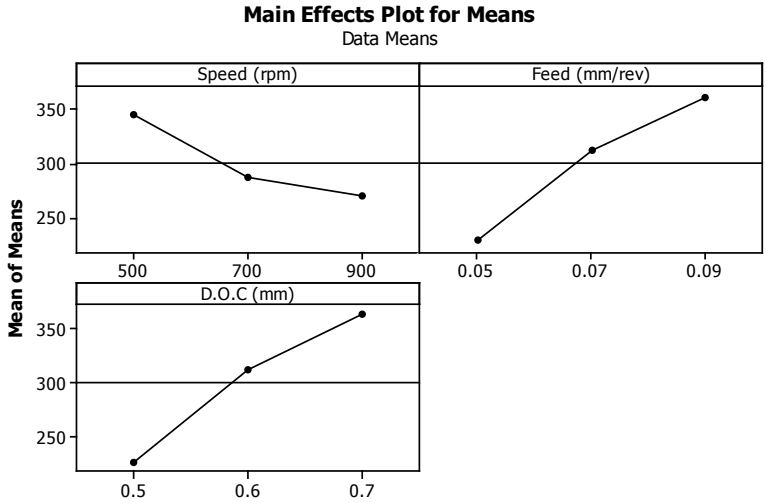

Fig. 8 Means plot for machining force

The characteristic for surface roughness is smaller the better.

$$\text{S/N} = -10\,\log 10\ \text{sum}\ (Y2/n)$$

Signal-to-noise ratio and Data mean.

Table 7 Surface roughness for normal hard turning

Exp. No.	Speed (rpm)	Feed (mm/rev)	Depth of cut (mm)	Surface roughness (μ)	SNRA
1	500	0.05	0.5	0.8	1.93820
2	500	0.07	0.6	0.925	0.67717
3	500	0.09	0.7	1.075	−0.62817
4	700	0.05	0.6	0.755	2.44106
5	700	0.07	0.7	0.865	1.25968
6	700	0.09	0.5	0.93	0.63034
7	900	0.05	0.7	0.73	2.73354
8	900	0.07	0.5	0.795	1.99266
9	900	0.09	0.6	0.88	1.11035

Table 8 Signal-to-noise ratios (smaller the better) response table

Level	Cutting speed (rpm)	Feed (mm/rev)	Doc (mm)
1	0.6624	2.3709	1.5204
2	1.4437	1.3098	1.4095
3	1.9455	0.3708	1.1217
Delta	1.2947	2.0001	0.3987
Rank	2	1	3

Factors are classified into noise factors and control factors. For the obtained results, the DOE of graph of signal-to-noise ratio and data mean has obtained. The response table of the signal-to-noise ratio and data mean, and the ranking of all input parameters are obtained as follows.

Table 8 shows the signal-to-noise ratio response table for surface roughness. From the examination, compared to the cutting speed and depth of cut, the feed is greater influencing parameter. Graph from Figs. 9 and 10 shows that surface roughness will be better with decrease in feed and depth of cut and increase in speed. From this experiment, cutting speed (900 rpm), feed (0.05 mm/rev), depth of cut (0.5 mm), and the lower surface roughness have acquired.

5.1.3 Grey Relation Analysis

Since there are two output parameters used in this experiment, Grey relation analysis strategy is utilized to locate the best ideal qualities. Grey relation grade is tabulated in Table 9.

The optimal setting of the level of factors can be inferred based on higher is better characteristics. From Table 10 the higher average of Grey relation grade is selected. The optimal settings of the level of factors are speed—900 rpm, feed—0.05 mm/rev, and depth of cut—0.5 mm.

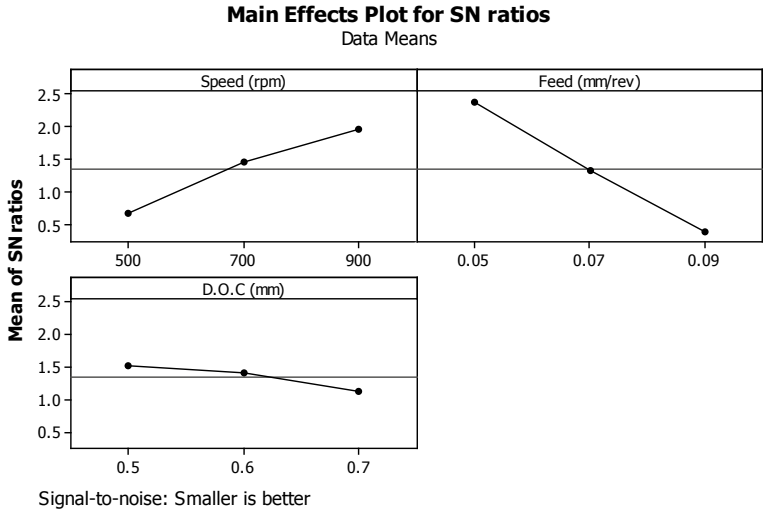

Fig. 9 SN plot for surface roughness

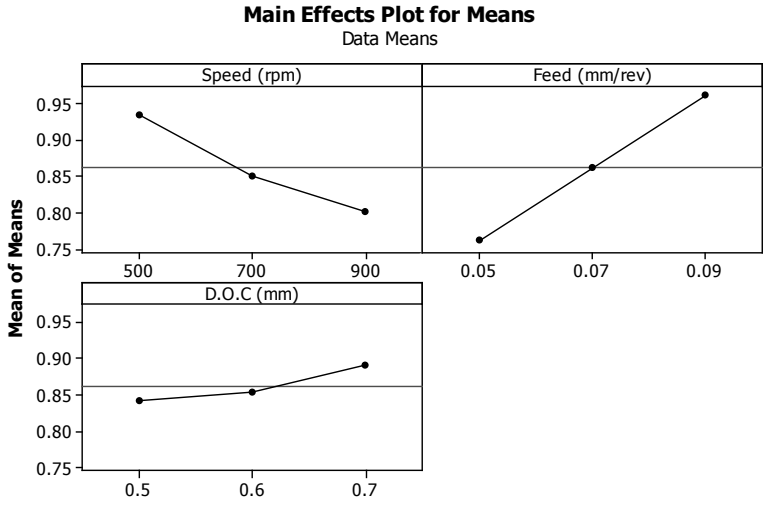

Fig. 10 Means plot for surface roughness

5.1.4 ANOVA Results for Grey Relation Grade

The ANOVA results in Table 11 show identification in machining force with percentage of contribution by various factors. The feed is most overwhelming variable then just profundity of cut and speed. The percentage contribution of feed, depth of cut, and speed towards machining force is 70.34, 15.33, and 13.25%, respectively.

Table 9 Grey relation grade

Speed (rpm)	Feed (mm/rev)	Depth of cut (mm)	Machining force (N)	Surface roughness (μ)	Grey relation grade
500	0.05	0.5	191.06	0.8	0.85567
500	0.07	0.6	364.25	0.925	0.461743
500	0.09	0.7	479.19	1.075	0.333333
700	0.05	0.6	238.51	0.755	0.812828
700	0.07	0.7	353.46	0.865	0.515531
700	0.09	0.5	269.69	0.93	0.555002
900	0.05	0.7	258.03	0.73	0.84133
900	0.07	0.5	219.42	0.795	0.780919
900	0.09	0.6	331.6	0.88	0.520538

Table 10 Average Grey relation grade

Average Grey relation grades			
Level 1	0.550249	0.836609	0.73053
Level 2	0.627787	0.586064	0.59837
Level 3	0.714262	0.469624	0.563398

Table 11 ANOVA for GRG

Factors	D.O.F	S.S	M.S	Ftest	Ptest	Pr%
Speed (rpm)	2	0.040391	0.020195	50.88245	0.019274	13.25123
Feed (mm/rev)	2	0.211009	0.105504	265.8205	0.003748	70.34936
Depth of cut (mm)	2	0.046623	0.023311	58.73335	0.016741	15.33682
Error	2	0.000794	0.000397			
TOTAL	8	0.298816				98.9374

6 Conclusions

From the investigation on Normal HT of AISI 4340 steel, some conclusions are as follows: During the consideration of machining force, it is noted that the most influencing parameters in this normal HT is depth of cut, and later, the feed rate and cutting speed. Minimum machining force is achieved at the cutting speed of 500 rpm, feed rate is 0.05 mm/rev, and depth of cut is 0.5 mm. Feed rate is most dominating parameter and later cutting speed and depth of cut, while the surface roughness considered. Minimum surface roughness is achieved at cutting speed is 900 rpm, feed rate is 0.05 mm/rev, and depth of cut is 0.5 mm. The optimal setting for this normal hard turning with consideration of machining force & surface roughness to the

level of factors applying Grey relation grade is speed—900 rpm, feed—0.05 mm/rev, and depth of cut—0.5 mm.

References

1. Bartarya G, Choudhury SK (2012) State of the art in hard turning. Int J Mach Tools Manuf 53(1):1–14
2. Chinchanikar S, Choudhury SK (2013) Investigations on machinability aspects of hardened AISI 4340 steel at different levels of hardness using coated carbide tools. Int J Refract Met Hard Mater 38:124–133
3. Paul BKM, Raju T (2014) Optimization of cutting parameters in hard turning of AISI 4340 steel. Int J Innov Res Adv Eng 1(8):93–98

Estimation of Thermo Oxidation on Chromel–Alumel Thermocouple

P. Narendra Ilaya Pallavan, S. Srinivasan, and V. Arumugam

Abstract Temperature is one of the most measured parameters within industry. Thermocouple is an extremely versatile device widely used in industry for critical high temperature, achieving extremely high accuracy with a thermocouple can be more difficult because of their inhomogeneity. Temperature drift in thermocouple is a common problem that affects the accuracy of a measurement system. Due to prolonged usage of thermocouple under different conditions causes changes in the properties of the thermocouple and in turn degrade the thermocouple which is followed by drift. Hence it is important to analyze the rate of degradation of the thermocouple material. In this work, material analysis using scanning electron microscopy by an energy dispersive X-ray (SEM-EDAX) has been performed on the thermocouple, due to change in temperature gradient at different insertion positions.

Keywords Thermoocuple · Chromel Alumel · Temperature gradient

1 Introduction

Thermocouple is a widely used device in industry for the measurements of high temperature. It is a cable of two wires made from two dissimilar alloys that are fused together at one end. Thermocouple produces a small potential created by the junction of two dissimilar alloys. The reality is that it is the temperature difference between one end of a conductor and the other end that produces the small electro

P. Narendra Ilaya Pallavan (✉)
Department of Electronics and Instrumentation Engineering, Bannari Amman Institute of Technology, Tamil Nadu, Sathyamangalam, Erode 638401, Tamil Nadu, India
e-mail: narendrapallavan@gmail.com

S. Srinivasan
Department of Instrumentation Engineering, Madras Institute of Technology, Chennai 600044, Tamil Nadu, India

V. Arumugam
Department of Aeronatical Engineering, Madras Institute of Technology, Chennai 600044, Tamil Nadu, India

G. Kumaresan et al. (eds.), *Advances in Materials Research*, Springer Proceedings in Materials 5, https://doi.org/10.1007/978-981-15-8319-3_89

motive force (EMF), or charge imbalance. When a thermocouple is used to measure the temperature of a process, it is expected that the acquired potential does not vary if the temperature of the atmosphere is constant. In certainty, the voltage can change with period, even though the temperature of the atmosphere is constant, this phenomenon is called Drift and is a source of error in thermocouple measurement [1].

The objective of the work is to measure the thermocouple drifts by subjecting the thermocouple at:

Analyze the effect due to change in temperature gradient at different insertion position [2].

The initial deviation of the conversion characteristics due to the in-homogeneity of the thermocouple [3].

Su Jun et al. [4] have experimentally determined the error of the thermocouple with controlled profile of temperature field and also compared with the theoretical estimations. Su Jun and Kochan [5] have adopted neural network methods for error correction which occurs due to inhomogeneity of thermocouple electrodes during prolonged use. It is shown that the error does not exceed ±0.46 °C at 5% significance level. Amagai and Nakamura [6] have determined the exponentially reducing thermal drift of a single junction thermal converter from the increase in temperature on the cold side of thermocouple which is obtained using thermal model. Ahmed et al. [7] has conducted analytical, experimental, and numerical analyses to inspect the effect of K-type thermocouple wire electrical protection on temperature measurement. It has been inferred that the effect of electrical protection on large diameter thermocouple must be accounted where as it can be neglected for small diameter thermocouple. Rokosz et al. [8] have examined the external layer formed on pure titanium after plasma electrolytic oxidation using SEM, EDAX, and X-ray photoelectron spectroscopy (XPS).

2 Material

Bare K-type thermocouple (Chromel–Alumel) of length 28 cm and diameter of 16 SWG, i.e., diameter is 0.16256 cm (0.064 inch) is considered for the case study. Fluke temperature furnace (Model No. 9150) is used as the reference source, which has a temperature range of 150–1200 °C, display resolution of 0.1 °C to 999.9 °C, stability ±0.5 °C, and display accuracy ±5.0 °C. The depth and diameter of the well is are inch and 1.25 inch, respectively. Hitachi SEM/EDAX (Model No. S3400N) scanning electron microscope is used for obtaining the elemental characterization that has a magnification capability of 5× to 300,000× and a resolution of up to 10.0 nm (10KV HV mode).

3 Procedure

3.1 Measurement Based on Temperature Gradient

The existent thermocouples are not homogeneous to same prolong period, *i.e.,* inhomogeneous. In this situation, the thermocouple is partitioned into small areas of equal size and the thermocouple is considered as homogeneous in each area. The temperature gradient at each area was measured in the experiment with the help of thermistors (Fig. 1).

A Negative Temperature Coefficient (NTC) thermistor is used in each area to measure the temperature. Here, the bottom most part which is emerged inside the RTC is consider as area 5 and the part where the cold junction exhibits is taken as area 1. The thermistors which are used here produce resistance change corresponding to the changes in the temperature.

K-type thermocouples were exposed to thermocyclic oxidation tests at 1000 °C in silicon carbide tube heater for 70 cycles. The experimental procedure includes a heating cycle of 1 h and an air cooling period of 20 min. Initially, the furnace was calibrated using the reference thermocouple and by multi-product calibrator (Model No.5502A). The steps involved in the tests are as follows:

(1) Physical dimensions of the K-type thermocouple samples are measured with the help of Venire caliper to check the validity of the dimensions.
(2) The samples are then introduced into hot zone of the heater well, which is set at 1000 ˚C temperature.
(3) After a holding time of 1 h in the furnace, the samples are taken out and ventilated at ambient temperature for 20 min.
(4) Visual observations are made after the end of each cycle regarding color, luster, or any other physical aspects of the oxide scales being formed.
(5) The samples hence collected after subjecting to oxidation are analyzed using SEM/EDAX analysis. The reproducibility of the test procedures should be ensured for few more samples.

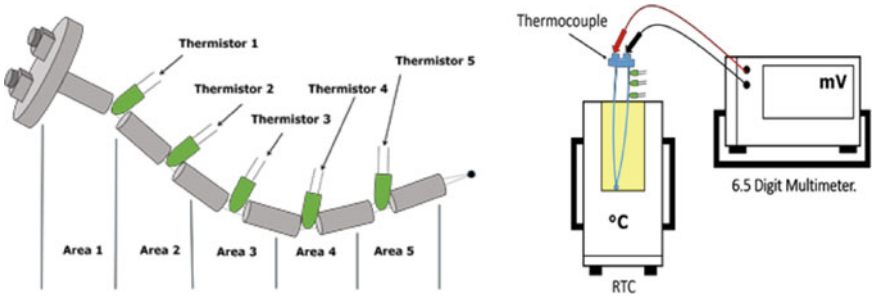

Fig. 1 Schematic representation of temperature gradient **a** Different regions; **b** Measurement system

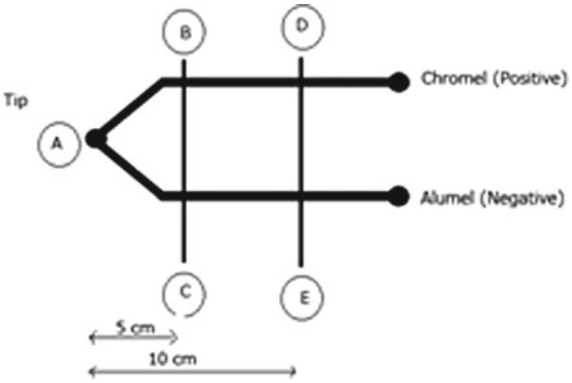

Fig. 2 Thermocouple sample preparation

3.2 SEM/EDAX Sample Preparation

SEM and EDAX analyses can be executed for conductive/non-conductive/magnetic material and the samples used for the analysis can be in powder form/pellet form/film/biological. In this paper, pellet form is taken to analyze the degradation of the sample. To conduct the analysis, samples are taken from both positive and negative terminals of the thermocouple at 5 and 10 cm above from the tip of the thermocouple as shown in Fig. 2. The sample size in SEM and EDAX is restricted to few millimeters only. So, the sample is prepared from 500 to 700 mm. Sample collected from tip of the thermocouple is A. Sample B is 5 cm above from tip of the thermocouple in Positive (Chromel) terminal, Sample C is 5 cm above from tip of the thermocouple in Negative (Alumel) terminal, Sample D is 10 cm above from tip of the thermocouple in Positive (Chromel) terminal, and E is 10 cm above from tip of the thermocouple in Negative (Alumel) terminal.

4 Experimental Results

The aim of the current paper is to evaluate the surface degradation of K-type thermocouple due to its prolonged usage at very high temperature. Nominal composition present in normal K-type thermocouple is Chromel (Positive)—90% Ni, 10% Cr and Alumel (Negative)—95% Ni, 2% Mn, 2% Al. Table 1 shows the presence of oxygen component in the normal K-type thermocouple which is used for the experimental analysis. Figure 3 shows the SEM image and the corresponding elemental analysis or chemical characterization performed using EDAX at tip, positive and negative sides of the thermocouple. The characterization of the elements in K-type thermocouple is based on the basic principle that each element has a distinctive atomic structure consenting a unique set of peak on its electromagnetic emission spectrum as follows.

Table 1 Oxygen composition (wt %) of thermocouple

Position	Oxygen (O2)
Sample A	10.28
Sample B	13.03
Sample C	24.37
Sample D	29.53
Sample E	45.93

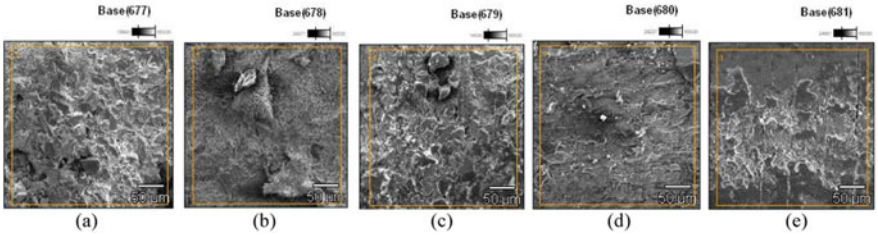

Fig. 3 Surface morphology, **a** Sample A, **b** Sample B, **c** Sample C, **d** Sample D, **e** Sample E

This entire procedure is repeated for 7 times. After 7 times, five different samples say A, B, C, D, and E are taken and the corresponding SEM images are obtained to a size of 50 μm as shown in Fig. 3.

The highlights of observation from the SEM image of degraded thermocouple are as follows:

- Sample A is highly degraded due to expose of high temperature at tip of the thermocouple.
- Sample B and C show the broken oxide layers and severe formation of new oxide layer due to thermocyclic oxidation. This samples being close to the tip of the thermocouple, degradation will be faster compared to samples D and E.
- Sample D and E show mild oxide layer growth, loss of adhesion, and surface roughening.

An elemental analysis of degraded thermocouple is conducted by using EDAX and the results are shown in Fig. 3. EDAX represents net count of the material for each sample with increasing accelerating voltage in the range 1 to 10 keV. Peaks are recorded based on the characteristics of each element in the thermocouple which is nominally sharp lines. Brehmstrahlungen (Baseline/Background) is broad and featureless background. The major components of K-type thermocouple are Ni, Cr and Al. During quenching, Ni formed as Nickel Oxide (NiO2), Cr formed as Chromium Oxide (CrO2), and Al formed as Aluminum Oxide (AlO2). These oxides form an oxide layer on the surface of the thermocouple. Due to this, the oxygen content is increased for all samples when compared with normal thermocouple as

seen from Table 1. Hence, it is inferred that continuous measurement at high temperature followed by air quenching will result in increased oxide layer, and at certain point, these oxide layer get brittle and again it will form a new layer.

5 Conclusion

The degradation of K-type thermocouple due to exposure of high temperature is analyzed using SEM-EDAX test. The test results inferred that material degradation is due to prominent oxide layer formation. As an extension of future work, the increase in resistance due to the increased oxide layer formation and hence the life span of the thermocouple can be determined.

References

1. Hamada T (2007) A calculation ofE.M.F. Drift from the Rh contents for platinum based thermocouples. SICE annual conference 2007
2. Ogura H, Tamba J, Izuclii M, Arai M (2002) Effect of temperature distribution on Emf of thermocouples. SICE Aug. 5–7, Osaka, pp 19–21
3. Hamada T (2000) Calibration and drift of platinum based thermocouples. Boundary pp 22–27
4. Jun S, Kochan O, Chunzhi W, Kochan R (2015) Theoretical and experimental research of error of method of thermocouple with controlled profile of temperature field. Measur Sci Rev 15(6)
5. Jun S, Kochan O (2014) Investigations of thermocouple drift irregularity impact on error of their inhomogeneity correction. Measur Sci Rev 14(1):29–34
6. Amagai Y, Nakamura Y (2012) Numerical analysis of low-frequency properties in single-junction thermal converters. IEEJ Trans Electr Electron Eng 7(4):350–354
7. Alwaaly AAY, Paul MC, Dobson PS (2015) Effects of thermocouple electrical insulation on the measurement of surface temperature. Appl Therm Eng
8. Rokosz K, Hryniewicz T, Raaen S, Chapon P, Dudek Ł (2016) GDOES, XPS and SEM with EDS analysis of porous coatings obtained on titanium after plasma electrolytic oxidation. Surf Interf Anal

Experimental Investigation of Solar-Based Air Heater Rectangular Duct Having Uniform Spaced Dimple Shaped as Roughness Element on the Absorber Plate

P. Rajesh Kanna, M. Chandrasekaran, and M. Ravikumar

Abstract This test examination has been completed to look at the thermal performance of the sunlight-based air heater rectangular duct with dimple form harshness geometry on surface of the plate and plate without dimple form harshness geometry. The thermal efficiency and outlet temperature of air are analyzed based on various mass streams per unit time. Investigations are led for various mass stream per unit time of air in extend (0.00528–0.01321 kg/s). The most extreme efficiency got for the mass stream per unit time of air is 53.22 and 39.33% for absorber plate with dimple form and without dimple form separately. The most extreme temperature contrast among outlet and inlet for sun-powered air heater conduit with dimple and without dimple form is 25.2–19.8 °C.

Keywords Solar air heater · Dimple · Thermal efficiency

1 Introduction

Sun-powered vitality is an enormous endless wellspring of vitality. The power got by the earth from the sun is 1.8×10^{11} Mega Watt, this value is ordinarily bigger compared to the present utilization on the earth of all business vitality assets. The energy from the sun has clean energy compared to fossil and nuclear energy and it is free and available in all over the world. The main application of the solar-based air heater is cloth or seeds drying and room heating.

Correlation of the four sunlight-based air collector obstructions was finished by the individual collector performance. The collector efficiency relies upon the sunlight-based radiation, expansion of the wind stream, and surface geometry of the gatherers. The collector efficiency improves with expanding mass stream rates because of upgraded heat move to the wind current [1, 2]. Then again, establishment of wings and baffles improves heat move among absorber and air that favors increment the

P. R. Kanna (✉) · M. Chandrasekaran · M. Ravikumar
Department of Mechanical Engineering, Bannari Amman Institute of Technology, Sathyamangalam, Tamil Nadu, India
e-mail: rajkannpmech@gmail.com

G. Kumaresan et al. (eds.), *Advances in Materials Research*, Springer Proceedings in Materials 5, https://doi.org/10.1007/978-981-15-8319-3_90

effectiveness and guaranteeing a greatest increment of temperature. More pressure drop expands the power utilization [3]. The results of single and two-fold pass sun-based air heater have been compared. The result shows that efficiency increased with expanding the mass stream rate. The difference between the exit stream temperature and atmosphere temperature ΔT decreases as the air mass stream rate increment [4].

Few studies have been completed on numerical performance along with entropy generation for double pass flat plate solar-based air heater contain longitudinal fins [5]. Fins gave better heat transfer increment in sun-based air heaters but it provides pressure drop increment in stream channels. Consequence demonstrates heat absorption of heat and dissipation potential of a solar-based air heater improved by using high efficiency optimized fin [6]. The experiment investigation exhibits that double pass-finned plate solar air heater has 9.3–11.9% less proficient compared with double pass v-corrugated plate oriented air heater [7].

Offset rectangular plate fin absorber plates system has been created to increase the heat transfer compared with fully developed turbulent flow. The offset rectangular plate is arranged above the plate surface and situated parallel to the liquid stream. The offset rectangular plate was welded to the bottom side of the absorber plate. High thermal performances are gotten with low friction loss and in result, low electrical power utilization by the fan in contrast with the flat plate collector [8]. Exploratory study has been completed for three kinds of sunlight-based air collectors, specifically flat plate, plate contain fins, and plate contain v-corrugated sun-powered air heater setup. The v-corrugated collector is seen as the high efficient gatherer and the flat plate gatherer is less efficient [9]. The point of utilization of the cross-corrugated absorbing plate and base plate was used to upgrade the turbulence and improvement in heat transfer rate in the wind stream channel and these are significant to the improvement of efficiencies of air heaters [10]. This paper demonstrated a novel sun-powered air collector with pin fin absorber plate to upgrade the thermal efficiency [11]. A few ponders have been done for the impact of two diverse mass stream rate 0.012 kg/second and 0.016 kg/second in collector with longitudinal fins [12]. This article displays an examination for a novel sort of sun-powered air heater. This article idea is to reduce the front side cover heat losses of the collector along with to augument heat extraction from the gatherer plate. Due to this idea, it is possible to preheat the air by passed through the front glass spread before entered in to the gatherer plate. Henceforth, this plan needs an additional setup cover to form a counter flow heat exchanger [13]. Examinations for thermo hydraulic performance of falsely roughened sun-powered air heaters have been done covering a wide scope of working parameters. Thermal performances of such gatherers have been discovered better than plane ones for the equivalent working parameters. Be that as it may, pressure drop increments in such collectors [14]. Significant collector efficiency improvement of sunlight-based air heaters can be acquired if the baffles in the gatherer have appended astounds to make air disturbance and an all-inclusive heat-move territory [15]. Examinations of the impact of geometrical parameters of multiple arc-shaped formed harshness component on heat transfer along with rubbing attributes of channel sun-based air heater having unpleasantness on the underside of the absorber plate have been completed. Most extreme upgrade in friction factor and Nusselt number

was 3.71 and 5.07 occasions separately when contrasted with smooth type [16]. In this title, different examinations have been done to decide the impact of various artificial geometries on heat transfer along with friction characteristics in air heater ducts. Artificial roughness is best method among other methods for improving the performance of sun-based heater duct [17]. Trial examinations state that the impact of artificial roughness leaning on heat transfer together with rubbing attributes in sun-based air heater channel and it has dimple molded components arranged in curved type as harshness components on absorber plate was carried out. The friction loss along with heat transfer increment was observed [18]. Tentatively examined the impact of friction together with heat transfer characteristic of turbulent stream of air going through rectangular channel which is roughened by circular protrusions organized in precise curve design. The most extreme upgrade in Nusselt number and friction factor is 2.89 and 2.93 occasions as contrasted and smooth conduit [19]. Tentatively explored the impact of geometrical parameters of the *V*-shaped perforated squares on heat transfer and stream attributes of rectangular duct. The greatest upgrade in Nusselt and friction factor has been seen as 6.76 and 28.84 occasions to that of smooth pipe, separately [20]. A test study has been done to research the effective efficiency of a sunlight-based air heater channel gave transverse and slanted ribs as artificial roughness components on the absorber plate. The most extreme estimation of powerful proficiency has been found for roughness parameters comparing to relative roughness pitch (p/e) of 8 under the scope of parameters researched [21]. A test examination demonstrates the thermal performance of flat plate and spherical dimple plate sun-based air heater. The outcome displays that the heat transfer rate of spherical dimple plate sun-based air heater is 1.5 times higher compared to flat plate sun-based air heater. The spherical dimple plate air heater efficiency is 23.45% to 35.50% more noteworthy than the relating flat plate air heater. They conducted that test for mass stream rate from 0.009 to 0.028 kg/s [22]. Factual connections for Nusselt number and friction factor as far as harshness and stream parameters were determined dependent on information gathered from explore. Advanced estimation of stream and harshness parameter yielding greatest execution is resolved. The most extreme improvement in Nusselt number for shifting relative dimple pitch, relative dimple depth, and relative dimple height was individually of the request for 2.6–3.55, 1.91–3.42, 3.09–3.94 occasions and that of friction factor was of the request for 1.62–2.79, 1.52–2.34, and 2.21–2.56 occasions over those of 1-side roughened ones [23].

2 The Experimental Setup

A schematic and photographic perspectives on the sun-powered air heater rectangular duct with dimple as harshness component on the absorber plate is appeared in Figs. 1 and 2. In the investigation of the exploratory arrangement comprises of rectangular pipe, absorber plate, blower, control valve, advanced thermometer, solarimeter, computerized anemometer, PVC pipe as appeared in Fig. 1. The inward

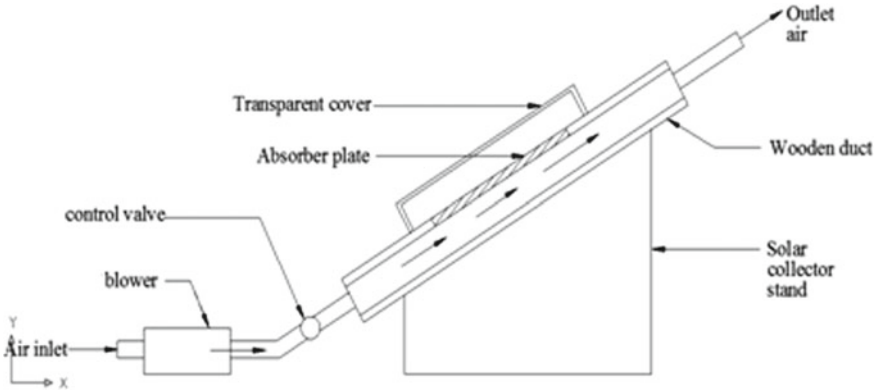

Fig. 1 Side view of the sun-based air heater

Fig. 2 Photographic view of sun-based air heater

cross-segment zone of the rectangular channel is having 2300 × 330 × 30 mm according to ASHRAE standard 97–77 [16]. The rectangular duct is partitioned in to three areas and they are inlet segment, test segment, exit segment. The length of the inlet segment, test segment, and exit area is 680 mm, 1200 mm, and 420 mm separately. In this investigation, two kinds of absorber plate are utilized. The absorber plate has comprised of aluminum. The thickness of the absorber plate is 2 mm. The spread window type, the Plexiglas thickness is 4 mm. The separation between absorber plate and straight forward spread is 2.5 mm. Advanced thermometers are situated equally, on the top surface of the absorber plates, at indistinguishable situations along the course of stream, for all cases tried. Channel entrance and exit air temperatures are estimated by two advanced thermometers. The yield of the thermometer is in degree Celsius estimation extend,—50–300 °C (–58–572 °F); goals, 0.1 °C; exactness, ± 1 °C or (±2 °F). An advanced multi-stem thermometer is utilized to quantify the surrounding temperature. The complete sun-based radiation occurrence

on the outside of the authority was estimated with a sunlight-based power meter. This meter is put above to the coating spread during taking readings, at a similar plane, looking due south. The deliberate factors are recorded at interims of 1 h and incorporate insolation, entrance and exit temperatures of the air circling through the gatherers, encompassing ambient temperature, absorber plate temperatures at a few chose areas, and wind stream rates (computerized anemometer Lutron AM-4201). The test started at morning 10 o'clock and finished at evening 4 o'clock.

3 Results and Discussion

This experimental analysis work displays the consequences of the test examination of a sun-based air warmer with and without dimple shape on the absorber plate during January 1, 2019, to April 20, 2019, in the city of Salem in Tamil Nadu, India. Figures 3 and 4 display the hourly fluctuation of sun intensity versus time when the wind stream rate is (0.00528–0.01321 kg/s) for the sunlight-based air heater with and without dimple molded surface on the absorber plate. The maximum solar radiation is 1324 W/square meter at afternoon 1 O'clock. Figures 5 and 6 display the entry and exit temperatures of air for the diverse mass stream flow of air. The most extreme estimation of inlet temperature, T_i at 14.00 pm of local time is 36.5 and 36.6 °C for the absorber plate with dimple shape and without dimple shape individually, which rely upon the ecological conditions, for example, wind speed and humidity. It is seen from Figs. 5 and 6 that the exit temperature diminishes as the mass stream rate is increased.

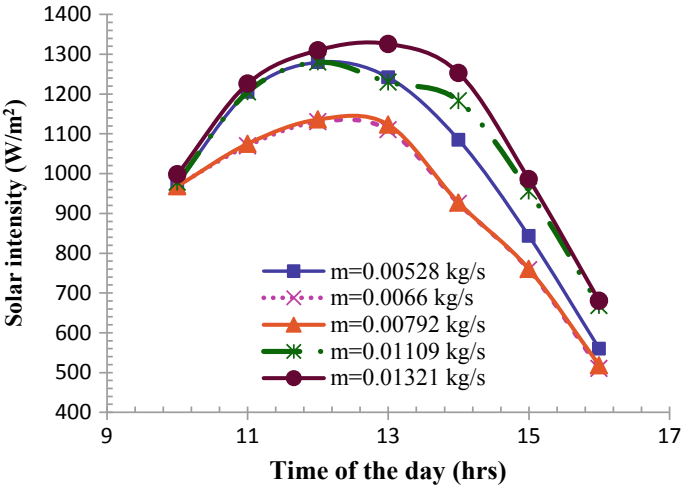

Fig. 3 Solar intensity versus time with protrusion

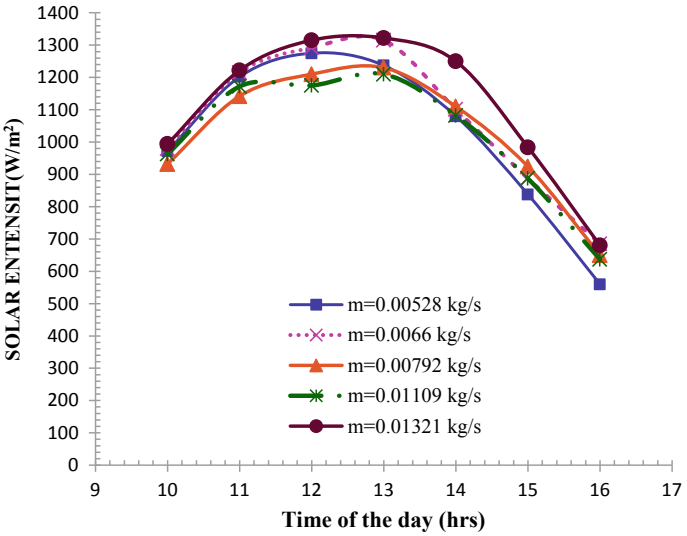

Fig. 4 Solar intensity versus time without dimple shape

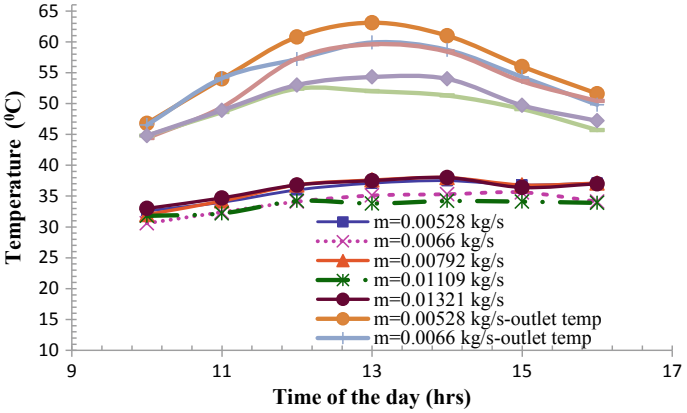

Fig. 5 Time versus temperature with dimple shape

Figures 7 and 8 shows the hourly variety of temperature distinction (ΔT) versus neighbourhood time when the wind stream rate go is 0.00528–0.01321 kg/s. As observed from Figs. 7 and 8, the temperature distinction esteems increment in the first part of the day as the solar intensity increases, to a most extreme incentive between 12.00 pm and 1.00 pm of neighborhood time and afterward diminishes toward the evening as the time passes. The most noteworthy temperature contrast esteems are 25.2 and 19.8 °C for the absorber plate with dimple formed surface and without dimple molded surface for a similar wind current pace of 0.00528 kg/s.

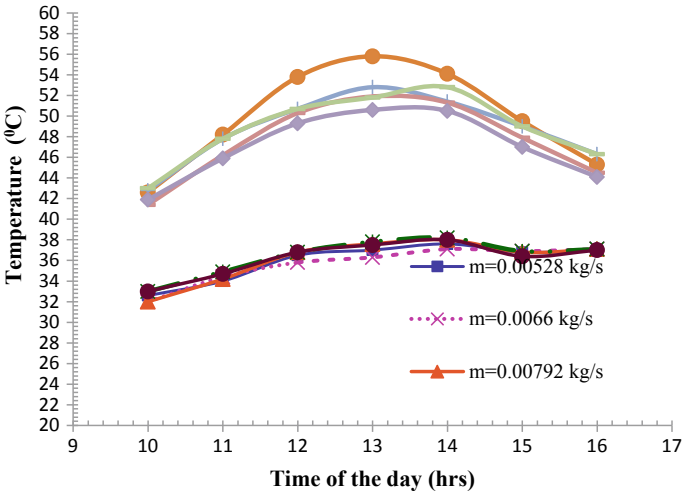

Fig. 6 Time versus temperature without dimple shape

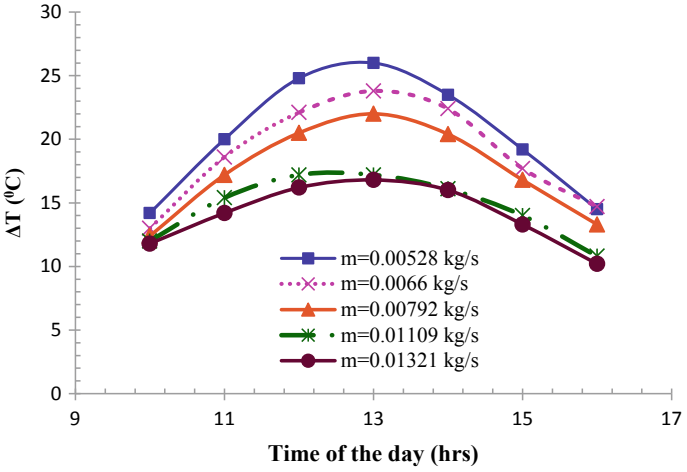

Fig. 7 Time versus temperature difference with dimple shape

Figures 9 and 10 show the hourly variety of thermal conductivity versus time for the distinctive wind stream rates. The effectiveness increments with the expanding wind current rate for both absorber plates. The most extreme effectiveness got for the absorber plate with dimple formed surface and without dimple molded surface is 53.22% and 39.93% separately for the wind stream pace of 0.01321 kg/s. As observed from Figs. 9 and 10, the effectiveness for practically every one of the cases tried is persistently expanded from morning until night. These outcomes are like those got from Mahmood et al. [22].

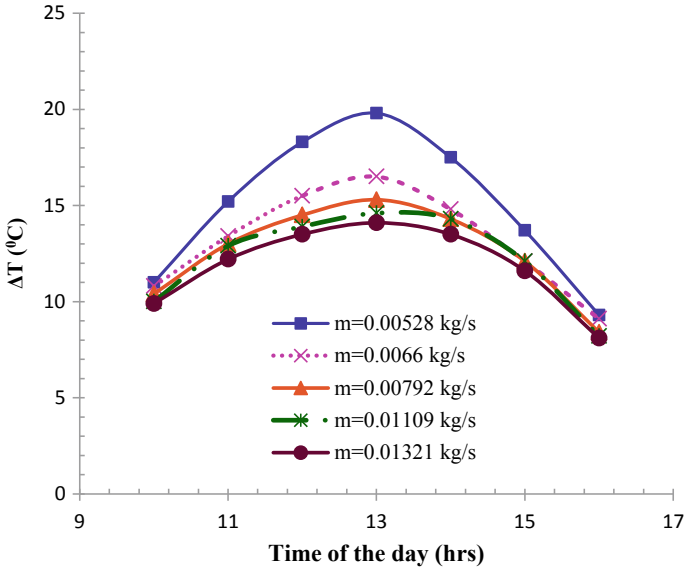

Fig. 8 Time versus temperature difference without dimple shape

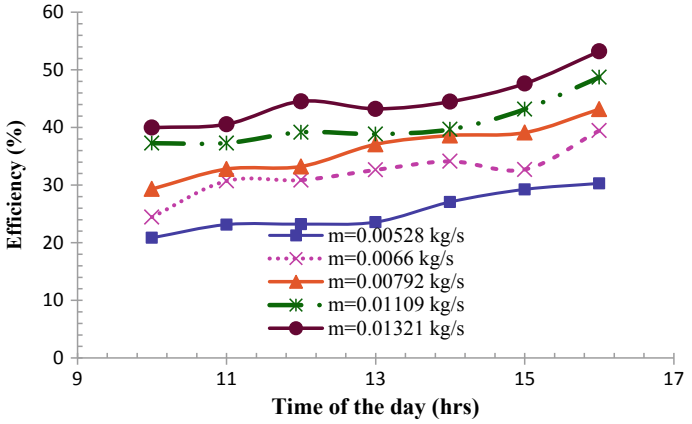

Fig. 9 Time versus efficiency with dimple shape

4 Conclusion

The sunlight-based air heater with and without dimple molded on the absorber plate is developed and tried for various mass stream pace of air. The accompanying ends are drawn:

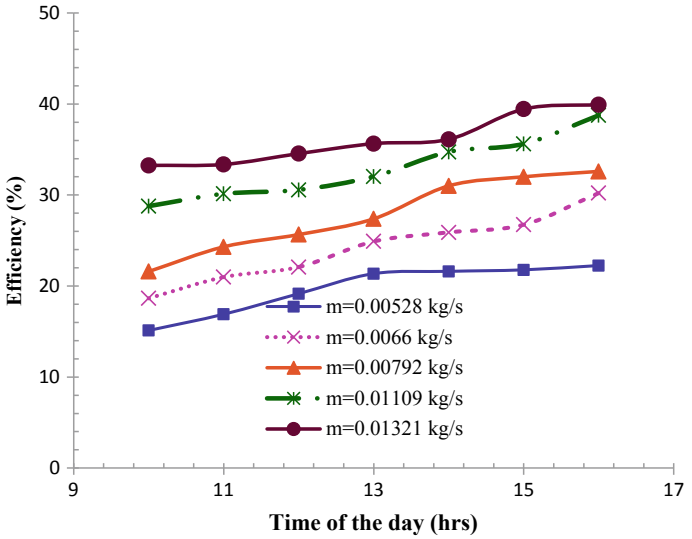

Fig. 10 Time versus efficiency without dimple shape

1. The thermal efficiency for the sun-powered air heater with dimple shape on the absorber plate is higher than that of without dimple shape for the most noteworthy mass stream pace of air.
2. In expansion, the temperature contrast between the inlet and outlet temperature diminishes with expanding mass stream pace of air in between 0.00528 and 0.01321 kg/s.
3. The most extreme effectiveness got for the absorber plate with dimple formed surface and without dimple molded surface are 53.22 and 39.93% separately for the wind stream pace of 0.01321 kg/s.
4. Finally, these outcomes demonstrate that there is an improvement with the utilization of dimple formed in the absorber plate.

References

1. Akpinar EK, Kocyigit F (2010) Experimental investigation of thermal performance of solar air heater having different obstacles on absorber plates. Int Commun Heat Mass Transf 37:416–421
2. Karsli S (2007) Performance analysis of new-design solar air collectors for drying applications. Renew Energy 32:1645–1660
3. Romdhane BS (2007) The air solar collectors: comparative study, introduction of baffles to favour the heat transfer. Sol Energy 81:139–149
4. Omojaro AP, Aldabbagh LBY (2010) Experimental performance of single and double pass solar air heater with fins and steel wire mesh as absorber. Appl Energy 87:3759–3765
5. Paisarn N (2005) On the performance and entropy generation of the double-pass solar air heater with longitudinal fins. Renew Energy 30:1345–1357

6. Nwachukwu PN (2010) Employing energy-optimized pin fins in the design of an absorber in a solar air heater. Energy 35:571–575
7. El-Sebaii AA, Aboul-Enein S, Ramadan MRI, Shalaby SM, Moharram BM (2011) Thermal performance investigation of double pass-finned plate solar air heater. Appl Energy 88:1727–1739
8. Hachemi A (1999) Experimental study of thermal performance of offset rectangular plate fin absorber-plates. Renew Energy 17:371–384
9. Karim MA, Hawlader MNA (2004) Development of solar air collectors for drying applications. Energy Converserv Manage 45:329–344
10. Gao W, Lin W, Liu T, Xia C (2007) Analytical and experimental studies on the thermal performance of cross-corrugated and flat plate solar air heaters. Appl Energy 84:425–441
11. Donggen P, Xiaosong Z, Hua D, Kun L (2010) Performance study of a novel solar air collector. Appl Therm Eng 30:2594–2601
12. Chabane F, Moummi N, Benramache S, Tolba AS (2012) Experimental study of heat transfer and an effect the tilt angle with variation of the mass flow rates on the solar air heater. Int J Sci Eng Invest 1:61–65
13. Mohamad AA (1997) High efficiency solar air heater. Sol Energy 60:71–76
14. Verma SK, Prasad BN (2000) Investigation for the optimal thermohydraulic performance of artificially roughened solar air heaters. Renew Energy 20:19–36
15. Yeh HM (1992) (1992) Theory of baffled solar air heaters. Energy 17:697–702
16. Singh AP, Varun S (2014) Investigated the Effect of artificial roughness on heat transfer and friction characteristics having multiple arc shaped roughness element on the absorber plate. Sol Energy 105:479–493
17. Kumar A, Saini RP, Saini JS (2012) Heat and fluid flow characteristics of roughened solar air heater ducts. Renew Energy 47:77–94
18. Sethi M, Varun NST (2012) Correlations for solar air heater duct with dimpled shape roughness elements on absorber plate. Sol Energy 86:2852–2861
19. Yadav S, Kaushal M, Varun S (2013) Investigated Nusselt number and friction factor correlations for solar air heater duct having protrusions as roughness elements on absorber plate. Energy 44:34–41
20. Tabish Alam RP, Saini JSS (2014) Experimental investigation on heat transfer enhancement due to V-shaped perforated blocks in a rectangular duct of solar air heater. Energy Conserv Manage 81:34–383
21. Varun AP, Saini RP, Singal SK, Siddhartha (2009) Investigated the performance prediction of solar air heater having roughened duct provided with transverse and inclined ribs as artificial roughness. Energy 34:2914–2922
22. Perwez A, Kumar R (2019) Thermal performance investigation of the flat and spherical dimple absorber plate solar air heaters. Sol Energy 193:309–323
23. Kumar V (2019) Nusselt number and friction factor correlations of three sides concave dimple roughened solar air heater. Renew Energy 135:355–377

Investigation and Experimental Study on Microstructure and Characterization of Silicon Carbide Synthesized by High Energy Ball Milling

M. Kalil Rahiman, S. Santhoshkumar, and P. Mathan Kumar

Abstract In recent years, nanopowders have been grabbed the attention in automobile and mechanical industries due to its enhanced mechanical properties such as high strength, hardness, and ductility. In this present work, microstructure and mechanical properties of Silicon Carbide (SiC) powder are investigated. An average size of 20 μ SiC is ground to obtain into nanoscale in a planetary ball mill. The powder is taken in different ball to weight ratios and milled in an argon atmosphere. Sample collection is done for every 10 h and the rotational speed is maintained from 300 to 400 rpm. Eventually, collected samples are characterized by X-ray Diffraction (XRD), Transmission Electron Microscope (TEM), and Energy Dispersive X-Ray Spectroscopy (EDAX). The particle size is availed in smaller grain sizes and varied from 101 to 21 nm after milling of powder with successive time periods.

Keywords High energy ball milling · X-Ray Diffraction (XRD) · Transmission Electron Microscope (TEM) · Energy Dispersive X-Ray Spectroscopy (EDAX)

1 Introduction

In automobile and mechanical industries, nanomaterials exhibit superior mechanical properties such as higher strength, hardness, and ductility. To improve the microstructure and mechanical properties of nanomaterials, high energy ball milling is used for the production of micron-sized powder into nano-sized powder [1, 2]. Metal matrix

M. Kalil Rahiman (✉)
Department of Aeronautical Engineering, Bannari Amman Institute of Technology, Sathyamangalam, Tamil Nadu 638401, India
e-mail: kalilrahimanm@bitsathy.ac.in

S. Santhoshkumar
Department of Automobile Engineering, Bannari Amman Institute of Technology, Sathyamangalam, Tamil Nadu 638401, India

P. Mathan Kumar
Department of Mechanical Engineering, Bannari Amman Institute of Technology, Sathyamangalam, Tamil Nadu 638401, India

G. Kumaresan et al. (eds.), *Advances in Materials Research*, Springer Proceedings in Materials 5, https://doi.org/10.1007/978-981-15-8319-3_91

composites are also the combination materials and it proves superior mechanical properties in many engineering fields. In industries, several fabrication methods are utilized for the production of nanopowders in which high energy ball milling is an important technique to fabricate nanopowders [3, 4].

To achieve high strength, hardness and ductility in nanopowders, various techniques are developed to reduce the size of the powder from micron-sized into nano-sized and accordingly improve its mechanical properties. High energy ball milling, rapid solidification, electro-deposition, plasma processing, vapour deposition are significant techniques for the production of nanomaterial and among these techniques, high energy ball milling technique is very popular for the fabrication of nanomaterials.

Grain size or particle size plays a vital role in nanomaterials. High energy ball milling produces micron-size particles with Nanocrystalline powders or nano-sized grains. Milling impact energy created by the specially designed high energy planetary ball mill due to the collision of the balls with the powder charge is sufficient to plastically deform the powder particles and, in so doing, to develop refined microstructures with enhanced properties [5, 6].

In metal cutting industries, chips being generated during machining process are utilized for the production of nanopowders. Silicon Carbide powder with Aluminum or Copper-based alloys are prepared for composition and milled by high-energy ball mill technique. By using the technique, low strength alloy to high strength alloy is possible at low cost [7, 8]. However, parameters such as types of mills, time, speed and atmosphere are the important variables for the fabrication process.

By recent literature surveys, few researchers made an attempt for the analysis of SiC and characterization using high energy ball milling method. In this research article, Silicon Carbide with micron-sized particle is taken into nano-structured silicon carbide using high-energy ball mill and analysis of microstructure and characterization is also studied.

2 Synthesis of SiC

Nanomaterials such as Silicon Carbide are synthesized either by the combination of nanomaterial or fracturing the nanomaterial from larger size into smaller size. For the production of nanomaterials, inert gas condensation and ultra high vacuum methods are deployed to improve the mechanical properties of nanomaterials [9, 10].

In recent years, Mechanical alloying is the most popular technique for processing metal powders. In this technique, metal powders are mixed to produce superalloys and two steps are followed for the production of powders. In the first step, alloys and powders are mixed in a certain ratio and in the second step, powder and alloy are ground in the mill to produce a nano-sized powder. During the operation of the mill, the powder and its compositions are mixed and eventually fine grain size particles are produced due to repetitive welding, fracturing [11, 12].

3 High Energy Ball Milling

3.1 Principle

High Energy Ball Milling is a technique for the production of nanopowder particles and alloys. For the production of Silicon Carbide powder, steel or tungsten carbide balls are repeatedly used for the deformation, cold welding and fracturing between the particles inside the vial. Due to plastic deformation in the mill, the internal structure of Silicon Carbide is reshaped from micron-sized particle into nano-sized particle. For grinding Silicon Carbide, Tungsten Carbide balls are used inside the vial during the operation of the mill and the powder sample is accordingly ground due to deformation.

4 Methodology

In this research work, an attempt has been made to grind silicon carbide with an average size of 20 μ and these powders are characterized by X-ray Diffraction, Transmission Electron Microscope (TEM) and Energy Dispersive X Ray Spectrometer (EDS) as shown in Fig. 1.

5 Experimental Work

For the production of silicon carbide nano-sized powder, the planetary ball mill is used which consists of ten numbers of 20 mm diameter balls in a 120 ml vial and hardened stainless steel is used as ball material. In high energy ball milling, the bowl rotation speed is maintained at approximately 300–400 rpm. An average size of 20 μ Silicon Carbide powder is chosen for the milling process and milling speed of 300–400 rpm is maintained for the production of Silicon Carbide from micron-Sized particle to nano-sized particle [13, 14].

For reducing oxidation in the milling environment during the milling process, argon gas is supplied in the milling area and glove box is used to handle all samples. The milling time for grinding Silicon Carbide powder is maintained up to 60 h and sample collection is done for every 10, 20, 30, 40, 50, 60 h.

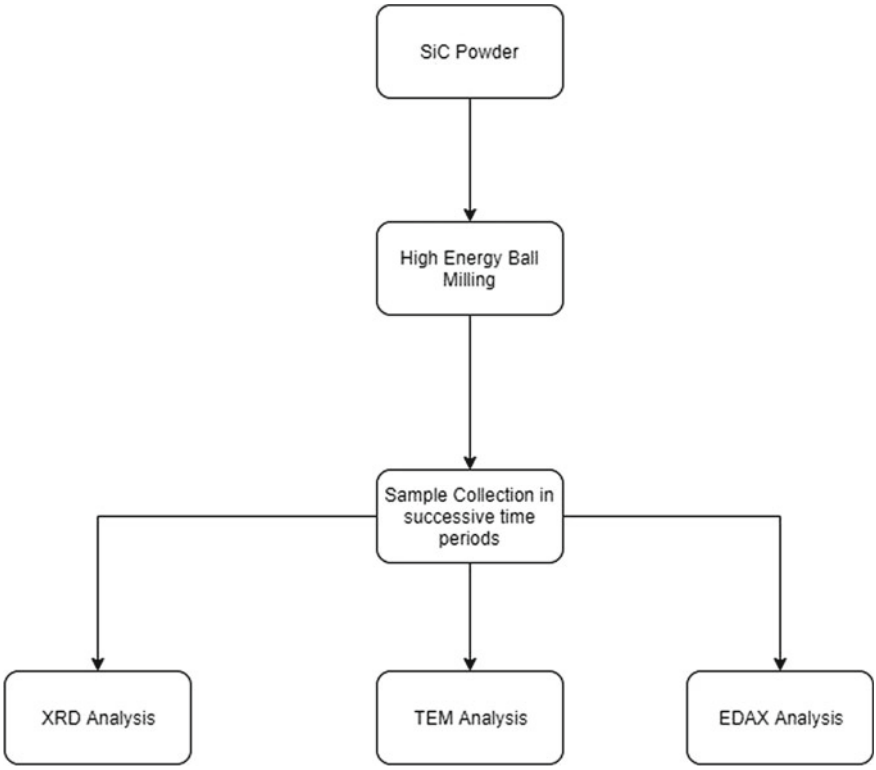

Fig. 1 Methodology

5.1 Parameters for Milling Process

Milling parameters such as speed, time, ball weight, powder weight and ball to powder weight ratio are the important parameters for the analysis of microstructure and characterization of Silicon Carbide.

In High Energy Ball Milling, the ball mill is allowed to rotate for about 60 h. During milling process, the SiC powder is agglomerated which is caused due to the ball impaction and the heat generated inside the planetary milling machine [15, 16].

5.2 Sample Collections

Silicon Carbide powders are collected from the planetary ball mill in every 10 h of milling and milling speed, for the process is 300–400 rpm. The average size of 20 μ is chosen for milling process [17–19]. The following Figs. 3a–g depict the collection of powders in successive time periods (Fig. 2).

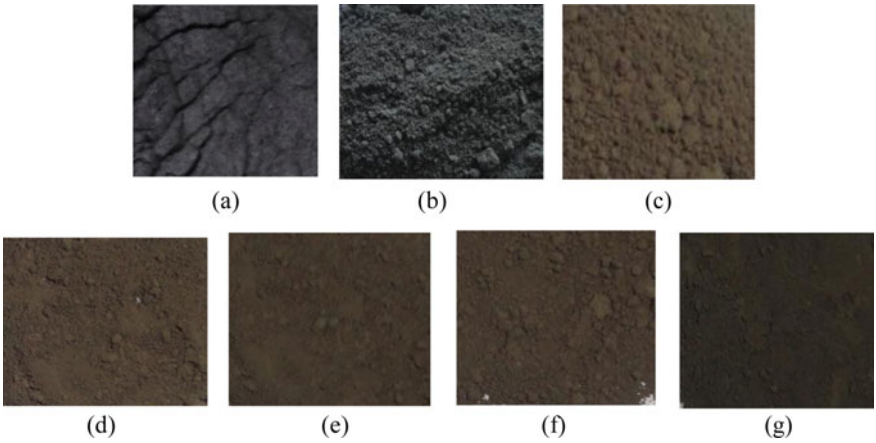

Fig. 2 Sample collections for **a** 10 h, **b** 20 h, **c** 30 h, **d** 40 h, **e** 50 h, **f** 60 h

The collected Silicon Carbide powders are further characterized by X-ray Diffraction, Transmission Electron Microscope (TEM) and Energy Dispersive X-Ray Spectrometer (EDS).

6 X-Ray Diffraction (XRD)

The grain size of Silicon Carbide powder is analyzed by X-Ray Diffraction or XRD and it is an important tool to find the size of grain and distortion. By using this method, X-ray is produced and the texture is analyzed by diffraction. Bragg's law is applied to find the grain size of the silicon carbide powder after the synthesis process.

By using the XRD analysis, broadened peaks are obtained when the grain sizes are in the nanometre, and the smaller the grain size, the broader the peak is obtained. To find the exact crystalline size of Silicon Carbide powder, Scherer equation is applied and It is used to find the size of the nanograins from the synthesized silicon carbide powders [20, 21]. It is based on Wolf–Bragg angle which results in size broadening of X-ray peaks.

The XRD analysis of silicon carbide samples collected from 10, 20, 30, 40, 50, 60 h are shown in Fig. 4a–f. X-ray diffractometer is used for calculating the crystalline size of the powder. XRD graph is generated with various peaks. By calculating the width of the peak, the crystalline size is calculated using Scherrer's formula. By using this method, the average size of 21 nm is found in XRD analysis [22, 23].

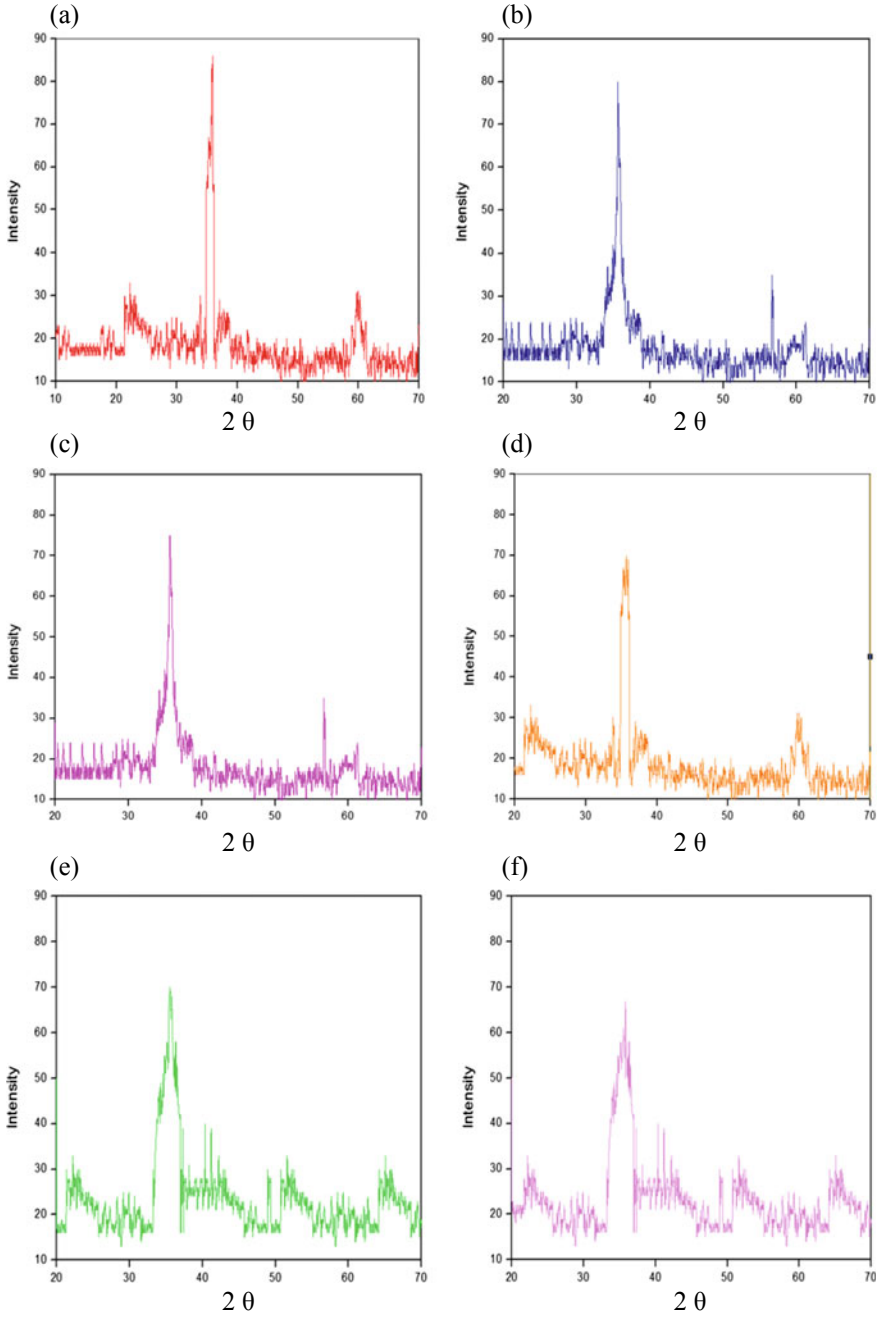

Fig. 3 XRD analysis for **a** 10 h, **b** 20 h, **c** 30 h, **d** 40 h, **e** 50 h and **f** 60 h

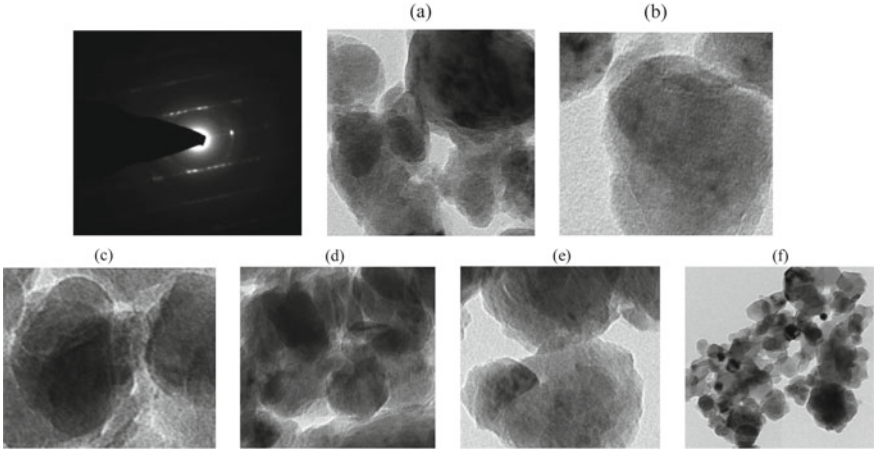

Fig. 4 TEM images of SiC for **a** 10 h, **b** 20 h, **c** 30 h,**d** 40 h,**e** 50 h and **f** 60 h

7 Transmission Electron Microscope (TEM)

Transmission Electron Microscope (TEM) is a largely magnified image by using light to form an image. The path of the electron is vertical in Vacuum of the microscope which travels into the lenses. It focuses on the sample at the bottom of the microscope. After the penetration of X-ray in the sample, electrons and X-rays are escaped from the sample [24, 25]. The beam of electrons is interfacing with the atoms of molecule with one another. The nano-sized powder is more precise and the unique size is attained after the successive time periods. The size of silicon carbide powder is also decreased from 101 nm as the time of milling is increased in TEM analysis.

From Fig. 4a–f, an unique and oval-shaped structure is found in successive time periods and the SiC powder is further analyzed by EDAX (Energy Dispersive X-Ray Spectroscopy).

Lattice strains and defects in crystals are unavoidable during the milling process. However, lattice strain is developed during the process [26, 27]. Due to fracturing and cold welding process during the operation of milling process, the structural changes such as lattice strain and defects in crystals occur. It is occurred due to phase transformation and the grain size is compared with frequency to find the exactness of SiC powder [28, 29] (Fig. 5).

8 EDAX (Energy Dispersive X-Ray Spectroscopy)

Energy Dispersive X-ray Spectroscopy is a technique is to identify the elements in silicon carbide powder or nanomaterials. In EDAX analysis, high beam electron is

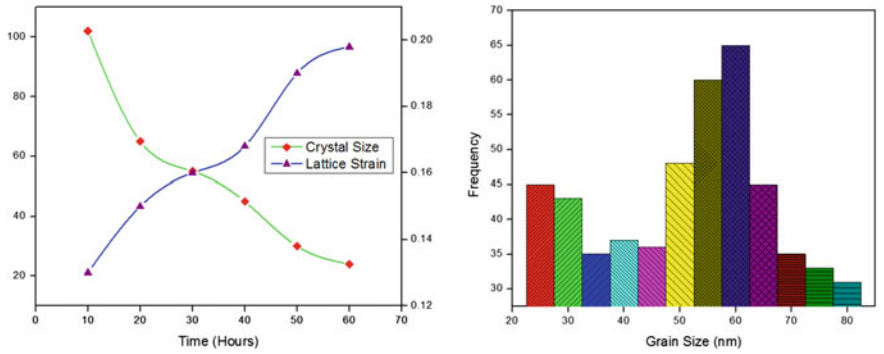

Fig. 5 Grain size analysis

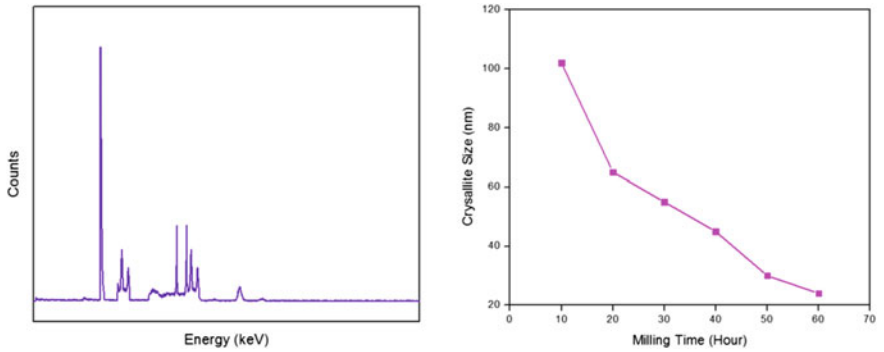

Fig. 6 EDAX analysis

produced to bombard on the Specimen where SiC powder is placed and the composition of powder is analyzed by EDAX. By this analysis, the presence of Si, Cl, Fe, Cu are found and the highest peak in Fig. 6 confirms the presence of silicon carbide and other peaks represent Cl, Fe, Cu, WC [30, 31].

In Fig. 6, as the milling time increases during the operation of milling process, the crystallite size decreases in successive time periods.

9 Conclusions

In past decades, researchers are carried out with alloys and silicon carbide powder using different percentage such as 15, 20 and 25%. In this research article, silicon carbide powder is only used to modify the micron-sized powder into nano-sized powder and it is observed that the average crystal size of 21 nm is found by X-ray

Table 1 Milling parameters

S. No.	Speed (rpm)	Maximum time (h)	Ball to powder ratio	Sample collection
1	300	10	15:1	Every 10 h
2	320	20	15:1	
3	340	30	20:1	
4	360	40	20:1	
5	380	50	25:1	
6	400	60	25:1	

diffraction method. By using this method, the size of the silicon carbide is successfully reduced as the milling time of SiC is increased and the complete silicon carbide phase formation is identified after 50 and 60 h milling by the comparison of the peak heights. In TEM analysis, unique structure and oval shape of silicon carbide powder is formed after successive time periods such as 10, 20, 30,40,50,60 h and EDAX reveals the presence of silicon carbide with maximum range and other elements such as Cl, Fe, Cu, WC are also distributed in silicon carbide powder. In mechanical, automobile and electronic industries, silicon carbide and its materials are employed because of its thermal and mechanical properties but nano-sized silicon carbide is not applied due to its processing techniques. Since high energy ball milling is a low-cost technique, it is recommended to deploy in industries to improve the mechanical and thermal properties of materials.

References

1. Wua Y, Kim GY, Anderson IE, Lograsso TA (2010) Fabrication of Al6061 composite with high SiC particle loading by semi-solid powder processing. Acta Mater 58:4398–4405
2. Ozdemir I, Ahrens S, Mucklich S, Wielage B (2008a) Nanocrystalline Al-Al_2O_3p and SiCp composites produced by high-energy ball milling. J Mater Process Technol 205(1–3):111–118
3. Li GW (2006) Bulk Al/SiC nanocomposite prepared by ball milling and hot pressing method. Trans Nonferrous Metals Soc China 16:398–401
4. Yang Y, Lan J, Li X (2004) Study on bulk aluminium matrix nano- composite fabricated by ultrasonic dispersion on nano sized SiC particles in molten aluminium alloy. Mater Sci Eng-A 380:378–383
5. Beffort O, Long S, Cayron C, Kuebler J, Buffat PA (2007) Alloying effects on microstructure and mechanical properties of high volume fraction SiC-particle reinforced Al-MMCs made by squeeze casting infiltration. Compos Sci Technol 67(3–4):737–745
6. Ozdemir I, Ahrens S, Mucklich S, Wielage B (2008b) The production of ultra fine grained Al-SiCp composites produced via high energy ball milling. Prakt Met 45(3):136
7. Park JJ, Choe HJ, Hong SM, Lee MK, Rhee CK (2012) Synthesis of Ni–Y_2O_3 nanocomposite powders by a very high speed planetary milling process: micro structural development and refinement behaviour. Powder Technol 230:139–144
8. Lopez B, Martinez Franco E, Zoz H, Trapaga-Martinez L (2011) Structural evolution of Ni–20Cr alloy during ball milling of elemental powders. Revista Mexicana De Física 57:176–s183
9. Suryanarayana C (2001) Mechanical alloying and milling. Prog Mater Sci 46:1–184

10. Saravanan MS, Sivaprasad K, Susila P, Babu SK (2011) Anisotropy models in precise crystallite size determination of mechanically alloyed powders. Phys B 406:165–168
11. Mohanasundaram N, Dhanavel D, Subramanian R, Nazirudeen MS, Ramakrishnan SS (1996) Production of aluminum silicon carbide particulate composites by powder metallurgy route. J Metal Mater Trans 77:57–59
12. Ling CP, Bush MB, Perera DS (1995) The effect of fabrication techniques on the properties of Al–SiC composites. J Mater Process Technol 48:325–331
13. Shorowordi KM, Laoui T, Haseeb A, Celis JP, Froyen L (2003) Microstructure and interface characteristics of B_4C, SiC and Al_2O_3 reinforced Al matrix composites: a comparative study. J Mater Process Technol 142(3):738–743
14. Cheng NP, Zeng SM, Liu ZY (2008) Preparation, microstructures and deformation behavior of SiCP/6066Al composites produced by PM route. J Mater Process Technol 202(1–3):27–40
15. Suryanarayana C (2008) Recent developments in mechanical alloying. Rev Adv Mater Sci 18:203–211
16. Sebastian V, Lakshmi N, Venugopalan K (2007) Evolution of magnetic order in mechanically alloyed Al–1 at% Fe. J Magn Magn Mater 309:153–159
17. Fang Q, Kang Z (2015) An investigation on morphology and structure of Cu–Cr alloy powders prepared by mechanical milling and alloying. Powder Technol. 270:104–111
18. Suryanarayana C, Ivanov E, Boldyrev VV (2001) The science and technology of mechanical alloying. Mater Sci Eng A 304–306:151–158
19. Shiau FS, Fang TT, Leu TH (1998) Effects of milling and particle size distribution on the sintering behavior and the evolution of the microstructure in sintering powder compacts. Mater Chem Phys 57:33–40
20. Wang J (2008) Mechanical alloying of amorphous Al–SiO2 powders. J Alloys Compd 456:139–142
21. Swamy V, Dubrovinskaya N, Dubrovinsky L (1999) High-temperature powder X-ray diffraction of yttria to melting point. J Mater Res 14:456–459
22. Torralba JM, Fuentes Pacheco L, Garcia Rodriguez N, Campos M (2013) Development of high performance powder metallurgy steels by high-energy milling. Adv Powder Technol 24:813–817
23. Meyers MA, Mishra A, Benson DJ (2006) Mechanical properties of nanocrystalline materials. Prog Mater Sci 51(4):427–556
24. Bahrami AH, Sharafi S, Baghbaderani HH (2013) The effect of Si addition on the microstructure and magnetic properties of Permalloy prepared by mechanical alloying method. Adv Powder Technol 24(1):235–241
25. Utriga Filho SL, Rodriguez R, Eartman JC, Lavernia EJ (2003) Powder metallurgy-metal matrix composites-synthesis of diamond reinforced Al-Mg nano crystalline composite powder using ball milling. Mater Sci Forum 416–418:213–218
26. Thakur PY, Ram MY, Dinesh PS (2012) Mechanical milling: a top to down approach for the synthesis of nanomaterials and nanocomposite. Nano Sci Nanotechnol 2(3):22–48
27. Lan J, Yang Y, Li X (2004) Microstructure and microhardness of SiC nano particles reinforced magnesium composites fabricated by ultrasonic method. Mater Sci Eng-A 386:284–290.28
28. Koohkan R, Sharafi S, Shokrollahi H, Janghorban K (2008) Preparation of nanocrystalline Fe–Ni powders by mechanical alloying used in soft magnetic composites. J Magn Magn Mater 320:1089–1094
29. Nishisawa T, Ishida K (1983) The Co (cobalt) system. Bull Alloy Phase Diagram 4(4):387–390
30. Schaffer B, Sercombe TB, Lumley RN (2001) Liquid phase sintering of aluminium alloys. Mater Chem Phys 67:85–91
31. Wan-li G (2006) Bulk Al/SiC nanocomposite prepared by ball milling and hot pressing method. Trans Nonferrous Metals Soc China 16:398–401

Advanced Bidirectional Switches-Based Three-Phase to N-Phase High-Power Impedance Source Matrix Converter

S. Manivannan, N. Shankar, A. Santhoshkumar, P. Selvabharathi, and N. Saravanakumar

Abstract The highly efficient three-phase into five-phase impedance source matrix converters used by gallium nitride (Ga-N) bidirectional switches with high-current and high-breakdown voltage are validated. The dual-gate Ga-N switches act as a single device bidirectional switch; whereas, a traditional bidirectional switch is made up of four modules with two insulated-gate bipolar transistors (IGBTs) and two diodes. Improving system efficiency including the implementation of the insulated gate allows small on-state opposition with secure, current collapse-free operation. The manufactured switches having the capabilities of breakdown voltage of 1340 V and the peak drain current exceeds 100 A are used to develop a three-phase to five-phase impedance source matrix converter which displays a maximum transformation effectiveness of 98% at 1 kW amount produced power with the expectancy that the high-current device can achieve a maximum output power of 10 kW or more. Furthermore, the Ga-N bidirectional switches are likewise free for current conduction commencing voltage balances so that the Ga-N-based matrix converter allows for unimportant size and extremely efficient AC/AC power transformation. So this paper presented the performance of highly efficient three-phase into five-phase impedance source matrix converters used by gallium nitride (Ga-N) bidirectional switches with high-current and high-breakdown voltages.

Keywords AC/AC power transmission · Breakdown voltage · Ga-N · Bidirectional switch · Impedance source · Matrix converter

S. Manivannan (✉) · N. Shankar · A. Santhoshkumar · P. Selvabharathi
Department of Electrical and Electronics Engineering, Bannari Amman Institute of Technology, Sathyamangalam, Erode, Tamil Nadu 638401, India
e-mail: manivannans@bitsathy.ac.in

N. Saravanakumar
Department of Electronics and Communication Engineering, Dr.Mahalingam College of Engineering and Technology, Pollachi, Coimbatore, Tamilnadu 642003, India

G. Kumaresan et al. (eds.), *Advances in Materials Research*, Springer Proceedings in Materials 5, https://doi.org/10.1007/978-981-15-8319-3_92

1 Introduction

Matrix converters were probable to be the most resourceful AC/AC power transformation topology since single-stage renovation could decrease various operating sufferers in conventional AC/DC/AC double-stage translation. The utmost serious module in a matrix converter is a bidirectional switch made up of two insulated-gate bipolar transistors (IGBTs) and fast recovery diodes (FRDs) series and anti-parallel connection [1]. The whole dimension of the manifold devices is larger in the conventional bidirectional switch, as well as the forward and reverse conductions are affected by the on-state voltage compensation. These drawbacks are the consequence in reducing the size of the system and the operating loss [2].

The bidirectional switch based on gallium nitride (Ga-N) with double gates was planned as a feasible answer to the aforementioned problems. At very compact matrix converters, monolithic addition of manifold bidirectional adjustments packed with sequestered gate motorists has also been projected [3]. However, in a small chip, the expedient can only grip low power so that the attainable productivity control remains low and the combined expedient is not suitable for everyday use [4]. In this broadside, highly effective action of three-phase to five-phase (3×5) impedance source matrix converters is established by means of Ga-N bidirectional alterations with the extraordinary extreme drain current (I_{max}) of 100 A and the interruption voltage of 1340 V. The on-state opposition (R_{on}) is concentrated miserable to 42 mΩ. The Ga-N-based matrix converter can reach the productivity influence over 10 kW or more by the high-current device and thus very capable of forthcoming compacted and highly well-organized AC/AC power renovation systems [5].

2 Ga-N-Based Bidirectional Switch Characteristics

Figure 1 shows the path illustration of a 3×5 impedance source matrix converter in which fifteen bidirectional adjustments are used. The comprehensive formation of the apparatuses for a bidirectional modification is also exposed in Fig. 2. Just unique single Ga-N scheme with dual entries allows the bidirectional switch, while the traditional one requires a maximum of four expedients with two IGBTs and two FRDs [6]. Figure 3 displays the fabricated Ga-N bidirectional switch's schematic cross section. In order to condense on-state resistance and beginning voltage variance over the broad wafer, settled gates created by p-Ga-N/i-Al-Ga-N regrowth method are implemented [7].

Figure 2 displays the Ga-N switch's current–voltage (I-V) characteristics for three gate bias situations [8]. The three I-V curvatures are the operating modes essential for three different matrix converters. The R_{on} is condensed down to 42 mΩ organized with the I_{max} of 100 A as revealed in Fig. 4. The interruption voltage is enlarged to 1340 V by growing the buffer depth on Si substrate as exposed in Fig. 4.

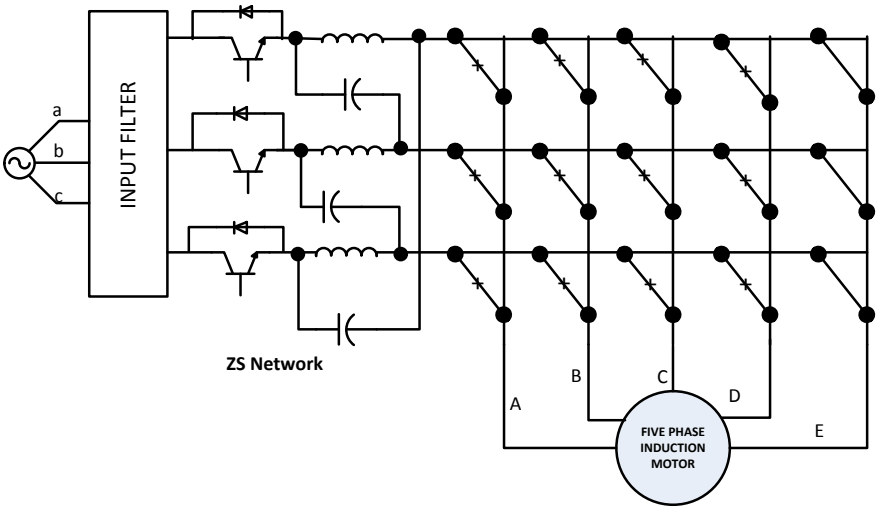

Fig. 1 Circuit diagram of 3 × 5 matrix converter with fifteen bidirectional switches

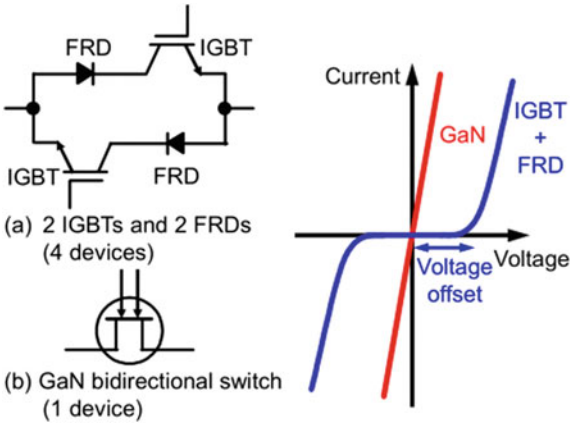

Fig. 2 Arrangements and I-V appearances of Ga-N and IGBT built bidirectional switches

The interruption voltage here is completely augmented to withstand the amplified input voltage besides the unwanted overvoltage induced by the inductive consignment action between the terminals. Adjustment operation as if a diode with opposite obstructive volume is mandatory as portion of the switching arrangement as exposed in Fig. 4. It is likewise well known that the current breakdown in which the R_{on} is enlarged after in height operating voltage is completely eradicated by improving the system structure and storage in the manufactured Ga-N switch [8].

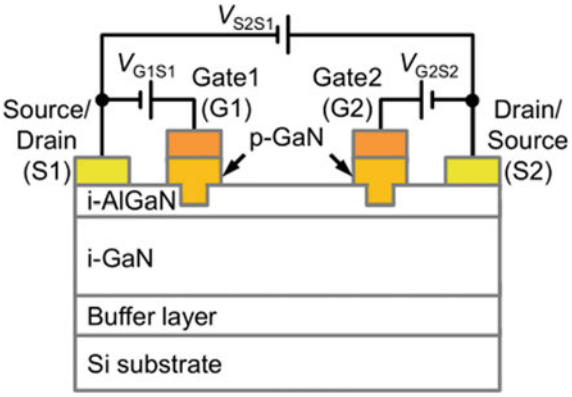

Fig. 3 Representation cross sections of Ga-N bidirectional adjustment with dual-gate construction

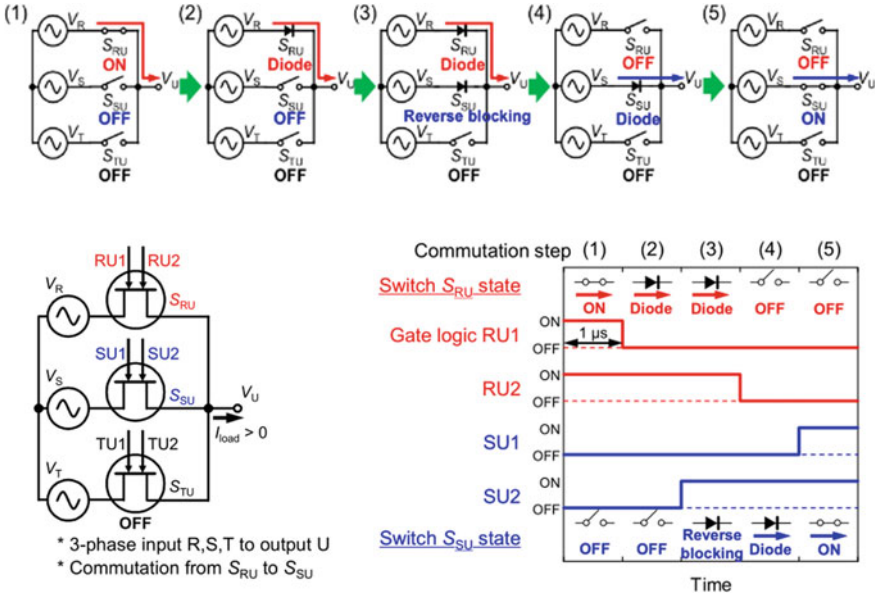

Fig. 4 Regulator arrangements of current commutation for Ga-N bidirectional switches

3 High-Power Ga-N 3 × 5 Impedance Source Matrix Converter

The switching arrangement of the gate controller must be judiciously considered to avoid the unwanted open/short circuits between the switches in that Ga-N 3 ambient matrix converter [10]. The current Ga-N matrix converter switching strategy is brief in Fig. 4. For a single-phase output, three modifications are a sole set, where first one switch requests to be on. To switch the on-state alteration to the further,

antithesis diode spoiling mode must be introduced as revealed in Fig. 4. As exposed in Fig. 4 rotating on solitary, a single gateway of the Ga-N switch permits the contrary obstructive diode manner that is desirable for the commutation [11].

Instantaneous turn-on and turn-off for together Ga-N bidirectional switch gates allow for both on-state and off-state strategies. As a consequence, the switching approach is applied by location gate control arrangements with a 1 μs switching step. Figure 5 shows a picture of the control pulse generated for impedance source matrix converter Ga-N 3, where fifteen sets of bidirectional Ga-N changes and gate pouring circuits are riding on a single-circuit board. For the impedance source matrix converter, a three-phase, 230 V, 50 Hz AC voltage is smeared. Matrix converter connected to resistive and inductive (RL) loads of 5.5–45.5 mH and 1.2 mH, respectively, with production frequencies and exporter frequencies of 50 Hz and 10 kHz [9–11].

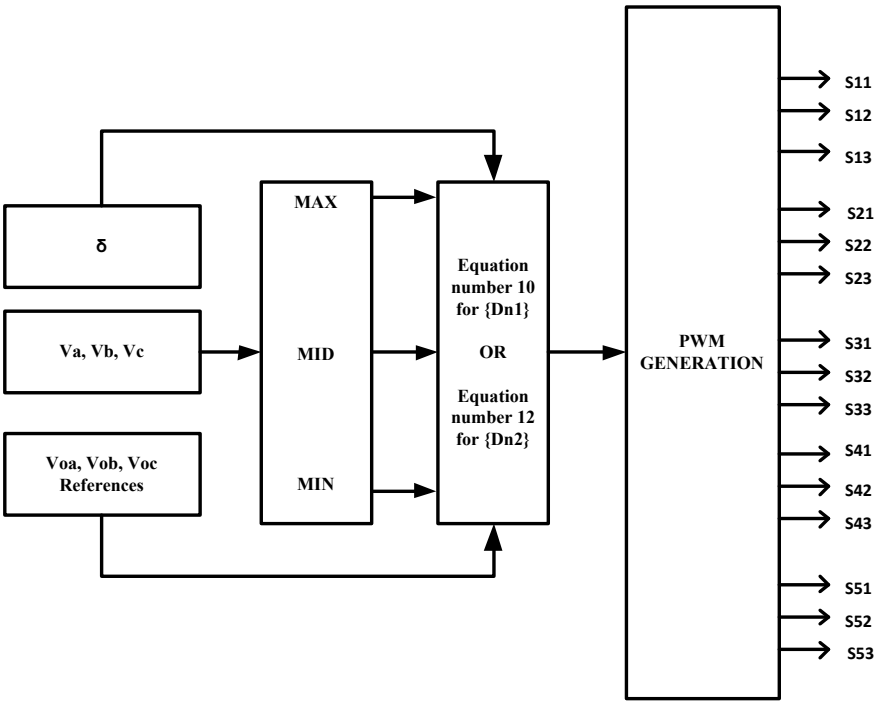

Fig. 5 Gating pulse generation for 3 × 5 impedance source matrix converter

4 Hardware Implementation and Output Discussion

Figure 4 summarizes the functioning waveforms, calculated functioning productivities and sufferers for different productivity power. Here, at the productivity supremacy of 1 kW, the peak conversion efficiency exceeds 98%, which is expressively developed than that of the IGBT-based matrix converter [12].

Figure 5 shows gating pulse generation for 3 × 5 impedance source matrix converter.

$$D_{n1} = \frac{\mathrm{MAX}(V_A, V_B, V_C) - V_{\mathrm{on}}^*}{\Delta + \delta(\mathrm{MID}(V_A, V_B, V_C) - \mathrm{MIN}(V_A, V_B, V_C))} \tag{1}$$

$$D_{n2} = \frac{\delta.\Delta + (\mathrm{MID}(V_A, V_B, V_C) - V_{\mathrm{on}}^*)}{\delta.\Delta + (\mathrm{MID}(V_A, V_B, V_C) - \mathrm{MIN}(V_A, V_B, V_C))} \tag{2}$$

Equations 1 and 2 are used to generate the duty ration and pulses for matrix converter. Figure 6 represents hardware implementation model for proposed 3 × 5 impedance source matrix converter. It shows all the basic components required to develop the prototype model of 3 × 5 impedance source matrix converter [13].

Figure 7 shows the three-phase input given to the 3 × 5 impedance source matrix converter. The magnitude voltage of 100 V is set in the input side. Figure 8 shows the five-phase output getting from the output stations of the 3 × 5 impedance foundation

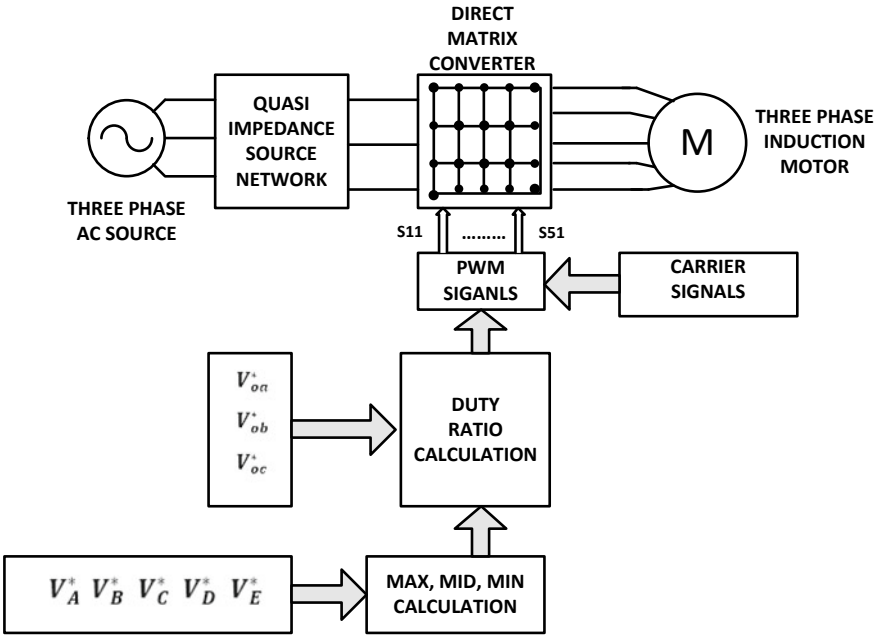

Fig. 6 Hardware implementation model for proposed 3 × 5 impedance source matrix converter

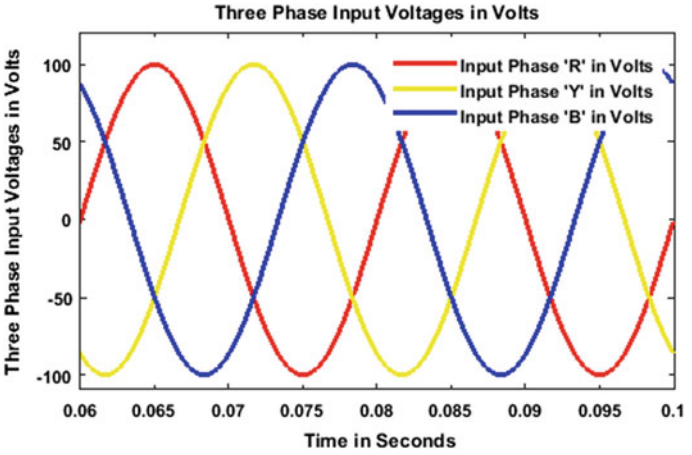

Fig. 7 Three-phase input given to the 3 × 5 impedance source matrix converter

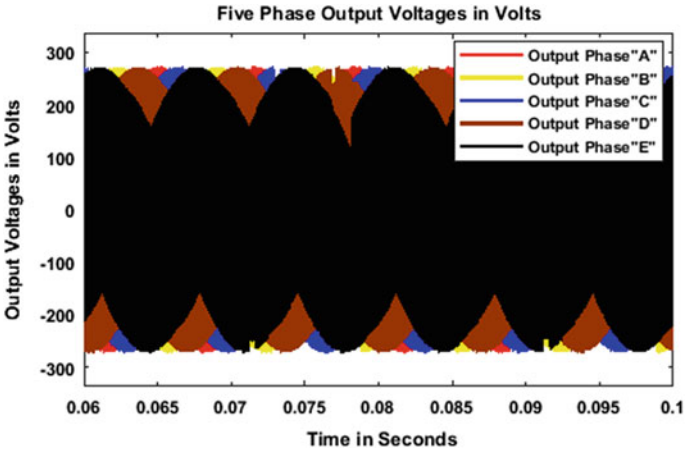

Fig. 8 Five-phase output getting from the output terminals

matrix converter. The production voltage is approximately 270 V with modulation index of 0.866. Figure 9 shows the shoot through signals generation for 3 × 5 impedance source matrix converter [14].

Figures 10 and 11 display the thorough operating loss study for both matrix converters based on Ga-N and IGBT. The resulting functioning loss is decreased by nearly partial in the IGBT-based Ga-N-based matrix converter, where the conductive loss is melodramatically abridged by increasing on-state confrontation and eliminating onward voltage counterbalance from Ga-N campaigns [15]. While the engaged Ga-N adjustments with the R_{on} of 42 mΩ, the I_{max} of 100A and the collapse voltage of 1340 V would establish the 3 × 5 matrix converter with advanced productivity

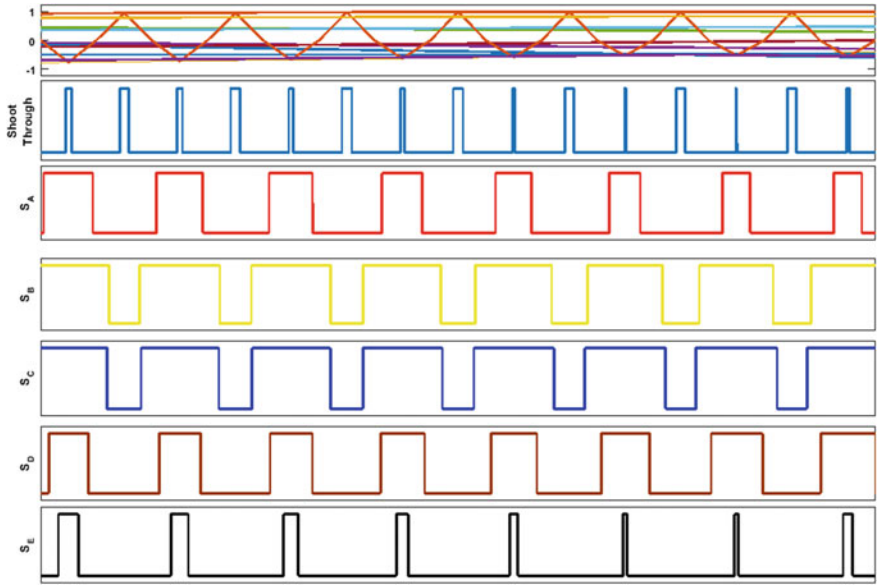

Fig. 9 Shoot through signals generation for 3 × 5 impedance source matrix converter

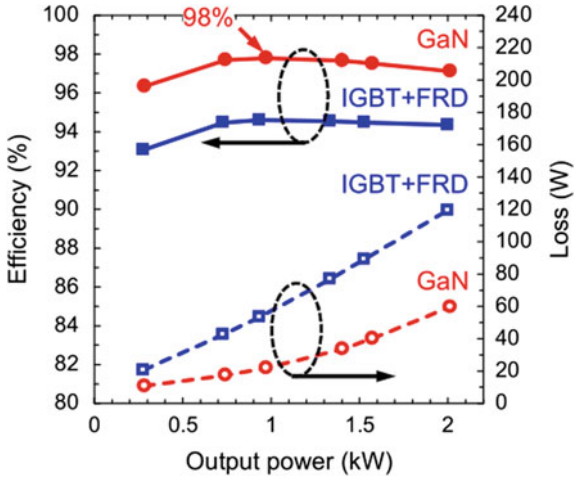

Fig. 10 Restrained adaptation efficacies and sufferers for various output power

power in the choice of 10 kW or more, the dimensions are just up to 2 kW since of the restraint of the quantity setup [16, 17].

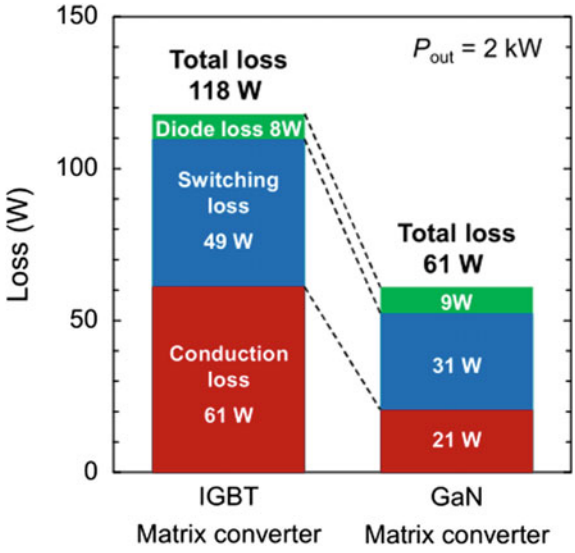

Fig. 11 Comprehensive analysis of the functioning loss for Ga-N-based and IGBT-based matrix converters at the productivity supremacy of 2 kW

5 Conclusions

This paper demonstrates the effective process of 3 × 5 impedance source matrix converters using Ga-N bidirectional adjustments. The Ga-N difference with dual entries allows bidirectional procedure with low R in conjunction with converse hindering diode method operation. By improving the device structure and processing, the I_{max} influences 100 A organized with the interruption voltage of 1340 V. The manufactured matrix converter Ga-N 3 befits the maximum operational proficiency at 1 kW productivity supremacy of 98 percent. The high-current Ga-N adjustments are capable of achieving extraordinary productivity power in the 10 kW assortment, of which the untried authorization remainders as a forthcoming work. This specifies that for compressed and effectual AC/AC power adaptation, Ga-N bidirectional switches are very promising. This paper presented the performance of highly efficient three-phase into five-phase impedance source matrix converters used by gallium nitride (Ga-N) bidirectional switches with high-current and high-breakdown voltages.

References

1. Wheeler PW, Rodriguez J, Clare JC, Empringham L, Weinstein A (2002) Matrix converters: a technology review. IEEE Trans Ind Electron 49(2):276–288
2. Morita T, Yanagihara M, Ishida H, Ishida M, Kaibara K, Matsuo H, Uemoto Y, Ueda T, Tanaka T, Ueda D (2007) 650 V, 3.1 mΩ cm^2 GaN-based monolithic bidirectional switch using normally-off gate injection transistor. In: International electron devices meeting (IEDM), pp 865–868

3. Nagai S, Yamada Y, Negoro N, Handa H, Kudoh Y, Ueno H, Ishida M, Otsuka N, Ueda D (2014) A GaN 3 × 3 matrix converter chipset with Drive-by-Microwave technologies. In: International solid-state circuits conference (ISSCC), pp 15–17 (2014)
4. Kaneko S, Kuroda M, Yanagihara M, Ikoshi A, Okita H, Morita T, Tanaka K, Hikita M, Uemoto Y, Takahashi S, Ueda T (2015) Current-collapse-free operations up to 850 V by GaN-GIT utilizing hole injection from drain. In International symposium on power semiconductor device sand ICs (ISPSD), pp 41–44
5. Okita H, Hikita M, Nishio A, Sato T, Matsunaga K, Matsuo H, Mannoh M, Uemoto Y (2016) Through recessed and regrowth gate technology for realizing process stability of GaN-GITs. In International symposium on power semiconductor devices and ICs (ISPSD), pp 23–26
6. Fedyczak Z, Szczesniak P (2012) Matrix-reactance frequency converters using an low frequency transfer matrix modulation method. Electr Power Syst Res 83(1):91–103
7. Szcześniak P (2014) A static and dynamic model of a space vector modulated matrix-reactance frequency converter. Electr Power Syst Res 108:82–92
8. Ge B, Lei Q, Qian W, Peng FZ (2012) A family of Z-source matrix converters. IEEE Trans Ind Electron 59(1):35–46
9. Lei Q, Peng FZ, Ge B (2012) Pulse-width-amplitude-modulated voltage-fed quasi-Z-source direct matrix converter with maximum constant boost. In: Twenty-seventh annual IEEE applied power electronics conference and exposition (APEC), pp 641–646
10. Liu S, Ge B, Abu-Rub H, Peng FZ, Liu Y (2012) Quasi-Z-source matrix converter based induction motor drives. In: IECON 2012—38th Annual conference on IEEE industrial electronics society, pp 5303–5307
11. He L, Duan S, Peng F (2013) Safe-commutation strategy for the novel family of quasi-Z-source AC–AC converter. IEEE Trans Ind Inform 9(3):1538–1547
12. Alesina A, Venturini M (1981) Solid-state power conversion: A Fourier analysis approach to generalized transformer synthesis. IEEE Trans Circ Syst 28(4):319–330
13. Alesina A, Venturini MGB (1989) Analysis and design of optimum-amplitude nine-switch direct AC–AC converters. IEEE Trans Power Electron 4(1):101–112
14. Correa P, Rodríguez J, Rivera M, Espinozav JR, Kolar JW (2009) Predictive control of an indirect matrix converter. IEEE Trans Ind Electron 56(6):1847–1853
15. Vargas R, Rodriguez J, Ammann U, Wheeler PW (2008) Predictive Current control of an induction machine fed by a matrix converter with reactive power control. Ind Electron IEEE Trans 55(12):4362–4371
16. Rivera M et al (2013) A simple predictive current control of a single-phase matrix converter. In: 2013 Fourth international conference on power engineering, energy and electrical drives (POWERENG), vol 5, pp 235–239
17. Toledo S, Rivera M, Rodas J, Comparatore L (2016) Predictive current control with reactive power minimization in six-phase wind energy generator using multi-modular direct matrix converter, pp 0–3

Design Implementation and Evaluation of Password Protected Circuit Breaker for Reliable Power System Protection and Maintenance

S. Manivannan, S. Sudhahar, G. M. Oorappan, K. Rajalashmi, and N. Saravanakumar

Abstract Password-based circuit breaker is a blueprint that empowers us in controlling the electrical lines with the help of password. This project gives this problem to ensure line safety. In this project, the schedule is done along these lines that the lineman is free to control the electrical line by entering the password to ON/OFF the electrical line. To achieve this, we have made use of PIC16F877A microcontroller. This microcontroller is one of the most eminent microcontrollers because of its flash memory technology which makes the write–erase process done as many times as possible. Also this plays a major role in digital electronic circuits. To develop the password-based circuit breaker to reduce the number of accidents to linemen in their working field, lineman has to do the task by turning ON/OFF.

Keywords Circuit breaker · Microcontroller · Lineman · Digital circuits · Password · Digital electronics

1 Introduction

The major challenge faced by the electric board is the increasing accident rates at level crosses. Due to increase in fatal death of lineman working in electric area, we

S. Manivannan (✉) · K. Rajalashmi
Department of Electrical and Electronics Engineering, Bannari Amman Institute of Technology, Sathyamangalam, Erode, Tamil Nadu 638401, India
e-mail: manivannans@bitsathy.ac.in

S. Sudhahar
Department of Electronics and Instrumentation Engineering, Bannari Amman Institute of Technology, Sathyamangalam, Erode, Tamil Nadu 638401, India

G. M. Oorappan
Department of Mechatronics Engineering, Bannari Amman Institute of Technology, Sathyamangalam, Erode, Tamil Nadu 638401, India

N. Saravanakumar
Department of Electronics and Communication Engineering, Dr. Mahalingam College of Engineering and Technology, Pollachi, Coimbatore, Tamil Nadu 642003, India

G. Kumaresan et al. (eds.), *Advances in Materials Research*, Springer Proceedings in Materials 5, https://doi.org/10.1007/978-981-15-8319-3_93

have one up with this idea [1]. This project does not allow to control the circuit to be located in the working field ensuring to minimize the fatal accidents occurring with the linemen in the working field. The system's control will be provided only to the linemen working on that area in his substation. To develop the password-based circuit breaker to reduce the number of accidents to linemen in their working field [2], lineman has to do the task by turning ON/OFF the loads with the help of a password. Since the control of the switches is in the hand of the linemen itself, there is no chance of accidents occurring. The main aim is to develop the password-based circuit breaker to reduce the number of accidents to linemen in their working field. Lineman has to do the task by turning ON/OFF the loads with the help of a password [3, 4].

2 Components Requirements for Reliable Power System Protection

2.1 IC16F877A Controller

PIC16F877A is an advanced controller produced by microchip technology. Its maximum operating frequency is 20 Hz, and the data memory is of 368 bytes. The ascendancy of this controller is that it uses flash memory technology that it can be readable and writable as many times as possible [5]. Pin configurations have total of 40 pin which includes 33 I/O pins. This controller is widely used because of its availability, cost efficiency, and quality.

2.2 877A Baseboard

The PIC16F877A baseboard is used to assess and reveal the capability of microchip microcontroller. This board is developed for general-purpose applications and to exercise variety of microcontroller peripherals [6]. The MCU socket on the board proffer supports for 40 pin DIP package of PIC16F877A controller. It is used for training and development purpose. It is designed to facilitate on-board programmer for PIC controller through ISP on universal serial port. The bridge rectifier in it permits this board to be powered with both AC and DC power supply adapters. Reset switches, user switches for input and output and port extension for all five ports [7].

Fig. 1 Keypad for input

*2.3 Keypad (4 * 3)*

Keypads are required to take user inputs to perform specific functions as shown in Fig. 1. Pads mostly containing numbers are called a numeric keypad. Many devices follow the standard for their arrangement [8].

A matrix keyboard contains set of switches and push buttons which are placed as rows and columns in the form of a matrix. The interfacing of matrix keypad is quite simple as they can be connected in many ways, but the only thing is that the rows are inputs and the columns are outputs. So, it is acceptable to read which key is pressed, and the column is made low one by one and then to read the columns.

2.4 LCD Display

The technology of LCD is used for displays in notebook and other smaller digital electronic applications as shown in Fig. 2. Through technologies like LEDs and gas plasma, LCDs allow displays to be much slimmer than technology of cathode ray tube [9]. Power required by LCDs is much less than light-emitting diode and displays of gas display since the working principles based on the blocking of light rather than dissipating it.

Fig. 2 LCD display for indicating position of circuit breakers

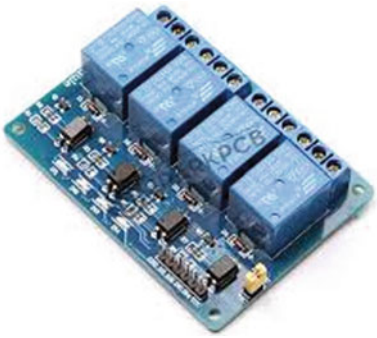

Fig. 3 Relay board for executing operation

2.5 Relay Board

A relay is an electrical switch shown in Fig. 3. Generally, these terms are used for cables using a power plug to make a connection with an alternating current of single-phase power source at the line voltage of local area. A zip cord is a weightless, not grounded, two wire which is insulated singly is a cord needed for small loads such as a floor or table light [10]. Sets of cord are separable from both the power supply and the electrical equipment and comprise a cord which is flexible with electrical connectors at the ends, one female, and one male. Finally, one end of the cord set is attached to a molded electrical plug.

2.6 Power Supply Board

The first performance of an influence is provided to convert electrical phenomenon from a supply to the right voltage, current, and frequency to power the load. As a result, power providers are typically remarked as power converters. Some power provides are separate stand-alone items of kit; whereas, others are designed into the load appliances that the power completely different functions and that power

Fig. 4 Power cord for providing power supplies to the relay circuits

provided may perform embody limiting this drawn by the load to safe levels, move off this inside the event of academic degree electrical fault, power learning to forestall electronic noise. A zip cord is a weightless, not grounded, two wire which is insulated singly and is a cord needed for small loads such as a floor or table light [11].

2.7 Power Cord

A mains cable or power cords an electrical wire that connects temporarily the mains electricity supply to an appliance through a wall sockets shown in Fig. 4. Generally, these terms are used for cables using a power plug to make connection with an alternating current of single-phase power source at the line voltage of local area [12]. A zip cord is a weightless, not grounded, two wire which is insulated singly and is a cord needed for small loads such as a floor or table light. Sets of cord are separable from both the power supply and the electrical equipment and comprise a cord which is flexible with electrical connectors at the ends, one female, and one male. Finally, one end of the cord set is attached to a molded electrical plug.

2.8 Insulation Tape

Electrical tape or insulating tape may be a sort of pressure-sensitive tape accustomed insulates electrical wires and alternative materials that conduct electricity. It is manufactured from several plastics; however, vinyl is most well-liked, because it stretches well and provides a good and long-lasting insulation. Electrical tape for sophistication of H insulation is formed of covering material [13].

2.9 Connecting Wires

Connecting wires permit associate electrical current to travel from one purpose on a circuit to a different as a result of electricity wants a medium through that it will

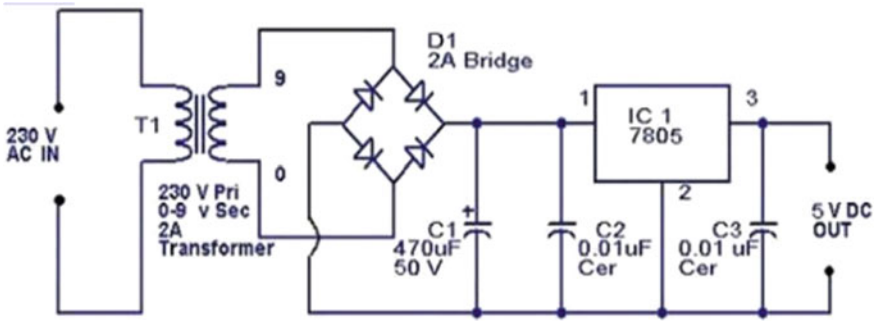

Fig. 5 Power supply

move. Most of the connecting wires area unit is created from copper or aluminum. Copper is an affordable and smart physical phenomenon. Rather than the copper, we will additionally use silver that has high physical phenomenon; however, it is too pricey to use [14].

2.10 MikroC PRO

MikroC PRO for PIC compiler coding—the software MikroC PRO for PIC is an advanced powerful tool for designing PIC programs, and it provides the programmer to develop easier and possible ways to develop many applications. It is used in various applications in C and also in other languages due to its efficiency and easier programming capability [15].

2.11 Power Supply

Microcontroller requires +5 V supply for its working as shown in Fig. 5. This is derived from 9 V transformer. 9 V transformer is connected to diode rectifier circuit, after converting AC to DC by using rectifier is 9 V DC is regulated to +5 V by using voltage regulator 7805. This +5 V supply is applied to microcontroller [16].

3 Working Password Protected Circuit Breaker for Reliable Power System Protection

Now let us see however the password protected circuit breaker works as shown in Fig. 6. First, once the ability is turned ON, the digital display displays a welcome

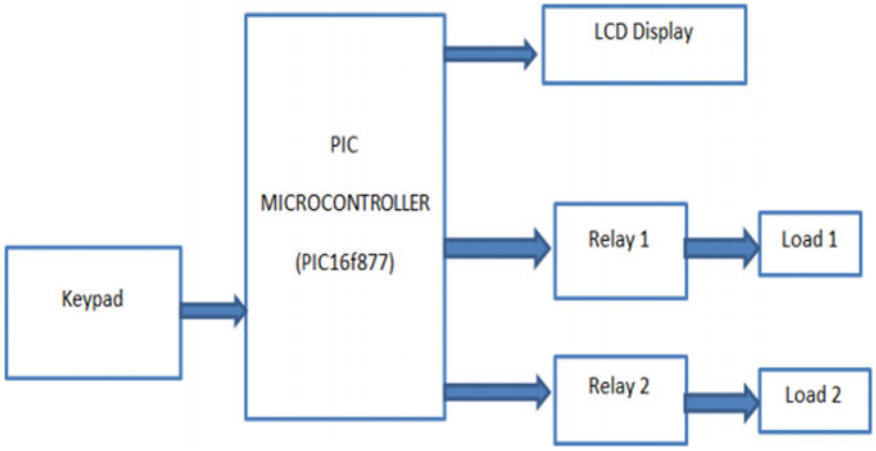

Fig. 6 Block diagram representation of password protected circuit breaker for reliable power system protection

screen and so asks you to enter the positive identification to unlock it. In our case, the positive identification is fastened, i.e., 1234. By mistreatment of the input device, positive identification is imputed, and as we tend to sort it the positive identification is seen on the digital display. If the incorrect positive identification is entered, it will show a wrong positive identification message and raise you to enter it once more.

When the right secret is entered, main screen of the breaker is opened. Currently, the standing of the four hundreds connected to the microcontroller square measure is shown on the alphanumeric display as *N* for on and *F* for off. By the assistance of the keyboard, after you press the specified button, the output goes to portal and activates the relay driver IC that successively switches the magnetic relay and so the load activates [17].

The applications are password-based electrical appliance control which can also be made using this. It can work on a single password. The password to operate can be changed. No other person can access the password is given into a system other than the person who had changed it as shown in Fig. 7. The advantages are it is a double fault protection, manually, it is a switchable mode, built in safety features to prevent spark ignition, very much effective and compact in nature. The disadvantages are harder and more costly to obtain high short-circuit interrupting capacities.

4 Result and Discussion

Refer the Annexure diagram, initialize all the inputs that are required to make the decision for protecting the human in the working place. Read the inputs and password from the input data logger. If the password is correct, then the control signals are

Fig. 7 Flowchart

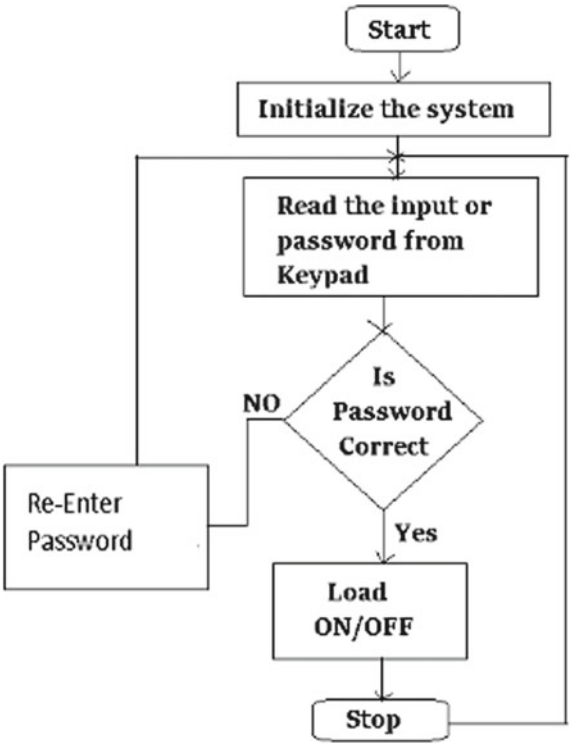

generated by the controller to operate the machine; otherwise, it once again reads the data and weight for the responses. Liken using this setup, the unwanted human error gets eradicated and system will run in smooth manner.

5 Conclusion

Security is the prime concern in our day-to-day life. Everybody desires to be the maximum amount as secure as potential. This method provides a brand new approach to secure the lifetime of a lineman. The word to work is often modified, and systems are often operated with efficiency with the modified word. No different person will close the circuit breaker once the changed password is given in the system apart from the one who had changed it. It provides no scope of password hacking. It provides safety to the lineman. This can be made more secured using EPROM in further development of the project. Electronic circuit breaker can be developed by interfacing it with GSM module and controlling via SMS.

Annexure

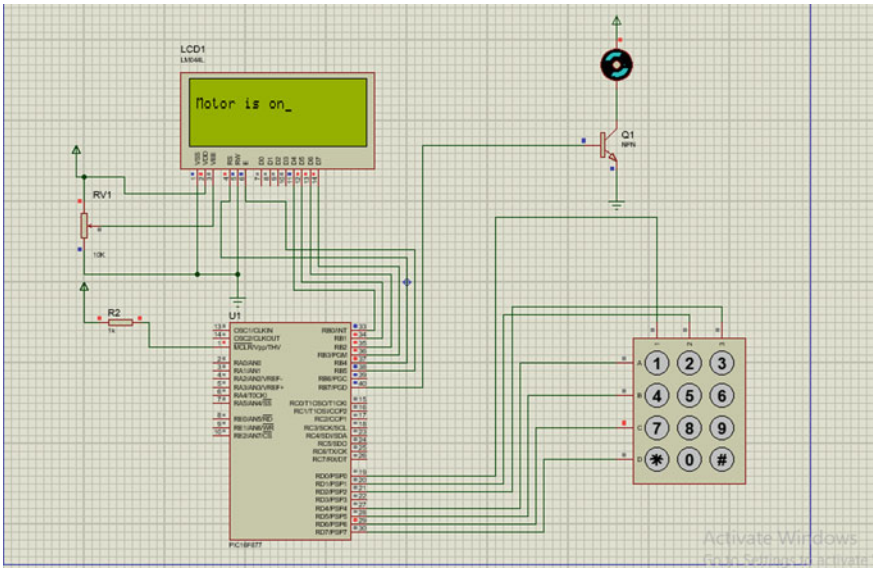

References

1. Veena (2015) Electric line man safety system with OTP based circuit breaker, vol 2. SR Engineering College
2. Mazidi MA, Mazid JG (1999) The Microcontroller and embedded system, 2nd edn. Person Education
3. Dr. Neelam Rup P (2014) Int. J. Eng. Trends Technol (IJETT) 13(3):261
4. Halpin M (2002) National code committee, vol 40, p 228
5. Sharma D, Major Goraga S (2015) Int J Curr Eng Sci Res (IJCESR) 2
6. Nair AP (2013): Electric line man safety system with OTP based circuit breaker, vol 4. BTC College of Engineering, Kerala
7. Del Toro V (1986) Electrical engineering fundamentals
8. Osepchuk JM (1996) IEEE Engineering in Medicine and Biology, vol 15, no 1, pp 116–120
9. Marne DJ (1997) National electrical safety code
10. Tasdighi M 2013) Inductive FCL's impact on circuit breaker's interruption condition during short-line faults. In: North American power symposium (NAPS), Issue 22–24
11. Matsumura T, Uchii T, Yokomiz Y (1997) Development of flux-lock type fault current limiter with high-Tc superconducting element. IEEE Trans Appl Supercond 7(2)
12. Solanki VP, Parmar AJ, Limbachiya NS, Koringa R, Patel S (2015) Arduino based protection system for wireman. Int J Electr Electron Res 3(1):76–79
13. Veena J, Srivani G, Afreen, Sunil Kumar M, Santhosh J, Subrahmanyam KBVSR (2015) Electric lineman protection using user changeable password based circuit breaker. Int J Curr Eng Sci Res 2(5):44–49 (2015)

14. Mahadik PN, Yadav PA, Gotpagar SB, Pawar HP (2016) Electric line man safety using micro controller with GSM module. Int J Sci Res Dev 4(1):205–207
15. Hassan Ali M (2015), Enhancement of a GSM based control system. Adva Circ Syst Signal Process Telecommun 189–202
16. Brooks DR (2016) Arduino-based dataloggers: hardware and software. 1(3)
17. Gibb M (2010) New media art, design, and the arduino microcontroller: a malleable tool. School of Art and Design, Pratt Institute, New York

Surface Texturing in Piston Ring Cylinder Liner Pair for Friction Reduction: A Review

S. Prakash, C. Sasikumar, S. Aravind, V. Mohan Prasath, and C. Udhayakumar

Abstract In most of the internal combustion engines (IC Engines) to increasing the efficiency, engineers are concerned with reducing the friction. As one of the options, when it comes to reducing engine friction power losses, piston ring cylinder liner (PRCL) assembly offers great potential. The texturing on the periphery has a main role in the PRCL to increases tribological performances. This paper covers the review of piston top compression ring and cylinder liners surface texturing about analytical and also the experimental work.

Keywords IC engine · Surface texturing · Cylinder liner · Piston ring · Engine friction

1 Introduction

The lubrication film thickness is very thin when the machine parts operate under boundary lubricating condition. When the thickness of the lubrication is minimum it will lead to dry contact or metal to metal contact. It also increases the friction losses in the engines [1]. In all type of IC Engines, 50% of the power loss occurs between cylinder liner and piston compression ring pair [2] and especially piston ring and cylinder liner pair consists of 5% of fuel consumption [3]. Now a day's many researchers focus on using surface texturing on cylinder liner and piston ring to improve the thickness of the lubrication system and introducing hydrodynamic lubrication to reduce the friction power loss in IC Engine.

References [4–6], reported the effect of texturing, the research people investigated the effect of dimples and perfect geometric arrangement for the surface texturing, analytically and experimentally, for the water-lubricated sealing ring applications. The load-carrying capacity of bearing is increased because of surface texturing and surface texturing in the solids modified frictional properties and reduces wear rate.

S. Prakash (✉) · C. Sasikumar · S. Aravind · V. Mohan Prasath · C. Udhayakumar
Department of Mechanical Engineering, Bannari Amman Institute of Technology, Sathyamangalam, Erode, Tamilnadu 638401, India
e-mail: prakashsedu@gmail.com

G. Kumaresan et al. (eds.), *Advances in Materials Research*, Springer Proceedings in Materials 5, https://doi.org/10.1007/978-981-15-8319-3_94

Shinkarenko et al. [7] develops a model to experimentally analyze the laser surface texturing (LST) for hydrodynamic lubrication. In the result, the aspect ratio is varied from 0.02 to 0.1 and they suggest suitable dimple density 3. Etsion and Sher [8] investigated and develops partial laser surface texturing on the top of piston ring. They found partial laser surface texturing piston ring reduces the fuel consumption upto 4% while comparing with the ordinary piston rings. Zhou et al. [9] created the theoretical model for finding the suitable parameters of cylinder liner for surface texturing. They suggested that suitable depth over diameter ratio is 0.1 at any operating condition. Kim et al. [10] experimentally investigated the effects of frictional behavior of brittle material like cast iron surfaces with surface texturing effects. And they found that dimple depth varies to diameter ratio 0.14 for the lower coefficient of friction than comparing with a depth over diameter ratio 0.3 and there are fewer researches in surface texturing about suitable designing model for piston ring and cylinder liner pairs [9, 10].

However, a small observation has been given to the working condition in piston compression ring and cylinder liner pair. The main aim of the present paper work is to summarize the analytical and experimental work of surface texturing which is the effect on the frictional behavior and friction reduction.

2 Background

2.1 Virtual Texturing

Identify the influential parameters of surface roughness by virtual texturing [11]. To analyze the texturing parameter like density, depth, diameter between the dimples or groves for the fine surface (average skewness $R_{sk} = 0.24$, surface roughness $R_a = 0.05$ μm, kurtosis $R_{ku} = 3.1$) values are altered, artificially forming indents. The virtually textured profiles are investigated with NIST SMATS soft gauge apparatus [12] and the surface roughness parameters were calculated for different geometries and different shape of textures.

2.2 Surface Texturing

Surface texturing is creating a defined surface features like dimples or grooves in the surfaces. Recently laser is used for creating surface texturing. By Laser surface texturing (LST) method we can make a surface texturing in different depth and different diameters. In contrast to surface textures, parameters like surface roughness is considered randomly and not characterized [13]. Surface texturing is used to increase the load-carrying capacity of the piston and improves the tribological behavior of top piston ring and cylinder liner pair.

3 Modeling of Surface Texture

3.1 Surface Texturing in Piston

Kligerman et al. [14] investigated in the top piston ring with a partial surface texturing. Figure 1 shows the piston ring with Laser surface texturing partially in the mid position of piston ring. Texturing can create in the entire position of the piston ring as shown in Fig. 2. Here W^* is the width of the piston ring and B is the textured zone axial length, x is the cylinder liner's axial direction, and z is piston ring circumferential direction. Partial LST segment is in Fig. 2. The texturing is distributed uniformly in the piston ring, Fig. 1a with a strip b_p, area density S_p and piston ring actual width W^*. Every dimple is designed symmetrically about its axis spherical with a radius r_p and sides of square cell is $2r_1 \times 2r_1$ in Fig. 1b.

$$\rho h_r \frac{\partial^2 c}{\partial t^2} = p_h - p_e \tag{1}$$

$$\frac{\partial}{\partial x}\left(h^3 \frac{\partial p}{\partial x}\right) + \frac{\partial}{\partial z}\left(h^3 \frac{\partial p}{\partial z}\right) = 6U\mu \frac{\partial h}{\partial x} + 12\mu \frac{\partial h}{\partial t} \tag{2}$$

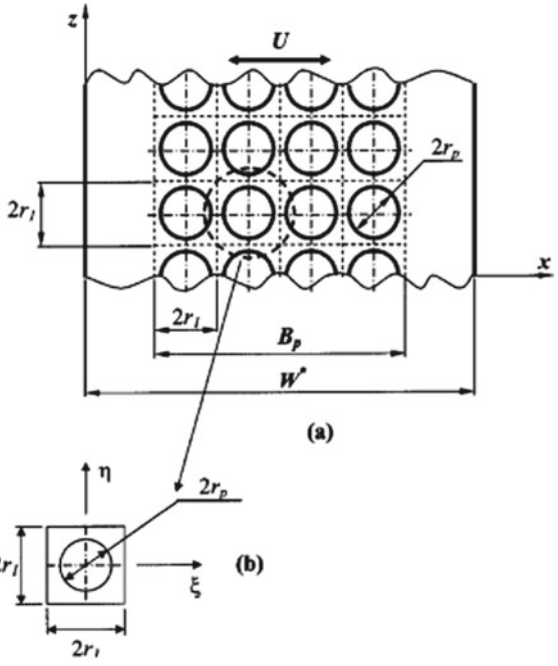

Fig. 1 **a** A textured surface model [14]. **b** A single dimple [14]

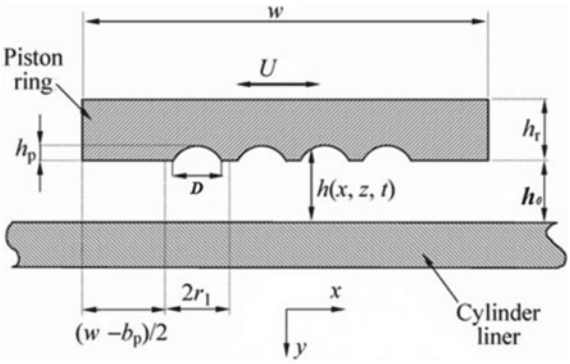

Fig. 2 Cylinder liner and piston ring [14]

where h represents the instantaneous local oil film thickness value, p is the instantaneous local hydrodynamic pressure, ρ is piston ring density and h_r is height. p_e and p_h are represents the total external pressure and instantaneous average hydrodynamic pressure values [15].

Tomanik [16] analyses the surface texturing on the top piston ring and cylinder bore and also partially on oil ring by using the simple mixed lubrication model. Comparison of flat shaped and barrel textured piston ring by reciprocating tests and engine operating conditions. Etsion and Sher [8] investigated experimentally by using a compression-ignition IC engine test bench as in Fig. 3. And they used partial textured ring and also measured composition of exhaust gases. A 2500 cm^3 naturally-aspirated four-cylinder Ford Transit Diesel engine without the exhaust gas retreatment with the surface textured piston ring and texturing was done on the top piston ring. The total engine was run 1800 h. And also the fuel consumption is measured periodically by a fuel container.

The composition of exhaust gas emissions was analyzed for HC, CO, O_2, CO_2 and NO_x with the help of SUN DGA-1000 device, and the engine smoke level was measured with the help of SUN DG8000 smoke-measuring device in opacity percentages [8]. References [10, 17] were used a pin-on-disk tribometer for friction tests. The strain gauges attached in the holder to measure frictional force [17].

Usman and Park [18] studied asymmetric piston ring and liner contact of textured piston ring. Solved 2D Reynolds equation with continuity equation, cavitation algorithm, and asperity interaction in the mixed lubrication, variable ring conformability, axial ring dynamics are also considered [18]. A simplified analytical 1D model of load-carrying capacity and the pressure distribution is used to analyze the load-carrying capacity of piston and ring with large radius of curvature and also a ring with a small radius is considered [19].

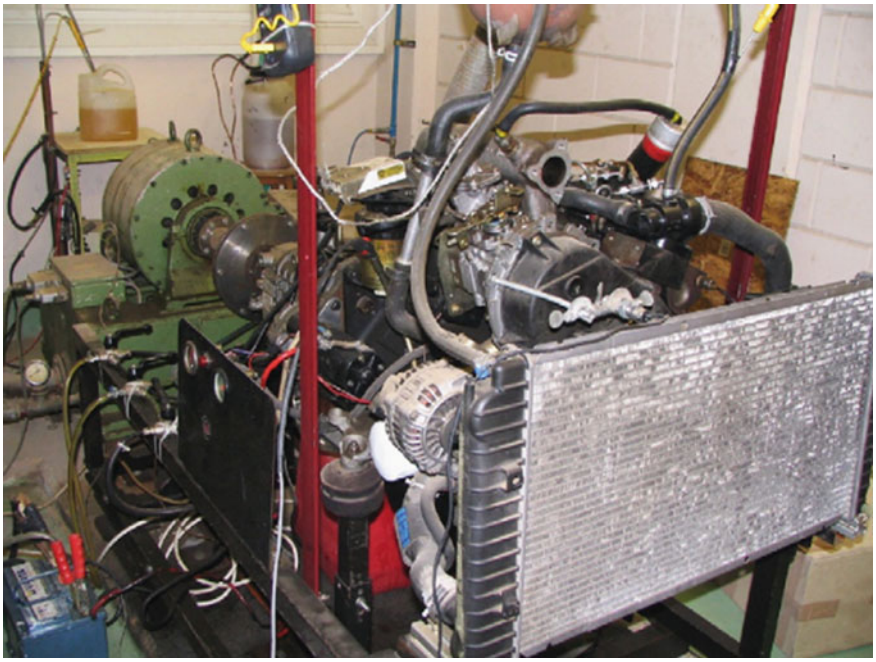

Fig. 3 Engine test bench picture [8]

3.2 Surface Texturing in Cylinder Liner

Guo et al. [20] investigated experimentally on a diesel engine setup. Created surface texturing (Dimples and grooves) on the cylinder liner fine surfaces with a two different diameters and different width of grooves shown in Fig. 4. Grabon et al [21] studied experimentally using reciprocating tester about the performance of honed cylinder liner surface by burnishing technique. The tribo system has stationary sample made

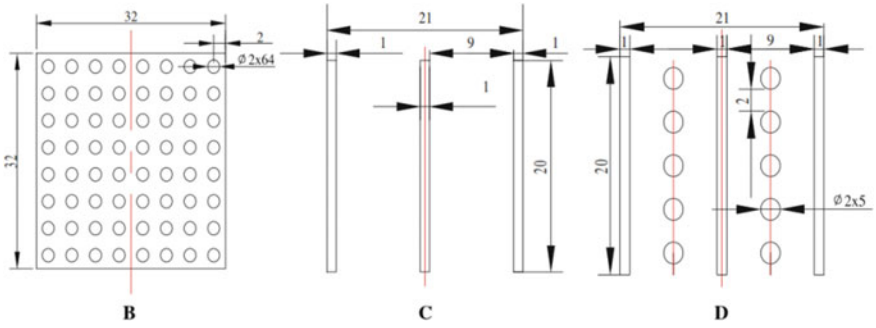

Fig. 4 Three types of cylinder liner [20]

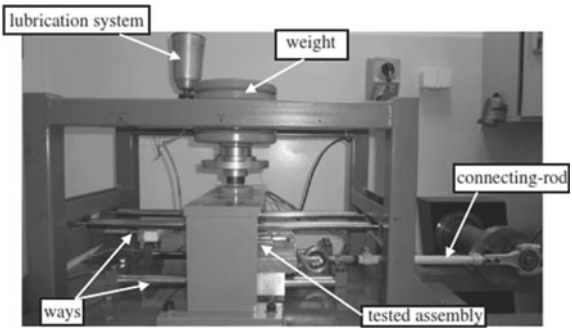

Fig. 5 Tribological tester [21]

by piston ring and cylinder liner performs reciprocating motion. Crankshaft assembly is used for changing the rotating movement into reciprocating movement [21].

V-belt transmission is driven by the electric motor with the transmission ratio of 1:2 was transmitted to crankshaft. Three average sliding speed is considered for friction test is shown in Fig. 5 and the average sliding speed as follows 0.44, 0.66 and 0.88 m/s [21]. Surface topography was done by the white light interferometer Talysurf CCI Lite and the height resolution is about 0.01 nm because wear sample was within the limit of original surface topography [21].

Noutary et al. [22] developed 2D analytical model of grooves with hatches and the result was compared with 1D analytical model. Author used code of multigrid [23] to solve the lubricating equation for the contact of cylinder liner–piston ring and compared analytical result with [19] one dimension model.

4 Result and Discussion

4.1 Surface Texturing in Piston Ring

Surface texturing can be measured from friction measurements. And the need for parametric analysis is to find the suitable parameters of surface texturing and also to analyze the engine operating conditions. Reference [14] suggested that optimum value dimensionless textured portion (γ) of the piston ring is 0.6.

Dimple diameter is not affecting the average friction force. The average friction force is decreasing when the increasing dimple density [14]. Minimum average friction force is less in partially textured piston ring compared to optimum fully textured ring [14]. Figure 6 shows the 30% of average friction force reduces in the narrow rings and 55% of average friction force reduces in the wide rings [14]. Tomanik [16] Investigation results show that higher oil film at the middle stroke and the reversal of piston because of hydrodynamic pressure generated in the micro dimples shown in Fig. 7. Because of high computational work for discretization the researcher was not considered full stroke of LST.

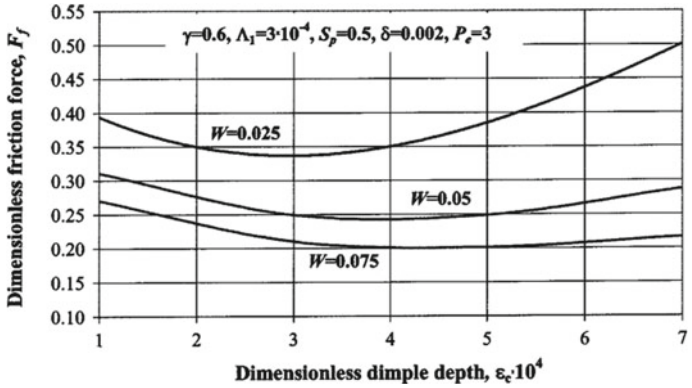

Fig. 6 Dimensionless friction force (Ff) versus Dimensionless dimple depth [14]

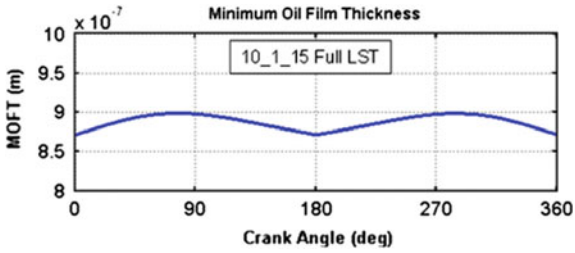

Fig. 7 Minimum oil film thickness versus crank angle [16]

LST on cylinder bore can easily generate the hydrodynamic support in the thin and oil compression ring lands and also reduce the wear, friction. Negligible effect by the barrel profile top ring of cylinder bore Laser surface texturing [16]. Dimple geometries like dimple diameter are about 100 μm and dimple depth is 10 μm cannot be applied on the oil control ring but small geometries LST can be applied on oil control ring. Partial LST can produce about 50% hydrodynamic support in top dead center and nearly 90% hydrodynamic support at middle stroke [16].

Etsion and Sher [8] used Cr-coated barrel-shaped untextured ring for the reference and the two different LST piston rings. Theoretical modeling suggested that optimum laser texturing parameters which gives the minimum friction. Laser is used for creating surface texturing and the LST texturing was not given significant changes in the engine emissions [8]. The changes of exhaust emissions were within the range of 2–5%. Figure 7 shows that fuel consumption reduces about 4% in the LST rings (Series 1: Barrel, coated chrome, baseline, series 2: Flat, chrome coated, and laser-treated, series 3: Flat and laser-treated, no chrome) [8] (Fig. 8).

Analytical results [19] showed that grooves with deep, dense, and wide have significant effects on the load-carrying capacity for piston rings with a small radius of curvature. Researcher suggested that groove location plays a major role in the pressure perturbation and the groove shape plays a secondary role [19].Investigation results [10] shows depth to diameter ratio of 0.14 with lower coefficients of friction

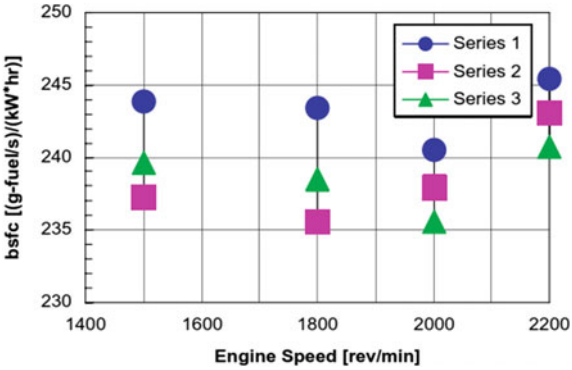

Fig. 8 Engine specific fuel consumption versus engine speed [8]

compared with a depth over diameter ratio of 0.30 and the results were validated with [24].

4.2 Surface Texturing in Cylinder Liner

Guo et al. [20] suggested that regular concave surface texture improves the operation condition of piston ring and cylinder liner pair. Concave surfaces with a depth to diameter ratio are 0.1 giving better lubrication compare with a depth-diameter ratio of 0.3. Grabon et al. [21] creates surface texture by burnishing method on honed cylinder liners. Average depths of oil pockets were 5 μ and its area, density of texture with oil pockets is 13%. Coefficient of friction is deceased by using burnishing technique comparing to plateau honed cylinder liner. The friction force is decreased by twice using the burnishing technique surface textured cylinder liner and this can identify in higher speeds and low loads [21]. The statistical parameters S_a and S_q are decreased, and the skewness S_{sk} also decreased, but the kurtosis S_{ku} increased for two types of surfaces [21].

Noutary et al. [22] found that the groove depth and density of texturing are the main factors to determine the load-carrying capacity but the groove shape only acts as a secondary role. Zhou et al. [9] found that suitable area densities are 16–22%, 14–18%, and 10–12% for low, medium, and high-velocity ranges, respectively and they suggested that required depth over diameter ratio is 0.1 for all operating conditions.

5 Conclusion

Surface texturing in piston ring or cylinder liner has shown a significant improvement in the tribological properties of rubbing pairs. Surface texturing is used to increase the load-carrying capacity and reduce the friction between piston ring and cylinder

pair. Creation of surface texturing can reduce the specific fuel consumption of an internal combustion engine without considerable exhaust gases. Laser is mainly used for creation of dimples by most of the researchers. In surface texturing; it is important find optimum texturing parameters like dimple depth, dimple diameter, and dimple density. A lot of research has been done numerically for finding the optimum texturing parameters, but the major issue is violating the assumptions made by using reynolds equation and creating meshes for micro-level that increase the computation time. Surface texturing is a possible method for the piston compression ring and cylinder liner and surface texturing can improve the load-carrying capacity, reduce the friction force between the rubbing pairs and increase the efficiency of an engine without the traceable changes in the emissions.

References

1. Stachowiak GW, Batchelor AW (2005) Engineering tribology. 4th edn. Oxford, UK
2. Ryk G, Etsion I (2006) Testing piston ring with partial laser surface texturing for friction reduction. Wear 261:792–796
3. Holmberg K, Andersson P, Erdemir A (2012) Global energy consumption due to friction in passenger cars. Tribol Int 47:221–234
4. Etsion I, Kligerman Y, Halperin G (1999) Analytical and experimental investigation of laser-textured mechanical seal faces. Tribol Trans 42:511–516
5. Etsion I, Halperin G (2002) A laser surface textured hydrostatic mechanical seal. Tribol Trans 45:430–434
6. Etsion I, Halperin G, Brizmer V, Kligerman Y (2004) Experimental investigation of laser surface textured parallel thrust bearings. Tribol Lett 17:295–300
7. Shinkarenko A, Kligerman Y, Etsion I (2009) The effect of surface texturing in soft elasto-hydrodynamic lubrication. Tribol Int 42:284–292
8. Etsion I, Sher E (2008) Improving fuel efficiency with laser surface textured piston rings. Tribol Int 42:542–547
9. Zhou Y, Zhu H, Tang W (2012) Development of the theoretical model for the optimal design of surface texturing on cylinder liner. Tribol Int 52:1–6
10. Kim B, Chae YH, Choi HS (2014) Effects of surface texturing on the frictional behavior of cast iron surfaces. Tribol Int 70:128–135
11. Podgornik B, Sedlacek M (2012) Performance, characterization and design of textured surfaces. J Tribol 134(4):41701–41707
12. NIST-internet based surface metrology algorithm testing system. https://physics.nist.gov/VSC/jsp/index.jsp
13. Gropper D, Wang L, Harvey TJ (2016) Hydrodynamic lubrication of textured surfaces: a review of modeling techniques and key findings. Tribol Int 94:509–529
14. Kligerman Y, Etsion I, Shinkarenko A (2005) Improving tribological performance of piston rings by partial surface texturing. J Tribol 127(3):632–638
15. Ronen A, Etsion I, Kligerman Y (2001) Friction reducing surface texturing in reciprocating automotive components. STLE Tribol Trans 44:359–366
16. Tomanik E (2013) Modelling the hydrodynamic support of cylinder bore and piston rings with laser textured surfaces. Tribol Int 59:90–96
17. ASTM Ed (2006) Standard test method for wear testing with a pin-on-disk apparatus. Annual Book of ASTM Standards G99
18. Usman A, Park CW (2017) Numerical investigation of tribological performance in mixed lubrication of textured piston ring-liner conjunction with a non-circular cylinder bore. Tribol Int 105:148–157

19. Biboulet N, Lubrecht AA (2016) Analytical solution for textured piston ring—Cylinder liner contacts (1D analysis). Tribol Int 96:269–278
20. Guo Z, Yuan C, Liu P, Peng Z, Yan X (2013) Study on influence of cylinder liner surface texture on lubrication performance for cylinder liner-piston ring components. Tribol Lett 51(1):9–23
21. Grabon W, Koszela W, Pawlus P, Ochwat S (2013) Improving tribological behaviour of piston ring-cylinder liner frictional pair by liner surface texturing. Tribol Int 61:102–108
22. Noutary M, Biboulet N, Lubrecht AA (2016) A robust piston ring lubrication solver: in fluence of liner groove shape, depth and density. Tribol Int 100:35–40
23. Alcouffe RE, Brandt A, Dendy JE, Painter JW (1981) The multi-grid method for the diffusion equation with strongly discontinuous coefficients. SIAM J Sci Stat Comput 2:430–454
24. Ronen A, Kligerman Y, Etsion I (2001) Friction-reducing surface-texturing in reciprocating automotive components. Tribol Trans 44:359–366

Mitigation of Frequency Variation Through Voltage Control in Islanded Microgrid

C. Kokila Vani, E. Sarangapani, and R. Kumaresan

Abstract The islanded microgrid should meet certain adequacy standards that necessitate the system frequency and voltage within the acceptable limit to provide a reliable power supply to remote people. This paper presents a frequency controller based on voltage regulation for the standalone microgrids. The controller proposed uses the sensitivity of load to operating voltages by which the consumption of the load is regulated. The scheme proposed has significant merits over conventional controllers such as enabling higher renewable energy penetration into standalone microgrids without depending on expensive energy storage systems. The main feature of the controller is to use only local frequency and voltage for feedback which avoids time-consuming additional infrastructure for communication. The simulation studies are carried out in MATLAB software to evaluate the performance of the controller.

Keywords Frequency control · Isolated microgrid · Voltage-based frequency controller (VFC) · Voltage regulation · Voltage source converter (VSC)

1 Introduction

Today, the electricity system has emerged as one of the most important infrastructures which supports all other commercial and developmental activities. In India, most of the consumers accessing the electricity receive intermittent and unreliable power from conventional power delivery grids. It also failed to meet out the challenges of future requirement with greater reliability and more economic benefits.

Thus, the concept of decentralized power delivery systems has come up as a new alternative. Microgrid was initiated as part of decentralized energy production and

C. Kokila Vani (✉) · E. Sarangapani
Department of Electrical Engineering, Bannari Amman Institute of Technology, Sathyamangalam, Tamil Nadu 638401, India
e-mail: kokilavani@bitsathy.ac.in

R. Kumaresan
Department of Electrical Engineering, Adhi College of Engineering and Technology, Kanchipuram, Tamil Nadu 631605, India

G. Kumaresan et al. (eds.), *Advances in Materials Research*, Springer Proceedings in Materials 5, https://doi.org/10.1007/978-981-15-8319-3_95

basically it is defined as an aggregation of generating sources and loads [1]. Isolated microgrid seems to be the better option for remote people in case of providing reliable power [2]. However, islanded microgrid should maintain the system voltage and frequency within acceptable levels [3]. The frequency response of droop-based controller which is a strategy for islanded microgrid operation seems to be poor due to sudden changes in wind and PV sources [4]. Also, ESS is too costly to maintain which has great financial impact on the system [5].

In view of aforementioned drawbacks, a controller based on voltage has been proposed to improve frequency response of the islanded microgrid through voltage regulation [6] and also to balance the mismatch between the demand and the output power [7]. Hence, it minimizes the system dependency on large energy storage system. By integrating the VFC with voltage source converters (VSC) [8], the effectiveness of the controller is investigated.

2 Proposed Control Structure of an Electronically Interfaced DER with VFC

The structure of a DER connected to the microgrid through a VSC [9] is illustrated in Fig. 1 where a PWM block provides the firing pulses to the switches of a bidirectional VSC. The power controller block [3] helps to calculate instantaneous active and reactive power. The primary function of the power controller is to offer the voltage and frequency reference set-points based on a drooping mechanism.

The voltage controller block is used to reap *d*-axis and *q*-axis current references. Feed-forward terms included here are used to decouple the two-axis controls. Current controller block is used to obtain voltage references [10].

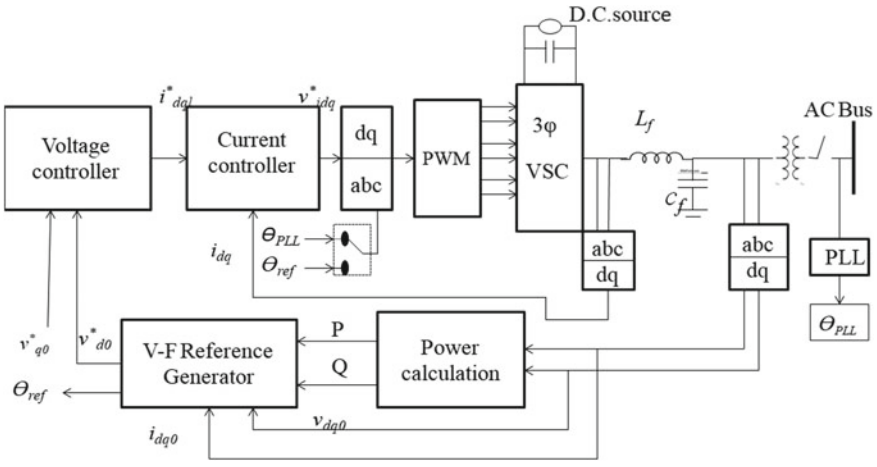

Fig. 1 Proposed control schematic of an electronically interfaced DER

The block diagram of proposed voltage-based frequency controller [9] is shown in Fig. 2. The frequency deviation of the system from the nominal set-point Δ_f is the enter sign to the controller. This frequency deviation is made to bypass via.

A PI controller to ensure that the steady-state error is zero [11], and K_{VFC} is the gain which determines the damping element provided by the VFC [12]. Then, the signal is allowed to enter via a lead-lag block which compensates the phase difference between the voltage regulator input and output.

The limits VFC_{max} and VFC_{min} are used to maintain output voltage within a desired range [13]. The block diagram of proposed VFC integration with the voltage controller block of VSC is shown in Fig. 3.

$$V_{d0}^{*} = V_n - n_q Q + \Delta f (K_{VFC} \frac{1 + \propto s + \beta s^2}{\tau_i s + \gamma s^2} \tag{1}$$

$$\propto = (K_p + 1)\tau_i + \tau_2 \tag{2}$$

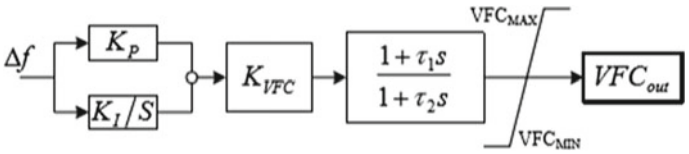

Fig. 2 Proposed voltage-based frequency controller block diagram

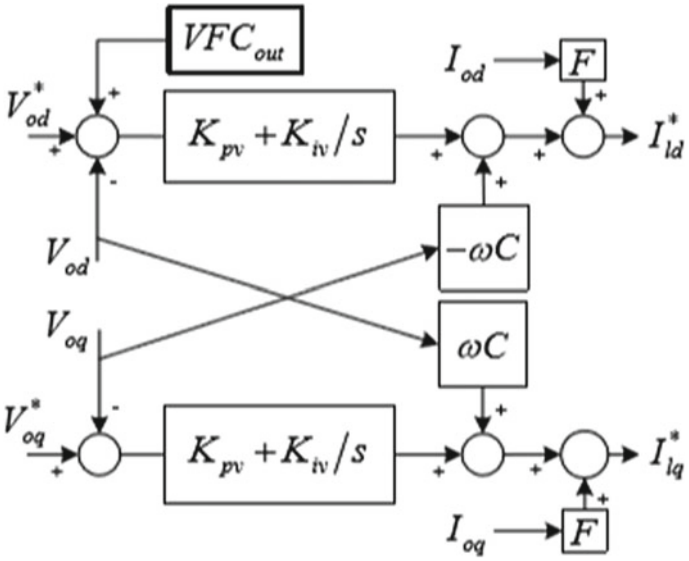

Fig. 3 Block diagram of proposed VFC integration with the voltage controller block of VSC

$$\beta = K_p \tau_i \tau_2 + \tau_i \tau_1 \tag{3}$$

$$\gamma = \tau_i \tau_2 \tag{4}$$

3 Results and Discussion

The test system for proposed work is shown in Fig. 4. A DC source of 230 V is supplied to the three-phase voltage source inverter.

3.1 Load Measurements

The type of load used in the AC bus is resistive and inductive load (RL load). Three different loads are used at different initial conditions with switching times 2 and 3.5 s. The simulation results of voltage and current of load at different loading conditions and switching times are shown in Fig. 5.

From Fig. 5, it is clear that the voltage is regulated even under various load conditions. By using VFC output signal to the voltage controller block of VSC, the voltage is regulated without much deviation.

3.2 Three-Phase VSI Measurements

Three-phase VSI is modeled with closed loop voltage and current control with 230 DC voltage source. This three-phase VSI is integrated with AC bus through a LC filter and a three-phase transformer.

The simulation results for voltage and current of secondary of the transformer using VFC is shown in Fig. 6. From Fig. 6, it is clear that the voltage is regulated even under various load conditions. By using VFC output signal to the voltage controller block of VSC, the voltage is regulated without much deviation. The results for voltage

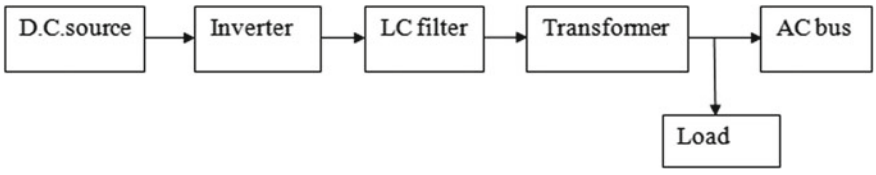

Fig. 4 Block diagram of test system for the proposed work

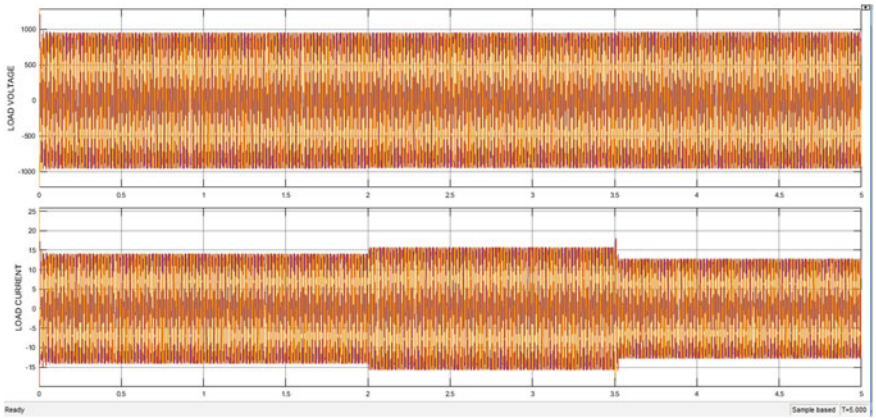

Fig. 5 Voltage and current with different loading conditions using VFC

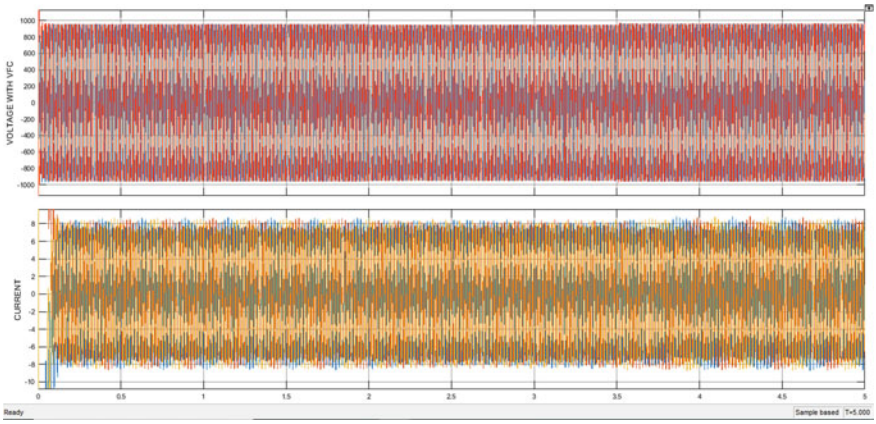

Fig. 6 Voltage and current of secondary of the transformer using VFC

and current of secondary of the transformer using VFC at different switching times are given in Table 1.

Table 1 Voltage and current measurements of secondary of the transformer using VFC

Switching times (s)	Voltage (V)	Current (A)
0–2	955	8.6
2–3.5	950	8.4
3.5–5	960	8.8

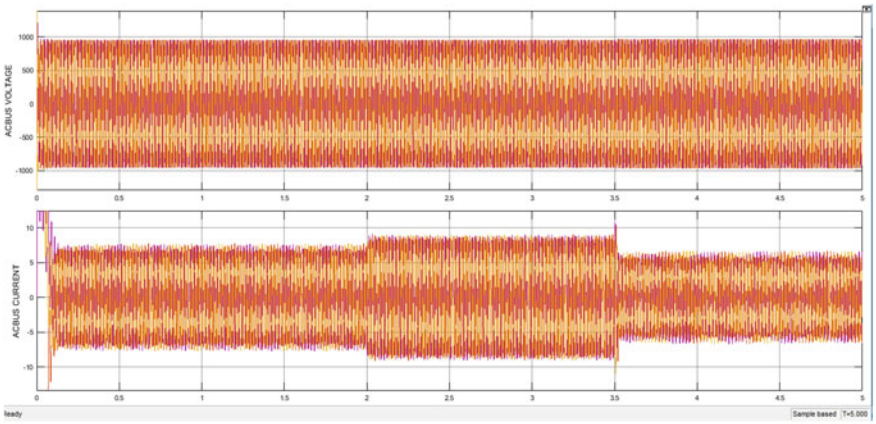

Fig. 7 Simulation results for voltage and current measurements of AC bus

3.3 AC Bus Measurements

The AC bus used for islanded microgrid is synchronous generator. Various parameters are used to design and model the synchronous generator. The input mechanical power supplied to the machine is 5 kW and supply voltage to the machine is 690 V. The simulation results for voltage and current measurements of AC bus are shown in Fig. 7.

3.4 Frequency Measurements with and Without VFC Measurements

Phase locked loop (PLL) is used to measure the frequency of the AC bus. The frequency measurements are done using PLL for the load parameters [14]. The simulation results for frequency of the system with and without VFC are shown in Fig. 8. The parameters of voltage-based frequency controller (VFC) are tabulated in Table 2.

The simulation results show that the frequency is not in the allowable limit of frequency in India. Also, there will be a power mismatch between load, inverter and AC bus. Hence, a controller is required to balance the power mismatch and to make the frequency within the allowable limit [15]. Here, voltage-based frequency controller (VFC) is used to mitigate the large frequency deviation. The simulation results show that the frequency is within the allowable limit of frequency in India. From Table 3, it is clear that frequency is improved efficiently by using voltage-based frequency controller.

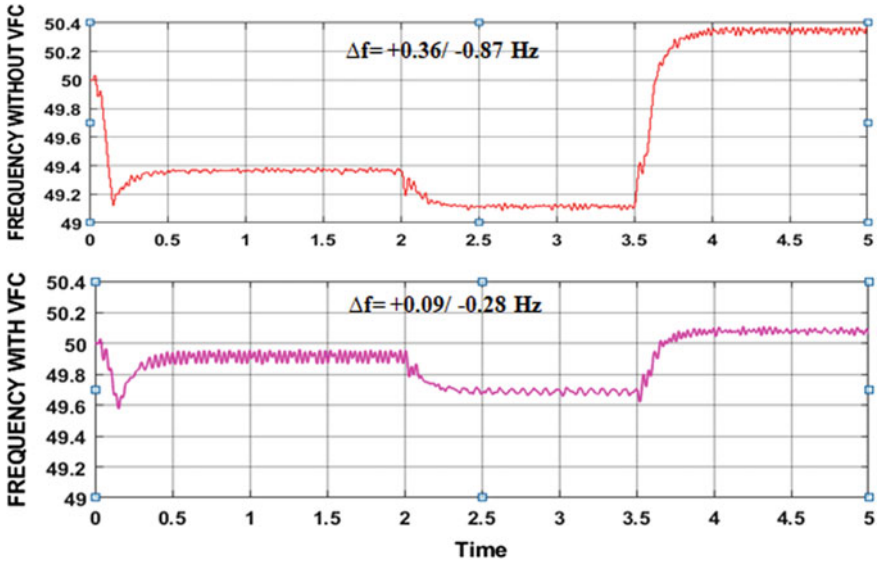

Fig. 8 Frequency of the system with and without VFC

Table 2 Parameters of voltage-based frequency controller (VFC)

Parameters	Units
Proportional gain, K_p	0.2
Integral gain, K_I	0.377
Integrator time constant, τ_i	2.65
Lead-lag block time constants, τ_1 and τ_2	0.01 and 0.9

Table 3 Frequency of the system with and without VFC

Frequency level	Frequency without VFC (Hz)	Frequency with VFC (Hz)	Frequency improvement using VFC (Hz)
Minimum frequency	49.13	49.72	0.59
Maximum frequency	50.36	50.09	0.27

3.5 Power Balance of Inverter, AC Bus and Load

The system without VFC has power unbalance so that its frequency is much reduced. To restore the frequency to the nominal value or near to the nominal value, the power has to get balanced or nearly balanced, respectively.

By using VFC, it is shown that the frequency is improved so that power should also get balanced. The results for power balance among inverter, AC bus and load are tabulated in Table 4. Load power should be equal to the inverter and AC bus

Table 4 Power balance of inverter, AC bus and load

Switching times (s)	RL load	Inverter power (kW)	AC *bus power (kW)	Total power (kW)	Load power (kW)
0–2	68 Ω and 1 mH	10.8	6.9	17.7	17.15
2–3.5	320 Ω and 1 mH	10.7	8.8	19.5	19
3.5–5	90 Ω and 1 mH	10.85	5.4	16.25	15.66

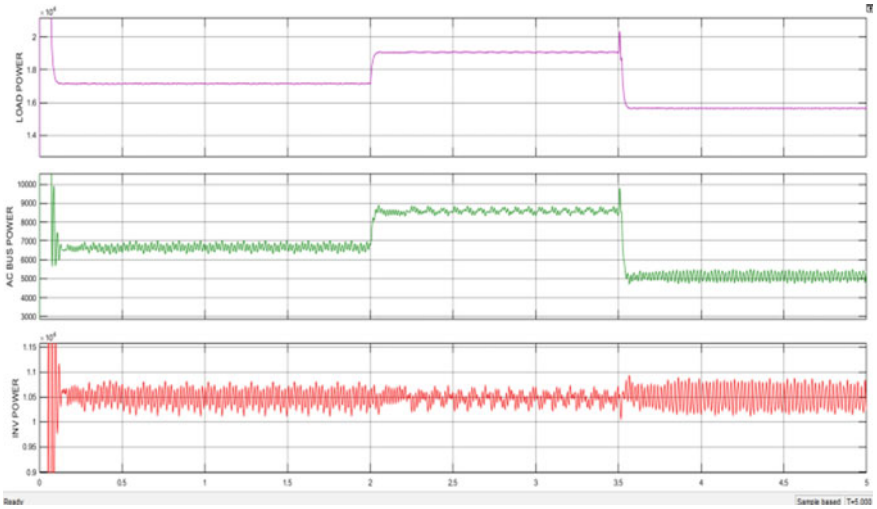

Fig. 9 Power balance of inverter, AC bus and load

power for power balance. Hence, in Table 4, it is evident from the column 5 and 6 that the power of the load is nearly equal to the power of the inverter and AC bus. The simulation results for power balance of inverter, AC bus and load are shown in Fig. 9.

4 Conclusion

In this paper, a frequency controller based on voltage is implemented for standalone microgrids which serve as control in addition to traditional frequency controllers to improve the system's frequency response. During the frequent variations in power outputs of RES, the controller acts as virtual storage for the system. Further, the VFC rectifies the drawbacks of conventional frequency control methods as it only

includes the local feedback signals such as frequency and voltage for communication. This makes the controller a simple and cost-effective one. Also, the response of VFC is almost immediate in case of frequent power output variations during large disturbances. However, the controller's performance is highly dependent on the composition of the load and acceptable operating voltage range.

References

1. Dellile G, Francois B, Malarange G (2012) Dynamic frequency control support by energy storage to reduce the impact of wind and solar generation on isolated power system's inertia. IEEE Trans Sustain Energy 3(4):931–939
2. Arriaga M, Canizares C, Kazerani M (2014) Northern lights: access to electricity in Canada's northern and remote communities. IEEE Power Energy Mag. 12(4):50–59
3. Farrokhabadi M, Canizares C, Bhattacharya K (2015) Evaluation of Droop-based controls in an islanded microgrid with electronically interfaced distributed energy resources. In: IEEE Eindhoven Powertech
4. Delille G, Yuan J, Capely L (2013) Taking advantage of load voltage sensitivity to stabilize power system frequency. In: IEEE Grenoble Conference
5. Mohamed YA, El-Saadany EF (2008) Adaptive decentralized droop controller to preserve power sharing stability of paralleled inverters in distributed generation microgrids. IEEE Trans Power Electron 23(6):2806–2816
6. Lalor G, Mullane A, Malley M. Frequency wind turbine technologies. IEEE Trans Power Syst 20(4):1905–1913
7. Liu K, Liu T, Hill DJ (2016) Frequency control in networked microgrids with voltage-sensitive loads. IEEE Transa Smart Grid 16(2):1–12
8. Karimi H, Nikkhajoei H, Iravani R (2008) Control of an electronically-coupled distributed resource unit subsequent to an islanding event. IEEE Trans Power Deliv 23(1):493–901
9. Farrokhabadi M, Bhattacharya K (2017) Frequency control in isolated/islanded microgrids through voltage regulation. IEEE Trans Smart Grid 8(3):1185–1194
10. Majumder R, Ghosh A, Ledwich G, Zare F (2009) Load sharing and power quality enhanced operation of a distributed microgrid. IET Renew Power Gener 3(2):109–119
11. Molina-Garcia A, Bouffard F, Kirschen D (2011) Decentralized Demand-Side Contribution to Primary Frequency Control. IEEE Trans. Power Syst. 26(1):411–419
12. Majumder R, Ledwich G, Ghosh A, Chakrabarti S, Zare F (2010) Droop control of converter-interfaced microsources in rural distributed generation. IEEE Trans Power Deliv 25(4):2768–2778
13. Strunz K (2006) Developing benchmark models for studying the integration of distributed energy resources. In: IEEE power & energy society general meeting, Montreal, QC, Canada
14. Erickson JC, Gilligan SR (1982) The effects of voltage reduction on distribution circuit loads. IEEE Trans Power App Syst 101(7):2014–2018
15. Wang Z, Wang J (2014) Review on implementation and assessment of conservation voltage reduction. IEEE Trans Power Syst 29(3):1306–1315

Analyzing the Performance of CO_2 Heat Pump for Mushroom Drying Application

C. Subramaniyan, R. Naveen Kumar, S. Siva Ranjith, and S. Thiyagu

Abstract Heat pump is mainly applied for HVAC in domestic and industrial applications in many countries. One of key applications of heat pump is dryer of fruits and vegetables. Many noted research is going on heat pump dryer with respect to the required conditions. Most commonly used refrigerants in the heat pumps are CFCs and HCFCs. Due to the ozone depletion, those refrigerants are unfit for the heat pump applications for better environmental considerations. So the alternative refrigerant for heat pump is to be applied for avoiding environmental pollution. Forbetter performance, many researches are going on CO_2 as an alternative refrigerant for HVAC applications. In this paper, a heat pump dryer setup was proposed and numerical modeling was done for mushroom drying application. The performance of heat pump was also been studied for various required conditions.

Keywords Mushroom dryer · Heat pump · Carbon dioxide (CO_2)

1 Introduction

Drying Kinetics of Milky Mushroom cuts (10 mm) in a fluidized bed dryer was studied with the model and the optimum datas were also been found. The result shows that the effective moisture diffusivity of mushroom is increased while the drying air temperature increased [1]. Analyzing the performance of solar tunnel dryer for drying mushrooms were also been investigated. The drying chamber temperature is varied from 37.0 to 66.5 °C and the performance of the dryer was also analyzed for the required conditions [2]. Energy consumption for drying of mushroom slices was studied in various methods such as hot air, microwave, vacuum, infrared, microwave-vacuum, and hot air-infrared. During data analysis the energy consumption levels in drying mushroom slices were associated with microwave and vacuum dryers, respectively was analyzed. Energy consumption in the hot air dryer is in downward

C. Subramaniyan (✉) · R. Naveen Kumar · S. Siva Ranjith · S. Thiyagu
Department of Mechanical Engineering, Bannari Amman Institute of Technology, Sathyamangalam, Erode 638401, Tamil Nadu, India
e-mail: subra.csm@gmail.com

G. Kumaresan et al. (eds.), *Advances in Materials Research*, Springer Proceedings in Materials 5, https://doi.org/10.1007/978-981-15-8319-3_96

trend with increasing temperature and an upward trend with increasing air velocity. In drying mushroom using infrared radiation, it was observed that the increased air velocity increases drying time and consequently reducing the amount of consumed energy. Using both the hot air and infrared sources on drying it is noted that energy consumption is reduced compared to the infrared drying alone [3].

Normally mushroom is dried in sunlight depend upon the weather conditions which affect the quantity of mushroom. Hence artificial drying of mushroom is promoted in order to maintain their quality with required drying conditions. The performance of dryer with respect to the various drying condition were analyzed [4]. Analyzing the performance of vapor compression system using CO_2 as refrigerant was done. The irreversibility in the system with CO_2 as refrigerant were also been analyzed with intercooler [5]. A theoretical study on CO_2 heat pumps for heating application are studied in which the desired temperature of water is obtained by reducing the mass flow rate of water and resulted in increase in efficiency with minimum heat loss [5]. In order to reduce the losses in expansion process with high-temperature change, the temperature of refrigerant at the exit of compressor can be reduced by multistage compression with inter cooling [6].

The heating tower heat pump (HTHP) is proposed as an opportunity to the conventional air-source heat pump (ASHP). To inspect the enhancement of the overall performance of the HTHP over the ASHP, a comprehensive comparison between the two systems was carried out primarily based on a simulation study. Physics-primarily based models for the ASHP and HTHP were evolved. The overall performance of the ASHP underneath frosting conditions changed into corrected with a newly advanced frosting map, and the regeneration penalization become taken into consideration for the HTHP [7]. The use of high-temperature heat pumps (HTHPs) running with natural fluids has been proven to be a capacity environmentally friendly solution to increase energy power performance in industrial methods. Industrial approaches release a tremendous amount of strength as low-quality waste heat to the environment [8].

Heat pump dryer is established as drying machine that certain the product's pleasant mainly meals and agriculture products, capable of manage drying temperature, relative humidity, moisture include extraction, drying air velocity, drying period, etc. Improving a heat pump dryer includes the setup cost, drying performance which includes air velocity, drying temperature and relative humidity, overall performance of the component hybrid to heat pump dryer, power required to run the machine, and also payback length [9]. Enhancing the performance of dryer with reduced energy consumption and product satisfactory in addition reduce environmental impact remained as the primary goal of any improvement of drying system. A solar-assisted chemical heat pump dryer is a new solar drying system, which have contributed to better cost-effectiveness and better excellent dried products as well as saving energy. A solar collector is customized to offer thermal energy in a reactor, so a chemical reaction can take place. This reduces the dependency of the drying generation on fossil energy for heating [10].

Although heat pumps have been used extensively in enterprise for lot of years, their use for drying, particularly foods, has been limited. Evaluating the potential

of heat pump dehumidifier (HPD) dryer has been done. HPD dryers offer several advantages over traditional hot-air dryers for the drying of food products, together with higher electricity efficiency, higher product quality, and the capability to function independently of out of doors ambient climate conditions. In addition, this technology is environmentally friendly because the gases and fumes are not given off into the atmosphere [11]. The overall performance of the drying system components is discussed, while the crucial device components are determined to improve the system efficiency. The overall performance of the drying process is also analyzed for three different medicinal and aromatic plants from the exergoeconomic point of view. A comprehensive parametric take a look is conducted to investigate the effect of varying dead (reference) state temperatures on exergoeconomic performance parameters for both drying system components and drying process. The correlations between the performance parameters and dead state temperatures are developed [12].

The performance of dryers have been improved by using different methodology such as heat recovery unit, proportional control (PC) of drying air temperature, simultaneous control of the relative humidity–temperature–air flow rate, water cycle dehumidifier, and closed-loop cycle to increase the drying efficiency of industrial drying applications. The highest coefficient of performance of the whole heat pump system (COPws,HP) was calculated as 3.7 and drying efficiencies of the IRD and HPD systems were calculated as 39% and 25%, respectively [13]. The study is to obtain the drying curves and calculate the effective diffusivity to predict drying kinetics and thermodynamic characteristics of tomatoes drying. The tomato samples were cut in two different shapes namely flat slices and wedges. In the case of flat slices, there were four different thicknesses, 0.5, 1, 1.5, 2 cm. For the wedged slices, the tomatoes were slit into 2, 4, 8, and 16 equal sections. The moisture content of the tomatoes varied between 92.5 and 93.6%. The tomatoes were weighed regularly until moisture content fell between 18 and 25% [14].

2 Methodology

One of the most important issues in mushroom production is the handling of the aftermath of the harvesting. The mushrooms are maintained for required temperature conditions like 50, 60, and 70 °C temperature. Therefore there is a need for anyone of the heating sources for maintaining the temperature of the mushroom. Mushroom will be drying in various methods including such as Sunlight, heat pump, etc. However, the availability of the sunlight is not continuous and uniform all over the day. The fluctuation in the output energy from the solar dryer causes quality reduction in the mushroom production. To avoid that non-uniformity of heat source from the solar dryer system it is proposed to place a heat pump dryer. This dryer is continuously giving heat source which can be easily varied for the required temperature. The CO_2 refrigerant fluid is also been used for drying process. At the quality approach, the mushrooms are considered good if they have a moisture content of 90.56%.

The working principle of heat pumps is reversed Carnot cycle. This cycle consists of two reversible isothermal processes and two isentropic processes. The working refrigerant (CO_2) fluid is sent through the evaporator which converts the liquid into gaseous stage. Then the gaseous state condition CO_2 is sent to compression and the compressor increases the pressure and temperature of the CO_2. Basically, five types of compressors are used for the heat pump dryer operation (Reciprocating compressor, Screw compressor, Rotary compressor, Centrifugal compressor, and finally Scroll compressor). The high pressurized CO_2 is sent to the heat exchanger where the CO_2 loses its heat energy and same is sent to the expansion valve for depressurizing. The low-pressure CO_2 is sent to the condenser which converts all the CO_2 in to liquid. Finally the same CO_2 is sent to the compressor again for another cycle.

The mathematical model was derived and the same was coded in Microsoft excel. The mass flow rate of mushroom is initially taken as the primary parameter for the modeling. The temperature of mushroom is taken for the required conditions and based on the temperature the heat load on the heat exchanger weas modeled. The initial temperature of the mushroom is considered constant and it doesn't play any role of load variation. The compressor work done is modeled for the corresponding value of pressure and the condenser heat transfer is also modeled. The mass flow rate of refrigerant and COP of the heat pump is derived and all the parameters are derived into the primary variables.

3 Numerical Analysis

Based on the mathematical model the drying of mushroom was done for heat pump by using CO_2 as the refrigerant fluid for the required conditions. The corresponding enthalpy values of CO_2 are taken from the property chart with respect to its temperature and pressure. Initial temperature of mushroom is taken as 25 °C and final required temperature is assumed as 60 °C. The compressor pressure is limited to 90 bar at 60 °C. Mass of mushroom to be dried is assumed as 0.4 kg and mass flow rate of refrigerant is calculated based on the required conditions. Finally, the COP is also derived from the output parameters. The compressed working temperature is varied from 60 to 80 °C and the corresponding values of COP, refrigerant mass flow rate is calculated. The simulated results are tabulated in Table 1 (Fig. 1).

Heat is supplied to the mushrooms Q_s which is to be supplied by the heat pump is given by the following the Eq. (1)

$$\mathrm{Q_s} = M_\mathrm{m} * C_\mathrm{p}\left(T_{m_2} - T_{m_1}\right) \tag{1}$$

Enthalpy of the refrigerant after heat exchanger and compressor work is given by Eqs. (2), (3) respectively

$$h_3 = h_2 - (Q_\mathrm{s}/M_\mathrm{ref}) \tag{2}$$

Table 1 Experimental parameters

M_m	C_p	T_{m_1}	T_{m_2}	Q_s	P	T_2	h_1	h_2	h_3	W_c	COP	M_{ref}
Kg	kJ/kg k	°C	°C	J	bar	°C	kJ/kg	kJ/kg	kJ/kg	kJ/s	–	kg/s
0.40	29.50	25	60	413.00	90	60	395	425	277.5	30	13.77	2.8
0.40	29.50	25	60	413.00	90	65	395	435	287.5	40	10.33	2.8
0.40	29.50	25	60	413.00	90	70	395	445	297.5	50	8.26	2.8
0.40	29.50	25	60	413.00	90	75	395	455	307.5	60	6.88	2.8
0.40	29.50	25	60	413.00	90	80	395	465	317.5	70	5.90	2.8

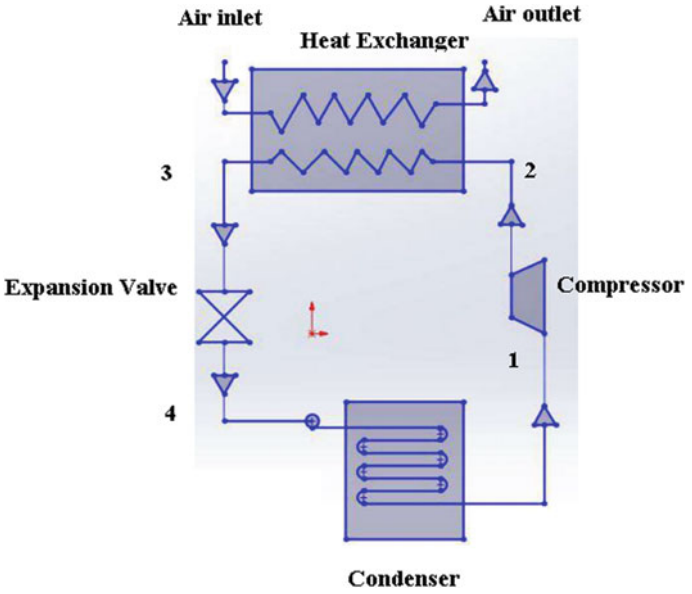

Fig. 1 Proposed layout of experimental setup

$$W_c = M_{ref}(h_2 - h_1) \tag{3}$$

Co-efficient of performance (COP) of the heat pump is given by

$$\text{COP} = Q_s / W_c. \tag{4}$$

4 Result and Discussion

The corresponding reversed Carnot cycle is drawn for all the results mentioned in Fig. 2 and the enthalpy is taken for all the required conditions. The graph was plotted for the COP of the heat pump with respect to the refrigerant temperature after compression for the mass of mushroom as 0.05 kg/s which is shown in Fig. 3. The COP varies from 5.25 to 3.41 for the variation in the refrigerant temperature (T_2) 50–70 °C. The mass flow rate of the mushroom is also varied from 0.05 to 0.4 kg/s. From the result, it was found that the co-efficient of performance (COP) is very less for the higher refrigerant temperature (T_2). When the refrigerant temperature (T_2) increases, the co-efficient of performance (COP) decreases gradually. Therefore the optimum temperature should be kept for compression for better COP. For higher the mass flow of mushroom the COP is also high.

The enthalpy of the refrigerant after the compression is also plotted on graph and it is shown in Fig. 4 for the various working temperatures of refrigerant and mass flow rate of mushroom. The compressor work input is also plotted in graph which is shown in Fig. 5 for the various working temperatures of refrigerant and mass flow rate of mushroom. The compressor work input is higher for the higher working temperatures of refrigerant and high mass flow rate of mushroom.

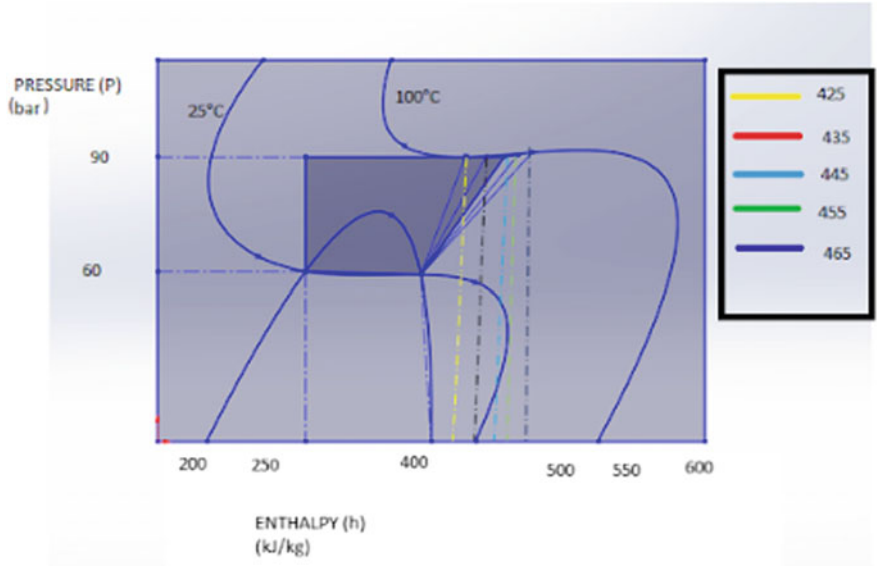

Fig. 2 Pressure-enthalpy diagram of CO_2

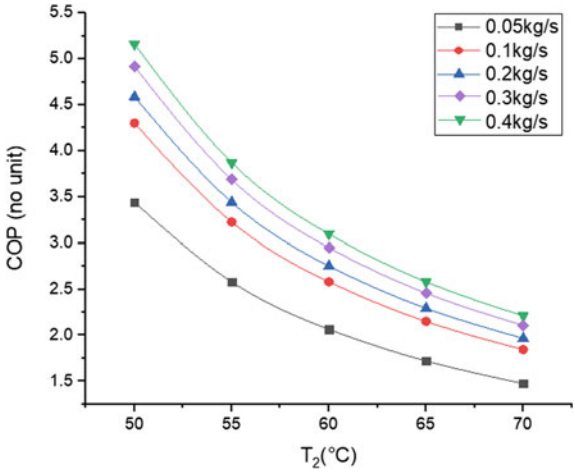

Fig. 3 Temperature (T_2) versus coefficient of performance (COP)

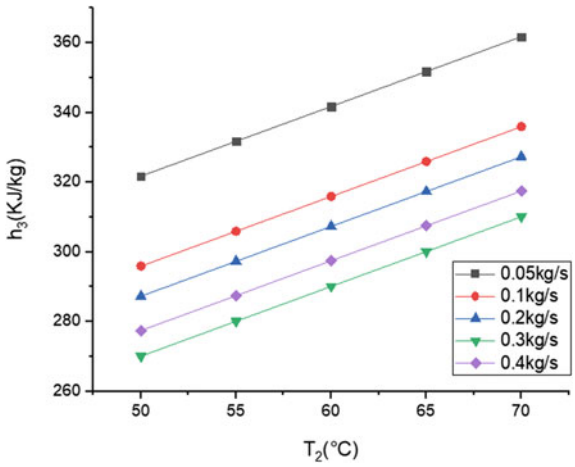

Fig. 4 Temperature (T_2) versus enthalpy (h_3)

5 Conclusion

For the better quality of the dried mushroom product, it is suggested to go for the proposed heat pump dryer system which gives uniform heat constantly. The optimum COP of heat pump can be achieved at the lower working temperature of the refrigerant after compression and the mass flow rate is higher for the mushroom. The working temperature of the refrigerant after compression increases, the efficiency decreases.

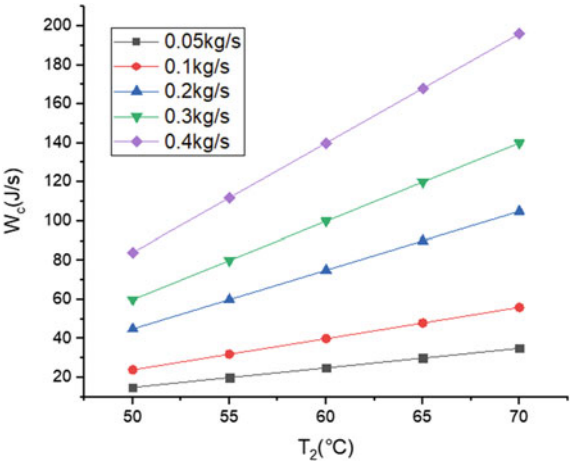

Fig. 5 Temperature (T_2) versus work done of compressor (W_c)

References

1. Arumuganathan T, Manikantan MR, Rai RD, Anandakumar S, Khare V (2009) Mathematical modeling of drying kinetics of milky mushroom in a fluidized bed dryer. Int Agrophys 23(1):1–7
2. Bala BK, Morshed MA, Rahman MF (2009) Solar drying of mushroom using solar tunnel dryer. In: International solar food processing conference, pp 1–11
3. Motevali A, Minaei S, Khoshtaghaza MH, Amirnejat H (2011) Comparison of energy consumption and specific energy requirements of different methods for drying mushroom slices. Energy 36(11):6433–6441
4. Wibowo IA, Indah N, Sebayang D, Adam NH (2018) Temperature control system for mushroom dryer. In: IOP conference series: materials science and engineering, vol 343, no 1. IOP Publishing, p 012036
5. Försterling S, Tegethoff W, Köhler J (2002) Theoretical and experimental investigations on carbon dioxide compressors for mobile air conditioning systems and transport refrigeration
6. Bullard C (2004) Trans-critical CO_2 systems-recent progress and new challenges. In: Bulletin of the IIF, vol 5
7. Huang S, Zuo W, Lu H, Liang C, Zhang X (2019) Performance comparison of a heating tower heat pump and an air-source heat pump: A comprehensive modeling and simulation study. Energy Convers Manage 180:1039–1054
8. Bamigbetan O, Eikevik TM, Nekså P, Bantle M (2017) Review of vapour compression heat pumps for high temperature heating using natural working fluids. Int J Refrig 80:197–211
9. Goh LJ, Othman MY, Mat S, Ruslan H, Sopian K (2011) Review of heat pump systems for drying application. Renew Sustain Energy Rev 15(9):4788–4796
10. Fadhel MI, Sopian K, Daud WRW, Alghoul MA (2011) Review on advanced of solar assisted chemical heat pump dryer for agriculture produce. Renew Sustain Energy Rev 15(2):1152–1168
11. Perera CO, Rahman MS (1997) Heat pump dehumidifier drying of food. Trends Food Sci Technol 8(3):75–79
12. Djebli A, Hanini S, Badaoui O, Boumahdi M (2019) A new approach to the thermodynamics study of drying tomatoes in mixed solar dryer. Sol Energy 193:164–174
13. Aktaş M, Şevik S, Aktekeli B (2016) Development of heat pump and infrared-convective dryer and performance analysis for stale bread drying. Energy Convers Manage 113:82–94
14. Gungor A, Erbay Z, Hepbasli A (2011) Exergoeconomic analyses of a gas engine driven heat pump drier and food drying process. Appl Energy 88(8):2677–2684

System Identification Using Adaptive Algorithms

J. Reena Catherine, N. Bhuvanesh, M. Prasanna, and S. Manojj

Abstract In this paper, System Identification is accomplished using various adaptive filters. System Identification is the one which is used in identifying the unknown model of a system and it is the mathematical modeling of the plant or process. It is said to be the bridge between the real-time application and the mathematical model of a particular system with respect to control theory and abstraction of model. In order to identify the unknown system, LMS (Least Mean Square), RLS (Recursive Least Square), NLMS (Normalized Least Mean Square), Leaky LMS, and Block LMS algorithms are used. Based on the mean square error obtained from the above-mentioned algorithms for the unknown system, the comparison of simulation results is done for the performance analysis of the adaptive algorithms.

Keywords Adaptive algorithms · Bilinear system · Mean square error · System identification · Mathematical model

1 Introduction

A Mathematical model serves as a good replica for the plant or a process. Models are qualitative understanding of a process. The determination of a process on the basis of input and output of a model which the system under test is equivalent is

J. Reena Catherine (✉) · M. Prasanna · S. Manojj
Department of Electrical and Electronics Engineering, Bannari Amman Institute of Technology, Sathyamangalam, Erode, Tamil Nadu 638401, India
e-mail: reenacatherinej@bitsathy.ac.in

M. Prasanna
e-mail: prasanna.ee17@bitsathy.ac.in

S. Manojj
e-mail: manojj.ee17@bitsathy.ac.in

N. Bhuvanesh
Department of Mechanical Engineering, Bannari Amman Institute of Technology, Sathyamangalam, Erode, Tamil Nadu 638401, India
e-mail: bhuvaneshn@bitsathy.ac.in

G. Kumaresan et al. (eds.), *Advances in Materials Research*, Springer Proceedings in Materials 5, https://doi.org/10.1007/978-981-15-8319-3_97

the process of System Identification. Performing various tests on a data based on an algorithm, the system to be identified can be determined. Modeling, Design, Control and Monitoring are the major tasks in the process of System Identification. Basically, the process of System Identification involves the process of estimation of black model or grey model of a system. It involves the estimation and prediction of the input-output relationship of a system and also the determination of the parameters related to the physical features of the system.

In [1], it is explained about various adaptive algorithms such as Least Mean Square algorithm, Normalized Least Mean Square algorithm and Recursive Least Squares algorithm in system identification. The performance evaluation of system identification is performed by these adaptive algorithms. The results show that all these algorithms have achieved accuracies with mean square values. The advantage of the descriptive algorithm of the literature lies in its simplicity. The calculation of weight updation in adaptive algorithms is almost straightforward and is based on iteration process. In [2], it is discussed about blind identification of a class of bilinear systems which has experienced the non-Gaussian higher order white noise. The system output is also corrupted by Gaussian measurement noise.

The main purpose is that the experiment design of plant must satisfy the constraints. The simulation results are provided such that it approves of the parameters identified by an array of linear systems. For identifying the unknown system from the response of the process with respect to the input signal, it is explained in [3]. The identification of the system is done by using adaptive algorithms such as LMS, NLMS, and RLS algorithms, which works on weight updation process and is based on the Least Mean Square Error. These algorithms are used to identify the unknown system and the simulation result shows the performance analysis of these algorithms in comparative manner.

In [4], it is discussed about the fractional adaptive signal processing. By using weight updation mechanism in standard Volterra LMS algorithm, the input-output relation of the Modified Standard Volterra LMS algorithm is derived. The parameters obtained in the Standard Volterra LMS algorithm and Modified Standard Volterra LMS algorithms are compared with the true parameters of the Box Jenkins model considered. The performance analysis is done through the performance measures obtained from the algorithms. The least mean square adaptive algorithm for the identification of the system with bilinear form is discussed in [5]. The bilinear term is given in terms of the impulse response of the spatiotemporal model. This spatiotemporal model features the multiple input and single output model. The performance analysis is done on the basis of convergence bounding the main features of the algorithm.

2 Materials and Methods

2.1 System Identification

Identification is the exercise of describing the relationship between the input and output of the system i.e., the cause and response of the system from the measured data. Modeling is crucially an important way of exploring, studying, and understanding the surrounding world. A model is used to describe imperative aspects of a system. A mathematical model is said to be a substitute for a process. The requirements which determine the complexity of the model are Modeling and Design, Control, and Monitoring. From Fig. 1, the basic block diagram of identification process is discussed. The input signal is given to the actuator, which gives the output to the process. In the process block, it processes the signal with disturbance and gives the output to the sensor. It evaluates the output with the measurable signal along with sensor noise, in order to obtain the response from the system.

Models obtained from the fundamental laws like continuity equation and energy conversion are known as first principle models. By conducting experiments, the alternative approach is used to build the models; such models are called empirical models. From Fig. 2, the block diagram of System Identification process is explained below.

2.1.1 Experimental Design

In Experimental Design, collection of data is done with respect to the prior knowledge of the system. The input signal or data must be chosen such that the data is more informative and the influence of noise must be reduced by choosing the input signal correspondingly.

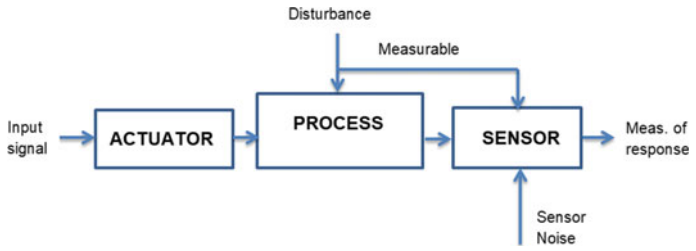

Fig. 1 Block diagram of the process of identification

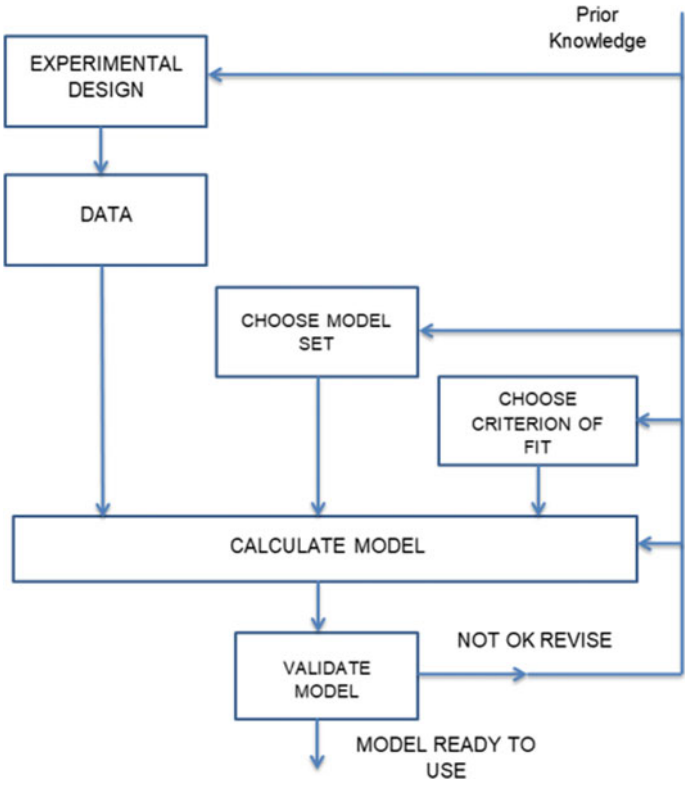

Fig. 2 Block diagram of system identification process

2.1.2 Data

By using some known parameters, on using estimation process, the unknown parameter can be determined. If we have no knowledge of the system, then the identification methods like black box identification and grey box identification are used in order to determine the parameters of the system.

2.1.3 Model Structure Selection

A group of models must be specified priorly such that the valid model based on the constraints can be chosen. By using the black box method, trial and error method, the suitable model is chosen. Both the parametric and non-parametric models are chosen.

The parametric model structure is given by,

$$A(q)y(t) = \frac{B(q)}{F(q)}u(t - n_k) + \frac{c(q)}{D(q)}e(t) \tag{1}$$

where, u and y are the input and output sequences, respectively, and e is the white noise sequence.

Different types of model are given as follows:

1. **AR Model**: The Auto Regressive (AR) model is a time series model, which is given by,

$$A(q)y(q) = e(t) \tag{2}$$

   where, the exogenous input u is zero.
2. **ARX Model**: The Auto Regressive Exogenous (ARX) model is given by,

$$A(q)y(t) = B(q)u(t - n_k) + e(t) \tag{3}$$

   The identification method for ARX model is least squares method, which is a special case of prediction error model.
3. **ARMAX Model**: The Auto Regressive Moving Average Exogenous (ARMAX) model is given by,

$$A(q)y(t) = B(q)u(t - n_k) + C(q)e(t) \tag{4}$$

   The ARMAX model has more flexibility than the ARX model, since it can handle with the disturbances in the system.
4. **OE Model**: The Output Error Model is given by,

$$A(q)y(t) = \frac{B(q)}{F(q)}u(t - n_k) + e(t) \tag{5}$$

   The OE model does not use any parameters for simulating the disturbance and the identification method is prediction error method which is the same as that of ARMAX model.
5. **BJ Model**: The Box Jenkins Model is given by,

$$A(q)y(t) = \frac{B(q)}{F(q)}u(t - n_k) + \frac{C(q)}{D(q)}e(t) \tag{6}$$

In the above-specified models, the polynomials A, B, C, D, F are defined by the backward shift operator (q^{-1}), which are given by,

$$A(q) = 1 + a_1 q^{-1} + \cdots + a_{na} q^{-na}$$
$$B(q) = b_1 + b_2 q^{-1} + \cdots + b_{nb} q^{-nb+1}$$

$$C(q) = 1 + c_1 q^{-1} + \cdots + c_{nc} q^{-nc}$$
$$D(q) = 1 + d_1 q^{-1} + \cdots + d_{nd} q^{-nd} \tag{7}$$

$$F(q) = 1 + f_1 q^{-1} + \cdots + f_{nf} q^{-nf} \tag{8}$$

where *na* is the number of past output terms used to predict the current output and *nb* is the number of past input terms used to predict the current output.

2.1.4 Criterion Fit

When System identification focuses on selecting a specific parametric model, it is appropriate to design and estimate the input-output relationship of the system with a transfer function. This process of estimation of the transfer function of the system with respect to the input-output relationship, gives clues to determine the complexity of the model and the appropriate model structure.

2.1.5 Validation

The model validation is used in order to check whether the model is satisfactory and to check whether it serves the purpose. But, this process is more dangerous because different sets of measurements must be used to crosscheck the above-specified constraints. In the model validation, the comparison is carried out between parameter estimates and the values determined using the algorithms and techniques.

2.2 Adaptive Algorithms

An algorithm that helps in altering the behavior during the execution of the process is said to be the adaptive algorithm. The block diagram from Fig. 3 is described as

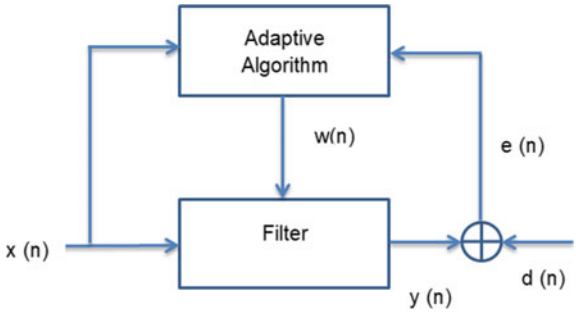

Fig. 3 Block diagram for adaptive algorithm

follows: the input $x(n)$ is given to the filter and adaptive algorithm block simultaneously. The filter which has the input as the input signal $x(n)$ has another input, which is the output of the adaptive algorithm process $w(n)$. After processing, the output of the filter $y(n)$ is obtained.

The desired output based on the requirement is given as $d(n)$. The comparative process takes place between the output of the filter after processing and the desired output. The comparative value obtained is the error between the outputs which is denoted by $e(n)$. This is then fed back to the adaptive algorithm block, where the error is used in updating the weights, since the adaptive algorithms are based on the weights of the previous data, the error between the filter output and the desired output, and learning rate.

2.2.1 Types of Adaptive Algorithm

The adaptive algorithms are classified based on the least square criterion. Since the complete process of adaptive algorithm is based on the weight updation, which depends on the past weights of the system, the algorithm is an iterative process where the weights are altered every instant.

LMS Algorithm

The LMS algorithm is Least Mean Square Algorithm which works on the basis of the weight updation equation. It involves the following algorithm steps:

LMS Algorithm Steps
The adaption process in the Least Mean Square algorithm involves three steps. They are:

1. The filter output is given by the input and the coefficient of weight obtained. It is given by,

$$y(n) = x(n)w^*(n) \tag{9}$$

2. The estimation of error is carried out by the comparison between the output of the filter and the desired output. It is given by,

$$e(n) = d(n) - y(n) \tag{10}$$

3. The updation of weight in the adaptation process takes place in iterative manner. The weight updation equation is given by,

$$w(n) = w(n-1) + \mu u(n)e(n) \tag{11}$$

NLMS Algorithm

The NLMS algorithm is the Normalized Least Mean Square Algorithm. The NLMS algorithm is considered as an extension of the LMS algorithm, which ignores this issue by the determination of maximum step size value.

NLMS Algorithm Steps
The adaptation process in the Normalized Least Mean Square algorithm is given by the following steps:

1. The filter output is given by the input and the coefficient of weight obtained. It is given by,

$$y(n) = x(n)w^*(n) \tag{12}$$

2. The estimation of error is carried out by the comparison between the output of the filter and the desired output. It is given by,

$$e(n) = d(n) - y(n) \tag{13}$$

   The step size value of the normalised mean square algorithm is calculated by using,

$$\mu(n) = \frac{1}{x(n)x^*(n)} \tag{14}$$

3. The updation of weight in the adaptation process takes place in iterative manner. The weight updation equation is given by,

$$w(n) = w(n-1) + \mu(n)u(n)e(n) \tag{15}$$

Because of its simplicity which is approximately equally simple as LMS algorithm, the NLMS algorithm exhibits better balance between the performance of the algorithm and the property of simplicity.

RLS Algorithm

The RLS algorithm is Recursive Least Squares Algorithm. In this algorithm, the weight updation is performed by deriving the minimized least squares error and

deriving an algorithm for the weight adaptation is said to be the Recursive Least Square algorithm.

RLS Algorithm Steps
The adaptation process in the Recursive Least Square algorithm is given by the following steps:

1. The filter output is given by the input and the coefficient of weight obtained. It is given by,

$$y(n) = x(n)w^*(n) \tag{16}$$

2. The estimation of error is carried out by the comparison between the output of the filter and the desired output. It is given by,

$$e(n) = d(n) - y(n) \tag{17}$$

3. The updation of weight in the adaptation process takes place in iterative manner. The weight updation equation is given by,

$$w(n) = w(n-1) + k(n)e(n) \tag{18}$$

where

$$k(n) = \frac{\pi(n)}{\gamma + x(n)\pi(n)}$$

The Recursive least squares algorithm has high convergence rate inspite of its complexity and requires p multiplications, RLS algorithm requires p^2 multiplications.

2.2.2 Variants of LMS Algorithm

Leaky LMS

In regular LMS algorithm, when the input is turned off, the weight vector the stalls. But in case of leaky LMS in the same scenario, the weight vector instead "leaks" out due to the leakage factor.

Leaky LMS Algorithm Steps
The adaptation process in the Leaky Least Mean Square algorithm is given by the following steps:

1. The filter output is given by the input and the coefficient of weight obtained. It is given by,

$$y(n) = x(n)w^*(n) \tag{19}$$

2. The estimation of error is carried out by the comparison between the output of the filter and the desired output. It is given by,

$$e(n) = d(n) - y(n) \tag{20}$$

3. The updation of weight in the adaptation process takes place in iterative manner. The weight updation equation is given by,

$$\omega(n+1) = (1 - \mu\gamma)\omega(n) + \mu e(n)x(n) \tag{21}$$

where, γ is the leakage factor which is the compromise between the bias and coefficient protection.

Block LMS

The Block LMS is Block Least Mean Square algorithm. In case of block LMS, we can update the coefficients of N samples by using block update.

Block LMS Algorithm Steps

1. The filter output is given by the input and the coefficient of weight obtained. It is given by,

$$y(n) = x(n)w^*(n) \tag{22}$$

2. The estimation of error is carried out by the comparison between the output of the filter and the desired output. It is given by,

$$e(n) = d(n) - y(n) \tag{23}$$

3. The updation of weight in the adaptation process takes place in iterative manner. The weight updation equation is given by,

$$\omega(n+1) = \omega(n) + \left(\frac{\mu e(n)x(n)}{N}\right) \tag{24}$$

where, N is the total number of samples.

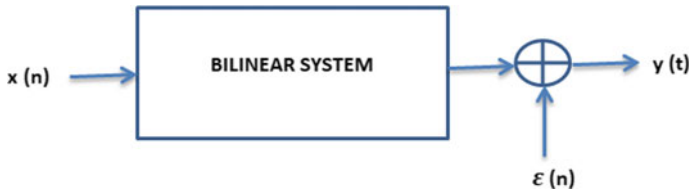

Fig. 4 Block diagram of input-output relationship of bilinear system

2.3 Bilinear System

Bilinear System means many real physical processes in the world. Thus, it is important to understand their stability property, their real properties by using various control methodologies. These systems can be considered as a class of nonlinear systems. The Bilinear System can be represented as natural models for many dynamic processes [6–9]. It has an ability to represent all the nonlinear systems efficiently and with relatively small number of parameters with respect to the system considered. A Bilinear System can be represented as,

$$\dot{x} = Ax + Bux \tag{25}$$

is the control input and x is the state. From the above state equation, it is expressed that, it is linear in state and linear in control; but not jointly linear in state and control. Also, the Bilinear System is a two factor model with respect to the state and the control. The Bilinear System can be given in the block diagram in Fig. 4:

The bilinear system in matrix form is expressed as,

$$\begin{pmatrix} \dot{x}_1 \\ \vdots \\ \dot{x}_n \end{pmatrix} = \begin{pmatrix} a_{11} \cdots a_{n1} \\ \vdots \ \ddots \ \vdots \\ a_{1n} \cdots a_{nn} \end{pmatrix} \begin{pmatrix} x_1 \\ \vdots \\ x_n \end{pmatrix} + \begin{pmatrix} b_{11} \cdots b_{n1} \\ \vdots \ \ddots \ \vdots \\ b_{1n} \cdots b_{nn} \end{pmatrix} u \begin{pmatrix} x_1 \\ \vdots \\ x_n \end{pmatrix} + \begin{pmatrix} c_1 \\ \vdots \\ c_n \end{pmatrix} u \tag{26}$$

3 Results and Discussions

This work is implemented in MATLAB 2015a. The technique followed in the system identification process using adaptive algorithm for a bilinear system is given by the Block Diagram in Fig. 5.

The input data given for the identification of the system is gas furnace data. This is obtained from the Gas Furnace Box Jenkins model. The System to be identified is

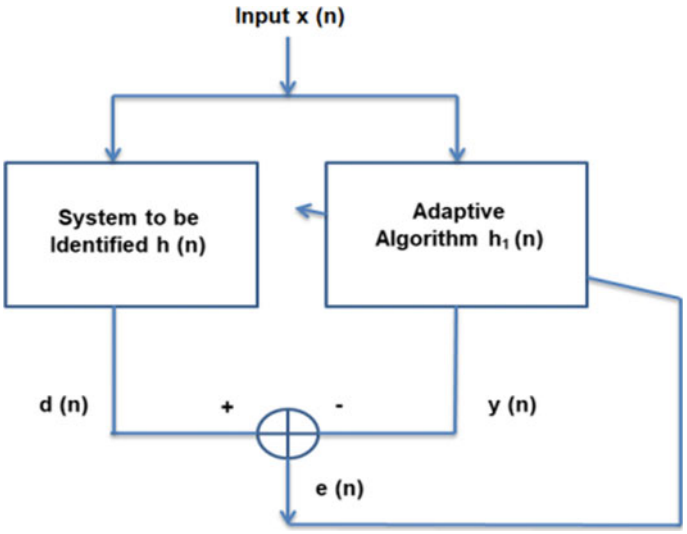

Fig. 5 Methodology for system identification using adaptive algorithm

given as true parameters in the particular block. The true parameters are estimated in the adaptive algorithm block which mimics the true values of the system [10–13].

They are explained as follows: The plot Fig. 6 is obtained for LMS algorithm with various step sizes$\mu = 0.007$, $\mu = 0.1$. The Step Size value chosen must be chosen such that it lies between the range [0, 1]. By applying the values 0.007 and 0.1 for μ, it is observed that the error is less for the smaller step size value comparatively. So, it confirms the property that, smaller the step size value, greater is the convergence rate.

In Figs 7, 8, 9, 10 and 11, the *x*-axis and *y*-axis are parameters and iterations respectively. In Figs 6, 7, 8, 9, 10, 11 and 12, the *x*-axis and *y*-axis are error and

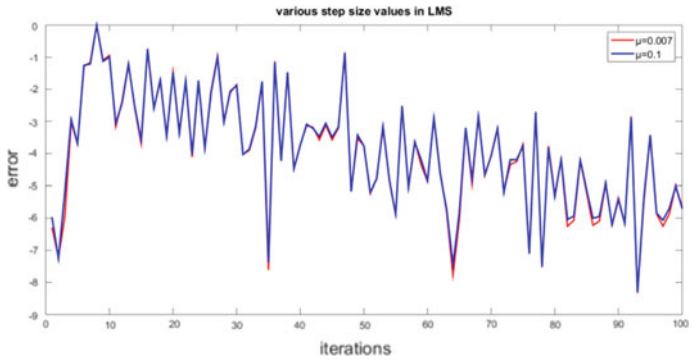

Fig. 6 Comparison of different values of step size for LMS

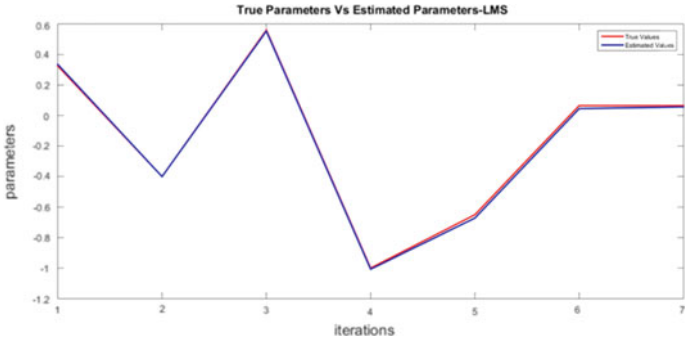

Fig. 7 True parameters versus estimated parameters of LMS

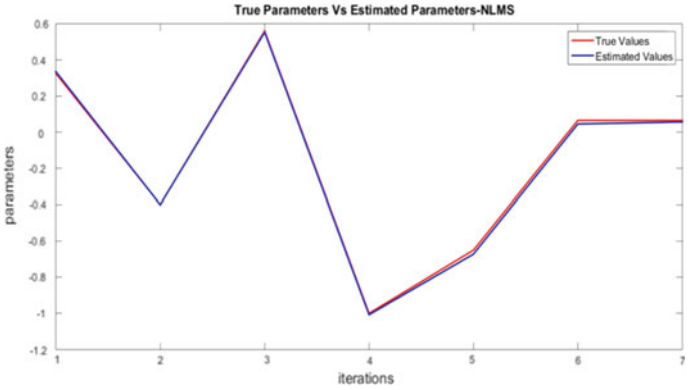

Fig. 8 True parameters versus estimated parameters of NLMS

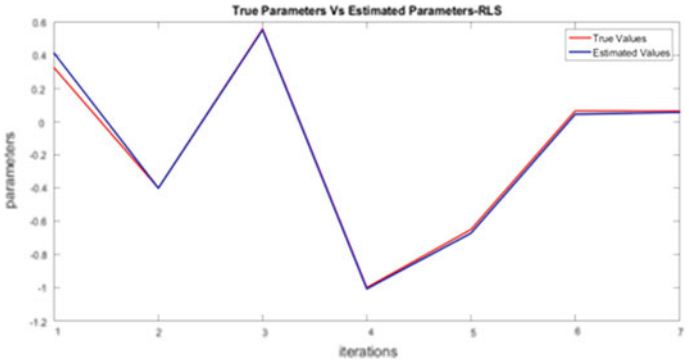

Fig. 9 True parameters versus estimated parameters of RLS

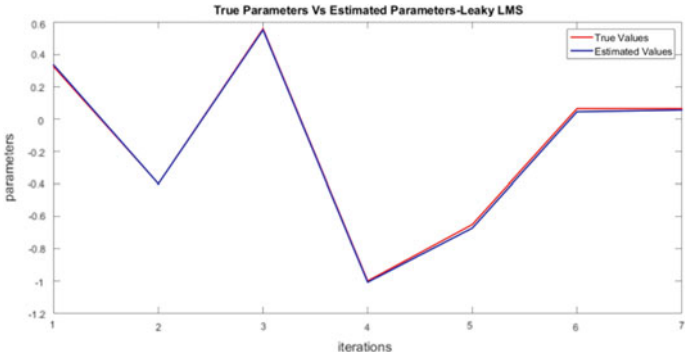

Fig. 10 True parameters versus estimated parameters of leaky LMS

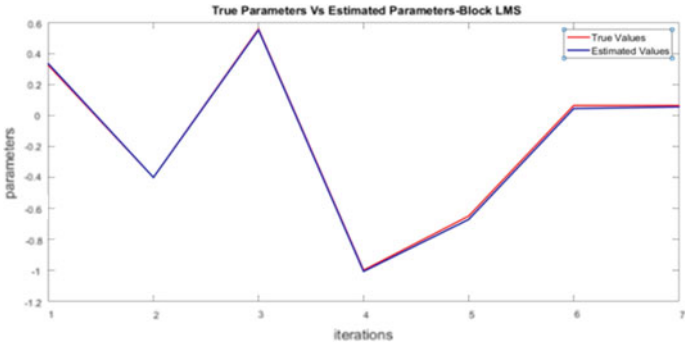

Fig. 11 True parameters versus estimated parameters of block LMS

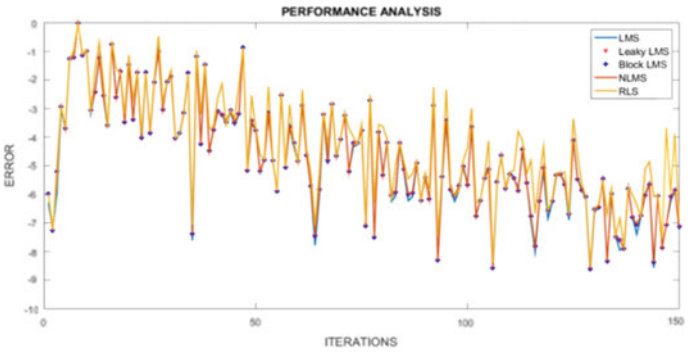

Fig. 12 Performance analysis of adaptive algorithms with respect to MSE

iterations respectively. The following plots Figs. 7, 8, 9, 10 and 11 are the comparison between the true parameters and estimated parameters of the system using different adaptive algorithms. From Fig. 6, it can be observed that the parameters can be estimated for different values of step size for LMS algorithm. From Fig. 7, it can be observed that the parameters estimated using LMS algorithm is approximately equal to the true parameters of the system. From Fig. 8, it can be observed that the parameters estimated using NLMS algorithm is approximately equal to the true parameters of the system [14, 15]. From Fig. 9, it can be observed that the parameters estimated using RLS algorithm is approximately equal to the true parameters of the system. From the below mentioned Fig. 10, it can be observed that the parameters estimated using Leaky LMS algorithm is approximately equal to the true parameters of the system.

From Fig. 11, it can be observed that the parameters estimated using Block LMS algorithm is approximately equal to the true parameters of the system. From Fig. 12, the performance analysis of various Adaptive algorithms is done based on the mean square error which determines the convergence rate of the system.

4 Conclusion

The main aim is to identify the unknown system using various adaptive algorithms, which works on the basis of weight updation process. To identify the system, the adaptive algorithms are used which are straightforward methods and are iterative in their process. From those results, it is concluded that the convergence rate of RLS is faster than the other Adaptive Algorithms. Though the complexity of RLS is higher than the complexity of the other Adaptive Algorithms, RLS has very less error after the end of iterations in order to obtain the true parameters. On the whole, the simulation results support the theoretical analysis. Those results indicate the good performance of these algorithms used for system identification.

References

1. Paleologu C, Benesty J, Ciochina S (2018) Adaptive filtering for identification of bilinear forms. Digit Signal Process 75:153–167
2. Kalouptsidis N, Koukoulas P, Mathews VJ (2003) Blind identification of bilinear systems. IEEE Trans Signal Process 51(2)
3. Ghauri SA, Sohail MF (2013) System identification using LMS, NLMS and RLS. In: IEEE student conference on research and development (SCOReD), 16–17 Dec 2013
4. Paleologu C, Benesty J, Ciochina S (2017) Analysis of LMS algorithm for bilinear forms. In: 22nd International conference on digital signal processing, 23–25 Aug 2017
5. Benesty J, Ciochina S, Paleologu C (2017) An NLMS algorithm for the identification of bilinear forms. In: 25th European signal processing conference (EUSIPCO)
6. Ciochina S, Paleologu C, Benesty J (2017) On the identification of bilinear forms with Wiener filter. IEEE Signal Process. Lett. 24(5)

7. Tan L, Jiang J (2014) Nonlinear active noise control using diagonal-channel LMS and RLS bilinear filters. In: Proceedings of 57th IEEE international Midwest symposium on circuits system, pp 789–792
8. Zhao H, Zeng X, He Z (2011) Low-complexity nonlinear adaptive filter based on a pipelined bilinear recurrent neural network. IEEE Trans Neural Netw 22(9):1494–1507
9. Zhu Z, Leung H (1999) Adaptive identification of bilinear systems. In: International conference on acoustics, speech and signal processing proceeding, 15–19 Mar 1999
10. Astrom KJ, Eykhoff P. System identification—A survey. Automatica 7:123–162
11. Söderström T, Stoica P (1988) On some system identification techniques for adaptive filtering. IEEE Trans Circ Syst 35:457–461
12. Reddy DC, Deergha Rao K (19991) An adaptive algorithm for nonlinear system identification. 16(3):263–274
13. Wang Z, Gu H (2007) Parameter identification of bilinear system based on genetic algorithm. In: International conference on life system modelling and simulation, LSMS 2007, pp 83–91
14. Paleologu C, Benesty J, Ciochina S (2017) An NLMS algorithm for the identification of bilinear forms. In: Proceedings of EUSIPCO, pp 2689–2693
15. Iqbal MA, Grant SL (2008) Novel variable step size NLMS algorithms for echo cancellation. Proceedings of IEEE ICASSP, pp 241–244

Design of Compact Paper Counting Machine

C. Sathishkumar, J. Selvakumar, S. R. Venkatesh, and M. Thoufeekahamed

Abstract In today's world, handing of papers is increased in shops and in institutions. In this generation, time has become the more important thing in every one's life. Counting and handling of papers in reprographies, stationeries, offices and educational institutions were done manually. It is difficult to count papers during peak working hours. Maintaining of big database in industries is difficult and it becomes too difficult in counting them. This generation people focuses to not waste their precious valuable time, manual counting will not be efficient and effective. Nowadays, in shopping malls, there are many vending machines which save the time of humans. The same is not followed in institutions and industries. The available paper counting machines are huge in size and it is too difficult to handle it. Counting of one or two papers is easy but counting many papers arises a problem and results in tedious process involving more time also. To overcome this problem, we have introduced a paper counting machine which will be useful for multiple applications. The machine consists of rollers, motors and electrical devices. The sensor used will detect the paper and the papers counted will be displayed on the LCD screen. Finally, the result will be of high accuracy in counting of papers automatically.

Keywords Counting · Vending · Rollers · LCD screen

1 Introduction

Time is the most powerful thing in coming generations; manual work in counting will not be efficient and effective. In places like shopping malls, the incorporation of automation plays a vital role in delivery of different products according to the need of customers. A vending machine is a type of machine which dispenses products or items such as water, chocolates, tea, coffee, and cool drinks. Those kinds of machines are seen in many places nowadays. These vending machines reduce the human effort

C. Sathishkumar (✉) · J. Selvakumar · S. R. Venkatesh · M. Thoufeekahamed
Department of Mechanical Engineering, Bannari Amman Institute of Technology, Sathyamangalam 638401, India
e-mail: sathishkumarc@bitsathy.ac.in

G. Kumaresan et al. (eds.), *Advances in Materials Research*, Springer Proceedings in Materials 5, https://doi.org/10.1007/978-981-15-8319-3_98

and save the time of every human. The vending machines operate on the principle of engineering. Automation is incorporated in shopping malls and industries but why not in institutes [1]. There is a demand for paper counting machines in offices and in institutes. The available invention purely lies on the principle of the field of mechatronics [2]. The automatic paper counting machine uses Arduino which is an embedded system for the proper required functioning of the machine. In this, the Arduino board receives the signal and sends signals to the input pins of a LCD display which shows the number of paper counted [3]. A sensing technology is used in the machine to sense the entered count and to send the corresponding signals to the Arduino board [4]. The paper counting machine is to count the paper which is performed by using a DC motor, paper feed mechanism, counting proximate sensors and pre-settable timer [5]. The paper is held in a paper tray, one end of which is passed through three guide rollers. This machine is designed and developed to deliver papers by inputting the suitable program in the system. The motto is to locate, identify, and count papers in the output area [6]. Thus, it is proposed in this project to design and fabricate an automatic paper counting machine, with the application of engineering principles, so as to save the time taken and to reduce the human effort taken to deliver the paper to the customer in required quantity and size. This machine also meets the higher demand for paper counting at the peak time in institutes during examination times. The machine is small in size, portable, and it is easy to handle.

2 Working Process

The concept lies on the automation area where the working or operating logic becomes simple. It lies in the manufacturing field, information technology field, and followed by electrical field. The machine is made with incorporating automation with the unique innovative arrangement for working. The logic involved here is giving input (i.e., giving the count of papers) and actuating the motors with the help of program to process the work and terminate the motors when the count becomes null (i.e., zero). The basic working principle is of paper counting and separating the bunch of paper to one by one. This paper counting machine consists of roller, key button, trays, DC motor, LCD display, and IR sensor. In this machine, initially, we insert the papers in the feeding tray, after that input is given. The LCD displays the number of papers. DC motor is connected to the axis of roller by using the DC clamp, with that command makes the DC motor to rotate and count the pages as well as sort out pages by the IR sensor's output data [7]. Our project basically designed for counting the A4 size paper. The rollers are mounted to the motors assembly. The roller is used to separate the paper from bunch of papers. The rollers are rotated at different RPM which is designated by the length of paper. The programming language used here is C language. The programming which is done controls the Arduino microcontroller. Finally, papers are collected by collecting tray (Fig. 1).

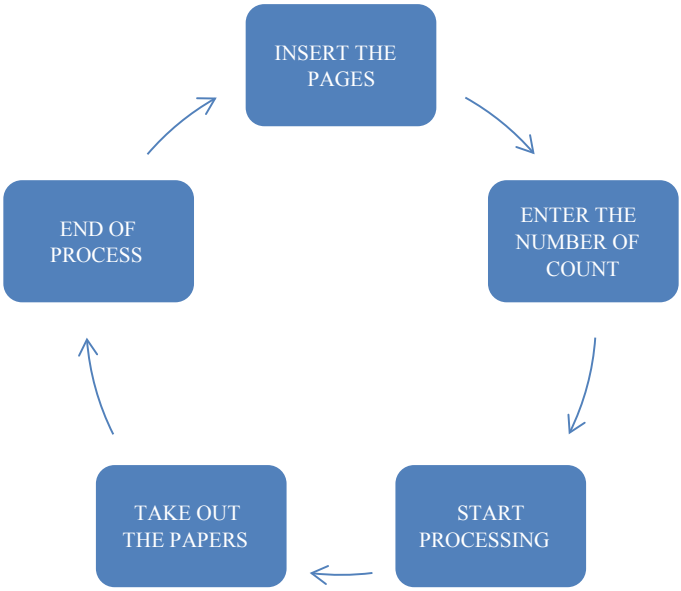

Fig. 1 Simple working representation of the automatic paper counting machine

3 Algorithm

The algorithm represents the step by step procedure of the program execution (Fig. 2).

The machine comprises of mechanical and electrical elements. Input is given as (count of papers) displayed in LCD display. The three-DC motor starts rotating clockwise. Motor shaft is connected to rollers. The four rollers are of different sizes used to pull the paper toward front and hence the processing starts [8]. Paper moves in paper feeding tray (sheet metal) attached with the help of acrylic side member which is connected with aluminum frame. The motors are actuated by using L239D drivers with the help of Arduino. The fourth roller is connected by means of pulley and belt with the third roller. Third roller connected to DC motor. The third and the fourth rollers are parallel to each other helping in getting the output of the incoming papers in the collecting tray. The IR sensor attached with the IR supporting card above the rollers detects the paper count [9]. As per programming logic, the input decrements (–) and if the count becomes zero the machine functioning stops (motors off).

4 Machine Image

See Figs. 3 and 4.

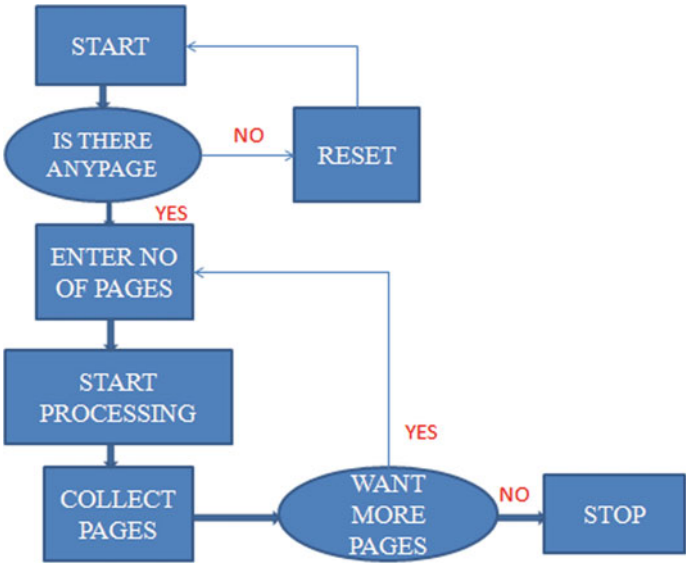

Fig. 2 Algorithm

Fig. 3 Design of paper counting machine

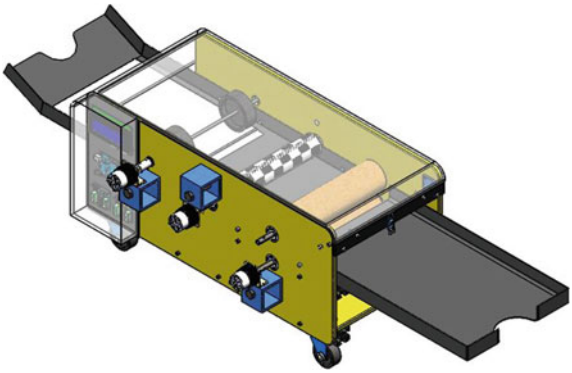

5 Result

The paper counting machine is tested in institutions, reprographies for counting of papers. By testing, it is found that the time involved in delivering the paper to the customer is reduced. The process of obtaining the count of paper is accurate. During peak hours, the papers were delivered efficiently. Human effort is reduced. Almost one paper per second is obtained as an output. The work is made easier in the machine and our entire objective is obtained.

Fig. 4 Real product machine

6 Conclusion

Many automatic vending machines are available now to deliver various products, but the counting machine to deliver bundle of paper is not available to the required need, which is a much needed one. The study is to develop a machine to count paper at low cost. After fabrication, the handling of this machine becomes very simple and it occupied only less space. This machine has a capacity of counting thousands of papers. The application of using paper is everywhere, so this counting machine can be used to reduce the time taken and human effort with higher accuracy in counting papers. Further improvements in this paper counting machine can be implemented when it becomes necessary.

References

1. Irshath Ahamed R, Mohamed Amir, Kamalnathan P, Kalaiselvan P (2015) Automatic paper vending machine. Int J Sci Eng Technol Res (IJSETR) 4(4)
2. Li Y, Tang Y, Zhang X, Liu N (2013) Study on paper separating mechanism of counting machine. In: Applied mechanics and materials, vol 312, 226–230. Trans Tech Publications Ltd.
3. Anju S, Chippy SR, Haritha H, Nijo VC, Er. Beena AO (2016) Automatic paper counting machine. Int J Sci Technol Eng (IJSTE) 2(10):917–921
4. Shaikh DA, Kedare AH, Sonawane PB, Jogdand SP (2016a) Cash Validation and exchange using arm 7. Int J Adv Res Innov Ideas Educ (IJARIIE) 2(2):994–1002
5. Wen L, Xuekai Y, Jin Y (2006) Design of automated packaging machine. Worcester Polytechnic Institute
6. Liu Y, Meng Q, Song X, Li A (2011) Research of automatic counting paper money technology based on two-dimensional histogram theta-division. In: MIPPR 2011: remote sensing image processing, geographic information systems, and other applications, vol 8006, p 80062A
7. Xuanju D, Jursheng Y (1995) Paper money sensors applied to counterfeit notes counting machine. J Trans Technol 1

8. Colijn A (2013) Automating and improving the printing planning process. University of Twente
9. Liang MIAO, Xi-Jian PING (2005) Algorithm of paper counting based on texture feature. J Inf Eng Univ 4

Sports Prediction Based on Random Forest Algorithm

G. Shobana and M. Suguna

Abstract The prediction of teams in sports plays an important role in today's world. The analysis of the team player based on past history helps users to choose players and place the players for match. It enables users to analyze the results of sports and predict the relevant outcome based on the tips provided. The main aim is to entertain users and engage them in online sports applications by providing information about previous matches and additional details about players, such as credits, number of balls with runs, time send on each ball, wicket placed, bowling, money earned, are made available. It also helps us to give suggestion for choosing best player by predictive analysis. The payment option is also made simple. User-friendly environment is created for effective usage of the system.

Keywords User interface · Sports prediction · Credits · Random forest algorithm · Fixture · Betting

1 Introduction

As the technology is growing, the online sports betting has become rapidly increase in the world. The most newly introduced betting on sports with their behavior of the matches in football, cricket, etc. The advertisement promotes betting on sports can be accessible anywhere with only Internet facility by using mobile itself. Placing the matches on betting process which was held on worldwide competitors with large events or fixture, the outcomes of betting process by winning or losing of the match. The betting of sports with the vast area such as basketball, cricket, boxing, hockey, baseball, auto racing, etc.

The popularity of online sports prediction has reached a greater extent. Cricket is one of the most popular sports. As the technology is growing at a faster pace, and the huge market in betting and huge demand for cricket has influenced the general

G. Shobana (✉) · M. Suguna
Department of Computer Science and Engineering, Kumaraguru College of Technology, Coimbatore, Tamil Nadu 641049, India
e-mail: shobana.g.cse@kct.ac.in

G. Kumaresan et al. (eds.), *Advances in Materials Research*, Springer Proceedings in Materials 5, https://doi.org/10.1007/978-981-15-8319-3_99

population to utilize machine learning calculations to predict the results of cricket matches. The playing can be done easily in online by using credit cards and debit card for playing the game. Online sports gaming can be playing from home itself from anywhere at any times thus based on consumer with convenience, the money can be placed in online bettors account by online.

The rest of the paper is organized as follows. Literature reviews are explained. Proposed system and their criteria are explained in Sect. 3. Experimental results are presented in Sect. 4. Concluding remarks are given in Sect. 5.

2 Existing System

Betting of online sports such as cricket, football, poker and other games involves placing a wager with some significance on the outcome of the games betting (2004). The past few years playing the games in online are increased in popularity and also provide some legal public health concerns, other jurisdictions, current legislation, and future outlooks [1].

Online gaming involves playing with software games and result are generated by software randomly based on some criteria. The betting on real-time matches in online based on how players perform the match [2]. Suggestions for future research includes: Dedicated studies based on experience in sports, experiences of young males, exploring how sports betting industry may affect the attitude and behaviors of risk groups [3]. Given minimal prior research on the topic, this study was considered exploratory. It used a mixed method design involving qualitative and quantitative elements..

2.1 Method 1

The literature review provides context for the study by outlining the growth of sports betting in Australia and factors that catalyzed the embedding of gambling promotions into sport broadcasts. The types and extent of sports betting promotions are reviewed along with the limited research examining these practices. Community concerns about these promotions are discussed, especially in relation to previous research on effects of gambling advertising on gambling attitudes, intentions and behaviors [4, 5].

2.2 Method 2

Stage two aimed to explore Queensland sports viewers' responses to gambling promotions during televised sport and inform instrumentation for stages three and

four. Thirty-nine regular sports viewers participated in eight online focus groups, comprising 21 men and 18 women. Eighteen were aged 18–29 years and 21 were aged 30–60 years, with a similar distribution of regular sports bettors (18) and non-spots bettors (21). To accommodate the geographic dispersion of participants and preserve anonymity, focus groups utilized blackboard collaborate, an online conferencing program. This allowed participants to converse in real time while sharing text, images and online video content [6, 7].

2.3 Issues in Existing Systems

1. No chance to change a selected player: If a player chosen by the user, the chance to change the player (adding substitute) is not given [8].
2. No provision of information on past records: The information about previous match records and player statistics is not provided to the user.
3. Betting option: Only player-wise betting option is provided in existing system. No alternative like toss-wise betting and over-wise betting are included.
4. Payment option: Payments through existing online sports betting apps seem to be more complicated. Deposition and transaction of money through the app are a difficult task for the users.

3 Proposed System

The prediction of the sports provides user-friendly environment. The machine learning algorithm can be used to make prediction in real-time sports, by using past history from the various sources about the teams [9]. It predicts which player is best in less time consumption, high efficiency level. Each record is verified from the sites before uploading in databases. The activity of predicting the sports results and wagering on the outcome, analyze the sport results and predict the probable outcome based on the provided ideas and hints. It also displays additional details about the user data, credits and money earned.

- Prediction of winning or losing of a particular team based on information from previous records.
- According to the game played, the betting strategies will change.
- Each user is given a chance to change player at a given time interval.
- Betting happens right from the toss up to match end.
- Equal distribution of prize money among the winners with maximum points.
- In order to make predictions, certain tips will be provided to the user (Fig. 1).

The users can choose any of the events such as (1) user can choose a currently running match of his choice and place the bet. (2) Prediction is categorized into toss-wise, over-wise, player-wise prediction. (3) The user can place the bet according to

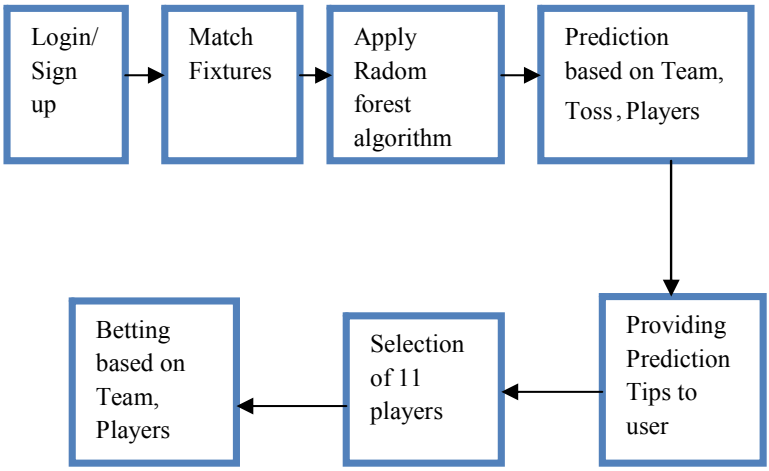

Fig. 1 Architecture of prediction system

his choice. User has to pay the amount demanded by the app to place the bet on a certain match. After the creation of account, the user will be provided a wallet. User is able to use wallet for banking, transactions, depositing money and payment.

3.1 Random Forest Algorithm

Historical data about the match records and player's performance is be fetched from various sources. A random forest algorithm builds multiple decision trees and those trees are combining to get better results. It can be used for both classification and regression tasks. The importance values of each feature used are obtained using random forest classifier algorithm and by knowing the importance of each attribute, clustering techniques are performed to do prediction. It will be provided to the user as prediction tips. With the help of tips displayed, the user can make wise decisions in betting. Selecting, altering and changing a team player at a given interval time are done in this application distribution of prize money among winners according to the rank.

3.2 Prediction Categories

Prediction are categorized into toss-wise, player-wise and team-wise prediction.

Selection of 11 Players
From a total of 30 players from 2 teams, 11 best players must be selected by the user to place the best. Prediction tips will be provided to users to select the best batsmen based on detailed analysis of best batting average and best strike rate of each player. Tips for selecting best bowlers will be based on analysis of best bowling average and number of wickets taken by each player. The user can select batsmen and bowlers in ratio of 6:5 or 7:4 accordingly. The dataset is taken from prediction for cricket match as shown in Fig. 2.

Team-Wise Prediction
For team-wise betting, comparisons between team 1 and team 2 are performed by considering factors like toss winner, match winner and toss decision. A prediction rule is implemented to get the count of

	game_id	match_type	team_inn1	team_inn2	toss_winner	toss_decision	match_winner
0	386530	ODI	Sri Lanka	India	India	field	India
1	386531	ODI	India	Sri Lanka	India	bat	India
2	386532	ODI	India	Sri Lanka	India	bat	India
3	386533	ODI	India	Sri Lanka	India	bat	India
4	386534	ODI	Sri Lanka	India	Sri Lanka	bat	Sri Lanka
5	386623	ODI	India	New Zealand	India	bat	India
6	386626	ODI	India	New Zealand	India	bat	no result
7	386627	ODI	India	New Zealand	New Zealand	field	India
8	386624	ODI	New Zealand	India	New Zealand	bat	India
9	386625	ODI	India	New Zealand	India	bat	New Zealand
10	377313	ODI	India	West Indies	India	bat	India
11	377314	ODI	India	West Indies	India	bat	West Indies
12	377315	ODI	West Indies	India	India	field	India
13	377316	ODI	West Indies	India	India	field	no result
14	403382	ODI	New Zealand	India	New Zealand	bat	India
15	403381	ODI	Sri Lanka	India	Sri Lanka	bat	Sri Lanka
16	403383	ODI	India	Sri Lanka	India	bat	India
17	415278	ODI	Pakistan	India	Pakistan	bat	Pakistan
18	415281	ODI	Australia	India	Australia	bat	no result
19	415284	ODI	West Indies	India	India	field	India
20	416236	ODI	Australia	India	Australia	bat	Australia
21	416237	ODI	India	Australia	Australia	field	India

Fig. 2 Dataset for prediction of cricket match

- Toss won, chosen batting, match won
- Toss won, chosen bowling, match won
- Toss won, chosen batting, match lost
- Toss won, chosen bowling, match lost
- Toss lost, match won
- Toss lost, match lost of the two teams between which the match will happen.

With the help of this information, accurate prediction tips are provided to place bet in upcoming matches are given Fig. 3 for cricket match.

Fig. 3 Toss- and team-wise prediction

Player-Wise Prediction (Batsman)
In player-wise betting, the best batsmen is selected by prediction using the conditions:

$$\text{Best\_Player} = ((\text{Matches played} - \text{Innings Batted})/\text{Innings Batted}) < 0.05 \quad (1)$$

$$\text{Best\_player} = (\text{Runs scored}/\text{Innings batted}) > 40 \quad (2)$$

The batsmen records which satisfy these conditions from Eqs. 1 and 2 are taken and those batsmens are referred to users through prediction tips.

Player-Wise Prediction (Bowlers)
In player-wise betting, the best bowlers are selected by prediction using the conditions

$$\text{Best\_ blower} = \text{Bowlig strike rate} > 0 \quad (3)$$

$$\text{Best\_blower} = \text{Innings bowled} > 10 \quad (4)$$

The bowler's records which satisfy these conditions from Eqs. 3 and 4 are sorted in ascending order according to their bowling strike rate and topmost bowlers in list are referred to users through prediction tips. The player-wise prediction based on bowlers is shown in Fig. 4.

	Player	Innings Bowled In	Balls Bowled	Runs Conceded	Wickets Taken	Bowling Avg	Economy Rate	Bowling Strike Rate	Four Wickets In An Innings	Five Wickets In An Innings
0	JM Anderson (200202015)	191	9504	7861	269	29.22	4.92	35.6	11	2
1	D Gough (199402009)	155	8422	6154	234	26.29	4.38	35.9	10	2
2	SCJ Broad (200602016)	121	6109	5364	178	30.13	5.26	34.3	9	1
3	A Flintoff (199602009)	116	5490	3968	168	23.61	4.33	32.7	6	2
4	IT Botham (197601992)	115	6271	4139	145	28.54	3.96	43.2	3	0
5	PAJ DeFreitas (198701997)	103	5712	3775	115	32.82	3.96	49.6	1	0
6	PD Collingwood (200102011)	151	5186	4294	111	38.68	4.96	46.7	3	1
7	TT Bresnan (200602015)	84	4221	3813	109	34.98	5.42	38.7	3	1
8	CR Woakes (201102018)	74	3654	3355	109	30.77	5.50	33.5	8	2

Fig. 4 Player-wise prediction based on bowlers

4 Conclusion

As the results, sports fans increase their engagement and connect deeper with the sport along with a profitable outcome in economy. The results and decision values are obtained using random forest algorithm by doing a detailed analysis with information from previous records and performing predictions, the most accurate results are provided as tips to the users which will be very useful for them to place the bet and gain profits. This will induce more interest among users in sports and people will use it as a good tool to make money as well.

References

1. Hing N (2014) Sports betting and advertising. Australian Gambling Research Centre, Australian Institute of Family Studies, Melbourne, pp 1–11
2. Jacobs DF (2000) Juvenile gambling in North America: An analysis of long term trends and future prospects. J Gambling Stud 16:2-3119-152
3. Wicker P, Soebbing BP (2013) Examining participating in sports betting in Germany. J Gambling Bus Econ 6(3):17–33
4. Gainsbury SM, Blaszczynski A, Sadeque S (2012) Wagering in Australia: a retrospective behavioural analysis of betting patterns based on player account data. J Gambling Bus Econ
5. McCormack A, Shorter GW, Griffiths MD (2013) An examination of participation in online gambling activities and the relationship with problem gambling. J Behav Addict 2(1):31–41
6. Killick EA, Griffiths MD (2019) In-play sports betting: a scoping study. Int J Mental Health Addict 17(6):1456–1495
7. Deans EG, Thomas SL Derevensky J, Daube M (2017) The influence of marketing on the sports betting attitudes and consumption behaviors of young men: implications for harm reduction and prevention strategies. J Harm Reduction 5
8. Davide C, Orazi JL (2015) The nature and framing of gambling consequences in advertising. J Bus Res 68(10):2049–2056
9. Parke A, Parke J (2018) Transformation of sports betting into a rapid and continuous gambling activity: a grounded theoretical investigation of problem sports betting in online settings. Int J Mental Health Addict 1340–1359

Experimental Study on Machinability of Metal Matrix Composite by Abrasive Water Jets

B. Siddharthan and A. Kumaravel

Abstract The unconventional machining of ceramic reinforced metal matrix composites is innovative. The machinability of aluminium alloy and boron carbide metal matrix composite with the abrasive water jets is discussed here. Two discrete proportions of Al-B_4C metal matrix composites were prepared with different mesh size, transverse rate, flow rate of abrasives and water pressure so as to distinguish the effectiveness of the AWJ machine for possible handling of metal matrix composites with abrasive water jets (AWJs). The penetration capability of abrasive water jets in various cases of metal matrix composites (MMCs) was experimented in trapezoidal-shaped aluminium boron metal matrix composite specimens which are prepared by stir casting method. Optical micrographs of metal matrix composite tests and scanning electron microscopic (SEM) examination of abrasive water jet cut surfaces empower to clarify the trends of material evacuation by the abrasives. Examination of results distinctly demonstrated the decision of abrasives of mesh size 80 with high water pressure and stream rate and low transverse rate results in effective processing of Al-B_4C MMCs with AWJs.

Keywords Metal matrix composites · Abrasive water jets · Depth of cut

1 Introduction

Metal matrix composites (MMCs) are materials comprising of at least two material constituents (matrix and reinforcement). On account of MMCs, matrix materials are like aluminium, magnesium, titanium, etc., and other is the reinforcement materials like silicon carbide, boron carbide and alumina in different structures (particles,

B. Siddharthan (✉)
Department of Mechatronics, Bannari Amman Institute of Technology, Sathyamangalam, Tamil Nadu, India
e-mail: siddharthan@bitsathy.ac.in

A. Kumaravel
Department of Mechanical Engineering, K.S. Rangasamy College of Technology, Tiruchengode, Tamil Nadu, India

G. Kumaresan et al. (eds.), *Advances in Materials Research*, Springer Proceedings in Materials 5, https://doi.org/10.1007/978-981-15-8319-3_100

whiskers and fibres). The unconventional machining processes, especially abrasive water jet machining plays an interesting role in the field of space vehicles and automotive sectors [1]. The samples were experimented for different input parameters of feed rate and transverse rate with fixed standoff distance. The machinability index of the composites was determined. Srivastava et al. [2] deals with the microhardness measurements on an aluminium alloy-based hybrid metal matrix composite with alumina and boron carbide as the reinforcements. In this work, the composites were machined by wire cut EDM and abrasive water jet turning process. The results reflect that the hardness value and the residual stress of the composite show better results when compared to wire cut EDM machined samples. The kerf taper angle and width were the ban to the machining of the composites. It was optimized using Taguchi's method by Gupta et al. [3]. The result reveals that optimizing the transverse speed of nozzle minimizes the kerf width and taper. The carbon fibre reinforced polymer (CFRP) composites along with the metallic material is conducted with 3D cutting and 2.5D cutting by Putz et al. [4]. In this case, the composite is prepared by the alternation layers of CFRP and metals for the dimensions of 2.5D and 3D machining, and it is concluded as 3D machining were promising for maximum tolerable forces. When a number of literatures were discussing about the testing, mathematical modelling [5] discussed the surface integrity of the machined surfaces. In this case, aluminium, magnesium, titanium and copper alloys were taken as the test sample materials. The materials were reinforced with ceramics and they are machined by electro discharge machining and were tested for microhardness and detected for surface defects. James and Narkhede [6] experimented with CFRP and titanium and with the submerged abrasive water and the find out that the higher the reinforcement, higher will be the hardness and lower will be the machinability.

Hejjaji et al. [7] conducted experiments with the carbon fibre reinforced epoxy composite specimens. The specimens were milled with abrasive water jets to study about their impact and tensile behaviour. It is concluded that the milling depth is purely influenced by the jet pressure and transverse speed of jet. Surface waviness is the result of variation in the standoff distance and the machined surfaces exhibit higher tensile strength for best machining parameters. CFRP with multidirectional chopped reinforced composites were studied by Deepak and Paulo Davim [8], El-Hofy et al. [9]. They experimented with the CFRP laminates with abrasive water jets for multilaminates with varying input parameters like feed rate and standoff distance and are evaluated by ANOVA technique. The results show that kerf width increase with increasing pressure and standoff distance. Uhlmann amd Männel [10] modelled titanium aluminide in ductile and brittle states and tested with abrasive water jets for kerf cutting operations. Josyula et al. [11], James and Narkhede [6] explained about the non-traditional method of machining the metal matrix composites using liquid nitrogen. In this method, the liquid nitrogen is sprayed over the conventional tool such that the wear of the conventional tool gets reduced.

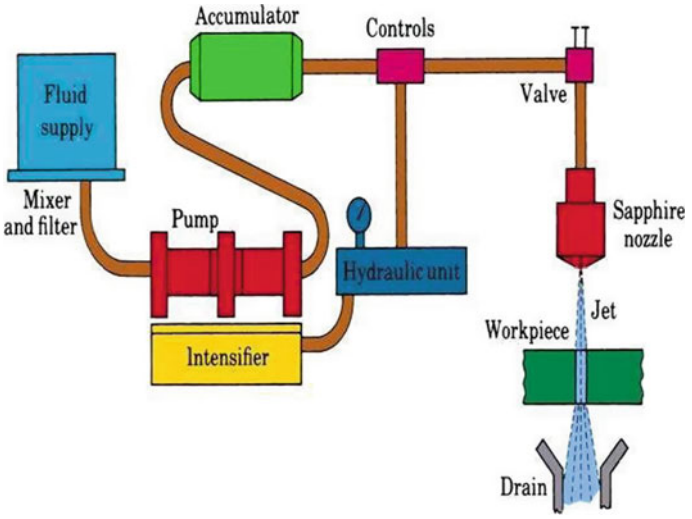

Fig. 1 Schematic view of abrasive water jet machining

2 Experimental Setup

The schematic view of the abrasive water jet machining is shown in Fig. 1. In the setup, the water at high pressure and the abrasive particles are mixed together and passed through the nozzle to achieve the machining [12, 13]. The machining is carried out in aluminium alloy with boron carbide in various proportions. The workpieces were fabricated into trapezoidal shapes by stir casting method such that the depth of cut $d = h_{\max} \sin 35^\circ$ can be estimated.

3 Process Parameters

Various parameters were utilized in the process of machining of composites by abrasive water jets. The input parameters include pressure, transverse rate, mesh size and flow rate of abrasives. Depth of cut is the net output of the process.

Materials selected.

Aluminium + Boron Carbide.

4 Experimental Procedure

4.1 Preparation of Al7075-B_4C Metal Matrix Composites

Stir casting method is constantly utilized to fabricate aluminium metal matrix composites. In stir casting technique, metal matrix composites were fabricated by dispersing reinforcement into the matrix material in molten state by continuous stirring activity and transferring it into the die and then solidified. To fabricate complex size, metal matrix composites by stir casting process, it is least difficult and the savviest technique to manufacture. A special shape of sample in trapezoidal shape at 35° of the objective material has been selected for trial and maximum depth of cut is investigated by abrasive water jet pressure in the various MMC samples performed by abrasive water jets cutting. The maximum depth of cut (h max) in the manufactured composites with chosen suitable process parameters can be evaluated using the relationship $h_{\max} = L \sin 35°$, where L is the slant length of cut in the wedge shape. The metal matrix composites utilized in this examination comprise of Al7075 compound strengthened with boron carbide (B_4C) particulate of 400 work sizes. Table 1 gives the chemical composition of Al7075 alloy.

Table 1 gives the various proportions of materials in Al7075 alloy. The quantity of Al7075 alloy and B_4C required to fabricate unreinforced aluminium alloy and 5% volume level of B_4C are taken by weight basic requirements. Aluminium alloy (Al7075) were placed in gas-fired crucible and elevated to temperature of about 500 °C to melt the matrix material completely and place it in semi-solid state [14]. The boron carbide is preheated up to 400–500 °C for 60 min to remove the moisture property by expelling the retained water molecules and different gases. The heated matrix material at liquid state is introduced with the stirring action at 200–300 rpm for 10 min. Degassing tablet (cupflux) is introduced into the molten mixture to expel the slag. The preheated boron carbide particles were included into the molten matrix material by stirring action at a velocity of 20 m/s for 10 min, and the furnace is kept at the temperature of 750 °C. The blend is kept underneath, the 75% of the liquid metal in crucible furnace and more than 25% at the base of furnace at this stage. This helps the valuable to uniform distribution of the Al7075 and B_4C. Figures 2 and 3 show gas-fired furnaces and the blend is transferred to the die in trapezoidal shape.

During pouring, the molten melt into a wedge shape die at the temperature maintained around 600 °C which was allowed to solidify in the wedge shape die. Figure 4 shows the pictorial of trapezoidal shape of casted composite specimen produced by the stir casting process.

Table. 1. Al7075 alloy—composition

Alloy	Zinc	Magnesium	Copper	Silicon	Manganese	Titanium	Chromium	Aluminium
Al7075	5.6—6.1	2.1–2.9	1.2–2.0	0.4	0.3	0.2	0.2	87.1–91.4

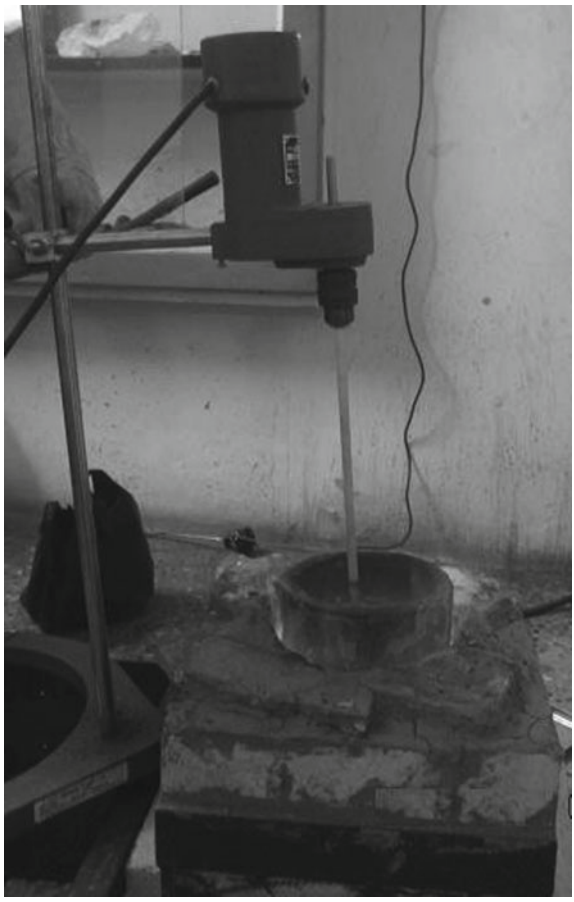

Fig. 2 Gas-fired furnace and setup of stir casting

Fig. 3 Pouring mixture MMCs in wedge-shaped die

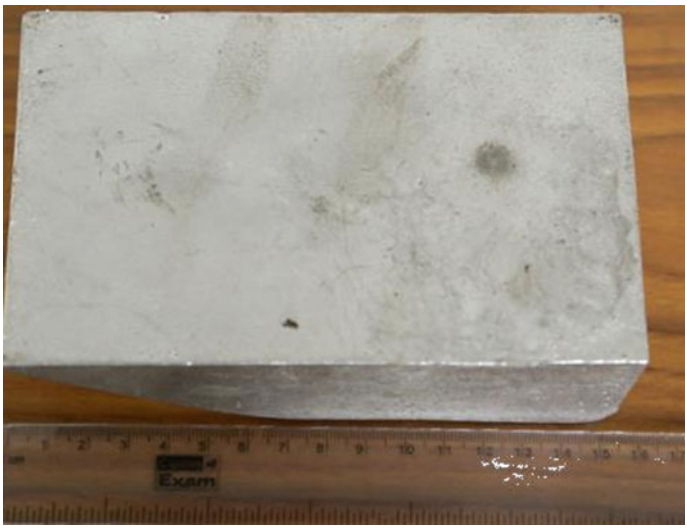

Fig. 4 Casted composite

The presence of reinforcement through the specimen was inspection by cutting the casting at different locations and under microscopic test, tensile test, SEM and EDAX test.

5 Experimental Method

To contemplate the impact of water jet pressure, transverse rate, abrasive flow rate and size of abrasive particles were experimented on various specimens by utilizing abrasive water jet machining system. The objective material was manufactured to trapezoidal in shape. An apparatus was intended to grasp the specimens in order to evade its dislocation during the process. In abrasive water jet machining course of action, the stream was made to impinge the sample at a point of 90° and most extreme depth of cut was noted. The extreme depth of cut of water stream into the objective material was acknowledged by analyzing the sprinkling of jet. With a standoff distance of 2 mm between the nozzle and the base material, trials were conducted with considering the input parameters factors like water jet pressure, traverse rate and flow rate of abrasive and mesh size of abrasives with the entire factor being changed at various levels as shown in Table 2.

Table 2 Process parameters

S. No	Process parameters	Minimum	Medium	Maximum
1	Size of abrasive particles (μm)	80	100	120
2	Water jet pressure (Mpa)	125	200	275
3	Abrasive flow rate (kg/min)	0.24	0.34	0.44
4	Traverse rate (mm/min)	60	90	120
5	Diamond water jet orifice diameter (mm)	0.25		
6	No. of passes	1		
7	Angle of cutting (degree)	90°		
8	Abrasive material	Calcite		
9	Focusing nozzle diameter (mm)	0.75		

5.1 Input Process Parameter

The machined workpiece is shown in Fig. 5. The figure indicates the wedge-shaped workpiece in which the lines show the number of passes that the machining of the workpiece has undergone. Totally, a series of 21 passes has been done on each sample with the aid of ANOVA method.

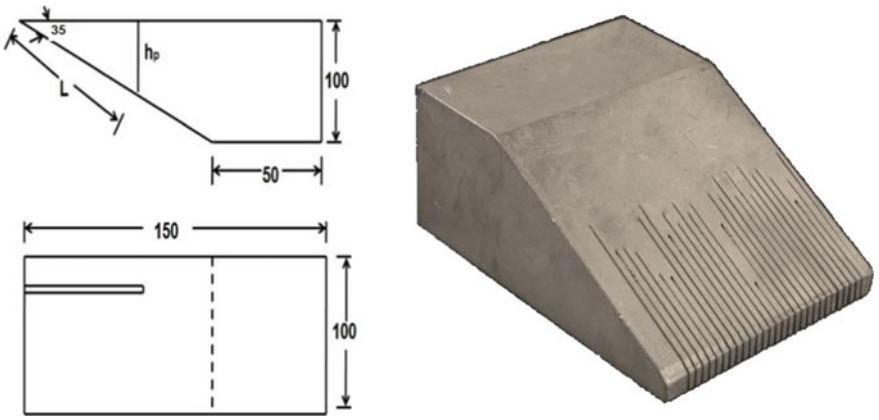

Fig. 5 Photograph of aluminium work piece

6 Results and Discussion

6.1 SEM TEST (Scanning Electron Microscopy)

The device that produces the images of the target material by utilizing the converged light emission of the electrons is the scanning electron microscope (SEM). The electrons emitted from the source examine and publish information about the surface of the target specimens and their chemical compositions.

The most comprehensively strategy of acknowledgment is by secondary electrons transmitted by particles invigorated by the electron beam. On a target surface, the tuft of secondary electrons is commonly contained by the target, yet on a tilted surface, the outside is mostly secured and more electrons are released. By checking the example and recognizing the secondary electrons, an image demonstrating the topography of the surface is made. Since the marker is not a camera, there is no diffraction limit for goals as in optical magnifying lens and telescopes. The SEM test of two compositions is appeared in Fig. 6a, b. The images are captured at the magnification of 100 μm. Figure 6a shows the microstructure of the pure aluminium, which is dominantly covered with grey surface. The lines show the presence of other constituents in the aluminium 7075 grade. Figure 6b indicates the microstructure of boron carbide reinforced composite samples. The dispersion of boron carbide is clearly visible at the 100 μm magnification.

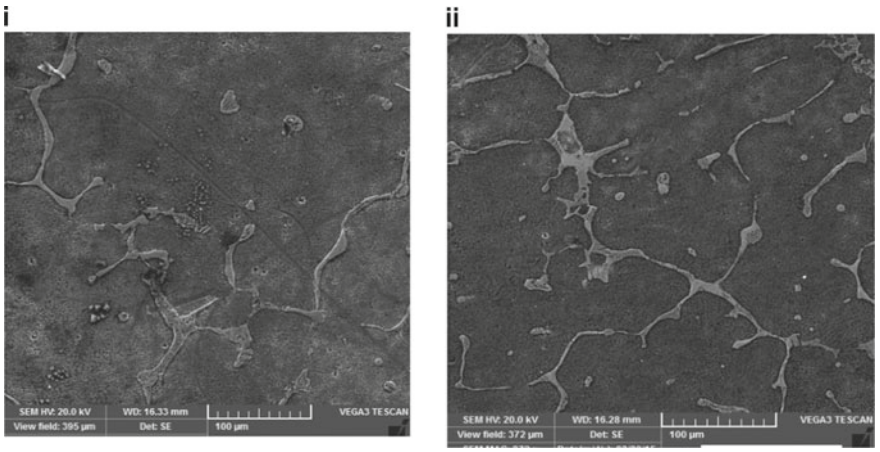

Fig. 6 **a** Pure Al. **b** 5% B_4C and 95% Al

Table 3 Hardness value for metal matrix composites

Sample	Hardness measurement (HV) at various locations			Average hardness (HV)
Al7075	60.2	60.4	59.7	60.1
Al7075 + 5% B_4C	64.9	65.1	64.6	64.3

6.2 Hardness Measurement

The hardness test was carried in Vickers hardness tester which has a testing load range of 10 g–1 kg load and testing scale used is HV. The prepared samples have undergone a load of 0.5 kg with reside time 10 s in three locations of each sample. The hardness value of the specimen is determined by taking the average of the hardness values taken at multiple locations as stated in Table 3.

6.3 Tensile Test

The tensile tests were conducted on the prepared specimen and the following results are obtained.

The above graphs 7a, b show the tensile strength of the pure aluminium alloy cast and boron carbide reinforced aluminium alloy cast. The stress–strain curve for the pure aluminium indicates the elastic and plastic flow of the material. When the load is further increased the material undergoes plastic deformation and reaches the ultimate point. At the same time, the 5% B_4C reinforced aluminium composite fails at the same loading condition, where the pure aluminium alloy yields. This is due to the presence of reinforcement in the aluminium alloy. From the results, it is found that the breaking load increases with increase in reinforcement. Figure 7b show that the breaking point occurs suddenly as a result of increase in brittleness, which is a property of composites.

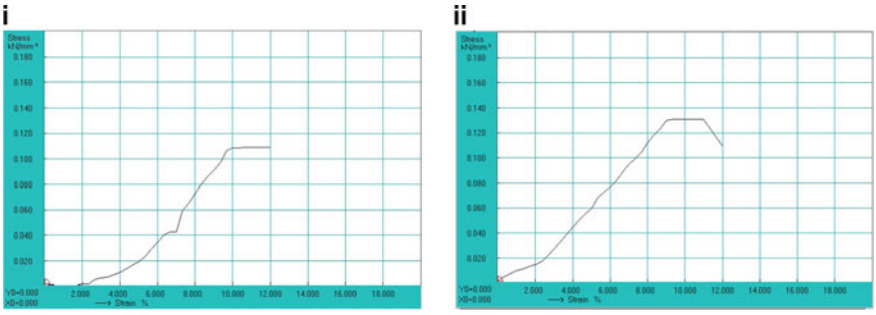

Fig. 7 **a** Pure aluminium. **b** 5% B_4C and 95% Al

7 Depth of Cut

The prepared sample is machined by varying the associated input parameters. From the experiments, it is seen that the depth of cut value decreases with increase in mesh size of abrasives, and furthermore maximum depth of cut is accomplished with maximum flow rate of abrasives, maximum water pressure with lower traverse rate. These observations can be easily visualized through a three-dimensional graph which is shown below.

Figure 8a–d shows the three-dimensional analysis graphs of depth of cut readings of the pure aluminium alloy casts.

The above graphs show that the depth of cut values increase with decrease in size of abrasive particles. Maximum depth of penetration is achieved with higher water pressure and abrasive flow rate with low traverse rate.

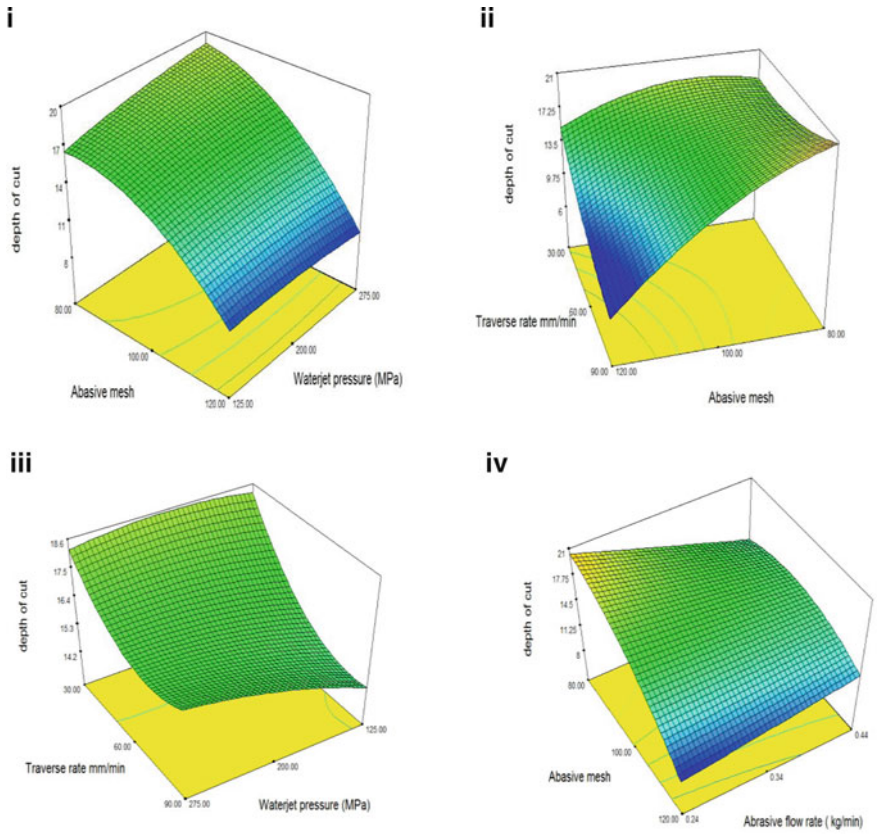

Fig. 8 **a** Abrasive mesh versus jet pressure. **b** Traverse rate versus abrasive mesh. **c** Traverse rate versus jet pressure. **d** Abrasive mesh versus abrasive flow rate

In following graphs, Fig. 9a–d show the analysis of depth of cut on the 8% boron carbide reinforced aluminium composite.

The above figures show the analysis of depth of penetration for MMCs (Al7075 + 5% B_4C). With decrease in the mesh size of abrasives, the depth of cut value increases. Higher depth of penetration is achieved with higher water pressure and abrasive flow rate with lower traverse rate. Unreinforced aluminium alloy exhibits higher depth of cut than that of the aluminium metal matrix composite (Al7075 + 5% B_4C).

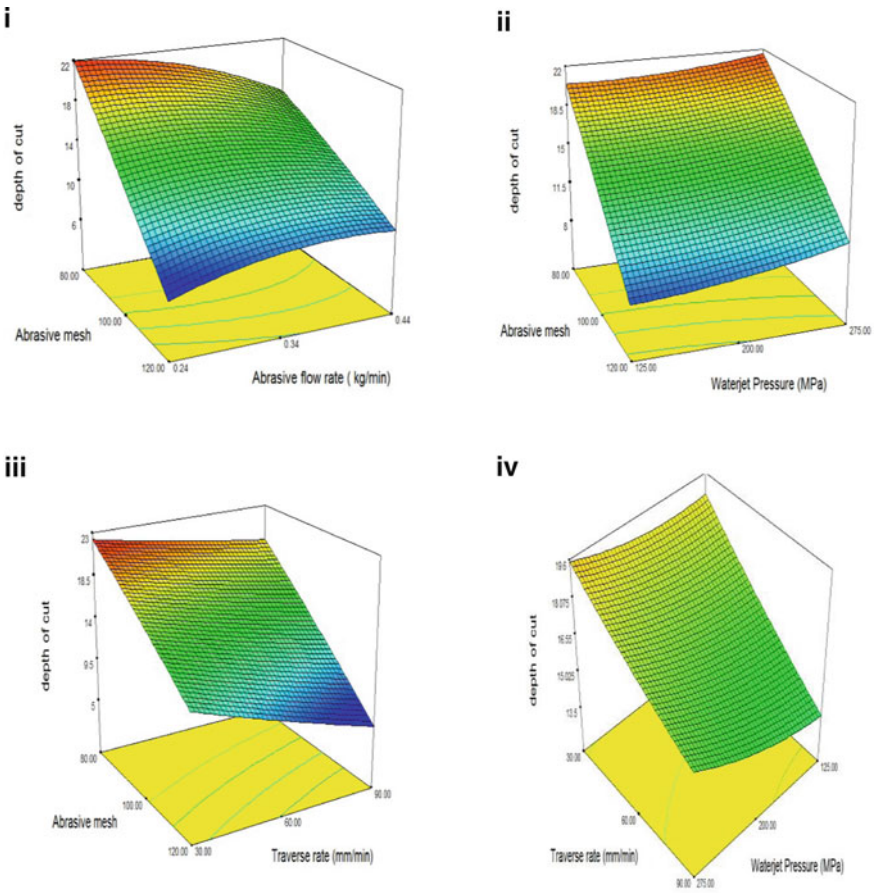

Fig. 9 **a** Abrasive mesh versus abrasive flow rate. **b** Abrasive mesh versus jet pressure. **c** Abrasive mesh versus traverse rate. **d** Waterjet pressure versus traverse rate

8 Conclusion

From the perceptions, the results were concluded as follows: The presence of boron carbide reinforcement in the aluminium alloy enhances the material properties like hardness and tensile strength of the composite. The improvement is due to the brittle nature of the ceramic reinforcement boron carbide. Depth of cut can be increased decreasing the transverse rate of machining. Maximum depth of cut is accomplished when the abrasive flow rate and water jet pressure are maximum. At a lower mesh size, higher depth of cut is achieved. The abrasive size of #80, water jet pressure of 275 psi, abrasive flow rate of 0.44 g/s and the transverse rate of 60 m/s give the perfect machining of the composites. Pure aluminium alloy exhibits higher depth of cut than that of the metal matrix composite (Al7075 + 5% B_4C). This is because of the reality that the higher level of boron carbide in the metal matrix composite prompts improvement in the mechanical properties.

References

1. Alberdi A, Suárez A, Artaza T, Escobar-Palafox GA, Ridgway K (2013) Composite cutting with abrasive water jet. Procedia Eng 63:421–429
2. Srivastava AK, Nag A, Dixit AR, Scucka J, Hloch S, Klichová D, Hlaváček P, Tiwari S (2019) Hardness measurement of surfaces on hybrid metal matrix composite created by turning using an abrasive water jet and WED. Measure: J Int Meas Confederation 131:628–639
3. Gupta V, Pandey PM, Garg MP, Khanna R, Batra NK (2014) Minimization of Kerf Taper angle and Kerf width using Taguchi's method in abrasive water jet machining of marble. Procedia Mater Sci 6:140–149
4. Putz M, Rennau A, Dix M (2018) High precision machining of hybrid layer composites by abrasive waterjet cutting. Procedia Manuf 21:583–590
5. Liao Z, Abdelhafeez A, Li H, Yang Y, Diaz OG, Axinte D (2019) State-of-the-art of surface integrity in machining of metal matrix composites. Int J Mach Tools Manuf 143:63–91
6. James S, Narkhede M (2019) Analytical modeling and experimental study on machining of CFRP/Ti stacks with submerged abrasive waterjet machining. Procedia Manuf 34:328–334
7. Hejjaji A, Zitoune R, Crouzeix L, Le RS, Collombet F (2017) Surface and machining induced damage characterization of abrasive water jet milled carbon/epoxy composite specimens and their impact on tensile behavior. Wear 376–377:1356–1364
8. Deepak D, Paulo Davim J (2019) Multi-response optimization of process parameters in AWJ machining of hybrid GFRP composite by grey relational method. Procedia Manuf 35:1211–1221
9. El-Hofy M, Helmy MO, Escobar-Palafox G, Kerrigan K, Scaife R, El-Hofy H (2018) Abrasive water jet machining of multidirectional CFRP laminates. Procedia CIRP 68:535–540
10. Uhlmann E, Männel C (2019) Modelling of abrasive water jet cutting with controlled depth for near-net- shape fabrication. Procedia CIRP 81:920–925
11. Josyula SK, Narala SKR, Charan EG, Kishawy HA (2016) Sustainable machining of metal matrix composites using liquid nitrogen. Procedia CIRP 40:568–573
12. Uhlmann E, Flögel K, Sammler F, Rieck I, Dethlefs A (2014) Machining of hypereutectic aluminum silicon alloys. Procedia CIRP 14:223–228

13. Kumar SS, Hiremath SS (2016) A review on abrasive flow machining (AFM). Procedia Technol 25:1297–1304
14. Marimuthu S, Dunleavey J, Smith B (2019) Laser based machining of aluminum metal matrix composites. Procedia CIRP 85:243–248

Study on Effect of Deposition Thickness on Temperature Distribution of Various Shaped 3D Printed Components

Arundeep Murugan, Mulatu Mengistayehu, N. Ummal Salmaan, and C. Sasikumar

Abstract In the modern-day manufacturing process most of the precision components are made by 3D printing technique, the quality of these components is decided by the layer deposition rate and the temperature distribution during printing. Experimental investigation of temperature distribution analysis on the 3D printing machine due to the variations of supply material thickness and heat flux produced with the help of connected thermocouples on the 3D printer machine was carried out in this research work. Two shapes (cube and cylinder) were used for comparison. Thickness variations were created from 5 to 15 micron. Heat flux variations were created from 10 to 30 W. These variations were used to produce simple cube and cylinder for the temperature distribution analysis.

Keywords 3D printer · Temperature distribution · Thickness · Heat flux · Cube · Cylinder

1 Introduction

3D printing is also said to be additive manufacturing (AM). It refers to processes under computer control used to manufacture 3D objects in which consecutive layers of substance are shaped to create an object.

Szykiedans and Credo [1] experimentally investigate about various mechanical properties of FDM and SLA low-cost 3-D prints especially for tensile modulus. They

A. Murugan (✉) · M. Mengistayehu
School of Mechanical & Industrial Engineering, Institute of Technology, Debre Markos University, 269 Debre Markos, Ethiopia
e-mail: arundeepmurugan@gmail.com

N. Ummal Salmaan
Faculty of Mechanical Engineering, Aksum Institute of Technology, Aksum University, 1010 Aksum, Ethiopia

C. Sasikumar
Department of Mechanical Engineering, Bannari Amman Institute of Technology, Sathyamangalam, Erode 638401, Tamil Nadu, India

G. Kumaresan et al. (eds.), *Advances in Materials Research*, Springer Proceedings in Materials 5, https://doi.org/10.1007/978-981-15-8319-3_101

mentioned mean, maximum and minimum tensile modulus of a tested various 3-D printers materials.

Rahman et al. [2] clearly showed that the plastic ribbon feed from a huge coil all the way through a set of moving gears to a heated barrel of an extruder of a 3D printer head as a schematic diagrammatic representation.

Lee et al. [3] completely explained about controllable-pitch Archimedean screw for Pico-hydropower generation design and 3D printing method. They showed prime variables of Archimedean screw. They mentioned the fabrication process of CPAS (Controllable-pitch Archimedean screw) and also fabricated CPAS images.

Felber et al. [4] experimentally explained about Air-Cooled Heat Exchangers design and Modelling in 3D-Printing. They clearly mentioned geometric configuration air-side microstructure, macrostructure for left side and right side respectively and also mentioned the effect of thermal conductivity on heat exchanger volume as a graph. They concluded that 3D-printed heat exchangers performance away from the thermal conductivity of the printed material.

Jerez-Mesa et al. [5] described that thermal performance of easily available open-source 3D printer (d-printer) extruder new design of liquefier (twist 3D) and modelling with the help of FEA. They showed the self-defined and mesh defined BC Nozzle liquefier with parts also illustrate 3D isothermal map of extruding liquefiers and streamlines for airflow around heat sink for BC Nozzle and B-Twist3D.

Jerez-Mesa et al. [6] explained about thermal performance of a RepRap 3D printer liquefier. They showed the segment of the geometrical domains defined in the finite element method for joint compose the liquefier body and also section of the analyzed BC Nozzle liquefier and materials, viewing the diverse components. They mentioned the boundary conditions and initial values for the FEM of Planar symmetry, Air inflow surface, Air outflow surface and Embedding hole for the heating resistor also mesh convergence study based on the minimum relative error criterion.

Günther et al. [7] explained about a variety of additive manufacturing technologies, compound filament production has freshly encouraged open-source proposal to build up 3D printing devices capable to fulfil the needs of customers' side.

Singh et al. [8] discussed about mathematical and systematic study of 3D printer extruder in Fused Deposition Modelling and they create complete solid CFD model of liquefier with PLA space filled for the computation. They showed the pictorial representations of liquefier temperature gradient, temperature distribution throughout the extruder of heat sink and the temperature distribution for triangular fins heat sink, heat sink having the elliptical fin and extruder having the rectangular with elliptical perforation fins.

Temperature distribution uniformity enhancement during casting solidification was carried out by Mageshwaran et al. [9] using methoding process.

Kostakis et al. [10] completely discussed about the 3D printing for educational experimental usage of two schools in Greece. They showed the schematic demonstrations of various parts.

2 Experimental Setup and Procedure

The experimental procedure followed [11–13] as per flow chart in Fig. 1. Figure 2a showed the Cube with sides of 40 mm and the cylinder with diameter 40 mm and height 40 mm shown in Fig. 2b. These shapes based on [14] were selected for this temperature distribution analysis of the 3D printer. There are three different layers of material flow rate with three different heat flux range considered for analysis of cube and cylinder. Temperatures were measured with the help of thermocouples connected

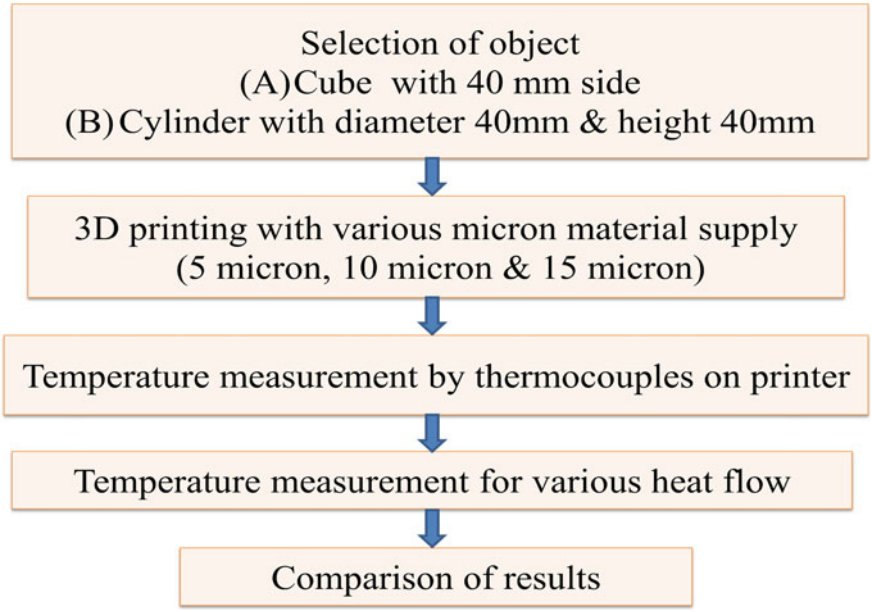

Fig. 1 Experimental procedure

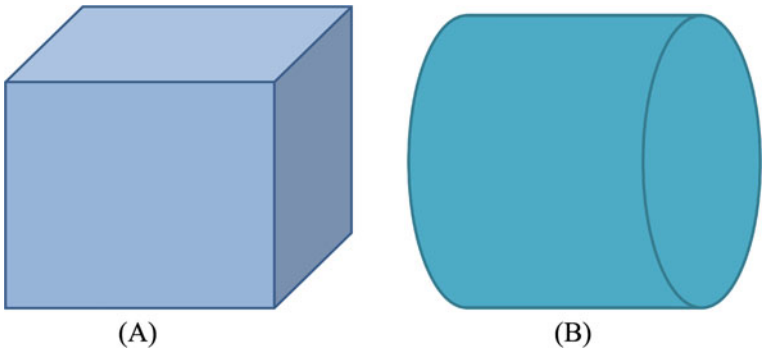

Fig. 2 **a** Cylinder with diameter 40 mm and height 40 mm, **b** cube with sides of 40 mm

with the printer surface and the average temperature used for analysis similar to [10, 15].

3 Results and Discussion

The measured temperature values after printing in 3D printer plotted with respect to the time in seconds. Figures 3, 4 and 5 showed the Time versus Average temperature plot for 10 W heat fluxes, 20 W heat fluxes and 30 W heat fluxes respectively for cube. Also Fig. 6 clearly mentioned the Time versus Average temperature plot for different heat flux with various thicknesses of materials supplied by the printer which combines all the values corresponding to their conditions for cube. Figures 7, 8 and 9 without a doubt plot the graphical representation between average temperatures and time for range for 5, 10 and 15 micron thickness of material supplied by 3D printer respectively for cube. Temperatures range for different thickness of material

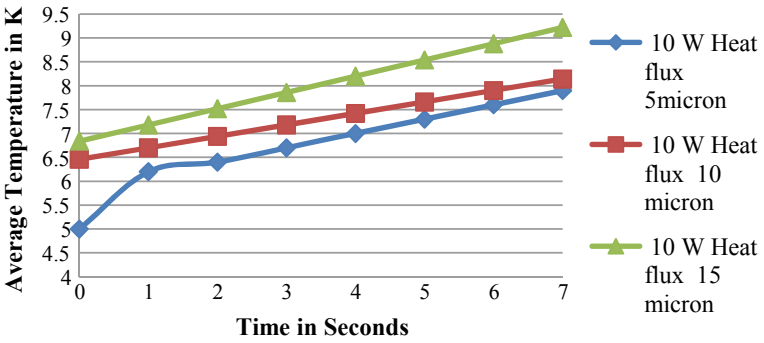

Fig. 3 Time versus average temperature for 10 W heat fluxes for cube

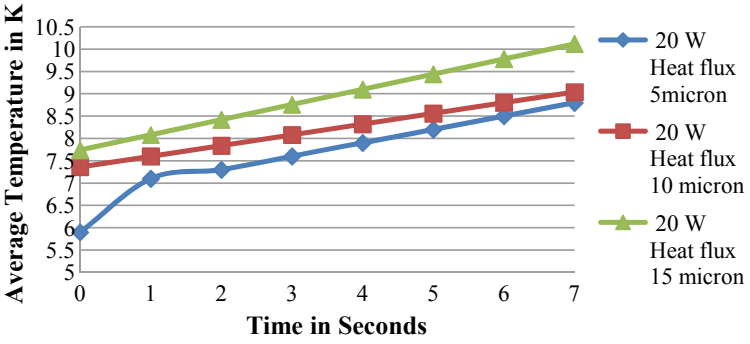

Fig. 4 Time versus average temperature for 20 W heat fluxes for cube

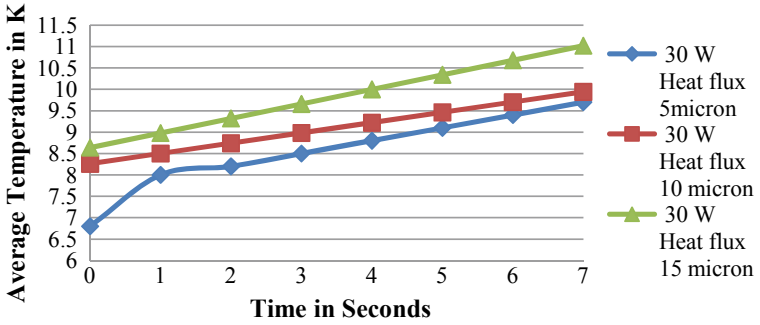

Fig. 5 Time versus average temperature for 30 W heat fluxes for cube

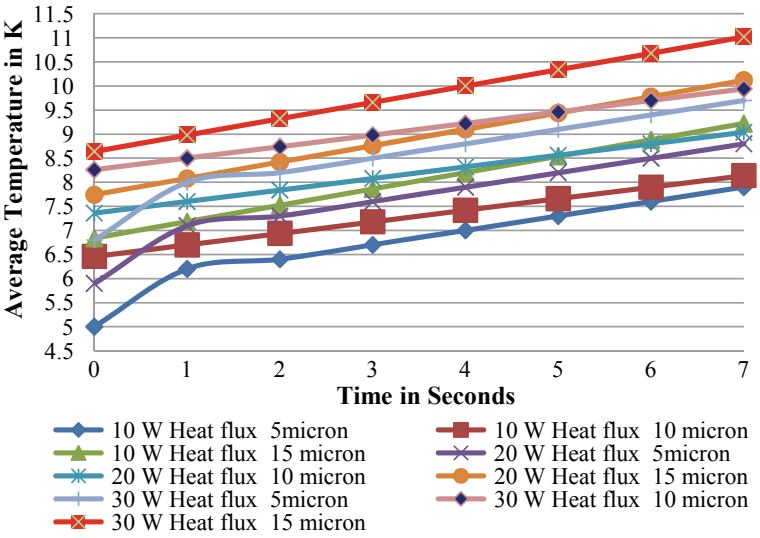

Fig. 6 Time versus average temperature for different heat flux with various thicknesses of materials for cube

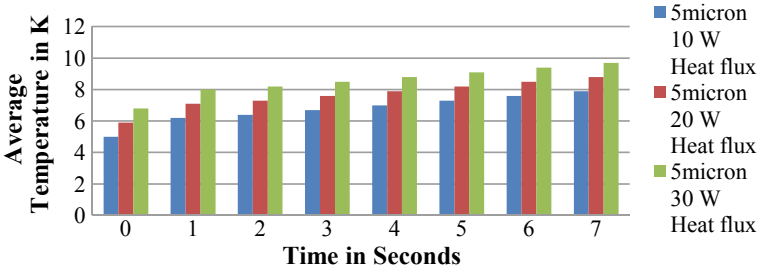

Fig. 7 Temperatures range for 5-micron thickness of material supply for cube

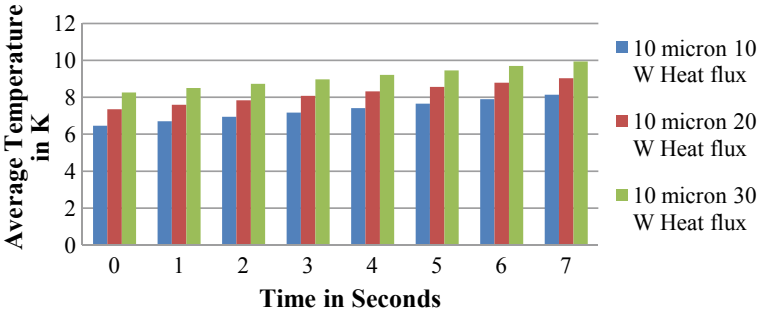

Fig. 8 Temperatures range for 10-micron thickness of material supply for cube

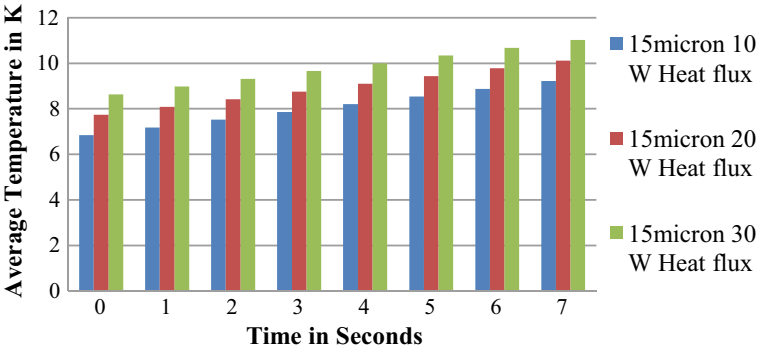

Fig. 9 Temperatures range for 15-micron thickness of material supply for cube

supplied by the 3D printer with various heat fluxes for cube with respect to different thickness of supplied material was undoubtedly shown in Fig. 10.

Figure 11 mentioned between Time and Average temperature for different heat flux with various thicknesses of materials for cylinder and also Temperatures range for different thickness of material supply with various heat fluxes with respect to different thickness of supplied material for cylinder values were noted in Fig. 12. The maximum and minimum average temperature values for cube and cylinder were mentioned in Fig. 13.

4 Conclusions

By this experimental investigation of temperature distribution on the 3D printer for two shapes produced the following conclusions.

- Heat flux and thickness of the material supplied by the 3D printer also create influence in the temperature distribution on that for both cube and cylinder.

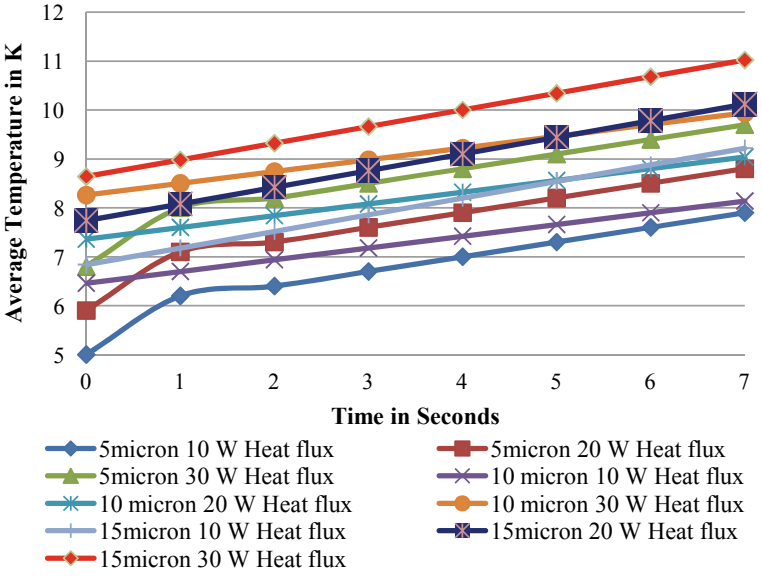

Fig. 10 Temperatures range for different thickness of material supply with various heat fluxes with respect to different thickness of supplied material for cube

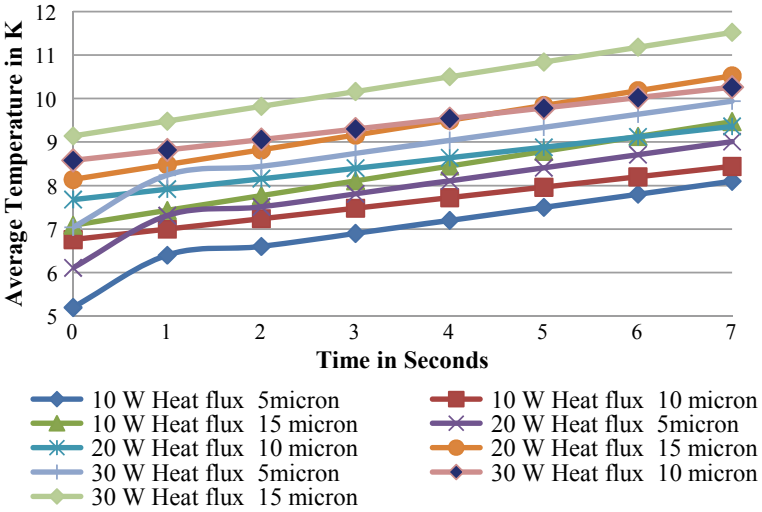

Fig. 11 Time versus average temperature for different heat flux with various thicknesses of materials for cylinder

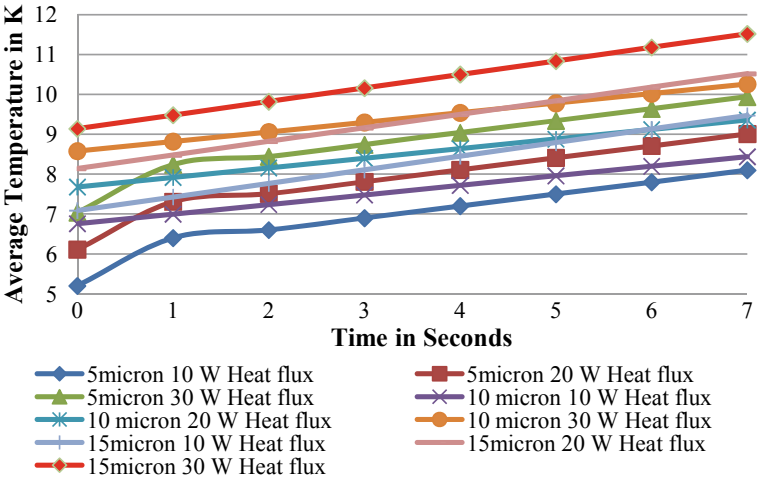

Fig. 12 Temperatures range for different thickness of material supply with various heat fluxes with respect to different thickness of supplied material for cylinder

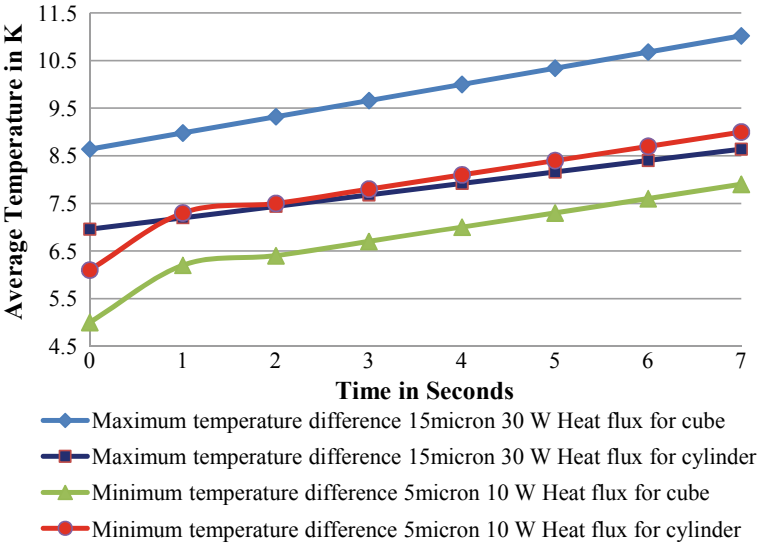

Fig. 13 Temperatures range for maximum and minimum values of cube and cylinder

- Heat flux is directly proportional to the temperature produced on the 3D printer.
- Thickness of material supplied by 3D printer is directly proportional to the temperature produced on the 3D printer for both cube and cylinder.
- Maximum average temperature reached on the 3D printer for 15 micron of thickness material supplied with 30 W of heat flux and also the minimum average

temperature reached at 5 micron of thickness of material supplied and 10 W of heat flux after fabrication for both cube and cylinder.

- The cube has the maximum average temperature values when compared to cylinder similarly, cylinder has the lower average temperature values when compared to cube for the same conditions.

References

1. Szykiedans K, Credo W (2016) Mechanical properties of FDM and SLA low-cost 3-D prints. Procedia Eng 136(2016):257–262
2. Rahman M, Schott NR, Sadhu LK (2016) Glass transition of ABS in 3D printing. https://www.comsol.com/paper/download/361301/rahmanpaper.pdf
3. Lee KT, Kim E-S, Chu W-S, Ahn S-H (2015) Design and 3D printing of controllable-pitch archimedean screw for pico-hydropower generation. J Mech Sci Technol 29(2015):4851–4857
4. Felber R, Nellis G, Rudolph N (2016) Design and modeling of 3D-printed air-cooled heat exchangers. In: International refrigeration and air conditioning conference. https://docs.lib.purdue.edu/iracc/1763
5. Jerez-Mesa R, Travieso-Rodriguez JA, Gomez-Gras G, Freixedes J (2015) Design of open source 3D printer extruder and modelling of thermal performance with FEA. J Trends Dev Mach Assoc Technol 19(1):189–192
6. Jerez-Mesa R, Travieso-Rodriguez JA, Corbella X, Busqué R, Gomez-Gras G (2016) Finite element analysis of the thermal behavior of a RepRap 3D printer liquefier. Mechatronics 000(2016):1–8
7. Günther D, Heymel B, Günther JF, Ederer I (2014) Continuous 3D-printing for additive manufacturing. Rapid Prototyping J 20(4):320–327
8. Singh SK, Prof. Satankar RK (2017) Numerical and analytical analysis of 3D printer extruder in fused deposition modelling. J. Emerging Technol Innov Res 4(10):10–22
9. Mageshwaran G, Polisetti SR, Jeya Jeevahan G, Joseph B (2016) Enhancement of uniform temperature distribution during casting solidification by methoding process. Int J Ambient Energy 38(8):774–780
10. Kostakis V, Niaros V, Giotitsas C (2014) Open source 3D printing as a means of learning: An educational experiment in two high schools in Greece. Telematics Inform 32(2015):118–128
11. Durairaj RB, Mageshwaran G, Sriram V (2016) Investigation on Mechanical properties of glass and carbon fiber reinforced with polyester resin composite. Int J Chem Tech Res 9(6):417–423
12. Schmutzler C, Zimmermann A, Zaeh MF (2016) Compensating warpage of 3D printed parts using free-form deformation. In: 48th CIRP conference on manufacturing systems 2015, vol 41, pp 1017–1022
13. Casavola C, Cazzato A, Moramarco V, Pappalettere C (2016) Orthotropic mechanical properties of fused deposition modelling parts described by classical laminate theory. Mater Des 90(2016):453–458
14. Li D, Dai N, Jiang X, Chen X (2015) Interior structural optimization based on the density-variable shape modeling of 3D printed objects. Int J Adv Manuf Technol 83(2016):1627–1635
15. Durairaj RB, Chereyala M, Mageshwaran G, Jeevahan J (2016) Surface roughness and corrosion characterisation of multi-walled carbon-nanotube-reinforced zirconium composite coated over SS316L. Int J Ambient Energy 39(1):54–57

Computer-Aided Thermal Control System of 3L-ANPCI Using LabVIEW

E. Sarangapani, N. Narmadhai, and C. Kokila Vani

Abstract In this paper, computer-aided (IoT) thermal control system of three-level active neutral point clamped inverter (3L-ANPCI) was proposed using LabVIEW. The Internet of Things (IoT) allows objects to be sensed or remotely controlled through existing network, creating opportunities to incorporate the physical world more deeply into the computer-based system. In addition to reducing human intervention, this results in improved efficiency, reliability and economic benefit. In many applications such as a PV network, active neutral point clamped inverter is the most desirable inverter topology due to the equal distribution of losses for switches. This topology helps the capacitors to achieve voltage balancing. The goal is to control the temperature of the junction and protect the system's uneven switching losses. LabVIEW is commonly used as an industrial monitoring and control system interface. Multisim can be used to co-simulate the three-level neutral point clamped inverter. The inverter input SPWM pulse can be supplied from LabVIEW to Multisim. The results of the simulation are confirmed by those derived from a mathematical calculation. The analysis of both tests verifies the reliability and validity of the IoT temperature monitoring from the specific IP address.

Keywords Internet of Things (IoT) · NPC inverter · ANPC inverter · IOT control · Junction temperature

1 Introduction

For over 25 years, multilevel structures have been studied and are an insightful solution for linking serial switches. The inner switches and the two clamp diodes take

E. Sarangapani (✉) · C. Kokila Vani
Department of Electrical Engineering, Bannari Amman Institute of Technology, Sathyamangalam, Erode, Tamilnadu 638401, India
e-mail: eeesaranga22@gmail.com

N. Narmadhai
Department of Electrical Engineering, Government College of Technology, Coimbatore, Tamil Nadu 641013, India

G. Kumaresan et al. (eds.), *Advances in Materials Research*, Springer Proceedings in Materials 5, https://doi.org/10.1007/978-981-15-8319-3_102

the role of the middle switches in the three-level stacked cells structure. The concept of the 3L converter with flying capacitors was later introduced by another invention. The design of static converters must ensure that the temperature of the junction for the power devices will not exceed acceptable limits in all different operating conditions. Power devices junction temperature is at result of losses in switching and conduction. The increased level of equal distribution of temperature between semiconductor and junction allows for a subsequent hike in the output power of the converter or results in increased frequency of switching. The unequal distribution of losses among semiconductors is a major drawback to the structure of three-level neutral point clamped inverter. A better balance of total power system losses has been achieved through the use of topologies: three-level active neutral point clamped and three-level stacked neutral point clamped inverter. The paper compares the three-level neutral point clamped inverter and three-level active neutral point clamped converter performance. Such converters' switching states are also examined, and their effect on the power system loss balance is clarified. The results of the MULTISIM and LabVIEW conduction and simulation are shown to verify the switching state analysis.

2 Comparison of Existing System with Proposed Methodology

2.1 Neutral Point Clamped Inverter

NPC [1]-style multilevel inverters play a vital role in power electronics and are commonly used in various industrial and commercial applications because they have low electromagnetic interference and significantly high performance (Fig. 1).

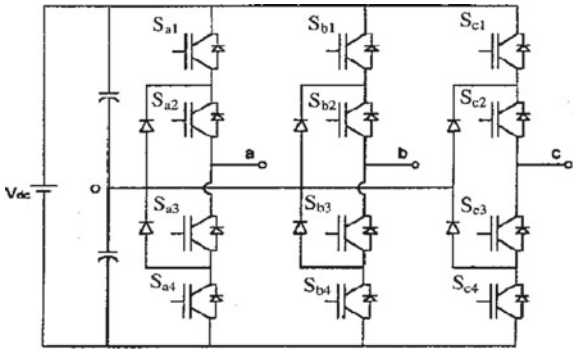

Fig. 1 Neutral point clamped inverter

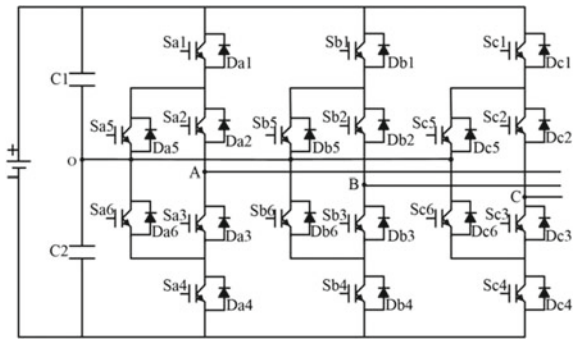

Fig. 2 Active neutral point clamped inverter

2.2 Active Neutral Point Clamped Inverter

For high-power, medium-voltage applications, the three-level neutral point clamped inverter [1] is widely used. The NPC inverter's main downside is that the switching failure will not be distributed evenly among the switches. The effective neutral point clamped switches were proposed to solve this problem [2].

For high-voltage applications, the active neutral point clamped inverter (ANPC) [2] is suitable. It is a combination of a multilevel inverter clamped neutral point. This is achieved by replacing clamping diodes with semiconductor switches, with proper selection of switching states controlling voltage balancing across condensers. The three-level ANPC multilevel inverter is as shown in Fig. 2. A single leg per phase of three-level ANPC inverter is made of six bidirectional switches, each switch composed of IGBT and antiparallel diode. Switches are grouped into three commutation combinations (S1, S1′), (S2, S2′) and (S3, S3′) as a complementary of switch pair. Thus, if one switch from complementary switch pair is turned on, the other of the same pair must be in off condition. Two switches are always turned on at the same time. State "1" means switch is ON, and state "0" means switch is OFF.

2.3 Control Technique for Three-Level ANPC MLI Point Clamped Inverter

PWM technique is used for inverter output voltage control [3]. The switching signal is created in pulse width modulation technique by comparing the basic reference signal with the carrier wave of the appropriate switching frequency. The reference signal frequency defines the frequency of the basic output wave, and the modulation index is determined by its amplitude. There are various PWM schemes available for controlling multilevel inverters. Among all SPWM [3] are selected for ANPCMLI control, further classified as phase disposition, phase opposite disposition and alternate phase opposite disposition SPWM. Two triangular carrier signals are required for three-level active neutral point clamped inverter. The carriers are expected to

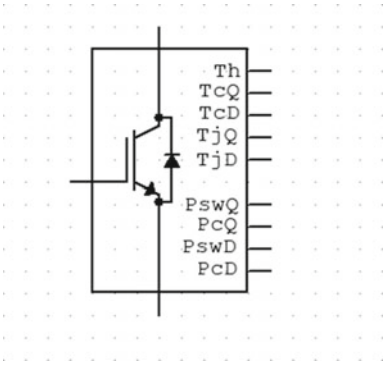

Fig. 3 IGBT thermal module

have the same frequency and high to low amplitude. The carrier is compared to the modulating signal at each moment. Every comparison switches the switch ON and is greater than the triangular carrier signal assigned to the switch. SPWM control signal for three-level ANPC is presented in Fig. 3 [4].

2.4 Switching Sequence

Complementary [5] switch pair presents in each phase (S1, S1′), (S2, S2′) and (S3, S3′), and gating signals S1′, S2′ and S3′ are generated by inverting S1, S2 and S3. Carrier-1 generated pulses are given to cell-1 and carrier-2 generated pulses cell-2.

2.5 Junction Temperature

Power electronic switches are essential components of electronic power converters and work in thermally Strengthy environments. A power semiconductor's junction temperature [6] directly affects its power loss and is eventually related to various mechanisms of failure. Therefore, knowing this temperature is important for purposes of optimal operation and reliability. If the T_j is known during a converter operation, it is possible to build real-time condition monitoring and active thermal control systems to improve system performance. Direct T_j measurements are difficult to perform since the power semiconductor is usually encapsulated in a variety of packaging materials. In fact, a semiconductor's electrical activity is highly temperature-dependent. If this relationship is established, it is possible to monitor the system's electrical parameters and use them to calculate the T_j.

2.6 Conduction Losses

The conduction losses [7] are the sum of the conduction loss in IGBT [7] and diodes, which are determined by static characteristics of the devices. The total losses consist of conduction losses

$$P_{\text{CON}} \text{ and swit } P_{\text{TOTAL}} = P_{\text{CON}} + P_{\text{SW}} \tag{1}$$

$$P_{\text{con,T}} = v_{\text{T}}.I_{\text{avg}}^{\text{con,T}} + r_{\text{r}}.\left(I_{\text{rms}}^{\text{con,T}}\right)^2 \tag{2}$$

$$P_{\text{con,D}} = v_{\text{D}}.I_{\text{avg}}^{\text{con,D}} + r_{\text{D}}.(I_{\text{rms}}^{\text{con,D}})^2 \tag{3}$$

$$V_{\text{T}} = V_{\text{o,T}} + K_{\text{V,T}}\left(T_{\text{j,T}} - T_{\theta}\right) \tag{4}$$

where V_{D}, r_{t} and r_{D} in (3), (4) can be described as follows,

$$V_{\text{D}} = V_{\text{o,D}} + K_{\text{v,D}}\left(T_{\text{j,D}} - T_{\theta}\right) \tag{5}$$

$$r_{\text{T}} = r_{\text{o,D}} + K_{\text{v,T}}\left(T_{\text{j,D}} - T_{\theta}\right) \tag{6}$$

$$r_{\text{D}} = r_{\text{o,D}} + K_{\text{v,D}}\left(T_{\text{j,D}} - T_{\theta}\right) \tag{7}$$

Switching losses P_{SW} as expressed below.

2.7 Switching Losses

Total energy losses from switching are obtained in IGBTs and diodes as a sum of energy losses during switches on and off. The losses of switching can be expressed by the equation below [8].

$$P_{\text{SW,T/D}} = \frac{1}{2\pi}\frac{(\alpha_2 - \alpha_1)}{2\pi}\int_{\alpha_1}^{\alpha_2} f_{\text{SW}} E_{\text{SW,T/D}}\,(i_{\text{c}})d(\omega t)$$

Table 1 Switching sequence

S/W	S1	S2	S3	S4	S5	S6	O/P
V1	1	1	1	0	0	0	VDC/2
V2	0	1	0	1	0	0	0
V3	0	1	0	1	0	1	0
V4	0	0	1	0	0	1	0
V5	1	0	1	0	1	0	0
V6	0	0	0	1	1	1	−VDC/2

3 Results and Discussion

3.1 Simulation Circuit for 3L-ANP Inverter

The three-level neutral point clamped inverter was designed in Multisim [9]. The Multisim-designed circuit simulation diagrammatic representation is shown in Fig. 3. The power circuit was simulated in Multisim. The input pulses are given from the LabVIEW simulation for all switches. It is operated on the basis of Table 1 switching series. The sinusoidal pulse width modulations are shown in below Fig. 7. Initially, three levels can be represented for Vdc/2, o, −Vdc/2. The zero-voltage level can be applied to directly connect to the ground for the losses of the switching transmission [10]. The sinusoidal and triangular waves are compared, and it is possible to compare both the waveforms to obtain a three-stage output.

3.2 IGBT Thermal Module

Power semiconductor switches are key components of electronic power converters and operate in thermally stressful environments [11]. A power semiconductor's junction temperature directly affects its power loss and is ultimately related to various mechanisms of failure. Therefore, knowledge of this temperature is critical for optimal operation and for reasons of reliability. If the temperature of the junction is known during the operation of a converter, it is possible to develop real-time condition monitoring and effective thermal control systems to increase process performance. It is difficult to perform direct measurements of the junction temperature as the power semiconductor is usually encapsulated within a range of packaging materials. Alternatively, a semiconductor's electrical behavior depends largely on temperature. This above thermal module represents the values which are T_{jd} and T_{jq} are junction temperature and case temperature of IGBT. The IGBT thermal model notations are T_j and T_c, this is the most important part of IGBT thermal characteristics [12]. The notations represent T_j = Junction temperature of IGBT. T_c = case temperature of IGBT (Fig. 4).

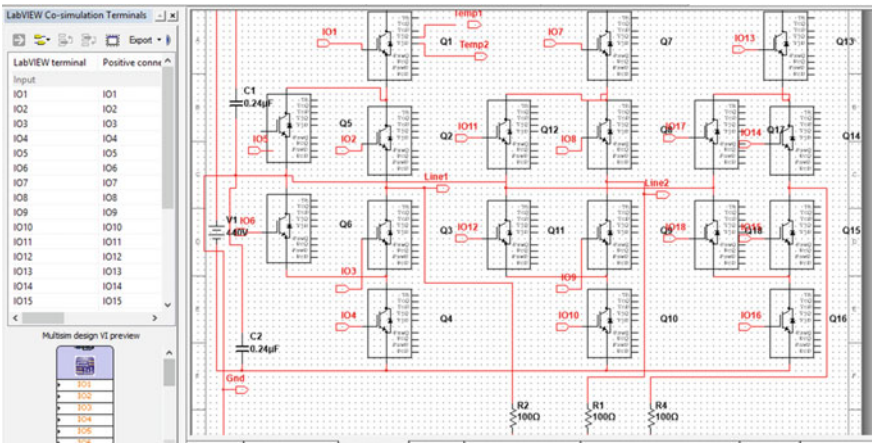

Fig. 4 Simulation of power circuit diagram

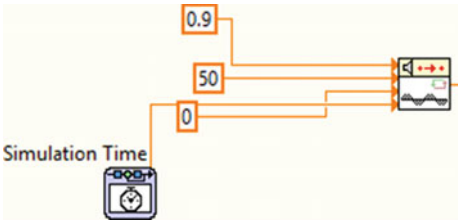

Fig. 5 LabVIEW sinewave generation circuit

3.3 Inverter Pulse Generation

The inverter pulses can be given from LabVIEW because, in order to overcome control from LabVIEW [4], Multisim does not provide individual modulation index control. LabVIEW is a good setting to design a modulation of the sinusoidal pulse width. The sinusoidal pulse width modulation LabVIEW simulations are shown in below Fig. 5. This is the 3L-ANPC inverter one leg pwm control structure. Initially, three levels can be represented for Vdc/2, o, −Vdc/2. Reference is sinusoidal, and carrier is triangular wave; both the waveforms can be compared; we will get a three-level output pulses.

3.4 Sinewave Generation Circuit

The below simulation circuits are sinusoidal waveform generation. The input parameter of modulation index value is 0.9, frequency 50 Hz, phase 0, 120, 240 and simulation time. Simulation time is common for the overall system [13].

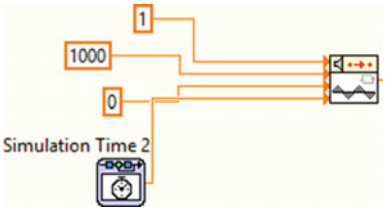

Fig. 6 Triangular wave generation circuit

3.5 *Triangular Wave Generation Circuit*

It is similar to above simulation circuit, but little bit variation because triangular wave generation simulation circuits are 1 KHz frequency and remaining values are common for sinusoidal wave generation (Fig. 6).

3.6 *Inverter Input SPWM Waveform*

Figure 7 shows the three-phase reference (sine) and carrier (triangular) wave comparison. The comparison output can be given to the inverter. Figure 7 shows that left-side waveform is inverter input pulse and right-side waveform is comparison output waveform.

The junction temperature variation output waveform is shown in below Fig. 8 The neutral point clamped inverter majorly used for medium-voltage application like a 600 and above voltage ranging industries. The inverter initial junction temperature

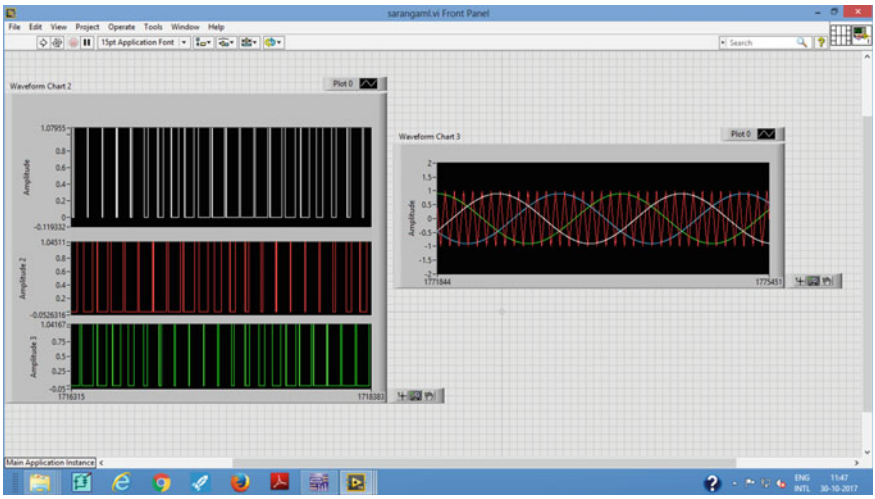

Fig. 7 Inverter input pulse comparison output waveform

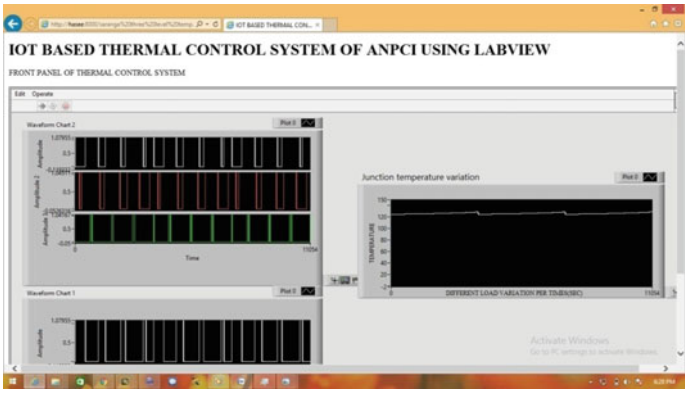

Fig. 8 Junction temperature variation output

Table 2 Different junction temperature values

S. No.	Input supply	Junction temperature
1	600	123.5
2	620	124.2
3	630	125.1
4	640	125.8

rating is 125 °C [14]. Simulation circuit different load values based on the related junction temperature are shown in Table 2 (Fig. 9).

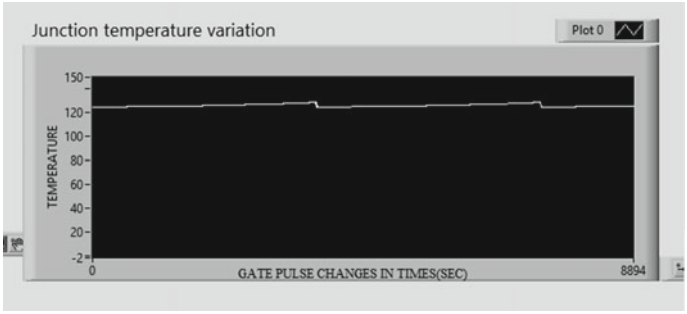

Fig. 9 Junction temperature variation

4 Conclusion

Thus, the computer-aided thermal control system of three-level active neutral point clamped inverter using LabVIEW is presented in this paper. The existing system is facing uneven distribution losses among the NPC inverter switches. To overcome this problem, the proposed system of ANPC inverter can be implemented with the help of Multisim. Finally, the inverter switching junction temperature can be monitored by LabVIEW web publishing tool (IoT), and it can be simulated and tested successfully by using software tools LabVIEW and MULTISIM.

References

1. Floricau D, Popescu CL, Popescu MO et al (2014) A comparison of efficiency for three level NPC and Active NPC voltage source converters. Compat Power Electron 09:331–336
2. Brunckner T, Bernet S (2005) The active NPC converter for medium voltage applications. In: Industry applications conference, 2005. Fortieth IAS annual meeting. Conference record of the 2005, vol 1. IEEE, pp 84–91
3. Nabe A, Takahashi T, Akagi H (1981) A new neutral point clamped PWM inverter. IEEE Trans Ind Appl IA-17(5):518–523
4. Stiasny T, Streit P, Lüscher M, Frecker M (2004) Large area IGCTs with improved SOA. In: Proceedings of PCIM conference, Nuremberg, Germany
5. Pan-dong Z, Jun-wei G, Shu K (2014) Power quality monitoring system of the distributed inverter based on Labview. Electr Measure Instrum 51(16):93–96
6. Karimi-Moghaddam G,Gould RD, Madhusoodhanan S et al (2012) Thermal design considerations for 12 kv Sic IGBT based 3LNPC converter. In: Energy conversion congress and exposition (ECCE), 2012. IEEE, pp 2180–2186
7. Honsberg M, Radke T (2009) 3-level IGBT modules with trench gate IGBT and their thermal analysis in ups, PFC and PV operation modes. In: 13th European conference on power electronics and applications, 2009, EPE'09. IEEE, pp 1–7
8. Brückner T, Bernet S (2001) Loss balancing in three-level voltage source inverters applying active NPC switches. In: Proceedings of IEEE-PESC, Vancouver, Canada, pp 1135–1140
9. Rodriguez J, Bernet S, Wu B, Pontt JO, Kouro S (2014) Multi level voltage source converter topologies for industrial medium voltage drives
10. Bhagwat P, Stefanovic VR (1980) Generalized structure of a multilevel PWM inverter. In: IEEE industry application society annual meeting, pp 761–76
11. Steimer PK, Apeldoorn O, Ødegård B, Bernet S, Brückner T (2005) Very high power IGCT PEBB technology. In: To be presented at IEEEPESC, Recife, Brazil
12. Pan Z, Peng PZ, Corzine KA, Stefanovic VR, Leuthen JM, Gataric S (2005) Voltage balancing control of diode clamped multilevel rectifier/inverter systems. IEEE Trans Ind App 41(6):169–1709
13. Steimer PK, Steinke JK, Grüning HE, Conner S (1999) A reliable, interface-friendly medium voltage drive based on the robust IGCT and DTC technologies. In: Conference record, IEEE-IAS annual meeting, Phoenix, AZ, pp 1505–1512
14. Nabae A, Takahashi I, Akagi H (1981) A new neutral-point-clamped PWM inverter. IEEE Trans Ind Appl 17:518–523

Experimental Investigation and Optimization of Machining Parameters of Aluminum Composite Material

K. Ramachandra Raju, G. Senthilkumar, D. Deepakraja, M. Vignesh, S. K. Surya, and G. Vivek

Abstract Machinability contribution to manufacturing is significant and its role for optimum has to be determined. Aluminum particulate reinforced compound has demand in some growing fields such as automotive, aircraft and locomotive industries. The research work focuses on machinability and optimization of machining parameters on Aluminum 6063 alloy reinforced with silicon carbide known as aluminum compound. Three specimens *A*, *B*, *C* reinforced with silicon carbide 3%, 6%, and 9%, respectively, were fabricated using stir cast. For each specimen, 13 experiments were conducted with varying input parameters such as speed, feed, and cutting depth in CNC vertical machining center using 10 mm end mill cutter. The recorded output responses are surface roughness and material removal rate. Using Design-Expert software's RSM method, number of runs and regression equations were decided. The Turbo C program utilized and carried out the sorting of output measurement. The more focus is laid on the significance of machinability. The objective is to enhance parametric optimization using particle swarm optimization (PSO) method to calculate the fitness value corresponding to speed, feed, and cutting depth. The Multiobjective optimization of the input parameters obtained from particle swarm optimization found to have optimum to measure the output responses of surface finish process and output responses of material removal rate of the both are compared.

Keywords Particulate reinforced composite milling forces · Surface roughness · Machinability · Particle swarm optimization

K. Ramachandra Raju (✉) · G. Senthilkumar · D. Deepakraja · M. Vignesh · S. K. Surya · G. Vivek
Department of Mechanical Engineering, Bannari Amman Institute of Technology, Sathyamangalam, TN 638401, India
e-mail: rajukrc@gmail.com

G. Kumaresan et al. (eds.), *Advances in Materials Research*, Springer Proceedings in Materials 5, https://doi.org/10.1007/978-981-15-8319-3_103

1 Introduction

Israelites using clay bricks and lined with straw are an early example of composites technology [1]. A composite generally defined as the combination of two or more macro-scale components with two or more distinct phases with recognizable interfaces between them. Composites are commonly used for their structural properties where the most commonly used reinforcing component is in particulate or fibrous form, and therefore the above definition can be limited to such systems containing a continuous/discontinuous fiber or particle reinforcement, all in a continuous supporting core phase, the matrix [1]. There are two phases that have continuous character namely matrix phase and primary phase. The second phases are reinforcement phase that is imbedded in the matrix in a discontinuous form. Composite efficiency depends on matrix and strengthening properties, size and distribution of constituents [2].

An evolutionary optimization technique includes single-pass SA, GA, and PSO, multi-pass turning and surface grinding. Input parameters are number of passes, cutting speed, feed and depth of cut, whereas output parameters are production cost and removal rate. Concluded that PSO meets this condition problem than GA and SA, since there is low number of iterations [3]. Alumina reinforced aluminum corrosion actions 6063 metal matrix composites. The influence of alumina volume percent and solution heat-treatment in salt water, basic, and acidic environments on the corrosion behavior of Al (6063) composites and their monolithic alloy. Al (6063) composites containing 6, 9, 15, and 18% of volume, and alumina were developed by using two-step stir casting [4]. Optimization of the end milling parameters and SiCp spindle speed and content was found to have greater influence on tool flank wear in end milling of LM25 Al/SiCp MMC, followed by feed rate. Tool flank wear is less influenced for depth of cut [5]. Estimation of optimum values of process variables such as speed, feed, and depth of cut, whereas the metal removal rate (MRR) and tool wear resistance were taken as the output [6]. Flexibility and reliability in the design of possible components depend on the reinforcement's combination and composition [7]. Particle swarm optimizations (PSO), a novel optimization algorithm for cutting parameters optimization (CPO), were discussed. Cutting experiment without and with optimized cutting parameters was conducted to demonstrate the effectiveness of optimization, respectively [8]. In order to minimize or maximize machining efficiency using current trend algorithms, researchers often consider process parameters such as cutting speed, depth of cut and radial rake angle [9]. Behavior of aluminum alloy reinforced with silicon carbide and alumina for different weight fractions produced by stir casting technique was studied and their results showed their effectiveness [10]. Increased reinforced percentages and sizes raise surface roughness. Cutting forces were much larger for tungsten carbide tools than PCD tools due to the formation of BUE [11]. Surface roughness increases first and then decrease with the increase in cutting speed [12]. Predicted surface roughness of fine turning using central composite experimental design [13]. Surface roughness on the thermoelectric behavior of friction clutches, developed axisymmetric finite element model

Table 1 Composition of Aluminum 6063 alloy

Si	Fe	Cu	Mn	Mg	Zn	Cr	Ti	Al
0.45	0.22	0.02	0.03	0.50	0.02	0.03	0.02	Balance

for a single-disk clutch system [14]. Optimized machining parameters for α–β for abrasive water jet machining [15]. Used ANN approach to predict drilling-induced thrust force and torque [16]. Cryogenic machining of stainless steel revealed feed rate is the most influencing process parameter on the performance characteristics [17].

Literatures reviewed are indicative that multiobjective optimization of milling machinability of Al6063 with SiC reinforced composites are limited. The present work uses particle swarm optimization to improve machinability of milling operation parameters speed, feed, and depth of cut for roughness and material removal rate.

2 Materials and Methods

2.1 Materials

The materials used in this study are 6xxx series aluminum alloy 6063 (6061, 6063) containing approximately the proportions needed for magnesium silicide (Mg_2Si) formation, making them heat treatable. Although not as strong as most 2xxx and 7xxx alloys, 6xxx series aluminum alloys have superior formability, weldability, machinability, and relatively good resistance to corrosion, with medium silicon carbide (SiC) resistance. It is a silicon-carbon compound with chemical formula SiC Aluminum 6063 alloy as a matrix and SiC as reinforcement. Aluminum 6063 alloy composition is shown in Table 1.

2.2 Stir Casting

The melting was carried in an induction furnace in a range of 760 ± 100 °C. A forced draft fan with 02 H.P, 2820 rpm motor was used to provide the necessary amount of air. Scraps of aluminum were preheated up to a temperature of 500 °C and silicon carbide particles in the core drying oven to a temperature of 200 °C. Die used as mold was also heated up to 200 °C.

The stir caster was mounted on the furnace with the help of links. The stirrer is used to agitate the liquid metal. The stirrer positioned such that 35% of material to be below the stirrer and 65% of material above the stirrer. Figure 1 represents cast composite from the stir casting setup. The molten composite is poured inside the die cavity which has graphite coating and the open view of the mold cavity.

Fig. 1 Composite cast sample

2.3 Machining

Unwanted piece of metal work removed in the form of chips is called machining. The method of machining will form the workpiece desired and usually done with machine and cutting tools [5]. Machinability studies have acquired greater importance in the area of composite.

End milling is commonly utilized in automobile and aerospace industries where quality is an important factor in manufacturing of slots, pockets, and molds/dies. End mills are used in milling applications like profile milling, tracer milling, face milling, and plunging. The end mills are used for light operations like cutting slots, precise machining of holes, producing narrow flat surfaces, and for profile milling operations [6].

Totally nine specimens are obtained from three cast composite specimens, named A, B, C with 240 mm height and 30 mm diameter of the above-mentioned composition. Figure 2 shows computer numerical control vertical milling center used for machining such as slots, profile, and present work involves taking a slot.

2.4 Design of Experiment

Experiments design is a systematic method for obtaining the most reliable results with minimal wastage of time/money and refining the procedures and identifying the most important factors that can require various experiments.

The Box–Behnken design fills out a polyhedron, approximating a sphere for three factors (13 runs). Figure 3 shows machining of the specimen carried out in the presence of coolant and the time for machining was noted with the help of stopwatch,

Fig. 2 CNC VMC 45 chetak

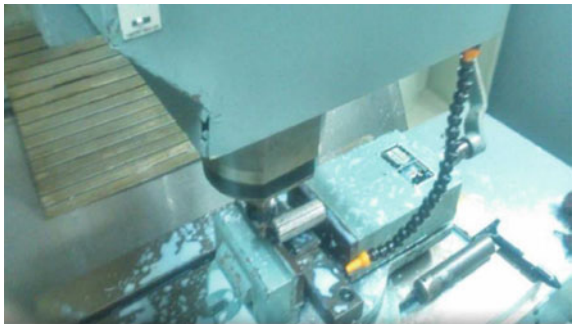

Fig. 3 Machining of the specimen

whereas Fig. 4 shows the machined specimen A, B, C, these specimens, similarly, there are nine individual specimens. Figures 5 and 6 represent machined specimen for surface roughness testing and Mitutoyo SJ 400 computer control surface roughness measuring system, respectively.

Fig. 4 A, B, C specimen of 3, 6, 9% of SiC

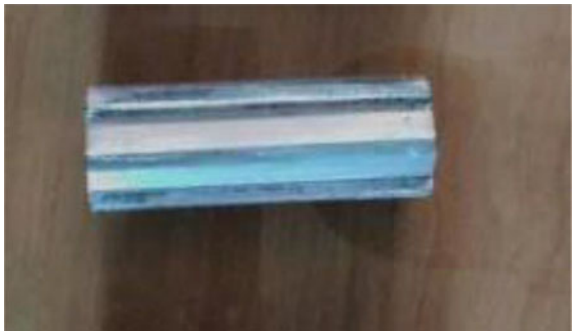

Fig. 5 Machined specimen

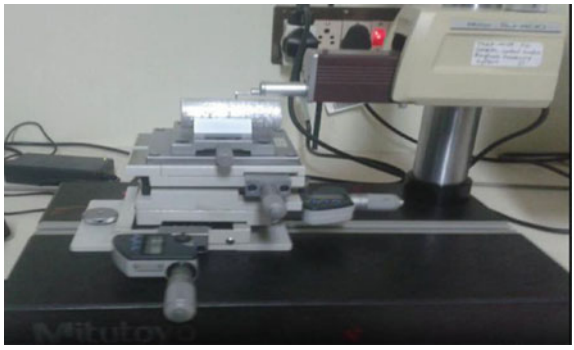

Fig. 6 Surface roughness tester

3 Result and Analysis

3.1 Experimental Work and Results

The input parameters used for recording the output responses, which are optimized in particle swarm optimization. The output response is surface roughness and metal removal rate. The specimen A, B, C with 3%, 6%, 9% of SiC, respectively, had 13 experiments conducted. Table 2 represents the measurement of responses for which the experiments are conducted.

3.2 Mathematical Model

Design-Expert 7.0 evaluation software aids to understand, evaluate the effects of parameters and their interacting effects on the response. The aim of the work is to simultaneously optimize surface roughness and material removal rate. The predicted regression equation responses are shown below for specimen A.

Table 2 Machinability results of specimens with different cutting parameters

Input parameters				Specimen A		Specimen B		Specimen C	
Exp. No.	Speed (rpm)	Feed (mm/rev)	Depth of cut (mm)	Roughness (μm)	MRR (mm^3/min)	Roughness (μm)	MRR (mm^3/min)	Roughness (μm)	MRR (mm^3/min)
1	500	0.1	3	0.38	584.9	0.51	768.8	0.58	425.8
2	500	0.2	4	0.37	634.1	0.52	905.8	0.59	124.1
3	1000	0.2	2	0.55	766.2	0.53	1115.5	0.45	395.8
4	750	0.1	4	0.47	490.1	0.55	952.5	0.58	168.4
5	1000	0.2	4	0.62	1915.4	0.63	1945.5	0.59	822.5
6	500	0.2	2	0.42	801.1	0.52	618.2	0.57	185.2
7	750	0.4	4	0.59	2461.7	0.66	2304.7	0.67	1158.2
8	750	0.1	2	0.49	460.6	0.54	893.2	0.52	638.2
9	750	0.3	2	0.55	972.1	0.58	1253.2	0.56	355.2
10	500	0.3	3	0.46	1182.3	0.56	1389.8	0.0.64	557.5
11	1000	0.3	3	0.66	2527.7	0.65	2685.7	0.58	1385.4
12	750	0.2	3	0.51	1741.4	0.57	2547.5	0.57	1485.6
13	1000	0.1	3	0.56	845.1	0.56	1256.3	0.51	542.3

$$\text{Response } Y = f(\text{A}, \text{B}, \text{C}) \tag{1}$$

$$\begin{aligned}\text{Ra} = {} & +0.4973 + 0.00016625 * \text{A} - 12.93875 * \text{B} \\ & - 0.19222 * \text{C} + 0.000655 * \text{A} * \text{B} \\ & + 0.0001075 * \text{A} * \text{C} + 2.91 * \text{B} * \text{C} \\ & - 0.0000000519 * \text{A} * \text{A} \\ & + 201.5 * \text{B} * \text{B} - 0.0158 * \text{C} * \text{C}\end{aligned} \tag{2}$$

$$\begin{aligned}\text{MRR} = {} & 4180.19175 + 1.92385 * \text{A} + 74033.575 * \text{B} \\ & + 2159.31575 * \text{C} + 48.35345 * \text{A} * \text{B} + 1.26678 * \text{A} * \text{C} \\ & + 68754.95000 * \text{B} * \text{C} - 0.0015248 * \text{A} * \text{A} - 317274 * \text{B} * \text{B} \\ & - 1847.099 * \text{C} * \text{C}\end{aligned} \tag{3}$$

Similar for specimen B, C, the regression equation is obtained.

3.3 Particle Swam Optimization (PSO)

Optimization is a discipline of adjusting the process parameters without violating the constraints. Response surface methodology can be applied, especially where several responses have to be simultaneously optimized. The behaviors of bird flocking are simulated by optimization of particle swarm. Suppose the following scenario: A group of birds are randomly searching food in an area. In search area, there contains only one piece of food. Not all birds know where the food is available. But they know how far the food is in each iteration. So what's the best strategy to find the food? The effective one is to follow the bird, which is nearest to the food. PSO understand from the situation and used it to solve the optimization problem. In PSO, each single solution is a "bird" in the search space, called as "particle." All the particles have fitness values that are measured by the fitness function and speeds that drive particle flight. The particles are "flown" through the problem space by following the current optimum particles [3]. The implementation of PSO is very simple and needs only a few lines programming code [9].

PSO is an evolutionary computing technique inspired by bird or fish schooling social behavior, developed by Eberhart and Kenedy in 1995. In PSO, there are three parameters considered: W, C_1, and C_2 where C_1 and C_2 where the cognitive and social parameter and w is weight of inertia. The particle associated with best solution is called leader and it is based on fitness value of function. Each particle keeps track of its coordinates in the problem space (search space). One more value considered in this technique is referred as "gbest" (also known as global best). Following equations are very important in PSO.

$$V_i + 1 = W V_i + C_1 r_1 (\text{Personal Best} - X_i) + C_2 r_2 \,\text{Gobal Best} - X_i) \quad (4)$$

$$X_i + 1 = X_i + V_{i+1} \quad (5)$$

In the above equation, V_{i+1} is denoted by new velocity for each particle based on its previous velocity and r_1, r_2 are the random numbers in the range between three ranges such as speed from 500 to 1000 rpm, feed from 0.1 to 0.3 mm/rev, and depth of cut from 2 to 4 mm. It is a relatively emerging and very fruitful technique for continuous and nonlinear functions optimization. It is not only very easy to implement computer codes in few lines but it also gives very promising result. The program code is written on platform Turbo C. The calculation time is under 5 s. The result could be retrieved in a very short time so it is very easy to apply and a technique to save time.

3.4 PSO Algorithm for Optimization Problem

Step 1 Initialize each particle.
Step 2 Calculate the fitness value for each particle. If the fitness value is better than best fitness value (pbest) in history, set the current value as the new 'pbest'.
Step 3 Choose the particle with best fitness value of all the particles as the 'gbest'.
Step 4 For each particle calculate the particle velocity.
Step 5 The termination criterion is maximum number of iterations or condition.

Based on this PSO algorithm, the following conclusions may be drawn from the optimization results of the PSO program. Table 3 shows the results for the three-aluminum specimen of particle swarm optimization. The values obtained by using the PSO algorithm correspondingly provide to satisfying the objective of the problem without violating the constraints. In the economics of machining, cutting parameters play a major role [8]. Thus, the particle swarm optimization seems to be a promising technique for optimizing the machining parameters like speed, feed, and depth of cut for recording the output responses such as surface roughness and material removal rate. The platform of work done is in the Turbo c, using Code Blocks.

Particle fitness equation developed in PSO, the optimal machining parametric combination was found varying for specimens based on their reinforcement weight

Table 3 Optimized results of A, B, C specimens

Specimens	Speed (rpm)	Feed rate (mm/rev)	Depth of cut (mm)	Material removal rate (mm^3/min)	Surface roughness (μm)
A	546	0.20	2.41	1210.73	0.408
B	642	0.27	2.23	1193.21	0.528
C	720	0.38	1.06	726.15	0.535

Table 4 Confirmatory test

Specimens	Speed (rpm)	Feed rate (mm/rev)	Depth of cut (mm)	Material removal rate (mm^3/min)	Surface roughness (μm)
C	720	0.38	1.061	729	0.55

percentage. The specimen B effect was proportional because of increase in addition of silicon carbide percentage, which is about 6%. It showed the higher hardness than the previous specimen did which is known from the surface roughness and material removal rate. Increase in silicon carbide to 9% found challenging in the casting. The specimen stirring time needed to increase from 15 min to greater extent. This ensured a better wettability and proper mixing of the silicon carbide with the matrix and other reinforcement. The 9% SiC needed a better speed, feed, and depth of cut compared to other two specimens. The speed increased gradually but the feed rate varied indifferently and depth of cut decreased showing the effect of SiC content in the composite.

Table 4 shows the confirmatory test that was conducted for specimen C to check the performance of PSO, proved to be efficient and obtained near results.

4 Conclusion

The preparation of three specimens with varying matrix and reinforcement (Al 6063 with silicon carbide) for was found successful through stir casting. The specimen with 3%, 6%, and 9% was prepared.

- In this research, the effects on surface roughness and material removal rate for Al/SiCp MMC of process parameters spindle speed, feed rate, depth of cut, and various percentage weights of silicon carbide were systematically studied.
- The parametric optimization is done to assess good machinability with prime focus as less surface roughness, without compensation of material removal rate. This lead to exploring particle swarm optimization technique with objective function framed as particle fitness, and it value is mapped for the obtained particle fitness and corresponding speed, feed, and depth of cut are noted to enhance the output responses.

References

1. Kaw AK (2006) Mechanics of composite materials. 2nd edn. CRC Press, Taylor & Francis Group
2. Akovali G (2001) Handbook of compound fabrication. RAPRA Technologies

3. Bharathi RS, Baskar N (2010) Optimization techniques for machining operations: a retrospective research based on various mathematical models. Int J Adv Manuf Technol 48(12):1075–1090
4. Alanema KK, Bodururin MO (2011) Corrosion behavior of aluminium reinforced aluminium (6063) metal matrix compounds. J Mater Miner Character Eng 10(12):1153–1165
5. Arokiadass R, Palaniradja K, Alagumoorthi N (2011) Surface roughness prediction model in end milling of Al/SiCp MMC by carbide tools. Int J Eng Sci Technol 3(6):78–87
6. Divya Theja K, Harinath Gowd G, Kareemulla S (2013) Prediction and Optimization of end milling process parameters using Artificial Neural Networks. Int J Emerging Technol Adv Eng 3(9):117–122
7. Singh J, Chauhan A (2016) Characterization of hybrid aluminum matrix compounds for advanced applications—A review. J Mater Res Technol 5(2):159–169
8. Li JG, Yao YX, Gao D, Liu CQ, Yuan ZJ (2008) Cutting parameters optimization by using particle swarm optimization (PSO). Appl Mech Mater 10(12):879–883
9. Yusup N, Zain AM, Hashim SZM (2012) Overview of PSO for optimizing process parameters of machining. In: International Workshop on information and electronics engineering (IWIEE), vol 29. Procedia Engineering, pp 914–923
10. Pulkit (2008) Mechanical behaviour of aluminium based metal matrix compounds reinforced with SiC and Alumina. M.E. thesis, Thapar university, Patiala
11. Suhasini G, Mamidala R, William P (2013) Machining of MMCs : a review. Mach Sci Technol 17(1):41–73
12. Xianhua T, Jun Z, Wenzhen Q, Feng G, Yintaowang, Helin P (2017) Performance of ceramic tools in high speed cutting iron-based super alloys. Mach Sci Technol 21(2):279–290
13. Toth-Laufer E, Horvarth R (2017) Fuzzy model based surface roughness prediction of fine turning. FME Trans 45:181–188
14. Abdullah OI, Schlattmann J, Lytkin M (2015) Effect of surface roughness on the thermoelastic behaviour of friction clutches. FME Trans 43:241–248
15. Marichamy S, Ravichandran M, Stalin B, Sridhar B (2019) Optimization of abrasive water jet machining parameters for α–β brass using Taguchi methodology. FME Trans 47:116–121
16. Dhawan V, Debnath K, Inderdeep S, Sehijpal S (2016) Prediction of forces during drilling of composite laminates using artificial neural network: a new approach. FME Trans 44:36–42
17. Sivaiah P, Chakradhar D (2018) Multi performance characteristics optimization in cryogenic turning of 17-4 PH stainless steel using Taguchi coupled grey relational analysis. Adv Mater Process Technol 3:431–447

FEM and Execution Analysis of Hardfaced Aluminium Alloy Impeller

C. Ramesh, P. Prakash, P. Sankar, and R. Prakash

Abstract An impeller is a pivoting segment of divergent pump, generally made of cast iron materials used in domestic applications that have low hardness value, impact strength and low wear resistance, which reduces the life of impellers. Due to poor wear resistance, the impeller has to undergo maintenance for every short interval of time. The other problem faced is the weight of impellers made of cast iron, which reduces the performances of the impeller. So as to improve life, impact strength, wear resistance, and performance, an alternate material is suggested using hardfaced aluminium alloy (6012). The alternate material for the existing impeller is selected, and the investigation on hardfacing is carried out for different grades of coating to increase the hardness, wear resistance, and life of the impeller. Then, the performance of the new material hardfaced aluminium impeller performance analysis can be carried out via erosion test and comparison between two materials. Von Mises pressure dispersion can be determined. In a planned way, the blended stream pump impeller having inclined inlet blade situating (case-I) in the meridional annulus is getting lesser twisted than the trapezoidal cutting edge situating (case-II) which itself connotes that the impeller with delta slanted sharp edges situating is a superior decision than the other one.

Keywords Hardfacing · Pump impeller · Aluminium alloy (6012) impeller · Meridional annulus · ANSYS · Von Mises stress · Blade

1 Introduction

An impeller is a turning fragment of different pump, which moves imperativeness from the motor that drives the pump to the fluid being pumped by animating the fluid outwards from the point of convergence of rotating [1]. The impeller made out of cast material, all things considered, maybe called rotor, also. It is more affordable

C. Ramesh (✉) · P. Prakash · P. Sankar · R. Prakash
Department of Mechanical Engineering, K.S. Rangasamy College of Technology, Tiruchengode, Tamilnadu 637215, India
e-mail: rameshc@ksrct.ac.in

G. Kumaresan et al. (eds.), *Advances in Materials Research*, Springer Proceedings in Materials 5, https://doi.org/10.1007/978-981-15-8319-3_104

to cast the winding impeller straightforwardly in the assistance it is fitted on, which is set moving by the gearbox from an electric motor, consuming engine or by the steam-driven turbine. The number of vanes will influence productivity when all is said in done more vanes are increasingly effective [2]. Additionally, the quantity of vanes influences the steepness of the trademark bend; see outward siphon tips for a chart on this impact [3]. The number of vanes will affect the efficiency in general more vanes are more efficient. Also the number of vanes affects the steepness of the characteristic curve; see centrifugal pump tips for a graph on this effect. An impeller with a high number of vanes reduces the amplitude of the pressure pulses that are caused as the impeller tip passes by the cutwater [4]. In certain applications, these pressure pulses are undesirable such as a paper machine head box pump which typically will be a double suction type with 4 or more vanes [5]. The head box is a large specialized nozzle that feeds a continuous stream of low consistency pulp on a travelling wire mesh which after drying produces a wide paper web [6]. If the pressure pulses are too high compared to the average, there will be a variation in the paper density which may affect printing quality and other operational factors [7].

2 Problem Identification

2.1 Impeller Troubleshooting

Problem causes and remedies of the impeller are mentioned in Table 1

3 Materials and Methods

Here the pump impeller has been coated with NiMo material in the process of Hardfacing.

Table 1 Impeller troubleshooting

Problem	Causes	Remedies
Pieces missing from cutting edges tips particularly in the focal point of the impeller. Edges look hollowed out or eaten away. Pitting on parts of the bargains of the impeller or all. The end faces hard, cleaned, broke, similar to carbon [8, 9].	Cavitation, for example, an excess of vacuum at the pump bay, liquid bubbles locally. Dry running normal finish of valuable life. A wrinkle on the trailing side of every sharp edge can likewise show over the top weight	Decreases pump speed Improving the bay pipe diameter. Reduce inlet pipe length and restrictions. Improving the bay pipe diameter It decreases the pressure and pumps speed

3.1 Hardfacing of Impeller

Impeller consisted of a three-piece bolted structure. It consolidated a circle, separate sharp edge and spread. The cutting edge was bolted to the plate by constructing agents, and a spread was then bolted to the sharp edges. Hardfacing is employed in aluminium alloy (6012) impeller. The assemblers and the blades are hardfaced using the TIG 410NiMo electrode [10, 11]. After hardfacing, the surface was machined to obtain a higher degree of smoothness by fettling or trimming process. Finally, the impeller has been assembled—blade was bolted to the circle by constructing agents, and a spread was then bolted to the blades. Hardfacing is carried out as per the TIG welding specifications [12].

The material properties of the existing material cast iron are compared to the new material hardfaced aluminium alloy. In this comparison, the material properties of the hardfaced aluminium alloy have the high values to the existing material cast iron [13].

4 Performance Analysis of Impeller

For material analysis, two materials cast iron and hard-faced aluminium alloy (6012) were considered. The materials properties are given in Table 2.

4.1 Material Analysis

Hardfaced aluminium alloy (6012) was tested for mechanical properties for different coating thicknesses (1, 2, 3 mm) in the material of TIG 410NiMo material. In this coating process, 3 mm thickness is having improved mechanical properties, which is related to the material analysis of the impeller. The results are referenced from the paper [14].

Table 2 Material properties of cast iron and hard-faced aluminium alloy (6012)

Material	Cast iron	Hardfaced aluminium alloy
Young's modulus	120 GPa	89 GPa
Poisson ratio	0.3	0.2
Density	7.2 g/cm^3	4.886 g/cm^3
Thermal expansion	46 μm/m K	21.6 μm/m K
Specific heat	450 kg K	810 kg K

Table 3 Mesh properties of cast iron impeller

Mesh	Element family	Elements	Nodes
Cast iron: PSOLID1, Iron_Cast_G25			
3d_mesh(1)	Tetra4	3468	1210

Table 4 Load values of cast iron impeller

Step name	Number of referenced loads			Loads
Subcase—Static loads 1	1	Hydrostatic (1)	Type	Hydrostatic
			Solver card name	PLOAD4
			Layer	1
			Applied to	14 Polygon face
			Description	
			Liquid surface	
			Liquid density	1e−006 kg/mm^3
			Gravitation constant	9810 mm/s^2
			Surface pressure	1000 N/mm^2 (MPa)

4.2 Stress Analysis of Cast Iron Impeller

ANSYS software was used for the analysis, Tetra4 element was chosen for meshing—considering the element size as 4.25 Kumar et al. [15], meshing properties of the cast iron impeller given in Table 3 and the loading conditions are given in Table 4 and also the stress distribution of cast iron impeller shown in Fig. 1.

4.3 Stress Analysis of Hardfaced Aluminium Alloy (6012) Impeller

ANSYS software was used for the analysis, Tetra4 element was chosen for meshing, considering the element size as 4.25 Kumar et al. [15], meshing properties of the hardfaced aluminium alloy (6012) impeller given in Table 5 and the loading conditions are given in Table 6 and also the stress distribution of aluminium alloy (6012) impeller shown in Fig. 2.

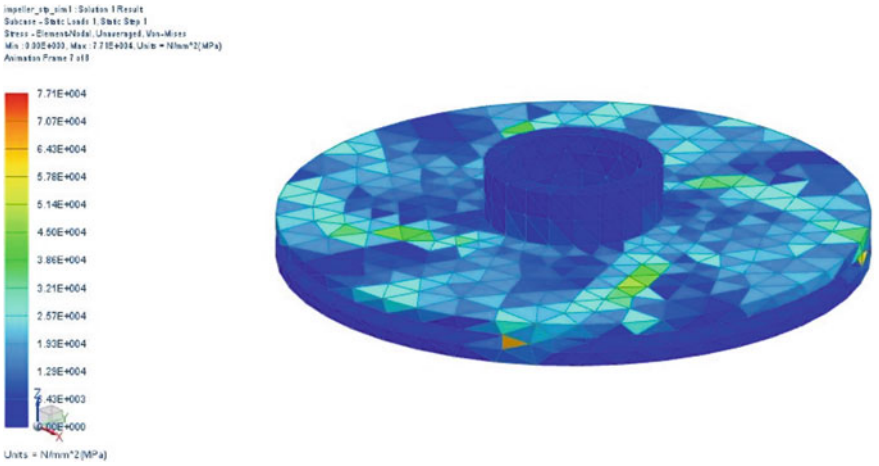

Fig. 1 Stress distributions of Cast iron impeller

Table 5 Mesh properties of hardfaced aluminium alloy (6012) impeller

Mesh	Element family	Elements	Nodes
Alu: PSOLID1, Aluminum_6012			
3d_mesh(1)	Tetra4	3468	1210

Table 6 Load values of hardfaced aluminium alloy (6012) impeller

Step name	Number of referenced loads		Loads
Subcase—Static loads 1		1	
	Hydrostatic(1)	Type	Hydrostatic–Hydrostatic
		Solver card name	PLOAD4
		Layer	1
		Applied to	14 Polygon Face
		Description	
		Liquid surface	
		Liquid density	1e−006 kg/mm^3
		Gravitation Constant	9810 mm/s^2
		Surface pressure	1000 N/mm^2 (MPa)

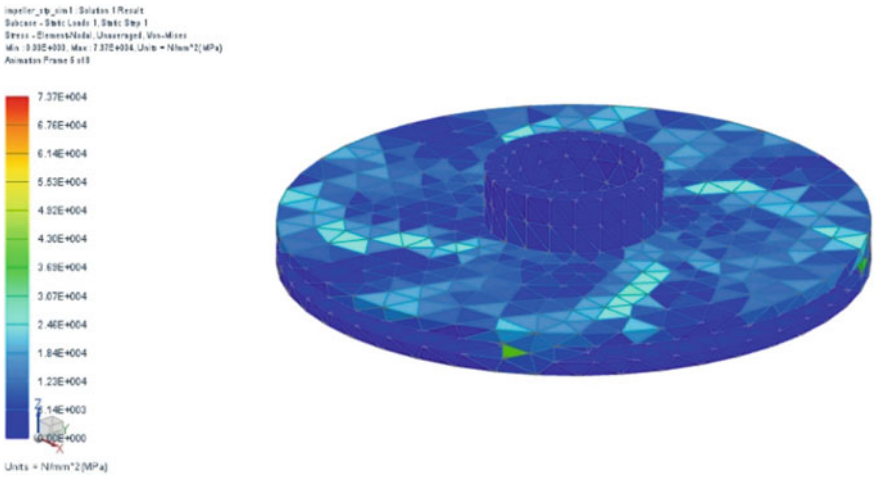

Fig. 2 Stress distributions of hardfaced aluminium alloy impeller

4.4 Blade Position Analysis

The plan parameters, as an example of sharp edge edges, camber points, stun edges, harmony measurements, were determined at various segments along the cutting-edge length for two diverse edges situating in the meridional annulus [16, 17]. For modelling both the blade positions, the blade angle can be calculated from hub to tip are varied, spanwise variety of cutting-edge plots for channel slanted edge position and trapezoidal sharp edge situating in the meridional annulus are analysed and the stress distribution of various blade positions are shown in Figs. 3 and 4. Mesh properties and load values of the inclined blade position are discussed in Tables 7 and 8.

4.5 Stress Analysis of Trapezoidal Blade Position

For modelling both the blade positions, the blade angle can be calculated from hub to tip are varied, mesh properties of trapezoidal blade position impeller given in Table 9 and the load conditions of that impeller given in Table 10.

5 Results and Discussion

Performance analysis of a mixed flow pump impeller was carried out in two aspects; one is based on the selection of material for the existing material cast iron, and another

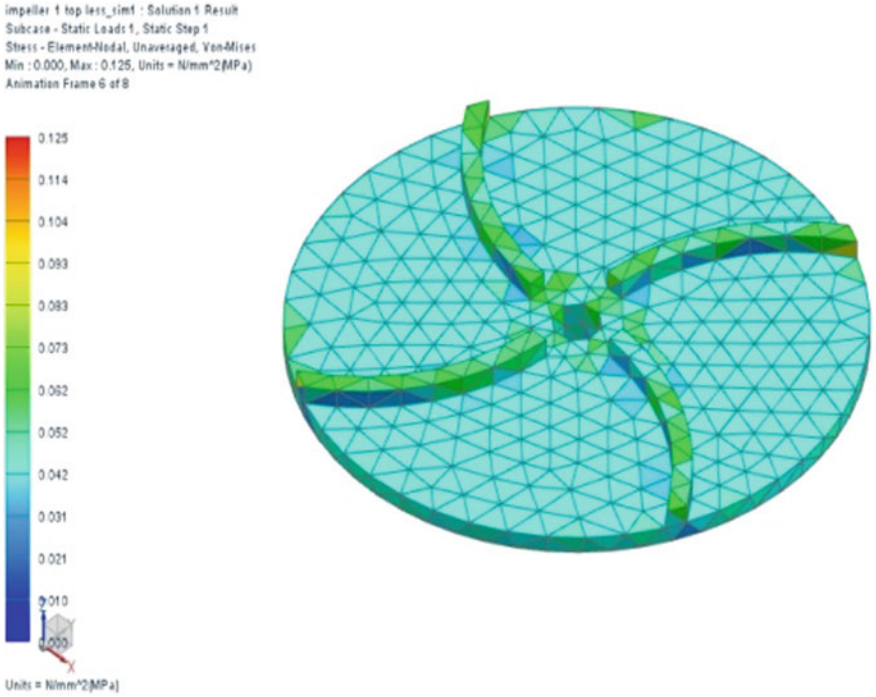

Fig. 3 Stress distributions of inclined blade position

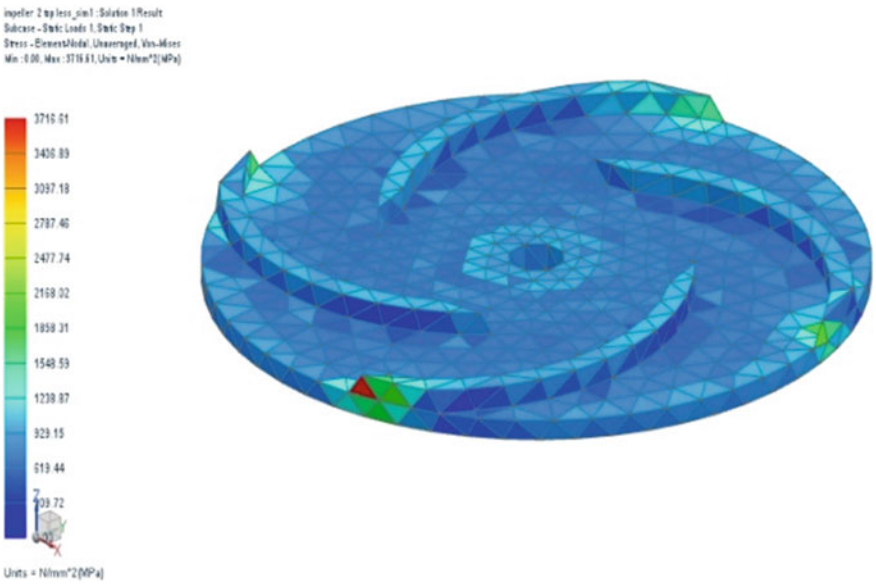

Fig. 4 Stress distributions of trapezoidal blade position

Table 7 Mesh properties of inclined blade position

Mesh	Element family	Elements	Nodes
alu: alu, Aluminum_6012			
3d_mesh(1)	Tetra4	2343	840

Table 8 Load values of inclined blade position

Step name	Number of referenced loads	Loads	
Subcase—Static loads 1	1		
	Hydrostatic(1)	Type	Hydrostatic
		Solver card name	PLOAD4
		Layer	1
		Applied to	14 Polygon face
		Description	
		Liquid surface	
		Liquid density	1e−006 kg/mm^3
		Gravitation constant	9810 mm/s^2
		Surface pressure	1000 N/mm^2 (MPa)

Table 9 Mesh properties of trapezoidal blade position

Mesh	Element family	Elements	Nodes
alu: PSOLID1, Aluminum_6012			
3d_mesh(1)	Tetra4	2668	954

Table 10 Load values of trapezoidal blade position

Step name	Number of referenced loads	Loads
Subcase—Static loads 1		1
Hydrostatic(1)	Type	Hydrostatic
	Solver card name	PLOAD4
	Layer	1
	Applied to	13 Polygon face
	Description	
	Liquid surface	
	Liquid density	1e−006 kg/mm^3
	Gravitation constant	9810 mm/s^2

Table 11 Result evaluation of the two different material impellers

Impeller material	Cast iron	Hardfaced aluminium alloy (6012)
Stress analysis	Von Mises stress	Von Mises stress
Element	3468	3468
Node	1210	1210
Max. von Mises stress	1.843e+007	1.825e+007

Table 12 Result evaluation of the two different blade positions

Impeller material	Hardfaced aluminium alloy	Hardfaced aluminium alloy
Impeller position	Inclined blade position	Trapezoidal blade position
Element family	Tetra4	Tetra4
Element	2343	2668
Node	840	954
Max. von Mises Stress	2.025e+007	2.549e+007

one is based on different blade positioning in the meridional annulus; inclined blade position and trapezoidal blade position results are shown in Table 11.

The max von Mises stress in the hardfaced aluminium alloy impeller is lesser than the cast iron impeller; this is because of the hardfacing material effect.

5.1 Blade Position Analysis

Results for the stress distribution analysis of inclined blade position and trapezoidal blade position are shown in Table 12.

It can be concluded from the above results that the mixed flow pump impeller having inlet inclined blade positioning (case-I) in the meridional annulus is getting lesser stress distribution than the trapezoidal blade positioning (case-II) which itself signifies that the impeller with inlet inclined blades positioning is a better choice than the other one as shown in Table 12.

6 Conclusion

- Comparing the 1, 2 and 3 mm thickness hardfaced aluminium alloy (6012), 3 mm hardfaced aluminium alloy is having more hardness and impact energy.

- Wear test results reveal that the hardfacing increases the wear characteristics of the samples. The plate with higher hardfacing (3 mm) showed better wear properties [14].
- It can be understood that the tribological properties were improved through hardfacing. The performance analysis of cast iron and hardfaced aluminium alloy (6012) impeller showed that the maximum stress developed in hardfaced aluminium alloy impeller is lesser than the cast iron impeller.
- It can be concluded from the above results that the mixed flow pump impeller having inlet inclined blade positioning (case-I) in the meridional annulus is getting lesser deformed than the trapezoidal blade positioning (case-II) which signifies that the impeller with inlet inclined blades positioning is a better choice than the other one.

References

1. Allen TT, Richardson RW, Tagliable DP, Maul GP (2002) Statistical process design for robotic GMA welding of sheet metal. Welding 81(5):69–172
2. Bergmann JB, Bielenin M, Stambke M, Feustel T, Witzendorff P (2013) Effects of diode laser superposition on pulsed laser welding of aluminium. Phys Procedia 41:180–189
3. Casalino G, Campanelli SL, Dal Maso U, Ludovico AD (2013) Arc leading versus laser leading in the hybrid welding of aluminium alloy using a fiber laser. Procedia CIRP 12:151–156
4. Das CR, Albert AK, Bhaduri G, Kempulraj (2003) A novel procedure for fabrication of wear resistant bushes for high temperature application. J Mater Process Technol 141:60–66
5. Deng DW, Zhang CP, Chen R, Xiad H (2013) Microstructure and microhardness of 17-4PH deposited with co-based alloy hardfacing coating. Phys Procedia 50:177–184
6. Eschnauer H (1998) Hard material powders and hard alloy powders for plasma surface coating. Thin Solid Films 73:1–17
7. Gandra J, Pereira D, Miranda RM, Vilaca P (2013) Influence of process parameters in the friction surfacing of AA 6082-T6 over AA 2024–T3. Procedia CIRP 7:341–346
8. Kirchga BM, Badisch E, Franek F (2008) Behaviour of iron-based hardfacing alloys under abrasion & impact. Procedia Eng 265:772–777
9. Marimuthu K, Murugan N (2013) Prediction and optimization of weld bead geometry of Plasma transferred arc hardfaced valve seat rings. Surf Eng 19:143–149
10. Gualco A, Hernan G, Svoboda ES, Surian, de Vedia LA (2010) Effect of welding procedure on wear behaviour of a modified martensitic tool steel hardfacing deposit. In: Materials & design, vol 9. Elsevier, Article in Press, Corrected Proof, pp 445–468
11. Balakrishnan M, Balasubramanian V, Madhusudhan Reddy G (2013) Effect of hardfacing consumables on ballistic performance of Q&T steel joints. Defence Technol 9:249–258
12. Buchely MF, Gutierrez JC, Leon LM, Toro A (2005) The effect of microstructure on abrasive wear of hardfacing alloys. 259:52–61
13. Glaesar WA (1992) Friction and wear of carbon alloy steels. ASM Int 18:702–709
14. Ramesh C, Prakash P, Siddharthan B, Naveen TK (2016) Theoretical and experimental analysis of Hardfaced aluminium alloy (6012). Adv Nat Appl Sci 10:18–26
15. Srivastava S, Roy AK, Kumar K (2014) Design of a mixed flow pump impeller blade and its validation using stress analysis. Procedia Mater Sci 6:417–424
16. Chu Q, Zhang M, Li J (2013) Failure analysis of impeller made of FV520B martensitic precipitated hardening stainless steel. Eng Fail Anal 34:501–510

17. Srivastava S, Roy AK (2014) Design of a mixed flow pump impeller and its validation using FEM analysis. Procedia Technol 14:181–187
18. Kim JS, Son YJ, Jeung K (2001) Control and optimization of bead width for multi-pass welding in robotic arc welding processes. Austr Welding J 46:43–46

Sensor-Based Gamified Rehabilitation Therapy to Enhance and Manage Human Physical Kinematics

S. J. Syed Ali Fathima, S. Amritha Shankar, and A. Ahamed Thajudeen

Abstract Over the period of technological development, the way in which the human interact with the computing devices is evolving continuously from command line to natural user interface. At the beginning, only commands were used to instruct the computers which were enriched after the development of graphical user interface (GUI) in the year 1980 with the usage of keyboard and pointing devices for computing interactions. Though GUI made easier interactive computing environment for almost all the users of that generation, it does not offer natural way of interaction. Current technologies proposed the next generation interface called as natural user interface (NUI) where the human's intuitive actions like touch, speech, thoughts and gestures become an input for computing interactions that aim to offer better user experience. In general, the NUI is made possible through small or large physical body movements intending to inform a message or information non-verbally and naturally consenting its opportunity in wide range of rehabilitative health applications. In this paper, the recent advancement of computing interfaces and NUI sensor-based technologies to enhance and manage human physical kinematics are reviewed. The current trends of using sensors and technologies in real-time applications of health care therapy are presented with a design of experimental sensor-based gamified therapy for hand rehabilitation.

S. J. Syed Ali Fathima (✉)
Department of Computer Science and Engineering, Kumaraguru College of Technology, Coimbatore, TN 641049, India
e-mail: syedalifathima.sj.cse@kct.ac.in

S. A. Shankar
Department of Computer Science and Engineering, Hindusthan College of Engineering and Technology, Coimbatore, TN 641012, India
e-mail: shankarhicet@hindusthan.net

A. Ahamed Thajudeen
College of Physiotherapy, Sri Ramakrishna Institute of Paramedical Sciences, Sidhapudur, Coimbatore, TN 641044, India
e-mail: ahamptsp@gmail.com

G. Kumaresan et al. (eds.), *Advances in Materials Research*, Springer Proceedings in Materials 5, https://doi.org/10.1007/978-981-15-8319-3_105

Keywords Natural user interface · Sensors · Healthcare · Rehabilitation · Therapy · Augmented reality · Virtual reality

1 Introduction

Artificial intelligence (AI) technologies seeking to imitate human intelligence, is receiving lot of attention and is being integrated into various fields, including medication and diagnosis. Interaction of human with computer machines is made possible by means of natural actions of human using their gestures, senses, thoughts and speech tracked using natural user interface (NUI) inspired by AI algorithms instead of making use of keyboard and mouse which is the part of graphical user interface (GUI). There exist multiple possibilities for operating NUI depending upon the state of purpose and the requirements from user. In healthcare domain, NUI kind of technology intervention could improve the rehabilitation environment by creating a motivational, engaging and optimistic impact for the patient's recovery. The application of gamified system in medical rehabilitation is greater than ever, since they have been proven to raise patients' engagement toward treatment and increases therapy's effectiveness. The gaming environment offering space for exercise training using video games will possibly create certain general healthcare benefits and as well encouraging outcomes in intensifying the recovery process in various disorders [1]. The forthcoming sections will review the assistive technology using emerging NUI computing techniques like touch computing, gesture computing, surface computing, brain computing and NUI application technologies like virtual reality and augmented reality. The paper also presents the design of experimental sensor-based gamified therapy to support and augment hand rehabilitation.

2 Literature Review

2.1 Computing Interfaces

Command line interface(CLI) is also known as command language interpreter, in which user issues text commands or shell scripts through the console interface using the typewriter or keyboard input device to interact with computer systems. CLI is mostly preferred by advanced programmers as they are keen and strong in controlling a program or operating systems using crisp commands. Scripting languages. like Python, Ruby and Perl are well known and widely used text processing programming languages in medical and bio-informatics to access and manage medical datasets, disease diagnosis and drug design, evaluate treatment plan and medical discovery [2]. Graphical user interface (GUI) is the system interface using which the users are allowed to interact with systems through visual markers, indicators and graphical

icons with the yield of capabilities offered by computers graphic techniques in addition to CLI features. The invention of various hardware devices like speech synthesis, tactile displays, sensors, etc., and appropriate software applications enabled GUI systems to be useful in medical rehabilitation for blind and disabled people for the improvements in orientation and mobility. GUI has now become more significant for a healthcare treatment tracking and analyzing devices. The facility to manage and administrate the device using GUI expands the easy handling, safety, control and accurate communication between the system and the user [3].

The enhancement to CLI and GUI with an ability to interact with computers or smart devices using the human body is proposed using natural user interface and it is powered by human touch, gesture, voice and senses. The implementation of NUI is possible by using appropriate sensing devices as an intermediate gateway for interaction that is either directly or indirectly integrated to the computing system. This facilitates the computers to be supplemented in different fields of applications like healthcare treatment with technological innovations which was found to be quite tough and tedious previously. The idea of developing gaming prototypes using NUI sensors for physical rehabilitation exercises has improved the interest and changed the exercise perception, making the patients to undertake training with enthusiasm and without the feel of treatment session [4]. The generalized model of NUI-based healthcare therapy is shown in Fig. 1. The sensors like Microsoft Kinect, Intel Real Sense, Leap Motion Controller, Nintendo Wii, etc., support natural user interface which enables AI-based computerized therapy.

The Comparison of computing interfaces is given in Table 1.

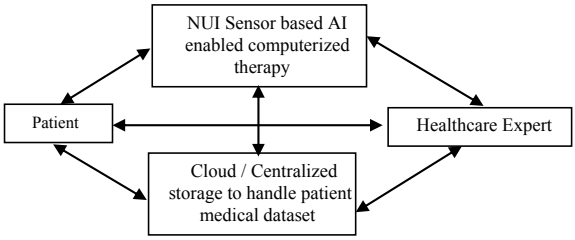

Fig. 1 Generalized model of sensor-based healthcare therapy

Table 1 Comparison of computing interfaces

Computing interfaces	Input mode	Support level in healthcare domain
CLI	Text commands	Low
GUI	Graphical commands using pointers and pointing devices	Medium
NUI	Voice/speech, body gestures, brain signals, touch, object's skeletal structure	High

2.2 NUI Sensor-Based Computing Techniques

The major classification of NUI-based computing techniques and the review of application of these techniques in healthcare rehabilitation is discussed.

2.2.1 Touch Computing

Touch computing enables the users to interact with controls and applications more intuitively using their touch input. For example: touching a graphical icon to open an application. The wall surfaces, flat tables, smartphones, PC screens and tablets are the most popularly used touch devices. The touch input signal using fingers is made active through a built-in panel that carries electrical charge in which the electric field will get interrupted on a touch in these handheld computing devices. This interruption is recorded as a computer event and sent to the software program for processing to initiate a response to the touch event. The games developed using touch panels are now introduced in cognitive exercise therapy. In recent days, the early learning is improved through the common use of touch screens in our day-to-day life [5].

2.2.2 Surface Computing

Human interaction with systems is also enabled through surface computing in which the normal surface of an object acts as an interaction interface. Touch computing deals with flat surface, whereas surface computing concentrates on non-flat three-dimensional objects surfaces like spherical, cylindrical and parabolic surfaces. It provides a means to ubiquitous computing of making every surface as interactive in our day-to-day environment. It can be implemented using displays like LCD or projection screens, projector and infrared cameras. Infrared cameras are main component that operate independent of light and allows for gesture detection in all lighting conditions. Microsoft research is on 3D surface computing which deals with sensing of 3D input data above 2D surfaces. The computer-aided seating system (CASS) with contour sensing and evaluation devices is used as assistance in the design of clinical seat contours which provides the examination of tissue distortion through the surface interface when the seats are loaded [6].

2.2.3 Gesture Computing

In general, the gestures are defined as small or large physical body movements intending to inform a message or information non-verbally. The ability of the computers to understand the natural human gestures as input and responds to the input in the right way as intended refers to the gesture recognition (GR) and it is implemented and interpreted with the aid of motion sensing devices called gesture

recognition sensing devices. The human physical kinetics by means of arms, eyes, facial expressions and any gesture act as an input signal to interact with systems using gesture computing. GR works with the principle in which the physical actions of the user are sensed as the input data signal by the camera-enabled sensor which is then sent to the application programming interface (API) to control devices or any other application. The infrared rays that are invisible are posed on the user and it is reflected back to sensor built-in with the GR integrated chip [7].

2.2.4 Brain Computing

The interaction between the computing system and human is also made possible using the direct brain signals through brain computing interface termed as BCI. The human physical motion and motor functions with effect from cognitive and sensory inputs can be recovered with the help of BCI. BCI using the thought processing offers a means for paralyzed to operate a computer, prosthetic limb, or motorized wheelchair. Thought-based control of a neuro-prosthesis has been developed in which hand grasp is supported with implanted stimulation electrodes [8]. Post-stroke rehabilitation with feedback training using virtual hands has been developed in which BCI use the classified brain patterns to generate virtual hand movements like opening and closing of the left or right upper limbs [9].

The comparison of NUI-based computing techniques is given in Table 2.

2.3 NUI Sensor-Based Computing Techniques

This section focuses on two major technologies with the application of NUI sensor that widely supports healthcare field.

Table 2 Comparison of NUI sensor-based computing techniques

NUI-based computing technique	Input mode	Support level in healthcare domain
Touch computing	Touch/multi-touch on flat surface	Low
Surface computing	Touch/multi-touch on flat or non-flat surface	Advanced hand gesture exercises and supports design of surfaces for assistive devices
Gesture computing	Speech, body movements (or) gestures, facial expressions, skeletal structure	Whole body gesture exercises
Brain computing	Thoughts as brain signals	Treatments relating physical and metal thoughts (or) controlling physical gestures by thoughts (brain signals)

2.3.1 Virtual Reality (VR)

VR represents the 3D space generated virtually by computers that can be explored, interacted and experienced by the humans directly using their sight and sound senses with the help of NUI. The simulated environment created using the software offers the user with the feel of real-time environment and the person becomes a part of it and is able to perform actions and manipulate objects. Interactive VR exercising system is one of the stimulated world of VR-based rehabilitation therapy developed to direct patients targeting specific body parts through therapist prescribed rehabilitation training exercises, games and activities that are interactive naturally [10].

2.3.2 Augmented Reality (AR)

The real-world environment with the computer-generated augmented virtual objects allowing the users to interact using the natural input signals generated through human speech, touch or gestures by the means of NUI sensors is termed to be AR technology. A mixture of real and virtual environment is projected in front of the patient to play with the augmented objects inside the environment with the tangible feeling. No visuo-spatial change by the patient is needed because of the fact that the patient communicates directly with the system [11]. AR technology supports rehabilitation by providing an entertaining, engaging and natural environment for treatments [12].

3 Methodology

3.1 Gamified Therapy

Gamified therapy can be employed to supplement the techniques of treatments in the area of rehabilitation, helping to satisfy different motor learning principles that are steadily acquiring substantial ground in terms of attracting an immensely accepted method [13]. The game design principles namely feedback, play, rewards, goals, difficulty, challenge, flow and failure can be an essential part for the development of customized games for rehabilitation of stroke survivors as they act as the makers of commercial games [14]. VR and AR gamified therapy offers the concept with multi-sensory feedback that needs various action levels. The gamified therapy and VR provide the benefit of training patients in certain target-oriented task that can be repetitive in the context of enriched virtual space that provides the feasibility of solving both motor and cognitive tasks and of studying new skills [15].

3.2 Experimentation

The experimental study uses Microsoft© Kinect gesture capturing sensor device as an interface for a sensor-based gamified therapy designed for hand movement rehabilitation to enhance reaching and touching objects around the subject [16]. Since the current examination is of experimental study and consists human respondents' ethical approval and information accessibility from institutional ethical committee, TOCPTRBR, The Oxford College of Physiotherapy, Bangalore has been gained prior accumulating data; similarly, respondents' details/information were kept anonymous and both parties (researcher and participant) signed the IC form under medical observation and regulations [17]. Finally, the data were not replicated or shared with other researchers for any other purposes.

Kinect is the NUI-based marker less motion sensing device consist of 3D depth sensor camera, vision camera, red–green–blue (RGB) camera, depth sensor, LED and a microphone array. The Microsoft's proprietary software to control these sensors is offered to enable 3D motion capture of the whole body with skeletal tracking features, facial expressions identification and voice or speech recognition capabilities.

The game scenario comprises of five jumper objects which is distributed virtually around the user environment within the reachable distance. In this case, the environment defines to the integration of virtual objects into real creative scene seized using Microsoft© Kinect's camera. The game play refers that the user must reach and bump the object to make it disappear, and for each single play, this must be repeated for the entire five objects with the timer and count variables set. Each bumping action and object vanishing within the time limit are considered to be hit and will get the reward score value of 10. For every appropriate hit action, the update of game score is performed and the range of motion angles of shoulder and elbow is measured using skeletal tracking feature of Kinect sensor and is recorded. When the timer is 0, the count is reduced and the game play repeat again until the count reaches to zero.

Kinect is a horizontal bar connected to a small base with a motorized pivot and fixed to a tripod and the target location is calibrated. Kinect camera should be located within 30 cm $\times$ 30 cm square at a distance of between 1.45 and 1.75 m from the user, and at either 0.15 m to the left or right. It was made to constrain the hand movement of the subject to a circular or a linear motion. Subject is placed in the frontal plane toward Kinect camera and performs training in sitting or standing position as per instruction. The experimental setup and illustration of reach and touch training scenario of sensor-based gamified therapy are shown in Fig. 2.

4 Results and Discussion

The usability test was conducted by toward measuring the ease or comfort of the user toward the developed experimental system. Thirty participants experienced sensor-based gamified therapy and are presented with set of questions to answer manually or

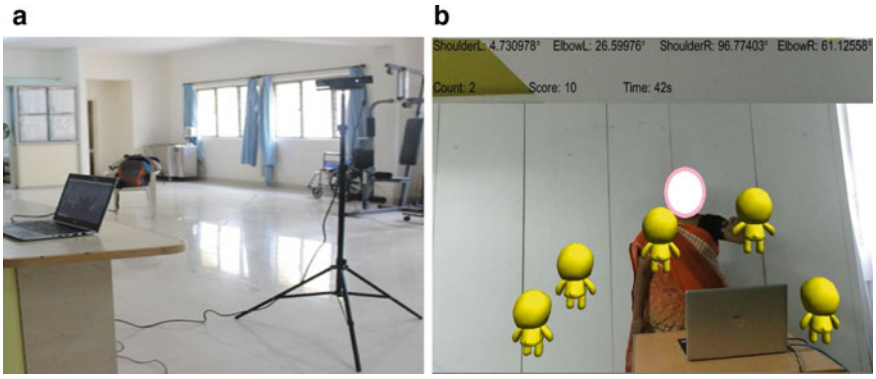

Fig. 2 **a** Experimental setup and **b** reach and touch—sensor-based gamified therapy

Table 3 Usability analysis of sensor-based gamified therapy for hand rehabilitation

Questions	Mean score
Scenarios are simple and easily understandable	4.4
Easy to use	4.3
Appropriate for upper limb functionality improvement	4.1
Hand gestures are captured and actions are performed correctly without any delay	4.3
Game training is taken without any feel of treatment session	4.2
Training environment is fun, interesting and engaging	3.8
Audio-visual feedback given motivates the training	3.2

through the computer programmed questionnaire. Once the respondents offered their real-time experiences through the scoring card or scoring options, the mean value is calculated and the score would be compared to reveal the system's efficiency. The usability test was designed with seven questions toward measuring the environment and effects of sensor-based gamified training offered to the participants as shown in Table 3. Through the developed experiment, the level of comfort and satisfaction experienced by the participants was the score as overall mean result was measured as 4.04. This proves that the developed system is rather pleasing and easy to adapt with the regular therapies and treatments.

5 Conclusions

In this paper, the evolvement of different types of computing interfaces, advancement of NUI-based computing techniques, like touch computing, surface computing, gesture computing and brain computing, and the technologies like VR and AR with

the application of NUI, experiment on sensor-based gamified therapy aiding the assistive technology to support and enhance healthcare rehabilitation were discussed. With smart machines communication has become much natural due to the greatest use of artificial intelligence techniques. Sensors can acquire gestures of human body as commands with smart NUI. The use of human–computer interaction-based products in the field of medical rehabilitation is consistently developing. Numerous researches are being carried out on these computing techniques to make it practical in medical practice. The research should also focus on developing suitable protocols for creating and delivery of rehabilitation services and products with these computing techniques to meet medical device standards.

References

1. Jain A, Lund D, Wixon (2011) The future of natural user interfaces. In: Proceeding of CHI'11 extended abstracts on human factors in computing systems, pp 211–214
2. Jules JB (2010) Methods in medical informatics: fundamentals of healthcare programming in perl, python, and ruby. Chapman & Hall/CRC Mathematical and Computational Biology
3. Laura DR (2013) Development of a graphical user interface for a rehabilitation exoskeleton. Vrije Univeriteit Brussel
4. Rego PA, Moreira PM, Reis LP (2011) Natural user interfaces in serious games for rehabilitation. In: Proceedings in 6th Iberian conference on information systems and technologies (CISTI) pp 1–4, 15–18
5. Matsushima F, Vilar RG, Mitani K, Hoshino Y (2014) Touch screen rehabilitation system prototype based on cognitive exercise therapy. In: Part II, Proceedings of HCI international conference, Heraklion, Crete, Greece
6. Brienza DM, Chung KC, Brubaker CE, Kwiatkowski RJ (1993) Design of a computer-controlled seating surface for research applications. IEEE Trans Rehabil Eng 1(1):63–66
7. Top 18 gesture recognition technology companies. https://www.technavio.com/blog/top-18-gesture-recognition-technology-companies. Last accessed on 28 Jan 2020
8. Guillot A, Collet C (2010) The neurophysiological foundations of mental and motor imagery. Oxford University Press
9. Pfurtscheller G, Muller-Putz GR, Scherer R, Neuper C (2008) Rehabilitation with brain–computer interface systems. Computer 41(10):58–65
10. Enabling-and-assistive-technology-disabilities. https://www.gesturetekhealth.com/solutions/enabling-and-assistive-technology-disabilities. Last accessed on 28 Jan 2020
11. Merians A, Jack D, Boian R, Tremaine M, Burdea G, Adamovich S, Recce M, Poizner H (2002) Virtual reality-augmented rehabilitation for patients following stroke. Phys Ther 82(9):898–915
12. Viaud-Delmon I, Gaggioli A, Ferscha A, Dunne S (2012) Human computer influence applied in healthcare and rehabilitation. Student Health Technol Inf 181:42–45
13. Barrett N (2016) The use and effect of video game design theory in the creation of game-based systems for upper limb stroke rehabilitation. J Rehabil Assist Technol Eng 3:1–16
14. Lohse K, Shirzad N, Verster A (2013) Video games and rehabilitation: using design principles to enhance engagement in physical therapy. J Neurol Phys Ther 37:166–175
15. Morone G, Tramontane M, Iosa M, Shofany J, Iemma A, Musicco M, Caltagirone C (2014) The efficacy of balance training with video game-based therapy in subacute stroke patients: a randomized controlled trial. BioMed Res Int
16. Syed Ali Fathima SJ, Shankar S, Ahamed Thajudeen A (2018) Activities of daily living rehab game play system with augmented reality based gamification therapy for automation of post stroke upper limb rehabilitation. J Comput Theor Nanosci 15(5):1–7

17. Grady C (2015) Enduring and emerging challenges of informed consent. New Eng J Med 372(9):855–862

A Review on Analysis of Performance Parameters in Low Voltage Current Mirror Circuits

S. Saranya, R. Saravana Kumar, S. Praveen Kumar, S. Dharani, and P. M. Rubesh Anand

Abstract Electronics industries often require low voltage and low power current mirror circuits with high performance in analog and mixed VLSI signal applications. The current mirror circuits trace the input current into an output device without any degradation for any load conditions. The major challenges while designing the current mirror circuits include low input and high output resistance, low input–output voltage and low noise considerations. Different topologies are developed in current mirror circuits to overcome these limitations but it is hard to satisfy all these requirements in a single circuit design. A detailed analysis of different current mirrors circuits is very essential for modern mixed VLSI signal applications. In this paper, the performance parameters of different current mirror circuits with the various topologies like low voltage CMOS analog design, MOSFETs devices in sub-threshold region, bulk driven and FGMOS in circuit level are compared and analyzed. The comparative analysis shows that the combination of two or more topologies performs better in analog VLSI design applications.

Keywords Low power CMOS · Bulk driven · FGMOS · Analog and mixed VLSI · Cascode topology

1 Introduction

The invention of CMOS technology has made a huge revolution in modern VLSI industry for consumer, industrial robotics and defense applications [1–3]. In order to enhance the speed of CMOS device operation and increase the density of the device with lower power consumption, the transistor size scaling is essential. In the same time, the supply voltage is not possible to be reduced correspondingly with transistor scaling [4] due to fundamental limitation of reduction of the input voltage. Equation (1) represents the power supply requirements of MOS circuits [5].

S. Saranya · R. Saravana Kumar (✉) · S. Praveen Kumar · S. Dharani · P. M. Rubesh Anand
Department of Electronics and Communication Engineering, Bannari Amman Institute of Technology, Sathyamangalam, Erode, Tamil Nadu 638401, India
e-mail: saravanaelectron@gmail.com

G. Kumaresan et al. (eds.), *Advances in Materials Research*, Springer Proceedings in Materials 5, https://doi.org/10.1007/978-981-15-8319-3_106

$$|V_{DD} - V_{SS}| \geq V_{tn} + |V_{tp}| \quad (1)$$

where

V_{DD} Positive supply voltage.
V_{SS} Negative supply voltage.
V_{tn} Threshold voltage of NMOS device.
V_{tp} Threshold voltage of PMOS device.

It is clear from the Eq. (1) that the supply voltage not less than the sum of *P* type and *N* type transistor threshold voltages. But in current CMOS technology, the reduction of supply voltage and low power consumption circuit designs is much essential. Hence, to design low voltage circuits in analog integrated circuits is a great challenge, especially in current mirror circuits [4]. The current mirror circuits are basic building blocks for almost all analog and mixed circuit systems. This circuit consists of two terminals and its output current is only based on input current and not influenced by the output load. The current mirror circuits are basically employed in biasing, loading and level shifting circuits and it is mainly used in amplifier, analog-to-digital (A/D) and digital-to-analog (D/A) converters.

The ideal current mirror circuits should attain the following requirements [6] as,

- Low input impedance
- High output impedance
- High accuracy
- Low input voltage
- Output current should be constant over wide range of load variation
- Low noise.

The current mirror circuits that are designed with different topologies possess their own advantages and drawbacks. The main consideration while designing the current mirror circuits are high output impedance and low output voltage. In order to attain linearity and high output impedance, regulated body-driven cascode current mirror circuits are implemented. In this technique, the output impedance increases while increasing the number of stages of current mirror circuits. But at the same time, it increases the minimum output voltage. Hence, there is always a trade-off between output impedance and minimal output voltage [6]. Cascode technique improves the accuracy and output resistance of the circuit, but meanwhile it increases the power requirements [6, 7].

Different cascode current mirror circuits are implemented for further performance improvement [5] as,

1. Double cascode
2. Wide swing cascode
3. Triple cascode
4. Regulated cascade

2 Methodology

In the last few decades, the current mirror circuits operations are enhanced by different topologies which include level shifter technique, bulk-driven technique and floating gate MOS technique (FGMOS). The level shifter circuits require an extra circuit to compensate the offset current which requires additional power for this technique. It increases the overall power consumption of the system [7]. The bulk-driven technique is adopted in CMOS design for low voltage and low power design. This technique controls the weak bias voltage between the bulk and source of MOSFET so that consequently input bias voltage is reduced [6]. The bulk-driven technique supports for low voltage design but other parameters are suffers from some limitations such as accuracy, input impedance, output impedance and linearity. Bulk-driven techniques is not used for wide voltage swing and it decays the bandwidth of current mirror circuits [4, 7].

FGMOS design is preferred compared to other techniques as it consists of multiple inputs and due to this configuration, effective threshold can be reduced [8]. FGMOS technique creates an additional parasitic resistance and capacitances which degrades the bandwidth of the circuit. Traditional current mirror circuits have low input and high output compliance voltages which indeed provides a high offset current and limit the operating range. In order to improve the operating range, multiple inputs floating gate technique is used [9]. This method satisfies the lower supply voltage but transconductance value and gain bandwidth product are degraded. Self-biased self-cascode bulk-driven quasi-FGMOS current mirror is proposed to prevent the above effects. In this topology, input supply is connected in bulk terminal of quasi-FGMOS transistor and output is taken at self-cascode FGMOS structure [10].

3 Results and Discussion

The comparison of supply voltage with power dissipation and output impedance of different current mirror circuits of various reported published state of art is presented in Fig. 1. From this graph, it is clear that [8] shows the lower power dissipation [0.14 mW] at low supply voltage (0.75 V). In the considered reference article [8], the current mirror circuit was designed by floating gate structure in Wilson current mirror circuit model. The various performance parameters of current mirror circuits with different topologies are listed in Table1. From this table, it is clear that researchers mainly used cascode, bulk driven and FGMOS techniques to achieve the device performance**.**

From Table 1, it is clear that researchers mainly used cascode, bulk driven and FGMOS techniques to achieve the device performance. The cascode techniques improve the output impedance level with degraded power supply [7, 10, 12, 15]. To improve the supply voltage performance, bulk-driven topology is adopted [4, 8, 13] and FGMOS technique is used for improve the supply voltage and power dissipation

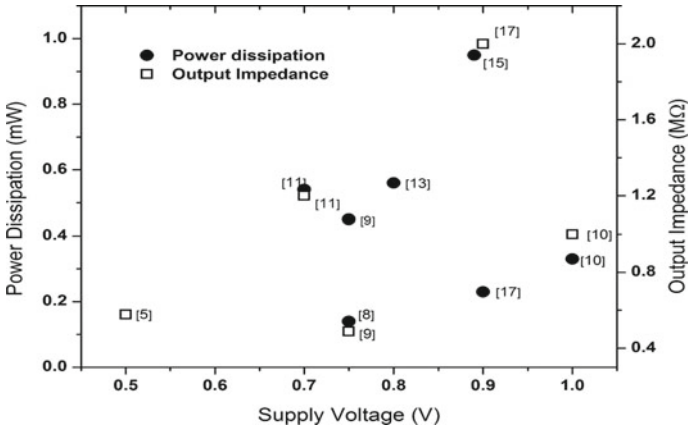

Fig. 1 Comparison of supply voltage with power dissipation and output impedance of various current mirror circuits

but bandwidth degraded [5, 11, 16]. Some researchers combine the above topologies to achieve the overall requirements of current mirror circuits [16, 17]. The voltage level shifting process is improved through the dual current mirror circuits through the lowest delay and low power consumption [18, 19].

4 Conclusions

In this work, different performance parameters of various current mirror circuits such as cascode, level shifter, bulk driven and FGMOS topologies are reviewed. Each of the current mirror circuits had its own advantages and drawbacks. The current mirror circuits are designed with minimum supply voltage and high output impedance, but balancing between these two parameters is difficult in single topology circuits. So hybrid techniques like combination of two topologies such as bulk drive, cascode, level shifter and FGMOS can be used to improve the analog and mixed VLSI circuit performance.

Table 1 Comparison of state of art of various performance parameters of current mirror circuits with different topologies

Refs.	Design methodology	Simulation tool	Output parameters	Parameter values
[7]	Wide swing cascode current mirror (WSSCM)	Cadence specter 35 nm MIMO	High amplification	0.33 μA
			Power dissipation	0.33 mW
			Supply voltage	1 V
			High output resistance	12 MΩ
			Output impedance	1.0 MΩ
[8]	Low voltage current mirror FGMOS	PSpice	High amplification	0.21 μA
			Power dissipation	0.54 mW
			Supply voltage	0.7 V
			High output resistance	15 MΩ
			Output impedance	1.2 MΩ
[2]	FGMOS-based WCM	SPICE and TSMC	High amplification	2.05 μA
			Supply voltage	0.5 V
			No. of transistor	2
			Upper cutoff frequency	5 MHz
			Output impedance	0.578 MΩ
			Bandwidth	257
[5]	Basic current mirror	Mentor graphics	High amplification	1.98 μA
			Power dissipation	0. 14 mW
			Supply voltage	0.75 V
			Output impedance	71.16 MΩ
			Output voltage	0.122 V
			Bandwidth	5.89 GHz
			Upper cutoff frequency	7 MHz

(continued)

Table 1 (continued)

Refs.	Design methodology	Simulation tool	Output parameters	Parameter values
			Output resistance	119 KΩ
[9]	Self-bias cascode current mirror	Cadence virtuoso 180 nm	Supply voltage	1.7 V
			Output voltage	0.65 V
			No. of transistor	5
			Upper cutoff frequency	7 MHz
[10]	Bulk driven	Cadence virtuoso 180 nm	Supply voltage	0.7 V
			Output voltage	0.67 V
			No. of transistor	2
			Upper cutoff frequency	10 MHz
	Self-biases cascode current mirror	Cadence virtuoso 180 nm	Supply voltage	0.67 V
			Output voltage	0.38 V
			No. of transistor	5
			Upper cutoff frequency	5 GHz
	Bulk-driven Wilson current mirror	Cadence virtuoso 180 nm	Power dissipation	0.56 mW
			Supply voltage	0.8 V
			Output voltage	0.9 V
			No. of transistor	4
			Upper cutoff frequency	6 MHz
[11]	Conventional current mirror	PSpice	High amplification	0.23 μA
			Power dissipation	0.23 mW
			Supply voltage	0.9 V
			High output resistance	1.37 MΩ
			Output impedance	2.0 MΩ

(continued)

Table 1 (continued)

Refs.	Design methodology	Simulation tool	Output parameters	Parameter values
[12]	Triple cascade current mirror	Mentor graphics	High amplification	0.23 μA
			Power dissipation	0. 95 mW
			Supply voltage	0.89 V
			High output resistance	1.37 MΩ
			Bandwidth	5.89GH
			Output resistance	45.26 M Ω
[5]	Bulk driven	SPICE	Power dissipation	0.8 mW
			Supply voltage	0.75 V
			High output resistance	1.37 MΩ
			Bandwidth	65 MHz
			Output resistance	45.26 M Ω
[6]	Folding gate	Cadence spectra using CMOS 180 nm	Power dissipation	0.45 mW
			Supply voltage	0.75 V
			Input impedance	1.49 KΩ
			Output impedance	0.488 MΩ
			Bandwidth	57 MHz
[4]	Flipped voltage follower self-cascode	TSMC of MOSIS 180 nm	Supply voltage	1 V
			Input resistance	2.133 KΩ
			Power dissipation	0.33 mW
	Flipped voltage follower	CMOS TSMC of MOSIC in 0.25 μm	Supply voltage	1.2 V
			Frequency	168.48 MHz
[1]	Level shifted FVF	Mentor graphics Eldospice based on TSMC 0.18 μm level shifted FVF	Supply voltage	1 V
			Power dissipation	0.33 mW
	Bulk driven Bulk driven	Cadence spectra and BSIM3v3	Input voltage	0.4 V
			Output voltage	0.39 V

(continued)

Table 1 (continued)

Refs.	Design methodology	Simulation tool	Output parameters	Parameter values
			Low supply voltage	0.7 V
	Level shifted FVF	Mentor graphics Eldospice based on TSMC 0.18 μm	Supply voltage	1 V
			Power consumption	0.54 μW
[13]	FGMOS and WCM	Cadence spectra and TSMC	Power supply	1 V
			Bandwidth	5 GHz
			Power consumption	0.58 mW
			Output impedance	10 MΩ
[14]	CMOS-memristive cascode current mirror	SPICE	Power consumption	14.142 μW
			On chip area	1.47 10^{-12} m^2
[15]	Cascode current mirror array	PUF CMOS process 65 nm	Power consumption	1.53 mW
			Supply voltage	0.95 V
			Throughput	10 Mb/s
[16]	Cascode current mirror array-based PUF	PUF using CMOS process 35 nm	Supply voltage	1 V
			Power consumption	18.8 mW
			Output impedance	12.5 MΩ

References

1. Saravana Kumar R, Mohanbabu A, Mohankumar N, Godwin Raj D (2018) Simulation of InGaAs sub-channel DG-HEMT for analogue/RF applications. Int J Electron 105(3):446–456
2. Bhanu Chander V, Asokan T, Ravindran B (2017) Recovering free space from a single two-point perspective image for mobile robot navigation for indoor applications. Lecture notes in mechanical engineering mechanism and robotics proceedings of iNaCoMM 2017, pp 15–26
3. Saravana Kumar R, Mohanbabu A, Mohankumar N, Godwin Raj D (2017) $In_{0.7}Ga_{0.3}As/InAs/In_{0.7}Ga_{0.3}As$ composite channel double gate (DG)-HEMT devices for high-frequency applications. J Comput Electron 16(3):732–740
4. Lakkamraju N, Mal AK (2004) Low supply voltage high-output impedance regulated cascode current mirror. IEEE Trans Circuits Syst II Express Briefs 51(3):124–129
5. Aggarwal B, Gupta (2009) Low-voltage cascode current mirror based on bulk-driven MOSFET and FGMOS techniques. In: International conference on advances in recent technologies in communication and computing ARTCom 09, pp 473–477
6. Chikani J, Chaudhari P, Savani V (2012) Analysis and characterization of various current mirror topologies in 90 nm technology. Int J Emerging Technol Adv Eng 2(12)
7. Main MU, Dennis JO, Khir Md, Tang TB, Sutri NY (2012) Noise and bandwidth analysis for PMOS based wide cascode current mirror using 0.35 μm CMOS-MEMS technology. Int J Emerging Technol Adv Eng 2(12)

8. Gupta M, Srivastava R, Singh U (2014) Low voltage high performance FGMOS based Wilson current mirror. In: IEEE International conference on signal processing and integrated networks SPIN, pp 565–570
9. Sharma S, Rajput SS, Magotra LK, Jamuar S (2015) FGMOS based wide range low voltage current mirror and its applications. In: Asia-Pacific conference on circuits and systems, APCCAS, vol 2, pp 331–334
10. Rana C, Afzal N, Prasad D (2015) A high-performance bulk driven quasi floating gate MOSFET based current mirror. APCCAS'02, vol 2, pp 331–334
11. Hamed HFA, Kaya S (2007) Low voltage Programmable double gate MOSFETs current mirror and its application as programmable-gain current amplifier. In: IEEE conferences on electronics circuits and system, pp 391–394
12. Lattenberg I, Vrba K (2007) Low input impedance current Mirror for high speed data communication. In: IEEE sixth international conference on networking, ICN 07
13. Akbari M, Javid A, Hashemipour O (2015) A high input dynamic range, low voltage cascode current mirror and enhanced phase-margin folded cascode amplifier. In: IEEE 22nd Iranian conference on Electrical Engineering, pp 77–81
14. Khateb F, Biolek D, Musil V, Shehab S (2007) Low voltage current differencing transconductance amplifier. Electronic Devices Syst EDS 07:311–315
15. Sung S-H, Hsia J, Yu C-P (2018) A 10-bit 200-MS/s switched-current pipelined ADC for analog front end of XDSL. In: 7th International symposium on next generation electronics (ISNE)
16. Singh P, Gupta M (2018) Application of FGMOS based Wilson current mirror in transimpedance amplifier. In: 8th IEEE transaction on power electronics (IICPE), pp 1–5
17. Satuyeva B, Krestinskaya O (2018) Design and analysis of CMOS-memristive cascode current mirror. In: International conference on computing and network communications (CoCoNet)
18. Lin S, Zhao X, Li B, Pan X (2017) An ultra-low power common source-amplifier-based physical unclonable function. In: Proceedings of IEEE transaction. Electron devices solid-state circuits (EDSSC), pp 269–272
19. Zhao X, Gan P, Zhao Q, Liang D, Cao Y, Pan X, Bermak A (2019) A 124 fJ/bit cascode current mirror array based PUF with 1.50% native unstable bit ratio. IEEE Trans Circ Syst 66(9):3494–3503
20. Yong Z, Xiang X, Chen C, Meng J (2017) An energy efficient and wide range voltage level shifter with dual current mirror. IEEE Trans Very Large Scale Integr (VLSI) Syst 25(12):3534–3538
21. Zhou J, Wang C, Liu X, Zhang X, Je M (2015) An Ultra-low voltage level shifter using revised wilson current mirror for fast and energy-efficient wide-range voltage conversion from sub-threshold to I/O voltage. IEEE Trans Circ Syst 62(3):697–706

Experimental Investigation on Mechanical Properties of Banana Fiber Reinforced Vinyl Ester Resin Composites

J. Harish Kumar, S. Prabhakaran, K. Alagar Pandi, and K. N. Karthick

Abstract In recent years, many types of composites materials are used in leading edges of materials technology, with ultra-demanding applications such as automotive, structural applications etc. Among the various composites, the widely used and oldest composite material is fiber-reinforced composites. Banana fibers act as the most common of all reinforcing fibers for FRP composites. Although these composites have some principal merits such as high strength, high chemical resistance, and excellent insulating properties, etc., natural fibers are now considered as serious alternatives for the use in composites, due to increased environmental awareness and consciousness throughout the world. For various engineering applications, natural fiber-reinforced polymer composites are being worked with. Various natural fibers such as jute, sisal, palm, coir, and banana are used as reinforcements. The reinforcement that is used in vinyl ester resin matrix is banana fiber. This work shows the study of treatment of sodium hydroxide (NaOH) in addition with alumina (Al_2O_3) particulate on fibers. The result that is inferred from the study is that the flexural strength value of UT, UT + Al_2O_3, T + Al_2O_3 has increased with increase in fiber content.

Keywords Scanning electron microscopy · UT—Untreated · T—Treated · Composite fabrication and Vinyl ester

J. Harish Kumar (✉) · S. Prabhakaran
Department of Mechanical Engineering, Academy of Maritime Education and Training, East Coast Road, Kanathur, Chennai, Tamil Nadu 600100, India
e-mail: harishkumarj20@gmail.com

K. Alagar Pandi
Department of Mechanical Engineering, Solamalai College of Engineering, Veerapanjan, Madurai, Tamil Nadu 625020, India

K. N. Karthick
Department of Mechanical Engineering, Bannari Amman Institute of Technology, Sathyamangalam, Erode, Tamil Nadu 638401, India

G. Kumaresan et al. (eds.), *Advances in Materials Research*, Springer Proceedings in Materials 5, https://doi.org/10.1007/978-981-15-8319-3_107

1 Introduction

Despite the growing familiarity with composite materials and ever-increasing range of applications, a clear definition is given by this term. Some of the natural composites like timber, organic materials like tissue surrounding the skeletal system, soil aggregates, minerals, and rock were described using some loose terms like "materials composed of two or more distinctly identifiable constituents". This lapse was made up as a fact that new types of composites were being innovated all that time with their own specific purposes like the filled, flake, particulate, and laminar composites**.** A good example for modern-day composite materials is fibers or particles that are embedded in a matrix of another material, which are mostly structural too.

When a strong load-carrying material (reinforcement) is imbedded in weaker material (matrix) it combines to form a composite. The strength and rigidity is provided by reinforcement which helps to support structural load. The matrix or binder (organic or inorganic) maintains the position and orientation of the reinforcement. The physical and chemical properties of the constituents of the composite are retained significantly. Composite materials in which different layers of materials give a specific character of a composite material having a specific function to perform are called as laminates. Fabrics have no matrix to fall back on, but in them, fibers of different compositions combine to give them a specific character. The materials that are reinforced can withstand maximum load and serve with the desirable properties.

1.1 Composite Materials

Composite materials were known to mankind in the Paleolithic age (also known as Old Stone age). The 300 ft high ziggurat or temple tower built in the city center of Babylon was made with clay mixed with finely chopped straw [1, 2].In recent years, polymeric based composite materials are being used in many applications, such as automotive, sporting goods, marine, electrical, industrial, construction, household appliances, etc. Polymeric composites have high strength and stiffness, light weight, and high corrosion resistance. In the past decade, extensive research work has been carried out on the natural fiber-reinforced composite materials in many applications. Natural fibers are available in abundance in nature and can be used to reinforce polymers to obtain light and strong materials.

Natural fibers from plants are beginning to find their way into commercial applications such as automotive industries, household applications, etc. A number of investigations have been conducted on several types of natural fibers such as kenaf, hemp, flax, bamboo, and jute to study the effect of these fibers on the mechanical properties of composite materials [3–6]. Mansur and Aziz [5] studied bamboo-mesh reinforced cement composites and found that this reinforcing material could enhance the ductility and toughness of the cement matrix, and increase significantly its tensile, flexural, and impact strengths. On the other hand, jute fabric-reinforced polyester

composites were tested for the evaluation of mechanical properties and compared with wood composite [6], and it was found that the jute fiber composite has better strengths than wood composites. A pulp fiber reinforced thermoplastic composite was investigated and found to have a combination of stiffness increased by a factor of 5.2 and strength increased by a factor of 2.3 relative to the virgin polymer [7].

Information on the usage of banana fibers in reinforcing polymers is limited in the literature. In dynamic mechanical analysis, Laly et al. [8] have investigated banana fiber reinforced polyester composites and found that the optimum content of banana fiber is 40%. Mechanical properties of banana–fiber–cement composites were investigated physically and mechanically by Corbiere-Nicollier et al. [8]. It was reported that Kraft pulped banana fiber composite has good flexural strength. In addition, short banana fiber reinforced polyester composite was studied by Pothan et al. [9]; the study concentrated on the effect of fiber length and fiber content. The maximum tensile strength was observed at 30 mm fiber length while maximum impact strength was observed at 40 mm fiber length. Incorporation of 40% untreated fibers Provides a 20% increase in the tensile strength and a 34% increase in impact strength tested with banana fiber and glass fiber with varying fiber length and fiber content as well. [10, 11]

1.2 Natural Fiber

1.2.1 Banana Fiber

By using Retting, Boiling, and Mechanical extraction methods banana fiber can be extracted from its leaves. A traditional biodegradation process that involves in microbial decomposition (breaking of the chemical bonds) of sisal leaves, which separates the fiber from the pith is called water retting. Then the fibers are thoroughly washed and processed further. This process takes 15–21 days for a single cycle of extraction. The process of water retting is a very slow, water-intensive process, unhygienic, and non-eco-friendly. Fibers that are extracted by this method are very poor in quality. Boiling is another extraction method, in which banana leaves are boiled and subsequent beating is done. Then washing is done and after which it is dried under sun to get the usable clean fiber. But for large-scale extraction this method is not suitable. Mechanical extraction involves inserting leaves into a machine "raspador machine "and pulling the raw material out. This process of mechanical extraction will not deteriorate the quality of the fiber and also suitable for small-scale operations. This process is efficient, versatile, cost-effective and eco-friendly. Residues that are produced during and after extraction of fiber are about 96% which is useful in generating biogas, composting, and isolation of a steroid, eco-genin, making of paper, biodegradable polymer, and wax (Figs. 1, 2 and 3).

Fig. 1 Mechanical process of sisal fibre extraction using raspador machine

Fig. 2 Thin strands of banana fiber

2 Materials and Methods

2.1 Chemical Treatment of Fibers

The untreated Banana fibers are shown in Fig. 4 were procured from YMC Marthandam in Tamil Nadu, India. The banana fibers that were procured are then treated with 10% of NaOH solution for 4 h of duration. After which the fibers were washed thoroughly using distilled water. Later the washed banana fibers were put in an oven for 24 h at an oven temperature of 80 °C in order to remove the traces of moisture in it.

Fig. 3 Thick strands of banana fiber

Fig. 4 Untreated banana fiber

2.2 Matrix

Vinyl ester resin is obtained from under the trade name of Ecmalon 9911. It appears as a clear yellow color liquid with viscosity of 400 cps and specific gravity of 1.05. The tensile strength and modulus of the cast resin are 70 MPa and 3200 MPa, respectively.

2.3 Composite Preparation

Hand lay-up technique was used to make the composite. Fig. 6 shows the mould that is prepared for making the composite. The mould is made up of mild steel with plywood sheet placed on the inner surface. A debonding agent is applied on the plywood sheet using which the composite specimen is casted in the mould. The dimensions of the inner cavity of the mould are 150 mm × 150 mm × 6 mm. The

upper plate is bolted to the mould prepared and this setup is left for curing at room temperature for 24 h. The composite plate so formed is then oven cured for 24 h at a temperature of 80 °C. After this, the specimens are cut for testing as per ASTM standards.

2.4 Materials

Reinforcing materials: Fiber materials used as the reinforcing material in the hybrid composite laminates were treated and untreated banana fibers of different dimensions in the form of non-woven mat. Matrix material: thermosetting resin such as Vinyl ester was used as matrix polymer. Polyester, catalyst-cobalt naphthenate, and accelerator—methane ethane ketone peroxide (GVR Traders, Satyan Polymers) were used as received.

2.5 Mould Preparation

The mould is prepared as per the ASTM standard D 5687. The size of the mould is 150 mm × 150 mm × 6 mm. The mould was prepared at Casmo Plastics, Madurai, Tamilnadu, India. The prepared mould is shown in Figs. 5, 6 and 7.

Fig. 5 Digital image of mould prepared in this investigation

Fig. 6 Fabrication process using banana fibre

Fig. 7 Fabrication process using banana fibre

2.6 Specimen Preparation

The mould has to be well cleaned and dried using releasing agent (wax) before the vinyl ester resin is filled up in the mould. On the mould, in order to lay up the first layer of vinyl ester mixture uniformly a special brush is used. The first layer of non-woven fiber mat was placed into the mould. Next to this, a layer of Vinyl ester was applied uniformly on the first layer of non-woven fiber mat.

Table 1 Designation of non-woven composite laminates used in this study

S. No	Designations
1	Vinyl ester resin
2	Fiber material—Banana fiber Different microns
3	Accelarato—Methyl ethene ketone Peroxide
4	Catalyst—Cobolt octate
5	Releasing agent—PVA
6	Particulate material—Al_2O_3

After which the second layer of non-woven fiber mat is then placed. These procedures are continuously followed to get the required composite laminates. Then the mould is closed and the composite laminates were rammed (Pressed) uniformly for 24 h to obtain the required thickness and after that curing process is done. Later the composite is allowed to get dried completely and then it is separated from the mould. The composite laminates are cut into specimen size as per ASTM standard for testing. The non-woven composite laminate's designations that are used in this study are tabulated in Table 1 (Figs. 8, 9, 10 and 11; Table 2).

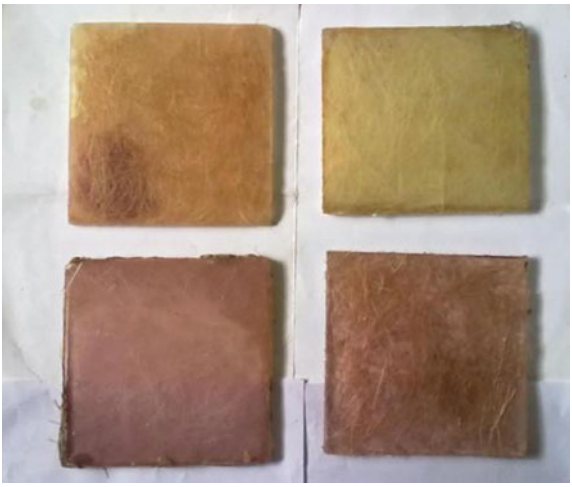

Fig. 8 Sample specimen of composite material

Fig. 9 Specimen before tensile test

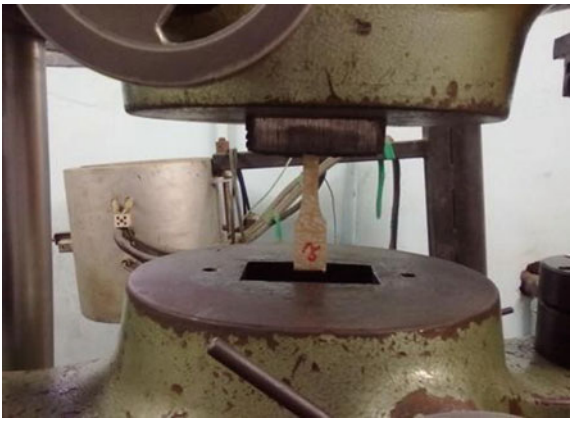

Fig. 10 Clamping of specimen in universal testing machine

3 Tensile Testing

3.1 Objective

The main objectives of this experiment are to determine the following properties:

Yield stress.

Proportional limit.

Ultimate stress.

Modulus of elasticity.

Fig. 11 Specimen after tensile test

Table 2 Various composite samples and its tensile strength

Samples	Tensile strength in Mpa
Sample 1	
UT	390
UT + Al_2O_3	330
T	380
T + Al_2O_3	470
Sample 2	
UT	340
UT + Al_2O_3	240
T	390
T + Al_2O_3	470
Sample 3	
UT	90
UT + Al_2O_3	240
T	300
T + Al_2O_3	360

3.2 Testing Procedure

Step 1 Identify the material to be tested for each specimen.
Step 2 Mark 2 inch of gauge length on each specimen using the jig provided.
Step 3 Specimen is prepared by ASTM Standard Torque Bone Size.
Step 4 Then the specimen is clamped in the machine using fixtures.
Step 5 Now tensile load is being applied over the specimen till the specimen breaks.

Step 6 Data of each specimen will be recorded and plot of the Stress-strain curve is generated using MatLab.

4 Result and Discussion

4.1 Mechanical Performance of Hybrid Composite

Tensile Strength n The results of tensile tests of UT, UT + Al_2O_3, T and T + Al_2O_3 cases and 1,2,3 samples are shown in Figs. 12a, b, 13a, b and 14a, b. As expected, surface modification of fibers using NaOH and Addition of Al_2O_3 resulted in a significant increase in tensile strength of the material. From the tables and figures we can easily find that the NaOH treatment and incorporation of Al_2O_3 provides a better improvement in the tensile strength of about 23.68, 20.51, and 20% for T + Al_2O_3 when compared with treated composites in all the cases. Variation of tensile strength Sample 1, 2, and 3 in single layer composite laminate, and Sample 1, 2, and 3 in two-layer composite laminate as shown in Figs. 12a, b, 13a, b and 14a, b.

5 Conclusion

The present work deals with fiber treatment and addition of Al_2O_3Mechanical properties of composites have been improved by Surface modification and addition of Al_2O_3. Therefore, that concluded the above results that NaOH treatment and addition of Al_2O_3 had provided better mechanical properties. The mechanical properties can even be increased more if this hybrid composite undergoes surface treatment of fibre.

Hybridization of Synthetic and Natural fibre polymer composites has been developed and characterized so as to arrive at a series of composites which can be used in many engineering and industrial areas such as marine, structural, consumer articles, and industrials applications. Hence it is to be concluded that with systematic and persistent research there will be a good scope and better future for Synthetic and Natural fibre—polymer hybrid composites in the coming years.

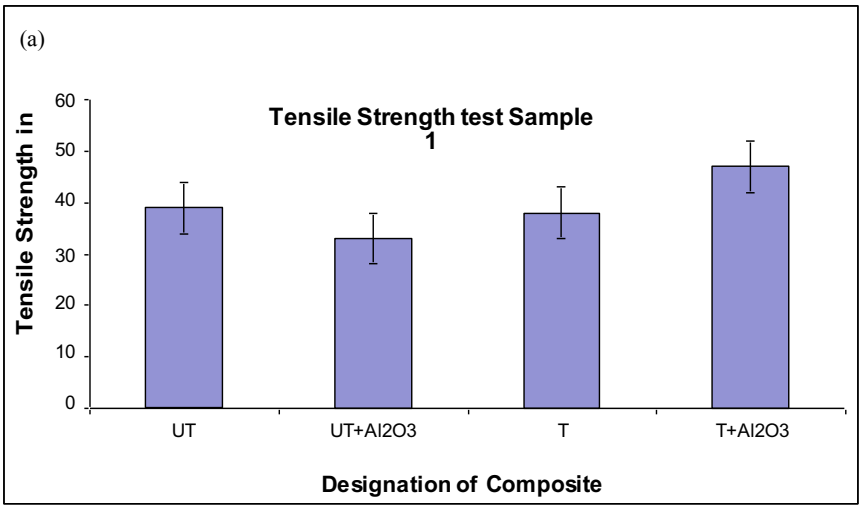

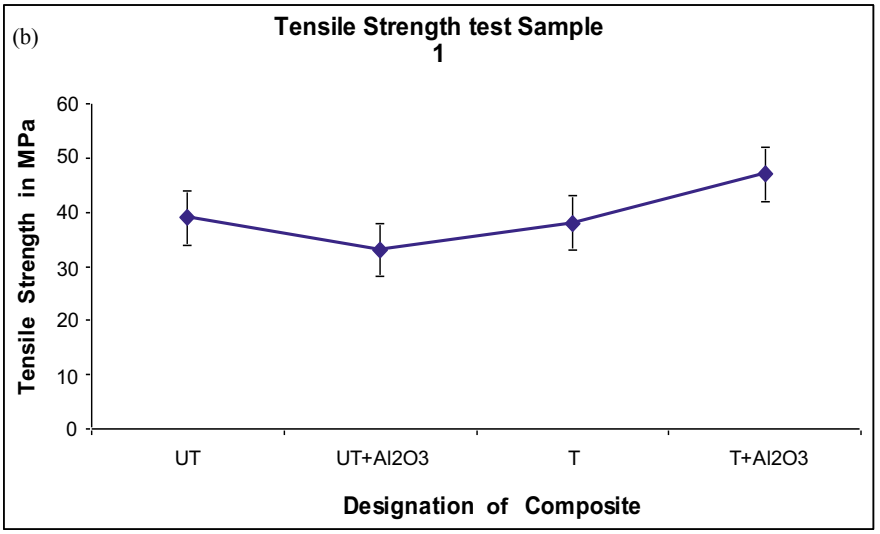

Fig. 12 **a**, **b** Tensile test result for Sample 1

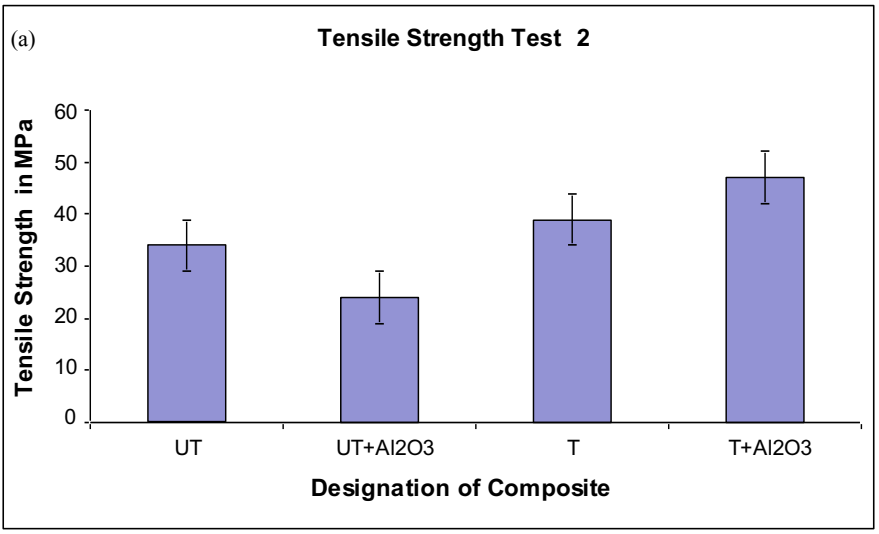

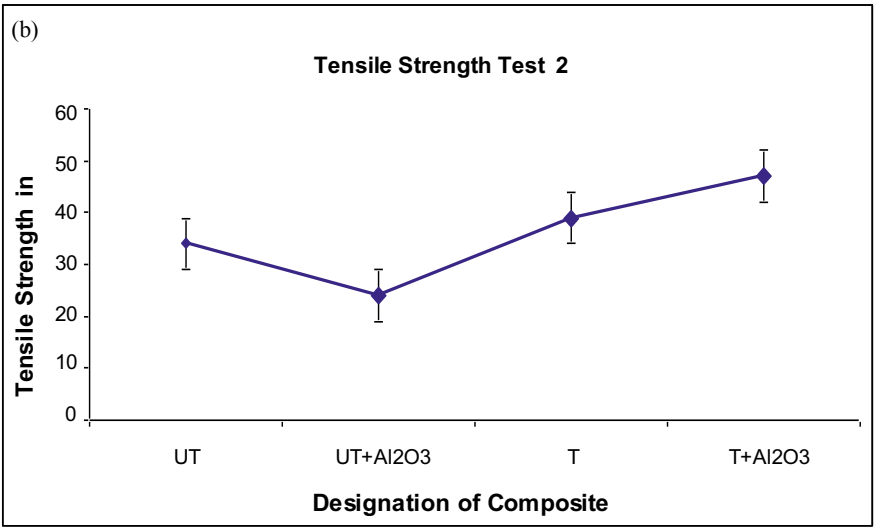

Fig. 13 **a**, **b** Tensile test result for Sample 2

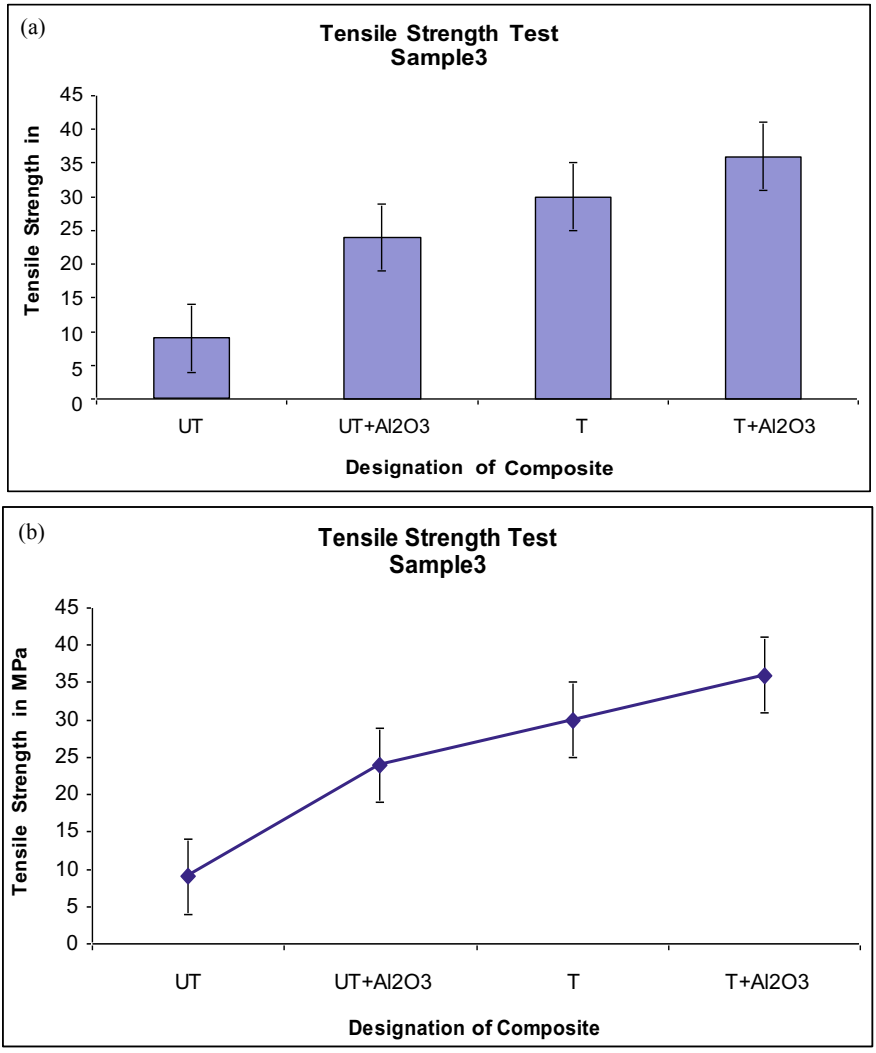

Fig. 14 **a**, **b** Tensile test result for Sample 3

References

1. Sreekumar PA, Albert P, Unnikrishnan G, Joseph K, Thomas S (2008) Mechanical and water sorption studies of ecofriendly banana fiber reinforced polyester composites fabricated by RTM. J App Poly Sci 109:1547–1555 (2008)
2. Belmares H, Barrera A, Monjaras M (1983) New composite materials from natural hard fibers. Part 2: fatigue studies and a novel fatigue degradation model. Ind Eng Chem Prod Res Dev 22:643–652
3. Maldas D, Kokta BV, Raj RG, Daneault C (1988) Polystyrene composites by chemical treatment. Polymer 29(7):1255–1265

4. Paul SA et al (2008) Effect of fiber loading and chemical treatments on thermophysical properties of banana fiber/polypropylene commingled composite materials. Compos Part A Appl Sci Manuf 39(9):1582–1588
5. Mansur MA, Aziz MA (1983) Study of bamboo—Mesh reinforced cement composite. Int J Cement Compos Lightweight Concrete 5(3):165–171
6. Gowda TM, Naidu ACB, Chhaya R (1999) Some mechanical properties of untreated jute fabric-reinforced polyester composites. J Compos Part A: Appl Sci Manuf 30(3):277–284
7. Mohanty S, Nayak SK, Verma SK, Tripathy SS (2004) Influence of fiber treatment on the performance of sisal-polypropylene composites. J Reinforced Plastic Compos 23:625
8. Laly Pothan A, Oommenb Z, Thomas S (2003) Dynamic mechanical analysis of banana fiber reinforced polyester composites. Compos Sci Technol 63(2):283–293
9. Pothan LA, Sabu T, Neelakantan (1997) Short banana fiber reinforced polyester composites: mechanical, failure and aging characteristics. J Reinforced Plastics Compos 16(8):744–765
10. Dhakal S, Keerthi Gowda BS (2017) An experimental study on mechanical properties of banana polyester composite. Mater Today: Proc 4(8):7592–7598
11. Jordan W, Chester P (2017) Improving the properties of banana fiber reinforced polymeric composites by treating the fibers. Proceedia Eng 200(2017):283–289

Wear Characterization of AlTiCrN and TiCN Coatings on SG Cast Iron

P. Sivasankar, S. K. Rajesh Kanna, N. Lingaraj, and P. Chandrasekar

Abstract This paper presents the methodology of reducing the wear rate of SG iron component by coating on the material and comparatively analysing the microstructure and wear behaviour of the coated and uncoated spheroidal graphite (SG) iron. The components like piston, valves and spring shackle are made of SG which has a wide range of application in field of automobile industry. These components are subjected to high wear due to their working condition, which affect the life of the product and its performance. The physical vapour deposition method is adapted to coat on the substrate material and the two coating materials are selected to be coated. The best material which resists the wear is to be selected among the coated samples. The pin-on-disc (POD) wear tester machine is used to test the wear behaviour of the uncoated and coated SG iron sample by varying the parameters like load, speed and time. The scanning electron microscope (SEM) images of the samples are taken, and the microstructural analysis and the wear behaviour of the worn surface material are found out.

Keywords Spheroidal graphite · Scanning electron microscope · Physical vapour deposition

1 Introduction

Ductile iron, which is widely called as ductile CI, nodular CI, spheroidal graphite iron, spheroidal graphite CI and SG iron. Ductile iron is composed of Fe as major constituent which has direct influence on its microstructural characterization. SG iron castings are used for wide variety of structural applications such as tractor parts, axial housings, carrier housings, trunnion housings and manifolds. SG iron provides

P. Sivasankar (✉) · S. K. Rajesh Kanna · N. Lingaraj
Mechanical Engineering Department, Rajalakshmi Institute of Technology, Kutthambakkam, Chennai 600124, India
e-mail: psivasankar89@gmail.com

P. Chandrasekar
Mechanical Engineering Department, Vellore Institute of Technology, Vellore 600124, India

G. Kumaresan et al. (eds.), *Advances in Materials Research*, Springer Proceedings in Materials 5, https://doi.org/10.1007/978-981-15-8319-3_108

high toughness and strength with better machinability and excellent product life. It provides ultimate surface characterizations among other CI [1]. The dry sliding wear test is used to characterize the surface property of a material by varying different process parameters like distance, speed and time. It is evident that the wear characteristics of the spheroidal graphite CI are similar to that of flake graphite CI. By means of adding TiC during re-solidification after laser surface treatment, it results in the improvement of surface properties like wear and hardness [2].

Recently, the samples made of SG CI are coated with steel electrodes by manual shielded metal arc welding. The results showed carbides deposition on the surface layers was minimum due to the surface characteristics of coated materials. It also gives as the clear results that wear resistance properties not only depends on the surface hardness properties of samples, but by also on factors such as microstructural layers, modulus of elasticity, size and the hard particles present on it [3–5].

In order to study the wear resistance of power transmission, reciprocating wear tests are conducted on components of commercial farm tractors, under lubricated and non-lubricated conditions [6–10]. In the past few decades, the test results have shown that all the tested coated samples by physical vapour deposition techniques showed better reduction in adhesive wear and volume loss, low friction rate and an abrasive type of wear [11–13]. Hence, it may be concluded that the modern PVD processes [14, 15] offer optimum conditions for the development, realization and industrial use of multicomponent and multilayer coatings. Hence, this paper concentrates on the methodology of reducing the wear rate of SG iron component by coating on the material and comparatively analysing the microstructure and wear behaviour of the coated and uncoated spheroidal graphite (SG) iron.

From the literature, it has been observed that many of the researchers had given an attempt to optimize the welding process parameters using different optimization techniques. But, none of the researchers has used the IWO algorithm to perform the optimization of the PAW process. In the present work, an attempt has been made to optimize the bead geometry of plasma arc welded Inconel 617 plates using two different techniques, namely GA and IWO.

2 Sample Preparation

In the present work, the SG iron casting is formed by melting the pig iron and other material constituents in an induction furnace. The casting is cut to required dimensions by wire cut EDM and 9 samples of pin material are prepared. In this work, the uncoated and the coated samples have to be tested for wear resistance.

The TiCN coatings are done on 3 samples of 3 μm coating thickness, and AlTiCrN coatings are done on 3 samples of 3 μm coating thickness. The microhardness of the coated samples is tested. The disc material is required according to specification of the wear tester machine. The wear test is conducted in POD wear tester machine varying the parameters like load, speed and sliding distance. The volume loss, wear rate,

Table 1 Chemical composition of SG cast iron

Chemical composition	C	Si	Mn	Mg	P	S	Cu	Ni	Fe
%	3.51	2.69	0.56	0.035	0.03	0.015	0.04	0.018	Balance

wear and friction coefficient are to be found out. The scanning electron microscope is used to form the surface images of the coated sample.

2.1 SG Iron 500/7 Grade

The SG iron 500/7 grade has been selected to analysis the wear characteristics (pin material). A typical chemical composition of this material is given in Table 1. Mechanical property: tensile strength—510 MPa, yield strength—320 MPa, % elongation—7%, hardness—228 HB, structure—ferrite and pearlite matrix. Cast iron 500-7 was cut by wire electric discharge machining process as per the given parameter of the pin. Length and diameter of the pin are 50 and 7 mm. The hardness of the pin material (cast iron 500-7) must be less than the disc material (EN 31) to find the wear resistance of cast iron 500-7. Hardness of the cast iron 500-7 is 32 HRC, and the hardness of EN31 is 62 HRC. The EN31 material is an high carbon alloy steel with superior quality which offers a high degree of hardness with high compressive strength and resistance over abrasion. The diameter of the disc is 55 mm, centre hole of the disc is 6 mm and the thickness of the disc is 10 mm.

2.2 Coating

Coatings produced by physical vapour deposition (PVD) in which the coating vapour flux is created by a physical process such as evaporation or sputtering from a solid target have been available since the technology necessary to sustain the required vacuum was developed. Although evaporated metal coatings have been used in some tribological applications, such as to lubricate threads on fasteners for the food industry, it has been the development of more advanced PVD processes enabling compound and ceramic coatings to be deposited with a high density which has revolutionized the PVD wear-resistant coatings market. The TiCN and AlTiCrN coatings are selected due to its tendency towards the wear characterization. These coatings were selected due to their superior functions such as less porosity towards molecular interaction of atoms, greater avoidance of coating delamination and minimum level of crank initiation and propagation. The above coatings are coated on the substrate of minimum 2–3 μm which will satisfy the above-mentioned conditions. The parameters for coating TiCN and AlTiCrN using PVD are given in Tables 2 and 3.

Table 2 Process parameter for coating TiCN

Parameter	Range
Coating thickness	2–3 μm
Service temp.	300 °C
Deposition temp.	425 °C
Hardness HV 0.05	2800
Deposition method	PVD arc
Friction versus steel, dry	0.15–0.3
Colour	Grey

Table 3 Process parameter for coating AlTiCrN

Parameter	Range
Coating thickness	3–8 μm
Service temp.	850 °C
Deposition temp.	450–550 °C
Hardness HV 0.05	3200
Deposition method	PVD arc
Friction versus steel, dry	0.55
Colour	Silver

3 Results and Discussion

3.1 Hardness Measurement

The coated samples will show characteristics changes on its surface due the deposition of TiCN and AlTiCrN on SG cast iron. Hence, microhardness testing is used to measure the depth or area of an indentation left by an diamond indenter of a specific shape, with a specific force of 0.981 N is applied for a specific time of 10 s (Fig. 1).

3.2 POD Wear Tester

A pod tribometer possess a stationary "pin" where applied load is in contact with a rotating disc. The pin can be of any shape to have a specific contact, but flat tipped pin are mostly used. Coefficient of friction is determined by the ratio of the frictional force to the loading force on the pin. The pod tester has proved its efficiency in providing a simple wear and friction test for low friction coatings such as DLC coatings on valves components in internal combustion engines. Pin of diameter 7 mm and length 50 mm, disc of 55 mm diameter and 10 mm thickness is used for POD wear testing.

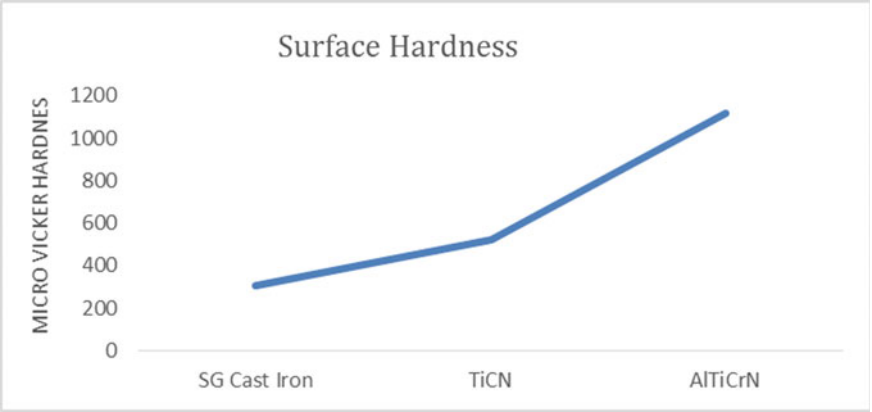

Fig. 1 Surface hardness of coated and uncoated sample

The operating parameters for POD tester is tabulated in Table 4. Wear rate for the uncoated and coated electrodes are shown in Fig. 2.

Table 4 Operating parameter for POD wear tester

Pin material	Operating parameters		
	Load (N)	Speed (rpm)	Time (min)
SG iron, TiCN coated, AlTiCrN coated	10	600	5
	15	600	5
	20	600	5

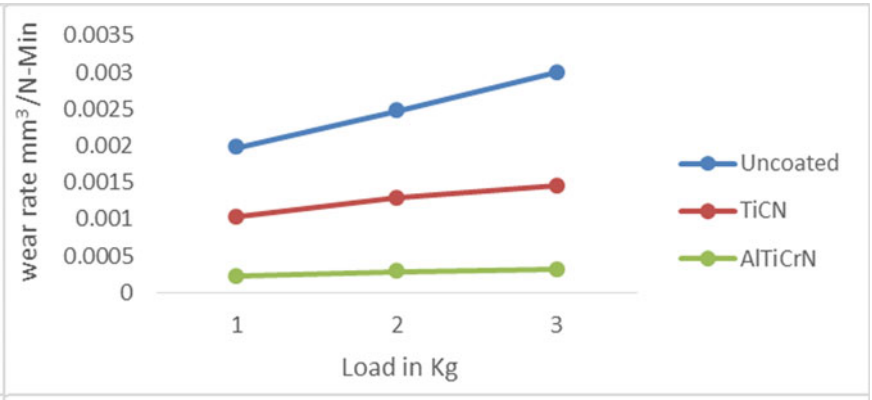

Fig. 2 Load versus wear rate for uncoated and coated samples

3.3 SEM Test

It shows clearly that the graphite nodules are present in the microstructure of SG cast iron as shown in Fig. 3a. Drastic erosion of material from the surface of SG cast iron is evident. Large number of cracks and pores are visible in the magnified image of the wearer cast iron surface as shown in Fig. 3b, c. The coating of TiCN and AlTiCrN over the substrate is shown in Fig. 3d, g. After wear, it is found that wear rate is more in the TiCN coated samples (Fig. 3e) as compared to the base material SG cast iron (Fig. 3e) and AlTiCrN coated samples (Fig. 3e) due to the adhesion property of the AlTiCrN coating on the SG cast iron. Presence of the chromium atom in the AlTiCrN coating enhances the wear characteristics is shown in Fig. 3i.

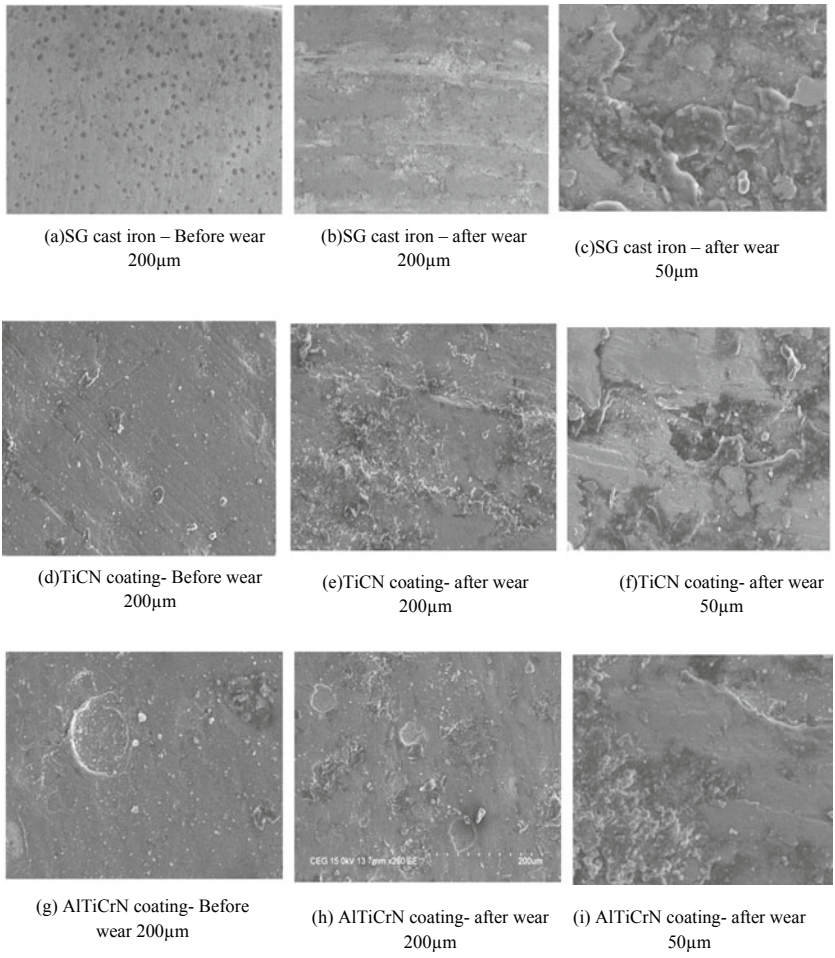

Fig. 3 SEM images of coated and uncoated samples

4 Conclusions

The experimental work was done by means of pin-on-disc wear tester machine to find the wear resistance, frictional force and frictional co-efficient of uncoated and coated SG cast iron samples and the results showed as follows,

1. For coated SG cast iron, it is found that hardness value has been increased as the result of which surface characteristics are improved.
2. It is evident that the adhesion of coating of 2–3 μm with the substrate is more as compared to uncoated samples, so that coating fractures and delaminates of coating substance can be reduced.
3. Volume loss of coated samples is lesser than the coated samples. Wear rate of the coated samples is lesser than the coated samples.
4. Frictional force and frictional co-efficient of uncoated samples were higher than that of the coated samples. This implies the influence of coating on the frictional behaviour of the sliding components.
5. The PVD coated samples showed improved surface hardness.
6. Among the coated samples, AlTiCrN coating showed better wear resistance than TiCN coatings. So, AlTiCrN coating is selected as the best coating material when compared with TiCN coating.
7. This experimental work tells as that even a very few micron level changes on the surface has direct influence on the wear behaviour of the material.
8. The acting wear mechanisms was investigated by means of metallographic observations of the worn surfaces, and subsurface damaged region were it results SG iron having more wear than coated samples.

References

1. Takeuchi E (2012) The mechanism of wear of spheroidal graphite cast iron in dry sliding. Wear, Elsevier Sequoia S.A
2. Mahmoud ERI, El-Labban HF (2014) Microstructure and wear behavior of TiC coating deposited on spheroidized graphite cast iron using laser surfacing. Eng Technol Appl Sci Res 4(5):696–701
3. Shamanian M, Mousavi Abarghouie SMR (2010) Effects of surface alloying on microstructure and wear behavior of ductile iron. Mater Des 31:2760–2766 (Elsevier)
4. Xiaoben Qi, Shigen Zhu (2013) Microstructure and wear behaviors of WC—12%Co coating deposited on ductile iron by electric contact surface strengthening. Appl Surf Sci 282:672– 679 (Elsevier)
5. Arabi Jeshvaghani R, Shamanian M (2011) Enhancement of wear resistance of ductile iron surface alloyed by stellite 6. Mater Des 32:2028–2033 (Elsevier)
6. Beltowksi M (2009) Wear of spheroidal graphite cast irons for tractor drive train components. Wear 267:1752–1756 (Elsevier)
7. Gadag SP, Srinivasan MN (1994) Dry sliding wear and friction: laser-treated ductile iron. Wear 173:21–29
8. Stanford MK (2001) Friction and wear characteristics of hard coatings. Wear 251:990–996 (Elsevier)

9. Santecchia E (2015) Wear resistance investigation of titanium nitride-based coatings. Ceram Int 41:10349–10379 (Elsevier)
10. Bienk EJ, Reitz H (1995) Wear and friction properties of hard PVD coatings. Surf Coat Technol 76–77, 475–480 (Elsevier)
11. Yang Q, Zhao L R (2008) Wear, erosion and corrosion resistance of CrTiAlN coating deposited by magnetron sputtering. Surf Coat Technol 202:3886–3892 (Elsevier)
12. Navinsek B, Panjan P (1999) PVD coatings as an environmentally clean alternative to electroplating and electroless processes. Surf Coat Technol 116–119, 476–487 (Elsevier)
13. V. Imbeni , C. Martini (2001) Tribological behaviour of multi-layered PVD nitride coatings. Wear 251:997–1002 (Elsevier)
14. Nicoletto G, Tucci A (1996) Sliding wear behavior of nitrided and nitrocarburized cast irons. Wear 197:38–44 (Elsevier)
15. Knotek FL (1993) Process and advantage of multicomponent and multilayer PVD coatings. Surf Coat Technol 59:14–20

Optimization of Process Parameters on the Electrical Discharge Machining of Al6061-SiC MMC Through Evolutionary Approach

S. K. Rajesh Kanna, N. Lingaraj, P. Sivasankar, and P. Chandrasekar

Abstract This research is a multi-objective optimization of major machining parameters EDM process during drilling of AL6061-SiC metal matrix composite. The major machining process parameters investigated in this research are supply current, flushing pressure and pulse on time along with SiC particles. AL6061 has been used as the matrix with 5, 10 and 15% of SiC of the sizes 15, 20, 25 and 30 μm. The experiments have been conducted, and the machining parameters have optimized through the evolutionary genetic algorithm to chalk up the best possible value for the tool wear rate, material removal rate and surface roughness. Fitness function had developed with multiple conflicting objectives to predict the better performance measures. By experimentation, it had been found that rate of material removal is proportionally increasing with increase of flushing pressure, supply current and pulse on time. Tool wear rate is also proportionally increasing with increase in the supply current and inversely proportional to the pulse on time. So genetic algorithm modules have been developed, and the output from the module is producing the better surface finish, higher rate of material removal with minimal tool wear.

Keywords Metal matrix composites · EDM · Al6061 · Optimization · Genetic algorithm · Invasive weed optimization

1 Introduction

Among the various unconventional machining process, electrical discharge machining (EDM) is the commonly adopted unconventional machining process to machine the complex intricate shapes on the conductive materials with high precision. In the EDM process, the current has been supplied to the electrodes and in turn sparks battered between the tool (electrode) and the conductive workpiece material, by means of this sparks, the materials have been removed from the workpiece [1–3].

S. K. Rajesh Kanna (✉) · N. Lingaraj · P. Sivasankar · P. Chandrasekar
Department of Mechanical Engineering, Rajalakshmi Institute of Technology, Kutthambakkam, Chennai, Tamilnadu 600124, India
e-mail: skrkanna@gmail.com

G. Kumaresan et al. (eds.), *Advances in Materials Research*, Springer Proceedings in Materials 5, https://doi.org/10.1007/978-981-15-8319-3_109

In the process of EDM, tool wear rate (TWR), material removal rate (MRR) and surface roughness (Ra) are mainly relied on the supply current, flushing pressure and pulse on time [4].

So in this research, the primary goal is to identify the best feasible and optimal parameters for obtaining the better surface finish, better surface roughness with minimal tool wear for the higher rate of material removal. For optimizing the parameters, in this research, genetic algorithm has been used.

The recent era of material science paved the way for many new combinations of materials. Among the various composite materials, aluminum-based metal matrix composites (MMC) are having a very extensive range of applications, as it is of less weight and high strength [5, 6]. For reinforcing and enhancing the better properties into the aluminum-based MMC, in recent years, many researchers [7–9] have experimented tremendous research and optimized various parameters. As the outcome of the previous researches, the major parameters which influence to improve the MRR, Ra and TWR are the supply current (I), flushing pressure (P), pulse on time (POT), pulse off time, intensity, etc. [8–10]. In this research, supply current along with the flushing pressure and pulse on time had been taken for the experimentation. In the current scenario, it is very essential to identify the optimal value for the machining parameters which can yield the best machining fulfillment [11]. Researchers are developing various mathematical instances for obtaining better MRR, TWR and Ra in machining the aluminum-based MMC [10–12]. The mathematical models used in optimization are either heuristic or can produce better solution for the single objective problems. Unfortunately, it might not be advisable to develop heuristic models for each and every problem, and at the same time the real-world problems might not necessarily to have an objective [13–19]. So the traditional mathematical models might not suitable for the real-time multi-objective problems. So genetic algorithm has been used, and many researchers proved that the genetic algorithm is producing better solution to the multi-objective optimization problems. John Holland introduced the methodology of evolutionary genetic algorithm (GA) in 1975 at the University of Michigan [16]. GA is identified as the powerful optimization tool for the NP-hard problems, because it uses random search procedure in coincidence with the natural selection procedures and can be applied to variety of complex non-deterministic polynomial problems for getting a feasible and optimal solution from the available possible solutions [19]. So GA has been implemented in this study for finding the optimal and feasible machining process parameters for the given conditions in the EDM.

2 Experimental Methodologies

In this experimentation method, the experiments were executed with five input machining process parameters, and with four different levels, each level having

Table 1 Input machining parameters for experimentation

Parameters	Notation	Unit	1	2	3	4
Current	I	Amps	4	8	12	16
Pulse on time	POT	μs	200	300	400	500
Voltage	V	Volts	30	30	30	30
Flushing Pr	Pr	MPa	0.0200	0.030	0.040	0.05
Particle size	Ps	μm	15	20	25	30

different combinations and as the total of 29 samples were studied. The incorporated levels and the factors considered for the optimization of the EDM parameters are given in Table 1.

2.1 Experimentation

In the present research, Inconel 617 superalloy plates of thickness 2 mm are used as the base material. Plasma arc welding in melt in mode is used to conduct bead-on-plate (BoP) experiments on the Inconel material. Initially, trial/pilot experiments are conducted to determine the range of the input parameters at full depth of penetration. The welding speed, welding current and plasma gas flow rate are considered as the input process parameters [12]. The working ranges of the input process parameters are given in Table 1.

Central composite design (CCD) is used to conduct the experiments. After experimentation, the plates are cross sectioned using wire-cut electric discharge machine to measure the bead dimensions [13]. The sectioned pieces are mounted with the help of specimen mounting machine, and then, proper etching is applied on the round specimen. The mounted specimens are used to measure the weld-bead dimensions.

The removal of the scrap materials was carried out by a flushing jet of dielectric fluid, i.e., kerosene pumped through the nozzle to the desired pressure. Al 6061-SiC of different composition and different sizes was taken as the workpiece material with 12 millimeter diameter copper electrode as the tool in the EDM. All other machining parameters of the EDM had been kept constant, and experimentation done only by varying parameters such as supply current, pulse on time, flushing pressure and particle size, twenty-seven experiments (L27) had been conducted on Al 6061-SiC composites. To avoid the human and the machine errors, two trials of machining had performed with the same setup to drill the 8 mm depth blind holes having the diameter of 12 mm. For each and every trial, the required parameters were measured before and after machining, and the parameters are machining time, electrode and workpiece weight. In reference to the recorded data, MRR and TWR were calculated using the Eqs. (1–2).

$$\mathrm{MRR} = \left(\mathrm{WP}_{\mathrm{wi}} - \mathrm{WP}_{\mathrm{wj}}\right)/T_k, \text{ (grams/mins)} \tag{1}$$

$$\mathrm{TWR} = \left(\mathrm{E_{wi}} - \mathrm{E_{wj}}\right)/\mathrm{T_k}, \text{ (grams/mins)} \quad (2)$$

whereas, $\mathrm{Ew_i}$ and $\mathrm{Ew_j}$ demote the weight of the electrode before and after machining,

$\mathrm{T_k}$ denotes the time taken to machine the workpiece.

The surface roughness value had been taken as the average of the roughness measured at two different points on the machined surface using Mitutoyo roughness measurement device. The obtained data for the different experimentation are given in Table 2.

Table 2 Experimental input and output

Trials	Current (A)	POT (μs)	Volt (V)	Pressure (Mpa)	Ps (μm)	MRR (g/Min)	TWR (g/min)	Ra (μm)
1	4	200	30	0.02	15	0.0315	0.0021	1.52
2	4	200	30	0.03	20	0.0321	0.0023	1.74
3	4	200	30	0.04	25	0.0329	0.0035	1.69
4	4	300	30	0.02	15	0.0318	0.0023	1.56
5	4	300	30	0.03	20	0.0336	0.0029	1.76
6	4	300	30	0.04	25	0.0344	0.0036	1.71
7	4	400	30	0.02	15	0.0329	0.0024	1.57
8	4	400	30	0.03	20	0.0356	0.0032	1.65
9	4	400	30	0.04	25	0.0365	0.0034	1.78
10	8	200	30	0.02	15	0.0342	0.0031	1.85
11	8	200	30	0.03	20	0.0378	0.0039	1.93
12	8	200	30	0.04	25	0.0396	0.0046	2.02
13	8	300	30	0.02	15	0.0384	0.0038	1.88
14	8	300	30	0.03	20	0.0413	0.0041	1.99
15	8	300	30	0.04	25	0.0408	0.0049	2.06
16	8	400	30	0.02	15	0.0396	0.0039	1.92
17	8	400	30	0.03	20	0.0426	0.0045	1.97
18	8	400	30	0.04	25	0.0426	0.0052	2.11
19	12	200	30	0.02	15	0.0411	0.0051	2.15
20	12	200	30	0.03	20	0.0457	0.0053	2.18
21	12	200	30	0.04	25	0.0481	0.0062	2.41
22	12	300	30	0.02	15	0.0457	0.0052	2.16
23	12	300	30	0.03	20	0.0478	0.0057	2.26
24	12	300	30	0.04	25	0.0496	0.0064	2.45
25	12	400	30	0.02	15	0.0489	0.0062	2.41
26	12	400	30	0.03	20	0.0492	0.0059	2.46
27	12	400	30	0.04	25	0.0498	0.0064	2.49

From the obtained set of input and output data, it is clear that there exist conflicting proportionality among the MRR, TWR and Ra. The obtained data are given as the input to the SPSS software as L27 array, and the obtained function for MRR, TWR and Ra is shown in Equations 3, 4 and 5, respectively.

$$\begin{aligned}\text{MRR} = 0.0624 &+ \left(5.04256\text{e}^{-560} \times \text{I}\right) + \left(4.5942\text{e}^{-003} \times \text{Pr}\right) \\ &+ \left(5.9882\text{e}^{-005} \times \text{Ps}\right) + \left(2.1123\text{e}^{-006} \times \text{POT}\right) \\ &- \left(1.9280\text{e}^{-006} \times \text{I} \times \text{Ps}\right) - \left(1.7541\text{e}^{-005} \times \text{Pr} \times \text{Ps}\right)\end{aligned} \tag{3}$$

From Eq. 3, it has been explored that the supply current has proportional effect on MRR, i.e., MRR increases with increase in I, POT, Pr and Ps and vice versa. From the TWR model, it is observed by experimentation that the current supplied for arc generation is inversely proportional to the EDM parameters, and the formulated equation is given as follows:

$$\begin{aligned}\text{TWR} = 9.0077\text{e}^{-004} &+ \left(3.0654\text{e}^{-004} \times \text{I}\right) + \left(5.9874\text{e}^{-004} \times \text{Pr}\right) \\ &+ \left(2.6854\text{e}^{-006} * \text{Ps}\right) + \left(5.3254\text{e}^{-007} \times \text{POT}\right) \\ &- \left(6.901\text{e}^{-007} \times \text{I} \times \text{Ps}\right) - \left(3.8931\text{e}^{-005} \times \text{Pr} \times \text{Ps}\right)\end{aligned} \tag{4}$$

The mathematical empirical equation generated for Ra is shown in Eq. 5, which implies that flushing pressure plays a major role in deciding the surface roughness. Higher the flushing pressure removes extra materials and on the other side, lesser the flushing pressure will lead to formation of deposition of removed materials on the surface. So it became essential to set the pressure within the limit based on the machining conditions.

$$\begin{aligned}\text{Ra} = 7.9902 &+ (1.5412 \times \text{I}) + (1.6215 \times \text{Pr}) + (2.3254 \times \text{Ps}) \\ &- \left(6.2351\text{e}^{-005} \times \text{POT}\right) - \left(3.8745\text{e}^{-004} \times \text{I} \times \text{Ps}\right) \\ &- (1.0268 \times \text{Pr} \times \text{Ps})\end{aligned} \tag{5}$$

So these three equations are having arbitrary proportionality, and these variations create the need for a combined mathematical model which can be able to identify the best optimal input machining parameters which produced better output. The mathematical model used in this research to optimize the input parameters is genetic algorithm model.

3 Genetic Algorithm Methodology

The GA is a random search technique that is useful for identifying the optimal solution in the larger number of samples with conflicting constraints and multi-objectives

in less time [17]. Effectiveness of the GA technique is influenced by several variables and mainly depends on its fitness function. Fitness function is the empirical mathematical function showing the correlation between process variable and the performance measures [18]. Genetic algorithm is having submodules like population generation, crossover, mutation and termination. In the population generation module, the population denotes the possible values for the parameters [19]. So the first stage is the construction of the population with the available parameters limits and the step size. Higher the step size, better the result and more the computational time [20]. Thus, the population have to be generated with the I, V, POT, Pr and Ps. The population size has been set to 100 with the step size of 0.5, 0, 50, 0.01, 5 for I, V, POT, Pr and Ps, respectively. In this research, voltage value has been kept at constant, as there is not a much variation in the output by varying the voltage value. The sample randomly generated GA chromosomes are as follows:

Parent 1 : 00110111111000011010111110001000110101110
Parent 2 : 01001001111001011000110001010101000010001
Parent 3 : 00000001111000000100101100111110110110011
Parent 4 : 01000001111011010110001101111110101001110

The first 4 digits denote the binary digits of the current value in the range of 4 to 12 units. The next three digits denote the decimal step up to 0.5. The next 5 digits are the constant of 11110 which denotes 30v. The next 9 and 6 digits denote the PoT value and its step increment. The next 2, 2, 5 and 3 digits denote pressure and particle size with its increments, respectively. The last 5 digits denote the dummy digits. Thus, each parent having 41 digits and similarly 100 parents will be generated for a generation. Once the population has been generated, and the next step is the crossover. Crossover is the second stage of genetic process of exchanging a random set of strings at random location between two random parents, and as the result, it generates two child chromosomes with the properties of their parents [1]. In this research, double crossovers have been performed, and in the double crossover, the child chromosomes obtained from the crossover of the two parents have been allowed to crossover with the third random parent, thereby the child having the property of the three parents. Thus, the population size has doubled. Also to increase the convergence rate, 80% of the parents only allowed to do crossover operation at random. The third stage of the GA is the mutation operation. To overcome the stagnation of the solution at a point, mutation operation has been performed by swapping the individual string from a random parent at random location with a random value. The mutation probability is set to 10 %. The next stage is the identification of the best-fit parent for producing the next-generation children with better properties. So the fitness function value or survival fitness of the every chromosome available in the population has to be calculated. The fitness function equation for calculating the fitness value is given in Equation 6.

$$f(x) = \frac{\alpha + \max.(\beta x MRR) + \text{Min.}(\delta x TWR) + \text{Min.}(\varepsilon x Ra)}{\sum(\text{Max.}MRR + \text{Min}\ TWR + \text{Min.}Ra)} \tag{6}$$

whereas, the α, β, δ and ε are the constants with the value of 0.5478, 0.5896, 0.9584 and 0.125, respectively, and vary with the applications. These values have to be identified by doing the sensitivity analysis with the formulated equations. Once the fitness function value for the populations had been calculated, then the half of the population have to be retained for the next iteration and the remaining worst population have to be discarded to avoid the worst results. The same methodologies of operations have to be repeated till any of the desired termination condition is achieved. In this research, the genetic generations terminated once 100 iterations were reached. Experimentations were carried out with higher and lower iterations, and it had been found that there were no much variations in the results.

4 Results and Discussion

The developed genetic algorithm model for optimizing I, POT, Pr, Ps to get the higher MRR, lesser TWR and better Ra has been successfully implemented, and the implementation had been done under two stages. In the first stage, the developed model had implemented to the single objective optimization functions, and in the second stage, it had implemented to the multi-objective optimization function. The genetic algorithm model proved that the effect of particle size, i.e., SiC size has significance effect in MRR, TWR and Ra compared with the other machining parameters. The single objective optimization model had tested with MRR, TWR and Ra independently, and the obtained experimental results are discussed in the following sections. By considering the material removal rate as the objective function, the genetic algorithm module produces the solution with the maximum current, higher pulse on time, higher flushing pressure and larger particle size will lead to higher material removal. The optimal values identified by the GA for I, POT, Pr and Ps are 16Amps, 500 μs, 0.05 MPa and 30 μm to produce the material removal rate of 0.05 g/min, and the value generated by the genetic algorithm is in par with the experimental values. From the GA model developed for the TWR to establish the lesser wear rate, the obtained values for the parameters for I, POT, Pr and Ps are 04Amps, 200 μs, 0.02 MPa and 15 μm to produce the tool wear rate of 0.0189 g/min. Lesser the current value, lesser the heat energy produced and the melting of the electrode can be avoided. Also lesser the POT value reduced the arc striking and thereby reduces the wear rate. GA models have also been applied to optimize the Ra, and the optimal machining parameter values for I, POT, Pr and Ps are 8 Amps, 300 μs, 0.04 MPa and 15 μm to produce the material removal rate of 1.25 μm. The machining parameters are having arbitrary effect over the surface roughness. In the second stage, the developed GA model has been applied to optimize the combined fitness function for the better machining. The output obtained for sample iteration with the error value of 0.2356 for 100 iterations is *"01111001111011001000000101010101111101111111"* The predicted optimum machining parameters values by decoding the genetic output and the experimental values are given in Table 3.

Table 3 Predicted optimum machining parameters values and the experimental values

	Current (A)	POT (μs)	Pressure (Mpa)	Ps (μm)	MRR (g/Min)	TWR(g/min)	Ra (μm)
Set limit	4–16	Max.500	0.02–0.05	15–30	–	–	–
GA model value	6	400	0.025	15	0.0357	0.0054	1.95
Experimental value	6	400	0.025	15	0.0415	0.0065	2.45

5 Conclusions

In this research, Al-SiC metal matrix composites were selected as the workpiece to optimize the EDM parameters to achieve the better material removal rate, lesser tool wear rate and perfect surface roughness. Different sized SiC particles have been used with 12 mm diameter copper electrode to drill the blend hole on the plate. Using the sample experimental data, the developed genetic algorithm model identified the best suitable optimal value for the supply current, pulse on time, flushing pressure and the SiC size to get higher MRR, lesser TWR and better Ra on the machined surface. The supply current is found to be the most significant parameter, and the developed module can be implemented to all the types of EDM machining process optimization with minor modifications.

Some of the observations made during the research are as follows. MRR increases with increase in the current, as higher current leads to higher temperature and results in excess material removal. MRR is less for the larger SiC. For most of the particle sizes, the effect of flushing pressure remains more or less same. Increase in the flushing pressure will also proportionally increase the MRR. TWR also increases with the increase in the supply current and slightly increases with the size of the particle. For larger particle size and with higher flushing pressure, TWR is maximum. The particle size and the flushing pressure mainly affect Ra. Beyond certain allowable limit of Ps and Pr, the Ra value increases. The result produced by the genetic algorithm module is mapping with the experimental data within the allowable limits. So the genetic algorithm module can be used to optimize the machining parameters.

References

1. Luis CJ, Puertas I, Villa G (2005) Material removal rate and electrode wear study on the EDM of silicon carbide. J Mater Process Technol 164:889–896
2. Puertas I, Luis CJ (2012) Optimization of EDM conditions in the manufacturing process of B4C and WC-Co conductive ceramics. Int J Adv Manuf Technol 59:575–582
3. Khan AA (2008) Electrode wear and material removal rate during EDM of aluminum and mild steel using copper and brass electrodes. Int J Adv Manuf Technol 39(5–6):482–487
4. Tamiloli N, Venkatesan J, Murali G, Kodali SP, Sampath Kumar T, Arunkumar MP (2019) Optimization of end milling on Al–SiC-fly ash metal matrix composite using Topsis and fuzzy

logic. SN Appl Sci 1(1):204
5. Singh S, Maheshwari S, Pandey PC (2004) Some investigations into the electric discharge machining of hardened tool steel using different electrode materials. J Mater Process Technol 149(1):272–277
6. Rozenek M, Kozak J, Dabrowski L, Łubkowski K (2001) Electrical discharge machining characteristics of metal matrix composites. J Mater Process Technol 109(3):367–370
7. Dhar S, Purohit R, Saini N, Sharma A, Kumar GH (2007) Mathematical modeling of electric discharge machining of cast Al–4Cu–6Si alloy–10wt % SiCP composites. J Mater Process Technol 194(1):24–29
8. Mandal D, Pal SK, Saha P (2007) Modeling of electrical discharge machining process using back propagation neural network and multi-objective optimization using non-dominating sorting genetic algorithm-II. J Mater Process Technol 186(1):154–162
9. Dvivedi A, Kumar P, Singh I (2008) Experimental investigation and optimisation in EDM of Al 6063 SiCp metal matrix composite. Int J Mach Mach Mater 3(3):293–308
10. Habib SS (2009) Study of the parameters in electrical discharge machining through response surface methodology approach. Appl Math Model 33(12):4397–4407
11. Müller F, Monaghan J (2000) Non-conventional machining of particle reinforced metal matrix composite. Int J Mach Tools Manuf 40(9):1351–1366
12. Bai X, Zhang QH, Yang TY, Zhang JH (2013) Research on material removal rate of powder mixed near dry electrical discharge machining. Int J Adv Manuf Technol 68(5–8):1757–1766
13. Rajesh Kanna SK, Kumar D (2011) Overloading Orientation Constraint over Genetic Mutation for Solving 3D Heterogeneous Bin Packing Problem. European J Sci Res 66(3):366–376
14. Rajesh Kanna SK, Malliga P (2012) Multi-Constrained Optimization of Rectangular Bin Packing Problem using Binary Coded Evolutionary Algorithm. Int J Mater Manuf Opt 3(1):27–35
15. Rajesh Kanna SK, Malliga P, Sarukesi K (2012) A 3D-Multi constrained arbitrary sized heterogeneous box packing optimization using hybrid genetic approach. J Adv Mater Res 479–481:1825–1830
16. Kanna SK, Jaisree AD, Balasundaram K, Kumar SB (2015) Optimization of 3D constrained rectangular bin packing problem using recursive ant colony algorithm. IOSR J Mech Civil Eng 12(4):65–70
17. Rajesh Kanna SK, Udaiyakumar KC (2017) A Complete framework for multi-constrained 3d bin packing optimization using Firefly algorithm. Int J Pure Appl Math 114(6):267–282
18. Kanna SK, Udaiyakumar KC, Kumar SD, Lingaraj N (2018) 3D heterogeneous bin packing framework for multi constrained problems using hybrid genetic approach. IOP Conf Series Mater Sci Eng 402:1–9
19. Jaisree AD, Umagowri R, Rajesh Kanna SK (2016) Evolutionary approach for optimizing 3D heterogeneous bin packing problems. Int J Trend Res Dev 3(1):447–452

Numerical Investigation on Aluminum Alloys Under Medium Velocity Impact of Projectiles

N. Nandhini, M. Vijayan, and M. A. Rajesh Kumar

Abstract Aluminum alloys are widely used for aircraft structures in larger ratios, where lightweight is the most desired property. Aluminum alloys Al2024 and Al7075 are tested for its ballistic resistance by numerical simulation using the software ANSYS. Here the Al alloy sheets of two different thicknesses 10 and 8 mm are hit with a projectile, and the energy absorbed by the plate is found. The projectile is hit perpendicular to the target, and the ballistic resistance is studied. The material behavior of the target was predicted for different parameters. The numerical results were compared for two varying thicknesses for the incident velocities were taken as 1500 m/s. Based on the numerical analysis using ANSYS, the velocity, acceleration, kinetic energy, ballistic resistance and energy absorbed for the plates of two different thickness are studied.

Keywords Ballistic resistance · ANSYS · Velocity impact · Kinetic energy

1 Introduction

The important features considered for airframes and engines are fatigue sensitive, lightweight, with more stiffness and damage tolerance. During the twenty-first century, the composites and alloys were preferred for lightweight which proved to be

N. Nandhini (✉)
Assistant Professor, Department of Mechanical Engineering, Bannari Amman Institute of Technology, Erode 638401, India
e-mail: nandhinin@bitsathy.ac.in

M. Vijayan
Research Scholar, Department of Mechanical Engineering, Coimbatore Institute of Technology, Coimbatore 641014, India
e-mail: aerovijay97@gmail.com

M. A. Rajesh Kumar
Placement Officer, Rathnavel Subramaniam College of Arts and Science, Coimbatore 641402, India
e-mail: mark4mech@gmail.com

G. Kumaresan et al. (eds.), *Advances in Materials Research*, Springer Proceedings in Materials 5, https://doi.org/10.1007/978-981-15-8319-3_110

Table 1 Properties of the Al2024 and Al7075 plates and Steel 1006 projectile [10]

Properties required for analysis	Density (kg/m3)	Shear modulus (MPa)	Maximum yield stress (MPa)	Initial yield stress (MPa)	Specific heat (J/kg/K)
Al2024 T4	2785	28,600	760	260	863
Al7075 T6	2804	26,700	810	420	848
Steel 1006 projectile	7896	81,800	–	350	452

more economical and led to an increase in engine performance. The state–of-the-art, new materials with desired properties are being developed in aerospace applications [1]. The new materials with high strength to weight ratios having properties such as lightweight with high strength, resistance to corrosion and creep are needed the most. The parameters considered include cost without any compromise in quality [2].

Few materials that comply with the requirements like aluminum, titanium, magnesium and their alloys are used. In this paper, a numerical investigation on Al based alloy is presented that is widely used in manufacturing aircraft components [3]. The characteristics of metallic components for aircraft seats are discussed. It has been found that the aluminum alloys are the major contributors for aircraft components. The aluminum alloys (2xxx, 6xxx, 7xxx and 8xxx) are found to be the prominent ones. Among these, the 8xxx series is widely used due to its low density [4–6].

Ballistic limit is the velocity at which the projectile penetrates a plate. The ballistic limit varies with varying thickness. The velocity of the projectile is considered medium to analyze the impact. The energy absorbed by the plate shows the ballistic limit of the plate depending on the initial velocity of impact and the varying thickness [7, 8]. Two different materials of more significance in aircraft applications were considered for analysis. A steel 1006 projectile of blunt face acts as the projectile that hits the plate with medium velocity to analyze the penetration behavior [9] (Table 1).

2 Numerical Modeling of Plate and Projectile

Software ANSYS/AUTODYN V18, a commercial hydrocode is used for modeling and analysis of the plate and the projectile. Steel projectile is modeled by Lagrangian process. Aluminum plate is taken as flexible material and projectile to be a rigid one for proper and perfect perforation. Frictionless contact is maintained between the plate and projectile for which the interaction gap is fixed as 1 mm. The plate is modeled to be symmetrical about both the perpendicular axes [11].

Numerical modeling is done to study the impact characteristics of both the materials. The dimensions of the aluminum plate chosen are $150 \times 150 \times 10$ mm. Al2024 T4, Al7075 T6 and the steel 1006 projectile of length 10 mm and radius 12.6 mm

are modeled by Lagrangian process [12]. Aluminum plate is considered as a flexible material and projectile as a rigid one for proper and perfect perforation. The projectile is initially positioned in a way such that there is a frictionless contact maintained between the plate and projectile. The initial interaction gap between plate and projectile is fixed as 1 mm. The plate is modeled to be symmetrical about both the perpendicular axes.

2.1 Simulation of Impact by Steel Projectile at Different Thickness of Al2024

The modeled plate and the projectile are meshed to incorporate the desired material properties into the model. The Al2024 T4 plate is meshed to be a coarse one, and the projectile has a fine mesh. The edges of the plate are fixed to resist deformation during perforation. The initial velocity of the projectile is set to be 1500 m/s, and the total time taken for the impact is calculated for the above conditions. The end time is set as 0.0001 s for a thickness of 10 mm [13].

2.2 Simulation of Impact by Steel Projectile at Different Thickness of Al7075

The Al7075 T6 plate is meshed with similar conditions. The plate is fixed in the edges. The initial velocity is 1500 m/s for the same thickness of 10 mm. The perforation is observed for the two different materials for the same thickness.

2.3 Mesh Statistics for the Different Geometry

Table 2 shows the number of nodes and elements of the Al2024 and Al7075 plates and the steel projectile for analysis. The elements of the geometries are meshed for coarse mesh in case of plates and fine mesh for projectile (Fig. 1).

Table 2 Mesh statistics for the different geometry considered for analysis

Geometry	Node	Element	Mesh size
Al2024 T4 plate (8 mm)	2304	1587	coarse
Al7075 T6 plate(10 mm)	2880	2116	coarse
Steel 1006 projectile	6475	5520	Fine

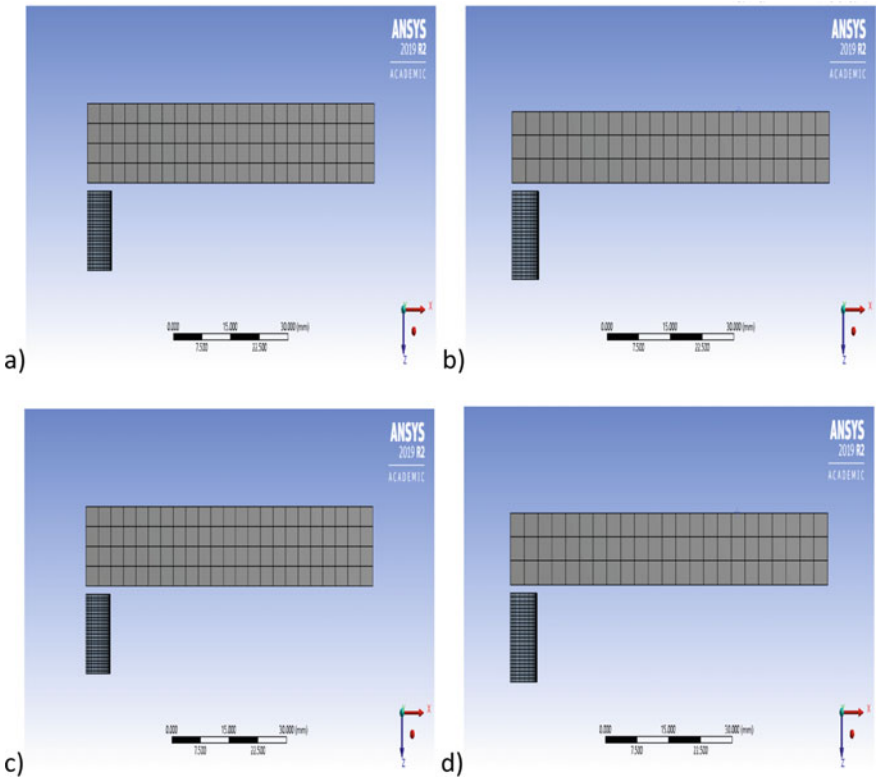

Fig. 1 Mesh diagram of **a** Al2024 T4 plate 10 mm thick and steel projectile **b** Al2024 T4 plate 8 mm thick and steel projectile **c** Al7075 T6 plate 10 mm thick and steel projectile and **d** Al7075 T6 plate 8 mm thick and steel projectile

3 Results and Discussions of the Problem

The tests were performed to investigate the perforation of the plates. Notch formation in the plate can be seen clearly as shown in Fig. 2, and it matches well with the results shown in literature. The difference in the time at which the notch formation occurs may be due to the different thickness of the plates. The delay in notch formation may be owed to the increased thickness which also indicates an increased ballistic resistance.

The structural failure occurring due to the fracture due to which crack may occur propagates resulting in failure. It shows the importance of learning the deformation, i.e., the formation of notch and the damage mechanism which needs to be avoided for better results.

Figure 3 shows the trend with which the velocity of projectile varies with time. The initial velocity with which the projectile moves is taken to be 1500 m/s. The projectile touches the plate after a while. The notch is formed around the time when

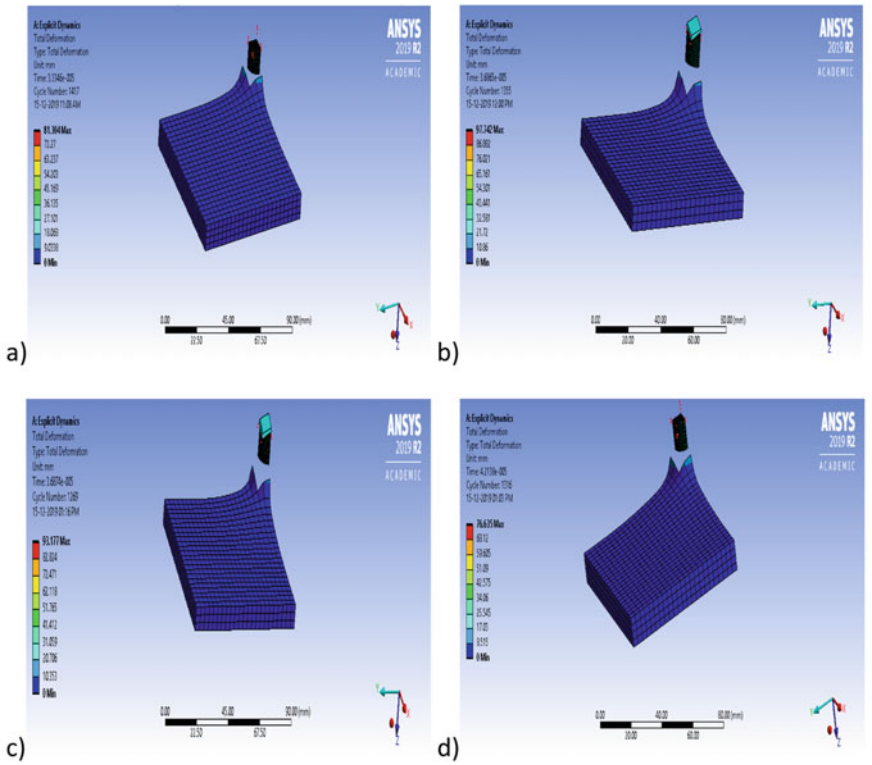

Fig. 2 Notch formation images of **a** Al2024 T4 plate 10 mm thick and steel projectile **b** Al2024 T4 plate 8 mm thick and steel projectile **c** Al7075 T6 plate 10 mm thick and steel projectile and **d** Al7075 T6 plate 8 mm thick and steel projectile

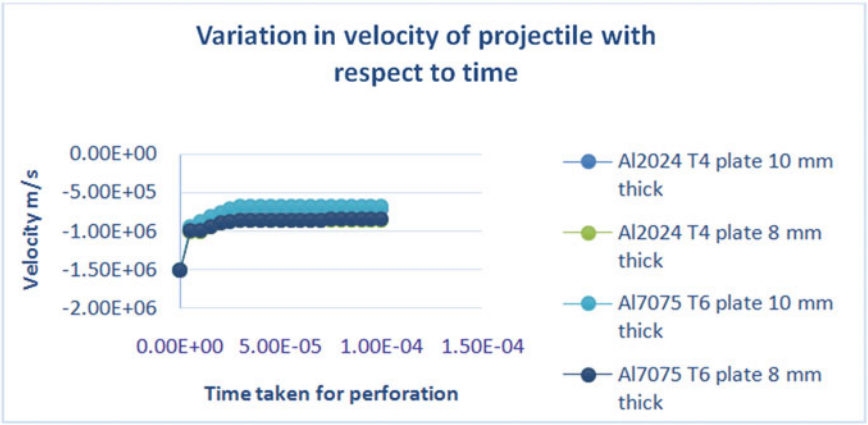

Fig. 3 Graph showing the variation in velocity of the projectile with respect to time

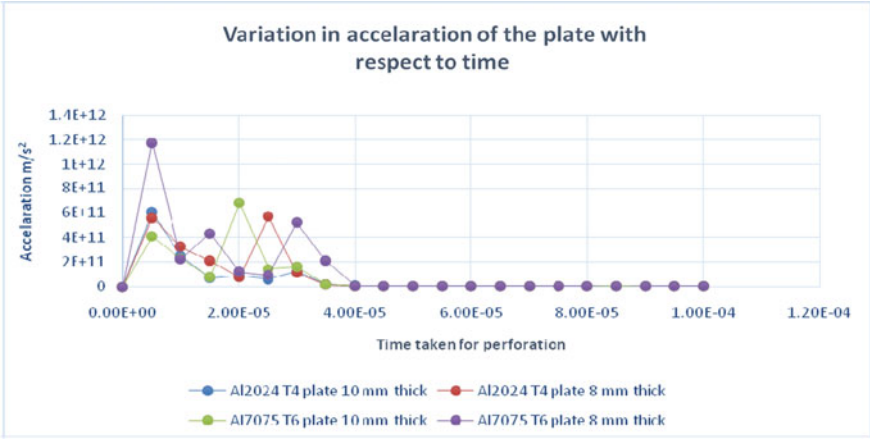

Fig. 4 Graph showing the variation in acceleration of the plate with respect to time

the graph shows nonlinear variation showing lowering of velocity. The projectile once passed through the plate moves with increased velocity, and later it travels with a constant velocity. The lowest value of velocity can be seen when the projectile passes through Al7075 T6 plate of 8 mm thickness that is due to higher resistance for penetration.

Acceleration varies in a nonlinear fashion during and after perforation which could be observed apparently from Fig. 4. Al7075 T6 plate of 8 mm thickness has the highest acceleration after penetration showing the higher resistance offered by the plate against impact. The acceleration produced in the plate is of nominal range that may lead to delamination. When a higher acceleration is created as seen in Al7075 T6 plate of 8 mm thickness, it may lead to increased vibration in the plate because of the increased resistance offered (Fig. 5).

The residual kinetic energy was calculated from the initial impact velocity and residual velocity after the penetration by the projectile. A good mesh convergence gives appropriate results which could be used to analyze the plate for variations in kinetic energy for different thickness [14]. The 8 mm plate in both the material has the higher kinetic energy value compared to other thickness. Changes in the thicknesses influence the amount of kinetic energy absorbed. Energy absorption in the target plates is largely independent of the projectile nose geometry reported by [9, 15] (Fig. 6).

The mass of the projectile and its diameter have a significant effect in the energy variation trend of the projectile. The fixed mass and diameter of the projectile explain the ballistic resistance of the plate for varying thickness and material. Ballistic analysis of the plate that shows complete perforation is studied to understand the ballistic limit and proportional energy absorption by ANSYS.

The aircraft is designed in a such a way that it has to resist damage under impact loading since it occurs in an unplanned way like hail, foreign object, bird strike, etc.

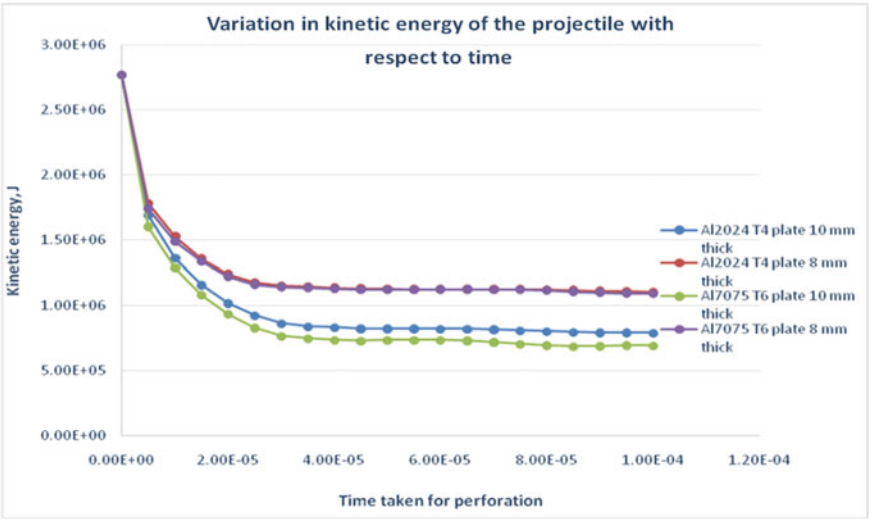

Fig.5 Graph showing the variation in kinetic energy of the projectile with respect to time

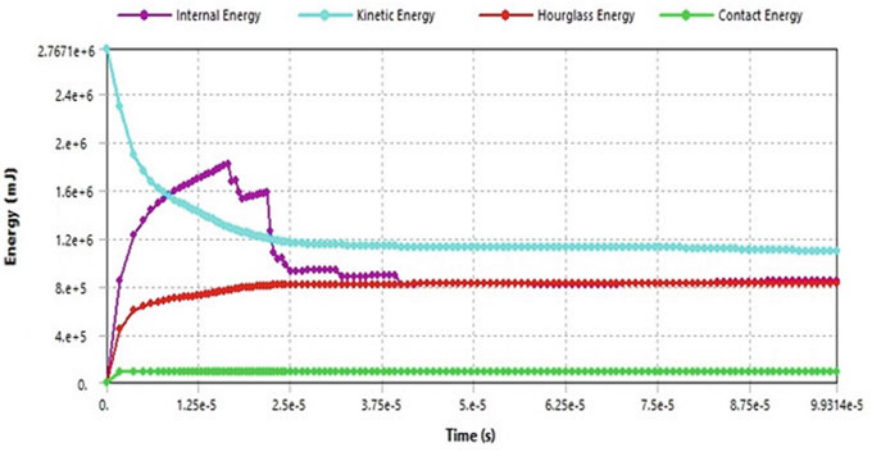

Fig. 6 Graph showing the energy summary of the projectile with respect to time

4 Conclusion

The behavior of the Al plates after being penetrated by a blunt projectile is investigated using ANSYS/AUTODYN V18, a commercial hydrocode. A simple yet a model with required details is presented and analyzed to study the progress of penetration. Variation of velocity, acceleration and kinetic energy has been studied with varying thickness of plate for the same size of projectile and impact velocity.

The test results give the interconnection between velocity, acceleration and kinetic energy with respect to the two different thicknesses considered for the different materials considered for analysis. As per the results from the analyses, it shall be concluded that the damage in the plate is lesser due to the impact of the projectile when the thickness is more for the same material. Since the body is constrained on all edges, the ease of penetration is lesser.

From the numerical analysis, we can conclude that the results obtained for impact velocity of projectile, acceleration of the Al plates, energy absorbed by the plates comply with the results from the literatures referred. Medium velocity impact behavior of the plates with parametric variations was analyzed to get different results which could be useful for future study.

This investigation on medium velocity impact projectiles is considered for the projectiles like runway debris that hit the aircraft base while taking off or landing because of the speed with which it travels [16].

References

1. Senthil K, Arindam B, Iqbal MA, Gupta NK (2017) Ballistic response of 2024 Aluminium plates against blunt nose projectiles. Procedia Eng. https://doi.org/10.1016/j.proeng.2016.12.030
2. Woodward RL, Cimpoeru SJ (1998) A study of the perforation of aluminium laminate targets. Int J Impact Eng. https://doi.org/10.1016/S0734-743X(97)00034-1
3. Senthil K, Iqbal MA, Bhargava P, Gupta NK (2017) Experimental and Numerical Studies on Mild Steel Plates against 7.62 API Projectiles. Procedia Eng. https://doi.org/https://doi.org/10.1016/j.proeng.2016.12.032
4. Jawalkar CS, Kant S (2015) A Review on use of Aluminium Alloys in Aircraft Components. i-manager's J Mater Sci 3:33–38
5. Dursun T, Soutis C (2014) Recent developments in advanced aircraft aluminium alloys. Mater Des. https://doi.org/10.1016/j.matdes.2013.12.002
6. Heinz A, Haszler A, Keidel C, Moldenhauer S, Benedictus R, Miller WS (2000) Recent development in aluminium alloys for aerospace applications. Mater Sci Eng a. https://doi.org/10.1016/S0921-5093(99)00674-7
7. Ansari MM, Chakrabarti A (2016) Impact behavior of FRP composite plate under low to hyper velocity impact. Compos Part B Eng. https://doi.org/10.1016/j.compositesb.2016.04.021
8. Radin J, Goldsmith W (1988) Normal projectile penetration and perforation of layered targets. Int J Impact Eng. https://doi.org/10.1016/0734-743X(88)90028-0
9. Gellert EP, Cimpoeru SJ, Woodward RL (2000) Study of the effect of target thickness on the ballistic perforation of glass-fibre-reinforced plastic composites. Int J Impact Eng 24:445–456
10. ASM Aerospace Specifications Metals Inc.
11. Bhuarya MK, Rajput MS, Gupta A (2017) Finite element simulation of impact on metal plate. Procedia Eng. https://doi.org/10.1016/j.proeng.2016.12.009
12. Børvik T, Clausen AH, Hopperstad OS, Langseth M (2004) Perforation of AA5083-H116 aluminium plates with conical-nose steel projectiles—experimental study. Int J Impact Eng 30:367–384
13. Seidt JD, Michael Pereira J, Gilat A, Revilock DM, Nandwana K (2013) Ballistic impact of anisotropic 2024 aluminum sheet and plate. Int J Impact Eng 62:27–34

14. Backman ME, Goldsmith W (1978) The mechanics of penetration of projectiles into targets. Int J Eng Sci. https://doi.org/10.1016/0020-7225(78)90002-2
15. Senthil K, Iqbal MA (2013) Effect of projectile diameter on ballistic resistance and failure mechanism of single and layered aluminum plates. Theor Appl Fract Mech 67–68:53–64
16. Safri S, Sultan M, Yidris N, Mustapha F (2014) Low velocity and high velocity impact test on composite materials–a review. Int J Eng Sci 50–60

Priority-Based Task Allocation and Scheduling in WSN Using DMPS

M. Suguna, D. Prakash, G. Shobana, and J. Cynthia

Abstract The network outturn can modify once the network size has changed, and the right to scale property will be granted. In dense wireless networks, it gives substantive performance. Dynamic multilevel priority (DMP)—except for those present at the last level in the zone-based topology of wireless networks, the proposed system schedules tasks have more than two levels of priority queues. The highest priority queues are placed by real-time task and can forestall data packets in other queues. Based on the threshold value, the non-real-time task is estimating the processing time hierarchy leaf nodes have two separate queues, one for real-time purposes and one for non-real-time tasks. This process evaluates the performance of the proposed scheduling of DMP tasks which performs much better than traditional schemes by averaging the waiting time for data processing and the delay in delivering the output.

Keywords Capacity of network · Partition · Task scheduling · Dynamic multilevel priority · Localized scheduling algorithm · CSMA algorithm

1 Introduction

A wireless network is any form of electronic network that uses wireless information connections for connecting network nodes. Task scheduling in the TCP connection is established when a packet is arrived, and it automates the insertion of packets to the MAC layer [1, 2]. Scheduling system must decide at any time on which it links to transmit the packet. The goal is to reduce short files and high latencies waiting time. DMP task—the scheduling nodes are virtually arranged in a hierarchical way

M. Suguna (✉) · G. Shobana · J. Cynthia
Computer Science and Engineering Department, Kumaraguru College of Technology, Coimbatore, Tamilnadu 641049, India
e-mail: suguna.m.cse@kct.ac.in

D. Prakash
Electrical and Electronics Engineering Department, Vel Tech Multi Tech Dr.RR and Dr.SR Engineering College, Chennai, Tamilnadu, India
e-mail: pp_d@rediffmail.com

G. Kumaresan et al. (eds.), *Advances in Materials Research*, Springer Proceedings in Materials 5, https://doi.org/10.1007/978-981-15-8319-3_111

[3]. There are three types as follows (i) real-time data packets (priority 1), (ii) non-real-time remote data packets received from lower-level nodes (priority 2) and (iii) non-real-time local data packets sensed from the node itself (priority 3).

2 Literature Work

The traditional view of wireless networks as connected graphs over which end-to-end paths have to be established is carried over from conventional computer communication networks [4]. The concept could not be applicable to some previous and emerging wireless networks, where there may be no contemporaneous end-to-end paths between the source and destination pairs for a variety of reasons, including node mobility, wireless propagation phenomena, malicious attacks and power limitations [5]. To provide communication services in such highly challenging wireless networks, delay/disruption tolerant networks (DTNs) are proposed which exploit the opportunistic connectivity and node mobility to relay and carry messages around the network. Suppose, when the next hop is not immediately available for the current node to deliver a message, some relay nodes will store the message in their buffers, carry the message along their movements and forward the message to other nodes when a communication opportunity is occurring, which helps to transmit the message further. Efficient CSMA algorithms are using an appropriate queue-based weight in CSMA parameters. Main purpose of this paper is to reduce the waiting time of the short files and high latencies [3, 1].

3 System Architecture and Scheduling Methods

3.1 Dataflow Diagram

Figure 1 describes the data flow structure of the CSMA method. Initially, the nodes are using AODV routing [6]. Then the packet will be sent from source to destination using LSA algorithm. The network will be partitioned into more no. of distributed area that performs the link scheduling, since it produced a minimum throughput and maximum throughput. So, in this work implement an MWS and CSMA algorithm [7]. The MWS algorithm work is based on the packet weight basis. After that implement a CSMA algorithm. The CSMA algorithm is mainly used to avoid the collision and improve the throughput [8, 9]. The advantages of the scheme are reducing the communication overhead and no time synchronization. If the transmission is successfully reaching the destination means, it will store in base station. Otherwise, it will repeat the step until reaching the destination.

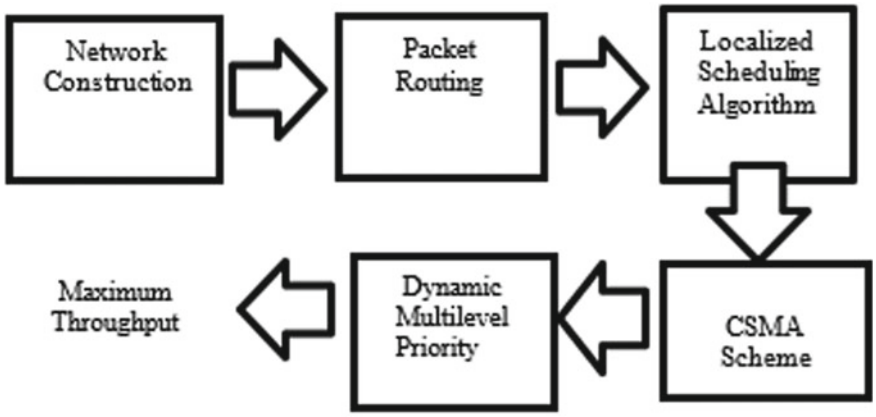

Fig. 1 System architecture

3.2 Scheduling Partition

(A) ***Distributed Partitioned Protocol***

The measurements of each partition in the network should be less than the critical radius of transmission. Initially, the large wireless network will decompose into multiple small networks using distributed partition protocol [10] and [11]. Specifically, to partition localities should be enclosed between an inner computer disk of radius. Protocol structure contains below listed steps.

Step 1: Control slot chooses a decision schedule to set of links m(a).
Step 2: It will change the previous state from next.
Step 3: Link I in m(a) active with probability $x(a) = 1$.
Step 4: Link I in m(a) inactive with probability $x(a) = 0$.
Step 5: After that use x(t) as a transmission schedule.

(B) Localized Scheduling Scheme

The (LSA) localized scheduling algorithm [8] steps are as follows:

Step 1: Collections of links that are ready to transmit as an input.
Step 2: After that they choose a link indefinitely from an entire network.
Step 3: Finally, the link satisfies the main result will have a minimum delay.
Step 4: Then move to the CSMA and DMP algorithms.

3.3 Carrier Sensing Multiple Access Algorithm

This section presents a model for collision-based CSMA/CA scheduling [5, 7, 12]. To measure the network's bandwidth in Eq. 1 below.

$$\Pi(s) = 1/z \exp(\sum wi); s \in M \quad (1)$$

i∈s where z is a constant, w is the weight of the scheduling task, so is the set of nodes. A proper schedule not solely avoid collisions of every receiving node within the whenever slot and additionally reduce the number of your time slots, latency.

3.4 Dynamic Multilevel Priority Scheduling Algorithm

The general nodes are virtually organized, and it follows a hierarchical flow. At the same level are the nodes that are at the same hop distance from the base station. The three levels of queues in the ready queue are priority 1, 2 and 3. [1, 6].DMP scheduling algorithm is defined as below.

Step1: **while** *taska, b* is received by *node*at level *a*
do
if *Type* (*taska, b*) = *real* − *time* **then**
put *taska, b* into *p*1 queue
else if *node*is not at lowest levels **then if** *taska, b* is not local **then**
put *taska, b* into *p2* queue **else** put *taska,* binto *p*3 queue **end if**
else put *taska, b* into *p*2 queue **end if**
Step2: here assumption of timeslot at la = t(k) Data sensing time at lkof nodei = stimea(t) Remaining time tl(a) = t(a)-stimea(t)
Let total real-time tasks for *node*at *la* ← *na*(*p*1) Let *procTime p*1(*a*) ← _*na*(*p*1)
e = 1 *procTime* (*e*)
if *procTime p*1(*a*) < *t*1(*a*) **then**
Step 3: All *p*1 tasks are processed as FCFS
Remaining time *t*2(*a*) ← *t*1(*a*) – *procTime p*1(*a*)
Let *procTime p*2(*c*) ← _*nc*(*p*2).
e = 1 *procTime*(*e*)
if *procTime p*2(*a*) < *t*2(*a*) **then**
Step 4: All *p*2 tasks are processed as FCFS
end if
Finally, to the lowest priority queue, the non-real-time data packets will be sent.

4 Results and Discussions

The network simulations, the propagation time of all links and the backoff time of contact k are distributed exponentially with average 1 ms and 1/exp (rk) ms. Table 1 is usedin the DMP scheduling to represent simulation parameters. The simulation starts with 200 nodes. After that it will be decomposed into many small partitions and will transmit the packet with the speed of 250kbps. The simulation results are

Table 1 Simulation parameters

Parameter	Value and size
Network bandwidth	100 m × 100 m
Node size	50–200
Zone size	5–15
Base station position	50 m × 100 m
Initial node energy	2 J
Propagation speed	198 × 10ˆ6meter/sec
Transmission speed	250Kbps

listed below. It consists of mainly three parameters: They are throughput, time delay and overhead. It will compare the existing and our proposed algorithm. Comparing the existing DMP scheduling algorithm is providing good performance [1, 3, 7].

Figure 2 shows the comparison of overhead analysis in CSMA algorithm, MWS with the existing LSA method. The packet overhead can be expressed as a percentage of non-application bytes divided by the total number of bytes in the message. Using the LSA scheme got 95% overhead, but using CSMA, reduce an overhead into <60%.

The routing will be performed between the intermediate nodes using AODV routing. And, the nodes also move dynamically [10]. The size of the nodes is 50, and the length of the network is 100 m × 100 m. Transmission energy consumptions are 50 n joule/bit. The transmission speed of the nodes is 250kbps. Each node has been linked within network.

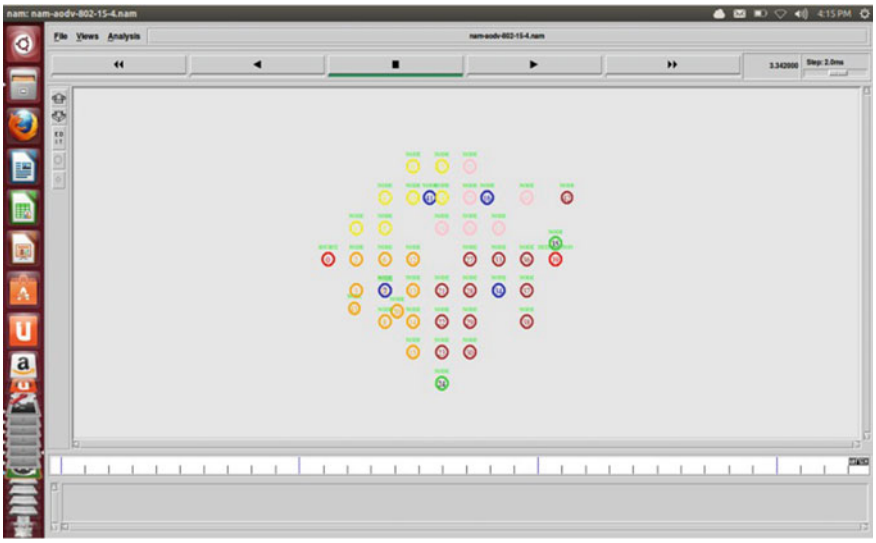

Fig. 2 Deployment of node

In Fig. 3, communication is established between node 0 and node 8, node 24 and node 25. The network will be divided into more number of partitions. Then connect the partition networks using LSA scheme. Using LSA, obtain some packet losses. Messages will be sent between nodes, and there will be packet drops between the nodes. In Fig. 4, the source node will initiate the routing and transmit the packet to the destination via neighbor sink and partition node. After LSA implement MWS and

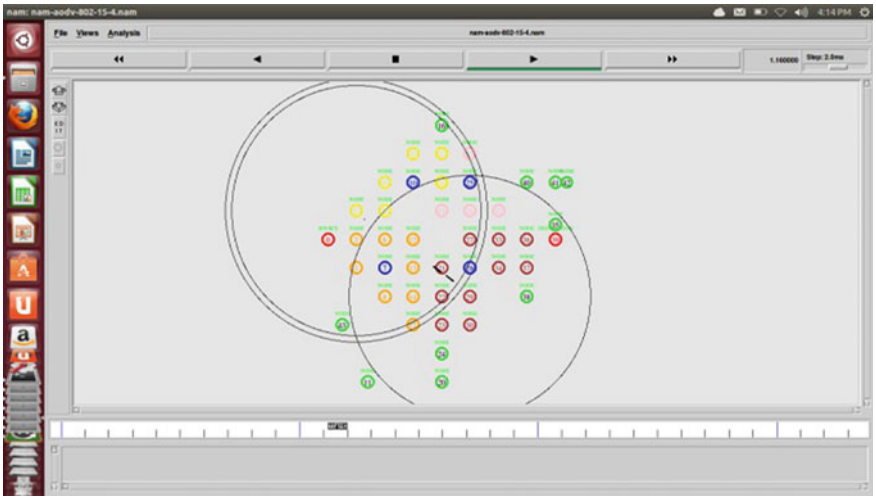

Fig. 3 Communication between nodes

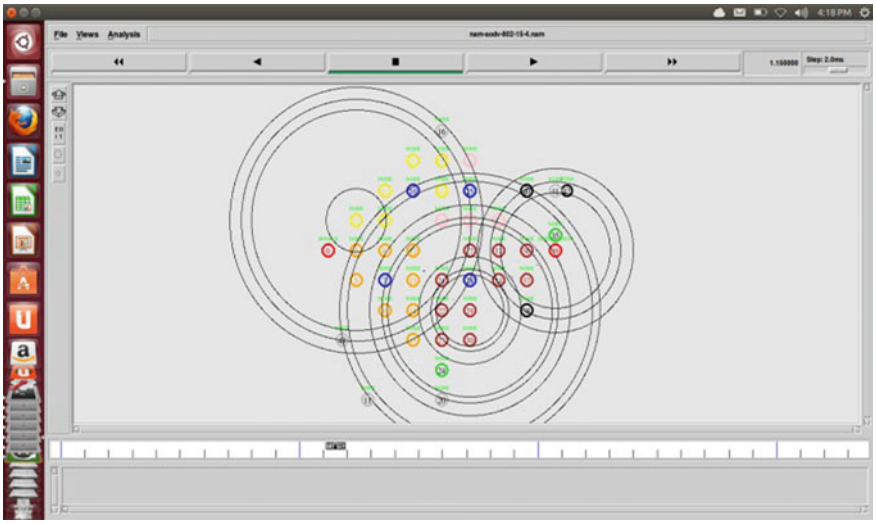

Fig. 4 Source send packet to destination without collision

CSMA algorithm. After implementation of CSMA, obtain a maximum throughput, minimum collision, minimum delay and minimum overhead. So CSMA is better than the existing scheme.

Figure 5 represents the comparison of overhead analysis in CSMA algorithm, MWS with existing LSA method. Using the LSA scheme got 95% overhead, but using CSMA, reduce an overhead into <60%.

Figure 6 shows that the comparison of time delay ratio of CSMA algorithm, MWS with existing LSA method. The graph is plotted between the timescale. The propagation delay is a measurement of the time for a data to reach its destination.

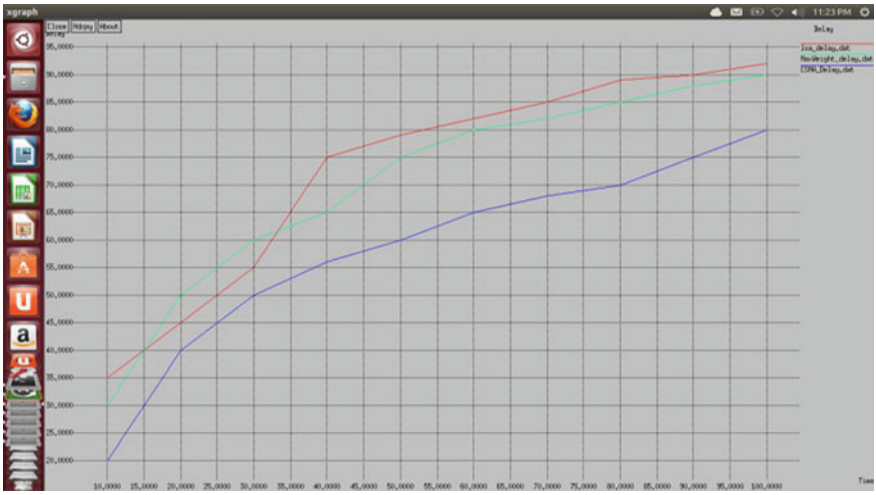

Fig. 5 Overhead comparison graph

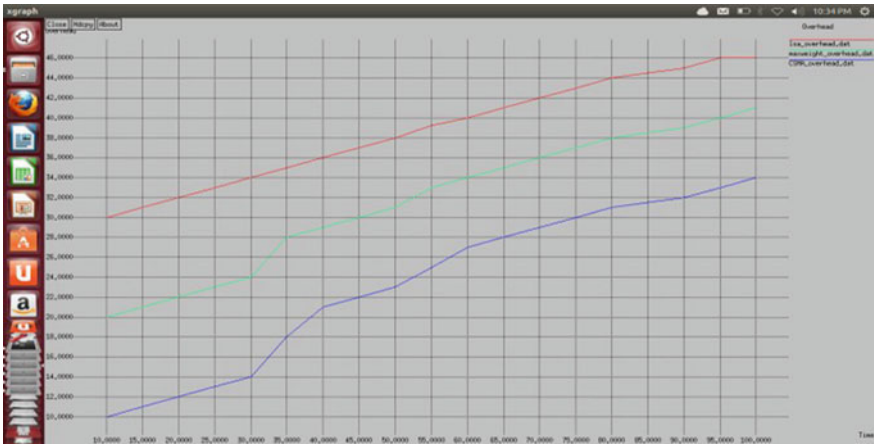

Fig. 6 Time delay comparison graph

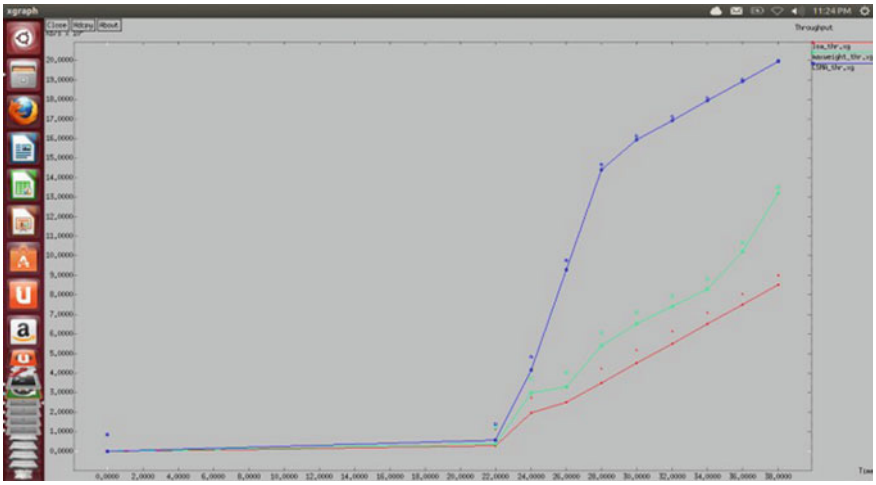

Fig. 7 Throughput comparison graph

Table 2 Simulation comparison

Algorithm/parameters	No of nodes	Time delay (ms)	Overhead (ms)	Throughput (bps)
LSA	100	92	46	40
CSMA	100	90	41	65
DMP	100	80	32	90

Using LSA, scheme got >90%, and finally using CSMA it will reduce in to <75%. So, the time delay will reduce compared to previous algorithms.

Figure 7 shows the comparison of throughput ratio of CSMA algorithm, MWS with the existing LSA method. And it will be denoted by packets per time unit. Hence, it achieves maximum throughput.

Table 2 represents the performance of each algorithm. Comparing localized scheduling and carrier sense multiple access, dynamic multilevel priority scheduling providing better result. Here the time delay reduced from 92 to 80 ms, overhead reduced from 46 to 32 and throughput increased from 40 to 90bps.

5 Conclusions

The task scheduling is implemented in wireless networks using DMP using NS2 simulator [7]. It reduces the waiting time to process data and to improve the performance and CPU utilization. The technique of scheduling partition is to achieve optimal scaling of resources in large wireless networks in order. The complexity is reduced, and it achieves the same result as theoretical method. Based on the

design principles, they proposed a CSMA distributed protocol. The nodes need to be informed with the MAC and carrier sensing information. This is the practical solution to increase the capacity of large wireless networks.

References

1. Ghaderi J, Ji T, Srikant R (2012) Connection-level scheduling in wireless networks using only MAC-layer information. In: 2012 proceedings IEEE INFOCOM, pp 2696–2700
2. Zhang XM, Wang EB, Xia JJ, Sung DK (2013) A neighbor coverage-based probabilistic rebroadcast for reducing routing overhead in mobile ad hoc networks. IEEE Trans Mobile Comput 12: 1–10
3. Fiore M, Ettore Casetti C, Chiasserini CF, Papadimitratos P (2013) Discovery and verification of neighbor positions in mobile Ad Hoc networks. IEEE Trans Mobile Comput 12(2):289–303
4. Mahjourian R, Chen F, Tiwari R, Thai M, Zhai H, Fang Y (2008) An approximation algorithm for conflict-aware broadcast scheduling in wireless ad hoc networks. In Proceeddings ACM Mobile AdHoc network and computing, pp 331–340
5. Jiang L, Walrand J (2009) Approaching throughput- optimality in a distributed CSMA algorithm with contention resolution. Technical Report, UC berkeley
6. Nasser N, Karim L, Talab T (2013) Dynamic multilevel priority packet scheduling scheme for wireless sensor network. IEEE Trans Wireless Commun 12(4):1448–1459
7. Rajeshwaran M, Suguna M, Sharmila D (2014) Localized scheduling for dense wireless networks using CSMA algorithm. Int J Innov Res Sci Eng Technol 3(3)
8. Zhou Y, Li X, Liu M, Mao X, Tang S, Li Z (2013) Throughput optimizing localized link scheduling for multihop wireless networks under physical interference model. arxiv 1301.4738v2 21 Jan 2013 (v1)
9. Xu Y, Wang W (2009) Scheduling partition for order optimal capacity in large scale wireless networks. In Proceedings of ACM MobiCom, pp 109-120
10. Wang Yu, Wang W, Li Mo, Song W-Z (2008) Interference-aware joint routing and TDMA link scheduling for static wireless networks. IEEE Trans Parallel Distributed Syste 19(12):1709–1726
11. Andrew M, Jung K, Stolyar A (2007) Stability of the max weight routing and scheduling protocol in dynamic networks STOC'07, 11–13 Jun 2007
12. Jiang L, Walrand J (2008) A distributed CSMA algorithm for throughput and utility maximization in wireless networks, pp 1511–1519

Characterization of Conformal Antenna for 5G-Enabled Industrial Robots

P. Hamsagayathri, P. Ramya, T. Perarasi, and R.Gayathri

Abstract The conformal microstrip patch with circular slot antenna with coplanar waveguide feed is developed to operate in millimeter wave for industrial robot communications. The proposed antenna structure is designed on conformal substrate RT/Duroid 5880 and portion of the ground plane are tapered to realize the broad bandwidth characteristics. The circular slots are made at the center of the patch to attain stable radiation pattern over the frequency range of 24.75–27.25 GHz. Both the impedance and radiation characteristics of the proposed structure are simulated using ADS software, where it resonates at 26 GHz with minimum return loss of 48 dB and VSWR of 1.023. Moreover, radiation characteristics of the proposed antenna are observed at 26 GHz. The proposed antenna achieves maximum gain of 4.22 dBi with radiation efficiency of 88.65%.

Keywords Microstrip patch · Robots · Circular slot · 5G communication · Coplanar waveguide

1 Introduction

In the recent years, 5G technology is gaining interest in wireless communication, where technology and innovation promise to transform the state-of-the-art communication in robotics. Known by the International Telecommunications Union (ITU)—the global regulator—as IMT-2020, the standard seeks to push boundaries. It aims to transform the cellular networks, communication devices that connect to them along with their operating frequencies [1–5].

Industrial robotics are high beneficiary, with wireless control of highly sophisticated mobile machines becoming feasible—as well as the possibility for robots to exploit the tremendous computational power and storage capacity in the cloud,

P. Hamsagayathri (✉) · P. Ramya · T. Perarasi · R.Gayathri
Department of Electronics and Communication Engineering, Bannari Amman Institute of Technology, Sathyamangalam, Tamilnadu 638401, India
e-mail: palanisamy.hamsagayathri@gmail.com

G. Kumaresan et al. (eds.), *Advances in Materials Research*, Springer Proceedings in Materials 5, https://doi.org/10.1007/978-981-15-8319-3_112

without being fastened by physical wires. Moreover, 5G redefines the robotic capability and shows the massive leap forward transformation in the industries [6, 7]. Most modern manufacturing facilities already make extensive use of robots in the car industry. The medical sector is another domain where the use of robotics is growing and is a great example of how combining robotics with 5G communications has the potential to change lives. Using 5G communications and global navigation and satellite systems can communicate future robots and enable them to perform required actions. Robots also play vital role in agriculture where they improve farming operations by moving through a field of crops to monitor growing conditions. Robots are able to send near-real-time video imagery and other information to a central control system and then perform actions such as pruning, spraying or harvesting crops.

Dual band antenna was designed in [2] to operate in both 2.4 and 5.5 GHz, where it was highly flexible and robust when compared with conventional patch antennas. Antenna in [3] was designed using CPW-fed to reduce the dispersion and smooth radiation characteristics were achieved. Moreover in [4], slots were introduced to obtain the wideband characteristics by means of coupling between the slots in the patch. The slotted structure also reduces the antenna size by 37%. Graphene-based antenna was proposed in various literatures [6, 8, 9] for high-speed communication. The performance of such antennas was also evaluated for different substrates like silica, quartz, aluminum nitrate and so on, and its both impedance and radiation characteristics were studied.

5G creates new era of communications that enable pioneering use cases in robotics, and this can be achieved by enabling the robots to operate in close proximity without interfering with one another. In addition, 5G technology is gaining over other due to its characteristics such as wide bandwidth, shorter wavelength and its propagation behavior in different mediums. Different antenna structures have been proposed for 5G communications in the literature [9–15]. However, each has its own pros and cons. In this paper, conformal printed antenna is designed on RT/Duroid 5880 substrate to achieve broader bandwidth at the operating frequency of 26 GHz.

2 Methodology

2.1 Design

The substrate dielectric constant, thickness of the substrate and operating frequency are three key parameters required for designing an antenna.

The selection of substrate is the crucial factor in antenna design, where microstrip losses are high in millimeter wave bands and they are categorized into dielectric, conductor and radiation losses. “The dielectric constant for the substrates is chosen in the range of $2.2 \leq \varepsilon r \leq 12$ to design microstrip antennas.” “Thick substrate with low dielectric constants provides better radiation efficiency, wider bandwidth but it increases the total size of the antenna”; whereas, thin substrate with high

dielectric constant reduces the undesired surface waves excitation and coupling but they produce less radiation efficiency with narrow bandwidth.

By considering all these factors, "RT/Duroid 5880 substrate with εr = 2.2 is used for antenna design with thickness of 0.5 mm at operating frequency of 26 GHz." Width of the patch is calculated as

$$W = \frac{C_0}{2f_r}\sqrt{\frac{2}{\epsilon_r + 1}} \tag{1}$$

The step by step antenna design calculations are listed below [8, 16].The radiation characteristics of the proposed antenna vary with the width of the patch, and it greatly affects its bandwidth and radiation efficiency. Due to fringing effect, electrical width of microstrip antenna is larger compared to its physical dimensions and hence electric field lines incident on the antenna pass through both in the air and substrate. Hence, "effective dielectric constant" is formulated as below

$$\epsilon_{\text{reff}} = \frac{\epsilon_r + 1}{2} + \frac{\epsilon_r - 1}{2}\left[1 + 12\frac{h}{W}\right]^{\frac{1}{2}} \tag{2}$$

$$\frac{\triangle L}{h} = \frac{0.412(\epsilon_{\text{reff}} + 0.3)\left(\frac{w}{h} + 0.264\right)}{(\epsilon_{\text{reff}} - 0.258)\left(\frac{W}{h} + 0.8\right)} \tag{3}$$

Extension in electrical length of the patch is usually calculated using the above equation, where ΔL is the function of "effective dielectric constant ϵ_reff, height of the substrate h and the width-to-height ratio (W/h)."

In general, length of the patch is half of the operating wavelength and the actual length is calculated by subtracting the length extended on both edges from effective length.

$$L_{reff} = \frac{C}{2f_0\sqrt{\varepsilon_{reff}}} \tag{4}$$

$$L = L_{\text{eff}} - 2 \triangle L \tag{5}$$

The dimensions of the conformal patch antenna are calculated using the above listed design equations. The general layout of the antenna structure and its parameters is given in Fig. 1 and Table 1.

2.2 Analysis

The proposed conformal center circular slotted antenna is analyzed using transmission line model. The microstrip antenna is represented as two radiating slots with

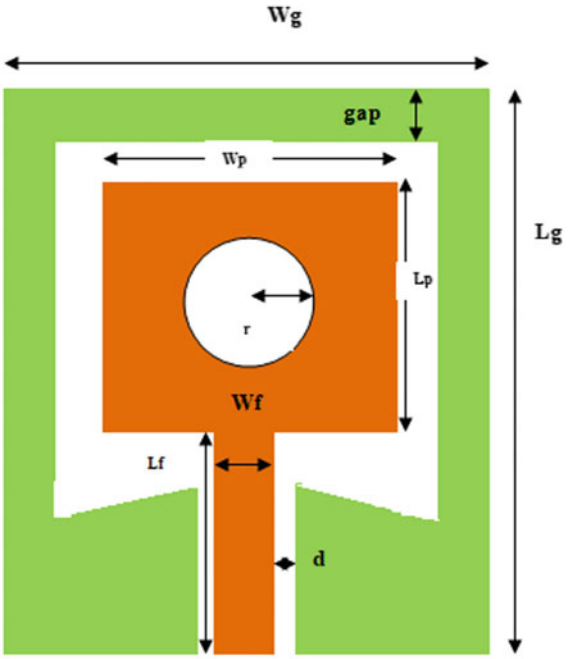

Fig. 1 Structure of the proposed antenna

Table 1 Layout parameters of the proposed antenna

Layout parameter	Value(mm)
Lp	3.5
Wp	4.5
Wf	2.1
Lf	1.5
Lg	5
Wg	5
D	0.3
R	0.5
Gap	0.5

each of width (W) and length (L), where they are "separated by the transmission line with low impedance" of length "d" [17]. Due to finite patch dimensions, electric and magnetic field lines are uniformly distributed along patch and the lines at the edges undergo fringing. "The amount of fringing depends upon the dimension of the patch and height of the substrate."

Substrate and radiator materials have great influence over the antenna performance. Because of high electrical conductivity, graphene material is chosen as the radiating element and the simulation is carried out for designed antenna structure. In addition, as the height of the substrate increases, fringing also increases with

large separation between the two radiating edges and lowers the resonant frequency. Hence, antenna for millimeter wave is designed with substrate with thickness (h) of 0.5 mm. The proposed antenna structure is fed using coplanar waveguide, where it reduces the dispersion by minimizing the parasitic effects of discontinuities in ground plane. It also aids to realize the broadband characteristics. However, such feed requires thick substrates, and hence the thickness is optimized in the antenna design.

3 Simulation Results and Discussion

The antenna proposed for 5G communication in robots is designed and simulated using ADS (2016). In ADS, antenna structure is meshed into tetrahedral shapes, and direct dense solver is applied to solve the Maxwell's integral equations. The impedance and radiation characteristics of the proposed antenna are studied and analyzed to evaluate its performance.

3.1 Impedance Characteristics

The impedance characteristics of the antenna are analyzed by its return loss and VSWR curves. "Return loss quantifies the loss of the power in the incident signal that reflected or returned back to the source due to discontinuity in the transmission line." The return loss is always minimum at the resonant frequency. As the equivalent circuit of microstrip antenna has R,L,G and C elements, antenna is neither inductive nor capacitive at the resonance and hence it is able to radiate the radio waves efficiently. "The return loss characteristics of the proposed antenna structure are shown in Fig. 2 where it exhibits the minimum return loss of −48 dB."

With reference to −10 dB, the impedance bandwidth is calculated and from the simulation result it is examined that proposed antenna structure realizes broad bandwidth of 2.5 GHz in the range of (24.75–27.25 GHz) which achieve the requirement of the millimeter wave applications.

"The voltage standing wave ratio (VSWR) measures the impedance mismatch between the antenna port and feed line connecting to it." The proposed antenna design attains minimum VSWR of 1.023 at the resonant frequency of 26 GHz, which is well below the industrial standard, and it is shown in Fig. 3.

The impedance curve of the proposed antenna structure is shown in Fig. 4, where it attains the impedance of 50.2 at the operating frequency of 26 GHz.

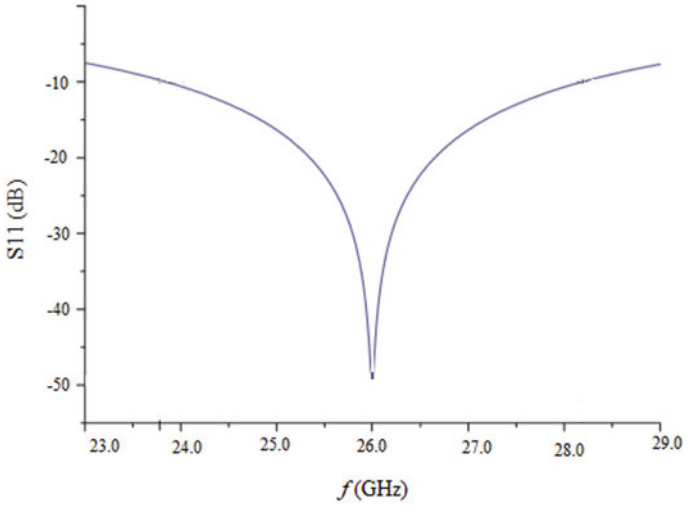

Fig. 2 S11 characteristics of proposed antenna

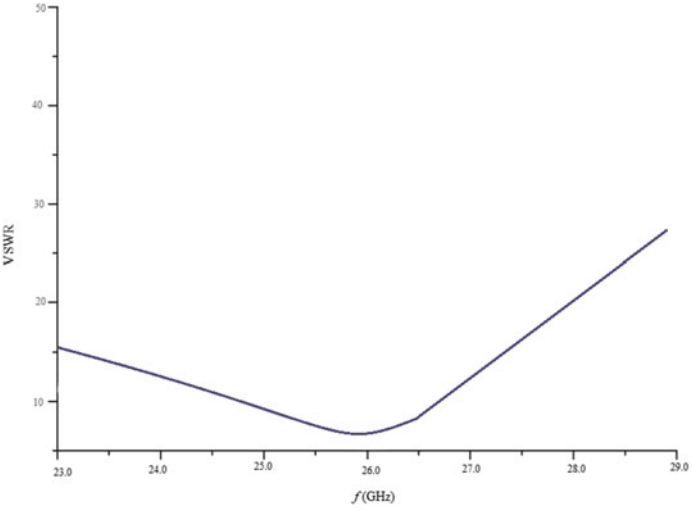

Fig. 3 VSWR of proposed antenna

3.2 Radiation Characteristics

The radiation characteristics of the antenna are analyzed by considering different parameters like gain, directivity, efficiency, polarization, current distribution and its radiation pattern in E-plane and H-Plane.

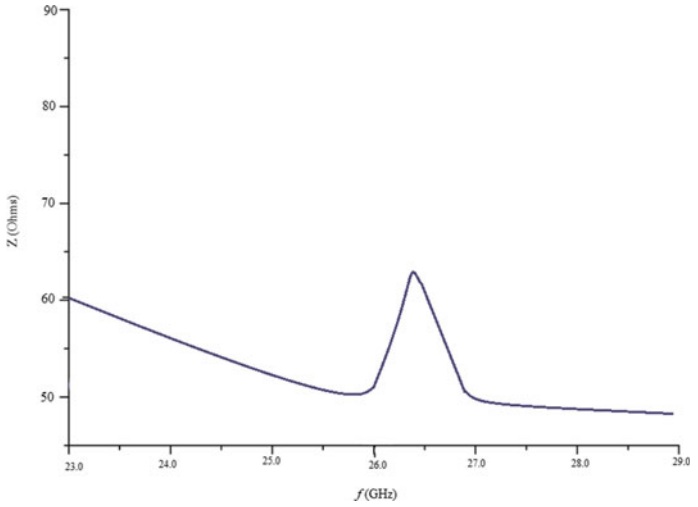

Fig. 4 Impedance curve of proposed antenna

The tapered sections in the ground plane in CPW-fed increase the bandwidth with slight decrease in the gain, and it attains 4.22 dBi. The antenna gain is always measured with respect to isotropic antenna. The directivity defines the ability of the antenna to radiate the accepted power in particular direction. The proposed antenna achieves the maximum directivity of 4.76 dBi with radiation efficiency of 88.65%. The radiation parameters of the proposed structure and conventional antenna are compared in Table2 (Fig. 5).

The circular slots are made at the center of the patch to increase its electrical length of the antenna which enhances its radiation pattern. "The shape of radiation pattern is constant at far fields, and hence radiation characteristics of the proposed antenna are evaluated in that region." Fields in E- and H-plane are not only normal to each other but also with the direction of propagation. The strong and weak radiating fields of the antenna are indicated in red and blue color.

Table 2 Variations in radiation characteristics for different substrates

Parameters	Rectangular patch	Proposed antenna structure
Gain	1.64	4.22
Directivity	2.18	4.76
Efficiency	76	88.65

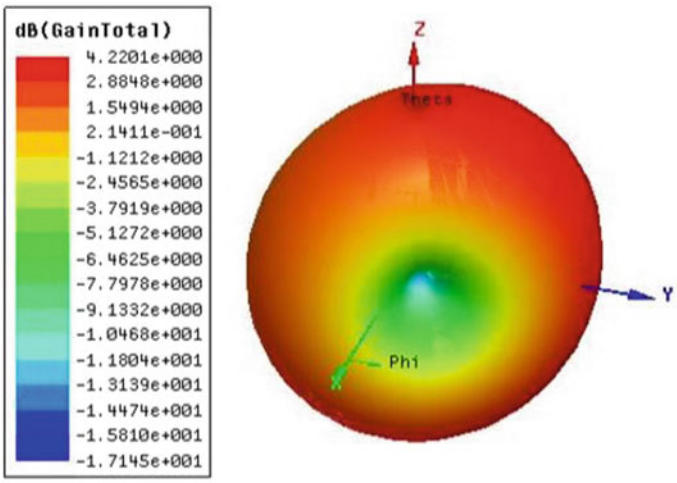

Fig. 5 Radiation pattern

4 Conclusions

In this paper, the performance of the antenna is studied to meet the requirements of 5G communication in robots. The tapered section in the ground plane increases the impedance bandwidth of 2.5 GHz (24.75–27.25 GHz) and helps to speed up the data transmission in 5G communications. The dimension and position of the circular slots are adjusted to control the shape and direction of the main lobe of radiation pattern. The proposed antenna structure achieves the radiation pattern with no side lobes. It attains the maximum gain or 4.22 dBi with radiation efficiency of 88.65%. The performance characteristics of the antenna can be studied on different conformal structures of robots in the future.

References

1. Ghaffarian MS, Moradi G (2011) A novel harmonic suppressed coplanar waveguide (CPW)-fed slot antenna. IEEE Antennas Wireless Propag. Lett 10:788–791
2. Ashok Kumar S, Shanmuganantham T, Dileepana D (2017) Design and development of CPW fed monopole antenna at 2.45 GHz and 5.5 GHz for wireless applications. Alexandria Eng J 56(2):231–234
3. Zhu S (2007) Development of conformal antenna and its application in electronic warfare. J Chinese Acad Electron Sci 12
4. Zhou L, Jiao Y-C, Qi Y, Weng Z, Ni T (2014) Wideband ceiling mount omnidirectional antenna for indoor distributed antenna system applications. Electron Lett 50(2):253–255
5. Koohi MZ, Neshat M (2015) Evaluation of Graphene-based terahertz photoconductive antennas. Trans F Nanotech 22:1299–1305

6. Llatser I et al (2012) Radiation characteristics of tunable graphene in the terahertz band. Radioengineering 21(4):946
7. Pozar DM (2009) Microwave engineering. Wiley
8. Chen PY, Argyropoulos C, Alu A (2013) Terahertz antenna phase shifters using integrally-gated 6rapheme transmission-lines. IEEE Trans Antennas Propag 61(4):1528–1537
9. Bala R, Marwaha A (2016) Investigation of Graphene based miniaturized terahertz antenna for novel substrate materials. Int J Eng Sci Technol 19(1):531–537
10. Amanatiadis S, Karamanos T, Kantartzis N (2017) Radiation efficiency enhancement of Graphene THz antennas utilizing metamaterial substrates. IEEE Antennas Wirel Propag Lett 16(4):2054–2057
11. Akyildiz IF, Jornet JM (2016) Realizing ultra-massive MIMO (1024 × 1024) communication in the (0.06–10) terahertz band. Nano Commun Netw 8(2):46–54
12. Hong W, Jiang ZH, Yu C et al (2017) Multibeam antenna technologies for 5G wireless communications. IEEE Trans Antennas Propag 65(12):6231–6249
13. Chin WH, Fan Z, Haines R (2014) Emerging technologies and research challenges for 5G wireless networks. IEEE Wireless Commun Magaz 21(2):106–112
14. Jilani SF, Alomainy A (2016) Planar millimeter wave antenna on low cost flexible PET substrate for 5G communications. In: 10th European conference on antennas and propagation
15. Omar A, Shubair R (216) UWB coplanar waveguide fed coplanar strips spiral antenna. In: 10th European conference on antennas and propagation
16. Balanis CA (2012) Advanced Eng Electromag. Wiley
17. John M, Manoj B, Jagadish Chandran G (2016) Design of a slotted rectangular microstrip patch antenna operated in ISM band using RT-duroid substrate. Int J Adv Res Electric Electron Instrument Eng 5(4)

Performance Analysis of Booth Multiplier-Based FIR in DWT Image Processing Applications

S. Tamilselvan, R. Ramesh, K. Hema Priya, and B. Nithya

Abstract The main objective of this work is to suggest an FIR filter for convolution-based DWT in image processing. Image processing using filters mainly suffers from the delay caused by the multiplier unit. Herewith, we have proposed booth multiplier-based MAC architecture for the design of FIR filter. Hence, the overall system achieves maximum speed improvement of 13.83% and area reduction by 22.39%. This work assures that the performance improved VLSI architecture for image processing with DWT techniques.

Keywords FIR filter · DWT image processor · Multiplier

1 Introduction

Recent days, the usage of DWT-based image processing is of the essence in reducing the storage space needed for an image. This also can be enhanced by many different compression techniques. But the resultant image may not have higher order of reduction. But by using DWT scheme, the order can be improved up to the level of 1/N, where the N is the number of quadrants (LL, LH, HH, HL). While performing the wavelet compression, the invisible high-frequency, high resolution part of images can be neglected [1]. This will make the compression as most efficient one, as the ¼ of the image is only used to store. A convolution-based three-level architecture is

S. Tamilselvan (✉) · R. Ramesh · K. Hema Priya · B. Nithya
Department of Electronics and Communication Engineering, Bannari Amman Institute of Technology, Coimbatore, Tamilnadu, India
e-mail: tamilselvans@bitsathy.ac.in

R. Ramesh
e-mail: rameshravi20597@gmail.com

K. Hema Priya
e-mail: hema.vd19@bitsathy.ac.in

B. Nithya
e-mail: nithya.vd19@bitsathy.ac.in

G. Kumaresan et al. (eds.), *Advances in Materials Research*, Springer Proceedings in Materials 5, https://doi.org/10.1007/978-981-15-8319-3_113

also proposed in [2]. However, the two level itself is a popular technique to produce compact image. High throughput and less computation time applications can be appropriate for this architecture, which reduces the computation time by half. Also the lifting base structures save considerable area. The two-dimensional multi-level DWT is discussed in the paper [2] and extended the same up to the dimensions of three using bi-orthogonal and Daubechies filters. The line buffered wavelet filer having M as the number of image proposed in [2] has the benefit when it is used in top throughput.

This leads to the drawback of having more adders and multipliers. If there is more mutual architecture available which computes data streams, then 100% hardware utilization is possible [3] and [4–7].

2 Booth Multiplier-Based Fir

Booth multiplier-based product generation has the advantage that the number of partial product rows required to calculate the product will be exactly half that of number of partial products needed for the ordinary multiplication methods.

For an example, the number of partial product rows needed for 64 bit ordinary multiplier is 64 rows, wherein the same multiplier would generate only 32 rows in the case of booth-based techniques.

An example for booth multiplier was shown in Fig. 1. Here 6 × 6 bit multiplications were performed. But instead of producing six PPR rows, only three rows were generated to produce the product values.

This makes the number of multiplier component that will be reduced in numbers and thereby the architecture size reduced [8, 9] and [10–15].

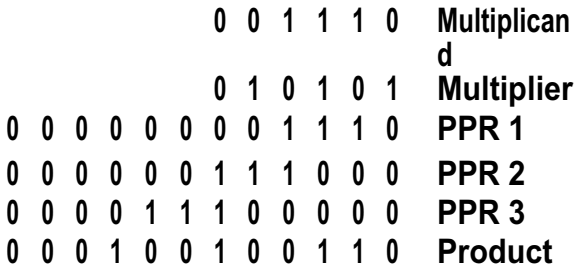

Fig. 1 Example 6 × 6 booth multiplier

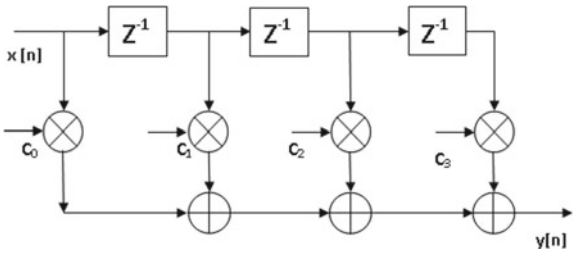

Fig. 2 Simple FIR filter structure

3 FIR Filter

The filters are playing important role in selecting the required value from the large numbers. Here in the case of DWT as a compression technique, only the most important information alone is to be taken for defining the images. The high-frequency values will be neglected while the picture is being compressed.

For selecting the low-frequency values from the available image samples, the FIR filer is used.

A simple FIR filter structure is shown in Fig. 2. So this filter is also called as low-pass FIR filter in DWT process.

4 DWT System

The image compression techniques can be split into two types, known as lossy compression and lossless compression. Further, the lossless compression has entropy coding and decorrelation technique. The RLC and statistical codes fall under the category of entropy coding, wherein the prediction-based compression, transform-based compression and multi-resolution-based compression are the types under the category of decorrelation method. On the other hand, the lossy compression technique has transform-based and non-transform-based compression as types. Vector quantization and fractals are the types of non-transform-based compression techniques. The advanced and high efficient compression techniques like DCT and DWT fall under the category of lossy transform-based compression techniques. The DWT removes the drawback of DCT. A wavelet is a function which has the properties like average value as 0, duration limit and frequency varying, with waves on the top and underneath the x-axis. Sometimes, high frequencies use narrow windows, and low frequencies would be preferred at wider windows. A wavelet is like sin and cos functions with ψk(t) function as given below

$$f(t) = \sum a_k \psi_k(t)$$

Table 1 Sub-bands of DWT

Frequency band	Horizontally	Vertically
LL	Low pass	Low pass
LH	Low pass	High pass
HL	High pass	Low pass
HH	High pass	High pass

A full image will be applied to DWT compression process. So that better compaction in energy is achieved as compared to DCT techniques. There are four sub-bands available in terms of frequency as shown in Table 1.

Usually, a low-pass filer will be used as FIR filter, and the image is passed in it. The undisclosed information of the images will be put out of sight in the LH, HL and HH portions, and only LL portion of low-frequency image element is more perceptive to our human eyes. It is obvious that the disclosed information in three portions has no data in it, and this high-frequency parts will not affect the quality of the image [16]. Three more important properties are linear time complexity, adaptability and sparsity. In special case of finger print image compression, image fusion, image matching and retrieval, image recognition and noise filtering, the wavelet compressions can be applied [17, 18].

4.1 Convolution-Based DWT System

The multiply and accumulation unit is a heart of FIR filer design. This MAC unit has multipliers and accumulators [19]. The multipliers produce product for floating point input numbers. The addition process is repeated every time to add the product with the previous MAC output. This can be given by the equation

$$\mathrm{m[i]} = \mathrm{m[i-1]} + \mathrm{x[i].y[i]}$$

where m[i] is the MAC output at ith iteration, and x[i] and y[i] represent the input for the multipliers. Here instead of ordinary multiplier, booth multiplication is used to generate the products, so as to minimize the number of partial product rows. Solo stage pipelined 8 bit floating point filter structure is shown in Fig. 3.

Input bit D decides the type of operation performed. If D = 1, then it performs multiplication, and if I is 0 then MAC operation is performed. Select line decides the input to be passed through it during the row and column processing. Totally, 96 clock cycles are needed to complete the row processing. Number multiplicands will decide the number of clock cycles.

By using pipelined structure with two MAC units, convolution time can be reduced by half and requires small area and very small power consumption for the operation.

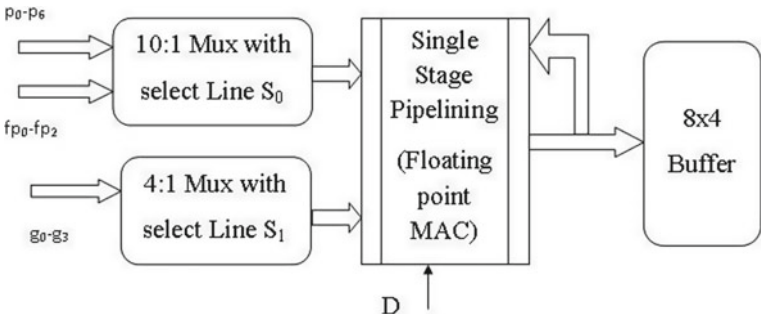

Fig. 3 Single-stage pipelining structure

4.2 Model for DWT Implementation

HDL codes for both existing and proposed designs are modeled and simulated in Xilinx ISE simulator, and by Cadence tool, the codes were synthesized. The overall architecture is shown in figure (Fig. 4).

Proposed DWT gets the selected address lines from the lookup table, where all the select lines are being stored. A preset register operated by means of clock will be continuously incremented by the adder with default '1' as one of the inputs. This will help the address lines of be continual values are stored in lookup table. The DWT of the image is obtained by using direct DWT2 function in MATLAB code [10, 20–24]. The same can be obtained by using the DWT algorithm, which is explained in this section. The algorithm setup can be written in hardware description code. The HDL code again simulated in Xilinx tool to verify its functionality, and the same can be used with the booth multiplier instead of the ordinary multipliers. Here the number of partial product rows can be minimized into half of the actual no. of rows required. This will be an added advantage for the area wise reduction of the architecture, and speed of the circuit can also be improved to better extent. Again the HDL code with booth multiplier for the DWT was simulated to get the DWT transformed image. This can be extended up to N number of dimensions as like MATLAB code does. The extended dimensions like 2D and 3D DWT are also

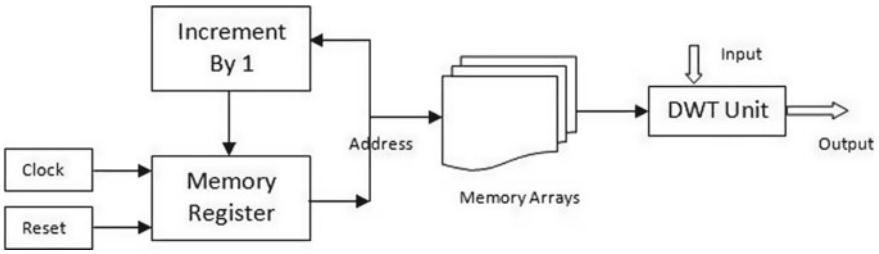

Fig. 4 Overall architecture of DWT

possible with this technique, finally the proposed architecture is implemented in the FPGA kit, and the performance analyses were done.

4.3 Simulation Result Analysis

The simulation result shows that the PSNR values are high, and the pictures look in same as other compression techniques. The simulations were done by using MATLAB software. Also the VHDL simulation was done by using ModelSim, and the parameters evaluation is carried out by Cadence software. The mean square error (MSE) is given by, $\text{MSE} = \frac{1}{L}\sum_{i=1}^{L}[p_i - q_i]^2$ where the input sequence is pi, output sequence is qi, and data sequence length is denoted by L. Also the pixel to noise ratio is given as, $\text{PSNR} = 10\log_{10}\left(\frac{p^2}{\text{MSE}}\right)$ where p is the peak value of the input sequence (Fig. 5).

Tables and Graph

The area and delay values for different compression techniques were shown in Table 2. It is observed that the performance of the DWT is more suitable for the image processing where there is a lack of storage space with improved performances as tabulated (Table 2).

Average performance of the proposed technique satisfies the significant reduction in both area and delay values as shown in Figs. 6 and 7.

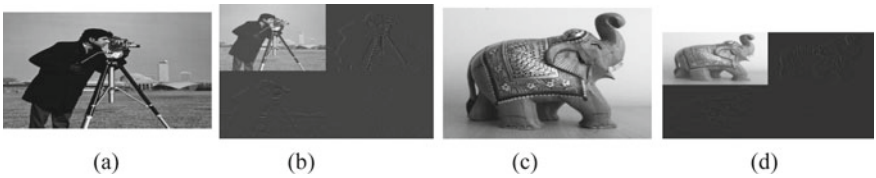

Fig. 5 **a** and **c** Original images, **b** and **d** DWT image

Table 2 Performance analysis

Methods	Area (μm2)	Delay(ps)
Floating point DWT in [11]	52,678.3	26,479.2
Floating point DWT in [12]	29,458.1	27,968.4
Floating point DWT in [13]	58,945.6	253,147
Proposed DWT	45,746.2	24,569.2

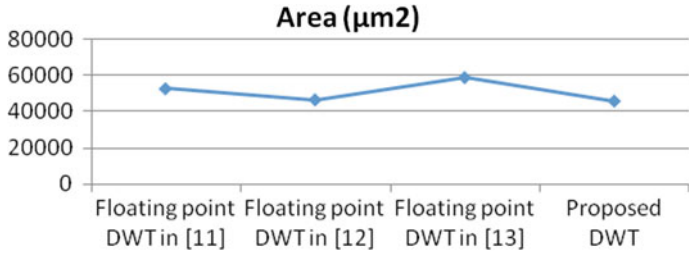

Fig. 6 Area comparison

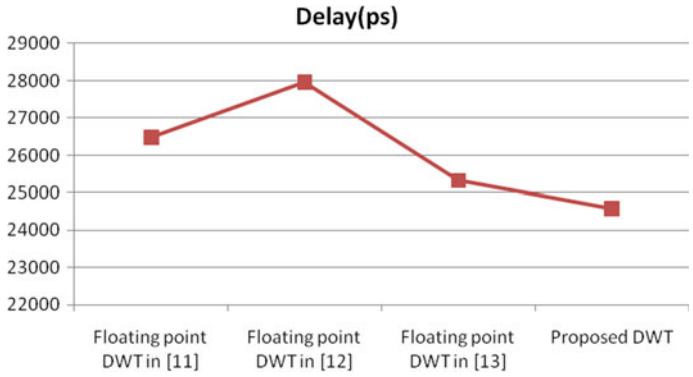

Fig. 7 Delay comparison

5 Results and Discussion

The result shows that the proposed work and the existing work will produce same image output. But in the performance wise and area utilization wise, the proposed architecture stands in its place. So this proposed architecture can be used in DWT-based image processing applications like convolution-based compression with minimum number of resources, energy and time.

References

1. Antonini M, Barlaud M, Mathieu P, Daubechies I (1992) Image coding using wavelet transform. IEEE Trans Image Process 1(2):205–220
2. Mohanty BK, Meher PK (2013) Memory-efficient high-speed convolution-based generic structure for multilevel 2-D DWT. IEEE Trans Circuits Syst Video Technol 23(2):353–363
3. Liu HJ, Shao Y, He X, Zhang TJ, Wang DH, Hou CH (2007) A novel VLSI architecture for 2-D discrete wavelet transform. IEEE Int Conf ASIC 40–43
4. Saravana Kumar R, Mohanbabu A, Mohankumar N, Godwin Raj D (2019) Simulation of InGaAs subchannel DG-HEMTs for analogue/RF applications. Int J Electron 105(3):446–456

5. Mohanbabu A, Saravana Kumar R, Mohankumar N (2017) Noise characterization of enhancement-mode AlGaN graded barrier MIS-HEMT devices. Superlattices and Microstructures
6. Poornachandran R, Mohankumar N, Saravana Kumar R, Sujatha G (2019) Sheet—carrier density and I—V analysis of In0.7Ga0.3As/InAs/In0.7Ga0.3As/InAs/In0.7Ga0.3As dual channel double M gateHEMT for THz applications. Int J Numer Model e2625
7. Poornachandran R, Mohankumar N, Saravanakumar R, Sujatha G (2019) Analysis of microwave noise in an enhancement-mode dual-quantum-well InAs HEMT. J Comput Electron © Springer Science+Business Media, LLC, part of SpringerNature 2019
8. Tamilselvan S, Nithya P (2017) Efficient modified booth multiplier for signal processing applications. Indian J Sci Technol 10(14)
9. Tamilselvan S, Selvambal J, Sharan Karunya K, Sri Suruthi R, Sumalin Briskilla J (2018) Design and implementation of area efficient fast multiplier. Int J Pure Appl Math 118(20):4971–4975
10. Vijaykumar VR, Elango S (2014) Hardware implementation of tag-reader mutual authentication protocolfor RFIDsystems. Integration VLSI J 47123–129
11. Vijeyakumar KN, Sumathy V, Elango S (2014) VLSI implementation of area-efficient truncated modified booth multiplier forsignal processing applications. Arabian J Sci Eng. Arab J Sci Eng 39:7795–7806
12. Vijaykumar VR, Raja Sekar S, Elango S, Ramakrishnan S (2018)Implementation of2*n*—2*k*—1 modulo adder based rfid mutual authentication protocol. IEEE Transactions on Industrial Electronics 65(1)
13. Philip SP, Sampath P, Devakumar PV, Elango S (2018) FPGA implementation of low power adaptive filter architecture. Int J Eng Adv Technol 8(2S). ISSN: 2249-8958
14. Saravana Kumar R, Mohanbabu A, Mohankumar N, Godwin Raj D (2017)$$\hbox {In}_{0.7}\hbox {Ga}_{0.3}\hbox{As}/\hbox {InAs}/\hbox {In}_{0.7}\hbox{Ga}_{0.3}\hbox {As}$$ In 0.7 Ga 0.3 As/InAs / In 0.7 Ga 0.3 As composite-channel double-gate (DG)-HEMT devices for high frequency applications. J Comput Electron 16(3). ISSN 1569–8025
15. Radhakrishnan SK, Subramaniyan B, Anandan M, Nagarajan M (2018) Comparative assessment of InGaAs sub-channel and InAs composite channeldouble gate (DG)-HEMT for submillimeter wave applications. Int J Electron Commun (AEÜ) Int. J Electron Commun (AEÜ) 83:462–469
16. Zervas ND, Anagnostopoulos GP, Spiliotopoulos V, Andreopoulos Y, Goutis CE (2001) Evaluation of design alternatives for the 2-D-discrete wavelet transform. IEEE Trans Circuits Syst Video Technol 11(12):1246–1262
17. Bebis G, Gyaourova A, Singh S, Pavlidis I (2006) Face recognition by fusing thermal infrared and visible imagery. Image Vision Comput 24(7):727–742
18. Jacobs CE, Finkelstein A, Salesin DH (1995) Fast multiresolution image querying. SIGRAPH
19. Tamilselvan S, Arun A (2018) An efficient MAC design for image processing application. Indian J Sci Technol 11(19)
20. Huang CT, Tseng PC, Chen LG (2004) Flipping structure: an efficient vlsi architecture for lifting-based discrete wavelet transform. IEEE Trans Signal Process 52(4): 1080–1089
21. Po-Cheng Wu and Liang-Gee Chen (2001) An efficient architecture for two-dimensional discrete wavelet transform. IEEE Trans Circuits Syst Video Technol 11(4):536–545
22. Chu Yu and Sao-Jie Chen (1997) VLSI implementation of 2-D discrete wavelet transform for real-time video signal processing. IEEE Trans Consum Electron 43(4):1270–1279
23. Marino F (2000) Efficient high-speed/low-power pipelined architecture for the direct 2-D discrete wavelet transfor. IEEE Trans Circuits Systems—II: Analog Digital Signal Process 47(12):1476–1491
24. Vijeyakumar KN, Elango S, Kalaiselvi S (2018) VLSI implementation of high speed energy—efficienttruncated multiplier. J Circuits Syst Comput 27(5):1850077

Structural and Optical Studies on Radio Frequency (Rf) Magnetron Sputter Deposited Nickel Oxide Thin Films

K. S. Usha, R. Sivakumar, and C. Sanjeeviraja

Abstract Nickel oxide, an example for metal oxide has its own remarkable impact as anodic coloring material in the field of electrochromic smart window. Radio frequency sputtering technique is implemented in preparing thin film of nickel oxide (NiO) over microscopic glass substrate. The conformational analysis is done by X-ray diffraction technique (XRD) and UV–Vis–NIR spectrophotometer. XRD reveals the crystalline nature of the deposited NiO thin film. A maximum transparency of 92% is obtained for the film deposited at 160 W RF which finds a wide application in optoelectronic devices.

Keywords Radio frequency magnetron sputtering · NiO · Optical properties · Transmittance · Optoelectronic devices

1 Introduction

Electrochromic devices (ECD) are the one which vary its optical properties to the external electric field applied which made them to retain its position in various advanced applications. To name a few, they are being used in smart windows where the transmission of the solar radiation is being altered, as output displays and in automotive mirrors where they prevent glaring during night driving. The attractive interests of ECD are its low-power conception and open-circuit memory which is being decided by the imperative layer used. This electrochromic film layer is formed either by amorphous material or by crystalline oxide which is deposited over a transparent conducting oxide-coated glass or plastic sheet. Among the conventional EC

K. S. Usha (✉)
Department of Physics, Bannari Amman Institute of Technology, Sathyamangalam 638401, India
e-mail: usha@bitsathy.ac.in; ushathinfilm@gmail.com

R. Sivakumar
Department of Physics, Alagappa University, Karaikudi 630003, India

C. Sanjeeviraja
Alagappa Chettiar College of Engineering and Technology, Karaikudi 630003, India

G. Kumaresan et al. (eds.), *Advances in Materials Research*, Springer Proceedings in Materials 5, https://doi.org/10.1007/978-981-15-8319-3_114

materials, NiO having polycrystalline structure and amorphous tungsten oxide (WO_3) are widely used due to its desirable optical properties [1–3].

Tunable optical properties with the external stimulus made these electrochromic devices to find a wide variety of applicational aspects [4–7]. The transition metals used find their significant applications in electrical conductivity and magnetic properties; whereas, tungstates fit them in laser and fluorescent lamps. Their utility is being extended as humidity sensors and catalysts [8, 9]. In this investigation, nickel oxide film is being coated as thin film by RF sputtering technique, and their structural and optical properties are investigated further to fit them for the apt applications.

2 Materials and Methods

2.1 Experimentation

A transparent glass material is used as substrate for depositing electrochromic film layer. Thin film of nickel oxide is prepared and deposited on the transparent glass substrate via RF magnetron sputtering technique. The target nickel oxide is manually prepared whose diameter is measured to be 5 cm. While depositing the prepared thin film, a uniform pressure of 5×10^{-3} mbar is maintained inside the chamber. The gap between the anode and the cathode is fixed approximately to be ~6 cm throughout the deposition process. This deposition is carried out at ambient temperature for about thirty minutes with an RF power of 160 W. After successful completion of the deposition, the thickness of the film deposited is measured using Stylus profilometer (Mitytoyo, SJ-301). The structural pattern of the film deposited is confirmed by X-ray diffraction analysis (XRD, X' pert Pro PANanalytical), and the optical properties are elucidated from UV–Vis–NIR spectrophotometer (JASCO;V-670).

3 Results and Discussions

3.1 Structural Study

Nickel oxide thin film deposited at RF power of 160 W shows thickness (t) of 0.78 μm. The XRD pattern obtained for the deposited thin film is depicted in Fig. 1. From the spectra obtained, it is well noticed that the film formed is of cubic structure which is further confirmed from the peak obtained at 42.9° which corresponds to (2 0 0) orientation. The data obtained experimentally is compared with the (JCPDS Card No. 89–7130) data and fits well. Thus, the XRD analysis carried out confirms the prepared NiO film as crystalline one.

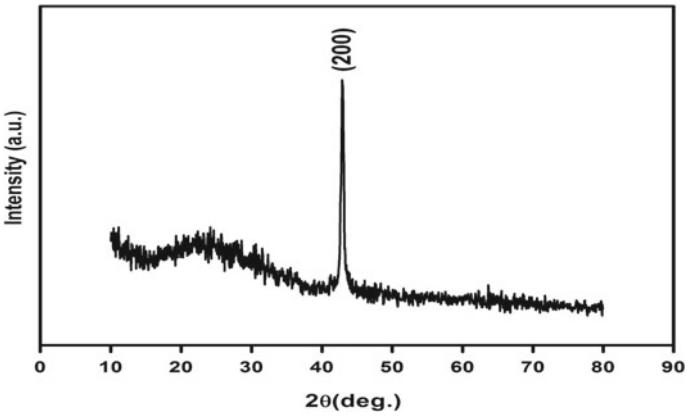

Fig. 1 X-ray diffraction pattern of NiO thin film

3.2 Optical Transmittance

The optical transmission spectra of the deposited NiO thin film are recorded in the wavelength of 300–2500 nm, and the obtained spectra is depicted in Fig. 2. It is concluded that nickel oxide thin film deposited at RF power of 160 W shows the highest transmittance (92%) in the VIS–NIR regions. MnS thin films prepared by sol–gel technique [10] show a transmittance of 85% only.

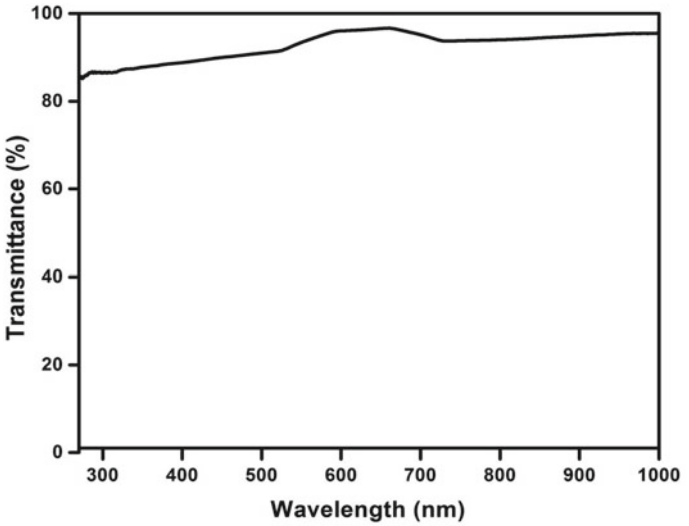

Fig. 2 Optical transmittance spectra of NiO thin film

4 Conclusions

Nickel oxide film deposited by RF sputtering technique has been investigated for their optical and structural properties. The thickness of the film deposited is calculated by Stylus profilometer. XRD reveals the crystalline nature while the transmittance is confirmed through UV–Vis–NIR spectrophotometer. The highest transmittance obtained remains a token of evidence for the material prepared to be used in electrochromic and optoelectronic device applications.

Acknowledgements Usha. K.S (one of the authors) is grateful for the financial support provided by DST, New Delhi, through Innovation in Science Pursuit for Inspired Research (INSPIRE).

References

1. Granqvist CG (1995) Handbook of Inorganic Electrochromic Materials, Elsevier, Amsterdam, the Netherlands.
2. Niklasson GA, Granqvist CG (2007), Electrochromics for smart windows: thin films of tungsten oxide and nickel oxide, and devices based on these J Mater Chem 17:127–156
3. Granqvist CG (2007) Transparent conductors as solar energy materials: a panoramic review. Solar Energy Mater Solar Cells 91(17):1529–1598
4. Demiryont H (1990), Electrochromics and potential automotive applications, Proc.SPIE 1323 (1) 171–187.
5. Agnihotry SA,. Saini KK, Chandra S (1986) Physics and technology of thin film electrochromic displays Indian J Pure Appl Phys. (24) 19–29.
6. Sbar N, Baddins M, Budziak R, Coprtez K, Laby L, Michalski L, Ngo T, Chulz S, Urbanik K (1999) Progress toward durable, cost effective electrochromic window glazings. Sol Energy Sol Cells 56:321–341
7. Wigginton M (1984) Glass in Architecture 24. Phaidon, London, p 221
8. Tamaki J, Fujii T, Fujimori K, Miura N, Yamazoe N (1995) Application of metal tungstate-carbonate composite to nitrogen oxides sensor operative at elevated temperature. Sensors and Actuators B 24(5):396–399
9. Stern DL, Grasselli RK (1997) Propane oxydehydrogenation over metal tungstates. J Catal 167(2):570–572
10. Yoshimura K, Miki T, Tanemuna S (1995) Nickel oxide electrochromic thin films prepared by reactive DC magnetron sputtering. Jpn J Appl Phys 34:2440–2446

Classification and Detection Techniques of Fault in Solar PV System: A Review

V. Mohanapriya, B. Sharmila, and V. Manimegalai

Abstract Nowadays, solar Photo-Voltaic (PV) system has become more significant than any other system for power generation. PV systems suffer from huge amount of power loss due to various faults that occurs in both internally and externally of the system. Faults are caused due to various factors and these faults must be identified and eliminated it as soon as possible, if it is not eliminated the faults are plunged throughout the system. It is essential to analysis fault in system in order to increase reliability, to extract maximum power (efficiency), and to provide a safety to the system. By comparing the measured V-I characteristics with actual characteristics, power loss can be calculated. A change in output voltage helps to estimate the number of faulty cells in PV system. By using various configuration method, fault in the solar photo voltaic system is detected and the location of faults are identified. This paper helps in analyzing the various faults types, causes and some of the method of fault detection in the PV system.

Keywords Classification · Detection · Faults · PV system·

1 Introduction

PV system provides/generates pollution free eco friendly power as it consists of monocrystalline silicon which converts light energy (energy from sunlight) in to electrical energy. PV fault may lead to adverse and deleterious situation, these faults cannot be easily identified or perceive [1]. Output voltage is based on the temperature and irradiance level of the PV system, even when fault is occurred the changes in

V. Mohanapriya (✉)
Bannari Amman Institute of Technology, Sathyamangalam 638401, Tamilnadu, India
e-mail: mohanapriyav@bitsathy.ac.in

B. Sharmila
Sri Ramakrishna Engineering College, Vattamalaipalaym, Coimbatore 64102, India

V. Manimegalai
Sri Krishna College of Technology, Coimbatore 641042, India

G. Kumaresan et al. (eds.), *Advances in Materials Research*, Springer Proceedings in Materials 5, https://doi.org/10.1007/978-981-15-8319-3_115

voltage level will be higher than normal voltage. Some faults like DC arc fault which occur due to various reason such as aging of component, rupture of cable and loose contact. This type of fault can be easily identified or located as it has its own characteristics [2]. Regular monitoring of voltage and current values is required while these values are compared with the maximum measured (during normal condition) voltage and current values to localize and identify the fault in the PV system [3]. Before protecting the PV system analysis of fault is fundamental task. Line to line fault are caused due to short circuit fault or double ground fault [4].

One of the major power losses in PV system is caused due to partial shading fault, hence it is necessary to identify the fault in order to maximize the efficiency of the system. It can be done by collected values of array current, voltages and irradiance [5]. High impedance fault is mainly due to unwanted contact of the system which should be detected, mathematical morphology is one type of method which is used to detect high impedance fault [6]. The faults in PV system are detected using various method one of such method is artificial neural network. With the output power during normal and faulty condition help to identify various types of fault with help of data collected during these faults [7]. This paper is completely based on the types of fault and how these faults are detected using various fault detection techniques.

2 Photovoltaic Module

2.1 Mathematical Modelling of Solar Cell

Single diode model is commonly used in solar modules [8]. Figure 1 shows the ideal and practical solar PV. In ideal PV cell there will be zero series and shunt resistance where as these resistance will be higher in the practical solar cell.

The output equation of the solar photo voltaic module is expressed as

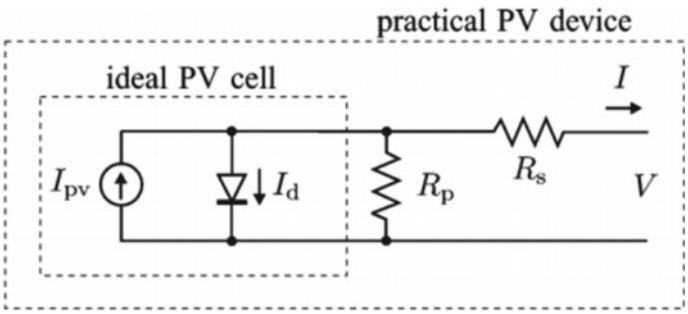

Fig. 1 Single diode diagram of PV cell and practical PV equivalent circuit

$$I = I_{pv} - I_o\left[\exp\left(\frac{V + RsI}{Vt \propto}\right) - 1\right] - \frac{V + RsI}{Rp} \quad (1)$$

Where

I_{pv} Photovoltaic current.
I_o Saturation current.
Vt Array thermal voltage.
Rs Array equivalent series resistance.
Rp Array equivalent parallel resistance.
$\propto$ Ideality constant of diode.

2.2 Characteristics of Solar Cell

The charcteristics of solar cell is represented by current versus voltage and power versus voltage. Figure 2 shows the VI and PV characteristics of ideal solar cell [8].

The MPP is the point at which maximum output power is obtained by PV panel or PV array. Below Vmpp the current is independent of output voltage, as voltage increases current starts to decrease. Isc and Voc are same in I-V characteristics of two individual PV modules, more power is produced when the array fill factor is higher.

3 Classification of Fault in PV System

The faults are caused both internally and externally. It includes DC side fault and AC side fault. Figure 3 shows the different types of faults.

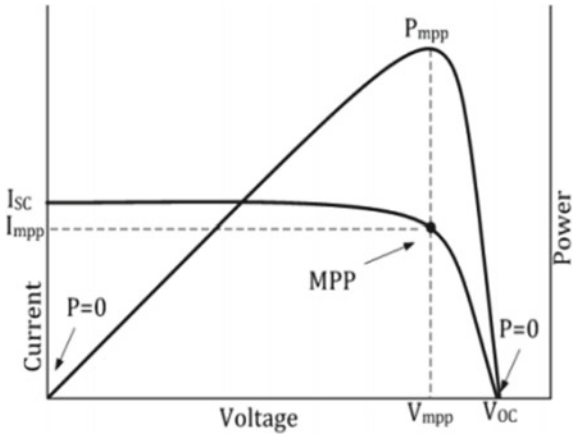

Fig. 2 characteristics of PV cell

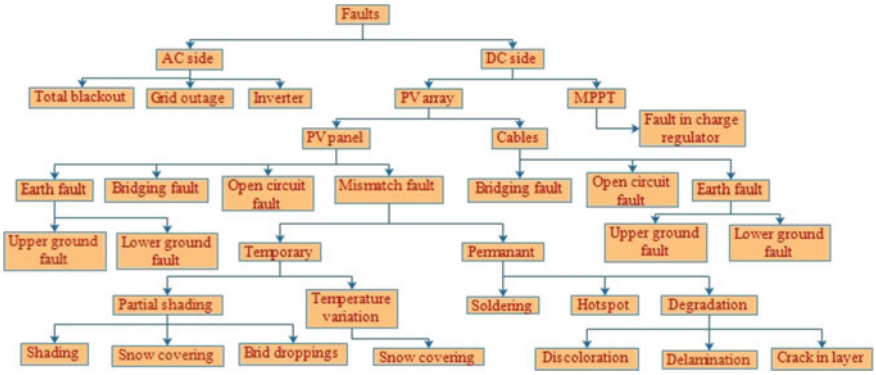

Fig. 3 Classification of faults PV system

3.1 DC Side Fault

The fault in DC side is divided into two major types: PV array fault and maximum power point tracking (MPPT) fault [9].

PV Array Fault

PV array fault further divided into two main groups PV panel fault and fault in cable. Main faults in PV array fault include bridging fault, ground fault, open circuit fault and mismatch fault [10].

Ground Fault and Bridging Fault

Large fault current causes ground fault which damage the entire system and lead to danger and it is most commonly occurred fault. Ground fault is a fault when there is a short circuiting between the conductor and ground [10]. Lower ground fault and upper ground fault are types of ground fault. In lower fault, the voltage will be higher than the half of the maximum output voltage. Upper ground fault will lead to large fault current [9]. Ground fault causes a drop in voltage and sudden changes in the characteristics of PV array system [11]. Cable insulation during installing, aging, corrosion, leakage of water are some causes of ground fault [12].

Bridging fault can be described as line to line fault, a low resistance between the two module points leads to bridging fault. Main reason for this type of fault is mainly due to insulation failure between the modules [9, 10]. This fault may occur between cables of different potential in an array. The term bridging describes only when the fault occurs between the two modules in a two different string. This fault reduces open circuit voltage, same short circuit is maintained or no change in short circuit current [11].

Open Circuit Fault and Mismatch Fault

Open circuit fault is due to the poor connection between the cell modules and also in current carrying paths, poor load connection and at breaker point. Main reason is destruction of interconnected wires [9, 10]. It reduces short circuit current but the open circuit voltage almost maintained constant. As short circuit current decreases maximum power obtained will also reduce [11].

Mismatch fault is one of the main reasons for major power loss as it changes the cells electrical parameters. Mismatch fault is either temporary or permanent fault. Temporary fault occur due to shading of cells caused by falling of shadows of trees, nearby buildings etc., [10]. Hot spot, degradation and soldering are the causes of permanent mismatch fault. Hotspot is produced when the operating current increases beyond short-circuit current inside the fault [9].

Partial Shading and By-Pass Diode Fault

Partial shading is a temporary mismatch fault. It due to covering of PV array cells due to high building, trees etc. The partial shading fault causes very high noisy frequency IV characteristics of PV array and hence produced decreased output power which results in hotspots [11]. Shading is a block in power flow. Shading is also due to overhead lines, if one panel in a array is shaded entire power flow is affected. As long as showdown is present in the PV array output power is reduced [10]. If fault occurs in smaller no of cells it is very difficult to detect, by pass diode are highly detachable during the fault because the effect of fault is easily visible in characteristics [13]. Shading is classified as shaded area of PV system: (1) from zero and keeps increasing, (2) zero to maximum values and return back zero, (3) maximum value during day and decreasing gradually and attains zero at some point of time [5].

By-pass diodes are connected parallel to the some solar cells in the PV module [11].By-pass diode fault is used to reduce the shading effect in PV string. If any shading occurs in a string diode in a string become forward biased. The current higher than the short circuit current flows through the diode and hence it reduces the hazards such as overheating [10]. Due to heating in an array lead to hotspots even fire or burn marks are produced. IV and PV characteristics of PV module changes during shading in a PV array, if diode is connected in parallel the changes do not occur in characteristics of PV array [11].

Arc Fault and MPPT Fault

Fault is due to the high electric charge flow between the conductors. Due to high discharge wire's insulation is damaged which leads to fire. Arcs ranges vary from few amperes to thousands of amperes. Types of arc fault include series arc fault, parallel arc fault [10]. Any intermittent connection in modules and even in solder joints produces arc faults. Arc lead to high frequency noise in string output voltage or current [11].

MPPT is mainly introduced in order to obtain maximum power in PV panels at any conditions/situations. If MPPT fails to extract maximum power there will be huge power loss in the system. Charge regulators are the reason for MPPT failure [9].

3.2 Fault in AC Side

In AC side grid outage and total blackout can be identified. If any fault occurs in inverter the DC output remains same only the AC output is reduced. With the output voltage from both DC and AC side it can be easily identified inverter is the only reason for power loss [9]. Various faults in PV array is shown in Fig. 4.

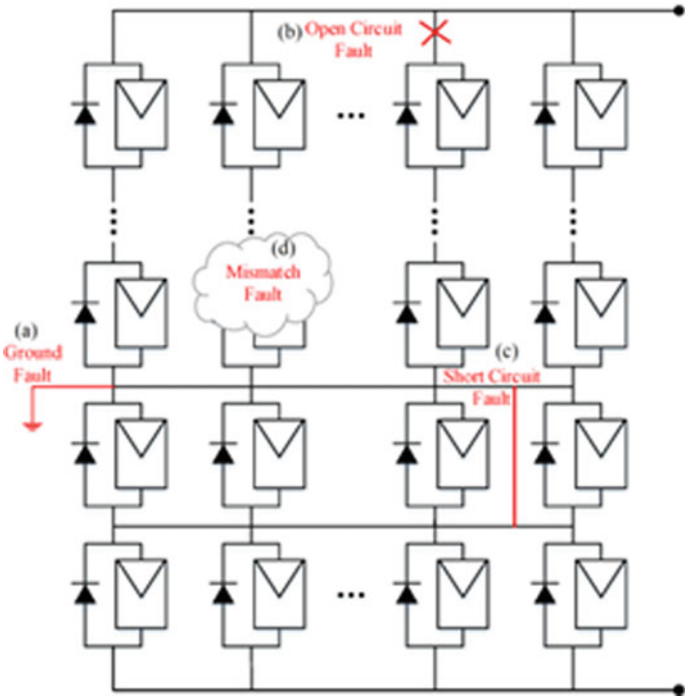

Fig. 4 Faults in solar array **a** ground fault **b** open circuit fault **c** short circuit fault **d** Mismatch fault

4 Fault Detection Method

There are various types of methods to detect above faults. It is required to detect the fault and it should be eliminated as soon as possible in order extract maximum power in the PV system.

4.1 Fault Diagnosis Method

It is novel method to detect fault in a system. Steps involved in fault diagnosis are as follows.

Step 1 Measured output power is compared to actual power output. If 13% or above 13% power loss is observed it is identified that there is a fault in a system.
Step 2 Irradiation at several points are measured if there is change in irradiation it is due to shading of cells or it is due to faults.
Step 3 open circuit voltage is observed whether the fault is occurred due to open circuit fault and number of cells are roughly estimated which causes open circuit fault.
Step 4 Fill Factor is calculated based n irradiance and temperature. With fill factor aging fault of PV panels can be determined [14].

Estimated values are compared with measured values and error residual vector. This vector is helpful to detect the faults in PV system or power converter. It is all programmed in Soc (System-of-Chip) system [15].

4.2 ARC Detection Based on Time, Frequency and Parallel Capacitor

If ARC fault is produced, there will be change in current and voltage. With help of characteristics of voltage and current arc fault can be identified [2].

Arc is a chaotic process, where it produces a high frequency noise in both current and voltage wave form. Amplitude of current is proportional to 1/f, as frequency increases current starts to decreases. If any low frequency is detected arc fault is produced [2].

Capacitors are paralleled with the PV system. Amplitude and polarities of Parallel capacitors are observed, DWT (Discrete Wavelet Transformation) is applied to current of capacitor [16]. For each fault polarities, spectrum and amplitude of current are different which is help full to detect fault [17].

4.3 SLIC and Thermal Images and SCADA Data

Simple Linear Iterative Clustering is a super pixel technique which is used to detect hotspot. With the infrared images of the solar array faults like hotspot can be detected. Working of solar cell at any condition can be identified with the help of thermal images. This is automatic fault detection method, it reduces time to detect fault and maximum efficiency is achieved [18] .

Supervisory control and data acquisition system technique is used to detect fault. SCADA include three main techniques are as follows: (1) statistical fault detection, (2) fault isolation using CPR ratio, (3) recoverability of faults by anomaly degree index. Over 90% accuracy of detection of fault is achieved using SCADA [19].

4.4 Fault Detection Through IV Curve and Optimized Fading

By comparing actual curve with the measured cure of the system, the deviation of measured curve shows the fault in the system [3]. Mismatch fault, partial shading, open circuit fault are some type of fault which can be detected with the help of IV curve. With the open circuit voltage, number of cells short-circuited may be identified by comparing actual open circuit voltage with measured voltage [20]. With IV characteristics six categories are identified/generated: normal operation, connection fault, shadow effect, partial shading, by-pass diode fault and group fault: cell, module, bypass-diode and connection [21].

Voltage sensor help to detect fault and to localize the shading part of cells quickly and accurately. Even the intensity of illumination of photovoltaic cells is forecasted online through this optimized fading technique. It simplifies the topology to detect fault [22].

5 SSTDR, Over Current Protection Devices and Mathematical Morphology

SSTDR is help full to detect arc fault but it cannot detect ground fault more accurately. Its advantages are: it detect fault even after sunset/absence of sunlight, it also detect future arc fault. It will not measure current and voltage of PV array system. It can trip due to inverter failure [12].

Over current protection device is mainly used to protect line to line fault. It also locates fault, measure fault impedance, irradiance level and blocking diodes. Even low irradiance fault, nigh-to-day fault are also detected [4]. Dual fusing and string level are identified using over current protection devices [23].

Mathematical morphology is used to detect fault mainly in AC system and arc detection. Mathematical morphology is a filtering technique is a successful method to detect fault in the PV system [6].

Line to line faults in solar PV system can be identified with help of IV curve (steady-state analysis) and also fault current evolution through MPPT (transient in time domain). Over current Protection devices are used to clear line to line fault, parallel capacitor can be used to detect the ARC fault. SSTDR are most popular method to detect fault in the solar PV system. For hotspot fault SLIC method is preferred.

6 Conclusion

This paper discuses fault types and detection technique of faults. Various methods are introduced to detect fault and differentiate it. Every method is discussed in short and which type of fault it can detect. Parallel capacitors are mainly used to detect arc fault, whereas SSTDR is also used to detect arc fault. SSTDR can also be used for line to line fault detection but it cannot provide accurate data. This review provides some fault detection techniques that are used to detect fault in a PV system. IV curve technique is used to detect fault such as mismatch fault and partial shading fault.

References

1. Stellbogen D (1993) Use of PV circuit simulation for fault detection in pv array fields, IEEE
2. Yongfei M, Jun Y, Libin Y, Chunlai L, Yanjiao H, Huabiao W, Canghai W, Xianmin W (2018) DC fault arc identification and detection analysis of photovoltaic power generation system. In: 2018 international conference and intelligent system
3. Alajmi M, Ikhlas A-Q (2016) Fault detection and localization in solar photovoltaic arrays using the current-voltage sensing framework. IEEE
4. Zhao Y, de Palma JF, Mosesian J, Lyons R, Lehman B (2013) Line–line fault analysis and protection challenges in solar photovoltaic arrays. IEEE Trans Indus Electron 60(9)
5. Hariharan R, Chakkarapani M, Saravana Ilango G, Nagamani C (2016) A method to detect photovoltaic array faults and partial shading in PV systems. IEEE Journal Photovoltaics 6(5)
6. Weerasekara M, Vilathgamuwa M, Mishra Y (2018) Detection of high impedance faults in PV systems using mathematical morphology, IEEE
7. Jenitha P, Immanuel Selvakumar A (2017) Fault detection in PV systems. Appl Solar Energy 53(3):229–237
8. Keshavani K, Joshi J, Trivedi V, Bhavsa M (2014) Modelling and simulation of photovoltaic array using Matlab/Simulink. IJEDR 2(4):2321–9939
9. Mano Raja Pau1 M, Mahalakshmi R, Karuppasamypandiyan M, Bhuvanesh A, Jai Ganesh R (2016) Classification and detection of faults in grid connected photovoltaic system. Int J Sci Eng Res 7(4). ISSN 2229-5518
10. Ghosh R, Das S, Panigrahi CK (2018) Classification of different types of faults in photovoltaic system. In: 2018 international conference on computation power, energy, information and communication (ICCPEIC)

11. Mawjood KA, Refaat SS, Morsi WG Detection and prediction of faults in photovoltaic arrays: a review, IEEE
12. Alam MK, Khan F, Johnson J, Flicker J (2015) A comprehensive review of catastrophic fault in PV arrays: types, etection, and mitigation techniques. IEEE J Photovoltaics 5(3)
13. Laamami S, Benhamed M, Sbita L (2017) Analysis of shading effect on a photovoltaic array. IEEE
14. Chen YH, Liang R, Tian Y, Wang F (2016) A novel fault diagnosis method of PV based on power loss and IV characteristics. In: 2016 international conference on new energy and future energy system (NEFES 2016)
15. Jain P, Xu JX, Panda SK, Poon J, Spanos C, Sanders SR (2016) Fault diagnosis via PV panel-integrated power electronics. IEEE
16. Xiong Q, Feng X, Gattozzi AL, Liu X, Yang H, Ji S, Zhu L, Hebner RE (2018) Arc fault detection and localization in photovoltaic system using parallel capacitor. IEEE
17. Xiong Q, Liu X, Feng X, Gattozzi AL, Shi Y, Zhu L, Ji S, Hebner, RE (2018) Arc fault detection and localization in photovoltaic systems using feature distribution maps of parallel capacitor currents. IEEE J Photovoltaics 8(4)
18. Alsafasfeh M, Abdel-Qader I, Bazuin B (2017) Fault detection in photovoltaic system using SLIC and thermal images. In: 2017 8th international conference on information technology (ICIT).
19. Dong A, Zhao Y, Liu X, Liu Q, Kang D (2017) Fault diagnosis and classification in photovoltaic system using SCADA data. In: 2017 international conference on sensing, diagnostics, prognostics, and control
20. Sarika S, Raoufi M, Bennouna A, benlarabi A, Ikken B (2018) Fault diagnosis in a photovoltaic system through IV characteristics analysis. In: The 9th international renewable energy congress (IREC 2018)
21. Chine W, Mellit A, Pavan A M, Lughi V (2015) Fault diagnosis in photovoltaic array. IEEE
22. Liao Z, Wang D, Ren J, Lin Z (2016) An optimized fading fault localization method applied in series-parallel photovoltaic array. In: 2016 international conference on smart grid and clean energy technologies
23. Albers MJ and Ball G (2015) Comparative evaluation of DC fault-mitigation techniques in large PV systems. IEEE J Photovoltaics 5(4)

Power Generation Enhancement Using Hybrid Thermoelectric Generator with Synthetic Oil-Based Nanofluids

V. George Samuel Raj, Godson Asirvatham Lazarus, Elangovan Daniel, Anitha Angeline Appadurai, and Stephen Manova

Abstract Power generation enhancement of hybrid thermoelectric generator (TEG) using the synthetic oil (Therminol 55) and a small volume concentration of Al_2O_3 nanoparticles (0.05 and 0.1%) is experimentally studied. The hot side of the hybrid TEG is varied from 150 to 380 °C and load resistance up to 2 ohms, respectively, while the cold side temperature is kept constant at 30 °C. The effect of hot side temperature and load resistance on the power generation is experimentally analyzed. The experimental results showed that the use of single hybrid TEG gave a power output of about 9.262 W with a temperature difference of 350 °C between hot and cold sides when using Therminol 55. By adding a small amount of Al_2O_3 nanoparticles to Therminol 55, the heat transfer capacity has increased and resulted in the enhancement of power output to 13.2 W for 0.05% concentration and 19.22 W for 0.1% concentration for the same temperature difference. Also, the use of nanoparticles resulted in increasing the efficiency of the hybrid TEG system. An enhancement of 2.65% is observed in the power output when nanoparticles suspended synthetic oil and used as the hot side fluid.

Keywords Hybrid thermoelectric generator · Nanofluid · Load resistance · Synthetic oil · Therminol 55 · Power output

1 Introduction

Consumption of fossil fuels by human activities leads to serious environmental problems. As a consequence, climate change, ozone layer depletion, greenhouse gas emission, global warming, and acid rain terminologies have started to appear commonly

V. George Samuel Raj · G. Asirvatham Lazarus (✉) · E. Daniel · S. Manova
Department of Mechanical Engineering, Karunya Institute of Technology and Sciences, Coimbatore, Tamilnadu 641114, India
e-mail: godson@karunya.edu

A. Angeline Appadurai
Department of Electrical and Electronics Engineering, Karunya Institute of Technology and Sciences, Coimbatore, Tamilnadu 641114, India

G. Kumaresan et al. (eds.), *Advances in Materials Research*, Springer Proceedings in Materials 5, https://doi.org/10.1007/978-981-15-8319-3_116

in the literature. To reduce the effect of the above-mentioned disasters, the thermoelectric (TE) energy converters are proposed as one possible method which gains popularity as it has an ability to convert exhaust heat from vehicles, electrical equipments, etc., into the electricity. 85% of world's energy are non-renewable energy resources in which 68% of fossil fuels are used in the generation of electric power [1].Institute of Sustainable Energy Policies predicted that only 33% of non-renewable energy will exist for power generation in the year of 2050, whereas 67% will be substituted by renewable energy [2]. Thermoelectric generators which are semiconductor devices converts heat energy into electrical energy [3]. Payal et al. [4] stated that the TEG module conveys 1.7 W of intensity, when hot side temperature was maintained at 75 °C and cool side at 30 °C which is likeness about 1.4% of effectiveness on a normal temperature contrast of 60 °C. The nanoheat transfer fluid comprising Al_2O_3-Therminol 55 of volumetric proportions ranging from 0.025 vol% to 0.3 vol% have been characterized and evaluated as directly solar absorbing working fluid. Muraleedharan et al. [5] experimented and found that the thermal efficiency of the solar collector has been increased with the nanoparticles attaining a maximum of 62% for 0.1% vol concentration. Quasim et al. [6] reviewed that in automobile field the maximum efficiency achieved by TEG is 5% and TEG which is made up of Bi_2Te_3 is used automobile industry. Changwei et al. [7] experimentally found that the efficiency of the TEG system reached 4.5% with a temperature difference of 65 °C, and in this study, the cost of the TEG system is low when compared to wind power system and PV and experimentally connected 600 thermoelectric modules in series with a temperature difference of 120 °C and the power reached 1 kW. Jun et al. [8] conducted experiments in multi-stage thermoelectric module ($PbTe/Bi_2Te_3$) which resulted in 9.5% maximum efficiency in the temperature range from 303 to 923 K. Shiho Kim [9] derived an analytical model for the description of interior temperature difference as a function of the load current of a TEG. Godson et al. [10] stated that the nanofluids have substantial capacity to enhance heat transfer.

Thermoelectric generation technology which is a solid-state energy conversion method can transform thermal energy into electricity by using thermoelectric transformation materials. A thermoelectric generator has some advantages such as no moving parts, compact size, and highly reliable. Thus, this system can be simplified and functioned over a prolonged period of time with less maintenance cost. Moreover, it has a wider choice of thermal sources that utilize both the high and low-quality heat to generate electricity.

2 Experimental Method

2.1 Preparation of Nanofluids

Two-step method is used to prepare Therminol 55 - Al_2O_3 nanofluid. The average size of Al_2O_3 nanoparticle is noted to be less than 50 nm. The Al_2O_3 nanoparticle was

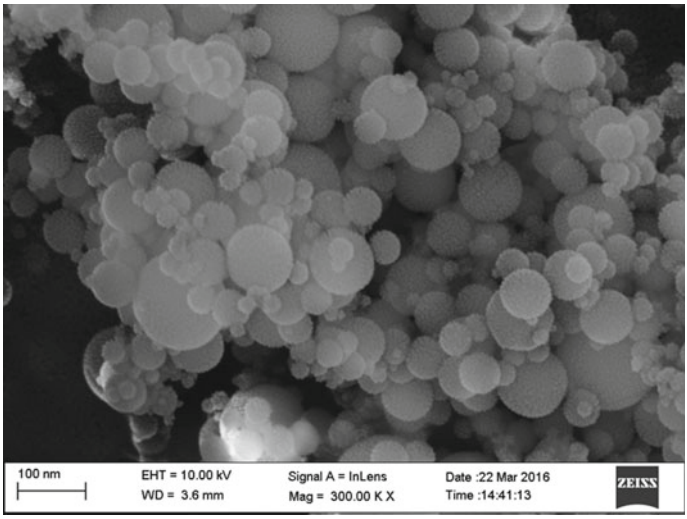

Fig. 1 SEM image of Al_2O_3 nanoparticle

distinguished by scanning electron microscope (SEM, JSM 6390, JEOL, USA) to study the particle size and shape. Figure 1 shows SEM image of Al_2O_3 nanoparticle taken at 300X magnification. To stabilize the Al_2O_3 nanoparticles in the base fluid, required quantity (5% of each volume concentration) of surfactant Sodium dodecyl benzene sulfonate (SDBS) is added.

Initially, the surfactant is dispersed in to Therminol 55 and then required quantity of Al_2O_3 nanoparticles is added. Ultrasonic vibrator (Model: UP400S, Hielscher Ultrasound technology, Germany) is used to homogenize the mixture for 30 min to separate the agglomerates of Al_2O_3 nanoparticles. Therminol 55–Al_2O_3 nanofluid was prepared with the volume concentrations of Al_2O_3 at 0.05% and 0.1% for different samples.

2.2 Experimental Setup

The performance of the thermoelectric generator is experimentally studied in detail by developing a test rig which is shown in Fig. 2. The components of test rig include hybrid TEG, heat exchanger, heater, heat sink, electric load, and data acquisition unit. The hybrid thermoelectric generator (TEG) is placed between the two-copper block. One of the copper blocks is fitted with cartridge heater with the capacity of 400 W to supply heat to hot side of TEG, and another copper block which acts as a heat exchanger is placed on the cold side of TEG with water circulating inside the copper block. The heater is connected to the variac and varied for different watts. A rheostat is connected to the hybrid TEG as an external load is to compute the output current

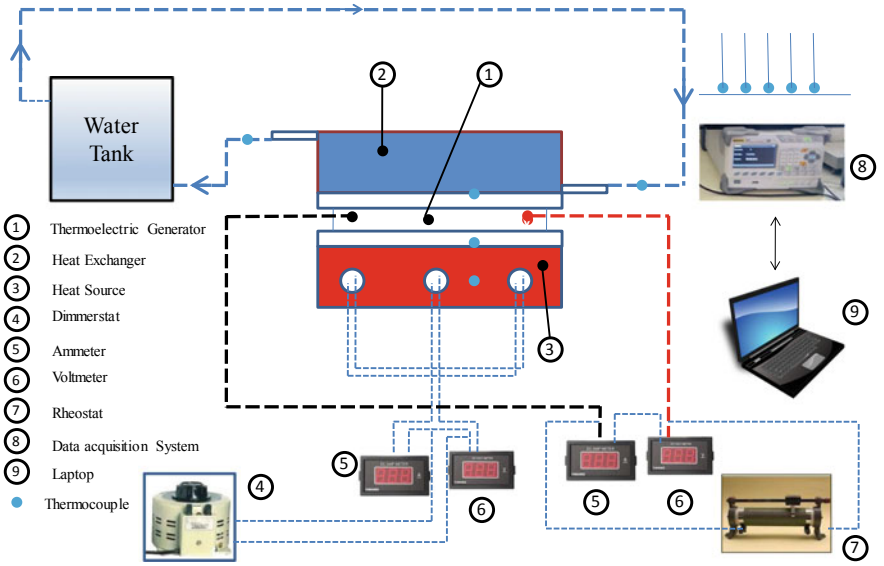

Fig. 2 Experimental test rig

and voltage through DC voltmeter and ammeter to obtain the power of the hybrid TEG, and the time is noted down and the load resistance is varied correspondingly for different temperature difference. Thermocouple of type-T (micro) is used for tracking the temperature of hot and cold side of hybrid TEG, heater temperature, and water inlet and water outlet temperature of the copper block placed on the cold side of hybrid TEG. Insulation is done using glass wool so that no heat goes to the surrounding.

2.3 Calculation for Efficiency

The efficiency of the thermoelectric module for power generation (η) is calculated from the thermoelectric generator efficiency using Eq. (1) where η is the thermoelectric module efficiency, P_{out} is the output power, Q_{in} is the heat load

$$\eta = P_{\text{out}}/Q_{\text{in}} \tag{1}$$

The output power P is calculated as the product of output voltage and current as given in Eq. (2)

$$P_{\text{out}} = V\text{X}I \tag{2}$$

3 Results and Discussions

3.1 Viscosity of Therminol 55—Al_2O_3 Nanofluids

Figure 3 shows the viscosity variation with respect to temperature for various volume concentrations. It can be clearly noted that when the volume concentration is increased, there is an increase in viscosity of Therminol 55/Al_2O_3 nanofluid. However, viscosity decreases for increase in temperature. The viscosity of the Therminol 55/Al_2O_3 nanofluid at 30 and 70 °C is 37.89 and 12.43 m Pa S, respectively, for 0.1% volume concentration with an increase of 21.9% and 54.06% when compared with that of Therminol 55. The main reason for increase in viscosity is the addition of the nanoparticles which increases the fluid friction and flow resistance [11]. The viscosity is measured using the Brookfield digital viscometer (DV-E, Brookfield, USA).

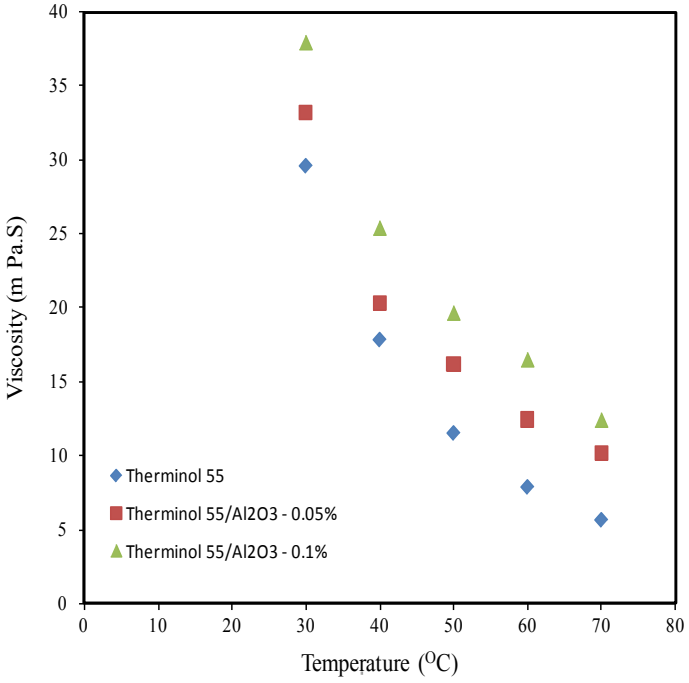

Fig. 3 Variation in viscosity with temperature for Therminol 55/Al_2O_3 nanofluid

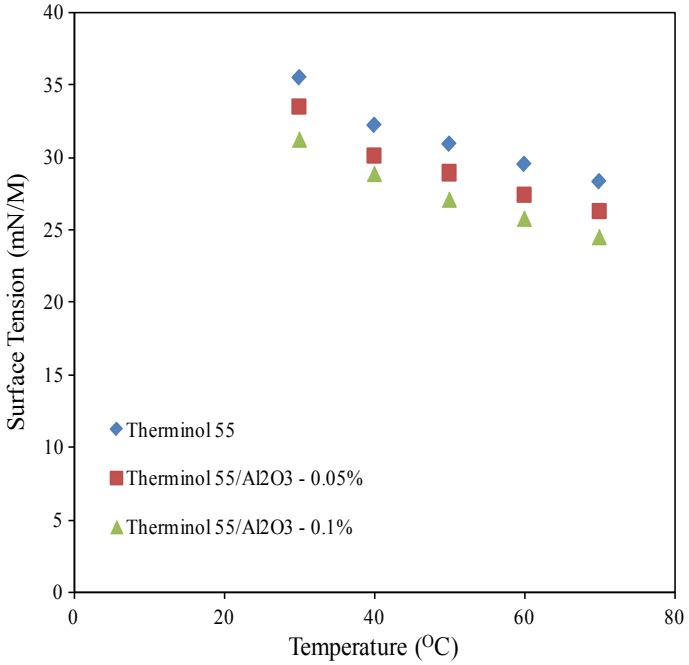

Fig. 4 Variation in surface tension with temperature for Therminol 55/Al_2O_3 nanofluid

3.2 *Surface Tension of Therminol 55—Al_2O_3 Nanofluids*

Figure 4 shows the comparison of surface tension with temperature for two different volume concentrations. It can be noted that the surface tension decreases when both the temperature and volume concentration of Therminol 55/Al_2O_3 nanofluid increases. The surface tension of the Therminol 55/Al_2O_3 nanofluid at 30 °C and 70 °C is 31.28 and 24.52 mN/M, respectively, for 0.1% volume concentration, with a decrease of 13.81% and 15.82% when compared to Therminol 55. The inter-attractive forces of molecules weaken when the temperature is increased, resulting in a lower surface tension [11]. The measurement of surface tension was done by SITA dynotester (SITA Process Solutions, Germany).

3.3 *Thermal Conductivity of Therminol 55—Al_2O_3 Nanofluids*

Figure 5 shows the comparison of thermal conductivity with temperature for various volume concentrations. It is clearly noted that the thermal conductivity of the working fluid decreases with an increase in both volume concentration and also for the base

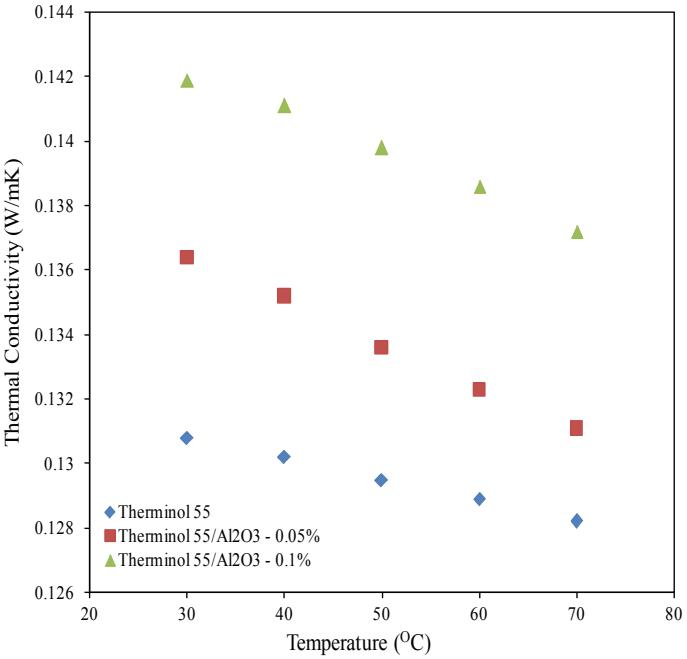

Fig. 5 Variation in thermal conductivity with temperature for Therminol 55/Al_2O_3 nanofluid

fluid. The values of thermal conductivity of the Therminol 55/Al_2O_3 nanofluid at 30 °C and 70 °C are 0.1419 W/m K and 0.1372 W/m K, respectively for 0.1% volume concentration, which is lower by 7.82 and 6.55% when compared with that of Therminol 55.

As the temperature increases, the solid nanoparticles experience a random motion and this movement obstructs transport of heat through liquids. Thus, with increase in temperature, the thermal conductivity of liquids decreases. The measurement of thermal conductivity was done by KD2 Pro (Decagon Devices, USA).

3.4 Temperature Difference and Power of Therminol 55—Al_2O_3 Nanofluids

Figure 6 shows variation in power generation with temperature difference of thermoelectric generator for various volume concentrations Therminol 55/Al_2O_3 nanofluid and is compared with Therminol 55. The highest temperature difference of TEG is noted for Therminol 55/Al_2O_3 nanofluid, whereas lowest value is noted for Therminol 55 (base fluid). In addition, increase in temperature difference enhances the power generation of TEG and 30% enhancement is noted when compared to the base

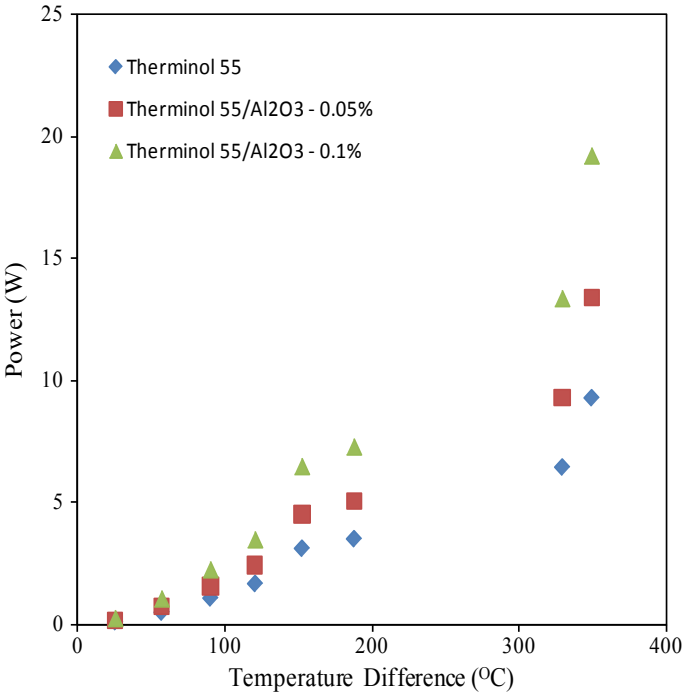

Fig. 6 Variation in power with temperature difference for Therminol 55/Al_2O_3 nanofluid

fluid. The output power obtained for Therminol 55/Al_2O_3 nanofluid for $\Delta T = 25$ °C and $\Delta T = 350$ °C is 0.25 W and 19.22 W, respectively, for 0.1% volume concentration. When nanoparticles are suspended in the base fluid, the heat absorbing capacity increases as thermal conductivity of Al_2O_3 nanoparticles is high. Thus, increase in thermal conductivity of nanofluid.

3.5 Temperature Difference and Efficiency of Therminol 55—Al_2O_3 Nanofluids

Figure 7 shows the variation in thermal efficiency of the system for the base fluid and Therminol 55/Al_2O_3 nanofluid with temperature difference of TEG. Increase in thermal efficiency is noted when the temperature difference increases. Volume concentration of 0.1% results in maximum thermal efficiency when compared to other concentration and the base fluid.

The highest thermal efficiency is noted to be 2.36% for the maximum temperature difference of 350 °C. The addition of nanoparticles in the base fluid increases the heat transfer rate and thus enhancing the thermal efficiency of the proposed system.

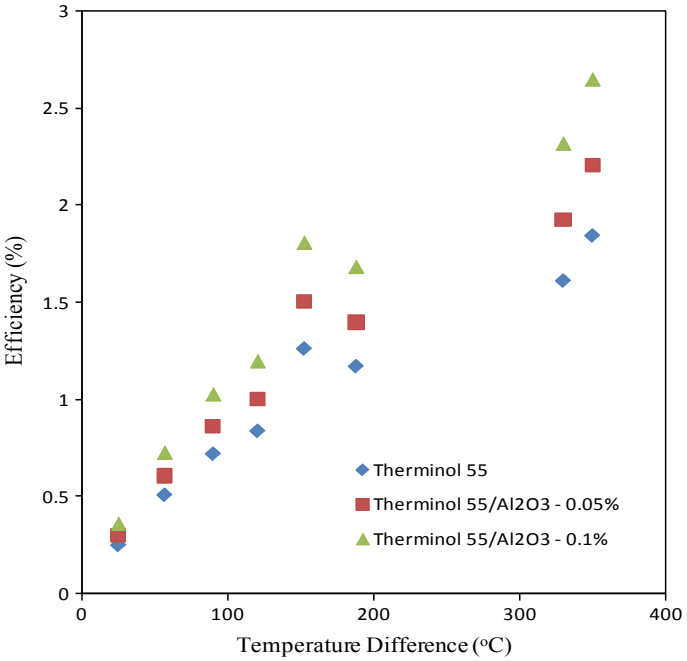

Fig. 7 Variation in efficiency with temperature difference for Therminol 55/Al_2O_3 nanofluid

Moreover, the insulation using glass wool is done to ensure that no heat loss occurs to the surrounding. Thus, reducing the heat loss to the ambient increases the thermal efficiency.

4 Conclusions

According to the current study, the following preliminary conclusions may be drawn:

(1) Electricity has been produced using Hybrid TEG module and tested. The power could reach about 9.262 W with a temperature difference of about 350°C between hot and cold sides for Therminol 55.
(2) By adding Al_2O_3 nanoparticles to the Therminol 55, the heat transfer capacity has increased and resulted in increase in power and efficiency for 0.05% and 0.1% volume concentration.
(3) The efficiency of the TEG system reached 2.2% and the power produced is about 13.2 W for 0.05% concentration and temperature difference of 350 °C.
(4) The efficiency of the TEG system reached 2.65% and the power produced is about 19.22 W for 0.1% concentration and temperature difference of 350 °C.

Acknowledgements The authors thankfully acknowledge the funding agency Department of Science and Technology (DST), Science and Engineering Research Board (SERB), (SB/FTP/ETA-362/2012), India, for providing the financial support. Also, the authors would like to thank Mr. Jayaseelan R of Karunya Institute of Technology and Sciences for helping in the fabrication of the experimental test facility.

References

1. Omer AM (2008) Energy, environment and sustainable development. Renew Sustain Energy Rev 12:2265–2300
2. Chan M (2009) Cutting carbon, improving health. Lancet 374:1870–1871
3. Peter AJD, Balaji D, Gowrishankar D (2013) Waste heat energy harvesting using thermoelectric generator, IOSR. J Eng 3:1–4
4. Ghusalikar PN, Landge KS, Raut PV Power generation from exhaust gas and engine heat using TEG. Int Res J Eng Technol (IRJET) 06(01). e-ISSN: 2395–0056
5. Liu C, Chen P, Li K (2014) A 1 kW low-temperature thermoelectric generator for low temperature geothermal resources. In: Proceedings, 39th workshop on geothermal reservoir engineering, Stanford University, Stanford, California
6. Khan MQ, Malarmannan S, Manikandaraja G (2018) Power generation from waste heat of vehicle exhaust using thermo electric generator: a review. IOP Conf Series Mater Sci Eng 402:012174
7. Liu C, Chen P, Li K (2015) A 1 kW thermoelectric generator for low-temperature geothermal resources. In: Proceedings world geothermal congress 2015, Melbourne, Australia
8. Pei J, Li LiangLiang, Liu DaWei, BoPing Zhang Yu, Xiao JL (2019) Science China Technological Sciences 62(9):1596–1604
9. Kim S (2013) Analysis and modeling of effective temperature differences and electrical parameters of thermoelectric generators. Appl Energy 102:1458–1463
10. Lazarus Godson B, Raja DM, Lal SW (2010) Enhancement of heat transfer using nanofluids—An overview. Renew Sustain Energy Rev 14:629–641
11. Ahammed N, Asirvatham LG, Wongwises S (2016) Effect of volume concentration and temperature on viscosity and surface tension of graphene–water nanofluid for heat transfer applications. J Therm Anal Calorim 123:1399–1409

Performance Analysis of Automobile Radiator Using Tungsten Trioxide Nano-Fluid

J. Vinoth Kumar, A. Amarkarthik, T. Santhosh, R. Solomon Allenjudah, and U. Sundreswaran

Abstract Conventional fluids (water and ethylene glycol) heat transfer performance results to be poor when incorporated with automobile radiator. An experimental study was performed to investigate the performance of automobile radiator using water and WO_3nanofluid as operational fluids. Analysis and comparison were carried out for heat transfer rate and outlet temperature of fluid for various flow rate ranging from 0.2m^3/hr. to 0.5 m^3/hr. Preparation of nanofluid was done for water with 0.0167%, 0.034%, and 0.0667% volume concentration of WO_3nanoparticle. The inlet condition of fluid was set at 50 ˚C as the impact for variation of temperature conditions on system performance was minimal. On experimentation, maximum increase in heat transfer rate was by 4.18% on comparison with base fluid.

Keywords Nanofluid · Radiator · Heat transfer rate · WO_3 · Performance

1 Introduction

Heat dissipation using conventional coolant fluid is employed in most of the engineering systems. At present, nanofluids (base fluid dispersed with nanoparticle) outperform significantly in most of the heat transfer systems. Enough precaution needs to be carried out to prevent fouling, sedimentation, and increase of pressure drop. To increase the performance of the heat transfer system needs either increase in size of the system or increase in the performance of cooling fluid. Due to the structural constraint, it is good for increasing the performance of the coolant.

Peyghambarzadehet al. [1] investigated the performance of radiator using Al_2O_3/waternanofluid for flow rate range 2–5 lit/min and coolant inlet temperature range 37–49 ˚C. They concluded an increase of 45% in heat transfer rate for 1% volume concentration nanofluid on comparison with water and minimal effect on performance for variation in inlet temperature of coolant. Sharma[2] conducted

J. Vinoth Kumar (✉) · A. Amarkarthik · T. Santhosh · R. Solomon Allenjudah · U. Sundreswaran
Department of Mechanical Engineering, Bannari Amman Institute of Technology-Sathyamangalam, Erode, Tamilnadu 638401, India
e-mail: vinothmech1809@gmail.com

G. Kumaresan et al. (eds.), *Advances in Materials Research*, Springer Proceedings in Materials 5, https://doi.org/10.1007/978-981-15-8319-3_117

experimental study on radiator using Al/water nanofluid of 0.2% vol. con. and 0.3 vol. con. with inlet coolant fluid temperature range from 45—55°°C.They resulted with 23.563% increase in heat transfer coefficient for 0.3% vol. con. Selvam et al. [3] summarized the enhancement of Nusselt number for 0.5% vol. con. GnP/ (water/EG) nanofluid by about 88% at 35 °°C and 90% at 40° °°C.

Oliveira et al. [4] studied the application of multi-walled carbon nanotube (MWCNT)/water of 0.05–0.16 wt. % in automotive radiator for coolant inlet temperature range 50°C-80°C and resulted in 17% decrement in heat transfer for 0.16 wt % nanofluid. Ali et al. [5] investigated the performance of radiator using ZnO/water nanofluid of 0.01–0.3% vol. con. for inlet temperature 45° C-55° C and concluded with an enhancement of 46.5% by using 0.2% vol. con. nanofluid. Ali et al. [6] conducted experimental study on radiator using 0.06, 0.09, and 0.12 vol. % MgO/water nanofluid and resulted with 31% increase in heat transfer rate for 0.12 vol. %. Naraki et al. [7] studied the application of CuO/water nanofluid of 0.04–0.4 vol. % and resulted in 8% enhancement in overall heat transfer coefficient for 0.4 vol. % nanofluid.

Hussain et al. [8] investigated the performance of radiator using SiO_2/water nanofluid of 1–2.5% vol. con. for inlet temperature 60°C-80°C and coolant flow rate of 2–8 lit/min.They concluded with an enhancement of 46% by using 2.5% vol. con. nanofluid. Ahmed et al. [9] conducted experimental study on radiator using TiO_2/water nanofluid of 0.1% vol. con., 0.2% vol. con. and 0.3 vol. con. with inlet coolant fluid temperature range from 20°C-80°C and found maximum overall heat transfer coefficient of 2050 W/m^{2}K 23.563 for 0.3% vol. con.

Palaniapan et al. [10] studied the application of fly ash nanofluid of about 2% vol.con. in automotive radiator for Reynolds number range 4000–8000 and resulted in 43.7% increase in heat transfer at Reynolds number 8000 and 2% vol.con. nanofluid. From the literature, there is no study for automobile radiator using tungsten trioxide nanofluid. Tungsten trioxide nanoparticles are a category of semiconductors that are broadly used in photothermal systems, based on the awareness of the authors; this type of particles has not been castoff yet in automobile radiator as the additive to working fluid. Hence, the current paper targets to analyze the result of using WO3/water nanofluids at various concentrations on the performance of radiator.

2 Analysis of Heat Transfer Rate

2.1 Analysis of Energy

Calculation of heat transfer rate in radiator is obtained by using Eqs. (1) and (2)

$$Q = \dot{m} c_p (T_i - T_0) \tag{1}$$

$$Q = hA(T_b - T_w) \tag{2}$$

The nanofluid's specific heat capacity can be calculated by using Eq. (3) [11]

$$c_{p,nf} = \frac{(1-\varphi)\rho_{bf} c_{p,bf} + \varphi\rho_n c_{p,n}}{(1-\varphi)\rho_{bf} + \varphi\rho_n} \tag{3}$$

The density of nanofluid is calculated from Eq. (4) [11]

$$\rho_{nf} = (1-\varphi)\rho_{bf} + \varphi\rho_n \tag{4}$$

The thermal conductivity of nanofluid is calculated from Eq. (5) [11]

$$k_{nf} = \frac{k_p + (n-1)k_{bf} - \varphi(n-1)(k_{bf} - k_p)}{k_p + (n-1)k_{bf} + \varphi(n-1)(k_{bf} - k_p)} \tag{5}$$

The viscosity of nanofluid is calculated from Eq. (6) [12]

$$\mu_{nf} = \mu_{bf}(1 + 2.5\varphi) \tag{6}$$

The Nusselt number for the entire radiator can be calculated Eq. (7) [13]

$$Nu_{exp} = \frac{h_{exp} x D_h}{k} \tag{7}$$

3 Preparation of Nanofluid and Experimentation

3.1 WO_3 Nanofluid Synthesis

Without extra processing and of diagnostic grade, all chemicals substances were used as received. Supplier of WO_3 nanoparticle: Nano Research labs, Jharkhand, India. The size of nanoparticle is of the range 40–50 nm and 99.9% purity. Due to the ease in preparation, nanofluid is prepared using two-step method. Initially, grinding of WO_3 nanoparticles is done by means of a mortar to prevent or minimize agglomeration. Later, addition of WO_3 nanoparticles with the distilled water by appropriate mass fraction and the mixture is manually agitated for minimal period of 10 min. The prepared mixture is placed in the ultrasonic bath (ANALAB, India) under sonication with a frequency of 30 kHz, 1000 watts power for a period of 4 h. Three different nanofluids of 0.0166%, 0.0334%, and 0.06667% volume concentration are prepared. Finally, stability testing of nanofluid is carried out using Zeta potential analyzer.

Table 1 Radiator specifications

S. No	Parameter	Value (cm)
1	Radiator length	38.4
2	Radiator width	33
3	Radiator height	2.2
4	Width of the radiator tube	0.2
5	Fin length	1
6	Distance between adjacent fins	0.1
7	Fin thickness	0.008

Table 2 Experiment test condition

Parameter	Water-based nanofluid
Nanoparticle concentration (vol %)	0–0.0667%
Nanoparticle	WO_3
Inlet temperature (K)	323
Volumetric flow rate (m^3/hr)	0.2 to 0.5
Reynolds number	200–600

3.2 Experimentation

The experimental setup comprises an automobile radiator with a fan, reservoir, connectors, rotameter, pump, thermometers, heater, small fuses, tubes, and expansion resource. Also, a thermometer has been used to measure air input temperature, air output temperatures, coolant inlet temperature, coolant output temperature, front surface temperature, and rear surface temperatures of the radiator. The experiment was conducted in Government College of Engineering, Salem, India. The circulation of operational fluid into the radiator is done through pump (500 W).On circulation, the working fluid enters the radiator initially and then it arrives a tank of 20 L capacity and continues the process. The constant temperature bath is utilized to cool the gain of heat obtained from solar collector. Flow rate adjustment with three-way valve, rotameter for desired flow rate upto 4 l/min, and pressure indicator for water and nanofluid. Radiator specification and test condition for experimentation are shown in Tables 1 and 2.Schematic layout of experiment apparatus is shown in Fig. 1.

4 Results and Discussion

In this study, the experimentation is carried out using WO3 nanofluid with concentrations 0.0167, 0.0334, and 0.0667 vol. % for various flow rates of 0.2, 0.3, 0.4, and 0.5 m^3/hr. as the working fluids. From Fig. 3, it depicts increase of heat transfer rate with the increase in flow rate and nanoparticle concentrations. Increase in heat

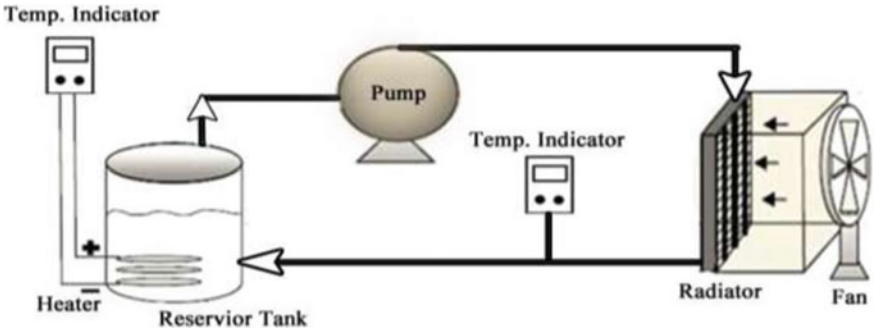

Fig. 1 Schematic layout of experiment apparatus

transfer coefficient is resulted at high flowrates due to mixing fluctuation produced by the effect of dispersion and chaotic movement of the nanoparticles. Increase in heat transfer was found with increase in volume concentration of nanoparticle addition with base fluid. Figure 2 shows radiator outlet temperatures, Tout, as a function of fluid volume flow rate circulating in the radiator. It can be observed that the accumulation nanoparticles to base fluid tend to reduce radiator outlet temperature. It can be concluded as for the equal mass flow rate in a heat transfer system tends to reduce fluid outlet temperature, thus enabling improvement in thermal performance of the radiator. Figure 3 also displays depreciation in heat transfer rate for rise in the volume flow rate passed through the system. The reason would be due to rise in fluid velocity impacted by the raise in volume flow rate. Thus, the coolant would have minimal duration for relating to air circulated through fan and results in rise of the exit temperature of coolant.

Figure 3 illustrates that the heat transfer enhancement in radiator is obtained due to the use nanofluids instead of base fluid. It can be perceived that ratio of heat transfer by nanofluid to base fluid increases with volume flow rate irrespective of nanofluid concentrations. In addition, the impact of volume flow rate is insignificant at higher concentration nanofluid. Also, Fig. 3 displays that for an addition of 0.0667 vol. % WO_3 nanoparticle to water mixture, the heat transfer rate was found to increase by 4.18% on comparison with the heat transfer rate on using water. Moreover, many suggestions by the researcher on enhancement of heat transfer due to the significant factor Brownian motion is detailed.

Finally, the replacement of conventional cooling fluid by nanofluid in car radiators would increase heat transfer rate. An increased heat transfer rate is depicted on addition of nanoparticle with the base fluid on using with the radiator. Thus, it results in possibility of reduction in the radiator size as well as reduced weight. So an improved fuel economy and reduced emission to environment would be achieved.

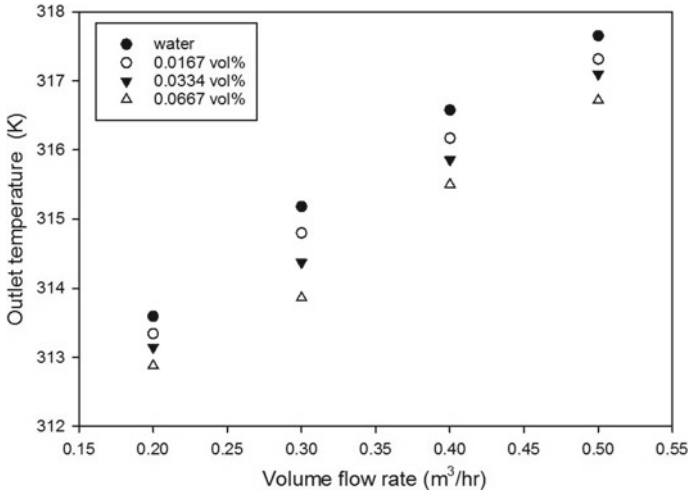

Fig. 2 Outlet temperature of coolant fluid based on variation of volume flow rate

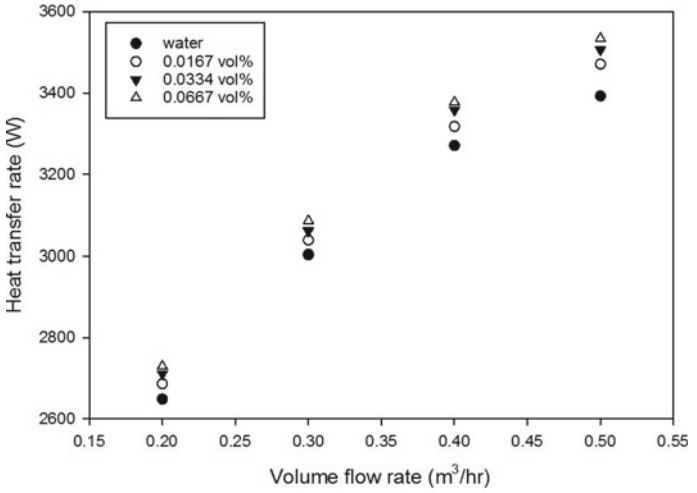

Fig. 3 Heat transfer rate of coolant fluid based on variation of volume flow rate

5 Conclusions

In this study, the impacts of WO_3/water nanofluids in an automobile radiator were explored. In comparison with base fluid, heat transfer rates were enhanced significantly for the usage of (WO_3/water) nanofluid in comparison with the base fluid. In the best condition, the maximum enhancement in heat transfer rate was obtained to be 4.18% for 0.067 vol. % of (WO_3/water) nanofluid. The experimental results

showed that heat transfer rate improved with the rise in flow rate of nanofluid. Also, the increase in volume concentration increased the heat transfer rate. The outcome specifies that using nanofluids can surge the heat transfer rate. Hence, providing hopeful means for scientists to improve extremely compact and effective automotive radiators. Weight reduction of radiator in turn reduces the consumption of fuel. Moreover, it can offer effective heat transfer and maximizes the lifespan of sections of a vehicle.

References

1. Peyghambarzadeh SM, Hashemabadi SH, Jamnani MS, Hoseini SM (2011) Improving the cooling performance of automobile radiator with Al_2O_3/water nanofluid, Appl Therm Eng 1833–1838. https://doi.org/10.1016/j.applthermaleng.2011.02.029
2. Sharma S (2018) Fabricating an experimental setup to investigate the performance of an automobile car radiator by using aluminum/water nanofluid. J Therm Anal Calorim 9. https://doi.org/10.1007/s10973-018-7224-9
3. Selvam C, Lal DM, Harish S (2017) Enhanced heat transfer performance of an automobile radiator with graphene based suspensions. Appl Therm Eng 123:50–60. https://doi.org/10.1016/j.applthermaleng.2017.05.076
4. Oliveira GA, Cardenas Contreras EA, Bandarra Filho EP (2017) Experimental study on the heat transfer of MWCNT/water nanofluid flowing in a car radiator. Appl Therm Eng 111:1450–1456. https://doi.org/10.1016/j.applthermaleng.2016.05.086
5. Ali HM, Ali H, Liaquat H, Bin Maqsood HT, Nadir MA (2015) Experimental investigation of convective heat transfer augmentation for car radiator using ZnO-water nanofluids. Energy 84:317–324. https://doi.org/10.1016/j.energy.2015.02.103
6. Ali H, Azhar M, Saleem M, Saeed Q, Saieed A (2015) Heat transfer enhancement of car radiator using aqua based magnesium oxide nanofluids. Therm Sci 19:2039–2048. https://doi.org/10.2298/TSCI150526130A
7. Naraki M, Peyghambarzadeh SM, Hashemabadi SH, Vermahmoudi Y (2013) Parametric study of overall heat transfer coefficient of CuO/water nanofluids in a car radiator. Int J Therm Sci 66:82–90. https://doi.org/10.1016/j.ijthermalsci.2012.11.013
8. Hussein AM, Bakar RA, Kadirgama K (2014) Case Studies in Thermal Engineering Study of forced convection nanofluid heat transfer in the automotive cooling system Case Stud. Therm Eng 2:50–61. https://doi.org/10.1016/j.csite.2013.12.001
9. Ahmed SA,Ozkaymak M, Sözen A, Menlik T, Fahed A (2018) Improving car radiator performance by using TiO_2-water nanofluid. Eng Sci Technol Int J 996–1005https://doi.org/10.1016/j.jestch.2018.07.008.
10. Palaniappan B, Ramasamy V (2018) Thermodynamic analysis of fly ash nanofluid for automobile (heavy vehicle) radiators. J Therm Anal Calorim. https://doi.org/10.1007/s10973-018-7844-0.
11. Devireddy S, Mekala CSR, Veeredhi VR (2016) Improving the cooling performance of automobile radiator with ethylene glycol water based TiO_2 nanofluids
12. Bejan AE (1988) Thermodynamics. Wiley Interscience, New York
13. Bejan (1995) Entropy generation minimization: the method of thermodynamic optimization of finite-size systems and finite-time processes. CRC Press, Boca Ratonm New York

Experimental Investigation on Corrosion Behaviour of Aluminium Alloy Nanoparticles Composite Material

K. Ramachandra Raju, G. Senthilkumar, Y. Arivu, T. Santhosh, T. Prasanth, and R. Pradeep

Abstract In this paper, the investigation on corrosion characteristics of aluminium alloy of standard A356 with nano-Al_2O_3 particles composite made in stir casting technique. Four samples were prepared that is A356 aluminium alloy without nano-Al_2O_3 and with different weight percentage of nano-Al_2O_3 particles (2.5, 3, 3.5%). The samples obtained from the stir casting process are subjected to accelerated corrosion test with 8% of NaCl solution. The results obtained reveal that A356 aluminium alloy with nano-Al_2O_3 MMCs has very low corrosion rates than unreinforced A356 aluminium alloy. Increasing the percentage of reinforcement was leading to rise in the corrosion resistance. Realized significant improvement in corrosion resistance for 3.5% nano-Al_2O_3 particles. Effect on density is 1% which is very marginal for the maximum reinforcement of 3.5% nano-Al_2O_3 particles.

Keywords Al_2O_3 nanoparticles · A356 aluminium alloy · NaCl · Mass loss · Corrosion · Stir casting composite

1 Introduction

Aluminium matrix composites are mainly used in valuable properties such as high wear resistivity, improvement in elevated temperature, high ductility and fatigue [1, 2]. The tribological structures of metal matrices have been widely studied, and the corrosion features are of high importance as composites of metal matrices have become applicants for the use of particular components to solve the corrosive problems [3–5]. The metal composites of aluminium show very low corrosive resistance compared to monolithic alloys, cause of reasons like gaps in the reinforcement interface, defects in production, internal and external stress, differences in structural behaviour and attractive effects due to merging of the metal matrix and reinforcement of the material [6, 7].

K. Ramachandra Raju (✉) · G. Senthilkumar · Y. Arivu · T. Santhosh · T. Prasanth · R. Pradeep
Department of Mechanical Engineering, Bannari Amman Institute of Technology, Coimbatore, Tamilnadu 638401, India
e-mail: rajukrc@gmail.com

G. Kumaresan et al. (eds.), *Advances in Materials Research*, Springer Proceedings in Materials 5, https://doi.org/10.1007/978-981-15-8319-3_118

In recent times, metal matrix nanocomposites have been used in a lot of applications because the mechanical properties are far superior than conservative microparticle strengthened MMCs [8]. They have an ability that provides corrosion resistance in the critical situations. Hence, corrosion resistance of the composite materials is identified, and reinforcement with nanoceramic additive material is most essential [9, 10]. Corrosion behaviour of Al 7075 matrix metal enhanced by nano-Al_2O_3 and nano-SiC [11, 12]. MMNCs are generated by using an electric stir casting technique [13, 14]. Pitting deterioration tests have been carried out to determine the corrosion resistance of Al_2O_3 and SiC nano-reinforced Al 7075 composites in HCl, H_2SO_4 and NaCl [15, 16].

The A356 aluminium alloy has been useful in a lot of application because of its excellent behaviour such as lightweight, corrosion resistance, good machinability and formability. The applications of A356 aluminium alloy can be increased by improving the properties of A356 aluminium alloy. Adding nano-Al_2O_3 particles with aluminium alloy has improved the properties. A356 aluminium alloy has good mechanical and corrosion properties with combination of nano-Al_2O_3 particles will make them more impressed for a variety of applications both from scientific and technological lookouts. Research works are limited on corrosion studies on marine condition by exposing aqueous (NaCl). Using nanoparticles less than 50 nm is limited. It is imperative to study the effect of corrosion of A356 alloys which is most suitable for marine application with nanoparticles reinforcements.

The objective of this work is to study the corrosion resistance of A356 alloy matrix composite reinforced with nano-Al2O3 particles 2.5, 3, 3.5% and test corrosion in 8% NaCl solution salt spray method for a period of time.

2 Experimental Procedure

2.1 Materials

In experimental work, stir casting method is applied for the manufacturing of composite by metal matrix. LM25 aluminium alloy composition (% of weight) as shown in Table 1 is preferred for matrix material and nano-alumina (Al_2O_3) particles supplied by Alfa Aesar, United Kingdom, are 40 nm for reinforcement material. After fabrication, corrosion test was done on the surface of the samples.

The resources used for this process are

Table 1 Chemical composition of A356 aluminium alloy

Cu	Mg	Si	Fe	Mn	Ni	Zn	Pb	Sn	Ti	Al
0.2 max	0.2–0.6	6.5–7.5	0.5 max	0.3 max	0.1 max	0.1 max	0.1 max	0.05 max	0.2 max	Bal

- Aluminium alloy of standard A356,
- Nano-Al_2O_3.

The composites of nano-metal particles are most relevant in a lot of applicational activities because the mechanical properties get progressed when similar to standard micro-particle strengthened MMCs. These materials predicted to show top corrosive resistant inside environments. Determining the corrosive resistant of composite substances supported by the nanoceramic components may be very vibrant. The experimental work was done for producing samples, and related corrosion test was conducted for determining the corrosion rate of samples.

Table 1 shows the chemical composition of aluminium alloy of grade A356. By varying the weight percentage of nano-Al_2O_3 (alumina), samples were obtained by stir casting method.

2.2 Stir Casting Process

The stir casting set-up is made of graphite crucible which is conical in shape for the fabrication of metal composites, as it survives at elevated temperature, which is considerably greater than the melting temperature (680 °C). This crucible which is made up of high ceramic alumina materials placed in the muffle around where the heating element is wound. The coil behaves itself as the heating element. This type of furnace is named as the resistance heating furnace. It can be heated very quickly up to 1000 °C within 55 min. An aluminium alloy of caste grade was applied as the matrix material, while the Al_2O_3 nanomaterials were used as the reinforcement material.

The alloy is kept in a resistance furnace and melted at the temperature of 8000 °C, and then the gas has been removed for 20 min in combination with argon gas through a graphite lance. To obtain uniformity in distribution of the particles, the discs are then added with the help of an electromagnetic stirrer (EMS) device. The current may vary from 50 to 80 A, while the voltage remains constant and is equal to 220 V. The effect of temperature gets lowered to convert the liquid to semisolid. During the solidification, the molten metal is immediately poured into the die cavity. This operation was repeated for producing each sample. The samples were prepared with different percentage of nano-Al_2O_3 particles, i.e. unreinforced A356 aluminium alloy and reinforced A356 aluminium alloy with 2.5, 3 and 3.5% of nano-Al_2O_3 particle.

2.3 Salt Spray Corrosion Test

The accelerated corrosive test produces a corrosive attack on the samples during this test. Salt spray test is most familiar and well-established corrosion tests compared to other tests.

Before testing, the samples were cleaned thoroughly. The solution used for this process is 8% sodium chloride salt solution. The samples were placed inside the chamber as shown in Fig. 1, followed by the salt-containing solution which is sprayed over the samples in the very fine fog mist. The constant temperature is maintained within the chamber. The samples get constantly wet due to spraying process, and hence, the samples undergo corrosion constantly. Here, ASTM G1 standard is used for corrosion test (Fig. 2 and 3).

The procedure is explained in summary, as follows:

- Salt fog chamber contains the wooden rocks.
- Samples are placed inside the chamber.
- 8% of NaCl solution is pumped from reservoir and gets sprayed on the samples.

Fig. 1 Salt spray test chamber

Fig. 2 Stir casted sample

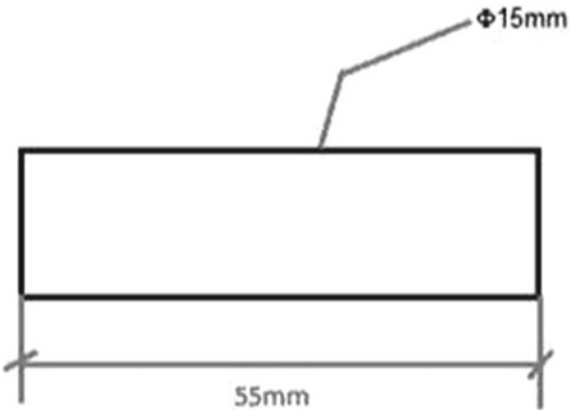

Fig. 3 Corrosion test samples size

- Solution is mixed with compressed air from the nozzle.
- Compressed air has done atomization of NaCl solution into fog at the nozzle.
- Heaters maintain the temperature of about 45 °C.
- Test carried out for about 48 h.

3 Results and Discussions

3.1 Density

The density of the samples was calculated as per Archimedes principle. Fig. 4 shows that after adding nano-Al_2O_3 particles with A356 aluminium alloy, the density is

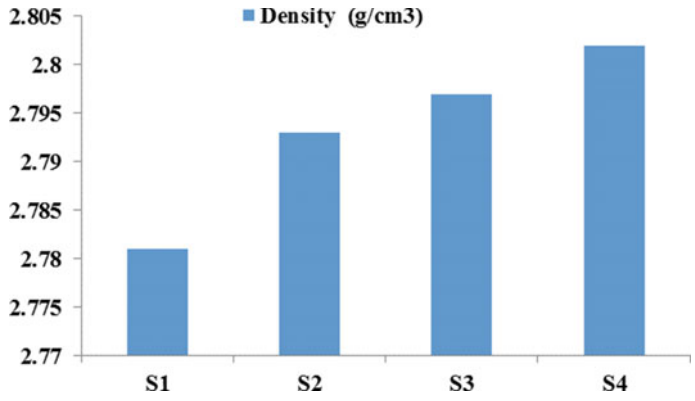

Fig. 4 Density values for the samples S1, S2, S3 and S4

increased. It infers that the density of the aluminium alloy is gradually increased with respect to weight percentage of nano-Al_2O_3 particles.

3.2 Mass Loss Corrosion Rate

The standard equation as per ASTM G1 for mass loss method to calculate corrosion rate is described below:

$$\text{Corrosion rate CR (mpy)} = 3.45 \times 10^6 * \text{W/ATD}$$

where

CR Corrosion rate in mills per year.
W Mass loss of specimen in grams.
D Density of specimen in g/cm^3.
A Area of specimen in cm^2.
T Time of exposure in hour.

Diameter of the specimen, d = 15 mm = 1.5 cm.
Height of the specimen, h = 55 mm = 5.5 cm.
Volume, $V = \pi r^2 h$,
Area, $A = 2\pi rh + 2\pi r^2$,

The mass of each sample was measured and tabulated after the corrosive test. Table 2 shows that the samples lost their mass after the completion of salt spray corrosive test. Reduction in mass was occurred in milligrams range. Corrosive rate of each sample was calculated by the help of corrosion expression. The result shows that the mass reduction of each sample is different. It indicates that for different percentage of nano-Al_2O_3, the mass reduction was varied.

Corrosion rate shown in Fig. 5 indicates that nano-Al_2O_3 particles added to the A356 alloy have given significant improvement. Size of the nanoparticles was 40 nm, smaller compared to other research works, and its corrosion rate is very minimal. Sample S1 unreinforced A356 alloy had higher corrosion rate by 50% compared 3.5% nano-Al_2O_3 particles reinforced sample S4. The effect of nanoparticles and increase in its % has given improved corrosion resistance which is most useful for aqueous salty environment marine applications.

Table 2 Weight of the samples

Specimens	Mass before corrosion test W1 (g)	Mass corrosion test W2 (g)
S1	27.054	27.05
S2	27.175	27.172
S3	27.215	27.212
S4	27.257	27.255

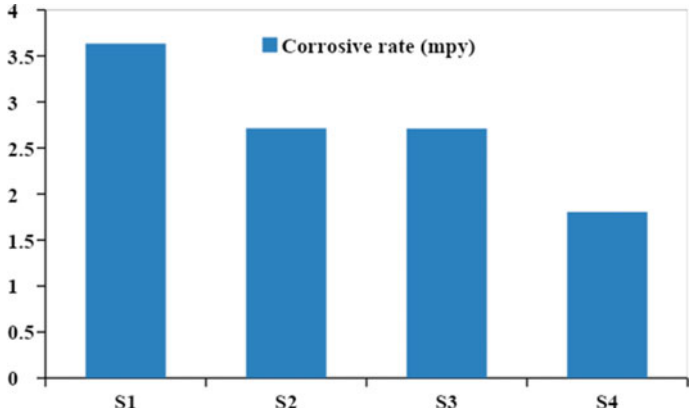

Fig. 5 Corrosion rate of the samples S1, S2, S3 and S4

4 Conclusions

In the present investigation, density and corrosion behaviour of A356 aluminium alloy with 2.5, 3 and 3.5% nano-Al_2O_3 particles reinforcements were studied. The following conclusion was made:

- Density of the samples is gradually increased by adding nano-Al_2O_3 particles. The density increase for the maximum reinforcement of 3.5% is about 0.75% which is very marginal and has less impact on density
- Corrosion rate of the samples after accelerated corrosion test shows that by adding nano-Al_2O_3 particles significantly improved the corrosive resistance of A356 aluminium alloy.
- The reinforced A356 aluminium alloy exhibited lower corrosion rate in 8% NaCl solution than unreinforced A356 aluminium alloy. Improvement of corrosion resistance of 3.5% nano-Al_2O_3 particles is 50% better than unreinforced A356 aluminium alloy.
- The nano-Al_2O_3 particles reinforcements with A356 alloy show significant improvement which can be widely used in marine applications.
- If the aqueous salt condition in oceans, rivers is lesser than 8% NaCl level and the corrosion resistance will be further higher and more beneficial.

References

1. Suresh SM, Mishra D, Srinivasan A, Arunachalam RM, Sasikumar R (2011) Production and characterization of micro and nano Al_2O_3 particle reinforced LM25 Aluminium alloy composites. ARPN J Eng Appl Sci 6(6):94–98

2. Chawla N, Williams JJ, Piotrowski G and Saha R (2001) Tensile and fatigue fracture of discontinuously reinforced Aluminum. D. Adv Fracture Res 1–6
3. Paciej RC, Agarwala VS (1986) Metallurgical variables influencing the corrosion susceptibility of a powder metallurgy Aluminium/Silicon composite. Corrosion 42(12):718–729
4. Shimizu Y, Nishimura T, Matsushima I (1995a) Corrosion resistance Al-based metal matrix composite. Mater Sci Eng 198(1–2):113–118
5. Liu ZS, Huangn B, Gu M (2006) Corrosion behavior of Al/AlN composite in alkaline solution. Mater Lett 60:2024–2028
6. Fontana MG Corrosion engineering. Mcgraw-Hill inernational editions, Material Science and Engineering Series
7. Ei M, Eigenfield K, Kouta F, Hussein A, Mahamoud TS and Ragaie RM (2008) Synthesis and characterization of new cast A356/(Al_2O_3) Metal matrix nano composites. In: Proceedings of the 2nd multifunctional nanocomposites & nanomaterials: international conference & exhibition MN2008 pp 1–8
8. Karabi DD, Das S (2007) Effect of mechanical milling on the corrosion behavior of Al-Zn/Al2O3 composite in NaCl solution. J Mater Sci 42:8209–8214
9. Hadleigh Casting Aluminium Technologies. Properties of LM25 aluminium alloy
10. Kok M (2005) Production and mechanical properties of Al2O3 particle-reinforced 2024 aluminium alloy composites. J Mater Process Technol 161:381–387
11. Roberge PR (2008) Corrosion engineering: principles and practice. McGraw-Hill, New York
12. Shimizu Y, Nishimura T, Matsushima I (1995b) Corrosion resistance of Al-based metal matrix composites. Mater Sci Eng A198(1–2):113–118
13. Yussof Z, Ahmad KR, Jamaluddin SB (2008) Comparative study of corrosion behavior of AA 2014/15 vol%Al and AA2009/20Vol%SiC. Port Electrochem Acta 26:291–301
14. Zhu J, Hihara LH (2010) Corrosion of continuous alumina-fibre reinforced Al2 wt% Cu-T6 metal matrix composite in 3.15 NaCl solution. Corros Sci J 52:406–415
15. De Salazar JMG, Urefia A, Manzanedo S, Barrena MI (1999) Corrosion behaviour of AA6061 and AA7005 reinforced with Al2O3 s in aerated 3.5% chloride solution: potentiodynamic measurements and microstructure evaluation. Corros Sci 41:529–545
16. Zhang Z, Chen DL (2008) Contribution of Orowan strengthen- ing effect in particulate-reinforced metal matrix nanocomposites. Mater Sci Eng A 483:148–152

Applications of Fuzzy Logic Approach for Assessment

V. Vaishnavi and M. Suresh

Abstract Appropriate Fuzzy set theory is acknowledged as the best problem modelling and solution method. Fuzzy logic approach is represented with mathematical and processing non-statistical information from uncertainty and provides tools to deal with imprecision intrinsic to many problems. Fuzzy set theory is mainly enforced to solve issues in health and natural sciences. The assessment of the various techniques implementation is gained attention of fuzzy logic mainly on triangular fuzzy number (TFN) and trapezoidal fuzzy number (TPFN). Thus the current study provides the outline of fuzzy logic and their application with the steps. The study helps the researcher and practitioner on the assessment of various implementation techniques in their organization easily and effectively.

Keywords Fuzzy logic · Assessment · Lean index · Agile index · Sustainability index · Leagility index

1 Introduction

Fuzzy logic approach is a methodology mainly used to solve the issues related to multifaceted and difficult to understand quantitatively by using fuzzy set theory [1]. Fuzzy set methods permit to capture the undefined and imprecise systems of the real world by using linguistic terms so that computers can follow human thought processes [2]. In currently, Fuzzy logic is used broadly in many industrial applications such as water treatment, travel time reduction, subway systems, washing machines, vacuum cleaners, rice cookers and aircraft flight control [3]. The fuzzy techniques help to reach an applicable truth by using the outcome of reasoning from such inexact, imprecise, and partial knowledge by collected replies are represented over a wide range [4]. A linguistic variable represented in words or sentences in natural or artificial language to get response from the experts easily [5]. For decision making various types of fuzzy numbers are used with linguistic data into quantitative

V. Vaishnavi · M. Suresh (✉)
Amrita School of Business, Amrita Vishwa Vidyapeetham, Coimbatore, India
e-mail: drsureshcontact@gmail.com

G. Kumaresan et al. (eds.), *Advances in Materials Research*, Springer Proceedings in Materials 5, https://doi.org/10.1007/978-981-15-8319-3_119

form [6] in which TFN and TPFN are used primarily in manufacturing, software and healthcare sector. Thus the current study focuses on the usage of fuzzy logic on TFN and TPFN in assessment of organizational current level and managers are forced to improve their strategy to enhance their performance.

2 Literature Review

Fuzzy logic was first introduced by [8] is a mathematical theory which allows uncertainty and vagueness can be exhibited and develop a framework using fuzzy numbers [9]. Narrow mode is said as logical system which is observed as a generalization of multi-appraised logic and wide mode is said as logical system [12] have defined as "Fuzzy logic is a system of reasoning and computation in which the objects of reasoning and computation are classes with unsharp (fuzzy) boundaries". In fuzzy logic, the whole thing is mentioned in degree and used mainly as wide mode.

Fuzzy logic includes an extensive range of theories and methods primarily built upon four concepts such as fuzzy sets, linguistic variables, probability distribution (membership function), and fuzzy if–then rules [3]. In qualitative assessments fuzzy sets and linguistic variables are mainly used to take decisions including complex and ambiguous with incomplete data. Fuzzy set is a set in which members' certainty of membership is rejected and every member belongs to the set with its own specific membership degree [13].

Linguistic variable is primarily useful for dealing with the situation which is complex or inadequate to explain in conservative quantitative expressions. A linguistic variable is a variable that uses values are words or sentences in natural or artificial language. The estimated fuzzy-set theory perspective is used in linguistic values to express fuzzy numbers. The TFN are mainly used because which is easily explained with exports and also used in assessment due to abstraction and impreciseness associated with predictable assessment of societal performance. TFNs' membership functions (fA(X)) are given in [2].

A TPFN form(a, b, c, d) is the most generic class of fuzzy numbers with linear membership function which is also used in the assessment with the ranking the fuzzy numbers. Ranking the fuzzy numbers would play a vital role in the resemble reasoning, optimization, forecasting, decision-making, scheduling and risk-based analysis practices [14]. A generalized TPFN [15] can be defined as a vector and the membership function $a(x)$: $R \rightarrow [0, 1]$.

Fuzzy set numbers like TFN and TPFN have gained attention from the researcher and practitioner from 90′s and have been used in the assessment of manufacturing, supply chain, healthcare and software. The detailed classification of fuzzy applications used in the field is given in Table 1.

Table 1 Detailed application of fuzzy logic approach on assessment

Assessment area	References
TFN	
Manufacturing	
• Lean	[13]
• Agility	[2]
• Agility—Supply Chain	[29]
• Leagility—Supply Chain	[32]
• Readiness—LSS	[33]
• Social Sustainability	[34]
• Safety practices	[35]
Software	
• Agility	[36]
Healthcare	
• Lean	[37]
• Agility	[38]
• Readiness—Lean	[4]
Banking	
• Lean	[39]
TPFN	
Construction project	
• Risk management	[40]
Logistics management	
• 3PL (third-party logistics)	[41]
Manufacturing	
• Agility	[42]
• Leanness	[44]
• Supply Chain	[14]
• Supply Chain—Agility	[46]
Information Technology	
• Risk management	[47]

3 Steps for TFN and TPRNs

The following steps have been from [2] and [6] for TFN and TPFNs. The notations used in the paper are given in Table 2.

Step 1 Selection of enabler, criteria and attributes based on context. The appropriate attributes relating to each criterion are identified from the literature review and expert opinion.

Table 2 Notations used in the current study

Indices	Abbreviations
L_i	Fuzzy importance weight of ith enabler
L_{ij}	Fuzzy importance weight of jth criterion in ith enabler
L_{ijk}	Fuzzy importance weight of kth attribute of jth criterion in ith enabler
P_i	Fuzzy importance rating of ith enabler
P_{ij}	Fuzzy importance rating of jth criterion in ith enabler
P_{ijk}	Fuzzy importance rating of kth attribute of jth criterion in ith enabler
FI	Fuzzy index
LE_i	Fuzzy number of natural language expression set
$fFI_i(x)$	TFN of FI_i
$fLE_i(x)$	TFN of LE_i

Step 2 Determination of linguistic scale. Linguistic languages are designated from natural-language expressions and allow more information than mathematical results for many situations.

Step 3 Quantification of performance ratings and prominent weighting from experts. The next step is a collection of importance weights and performance rating of enabler, criteria and attributes for evaluating the context.

Step 4 Transformation of linguistic terms to applicable fuzzy numbers. A TFN is generally used because they are simply specified by experts and are converted for performance rating and importance weights [2, 18, 23]. Likewise, TPFNs conversion also had been done for performance rating and importance weights [41].

Step 5 Aggregating fuzzy rating with fuzzy weights. The aggregate performance rating of the attributes is customized into criteria rating and the criteria rating is customized into enabler rating and equation is given in 1 and 2 respectively.

$$P_{ij} = \frac{\sum_{k=1}^{K} (L_{ijk} \otimes P_{ijk})}{\sum_{k=1}^{K} L_{ijk}} \tag{1}$$

$$P_i = \frac{\sum_{j=1}^{J} (L_{ij} \otimes P_{ij})}{\sum_{j=1}^{J} L_{ij}} \tag{2}$$

Once criteria rating is obtained, next step compute the Fuzzy Index (FI) is calculated by Eq. 3 given below.

$$FI = \frac{\sum_{i=1}^{I} (L_i \otimes P_i)}{\sum_{i=1}^{I} L_i} \tag{3}$$

Step 6 Match the FI with an appropriate level. The calculated FI is compared with the general linguistic term using Euclidean distance method. Euclidean

Table 3 Fuzzy intervals for Linguistic variables

Natural Language expression set	Fuzzy intervals
Most Favourable (*MF*)	(7, 8.5, 10)
Favourable (*FV*)	(5.5, 7, 8.5)
Fair (*F*)	(3.5, 5, 6.5)
Bad (*B*)	(1.5, 3, 4.5)
Worst (*W*)	(0, 1.5, 3)

distance method is conceived as the most spontaneous method for humans to calculate perceived closeness. Table 3 represents natural language expression set and its corresponding fuzzy interval. The Euclidean distance is calculated by the following Eq. (4).

$$D(FI, LE_i) = \sqrt{\sum (fFI(x) - fLE_i(x))^2} \tag{4}$$

Step 7 To identify weaker attributes Fuzzy Performance Importance Index (FPII) is calculated. The FPII computation consists of two steps: first is the calculation of was given in the Eq. (5) below.

$$FPII_{ijk} = U_{ijk} \otimes P_{ijk}; \tag{5}$$

where

$$U_{ijk} = (1, 1, 1) - L_{ijk}$$

Next step is the development of a ranking score for each attribute following centroid method. Here a, b & c denotes the lesser, middle and higher orders of the TFN, respectively are shown in Eq. (6).

$$Rank\ score = \frac{a + 4b + c}{6} \tag{6}$$

After obtaining ranks for all attributes, management will take corrective action to overcome the issues.

4 Results and Discussions

Fuzzy logic approaches are used widely in manufacturing sector and gained importance in healthcare sector with the linguistic variables to make decisions effectively. Organizational performance related to implementation of specific strategy like lean, agility, LSS and other techniques. The methods the manager to know their current

performance level and in which ways their organization needs improvement. Both, TFN and TPFNs are simple and easy to use which need to be explained to the experts before asking their views. The performance rating and importance weights are collected from the experts which should be sometimes vague, so the method helps to find the performance of the organization easily. The method can be used to develop their current level to the standard by periodic assessment of developed framework effectively. The assessment of techniques will helps for organization transformation from the current state to upgrade state easily and successfully.

5 Conclusion

The current study exposed mainly about the application of fuzzy logic approach with the TFN and TPFNs in the assessment of current performance of the organization. The major assessment areas are risk, implementation of lean, agility & sustainability in manufacturing, software and healthcare section. The researcher and practitioner paid more attention on implementing fuzzy logic towards healthcare sector. The method provides a structured procedure, which helps to identify the drivers related to the current business environment and provide a strategic direction to enhance organization capability. In addition, the method provides suggestions and convinced results for further development. The limitation of this methodology is membership function of natural language in linguistic variables. It depends on the managerial perception of experts. The membership function should be defined to evaluate the importance of key aspects of organization, which includes strategy, marketing, operations and finance.

References

1. Mittal H, Bhatia PK, Goswami P (2008) Software quality assessment based on fuzzy logic technique. Int J Softw Comput Appl 34(3):105–112
2. Lin CT, Chiu H, Tseng YH (2006a) Agility evaluation using fuzzy logic. Int J Prod Econ 101(2):353–368
3. Yen J, Langari R (1999) Fuzzy logic: intelligence, control, and information, vol 1. Prentice hall, Upper Saddle River, NJ
4. Narayanamurthy G, Gurumurthy A, Subramanian N, Moser R (2018) Assessing the readiness to implement lean in healthcare institutions–A case study. Int J Prod Econ 197:123–142
5. Zadeh LA (1975) Fuzzy logic and approximate reasoning. Synthese 30(3–4):407–428
6. Chen SM, Chen JH (2009) Fuzzy risk analysis based on ranking generalized fuzzy numbers with different heights and different spreads. Expert Syst Appl 36(3):6833–6842
7. Yang T, Hung CC (2007) Multiple-attribute decision making methods for plant layout design problem. Robotics Comput Integr Manuf 23(1):126–137
8. Zadeh LA (1965) Fuzzy Sets. Inf Control 8(3):338–353
9. Klir GJ, Yuan B (1995) Fuzzy sets and fuzzy logic: theory and applications. Upper Saddle River, 563

10. Zadeh LA (2002) From computing with numbers to computing with words: from manipulation of measurements to manipulation of perceptions. In: The Dynamics of Judicial Proof (pp 81–117). Physica, Heidelberg
11. Zadeh LA (2004) Precisiated natural language (PNL). AI Magazine 25(3):74–74
12. Zadeh LA (2015) Fuzzy logic—a personal perspective. Fuzzy Sets Syst 281:4–20
13. Zanjirchi SM, Tooranlo HS, Nejad LZ (2010) Measuring organizational leanness using fuzzy approach. In: Proceedings of the 2010 International Conference on Industrial Engineering and Operations Management (pp 144–156)
14. Sahu AK, Sahu SK, Datta S, Mahapatra SS (2015b) Supply chain flexibility assessment and decision-making: a fuzzy intelligent approach. Int J Bus Excell 8(6):675–699
15. Chen SH (1985) Ranking fuzzy numbers with maximizing set and minimizing set. Fuzzy Sets Syst 17(2):113–129
16. Gupta MM, Kaufmann A (1985) Introduction to fuzzy arithmetic: theory and applications. Van Nostrand Reinhold Company, New York, NY
17. Bansal A (2011) Trapezoidal fuzzy numbers (a, b, c, d): arithmetic behavior. Int J Phys Math Sci 2(1)
18. Vimal KEK, Vinodh S (2013) Application of artificial neural network for fuzzy logic based leanness assessment. J Manuf Technol Manag 24(2):274–292
19. Vinodh S, Balaji SR (2011) Fuzzy logic based leanness assessment and its decision support system. Int J Prod Res 49(13):4027–4041
20. Vinodh S, Vimal KEK (2012) Thirty criteria based leanness assessment using fuzzy logic approach. Int J Adv Manuf Technol 60(9–12):1185–1195
21. Agrawal R, Asokan P, Vinodh S (2017) Benchmarking fuzzy logic and ANFIS approaches for leanness evaluation in an Indian SME: a case study. Benchmarking An Int J 24(4):973–993
22. Abreu A, Calado JMF (2017) A fuzzy logic model to evaluate the lean level of an organization. Int J Artif Intell Appl (IJAIA) 8(5):59–75
23. Vinodh S, Aravindraj S (2015) Benchmarking agility assessment approaches: a case study. Benchmarking Int J 22(1):2–17
24. Vinodh S, Devadasan SR (2011) Twenty criteria based agility assessment using fuzzy logic approach. Int J Adv Manuf Technol 54(9–12):1219–1231
25. Aravindraj S, Vinodh S (2014) Forty criteria based agility assessment using scoring approach in an Indian relays manufacturing organization. J Eng Design Technol 12(4):507–518
26. Vinodh S, Kumar VU, Girubha RJ (2012) Thirty-criteria-based agility assessment: a case study in an Indian pump manufacturing organisation. Int J Adv Manuf Technol 63(9–12):915–929
27. Tsai CS, Chen CW, Lin CT (2008) Align agile drivers, capabilities and providers to achieve agility: A fuzzy-logic QFD approach. In Supply Chain, IntechOpen
28. Shahraki A, Yaghoobi NM, Fard SG (2011) Fuzzy evaluation to reach the required agility at manufacturing organizations. J Basic Appl Sci 1(9):1112–1123
29. Lin CT, Chiu H, Chu PY (2006b) Agility index in the supply chain. Int J Prod Econ 100(2):285–299
30. Vinodh S, Devadasan SR, Vimal KEK, Kumar D (2013) Design of agile supply chain assessment model and its case study in an Indian automotive components manufacturing organization. J Manuf Syst 32(4):620–631
31. Kumar D, Ramakrishna H (2011) Assessment of supply chain agility using Fuzzy Logic for a manufacturing organization. IUP J Supply Chain Management 8(4)
32. Vinodh S, Aravindraj S (2013) Evaluation of leagility in supply chains using fuzzy logic approach. Int J Prod Res 51(4):1186–1195
33. Sreedharan V, R., Raju, R., Sunder M, V., & Antony, J. (2019) Assessment of Lean Six Sigma Readiness (LESIRE) for manufacturing industries using fuzzy logic. Int J Quality Reliability Manage 36(2):137–161
34. Rajak S, Vinodh S (2015) Application of fuzzy logic for social sustainability performance evaluation: a case study of an Indian automotive component manufacturing organization. J Clean Prod 108:1184–1192

35. Ganesh J, Suresh M (2015) Safety practice level calculation in Indian manufacturing company using fuzzy logic approach. In: 2015 IEEE International Conference on Computational Intelligence and Computing Research (ICCIC) (pp 1–4). IEEE
36. Tseng YH, Lin CT (2011) Enhancing enterprise agility by deploying agile drivers, capabilities and providers. Inf Sci 181(17):3693–3708
37. Narayanamurthy G, Gurumurthy A (2018) Is the hospital lean? A mathematical model for assessing the implementation of lean thinking in healthcare institutions. Operations Research for Health Care 18:84–98
38. Suresh M, Patri R (2017) Agility assessment using fuzzy logic approach: a case of healthcare dispensary. BMC Health Services Research 17(1):394
39. Madhan K, Suresh M (2016) Leanness assessment using fuzzy logic approach: a case of Indian cooperative bank. In: 2016 International Conference on Advanced Communication Control and Computing Technologies (ICACCCT) (pp 341–346). IEEE
40. Samantra C, Datta S, Mahapatra SS (2017) Fuzzy based risk assessment module for metropolitan construction project: An empirical study. Eng Appl Artif Intell 65:449–464
41. Sahu NK, Datta S, Mahapatra SS (2015a) Fuzzy based appraisement module for 3PL evaluation and selection. Benchmarking Int J 22(3):354–392
42. Mishra S, Datta S, Mahapatra SS (2013) Agility Evaluation and Identification of Agile Obstacles by exploring fuzzy degree of similarity (DOS) concept. Int J Inf Comput Technol 3(1):82–86. International Research Publication House, New Delhi
43. Samantra C, Datta S, Mishra S, Mahapatra SS (2015) Fuzzy evaluation modelling to assess organisational agility. Int J Ind Syst Eng 21(1):50–67
44. Matawale CR, Datta S, Mahapatra SS (2014) Leanness estimation procedural hierarchy using interval-valued fuzzy sets (IVFS). Benchmarking Int J 21(2):150–183
45. Sahu AK, Datta S, Mahapatra SS (2017) Evaluation of performance index in resilient supply chain: a fuzzy-based approach. Benchmarking Int J 24(1):118–142
46. Samantra C, Datta S, Mishra S, Mahapatra SS (2013) Agility appraisal for integrated supply chain using generalized trapezoidal fuzzy numbers set. Int J Adv Manuf Technol 68(5–8):1491–1503
47. Samantra C, Datta S, Mahapatra SS (2014) Risk assessment in IT outsourcing using fuzzy decision-making approach: An Indian perspective. Expert Syst Appl 41(8):4010–4022

Study and Testing of Pneumatic Control of Ball Valve Using Actuator

G. Dinesh Kumar, K. S. Karthikeyan, and C. Sathishkumar

Abstract In recent days, the industry uses huge-sized valves to operate the flow of fluids from one area to another area. These huge-sized valves were completely operated on manual premises. The ball-type valves were located over the hot radiation transmitting regions as well as cold radiated regions, and this affects the human skin, also it interprets damages to the body and heath, ultimately it causes death. We can use safety instruments like aprons, gloves, etc., but this will increase the cost and the labor expense is also high. To avoid such circumstances, the actuator-based ball valves help to control the flow of fluid automatically, without any manual help. Hence, this will improvise the standard of the industries also this helps to detect the flow and measure the opening and closing data through graphical representation. This inter-fixing of actuator over a ball valve is analyzed by the hydro test which gives the result about the leakage data and thus provides information when a leakage has occurred. This helps to control the wastage of fluid over the flow path.

Keywords Manual premises · Ball-typed valves · Hot and cold regions · Actuator

1 Introduction

The ball valves were mechanical devices which control the pressure and flow with the working process [1]. These ball valves were mostly of manually operated, may be hydraulic or pneumatically operated. This is an important component in piping system which conveys [2] the gases, liquids, and slurries. The valves have different categories like gate, globe, ball, check, butterfly, plug, and diaphragm. These models have different features and functions. The actuators were capable of controlling the movements [3] and positioning that is operated by manual, sometimes pneumatic, hydraulic, and electrical. The basic movement of valve is linear movement and rotary

G. Dinesh Kumar (✉) · K. S. Karthikeyan · C. Sathishkumar
Department of Mechanical Engineering, Bannari Amman Institute of Technology, Sathyamangalam, Tamilnadu, India
e-mail: dineshkumar.me16@bitsathy.ac.in

G. Kumaresan et al. (eds.), *Advances in Materials Research*, Springer Proceedings in Materials 5, https://doi.org/10.1007/978-981-15-8319-3_120

movement [4]. These linear movement actuators transfer the energy to linear movements. This is mainly to position the valve may be of push and pull operations. The rotary movement [5] actuators transfer the energy into rotary movements. This is mainly to position the valve motion by ball and butterfly valves. These actuators were manually operated [6] with hand wheel or knob. They have different [7] types of configurations that were available in many shapes and sizes based on their usage [8]. These actuators make the movements with rigid chain. The ball valves [9] were connected to the actuators to control the movement more effectively and electrically. They provide a better feature to control the valves movement over a distance [10] and thus provide a safe platform for the industries.

2 Literature Survey

Ebenezer Sathish Paul [1] presented two systems of two-stage electrohydraulic servo valve with a nozzle flapper pilot stage, which is controlled by stack-type piezoelectric elements and a displacement magnifying mechanism.

Mandanaka [2] studied the performance of the poppet valve through investigation of inflow and outflow for the range of small and controllable openings made available from the employment of a practical piezoelectric stack driver.

Ali [3] introduced a pressure regulator which is used for controlling the reducing pressure in the piezoelectrically driven pneumatic valve. The pneumatic valve of this study object is two-stage type and consists of a piezoelectric actuator, a controller, a poppet valve, and a pressure regulator.

Dutt [4] presented a neural network pattern classifier to carry out fault diagnosis and identification upon the actuator of a Fisher–Rosemount 667 industrial process valve.

3 Actuator and Its Types

In order to control the mechanism or a system, an actuator is used to control the opening and closing of the valve. This actuator is operated by electric power, and it converts the energy into dynamic action.

The four types of actuator are as follows:

Manual.
Pneumatic.
Hydraulic.
Electric.

3.1 Manual

In manual actuators, it is operated by gears, levers, or wheels to move the complete valve system. These manual actuators were operated by human hand. These actuators are very much costless, easy to operate, and self-contained. It is difficult to operate large sized valves manually. Also it is difficult to operate valves that were located in toxic, remote, and hostile environments. Considering the safety, there must be a quicker operation at this situation.

3.2 Pneumatic

The pneumatic valve actuators use air pressure as their power source, used on linear and quarter-turn valves. They convert the air pressure into motion of the system. A linear force is created on the diaphragm by blowing air pressure on to it. The arrangement of it may be spring—closed or opened. Also in double acting actuators, they open and close by blowing air pressure through in and out of it. There is in need of a central compressor system.

3.3 Hydraulic

The hydraulic valve actuators use fluid pressure as their power source, used on linear thrust for gate valves and globe valves. They convert the fluid pressure into motion of the system. To operate a quarter-turn valve, torque is introduced to the system. The fluid may be of any composition depending on the systems need. The hydraulic pressure is created by a pump. It is also used in applications like water pumping stations, JCBs, etc.

3.4 Electric

The electric valve actuators use electricity as their power source and used to provide torque to control the opening and closing of the valves. This is mainly an energy-efficient system with no toxic and quiet reliable; however, without electricity this system fails to work. Battery packs can also be used instead of an external power source.

Fig. 1 Problem

4 Existing Problem

The man power required for this valve operation is comparatively more. Manual operation of very huge-sized valves is difficult in terms of physical work and perfection. Incorrect assembly, installation, or maintenance procedures would be performed in the absence of values in production and controlling units. In the absence of valve, the necessary movements to the disk and plug cannot be fixed in exact and required position within the short duration.

Frictional losses from straight pipe alone cannot be easily calculated without the presence of valves. The valves are present in Fig. 1 areas where the surrounding temperature is too high or too low or the high radiation areas where humans cannot be directly employed in the operation of valves. Working in these areas may cause diseases such as hypothermia, frostbite, trench foot and chilblain, heat exhaustion, heat cramps, and heat stroke, nausea, bloody vomiting and diarrhea, etc.

5 Objectives

(1) To study the automatic flow control of valves.
(2) To analyze on the manual efforts in operation of valves.
(3) To regulate the flow in valves.

6 Existing Problem

Project methodology is represented in Fig. 2.

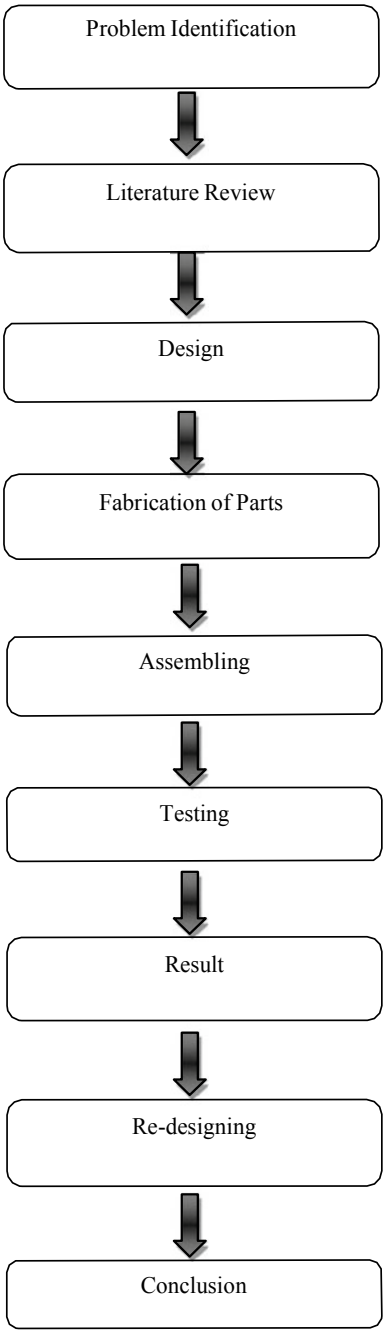

Fig. 2 Project methodology

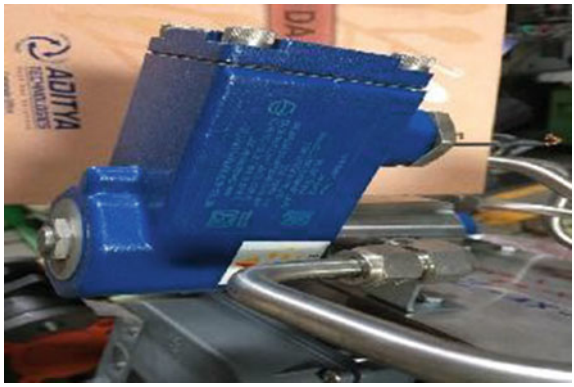

Fig. 3 Solenoid valve

6.1 Solenoid Coil

The solenoid is an electromagnetic device made up of coil of wire. This is a device which converts electric energy into mechanical energy into reciprocating motion. The solenoid when energized by an external power supply in the coil wires gets magnetized and creates a magnetic flux around it. This magnetic flux gives the reciprocating motion for the soft iron core in between the wires.

6.2 Solenoid Valve

The solenoid valve operates on the principle of electromechanical concept. These valves differ from several characteristics they are, the electric power they consume, the magnetic flux they generate, the regulation of fluid by some mechanism, and the control type of the fluid. Figure 3 mechanism may vary from linear motion to plunger type to pivoted-armature and rocker actuators. These actuators were the most familiar elements used to control the fluid motion. It benefits of fast action, safe switching, and the high reliability with long life span [11–15].

6.3 Air Regulator

Shavo's Fig. 4 is the combination unit for process control which is an efficient space saving design for general applications in filtration, and liquid water removal and controlled pressure are required.

Fig. 4 Air regulator

6.4 Volume Booster

There is a need to increase the speed of the actuators motion, as there is a requirement of the use of a Fig. 5 which is a high volume amplifier to prevent the time lags. The controller produces a volume signal and transmits the auxiliary signal supply of high volume to the control actuator which is separated by long piping runs. The volume boosters were mainly used along with the large capacity diaphragm actuator [16–18].

6.5 Positioner

The positioner valve is used on places where the air load pressure has to be increased or decreased to drive the actuator to reach a balanced position of the valves system to the output signal received from the variable controller. Figure 6 shows that it is very much effective in performance and eliminates the physical contact with linkage less feedback on wear parts. This capability of self-diagnostics helps in health evaluation by increase in performance, and this evaluation is done by digital communication to access the valve [19–22].

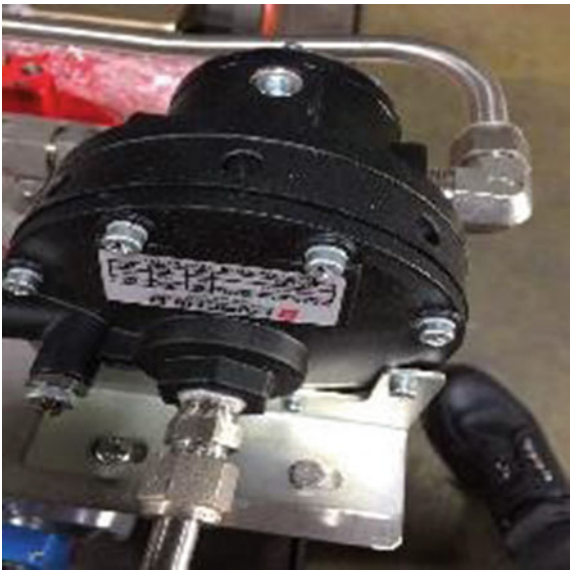

Fig. 5 Volume booster

Fig. 6 Positioner

6.6 Limit Switch

The limit switch is used to determine the opening and closing of valves by indicating the user with the signal and thus acts as a visual sign to the operator. Figure 7 indicates the extent of both opening and closing of the valves. They can open up to a degree of about 0 to 90 degree.

Fig. 7 Limit switch

Fig. 8 Pneumatic compressors

6.7 Pneumatic Compressor

The pneumatic compressor is used to compress the air molecules from the container or a cylinder tank. Figure 8 was connected to the pneumatic valves depending on their actuators like single, double, etc. Prominent features include sandwich mounting, travel stops, self-locking declutch mechanism, corrosion-resistant, and gear plating.

6.8 Ball Valve

The ball valve is in the form of a quarter-turn valves, and this Fig. 9 allows the use of hollow, perforated, and pivoting balls which helps in controlling the flow of

Fig. 9 Ball valve

any medium in to it. The ball valves were of high reliable characteristic which can perform well even after completing many cycle of process. On cold climates, the ball valves get freezed, and thus disable the valve; hence, the freeze-tolerant ball valve plug ruptures it and makes an easy repair to the valve. In cryogenics purposes, the ball valves expand inside itself. The safety is well determined in the ball valve.

7 Testing Methods

(1) Shell test
(2) Back seat test
(3) Hydro seat test
(4) Air seat test

7.1 Shell Test

The shell test is a process that is undergone to check the condition of the valve by sending pressure inside the inlet and by closing the outlet, if there is any packing gland tightly occurs, it is enough to maintain the test pressure, thereby testing the stuffing box. Application of internal hydrostatic pressure is 150% of the maximal rated pressure. Visual examination is performed for leakages/dripping, distortion, or other anomaly.

7.2 Back Seat Test

All the valves must undergo this backseat test, but the bellows seal valves have this feature, and it is performed by applying pressure inside the valve with valve end closed and valve fully opened. Minimal test pressure is 0.2 bar. Maximal test pressure is 150% of the maximal pressure rating. The valve outlet is exposed to atmospheric pressure, performing a drop-tight (zero leakage) sealing for minimal period of 30 s.

Dynamic test—the valve is opened and drop-tight closed, at 0.2 bar (3psi) pressure, inspecting its sealing and mechanical reliability at the varying low-pressure conditions. When tested, the packing is said to be loose. The manufacturer is mainly responsible for the demonstration of the pack that will not leak the valve's pressure rate is 100°F (38 °C).

7.3 Hydro Seat Test

The hydrostatic testing is done by filling the pressure into the component with the water completely to test purposes, removing the air contained within the unit, and pressurizing the system up to 1.5 times the design pressure limit of the unit. The pressure is then held for a specific amount of time to visually inspect the system for leaks. Visual inspection can be enhanced by applying either tracer or fluorescent dyes into the liquid medium in order to determine the location of cracks and leaks that are originating over it.

7.4 Air Seat Test

The valve is tested for its performance in automatic purging of small quantities of air, while the pipeline is pressurized. Air is injected to the valve inlet, in closed, pressurized position. Air release and re-sealing are inspect.

8 Application

The actuating valves were used to control the flow and pressure and also shut off of corrosive fluids and gases.

They are also used in the oil industry and natural gas industry.

Sectors like manufacturing, chemical storing; residential areas, etc., were these actuating valves actively perform its function.

Actuating valves were highly suitable in high-temperature and pressure conditions.

It is used for automatic on and off applications.
They can be used in high radiation areas.

9 Advantages

Their operation and maintenance on repair of gate valves seating surfaces are complex.

The main biggest advantage of ball valves is that they have a very poor throttling characteristics. This can cause the seat of a ball valve to erode easily and has high output capability and high actuator stiffness.

They provide laminar flow, and pressure loss is minimum.

There will be low-pressure drop when opened fully and then tightly sealed and has fast stroking speed.

10 Result and Discussion

The result of the project would be positive if it reaches the industrial persons, with all affordable commitments. If the pneumatic actuator becomes familiar in the industries, then everything will be automated and the operations become easy to access. This valve will be very much helpful for the operators to operate the ball valves from the distance itself. Also it is electrically operated which makes it open and close by itself. If there are any drawbacks that occur in the ball valves, it will be rectified in future with advanced technology.

11 Conclusions

Today, industries work on highly automated machinery processes than normal manual systems. With the tremendous increasing usage of automated machinery systems, it has also been a great rise in the demands of the actuators, which play a vital role in the automation process. Actuators are responsible for moving, controlling, and positioning of a mechanism or system that makes the working of automated equipment easy. In the coming years, the demand for industrial valves is anticipated to rise as they are used in various commercial construction projects, automation projects, and so on. Increased industrialization and expansion of existing facilities have spurred the demand owing to technological innovations and boost the industry growth. This inventory action would enhance the new supplements and eliminates labor in hazardous zones.

References

1. Ebenezer Sathish Paul P, Uthaya Kumar G, Durairaj S, Sundarrajan Dharmakrishnan D (2015) Design and analysis of industrial ball valve using computational fluid dynamics. Int J Recent Trends Mech Eng
2. Mandanaka P, Raiyani H (2016) Review on modeling and FEA analysis of ball valve. Int J Sci Res Dev 4(03)
3. Ali H, Mohd Noor SBB, Bashi SM, Marhaban MH (2009) A review of pneumatic actuators (modeling and control). Australian J Basic Appl Sci 3(2):440–454
4. Dutt K (2013) Analytical description of pneumatic system. Int J Sci Eng Res 4(9)
5. Gokilakrishnan G, Divya S, Rajesh R, Selvakumar V (2014) Operating torque in ball valves-a review. Int J Technol Res Eng 2(4)
6. AthifMohd Faudzi A, DinMustafa N, Osman K (2014) Force control for a pneumatic cylinder using generalized predictive controller approach. Hindawi Publishing Corporation Mathematical Problems in Engineering, vol 2014
7. Bagdi KH, Raiyani H (2019) Analysis and optimization of ball valve. Int J Innov Res Sci Eng Technol 8(3)
8. Dohta S, Akagi T, Masagoa Y, Matsushita H, Zhang Y (2012) Development of small-sized digital servo valve for wearable pneumatic actuator. Int Symp Robot Intell Sensors
9. Tabrizi AS, Asadi M, Xie G, Lorenzini G, Biserni C (2014) Computational fluid dynamics based analysis of a ball valve performance in the presence of cavitation. J Eng Thermophys 23(1):27–38
10. Uehara S, Hirai S (2005) Unconstrained vibrational pneumatic valves for miniaturized proportional control devices. In: Proceedings of 9th international conference on mechatronics technology
11. Shearer JL (1956) Study of pneumatic process in the continuous control of motion with compressed air. Trans ASME 233–249
12. Wang J et al (1999) Accurate position control of servo pneumatic actuator systems: an application to food packaging. Control Engineering Practice 7:699–706
13. Messina A et al (2005) Experimenting and modelling the dynamics of pneumatic actuators controlled by the pulse width modulation (PWM) technique. Mechatronics 15:859–881
14. Shaojuan Y et al. (2008) A new iterative learning controller for electro-pneumatic servo system. In: Intelligent systems design and applications, pp 101–105
15. Barth EJ, Goldfarb M (2002) A control design method for switching systems with application to pneumatic servo systems. ASME Conf Proceed 2002:463–469
16. Choi H-S et al (2005) Development of hybrid robot for construction works with pneumatic actuator. Automat Construction 14:452–459
17. Faudzi AAM et al. (2008) Distributed physical human machine interaction using intelligent pneumatic cylinders. In: International Symposium on Micro-Nano Mechatronics and Human Science, 2008, pp 249–254
18. Sang-Eun S et al (2010) Development of a pneumatic robot for MRI-guided transperineal prostate biopsy and brachytherapy: New approaches," in Robotics and Automation (ICRA). IEEE International Conference on 2010:2580–2585
19. Kubo et al (2009) Development of active 80-faced polyhedron for haptic physical human-machine interface. In: IEEE/RSJ International Conference on Intelligent Robots and Systems, 2009. IROS, pp 1259–1264
20. Rajendran S, Nanda PS (2009) Electro-pneumatic servo system. In: presented at the 14th National Conference on Machines and Mechanisms (NaCoMM09), NIT, Durgapur, India
21. Schindele D, Aschemann H (2009) Adaptive friction compensation based on the LuGre model for a pneumatic rodless cylinder. In: 35th Annual Conference of IEEE Industrial Electronics, IECON '09, pp 1432–1437
22. Ali HI et al (2009) Mathematical and intelligent modeling of electropneumatic servo actuator systems. Aust J Basic Appl Sci 3:3662–3670

Analysis of Six Sigma—Implementation of DIMAC Methodology in Foundry Industry

P. Nethaji, P. Kaliyappan, R. Sathya, S. R. Hariprakash, and K. Prakash

Abstract This paper work has the objective of suggesting improvements in the quality of a compressor housing work cell using SIX SIGMA concepts. Customers expect good quality products at the right time. Competition in the market is increasing day by day, to overcome this situation; Industries are compelled to develop their manufacturing processes to fulfil customer needs. Many defects occur during the casting process, resulting in poor quality of products there is, therefore need to find a compelling problem that makes the product in-to Critical to Quality (CTQ). A perusal of the relevant literature shows that SIX SIGMA provides a defined paradigm for large scale industries. The goal of this paper is to investigate how SIX SIGMA tool can be adapted to the manufacturing environment. With a reference to taking a leading foundry industry as a case study, the main objective of this project is to reduce the rework/rejection in gravity die casting process and to optimize the parameters using the application of SIX SIGMA methodology; Define-Measure-Analysis-improve-Control (DMAIC).

Keywords Casting defect · CTQ · Six sigma · Gravity dies casting process · DIMAIC

1 Introduction

Quality is based on the established utility of the product. When a product manufactured is free of defects, it is a good quality product. Six Sigma provides continuous improvement in an organization and helps to achieve customer satisfaction. Use of the Six Sigma approach in the organization helps boosting on an on-going basis the

P. Nethaji (✉) · P. Kaliyappan · S. R. Hariprakash · K. Prakash
Department of Mechanical Engineering, SKR Engineering College, Anna University, 600123 Tamilnadu, India
e-mail: nethaji13393@gmail.com

R. Sathya
Department of Electronics and Communication Engineering, Rajalakshmi Engineering College, Anna University, 602105 Tamilnadu, India

G. Kumaresan et al. (eds.), *Advances in Materials Research*, Springer Proceedings in Materials 5, https://doi.org/10.1007/978-981-15-8319-3_121

financial status of the industry. It is used mainly for quality improvement process by reducing the rejection/rework and also the production cost.

Joshi [1], has made an analysis of the various defects in the casting process with Pareto and cause and effect diagrams to locate the exact causes and the remedial factors to improve quality level and productivity of the organization [1]. Chintan [2], discusses various tools and techniques used in Six Sigma methodology and performance measurement of the organization DPMO, maintained at Six Sigma level [2]. Manohar and Balakrishna (2013), there is an analysis of various defects seen on the casting wheel and shows how Six Sigma methodology can be adapt in the casting wheel production process [3]. Sandhya and Ramakrishna [4], discuss Six Sigma DIMAIC methodology tools for reducing defects and optimizing the parameters. Their paper demonstrates their findings of various causes using a cause and effect diagram [4]. Sanjiv Kumar Tiwari [5], has taken up the study of a small scale foundry industry in India, for reducing rejections in a green sand casting using Six Sigma tools, response surface methodology using ANOVA and control chart [5].

Execution for this schema implies that the consolidation from claiming MCDM in six sigma prompt. An noteworthy change in the sigma level of the firm Regardless of unapproved unlucky deficiency for addition assets. This examines could help scientists Furthermore professionals will completely see all the Furthermore profit starting with BDA abilities Also change activities for example, such that LSS What's more GM same time overseeing Ecological issues [6–8]. Those later acquaintance of the six sigma methodology likewise helped large portions firm for effectively upgrading their generation capacities, lessening waste, What's more expanding effectiveness, also usage of the recommended six sigma approach might diminish the dismissal rate significantly [9–11].

Execution of a six sigma nature change one task clinched alongside Indian MSME association included in the creation about transportable enhancer frameworks with a point to decrease the repairs Furthermore rejections Also likewise discriminating survey with respect to detail cutoff points Also control cutoff points may be produced starting with the point of view for six sigma nature and the require to An solid security between the two will be pushed [12–15]. Incline manufacturing by and large used to dispense with waste What's more six sigma methodology utilized to decreasing the defects clinched alongside manufacturing procedure Toward eliminating the methodology variety for assistance for Factual instruments Furthermore systems Also Additionally it could tackle the issue from claiming insufficient specimens in the industry, Furthermore there will be an effective assessment transform accessible to applications [16, 17].

There are many types seen in the casting process to suit mass production. Defect creeping during the gravity die casting process, these deteriorate the quality of the product. The aim of this paper is to find methods for reducing defects in the gravity die casting process and to maintain at Six Sigma level (zero defects).

2 Methodology

This study was done in leading foundry industry, with an in-depth study of the gravity die casting process and controls the defect using Six Sigma methodology and concepts. Figure 1 shows the methodology used for this study.

2.1 Define Phase

The first phase shows the existing gravity die casting process and problem definition, with analysis of the internal and external customer voice. This phase provides the objective of the paper and goal statement as well as the relevant data collected.

$$Y = f(x) \tag{1}$$

where

Y Response (problem in the process), and
f(x) Suspected source of variance (cause for the problem).

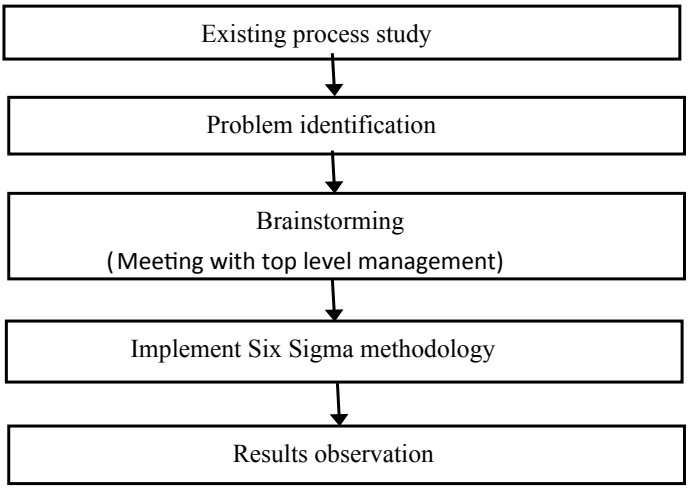

Fig. 1 Methodology six sigma implementation

2.2 Case Study

Six Sigma tools were planned for improvement in foundry industry. This manufacturing process is gravity die casting process; compressor housing products are manufactured here.

3 Measure Phase

A measure phase was used for gathering the current data for quality and cost of the rework, rejection rate, and locating critical defects. Pareto diagram (Fig. 2) shows the number of defects in y axis and the nature of the defects in x axis. It shows "Metal Not Filling defect" (MNF) accounts for bigger quality loss by the rule of 80–20. MNF defect contributes 13.3% of quality loss (Table 1).

3.1 Statement

Molten metal is not filling (MNF Defect) properly in the diffuser area resulting in gaps in the finished product, thereby increasing defects and reducing quality. This problem was identified only in final inspection (Fig. 3).

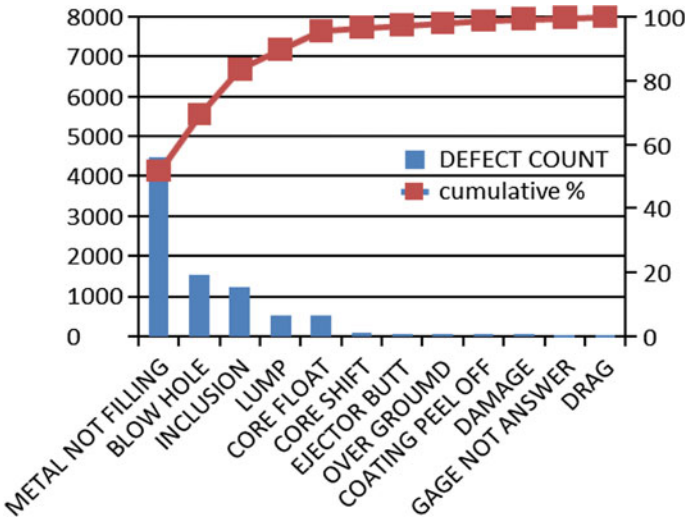

Fig. 2 Pareto diagram

Table 1 Table for Pareto diagram

Defects	Count	Cumulative count	Cumulative %
Metal Not Filling	4470	4470	51.73012383
Blow Hole	1534	6004	69.48269876
Inclusion	1226	7230	83.67087143
Lump	532	7762	89.82756625
Core Float	508	8270	95.70651545
Core Shift	79	8349	96.62076149
Ejector Butt	65	8414	97.37298924
Over Ground	64	8478	98.11364425
Coating Peel Off	63	8541	98.84272654
Damage	47	8588	99.38664506
Gage Not Answer	28	8616	99.71068163
Drag	25	8641	100

Fig. 3 MNF defect in diffuser area Problem

4 Analysis Phase

This phase helps to identify the critical cause for the MNF defect, suspected source of variance and find the root cause (X) for the CTQ and decide which vital cause requires controls (Y). Figure 4 shows the cause of the problem. Data was collected with the help of the production engineer and quality manager.

4.1 Improve Phase

The aim of the improvement phase is to improve quality and provide a solution for critical defects.

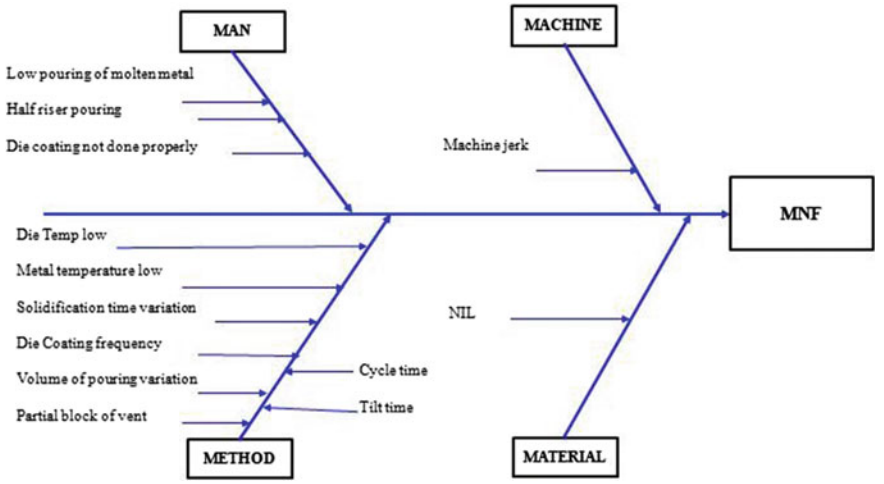

Fig. 4 Cause and effect diagram

5 Metal not Filling (MNF)-The Step

(1) Ensure that molten metal is not returned to the holding furnace.
(2) Avoid half raiser pouring
(3) Increase the vent hole size. This increases the rate of core gas escapes from the die during solidification.
(4) Decrease the tilt time. This helps to increase the filling effect of molten metal in the die.
(5) Ensure that die is clean.
(6) Standardize the pouring cup angle.

5.1 Full Factorial DOE Analysis

Full Factorial gives all possible combinations of factors and levels and these were all tested. Two factors were selected for the test (Tilt Time and Vent hole size). The following equation shows the relationship between Y(response) and Xs(factors).

$$Y = a_0 + a_1X_1 + a_2X_2 + \cdots \in + a_pX_1X_2 \ldots\ldots X_N + \varepsilon \tag{2}$$

where

Y	is the response and X_1, X2…. X_k are the factors.
a_0- a_1,a_2…..a_p	Intercept coefficients of the factors and interaction.
ε	Error of the model.

$2^k = 2^2$ = 4 treatment;
K Factor (Figs. 5 and 6: Tables 2, 3 and 4).

In the control phase, the result should be palpable control and sustain the new result and monitor it to ensure that problem seen earlier does not crop up. The following action was implemented by the production and quality department to sustain the new result.

- New design for the die should not be getting back into older design.

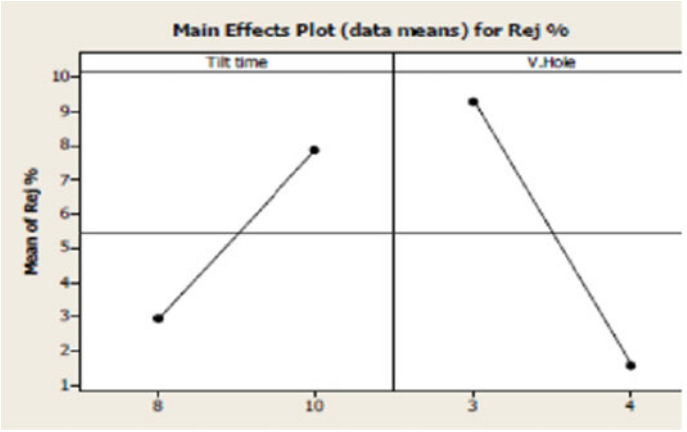

Fig. 5 Main effect plot

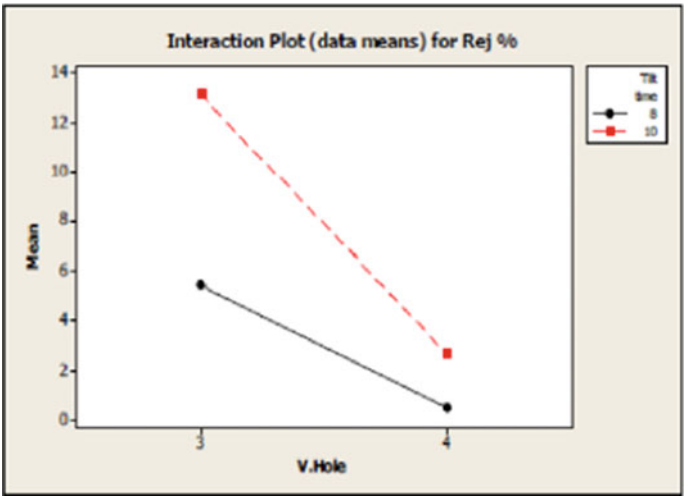

Fig. 6 Interaction plot control phase

- Tilt time for the machine should be monitor regularly. Proper training to be provided to the operator.

6 Concluding the Results

This paper shows how SIX SIGMA DMAIC methodology can be used for reducing critical defects in a foundry industry. Quality level of the compressor housing part is increased by the use of the six sigma approach and it helps to meet the customer demand quickly. After using the Six Sigma methodology, the rejection rate of MNF defect came down to 0.45% from 13.3% (Fig. 7).

Fig. 7 Defect-free job

Table 2 Factors and levels

Sl. No	Suspected source of variance	unit	Current setting (−)	New setting (+)
1	Tilt Time	seconds	10(−)	8(+)
2	Vent hole size	Millimetre	3(−)	4(+)

Table 3 Two factors, two leave full factorial

Run	Treatment	Factors	
		Tilt Time (A)	Vent size (B)
1	L	−1	−1
2	A	+1	−1
3	B	−1	+1
4	Ab	+1	+1
Trail 1 tilt time =10, vent size=3		**Trail 2 tilt time =8, vent size=3**	
Test	MNF rejection %	Test	MNF rejection %
1st	8.22	1st	5.24
2nd	13.20	2nd	6.28
3rd	13.16	3rd	5.42
Median	13.16	Median	5.42
Trail 3 tilt time =10, vent size=4		**Trail 4 tilt time =8, vent size=4**	
Test	MNF rejection %	Test	MNF rejection %
1st	2.63	1st	0.64
2nd	2.42	2nd	0.48
3rd	2.82	3rd	0.46
Median	2.63	Median	0.48

Table 4 Result of the trails

Trail no	Tilt time	Vent hole size	Treatment	Response (median of rejection %)
1	(−1) 10	(−1) 3	L	13.16
2	(+1) 8	(−1) 3	A	5.42
3	(−1) 10	(+1) 4	B	2.63
4	(+1) 8	(+1) 4	Ab	0.48

References

1. Joshi A (2014) Pritam kadam,: An application of Pareto analysis and cause and effect diagram for minimization of defects in manual casting process. Int J Mech Prod Eng 2(2):36–40
2. Chintan C, Rao A (2015) review of six sigma implementation in small scale foundry. Int J Innov Res Sci Eng Technol 4(12):11894–11902
3. Manohar C, Balakrishna A (2015) Defect analysis on cast wheel by SIX SIGMA methodology to reduce defects and improve the productivity in wheel production plant. Int Res J Eng Technol (IRJET), 02(03), 1659–1663
4. Sandhya MS, Ramakrishna H (2015) Optimization of foundry parameters for reducing casting defects. Int J Sci Res Dev 3(03):2673–2676
5. Tiwari SK, Tiwari RK (2016) Reduction of rework in green sand casting process: a six sigma prospective. J Appl Eng Res 11(5):3141–3150
6. Gupta A, Sharma P, Jain A, Xue H, Malik SC, Jha PC (2019) An integrated DEMATEL Six Sigma hybrid framework for manufacturing process improvement. Ann Oper Res

7. Belhadi A, Kamble SS, Zkik K, Cherrafi A, El fezazi S (2019) The integrated effect of big data analytics, lean six sigma, and green manufacturing on the environmental performance of manufacturing companies: The case of North Africa. pp 1–37
8. Barot RS, Patel J, Sharma B, Rathod B, Solanki H, Patel Y (2019) Lean six sigma feasibility and implementation aspect in cast iron foundry. Materials Today: Proceedings, pp 1–8
9. Cai W, Lai KH, Liu C, Wei F, Ma M, Jia S, Jiang J, Lv L (2019) Promoting sustainability of manufacturing industry through the lean energy-saving and emission-reduction strategy. Sci Total Environ 665: 23-32
10. Chen K-S, Wang C-H, Tan KH, Chiu S-F (2019) Developing one-sided specification six-sigma fuzzy quality index and testing model to measure the process performance of fuzzy information. Int J Prod Econ 208:560–565
11. Maged A, Haridy S, Kaytbay S, Bhuiyan N (2019) ontinuous improvement of injection moulding using Six Sigma: case study. Int J Indus Syst Eng 32(2):243–266
12. Sharma P, Anshu Gupta SC, Malik PCJ (2019) quality improvement in manufacturing process through six sigma: a case study of indian msme firm. Yugoslav J Oper Res 29:519–537
13. Singh Sodhi H, Singh D, Jit Singh B (2019) An empirical analysis of critical success factors of Lean Six Sigma in Indian SMEs. Int J Six Sigma and Competitive Advantage 11(4):227–252
14. Ravichandran J (2019) A review of specification limits and control limits from the perspective of Six Sigma quality processes. Int J Six Sigma and Competitive Advantage 11(1):58–72
15. Supapan J, Chutima P (2019) Defect reduction in the manufacturing process of in-mould decoration of injection moulded components. Mater Sci Forum 962:181–188
16. Swarnakar V, Singh AR, Tiwari AK (2019) Evaluating importance of critical success factors in successful implementation of Lean Six Sigma Framework. AIP Conf Proceed 030048–1–030048- 9
17. Wang C-H, Chen K-S (2019) New process yield index of asymmetric tolerances for bootstrap method and six sigma approach. Int J Prod Econ 219:216–223

Novel Metal-Organic Polymer [Ruthenium Bis(II) (2,2′–Bipyridyl 4,4′–Dicarboxylic Acid) (N-Methyl morpholine)]$_n$ $(BF_4)_{2n}$ for Dye-Sensitized Solar Cell Application

Sathishkumar Chinnasamy, Mohanraj Shanmugam, and Sivasubramanian Ramanathan

Abstract Herein, we have given the synthesis of a novel Ruthenium based metal-organic polymer dye $[Ru(L_1)_2(L_2)]_n(BF_4)_{2n}$, where L_1 = 2,2′bipyridyl 4,4′-dicarboxylic acid, L_2 = N-Methyl Morpholine, coded as RuMOP-NMM1, centered on long-drawn-out organic base (N-Methyl Morpholine) as linker unit and its photophysical and electrochemical properties. The material was characterized by UV–Vis absorption, Fluorescence, Infrared (FT-IR), Raman and Nuclear Magnetic Resonance (NMR) spectroscopy, Elemental Analyser (CHNS/O), Thermo Gravimetric/Differential Scanning calorimetry (TG/DSC) and Cyclic Voltametry (CV). The polynuclear complex displays an absorption band on longer wavelengths with high molar extinction coefficient. The metal-mediated supramolecular polymer complex, exhibit a strong luminescence emission. Henceforth, these metal-organic polymer (RuMOP-NMM1) have better thermal and chemical stability than the mononuclear complexes. These photoluminescence and electrochemical characterization results strongly suggest that the synthesized metal-organic polymer is kinetically and energetically suitable to aid as sensitizers in energy-relevant applications mainly in dye-sensitized solar cell (DSSC).

Keywords Methyl morpholine · Supramolecular · Polymer · Metal-organic · DSSC · Sensitizer · Ruthenium (II) · Solar cell

S. Chinnasamy (✉) · S. Ramanathan
Nanochemistry and Hybrid Solar Energy Lab, PSG Institute of Advanced Studies Coimbatore, Coimbatore, Tamil Nadu 641004, India
e-mail: chemistrysathish@gmail.com

M. Shanmugam
Sardar Vallabhbhai Patel International School of Textile and Management, Coimbatore, Tamil Nadu 641004, India

G. Kumaresan et al. (eds.), *Advances in Materials Research*, Springer Proceedings in Materials 5, https://doi.org/10.1007/978-981-15-8319-3_122

1 Introduction

In the present global scenario, the important need of the hour is to utilize renewable energy sources for commercial applications. In that, solar energy utilization is the prior one and important one. So in the last few years, research on conversion of solar energy into photovoltaic energy becomes a significant one. As a consequence, range of photovoltaic devices (solar cells) was raised such as silicon solar cells, organic Solar cells, dye-sensitized solar cells and polymer solar cells [1–6]. In that, dye-sensitized solar cells (DSSCs) have involved noteworthy attention of recent researchers due to their low production cost. As presence a multilayer stratagem, the efficiency of DSSC mostly rests on the act of sensitizers, TiO_2 photoanode, counter electrode and electrolyte [7]. Among these main components, dye sensitizer is accountable for the photon absorption, electron injection and enlightening the efficiency. Subsequently, dye sensitizer plays an energetic part in the device efficacy, different kinds of dyes have been used in DSSC. Amongst these dye sensitizers, ruthenium polypyridyl based dyes exposed the preeminent concert due to their better light-harvesting properties upon adsorption onto TiO_2. [8–11]. Though, Ruthenium polypyridyl based dyes were identified as the most competent sensitizers for DSSC applications. In specific, the dicarboxylated bipyridine ligand-based N3 referred to as the standard. Ruthenium polypyridyl complex centered sensitizers have attained 12% efficiency. So, there is a great entreaty to expand the performance of ruthenium complexes based DSSCs [12, 13].

In mandate to realize higher efficiency, sensitizers with appropriate structural sorts are required. Covering the aromatic units over various ligands, the photophysical electrochemical characteristics of DSSC might be amended. Supramolecular metallo-polymers have increased ample interest in current years [14]. These polymers through extended π—conjugation units can display unusual photophysical and electrochemical properties. Therefore, the transition metal founded main chain coordination polymers show greater photophysical properties and absorption bands within elevation extinction coefficients [15, 16]. These supramolecular metallo-polymers too display the grouping of both organic and organometallic compounds. The structure and the property of the metallopolymers can impart significant differences in the device performances. Ruthenium based metallo-polymers with conjugated units has many advantages, such as long-lived metal to ligand charge transfer (MLCT) and exhibit Ru(II, III) along with ligand centered redox process [17, 18].

In this work, we report the synthesis and characterization of novel Ruthenium based metal-organic polymer dye $[Ru(L_1)_2(L_2)]_n(BF_4)_{2n}$, where $L_1 = 2,2'$bipyridyl 4,4′-dicarboxylic acid, $L_2 =$ N-Methyl Morpholine, coded as RuMOP-NMM1, structure–property rapport as a sensitizer in DSSC has been considered. The polymeric dye presented exceptional performance closed to that of reference dyes.

2 Experimental Section

2.1 Materials and Methods

All reagents and solvents used in this synthesis are AR grade. All reactions are carried out under Argon gas atmosphere. The Ruthenium precursor $Ru(dcbpy)_2Cl_2$, reference dye (N_3 dye) was prepared according to the literature. P_{25} TiO_2 powder (<99%) were purchased from Sigma Aldrich.

2.2 Characterization

The UV–Vis spectra were obtained by using Shimadzu UV-1800 UV–VIS spectrophotometer (Japan). Flourescence spectra were taken by Shimadzu RF-6000 spectrofluorophotometer (Japan). FTIR spectra were measured in IR Affinity FTIR, (Shimadzu, Japan). ^{1}H NMR spectra were received by 400 MHz NMR spectrometer JEOL JMM-ECS 400. The elemental and mass analysis was completed by Perkin-Elmer elemental analyzer and JEOL GCMATEII correspondingly. The TGA/DSC analysis was conceded out in NETZCH STA Jupiter 4429. Raman analysis was ensured by Horiba Jobin-LabRam-HR UV–vis μ-Raman spe at ambient temperature with Argon laser with an excitation wavelength of 514 nm equipped with CCD detector.

3 Results and Discussion

3.1 Synthesis of RuMOP-NMM1

[Ru(L$_1$)$_2$(L$_2$)]$_n$(BF$_4$)$_{2n}$, Where L$_1$ = 2,2′bipyridyl 4,4′-Dicarboxylic Acid, L$_2$ = N-Methyl Morpholine]

Preparation of metal-organic polymer dye $[Ru(L_1)_2(L_2)]_n(BF_4)_{2n}$, where L_1 = 2,2′bipyridyl 4,4′-dicarboxylic acid, L_2 = N-Methyl Morpholine, coded as RuMOP-NMM1, was prepared by the following synthetic procedure (1), concerning the replacement of the two chloride ions in Ru(II) precursor $[RuCl_2(dcbpy)Cl_2]$ with the N-Methyl Morpholine as linker unit which is based on extended organic base group.

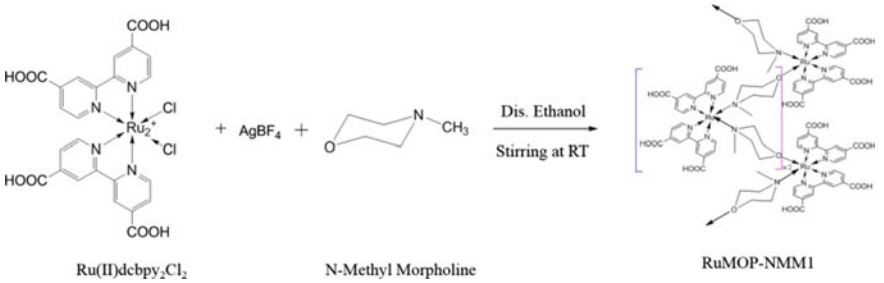

Scheme 1 Synthesis of RuMOP-NMM1

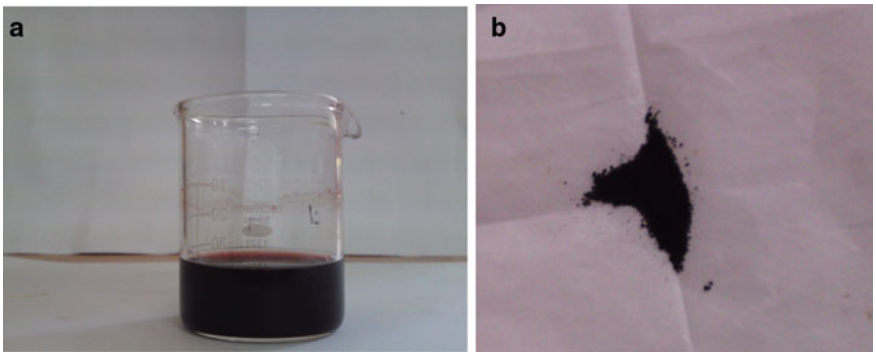

Fig. 1 **a** and **b** RuMOP-NMM1 in Methanol and in powder form

3.2 UV–Visible and Emission Spectroscopy

The UV–Vis spectra of (**RuMOP-NMM1)** show bands in the visible region due to MLCT transitions. The occurrence of carboxylated group exhibit two π to π* intraligand transitions. The two t_2 to π* MLCT bands is due to the visible and near–UV. The absorption and emission values were given in Table 1. The room temperature luminescence of (**RuMOP-NMM1)** complex is displayed the luminescence maximum is positioned centered at 534 nm.

Table 1 Absorption and luminescence properties of (**RuMOP-NMM1**)

Complex	Absorbance (nm)	Emission (nm)
(RuMOP-NMM1)	522	535
	390	
	312	

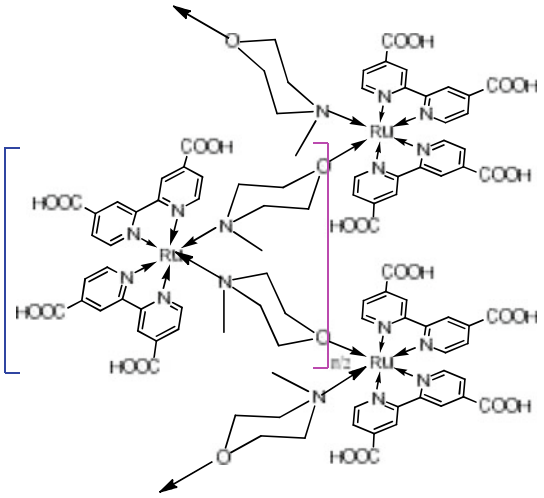

Structure of RuMOP-NMM1

3.3 FT–IR Spectroscopy

A sturdy band in the area of 3412 cm^{-1}, owing to the occurrence of O–H group of the carboxylic acid group. The quite durable absorption at 1711 cm^{-1} corresponds to the stretching vibration mode of C = O bond and the bands at 1359 cm^{-1} and 1601 cm^{-1} are due to the symmetric and asymmetric stretching in the C = O and C-H bands respectively. Due to the N-coordination from the N-methyl morpholine unit absorption at 2011 cm^{-1} was noted [19].

3.4 Thermal Gravimetric Analysis

The TGA curve of the metal-organic polymer (**RuMOP-NMM1)** is given in Fig. 1. 7.66% weight loss at 70–90 °C is due to the removal of solvent residues. A weight loss observed at 250–345 °C arise due to the loss of coordinated organic ligand. Overhead 400 °C a nearly horizontal curve was obtained due to the realization of metal oxides. The weight fraction of mass change is given in Table 2. The thermal behaviour is consistent with other Ru based dicarboxylic bipyridyl ligands [20].

Table 2 Thermal properties of (**RuMOP-NMM1)** sensitizer

Complex	Temp (ºC)	Mass Change (%)
RuMOP-NMM1	90	7.66
	345	23.81
	400	45.62

Table 3 Photovoltaic properties of DSC $[Ru(dcbpy)_2](NCS)_2$ as sensitizer

Complex	J_{sc} (mA cm^{-2})	V_{oc} (V)	FF (%)	Efficiency (%)
(RuMOP-MM1)	2.79	0.582	65.1	1.07

3.5 Fabrication of DSSCs

DSSC has been prepared using the synthesized (**RuMOP-NMM1)** dye as a photosensitizer and with a double layer TiO_2 coating on FTO plate as photo anode entailing of a transparent titania nanoparticles and BMMI electrolyte. We checked the photovoltaic response of the devices. The photovoltaic parameters are listed in Table 3.

The overall conversion efficiencies 2.3% were derived from the equation:

$$\text{IPCE} = J_{\text{sc}} \times V_o \times FF,$$

where

J_{sc} is the short circuit current density,
V_{oc} the open-circuit voltage and FF the fill factor.

By using N_3 dye the overall efficiency obtained was 10%. In this report the power conversion efficiencies were 1.07% only, we stress the detail that by tuning all other parameters these dyes can attain the literature mentioned efficiency. We believe that the use of more pi-conjugated extended schemes, with appropriate p-delocalized substituent's also would improve light harvesting possessions and, ultimately, photovoltaic performances.

3.6 I-V Characteristics

The current density (J) against voltage (V) curves of the DSSC is exposed in Fig. 2. The photovoltaic dimensions of open-circuit voltage (V_{oc}), short circuit current density (J_{sc}), fill factor (*FF*), and the PCE (η) values were abridged in Table 3. The metal-organic polymer ***(RuMOP-Pyz-1)***, based DSSC showed the photoconversion efficiency value (η) of 1.07% with short circuit current (J_{sc}) 2.79 mA/cm^2; open-circuit voltage (V_{oc}) 0.582 V and Fill Factor (*FF)* 65.1%. In compared with the

reference dye. The main-chain metal-organic polymer-based supramolecular ruthenium which has linker units, has better photovoltaic properties. So, in this synthesized main-chain metal-organic polymer which has efficient electron injection on TiO_2 surface (Fig. 3).

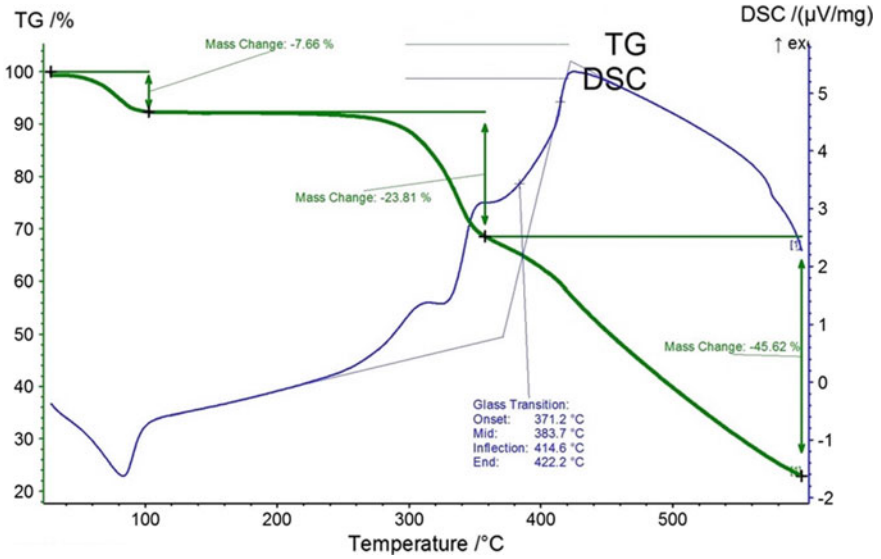

Fig. 2 TGA and DSC curves of (**RuMOP-NMM1**)

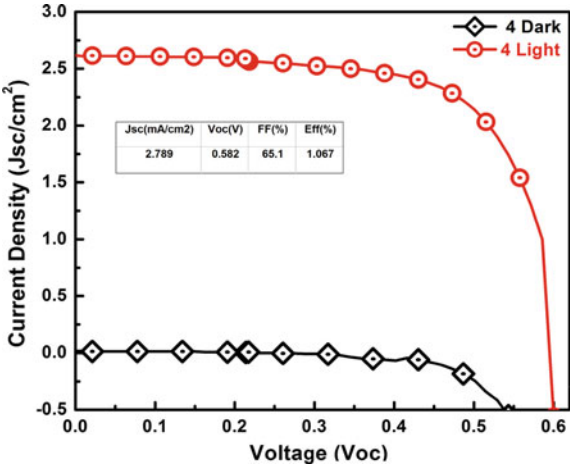

Fig. 3 *J-V* curves of (**RuMOP-NMM1**) as sensitizer in DSSC

4 Conclusions

In summary, **$[Ru(L_1)_2(L_2)]_n(BF_4)_{2n}$, where L_1= 2,2′bipyridyl 4,4′-dicarboxylic acid, L_2= N-Methyl Morpholine,** metal-organic polymer **RuMOP-NMM1** was effectively prepared and engaged as an energy material in the form of sensitizer in DSSC. The synthesized metal-organic polymer was characterized using several spectroscopic and microscopic techniques. A maximum conversion efficiency of 1.07% with short circuit current (J_{sc}) 3.22 mA/cm^2; open-circuit voltage (V_{oc}) 0.582 V and Fill Factor (FF) 65.1%. Under Air Mass (AM) 1.5 G simulated sunlight at a light intensity of 100 mW/cm^2 was obtained.

References

1. Grazia LS, Giacomo C, Salvatore C, Raphael S (2017) Geometric shape optimization of organic solar cells for efficiency enhancement by neural networks, Lecture note Mech. Eng 789–796
2. Mital C, Cheer S, Hong H (2017) Recovery of metals from solar cells by bioleaching. Lecture Note Mechanical Engineering, pp 277–284
3. Ping LX, Yun ZZ, Xu Z, Zen CD, Hsuan HM, Jia Z, Sheng LR, Jing Z, Hua ZY (2013) Technological collaboration patterns in solar cell industry based on patent inventors and assignees analysis. Lecture Note Mechanical Engineering, pp 427–441
4. Shivangi AK, Saxena M, Siddiqui S (2019) Effect of AR coating properties on diffused reflectance and overall efficiency of mc-Si Silicon solar cells. Lecture Note Mechanical Engineering, pp 407–412
5. Khadambari B, Bhattacharya SS, Rao MSR (2019) Fabrication and characterization of $Cu_{2-X}Zn_{1.3}SnS_4$ kesterite thin films synthesized by solvent based process method for photovoltaic solar energy applications. Lecture Note Mechanical Engineering, pp 241–247
6. Wangmo P. Jadoun VK, Agarwal A (2020) A review on solar energy-based smart Ggreenhouse. Lecture Notes Mechanical Engineering, pp 629–634
7. O' Regan B, Gratzel M (1991) A low-cost, high-efficiency solar cell based on dye-sensitized colloidal TiO2 films,. Nature 353 (1991):737–740.
8. Hagfeldt A, Boschloo G, Sun L, Kloo L, Pettersson H (2010) Dye-sensitized solar cells. Chem Rev 110:6595–6663
9. Yella A, Lee H-W, Tsao HN, Yi C, Chandiran AK, Nazeeruddin MK, Diau E, Yeh CY, Zakeeruddin SM, Gratzel M (2011) Porphyrin-sensitized solar cells with cobalt (II/III)–based redox electrolyte exceed 12 percent efficiency. Science 334:629–634
10. Loh L, Dunn S (2012) Recent progress in ZnO-based nanostructured ceramics in solar cell applications. J Nanosci Nanotechno 12:1–16
11. Chen HS, Lue SJ, Tung YL, Cheng KW, Huang FY, Ho KC (2011) Elucidation of electrochemical properties of electrolyte-impregnated micro-porous ceramic films as framework supports in dye-sensitized solar cells. J Power Sources 196:4162–4172
12. Yen YS, Chou HH, Chen YC, Hsu CY, Lin JT (2012) Recent developments in molecule-based organic materials for dye-sensitized solar cells. J Mater Chem 22:8734–8747
13. Wong WY (2009) Challenges in organometallic research–Great opportunity for solar cells and OLEDs. J Organomet Chem 694:2644–2647
14. Nagarajan B, Kushwaha S, Elumalai R, Mandal S, Ramanujam K, Raghavachari D (2017) Novel ethynyl-pyrene substituted phenothiazine based metal free organic dyes in DSSC with 12% conversion efficiency. J Mater Chem A 5:10289–10300
15. Daeneke T, Kwon TH, Holmes AB, Duffy NW, Bach U, Spiccia L (2011) High-efficiency dye-sensitized solar cells with ferrocene-based electrolytes. Nat Chem 3:211–215

16. Cuello-Garibo JA, James CC, Siegler MA, Bonnet S (2018) Influence of the Steric Bulk and Solvent on the Photoreactivity of Ruthenium Polypyridyl Complexes Coordinated to L-Proline. Eur J Inorg Chem 25:1260–1268
17. Billen P, Leccisi E, Dastidar S, Li S, Lobaton L, Spatari S, Baxter JB (2018) Comparative evaluation of lead emissions and toxicity potential in the life cycle of lead halide perovskite photovoltaics. Energy 166:1089–1096
18. Yun S, Qin Y, Uhl AR, Vlachopoulos N, Yin M, Li D, Hagfeldt A (2018) New-generation integrated devices based on dye-sensitized and perovskite solar cells. Energy Environ Sci 11:476–526
19. Greijer H, Lindgren J, Hagfeldt A (2001) Resonance Raman scattering of a dye-sensitized solar cell: mechanism of thiocyanato ligand exchange. J Phys Chem B 105:6314–6320
20. Sannino D, Vaiano V, Ciambelli P, Zama I, Gorni G (2013) Evaluation of N719 amount in TiO2 films for DSSC by thermo gravimetric analysis. J Therm Anal Calorim 453–458

Effect of Different SiCp Particle Sizes on the Behavior of AA 7075 Hot Deformation Composites Using Processing Maps

M. Rajamuthamilselvan, S. Rajakumar, and S. Kavitha

Abstract The mechanical reaction of 7075 Al alloy and Al 7075/15% SiCp with 5 μm, 20 μm, and 63 μm metal-matrix composites is investigated using a hot compression sample. In order to achieve the processing map of the studied material following the dynamic material model, the flow stress curves obtained in temperature ranges of 300–500 °C and strain rate ranges of 0.001–1.0 s-1, respectively. All flow instability zones are analyzed by an optical microscope. Microstructural characterization carried out using an optical microscope image analyzer on compressed composite specimens showed safe domains and non-safe domains. The composites of AA7075/20 μm SiCp showed higher efficiency, flow stress, and lower regimes of instability than alloy.

Keywords Mmcs · Processing maps · Dynamic recrystallization · Hot workability

1 Introduction

Hot deformation is an essential step in aluminum alloy production. Number of studies on the hot workability of these alloys has been carried out [1, 2]. Higher flow stress can be obtained for the alloy with unstable microstructure due to dynamic precipitation, and the flow curves often show significant softening due to subsequent coarsening of particles [1]. Due to their high mechanical properties and low density, the high-strength Al–Zn–Mg–Cu alloys were widely used in aeronautical structures. However,

M. Rajamuthamilselvan (✉)
Department of Mechanical Engineering, Government College of Engineering, Srirangam, Trichy, Tamilnadu 620012, India
e-mail: rajanarmi@yahoo.co.in

S. Rajakumar
Department of Manufacturing Engineering, Annamalai University, Annamlai Nagar, Chidambaram, Tamilnadu 608002, India

S. Kavitha
Department of Electronics and Instrumentation Engineering Annamalai University, Annamlai Nagar, Chidambaram, Tamilnadu 608002, India

G. Kumaresan et al. (eds.), *Advances in Materials Research*, Springer Proceedings in Materials 5, https://doi.org/10.1007/978-981-15-8319-3_123

due to the high concentration of Zn, Mg, and Cu elements, their hot workability is often reduced. Thus, to obtain only the required shape, but also more importantly the desired microstructure and properties, the hot deformation parameters need to be optimized. Because of the practical importance, the warm deformation behavior of some Al–Zn–Mg–Cu alloys [3] has been investigated.

Al-MMCs can substitute for steel to some degree when reinforced with ceramic particulate materials such as SiC, Al2O3, B4C, and TiC. Consequently, they have great potential of application in defense and automotive industries [4].The high-strength metal-matrix composites combine the high strength and hardness of the reinforcing phase with the ductility and toughness of light metals that the particulate-reinforced metal-matrix composites have emerged as attractive materials for use in a range of applications involving industry, military, and space-related applications [5]. The renewed interest in metal-matrix composites was encouraged by the production of reinforcement material that either offers improved properties or reduced costs compared to existing monolithic materials [6]. As a function of temperature, strain rate, and strain, the input to produce a processing map is the experimental flow stress information. Since the generated map will only be as good as the input data, it is important to use precise, reliable, and yet simple experimental technique to generate them [7].

Reinforcement of the size and volume fraction are two important factors controlling the mechanical properties of MMC. Clearly, the spacing between particles is an important geometric parameter to regulate an inhomogeneous plastic deformation in the composite. According to Liu et al.[8], the strain gradient can effectively describe this in homogenous plastic deformation. Comparative study on the effect of SiCp particle sizes and volume fraction on 7075 Al/SiCp composites deformation behavior is discussed below.

The processing map technique is based on the concept of dynamic materials, whose principles were mentioned earlier [9, 10]. In short, the work piece undergoing a hot deformation is considered to be a power dissipater, and the total power instantaneously dissipated is given by.

$$P = \int_0^{\acute{\epsilon}} \sigma . d\acute{\epsilon} + \int_0^{\sigma} \acute{\epsilon} . d\sigma = G + J \tag{1}$$

where there is the strength of flow and where there is the rate of stress. In terms of terminology of physical systems, the first integral is called G content representing heat deformation, and the second one is a J co-content representing microstructural dissipation, which is a complementary part of G content. The strain rate sensitivity (m) is the factor that divides energy between heat deformation and microstructural changes as follows:

$$\frac{dJ}{dG} = \frac{\acute{\epsilon} . d\sigma}{\sigma . d\acute{\epsilon}} = \frac{\acute{\epsilon}\sigma d \ln \sigma}{\sigma \acute{\epsilon} d \log \acute{\epsilon}} \approx \frac{\triangle \log \sigma}{\triangle \log \acute{\epsilon}} = m \tag{2}$$

The efficiency of power dissipation (η) which occurs during deformation by microstructural adjustments is derived by contrasting the nonlinear power dissipation which occurs instantaneously in the workpiece with that of a linear dissipater ($m = 1$).

$$\frac{\triangle J/\triangle P}{(\triangle J/\triangle P)linear} = \frac{m/(m+1)}{1/2} = \frac{m}{m+1} = \eta \tag{3}$$

The energy dissipation map represents the three-dimensional variance of temperature and strain efficiency that is generally viewed as a contour map of iso-efficiency. Furthermore, the extreme principles of irreversible thermodynamics applied to continuum mechanics of large plastic flow were explored to establish a criterion for the onset of flow instability provided by the parameter of instability ξ (έ)

$$\xi\left(\acute{\varepsilon}\right) = \frac{\delta \ln(m/m+1)}{\delta \ln \acute{\varepsilon}} + m < 0 \tag{4}$$

The variance of the parameter of instability as a function of temperature and stress level is a map of instability that delineates instability regimes where ξ is negative. A superimposition of the instability map on the energy dissipation map provides a processing map showing domains where individual microstructural processes dominate and limiting flow instability conditions for regimes. Processing maps help to identify hot working temperature–strain rate windows where the material's intrinsic workability is maximum (e.g., superplasticity or dynamic recrystallization (DRX)) and also prevent flow instability regimes (e.g., flow location or adiabatic shear bands) or cracking. Previously, the processing map technique was used to research the mechanisms of warm deformation in Al and its alloys [9, 11] including dynamic recrystallization (DRX) and flow instability.

The standard equation of the kinetic rate relative to the flow stress (σ) and the strain rate (έ) is given by [12, 13]:

$$\acute{\epsilon} = A\sigma^n \exp(-Q/RT) \tag{5}$$

where A = constant, n = stress exponent, Q = activation energy, and R = gas constant. The rate-controlling mechanisms are identified on the basis of the activation parameters n and Q.

2 Experimental Work

Stir-casting technique was used to produce 7075Al alloy, 7075 Al alloy with reinforcement size was 5 μm, 20 μm, and 63 μm SiCp with 15% silicon carbide composite volume fraction. The aluminum alloy matrix content was 7075. Using a revolving impeller in Argon setting, preheated SiCp (250° C) was applied to the melt

and mixed and poured in permanent mold. The cylindrical samples were made from the extruded rods, 10 mm in diameter and 10 mm in height. The hot compression tests were carried out on a universal testing machine controlled by 1OT servo for different strains (0.1–0.5), strain rates (0.001 s^{-1}–1.0 s^{-1}), and temperatures (300–500° C). The specimen's temperature was monitored using a chromel/alumel thermocouple embedded in a 0.5 mm hole drilled half of the specimen's height [14]. The samples were immediately quenched in water after compression analysis and microstructure were examined for the cross section. Specimens have been deformed to half of their original height. Parallel to the compression axis, deformed specimens were sectioned, and the cut surface was prepared for metallographic testing. Specimens have been etched with the solution from Keller [15]. The specimen microstructure was obtained through an optical microscope, and the deformation mechanism was studied. For different strain levels, temperatures at a constant strain of 0.5 were evaluated using the flow stress information, power dissipation efficiency, and flow instability. Processing maps for 7075 Al alloy and Al 7075/SiC/15 percent composites were produced for 0.5 strains.

3 Result and Discussions

3.1 Interpretation from Flow Curves

It is well known that mechanical performance also depends on the size of the reinforcement particle in particulate-reinforced metal-matrix composites. If the reinforcement particle size is larger, yield and flow stresses will be increased while the strength and ductility of the fracture will often be decreased. Therefore, reinforcement particles of large size have a high fracture propensity during low temperature deformation. This pattern may also tend to be at a moderately high temperature. In such a situation, under terms of flow pressure enhancement, the impact of additional reinforcement becomes less. Nonetheless, flow pressure is linear at high stress levels, indicating the effect of increased density of dislocation in the matrix [16].

Figure 1a–d shows the flow curves of 7075 aluminum alloy and 7075Al/15%SiCp composites deformed at 0.1 s^{-1} and different temperatures ranges from 300–500 °C, respectively. The materials flow stress increases as the stress rate increases and the temperature decreases. The typical behavior of warm working conditions deformed metals [17]. For the reinforced composites, the flow pressure is lower in all situations. In the curves, it is clearly observed that there is considerable softening of the flow in composites, especially at higher strain values. This shows that the variance in flow pressure with change in particle size for a constant 15 percent composite volume fraction. It is interesting to note that the flow pressure rises at 400° C with particle size, whereas at a higher deformation temperature of 450° C it shows a decreasing pattern. It is well known that enhancing the mechanical properties of hard ceramic particles in a soft metallic matrix [18]. Larger SiC particle size added in composites

shows higher strain durability index and lower strength coefficient values due to better SiC load transfer rate to the aluminum matrix compared to lower particle size [19]. Therefore, the flow pressure of composites increases with increased particle size of reinforcement. With increased size of SiCp of composites, the better densification increases.

Because of a steep rise in the same way as the particle size is finer; the fraction of smaller particles will create a high dislocation density relative to larger particles [20]. Due to this crucial variation in dislocation size, a large number would be generated locally in homogenous areas, which in turn would affect local flow behavior. This can lead to a non-uniform reduction in flow and flow stress, making the system plastically unstable. Experiments in which a steep increase in dislocation density is observed with a decrease in particle size can describe a critical size. An increase in particle size, on the other hand, reduced composite strength and increased ductility [21].

3.2 Interpretation from Processing Map

The ultimate goal is to produce components with regulated microstructure and properties on a repeatable basis in a manufacturing environment, without macro- or microstructural defects [9]. Microstructures of deformed samples showed that under these storage conditions, dynamic recovery is the mechanism. The approach to processing maps was found to be useful in achieving optimum processing parameters and preventing microstructural defects like flow instability [22]. Figure 2 shows the processing maps for 7075 Al alloy, and 7075Al/SiCp with 5 μm, 20 μm, and 63 μm composites obtained by superimposing the instability map on the 0.5 strain efficiency is shown in Fig. 2a–d, respectively. The contour numbers represent the efficiency of power dissipation, and the shaded domains show the flow instability regions. The difference of microscopic stress and strain distributions is lower in finer microstructure composites. Temperature rises in the DRX domain as the particle size increases [23]. It is in good agreement with the findings reviewed as, Fig. 2a the map exhibits a DRX domain in the temperature range 350–395 oC and strain rate range 0.013–0.12 s^{-1} with a peak efficiency of about 28% occurring at 350 °C and 0.1 s^{-1}. In Fig. 2b, the map exhibits that the DRX domain is obtained at the temperature, and strain rate ranges are 345–385 °C and 0.01–0.1 s^{-1} with a peak efficiency of about 26% at 365 °C and 0.05 s^{-1}(5 μm). In Fig. 2c, the DRX domain occurs in the region of 355–420 °C for a strain rate range of 0.01–0.1 s^{-1}. The maximum efficiency in this domain is 44%, increasing from 20%. In Fig. 2d, the DRX domain occurs in the region of 435–495 °C for a strain rate range of 0.02–0.16 s^{-1}. The maximum efficiency in this domain is 36%(63 μm). In the 7075Al/SiCp with 20 μm composites (Fig. 2c), the maximum efficiency is due to the high bonding area when compared with the small particle size, i.e., 5 μm reinforcement size.

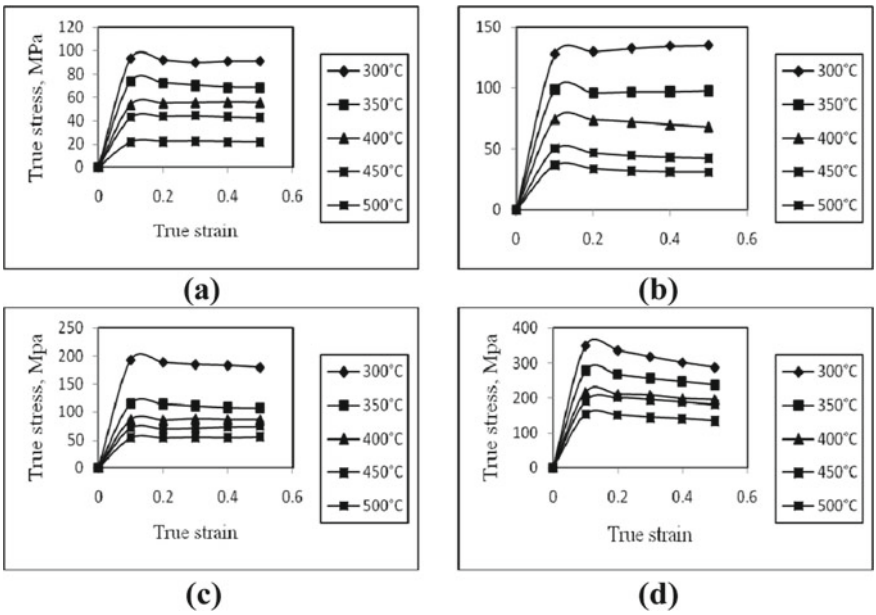

Fig. 1 **a** Flow curves of 7075 Al alloy for different temperatures at constant strain rate of 0.1 s^{-1} **b** Flow curves of 7075 Al/15%SiCp (5 μm) for different temperatures at constant strain rate of 0.1 s^{-1} **c** Flow curves of 7075 Al/15%SiCp (20 μm) for different temperatures at constant strain rate of 0.1 s^{-1} **d** Flow curves of 7075 Al/15%SiCp (63 μm) for different temperatures at constant strain rate of 0.1 s^{-1}

The stable efficiency value as a strain function indicates that the dissipation of power occurs through microstructural equilibrium processes that occur during deformation, i.e., dynamic restoration processes such as DRX and DRV. However, for verification, thorough microstructural analysis will still be required. A high efficiency in the stable environment suggests better conditions for process. Deformation efficiency of composites improves with an increase in reinforcement particle sizes up to 20 μm (5 μm—efficiency is 26%, 20 μm—efficiency is 44%), then the efficiency decreases for composites with a reinforcement particle size of 63 μm (36%), as larger particles fragment more easily during deformation than smaller ones [23].

3.3 Microstructural Examination

Interpretations of the various domains of deformation must be based on microstructural validation [22]. Figure 3a shows the micrograph of deformed 7075Al alloy at 350 °C and 0.1 s^{-1} and Fig. 3b, c deformed 7075Al/SiCp with 5 μm and 20 μm at 400 °C and 0.1 s^{-1}. Fig. 3d shows deformed 7075Al/SiCp with 63 μm at 450 °C and 0.1 s^{-1}. With wavy grain boundaries typical of grain processing by dynamic

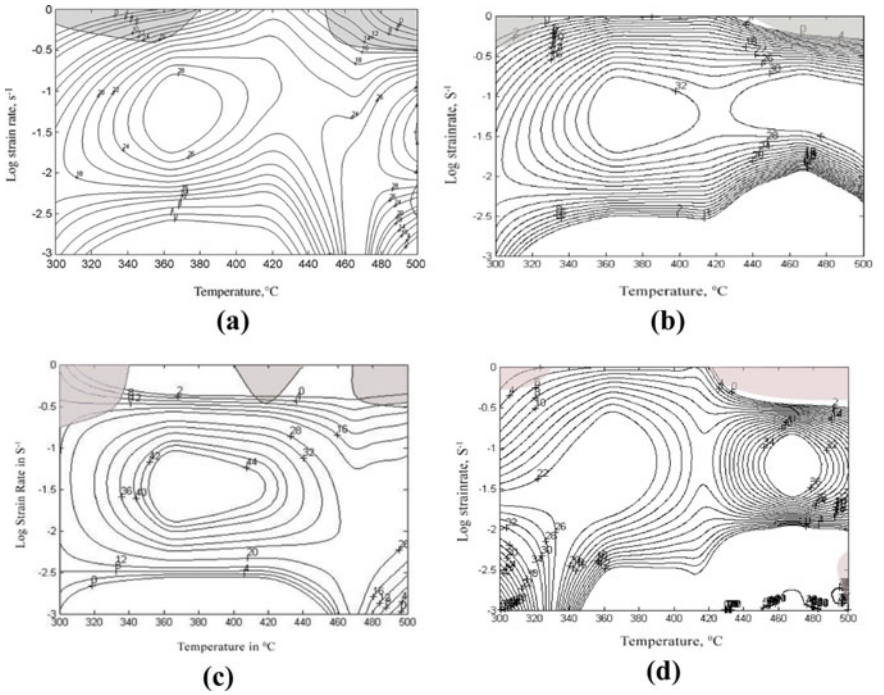

Fig. 2 **a** Processing map for 7075 alloy **b** Processing map for 7075Al/15%SiCp (5 μm) composites **c** Processing map for 7075Al/15% SiCp (20 μm) composites **d** Processing map for 7075Al/15% SiCp (63 μm) composites

recrystallization (DRX) [24], fine grains are observed in the above micrographs. The occurrence of dynamic recovery and dynamic recrystallization at higher temperatures and moderate strain rate deformation results in a significant reduction in flow stress. DRX is more successful than the DRY, however. DRX is a domain chosen to optimize hot workability and control good microstructure [24]. It is found that in the composites the dynamically recrystallized volume of grain is smaller than in alloy. This is done in the matrix by strong particles. The maximum power dissipation efficiency in the DRX domain of the 7075 Al/20 μm of SiCp is higher than that of 7075 Al alloys and 7075 Al/5 μm, 63 μm of SiCp. Large reinforcement particles are prone to fracture compared to smaller ones [25]. This particle fracture phenomenon is not expected to be an effective mechanism at high temperatures but to increase the relaxation temperature for a given strain rate for a large particle size composite reinforced lower temperature compared to temperature restoration can result in pressure accumulation at the particle/matrix interfaces. In the end, this leads to more fracture events involving the reinforcement of large particles and matrix cavitations [25, 26].

It is well agreement with the present study that particle cracking is identified in 7075Al/15% SiCp composites of higher reinforcement particle sizes (20 and 63 μm) which are as shown in Fig. 4a, b. Overall, during deformation, larger particles fracture

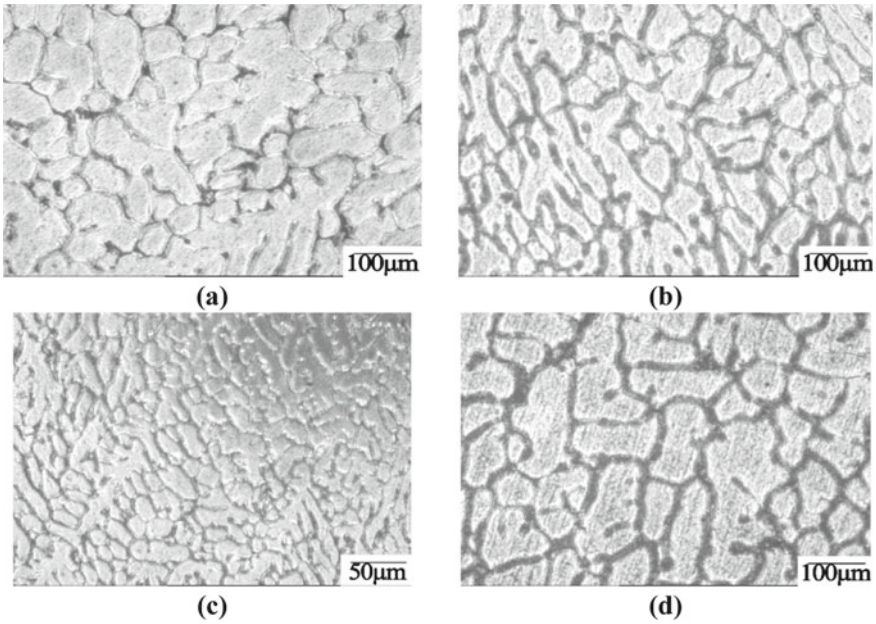

Fig. 3 **a** Dynamic recrystallization for 7075Al alloy at 350 °C at a strain rate of 0.1 s^{-1} **b** Dynamic recrystallization for 7075Al/15% SiCp (5 μm) composites at 400 °C at a strain rate of 0.1 s^{-1} **c** Dynamic recrystallization for 7075Al/15% SiCp (20 μm) composites at 400C and at a strain rate of 0.1 s^{-1} **d** Dynamic recrystallization for 7075Al/15% SiCp (63 μm) composites at 450 °C at a strain rate of 0.1 s^{-1}

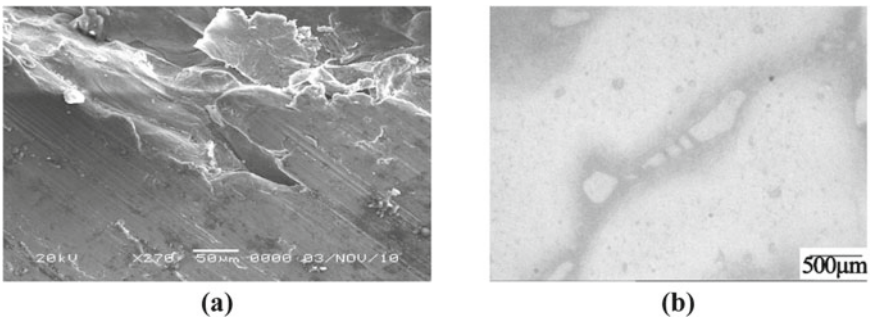

Fig. 4 **a** SEM image of particle breakage for 7075Al/15% SiCp (20 μm) composites at 400C and at a strain rate of 1.0 s^{-1} **b** Particle cracking for 7075Al/15% SiCp (63 μm) composites at 500 ∘52C and at a strain rate of 1.0 s^{-1}

more easily than smaller ones [23]. Larger particles have a larger interface area with the matrix and are therefore subject to higher concentration of stress. The force of the particle fracture is regulated by the intrinsic defects in the particle. Because the particle size of a flaw is small, larger particles are more likely to break because they are more likely to have a flaw greater than a certain critical size [27]. In addition, the composite containing large-size reinforcement particle shows more particle breakage at a higher strain rate. Srivastava et al. [20] stated that smaller particles increase the hardening of composites by plastic work, while particle/matrix interfacial decohesion does the contrary. Similarly, smaller 17 μm particle size may also result in poor workability. Large particle size with moderate volume reinforcement fraction would therefore give improved workability.

It was also pointed out that smaller particles lead to debonding of the interface, while larger ones often fractured during loading [20]. This argument is confirmed in the present investigation, i.e., debonding occurs in 7075 Al/15%SiCp (5 μm) composites as shown in Fig. 5, particle fracture occurs in7075 Al/15%SiCp (63 μm) composites. The particle size of reinforcement dominates MMC rupture, for example, cracks usually occur in particles with a dimension greater than 5 μm, whereas small particles (< 5 μm) tend to be deboned at the matrix–particle interface [28]. Matrix stress is inhomogeneous during the initial deformation stage due to the discrepancy between the particles and the matrix of the elastic modulus. In the matrix, which closes to the tip of the particles along the loading axis, high stress also develops. In the vicinity of the particles, the stress concentration is due to the stress restriction in the presence of SiC particles [29].

Due to inhomogeneity in the stress distribution, fracture and debonding occur locally at the interfaces. This can be avoided by processing the composites between reinforced particles that do not form deformation zones. It is well known in particulate-reinforced composites that debonding particle damage is easy to occur on large particles of reinforcement and difficult to occur on small particles of reinforcement. In order to consider the effect of particle size on damage, debonding damage is assumed to be controlled by a critical energy criterion for interfacial debonding of particle–matrix. The particle size is smaller, dislocation reinforcement is more

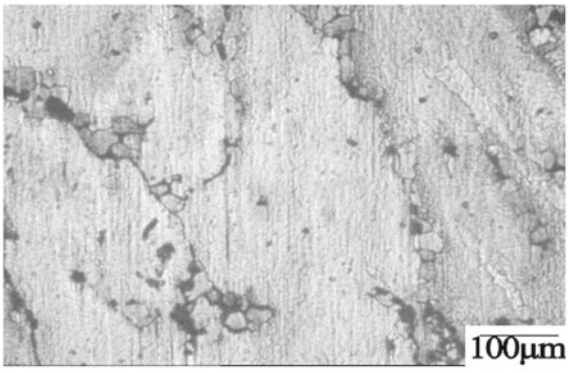

Fig. 5 Deboning for 7075Al/15% SiCp (5 μm) composites at 450 °C and at a strain rate of 1.0 s^{-1}

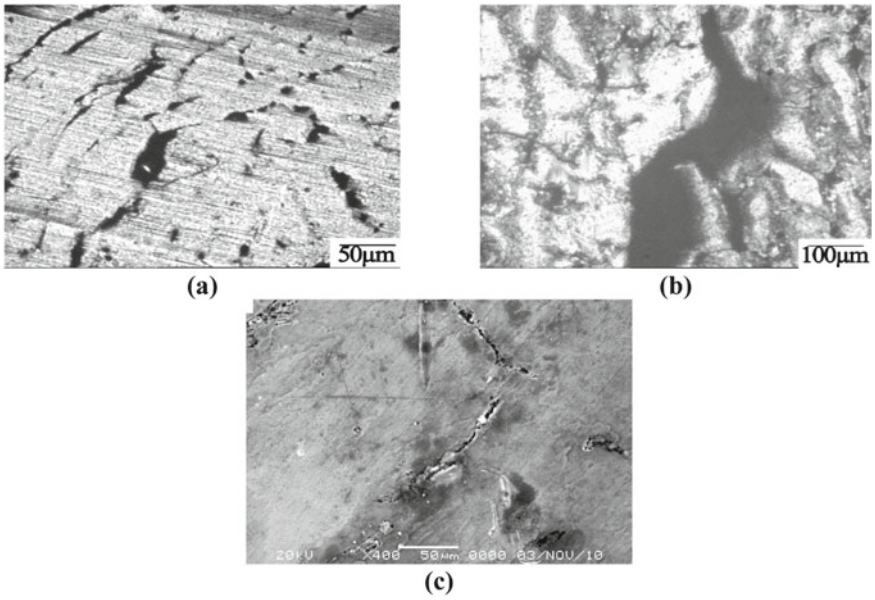

Fig. 6 **a** Matrix cracking for 7075Al/15% SiCp (5 μm) composites at 500 °C and a strain rate of 1.0 s^{-1}. **b** Interface crack for 7075Al/15% SiCp (20 μm) composites at 500C and at a strain rate of 1.0 s^{-1} **c** SEM image of interface cracking for 7075Al/15% SiCp (63 μm) composites at 500 °C and a strain rate of 1.0 s^{-1}

dominant, and debonding damage is more difficult to occur. The debonding damage occurs from larger particles to smaller particles in composites containing different sizes of particles, and the stress–strain relationship shifts to the lower side of stress [30].

The dynamic interplay of particle size, volume fraction, and strain frequency results in variability in the creation of voids and damage to particles. Low stress levels may relate large variation in the difference in porosity to the low value of matrix flow pressure, resulting in localized stress fields in turn. At a higher strain rate, high matrix flow stress does not allow large plastic strain around particles and thus fewer instances of particle breaking. At high stress frequency, particle breakage may be expected to be lower, but in such situations, the matrix cavitation phenomenon may become dominant due to inhomogeneous stress distribution in the matrix; hence matrix cracking or interface cracking may occur. Matrix cracking and interface cracking that occurs at higher strain rate and higher temperature in all the 7075Al/SiCp composite materials investigated are as shown in Fig. 6a–c.

4 Conclusions

The following conclusions were drawn from the investigation.

- Temperature rises in the DRX domain as the particle size increases. As the content of silicon carbide increases, the pore size becomes smaller, resulting in an increase in the value of the formability pressure index.
- During deformation, larger particles fracture more quickly than smaller ones. Larger particles have a wider interface with the matrix and are therefore subject to higher concentration of pressure.
- Higher reinforcement particle size of SiCp composites (7075Al (5 μm)) does not consider particle cracking. Since smaller particles improve the hardening of composites in the plastic work.
- Debonding particle damage on large reinforcement particles is easy to occur and is difficult to occur on small reinforcement particles due to the more prevalent dislocation reinforcement. Significant particle fracture and interface debonding at large strains can be related due to the low flow pressure of large particle size reinforced composites. Due to inhomogeneity in the stress distribution, fracture and debonding occur locally at the interfaces.
- Deformation efficiency of composites increases with an increase in reinforcement particle sizes up to 20 μm (5 μm—efficiency is 26%, 20 μm—efficiency is 30%), then the efficiency decreases for composites with a reinforcement particle size of 63 μm (28%)

Acknowledgements The authors thank the Department of Manufacturing Engineering, Annamalai University, Tamilnadu, India, for their support in the manufacture and testing of composites.

References

1. Zhang BL, Baker TN (2004) Effect of the heat treatment on the hot deformation behaviour of AA6082 alloy. J Mater Process Technol 153–154:881–885
2. Bardi F, Cabibbo M, Spigarelli S (2002) An Analysis of Thermo-Mechanical Treatments of A 2618 Aluminium Alloy: Study of Optimum Conditions for Warm forging". Materilas Science Engineering a 334:87–95
3. Hu HE, Zhen L, Yang L (2008) Deformation behavior and microstructure evolution of 7050 aluminum alloy during high temperature deformation. Materials Science Engineering a 488:64–71
4. Bedir F (2007) Characteristic properties of Al–Cu–SiCp and Al–Cu–B4Cp composites produced by hot pressing method under nitrogen atmosphere. Materials Design 28:1238–1244
5. Abouelmagd G (2004) Hot deformation and wear resistance of P/M aluminium metal composites. J Mater Process Technol 155–156:1395–1401
6. Kalkanl A, Yılmaz S (2008) Synthesis and characterization of aluminum alloy 7075 reinforced with silicon carbide particulates. Materials Design 29:775–780
7. Srinivasan N, Prasad YVRK, Ramarao P (2008) Hot deformation behaviour of Mg– 3A alloy a study using processing map. Mater Sci Eng, a 476:146–156

8. Liu LF, Dai LH, Yang GW (2003) Strain gradient effects on deformation strengthening behavior of particle reinforced metal matrix composites. Mater Sci Eng A 345:190–196
9. Cavaliere P, Cerri E, Leo P (2004) Hot deformation and processing maps of a particulate reinforced 2618/Al2O3/20p metal matrix composite. Compos Sci Technol 64:1287–1291
10. Prasad YVRK (2003) Processing maps—a status report, On the hot working characteristics of 2014 Al–20 vol% Al2O3 metal matrix composite. Journal of Material Engineering Performance. 12:638–645
11. Narayana Murty SVS, Nageswara Rao B, Kashyap BP (2005) On the hot working characteristics of 2014 Al–20 vol% Al2O3 metal matrix composite. J Mater Process Technol 166:279–285
12. McQueen HJ, Ryan ND (2002) Constitutive analysis in hot working. Materials Science Engineering. A 322:43–63
13. Narayana Murty SVS, Nageswara Rao B, Kashyap BP (2005) Identification of flow instabilities in the processing maps of AISI 304 stainless steel. J Mater Process Technol 166:268–278
14. Lin YC, Chen MS, Zhong J (2008) Prediction of 42CrMo steel flowstress at high temperature and strain rate. Mech Res Commun 35(3):142–150
15. Prasad YVRK, Rao KP (2005) Processing maps and rate controlling mechanisms of hot deformation of electrolytic tough pitch copper in the temperature range 300–950°C. Mater Sci Eng, a 391:141–150
16. Kouzeli M, Mortensen A (2002) Size dependent strengthening in particle reinforced aluminum. Acta Mater 50:39–51
17. Cerri E, Spigarelli S, Evangelista E, Cavaliere P (2002) Hot deformation and processing maps of a particulate-reinforced 6061+20% Al_2O_3 composite. Mater Sci Eng, a 324:157–161
18. Qu S, Siegmund T, Huang Y, Wu PD, Zhang F, Hwang K (2005) A study of particle size effect and interface fracture in aluminum alloy composite via an extended conventional theory of mechanism-based strain-gradient plasticity. Compos Sci Technol 65:1244–1253
19. Narayanasamy R, Ramesh T, Prabhakar M (2009) Effect of particle size of SiC in aluminium matrix on workability and strain hardening behaviour of P/M composite. Mater Sci Eng, a 504:13–23
20. Srivastava VC, Jindal V, Uhlenwinkel V, Bauckhage K (2008) Hot-deformation behaviour of spray-formed 2014 Al + SiCP metal matrix composites. Mater Sci Eng, a 477:86–95
21. Milan MT, Bowen P (2004) Tensile and Fracture Toughness Properties of SiCp Reinforced Al Alloys: Effects of Particle Size, Particle Volume Fraction, and Matrix Strength. the Journal of Materials Engineering and Performance. 13(6):775–783
22. Prasad YVRK, Sasidhara S (eds) (1997) Hot Working Guide: A Compendium of Processing Maps. ASM International, Materials Park, OH
23. Tham LM, Gupta M, Cheng L (2002) Effect of reinforcement volume fraction on the evolution of reinforcement size during the extrusion of Al-SiC composites. Mater Sci Eng, a 326:355–363
24. Xiao BL, Fan JZ, Tian XF, Zhang WY, Shi LK (2005) Hot deformation and processing map of 15%SiCp/2009 Al composite. J Mater Sci 40:5757–5762
25. Ferry M, Xiao Guo Z (Ed) (2005) The deformation and Processing of structural materials, Woodhead Publishing Ltd., Cambridge, England, p 203
26. Clyne TW, Withers PJ (1993) An introduction to metal matrix composites. Cambridge University Press, Cambridge
27. Wang Z, Song M, Sun C, Xiao D, He Y (2010) Effect of extrusion and particle volume fraction on the mechanical properties of SiC reinforced Al–Cu alloy composites. Mater Sci Eng, a 527:6537–6542
28. Balasivanandha Prabu S, Karunamoorthy I (2008) Microstructure-based finite element analysis of failure prediction in particle-reinforced metal matrix composite. J Mater Process Technol 207(1/3):53−62
29. Peng Z (2010) Li fu-guo, "Effect of particle characteristics on deformation of particle reinforced metal matrix composites." Transactions of Nonferrous Metals Society of China 20:655–661
30. Tohgo K, Itoh Y, Shimamura Y (2010) A constitutive model of particulate-reinforced composites taking account of particle size effects and damage evolution. Composites: Part A 41(2):313–321

Experimental Analysis of Forced Turbulent Convective Heat Transfer in a Circular Cross-Sectional Tube With Al_2O_3-Water Nanofluid

V. D. Tamilarasan, T. Rameshkumar, S. Saravanan, and A. Ramakrishnan

Abstract In a turbulent flow, heat transfer through convection and variation in pressure of a fluid through a circular cross-sectional tube with constant wall temperature using metallic nanopowder (Al_2O_3-aluminum oxide) in a base fluid (H_2O-water) is studied. The results can be utilized to increase heat transfer rates in many heat transfer applications. The heat transfer coefficient, Nusselt number and Reynolds number were obtained for different wall temperatures (45, 50, 55 and 60 °C) at different mass flow rates (60 LPH (Liter Per Hour),75 LPH & 90 LPH) of base and nanofluid (Al_2O_3/H_2O). Earlier researchers used millimeter and micrometer-sized particles to increase the heat transfer rates, but encountered problems of clogging and suspension stability. Nowadays, modern techniques are used to produce nanometer-sized particles as per requirement. In this study, the heat transfer coefficient of the base fluid is increased by dispersing Al_2O_3 nanoparticle in a particular concentration ($\varphi = 0.05\%$). Nanoparticles presence in base fluid slightly increases the heat transfer coefficient of the system when compared to the base fluid without nanoparticles. The study also analyzes the performance of heat transfer by varying mass flow rates with different wall temperatures and compares its results to nanofluid with water.

Keywords Nanoparticles · Turbulent flow · Particle size · Convective heat transfer · Aluminum oxide

Nomenclature

ρ	Density of fluid (Kg/m^3) (Subscript bf, nf & p denotes the base fluid, nanofluid & nanoparticles respectively)
k	Thermal conductivity (W/m^2K)
C_p	Specific heat (J/KgK)

V. D. Tamilarasan (✉) · T. Rameshkumar · S. Saravanan · A. Ramakrishnan
Department of Mechanical Engineering, Bannari Amman Institute of Technology, Sathyamangalam, Tamil Nadu 638 401, India
e-mail: tamil.maritime@gmail.com

G. Kumaresan et al. (eds.), *Advances in Materials Research*, Springer Proceedings in Materials 5, https://doi.org/10.1007/978-981-15-8319-3_124

d	Nano-particle diameter (nm)
D	Diameter of circular tube (m)
L	Length of the tube (m)
μ	Viscosity of the fluid (Pa s)
T	Nanofluid temperature (°C)
T_{fr}	Temperature at the freezing point of the base fluid (°C)
Pr	Prandtl number
Φ	Volume fraction
Re_p	Reynolds number
Kb	Boltzmann's constant
Nu	Nusselt number
H	Heat transfer coefficient (W/mK)
Q	Heat transfer rate (W/m^2)
A	Cross sectional area of tube (mm)
T_w	Average wall temperature (°C)
T_b	Bulk mean temperature (°C)
T_{in}	Inlet temperature of fluid (°C)
T_{out}	Outlet temperature of fluid (°C)
T1, T2, T3, T4	Measure the wall tem-perature of the tube (°C)

1 Introduction

Heat transfer through convection can be raised by dispersion of nanoparticles, which have an ability to raise the heat transfer more efficiently in a base fluid when compared with conventional fluids like water. The fluid properties, size and concentration of the nanoparticles play the important parameter for heat transfer enhancement in heat exchanger applications. Using different volumes of concentration of nanofluid in different flow patterns such as laminar flow, transition flow and turbulent flow would yield a number of different research papers. Observation of the above flow pattern of nanofluids in a circular tube and enhancements in heat transfer have been found and supported this research work.

Earlier research articles indicates that the coefficient of heat transfer of base fluids have lesser capability to transfer heat than the nanofluids, at a slight or no pressure drop. Pak and Cho (1998) [1] examined the convective heat transfer of water-based nanofluid (dilute y-Al_2O_3/Water) in a turbulent flow, at different mixture ratio and correlation of the Nusselt number. The experiment was conducted in a horizontal circular cross-sectional pipe at a constant wall heat flux using Al_2O_3 and TiO_2 nanoparticles. The results indicate that there is an increase in Reynolds number and bulk concentration of the particle by increasing the Nusselt number in nanoparticles. Choi [2] proposed that the nanoparticle dispersion in base fluid would cause higher thermal conductivity than the base liquid. Nanoparticles have better stability, less clogging and higher surface area.

Wen and Ding [3] studied the enhancement of convective heat in a laminar flow in a circular pipe by dispersed the nanoparticle Al_2O_3 in base fluid. The heat transfer is directly proportional to the Reynolds number, as well as particle concentration. This enhancement that takes place is high at the entrance area of pipe and decreases with axial length. Ding et al. [4] proposed an experimental setup to study the behavior of heat transfer due to suspending aqueous medium in a multi-walled carbon nanotubes (CNT). They discovered that the convective rate of heat transfer was enhanced with H_2O as the working fluid. Heat transfer relies on the condition of flow of fluid, pH level, the size of the nanotubes. The results from the experimental studies proposed that for Al_2O_3 and CuO nanofluid systems, the heat transfer coefficient gets enhanced with the effect of nanoparticles concentrations and Peclet number. When compared to CuO/H_2O nanofluid, the enhancement of heat transfer is high in Al_2O_3/H_2O nanofluids. Other factors that would affect heat transfer in nanoparticles are amount of dispersion, chaotic movement of the particle, Brownian motion and particle migration [5, 6, 8].

Anoop and Sundararajan [7] studied the behavior of nanofluid with varying particle sizes (45–150 nm) and found that the coefficient of heat transfer of particles of diameter 45 nm was higher to that of the particles of diameter 150 nm. For instance, at x/D = 147, 45 nm nanoparticle size-based nanofluid increases the coefficient of heat transfer around 25% when compared to the 150 nm nanoparticle. Increasing the concentration of nanoparticles in nanofluid and flow rate increases the average heat transfer coefficient. Nguyen et.al. [9]. Developed cooling system of microprocessor, which has Al_2O_3 Nanoparticles suspended in them for enhancing the coefficient of heat transfer of the system, under turbulent flow conditions. Fotukian and Nasr Esfahany [10] experimentally analyzed the turbulent convective transfer of heat of Al_2O_3/H_2O flowing in a circular cross-sectional pipe, maintaining uniform wall temperature throughout the tube in the laminar flow condition. It increases the coefficient of heat transfer by 48%, while maintaining nanoparticle concentration (0.05%). When compared to pure water, the coefficient of heat transfer increases by 25% and pressure drop increases by 20% when the concentration of particles is 0.24%. The heat transfer coefficient depends on the Reynolds number, nanoparticle concentration and its thermal conductivity. The size of nanoparticle plays an opposite effect on the heat transfer coefficient at a fixed flow rate of nanofluid [11–13].

2 Experimental Methods of Nanoparticle Preparation

2.1 Aluminum oxide (Al_2O_3)

Al_2O_3 is used as a nanoparticle in this work. It is dispersed in the water shown in Fig. 1. Totally, 12 g of Al_2O_3 nanopowder is dissolved in 6-L water. Al_2O_3 is commercially available powder and mostly used by the researchers. It is also cheap when compared

Fig. 1 Al_2O_3 Nanopowder

Table 1 Thermophysical properties of Al_2O_3

Powder name	α-Aluminum oxide(Al_2O_3) or Alumina (99.9%)
Average particle size	45 nm
Color	White
Crystal structure	Rhombohedral
Specific heat capacity	0.850 J/g-°C
Molecular weight	101.961 g/mol
Density	3.96 g/cc
Thermal conductivity	30 W/m–K
Melting point	2054 °C
Boiling point	≥3000 °C
Maximum service temperature, Air	1750 °C
Molar volume	25.575 cc/mol

to the other powders like CuO and Ag. The thermophysical properties of Al_2O_3 are shown in Table 1.

2.2 Preparation of Al_2O_3 Nanofluid

The nanofluid is prepared by mixing nanoparticle in a base fluid under proper mixing and non-sedimentation condition. Clustering is a major problem during this process. To resolve this clustering, there are two techniques that are used, namely one-step method and two-step method. In this process, nanoparticles are simultaneously formed with reduced agglomeration and uniformly dispersed throughout

Fig. 2 Magnetic stirrer

Fig. 3 Ultrasonic cleaner

the base fluid, with stable suspension. The shortcoming of this process is that one cannot assure the purity of the nanofluid from this method. It is also hard to make nanofluids of our required size and concentration. This method is used for nanofluid synthesis using commercially available nanoparticles. Nanoparticles are dispersed intensively and with reduced particle agglomeration by using ultrasonic equipment and magnetic stirrer, into water as shown in Fig. 2. The ultrasonic cleaner equipment used in two-step method for this research work is shown in Fig. 3 .

3 Experimental Setup

The experimental system consists of data logger (Agilent 34972A LXI Data Acquisition system), test section, cooling tank, reservoir and a flow controlling system (Rotometer) as shown in Fig. 4. A 20 L reservoir tank with drain valve was used to store nanofluid. The geometrical parameter of test section uses a copper tube which was 1.3 m length, 9 mm inner diameter and 12 mm outer diameter with 1.5 mm tube

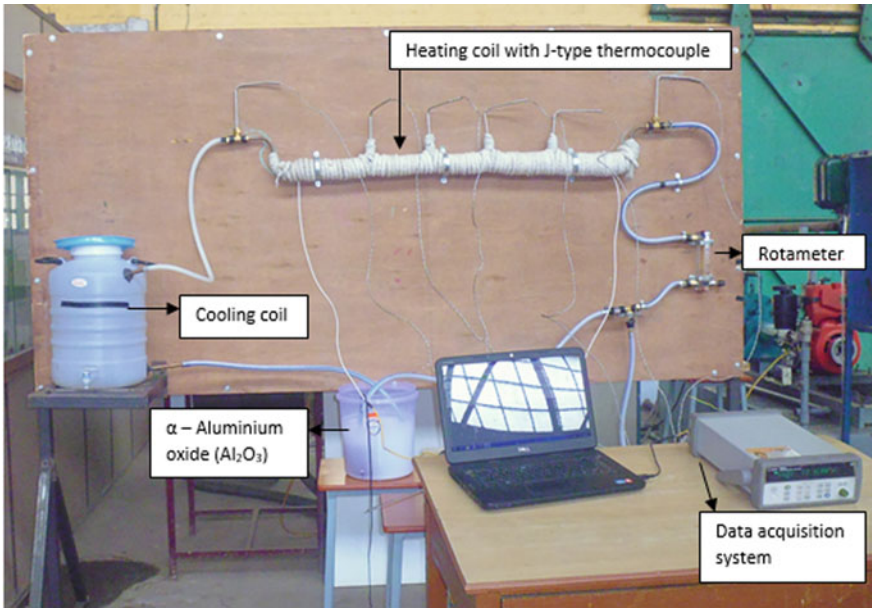

Fig. 4 Experimental setup run by nanofluid

wall thickness. Nanofluid flows inside the copper tube. The tube was initially covered by mica sheet. It is wounded by nichrome (Nickel + Chromium) heating coil over the surface of mica sheet. It is heated by electrical heating which maintains constant wall temperature boundary condition. Copper tube is divided into five sections. Each section is covered with mica sheet and heating coil. Each section is connected by connecting legs.

Six J-type thermocouples are fitted on the copper tube, equally distributed between two consecutive sections for measuring tube wall temperature. Copper tube is electrically insulated by ceramic wool blanket which is thermally insulated. After covering the tube with ceramic wool, it was wounded by the asbestos rope of 6 mm. Again asbestos rope of 12 mm was wounded tightly on the copper tube to reduce heat loss. To measure the inlet and outlet temperatures of fluid, two (J-type) thermocouples were inserted at the inlet and outlet flow regions of the test tube.

Nanofluid is prepared and stored at the reservoir tank. When the motor pump and electrical heating system get started, the tube wall temperature gets increased. Nanofluid is pumped through the copper tube. Tube wall temperature is maintained, and the current is controlled by an autotransformer. The experimental observations were noted for different voltages at a particular concentration of 0.2%. A total of six thermocouples are connected to a data logger nodal, which is coupled with the system. Each and every run, inlet, outlet and tube wall temperatures were noted. Left end of the test tube section was connected to cooling tank, and the loop is continued to the reservoir which has submersible pump inside. A flow control system (Rotameter)

was introduced between the cooling tank and test section. In the Rotameter, knob is adjusted for maintaining the different mass flow rates (60 LPH, 75LPH & 90LPH). This procedure is repeated by changing the coil temperature using autotransformer & surface temperature and fluid inlet & outlet temperature were noted. The above experiment is conducted for different mass flow rates (60 LPH, 75LPH & 90 LPH), different wall temperature and different voltage for the particle volume concentration ($\varphi = 0.05\%$), and the results were tabulated.

3.1 Analysis of Data

Density, viscosity, specific heat and thermal conductivity of nanofluid were determined based on the below correlations.

Density of nanofluid,

$$\rho_{nf} = \varphi\rho_p + (1-\varphi)\rho_{bf} \tag{1}$$

Specific heat of nanofluid,

$$(\rho Cp)_{nf} = \varphi(\rho Cp)_p + (1-\varphi)(\rho Cp)_{bf} \tag{2}$$

$$Cp_{nf} = (\rho Cp)_{nf}/\rho_{nf} \tag{3}$$

Absolute viscosity of nanofluid,

$$\frac{\mu_{nf}}{\mu_{bf}} = \frac{1}{1 - 24.375d^{-0.264}\varphi^{1.028}} \tag{4}$$

Thermal conductivity of the nanofluid,

$$\frac{k_{nf}}{k_{bf}} = 1 + 4.4Re_p^{0.4}Pr_{bf}^{0.66}\left(\frac{T}{T_{fr}}\right)^{10}\left(\frac{k_p}{k_{bf}}\right)^{0.03}\varphi^{0.66} \tag{5}$$

$\mathrm{Re_p}$ is the Reynolds number referred to the nanoparticle diameter, and it is defined as:

$$\mathrm{Re_p} = \frac{2\rho_{bf}k_bT}{\pi\mu_{bf}^2 d} \tag{6}$$

After calculating every value required for the Prandtl number, and Reynolds number is calculated as follows:

$$\text{Prandtl number, } Pr_{nf} = \left(\mu_{nf}Cp_{nf}\right)/k_{nf} \tag{7}$$

$$\text{Reynolds number, } Re_{nf} = \left(\rho_{nf} V D\right)/\mu_{nf} \tag{8}$$

For calculating Nusselt number of forced turbulent flow of nanoparticle inside the circular cross-sectional tube, Dittus-Boelter equation was used as it is independent of thermal boundary, and properties are evaluated at bulk mean temperatures.

According to the Dittus-Boelter equation,

$$Nu = 0.023 Re^{0.8} Pr^{0.4} \tag{9}$$

Valid for,

$$0.6 < \text{Pr} < 100, 2500 < \text{Re} < 1.25 * 106, \text{L/D} > 60$$

After finding the Nusselt number,
Heat transfer coefficient,

$$\text{h} = (\text{Nu}_{\text{nf}}\text{K}_{\text{nf}})/\text{D} \tag{10}$$

Heat transfer rate is calculated as follows:

$$\text{Q} = \text{hA}(\text{T}_{\text{w}} - \text{T}_{\text{b}}) \tag{11}$$

where
Average wall temperature,

$$\text{T}_{\text{w}} = (\text{T}_1 + \text{T}_2 + \text{T}_3 + \text{T}_4)/8 \tag{12}$$

Bulk mean temperature.

$$\text{T}_{\text{b}} = (\text{T}_{\text{in}} + \text{T}_{\text{out}})/2 \tag{13}$$

4 Result and Discussion

4.1 Compare the Experimental Result of Base Fluid (Pure Distilled Water) and Nanofluid ($AL_2O_3 + H_2O$)

In parliamentary law to demonstrate reliability and accuracy of experimental measurement, some tests were done with pure distilled water, and the test result was compared with the nanofluid. The experiment was conducted with constant

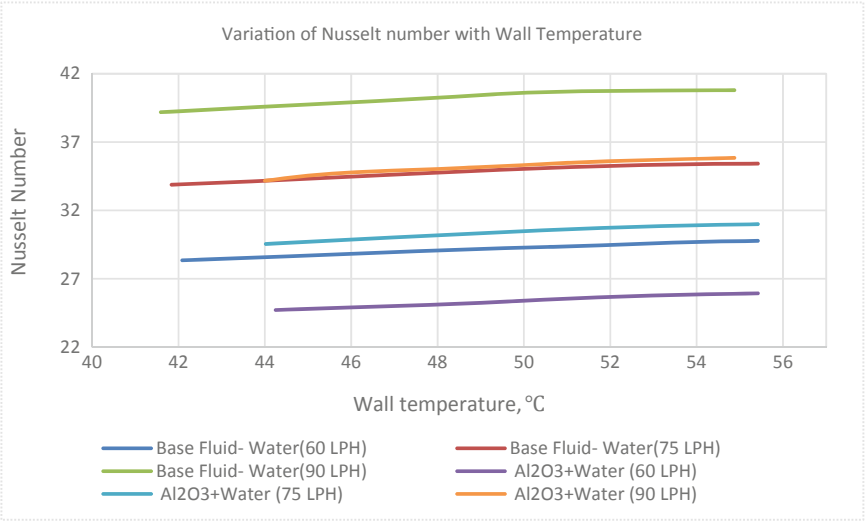

Fig. 5 Variation of experimental Nusselt number (Nu) with wall temperature (T_w) at varying mass flow rate

percentage of nanoparticle compared with pure base water for turbulent flow under constant wall temperature conditions.

Figure 5 shows the experimental Nusselt number of base fluid (H_2O) and nanofluid (Al_2O_3/H_2O) with the wall temperature at different mass flow rates (60LPH, 75LPH & 90LPH). It is found that high Nusselt number is attained at a 90 LPH mass flow rate at both the fluids. The result indicated that the Nusselt number of base fluid at 60 LPH, 75LPH mass flow rates are 16%, 18% lower to that at 90 LPH at all wall temperatures. From the graph showed the Nusselt number of nanofluid ($AL_2O_3 + H_2O$) for particular concentration ($\varphi = 0.05\%$) is 12% lesser than the base fluid (H_2O) at all mass flow rate

From our experiment observation, we noticed that Nusselt number increases with the increase in mass flow rate and wall temperature.

Figure 6 shows the experimental heat transfer coefficient of base fluid and nanofluid versus wall temperature at different mass flow rate (60LPH, 75LPH & 90LPH); the coefficient of heat transfer increases with increasing the wall temperature. The coefficient of heat transfer values 2867.15 W/m^{2}K and 3197.94 W/m^{2}K, achieved at 90 LPH, is the maximum in base fluid and nanofluid, respectively. At 60 LPH, the minimum value of 1966.62 W/m^{2}K and 2020.56 W/m^{2}K was obtained at wall temperature 42.08°C for base fluid and nanofluid, respectively. In this result, the mass flow rate of base fluid at 60 LPH and 75LPH is 16% and 13% lower than the 90 LPH at all wall temperature, respectively.

In the present investigation, the concentration of nanoparticle (AL_2O_3) is 0.05% dispersed in the base fluid (H_2O) are used to examine the heat transfer performance of heat exchanger application. From Fig. 7. The graph shows an increase of heat transfer

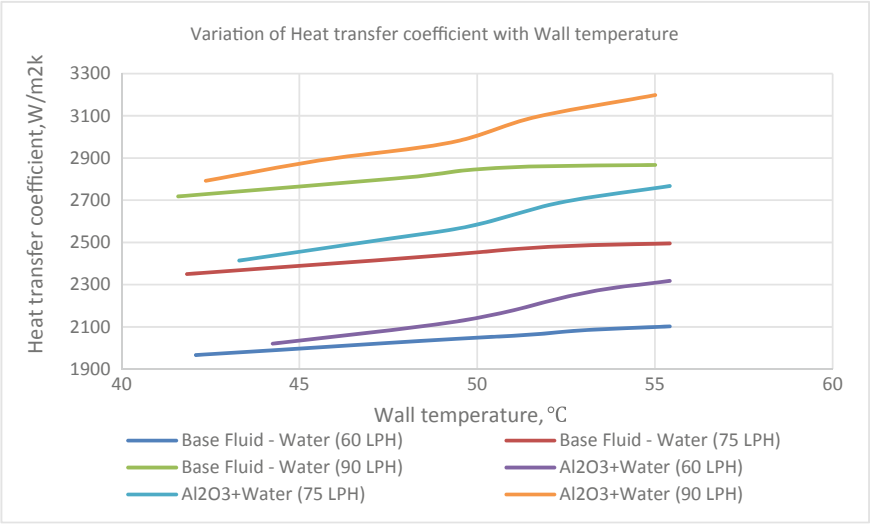

Fig. 6 Variation of experimental heat transfer coefficient (h) with wall temperature (T_w) at varying mass flow rate

at an increase of wall temperature and mass flow rate of fluid. Maximum value of heat transfer was achieved at 90 LPH, and a minimum value of it was observed at 60 LPH of both the conditions. Their values are 1085.02 W and 335.86 W at low for all temperature. Max heat transfer achieved at 90 LPH was 1571.30 W and the minimum value of 568.68 W was achieved at 60 LPH. Al_2O_3 nanofluid has maximum heat transfer than the water at 90 LPH.

The above graph shows the variation of Reynolds number with respect to wall temperature for different mass flow rates. When the wall temperature gets increased, dynamic viscosity gets decreased. This in turn increases the Reynolds number. Maximum Reynolds number (5660.63) was achieved at 90 LPH when the temperature was 52.875 °C.

From Fig. 8. when the temperature of the wall is increased, dynamic viscosity of nanofluid is decreased. Due to decrease in the dynamic viscosity, Reynolds number gets increased. Maximum Reynolds number (5996.427) was achieved at 90 LPH at 60.66 °C and minimum value of 3252.87 was noted at 60 LPH at 44.24 °C.

5 Conclusion

The experimental study investigated the heat transfer through convection of Al_2O_3/H_2O nanofluid when passed through a circular tube in a turbulent flow at different mass flow rates. Mass flow rates and thermal conductivity play a significant role in enhancing the heat transfer of the nanofluid.

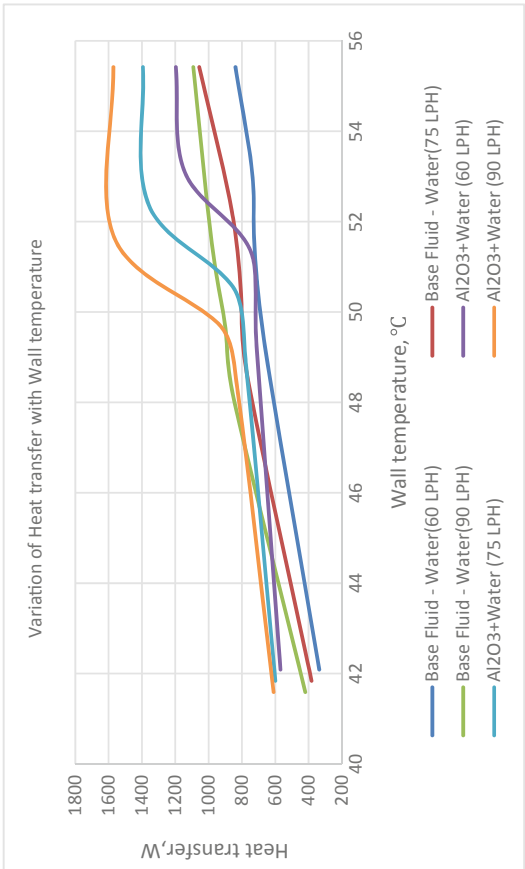

Fig. 7 Variation of experimental heat transfer (Q) with wall temperature (T_w) at varying mass flow rate

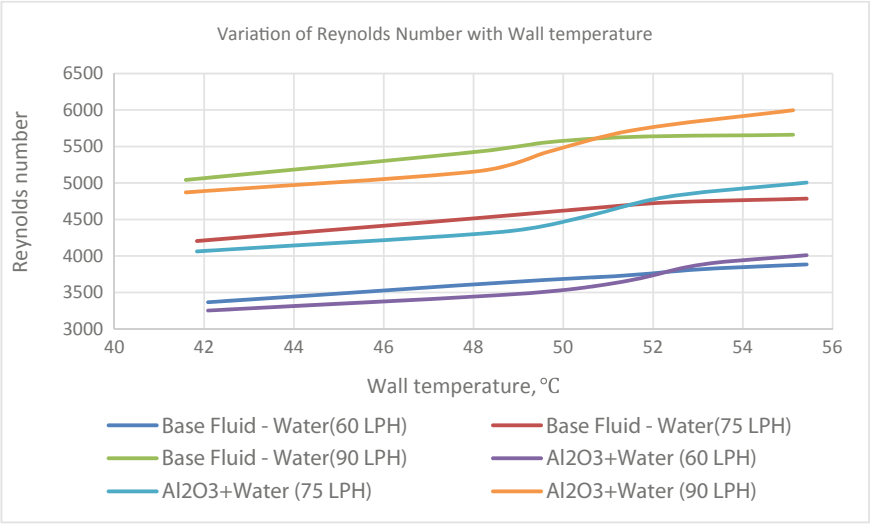

Fig. 8 Variation of experimental Reynolds number (Re) with wall temperature (T_w) at different mass flow rate

The results show that the coefficient of heat transfer of the nanofluids increases with an increase in thermal conductivity and mass flow rate. It is concluded that the sole reason of increase in heat transfer rate is not due to usage of a mere nanofluid. Factors of dispersion of nanoparticles in the base fluid, chaotic movement of nanoparticles, fluctuations of nanoparticles and its interactions, especially in high Reynolds number may cause a flow structure change, which in turn leads to an increase in heat transfer. The work describes the nanoparticles suspended in the water at 0.05% volume fraction for three different mass flow rates (60 LPH, 75 LPH and 90 LPH) with varying wall temperature. The coefficient of heat transfer and also the Nusselt number gets increased with an increase in mass flow rate. The highest value of coefficient of heat transfer and heat transfer was observed at 90 LPH.

At 60 LPH,

The coefficient of heat transfer, thermal conductivity and heat transfer of the nanofluid when compared to distilled water increased by 9.3%, 9.04% and 29.9%, respectively.

At 75 LPH,

The coefficient of heat transfer, thermal conductivity and heat transfer of the nanofluid when compared to distilled water increased by 9.87%, 21.1% and 28.2%, respectively.

At 90 LPH,

The coefficient of heat transfer, thermal conductivity and heat transfer of the nanofluid when compared to distilled water increased by 10.34%, 21.22% and 30.94%, respectively.

References

1. Pak BC, Cho YI (1998) Hydrodynamic and heat transfer study of dispersed fluids with submicron metallic oxide particles. Exp Heat Transf Int J 11(2):151–170
2. Choi SU, Eastman JA (1995) Enhancing thermal conductivity of fluid with nanoparticles. No. ANL/MSD/CP-84938, Argonne National Lab, United states
3. Wen D, Ding Y (2004) Experimental investigation into convective heat transfer of nanofluids at the entrance region under laminar flow conditions. Int J Heat Mass Transf 47(24):5181–5188
4. Ding Y, Alias H, Wen D, Williams RA (2006) Heat transfer of aqueous suspensions of carbon nanotubes (CNT nanofluids). Int J Heat Mass Transf 49(1-2):240–250
5. Heris SZ, Etemad SG, Esfahany MN (2006) Experimental investigation of oxide nanofluids laminar flow convective heat transfer. Int Commun Heat Mass Transfer 33(4):529–535
6. Heris SZ, Esfahany MN, Etemad SG, (2007) Experimental investigation of convective heat transfer of Al_2O_3/water nanofluid in circular tube. Int J Heat Fluid Flow 28(2):203–210
7. Anoop KB, Sundararajan T, Das SK (2009) Effect of particle size on the convective heat transfer in nanofluid in the developing region. Int J Heat Mass Transf 52(9-10):2189–2195
8. Godson L, Raja B, Lal MD, Wongwises SE (2010) Enhancement of heat transfer using nanofluids-An overview. Renew Sustain Energy Rev 14(2):629–641
9. Nguyen CT, Roy G, Gauthier C, Galanis N (2008) Heat transfer enhancement using Al_2O_3 – water nanofluid for electronics liquid cooling system. Appl Therm Eng 27(8-9):1501–1506
10. Fotukian SM, Esfahany N (2010) Experimental investigation of turbulent convective heat transfer of Al_2O_3/water nanofluid inside a circular tube. Int J Heat and Fluid Flow 31, 606–612
11. Fotukian SM , Esfahany MN (2010) Experimental study of turbulent convective heat transfer and pressure drop of dilute CuO/water nanofluid inside a circular Tube. Int Commun in Heat and Mass Transf 37(2):214–219
12. Ebrahimnia-Bajestan E, Moghandam MC, Niazmand H, Daungthongsuk W, Wongwises S (2016) Experimental and numerical investigation of nanofluids heat transfer characteristics for application in solar heat exchangers. Int J Heat Mass Transf 92:1041–1052
13. Minakov AV, Guzei DV, Pryazhnikov MI, Zhigarev VA, Rudyak VY (2016) Study of turbulent heat transfer of the nanofluids in a cylindrical channel. Int J Heat Mass Transf 102:745–755

Modelling the Factors of Buying Behaviour of Paint Products

M. Suresh and S. Bala Yogesh

Abstract Purchasing paint for domestic use has become a difficult decision making problem. Customers need to visit dealer shops exclusively for purchase of the paint products has become mandatory. There are various factors that will influence the customers' decision on choosing a particular dealer shop over the others. The customers who visit the dealer shops are predominantly painters and a few direct consumers. This paper primarily focus upon identifying the key factors that will influence paint buying behaviour in dealer shops. In this paper, a conceptual model has been developed using Interpretive Structural Modelling (ISM) approach. This study results indicate product variance is the key influencing factor, followed by compatible price and product reliability for the purchase decision of paint products by customers.

Keywords Buying behaviour · Purchase · Customer satisfaction · Products buying · Consumer behaviour · Interpretive structural modelling

1 Introduction

Paint products have become one of the major commodity product in our country. There are huge infrastructural changes happening in our country which indirectly will increase the paint consumption. The average paint consumption has increased considerably inrecent times. The market size of the paint industry in India is estimated to be around 350 billion. It is predicted that there will be 9–10% growth in the paint industry over the next 5 years [1]. Most of the paint purchasing happens only at dealer shops. It is difficult to convert this into online or e-commerce sector because for a particular shade having thousand colours, that influence purchasing experience. The consumers and painters visit the shop individually or together for the purchase of the paint. Thus, it makes a challenging task for the dealers to satisfy their need. Many

M. Suresh (✉) · S. B. Yogesh
Amrita School of Business, Amrita Vishwa Vidyapeetham, Coimbatore, India
e-mail: drsureshcontact@gmail.com

G. Kumaresan et al. (eds.), *Advances in Materials Research*, Springer Proceedings in Materials 5, https://doi.org/10.1007/978-981-15-8319-3_125

of the paint retail shops have different brands of paints in their own stores. But, only few shops have the exclusive dealership.

Many researchers studied the customers' buying behaviour in many fields, but very few researchers focused on the purchasing behaviour of paint products. The urge for the basic crux of this paper is based on the benefits that a dealer shop can reap upon choosing the right factors. This study identifies the factors that play a major role in influencing the purchase behaviour of the customers on paint products and a framework is prepared with the help of ISM approach.

2 Literature Review

Most of the companies have now started analyzing the buying behavior of their customer, and use it as a competitive tool in the market to stand apart from its competitors [2] analyzed the customer's experience have influenced by the smart phone purchase [3] identified how company behaviour can affect the buying behaviour of the customer. Whereas [4] studied various dimensions in offering the service that can influence the health care industry [5] analyzed the relationship between the customer dissatisfaction and buying a product [6] studied customers green purchase behaviour and the effect of customer perceived green wash fear [7] developed a customer satisfaction index for American customer from which the buying behavior could be identified [8] developed a customer satisfaction index system of express mail service.

3 Research Methodology

The paper focuses primarily on identifying the key factors that are influencing the customers' paint purchase behavior. Various factors that influence customer buying behavior are identified through literature review and experts opinion. The identified factors are shortlisted with the help of experts based on customer buying behavior in the paint dealer shop environment. The experts are sales representatives, service staffs, dealer shop managers, regular customers of selected paint dealer shops located in Tamil Nadu, India.

ISM method involves the following steps:

(1) Identification of factors that will affect the customer buying behaviour in dealer shops environment (Table 1).
(2) Self Structural Interaction Matrix (SSIM): It is prepared based on the contextual relationship between the pair of factors [9–12] and it's shown below:
Example: Relationship between the factors *m* and *n* ?
Option-1: V: *m* influences *n.*
Option-2: A: *n* influences *m.*
Option-3: X: mutual relationship between *m* and *n.*

Table 1 Identified factors for consumer buying behaviour in paint dealer shop

Factors	Definition	References / expert opinion
Product variance (H1)	The variety of products available of various types	[23]
Service quality (H2)	The quality of service being delivered at service scape	[24, 25]
Perceived quality (H3)	The assumed quality of service is attained	[26]
Perceived value (H4)	The customer expects a set of value for the product	[26]
Brand image (H5)	The brand picture that springs up to mentioning of a firm's name	[27]
Compatible price (H6)	The ideal price fixed for a particular product	Expert Opinion
Store environment (H7)	The environment created in the store in order to improve customer satisfaction	[28]
Product reliability (H8)	The trustiness created for a particular product to make the sale	[29]
Customer value (H9)	The value proposition for a particular brand instilled in the customer's mind	[30]
Customer loyalty (H10)	Making returning customers with a superior service	[31]

Option-4: O: no relationship between *m* and *n*.
SSIM is developed based on the consensus of the 25 experts' opinions and it's shown in Table 2.

(3) Initial Reachability Matrix (IRM): It's developed from SSIM [13–16]. The IRM has been depicted in the Table 3.

Table 2 SSIM for consumer buying behaviour

Factors	H1	H2	H3	H4	H5	H6	H7	H8	H9	H10
H1	1	O	O	O	V	V	V	V	O	O
H2		1	O	A	V	O	A	O	V	V
H3			1	V	X	A	O	A	O	O
H4				1	V	A	O	A	O	O
H5					1	O	V	A	O	O
H6						1	O	O	O	V
H7							1	O	V	O
H8								1	O	V
H9									1	V
H10										1

Table 3 IRM for consumer buying behaviour

Factors	H1	H2	H3	H4	H5	H6	H7	H8	H9	H10
H1	1	0	0	0	1	1	1	1	0	0
H2	0	1	0	0	1	0	0	0	1	1
H3	0	0	1	1	1	0	0	0	0	0
H4	0	1	0	1	1	0	0	0	0	0
H5	0	0	1	0	1	0	1	0	0	0
H6	0	0	1	1	0	1	0	0	0	1
H7	0	1	0	0	0	0	1	0	1	0
H8	0	0	1	1	1	0	0	1	0	1
H9	0	0	0	0	0	0	0	0	1	1
H10	0	0	0	0	0	0	0	0	0	1

Table 4 FRM for consumer buying behaviour

Factors	H1	H2	H3	H4	H5	H6	H7	H8	H9	H10	Driving Power ↓
H1	1	*1*	*1*	*1*	1	1	1	1	*1*	*1*	10
H2	0	1	*1*	*1*	1	0	*1*	0	1	1	7
H3	0	*1*	1	1	1	0	*1*	0	*1*	*1*	7
H4	0	1	*1*	1	1	0	*1*	0	*1*	*1*	7
H5	0	*1*	1	*1*	1	0	1	0	*1*	*1*	7
H6	0	*1*	1	1	*1*	1	*1*	0	*1*	1	8
H7	0	1	*1*	*1*	*1*	0	1	0	1	*1*	7
H8	0	*1*	1	1	1	0	*1*	1	*1*	1	8
H9	0	0	0	0	0	0	0	0	1	1	2
H10	0	0	0	0	0	0	0	0	0	1	1
Dependence →	1	8	8	8	8	2	8	2	9	10	

1 indicates transitive links

(4) Final Reachability Matrix (FRM): It's developed from IRM through transitivity analysis which follows that if F = G, G = H, then F = H [17–20]. The FRM has been shown in Table 4.
(5) Partition of the FRM: The FRM is then partitioned into different levels [21, 22]. The ISM levels and MICMAC ranks are captured in Table 5.

4 Results and Discussions

The ISM digraph is obtained from the final FRM and it depicts in Fig. 1. The digraph is a visual representation of the various relationships between the factors and the

Table 5 ISM factors level and rank

Sl. No	Factors	Factors level	Driving power/dependence	MICMAC rank
1	Product variance (H1)	5	10	1
2	Service quality (H2)	3	0.875	3
3	Perceived quality (H3)	3	0.875	3
4	Perceived value (H4)	3	0.875	3
5	Brand image (H5)	3	0.875	3
6	Compatible price (H6)	4	4	2
7	Store environment (H7)	3	0.875	3
8	Product reliability (H8)	4	4	2
9	Customer value (H9)	2	0.222	4
10	Customer loyalty (H10)	1	0.1	5

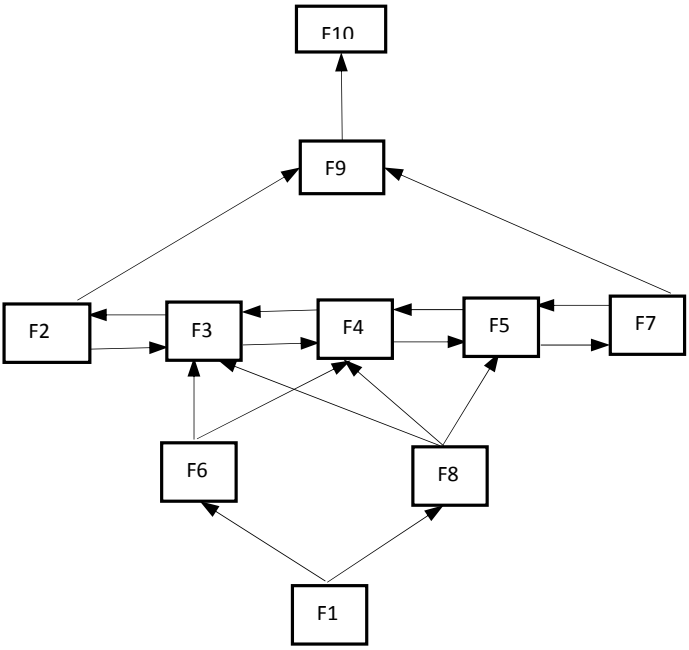

Fig. 1 ISM for the consumer buying behaviour factors

levels at which they are positioned. Top-level indicates level-1 and bottom level indicates least level.

The MICMAC diagram shown in Fig. 2 and it depicts the categorization of the various factors.

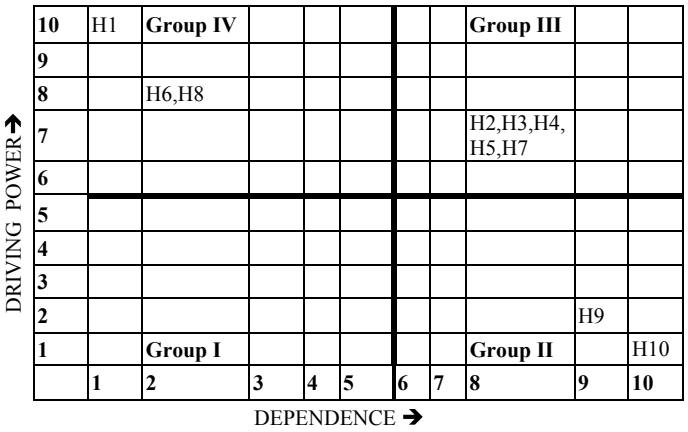

Fig. 2 MICMAC analysis for environmental sustainability factors

Group I:

Autonomous factors: These factors have weak driving power and weak dependence power [32, 33]. In this study, none of the factors associated with Group-I.

Group II:

Dependence factors: These factors have weak driving power and strong dependence power [34]. In this group, we have two factors, Customer Value (H9), Customer Loyalty (H10).

Group III:

Linkage factors: These factors have strong driving power as well as strong dependence power [35, 36]. In this group, we have five factors, Service Quality (H2), Perceived Quality (H3), Perceived Value (H4), Brand Image (H5), Store Environment (H7).

Group IV:

Driving factors: These factors also called key or triggering factors. These factors have strong driving power and weak dependence power [37, 38]. In this group, we have three factors, Product variance (H1), Compatible price (H6) and Product reliability (H8).

The MICMAC rank is calculated through driving power divided by dependence. It is depicted in

Table 5. This rank 1 factor indicates highest priority and rank 5 indicates least priority and appropriately given importance to the customer buying behaviour in paint dealer shops.

5 Conclusion

This paper discusses a comprehensive perspective on customer buying behavior at a dealer paint shop. The factors identified in this study determine customer buying behavior at a preliminary stage. The ISM approach enables us to understand the complexities of the identified factors and gain a comprehensive overview of the effects. The use of ISM in this study is very favorable because this framework not only allows the classification of the results reached into different classifications but also provides a deeper insight into the direct and indirect relationships between different factors by answering the following research questions.

1. What are the influencing factors for buying paint products at a dealer shop?
2. How are they interdependent with each other?
3. Can we rank these factors?

This framework helps improve the performance of the paint dealer shop by identifying key factors.

References

1. Rao R https://www.business-standard.com/content/b2b-chemicals/coatings-industry-paints-big-picture-with-pick-up-in-rural-demand-113102100391_1.html. Accessed on 17 Feb 2017
2. Shin DH (2015) Effect of the customer experience on satisfaction with smartphones: Assessing smart satisfaction index with partial least squares. Telecommunications Policy 39(8):627–641
3. Simon DH, DeVaro J (2006) Do the best companies to work for provide better customer satisfaction? Manag Decis Econ 27(8):667–683
4. Raposo ML, Alves HM, Duarte PA (2009) Dimensions of service quality and satisfaction in healthcare: a patient's satisfaction index. Service Business 3(1):85–100
5. Luo M X, Homburg C (2007) Neglected outcomes of customer satisfaction. J Market 71(2):133–149
6. Rejikumar G (2016) Antecedents of Green Purchase Behaviour: An Examination of Moderating Role of Green Wash Fear. Global Business Review 17(2):332–350
7. Fornell C, Johnson MD, Anderson EW, Cha J, Bryant BE (1996) The American customer satisfaction index: nature, purpose, and findings. Journal of Marketing 60(4):7–18
8. Liu HY, Jian LI, Ge YX (2006) Design of customer satisfaction measurement index system of EMS service. J China Univ Posts Telecommun 13(1):109–113
9. Gayathri K, Suresh M (2018) Modelling the factors of agile practices in project management a case of illumination project organization. Int J Eng Technol (UAE) 7(2.33):541–547.
10. Sankar H, Suresh M (2018) Modelling the factors of workplace spirituality in healthcare organization. Int J Eng Technol (UAE) 7(2.33):786–790
11. Keerthanaa P, Suresh M (2018) Informal learning in work place: a case of caregivers. Int J Eng Technol (UAE) 7(2.33):791–795
12. Gautham GR, Suresh M, Ranganathan R (2018) Factors affecting human performance in lathe machine shop operations. Int J Eng Technol (UAE), 7(2.33):882–885
13. Keerthana S, Suresh M (2016) Drivers influencing lean practices in street food vending process. In: 2016 IEEE International Conference on Computational Intelligence and Computing Research (ICCIC) (pp 1–5) IEEE
14. Haresh B, Suresh M, Ranganathan R (2018) Factors influencing success of new product launch: a case of SME stationery industry in India. Int J Eng Technol (UAE) 7(2.33):902–906

15. Jeevan S, Suresh M, Ranganathan R (2018) Risk factors influencing humanitarian operations: a case of temple cart festival. Int J Eng Technol (UAE) 7(2.33):946–949
16. Aarthi N, Suresh M (2018) Factors influencing people to approach micro finance institutions in India. Int J Eng Technol (UAE) 7(2.33):978–981
17. Amrita VV, Suresh M (2016) Factors influencing lean practices in Super market services using interpretive structural modeling. In: 2016 IEEE International Conference on Computational Intelligence and Computing Research (ICCIC) (pp 1–5). IEEE
18. Renganath K, Suresh M (2016) Analyzing the drivers for safety practices using interpretive structural modeling: A case of Indian manufacturing firms. In: 2016 IEEE International Conference on Computational Intelligence and Computing Research (ICCIC) (pp 1–6). IEEE
19. Abinaya R, Suresh M (2016) Analyzing the drivers for lean practices of commercial banking using interpretive structural modelling. In: 2016 IEEE International Conference on Computational Intelligence and Computing Research (ICCIC) (pp 1–4). IEEE
20. Patri R, Suresh M (2018) Factors influencing lean implementation in healthcare organizations: an ISM approach. International Journal of Healthcare Management 11(1):25–37
21. Venkatesh AB, Suresh M (2016) Factors influencing Indian tourism promotion in social media. In: 2016 IEEE International Conference on Computational Intelligence and Computing Research (ICCIC) (pp 1–5). IEEE
22. Sudharsan TM, Suresh M (2016) Factors influencing purchase decision of solar lanterns by street vendors. In: 2016 IEEE International Conference on Computational Intelligence and Computing Research (ICCIC) (pp 1–4). IEEE
23. Simonson I, Winer RS (1992) The influence of purchase quantity and display format on consumer preference for variety. Journal of Consumer Research 19(1):133–138
24. Deng WJ, Yeh ML, Sung ML (2013) A customer satisfaction index model for international tourist hotels: Integrating consumption emotions into the American Customer Satisfaction Index. International Journal of Hospitality Management 35:133–140
25. Suresh M, Mahadevan G, Abhishek RD (2019a) Modelling the factors influencing the service quality in supermarkets. Int J Syst Assurance Eng Manag 1-13. https://doi.org/10.1007/s13198-019-00897-4.
26. Ayraktar E, Tatoglu E, Turkyilmaz A, Delen D, Zaim S (2012) Measuring the efficiency of customer satisfaction and loyalty for mobile phone brands with DEA. Expert Syst Appl 39(1):99–106
27. Park CW, Jaworski BJ, MacInnis DJ (1986) Strategic brand concept-image management. Journal of Marketing 50(4):135–145
28. Mohan G, Sivakumaran B, Sharma P (2013) Impact of store environment on impulse buying behavior. Eur J Mark 47(10):1711–1732
29. Kelley CA (1988) An investigation of consumer product warranties as market signals of product reliability. J Acad Mark Sci 16(2):72–78
30. Anderson JC, Narus JA (1998) Business marketing: understand what customers value. Harvard Business Review 76:53–67
31. Oly Ndubisi N (2007) Relationship marketing and customer loyalty. Marketing Intelligence & Planning 25(1):98–106
32. Patri R, Suresh M (2017) Modelling the enablers of agile performance in healthcare organization: A TISM approach. Global J Flexible Syst Manage 18(3):251–272
33. Suresh M, Ganesh S, Raman R (2019) Modelling the factors of agility of humanitarian operations. Int J Agile Syst Manage 12(2):108–123
34. Patil M, Suresh M (2019) Modelling the enablers of workforce agility in IoT projects: a TISM approach. Global J Flexible Syst Manage 20(2):157–175
35. Miruthu Bashini R, Suresh M (2018) Modelling the ergonomics factors affecting the work system in hospital: An ISM approach. International Journal of Pure and Applied Mathematics 119(7):183–198
36. Vaishnavi V, Suresh M, Dutta P (2019a) A study on the influence of factors associated with organizational readiness for change in healthcare organizations using TISM. Benchmarking: An Int J 26(4):1290–1313

37. Shiyam Sundar T, Suresh M, Raghu Raman R (2018) Modelling the ergonomics factors affecting the work system in hospital: An ISM approach. Int J Pure Appl Math 119(7):107–125
38. Vaishnavi V, Suresh M, Dutta P (2019b) Modelling the readiness factors for agility in healthcare organization: a TISM approach. Benchmarking: An Int J 26(7):2372–2400